



Associate Directorate for Environmental Management

P.O. Box 1663, MS M992
Los Alamos, New Mexico 87545
(505) 606-2337

Environmental Management

P. O. Box 1663, MS M984
Los Alamos, New Mexico 87545
(505) 665-5658/FAX (505) 606-2132

Date: MAR 28 2018

Refer To: ADEM-18-0015

LAUR: 18-21450

John Kieling, Bureau Chief
Hazardous Waste Bureau
New Mexico Environment Department
2905 Rodeo Park Drive East, Building 1
Santa Fe, NM 87505-6303

Subject: Compendium of Technical Reports Conducted Under the Work Plan for Chromium Plume Center Characterization

Dear Mr. Kieling:

Enclosed please find two hard copies with electronic files of the Compendium of Technical Reports Conducted Under the Work Plan for Chromium Plume Center Characterization. A pre-submission review meeting was held between Los Alamos National Security, LLC, and the New Mexico Environment Department (NMED) on September 6, 2017. The submittal of this compendium of reports fulfills submittal of Milestone #1 in the Fiscal Year 2018 Appendix B of the 2016 Compliance Order on Consent between NMED and Department of Energy.

If you have any questions, please contact Danny Katzman at (505) 667-6333 (katzman@lanl.gov) or Cheryl Rodriguez at (505) 665-5330 (cheryl.rodriguez@em.doe.gov).

Sincerely,

Enrique Torres, Program Director
Environmental Remediation Program
Los Alamos National Laboratory

Sincerely,

David S. Rhodes, Director
Office of Quality and Regulatory Compliance
Environmental Management
Los Alamos Field Office

ET/DR/SS:sm

Enclosures: Compendium of Technical Reports Conducted Under the Work Plan for Chromium Plume Center Characterization (EP2018-0026)

Cy: (w/enc.)

Cheryl Rodriguez, DOE-EM-LA
Stephani Swickley, ADEM ER Program
Danny Katzman, ADEM ER Program
Gilles Bussod, EES-14

Cy: (w/electronic att.)

Laurie King, EPA Region 6, Dallas, TX
Raymond Martinez, San Ildefonso Pueblo
Dino Chavarria, Santa Clara Pueblo
Steve Yanicak, NMED-DOE-OB, MS M894
emla.docs@em.doe.gov
Public Reading Room (EPRR)
PRS Database
ADESH Records

Cy: (w/o enc./date-stamped letter emailed)

lasomailbox@nnsa.doe.gov
Peter Maggiore, DOE-NA-LA
David Rhodes, DOE-EM-LA
Enrique Torres, ADEM ER Program
Danny Katzman, ADEM ER Program
Randy Erickson, ADEM ER Program
Jocelyn Buckley, ADESH-EPC-CP
Mike Saladen, ADESH-EPC-CP
Benjamin Roberts, ADESH-EPC-DO
William Mairson, ADESH-EPC-DO/PADOPS
Craig Leasure, PADOPS

LA-UR-18-21450
March 2018
EP2018-0026

Compendium of Technical Reports Conducted Under the Work Plan for Chromium Plume Center Characterization

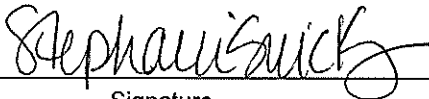
Prepared by the Associate Directorate for Environmental Management

Los Alamos National Laboratory, operated by Los Alamos National Security, LLC, for the U.S. Department of Energy (DOE) under Contract No. DE-AC52-06NA253 and under DOE Office of Environmental Management Contract No. DE-EM0003528, has prepared this document pursuant to the Compliance Order on Consent, signed June 24, 2016. The Compliance Order on Consent contains requirements for the investigation and cleanup, including corrective action, of contamination at Los Alamos National Laboratory. The U.S. government has rights to use, reproduce, and distribute this document. The public may copy and use this document without charge, provided that this notice and any statement of authorship are reproduced on all copies.

Compendium of Technical Reports Conducted Under the Work Plan for Chromium Plume Center Characterization

March 2018

Responsible project manager:

Stephani Swickley		Project Manager	Environmental Remediation Program	3/22/18
Printed Name	Signature	Title	Organization	Date

Responsible LANS representative:

for Randall Erickson		Associate Director	Associate Directorate for Environmental Management	3/22/18
Printed Name	Signature	Title	Organization	Date

Responsible DOE-EM-LA representative:

David S. Rhodes		Office Director	Quality and Regulatory Compliance	3-27-2018
Printed Name	Signature	Title	Organization	Date

CONTENTS

1.0 INTRODUCTION 1

1.1 Background and Regulatory Framework 1

1.2 Objectives of Studies Included in the Compendium 2

1.3 Organization of the Compendium 3

2.0 TECHNICAL REPORT SUMMARIES 4

2.1 Attachment 1: Results and Implications of Field Tracer Testing and Long-Term Pump Tests within the Chromium Plume at Los Alamos National Laboratory from 2013 to 2017 4

2.2 Attachment 2: Isotopic Signatures of Hexavalent Chromium in the Regional Aquifer: Evaluation of Natural Attenuation 5

2.3 Attachment 3: Stratigraphic and Sedimentological Studies and their Hydrogeological Features in the Chromium Investigation Area, Los Alamos National Laboratory 6

2.4 Attachment 4: Analysis of Groundwater Geochemical Fingerprints for Identification of Source Areas in the Chromium Project Area 8

2.5 Attachment 5: Evaluation of Potential Source Areas for the Chromium Plume Using Machine Learning Data Analyses of Geochemical Data 8

2.6 Attachment 6: Characterization of Natural Attenuation 10

2.7 Attachment 7: Bioremediation Bench-Scale Studies 11

2.8 Attachment 8: Chemical Remediation Bench-Scale Studies 12

2.9 Attachment 9: Groundwater Modeling Status Report 14

3.0 REFERENCES AND MAP DATA SOURCES 16

3.1 References 16

3.2 Map Data Sources 17

4.0 KEY CONTRIBUTORS TO THE CHROMIUM COMPENDIUM STUDIES 18

Figure

Figure 1.0-1 Map showing the approximate extent of the hexavalent chromium plume as defined by the 50-µg/L New Mexico groundwater standard 21

Attachments

Attachment 1 Results and Implications of Field Tracer Testing and Long-Term Pump Tests within the Chromium Plume at Los Alamos National Laboratory from 2013 to 2017

Attachment 2 Isotopic Signatures of Hexavalent Chromium in the Regional Aquifer: Evaluation of Natural Attenuation

Attachment 3 Stratigraphic and Sedimentological Studies and their Hydrogeological Features in the Chromium Investigation Area, Los Alamos National Laboratory

Attachment 4 Analysis of Groundwater Geochemical Fingerprints for Identification of Source Areas in the Chromium Project Area

Attachment 5 Evaluation of Potential Source Areas for the Chromium Plume Using Machine Learning Data Analyses of Geochemical Data

- Attachment 6 Characterization of Natural Attenuation
- Attachment 7 Bioremediation Bench-Scale Studies
- Attachment 8 Chemical Remediation Bench-Scale Studies
- Attachment 9 Groundwater Modeling Status Report

Acronyms and Abbreviations

3-D	three-dimensional
BSS	blind source separation
CdR	Cerros del Rio
CHROTRAN	Chromium Transport Bio-Chemical Remediation Code
CME	corrective measures evaluation
DOE	U.S. Department of Energy
FEHM	Finite Element Heat and Mass Transfer Code
gpd	gallons per day
gpm	gallons per minute
IM	interim measure
LANS	Los Alamos National Security, LLC
MADS	Model analysis and decision Support (code)
ML	machine learning
NMED	New Mexico Environment Department
NMF	nonnegative matrix factorization
NMFk	Nonnegative Matrix Factorization+ k-means clustering analysis
rNMF	Robust Nonnegative Matrix Factorization
NTF	nonnegative tensor factorization
RLWTF	Radioactive Liquid Wastewater Treatment Facility

1.0 INTRODUCTION

This compendium of technical reports presents results of studies that have been conducted over the last several years. The studies presented here constitute an integrated effort to provide a significant advancement in the understanding of the nature and extent of contamination and contaminant sources that are present within the overall chromium plume footprint and also advance the site conceptual model that supports the interim measure (IM) for plume control (LANL 2015, 600458) and future corrective measures. Several of the studies presented in the compendium also document ongoing work being conducted to evaluate remedial alternatives. The modeling work presented in this compendium provides an overarching framework for iteratively testing the conceptual model and for evaluating performance of the IM. It also supports quantitative evaluation of potential remedial alternatives and design of implementation strategies.

Figure 1.0-1 provides the context for the location of the chromium plume including monitoring wells, piezometers, and IM infrastructure wells.

1.1 Background and Regulatory Framework

The U.S. Department of Energy and Los Alamos National Security, LLC (DOE/LANS) has been conducting investigations directly related to understanding the fundamental nature and extent and fate and transport of chromium and related contaminants since 2006. Key documents that describe the evolution of the investigations include the “Investigation Report for Sandia Canyon” (LANL 2009, 107453) and the “Phase II Investigation Report for Sandia Canyon” (LANL 2012, 228624). More specific investigations began in 2014 with implementation of a coring program conducted under the “Drilling Work Plan for Chromium Project Coreholes” (LANL 2014, 259151), which was approved with modifications by the New Mexico Environment Department (NMED) in September 2014 (NMED 2014, 525201). Additional investigations were conducted under the “Work Plan for Chromium Plume Center Characterization” (LANL 2015, 600615), which was approved with modifications by NMED in October 2015 (NMED 2015, 600958). The two work plans set objectives for investigations and studies that would build an integrated hydrogeologic and geochemical framework for eventual development of an evaluation and recommendation of remedial alternatives to be presented in a corrective measures evaluation (CME) report. A “Pilot-Scale Amendments Testing Work Plan for Chromium in Groundwater beneath Mortandad Canyon” (LANL 2017, 602505) was also prepared and approved by NMED (NMED 2017, 602546) following approximately 1.5 y of extensive bench-scale and field tracer studies. The pilot-scale studies are underway at small-scale intrawell settings and will lead to development of a second-phase work plan that will be based on results of the initial phase. The Phase II work plan will be submitted to NMED by September 28, 2018.

Concurrent with the plume-center characterization work, DOE/LANS completed engineering and construction work for an IM to control plume migration in accordance with the NMED-approved “Interim Measures Work Plan for Chromium Plume Control” (LANL 2015, 600458; NMED 2015, 600959). The IM is expected to be fully operational in 2018. Evaluation of the performance of the IM will also likely provide useful insights into the hydrogeology and geochemistry of the plume area. That, along with the goal of creating a smaller plume footprint through the hydraulic control approach, means the IM is also highly integrated with the overall goal to develop an effective and efficient approach for remediation of the chromium plume.

Discussions and data sharing have been occurring with NMED over the past 2 yr as part of a process to guide the investigations. The reports included in the compendium document the status of the investigations, some of which could be considered essentially complete while others are ongoing and may be updated with additional information before the CME report is produced.

1.2 Objectives of Studies Included in the Compendium

The objectives of the “Work Plan for Chromium Plume Center Characterization” (LANL 2015, 600615) and other objectives of the studies included in this compendium are summarized below.

- Investigate the feasibility of chromium source removal from the center of the plume (as defined as the portion of the plume with the highest chromium concentrations).
 - ❖ Ongoing wellhead monitoring from the chromium extraction wells will provide insights into sustainability of mass removal rates. Only limited data are available to date because only extraction well, CrEX-1, has been pumped for an extended period. During approximately 6 mo of continuous pumping from January through June of 2017, CrEX-1 exhibited very steady chromium concentrations of about 170 µg/L. The three other extraction wells have not been pumped for extended periods, so the chromium transients at those wells are not well understood at this time. Additionally, trends in surrounding monitoring wells and piezometers will be monitored and evaluated for the purpose of characterizing capture zones associated with long-term extraction. These results are not presented in this compendium.
- Further characterize the distribution of chromium and related biogeochemical species and conditions in the aqueous and solid phases within the vadose zone and in the regional aquifer.
 - ❖ These results are presented in Attachment 1, “Results and Implications of Field Tracer Testing and Long-Term Pump Tests within the Chromium Plume at Los Alamos National Laboratory from 2013 to 2017.” Data from stratified sampling of “free” water collected during the sonic coring program and subsequent centrifuged water from stratified samples provide insight into the vertical distribution of contaminants in the lower vadose zone and regional aquifer.
- Further characterize key attributes of the aquifer, including heterogeneity and dual porosity, principally for the purpose of evaluating potential in situ remedial strategies for the plume.
 - ❖ This objective was addressed with tracer tests (Attachment 1) and with the detailed stratigraphic analysis that was conducted on material collected from the sonic coring program (Attachment 3, “Stratigraphic and Sedimentological Studies and their Hydrogeological Features in the Chromium Investigation Area, Los Alamos National Laboratory”). These studies will be used to refine the groundwater models of aquifer flow and contaminant transport properties (heterogeneity, dual porosity, etc.) and associated uncertainties related to potential remediation approaches.
- Study the geochemical conditions around injection wells in support of the IM. This information was considered important to understand long-term performance of injection wells and to guide potential maintenance activities at injection wells.
 - ❖ This study was addressed with geochemical modeling that was included in the DOE/LANS application for the injection well permit (DP-1835) (LANL 2016, 602906) and is not further discussed in this report. The modeling showed that no adverse geochemical conditions are likely to occur around injection well screens.

- Evaluate various approaches or engineered solutions that may be viable as remediation strategies for the chromium plume.
 - ❖ These studies were addressed with isotopic analysis of groundwater samples presented in Attachment 2 “Isotopic Signatures of Hexavalent Chromium in the Regional Aquifer: Evaluation of Natural Attenuation”, bench-scale studies including leaching studies and batch and column experiments presented in Attachment 6, “Characterization of Natural Attenuation,” Attachment 7, “Bioremediation Bench-Scale Studies,” and Attachment 8, “Chemical Remediation Bench-Scale Studies.” These studies eventually led to development of the field pilot-scale test currently underway (LANL 2017, 602505). Quarterly reports are used to report on the status of the test. The first quarterly report was submitted to NMED on January 28, 2018 (LANL 2018, 602862), and the next report is scheduled for submittal by April 30, 2018.
- Characterize the infiltration beneath the shallow alluvial groundwater in Sandia Canyon.
 - ❖ This objective is being addressed by monitoring water levels from nested sensors installed in boreholes within the alluvium in Sandia Canyon in accordance with the “Drilling Work Plan for Alluvial Piezometers in Sandia Canyon” (LANL 2015, 601047). Piezometer-completion details are provided in the “Field Summary Report for Alluvial Piezometers in Sandia Canyon” (LANL 2017, 602134). Understanding the nature and spatial variability of infiltration of alluvial groundwater in Sandia Canyon may be important to future remedial actions, so a baseline understanding is considered necessary for comparison with conditions that may be associated with future actions and for modeling purposes. To date, limited saturation has been observed, likely because of the substantial reduction in daily effluent volume released into Sandia Canyon. Effluent records indicate that effluent volumes have reduced from a high of greater than 400,000 gallons per day (gpd) to as little as 140,000 gpd in the last several years. Monitoring of the piezometers is ongoing and data are available in the Intellus database.

Additional studies presented in this compendium are focused on further discerning the geochemical domains that compose the plume. Attachment 4, “Analysis of Groundwater Geochemical Fingerprints for Identification of Source Areas in the Chromium Project Area,” uses a geochemical fingerprinting approach to identify domains, and Attachment 5, “Evaluation of Potential Source Areas for the Chromium Plume Using Machine Learning Data Analyses of Geochemical Data,” uses an advanced analytical modeling approach similar to principal component analysis to independently identify source areas and plume evolution to date. These tools can also inform and help reconcile observations of performance of future mitigation actions including the IM and final remedial actions.

The modeling presented in Attachment 9, “Groundwater Modeling Status Report,” describes the activities that have supported design of the IM and provides the overarching framework for evaluating performance of the IM and guiding future changes in operational strategies for the IM, including distribution of injection locations and rates. The modeling tools presented in Attachment 9 also provide a foundation for evaluation and development of remedial alternatives.

1.3 Organization of the Compendium

The compendium consists of nine attachments, each of which presents the objective, methodology, and results of the various studies that have been conducted over the last several years. Section 2 of the main body of this report provides summaries of each of the studies and how the studies integrate and support the overall goal of plume remediation.

2.0 TECHNICAL REPORT SUMMARIES

The subsections below provide a summary of each respective study included as attachments in this compendium.

2.1 Attachment 1: Results and Implications of Field Tracer Testing and Long-Term Pump Tests within the Chromium Plume at Los Alamos National Laboratory from 2013 to 2017

Several field tracer experiments and related field tests were conducted from 2013 to 2017 to better understand the regional aquifer hydrology and geochemistry within the hexavalent chromium [Cr(VI)] plume. These tests included

- nine borehole dilution tracer tests,
- two push-pull tracer tests (R-42 and R-28),
- four long-term pumping tests in which geochemical transients were observed (R-42, R-28, R-62 and R-43 S1),
- one push-drift test in which a solution buffered to pH ~9.8 was introduced to promote desorption of anion-exchanged Cr(VI) (R-42), and
- one cross-hole tracer test with three different tracer injection locations (CrPZ-2a, CrPZ-2b, and R-28), and one well in which tracers appeared (CrEX-3, with tracers from CrPZ-2a).

The borehole dilution tracer tests indicated that there is a wide range of natural flow velocities in the regional aquifer within the chromium plume. R-28 and R-43 S1 stand out as having the highest flow velocities intersecting their wellbores, with R-28 being on the order of 1 m/d (after accounting for an assumed flow porosity of 0.2) and R-43 S1 being on the order of 2 m/d. The flow velocity estimates can be used to calculate local Cr(VI) fluxes in the aquifer, and these estimates suggest that Cr(VI) fluxes at R-28 and R-43 S1 are considerably higher than at R-42 where the highest Cr(VI) concentrations are measured in the aquifer. The flow velocity estimates deduced from the push-pull tracer tests in R-42 and R-28 were in good agreement with the estimates deduced from the borehole dilution tracer tests in those wells.

One of primary objectives of the push-pull tracer testing, the long-term pumping tests, and the cross-hole tracer test was to interrogate diffusive mass transfer between rapidly flowing and non-flowing (or slower flowing) strata in the regional aquifer. Such diffusive mass transfer could have very important implications for a remediation strategy, as Cr(VI) residing in hydraulically tight, or slow-flowing zones or strata, could greatly extend the duration of potential pump-and-treat approaches and may play into in situ remediation strategies. The tests collectively yielded conflicting evidence for dual-porosity behavior in the regional aquifer, although intuitively it seems logical that some diffusion between fast-flowing pathways and slower-flowing pathways must be occurring. The push-pull tracer test in R-28 and the cross-hole tracer responses between CrPZ-2a and CrEX-3 both showed evidence of diffusion between preferential hydraulic strata and hydraulically tight, or slower-flowing, strata, but the push-pull test in R-42 and the geochemical responses to long-term pumping of R-42 and R-28 did not show definitive evidence of diffusive mass transfer within the aquifer. The best explanation for these observations is that the relative thicknesses or cross-sectional areas of preferential hydraulic strata varies considerably in different portions of the plume. Diffusive mass transfer over the time scales of the tests will be difficult to observe if preferential pathways are relatively wide along a flow path because diffusion out of such pathways will result in very little observable decrease in tracer concentrations; however, if preferential pathways are narrow along a flow path, diffusion will result in much greater observable decreases in tracer concentrations.

Another primary objective of the push-pull and cross-hole tracer tests, and the long-term pumping tests, was to look for evidence of Cr(VI) natural attenuation in the regional aquifer (in this case, natural attenuation is considered to be reduction of Cr(VI) to trivalent chromium [Cr(III)], not anion exchange of chromate (CrO_4^-), although evidence of the latter was also looked for in the R-42 push-pull test involving injection of a solution with pH 9.8). Collectively, the tests produced little evidence of natural attenuation of Cr(VI). Responses of Cr(VI) relative to major anions in push-pull, push-drift, and pumping tests in R-42, R-62, and R-43 S1, including the push-drift test at R-42 to induce CrO_4^- desorption, indicated no natural attenuation of Cr(VI), and there was also no evidence of natural attenuation during the drift period in R-28 after the cross-hole tracer injection into this well. A small amount of Cr(VI) natural attenuation was suggested in the vicinity of CrPZ-2a during the drift period after the cross-hole tracer injection into this piezometer, and natural attenuation was also suggested during the drift period in the 2014 R-28 push-pull test. Also, the drops in Cr(VI) concentrations during long-term pumping of R-42 and R-28 while concentrations of all other major anions remained essentially constant suggest that there is a possibility that Cr(VI) may be getting partially reduced to Cr(III) in secondary porosity in the aquifer. However, another explanation for the long-term pumping observations at R-42 and R-28 is that Cr(VI) is spatially distributed in the aquifer differently than the major anions that it is typically associated with. A possible explanation for the apparent natural attenuation of Cr(VI) at CrPZ-2a is that the bentonite known to be present in the completion of this piezometer may have caused some reduction of Cr(VI).

The rapid cross-hole tracer responses at CrEX-3 resulting from the tracers injected into CrPZ-2a, coupled with the lingering of the same tracers in CrPZ-2a long after they reached peak concentrations in CrEX-3, suggest a large contrast in hydraulic conductivity of various zones or lithologic layers near CrPZ-2a. Apparently, a significant fraction of the tracer mass was pushed into high-conductivity flow pathways that carried the tracers almost all the way to CrEX-3 in the 84 d after injection and before CrEX-3 began pumping. However, a significant fraction of tracer mass was also apparently pushed into low-conductivity zones or pathways near CrPZ-2a in which the tracers lingered for many months before slowly drifting back into the piezometer.

The field test results collectively indicate that the Cr(VI) plume is quite heterogeneous, both hydrologically and geochemically. The Cr(VI) concentrations in the plume apparently have a complex spatial distribution that is suggested not only by the distribution of observed concentrations in monitoring wells, but also by the responses of Cr(VI) concentrations to pumping at various locations in the aquifer, including different responses relative to anions that are known to have vadose-zone sources and are typically correlated with Cr(VI). It is apparent that pumping of CrEX-3 at ~40 gallons per minute (gpm) strongly captures Cr(VI) groundwater flow and contamination present in the vicinity of CrPZ-2a, but it does not capture much water from CrPZ-2b, which is completed just 15 ft below the bottom of CrPZ-2a. Pumping of CrEX-3 at ~40 gpm also does not appear to capture any of the Cr(VI) contamination present in the vicinity of R-28, which is screened starting at approximately 40 ft below the water table.

2.2 Attachment 2: Isotopic Signatures of Hexavalent Chromium in the Regional Aquifer: Evaluation of Natural Attenuation

The objective of this study was to investigate the presence of natural attenuation along the flow path using stable isotope data collected from perched-intermediate and regional aquifer monitoring wells. Evaluation of fractionation of stable isotopes of chromium (chromium-53 and chromium-52) from monitoring points along a contaminant flow path is a useful approach for assessing whether natural attenuation of [Cr(VI)] is occurring. During chemical or biotic reduction of dissolved-phase Cr(VI) to solid-phase trivalent chromium [Cr(III)] there is a shift in the isotopic signature of residual Cr(VI) in an aquifer. The magnitude of this isotopic shift can be an indicator of the degree of reduction that occurs along a contaminant flow path. Dilution and sorption will decrease Cr(VI) concentrations but do not significantly

affect chromium isotope signatures, so this technique is useful in distinguishing reduction from simple dilution or reversible sorption.

Chromium isotope signatures of monitoring wells in and around the chromium plume have been measured since 2007. An isotopic shift has been noted within perched-intermediate groundwater, likely related to reduction of Cr(VI) interacting with the iron-rich Cerros del Rio basalts. However, chromium isotope values show a high degree of similarity throughout the chromium-contaminated portion of the regional aquifer. This suggests that there is little natural attenuation in the form of reduction of Cr(VI) occurring. Even more importantly, chromium isotope and concentration trends at the downgradient periphery of the chrome plume, where residual reduction capacity might be expected to be present, are entirely consistent with simple mixing of an arriving chromium plume with background groundwater.

It is possible, though unlikely, that all Cr(VI) reduction occurs in secondary porosity where slow transport of Cr(VI) into secondary porosity limits the expression of the isotopic shift typically associated with reduction. The preponderance of evidence presented in this compendium, however, suggests that reduction either does not occur in the regional aquifer, or occurs at very low levels not detectable by the chromium-isotope technique. The simplest interpretation of the observed chromium isotope signatures supports these other lines of evidence in terms of suggesting Cr(VI) reduction in the regional aquifer is negligible.

2.3 Attachment 3: Stratigraphic and Sedimentological Studies and their Hydrogeological Features in the Chromium Investigation Area, Los Alamos National Laboratory

This study summarizes geological investigations that identify (1) lithostratigraphic surfaces that act as potential groundwater pathways in the vadose zone and (2) sedimentological properties of rocks that make up the regional aquifer. This work provides supplemental information for the sitewide geologic model by identifying additional geologic contacts internal to the major rock units that have the potential to influence vadose-zone groundwater pathways and flow directions. In addition, sedimentological data for rocks of the regional aquifer are combined with hydraulic properties to assess lithologic factors controlling groundwater flow paths in the upper regional aquifer.

Geologic contacts and internal bedding features have the potential to influence groundwater pathways and flow directions in the vadose zone. As a consequence, chromium-contaminated surface water that began an infiltration pathway in Sandia Canyon is believed to have percolated vertically to the regional aquifer and migrated southward through the vadose zone before entering the regional aquifer beneath Mortandad Canyon. This work addresses uncertainties in the sitewide geologic model by documenting the dips of geologic contacts and internal bedding features for rocks that make up the vadose zone. Borehole geophysical logs were used to identify the bedding orientations for three new geologic contacts: (1) in ash-flow tuffs in the Otowi Member of the Bandelier Tuff, (2) at a regional-scale stratigraphic break between alkali basalts and tholeiites in the Cerros del Rio basalts, and (3) at a laterally continuous depositional unit within the lower Puye Formation. Structure contour maps for the three new geologic contacts were combined with those in the current sitewide geologic model to assess the groundwater flow directions through the vadose zone. Bedding orientations within these geologic units are consistent with the interpretation that generally southerly translation of chromium-contaminated recharge is the result of lateral diversion associated with dipping geologic beds. Structure contour maps also revealed the locations of volcanic vents that were sources of the Cerros del Rio rocks beneath the eastern Pajarito Plateau. These vents define a north-northwest-trending volcanic lineament east of the chromium plume area that may represent a previously unrecognized fault or fracture system.

The sedimentological properties of the rocks of the regional aquifer were determined to assess heterogeneity and dual porosity in the regional aquifer by characterizing the lithology, grain size distributions, mineralogy, and chemistry of continuous sonic cores obtained from five core holes in Mortandad Canyon. The objective of this study is to characterize the stratigraphy and lithology of Pliocene and Miocene sedimentary rocks that make up primary chromium contaminant flow paths in the upper regional aquifer and to assess how the hydrogeological properties of these deposits may affect contaminant migration and flux. Individual depositional beds were identified by detailed lithologic descriptions of the core, and samples representing each bed were sieved into six size fractions to determine the particle-size distribution of aquifer materials. Estimates of the hydraulic conductivity for each bed were calculated from the particle-size data using the Kozney-Carman method. A subset of core samples was also analyzed using x-ray fluorescence and quantitative x-ray diffraction to characterize the chemistry and mineralogy of particle-size fractions. Key results of the investigation include the following:

- The upper regional aquifer in the chromium plume area is made up of three stratigraphic units: Puye Formation, Puye pumiceous subunit, Miocene pumiceous unit. These three units are alluvial fan deposits dominated by 0.2- to 4-ft-thick beds of silty to gravelly coarse sands that are mostly poorly sorted, massive, unconsolidated, and matrix- to clast-supported. Clast sizes generally decrease with depth through the stratigraphic sequence, and the bulk chemical and mineralogical compositions of the sediments vary from dacitic to rhyolitic compositions with increasing depth. The provenance of detritus making up these alluvial fans reflects changing activity of multiple volcanic source vents during development of the Jemez Mountains volcanic field.
- The Puye pumiceous subunit is a new stratigraphic unit that was identified at the base of the Puye Formation. It contains strata that include both dacite-rich lithic sands and gravels and rhyolitic pumice-rich sands. Thus it is a hybrid unit with similarities to the overlying Puye Formation and the underlying Miocene pumiceous unit. Because it contains abundant Rhyodacite of Rendija Canyon clasts, the new unit is Pliocene in age and probably represents an early stage of alluvial fan development when outcrops of Miocene rhyolitic tephra contributed detritus to the Puye Formation. The Puye pumiceous subunit marks renewed deposition of alluvial fan complexes in the western Española basin during the early Pliocene, following a late Miocene hiatus.
- Particle-size analyses of cores reveal that the regional aquifer is characterized by a high degree of heterogeneity and that dual porosity is likely to affect groundwater pathways. Hydraulic conductivities were calculated from the particle-size data for each of the beds making up the aquifer in the five core holes. In each core hole, a relatively small number of 0.2- to 4-ft-thick beds contain significantly greater hydraulic conductivities than those found in thick sequences of overlying and underlying strata. These thin transmissive beds may play a disproportionate role in groundwater and contaminant flux in the regional aquifer and may also play a major role in the quantity and chemistry of groundwater pumped from extraction and monitoring wells. The nature of these beds will also likely have to be factored into remediation strategies.
- Regional groundwater likely moves through interconnected transmissive strata that together form a network of preferential pathways that are largely blind to stratal dips and stratigraphic boundaries. As a result, regional groundwater pathways are dominated by lateral flow that is controlled by low-gradient hydraulic gradients dipping to the east and southeast rather than dip of beds.

2.4 Attachment 4: Analysis of Groundwater Geochemical Fingerprints for Identification of Source Areas in the Chromium Project Area

The goal of this study was to evaluate whether multiple original sources of contaminants are discernable within the overall chromium plume footprint. Insights derived from this study are considered potentially useful for interpreting observed concentration trends at monitoring wells within the plume area and overall plume dynamics. This report identifies geochemical domains that contribute to the chromium plume. Understanding different contaminant signatures in the chromium plume is important when identifying contaminant pathways and is a key element of the site conceptual model. The spatial distribution of the domains provides information about locations where contamination enters the regional aquifer. Delineating contaminant source domains and their spatial distributions is important for understanding current site conditions and supports optimization of remediation strategies.

The chromium footprint in the regional aquifer has been affected by a complex series of contaminant releases from different locations and time periods. The releases are associated with discharges from cooling towers, sewage treatment, and plutonium processing and associated releases in three different canyons. Releases have varied in terms of discharge location and timing as well as chemical makeup. This, along with complex mixing of contaminant sources within the vadose zone and regional aquifer, makes understanding the provenance of contaminant signatures in the regional aquifer difficult.

As a complement to more quantitative methods of contaminant source attribution (see Attachment 5 of this compendium), visual “fingerprint” diagrams were developed to allow easy comparison between monitoring well data with the goal of grouping wells into similar domains in terms of contaminant sources. Contaminant concentrations and isotopic signatures were considered in creating the fingerprints. Contaminants, including, but not limited to, chromium, tritium, and perchlorate, were normalized to background upper tolerance limits for species that also occur naturally, or to method detection limits for species with no natural background. The use of isotopic signatures added considerable complexity to the diagrams, but also significant value. For example, rather than just considering nitrate as a contaminant, the nitrogen and oxygen isotopic signature of nitrate was used to distinguish nitrate from modern sewage releases, older sewage releases, and nitric acid. Isotopic signatures were scaled from -1 to 3 based on deviations from established background isotopic ranges.

Using the fingerprint diagrams, five geochemical source domains were identified and delineated on a map of the chromium plume. Because contamination may still be entering the regional aquifer from the vadose zone, an improved understanding of contaminant source attribution may also allow for better design of regional aquifer remediation strategies. Such knowledge could also be useful were remediation efforts ever to be extended to the vadose zone to reduce residual contamination before it could enter the regional aquifer.

2.5 Attachment 5: Evaluation of Potential Source Areas for the Chromium Plume Using Machine Learning Data Analyses of Geochemical Data

A novel unsupervised machine learning (ML) method employing a blind source separation (BSS) model was used to assess geochemical variability within the chromium plume area for the purpose of identifying spatially or temporally unique source areas (groundwater types). Different contaminant sources are modified through water-rock interaction and can mix in the vadose zone or within the regional aquifer. The ML BSS method attempts to identify these contaminant sources and their potential breakthrough locations in the regional aquifer by deconvoluting geochemical data from individual monitoring wells. Identification of source-area groundwater types and their spatial distribution provides insight into plume dynamics and supports optimization of remediation strategies. The ML BSS method complements other

methods and modeling techniques (Attachments 4 and 9 of this compendium, respectively) that also use site geochemical data to identify contaminant sources in the chromium plume.

The ML BSS method uses the concentrations of 8 different geochemical species [chromium (Cr), chloride (Cl⁻), perchlorate (ClO₄), tritium (³H), nitrate (NO₃), calcium (Ca), magnesium (Mg), and sulfate (SO₄)] and their spatial and temporal trends in 19 monitoring wells to classify groundwater sources in the contaminated aquifer. Sources and mixing ratios were identified using rNMF (Robust Nonnegative Matrix Factorization), a new methodology and computational framework for inverse analysis and source identification that is based on nonnegative matrix factorization (NMF) techniques. Three different BSS algorithms were used to conduct the rNMF analyses:

- NMFk (Nonnegative Matrix Factorization + k-means clustering analysis) decouples the mixed geochemical data from wells to find the number of contaminant sources that may be present in well data. The analysis relies only on the robustness of the reconstructed solutions, without any additional information about the contaminant sources, aquifer properties, or the physical/biogeochemical processes of contaminant transport in the aquifer.
- ShiftNMFk uses transients in the geochemical data and the velocity of contaminant migration to identify (a) the number of contaminant sources, (b) the source locations (i.e., breakthrough locations into the regional aquifer), (c) the signal delays, and (d) velocity of signal propagation (advective transport velocity).
- GreenNMFk also uses transients in the geochemical data but accounts for the physics of the contaminant transport process (using “Green functions” of the advection-diffusion equation) to identify (a) the number of contaminant sources; (b) the source locations (i.e., breakthrough locations), (c) the transients in the source releases, (d) advective transport velocity, and (e) transport dispersivities (assuming a Fickian dispersion model).

In addition to the matrix techniques in the ML methods discussed above, a novel unsupervised ML based on nonnegative tensor factorization (NTF) has been developed, called NTFk, which allows analysis of multi-dimensional data (NMF applicability is limited to two-dimensional data sets). The analyses are performed using NTFk, which allows for accounting of transients of source mixing. The NTFk analysis identifies seven distinct groundwater sources, including two background sources and five contaminant sources. These sources make up the geochemical mixtures observed in current monitoring well data. Temporal changes in sources were captured by computing average concentrations of each chemical species for each year between 2005 and 2016. The NTFk results accurately reproduce the geochemical transients observed at the monitoring wells.

Sources identified by the NTFk analysis include the following:

- Source 1, which has values elevated for Cr, Cl⁻, NO₃, Ca, Mg, and SO₄ and is associated with power plant and sewage releases at the head of Sandia Canyon. This is the main source of chromium that constitutes the majority of the plume footprint.
- Source 2 has elevated ClO₄, which is a known contaminant in effluent from the Radioactive Liquid Wastewater Treatment Facility (RLWTF) in Mortandad Canyon.
- Source 3 represents background groundwater as defined by areas upgradient and downgradient of the main chromium plume area.
- Source 4 has elevated NO₃ and represents either sewage effluent released in Sandia Canyon or nitric acid effluent released from the RLWTF in Mortandad Canyon.

- Source 5 has elevated ^3H , Cr, Cl^- , Ca, Mg, and SO_4 . This is potentially a mixed source where contaminants originating in Los Alamos, Sandia, and Mortandad Canyons are mixing in perched-intermediate groundwater before their arrival at the regional aquifer.
- Source 6 has elevated Cl^- , Ca, Mg, and SO_4 . Source 6 is similar to Sources 1 and/or 5, but the low activity of ^3H and low Cr concentration suggest Source 6 post-dates cessation of chromium releases in 1972 and represents more recent infiltration through the vadose zone.
- Source 7 represents background groundwater.

Mixing ratios in the each of the monitoring wells were computed for the 7 sources. The mixing ratios were then extrapolated between the wells using an interpolation technique. The results of the interpolated data are presented as 12 time-series maps (2005 through 2016) that show the spatial and temporal distributions of mixing ratios for the 7 groundwater sources. These maps show the locations of source breakthrough in the regional aquifer and the temporal evolution of the sources in the chromium plume. Sources 1, 5 and 6 are centered in the area of wells R-28 and R-42. Source 2 is centered in the area of well R-15. Source 4 is centered in the area of wells R-43 and R-11; it also occurs in wells R-62 and R-15 but diminishing impacts in recent years suggest lateral plume migration or shifts in the infiltration pathways. Sources 7 and 3 represent the background groundwater types. Diminished mixing ratios for background Sources 3 and 7 occur in the chromium plume where mixing with contaminant sources is greatest. These spatial and temporal data can be used to infer flow and transport properties of the aquifer and contaminant source characteristics that are essential for reliable assessment of the contamination hazards and risks.

2.6 Attachment 6: Characterization of Natural Attenuation

Between 2013 and 2016, several laboratory experiments were conducted to evaluate the potential for regional aquifer sediments to reduce Cr(VI) to Cr(III), thus providing natural attenuation of Cr(VI) in the regional aquifer. These experiments included

- Cr(VI) “uptake” experiments, in which aquifer sediment samples were placed in contact with a solution containing a known amount of Cr(VI), either in a batch experiment or a column experiment, and the amount of Cr(VI) removed from solution was measured,
- sequential leaching experiments, in which aquifer sediment samples were leached with successively more aggressive solutions to remove any contaminant chromium that may be associated with sediments, and
- x-ray synchrotron experiments to confirm that Cr(VI) reduction to Cr(III) can potentially occur on aquifer sediments.

The Cr(VI) uptake experiments were conducted largely on geomaterials obtained from sonic coring into the plume. The experiments proved challenging because many sediment samples were contaminated with tiny amounts of iron from drill bits or casing, and the presence of even very small amounts of anthropogenic iron resulted in orders of magnitude more Cr(VI) uptake than was observed on sediment samples from which the anthropogenic iron contamination was carefully removed. Iron contamination was also a source of error in the sequential leaching experiments, but these experiments were further hampered by the large amounts of naturally occurring chromium that were leached from aquifer sediments, irrespective of whether or not the sediments had been exposed to contaminant Cr(VI). Leachates from samples exposed to Cr(VI) contamination were always compared with leachates from samples believed to not be exposed to contamination to draw inferences about the presence of anthropogenic chromium on the contaminated samples, but the naturally occurring chromium signal typically dwarfed any potential anthropogenic chromium signal. When Cr(VI) uptake onto sediments was

definitively observed (and iron contamination was ruled out), it was generally found to be associated with a very fine particle-size fraction of the sediments that was separated by gravity settling and constituted a small mass fraction of the bulk sediment sample (typically 1% or less). Desorption experiments were often conducted on samples that exhibited positive Cr(VI) uptake, and it was generally found that the Cr(VI) was not readily desorbed, so it was assumed that the Cr(VI) had been reduced to Cr(III). Cr(VI) reduction to Cr(III) was confirmed on fine-grained materials separated from aquifer sediments in x-ray synchrotron experiments.

The overall conclusion from the laboratory natural attenuation experiments was that the regional aquifer sediments in the Cr(VI) plume area appear to be capable of reducing no more than about 0.05 g Cr(VI) per gram of sediment to Cr(III). However, many laboratory experiments resulted in Cr(VI) uptake estimates that were indistinguishable from zero, so it is possible that the natural attenuation of Cr(VI) in the regional aquifer is even less than 0.05 g Cr(VI) per gram of sediment. Field observations of increases in Cr(VI) concentrations in monitoring wells at the chromium plume periphery relative to increases in concentrations of nonreactive anions with anthropogenic origins (e.g., Cl^- , SO_4^{2-}) support the conclusion of an upper-bound natural attenuation estimate of no more than 0.05 g Cr(VI) per gram of sediment.

2.7 Attachment 7: Bioremediation Bench-Scale Studies

This investigation summarizes batch and column studies that were conducted to evaluate feasibility of bioremediation for chromium in the regional aquifer and to define the experimental parameters needed to perform a pilot treatability test of in situ bioremediation treatment of chromium in the regional aquifer beneath Mortandad Canyon. The objectives of the batch and column studies were to investigate (1) the microbial profile of the regional aquifer at the areas of highest chromium concentrations within the plume, (2) how the microbes respond to biostimulation using sodium acetate and molasses, and (3) the impact of increased microbial activity on Cr(VI) speciation and groundwater quality. Biostimulation is currently being evaluated as a potential measure that may be implemented for plume remediation. This report summarizes the results of the initial characterization of the microbial diversity in the regional aquifer at the location of groundwater monitoring wells R-42 and R-28. The report also presents the data related to chromium reduction and the reduction of competing electron acceptors (i.e., nitrate, sulfate, and iron) for both batch and column studies.

The batch experiments were set up in sealed reactors under anaerobic conditions. The column experiments were set up with sediments collected from contaminated portions of the plume and groundwater collected from R-42. Analysis found that the bacterial community in the natural groundwater was dominated by proteobacteria, which represented 58.2% of the overall bacterial population [α -proteobacteria (25.5%), β -proteobacteria (12.7%), γ -proteobacteria (13.7%), δ -proteobacteria (6.2%)]. Biostimulation with sodium acetate in the batch reactors resulted in a slow but steady removal of Cr(VI) from solution. The rate of Cr(VI) reduction was strongly dependent on the initial geochemical conditions and the presence of competing electron acceptors. Biostimulation of groundwater samples with molasses in batch reactors resulted in a very rapid reduction of Cr(VI) to Cr(III). Chromate was also removed in the sterile controls, which was attributed to the reduction of Cr(VI) abiotically by molasses. Cr(VI) reduction in columns packed with sediment and biostimulated by amendments (i.e., acetate and molasses) was very fast. Longer pulses of amendment injections resulted in longer Cr(VI) attenuation capacities.

The microbial community in the column stimulated with acetate was primarily composed of β -proteobacteria, α -proteobacteria, γ -proteobacteria and Verrucomicrobia. These taxa composed 86% in both the influent (bottom) and effluent (top) ends of the column. In the molasses column, there was a greater divergence in the composition of the dominant taxa between the influent and effluent ends of the column. The influent end of the molasses column was primarily composed of β -proteobacteria (65%) and Verrucomicrobia (28%), whereas the dominant members in the effluent end of the column were almost

equally split amongst the β -proteobacteria (30%), Verrucomicrobia (27%) and Bacteroidetes (28%). This study revealed that both molasses and acetate can be used as carbon substrates to achieve Cr(VI) reduction. Molasses was determined to induce a much larger attenuation capacity compared with acetate, forming the basis for using molasses in the field pilot-scale study currently underway (LANL 2017, 602505).

2.8 Attachment 8: Chemical Remediation Bench-Scale Studies

A series of laboratory bench-scale experiments was conducted to evaluate sodium dithionite as a chemical reductant to reduce Cr(VI) to Cr(III) in Cr(VI)-contaminated portions of the regional aquifer. Sodium dithionite has been used successfully at other sites for Cr(VI) remediation, and it is believed to derive its benefit mainly from its ability to reduce iron in sediments, which in turn is efficient at reducing Cr(VI) to Cr(III). In effect, the dithionite-treated aquifer zone serves as an in situ permeable reactive zone to reduce Cr(VI) to Cr(III) as contaminated water moves through the zone.

Three general types of laboratory dithionite experiments were conducted:

1. Aqueous batch experiments, without sediments present, which were intended to evaluate dithionite degradation rates under various initial conditions, as well as mechanisms and reaction products of dithionite degradation under these conditions
2. Aqueous batch experiments, with aquifer sediments present, which were intended to evaluate dithionite reactions with sediments, and also whether metals or other species might be liberated from sediments in a manner that could adversely affect water quality
3. Column experiments in which sodium dithionite pulses were injected into aquifer sediments followed by the steady injection of contaminated aquifer water to determine the Cr(VI) reduction capacity imparted to the sediments by the dithionite treatment

Sodium dithionite reacts rapidly with dissolved oxygen, so most batch experiments were conducted in flame-sealed glass reactors that were purged of air. The batch experiments without sediments indicated that dithionite degradation under anaerobic conditions proceeds in two steps: (1) a rapid disproportionation that happens on the time scale of minutes and results in an almost immediate drop in dithionite concentrations that is larger at lower pH, and (2) a slower degradation reaction that happens on the time scale of days to weeks and follows a pseudo first-order rate law given by

$$\frac{dC_{S2O4}}{dt} = 10^{-4.81} [H^+]^{0.24} C_{S2O4}, \quad \text{Equation 1}$$

where C_{S2O4} = dithionite concentration in mol/L that remains after the initial rapid drop in concentration, $[H^+]$ = proton concentration in mol/L, and t = time in seconds. Reaction products observed in the experiments included sulfate, sulfite, and sulfide, and likely elemental sulfur species or polysulfur species that could not be quantified. A separate set of sediment-free batch experiments was kept open to air to simulate a field deployment scenario, and these experiments established that sodium sulfite (Na_2SO_3) effectively buffered dithionite solutions between pH 7 and 8, which extended the dithionite lifetime in the presence of oxygen to the point where a solution could be injected over several hours in the field. Previous dithionite field deployments have typically used bicarbonate/carbonate (HCO_3^-/CO_3^{2-}) buffers that maintain pH in the range of 10 to 11 to maximize dithionite lifetime, but this was considered impractical at Los Alamos because the regional aquifer is already saturated with respect to calcite ($CaCO_3$) and adding HCO_3^- or CO_3^{2-} would risk calcite precipitation that could result in permeability reduction near injection wells.

The aqueous batch experiments with sediments showed that the presence of sediments causes the additional rapid degradation of about 2×10^{-5} mol of dithionite per gram of sediment beyond the initial rapid degradation in the absence of sediments. During this rapid degradation, about 2×10^{-6} mol of dissolved Fe^{2+} and 2×10^{-7} mol of dissolved Mn^{2+} per gram of sediment were produced, and these quantities were found to be the same for four different aquifer sediments tested. If the initial dithionite present was less than 2×10^{-5} mol per gram of sediment, then essentially all the dithionite was rapidly consumed, leaving only very small residual concentrations. After the initial rapid degradation, any remaining dithionite was consumed about 2.5 to 3 times faster in the presence of sediments than in their absence, and about 0.35 mol of Fe^{2+} and 0.035 mol of Mn^{2+} were produced for every mole of dithionite consumed. Concentrations of arsenic and other metals observed in the experiments generally stayed below groundwater standards.

In a separate set of batch experiments involving the treatment of sediments with 1 M sodium dithionite, a post-test "titration" of the treated sediments with a 1% Cr(VI) solution indicated that nearly all of the iron in the sediments would have had to be reduced to ferrous oxide [Fe(II)] by the dithionite to be able to account for all of the Cr(VI) that was reduced. Given that a large percentage of the iron in the sediments was not accessible to the dithionite solution, this result clearly suggests that the reductive capacity imparted to the sediments cannot be entirely attributed to reduced iron, which has been a commonly held belief. These studies have indicated that reduced sulfur species contribute to the reduction capacity of dithionite-treated sediments as well.

The column experiments showed that the injection of two pore volumes of a 0.05 M sodium dithionite solution buffered with 0.05 M of Na_2SO_3 resulted in a Cr(VI) reduction capacity ranging from about 6×10^{-3} to 9×10^{-3} mol Cr(VI)/mole dithionite introduced. These capacities were measured by injecting non-deaerated R-42 water [Cr(VI) concentrations of about 900 $\mu\text{g/L}$] through the columns until Cr(VI) broke through in the column effluents. R-42 water nominally has a dissolved oxygen concentration of 6–7 mg/L and a nitrate concentration of 25–30 mg/L. Nitrate was not reduced by the dithionite-treated sediments, but some of the oxygen was probably reduced (dissolved oxygen was not measured in the column effluents because they became oxygenated before measurements could be made). The dithionite-treated sediments effectively prevented Cr(VI) breakthrough for 30 to 50 column pore volumes. Arsenic and other metal concentrations generally remained below standards except during the dithionite pulse. After chromium breakthrough was complete, the columns were frozen and cut into 1-cm-long sections, and each section was acid leached to determine the spatial distribution of chromium, iron and other constituents on the sediments. The results revealed that chromium [as Cr(III)] was rather evenly distributed throughout the columns, but the iron distribution in the sediments in one of the columns suggested that the dithionite had reached only about two-thirds of the way through the column before being consumed. The mass of sediments in the first two-thirds of the column corresponds to the mass that would be predicted to rapidly consume all the injected dithionite if the consumption were the same as in the batch experiments (i.e., 2×10^{-5} mol of dithionite per gram of sediment).

Although the chemistry associated with sodium dithionite reactions is complex and many mechanistic details are not fully understood, sodium dithionite appears to be a viable chemical reductant that should be capable of establishing an in situ permeable reactive zone in the regional aquifer that can reduce and immobilize many pore volumes of Cr(VI)-contaminated groundwater. The laboratory bench-scale experiments resulted in a recommendation that sodium dithionite be deployed in the field pilot test (LANL 2017, 602505) at a concentration of 0.05 mol/L with 0.05 mol/L Na_2SO_3 , and a field pilot deployment that followed this recommendation has so far proven successful.

2.9 Attachment 9: Groundwater Modeling Status Report

The modeling work presented in this compendium describes the work conducted to provide a quantitative framework for iterating with the site conceptual model, for evaluating performance of the IM, and for quantitative evaluation of potential remedial alternatives and design of implementation strategies. Historically, the models have guided siting of monitoring wells, interpretation of intrawell and interwell hydraulics, and design of the ongoing IM.

Attachment 9 describes ongoing groundwater modeling efforts, which are focused in three main areas:

- Three-dimensional (3-D) coupled vadose-zone/regional-aquifer model
- Regional-scale aquifer model
- Biogeochemical remediation model

The 3-D coupled vadose-zone/regional-aquifer model is designed to represent the groundwater flow and contaminant transport in the vadose zone and the regional aquifer in the vicinity of the chromium plume. The model spatial domain includes Mortandad, Sandia, and Los Alamos Canyons and extends from ground surface to approximately ~100 m below the regional water table. The computational grid is based on the geologic framework model with improvements to some hydrostratigraphic surfaces based on work presented in Attachment 3 of this compendium. In the vadose zone, water-phase flow and transport were adopted based on Richard's Equation and a van Genuchten relative-permeability capillary-pressure model in which vadose-zone permeabilities of various geologic units are represented as a function of saturation. The regional aquifer model uses the Finite Element Heat and Mass Transfer Code (FEHM) to simulate contaminant transport of chromium by advective dispersion. The major goals of the model are to simulate groundwater flow and contaminant transport conditions at the site, predict the fate of contaminant mass in the vadose zone (including the future impacts on the regional aquifer), and predict future system behavior under different natural and mitigation scenarios. The model is calibrated to

- reproduce the perching of infiltrated groundwater on the top of the Cerros del Rio (CdR) basalts within the vadose zone,
- match the model-predicted saturation thickness with existing observations for the perched-intermediate zone beneath Sandia and Mortandad Canyons,
- obtain groundwater and contaminant-mass fluxes through "hydraulic windows" through the CdR basalts in the vadose zone, and
- achieve advective travel times through the vadose zone consistent with existing site data and knowledge.

The 3-D Coupled vadose-zone/regional-aquifer model captures the significant heterogeneity of the vadose zone and regional aquifer, along with the transient initial conditions and boundary conditions that simulate the hydrologic environment. This calibrated model may be used to assess the potential future impacts of vadose-zone chromium inventory on the regional aquifer and simulate potential corrective action scenarios. Ultimately, the model is a critical component of a system model that simulates the behavior of future chromium migration in the regional aquifer, and it is the basis for uncertainty quantification of key model parameters.

The regional-scale aquifer model is designed to represent the groundwater flow and contaminant transport in the regional aquifer. The model is three dimensional with a spatial domain encompassing the entire Pajarito Plateau. The top of the model is defined by the regional aquifer water table. The model grid contains 766,283 nodes and 4,659,062 elements with local refinement in the area of the chromium plume.

The local refinement enables the model to include accurate locations for wells within the area of the chromium plume that are used in the model calibration. The model includes several areas where there is local groundwater recharge, including breakthrough areas (“sources”) of chromium contamination. The model represents flow and transport using spatially heterogeneous and anisotropic permeability and specific storage. Model properties are estimated by calibration against observed field data. The model accounts for transients in the municipal water-supply pumping occurring on the Pajarito Plateau and from pumping in the chromium plume during long-term field tests. The FEHM code is used to simulate contaminant transport of chromium by advective dispersion. Various types of model analyses (model inversions and calibrations, sensitivity analyses, uncertainty analyses, etc.) are carried out using the Model Analysis and Decision Support (MADS) open-source code. The model is calibrated to reproduce

- regional aquifer water levels from existing monitoring points,
- transients in the hydraulic drawdowns in the regional aquifer caused by water-supply pumping and project-related pumping activities, and
- chromium concentration transients observed in regional aquifer monitoring wells.

The regional-scale aquifer model estimates the location and shape of the contamination sources as a part of the inversion process. The model also estimates flux of infiltration from the vadose zone and contaminant concentration directly at the entry point into the regional aquifer. Chromium concentration data are used to characterize aquifer heterogeneity.

The biogeochemical remediation model is a multi-dimensional reactive transport model of relevant biogeochemical processes that are valuable for evaluating the deployment of various amendments for in situ remediation in the aquifer. CHROTRAN (Chromium Transport Bio-Chemical Remediation Code) was developed as a comprehensive modeling tool that provides a framework for modeling biostimulation, biodegradation, chemical degradation, growth inhibition, and biocide effects. CHROTRAN is optimized to model chromium remediation, and the full suite of biochemical processes implemented in CHROTRAN was used to model in situ biochemical remediation of chromium-contaminated groundwater using molasses as a biostimulant. In the exploratory models conducted for pilot-scale testing at the site, the following species, whose dynamics are governed by physical and biochemical aquifer processes, were considered:

- Cr(VI), the contaminant to be remediated
- Molasses, an electron donor that serves as the biostimulant and abiotic reductant
- Biomass, a collection of microbial consortia and their associated extracellular material
- Ethanol, a conservative amendment that serves as a microbial growth inhibitor
- Biocide, an amendment that kills excess biomass and is consumed in the process

CHROTRAN was also used to model in situ chemical remediation of chromium-contaminated groundwater using sodium dithionite, a strong chemical reductant capable of reducing iron in sediments from ferric oxide [Fe(III)] to Fe(II). Surface-bound Fe(II) becomes a long-term, stationary source of reductant capable of geochemically reducing dissolved Cr(VI) to Cr(III) through in situ redox manipulation. CHROTRAN is also capable of modeling other important processes that may influence remediation, such as mineral precipitation/dissolution, aqueous speciation, and pH.

3.0 REFERENCES AND MAP DATA SOURCES

The following reference list includes documents cited in this compendium. Parenthetical information following each reference provides the author(s), publication date, and ERID or ESHID. This information is also included in text citations. ERIDs were assigned by the Associate Directorate for Environmental Management's (ADEM's) Records Processing Facility (IDs through 599999), and ESHIDs are assigned by the Environment, Safety, and Health Directorate (IDs 600000 and above). IDs are used to locate documents in the Laboratory's Electronic Document Management System and in the Master Reference Set. The NMED Hazardous Waste Bureau and ADEM maintain copies of the Master Reference Set. The set ensures that NMED has the references to review documents. The set is updated when new references are cited in documents.

3.1 References

LANL (Los Alamos National Laboratory), October 2009. "Investigation Report for Sandia Canyon," Los Alamos National Laboratory document LA-UR-09-6450, Los Alamos, New Mexico. (LANL 2009, 107453)

LANL (Los Alamos National Laboratory), September 2012. "Phase II Investigation Report for Sandia Canyon," Los Alamos National Laboratory document LA-UR-12-24593, Los Alamos, New Mexico. (LANL 2012, 228624)

LANL (Los Alamos National Laboratory), July 2014. "Drilling Work Plan for Chromium Project Coreholes," Los Alamos National Laboratory document LA-UR-14-24829, Los Alamos, New Mexico. (LANL 2014, 259151)

LANL (Los Alamos National Laboratory), May 2015. "Interim Measures Work Plan for Chromium Plume Control," Los Alamos National Laboratory document LA-UR-15-23126, Los Alamos, New Mexico. (LANL 2015, 600458)

LANL (Los Alamos National Laboratory), July 2015. "Work Plan for Chromium Plume Center Characterization," Los Alamos National Laboratory document LA-UR-15-24861, Los Alamos, New Mexico. (LANL 2015, 600615)

LANL (Los Alamos National Laboratory), December 2015. "Drilling Work Plan for Alluvial Piezometers in Sandia Canyon," Los Alamos National Laboratory document LA-UR-15-29446, Los Alamos, New Mexico. (LANL 2015, 601047)

LANL (Los Alamos National Laboratory), May 12, 2016. "Additional Information for Discharge Permit Application DP-1835," Los Alamos National Laboratory letter (ENV-DO-16-118) to M. Hunter (NMED) from J.P. McCann (LANL), Los Alamos, New Mexico. (LANL 2016, 602906)

LANL (Los Alamos National Laboratory), January 2017. "Field Summary Report for Alluvial Piezometers in Sandia Canyon," Los Alamos National Laboratory document LA-UR-17-20200, Los Alamos, New Mexico. (LANL 2017, 602134)

LANL (Los Alamos National Laboratory), July 2017. "Pilot-Scale Amendments Testing Work Plan for Chromium in Groundwater beneath Mortandad Canyon," Los Alamos National Laboratory document LA-UR-17-25406, Los Alamos, New Mexico. (LANL 2017, 602505)

- LANL (Los Alamos National Laboratory), January 2018. "Quarterly Report on Pilot-Scale Amendments Testing for Chromium in Groundwater beneath Mortandad Canyon," Los Alamos National Laboratory document LA-UR-18-20467, Los Alamos, New Mexico. (LANL 2018, 602862)
- NMED (New Mexico Environment Department), September 26, 2014. "Approval with Modifications, Drilling Work Plan for Chromium Project Coreholes," New Mexico Environment Department letter to P. Maggiore (DOE-NA-LA) and J.D. Mousseau (LANL) from J.E. Kieling (NMED-HWB), Santa Fe, New Mexico. (NMED 2014, 525201)
- NMED (New Mexico Environment Department), October 15, 2015. "Approval with Modifications, Work Plan for Chromium Plume Center Characterization," New Mexico Environment Department letter to D. Hintze (DOE-NA-LA) and M. Brandt (LANL) from J.E. Kieling (NMED-HWB), Santa Fe, New Mexico. (NMED 2015, 600958)
- NMED (New Mexico Environment Department), October 15, 2015. "Approval with Modifications, Interim Measures Work Plan for Chromium Plume Control," New Mexico Environment Department letter to D. Hintze (DOE-NA-LA) and M. Brandt (LANL) from J.E. Kieling (NMED-HWB), Santa Fe, New Mexico. (NMED 2015, 600959)
- NMED (New Mexico Environment Department), July 31, 2017. "Approval, Pilot-Scale Amendments Testing Work Plan for Chromium in Groundwater beneath Mortandad Canyon," New Mexico Environment Department letter to D. Hintze (DOE-EM) and B. Robinson (LANL) from J.E. Kieling (NMED-HWB), Santa Fe, New Mexico. (NMED 2017, 602546)

3.2 Map Data Sources

- Hillshade; Los Alamos National Laboratory, ER-ES, As published;
\\slip\gis\Data\HYP\LiDAR\2014\Bare_Earth\BareEarth_DEM_Mosaic.gdb; 2014.
- Point features; As published; EIM data pull; 2017.
- Chromium plume > 50 ppb; Los Alamos National Laboratory, ER-ES, As published;
\\slip\gis\GIS\Projects\13-Projects\13-0065\shp\chromium_plume_2.shp; 2018.
- Structures; Los Alamos National Laboratory, KSL Site Support Services, Planning, Locating and Mapping Section; 06 January 2004; as published 29 November 2010.
- Drainage channel; Los Alamos National Laboratory, ER-ES, As published, GIS projects folder;
\\slip\gis\GIS\Projects\15-Projects\15-0080\project_data.gdb\correct_drainage; 2017.
- Technical Area Boundaries; Los Alamos National Laboratory, Site Planning & Project Initiation Group, Infrastructure Planning Office; September 2007; as published 13 August 2010.
- Unpaved roads; Los Alamos National Laboratory, ER-ES, As published, GIS projects folder;
\\slip\gis\GIS\Projects\14-Projects\14-0062\project_data.gdb\digitized_site_features\digitized_roads; 2017.
- U.S. Census populated places; Los Alamos National Laboratory, ER-ES, As published, GIS projects folder; \\slip\gis\GIS\Data\ESRI\census\places.sdc\places; 2018
- Rivers; Los Alamos National Laboratory, ER-ES, As published, GIS projects folder;
\\slip\gis\GIS\Data\ESRI\hydro\rivers.sdc\rivers; 2018.

4.0 KEY CONTRIBUTORS TO THE CHROMIUM COMPENDIUM STUDIES

Attachment 1: Results and Implications of Field Tracer Testing and Long-Term Pump Tests within the Chromium Plume at Los Alamos National Laboratory from 2013 to 2017

Paul Reimus (EES-14), Bennie Martinez (EES-14), Danny Katzman (ADEM-PO), Gary Garcia (ER-FS), Patrick Mahoney (ER-FS), Gabriel Vigil (ER-FS)

Attachment 2: Isotopic Signatures of Hexavalent Chromium in the Regional Aquifer: Evaluation of Natural Attenuation

Jeff Heikoop (EES-14), Dea Musa (EES-14), Kai Williams (EES-14), Tom Johnson (University of Illinois Urbana-Champaign)

Attachment 3: Stratigraphic and Sedimentological Studies and their Hydrogeological Features in the Chromium Investigation Area, Los Alamos National Laboratory

David Broxton (ADEM), Giday Woldegabriel (EES-14), Rose Harris (EES-14), Danny Katzman (ADEM-PO)

Attachment 4: Analysis of Groundwater Geochemical Fingerprints for Identification of Source Areas in the Chromium Project Area

Jeff Heikoop (EES-14), Dea Musa (EES-14), Danny Katzman (ADEM-PO)

Attachment 5: Evaluation of Potential Source Areas for the Chromium Plume Using Machine Learning Data Analyses of Geochemical Data

Velimir Vesselinov (EES-16), Dan O'Malley (EES-16), Boian Alexandrov (T-1), Sachin Pandey (EES-16)

Attachment 6: Characterization of Natural Attenuation

Paul Reimus (EES-14), Mei Ding (EES-14), Doug Ware (EES-14), Rose Harris (EES-14), Dea Musa (EES-14), Danny Katzman (ADEM-PO)

Attachment 7: Bioremediation Bench-Scale Studies

Hakim Boukhalfa (EES-14), Chris Yeager (C-CDE), Dongping Wang (EES-14), Artaches Migdissov (EES-14), Satish Karra (EES-16), Doug Ware (EES-14), Velimir Vesselinov (EES-16), Hajnalka Daligault (B-10), Cheryl Gleasner (B-10), Shannon Johnson (B-10), Po-E Li (B-10), Paul Reimus (EES-14), Danny Katzman (ADEM-PO)

Attachment 8: Chemical Remediation Bench-Scale Studies

Paul Reimus (EES-14), Katherine Telfeyan (EES-14), Artaches Migdissov (EES-14), Doug Ware (EES-14), Sachin Pandey (EES-16)

Attachment 9: Groundwater Modeling Status Report

Velimir Vesselinov (EES-16), Dan O'Malley (EES-16), Scott Hansen (EES-16), Terry Miller (EES-16), Zhiming Lu (EES-16), Satish Karra (EES-16), Qinjun Kang (EES-16), Maruti Mudunuru (EES-16), Sachin Pandey (EES-16), Boian Alexandrov (T-1), Jeffrey Hyman (EES-16), Daniel Livingston (EES-16)

Analytical support for these compendium studies was provided by staff in the Laboratory's Geochemistry and Geomaterials Research Laboratory (GGRL)

George Perkins (EES-14), Emily Kluk (EES-14), Oana Marina (EES-14), David Chu (EES-14), Kai Williams (EES-14), Zhenghua Li (EES-14), Mike Rearick (EES-14/C-AAC)

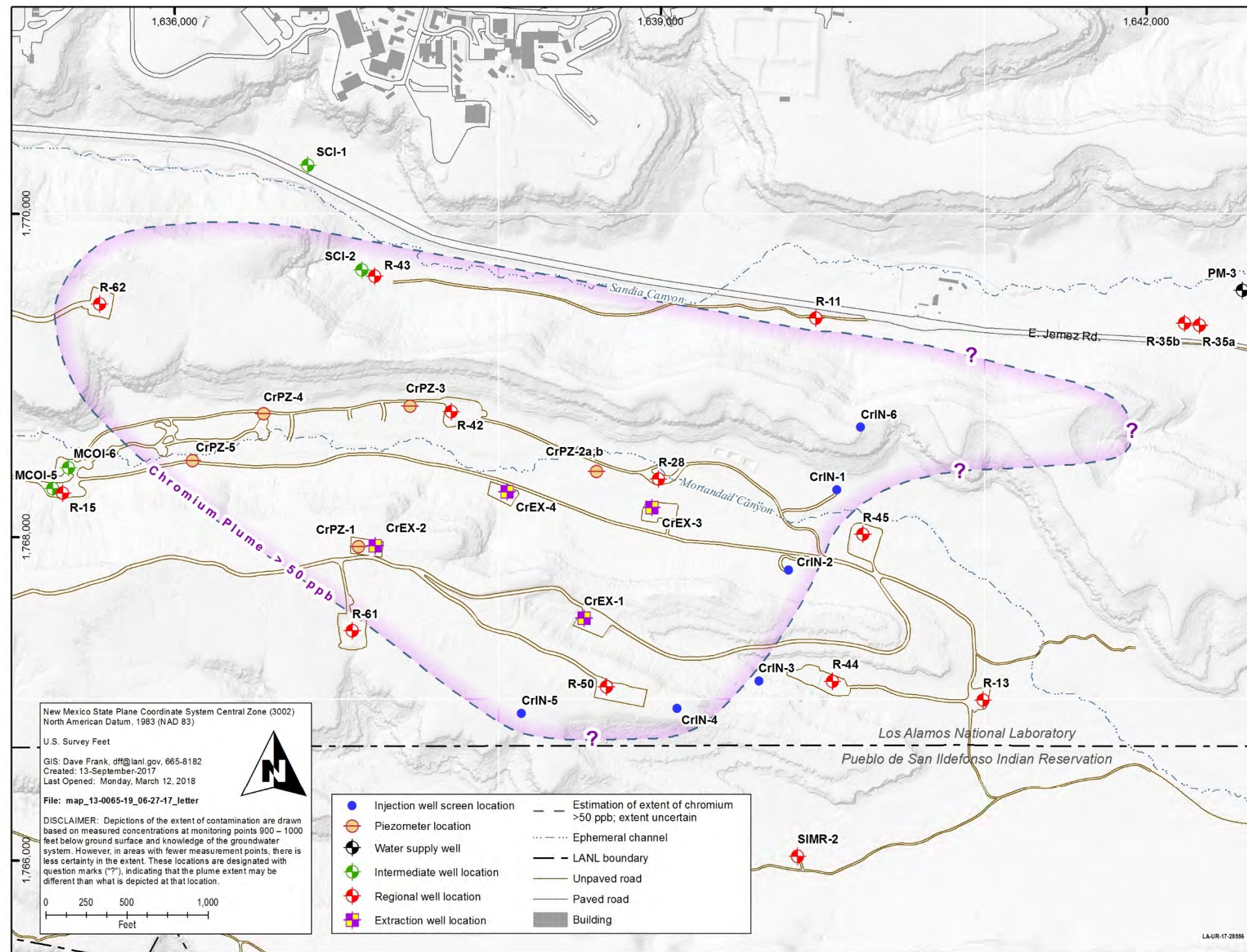


Figure 1.0-1 Map showing the approximate extent of the hexavalent chromium plume as defined by the 50-µg/L New Mexico groundwater standard. Locations of monitoring wells, piezometers, extraction wells and injection wells are also shown.

LA-UR-18-21450
March 2018
EP2018-0027

Results and Implications of Field Tracer Testing and Long-Term Pump Tests within the Chromium Plume at Los Alamos National Laboratory from 2013 to 2017

Attachment 1



Prepared by the Associate Directorate for Environmental Management

Los Alamos National Laboratory, operated by Los Alamos National Security, LLC, for the U.S. Department of Energy (DOE) under Contract No. DE-AC52-06NA253 and under DOE Office of Environmental Management Contract No. DE-EM0003528, has prepared this document pursuant to the Compliance Order on Consent, signed June 24, 2016. The Compliance Order on Consent contains requirements for the investigation and cleanup, including corrective action, of contamination at Los Alamos National Laboratory. The U.S. government has rights to use, reproduce, and distribute this document. The public may copy and use this document without charge, provided that this notice and any statement of authorship are reproduced on all copies.

CONTENTS

1.0	INTRODUCTION	1
2.0	BOREHOLE DILUTION TRACER TESTS	1
3.0	PUSH-PULL TRACER TESTS AT R-42 AND R-28	3
3.1	Dual-Porosity/Dual-Permeability Information—Flowing Layer Thicknesses	4
3.2	Natural Groundwater Flow-Velocity Estimates	6
3.3	Evidence for Natural Attenuation of Cr(VI)	9
4.0	GEOCHEMICAL TRANSIENTS DURING PUMPING TESTS OF R-42, R-28, R-62, AND R-43 S1	10
5.0	PUSH-DRIFT TEST WITH HIGH PH SOLUTION IN R-42	14
6.0	CROSS-HOLE TRACER TESTING	16
6.1	Pressure Responses during Injections into CrPZ-2a and CrPZ-2b	17
6.2	Tracer and Geochemistry Observations in Injection Wells	18
6.3	Cross-Hole Tracer Response at CrEX-3	21
7.0	OVERALL CONCLUSIONS FROM 2013-2017 FIELD TESTING	24
8.0	REFERENCES AND MAP DATA SOURCES	26
8.1	References	26
8.2	Map Data Sources	27

Figures

Figure 1.0-1	Map of the Cr(VI) plume area	29
Figure 2.0-1	Locations of dilution tracer tests with estimated linear groundwater flow velocities and Cr(VI) fluxes at each of the locations	30
Figure 2.0-2	Tracer concentration histories (ln C/Co vs time) in each dilution tracer test (plots intended to show quality of the test data)	31
Figure 3.1-1	Normalized tracer concentrations as a function of time in the R-42 push-pull tracer test	32
Figure 3.1-2	Normalized tracer concentrations as a function of time in the R-28 push-pull tracer test	33
Figure 3.1-3	Match of the 2-D numerical model to the tracer responses and the difference between the two tracer responses (showing both raw and background-subtracted bromide concentrations) during the R-28 push-pull test	34
Figure 3.2-1	Response of 1,5-NDS dilution tracer at R-42 during the push-pull test after subtracting out the contribution of the residual tracer that was still in the wellbore at the start of the test (approximately 52% of the tracer, which was assumed to be represented by the Br and 2,6-DFBA responses multiplied by 0.52)	35
Figure 3.2-2	Tracer and aquifer water breakthroughs during the R-28 push-pull tracer test, showing Br breakthrough relative to conservative anions that were in aquifer water but not in treated water (SO ₄ ⁻) or vice-versa (Cl ⁻ , which had a concentration of about 145 mg/L in treated water and 45 mg/L in aquifer water)	35
Figure 3.3-1	Breakthroughs of SO ₄ ⁻ and Cr(VI) in R-42 during the pull phase of the push-pull test in R-42	36

Figure 3.3-2	Breakthroughs of Cr(VI) and NO ₃ ⁻ relative to SO ₄ ⁼ in the R-28 push-pull test.....	36
Figure 3.3-3	Total organic carbon (TOC) concentrations superimposed on NO ₃ ⁻ and NO ₂ ⁻ concentrations during R-28 (top) and R-42 (bottom) push-pull tests.....	37
Figure 4.0-1	Concentrations of key constituents in R-42 during the long-term pumping test of R-42 in 2013, including the period after pumping ended (top: major anions and Cr(VI), bottom: major cations)	38
Figure 4.0-2	Charge balance in R-42 during long-term pump test of R-42 (at 7–8 gpm)	39
Figure 4.0-3	Concentrations of key constituents in R-28 during the long-term pumping test of R-28 (at 27–28 gpm), including the period after pumping ended (top: major anions and Cr(VI), bottom: major cations).....	40
Figure 4.0-4	Concentrations of key constituents in R-62 during the long-term pumping test of R-62 (at 1–1.5 gpm), including the period immediately after pumping ended.....	41
Figure 4.0-5	Concentrations of key constituents in R-43 S1 during the long-term pumping test of R-43 S1 (at 7–8 gpm), including the period immediately after pumping ended.....	42
Figure 5.0-1	Concentrations of major anions and Cr(VI) in R-42 during the drift phase of the high-pH push-drift test at R-42. Concentrations are expressed as fractions of pretest concentrations.....	43
Figure 5.0-2	pH, alkalinity, and sodium and calcium concentrations in R-42 during the drift phase of the high-pH push-drift test at R-42.....	44
Figure 6.1-1	Pressure responses in CrPZ-2a, CrPZ-2b and R-28 during the tracer and chase injections into CrPZ-2b.....	45
Figure 6.1-2	Pressure responses in CrPZ-2a, CrPZ-2b and R-28 during the tracer and chase injections into CrPZ-2a.....	46
Figure 6.1-3	Pressure responses in CrPZ-2a, CrPZ-2b, and R-28 during 12-h pump test of CrEX-3 (at ~40 gpm).....	47
Figure 6.2-1	Decline in bromide tracer concentration observed in CrPZ-2a after the chase started in CrPZ-2b.....	48
Figure 6.2-2	Rise in rhenium tracer concentration observed in CrPZ-2b after the tracer injection started in CrPZ-2a (top)	49
Figure 6.2-3	Concentration histories of tracers injected into CrPZ-2a measured in passive samples collected from CrPZ-2a after the injection and chase.....	50
Figure 6.2-4	Concentrations of major anions and Cr(VI) in CrPZ-2a measured in passive samples collected from CrPZ-2a after the injection and chase, which were both potable water. Concentrations are expressed as fractions of pretest concentrations.....	50
Figure 6.2-5	Concentration histories of major anions, bromide tracer, and Cr(VI) in CrPZ-2b, measured in passive samples collected from CrPZ-2b after the injection and chase.	51
Figure 6.2-6	Concentration histories of tracers injected into R-28 measured in passive samples collected from R-28 after the injection and chase.....	51
Figure 6.2-7	Concentrations of major anions and Cr(VI) in R-28 measured in passive samples collected from R-28 after the injection and chase, which were both potable water. Concentrations are expressed as fractions of pretest concentrations.....	52
Figure 6.3-1	Normalized breakthrough curves of tracers injected into CrPZ-2a in CrEX-3 during pumping of CrEX-3.....	52
Figure 6.3-2	Normalized concentrations of tracers injected into CrPZ-2a in CrEX-3, including additional samples collected after pumping ended.....	53

Figure 6.3-3 Model match to normalized breakthrough curves of tracers injected into CrPZ-2a in CrEX-3 through the end of pumping on 12/7/2016 53

Figure 6.3-4 Model match to *differences* in normalized breakthrough curves of tracers injected into CrPZ-2a in CrEX-3 54

Tables

Table 2.0-1 Circulation Loop Volumes, Volumetric Flow Rates, Flow Distortion and Linear Velocity Estimates for Each Borehole Dilution Tracer Test 55

Table 3.0-1 Tracer Identities/Masses, Injection and Chase Volumes, Key Dates/Times, and Withdrawal Rates in the Push-Pull Tracer Tests at R-42 and R-28 55

Table 6.0-1 Tracer Identities/Masses, Injection and Chase Volumes, Key Dates/Times, and (at ~40 gpm) at CrEX-3 in the Cross-Hole Tracer Test 56

Appendixes

Appendix A Moisture Content and Pore Water Chemistry Data from Sonic Core Holes CrCH-1 through CrCH-5, and Chemistry Data from Completed Piezometers (CrPZ-1 through CrPZ-5)

Appendix B Long-Term Trends (through mid-2017) in Selected Monitoring Wells in which there have been Notable Increases in Cr(VI) Concentrations

1.0 INTRODUCTION

Hexavalent chromium [Cr(VI)] contamination from legacy operations at Los Alamos National Laboratory (LANL or the Laboratory) was discovered in the regional aquifer beneath Mortandad canyon in 2005. In the years since then, numerous investigations have been conducted by the Laboratory to define the nature and extent of the Cr(VI) contamination, to understand the transient behavior of the plume, and to develop a strategy for remediating the plume, including an interim pump-and-treat measure that is currently being employed.

Among the many investigations carried out by the Laboratory for the chromium project, several field tracer studies and related tests were conducted from 2013 to 2017 to better understand the regional aquifer hydrology and geochemistry within the Cr(VI) plume in support of the various other studies and field amendments tests. These tests included nine borehole dilution tracer tests, two push-pull tracer tests, four long-term pumping tests in which geochemical transients were observed, a push-drift test in which a solution buffered to pH ~9.8 was introduced to promote desorption of anion-exchanged Cr(VI), and a cross-hole tracer test with three different tracer injection locations (and one well in which tracers appeared). Collectively, the results of these tests have provided valuable insights and constraints on ambient groundwater flow velocities in the plume area, natural attenuation processes for Cr(VI), diffusive mass transfer between primary and secondary porosity, capture zones for extraction wells, and the potential distribution of Cr(VI) and other groundwater constituents near the test wells. The purpose of this report is to present the results and preliminary interpretations of these tests and to discuss potential implications of the results.

The test results are presented in this report in separate sections for each type of test. Dilution tracer tests are presented first, followed by the two push-pull tracer tests, geochemical trends observed during long-term pump tests, the push-drift test, and finally the cross-hole tracer test. The order of presentation of the material corresponds roughly, but not exactly, to the chronological order in which the tests were conducted.

Appendix A of this report summarizes the moisture content and pore-water chemistry data obtained from five sonic core holes that were drilled into the Cr(VI) plume in 2014 and 2015 (designated as CrCH-1 through CrCH-5, although later completed as 2-in. piezometers designated as CrPZ-1 through CrPZ-5). The pore water was extracted from the sonic core by centrifugation (wherever the core contained enough moisture). The pore-water chemistry data provide valuable information on the distribution of anthropogenic constituents (SO_4^- , Cl^- , and NO_3^-) as a function of depth, particularly below the water table where the core was always moist enough to extract sufficient water for analysis. Although the pore water did not yield reliable measurements of Cr(VI) concentrations, the depth profiles of the other anthropogenic constituents, which tend to be correlated with Cr(VI) throughout the plume area, illustrate how Cr(VI) contamination is likely distributed with depth within the aquifer.

Figure 1.0-1 shows a map of the plume area that highlights the wells in which the field tests described in this report were conducted, and it also shows the locations of the sonic core holes (identified in this figure as CrPZ-1 through CrPZ-5).

2.0 BOREHOLE DILUTION TRACER TESTS

Borehole dilution tracer tests were conducted in several wells within the Cr(VI) plume area to obtain estimates of ambient groundwater flow velocities at the well locations. These tests were conducted by injecting a tracer solution at the top of the screened interval in a given well while withdrawing water at the same rate or a slightly higher rate from below the screened interval. The matching of the flow rates (or slightly higher extraction rate than injection rate) ensured that the tracer solution remained in the well

casing and was not pushed into the filter pack or the formation during the injection. When the tracer solution returned to the surface via the production tubing and reached a stable concentration approximately equal to the injection concentration, the tracer injection was stopped, and the withdrawal flow from the well was redirected into the injection tubing or directly into the well casing. This established a closed-loop circulation system in which the traced water was continuously cycled between the surface and the screened interval, with the tracer being forced to flow down the entire length of the interval inside the casing with each pass. The reinjection of all water pumped from the well (minus any small amount collected for samples) ensured that there was no net injection or withdrawal of water occurring. Under these conditions, the rate of decline in tracer concentration in the circulation loop can be related to the volumetric flow rate of the groundwater that is flowing naturally through the screened interval (Drost 1968; Palmer 1993). Mathematically,

$$\frac{d \ln C}{dt} = -\frac{Q}{V} \quad \text{Equation 1}$$

where C = tracer concentration

t = time, h

Q = volumetric flow rate, L/h

V = volume of circulation loop, L

Note that $\frac{d \ln C}{dt}$ is the slope of a plot of $\ln C$ vs t .

The volumetric flow rate Q is then related to the specific discharge in the aquifer in the vicinity of the well screen using the methods of Palmer (1993), which distribute the volumetric flow rate over the cross-sectional area of the well screen and account for flow field distortions in the aquifer caused by the presence of the filter pack, well screen, and casing. The specific discharge estimate can then be converted to a groundwater velocity estimate by dividing by an assumed flow porosity.

The tracer used in all dilution tracer tests was sodium 1,5 naphthalene disulfonate (1,5-NDS), which is known to not interact with aquifer sediments and has been used in numerous tracer tests, including in geothermal systems, as a conservative tracer (Rose et al. 2001; Nimmo et al. 2002). This tracer is readily analyzed by fluorescence spectrophotometry using an excitation wavelength of about 225 nm and an emission wavelength of approximately 330 nm. A Shimadzu RF-5301PC Spectrophotometer configured as a fluorimeter was used for all measurements, although a field fluorimeter (Ocean Optics USB4000 Fiber Optic Spectrometer) was used to make qualitative determinations of when tracer returned to the surface from the injection interval so that the tracer injections could be stopped and the circulation of tracer solution started. Except for the first dilution tracer test at regional aquifer monitoring well R-42, only a few grams of the tracer salt was used in each test; at R-42, about 200 g was used. The first test revealed that 200 g was excessive; the samples had to be diluted by large amounts for concentration measurements. The mass was therefore reduced by approximately 2 orders of magnitude for all subsequent tests. In all tests, the tracer mass injected was less than the mass prepared because the injection of tracer solution was stopped when tracer returned to the surface. The exact tracer masses or concentrations injected were not important because only the rate of decline in tracer concentrations is important for the test interpretation, not the absolute concentrations. Samples were collected in 60-mL amber glass bottles (Qorpak) with Teflon-lined screw caps, with most samples being collected using an autosampler (ISCO Foxy 200). In almost all cases, samples were analyzed without filtration or centrifugation, although in rare cases where samples had visible turbidity, they were filtered or centrifuged to remove the turbidity for the fluorescence measurements.

Figure 2.0-1 shows the locations at which dilution tracer tests were conducted for the chromium project in 2014 and 2015. This figure includes the estimated linear flow velocities and Cr(VI) fluxes (concentration multiplied by specific discharge) at each of the locations. Plots of the tracer concentration time histories (normalized to injection concentrations in all cases) in each test well are shown in Figure 2.0-2, and Table 2.0-1 provides a tabulation of the circulation loop volumes, volumetric flow rates (from Equation 1), flow distortion factors, and linear flow-velocity estimates for each well location. The flow distortion factors were estimated using the methods of Palmer (1993), and they should be considered somewhat uncertain because the degree to which the installation of the wells affected the hydraulic conductivity of the aquifer in the immediate vicinity of the well is not known (several parameters can be only estimated). The flow distortion factors for the piezometers CrPZ-2a, CrPZ-2b, and CrPZ-3 should be considered especially uncertain because these “wells” have much smaller casing radii relative to borehole radii than typical wells, and they go beyond the range of this ratio considered by Palmer (1993). Indeed, the specific discharges estimated for the piezometers seem to be rather low compared with the discharges estimated in nearby monitoring wells that have more conventional completions (namely R-42 for CrPZ-3, and R-28 for CrPZ-2a/2b), suggesting that the borehole flow distortion factors may be overestimated for these piezometers.

Although borehole dilution tests have their limitations and uncertainties, the results of the dilution tests conducted for the chromium project definitely suggest that there is considerable variability in local flow velocities across the uppermost regional aquifer. Specifically, flow velocities at R-28 and R-43 S1 (the upper of two screens in R-43) seem to be significantly higher than in any of the other regional aquifer locations tested. Also, the flow velocity in the only intermediate well tested, SCI-2, is quite high, suggesting that this well may be connected to or within a relatively high-velocity flow pathway that is transporting Cr(VI) within the vadose zone. These results support a conceptual flow model involving relatively discrete flow pathways in the regional aquifer that may account for the majority of the groundwater flux in the upper portion of the aquifer where the Cr(VI) contamination is located. The implication is that the Cr(VI) may be preferentially transported in “channels” of high flow velocity, although the nature of these channels cannot be deduced from the dilution tests alone, which provide only a very local measurement and no information on flow direction. It may be that such flow channels interconnect and form “braided” patterns that roughly equate to uniform, homogeneous flows when viewed at larger scales, or it is possible that R-28 and R-43 S1 represent areas where more uniform flow has been effectively “funneled” into high-permeability regions of a narrow cross-section that happen to intersect these wells. There is currently no evidence that channels of high permeability and high flow velocity persist over length scales that are similar to the dimensions of the plume, as the wells completed along the periphery of the plume (as currently mapped) all tend to have similar Cr(VI) concentrations. If narrow high-velocity channels were persistent over the entire length scale of the plume, such uniform concentrations would not be expected. Note that although borehole dilution tests have their uncertainties and detractors, the results of the push-pull tracer tests at R-42 and R-28 and the geochemical responses to long-term pumping in these wells (and also long-term pumping of R-43 S1 and R-62), all tend to qualitatively support the flow-velocity estimates from the borehole dilution tests. This supporting evidence will be discussed in sections 3 and 4.

3.0 PUSH-PULL TRACER TESTS AT R-42 AND R-28

In 2014, two push-pull tracer tests were conducted at regional aquifer monitoring wells R-42 and R-28. The locations of these wells are shown in Figures 1.0-1 and 2.0-1. The tests were conducted on the heels of the dilution tracer tests in these two wells, and they were preceded (in 2013) by continuous pumping of the wells for an extended period of time (geochemical transients from the continuous pumping are discussed in section 4).

The push-pull tests were conducted by first injecting approximately 1400 gal. of water containing two nonreactive tracers that had a difference of about a factor of 3 in free-water diffusion coefficient. The tracers used at R-42 were sodium bromide (NaBr) and sodium 2,6-difluorobenzoate (Na 2,6-DFBA), with the anions Br⁻ and 2,6-DFBA⁻ serving as the nonreactive tracers. The tracers at R-28 were NaBr and sodium 2,5-difluorobenzoate (Na 2,5-DFBA), with Br⁻ and 2,5-DFBA⁻ serving as the tracers. From previous work (Reimus et al. 2003; Reimus et al. 2007) it was known that none of these anionic tracers react with mineral surfaces at the pH of the groundwater, and it was also known that Br⁻ has a diffusion coefficient about a factor of 3 larger than that of the DFBA⁻ anions.

The tracer solution was followed by the injection of approximately 10,000 gal. of tracer-free “chase” water to “push” the tracers out into the aquifer away from the injection well. The chase water in both tests consisted of water that had been treated by ion exchange to remove Cr(VI), with the columns containing fresh ion exchange resin that also removed essentially all of the SO₄⁼ and NO₃⁻ from the water, replacing these anions with Cl⁻. After the injection of the chase water, the wells were allowed to “rest” without any net injection or withdrawal of water, which allowed the injected tracer solutions to “drift” with the ambient groundwater flow. However, during the “rest” or “drift” period, each well was continuously circulated by withdrawing water from the bottom of the screened interval and returning it to the top of the interval, with small-volume samples being collected at the surface to allow the concentration of tracers drifting back through the well to be monitored. After the rest or drift period was over, water was pumped from the wells to recover the tracers and determine their responses. The volumes of the tracer and chase water and the durations of the injection, rest, and pumping periods (and pumping rates) in each well are listed in Table 3.0-1.

Autosamplers (ISCO Foxy 200) were used to collect samples in 60-mL amber glass bottles (Qorpak) during the drift and net withdrawal periods of both push-pull tracer tests. Bromide was analyzed in the samples by ion chromatography using U.S. Environmental Protection Agency (EPA) Method 300 on a Dionex DX-600 system. The fluorinated benzoates were analyzed by high-performance liquid chromatography (HPLC) using a Dionex Ultimate 3000 RS Variable Wave Length Detector. The primary analytical column for the fluorinated benzoates was an Acclaim C-18 (4.6 x 150 mm). Typical HPLC operating parameters were as follows: 60/40 v/v 30 mM KH₂PO₄ buffer/methanol; 25°C; 0.8-mL/min flow rate; 200-μL injection volume; and analyte detection at 222 nm (ultraviolet [UV] absorbance). Selected samples were also analyzed for the 1,5-NDS dilution tracers using the fluorescence method described in section 2.

The remainder of this section is divided into 3 subsections that separately address different types of information obtained from the push-pull tracer tests: information on the dual-porosity/dual-permeability behavior of the aquifer, natural-flow-velocity estimates, and evidence of natural attenuation of Cr(VI) in the aquifer.

3.1 Dual-Porosity/Dual-Permeability Information—Flowing Layer Thicknesses

The use of the two simultaneously injected tracers with a difference of a factor of 3 in diffusion coefficient in each of the push-pull tests was intended to provide diagnostic information on diffusion between zones with flowing and stagnant water in the aquifer (or between faster- and slower-flowing water, as the case may be). If there is a significant amount of diffusive mass transfer between faster and slower flowing water in a push-pull test, the tracer with the smaller diffusion coefficient (the DFBA in this case) should have higher early normalized concentrations (concentration divided by injection mass or injection concentration) and a lower late concentration (i.e., tail) than the tracer with the larger diffusion coefficient. The rationale for this expectation is that proportionately less of the tracer with the smaller diffusion coefficient should diffuse out of the faster flow pathways into slower-flow pathways during the injection and rest period, and thus more of this tracer will show up early when the well is pumped back.

Conversely, more of the higher-diffusivity tracer will diffuse out of the faster-flow pathways during the injection and rest period, resulting in lower concentrations initially and higher concentrations later in the pumping period when this tracer back-diffuses out of the slower-flow pathways.

The normalized tracer concentrations as a function of time in the R-42 push-pull test are shown in Figure 3.1-1. Note that the response of the dilution tracer, 1,5-NDS, is shown along with the responses of the Br⁻ and 2,6 DFBA-. It is apparent that during the rest or drift period, very little of either of the push-pull tracers had drifted back into the well. However, almost immediately after net withdrawal began, 266.2 h after the end of the chase, these tracers appeared and rose rapidly in concentration. There are two possible explanations for this behavior: (1) Any tracer that had been injected directly upgradient of R-42 must have not quite drifted back into the wellbore (but was about to) when withdrawal began, or (2) very little of the tracer was injected directly upgradient, but nonetheless tracer was present near the wellbore so that when withdrawal began there was almost an immediate response. The exact explanation cannot be determined, but it is apparent that the normalized responses of the Br⁻ and 2,6 DFBA- are essentially identical, suggesting that there was very little diffusion out of flowing pathways and into nonflowing or slower-flowing pathways for both tracers.

Obviously, diffusion is a process that must have been occurring during the push-pull test, but its influence was apparently too small to cause a difference in the tracer responses. It is known that the stratigraphy in sonic core hole CrCH-3 (completed as piezometer CrPZ-3), located within about 80 m of R-42, is highly layered, with varying layer thicknesses of coarser and finer material (See Attachment 3 of this compendium, "Stratigraphic and Sedimentological Studies and their Hydrogeological Features in the Chromium Investigation Area, Los Alamos National Laboratory"). Thus, it was considered possible that the tracer responses might reflect diffusion into secondary porosity, particularly if flow was primarily through a thin horizontal layer of high permeability that was sandwiched between two lower-permeability layers into which diffusion could occur. The lack of a difference in the tracer responses suggests that any high-permeability layers must have been thick enough that the mass of tracer that diffused out of them was negligible relative to the mass that stayed in them. A simple analysis of expected tracer responses for different thicknesses of flowing vs nonflowing layers was conducted using a two-dimensional (2-D) numerical model, and the results suggested that, given the duration of the push-pull tracer test, the thickness of a flowing layer sandwiched between two low-permeability layers would have had to be on the order of a meter to result in no discernable differences in the tracer responses. That is, anything less than a meter in flowing layer thickness should have resulted in a notable difference in the tracer responses. This analysis cannot be considered completely definitive because it used an idealized geometry (horizontal layers of constant thickness), and it did not account for the possibility of advective flow in the low-permeability layers or of any flow between the layers, which could have smeared out a diffusion signature. The analysis also involved assuming the same porosities and tracer diffusion coefficients in different layers. In reality, lower-permeability layers might be expected to have slightly lower porosities and smaller diffusion coefficients than higher-permeability layers, and the effect would be to suppress diffusion out of higher-permeability layers, thus allowing somewhat narrower high-permeability layer thicknesses to be consistent with the observations. The analysis nevertheless suggests that preferential flow through relatively narrow layers of high permeability is inconsistent with the observed tracer responses.

The normalized tracer concentrations as a function of time in the R-28 push-pull test are shown in Figure 3.1-2. Note that no response is shown for the dilution tracer (1,5-NDS) because, in this case, the dilution tracer was not recovered at all during the net production phase of the test in R-28. Apparently, all of the dilution tracer drifted out of the pumping capture zone before establishing net withdrawal of water from this well. This result is in stark contrast to the R-42 result for the dilution tracer, especially when one considers that the rest/drift period was somewhat shorter at R-28 than R-42, and the R-28 pump was capable of pumping at approximately 4 times the volumetric flow rate as that of R-42. Clearly, this result qualitatively supports the dilution tracer test results in the two wells, which indicated a much higher flow

velocity at R-28 than at R-42 (Table 2.0-1). Another significant difference at R-28 relative to the R-42 push-pull test result is that the bromide and 2,5-DFBA both appeared in samples collected from R-28 long before any net withdrawal of water from the well, and, in fact, they both appear to have peaked in concentration before any net withdrawal. This result is also qualitatively consistent with a much higher natural flow velocity at R-28 relative to R-42, where no tracer appeared in the well until after net withdrawal was established.

Whereas in R-42 there were virtually no differences in the normalized concentrations of the bromide and 2,6-DFBA (Figure 3.1-1), it is apparent upon close inspection of Figure 3.1-2 that the 2,5-DFBA at R-28 appears to slightly precede the bromide during the early part of the drift phase of the test, and it peaks at a slightly higher normalized concentration than the bromide. Also, during the tailing part of the test, after net withdrawal was established, it appears that the bromide concentration becomes slightly higher than the 2,5 DFBA concentration (see Figure 3.1-2, bottom), even after subtracting out a background concentration of bromide that was non-zero. These results are qualitatively consistent with a small amount of diffusion of the tracers out of rapidly flowing porosity into slower-flowing porosity during the test. In a manner similar to the R-42 analysis described above, the 2-D numerical model was used to estimate how thick a flowing layer sandwiched between two nonflowing layers would have to be to yield the observed differences in the normalized tracer responses. It was found that the responses were consistent with a flowing layer that was about 20 cm thick, sandwiched between 20-cm-thick nonflowing layers (the predicted responses were sensitive not only to the thickness of the flowing layer but also the thickness of the nonflowing layers). The match of the model to the difference between the two tracer responses (after background subtraction of bromide) is shown in Figure 3.1-3.

Note that there is considerable scatter in the data that makes a quantitative conclusion from this analysis rather tenuous, but the 20-cm-thick flowing layer surrounded by 20-cm-thick nonflowing layers gave the best result of the model simulations attempted. The implication is that the thickness of flowing layers at R-28 appears to be less than at R-42, perhaps by as much as a factor of 5. This was a rather qualitative analysis that did not involve exhaustively varying parameters associated with layers, and the analysis had the same simplifications and caveats as the R-42 analysis. Note that if the porosity and diffusion coefficients were allowed to vary between the layers (with diffusion coefficients constrained to maintain their factor-of-3 difference between the two tracers), the analyses would be highly nonunique, with many potential combinations of porosity, diffusion coefficients, and layer thicknesses yielding equally good matches to the data. The intent was to obtain rough estimates of plausible layer thicknesses, and in particular, relative differences between high-permeability layer thicknesses at R-42 and R-28, so the layer thicknesses were the only parameters varied in both of the analyses (with the same porosities and diffusion coefficients assumed at both sites). Because porosities and diffusion coefficients were not assumed to be correlated with permeability, the high-permeability layer thicknesses obtained from the analyses should be considered upper bounds. If the other extreme of assuming very small porosities and/or small diffusion coefficients in the low-permeability layers was employed, the deduced high-permeability layer thicknesses would be considerably thinner.

3.2 Natural Groundwater Flow-Velocity Estimates

The push-pull tests at both R-42 and R-28 allowed independent estimates of natural groundwater flow velocities that could be compared with the dilution-tracer-test results. These estimates might be considered more representative than the dilution-tracer-test estimates because they involved interrogation of a larger volume of aquifer that was not confined to the immediate vicinity of the wellbores, as in the case of the dilution tracer tests. At R-42, an estimate was obtained by analyzing the dilution tracer response that occurred during the withdrawal phase of the push-pull test. The procedure was as follows.

The normalized concentrations of the two push-pull tracers were multiplied by 0.52 so that they had peak normalized concentrations that were the same as the peak normalized concentration of the dilution tracer (1,5-NDS). Note that this factor of 0.52 is quite consistent with the fraction of 1,5-NDS that was estimated to be remaining in the R-42 wellbore at the conclusion of the dilution tracer test, which was 0.55. The push-pull tracer injection was started within a day of the conclusion of the dilution tracer test, so the dilution tracer mass that remained in the wellbore was expected to behave much like the push-pull tracers when R-42 was pumped back in the push-pull test.

This adjusted normalized concentration of the push-pull tracers was subtracted from the normalized concentration of the dilution tracer to yield a response of the dilution tracer that was deemed to be representative of the dilution tracer mass that actually left the R-42 wellbore during the dilution tracer test. A plot of the tracer breakthrough curves showing the results of the previous step and this step is provided in Figure 3.2-1.

The difference between the mean return time of the push-pull tracers and of the dilution tracer that left the wellbore during the dilution tracer test (green curve of Figure 3.2-1) after the start of net withdrawal was estimated. The mean return time for the push-pull tracers was 34 h and the mean return time for the dilution tracer was 90 h.

Groundwater flow around R-42 during the net withdrawal period was assumed to be ideally radial, so the average distance that the push-pull tracers had moved from the wellbore during the chase and drift periods was estimated to be 3.7 m, and the average distance that the dilution tracer that left the wellbore during the dilution test had moved was 6.0 m. Both of these estimates assume a flow porosity in the aquifer of 0.2. The estimates were obtained from

$$L = \sqrt{\frac{Q\tau}{\pi b\phi}} \quad \text{Equation 2}$$

where L = mean distance of tracer from wellbore, m

Q = pumping extraction rate, m³/h

τ = mean return time of tracer, h (either 34 h or 90 h)

b = length of screened interval, m

ϕ = assumed flow porosity

The mean time that the dilution tracer that left the wellbore spent in the aquifer under natural groundwater flow conditions was taken to be 440 h, which is the sum of the push-pull drift period (~266 h), the time that at least half the tracer leaving the wellbore during the dilution test spent in the aquifer (~120 h) and the difference between the mean return times of the tracers during the push-pull test (56 h). The time of the tracer injection and chase were not counted because the tracers were being artificially pushed out into the aquifer during that time, and it was a relatively short time (less than 24 h). One might at first consider the drift period to be affecting all tracers the same and that it should therefore not be counted in this calculation, given that the overall estimate is based on the differences between the responses of the push-pull tracers and dilution tracer. However, the rationale for including the drift time in the calculation is that the push-pull tracers were assumed to be pushed approximately equally in all directions from the wellbore during injection and chase, but the dilution tracer that exited the wellbore during the dilution tracer test did so only in the downgradient direction. Thus, the movement of the push-pull tracers during the drift period would have caused some of the tracer to return earlier than if there was no drift and some to return later, having little net effect on the return time of these tracers. In contrast, the dilution tracer that left the wellbore during the dilution tracer test always drifted downgradient, increasing its return time when the well was pumped.

The natural groundwater flow velocity was taken to be the difference in the estimated distance the different types of tracers were from the wellbore at the time of pumping (6.0–3.7 = 2.3 m) divided by the 440 h obtained in the previous step, i.e., 0.0053 m/h or 0.13 m/d. This estimate is in excellent agreement with the estimate from the dilution tracer test in R-42 provided in Table 2.0-1 (0.14 m/d).

The procedure for obtaining an estimate of the natural groundwater flow velocity at R-28 was much different than at R-42 because there was no dilution tracer recovered at all at R-28. Rather, the estimate relied on the return times of the tracers relative to the return times of the aquifer water, with the appearance of sulfate and a decrease in chloride concentrations taken to be an indication of when the aquifer water was returning to the well. Unlike at R-42, where very little tracer or aquifer water were observed before initiating net water withdrawal from the well, the tracers and aquifer water both returned to R-28 during the drift period, and the tracer concentration actually appeared to peak during the drift period. The estimate of groundwater flow velocity was constrained by two separate calculations that together were intended to reduce uncertainty in the estimate. First, as Figure 3.2-2 (upper plot) shows, the time for the arrival of the peak concentration of the bromide tracer was approximately 110–120 h after the end of the chase period. Second, the difference between the arrival time of the bromide and the arrival time of the aquifer water was about 12 h (also in Figure 3.2-2, upper plot). Given that approximately 1500 gal. of tracer was injected (in treated water), followed by about 10,000 gal. of untraced treated water, the distances that the leading and trailing edges of the bromide pulse should have been injected into the aquifer can be readily estimated. Then, one estimate of the natural groundwater flow velocity can be taken to be the average distance the bromide pulse was injected divided by the time to the peak bromide concentration, and another estimate can be taken to be the difference between the distance of the leading and trailing edges of the pulse divided by the 12-h arrival time difference between the arrivals of the bromide tracer and the aquifer water (indicated by an increase in sulfate and a drop in chloride concentrations).

When radial flow was assumed during the injection, it was found that these estimates differed by about 50%, with the estimate from the time to peak bromide arrival being 50% larger than the estimate from the difference in the arrival times. To reconcile these differences, the assumption of radial flow was relaxed to allow the distance of penetration during injection to have a dependence on volume injected raised to an arbitrary power, with this arbitrary power treated as an adjustable parameter. Radial flow implies that the radial distance to the leading edge of an injection is proportional to the square root of volume injected (or time, if the flow rate is constant), consistent with Equation 2, where $Q\tau$ = volume injected. For nonradial flow, or more general flow, Equation 2 can be written as:

$$L = \left(\frac{Q\tau}{\pi b\phi} \right)^{1/x} \quad \text{Equation 3}$$

where x is called the “flow dimension,” and is equal to 2 for radial flow, 1 for linear flow, and 3 for spherical flow. Allowing the flow dimension to be variable in this case is permissible because the tracer being observed in the well during the drift period must be coming from almost directly upgradient of the well in a relatively narrow azimuthal range. If a disproportionate amount of the injection flow is pushed out of the well in this direction, then the flow dimension for this direction will tend more toward 1 (linear), and if it is pushed more in other directions, the flow dimension will tend more toward 3 (spherical). The natural flow velocities for the two different estimates (i.e., from the bromide peak time and the difference in bromide and aquifer water arrival times) were found to be in agreement when the flow dimension in the upgradient direction during the injection was taken to be 1.28. In this case, both estimates were approximately 1.2 m/d when it was assumed that the aquifer flow porosity was 0.2. This flow-velocity estimate has a weak dependence on the assumed flow porosity (i.e., the flow dimension yielding equal flow-velocity estimates would differ slightly if a different flow porosity were assumed, and the resulting estimate of flow velocity would be slightly different). Note that a flow dimension of 1.28 implies that a

disproportionate amount of flow was directed upgradient during the injection and chase periods of the test (more so than under ideal radial flow conditions).

The estimate of 1.2 m/d is in good agreement with the estimate of 1.1 m/d from the dilution tracer test at R-28 (Table 2.0-1). Thus, at both R-42 and R-28, the groundwater flow-velocity estimates obtained from the push-pull tests were in excellent agreement with velocity estimates from the dilution tracer tests, which lends confidence to the velocity estimates obtained from dilution tracer tests in other wells, where independent groundwater flow-velocity estimates were not available.

3.3 Evidence for Natural Attenuation of Cr(VI)

The push-pull tracer tests also provided a cursory assessment of the potential for natural attenuation of Cr(VI) in the regional aquifer in the vicinity of the Cr(VI) plume. This assessment was made by comparing the return arrivals of conservative anions in the aquifer with those of Cr(VI) during both the drift and pumping periods of the tracer tests as the treated water used for the tracer and chase injections was replaced with aquifer water. The anions were analyzed by ion chromatography in the same samples that were collected for tracers using EPA Method 300 on the Dionex DX-600 system (i.e., they were analyzed along with the bromide tracer). Total chromium was analyzed by inductively coupled plasma–mass spectrometry (ICP-MS) using EPA Method 200.8 on a Perkin Elmer NexION system. All the chromium measured was assumed to be Cr(VI) because of the very low solubility of Cr(III) at the pH of the groundwaters. Figure 3.3-1 shows that the return of SO_4^{2-} essentially mirrored the return of Cr(VI) into R-42 after net withdrawal started in this test. This result indicates that there was no natural attenuation at all of Cr(VI) at this location.

In contrast, Figure 3.3-2 shows a more complicated result at R-28. First, it is apparent that both Cr(VI) and NO_3^- are delayed in their arrivals into R-28 during the drift period of the test relative to SO_4^{2-} , with the delay being greater for NO_3^- than for Cr(VI). These delays hint at the possibility of biologically induced reduction in the aquifer upgradient of R-28 because it is known that NO_3^- is biogeochemically reduced before Cr(VI). This result was consistently observed during biostimulation laboratory studies conducted at Los Alamos (Attachment 7 of this compendium, “Bioremediation Bench-Scale Studies”), and it has also been reported in the literature (Rivett et al 2008). On the other hand, if reduction is abiotic (for instance, by reduced iron phases), it is often the case that Cr(VI) is reduced more rapidly than NO_3^- , and this does not appear to have been the case at R-28. Note that once pumping began, Cr(VI) concentrations rose rapidly and essentially in concert with SO_4^{2-} concentrations, and even NO_3^- rose in concentration and approached its pretest value at about the same rate as the SO_4^{2-} and Cr(VI). This observation suggests a reduction process that was probably quite close to the wellbore where the water residence times were too short under pumping conditions to allow a slow reduction reaction to occur. Biotic reduction is known to be a relatively slow process compared with abiotic reduction. Other indications that reduction of NO_3^- and Cr(VI) was likely biotic include the fact that once net pumping began, the concentrations of NO_3^- repeatedly dipped and tended to coincide with increases in NO_2^- concentrations, whereas Cr(VI) concentrations tended to remain more stable and close to their pretest concentrations in R-28 (Figure 3.3-2). However, Cr(VI) concentrations did decrease quite dramatically (along with NO_3^- concentrations) at around 210 h after the end of the chase; the cause of this decrease is potentially attributable to a pumping interruption that occurred at about this time without a corresponding interruption in the autosampler. During the pumping interruption, the residence time of the water in the sampling lines was much longer than during the rest of the test, so it seems plausible that the dramatic reduction of both Cr(VI) and NO_3^- may have occurred in the sampling lines at this time. The drops in NO_3^- concentrations with corresponding increases in NO_2^- concentrations definitely suggest a biotic process. A final piece of evidence suggesting that biotic reduction was occurring are the measurements of total organic carbon that were obtained throughout the test, which are shown in Figure 3.3-3 along with a similar plot during

the pumping phase of the R-42 push-pull test. The concentrations of organic carbon in both tests seem to be higher (red dots in Figure 3.3-3) when the NO_3^- concentrations drop and the NO_2^- concentrations rise, which is consistent with a greater-than-natural amount of microbial activity in both tests during these time periods.

Although it is tempting to attribute observations of apparent Cr(VI) and NO_3^- attenuation at R-28 to natural processes, the combined consideration of all the observations discussed above suggests that the attenuation was likely the result of some unnatural microbial activity near R-28. The source of this unnatural microbial activity is unknown, although video logs of R-28 have frequently shown significant biofilm buildup in the lower portion of the screened interval. Given that there was no attempt to rid the well of these biofilms before the test (for instance, by a well workover), it is possible that these films may have partially or completely broken loose during the tracer and chase injections and been pushed into the aquifer or filter pack where they induced reducing conditions that influenced the behavior of the groundwater constituents. It is also possible that there may have been some residual organic material in the tanks that were used for the tracer and chase water that biostimulated natural microbes in the vicinity of the well. The higher total organic carbon concentrations during the production phase of the test could reflect the presence of some of this material. Although a definitive explanation cannot be provided, the balance of the evidence suggests that caution should be taken in attributing any of the observed delays in Cr(VI) and NO_3^- arrivals at R-28 to natural attenuation processes. It also appears that the most possible credit one could take for Cr(VI) attenuation would be a retardation factor of about 1.3 to 1.4 based on the relative arrival times of the SO_4^{2-} and Cr(VI) during the drift phase of the R-28 test.

4.0 GEOCHEMICAL TRANSIENTS DURING PUMPING TESTS OF R-42, R-28, R-62, AND R-43 S1

R-42 and R-28 were each pumped for an extended period of time in 2013 to observe hydraulic responses within the Cr(VI) plume area to help constrain groundwater flow modeling of the area. During both of these tests, geochemical trends in the pumping wells were observed, which provided valuable insights into contaminant distributions and transport processes in the plume. After pumping, the wells were allowed to recover, and geochemical trends were again observed during the recovery period. In 2014, after dilution tracer testing in wells R-62 and R-43 S1, relatively long-term pump tests of these wells were conducted. These tests also offered the opportunity to observe geochemical trends in the pumping wells during both pumping and recovery of the wells.

In all cases samples were collected manually by Los Alamos Environmental Programs Field Services personnel or by their subcontractors. Anions (other than HCO_3^-) were analyzed by ion chromatography using EPA Method 300 on a Dionex DX-600 system. Samples for major cations and trace metals were filtered in the field with a 0.45-mm filter and then acidified for preservation using high-purity nitric acid. Major cations were analyzed by inductively coupled plasma–optical emission spectroscopy (ICP-OES) using EPA Method 200.7 on a Perkin Elmer Optima 2100 DV. High-purity nitric acid (Fisher Trace Metal Grade) was used for sample and calibration standard preparation. An internal standard (scandium) was added to both samples and standards to correct for matrix effects, which can result in varying sample introduction rates. Some samples were diluted before analysis to minimize matrix effects as well as allow the analytes of interest to remain within the linear dynamic range of the calibration. SPEX CertiPrep Instrument Check Standard 3 was used to check the accuracy of the multi-element calibrations. Typical ICP-OES parameters were 1350 W forward power, 15 L/min plasma gas flow, 0.2 L/min auxiliary flow; and 0.8 L/min nebulizer flow. Trace metals and other minor elements, including chromium, were analyzed by ICP-MS using EPA Method 200.8 on a Perkin Elmer NexION system. As with the ICP-OES samples, high-purity nitric acid (Fisher Trace Metal Grade) was used for sample and calibration standard preparation. Internal standards (yttrium, bismuth, and indium) were added to both samples and standards to correct for matrix effects, which can result in varying sample introduction rates. Some samples were

diluted before analysis to minimize matrix effects as well as allow the analytes of interest to remain within the linear dynamic range of the calibration. The National Institute of Standards and Technology (NIST) Standard Reference Material (SRM) 1640a, "Trace Elements in Natural Water," was used to check the accuracy of the multi-element calibrations. Typical ICP-MS parameters were 1600 W forward power, 18 L/min plasma gas flow, 1.2 L/min auxiliary flow; and 0.9 L/min nebulizer flow. The HCO_3^- concentrations were calculated from total alkalinity measurements made using a H_2SO_4 titration procedure and also from the measured pH of the samples. All of the samples had pH values indicating that CO_3^{2-} concentrations were negligible relative to HCO_3^- concentrations.

Figure 4.0-1 shows the responses of key constituents to pumping of R-42 (at 7–8 gallons per minute [gpm]), including the responses after pumping was stopped and the well was allowed to recover. Although the data are a bit noisy and there were some issues identified with charge balance (see Figure 4.0-2), the responses suggest that most constituents remained relatively constant in concentration throughout the test, with the primary exception being Cr(VI), which decreased in concentration when the well was pumped and then "rebounded" when pumping stopped. Note that the apparent rises in SO_4^{2-} and Cl^- concentrations just before the end of pumping, and then their subsequent drops after pumping ended, which are contrary to the Cr(VI) trends, are believed to be an analytical artifact that is explained in the Figure 4.0-2 caption. The rates of Cr(VI) decrease and rebound appear to be similar, which is a bit surprising because the well was pumped at 7–8 gpm and there was essentially only natural flow during the rebound period. Normally one might expect a more rapid change to occur under forced-gradient conditions than under natural-gradient conditions, but the fact that the decreases and increases occurred over similar time scales suggests that the capture zone induced by pumping may have been skewed in a direction different from that of the direction of the natural gradient. That is, the majority of the drop in chromium concentration during pumping may have occurred because water was disproportionately drawn into the well from a direction that was different than the direction of the natural gradient, and then when the pumping was stopped, the upgradient water containing chromium at pretest concentrations rather quickly reverted to dominating the geochemistry in the well. Of course, in three dimensions the situation could be considerably more complex, with the possibility that different horizontal layers were contributing different amounts of flow having different chromium concentrations to the well under pumping and nonpumping conditions. Dual-porosity effects (diffusion into and out of lower permeability zones) were also considered as a possible cause of the chromium concentration transients, and this is discussed below.

The fact that chromium was effectively the only constituent that dropped in concentration during pumping at R-42 and recovered after pumping ended is intriguing. Cr(VI) has frequently been associated with both SO_4^{2-} and Cl^- , and to a lesser degree with NO_3^- , in the plume area, yet none of these other constituents changed in concentration during the test as Cr(VI) did. In fact, SO_4^{2-} and Cl^- seemed to trend the opposite of Cr(VI) just before and after pumping ended, but this is believed to be an analytical artifact that is explained in the Figure 4.0-2 caption. CrO_4^{2-} and SO_4^{2-} are believed to have originated mainly from the same source location (the cooling tower operations at the head of Sandia Canyon), and these two anions have the same size, charge, and electronic structure, suggesting that they should have very similar diffusion properties. If both anions were completely nonreactive, then one would expect that if dual-porosity behavior affected one, it would affect the other in the same manner. There are two possible explanations for the differences in the behavior of these two anions during the R-42 pumping/recovery test. The first is that the CrO_4^{2-} had a different spatial distribution in the aquifer at the start of the pump test than all the other constituents, and it therefore had a different response to pumping. The CrO_4^{2-} and SO_4^{2-} were not simultaneously released at the head of Sandia Canyon; available data suggest that releases of SO_4^{2-} preceded CrO_4^{2-} by a few years, and furthermore, CrO_4^{2-} would have been attenuated to some degree by reduction processes known to be occurring in the wetland near the source and also potentially in the Cerros del Rio basalts within the vadose zone underlying Sandia and Mortandad Canyons. Thus,

the spatial distribution of CrO_4^- and SO_4^- should not be expected to be identical in the regional aquifer, even though they appear to be quite well correlated with each other across the site. It is certainly possible that the SO_4^- is more widely and evenly distributed across the aquifer than Cr(VI), which could explain why it did not change in concentration during the R-42 test whereas Cr(VI) did. The same would hold true for Cl^- and NO_3^- , although these constituents come from different and more widely distributed sources than either Cr(VI) or SO_4^- .

The second possible explanation for the difference in the behavior of the Cr(VI) relative to the other anions during the R-42 pump/recovery test is that the Cr(VI) is actually being partially reduced in secondary porosity (strata with lower or negligible groundwater flow rates), whereas the other anions are not reacting in the secondary porosity. In this case, it is possible that the primary and secondary porosity could be in disequilibrium with respect to Cr(VI) (i.e., the concentrations in the primary and secondary porosity are not equal, with a net flux of Cr(VI) from the primary to the secondary porosity), while they are essentially in equilibrium for the other anions. If there was a decrease in concentration in the primary porosity induced by pumping, then it is conceivable that the Cr(VI) concentration could decrease while the concentrations of the other anions do not decrease as much because of back-diffusion out of the secondary porosity. This back-diffusion could occur for the other anions while net diffusion into the secondary porosity is still occurring for the Cr(VI) because of the irreversible loss of Cr(VI) in the secondary porosity due to reduction. Then, when the pumping stopped and concentrations increased again in the primary porosity, the Cr(VI) would slowly recover in concentration, whereas the other anions would already be very close to their original concentrations because of the smoothing effect of the back diffusion process during pumping. However, this explanation can account only for smaller relative decreases in the concentrations of the other anions relative to Cr(VI) during pumping; it cannot explain a lack of any change in concentrations of the other anions. In fact, it was not possible to reproduce the observed responses during the R-42 test using a dual-porosity model if it was assumed that Cr(VI) and all the other anions have the same spatial distribution in the aquifer when pumping began. The concentrations of the other anions inevitably decreased along with the Cr(VI) concentrations, even if the relative drop was less for the other anions.

Another possibility related to dual-porosity behavior that wasn't explicitly considered via modeling is that the relative contributions of flows from the primary and secondary porosity in R-42 could have changed to favor a greater contribution from the secondary porosity as the test progressed. This could occur, for instance, if flow boundaries were encountered in primary porosity layers during the test, resulting in a reduction in flow within these layers at later times. If this occurred but no such boundaries were encountered in secondary porosity layers, then the secondary porosity layers would contribute more relative flow to the well during the latter part of the pumping period. In this case, if the concentration of Cr(VI) is lower in the secondary porosity because of an irreversible reduction process, then the observed concentration of Cr(VI) would decrease during pumping. However, if the concentrations of the other anions had effectively equilibrated in the primary and secondary porosities before pumping, their concentrations would remain stable during pumping. This explanation does not rely on back diffusion to sustain the concentrations of the other anions. This dual-permeability scenario seems inherently more plausible than the dual-porosity explanation of the previous paragraph, (where the secondary porosity was assumed to essentially be not flowing). However, the hydraulic drawdown in R-42 remained remarkably stable during the pump test, which argues against any significant flow boundaries being encountered in primary porosity layers.

Figure 4.0-3 shows the responses of key constituents to pumping of R-28 (at 27–28 gpm), including the responses after pumping was stopped and the well was allowed to recover. The responses are qualitatively very similar to what was observed in the R-42 pump test, and the possible explanations for the observations are therefore the same. As at R-42, it is apparent that when R-28 is pumped, it draws water that gets progressively lower in Cr(VI) concentrations while all other constituents remain effectively

unchanged, and then the process is reversed when pumping stops. The volumetric pumping rate at R-28 was approximately 4 times higher than at R-42, which makes the similarity in the relative rates of decline and recovery of Cr(VI) concentrations during the pumping and recovery periods seem even more surprising than at R-42. However, upon further reflection, the dilution-tracer-test results (Table 2.0-1) suggest that the natural groundwater flow velocity at R-28 is as much as 8 times higher than at R-42, so the rate of rebound at R-28 is perhaps not surprising at all. As at R-42, the best explanation for the observed behavior is that water was disproportionately drawn into the well from a direction that was different than the direction of the natural gradient during pumping, and when the pumping was stopped, the upgradient water containing Cr(VI) at pretest concentrations rather quickly reverted to dominating the geochemistry in the well.

Figure 4.0-4 shows the responses of key constituents to pumping of R-62 (at 1–1.5 gpm), including the responses after pumping was stopped and the well was allowed to recover. The notable features of the responses are that (1) all major cations and anions, including Cr(VI)/CrO₄⁼, responded with very rapid changes in concentrations (cations and HCO₃⁻ decreasing; anions and Cr(VI) increasing) despite the fact that the pumping rate was less than 2 gpm, and (2) when pumping stopped, none of the anions or cations reverted to their pretest concentrations immediately but remained relatively unchanged for quite a while. However, sampling several months later (not shown) indicated that all species eventually reverted to approximately their pretest concentrations. The interpretation for these observations is that the groundwater chemistry at R-62 before pumping reflected the influence of the infiltration of a vadose-zone water that was relatively high in HCO₃⁻ concentrations (because of intimate contact with atmospheric CO₂ in the unsaturated zone) and low in other anion concentrations but slightly higher in cation concentrations. The pumping apparently rapidly swept the signature of this water out of the well and replaced it with water that was presumably more representative of the regional aquifer in the immediate vicinity of R-62, which had much higher anion concentrations, lower HCO₃⁻ concentrations, and slightly lower major cation concentrations than the pretest water in the well. When the pumping stopped, the rebound in concentrations to pretest levels was clearly delayed, presumably because of the very low ambient flow velocity in the well, as estimated from the dilution tracer test (Table 2.0-1). However, the slow rebound may also reflect that the infiltration rate in the vicinity of the well is quite low, so it takes a while to re-establish the signature of this water. While it is possible that the observed changes in water chemistry simply reflect a spatial distribution of aquifer water chemistry in the immediate vicinity of R-62 that was perturbed by pumping, the inference of a pretest infiltration water chemistry signature is based on the observation that it was only the anions (and all of the major ones) that changed significantly when the well was pumped, with a very prominent change in HCO₃⁻ concentrations. Elsewhere in the aquifer when there are differences in major ion chemistry between monitoring wells, the major anions and cations tend to increase or decrease together and the HCO₃⁻ concentrations remain more or less very similar across the aquifer. The gradual reversion to pretest concentrations of major anions suggests that the vadose-zone infiltration signature eventually re-established itself, although clearly it takes much more time than the time to sweep the signature out of the well, even by a relatively low pumping rate.

Figure 4.0-5 shows the responses of key constituents to pumping of R-43 S1 (at 7–8 gpm), including the responses after pumping was stopped and the well was allowed to recover. The notable features of this test are (1) the concentrations of the anions CrO₄⁼, SO₄⁼, and to a lesser degree Cl⁻, all increased almost immediately upon pumping and then decreased immediately when pumping stopped, (2) the concentration of NO₃⁻ remained almost unchanged throughout the test, and (3) cation concentrations also increased slightly with the major anions, in contrast to what was observed at R-62. These observations are consistent with a contaminant flow pathway that contains both CrO₄⁼ and SO₄⁼ being relatively close to R-43 S1 and being “drawn into” the well when pumping starts. Then, as soon as pumping stops, the concentrations rebound quickly to pretest levels, which is consistent with the very high natural flow velocity in this well that was estimated from the dilution tracer test (Table 2.0-1). The long-term trends for

CrO_4^- and SO_4^- concentrations in R-43 S1 are increasing, which suggests that the flow pathway(s) responsible for the rapid increases with pumping may also be responsible for the more gradual long-term increasing trends when the well is not pumped.

Collectively, the geochemical transients observed during pumping of R-42, R-28, R-62, and R-43 S1 paint a complicated picture of the Cr(VI) plume, with both contaminants and major ions being quite heterogeneously distributed in the vicinity of the wells. The Cr(VI) concentrations in both R-42 and R-28 tended to decrease with pumping and slowly rebounded when pumping stopped, although no other constituents besides Cr(VI) changed significantly in concentration as a result of pumping. In contrast, R-62 and R-43 S1 both showed rapid increases in Cr(VI) and anion concentrations in response to pumping, although cation concentrations increased significantly only in R-43 S1, and HCO_3^- concentrations actually decreased in R-62. Also, the reversion back to prepumping concentrations was slow in R-62 and fast in R-43 S1, which presumably reflects the slow and fast natural flow rates, respectively, moving through these two wells. The rapid increases in Cr(VI) concentrations in R-62 and R-43 S1 that occurred essentially in unison with increases in anion concentrations are consistent with very little natural attenuation of Cr(VI) in the regional aquifer at these locations. If there were some natural attenuation, one might expect a delay in the arrival of Cr(VI) relative to the anions after pumping was initiated, but this was not observed. Also, the ratio of pumping to prepumping concentrations of Cr(VI) was generally equal to or larger than this ratio for other anions in R-62 and R-43 S1, even after correcting for background anion concentrations. The implication is that it does not appear there was any less of a relative rise in Cr(VI) concentrations during pumping than there was for other anions, which suggests that there was not a rate-limited Cr(VI) reduction process occurring during pumping.

Dual-porosity or dual-permeability transport behavior involving diffusion between fast and slow-moving water in the regional aquifer is not strongly implicated by the geochemical transients observed in response to pumping of the four wells. This does not mean that diffusive mass transfer processes do not occur in the aquifer, but it suggests that their influence was overshadowed by the influence of advective transport processes and also the spatial distributions of contaminants and other constituents in the aquifer, at least in the vicinity of the four wells that were pumped. The lack of any significant changes in concentrations of virtually all chemical constituents other than Cr(VI) at R-42 and R-28 might potentially be explained by some reduction of Cr(VI) in secondary porosity coupled with a gradual increase in the relative contribution of flow from secondary porosity in these wells during the pump tests, but it is not consistent with diffusion by itself between flowing porosity and nonflowing porosity. The responses to pumping in these wells, and also in R-62 and R-43 S1, collectively suggest a much greater likelihood that the geochemical transients were primarily the result of different spatial distributions of contaminants and constituents in the vicinity of the wells in relation to the permeability distribution around these wells. In the case of R-42 and R-28, these combined factors resulted in drawing in water with lower concentrations of Cr(VI) during pumping, and in the case of R-62 and R-43 S1, the combined factors resulted in drawing in water with higher concentrations of Cr(VI) during pumping.

5.0 PUSH-DRIFT TEST WITH HIGH PH SOLUTION IN R-42

In 2016, a test was conducted in well R-42 in which approximately 15,000 gal. of a solution of potable water containing 0.005 M NaHCO_3 + 0.005 M Na_2CO_3 was injected and then allowed to drift with the natural flow in the vicinity of the well while passive samples (no net pumping) were taken to observe the return of aquifer water into the well. The solution had a well-buffered pH of approximately 9.8, which was intended to induce desorption of any CrO_4^- that might be adsorbed by anion exchange onto aquifer mineral surfaces. Such anionic adsorption of CrO_4^- has been observed in systems with significant amounts of clay, iron oxide, or iron oxyhydroxide surfaces present (Zachara et al. 1987; Zachara et al. 1989) because these minerals tend to have positively charged surfaces at pHs less than about 7 to 8.

However, at higher pHs, there is virtually no anionic adsorption. Because the pH of the regional aquifer is typically around 8, it was thought that there may be some CrO_4^- adsorbed onto surfaces that would be liberated by the high-pH solution. Such liberation should be observable in a push-drift test, as it should result in early returns of Cr(VI) relative to returns of other aquifer constituents that have significantly lower concentrations in the potable water than the aquifer water, and/or it should result in higher concentrations of Cr(VI) relative to pretest concentrations once the aquifer water returns. Note that reversible anionic adsorption of Cr(VI) would not technically be considered a natural attenuation process according to EPA criteria because it does not result in permanent removal of Cr(VI) from the aquifer in the manner that a reduction process would. However, such adsorption would increase the potential for reduction processes to occur because Cr(VI) would presumably be preferentially adsorbed to iron-bearing phases that can transfer electrons to Cr(VI) and reduce it to Cr(III).

One of the immediate observations during the injection of the buffered potable water was that the permeability in the vicinity of the R-42 wellbore steadily decreased as the injection proceeded. In fact, original plans had called for 21,000 gal. of buffered potable water to be injected into R-42, but the permeability had decreased so significantly after 15,000 gal. that it was decided to not mix up and attempt to inject the last 6000 gal. The permeability reduction can be attributed to calcite precipitation in the aquifer, as the dramatic increase in pH and alkalinity resulting from the buffered water would have caused the calcite (CaCO_3) saturation index to be exceeded by orders of magnitude anywhere the injected water mixed with aquifer water, which had a Ca^{2+} concentration of about 50 mg/L and is essentially already saturated with respect to calcite. This possibility was recognized before the start of the test, but pessimistic calculations had suggested that the mass of calcite generated should not cause more than a 0.1% porosity reduction in the local aquifer. In hindsight, it is apparent that even though the porosity reduction was not expected to be large, its effect would be felt mainly in narrow pore throats that have a large influence on permeability because precipitating calcite should tend to become lodged in the narrowest pore throats. This observation of permeability reduction was considered fortuitous because it factored directly into plans for using sodium dithionite as a chemical reductant in a pilot-scale remediation test in Mortandad canyon. Sodium dithionite is typically buffered to a high pH using Na_2CO_3 to counter its tendency to degrade more rapidly under neutral or acidic conditions, but the observations at R-42 made it clear that carbonate or bicarbonate should not be used to buffer a dithionite solution in the regional aquifer beneath Mortandad canyon.

The concentrations of Cr(VI) and various anions in passive samples collected from R-42 in the aftermath of the injection are shown in Figure 5.0-1. Figure 5.0-2 shows the corresponding histories of pH, alkalinity, and sodium and calcium concentrations in the well during this same time period. The analytical methods used for the analytes were the same as those described in previous sections. However, the pH and alkalinity in this test were both measured in the field using a YSI 650XLM sonde and meter system for pH, and a Hach digital titrator with H_2SO_4 titration to a bromocresol green-methyl red indicator endpoint for alkalinity (Hach Method 8203). In Figure 5.0-1, it is apparent that there was initially a high concentration of all constituents, which were present in about the same concentration ratios as in pretest R-42 water. Figure 5.0-2 also shows that the initial pH and alkalinity were relatively low. Thus, for unknown reasons, it appears that a significant fraction of R-42 water remained in the wellbore even after the injection of approximately 15,000 gal. of potable water. The reason for this anomalous behavior is a mystery, although it is speculated that it may have been a result of the permeability reduction in the well during injection occurring disproportionately in the higher-permeability lithologic layers, which caused the less permeable layers to have greater contributions to flow as the injection proceeded. It is possible that some layers that received very little of the buffered solution because of their low natural permeability may have contributed an unnaturally large fraction of the flow in the immediate aftermath of the injection because of the reduction in permeability in all other layers. This would have resulted in an early R-42 geochemical signature. However, the surging of water in the well resulting from each sampling event, which involved

first pumping water to the surface and then returning the water to the aquifer in a closed flow loop, may have quickly dislodged enough calcite that layer flow rates quickly reverted to being more proportional to the original layer permeabilities. This would have resulted in the R-42 water signature being quickly replaced by the potable water signature, consistent with what is shown in both Figures 5.0-1 and 5.0-2.

Despite the initial puzzling transient, it is apparent that the potable water quickly dominated the geochemistry of the well and was gradually flushed out of the vicinity of R-42 and replaced with aquifer water to allow observation of the relative rates and magnitudes of the return of the various groundwater constituents. From Figure 5.0-2, it is apparent that the Cr(VI) returned into the well coincidentally with the conservative anions SO_4^- and Cl^- and it did not rise to a concentration that was higher than before the test, leading to the conclusion that there was no appreciable desorption of CrO_4^- that occurred as a result of the injection of the high pH solution. It is also apparent that there must have been no adsorption or reduction of Cr(VI) as the aquifer water drifted back into the well because there is no delay in the return of the Cr(VI) relative to the other anions. Thus, the push-drift test results suggest that there was virtually no prior adsorption of Cr(VI) onto aquifer surfaces nor any natural attenuation of Cr(VI) by reduction as the aquifer water drifted back into the well.

Figure 5.0-2 shows that the pH and alkalinity, as well as the Na^+ and Ca^{2+} concentrations, in the well remained perturbed much longer than the anion concentrations, which can be attributed to the slow dissolution of calcite as aquifer water replaced the potable water. The presence of an excess of calcite tended to keep the pH, alkalinity and Na^+ concentrations artificially high while the Ca^{2+} concentrations remained low. However, it is apparent that the pH and alkalinity in R-42 were trending toward their pretest values after nearly a year of drift (Figure 5.0-2), which is consistent with the calcite being slowly dissolved out of the system.

6.0 CROSS-HOLE TRACER TESTING

A cross-hole tracer test was initiated in 2016 with tracer injections into three separate locations, CrPZ-2a, CrPZ-2b, and R-28, with the primary anticipated recovery location being CrEX-3. CrPZ-2a and CrPZ-2b are nested piezometers with screened intervals at two different depths in the same borehole located about 125 m from CrEX-3. CrEX-3 started pumping after the injections in CrPZ-2a and CrPZ-2b but before the injection into R-28. The tracer identities, dates of injections, and volumes of both traced water and chase water are listed in Table 6.0-1. Each injection included two nonreactive tracers that had diffusion coefficients that differed by a factor of about 3 or 4, with the intent being to look for evidence of diffusion between primary and secondary porosity in the cross-hole tracer responses (and potentially in the injection wells also). The tracer and chase water in all cases was potable water, which offered a contrast in major ion chemistry with the resident aquifer water in CrPZ-2a and R-28 in the same way that there was a contrast in the 2014 push-pull tests with the R-42 and R-28 aquifer water and in the 2016 push-drift test with the R-42 aquifer water. CrPZ-2b had very low pretest concentrations of all major ions and Cr(VI), and it therefore did not have much contrast in chemistry with potable water. An integral part of the CrPZ-2a and R-28 tracer tests was observing the disappearance of the potable water signature and the return of the aquifer water in these wells so that information could be obtained on how rapidly the tracer solution was drifting out of the vicinity of the injection well/interval and also on potential natural attenuation of the Cr(VI) as it drifted back into the well. There were difficulties in sampling CrPZ-2b, so only sparse data were obtained from this location, although the low concentrations of major ions and Cr(VI) in this well would have precluded obtaining good information on natural attenuation of Cr(VI) anyway.

All samples were collected manually at both the injection wells and observation wells (CrEX-1 and CrEX-3). Tracers and major ions were analyzed by methods already described in preceding sections of this report. The ReO_4^- tracer injected into CrPZ-2a was analyzed by analysis of rhenium by ICP-MS using an adaptation of EPA Method 200.8 on a Perkin Elmer NexION system.

The injections into CrPZ-2a and CrPZ-2b had the added bonus of providing valuable information on anisotropy in hydraulic conductivity in the aquifer in the vicinity of CrPZ-2a/b because pressure responses were obtained in each piezometer screen as each injection was occurring. Although a formal analysis of the pressure responses is not provided in this report, the data are presented to facilitate such an analysis. In the remainder of this section, the hydraulic responses observed during the CrPZ-2a and CrPZ-2b injections are presented first, followed by the tracer and geochemistry data from the injection wells after the injections, and then finally the cross-hole tracer responses are presented. Of the three tracer injections, only one resulted in a cross-hole response (to date): the tracers injected into CrPZ-2a appeared in CrEX-3. None of the tracers ever appeared in CrEX-1, which was also sampled at regular intervals.

6.1 Pressure Responses during Injections into CrPZ-2a and CrPZ-2b

Figure 6.1-1 shows the pressure responses in CrPZ-2a, CrPZ-2b, and R-28 during the injection into CrPZ-2b. Note that the injection into CrPZ-2b was done in increments over several days because tanks were pumped out during the days (using a sump pump) and then allowed to gravity-drain into the night until they were empty. By the next morning the downhole pressures had reverted to being very close to their starting values before injection began. Note that the heads during injection cycles gradually increased as the injections progressed, because adjustments were made to allow for a faster injection rate (at least up until the last few injection cycles, where the rate was stabilized at around 15 gpm). Pressure data for R-28 was recorded only during the last four cycles. It is apparent that the pressure response in PZ-2a, for which the bottom of the filter pack is only about 15 ft above the top of the filter pack for PZ-2b, is very muted compared with the pressure elevation in PZ-2b. Although a formal analysis of this vertical pressure response was not conducted, it is intuitively obvious that the response implies a large horizontal-to-vertical anisotropy ratio of hydraulic conductivity in the aquifer (with a much greater horizontal hydraulic conductivity). The magnitude of the horizontal pressure response in R-28 over 100 m away from CrPZ-2b is about one-third of the vertical response in CrPZ-2a less than 5 m above CrPZ-2b. The injection rate into CrPZ-2b was about 15 gpm (not metered, but based on tank draining rates) during the last few cycles shown in Figure 6.1-2.

Figure 6.1-2 shows the pressure responses in CrPZ-2a, CrPZ-2b, and R-28 during the injection into CrPZ-2a. The upper half of Figure 6.1-2 shows the response to a very sharp pressure spike in CrPZ-2a that occurred when the tracer injection first started, before it was realized that CrPZ-2a was not capable of taking the initial flow rate. The spike amounted to nearly 230 ft of water-level elevation in CrPZ-2a, yet resulted in less than 1 ft of elevation in CrPZ-2b and less than 0.1 ft in R-28. The lower half of Figure 6.1-3 shows that over the remainder of the injection cycles in CrPZ-2a (which were controlled to keep the water-level rise in CrPZ-2b to no more than 100 ft), the water-level rise in CrPZ-2b never exceeded about 0.4–0.5 ft, and the rises in R-28 were nearly imperceptible (a fraction of 0.1 ft). There is again an implication of a very small vertical hydraulic conductivity, given that the system was able to sustain a head difference of nearly 100 ft between the two piezometer filter packs during the injection at about 3 gpm into CrPZ-2a.

To provide additional perspective, Figure 6.1-3 shows the pressure responses in CrPZ-2a, CrPZ-2b, and R-28 when CrEX-3 was pumped for about 12 h at around 40 gpm on June 24, 2016. Although the water-level scale for CrPZ-2a in this figure is offset from that of R-28 and CrPZ-2b, the magnitude of the scales are the same, and hence the drawdowns are directly comparable. Of interest is that despite the fact that

CrEX-3 is completed entirely in the Puye Formation that CrPZ-2a is completed in (it is not completed at all in the Miocene pumiceous unit that CrPZ-2b is completed in), the drawdown in CrPZ-2b is almost the same as it is for CrPZ-2a. This implies that there must be considerably more vertical hydraulic communication across the intervals/layers that separate CrPZ-2a from CrPZ-2b somewhere in the aquifer between CrPZ-2 and CrEX-3 than there is in the immediate vicinity of CrPZ-2. The greater drawdown in R-28 relative to CrPZ-2a and CrPZ-2b shown in Figure 6.1-3 is to be expected because R-28 is much closer to CrEX-3 than the piezometers are.

6.2 Tracer and Geochemistry Observations in Injection Wells

During the injections into CrPZ-2a and CrPZ-2b, sampling was conducted in the piezometer in which injection was not occurring to determine if there was any cross-communication of the tracers between the two injection intervals. Sampling in CrPZ-2a was done at the beginning of the chase phase in CrPZ-2b, and sampling in CrPZ-2b was done at the beginning of the tracer injection phase in CrPZ-2a. CrPZ-2a was sampled first, and when this was done the tracers that had been injected into CrPZ-2b were found at essentially their injection concentrations. This was rather surprising (especially considering the very large water-level differences between the piezometers observed during injections), so a flow circulation loop was established in CrPZ-2a that mimicked the configuration during the borehole dilution tests, allowing samples to be collected over time so that the concentration of the CrPZ-2b tracers could be monitored in CrPZ-2a as the chase took place in CrPZ-2b. Figure 6.2-1 shows the decline in bromide tracer concentration [plotted as $\ln(C/C_0)$, where C_0 is the initial concentration, vs time] observed after the chase started, and it is quite apparent that there is a very rapid tracer response between the two piezometers. An analysis analogous to that for a borehole dilution test was conducted, and it was estimated that the flushing rate of CrPZ-2a as a result of injecting chase water into CrPZ-2b was approximately 5.4 gal. per h. A similar circulation flow loop was established in CrPZ-2b at the start of the CrPZ-2a tracer injection, and Figure 6.2-2 shows the rise in rhenium concentration in CrPZ-2b resulting from the sodium perrhenate injection into CrPZ-2a. Figure 6.2-2 includes a second plot that shows $\ln(1-C/C_0)$, where C_0 is the final concentration, vs time, which is a plot suitable for a dilution-tracer-test interpretation. The flushing rate of the CrPZ-2b interval was estimated to be about 9 gal. per h. Given the injection flow rates of approximately 15 gpm into CrPZ-2b and about 3 gpm into CrPZ-2a at the times of the sample collections, the estimated fractions of tracer mass that ended up in the interval that was not being injected into was about 0.005 for the tracers injected into CrPZ-2b and nearly 0.05 for the tracers injected into CrPZ-2a. Thus, nearly 5% of the tracer mass injected into CrPZ-2a is estimated to have ended up in CrPZ-2b, whereas only about 0.5% of the tracer mass injected into CrPZ-2b ended up in CrPZ-2a. The rapid tracer responses between the two nested piezometers, along with the very large water-level differences that were sustained during the injections, suggests that the flow pathway(s) between the two piezometer filter packs had a very small dead volume. It seems logical that the pathway or pathways were located directly within the wellbore completion, and they likely represent some sort of a leakage pathway in the completion rather than natural flow pathways through the aquifer stratigraphy.

Despite the fact that a non-natural leak pathway within the wellbore completion is inferred from the cross-piezometer tracer responses, the flow-rate estimates between the piezometers can be used to obtain crude bounding estimates of vertical hydraulic conductivity over the ~5 m of intervening lithologic layers between the two filter packs. To do this, one has to assume a cross-sectional area that the flow is occurring in, and in this case a very conservative cross-sectional area of 1 m² is assumed, which effectively corresponds to a cylinder of about 1 m diameter centered around the well. Using the observed head differences and flow-rate estimates, an estimate of hydraulic conductivity can be obtained from

$$K = \frac{QL}{A\Delta H} \quad \text{Equation 4}$$

where K = hydraulic conductivity, m/day

Q = flow rate between intervals, m³/d

A = assumed cross-sectional area, m²

ΔH = head difference between intervals, m

L = distance between filter packs.

Using Equation 4, the estimate for CrPZ-2b to CrPZ-2a is about 0.27 m/d, and the estimate for CrPZ-2a to CrPZ-2b is about 0.12 m/d. Both of these estimates should be considered conservative upper bounds because it is strongly suspected that the flow between the intervals was not along natural flow pathways through the aquifer layers and also because the cross-sectional area sustaining the head difference was assumed to be very small. Even so, these estimates are a factor of 10 to 25 smaller than the horizontal hydraulic conductivity estimates of about 3 m/d obtained from analysis of pump tests in the vicinity of CrPZ-2 (Attachment 9 of this compendium, "Groundwater Modeling Status Report"). If a more realistic cross-sectional area of 10 m² is considered, which corresponds to a cylinder of about 3.5 m in diameter centered around the CrPZ-2 wellbore, then the horizontal to vertical hydraulic conductivity ratio would exceed 100.

Figure 6.2-3 shows the concentration histories of the tracers in CrPZ-2a, and Figure 6.2-4 shows the concentration histories of major anions and Cr(VI) in CrPZ-2a after the injection of the tracer water and chase water into the well. It is apparent from Figure 6.2-4 that the tracer concentrations went through an initial dip and then a subsequent rise, which undoubtedly corresponded to the chase water flowing through the well, followed by the tracer solution. The early high tracer concentrations in the aftermath of the injection must reflect that some of the tracer solution lingered in the vicinity of the wellbore during the injection of chase water. The apparent slow rate of tracer solution drifting back into the wellbore is in contrast to the rapid response of the CrPZ-2a tracers in CrEX-3, approximately 125 m away (see section 6.3). It can be surmised that some of the injected tracer mass must have been pushed into relatively fast-flowing pathways that are not reflected in the tracer responses in CrPZ-2a, whereas a significant amount of mass remained in slower-moving pathways that resulted in the CrPZ-2 observations.

Figure 6.2-4 shows that the return of major ions and Cr(VI) into CrPZ-2a began to occur long before tracer concentrations started to rise in the well. It also appears that the concentrations of major ions in the aquifer had leveled off to about 70–80% of their pretest concentrations at the time the tracer concentrations began to rise. This behavior suggests that most of the tracer signal in the piezometer once the tracer concentrations began to rise was the result of flow pathways that were contributing no more than about 20–30% or so of the flow into the piezometer, with the other 70–80% of the flow being aquifer water. An observation like this suggests that perhaps only a few relatively high-permeability flow layers contributed most of the flow through the screened interval, with the tracer that was injected into these layers being rapidly swept away and replaced with aquifer water while the tracer solution injected into other layers moved only very slowly. The tracer injected into the rapidly flowing layers may be the tracer that appeared rapidly in CrEX-3, ~125 m away.

Unlike the observations during the push-drift test in R-42, it appears that the Cr(VI) lagged slightly behind the major anions in returning into the CrPZ-2a wellbore. In fact, it appears that even NO₃⁻ lagged slightly behind the other major ions. These observations suggest that there may have been a small amount of natural attenuation of both Cr(VI) and NO₃⁻ occurring in the vicinity of CrPZ-2a as aquifer water drifted back into the wellbore. One potential explanation for the contrasting observations at CrPZ-2a and R-42 is that the pretest concentrations of Cr(VI) were much lower in CrPZ-2a than R-42, and therefore the reduction/attenuation capacity of the aquifer sediments with respect to Cr(VI) (and presumably NO₃⁻ as well) were already exhausted in the vicinity of R-42 but not at CrPZ-2a. However, another potential

explanation is that there may have been a considerable amount of bentonite in the CrPZ-2a well completion that had not been properly developed out of the piezometer before the test, and this bentonite could have reduced some of the Cr(VI) when the aquifer water flowed back into the piezometer. Laboratory testing had indicated that the bentonite the drillers used in the piezometer completions was quite effective at reducing Cr(VI), and it was also known that CrPZ-2a and -2b both had substantial amounts of bentonite in their screened intervals after completion. The bentonite had not been intentionally introduced to the intervals, but rather it had been intended to provide hydraulic isolation between the two nested piezometers. However, it was very apparent from video logs, and the limited development of the piezometers, that some bentonite had made its way into the screened intervals. Additionally, it is possible that the “leakage” of the seal between the two intervals observed during the injections into each piezometer (see above) may have mobilized more bentonite from between the two intervals. The large volume injections would have then pushed any suspended bentonite into the surrounding filter pack and aquifer, where it may have been quite efficient at reducing Cr(VI) as it flowed back into the well. The situation would have been much more noticeable for CrPZ-2a because the injection into this piezometer occurred after the injection into CrPZ-2b (hence there was greater potential for bentonite being mobilized into CrPZ-2a than into CrPZ-2b) and also because the pretest Cr(VI) concentrations in CrPZ-2b were already near background concentrations.

Figure 6.2-5 shows the concentrations of major anions, including the bromide tracer, and Cr(VI) in CrPZ-2b after the tracer and chase injection into this piezometer. CrPZ-2b was sampled much less frequently than CrPZ-2a because of the failure of a Bennett pump, which necessitated laborious bailing of the piezometer to obtain samples, and it was not sampled at all after Nov. 17, 2016. The samples indicated no notable increases in concentrations of any aquifer constituents through November 17, 2016. The bromide tracer showed a gradual increase in concentrations through early September, followed by a levelling off of concentrations in September and October, 2017, and then the last two samples taken on October 27 and November 17 showed dramatic increases in bromide concentrations, which suggested that the main tracer pulse may have been just beginning to appear in the piezometer when the sampling ended. The last sample also showed a slightly higher Cr(VI) concentration than previous samples, suggesting that it is possible that Cr(VI) from the aquifer was beginning to appear in the piezometer. However, there was such a small contrast between the aquifer water and the potable water in concentrations of all major ions and Cr(VI) that the results of Figure 6.2-5 are not considered conclusive with respect to any information on natural attenuation of Cr(VI). Also, it was difficult to assess how representative the bailed samples from CrPZ-2b were, and also how consistent they were from one sampling event to the next. Certainly they were not considered as representative as samples from CrPZ-2a, which were collected by pumping the piezometer for some time and then obtaining a sample.

Figure 6.2-6 shows the concentrations of tracers in R-28 after the injection of the tracers into this well. It is apparent that the tracer concentrations peaked rather quickly and then also declined rather quickly, indicating a high natural flow velocity through this well, which is consistent with the results of the dilution and push-pull tracer tests conducted in these wells in 2014. No analysis was attempted to estimate the flow velocity in R-28 during the 2016 tracer test, mainly because CrEX-3, only 54 m away from R-28, was being pumped at 40 gpm during almost the entire time period that tracers were observed in R-28. Thus, any estimate of flow velocity could not be considered an estimate of natural flow velocity.

Figure 6.2-7 shows the concentrations of major anions and Cr(VI) in R-28 after the tracer injection was completed. It is apparent that the return of aquifer water was essentially complete after about 2 mo, which is also about the amount of time it took for tracers to be almost completely flushed out of the borehole. In contrast to CrPZ-2a, which reached 70–80% of the concentrations of major ions in the aquifer water before tracer concentration even began to rise, the tracer concentrations in R-28 peaked before the concentrations of major ions reached even 40% of their concentrations in the pretest aquifer water. This would seem to indicate that the flow through R-28 was more uniformly distributed across the screened

interval than in CrPZ-2a (with less predominance of a few high-permeability layers, as seemed to be implied at CrPZ-2a), although it may also indicate that tracer was almost entirely injected into a few high-permeability layers and hardly any tracer mass made it into layers of lower permeability. It is also apparent from Figure 6.2-7 that Cr(VI) does not appear to be delayed much in its arrival in R-28 relative to the other major anions in the aquifer, suggesting very little natural attenuation of the Cr(VI). However, interestingly enough, the concentration of Cr(VI) actually increased to a factor of 1.4 over its pretest level. The concentrations of other anions also appear to have increased to higher than their pretest levels, although the increase is more like a factor of 1.1 to 1.2. The best explanation for this behavior would seem to be that the nearby pumping of CrEX-3 drew some water through R-28 that was higher in all anions, and especially higher in Cr(VI) concentrations, relative to the water that was flowing through the well under natural gradient conditions before CrEX-3 starting pumping. It can be presumed that this water came from north of R-28 because CrEX-3 is almost due south of R-28. It is noteworthy that when R-28 was pumped in 2013, the concentrations of Cr(VI) decreased, but when CrEX-3 was pumped and R-28 was not pumped in 2016, the Cr(VI) concentrations in R-28 increased. Given that Cr(VI) concentrations in CrEX-3 are only about half of what they are in R-28, it seems reasonable that more water from the general direction of CrEX-3 (to the south) may have been drawn into R-28 when it was pumped in 2013. However, it is still unclear why the concentrations of other anions in R-28 did not similarly decrease with pumping in 2013 because concentrations of other anions are also lower in the vicinity of CrEX-3 than at R-28. It is also noteworthy that despite the apparent influence of CrEX-3 on concentration trends in R-28, the tracers that were injected into R-28 never showed up at CrEX-3.

6.3 Cross-Hole Tracer Response at CrEX-3

CrEX-3 was pumped at about 40 gpm from September 12, 2016, to November 7, 2016, although pumping was not entirely continuous. Almost immediately after pumping began on September 12, 2016, the tracers that were injected into CrPZ-2a appeared in samples collected in CrEX-3. Figure 6.3-1 shows the normalized responses (concentrations divided by injection mass) of the tracers 2,7-NDS and ReO_4^- in CrEX-3 during the pumping period. The tracers that were injected into CrPZ-2b and R-28 never appeared in CrEX-3. After pumping stopped on November 7, 2016, samples were collected from CrEX-3 only very infrequently, as shown in Figure 6.3-2. Interestingly, the 2,7-NDS seems to have disappeared entirely from the samples collected after pumping stopped, although the ReO_4^- concentrations persisted at relatively elevated levels. Even before pumping stopped, it appeared that the 2,7-NDS concentrations were trending downward at an unnaturally high rate, and there were a few samples that had much lower concentrations than other samples in the overall trend. These results seem to imply that the 2,7-NDS may have experienced some degradation in the aquifer at later times during the test. It should be noted that laboratory experiments a couple of months in duration were previously conducted in which it was shown that 2,7-NDS did not degrade in aqueous solutions that were in contact with aquifer sediments, so apparently the degradation inferred from the tracer test data was a result of processes that occurred over longer time scales than in the laboratory experiments or possibly because of biogeochemical processes that did not occur in the laboratory experiments. It should also be noted that ReO_4^- concentrations measured in samples collected after pumping stopped (Figure 6.3-2) cannot be directly compared with those collected during pumping because pumping causes a significant amount of dilution to occur in the wellbore by drawing in a considerable amount of water that does not contain tracer. In contrast, when a well is pumped for just a short time to collect a sample, there is less dilution because the tracer has presumably flowed around the well during the period before sampling, and the water drawn in therefore has more tracer in it. The large spikes in tracer concentrations upon resumption of pumping between September 12 and November 7, 2016 (Figure 6.3-1) reflect this behavior; during the periods of no pumping that immediately precede the first samples collected upon resumption of pumping, the tracers moved around CrEX-3 and the first samples collected therefore contained much higher concentrations of the tracers.

The tracer responses shown in Figure 6.3-1 are qualitatively consistent with a small amount of dual-porosity behavior occurring in the aquifer between CrPZ-2a and CrEX-3. The normalized concentrations of 2,7-NDS are initially higher than those of ReO_4^- and then after both tracers have peaked in concentration, the normalized concentrations of ReO_4^- tend to be higher than those of 2,7-NDS. Also, when there was a pumping interruption during the early part of the test when concentrations were rising, the normalized concentration of 2,7-NDS was higher on resumption of pumping than ReO_4^- , and when there was a long interruption during the latter part of the test, the normalized concentration of ReO_4^- jumped more on resumption of pumping than 2,7-NDS. These observations are all consistent with the 2,7-NDS, which is the larger molecule and therefore the less-diffusive tracer, experiencing less diffusion out of primary porosity into secondary porosity during the test. In this case, the 2,7-NDS will have higher normalized concentrations before peak concentrations are reached because more ReO_4^- will have diffused into secondary porosity between CrPZ-2a and CrEX-3. However, after concentrations have peaked, the ReO_4^- should have higher concentrations because there will be more of this tracer back-diffusing out of secondary porosity into primary porosity. The apparent degradation of 2,7-NDS muddles the comparison of the tracer responses at late times because it is not possible to know whether the lower normalized concentrations of 2,7-NDS relative to ReO_4^- are due to dual-porosity effects or to degradation of the 2,7-NDS. However, the fact that normalized concentrations of 2,7-NDS are higher than ReO_4^- during the early part of the breakthrough curves seems to provide rather solid evidence of dual-porosity behavior because the degradation of 2,7-NDS could only cause its concentrations to be artificially lowered.

The semi-analytical RELAP model (Reimus et al. 2003) was used to obtain a crude match to the tracer breakthrough curves of Figure 6.3-1, and the result is shown in Figure 6.3-3. RELAP does not account for tracer drift during the pumping interruptions, so the spikes in concentration after each pumping interruption are not duplicated, and the match is not great in the tail of the breakthrough curves when there was an extended pumping interruption. The mean residence time and Peclet number (distance between wells divided by longitudinal dispersivity) that provided the best match to the data are not highly meaningful because the test involved significant periods of both natural flow and pumping, which would have caused these parameters to be different at different times during the test. The key feature that was matched was the difference between the concentrations of the two tracers, which was much more prominent than in either of the push-pull tracer tests conducted with multiple tracers in 2014. The main parameter adjusted to match these differences was the thickness of the flowing layer assumed to be responsible for the transport of the tracers between CrPZ-2a and CrEX-3. In this case, a planar geometry was assumed with a flowing layer sandwiched between two layers of infinite thickness that had a much lower hydraulic conductivity; an infinite thickness was assumed because the tracer concentrations in the lower conductivity layers should have been effectively zero over much of the distance between the two wells (this is in stark contrast to a push-pull test, where tracers would be expected to be present in many layers because the tracers are pulled back into the injection well). Both the flowing and nonflowing layers were assumed to have porosities of 0.25, and the diffusion coefficients in the layers were assumed to be $5 \times 10^{-6} \text{ cm}^2/\text{s}$ for the ReO_4^- and $1.5 \times 10^{-6} \text{ cm}^2/\text{s}$ for the 2,7-NDS (the same as what was assumed for the 2014 push-pull tracer tests). The results are more sensitive to the porosities assumed than the diffusion coefficients, although it is important to assume an appropriate difference between the tracer diffusion coefficients because there would be no difference in the modeled tracer responses if it weren't for the differences in diffusion coefficients. Figure 6.3-4 shows the match of the model to the differences between the two normalized tracer concentrations, and it is apparent that the model matches the differences during the peak and early tailing portion of the test quite well. The differences are underpredicted by the model at later times, but it is suspected that much of this discrepancy is due to the apparent degradation of the 2,7-NDS, which seemed to be reflected in the later samples. The model match shown in Figure 6.3-4 corresponds to a flowing layer thickness of 100 cm, or 1 m, which is somewhat larger than the flowing layer thickness of 20 cm deduced from the interpretation of the push-pull test in R-28 in 2014, but it is the same as the lower bound of 100 cm deduced from the push-pull test in R-42.

Irrespective of the dual-porosity implications of the tracer responses of Figure 6.3-1, the fact that the tracers from CrPZ-2a appeared so quickly after pumping of CrEX-3 began was quite surprising. It was also quite surprising that the recovery of tracers was estimated to be in the 35–40% range at the end of the pumping period, which seems quite remarkable given that concentrations of tracers in CrPZ-2a were still increasing long after the pumping period ended. The implication is that a fraction of the injected tracer mass was pushed into high-velocity flow pathways that transported the tracer rapidly toward CrEX-3 while much of the injected tracer mass remained in lower-velocity flow pathways in the vicinity of CrPZ-2a, lingering upgradient of CrPZ-2a and drifting into the piezometer very slowly. It seems evident that the tracers must have been present quite close to CrEX-3 when pumping began, which implies that they moved the majority of the 125 m between CrPZ-2a and CrEX-3 during the 84 d after the chase water injection into CrPZ-2a was finished and the pumping of CrEX-3 began. If flow during the injection into CrPZ-2a and during pumping from CrEX-3 were both ideally radial over the length of the screens in each well, then the calculated distance that the leading edge of the tracer would have been injected into the formation from CrPZ-2a (assuming a flow porosity of 0.2) would have been about 6.3 m, and the distance that pumping of CrEX-3 would have reached into the aquifer in the 3–4 d of pumping that it took for the tracer concentrations to dramatically increase would have been about 10.5 m. Thus, only about 17 of the 125 m between the injection and pumping points could be attributed to the flows induced by injection and pumping, and the remaining ~108 m would have to be attributed to natural flow during the 84 d of no injection or pumping. Of course, flow could have been very heterogeneously distributed around the boreholes rather than as ideal radial flow, and the possibility certainly exists that distances of penetration into or withdrawal from the aquifer could have been much greater than those suggested by the radial flow calculations, particularly if flow occurred primarily through a few very thin lithologic layers. However, even if a transport distance of only 90 m is assumed for the natural-gradient flow period of 84 d, the average flow velocity for the tracer mass that was recovered in CrEX-3 during this period would have been on the order of 1 m/d, which is about a factor of 30 higher than the velocity inferred from the dilution tracer test in CrPZ-2a. This result suggests that the relatively high natural flow velocity responsible for the tracer movement between CrPZ-2a and CrEX-3 either did not directly intersect the CrPZ-2a wellbore (but was somewhere close by), or it occurred over only a small fraction of the screened interval thickness. In the latter case, the dilution-tracer-test results would have been misleading because the volumetric flow rate out of the screened interval during the dilution test was attributed to the entire length of the screen instead of just a small fraction of the interval thickness. Either way, the combination of the rapid response of a large fraction of the CrPZ-2a tracer mass in CrEX-3 coupled with the lingering of tracers in the vicinity of CrPZ-2a long after concentrations peaked in CrEX-3 suggest the presence of zones or layers in the aquifer that have large contrasts in hydraulic conductivity.

The fact that tracers injected into CrPZ-2b and R-28 never showed up in CrEX-3 during its pumping period is also quite informative. The lack of a tracer response from CrPZ-2b suggests that CrEX-3 is drawing water mainly from the Puye Formation in which CrPZ-2a is completed; there is apparently much less water coming from the Miocene pumiceous unit in which CrPZ-2b is completed. Nevertheless, the hydraulic responses to pumping of CrEX-3 shown in Figure 6.1-3 indicate that there is almost as strong of a hydraulic communication between CrEX-3 and CrPZ-2b as there is between CrEX-3 and CrPZ-2a. This result underscores how hydraulic responses do not necessarily translate directly to an indication of good flow communication between wells. The lack of a response of the tracers injected into R-28 at CrEX-3 is a strong indication that the natural flow direction at R-28 is oriented from west-to-east or possibly even to the northeast, certainly not toward the south and unlikely toward the southeast. It is also a confirmation that the natural flow velocity must be quite fast, as the dilution tracer test and the push-pull tracer test in R-28 suggested. If the velocity weren't very rapid, the 40-gpm pumping rate from CrEX-3 would have likely drawn in at least some of the tracers from R-28, especially considering that about 30,000 gal. of tracer plus chase solution was injected into R-28, and CrEX-3 was pumping the entire time of the injection. As previously mentioned, the fact that chromium and major anion concentrations increased

above their pretest concentrations in R-28 during pumping of CrEX-3 (Figure 6.2-7) suggests that the pumping of CrEX-3 likely drew water into R-28 from north of R-28 (toward CrEX-3) even if the pumping wasn't strong enough to draw the tracers injected into R-28 all the way over to CrEX-3.

The tracers injected into CrPZ-2a and CrPZ-2b were also analyzed in selected samples collected from R-28 after the R-28 injection, and none of these tracers ever appeared in R-28 at concentrations above detection limits. This result is perhaps not surprising given that pumping of CrEX-3 would be expected to draw tracers away from R-28, although CrEX-3 was pumped for less than 2 mo. The very rapid response of the tracers injected into CrPZ-2a in CrEX-3 almost as soon as CrEX-3 started pumping suggests that the natural flow direction, at least in the Puye Formation in the vicinity of these wells, must be almost directly from CrPZ-2a to CrEX-3. One cannot necessarily assume that the same flow direction applies to the Miocene pumiceous unit at this location, although it would be logical to do so.

The cross-hole tracer test results have important implications for the capture zone created by pumping of CrEX-3 at ~40 gpm. It is apparent that CrEX-3 is able to effectively "reach" very far upgradient in the direction of CrPZ-2 in the Puye Formation, although the term "reach" is perhaps misleading given that it is really the natural flow that brings water to CrEX-3 more so than it is the pumping of CrEX-3 that draws water from this direction. The fact that the Cr(VI) concentrations observed in CrEX-3 are somewhat higher than in CrPZ-2a (about 170 mg/L vs about 120–140 mg/L in CrPZ-2a) indicates that the balance of the water being drawn into CrEX-3 has a slightly higher average Cr(VI) concentration than in CrPZ-2a, and the logical assumption is that this is reflecting the influence of water being drawn from the general direction of R-28 where Cr(VI) concentrations are notably higher. However, the CrEX-3 capture zone apparently does not include R-28, and the inference is that the high Cr(VI) concentrations and fluxes in the vicinity of R-28, and presumably anything to the north of R-28, are moving further downgradient without being captured at all by current extraction wells.

7.0 OVERALL CONCLUSIONS FROM 2013-2017 FIELD TESTING

There are several conclusions that can be drawn from the field testing that was conducted from 2013 to 2017 in the chromium plume area beneath Mortandad and Sandia Canyons. These are listed below:

Dilution tracer tests have indicated that there is a wide range of natural groundwater flow velocities in the regional aquifer within the chromium plume. R-28 and R-43 S1 stand out as having exceptionally high flow velocities intersecting their wellbores, with R-28 being on the order of 1 m/d (after accounting for an assumed flow porosity of 0.2) and R-43 S1 being on the order of 2 m/d. SCI-2 also has a relatively high flow velocity, which suggests that it may be part of a flow pathway in the vadose zone that is transporting Cr(VI) to the regional aquifer [given that it also contains relatively high concentrations of Cr(VI)]. The groundwater flow velocity estimates in the regional aquifer wells can be used to calculate local Cr(VI) fluxes in the aquifer, and these estimates suggest that fluxes at R-28 and R-43 S1 are considerably higher than at R-42, where the highest chromium concentrations are measured in the aquifer.

Push-drift testing in 2014 and cross-hole tracer testing in 2016–2017 yielded groundwater flow-velocity estimates that were generally consistent with dilution-tracer-test estimates in selected boreholes. However, one exception was that the cross-hole response of tracers injected into CrPZ-2a (at CrEX-3) suggested a natural groundwater flow velocity that was at least an order of magnitude larger than the dilution-tracer-test estimate in CrPZ-2a.

There is conflicting evidence for dual-porosity behavior in the regional aquifer, although intuitively it seems logical that some diffusion between fast-flowing pathways and slower-flowing pathways (or nonflowing zones) must be occurring. The push-pull test in R-28 and the cross-hole tracer responses between CrPZ-2a and CrEX-3 both showed evidence of diffusion between primary and secondary

porosity, but the push-pull test in R-42 and the responses to long-term pumping of R-42 and R-28 did not show definitive evidence of diffusive mass transfer. The best explanation for these observations is that the relative thicknesses or cross-sectional areas of rapidly flowing porosity varies considerably in different places in the regional aquifer. Wherever the cross-sectional area of primary porosity is rather small (i.e., thin layers transmitting a large amount of flow), a dual-porosity signature is seen, but wherever it is rather large, a dual-porosity signature is not observed (at least over the time scales of the observations).

There appears to be little evidence of natural attenuation of Cr(VI) in the regional aquifer [in this case, natural attenuation is considered to be reduction of Cr(VI) to Cr(III), not anion exchange of CrO_4^- , although evidence of the latter was also looked for]. Responses of Cr(VI) relative to major anions in push-pull, push-drift, and pumping tests in R-42, R-62, and R-43 S1, including a push-drift test at R-42 in which an alkaline solution was injected to induce CrO_4^- desorption, indicated no natural attenuation of Cr(VI), and there was also no evidence of natural attenuation during the drift period in R-28 after the cross-hole tracer injection into this well. A small amount of Cr(VI) natural attenuation was suggested in the vicinity of CrPZ-2a during the drift period after the cross-hole tracer injection into this piezometer, and natural attenuation was also suggested during the drift period in the 2014 R-28 push-pull test. Also, the drops in Cr(VI) concentrations during long-term pumping of R-42 and R-28 while concentrations of all other major anions remained essentially constant suggest that there is a possibility that Cr(VI) may be getting partially reduced in secondary porosity in the aquifer. However, the more likely explanation for the observations at R-42 and R-28 is that Cr(VI) is spatially distributed in the aquifer differently than the major anions that it is typically associated with. Also, a possible explanation for the apparent natural attenuation of Cr(VI) at CrPZ-2a is that the bentonite known to be present in the completion of this piezometer may have caused some reduction of Cr(VI). Collectively, the observations suggest that natural attenuation of Cr(VI) in the regional aquifer is quite minimal, if it occurs at all. These results are consistent with other lines of evidence from laboratory batch and column studies, from observed spatial and temporal trends of chromium isotopes, and from long-term trends in monitoring wells at the periphery of the chromium plume, all of which indicate little evidence of natural attenuation of Cr(VI) in the regional aquifer. The first two of these other lines of evidence are discussed in Attachment 6 of this compendium, "Characterization of Natural Attenuation," and Attachment 2 of this compendium, "Isotopic Signatures of Hexavalent Chromium in the Regional Aquifer: Evaluation of Natural Attenuation", and the third line of evidence is presented in a series of plots in Appendix B of this report.

The rapid cross-hole tracer responses at CrEX-3 resulting from the tracers injected into CrPZ-2a, coupled with the lingering of the same tracers in CrPZ-2a long after they reached peak concentrations in CrEX-3, suggests a large contrast in hydraulic conductivity of various zones or lithologic layers near CrPZ-2a. Apparently, a significant fraction of the tracer mass was pushed into high-conductivity flow pathways that carried the tracers almost all the way to CrEX-3 in the 84 d after injection and before CrEX-3 began pumping. However, a significant fraction of tracer mass was also apparently pushed upgradient in low-conductivity zones or pathways near CrPZ-2a in which the tracers lingered for many months before slowly drifting back into the piezometer.

The lack of responses of tracers from CrPZ-2b and R-28 in CrEX-3 during the cross-hole tracer test suggests that CrEX-3 is not drawing much water from the Miocene pumiceous unit in the direction of CrPZ-2, and it also indicates that R-28 does not appear to be within the CrEX-3 capture zone when the latter is pumped at ~40 gpm. Thus, it is evident that the high Cr(VI) concentrations and fluxes in the vicinity of R-28 are not being captured at all by current extraction wells (CrEX-1 or CrEX-3).

The field test results collectively indicate that the Cr(VI) plume is quite heterogeneous, both hydrologically and geochemically. The Cr(VI) concentrations in the plume apparently have a complex spatial distribution that is suggested not only by the distribution of observed concentrations in monitoring wells, but also by the responses of Cr(VI) concentrations to pumping at various locations in the aquifer, including different

responses relative to anions that are known to have vadose-zone sources and are typically correlated with Cr(VI). Tracer tests indicate that natural groundwater flow velocities in the aquifer vary widely from location to location, with evidence of relatively high-velocity zones/layers located in or near certain wells but not in or near other wells. Diffusion between faster- and slower-flowing groundwater must be occurring in the aquifer, but it is inconsistently observed in field tests, suggesting it probably occurs over different time and distance scales in different locations within the aquifer. Thicknesses of strata with higher groundwater flow rates were estimated to range from 20 cm to at least 100 cm based on differences (or lack thereof) in responses of nonreactive tracers with different diffusion coefficients in tracer tests. If natural attenuation of Cr(VI) is occurring at all in the aquifer, the available evidence suggests that it is not having a large effect on plume migration/evolution, and it is most likely occurring in secondary porosity where groundwater flow velocities are lower.

8.0 REFERENCES AND MAP DATA SOURCES

8.1 References

The following reference list includes documents cited in this report.

- Drost, W., D. Klotz, A. Koch, H. Moser, F. Neumaier, and W. Raurert. "Point Dilution Methods of Investigating Ground Water Flow by Means of Radisotopes," *Water Resources Research*, Vol. 4(1), 125–146 (1968).
- Nimmo, J.R., K.S. Perkins, P.E. Rose, J.P. Rousseau, B.R. Orr, B.V. Twining, and S.R. Anderson. "Kilometer-Scale Rapid Transport of Naphthalene Sulfonate Tracer in the Unsaturated Zone at the Idaho National Engineering and Environmental Laboratory," *Vadose Zone Journal*, Vol. 1, No. 1, pp. 89–101 (2002).
- Palmer, C. D. "Borehole dilution tests in the vicinity of an extraction well," *Journal of Hydrology*, Vol. 146, 245–266 (1993).
- Reimus, P., G. Pohll, T. Mihevc, J. Chapman, M. Haga, B. Lyles, S. Kosinski, R. Niswonger, and P. Sanders. "Testing and Parameterizing a Conceptual Model for Solute Transport in a Fractured Granite Using Multiple Tracers in a Forced-Gradient Test," *Water Resources Research*, Vol. 39, No. 12, pp. SBH 14-1 to SBH 14-15 (2003).
- Reimus, P. W., T. J. Callahan, S. D. Ware, M. J. Haga, and D. A. Counce. "Matrix Diffusion Coefficients in Volcanic Rocks at the Nevada Test Site: Influence of Matrix Porosity, Matrix Permeability, and Fracture Coating Minerals," *Journal of Contaminant Hydrology*, Vol. 93, pp 85–95 (2007).
- Rivett, M. O, S. R. Buss, P. Morgan, J. W.N. Smith, and C. D. Bemment. "Nitrate attenuation in groundwater: a review of biogeochemical controlling processes," *Water Research*, Vol. 42, 4215–4232 (2008).
- Rose, P.E., W.R. Benoit, and P.M. Kilbourn. "The Application of the Polyaromatic Sulfonates as Tracers in Geothermal Reservoirs," *Geothermics*, Vol. 30, No. 6, pp. 617–640 (2001).
- Zachara, J.M., D.C. Girvin, R.L Schmidt, and C.T. Resch. "Chromate Adsorption on Amorphous Iron Oxyhydroxide in the Presence of Major Groundwater Ions," *Environmental Science and Technology*, Vol. 21, 589–594 (1987).
- Zachara J. M., Ainsworth C. C., Cowan C. E., and Resch C. T. "Adsorption of chromate by subsurface soil horizons," *Soil Science Society of America Journal*, Vol. 53, 364–373 (1989).

8.2 Map Data Sources

Hillshade; Los Alamos National Laboratory, ER-ES, As published;
\\slip\gis\Data\HYP\LiDAR\2014\Bare_Earth\BareEarth_DEM_Mosaic.gdb; 2014.

Point features; As published; EIM data pull; 2017.

Chromium plume > 50 ppb; Los Alamos National Laboratory, ER-ES, As published;
\\slip\gis\GIS\Projects\13-Projects\13-0065\shp\chromium_plume_2.shp; 2018.

Structures; Los Alamos National Laboratory, KSL Site Support Services, Planning, Locating and Mapping Section; 06 January 2004; as published 29 November 2010.

Drainage channel; Los Alamos National Laboratory, ER-ES, As published, GIS projects folder;
\\slip\gis\GIS\Projects\15-Projects\15-0080\project_data.gdb\correct_drainage; 2017.

Technical Area Boundaries; Los Alamos National Laboratory, Site Planning & Project Initiation Group, Infrastructure Planning Office; September 2007; as published 13 August 2010.

Unpaved roads; Los Alamos National Laboratory, ER-ES, As published, GIS projects folder;
\\slip\gis\GIS\Projects\14-Projects\14-0062\project_data.gdb\digitized_site_features\digitized_roads; 2017.

U.S. Census populated places; Los Alamos National Laboratory, ER-ES, As published, GIS projects folder; \\slip\gis\GIS\Data\ESRI\census\places.sdc\places; 2018.

Rivers; Los Alamos National Laboratory, ER-ES, As published, GIS projects folder;
\\slip\gis\GIS\Data\ESRI\hydro\rivers.sdc\rivers; 2018.

Paved Road Arcs; Los Alamos National Laboratory, FWO Site Support Services, Planning, Locating and Mapping Section; 06 January 2004; as published 29 November 2010.

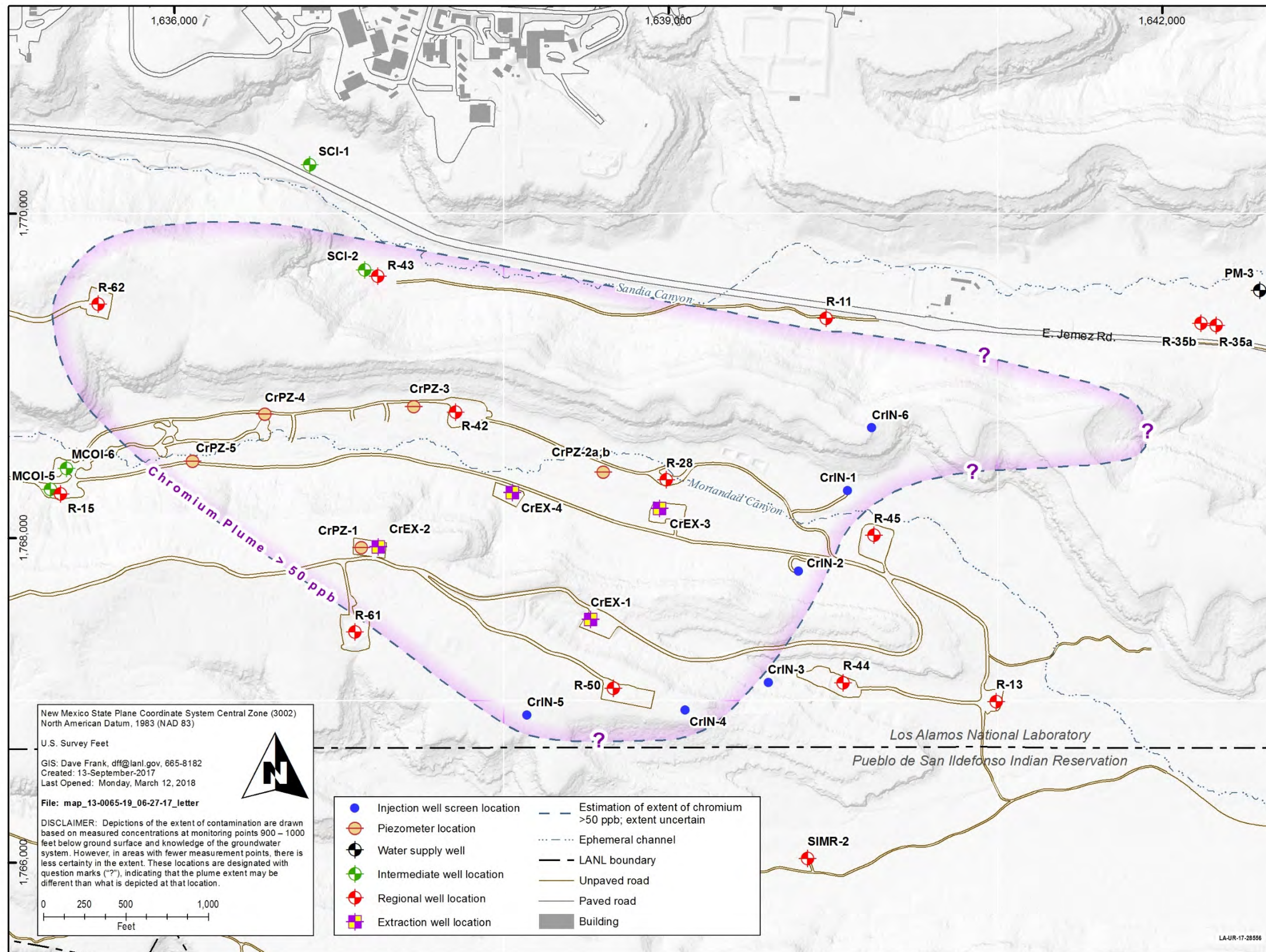


Figure 1.0-1 Map of the Cr(VI) plume area

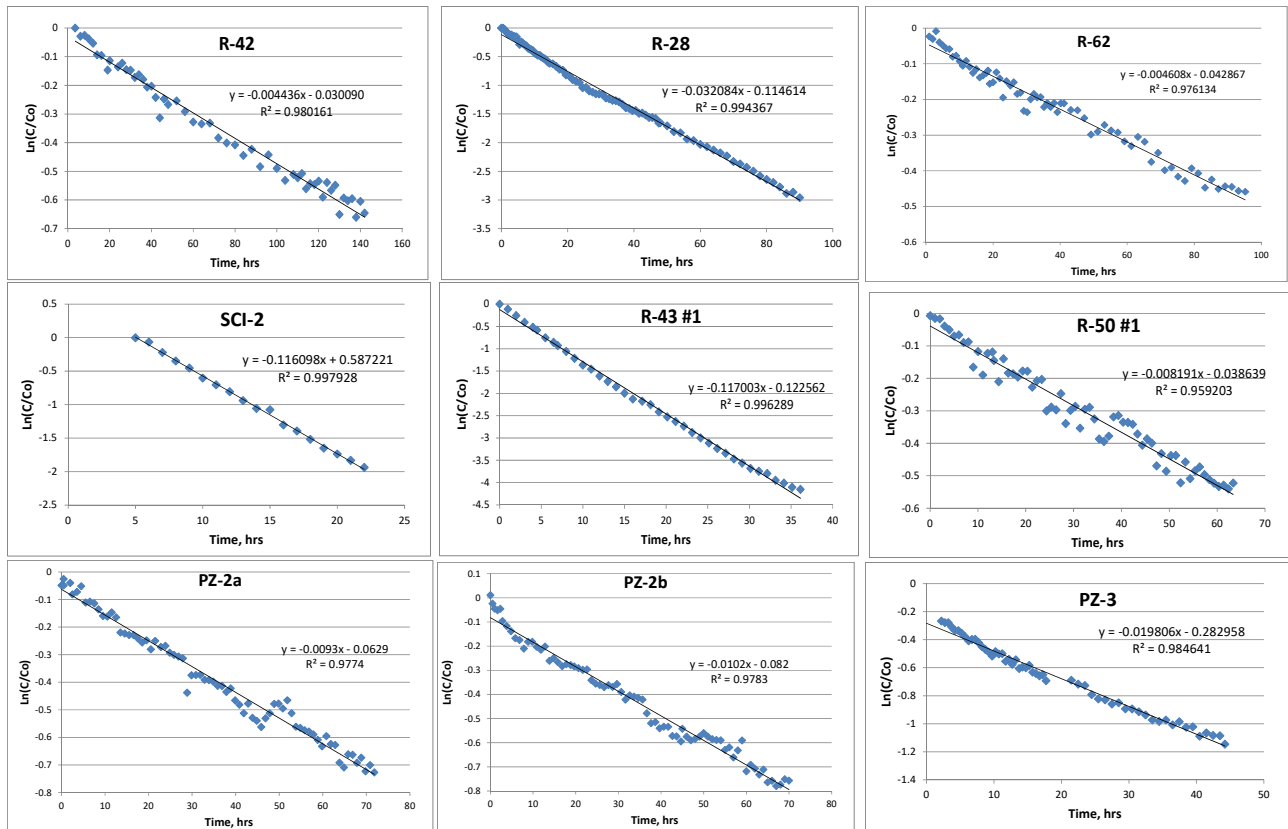


Figure 2.0-2 Tracer concentration histories ($\ln C/C_o$ vs time) in each dilution tracer test (plots intended to show quality of the test data)

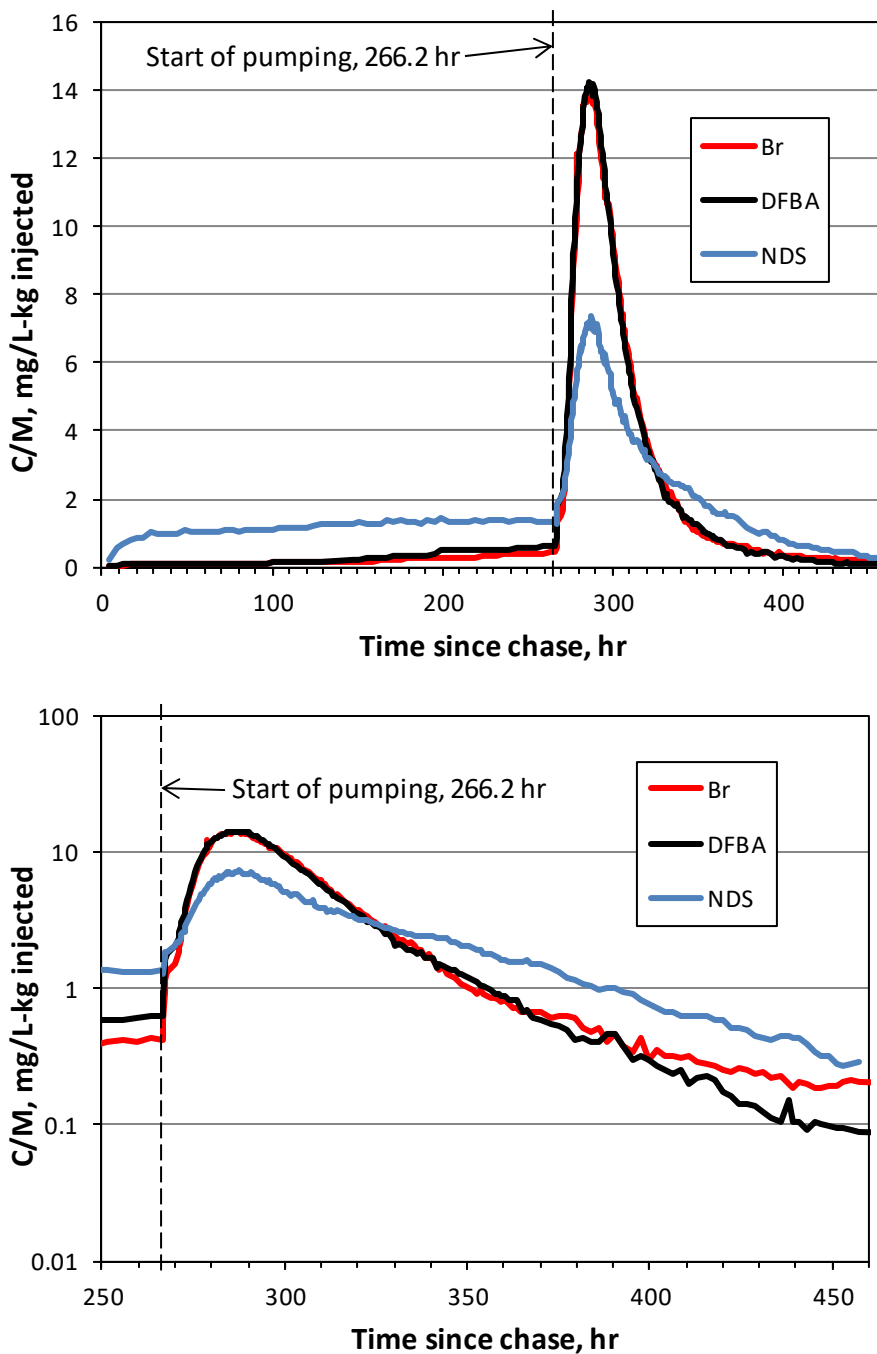


Figure 3.1-1 Normalized tracer concentrations as a function of time in the R-42 push-pull tracer test. Top shows entire test duration after chase, and bottom shows only the pumping period with a log scale for concentrations. Bromide concentrations were not background-subtracted.

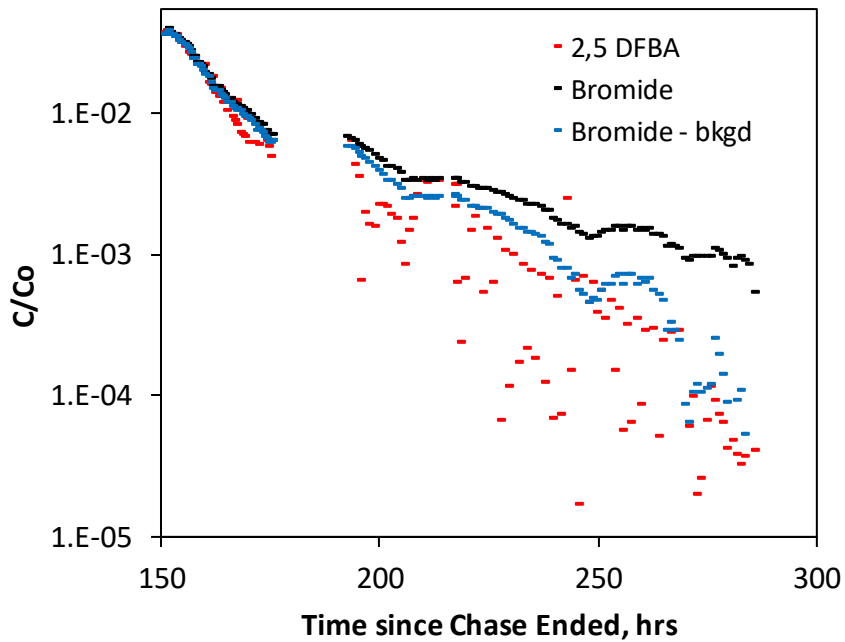


Figure 3.1-2 Normalized tracer concentrations as a function of time in the R-28 push-pull tracer test. Bromide concentrations are background-corrected in upper plot. Bottom plot shows late-time data with log concentration scale, highlighting differences between raw bromide and background-subtracted bromide concentrations. Note that concentrations are plotted as fractions of injection concentrations (as opposed to concentration divided by injection mass).

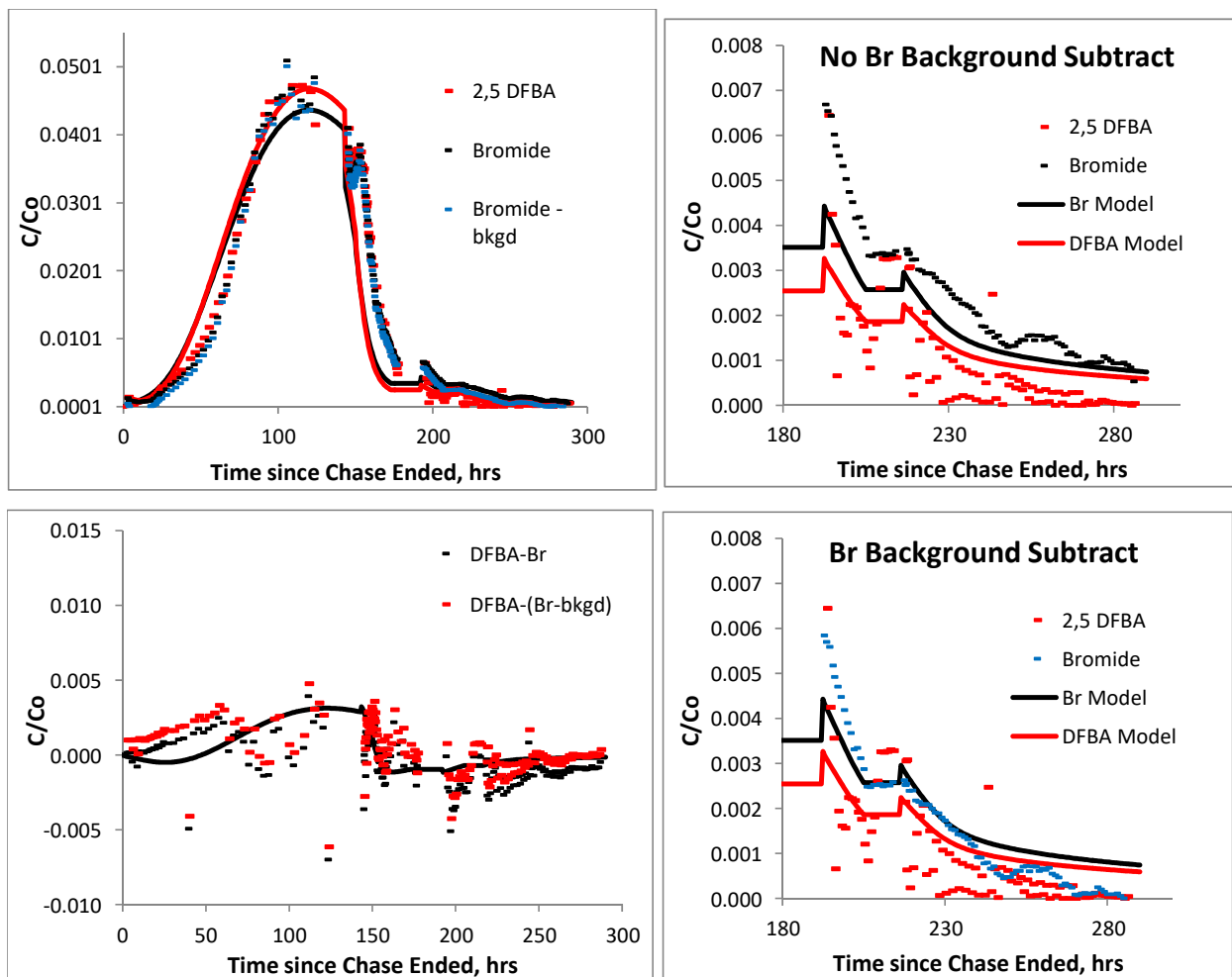


Figure 3.1-3 Match of the 2-D numerical model to the tracer responses and the difference between the two tracer responses (showing both raw and background-subtracted bromide concentrations) during the R-28 push-pull test. Note that the inability of the model to capture the secondary peak of tracers that occurred after pumping started (upper-left plot) is due to the fact that the model did not account for heterogeneity in the drift of the tracers before the pumping period started (pumping started at around 145 h).

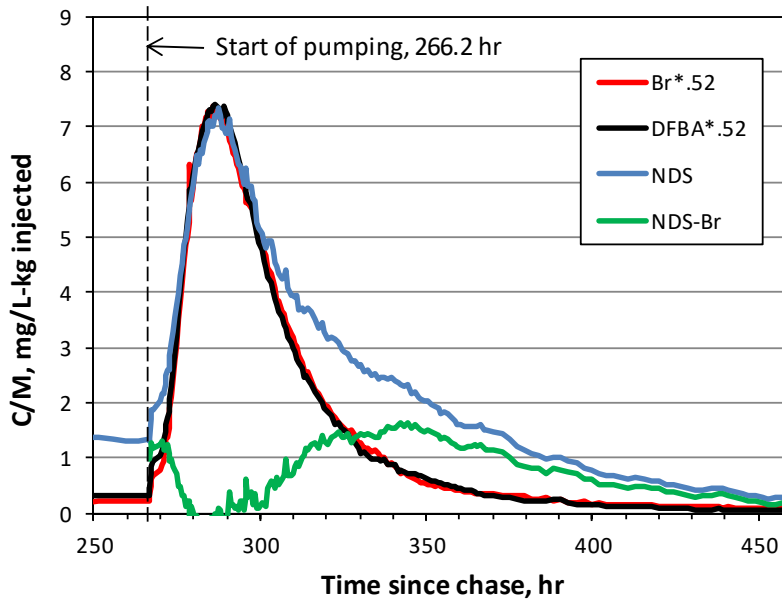


Figure 3.2-1 Response of 1,5-NDS dilution tracer at R-42 during the push-pull test after subtracting out the contribution of the residual tracer that was still in the wellbore at the start of the test (approximately 52% of the tracer, which was assumed to be represented by the Br and 2,6-DFBA responses multiplied by 0.52). The green curve is the resulting response of the dilution tracer that was assumed to have left the wellbore during the dilution tracer test.

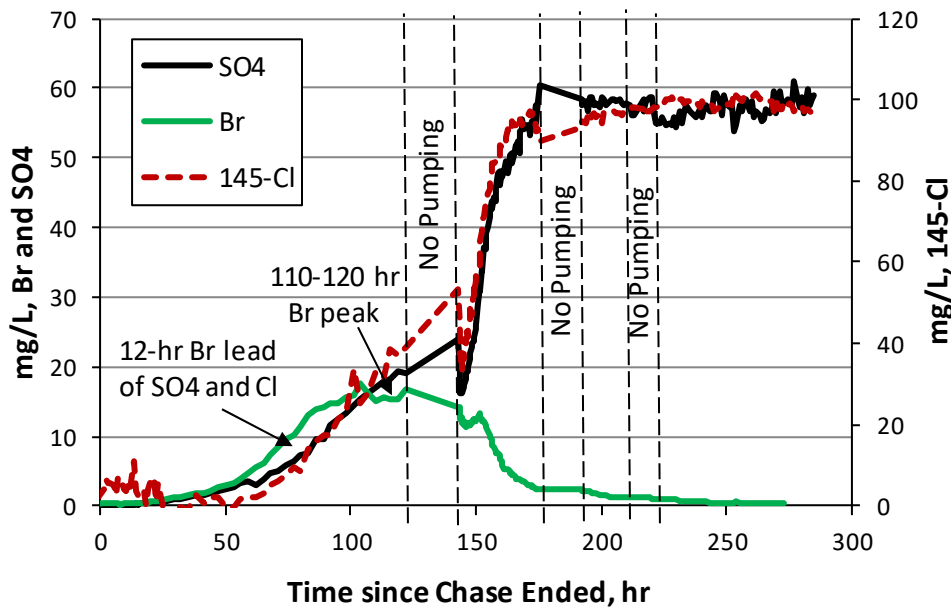


Figure 3.2-2 Tracer and aquifer water breakthroughs during the R-28 push-pull tracer test, showing Br breakthrough relative to conservative anions that were in aquifer water but not in treated water (SO_4^-) or vice-versa (Cl^- , which had a concentration of about 145 mg/L in treated water and 45 mg/L in aquifer water)

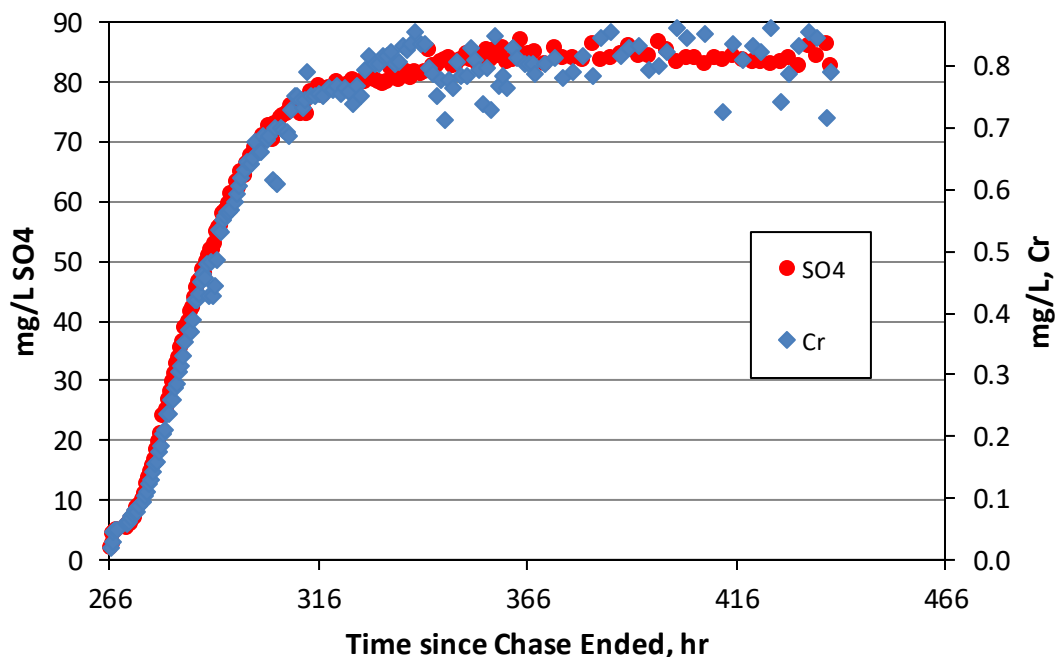


Figure 3.3-1 Breakthroughs of SO_4^- and Cr(VI) in R-42 during the pull phase of the push-pull test in R-42

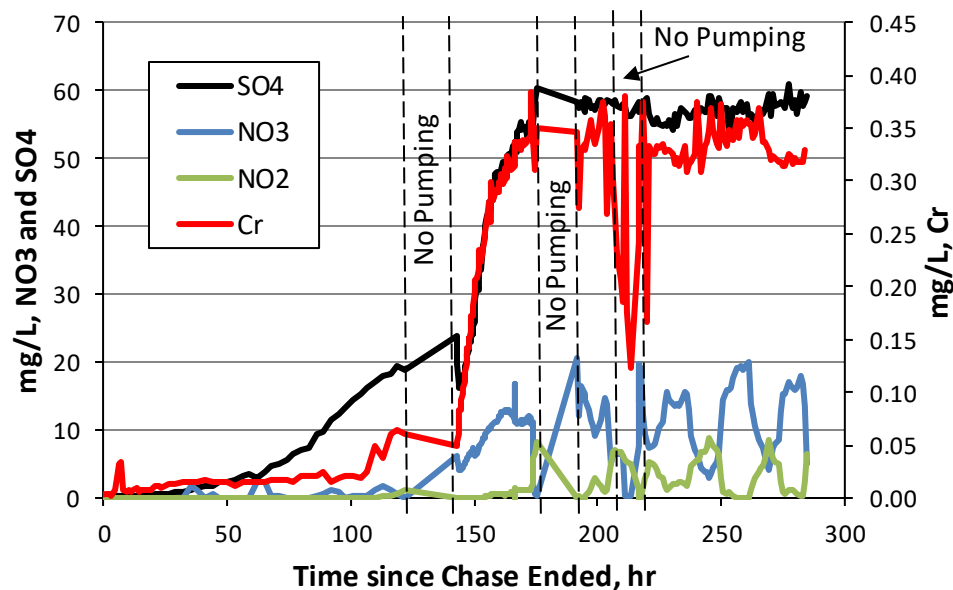


Figure 3.3-2 Breakthroughs of Cr(VI) and NO_3^- relative to SO_4^- in the R-28 push-pull test. Note that after pumping began, the NO_3^- concentrations cycled out of phase with NO_2^- concentrations, while Cr(VI) tended to remain quite constant except during the last nonpumping period when the autosampler continued to collect samples, which suggests that reduction may have occurred in the nearly stagnant sampling lines during this period.

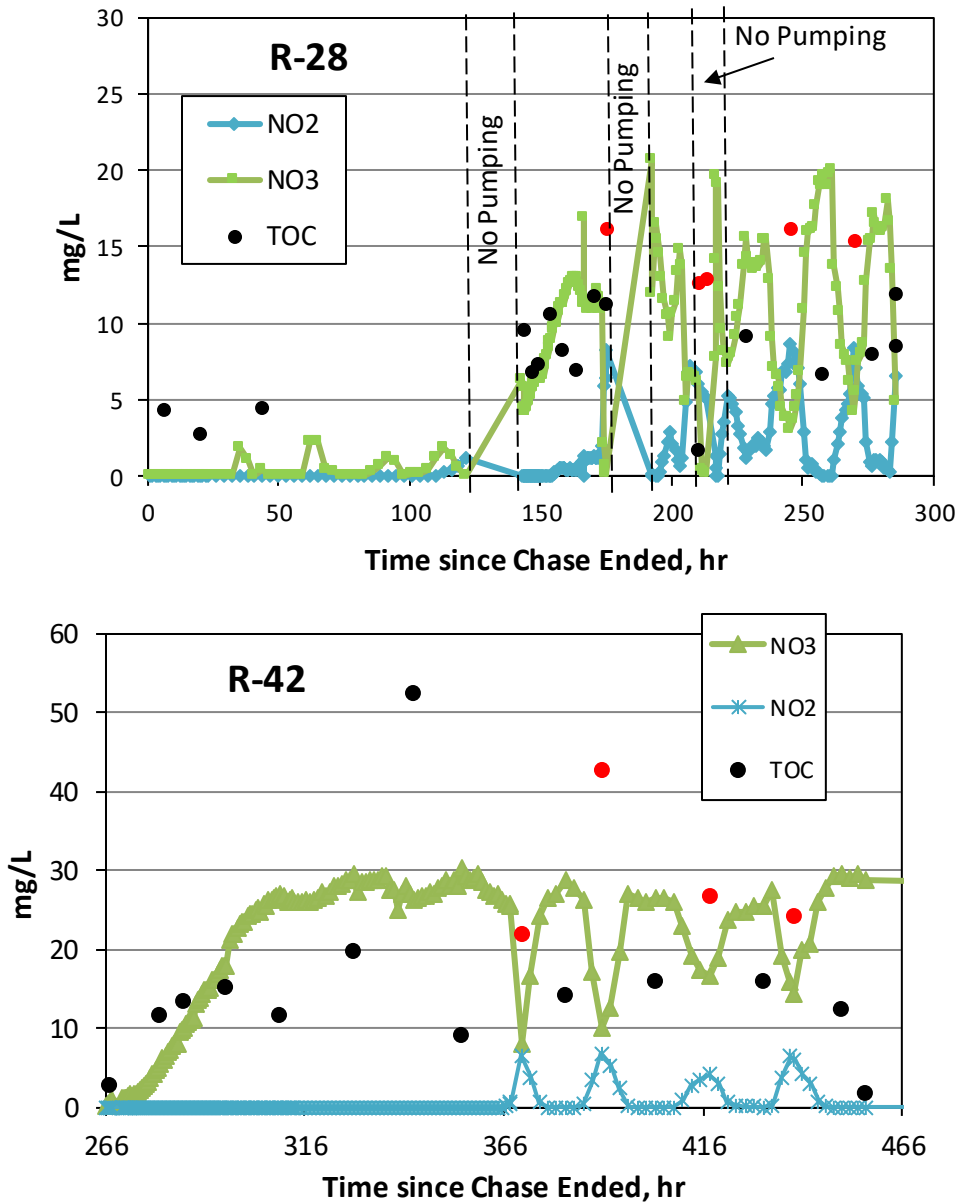


Figure 3.3-3 Total organic carbon (TOC) concentrations superimposed on NO_3^- and NO_2^- concentrations during R-28 (top) and R-42 (bottom) push-pull tests. Note the higher TOC concentration (red dots) tend to occur when NO_3^- concentrations drop and NO_2^- concentrations rise (i.e., when NO_3^- reduction seems to be occurring).

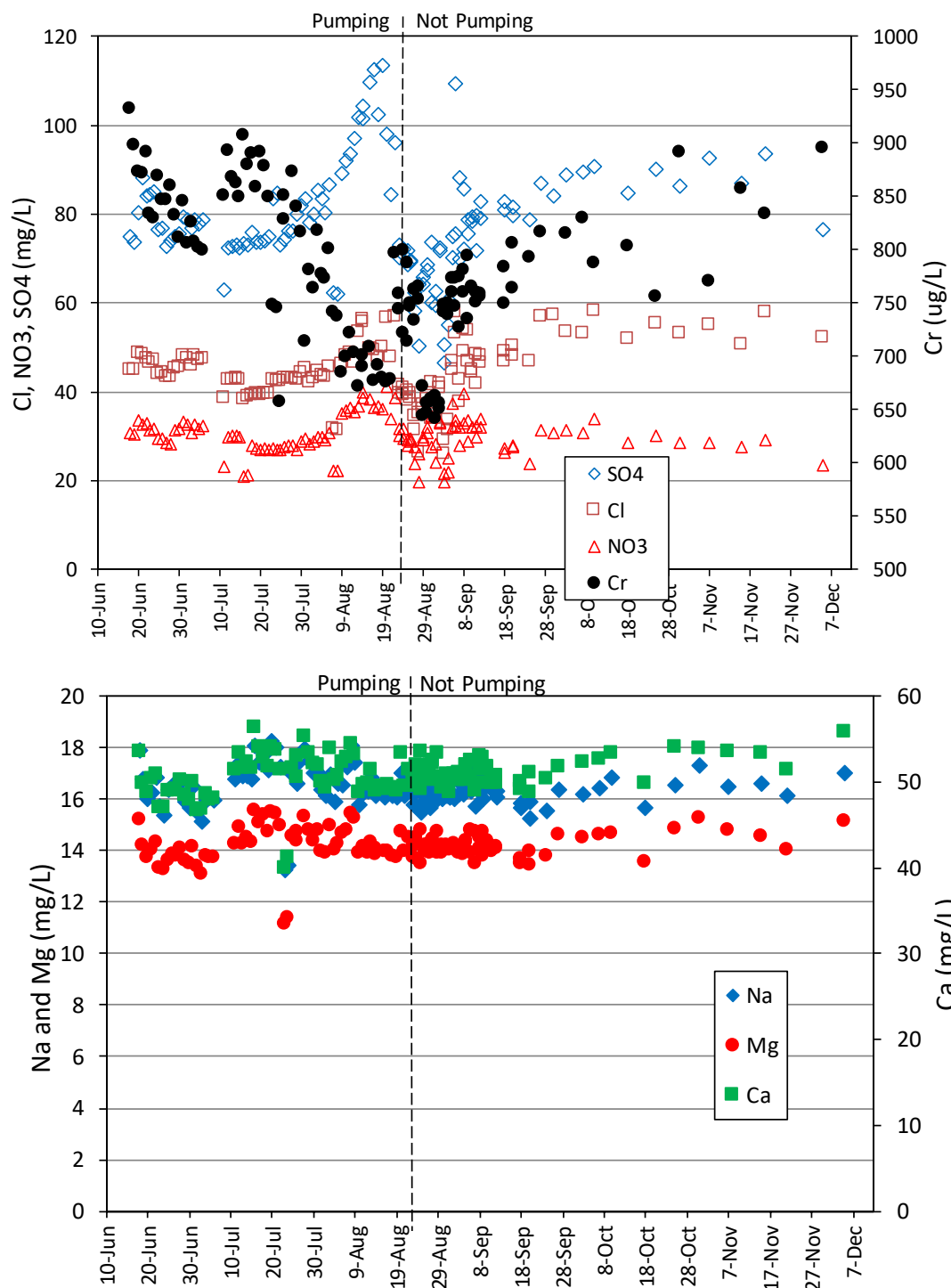


Figure 4.0-1 Concentrations of key constituents in R-42 during the long-term pumping test of R-42 in 2013, including the period after pumping ended (top: major anions and Cr(VI), bottom: major cations). Note the difference in the Cr concentration scale in the upper plot. The rise in concentration of SO₄⁻ and Cl⁻ before pumping ended, followed by the drop after pumping ended, are believed to be an analytical artifact (see Figure 4.0-2).

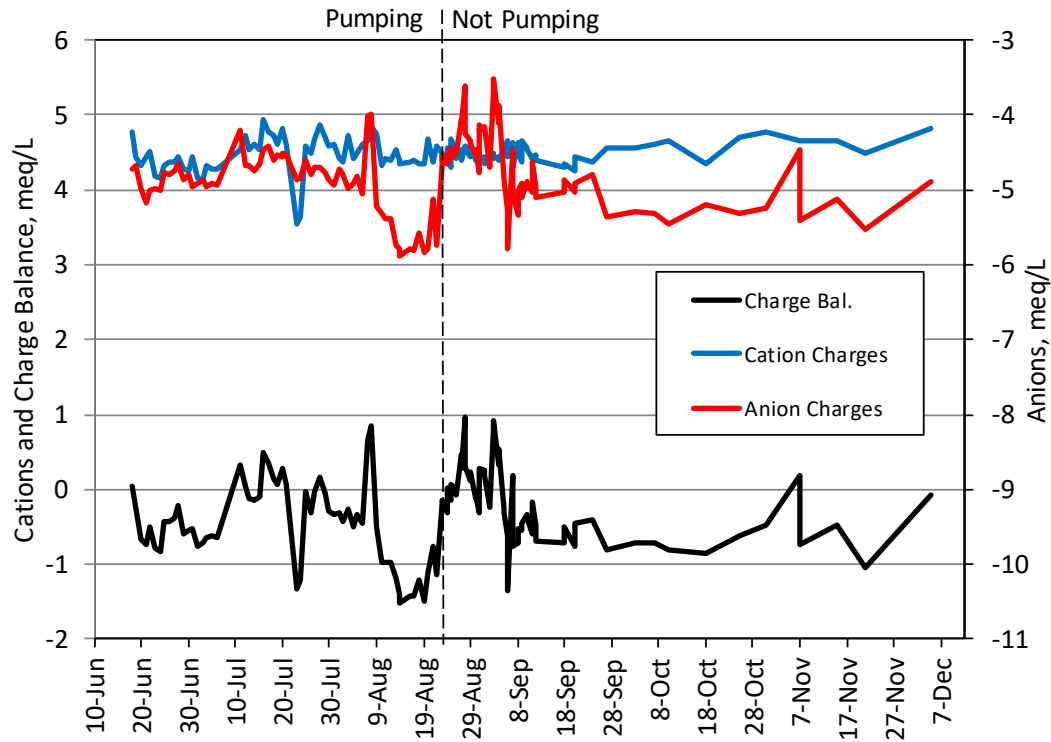


Figure 4.0-2 Charge balance in R-42 during long-term pump test of R-42 (at 7–8 gpm). Note the large drop in anion charge (increase in negative charge) just before the end of the pumping period, followed by the large rise in anion charge right after the end of the pumping period. In contrast, the cation charges are relatively steady with the exception of a downward spike around July 22. The large charge imbalances just before and after the pumping stopped suggest that the apparent sharp rise and drop in major anion concentrations around the time pumping stopped (shown in Figure 4.0-1) were an analytical artifact.

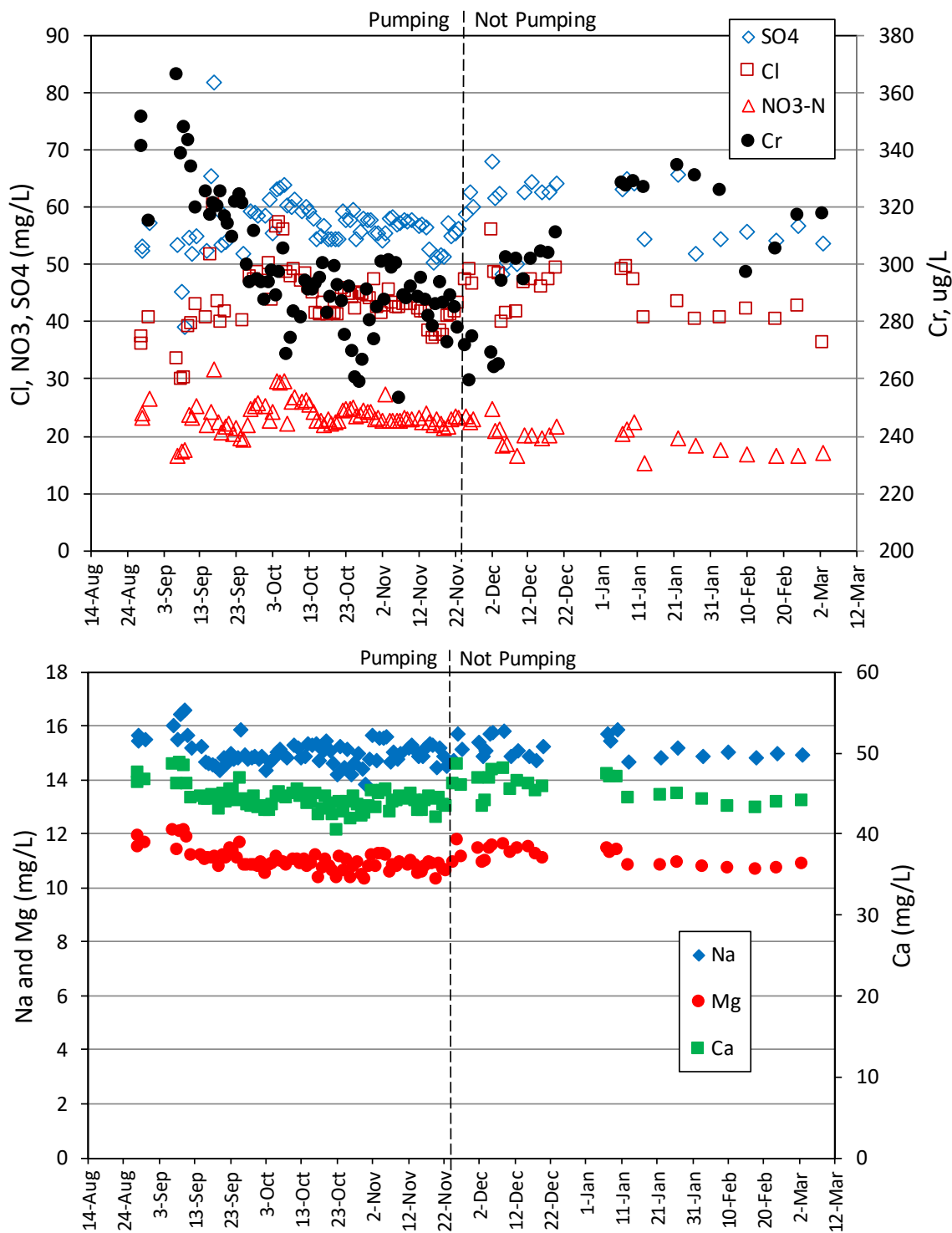


Figure 4.0-3 Concentrations of key constituents in R-28 during the long-term pumping test of R-28 (at 27–28 gpm), including the period after pumping ended (top: major anions and Cr(VI), bottom: major cations). Note the difference in the Cr concentration scale in the upper plot. Only Cr shows any significant changes (within the error of the measurements) over the time of the test. Charge balance errors were much smaller for the R-28 test than for the R-42 test.

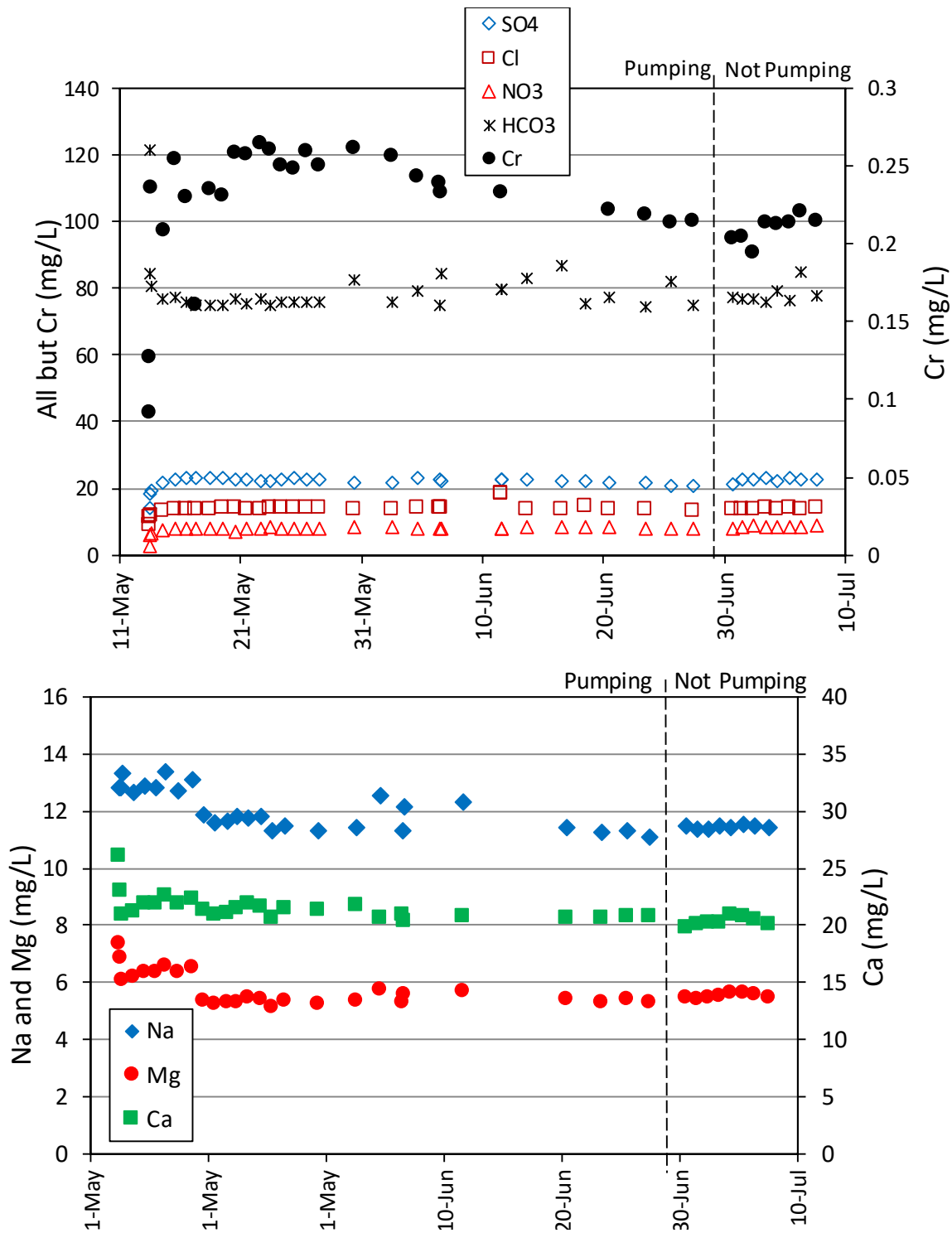


Figure 4.0-4 Concentrations of key constituents in R-62 during the long-term pumping test of R-62 (at 1–1.5 gpm), including the period immediately after pumping ended

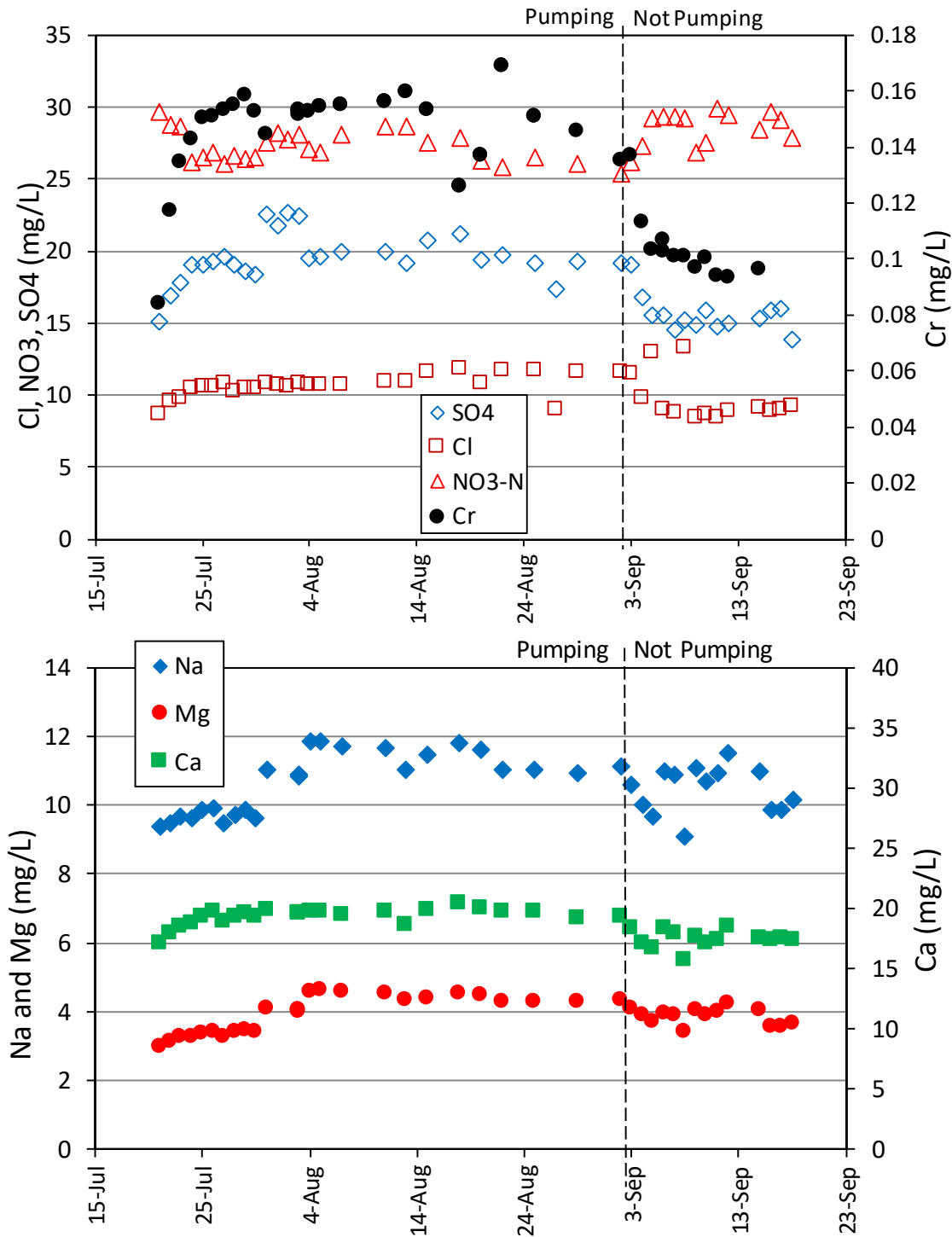


Figure 4.0-5 Concentrations of key constituents in R-43 S1 during the long-term pumping test of R-43 S1 (at 7–8 gpm), including the period immediately after pumping ended

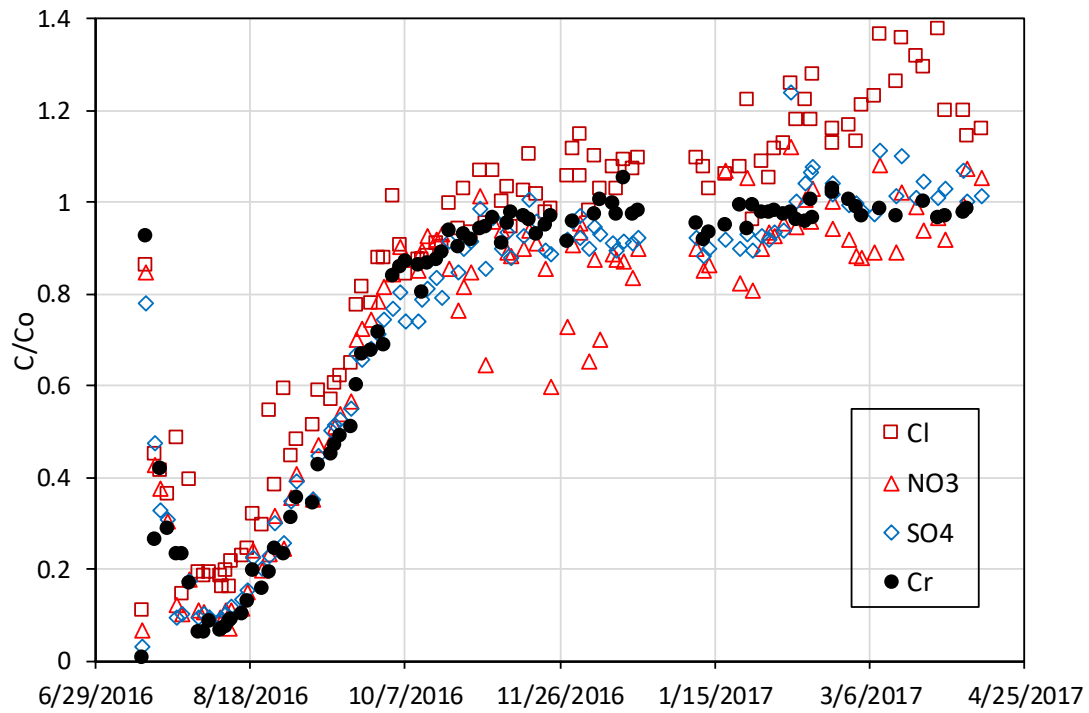


Figure 5.0-1 Concentrations of major anions and Cr(VI) in R-42 during the drift phase of the high-pH push-drift test at R-42. Concentrations are expressed as fractions of pretest concentrations.

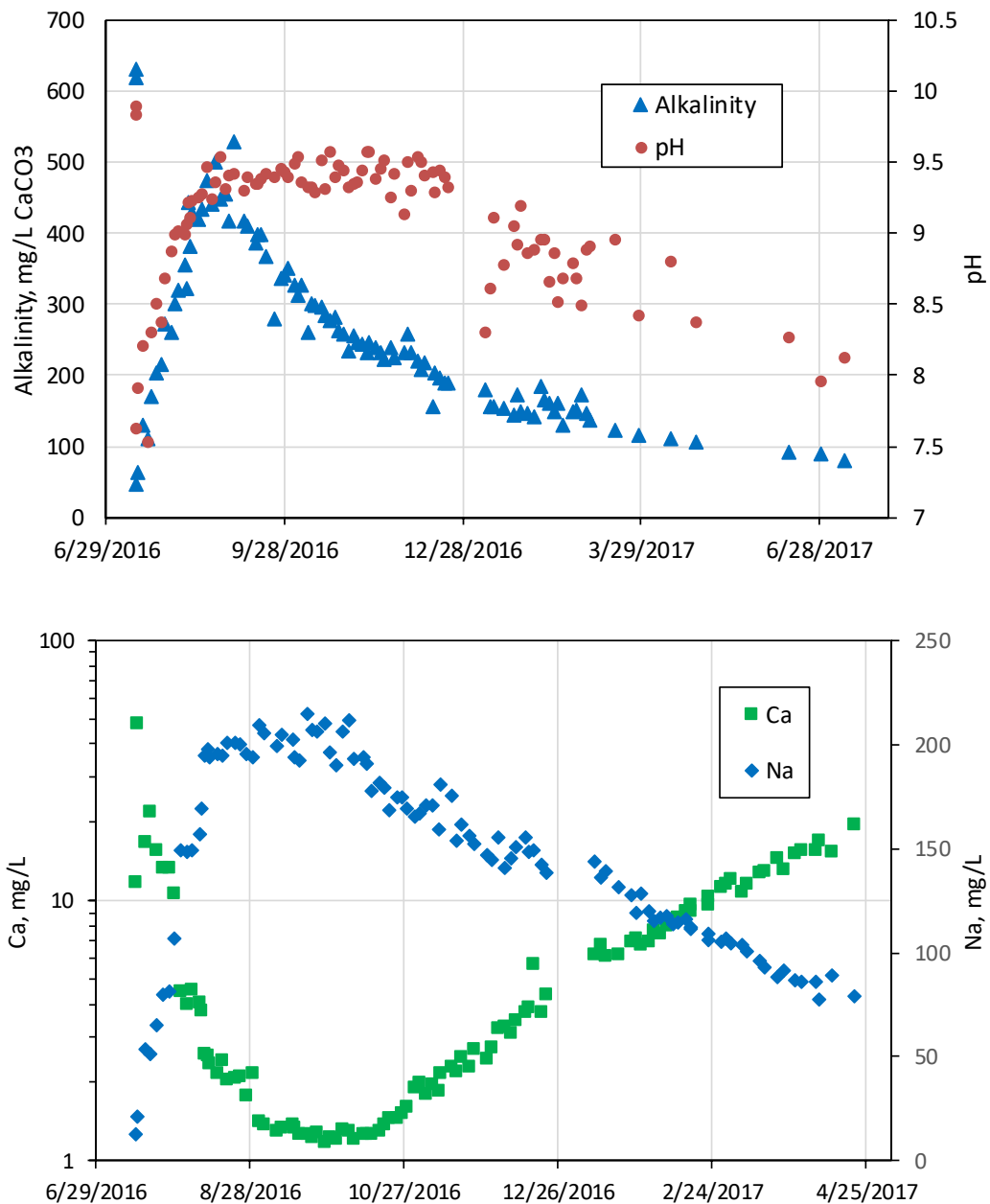


Figure 5.0-2 pH, alkalinity, and sodium and calcium concentrations in R-42 during the drift phase of the high-pH push-drift test at R-42. Note the log scale for calcium.

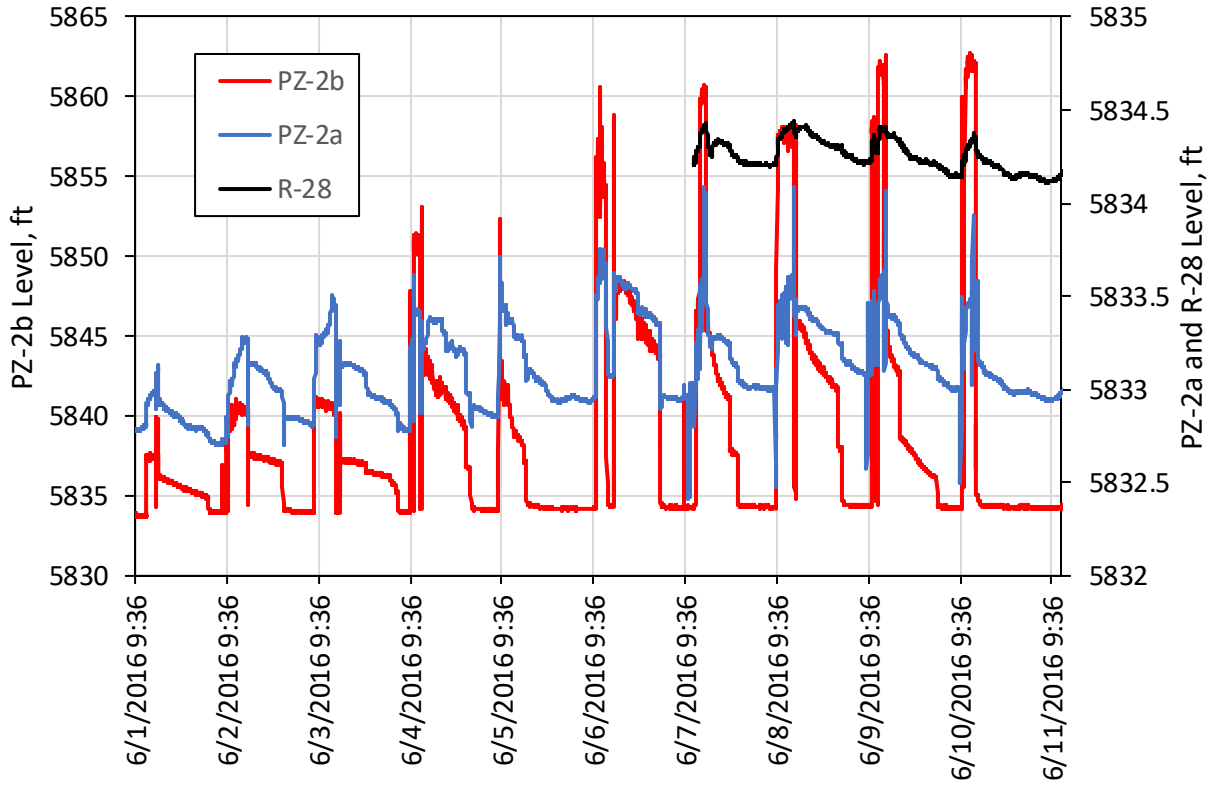


Figure 6.1-1 Pressure responses in CrPZ-2a, CrPZ-2b and R-28 during the tracer and chase injections into CrPZ-2b

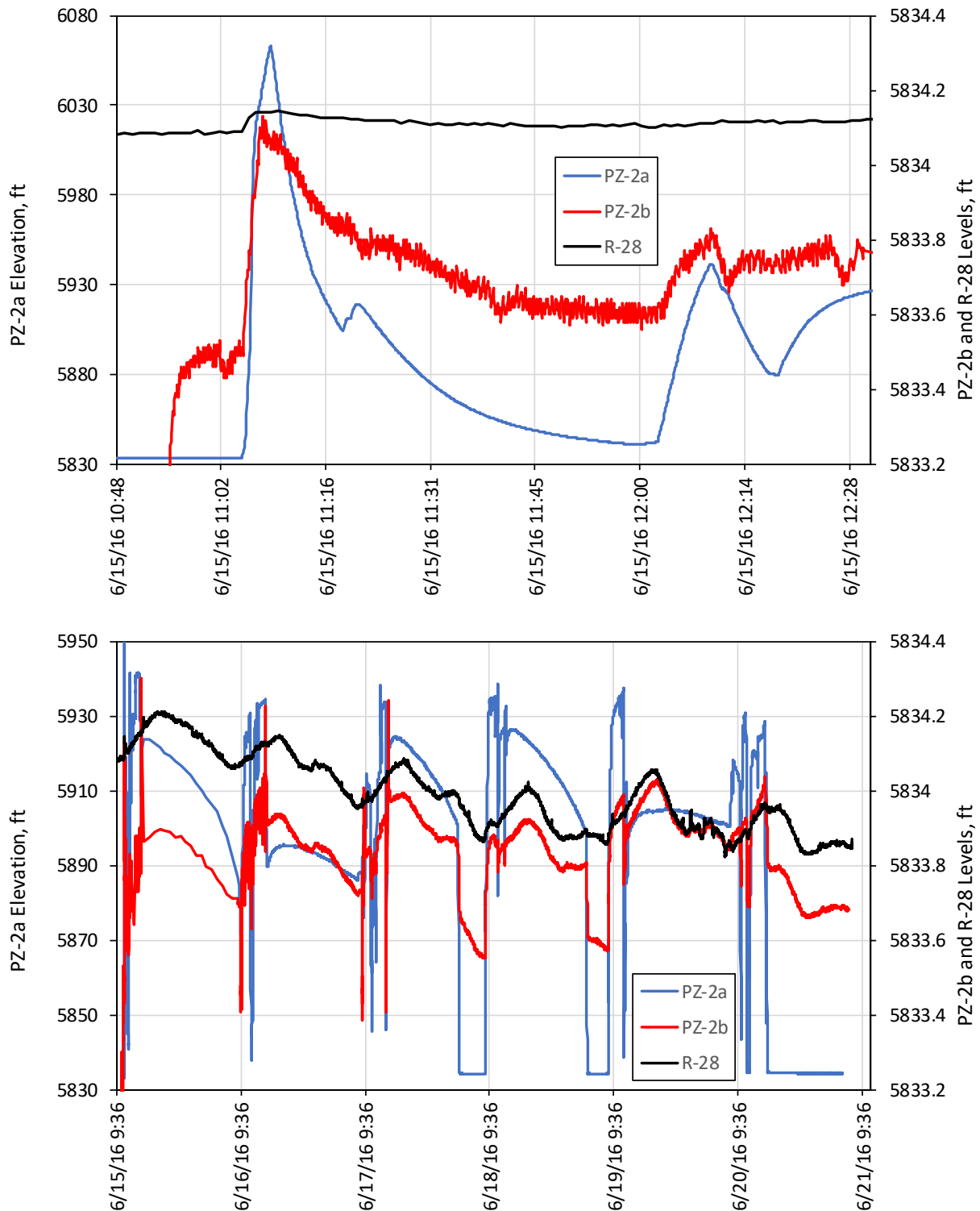


Figure 6.1-2 Pressure responses in CrPZ-2a, CrPZ-2b and R-28 during the tracer and chase injections into CrPZ-2a. Top shows responses to initial pressure spike in CrPZ-2a when injection rate was discovered to be too high, and bottom shows the entire history of the injection.

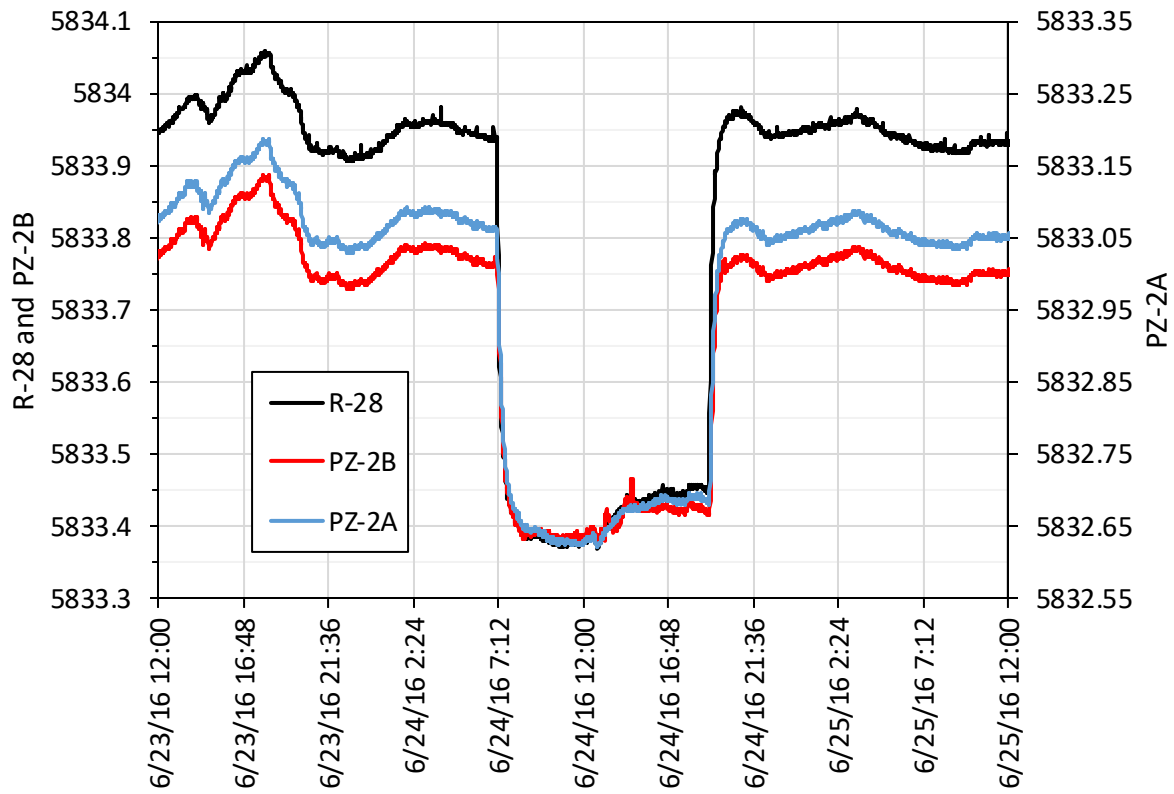


Figure 6.1-3 Pressure responses in CrPZ-2a, CrPZ-2b, and R-28 during 12-h pump test of CrEX-3 (at ~40 gpm)

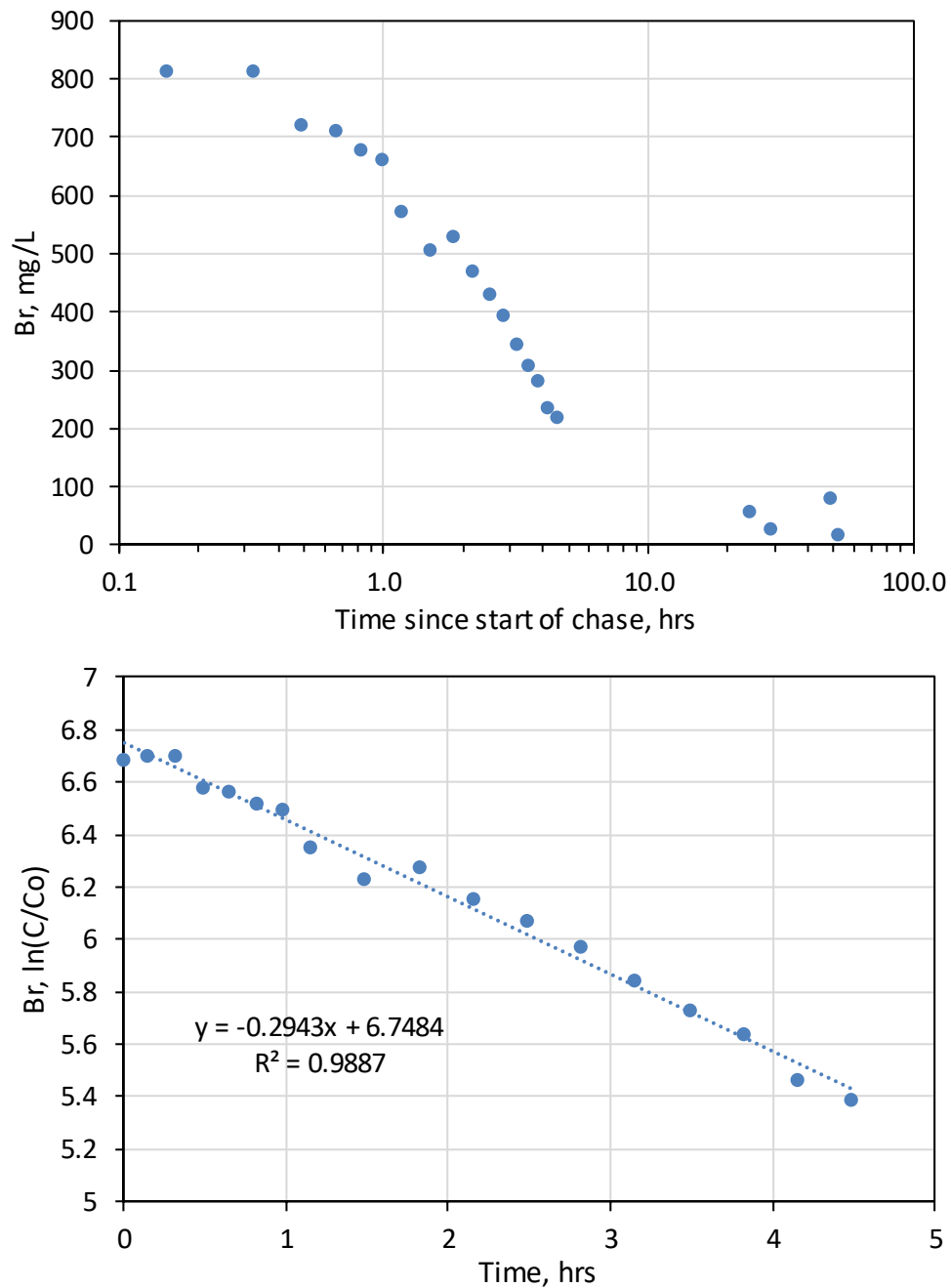


Figure 6.2-1 Decline in bromide tracer concentration observed in CrPZ-2a after the chase started in CrPZ-2b. Top: raw concentrations vs log time; bottom: $\ln(C/Co)$, where Co is the initial concentration, vs time. Note that the initial concentration was essentially the same as the concentration injected into CrPZ-2b.

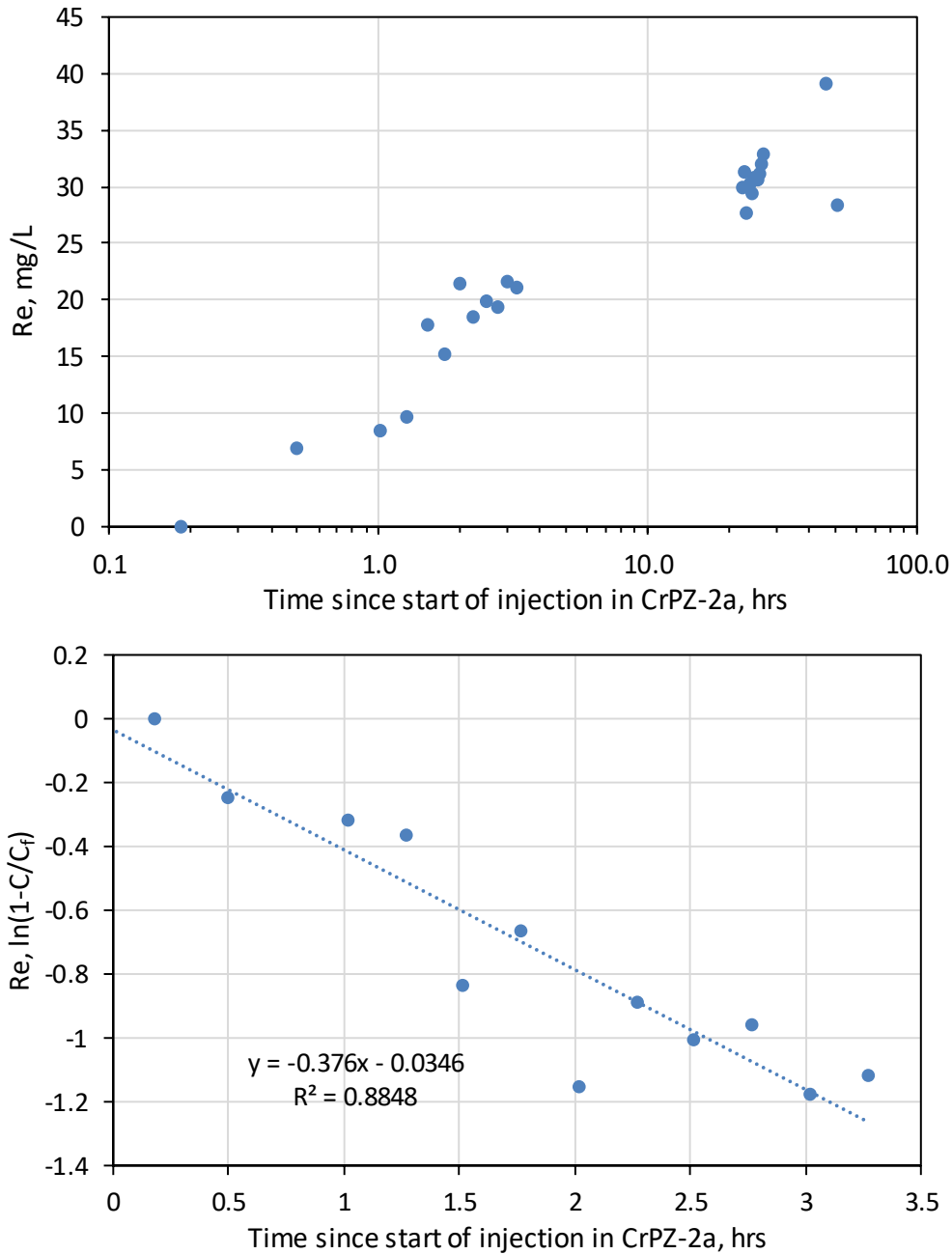


Figure 6.2-2 Rise in rhenium tracer concentration observed in CrPZ-2b after the tracer injection started in CrPZ-2a (top). Bottom figure is a plot of $\ln(1-C/C_f)$, where C_f is the final concentration, vs time. Note that the final concentration was essentially the same as the injection concentration in CrPZ-2a (a little over 30 mg/L Re).

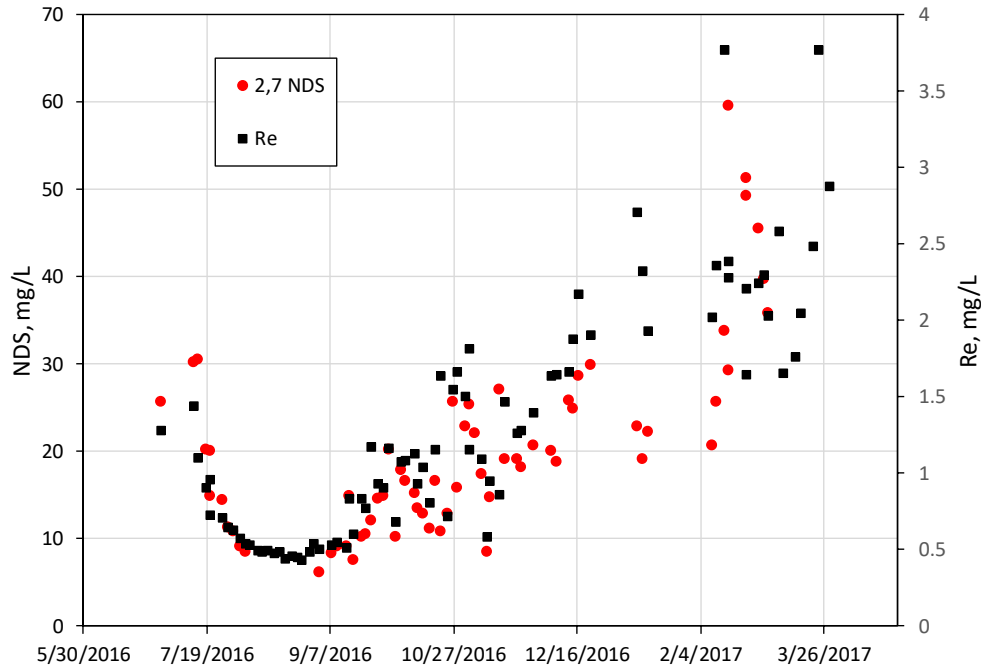


Figure 6.2-3 Concentration histories of tracers injected into CrPZ-2a measured in passive samples collected from CrPZ-2a after the injection and chase

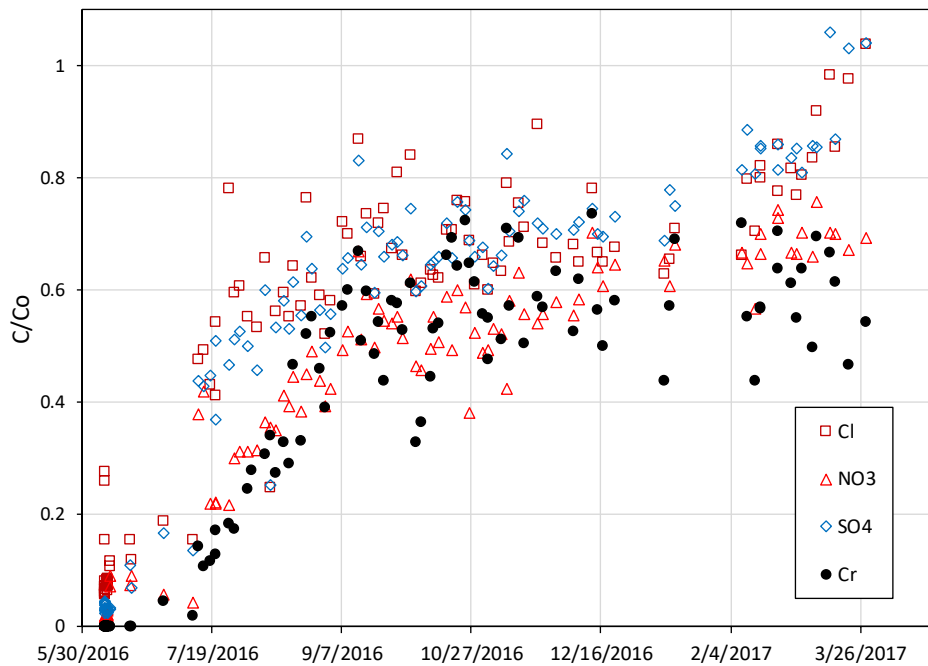


Figure 6.2-4 Concentrations of major anions and Cr(VI) in CrPZ-2a measured in passive samples collected from CrPZ-2a after the injection and chase, which were both potable water. Concentrations are expressed as fractions of pretest concentrations.

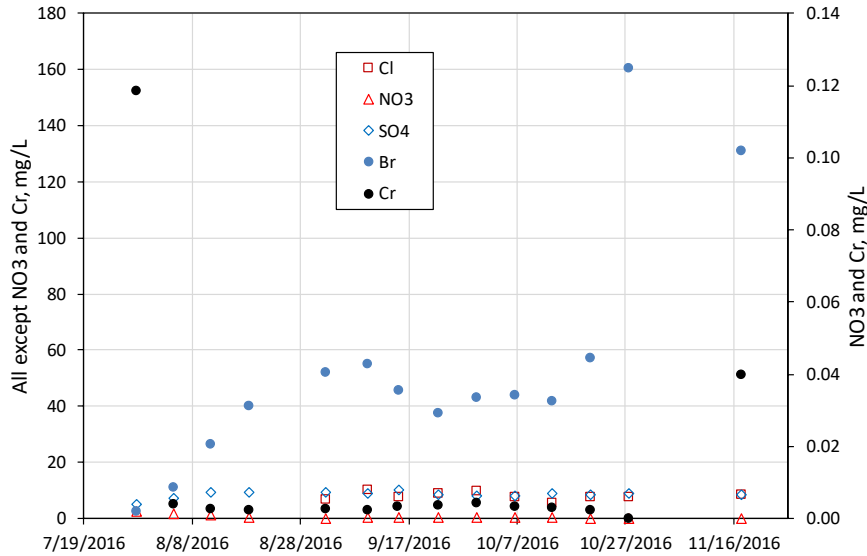


Figure 6.2-5 Concentration histories of major anions, bromide tracer, and Cr(VI) in CrPZ-2b, measured in passive samples collected from CrPZ-2b after the injection and chase. Note that the initial high Cr(VI) concentration is possibly a signature of water from CrPZ-2a that was pushed down into CrPZ-2b during the CrPZ-2a injection (the Cr value is higher than anything ever measured in CrPZ-2b, but somewhat lower than pretest Cr concentrations in CrPZ-2a).

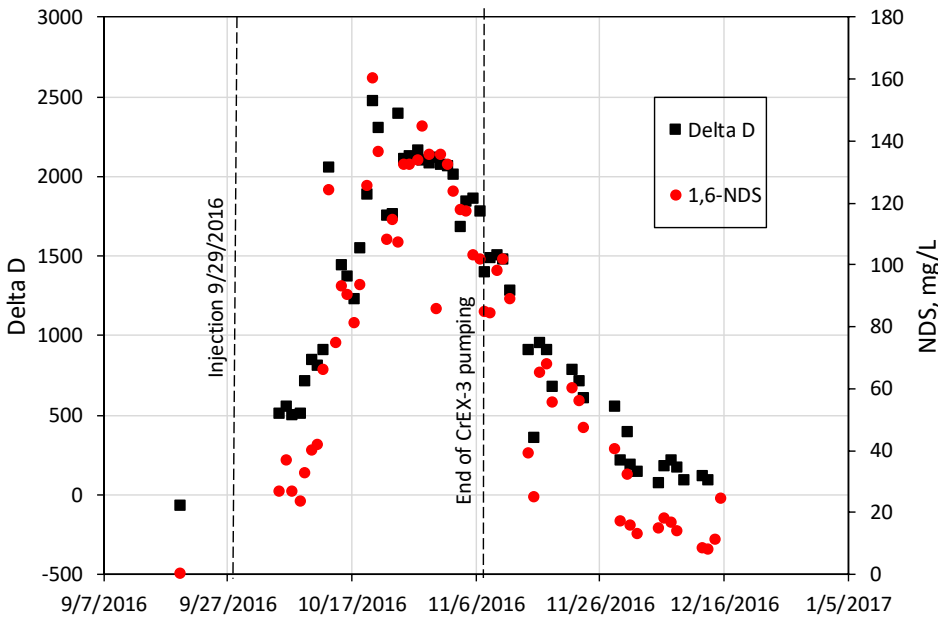


Figure 6.2-6 Concentration histories of tracers injected into R-28 measured in passive samples collected from R-28 after the injection and chase. Delta D is delta deuterium, expressed as per mille difference from standard mean ocean water.

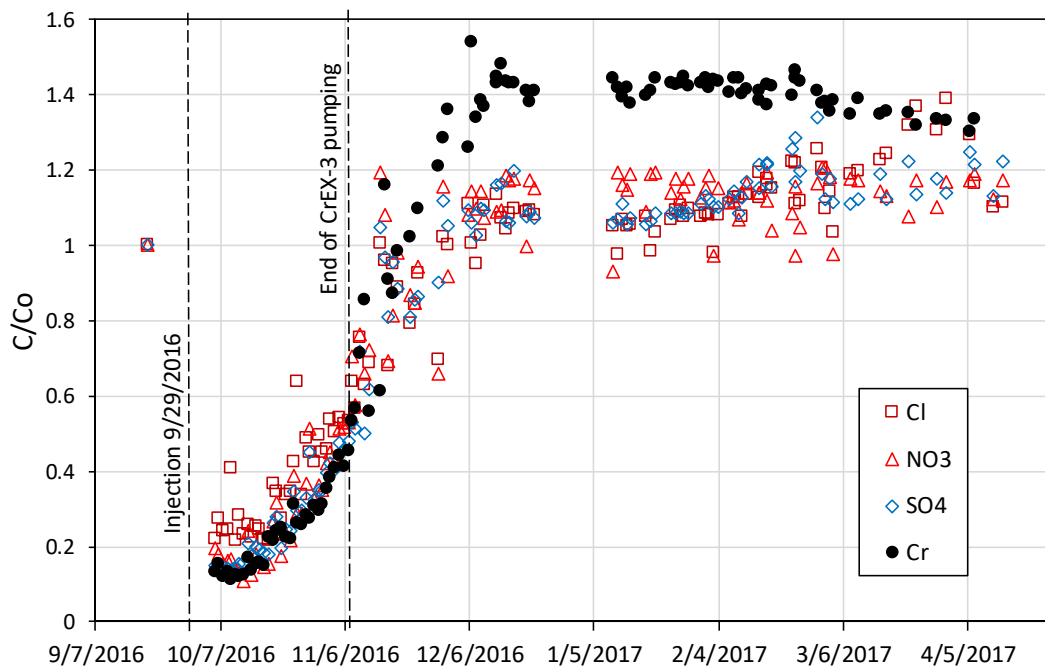


Figure 6.2-7 Concentrations of major anions and Cr(VI) in R-28 measured in passive samples collected from R-28 after the injection and chase, which were both potable water. Concentrations are expressed as fractions of pretest concentrations.

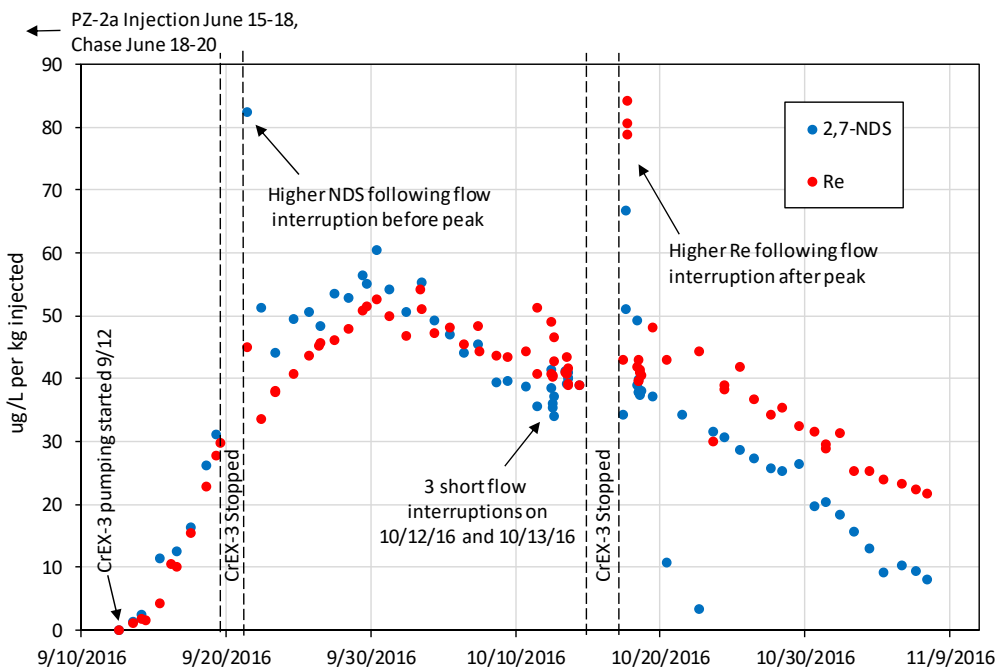


Figure 6.3-1 Normalized breakthrough curves of tracers injected into CrPZ-2a in CrEX-3 during pumping of CrEX-3

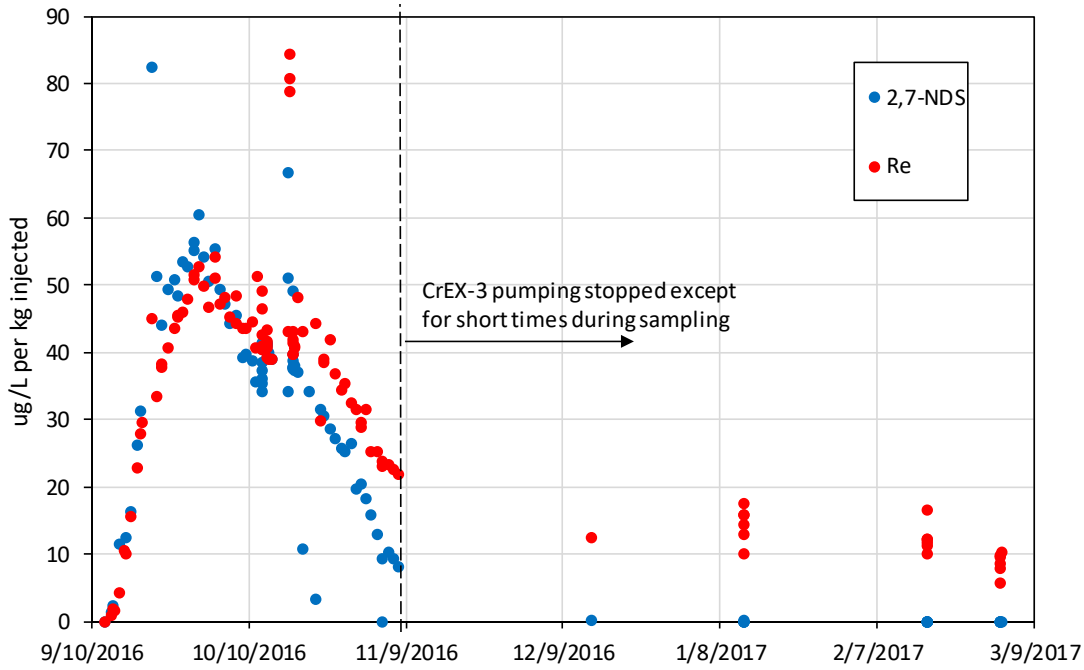


Figure 6.3-2 Normalized concentrations of tracers injected into CrPZ-2a in CrEX-3, including additional samples collected after pumping ended.

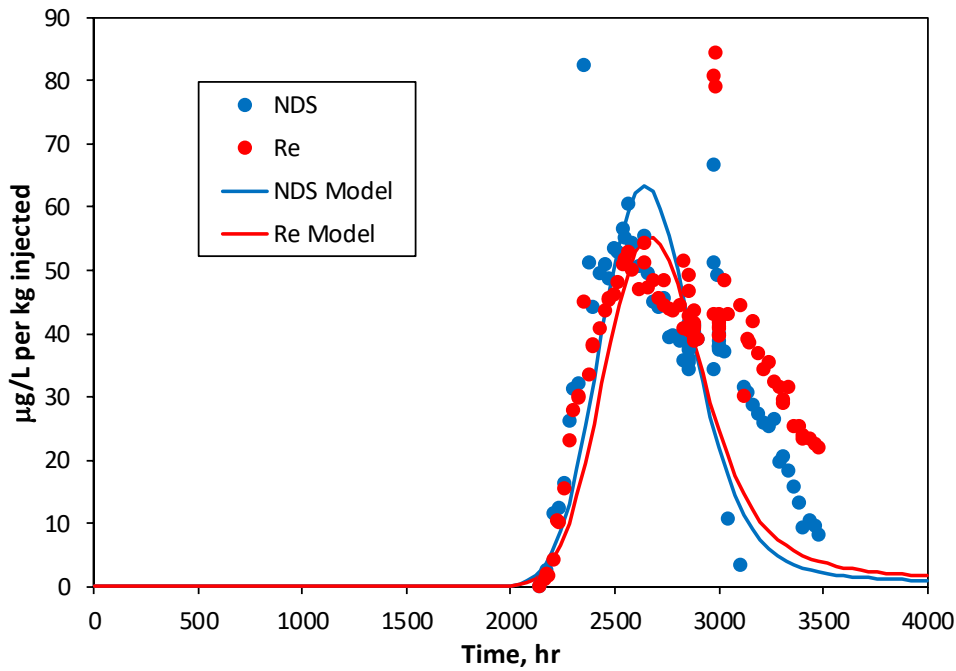


Figure 6.3-3 Model match to normalized breakthrough curves of tracers injected into CrPZ-2a in CrEX-3 through the end of pumping on 12/7/2016. Note that the model does not attempt to match the responses to flow interruptions.

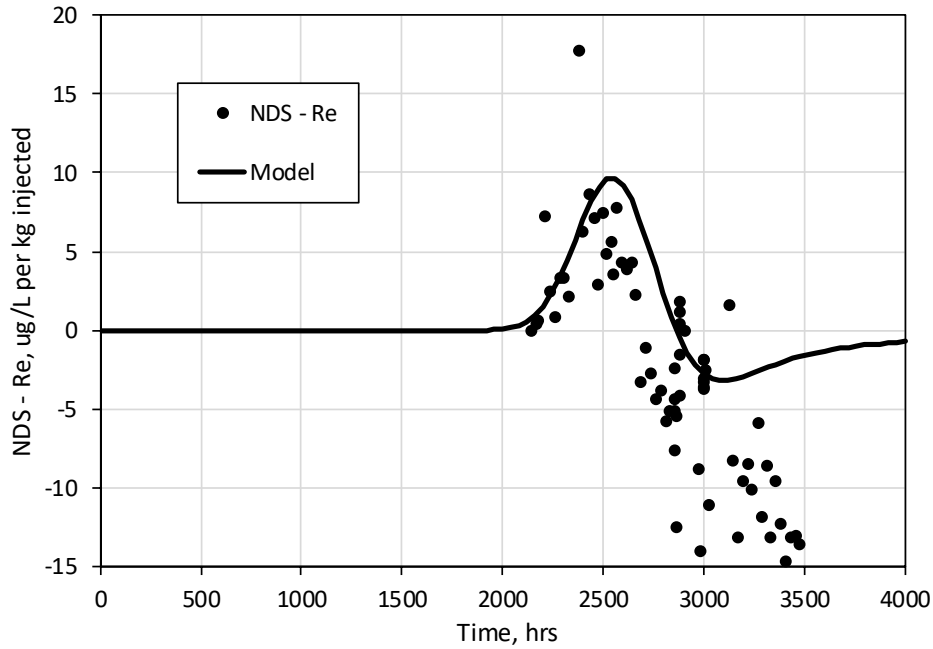


Figure 6.3-4 Model match to *differences* in normalized breakthrough curves of tracers injected into CrPZ-2a in CrEX-3. The model results are the same as for Figure 6.3-3. Note that the late-time differences are poorly matched presumably because of the degradation of 2,7 NDS.

Table 2.0-1
Circulation Loop Volumes, Volumetric Flow Rates, Flow Distortion
and Linear Velocity Estimates for Each Borehole Dilution Tracer Test

Well	V, L	Q, L/h	β (dist. Factor)	$V = Q/(\beta\phi)$, m/d*
R-42	795	3.5	3.7	0.14
R-28	833	26.7	3.3	1.1
R-62	454	2.1	3.8	0.08
SCI-2	76	9.2	4.2	0.85
R-43 S1	416	48.7	3.7	2.0
R-50 #1	379	3.1	3.8	0.25
CrPZ-2a	76	0.7	15.3	0.035
CrPZ-2b	95	0.96	15.3	0.025
CrPZ-3	76	1.5	10.6	0.06

* Linear flow-velocity estimate assumes a flow porosity of 0.2 (multiply by 0.2 for specific discharge estimate). Note that SCI-2 is in fractured/rubblized media, so flow porosity is likely less than 0.2).

Table 3.0-1
Tracer Identities/Masses, Injection and Chase Volumes,
Key Dates/Times, and Withdrawal Rates in the Push-Pull Tracer Tests at R-42 and R-28

	R-42	R-28
Tracers	Na Br (2001.4 g) Na 2,6-Difluorobenzoate (1499.1 g)	Na Br (2000.5 g) Na 2,5-Difluorobenzoate (1500.2 g)
Tracer Injection Vol. (gal.)	1440	1350
Chase Vol. (gal.)	10,000	9000-10,000 ^a
Time of Tracer Injection	4/9/14 9:30–12:30	5/21/14 9:45–15:48 (plus 14 min starting at 13:05 on 5/20/14, stopped by leak)
Time of Chase	4/9/14 12:45 – 4/10/14 8:34	5/21/14 15:54 – 5/22/14 10:45
End of Rest/Drift Time ^b	4/21/14 10:42	5/28/14 9:45
Withdrawal Rate(s) (gpm)	7.5	16.3 for first 7 h, then 27 thereafter

^a Volume uncertain, but estimated based on residual levels in three 5000-gal. poly tanks.

^b Rest/drift time started at end of chase, and withdrawal started at end of rest/drift time.

**Table 6.0-1
Tracer Identities/Masses, Injection and Chase Volumes,
Key Dates/Times, and (at ~40 gpm) at CrEX-3 in the Cross-Hole Tracer Test**

	CrPZ-2a	CrPZ-2b	R-28
Tracers	Na 2,7-NDS (24.87 kg) NaReO ₄ (2.0 kg)	Na 2-NS (25.15 kg) Na Br (144.8 kg)	Na 1,6-NDS (24.96 kg) D ₂ O (60 kg)
Tracer Inj. Vol. (gal.)	10,000	42,000	15,000
Chase Vol. (gal.)	10,000	21,000	15,000
Time of Tracer Injection	6/15/16 12:05 – 6/18/16 12:03	6/1/16 13:32 – 6/7/16 23:00 ^a	9/29/16 8:21 – 9/29/16 12:52
Time of Chase	6/18/16 12:06 – 6/20/16 15:50	6/8/16 10:30 – 6/10/16 14:50	9/29/16 12:55 – 9/29/16 16:30
Pumping Period at CrEX-3 (at ~40 gpm)	9/12/16 13:25 – 11/7/16 10:30 ^{b,c}	9/12/16 13:25 – 11/7/16 10:30 ^{b,c}	9/12/16 13:25 – 11/7/16 10:30 ^{b,c}

^a Tracer injection ended at around this time as tank drained by gravity during the night.

^b There was also a 12-h pump test in CrEX-3 on 6/24/16 at ~40 gpm.

^c There were the following significant CrEX-3 pump downtimes during the pumping period:

9/13/16 18:30 to 9/14/16 10:15 (15:45 h:min)

9/19/16 17:00 to 9/21/16 14:05 (45:05)

10/3/16 4:00 to 10/3/16 10:15 (6:15)

10/13/16 4:40 to 10/13/16 10:32 (5:52)

10/14/16 14:27 to 10/17/16 15:38 (73:11)

Appendix A

*Moisture Content and Pore Water Chemistry Data from
Sonic Core Holes CrCH-1 through CrCH-5, and Chemistry
Data from Completed Piezometers (CrPZ-1 through CrPZ-5)*

A-1.0 INTRODUCTION

This appendix presents the results of moisture content measurements and pore water chemistry measurements of sonic core samples from CrCH-1 through CrCH-5. The locations of CrCH-1 through CrCH-5 in relation to the footprint of the hexavalent chromium [Cr(VI)] plume are shown in Figure A.1.0-1. The sonic coring was conducted between October 2014 and March 2015. Each core hole was drilled by conventional methods until it penetrated the Cerros del Rio basalt in the unsaturated zone (typically 700–750 ft below land surface), and then sonic coring with a 5-in. bit was conducted until reaching about 100 ft below the water table (usually about 1000 ft below land surface). CrCH-1 was an exception because it was drilled from the top of a mesa, so the Cerros del Rio basalt was not penetrated until over 900 ft below land surface, and the core hole reached only about 25 ft below the water table to a final depth of about 1140 ft below land surface. During coring below the water table, a “simulprobe” water-sampling tool was used to collect groundwater samples every 20 ft in each core hole. This tool required a dedicated trip into the hole to collect a sample. The simulprobe samples were analyzed for water chemistry, and the results are reported in this section along with the pore water chemistry data.

The sonic core was collected in 3- to 5-ft increments in a 5-ft long sonic core barrel that was driven by sonic vibration into the sediments at the bottom of the hole each time the core barrel made a trip into the hole. The barrel was often not advanced the entire 5 ft, but even when a full 5 ft of core was extracted, it was often apparent that the upper portion of the core interval was slough that had fallen into the borehole between trips. Thus, often only the lower 3 ft or so of what appeared at the surface as a 5-ft interval actually appeared to be material that was freshly cored on the trip into the hole. The 5-ft core barrel was equipped with a Plexiglas/Lexan inner liner to facilitate easy removal of the core from the core barrel at the surface. After removal from the barrel, which was typically accomplished by hammering on the outside of the barrel, the liner was capped on both ends and the core was placed into cold storage within 10-12 h of extraction. In some cases, particularly below the water table, the sediments in the core barrel slid out of the Plexiglass liner before the liner could be extracted from the barrel. In these cases, the core was collected in long, thin plastic bags that were set up beneath the barrel to capture the core if it slid out. These bags were found to preserve the lithologic layering and moisture content of the core almost as well as the Plexiglas liners. Core recovery appeared to be nearly 100% regardless of whether the core was captured in Plexiglas liners or in plastic bags.

A-2.0 METHODS

A-2.1 Moisture Content Measurements and Collection of Pore Water

The core tubes or long plastic bags containing core were delivered to the Earth System Observations (EES-14) sample preparation laboratory in batches. Once in the lab, they were quickly processed by removing sediment samples from the interior of the liner or bag, generally at least 1 in. from bottom of the core interval (to avoid any contamination or artifacts that might occur near the walls or the bottom of the barrel). One relatively large sample was collected and weighed in a tared 125-mL glass bottle, and then the sample was dried out in an oven (110°C) and reweighed so that the moisture content could be determined [moisture content = (wet mass–dry mass)/(wet mass)]. Smaller wet sediment samples were collected and placed into centrifuge tubes equipped with 0.45- μ m filter inserts so that when the tubes were spun (4000 rpm), pore water was extracted beneath the filters for chemical analysis. The pore water was analyzed for major anions and cations, as well as Cr(VI) and trace elements, using the analytical methods described below. For many intervals in the unsaturated zone, the core was too dry to extract enough water for chemical analyses. However, almost all intervals collected from below the water table

contained sufficient pore water to extract for chemical analysis, and in some cases, multiple samples were collected from different locations/depths within a given core interval for chemical analysis.

A-2.2 Pore Eater Chemistry Analytical Methods

Anions (other than HCO_3^-) were analyzed by ion chromatography using U.S. Environmental Protection Agency (EPA) Method 300 on a Dionex DX-600 system. Major cations were analyzed by inductively coupled plasma–optical emission spectroscopy (ICP-OES) using EPA Method 200.7 on a Perkin Elmer Optima 2100 DV. High-purity nitric acid (Fisher Trace Metal Grade) was used for sample and calibration standard preparation. An internal standard (scandium) was added to both samples and standards to correct for matrix effects, which can result in varying sample introduction rates. Some samples were diluted before analysis to minimize matrix effects as well as allow the analytes of interest to remain within the linear dynamic range of the calibration. SPEX CertiPrep Instrument Check Standard 3 was used to check the accuracy of the multielement calibrations. Typical ICP-OES parameters were: 1350 W forward power, 15 L/min plasma gas flow, 0.2 L/min auxiliary flow; and 0.8 L/min nebulizer flow. Trace metals and other minor elements, including chromium, were analyzed by inductively coupled plasma–mass spectrometry (ICP-MS) using EPA Method 200.8 on a Perkin Elmer NexION system. As with the ICP-OES samples, high-purity nitric acid (Fisher Trace Metal Grade) was used for sample and calibration standard preparation. Internal standards (yttrium, bismuth, and indium) were added to both samples and standards to correct for matrix effects, which can result in varying sample introduction rates. Some samples were diluted before analysis to minimize matrix effects as well as allow the analytes of interest to remain within the linear dynamic range of the calibration. The National Institute of Standards and Technology (NIST) Standard Reference Material (SRM) 1640a, “Trace Elements in Natural Water,” was used to check the accuracy of the multielement calibrations. Typical ICP-MS parameters were 1600 W forward power, 18 L/min plasma gas flow, 1.2 L/min auxiliary flow; and 0.9 L/min nebulizer flow.

A.3-0 RESULTS

Figures A-3.0-1 through A-3.0-25 provide graphic depictions of the results from each of the core holes. These 25 figures are divided into 5 sets of 5 plots each; one set for each core hole. Each set contains, in the following order, plots of (1) moisture content vs depth, (2) pore water anion concentrations vs depth, (3) pore water chromium concentrations vs depth, (4) pore water anion concentrations vs depth below the water table, including simulprobe data, and (5) concentration trends in samples collected while purging the core holes with a low-flow-rate pump after they were completed as piezometers. The location of the water table, as identified at the time of the sonic coring, is shown in all figures. Note that any unsaturated zone depths for which pore water chemistry data are not shown on the plots correspond to depths for which there was insufficient water spun out of the sediment samples to measure pore water chemistry.

The anion concentration profiles include data only for SO_4^- , Cl^- , and NO_3^- , as these anions contribute the majority of the anion charge (other than HCO_3^-) in the plume area. The concentrations of these anions also tend to be correlated with Cr(VI) concentrations in the plume area, as they all have anthropogenic origins (superimposed on a background concentration in the case of SO_4^- and Cl^-), although only SO_4^- is believed to have a major contribution from the same source area as Cr(VI) (the upper Sandia Canyon wetland outfall). The anion profiles are given more emphasis than the chromium profiles because it became evident quite early in the work that chromium concentrations in the pore water samples were likely biased low in most, if not all, of the sonic core samples because of the presence of metallic iron contamination in the core from the steel coring bits that were used. As the chromium plots displayed in Figures A-3.0-1 through A-3.0-25 show, the chromium concentrations did not show any obvious trends with depth in the core holes, and they tended to jump up and down over relatively short vertical distances, which was contrary to what was observed for the anions. As discussed in Attachment 6 of this

compendium, "Characterization of Natural Attenuation," metallic iron contamination was identified in many sonic core samples, and it was found to produce a large amount of artificial uptake of Cr(VI) in batch uptake experiments. Also, after the sonic core holes were completed as piezometers, and when they were pumped to obtain representative groundwater samples, the Cr(VI) concentrations in the pumped water were generally significantly higher than in the vast majority of the pore water samples (compare 3rd and 5th plot of each set of plots). Thus, the chromium concentrations in the pore water samples were considered unreliable indicators of chromium concentrations within the plume. Instead, the anion concentration profiles were used as the best indicators of how the aquifer was geochemically stratified in the core holes, and it was assumed that Cr(VI) concentration trends in the absence of iron artifacts should follow the anion trends, especially the SO_4^- trends, in the core holes.

In the remainder of this section, the highlights of the results from each of the sonic core holes are discussed in turn. Refer to the data supplement accompanying this report to view all the moisture content and pore water chemistry data, including the concentrations of constituents not plotted here. Chemistry data during the purging of the core holes/piezometers are also provided in the data supplement.

A.3-1 CrCH-1

This core hole had a considerable amount of moisture just below the Cerros del Rio basalt, but at depths below about 1030 ft below land surface to the water table (1118 ft), it was not possible to obtain enough pore water to measure water chemistry. As with all the other core holes, the moisture content of the core samples increased dramatically below the water table relative to measurements from above the water table. Although the pore water sample density below the water table is not great in this core hole because only a little over 20 ft of saturated zone was penetrated, the anion profiles of Figure A-3.0-4 show that anion concentrations appear to increase markedly over the bottom 5 ft or so of the hole relative to the upper 15 ft of saturated zone. However, the chromium concentrations in pore water samples from the saturated zone (Figure A-3.0-3) show no such trend, and they are also much lower than pumped samples that were eventually collected from the piezometer (Figure A-3-0-5). The anion profile of Figure A-3.0-4 suggests that the upper 15 ft or so of the saturated zone at this location has lower concentrations of contaminants or anthropogenic constituents than the aquifer below 15 ft. This is the only core hole in which concentrations of such constituents appeared to increase with depth.

A.3-2 CrCH-2

This core hole had more moisture in the unsaturated zone than CrCH-1, as reflected by both the moisture content data and the number of unsaturated zone samples that yielded sufficient pore water for chemical analysis. There appeared to be anthropogenic constituents (as reflected by anion concentrations) throughout the unsaturated zone and in the upper 25 ft or so of the saturated zone. However, the bottom 75 ft of saturated zone in this core hole appeared to be relatively free of anthropogenic constituents. The geochemical stratification in this core hole was more pronounced than in any other core hole, with the suggestion of a confining layer of some sort preventing water with anthropogenic constituents from reaching more than 25 ft below the water table. CrCH-2 was completed as a nested piezometer that had a 10-ft sampling interval in the upper portion of the core hole where anthropogenic constituent concentrations were high, and a 20-ft interval in the lower portion of the core hole where concentrations were low. The two intervals were isolated from each other by a bentonite plug that was located just below the bottom of the upper section of higher concentrations. Subsequent pumping of the nested piezometers confirmed that Cr(VI) concentrations were significant in the upper zone but very low in the lower zone (Figure A-3.0-10). The pumping of the upper piezometer showed a dramatic increase in the Cr(VI) concentrations from their initial value (Figure A-3.0-10,left), which is believed to be a reflection of the large amount of bentonite that was present in this piezometer. As discussed in Attachment 6 of this

compendium, the bentonite used by the drillers was capable of reducing significant amounts of Cr(VI). Considerable bentonite “contamination” was present in both piezometers of CrCH-2, probably because of the bentonite that was introduced into the completion to isolate the two piezometer screens from each other.

A.3-3 CrCH-3

This core hole had considerable moisture content in the unsaturated zone, and similarly to CrCH-2, the unsaturated zone pore waters showed elevated concentrations of anthropogenic constituents. The pore waters below the water table also had elevated concentrations of anthropogenic constituents, but unlike CrCH-2, there was not an obvious separation between water containing and not containing anthropogenic constituents in the saturated zone. Rather, the concentrations of anthropogenic constituents in CrCH-3 appeared to be elevated throughout the 100 ft of saturated zone that was penetrated. However, the concentrations gradually decreased with depth, with those at the bottom of the core hole being about half what they were at the water table.

A-3.4 CrCH-4

This core hole was drier in the unsaturated zone than CrCH-2 or CrCH-3, although it exhibited a saturated zone profile of anthropogenic constituents that was similar to CrCH-3 (i.e., decreasing concentrations with depth). However, the anthropogenic constituents in CrCH-4 had much lower concentrations than in CrCH-3, and at the bottom of the hole, the SO_4^- and Cl^- concentrations were essentially equal to background concentrations in the regional aquifer (at least in places where there are no anthropogenic constituents). Subsequent pumping of this core hole after it was completed as a piezometer indicated that it was essentially free of Cr(VI) contamination, although it does contain elevated levels of NO_3^- . Pumped samples also contained much higher concentrations of ClO_4^- than observed anywhere else in the chromium plume area (not discussed here), which suggests that the water in this core hole/piezometer has a significant contribution from upper Mortandad canyon, where the source of ClO_4^- contamination was located.

A.3-5 CrCH-5

This core hole was quite dry in the unsaturated zone, and it exhibited a saturated zone profile of anthropogenic constituents that was similar to CrCH-2 (i.e., with what appears to be a relatively sharp drop in concentrations of anthropogenic constituents below about 25 ft below the water table). However, the boundary between high and low anthropogenic concentrations is not nearly as sharp as in CrCH-2. Pumped samples from this core hole after it was completed as a piezometer indicated Cr(VI) concentrations similar to CrCH-1 and CrCH-3. All of these piezometers had Cr(VI) concentrations in the 300–400 $\mu\text{g/L}$ range. Interestingly, CrCH-4, which had very little, if any, Cr(VI) contamination, is located between CrCH-1 and CrCH-3.

A-4.0 CONCLUSIONS

The chemical analysis of pore waters from sonic core holes CrCH-1 through CrCH-5 did not provide good information on Cr(VI) concentration profiles (concentrations vs depth) in the regional aquifer because of the presence of iron fragments in the core from the sonic coring bit(s). Subsequent pumping/sampling of the piezometers clearly showed that Cr(VI) concentrations in the pore waters were artificially depressed by the presence of iron in the core sediments. However, the pore waters yielded good information on concentration profiles of SO_4^- , Cl^- and NO_3^- , anions that have anthropogenic origins and are elevated

above background concentrations in much of the plume area. These anions tend to be positively correlated with Cr(VI) in the contaminated aquifer, so they are used here to provide an indirect indication of how Cr(VI) is likely to be distributed with depth at the locations of the core holes. The profiles of the anions generally reflect that anthropogenic constituents tend to be more concentrated near the water table (consistent with their transport through the vadose zone before reaching the water table), and their concentrations decrease with depth. However, an exception to this trend was observed at CrCH-1, where concentrations were lower in the upper 15 ft or so of the saturated zone than they were at depths below 15 ft (although the hole penetrated the saturated zone only about 20 ft). In CrCH-2 and CrCH-5, the anthropogenic constituents seem to be confined to the upper 25 ft or so of the saturated zone, with a very sharp demarcation between water containing these constituents and water not containing them in CrCH-2. In CrCH-3, it appears that the entire 100 ft of saturated zone penetrated by sonic coring contains anthropogenic constituents, although concentrations definitely decreased with depth. CrCH-4 shows similar trends to CrCH-3, although concentrations of anthropogenic constituents are much lower than in CrCH-3, and CrCH-4 appears to be almost entirely free of Cr(VI) contamination.

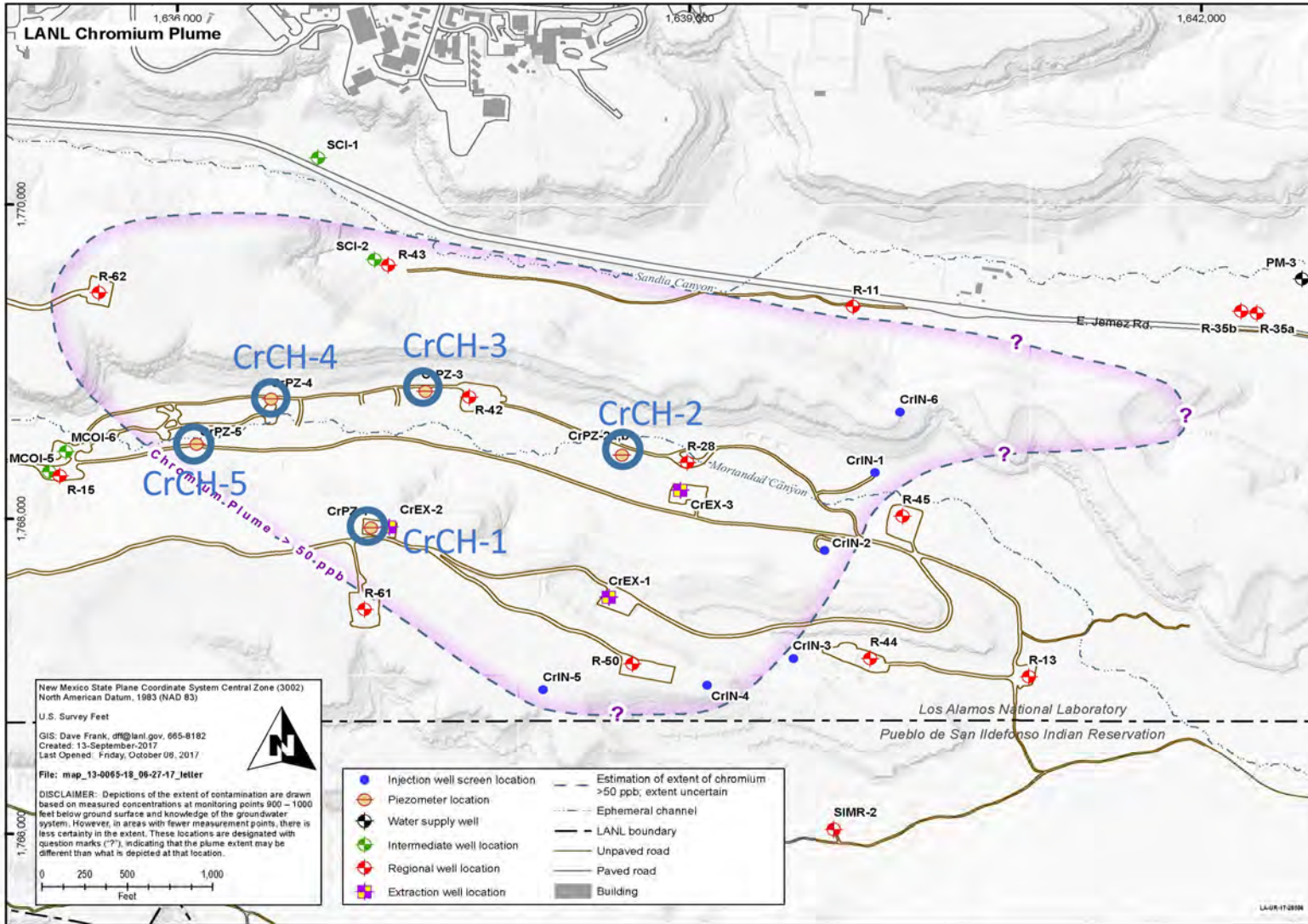


Figure A-1.0-1 Locations of the sonic core holes within the Cr(VI) plume, as demarcated by the inferred 50-μg/L contour

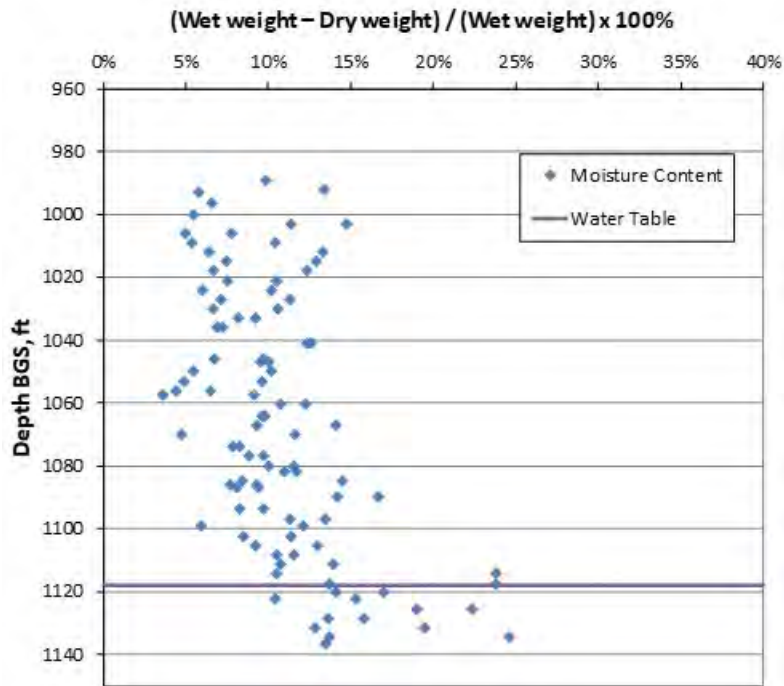


Figure A-3.0-1 Moisture content vs depth in CrCH-1

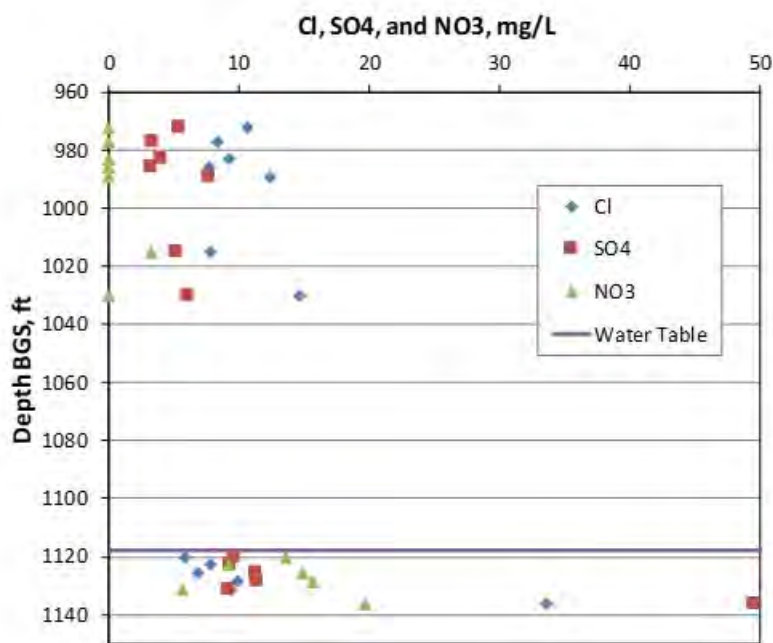


Figure A-3.0-2 Anion concentrations in pore water vs depth in CrCH-1

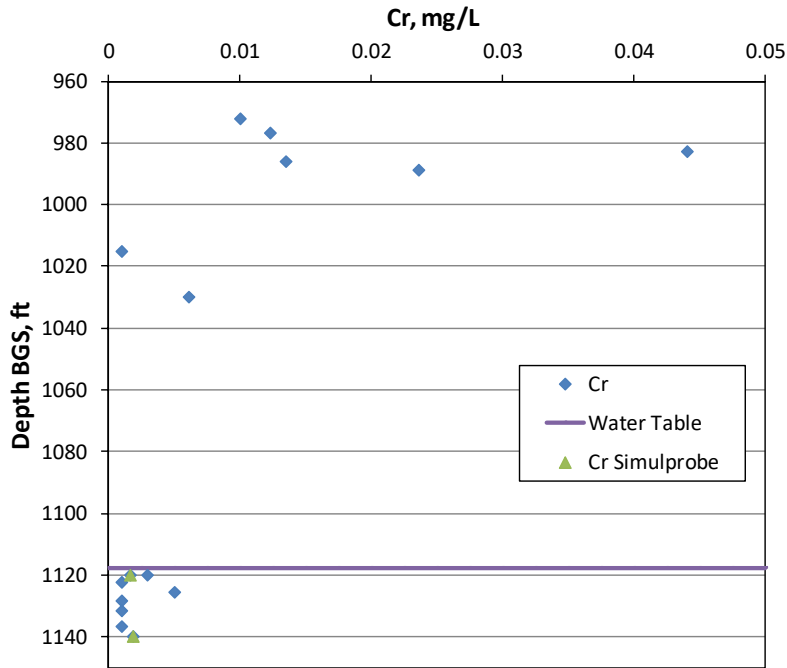


Figure A-3.0-3 Chromium concentrations vs depth in CrCH-1, including simulprobe data

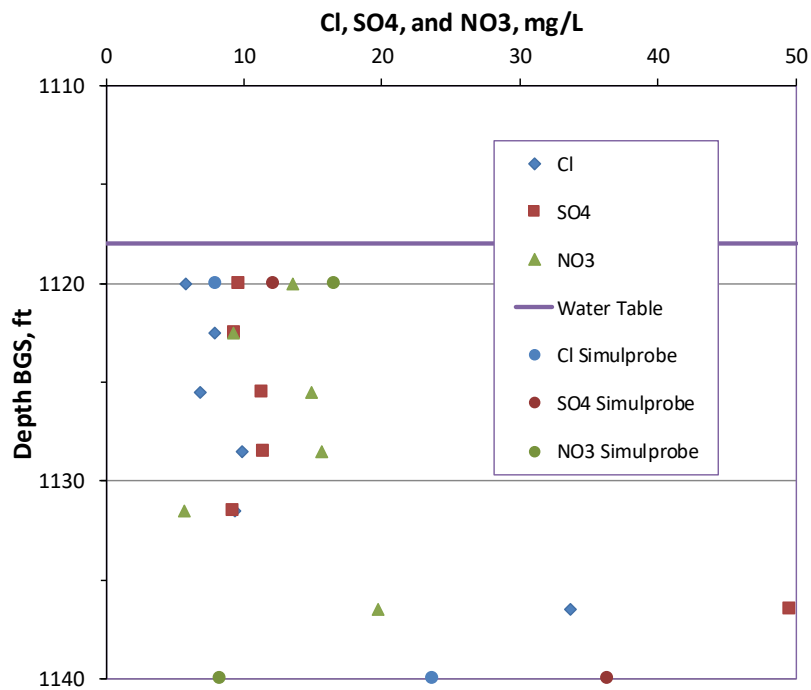


Figure A-3.0-4 Anion concentrations in pore water below the water table vs depth in CrCH-1. Simulprobe samples are included and shown as circles.

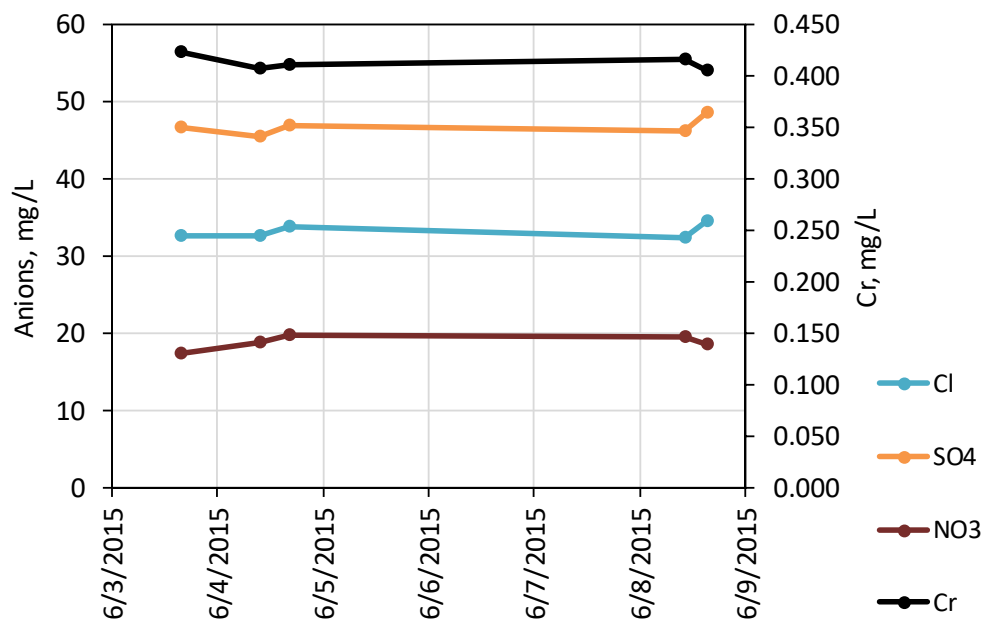


Figure A-3.0-5 Concentrations of anions and Cr as a function of time during pumping of CrCH-1 with a Bennett pump capable of about 0.5 gal. per minute

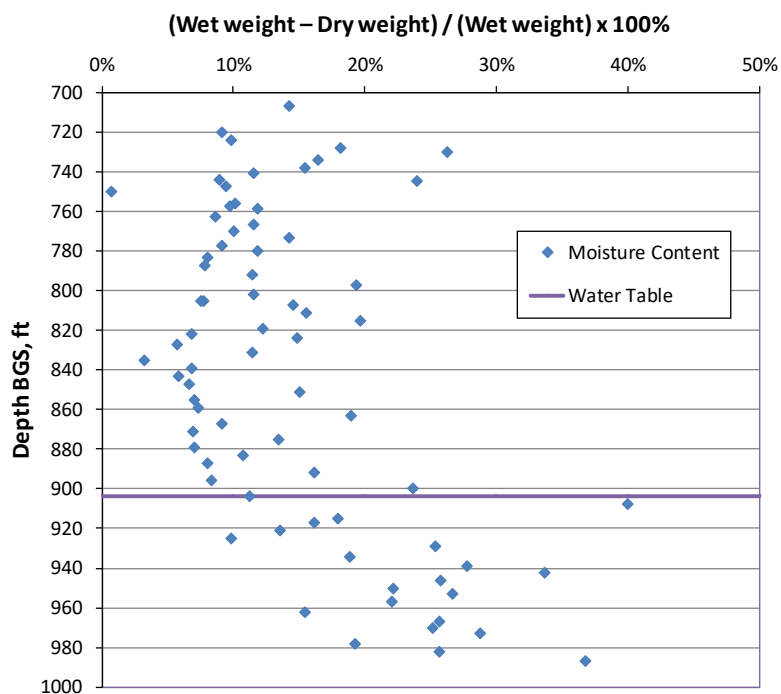


Figure A-3.0-6 Moisture content vs depth in CrCH-2

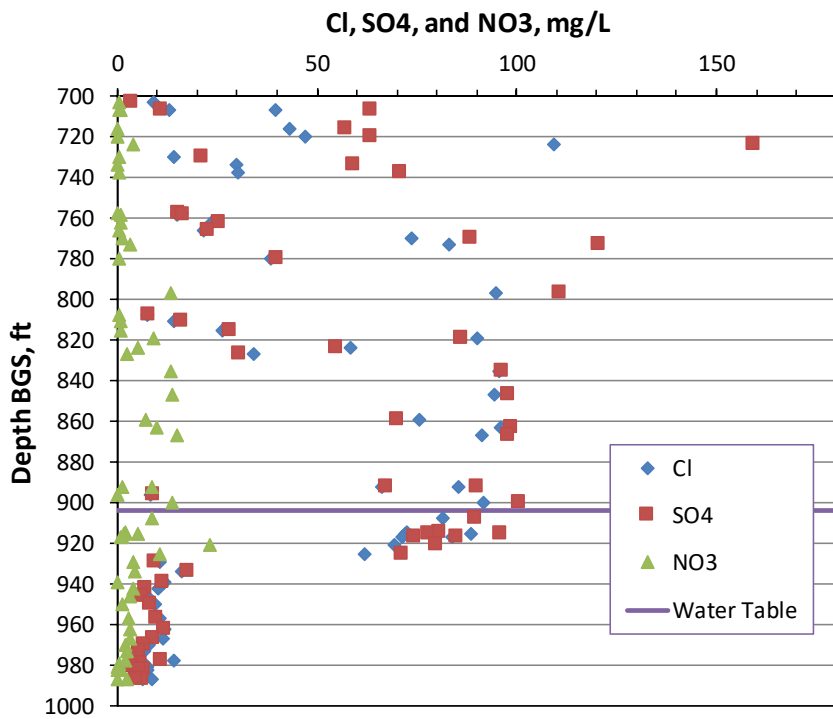


Figure A-3.0-7 Anion concentrations in pore water vs depth in CrCH-2

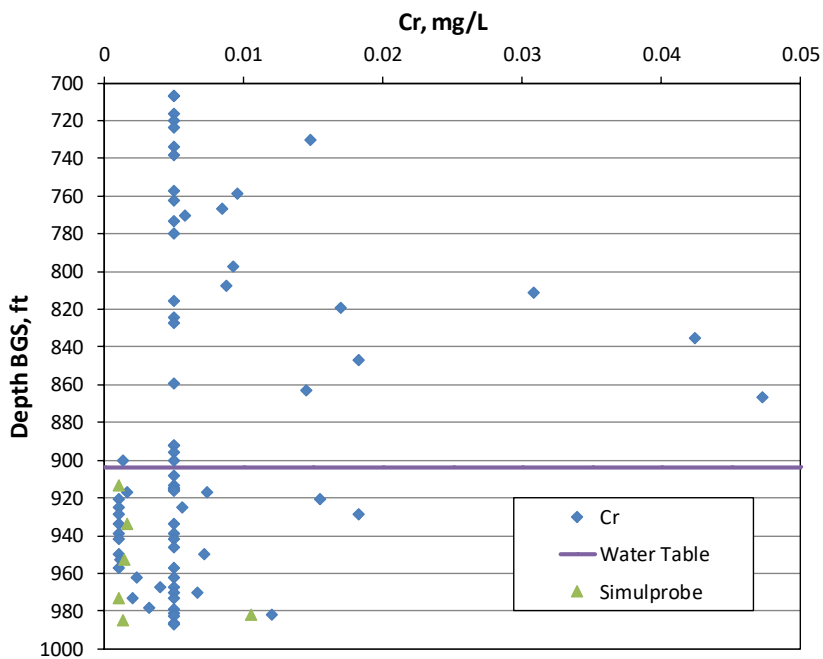


Figure A-3.0-8 Chromium concentrations vs. depth in CrCH-2, including simulprobe data

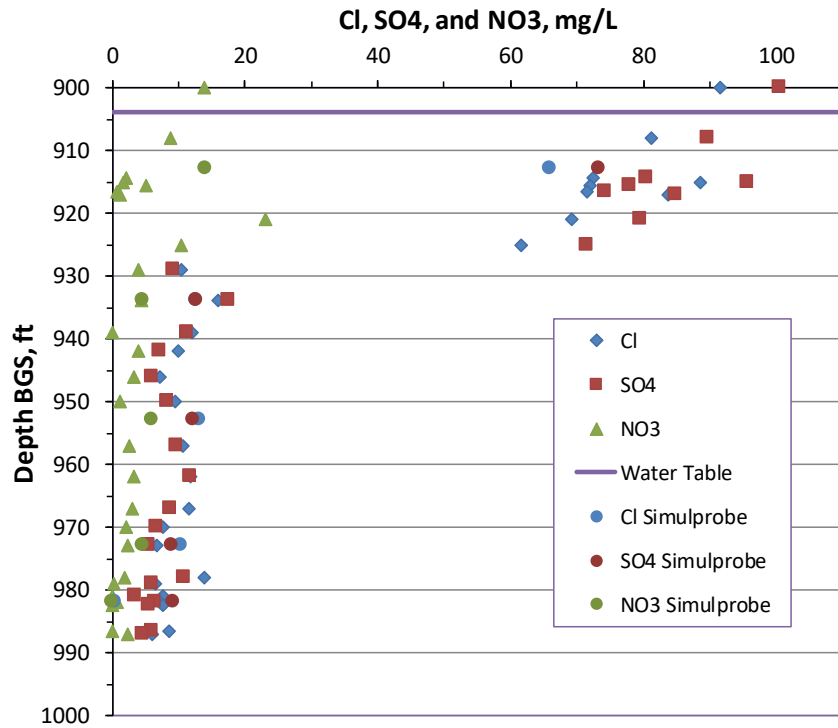


Figure A-3.0-9 Anion concentrations in pore water below the water table vs depth in CrCH-2. Simulprobe samples are included and shown as circles.

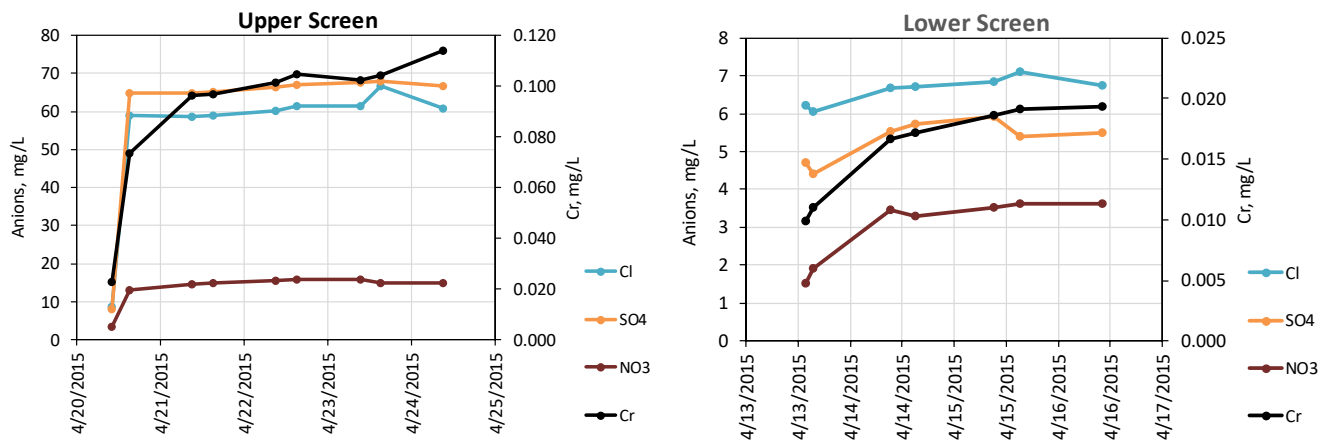


Figure A-3.0-10 Concentrations of anions and Cr as a function of time during pumping of both piezometers (upper and lower screens) of CrCH-2 with a Bennett pump capable of about 0.5 gal. per minute

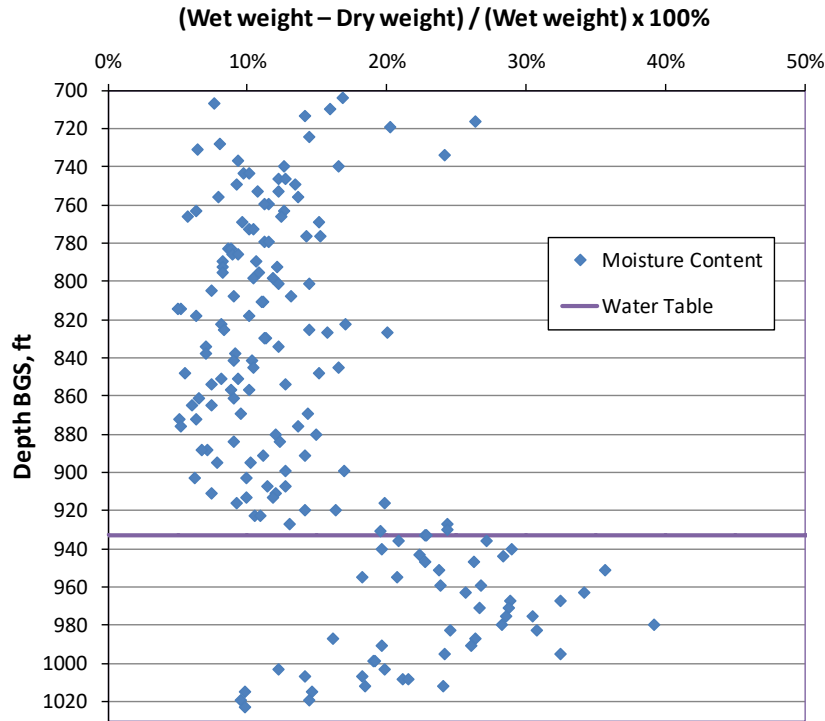


Figure A-3.0-11 Moisture content vs depth in CrCH-3

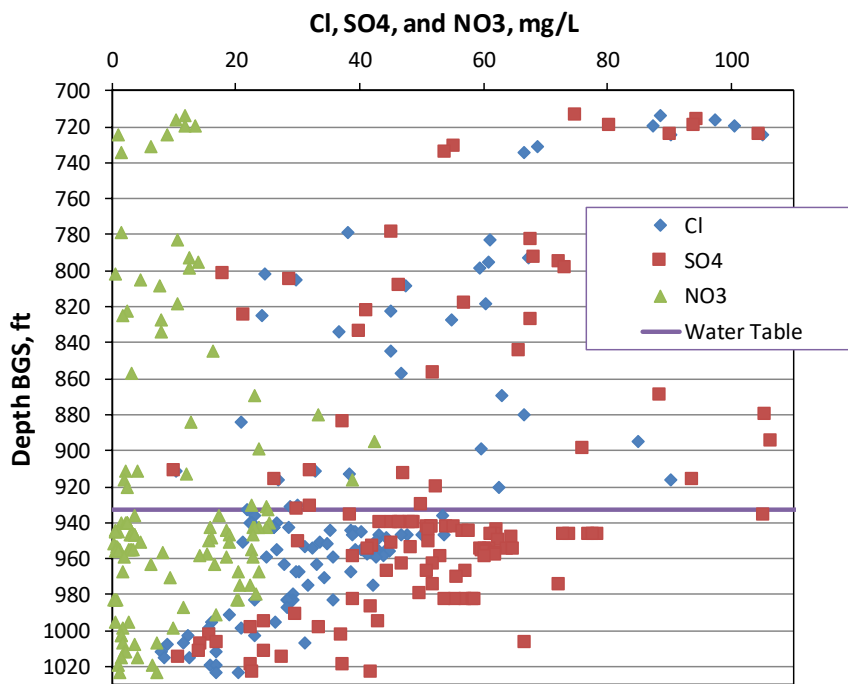


Figure A-3.0-12 Anion concentrations in pore water vs depth in CrCH-3

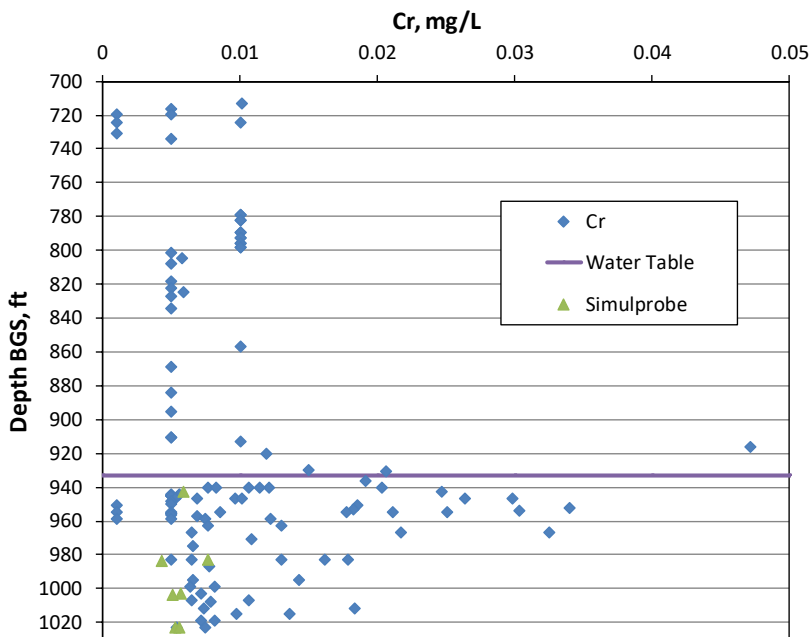


Figure A-3.0-13 Chromium concentrations vs depth in CrCH-3, including simulprobe data

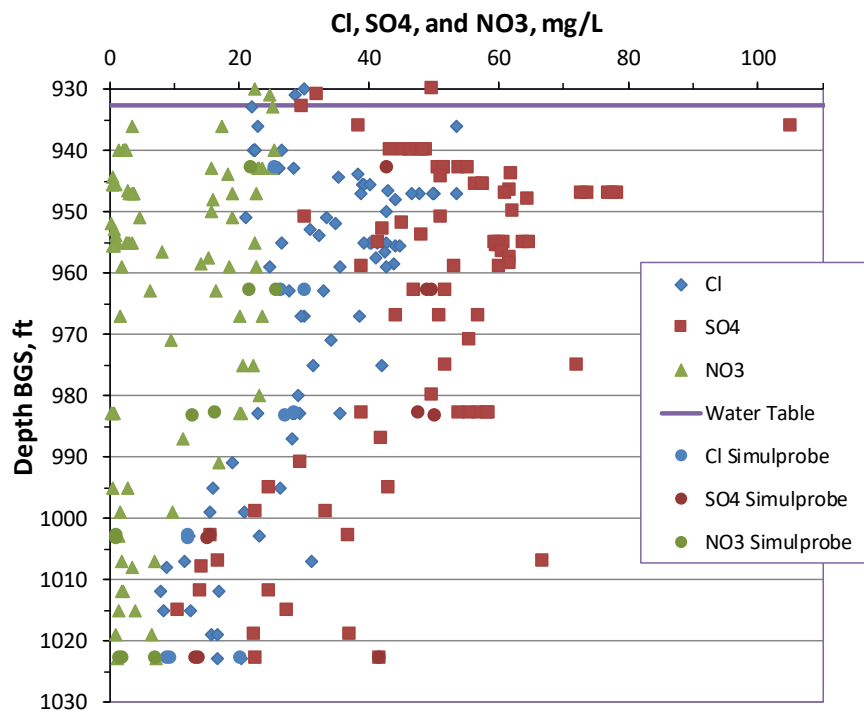


Figure A-3.0-14 Anion concentrations in pore water below the water table vs depth in CrCH-3. Simulprobe samples are included and shown as circles.

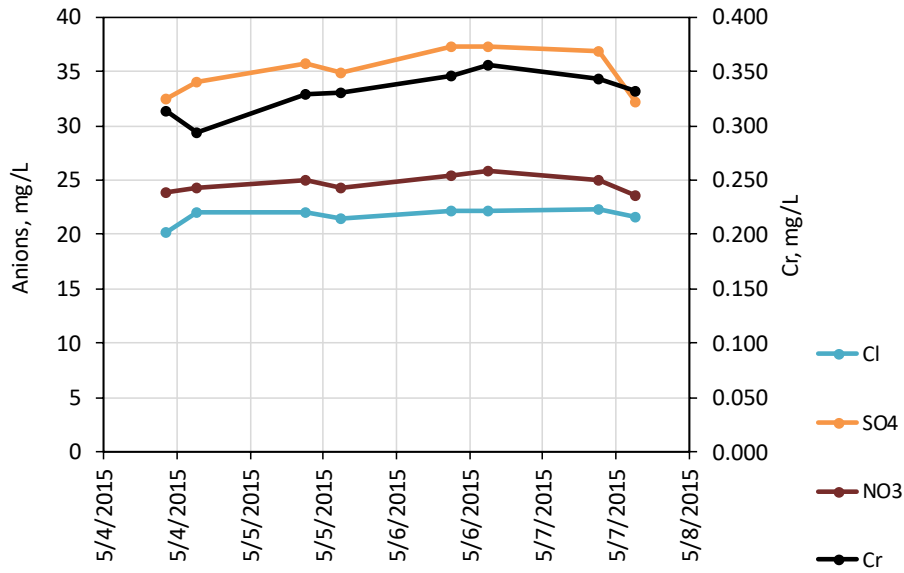


Figure A-3.0-15 Concentrations of anions and Cr as a function of time during pumping of CrCH-3 with a Bennett pump capable of about 0.5 gal. per minute

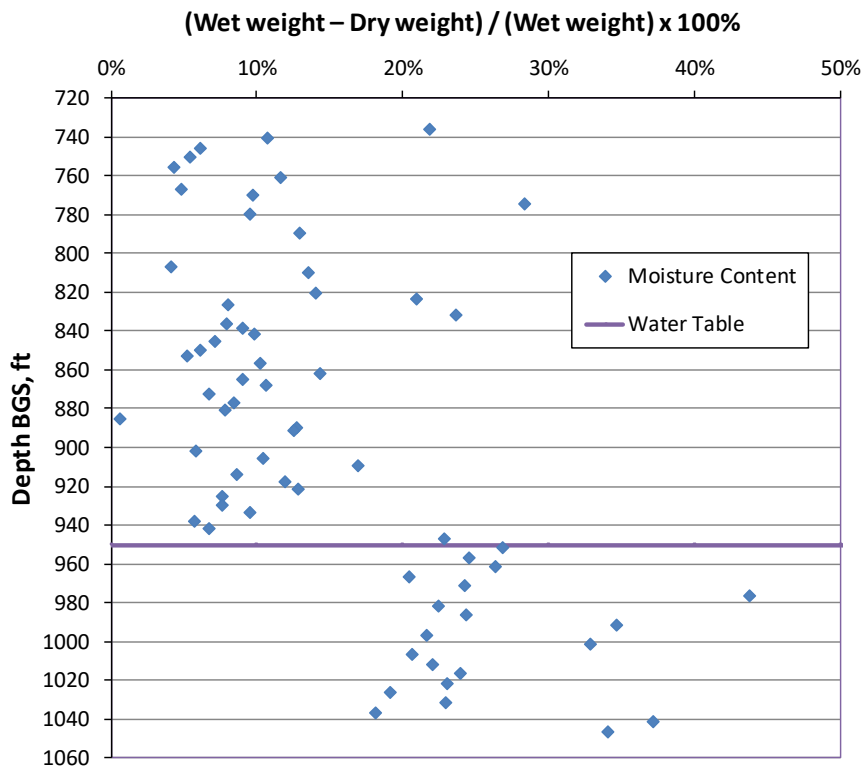


Figure A-3.0-16 Moisture content vs depth in CrCH-4

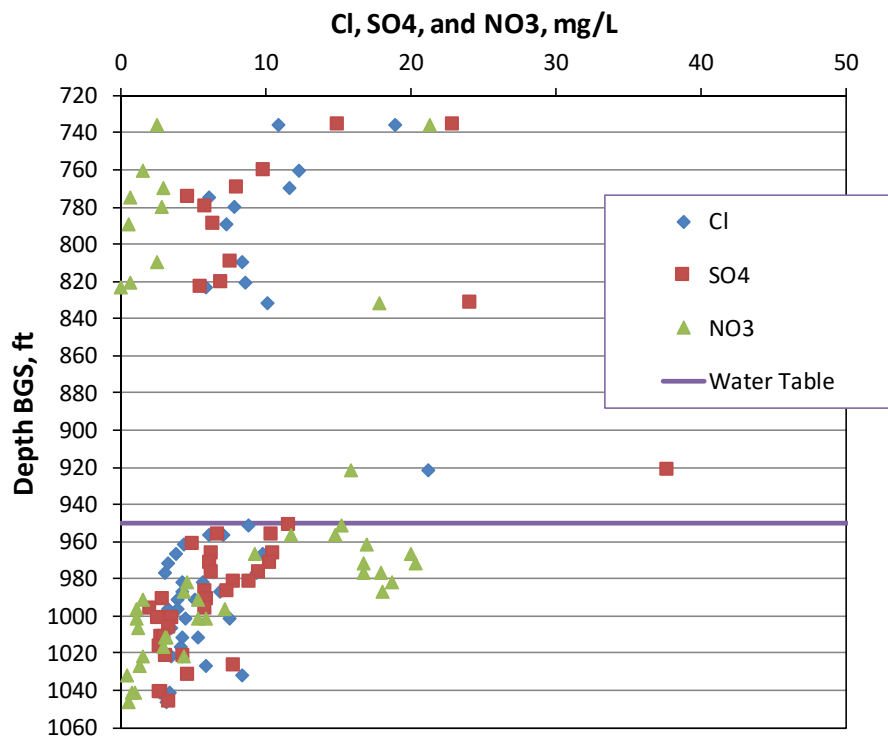


Figure A-3.0-17 Anion concentrations in pore water vs depth in CrCH-4

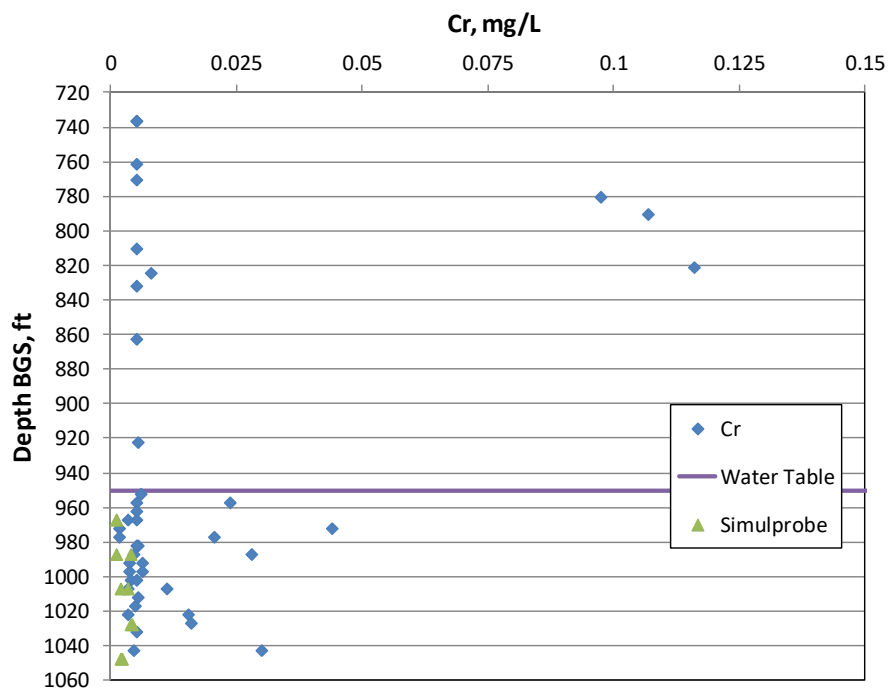


Figure A-3.0-18 Chromium concentrations vs depth in CrCH-4, including simulprobe data

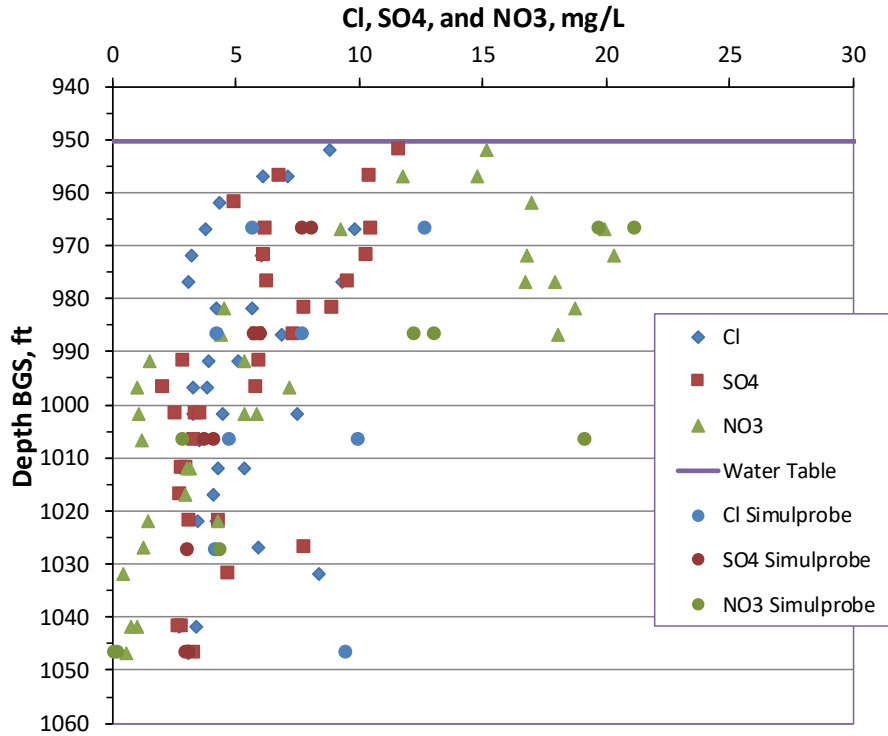


Figure A-3.0-19 Anion concentrations in pore water below the water table vs depth in CrCH-4. Simulprobe samples are included and shown as circles.

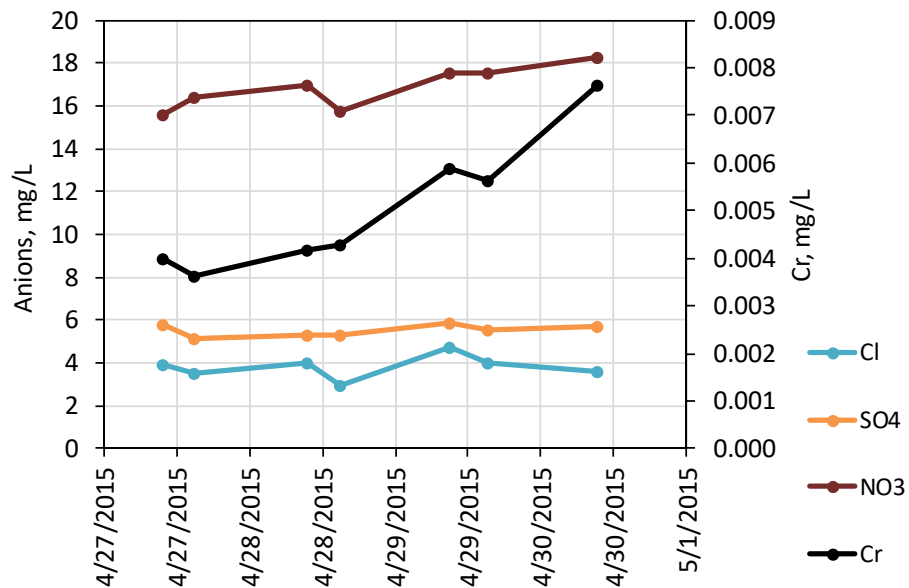


Figure A-3.0-20 Concentrations of anions and Cr as a function of time during pumping of CrCH-4 with a Bennett pump capable of about 1 gal. per minute

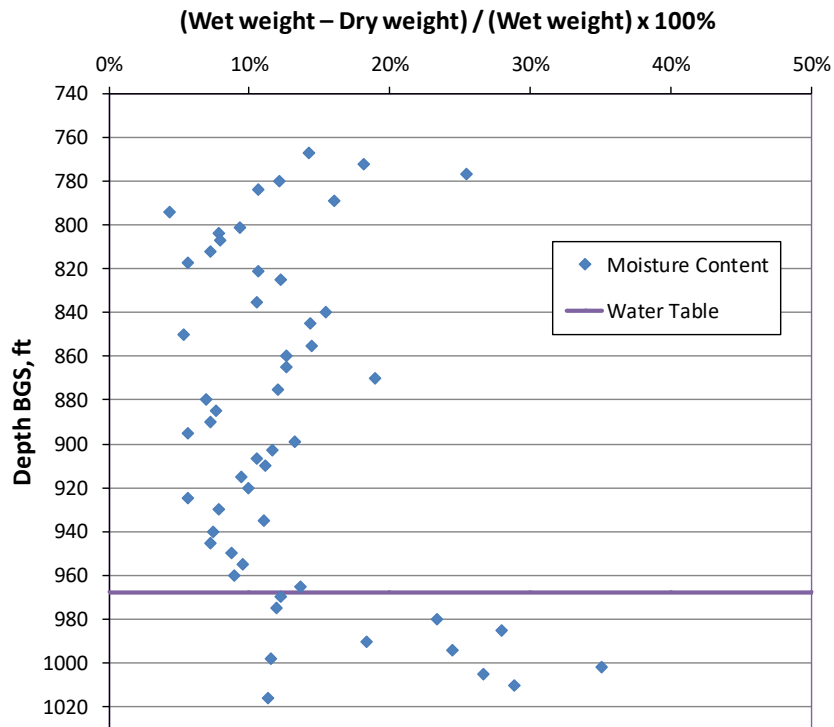


Figure A-3.0-21 Moisture content vs depth in CrCH-5

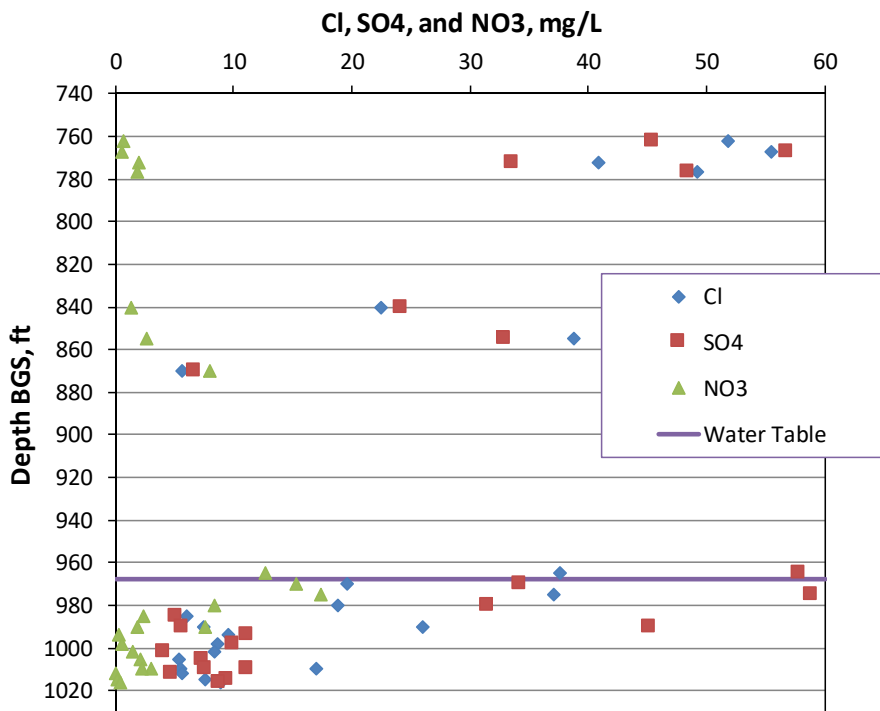


Figure A-3.0-22 Anion concentrations in pore water vs depth in CrCH-5

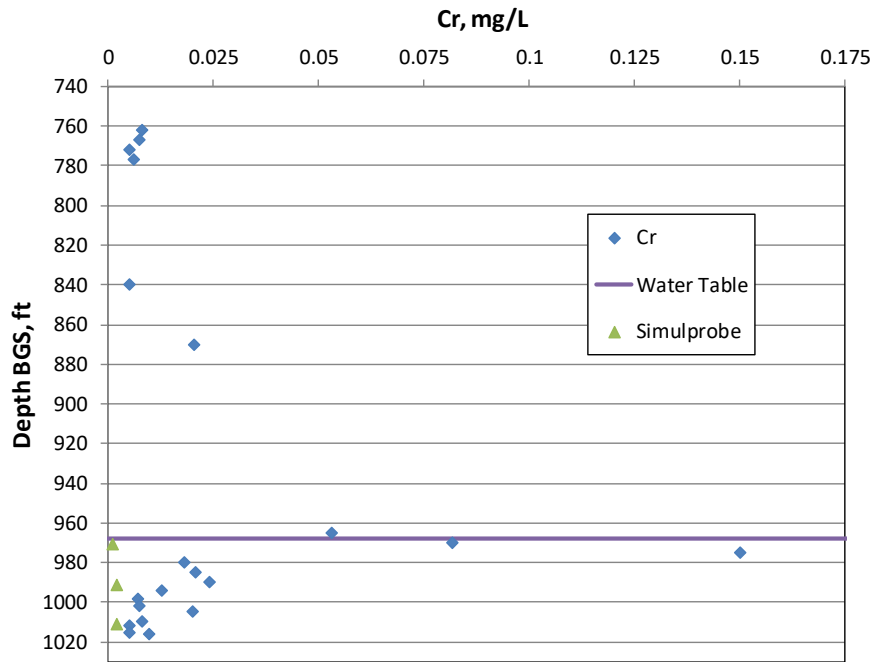


Figure A-3.0-23 Chromium concentrations vs depth in CrCH-5, including simulprobe data

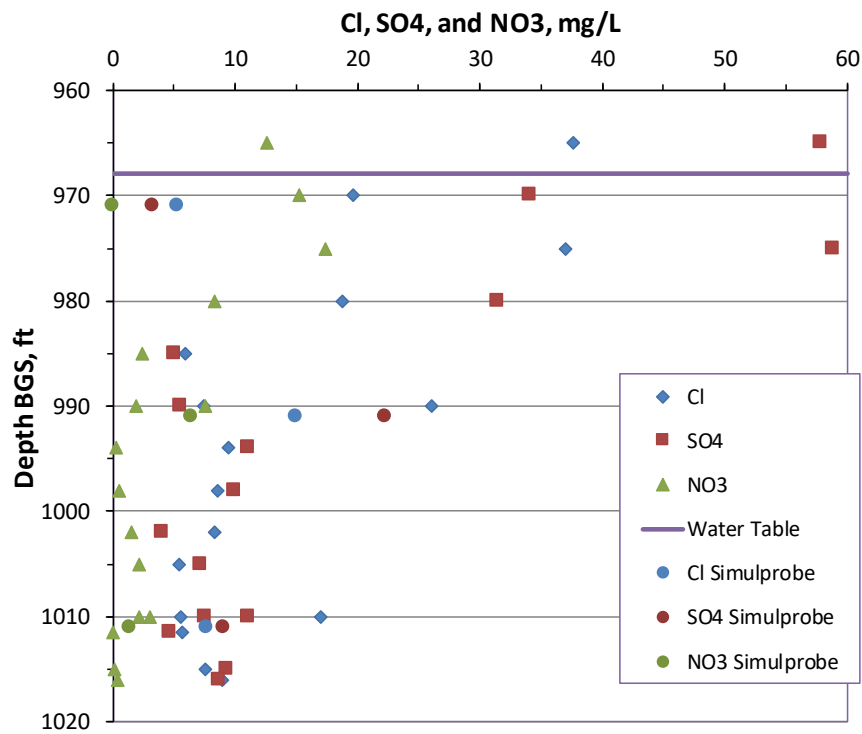


Figure A-3.0-24 Anion concentrations in pore water below the water table vs depth in CrCH-5. Simulprobe samples are included and shown as circles.

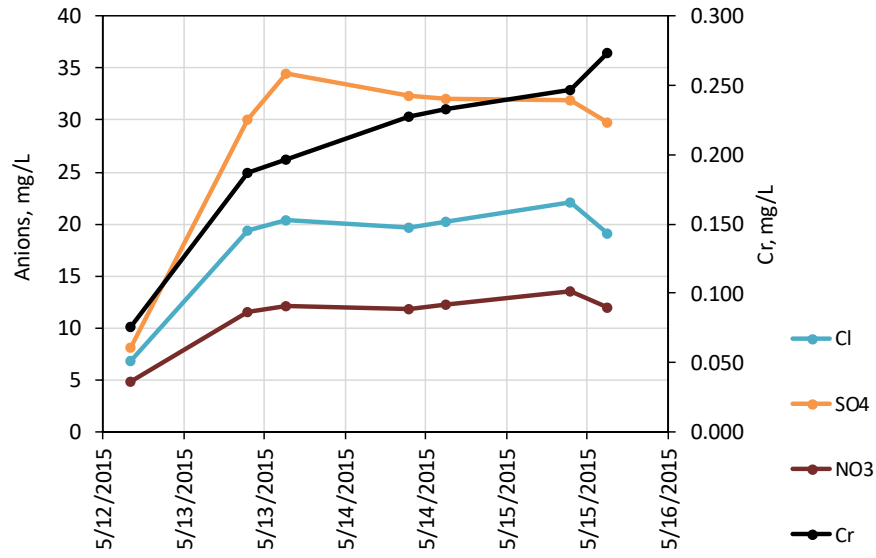


Figure A-3.0-25 Concentrations of anions and Cr as a function of time during pumping of CrCH-5 with a Bennett pump capable of about 0.5 gal. per minute

Appendix B

*Long-Term Trends (through mid-2017) in
Selected Monitoring Wells in which there have been
Notable Increases in Cr(VI) Concentrations*

B-1.0 INTRODUCTION

Collectively, the plots shown in Figures B.1-0-1 through B.1-0-5 of this appendix indicate that hexavalent chromium [Cr(VI)] is rising in concentration in monitoring wells at the periphery of the chromium plume essentially in tandem with anions that are known to be nonreactive/conservative and that also originate from surface sources (SO_4^- , Cl^- , and in some cases, NO_3^-). Although the surface source locations for the anions are not necessarily the same as the primary source for Cr(VI) (the head of Sandia Canyon), SO_4^- is believed to be predominantly from the same source location as Cr(VI). The only monitoring location where there appears to be any delay of Cr(VI) concentration rises relative to any of the anions is at perched-intermediate groundwater monitoring well MCOI-6 in Mortandad canyon, where SO_4^- is leading Cr(VI) by perhaps as much as a year (see Figure B-1.0-1). However, this result may be more affected by releases from a different source location, namely the Radioactive Liquid Effluent Facility outfall in Mortandad Canyon, than the majority of the Cr(VI) and SO_4^- , which was released at the head of Sandia Canyon. In all other monitoring wells, the conclusion is that Cr(VI) is not lagging any of the other anions, and the implication is that there is not any significant natural attenuation of Cr(VI) occurring within the chromium plume area. One cannot rule out the possibility that there is some natural attenuation occurring (i.e., Cr(VI) reduction to trivalent chromium [Cr(III)]), but if there is, its effect must be limited to the lowering of the concentrations of Cr(VI), not delaying the overall transport rate of Cr(VI). If this situation is indeed occurring, it would imply that natural attenuation must be occurring only in secondary porosity, and it would also imply that such attenuation must be rather limited because a significant amount of reduction in secondary porosity would still result in a delay in Cr(VI) transport relative to conservative anions.

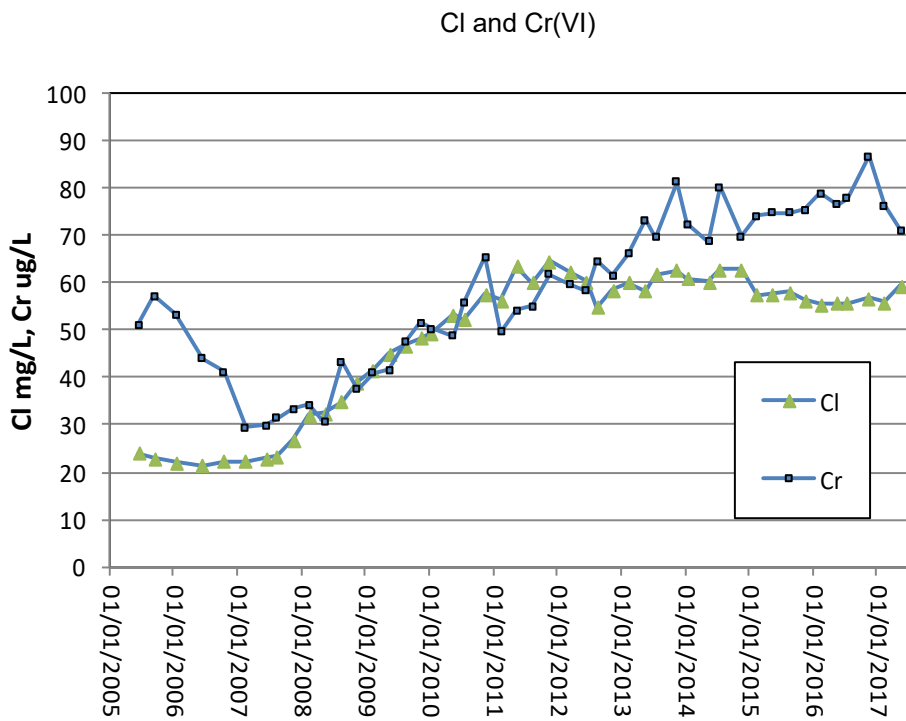
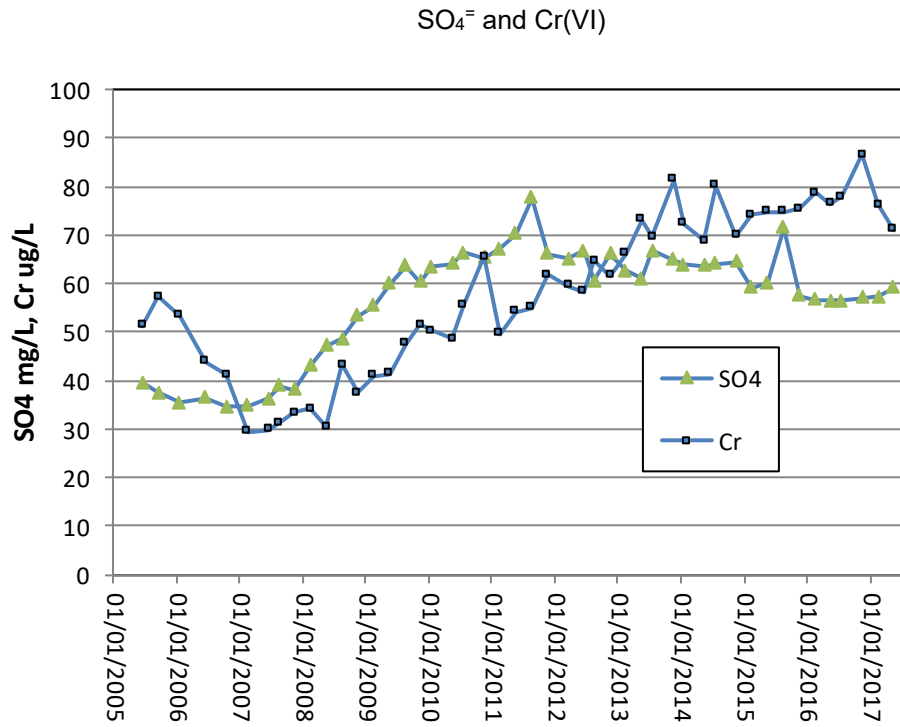


Figure B-1.0-1 Trends in MCOI-6 (intermediate well in Mortandad Canyon)

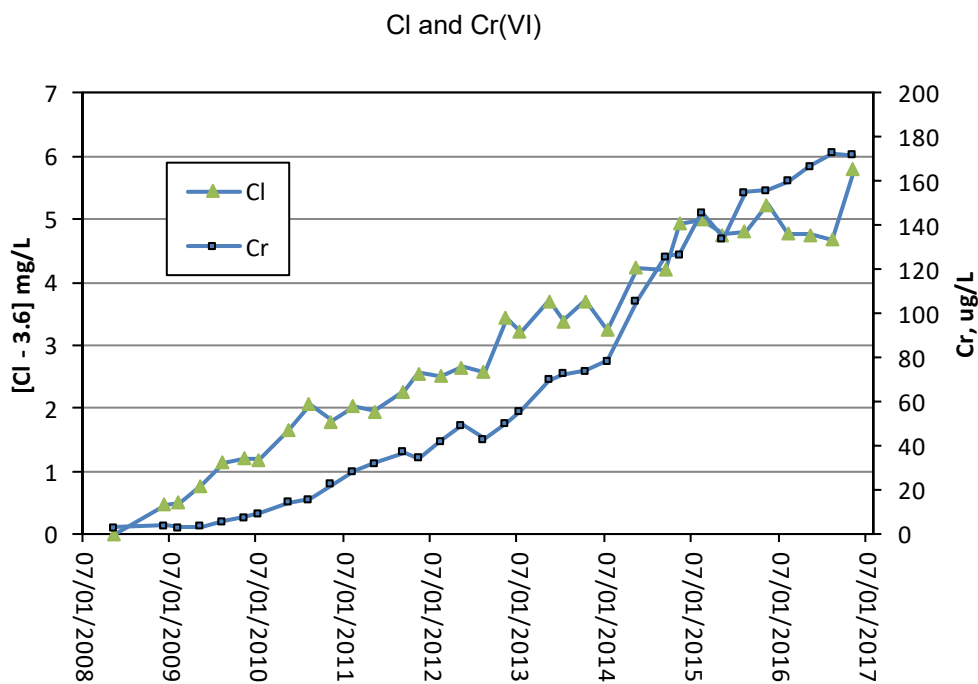
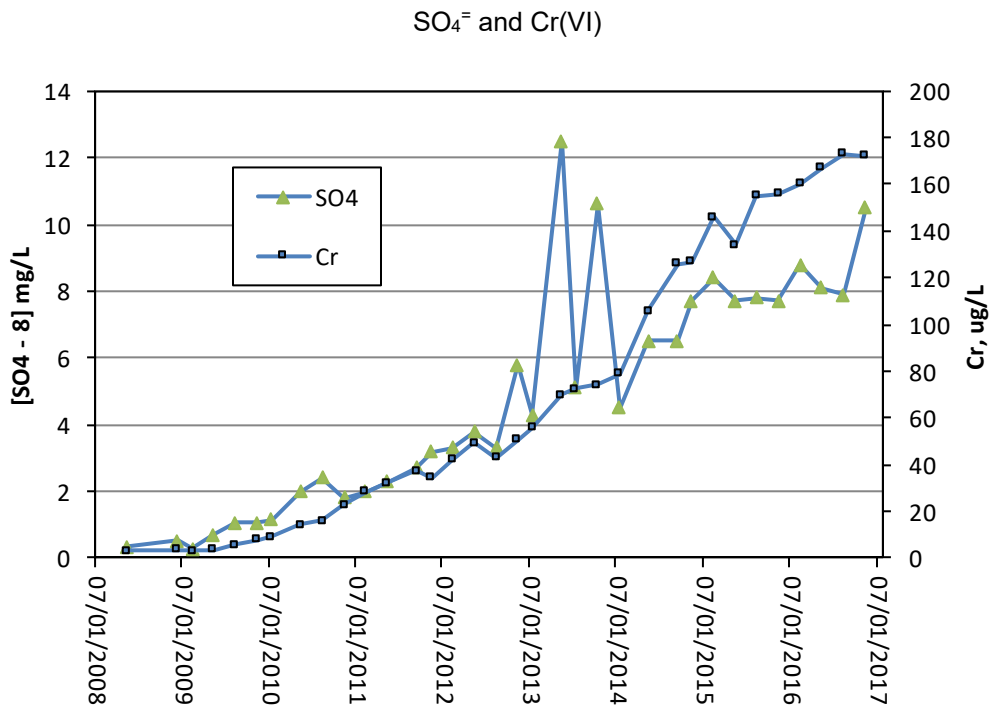


Figure B-1.0-2 Trends in R-43 S1

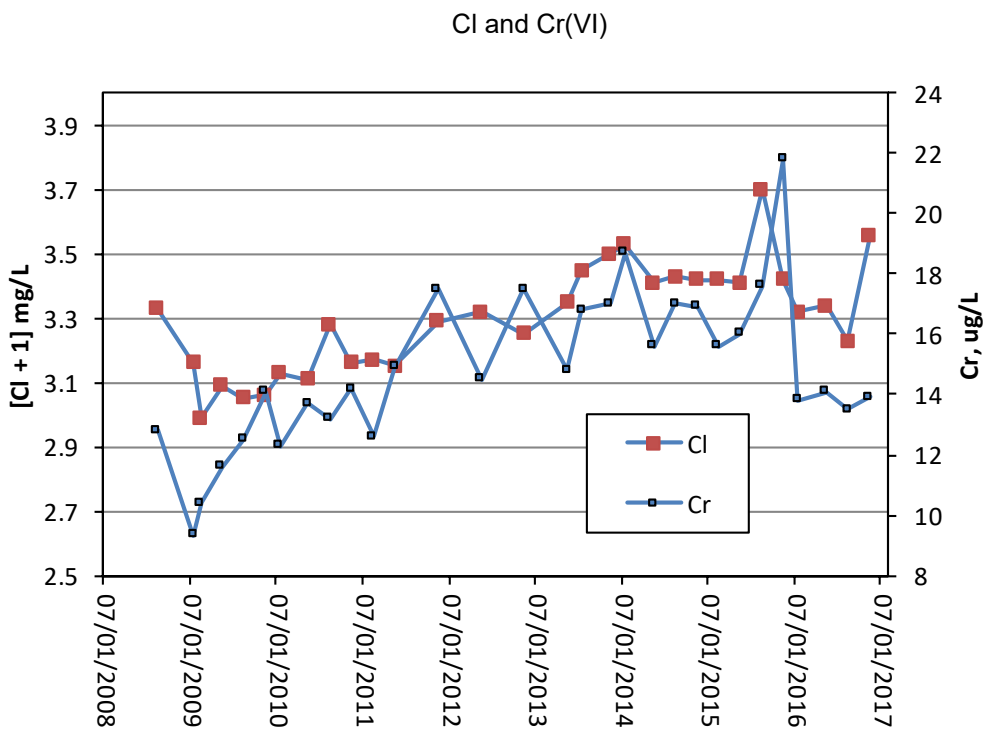
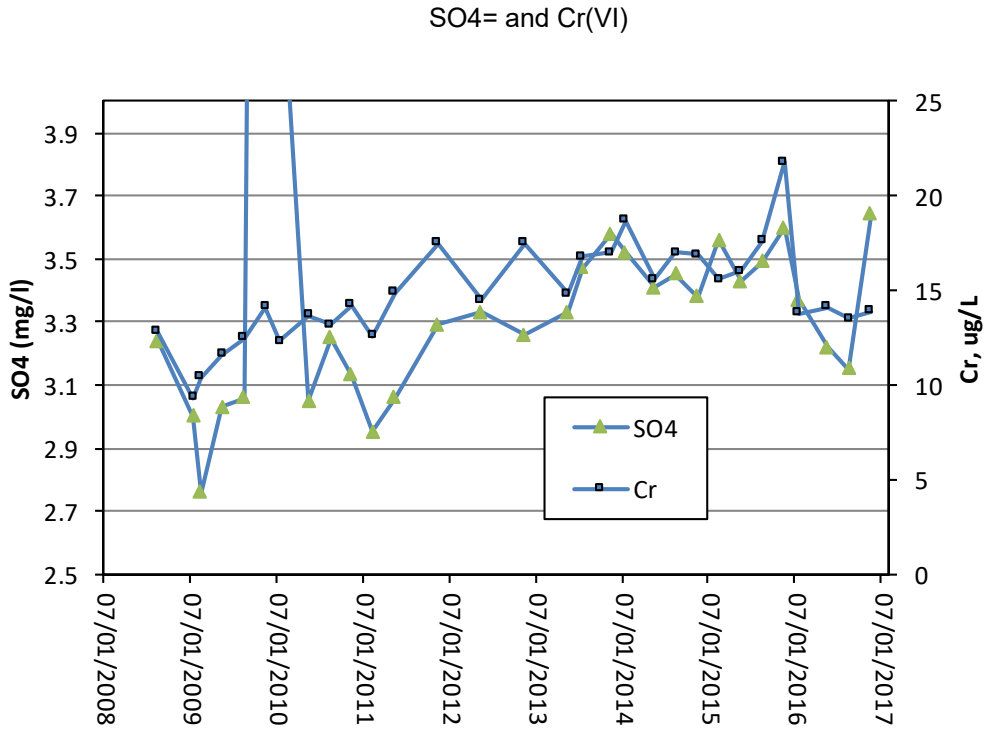


Figure B-1.0-3 Trends in R-44 S1

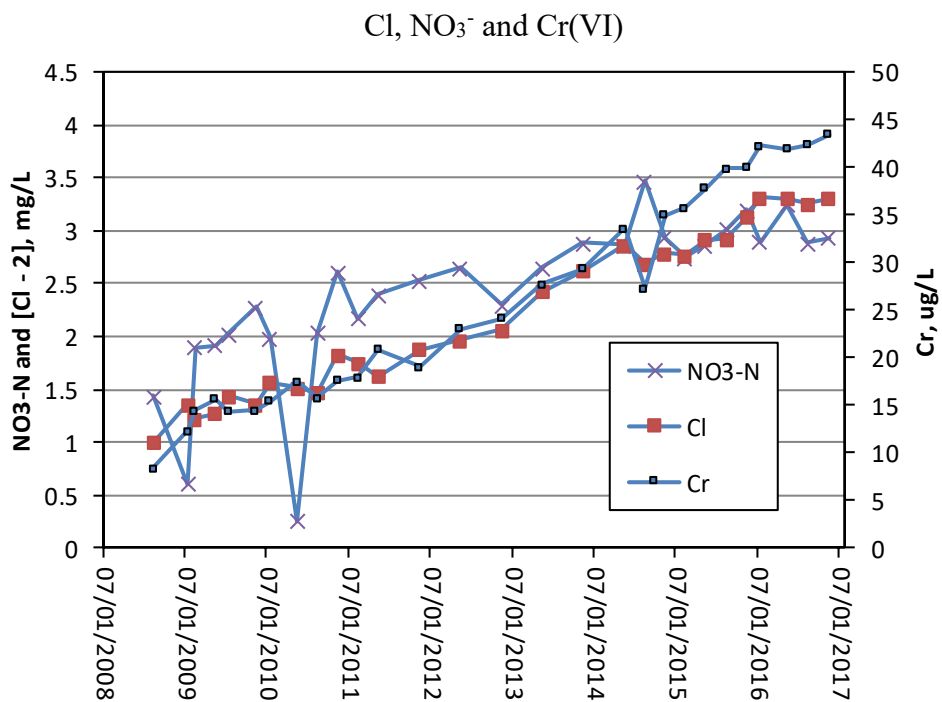
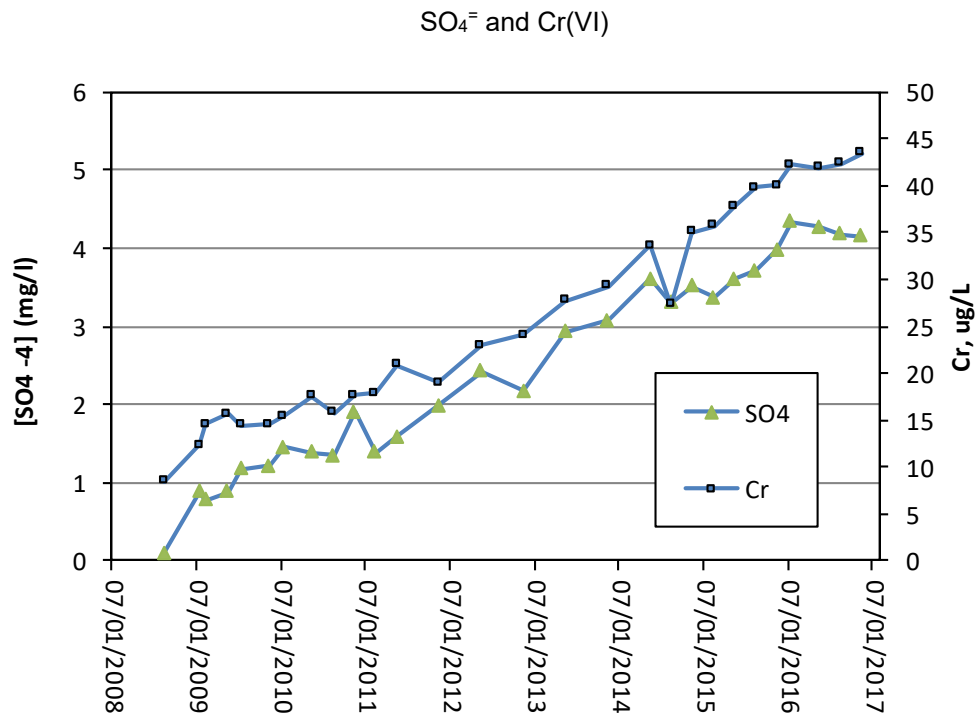


Figure B-1.0-4 Trends in R-45 S1

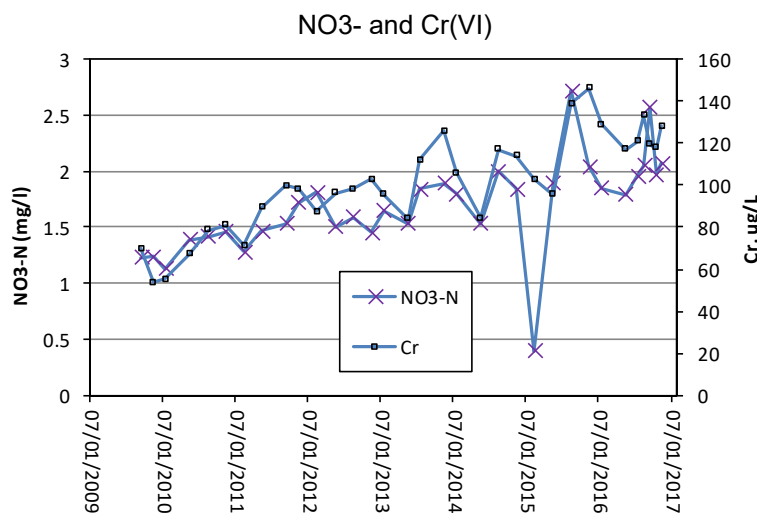
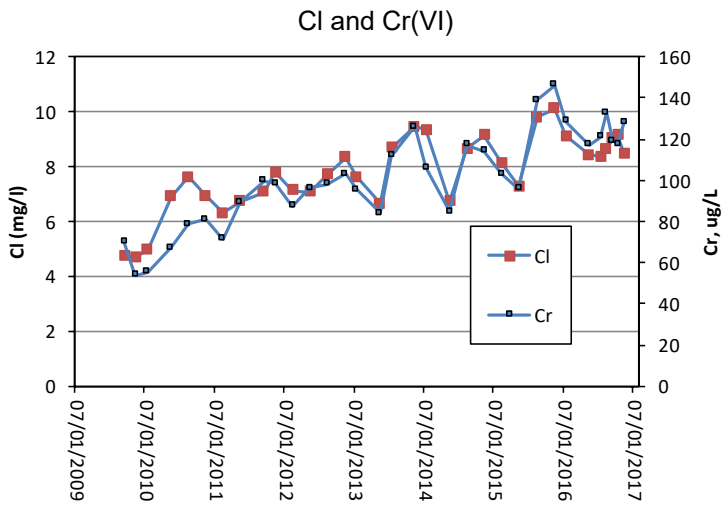
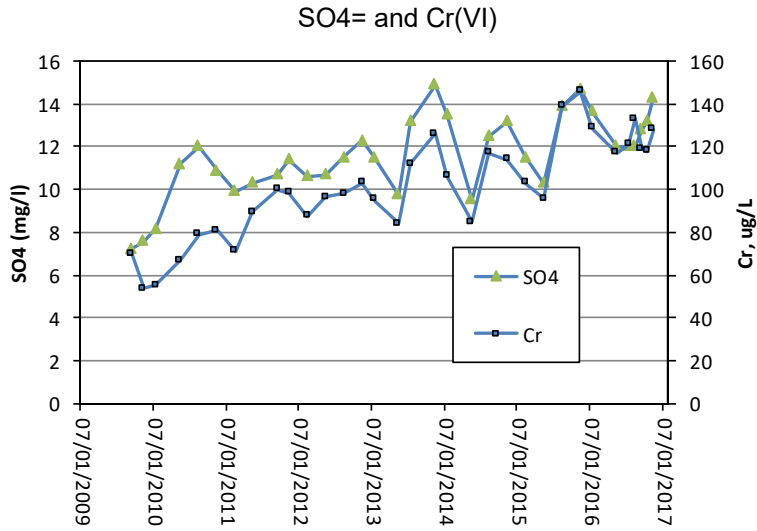


Figure B-1.0-5 Trends in R-50 S1

LA-UR-18-21450
March 2018
EP2018-0028

Isotopic Signatures of Hexavalent Chromium in the Regional Aquifer: Evaluation of Natural Attenuation

Attachment 2

Prepared by the Associate Directorate for Environmental Management

Los Alamos National Laboratory, operated by Los Alamos National Security, LLC, for the U.S. Department of Energy (DOE) under Contract No. DE-AC52-06NA253 and under DOE Office of Environmental Management Contract No. DE-EM0003528, has prepared this document pursuant to the Compliance Order on Consent, signed June 24, 2016. The Compliance Order on Consent contains requirements for the investigation and cleanup, including corrective action, of contamination at Los Alamos National Laboratory. The U.S. government has rights to use, reproduce, and distribute this document. The public may copy and use this document without charge, provided that this notice and any statement of authorship are reproduced on all copies.

CONTENTS

1.0	INTRODUCTION	1
2.0	ANALYTICAL METHOD	1
3.0	INVESTIGATION SCOPE	1
4.0	RESULTS AND DISCUSSION	2
5.0	CONCLUSION	4
6.0	REFERENCES AND MAP DATA SOURCES	5
6.1	References	5
6.2	Map Data Sources	6

Figures

Figure 1.0-1	Location Map showing outfalls, the Sandia Canyon wetland, the primary Cr(VI) infiltration zone, location of monitoring wells, and the area of Cr(VI) concentration exceeding 50 µg/L in the regional aquifer	7
Figure 4.0-1	Most recent $\delta^{53}\text{Cr}$ (‰) and Cr concentration (µg/l) for perched-intermediate and regional aquifer wells in Sandia Canyon and Mortandad Canyon (sample dates from 2007–2016)	8
Figure 4.0-2a	R-43(1) quarterly $\delta^{53}\text{Cr}$ sampling analysis with corresponding [Cr] from 2008 to 2016.	9
Figure 4.0-2b	R-43(2) quarterly $\delta^{53}\text{Cr}$ sampling analysis with corresponding [Cr] from 2008 to 2016.	9
Figure 4.0-2c	R-44(1) quarterly $\delta^{53}\text{Cr}$ sampling analysis with corresponding [Cr] from 2008 to 2016. ...	10
Figure 4.0-2d	R-45(1) quarterly $\delta^{53}\text{Cr}$ sampling analysis with corresponding [Cr] from 2008 to 2016. ...	10
Figure 4.0-2e	R-45(2) quarterly $\delta^{53}\text{Cr}$ sampling analysis with corresponding [Cr] from 2008 to 2016. ...	11
Figure 4.0-2f	R-50(1) quarterly $\delta^{53}\text{Cr}$ sampling analysis with corresponding [Cr] from 2008 to 2016. ...	11
Figure 4.0-3	$\delta^{53}\text{Cr}$ versus [Cr] for most recent data from each well	12
Figure 4.0-4a	$\delta^{53}\text{Cr}$ versus [Cr] for R-43(1) and R-43(2) time-series data	13
Figure 4.0-4b	$\delta^{53}\text{Cr}$ versus [Cr] for R-44(1) and R-44(2) time-series data	14
Figure 4.0-4c	$\delta^{53}\text{Cr}$ versus [Cr] for R-45(1) and R-45(2) time-series data	15
Figure 4.0-4d	$\delta^{53}\text{Cr}$ versus [Cr] for R-50(1) time-series data	16
Figure 4.0-5	Time series for chloride, sulfate and chromium at R45(1)	17
Figure 4.0-6a	Experimental $\delta^{53}\text{Cr}$ and [Cr] data for the initial ZVI experiment plotted as a time series .	17
Figure 4.0-6b	Experimental $\delta^{53}\text{Cr}$ and [Cr] data for a second ZVI experiment plotted as a time series .	18
Figure 4.0-6c	Microbial bioreduction experimental $\delta^{53}\text{Cr}$ and [Cr] concentration data plotted as a time series	18
Figure 4.0-7a	ZVI experimental $\delta^{53}\text{Cr}$ and associated f with $\epsilon = 1.91$	19
Figure 4.0-7b	Microbial reduction experimental $\delta^{53}\text{Cr}$ and associated f with $\epsilon = 3.57$	19

Tables

Table 3.0-1	Summary of Quarterly Data	21
Table 3.0-2	Summary of CrPZ Well Data.....	29
Table 3.0-3	Summary of Data from CrEX-1, CrEX-3, CrIN Wells and Regional Aquifer Pump Tests	31
Table 4.0-1	Summary of Experimental Data	34

1.0 INTRODUCTION

Chromium isotopes are key parameters to estimate hexavalent chromium [Cr(VI)] reduction and related geochemical processes such as sorption and dilution of Cr(VI) occurring within an aquifer. When Cr(VI) reduction occurs, the residual Cr(VI) in groundwater becomes enriched in heavier chromium isotopes, whereas the lighter isotopes are preferentially incorporated into precipitated trivalent chromium [Cr(III)] solids. The most common method used to quantify the degree of Cr(VI) reduction is a Rayleigh model. One limitation of using chromium isotopes to estimate reduction is that chromium isotopes can be used only to estimate how much reduction occurred along a particular flow path, not precisely where the reduction occurred.

In Heikoop et al. (2014), evidence of reduction was found in the vadose zone, likely related to reduction of Cr(VI) in the divalent iron– [Fe(II)]-rich Cerros del Rio basalts, but little evidence for Cr(VI) reduction in the regional aquifer was identified. This study provides an update on the results described by Heikoop et al. (2014; 255424) with the addition of geochemical and isotopic data from new wells to further assess natural attenuation in the regional aquifer. An updated map of the study area is shown in Figure 1.0-1.

2.0 ANALYTICAL METHOD

Groundwater samples were collected at perched-intermediate and regional monitoring wells (Figure 1.0-1) in 1-L high-density polypropylene bottles. Target analytes include total chromium ([Cr]) concentration, Cr(VI) concentration for a subset of samples, and chromium isotopic ratio ($\delta^{53}\text{Cr}$). Chromium isotope samples were filtered but not acidified. All samples were analyzed for $\delta^{53}\text{Cr}$ and concentrations on a Nu Instruments high-resolution multicollector inductively coupled plasma mass spectrometer at the University of Illinois at Urbana-Champaign using a $^{54}\text{Cr}/^{50}\text{Cr}$ double-isotope spike technique (Ellis et al. 2002; Schoenberg et al. 2008). For a detailed description of sample preparation and analytical techniques, see Raddatz et al. (2011). Uncertainty in $\delta^{53}\text{Cr}$ is $\pm 0.13\%$ (95% confidence interval; Heikoop et al. 2014).

3.0 INVESTIGATION SCOPE

This study was primarily focused on monitoring wells within and around the chromium plume in the regional aquifer (Table 3.0-1). Other regional aquifer and intermediate wells were also included for completeness, including CrPZ piezometers, the CrEX-1 and CrEX-3 extraction wells, CrIN injection wells, the Sandia Canyon SCI-2 intermediate well, and Mortandad Canyon intermediate wells. However, CrPZ data (Table 3.0-2) and CrEX-1, and CrEX-3 data (Table 3.0-3) should be used with caution, as these wells are not formal monitoring wells; temporal trends in $\delta^{53}\text{Cr}$ from these wells were not considered. In addition, data from chromium injection wells were included in Table 3.0-3 but were not plotted or subject to rigorous analysis. Well SCI-2 is completed in deep perched groundwater and may represent a recharge pathway from Sandia Canyon to the regional aquifer. Mortandad Canyon intermediate wells may contain Cr(VI) from multiple sources (Heikoop et al. 2014).

For the purposes of this study, wells with typical total chromium concentrations below 8 ppb are considered to be background wells, and wells with typical total chromium concentrations exceeding 50 ppb are considered to be within the chromium plume centroid. Any well with typical total chromium concentrations between 8 and 50 ppb are considered to be within the chromium plume but not within the chromium plume centroid.

Groundwater samples can provide only an estimate of the total chromium and hexavalent chromium concentrations and chromium isotope ratios in complex formations because of potential biases associated with preferential sampling from primary porosity (e.g., chromium reduction could occur preferentially in secondary porosity). In addition, uncertainty in the $\delta^{53}\text{Cr}$ of the industrial source adds uncertainty in calculating the Cr(VI) reduction occurring along a flow path. A discussion of the presence of reduction within the regional aquifer and a comparison of fractionation factors (ϵ) from experiments and literature follows, using these data and the relationship between $\delta^{53}\text{Cr}$ and chromium concentration as described in Ellis et al. (2002).

No samples of the potassium dichromate used in the Technical Area 03 (TA-03) cooling tower (the – chromium source from Sandia Canyon) were available for analysis. Potassium dichromate solutions used by Jamieson-Hanes et al. (2012) in batch and column experiments were close to 0‰. Here we assume a value of 0‰ for $\delta^{53}\text{Cr}$ of contaminant Cr(VI), consistent with measurements of industrial chromate solutions (Ellis et al. 2002; Schoenberg et al. 2008).

4.0 RESULTS AND DISCUSSION

The most recent quarterly $\delta^{53}\text{Cr}$ and [Cr] concentration (as a proxy for [Cr(VI)]) are shown in Figure 4.0-1 and Table 3.0-1. Background wells, such as R-67, are shown to have the highest $\delta^{53}\text{Cr}$, and wells within the regional aquifer chromium plume have a fairly constant $\delta^{53}\text{Cr}$ around 1‰ regardless of concentration. If significant reduction of Cr(VI) was occurring within the regional aquifer, $\delta^{53}\text{Cr}$ would be expected to be higher at the periphery, where any reduction capacity would be acting on lower Cr(VI) concentrations. However, that pattern is not observed in the data. Although not the focus of this study, intermediate wells had variable $\delta^{53}\text{Cr}$ depending on the interaction with the vadose zone basalts and Cr source (Sandia Canyon vs Mortandad Canyon) (Heikoop et al. 2014).

Time-series analysis reveals that most chromium plume periphery wells show increases in [Cr] and decreases in $\delta^{53}\text{Cr}$ approaching 1‰ over time, consistent with plume expansion/mixing with background waters. These results comparing $\delta^{53}\text{Cr}$ and [Cr] are shown in Figure 4.0-2, a–f. Only regional wells showing significant trends between $\delta^{53}\text{Cr}$ and [Cr] were plotted. Plume centroid wells show little variation in $\delta^{53}\text{Cr}$ over time. In addition to quarterly sampling, pump tests were conducted at R-28, R-42, SCI-2, R-43, and R-62 but significant $\delta^{53}\text{Cr}$ trends were not observed (Table 3.0-3). Extended pumping did not appear to access Cr(VI), showing greater evidence for reduction, regardless of whether the Cr(VI) sampled derived from primary or secondary porosity.

The most recent $\delta^{53}\text{Cr}$ and [Cr] data for the regional wells were plotted with an assumed ϵ value of 3.4‰ (following Ellis et al. 2002) (Figure 4.0-3). Small degrees of reduction in the vadose zone were observed, but most of the variation within the regional aquifer can be explained by mixing with background. Regional background wells have a signature of low [Cr] and slightly higher $\delta^{53}\text{Cr}$, whereas regional wells in the chromium plume show a high [Cr] and lower $\delta^{53}\text{Cr}$ signature similar to 1‰. The dominant geochemical processes affecting $\delta^{53}\text{Cr}$ and [Cr] can be hypothesized using these unique signatures. In Figure 4.0-4, a–d, the time series for $\delta^{53}\text{Cr}$ and [Cr] data of plume periphery wells R-43, R-44, R-45, and R-50 are plotted in similar fashion to Figure 4.0-3. These plots further suggest that mixing is the major geochemical process at the plume periphery, as the plotted points fall along a mixing trend between the contaminant source at the plume centroid and background. Given the relatively small isotopic difference between background wells and wells with significant Cr(VI) contamination, it could potentially be difficult to distinguish mixing and sorption, the latter resulting in Cr(VI) concentration decreases, but no significant isotopic shift (Figures 4.0-3, 4.0-4). The decreasing $\delta^{53}\text{C}$ with increasing [Cr] concentration trends shown in Figures 4.0-2 and 4.0-4, however, are entirely consistent with mixing. Moreover, alkaline leach tests at R-42 demonstrated no leaching of sorbed Cr(VI) (See Attachment 1 of this compendium, “Results and

Implications of Field Tracer Testing and Long-Term Tests within the Chromium Plume at Los Alamos National Laboratory from 2013 to 2017.”)

The mixing trends shown in Figures 4.0-3 and 4.0-4 assume a background end member with $\delta^{53}\text{Cr}$ of 1.8‰. This relatively high value was chosen to be conservative in identifying the presence of Cr(VI) reduction in the regional aquifer, thereby making it more difficult to reject the null hypothesis of no Cr(VI) reduction occurring. In determining the occurrence of reduction, the choice of background end member $\delta^{53}\text{Cr}$ is most significant for plume edge wells (wells that have concentrations and isotopic signatures more similar to background). These wells, however, show decreasing $\delta^{53}\text{Cr}$ with increasing concentration through time (Figure 4.0-2), the exact opposite pattern expected from reduction. Furthermore, in R-45(1), for example, the increases in Cr(VI) are closely mirrored by increases in contaminant sulfate and chloride, conservative species in an oxidizing aquifer (Figure 4.0-5).

An alternative explanation for the trends shown in Figure 4.0-2 is that they represent reduction capacity being quickly overwhelmed at the plume edge. In other words, the low starting concentrations might not represent background, but rather reduced contaminant Cr(VI), with reduction being overwhelmed as concentrations increase over time. The low $\delta^{53}\text{Cr}$ at the start of the time series (Figure 4.0-2), however, makes this scenario problematic. Assume, for example, that Cr(VI) reduction was occurring in 2009 at R-43(1) and that [Cr] concentrations would have been 100 ppb in the absence of reduction. In other words, concentrations were being reduced by more than 90%. With reference to Figure 4.0-3, the $\delta^{53}\text{Cr}$ of Cr(VI) at this point, assuming ϵ of 3.4‰, would have values greater than 8‰, which is clearly not what is observed. The only way to reconcile the results shown in Figure 4.0-2a and 4.0-4a with reduction of Cr(VI) in well R-43(1) would be a greater than 90% reduction with effective ϵ less than 0.3‰. While such a value for effective ϵ is theoretically possible, the preponderance of evidence suggests that such high levels of reduction (i.e. >90%) do not occur in the regional aquifer (see the introduction to this compendium, section 1; and Attachment 1 of this compendium) and that the isotopic and concentration patterns observed at the plume edge represent simple mixing between background and contaminant Cr(VI). Perhaps the strongest evidence precluding significant reduction comes from tests where potable water was injected into wells (\pm alkaline leach solutions) within the chromium plume and [Cr] concentrations were compared with concentrations of conservative species as contaminated water drifted back into the well screen (see Attachment 1 of this compendium). Two out of three wells (R-42 and R-28) showed no evidence of reduction in field testing. One well, CrPZ-2(1), did show evidence for reduction of Cr(VI), which could be due to residual bentonite in and around the well screen.

To assess potential remedial alternatives for the chromium plume, experiments conducted on groundwater associated with the chromium plume examined the effects of Cr(VI) reduction by zero valent iron (ZVI) and by natural regional aquifer microbial consortia stimulated by acetate in batch experiments with aquifer sediments (Table 4.0-1). Cr (VI) in groundwater from R-42 was readily reduced to Cr(III), showing the potential for reduction through the introduction of ZVI or stimulating the natural microbial population in the aquifer given optimal conditions (Figure 4.0-6a, 4.0-6b, and 4.0-6c). As discussed in Heikoop et al. (2014), the ϵ of batch and column Cr(VI) reduction experiments are generally between 0.4 to 5‰. In Figures 4.0-7a and 4.0-7b, the Rayleigh model was used to calculate the ϵ values for these experiments. For the ZVI and microbial reduction experiments, respectively, ϵ values equal to 1.91‰ and 3.57‰ were observed. The experiments resulted in ϵ values similar to those found in literature (Ellis et al. 2002; Kitchen et al. 2004; Berna et al. 2010; Jamieson-Hanes et al. 2012). The relatively low ϵ value observed for the ZVI experiment is consistent with the rapid reduction of chromium in a matter of hours rather than days, as in the microbial reduction experiment.

5.0 CONCLUSION

Overall, there is no evidence for Cr(VI) reduction in the regional aquifer based on the relationships between $\delta^{53}\text{Cr}$, [Cr], and Cr(VI) data. Therefore, the degree of reduction was not calculated using the Rayleigh model. Given the relevant paucity of evidence for reduction in core sediment leachate data, most Cr(VI) uptake experiments, and aquifer field testing (section 1 and Attachment 1 of this compendium), the simplest explanation is that reduction is not significant in the aquifer, even in secondary porosity. It could be argued that the natural attenuation capacity has been overwhelmed within the plume centroid, but patterns at the periphery of the chromium plume, where reduction would presumably still be occurring, are not consistent with reduction, but rather appear to reflect simple mixing with background as the plume expands.

It is possible that the ϵ value in the regional aquifer is anomalously low, perhaps due to high rates of reduction. Lower effective kinetic isotope enrichment factors are favored by intracellular reduction, higher reduction rates, and Cr(VI) transport limitation to either extracellular (e.g., diffusion through biofilms or passivation layers) or intracellular reduction sites. However, our lab-based reduction experiments were conducted with site waters, sediments, and microbes, and resulted in typical ϵ values. The microbial reduction experiment described here involved a natural microbial consortium, presumably with varying reduction mechanisms, reduction locations, and transport limitations. The relatively high ϵ value observed for the experiment suggests reduction may have been primarily extracellular (and relatively insensitive to reduction rate) or, if intracellular, that enzymatic Cr(VI) reduction steps (strongly fractionating) were rate limiting as opposed to Cr(VI) transport constraints. Even the experiment using site water and ZVI to reduce Cr(VI), which resulted in very rapid reduction of Cr(VI), still yielded a typical ϵ value of 1.91‰. These observations suggest that the chromium isotope ϵ value in the regional aquifer is not inherently low. Column and batch studies, however, can never fully replicate real aquifer porosity distributions and transport constraints.

The only way the chromium isotope data can be reconciled with the idea of significant reduction in the aquifer is if the reduction were to occur primarily in secondary porosity, with transport limitations leading to a lower effective ϵ value. If diffusion into secondary porosity is rate limiting, a lower effective ϵ value would be observed; moreover, if all Cr(VI) in secondary porosity was reduced, there would be no residual Cr(VI) to measure. Sampling biases associated with sampling of primary versus secondary porosity could also play a role. While this possibility cannot be ignored, it would be more compelling if evidence for reduction of anthropogenic chromium had been identified in core leachate results or during extended aquifer pump tests and other field tests designed to assess natural attenuation. It is possible that the isotope and core leachate techniques are simply not sensitive enough to detect a minor amount of reduction that has occurred in the aquifer.

6.0 REFERENCES AND MAP DATA SOURCES

6.1 References

The following reference list includes documents cited in this report.

- Berna, E.C., T.M. Johnson, R.S. Makdisi, and A. Basu. "Cr Stable Isotopes as Indicators of Cr(VI) Reduction in Groundwater: A Detailed Time-Series Study of a Point-Source Plume," *Environmental Science & Technology*, Vol. 44, No. 3, pp. 1043–1048 (2010).
- Ellis, A.S., T.M. Johnson, and T.D. Bullen. "Chromium Isotopes and the Fate of Hexavalent Chromium in the Environment," *Science*, Vol. 295, pp. 2060–2062 (2002).
- Heikoop, J.M., T.M. Johnson, K.H. Birdsell, P. Longmire, D.D. Hickmott, E.P. Jacobs, D.E. Broxton, D. Katzman, V.V. Vesselinov, M. Ding, D.T. Vaniman, S.L. Reneau, T.J. Goering, J. Glessner, and A. Basu. "Isotopic Evidence for Reduction of Anthropogenic Hexavalent Chromium in Los Alamos National Laboratory Groundwater," *Chemical Geology*, Vol. 373, pp. 1–9 (2014).
- Jamieson-Hanes, J.H., B.D. Gibson, M.B.J. Lindsay, Y. Kim, C.J. Ptacek, and D.W. Blowes. "Chromium Isotope Fractionation during Reduction of Cr(VI) under Saturated Flow Conditions," *Environmental Science & Technology*, Vol. 46, No. 12, pp. 6783–6789 (2012).
- Kitchen, J.W., T.M. Johnson, and T.D. Bullen. "Chromium Stable Isotope Fractionation During Abiotic Reduction of Hexavalent Chromium," *Eos Transactions, American Geophysical Union*, Vol. 85, No. 47, Fall Meeting Supplement, Abstract V51A-0519 (2004).
- Raddatz, A.L., T.M. Johnson, and T.L. McLing. "Cr Stable Isotopes in Snake River Plain Aquifer Groundwater: Evidence for Natural Reduction of Dissolved Cr(VI)," *Environmental Science & Technology*, Vol. 45, No. 2, pp. 502–507 (2011).
- Schoenberg, R., S. Zink, M. Staubwasser, and F. von Blanckenburg. "The Stable Cr Isotope Inventory of Solid Earth Reservoirs Determined by Double Spike MC-ICP-MS," *Chemical Geology*, Vol. 249, pp. 294–306 (2008).

6.2 Map Data Sources

Hillshade; Los Alamos National Laboratory, ER-ES, As published;
\\slip\gis\Data\HYP\LiDAR\2014\Bare_Earth\BareEarth_DEM_Mosaic.gdb; 2014.

Point features; As published; EIM data pull; 2017.

Chromium plume > 50 ppb; Los Alamos National Laboratory, ER-ES, As published;
\\slip\gis\GIS\Projects\13-Projects\13-0065\shp\chromium_plume_2.shp; 2018.

Structures; Los Alamos National Laboratory, KSL Site Support Services, Planning, Locating and Mapping Section; 06 January 2004; as published 29 November 2010.

Drainage channel; Los Alamos National Laboratory, ER-ES, As published, GIS projects folder;
\\slip\gis\GIS\Projects\15-Projects\15-0080\project_data.gdb\correct_drainage; 2017.

Technical Area Boundaries; Los Alamos National Laboratory, Site Planning & Project Initiation Group, Infrastructure Planning Office; September 2007; as published 13 August 2010.

Rivers; Los Alamos National Laboratory, ER-ES, As published, GIS projects folder;
\\slip\gis\GIS\Data\ESRI\hydro\rivers.sdc\rivers; 2018.

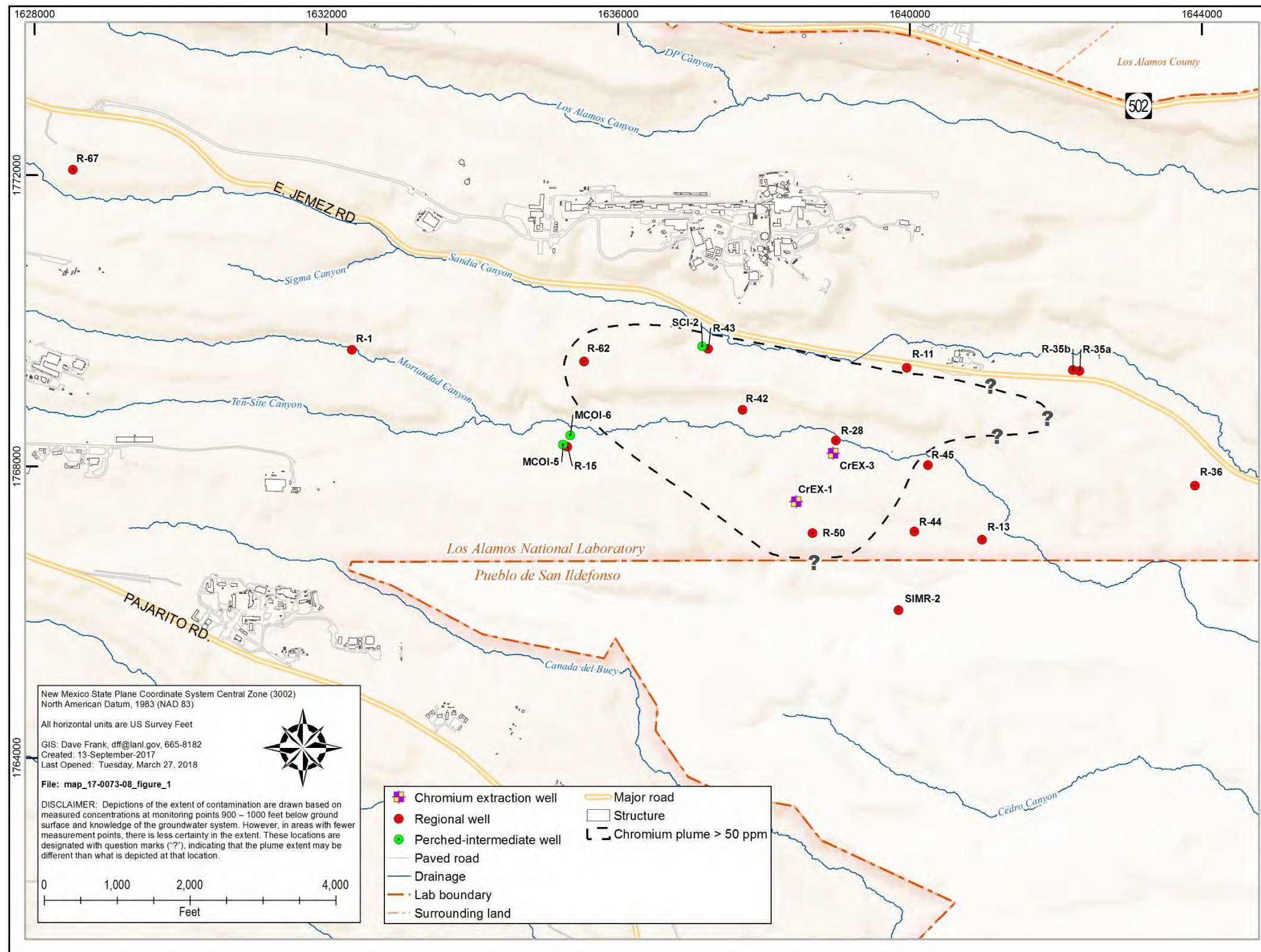


Figure 1.0-1 Location Map showing outfalls, the Sandia Canyon wetland, the primary Cr(VI) infiltration zone, location of monitoring wells, and the area of Cr(VI) concentration exceeding 50 µg/L in the regional aquifer. Well WST-600902 is off the map to the west, outside the area of influence of the chromium plume.

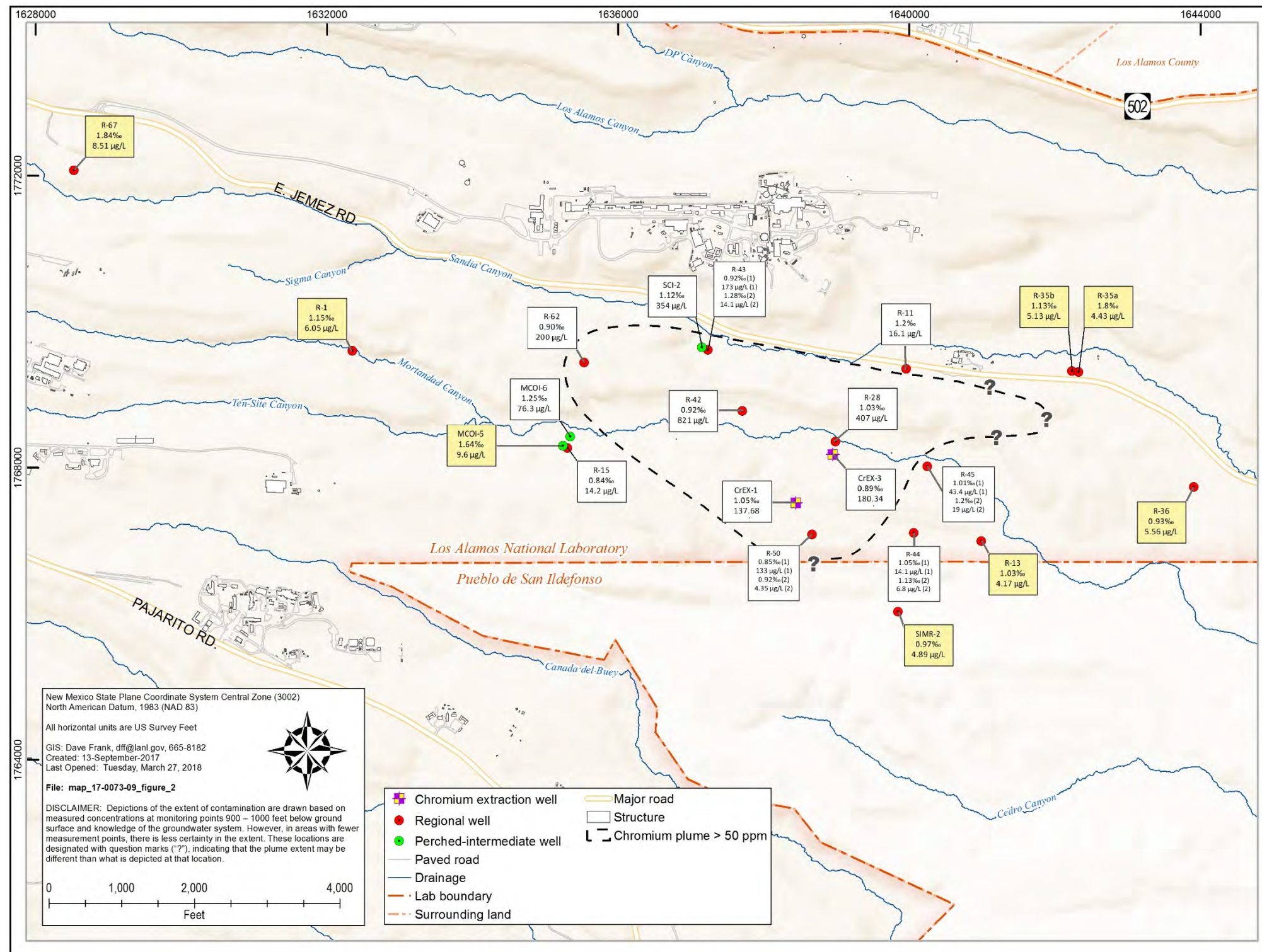


Figure 4.0-1 Most recent $\delta^{53}\text{Cr}$ (‰) and Cr concentration ($\mu\text{g/L}$) for perched-intermediate and regional aquifer wells in Sandia Canyon and Mortandad Canyon (sample dates from 2007–2016). Where two values are given for each parameter, those followed by (1) are from the upper screen and those followed by (2) are from the lower screen of the particular well. Text boxes shaded in yellow represent wells outside the chromium plume that have only natural background chromate present.

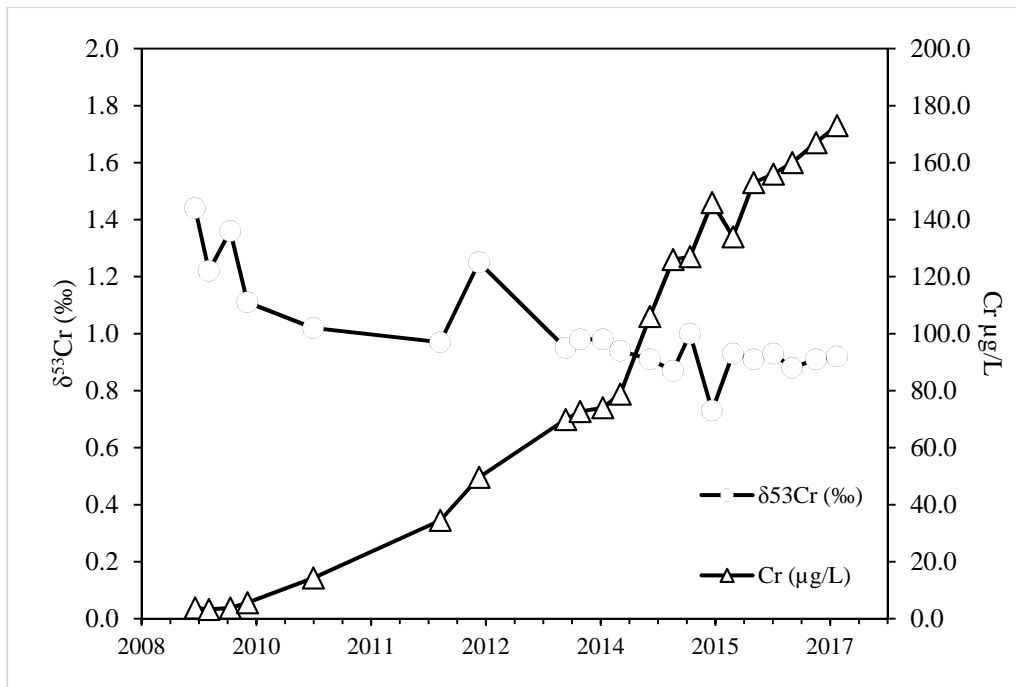


Figure 4.0-2a R-43(1) quarterly $\delta^{53}\text{Cr}$ sampling analysis with corresponding [Cr] from 2008 to 2016. Total chromium data were included in the study data set only if a $\delta^{53}\text{Cr}$ sample was acquired during the same time period.

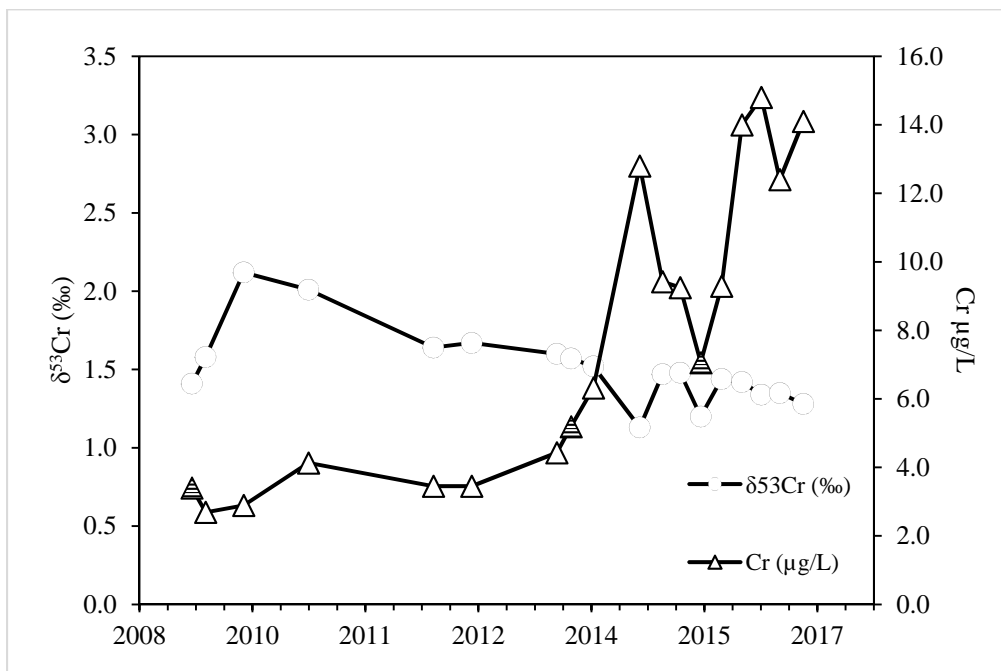


Figure 4.0-2b R-43(2) quarterly $\delta^{53}\text{Cr}$ sampling analysis with corresponding [Cr] from 2008 to 2016. Total chromium data were included in the study data set only if a $\delta^{53}\text{Cr}$ sample was acquired during the same time period. Hashed triangles represent non-detect samples for [Cr].

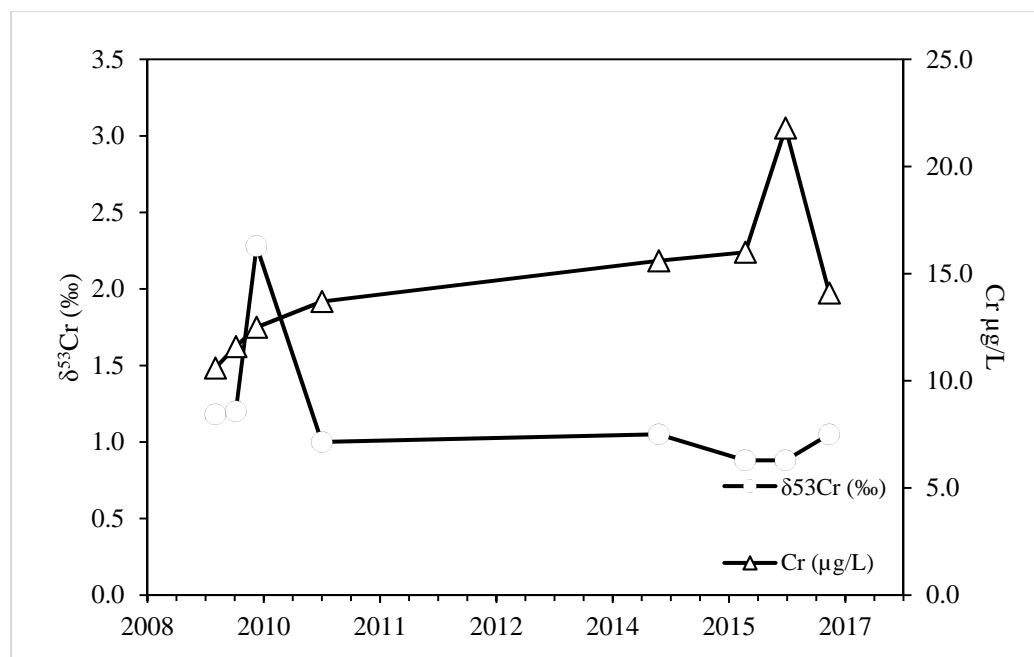


Figure 4.0-2c R-44(1) quarterly $\delta^{53}\text{Cr}$ sampling analysis with corresponding $[\text{Cr}]$ from 2008 to 2016. Total chromium data were included in the study data set only if a $\delta^{53}\text{Cr}$ sample was acquired during the same time period.

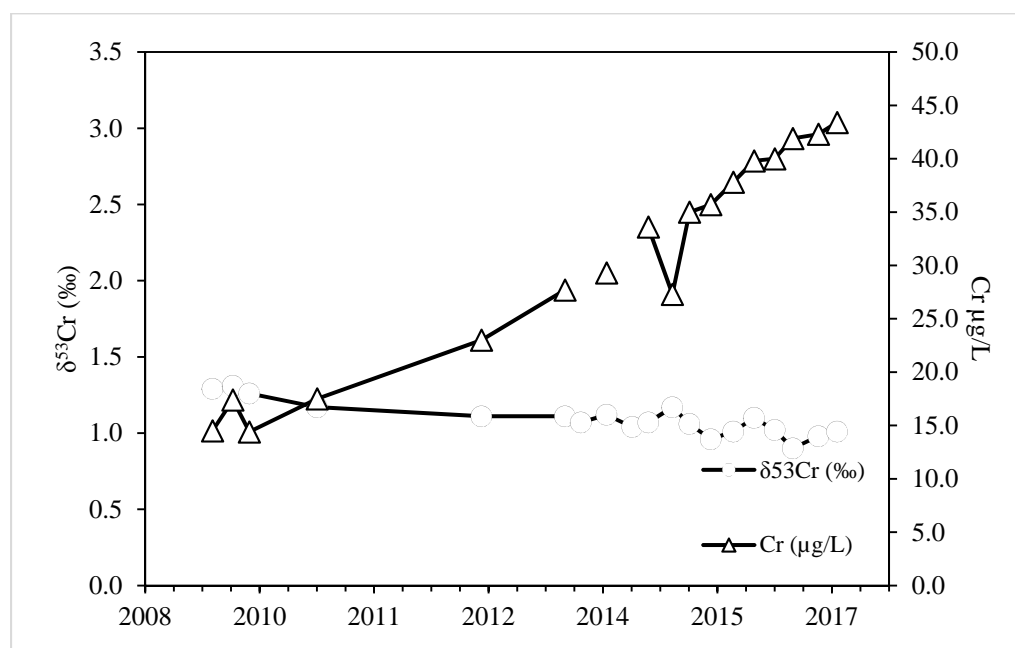


Figure 4.0-2d R-45(1) quarterly $\delta^{53}\text{Cr}$ sampling analysis with corresponding $[\text{Cr}]$ from 2008 to 2016. Total chromium data were included in the study data set only if a $\delta^{53}\text{Cr}$ sample was acquired during the same time period.

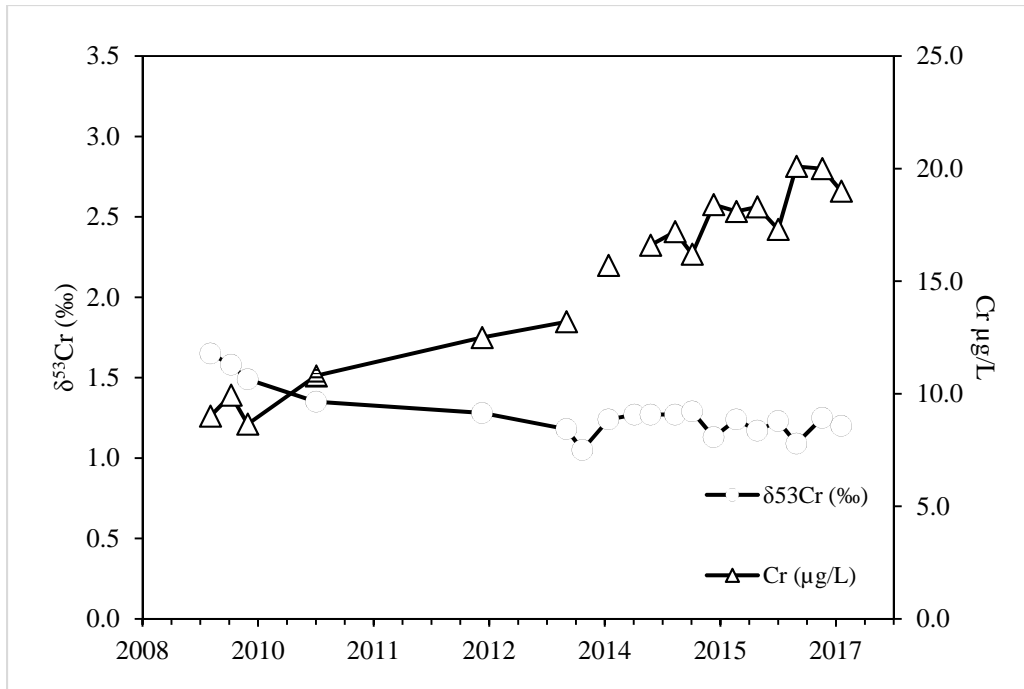


Figure 4.0-2e R-45(2) quarterly $\delta^{53}\text{Cr}$ sampling analysis with corresponding [Cr] from 2008 to 2016. Total chromium data were included in the study data set only if a $\delta^{53}\text{Cr}$ sample was acquired during the same time period.

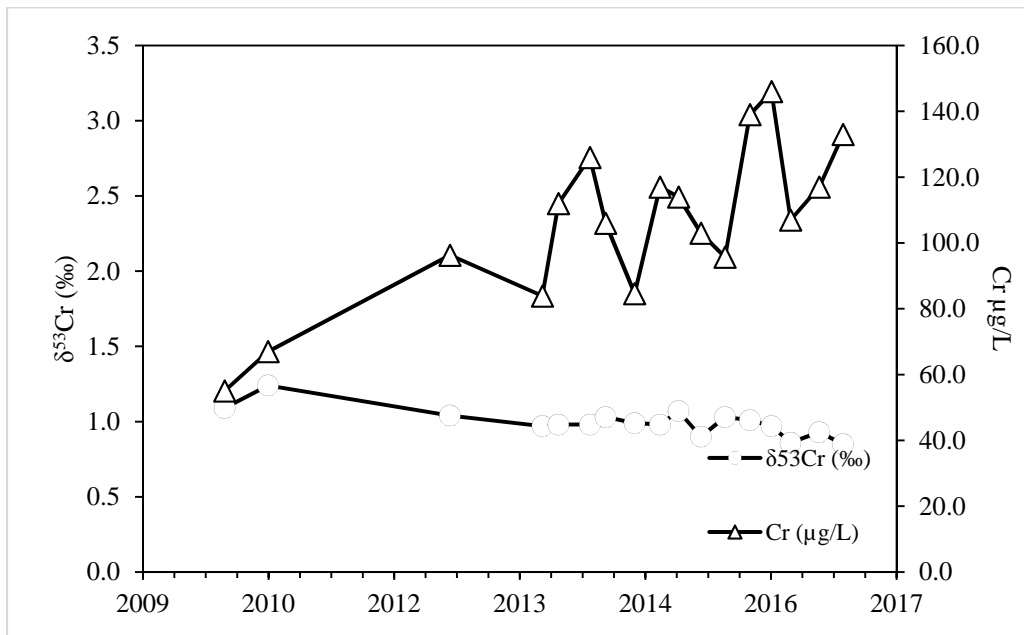


Figure 4.0-2f R-50(1) quarterly $\delta^{53}\text{Cr}$ sampling analysis with corresponding [Cr] from 2008 to 2016. Total chromium data were included in the study data set only if a $\delta^{53}\text{Cr}$ sample was acquired during the same time period.

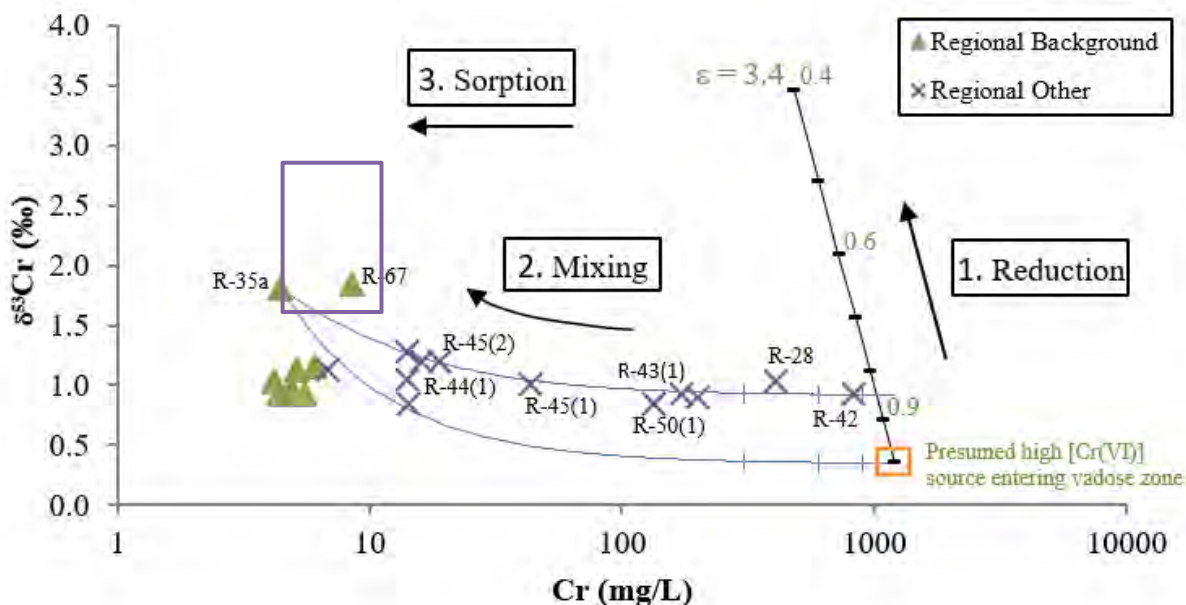


Figure 4.0-3 $\delta^{53}\text{Cr}$ versus [Cr] for most recent data from each well. Lower blue curve is a mixing line between a background water and a highly chromium-contaminated water (open orange box; estimated from the [Cr] concentration and $\delta^{53}\text{Cr}$ at well R-42; see Heikoop et al. [2014; 255424] for details) that has not undergone substantial reduction in the vadose zone or regional aquifer. Upper curve is a mixing line arbitrarily set to mix water from well R-42 with a high $\delta^{53}\text{Cr}$ background source. Ticks on mixing curve represent 25%, 50%, and 75% mixtures. The isotopic trend associated with reduction for $\epsilon = 3.4\text{‰}$ is shown, along with fraction [Cr] remaining as reduction proceeds. The value of 3.4‰ was chosen to be intermediate within the range of experimentally observed ϵ values. The lack of isotopic fractionation associated with sorption is also shown. Labeled panels with numbers 1, 2, and 3 show expected trends in both $\delta^{53}\text{Cr}$ and [Cr] concentration for the processes of reduction, mixing, and sorption, respectively. These processes likely occur concurrently, at least to some degree. To prevent cluttering of the diagram, not all data points are labeled. Total chromium data are used instead of Cr(VI), as these data are more complete and [Cr] and Cr(VI) compare favorably in the regional aquifer.

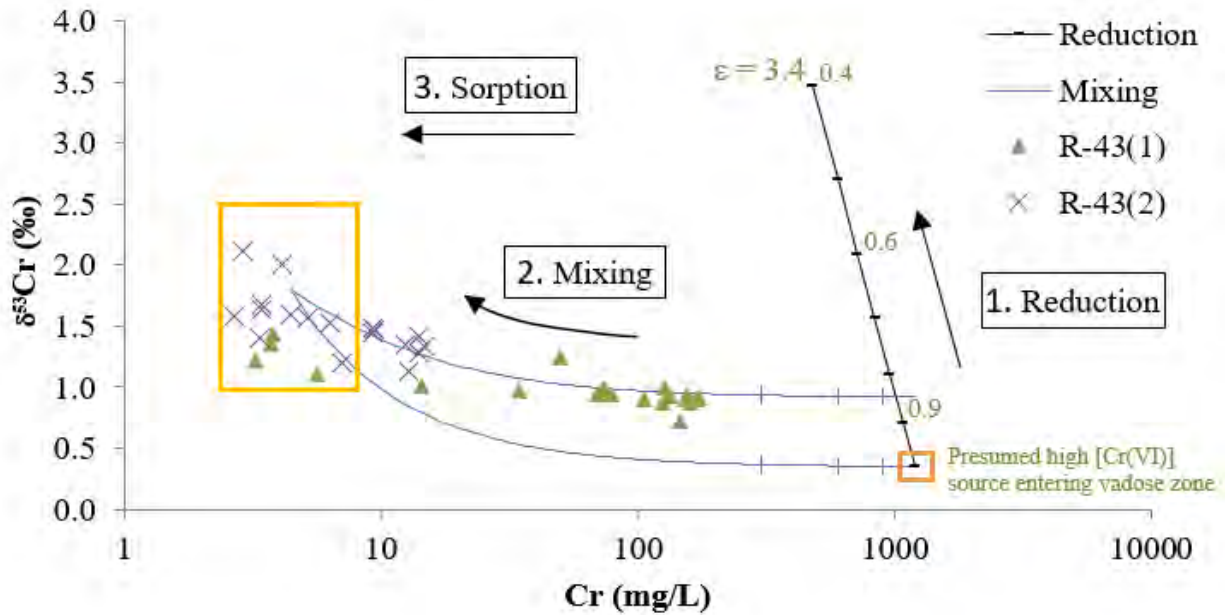


Figure 4.0-4a $\delta^{53}\text{Cr}$ versus $[\text{Cr}]$ for R-43(1) and R-43(2) time-series data. Lower blue curve is a mixing line between a background water (open yellow box; range of $[\text{Cr}]$ concentration from most recent background well data) and a highly chromium-contaminated water (open orange box; estimated from the $[\text{Cr}]$ concentration and $\delta^{53}\text{Cr}$ at well R-42) that has not undergone substantial reduction in the vadose zone or regional aquifer. Upper curve is a mixing line arbitrarily set to mix water from well R-42 with a high $\delta^{53}\text{Cr}$ background source. Ticks on mixing curve represent 25%, 50%, and 75% mixtures. The isotopic trend associated with reduction for $\epsilon = 3.4\text{‰}$ is shown, along with fraction $[\text{Cr}]$ remaining as reduction proceeds. The value of 3.4‰ was chosen to be intermediate within the range of experimentally observed ϵ values. The lack of isotopic fractionation associated with sorption is also shown. Labeled panels with numbers 1, 2, and 3 show expected trends in both $\delta^{53}\text{Cr}$ and $[\text{Cr}]$ concentration for the processes of reduction, mixing, and sorption, respectively. These processes likely occur concurrently, at least to some degree.

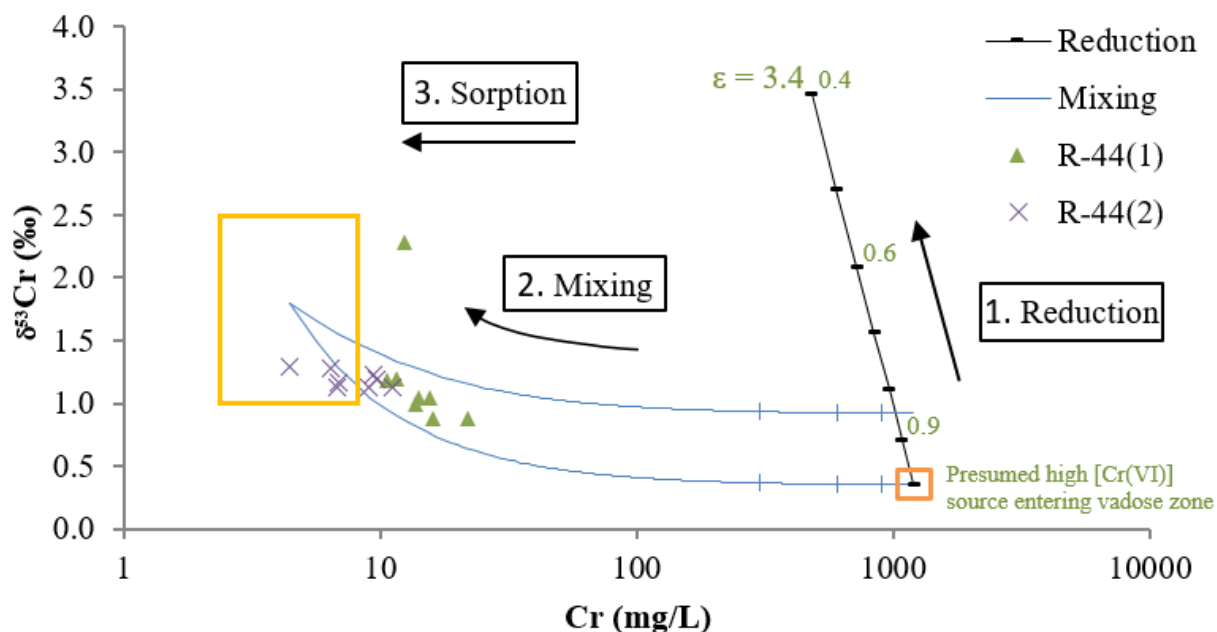


Figure 4.0-4b $\delta^{53}Cr$ versus $[Cr]$ for R-44(1) and R-44(2) time-series data. Lower blue curve is a mixing line between a background water (open yellow box; range of $[Cr]$ concentration from most recent background well data) and a highly chromium-contaminated water (open orange box; estimated from the $[Cr]$ concentration and $\delta^{53}Cr$ at well R-42) that has not undergone substantial reduction in the vadose zone or regional aquifer. Upper curve is a mixing line arbitrarily set to mix water from well R-42 with a high $\delta^{53}Cr$ background source. Ticks on mixing curve represent 25%, 50%, and 75% mixtures. The isotopic trend associated with reduction for $\epsilon = 3.4$ ‰ is shown, along with fraction $[Cr]$ remaining as reduction proceeds. The value of 3.4‰ was chosen to be intermediate within the range of experimentally observed ϵ values. The lack of isotopic fractionation associated with sorption is also shown. Labeled panels with numbers 1, 2, and 3 show expected trends in both $\delta^{53}Cr$ and $[Cr]$ concentration for the processes of reduction, mixing, and sorption, respectively. These processes likely occur concurrently, at least to some degree.

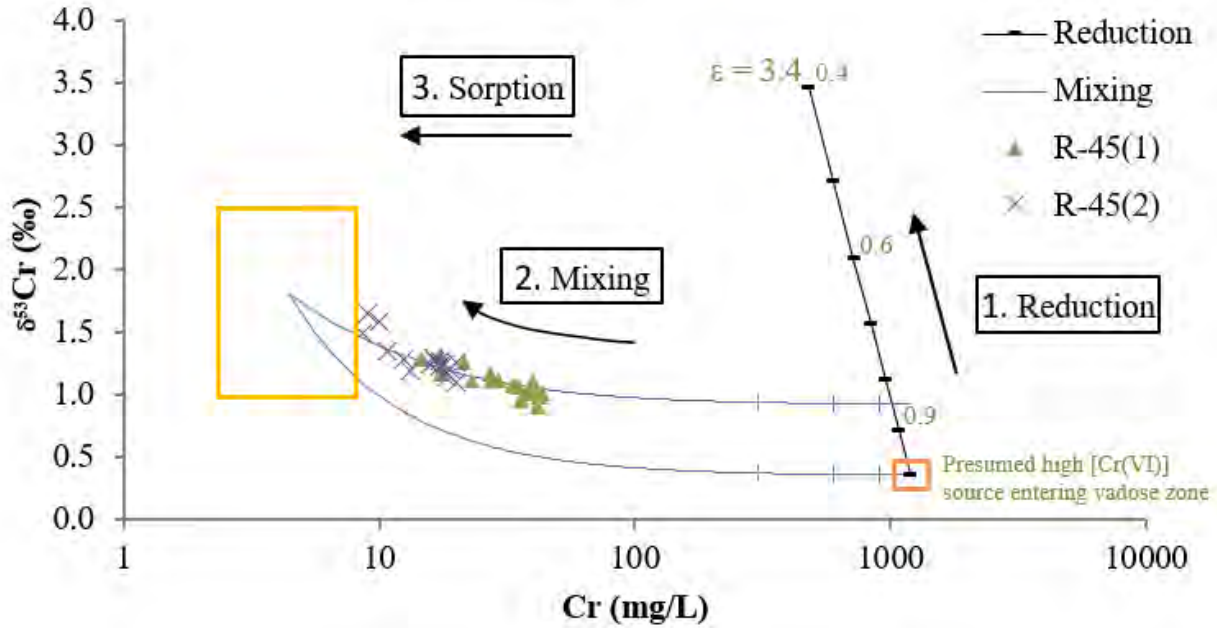


Figure 4.0-4c $\delta^{53}\text{Cr}$ versus $[\text{Cr}]$ for R-45(1) and R-45(2) time-series data. Lower blue curve is a mixing line between a background water (open yellow box; range of $[\text{Cr}]$ concentration from most recent background well data) and a highly chromium-contaminated water (open orange box; estimated from the Cr concentration and $\delta^{53}\text{Cr}$ at well R-42) that has not undergone substantial reduction in the vadose zone or regional aquifer. Upper curve is a mixing line arbitrarily set to mix water from well R-42 with a high $\delta^{53}\text{Cr}$ background source. Ticks on mixing curve represent 25%, 50%, and 75% mixtures. The isotopic trend associated with reduction for $\epsilon = 3.4\text{‰}$ is shown, along with fraction $[\text{Cr}]$ remaining as reduction proceeds. The value of 3.4‰ was chosen to be intermediate within the range of experimentally observed ϵ values. The lack of isotopic fractionation associated with sorption is also shown. Labeled panels with numbers 1, 2, and 3 show expected trends in both $\delta^{53}\text{Cr}$ and $[\text{Cr}]$ concentration for the processes of reduction, mixing, and sorption, respectively. These processes likely occur concurrently, at least to some degree.

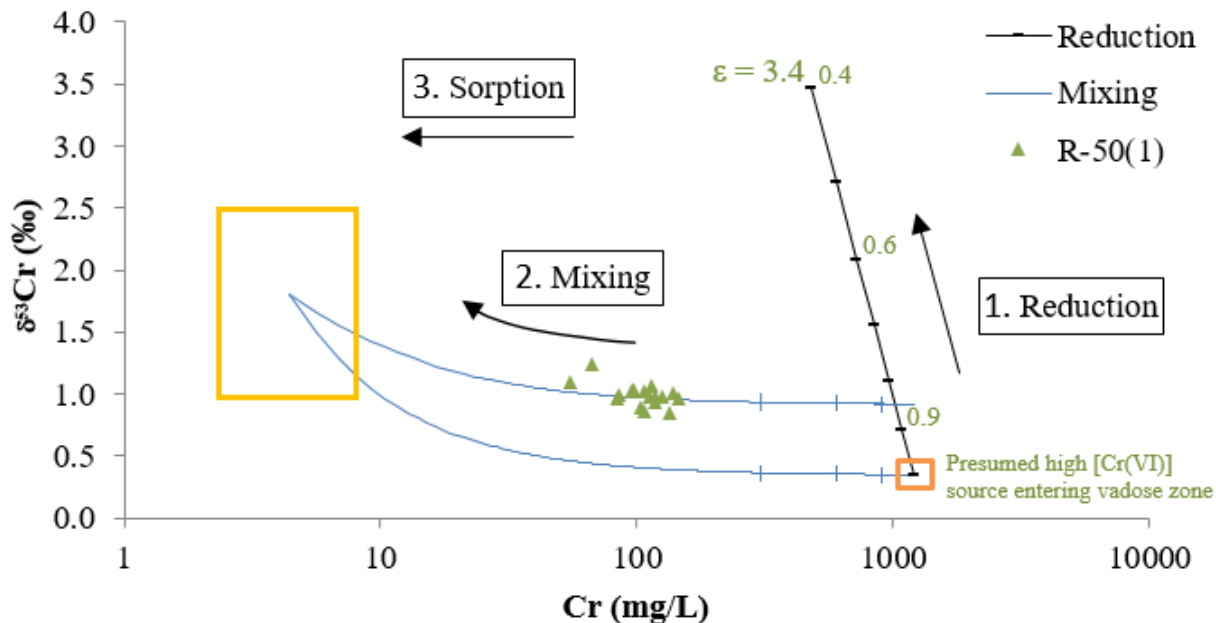


Figure 4.0-4d $\delta^{53}\text{Cr}$ versus [Cr] for R-50(1) time-series data. Lower blue curve is a mixing line between a background water (open yellow box; range of [Cr] concentration from most recent background well data) and a highly chromium-contaminated water (open orange box; estimated from the Cr concentration and $\delta^{53}\text{Cr}$ at well R-42) that has not undergone substantial reduction in the vadose zone or regional aquifer. Upper curve is a mixing line arbitrarily set to mix water from well R-42 with a high $\delta^{53}\text{Cr}$ background source. Ticks on mixing curve represent 25%, 50%, and 75% mixtures. The isotopic trend associated with reduction for $\epsilon = 3.4$ ‰ is shown, along with fraction [Cr] remaining as reduction proceeds. The value of 3.4‰ was chosen to be intermediate within the range of experimentally observed ϵ values. The lack of isotopic fractionation associated with sorption is also shown. Labeled panels with numbers 1, 2, and 3 show expected trends in both $\delta^{53}\text{Cr}$ and [Cr] concentration for the processes of reduction, mixing, and sorption, respectively. These processes likely occur concurrently, at least to some degree.



Figure 4.0-5 Time series for chloride, sulfate and chromium at R45(1)

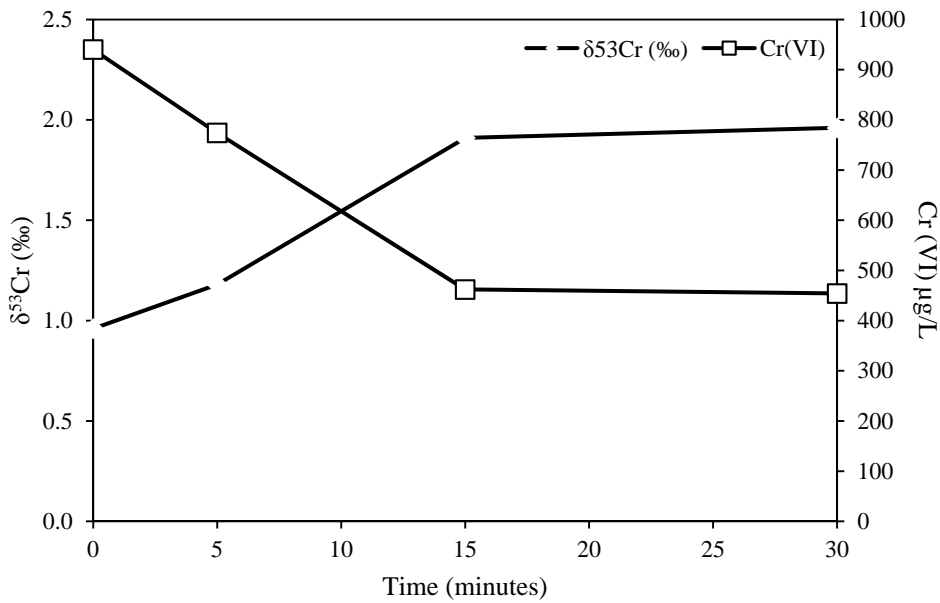


Figure 4.0-6a Experimental $\delta^{53}\text{Cr}$ and [Cr] data for the initial ZVI experiment plotted as a time series

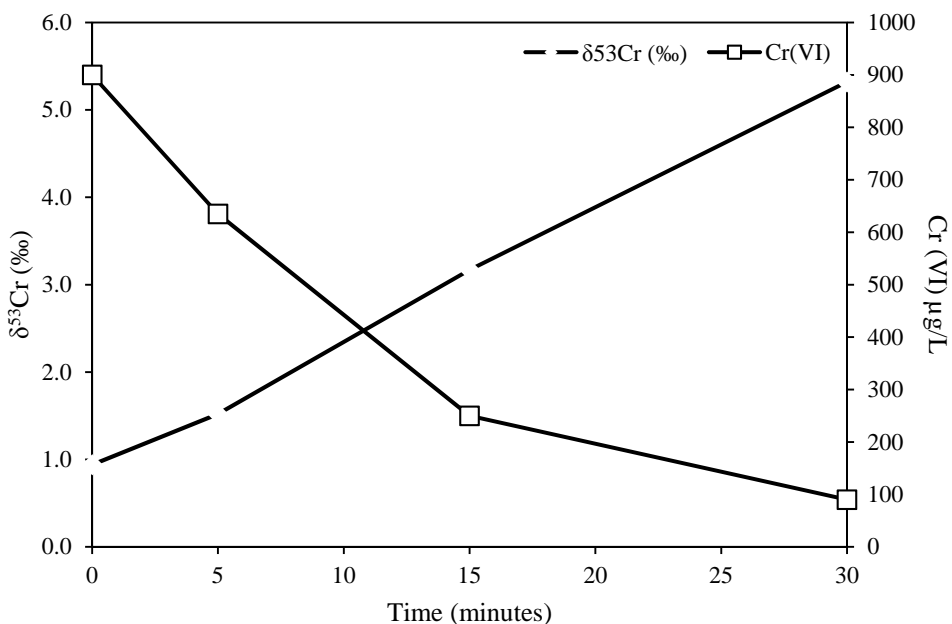


Figure 4.0-6b Experimental $\delta^{53}\text{Cr}$ and $[\text{Cr}]$ data for a second ZVI experiment plotted as a time series

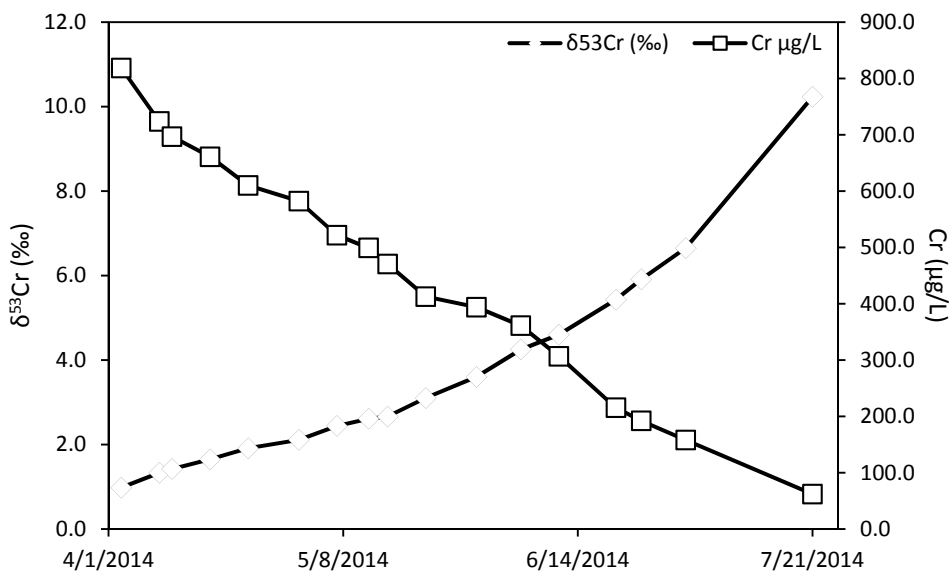


Figure 4.0-6c Microbial bioreduction experimental $\delta^{53}\text{Cr}$ and $[\text{Cr}]$ concentration data plotted as a time series

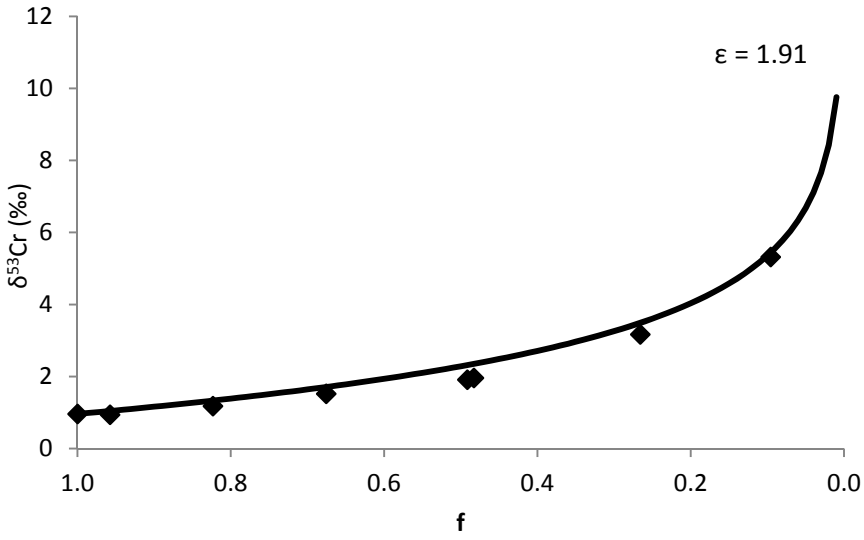


Figure 4.0-7a ZVI experimental $\delta^{53}\text{Cr}$ and associated f with $\epsilon = 1.91$

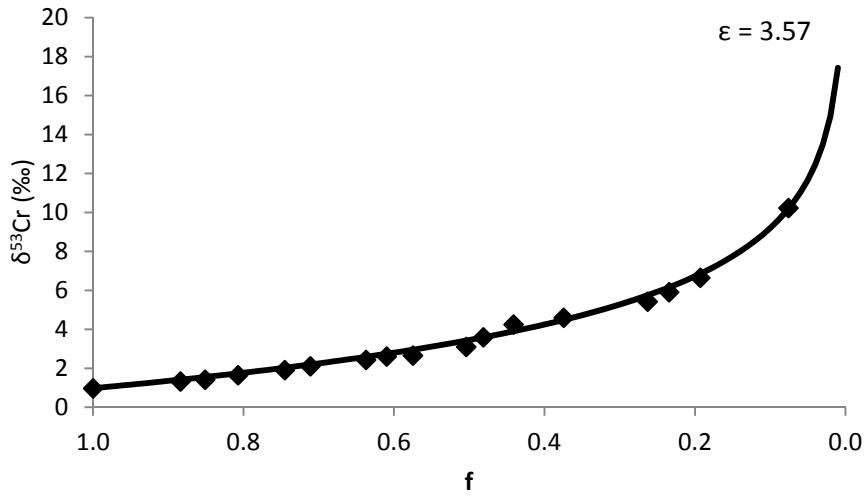


Figure 4.0-7b Microbial reduction experimental $\delta^{53}\text{Cr}$ and associated f with $\epsilon = 3.57$

Table 3.0-1
Summary of Quarterly Data

Location ID	Date Sampled	Field Sample ID	Time	$\delta^{53}\text{Cr}$ (‰)	Cr ($\mu\text{g/L}$)	Cr(VI) ($\mu\text{g/L}$)
MCOI-5	3/5/2007	UF070200GMC501	13:18	2.93	5.0	—*
MCOI-5	11/12/2007	CAMO-08-8625	14:55	2.0	1.1	—
MCOI-5	2/13/2008	CAMO-08-10422	14:00	2.84	4.6	1.60
MCOI-5	5/20/2008	CAMO-08-12738	14:15	2.42	10.0	1.77
MCOI-5	8/18/2008	CAMO-08-14499	16:26	2.22	2.2	2.40
MCOI-5	11/11/2008	CAMO-09-781	11:30	2.16	3.3	2.30
MCOI-5	5/4/2009	CAMO-09-8162	13:39	2.08	4.49	2.50
MCOI-5	8/6/2009	CAMO-09-9531	13:10	1.5	10.0	3.40
MCOI-5	11/3/2009	CAMO-10-3898	15:48	2.06	3.89	2.79
MCOI-5	1/25/2010	CAMO-10-9737	13:32	2.4	3.74	2.40
MCOI-5	11/18/2014	CAMO-15-90224	11:35	1.6	5.39	—
MCOI-5	11/16/2015	CAMO-16-106115	10:57	1.41	5.21	—
MCOI-5	11/8/2016	CAMO-17-127242	10:34	1.64	9.6	—
MCOI-6	2/26/2007	UF070200GMC601	14:51	1.6	29.4	—
MCOI-6	11/9/2007	CASA-08-7612	11:56	1.55	33.3	—
MCOI-6	2/22/2008	CAMO-08-10425	11:37	1.0	34.2	35.1
MCOI-6	5/20/2008	CAMO-08-12741	15:20	1.01	30.5	38.4
MCOI-6	8/12/2008	CAMO-08-14501	12:00	0.99	43.3	39.5
MCOI-6	11/10/2008	CAMO-09-785	15:35	1.16	37.0	40.7
MCOI-6	5/5/2009	CAMO-09-8167	13:25	0.99	41.5	49.8
MCOI-6	8/19/2009	CAMO-09-9535	15:15	1.21	47.5	41.9
MCOI-6	11/2/2012	CAMO-13-24256	12:03	1.43	61.6	68.0
MCOI-6	11/7/2013	CAMO-14-45760	13:19	1.46	81.3	61.9
MCOI-6	1/17/2014	CAMO-14-49674	11:06	1.45	72.4	60.6
MCOI-6	5/13/2014	CAMO-14-75510	12:24	1.42	68.8	—
MCOI-6	7/8/2014	CAMO-14-84007	12:02	1.4	80.1	—
MCOI-6	11/7/2014	CAMO-15-90225	11:53	1.33	69.8	—
MCOI-6	2/26/2015	CAMO-15-92494	14:07	1.36	74.1	—
MCOI-6	5/5/2015	CAMO-15-95795	11:20	1.27	74.7	—
MCOI-6	8/4/2015	CAMO-15-102597	13:49	1.13	74.7	—
MCOI-6	11/6/2015	CAMO-16-106116	12:48	1.11	75.4	—
MCOI-6	2/8/2016	CAMO-16-110034	12:16	1.31	78.8	—
MCOI-6	5/5/2016	CAMO-16-115270	13:56	1.17	76.5	—
MCOI-6	7/25/2016	CAMO-16-124285	12:39	1.18	77.8	—
MCOI-6	11/8/2016	CAMO-17-127243	13:34	1.14	86.6	—
MCOI-6	2/8/2017	CAMO-17-129290	13:00	1.25	76.3	—

Table 3.0-1 (continued)

Location ID	Date Sampled	Field Sample ID	Time	$\delta^{53}\text{Cr}$ (‰)	Cr ($\mu\text{g/L}$)	Cr(VI) ($\mu\text{g/L}$)
R-1	3/7/2007	GF070200G01R01	10:46	1.24	4.6	—
R-1	2/22/2008	CAMO-08-10453	14:40	1.22	7.2	5.50
R-1	5/20/2008	CAMO-08-12742	10:02	1.17	5.5	7.90
R-1	11/16/2009	CAMO-10-3899	14:35	1.47	8.7	5.52
R-1	2/11/2010	CAMO-10-9330	13:21	1.53	5.64	5.20
R-1	11/12/2010	CAMO-11-1260	10:16	1.35	6.69	5.22
R-1	11/10/2014	CAMO-15-90226	11:13	1.19	5.24	—
R-1	11/20/2015	CAMO-16-106117	11:54	1.08	5.83	—
R-1	11/15/2016	CAMO-17-127244	10:47	1.15	6.05	—
R-11	2/13/2007	GF070200G11R01	09:56	1.18	33.2	—
R-11	11/7/2007	CASA-08-7433	16:35	1.12	21.7	—
R-11	2/6/2008	CASA-08-10546	14:40	1.36	23.0	20.5
R-11	5/12/2008	CASA-08-12870	11:25	1.07	22.1	22.4
R-11	8/11/2008	CASA-08-14383	12:00	1.22	15.6	20.8
R-11	11/5/2008	CASA-09-883	12:00	1.34	17.5	18.5
R-11	4/29/2009	CASA-09-12365	12:05	1.21	17	18.4
R-11	11/19/2014	CASA-15-90257	15:05	1.19	23.1	—
R-11	5/14/2015	CASA-15-95827	11:51	1.28	21.1	—
R-11	11/11/2015	CASA-16-106253	11:28	1.25	20.9	—
R-11	5/17/2016	CASA-16-115488	14:06	1.16	23.8	—
R-11	11/16/2016	CASA-17-127290	14:58	1.2	16.1	—
R-13	2/28/2007	GF070200G13R01	12:45	1.0	3.8	—
R-13	2/14/2008	CAMO-08-10444	16:45	1.14	6.2	3.90
R-13	5/14/2008	CAMO-08-12772	13:58	1.07	3.6	3.60
R-13	8/14/2008	CAMO-08-14534	10:35	0.84	6.3	4.30
R-13	11/10/2008	CAMO-09-810	12:45	1.09	4.8	4.10
R-13	4/30/2009	CAMO-09-8179	14:00	1.15	3.88	3.90
R-13	11/19/2014	CAMO-15-90227	12:34	1.15	3.71	—
R-13	11/10/2015	CAMO-16-106118	13:14	1.07	3.75	—
R-13	11/7/2016	CAMO-17-127245	12:07	1.03	4.17	—
R-15	2/28/2007	GF070200G15R01	10:20	1.02	7.5	—
R-15	2/25/2008	CAMO-08-10436	12:55	1.02	7.3	7.80
R-15	5/20/2008	CAMO-08-12752	10:30	1.03	7.9	5.30
R-15	8/15/2008	CAMO-08-14540	13:45	0.97	9.8	8.50
R-15	11/10/2014	CAMO-15-90228	13:21	1.02	11.2	—
R-15	11/20/2015	CAMO-16-106120	10:30	0.86	12.6	—
R-15	11/15/2016	CAMO-17-127247	12:34	0.84	14.2	—
R-28	3/6/2007	GF070200G28R01	10:19	1.0	446.0	392
R-28	11/14/2007	CAMO-08-8712	14:16	1.0	385.0	373

Table 3.0-1 (continued)

Location ID	Date Sampled	Field Sample ID	Time	$\delta^{53}\text{Cr}$ (‰)	Cr ($\mu\text{g/L}$)	Cr(VI) ($\mu\text{g/L}$)
R-28	2/15/2008	CAMO-08-10441	11:15	1.08	419.0	417
R-28	5/14/2008	CAMO-08-12767	11:29	1.01	438.0	429
R-28	8/15/2008	CAMO-08-14542	11:30	1.05	373.0	—
R-28	11/10/2008	CAMO-09-809	15:53	1.13	468.0	436
R-28	5/1/2009	CAMO-09-8178	13:50	1.12	388.0	420
R-28	11/10/2010	CAMO-11-1272	13:05	0.98	402.0	411
R-28	11/13/2014	CAMO-15-90229	12:55	0.99	421.0	—
R-28	11/16/2015	CAMO-16-106121	12:37	1.03	407.0	—
R-35a	8/30/2007	GF07080GR35a01	10:24	3.93	2.4	—
R-35a	2/21/2008	CASA-08-10557	16:28	2.1	4.7	2.80
R-35a	5/13/2008	CASA-08-12874	10:40	3.17	10.0	1.61
R-35a	8/12/2008	CASA-08-14389	15:40	2.03	4.7	3.00
R-35a	11/6/2008	CASA-09-884	14:40	2.24	3.6	3.20
R-35a	2/4/2009	CASA-09-3014	12:50	2.02	4.9	3.50
R-35a	4/28/2009	CASA-09-9294	13:55	2.37	10.6	3.30
R-35a	8/3/2009	CASA-09-10390	03:35	2.32	6.57	3.35
R-35a	11/4/2009	CASA-10-3895	13:50	2.25	3.64	3.28
R-35a	2/11/2010	CASA-10-9846	14:12	2.1	3.88	3.30
R-35a	11/11/2010	CASA-11-1372	12:58	1.86	5.71	3.24
R-35a	11/10/2014	CASA-15-90258	12:38	1.93	4.92	—
R-35a	11/9/2015	CASA-16-106254	14:25	1.91	4.2	—
R-35a	11/9/2016	CASA-17-127291	12:29	1.8	4.43	—
R-35b	8/29/2007	GF07080GR35b01	10:51	1.23	4.8	—
R-35b	11/10/2007	GWR35b-08-8639	13:15	1.42	7.4	—
R-35b	2/7/2008	CASA-08-10558	13:25	1.51	5.9	—
R-35b	5/13/2008	CASA-08-12878	12:40	1.8	10.0	3.60
R-35b	8/12/2008	CASA-08-14385	11:20	1.31	5.6	4.60
R-35b	11/6/2008	CASA-09-886	10:35	1.35	3.2	4.70
R-35b	2/2/2009	CASA-09-3017	12:20	1.48	5.1	4.40
R-35b	4/27/2009	CASA-09-8307	12:30	1.49	7.48	4.50
R-35b	11/11/2010	CASA-11-1375	15:00	1.2	7.1	5.17
R-35b	11/6/2014	CASA-15-90259	10:45	1.27	4.71	—
R-35b	11/6/2015	CASA-16-106255	11:46	1.16	4.39	—
R-35b	11/9/2016	CASA-17-127292	12:27	1.13	5.13	—
R-36	3/12/2008	CASA-08-11172	12:45	0.94	11.1592	—
R-36	5/12/2008	CASA-08-12885	13:55	0.9	8.8	4.10
R-36	8/12/2008	CASA-08-14397	15:05	1.09	7.5	4.50
R-36	11/6/2008	CASA-09-892	13:45	1.16	5.6	4.80
R-36	2/5/2009	CASA-09-3024	13:55	1.27	6.2	4.60

Table 3.0-1 (continued)

Location ID	Date Sampled	Field Sample ID	Time	$\delta^{53}\text{Cr}$ (‰)	Cr ($\mu\text{g/L}$)	Cr(VI) ($\mu\text{g/L}$)
R-36	4/28/2009	CASA-09-9296	16:12	1.19	11.6	4.80
R-36	11/6/2014	CASA-15-90260	13:10	1.12	6.73	—
R-36	11/17/2015	CASA-16-106256	13:43	1.08	5.89	—
R-36	11/10/2016	CASA-17-127293	12:40	0.93	5.56	—
R-42	10/9/2008	CAMO-08-16443	12:57	1.05	848	893
R-42	11/20/2008	CAMO-09-826	10:10	1.06	768.0	916
R-42	2/20/2009	CAMO-09-2871	12:50	1.06	830.0	937
R-42	5/11/2009	CAMO-09-8210	13:30	1.07	886.0	1023
R-42	8/14/2009	CAMO-09-9570	14:10	0.96	1000.0	825
R-42	11/5/2009	CAMO-10-3900	13:40	1.19	961.0	1001
R-42	2/10/2010	CAMO-10-9739	15:41	1.21	894	977
R-42	11/10/2010	CAMO-11-1274	10:55	0.96	995.0	1022
R-42	11/7/2013	CAMO-14-45765	11:09	0.95	890.0	837
R-42	11/14/2014	CAMO-15-90232	11:06	0.93	908.0	—
R-42	11/16/2015	CAMO-16-106125	15:03	0.92	821.0	—
R-43 S1	6/19/2009	CAMO-09-10502	13:31	1.44	3.81	2.08
R-43 S1	8/18/2009	CASA-09-10396	17:15	1.22	3.25	2.25
R-43 S1	11/19/2009	CASA-10-3857	14:58	1.36	3.73	2.31
R-43 S1	2/2/2010	CASA-10-9481	13:50	1.11	5.63	3.40
R-43 S1	11/16/2010	CASA-11-1378	13:28	1.02	14.3	12.5
R-43 S1	5/22/2012	CASA-12-14063	13:03	0.97	34.5	—
R-43 S1	11/7/2012	CASA-13-24221	12:44	1.25	49.6	44.0
R-43 S1	11/19/2013	CASA-14-45716	13:06	0.95	69.9	64.0
R-43 S1	1/21/2014	CASA-14-49696	12:20	0.98	72.7	61.7
R-43 S1	4/30/2014	CASA-14-75536	14:55	0.98	74.0	—
R-43 S1	07/15/2014	CASA-14-81525	11:16	0.94	78.8	—
R-43 S1	11/21/2014	CASA-15-90261	11:28	0.91	106.0	—
R-43 S1	3/2/2015	CASA-15-92522	12:44	0.87	126.0	—
R-43 S1	5/15/2015	CASA-15-95831	12:20	1.0	127.0	—
R-43 S1	8/19/2015	CASA-15-102653	13:36	0.73	146.0	—
R-43 S1	11/18/2015	CASA-16-106257	13:17	0.93	134.0	—
R-43 S1	2/16/2016	CASA-16-110067	13:11	0.91	153.0	—
R-43 S1	5/12/2016	CASA-16-115492	12:51	0.93	156.0	—
R-43 S1	8/2/2016	CASA-16-124346	13:49	0.88	160.0	—
R-43 S1	11/14/2016	CASA-17-127294	12:51	0.91	167.0	—
R-43 S1	2/13/2017	CASA-17-129340	13:48	0.92	173.0	—
R-43 S2	6/18/2009	CAMO-09-10509	14:30	1.41	3.4	1.59
R-43 S2	8/18/2009	CASA-09-10401	12:40	1.58	2.69	1.58
R-43 S2	2/2/2010	CASA-10-9845	16:10	2.12	2.89	1.90

Table 3.0-1 (continued)

Location ID	Date Sampled	Field Sample ID	Time	$\delta^{53}\text{Cr}$ (‰)	Cr ($\mu\text{g/L}$)	Cr(VI) ($\mu\text{g/L}$)
R-43 S2	11/16/2010	CASA-11-1381	10:10	2.01	4.13	2.01
R-43 S2	5/22/2012	CASA-12-14064	15:00	1.64	3.45	—
R-43 S2	11/7/2012	CASA-13-24222	14:36	1.67	3.45	4.00
R-43 S2	11/19/2013	CASA-14-45717	15:03	1.6	4.43	4.20
R-43 S2	1/21/2014	CASA-14-49697	14:11	1.57	5.19	—
R-43 S2	4/30/2014	CASA-14-75537	11:26	1.52	6.32	—
R-43 S2	11/21/2014	CASA-15-90262	13:57	1.13	12.8	—
R-43 S2	3/2/2015	CASA-15-92523	14:13	1.47	9.42	—
R-43 S2	5/19/2015	CASA-15-95832	12:43	1.48	9.25	—
R-43 S2	8/18/2015	CAMO-15-104021	10:38	1.2	7.06	—
R-43 S2	11/18/2015	CASA-16-106258	15:03	1.44	9.29	—
R-43 S2	2/16/2016	CASA-16-110068	15:05	1.42	14	—
R-43 S2	5/12/2016	CASA-16-115493	14:45	1.34	14.8	—
R-43 S2	8/2/2016	CASA-16-124347	15:36	1.35	12.4	—
R-43 S2	11/14/2016	CASA-17-127295	14:26	1.28	14.1	—
R-44 S1	8/17/2009	CAMO-09-10295	12:35	1.18	10.6	8.24
R-44 S1	11/13/2009	CAMO-10-3224	13:15	1.2	11.6	13.1
R-44 S1	2/10/2010	CAMO-10-9372	11:55	2.28	12.5	8.30
R-44 S1	11/18/2010	CAMO-11-1275	12:20	1.0	13.7	12.0
R-44 S1	11/5/2014	CAMO-15-90233	11:41	1.05	15.6	—
R-44 S1	11/12/2015	CAMO-16-106126	11:31	0.88	16.0	—
R-44 S1	5/3/2016	CAMO-16-115280	12:55	0.88	21.8	—
R-44 S1	11/7/2016	CAMO-17-127252	11:49	1.05	14.1	—
R-44 S2	8/17/2009	CAMO-09-9925	14:15	1.13	11.2	8.74
R-44 S2	11/13/2009	CAMO-10-3227	11:15	1.23	9.48	10.6
R-44 S2	2/10/2010	CAMO-10-9374	14:04	1.29	4.43	4.40
R-44 S2	11/18/2010	CAMO-11-1277	10:50	1.28	6.45	4.94
R-44 S2	11/5/2014	CAMO-15-90234	14:28	1.16	6.89	—
R-44 S2	11/12/2015	CAMO-16-106127	13:41	1.19	9.63	—
R-44 S2	5/3/2016	CAMO-16-115281	14:56	1.13	9.04	—
R-44 S2	11/7/2016	CAMO-17-127253	14:05	1.13	6.8	—
R-45 S1	8/19/2009	CAMO-09-10252	14:36	1.29	14.5	12.0
R-45 S1	11/16/2009	CAMO-10-3903	14:22	1.31	17.4	13.4
R-45 S1	1/27/2010	CAMO-10-9378	14:17	1.26	14.4	13.6
R-45 S1	11/19/2010	CAMO-11-1280	12:26	1.17	17.5	16.6
R-45 S1	11/6/2012	CAMO-13-24264	12:40	1.11	23	25.0
R-45 S1	11/6/2013	CAMO-14-45768	13:15	1.11	27.7	24.7
R-45 S1	1/14/2014	CAMO-14-49679	12:17	1.07	—	24.1
R-45 S1	5/7/2014	CAMO-14-75517	12:52	1.12	29.3	—

Table 3.0-1 (continued)

Location ID	Date Sampled	Field Sample ID	Time	$\delta^{53}\text{Cr}$ (‰)	Cr ($\mu\text{g/L}$)	Cr(VI) ($\mu\text{g/L}$)
R-45 S1	8/27/2014	CAMO-14-84012	11:11	1.04	—	—
R-45 S1	11/5/2014	CAMO-15-90235	11:27	1.07	33.6	—
R-45 S1	2/18/2015	CAMO-15-92503	13:54	1.17	27.3	—
R-45 S1	5/4/2015	CAMO-15-95807	11:51	1.06	35.0	—
R-45 S1	8/5/2015	CAMO-15-102610	11:07	0.96	35.7	—
R-45 S1	11/11/2015	CAMO-16-106128	11:51	1.01	37.8	—
R-45 S1	2/10/2016	CAMO-16-110044	11:26	1.1	39.8	—
R-45 S1	5/10/2016	CAMO-16-115282	11:37	1.02	40.0	—
R-45 S1	7/28/2016	CAMO-16-124298	10:19	0.9	41.9	—
R-45 S1	11/17/2016	CAMO-17-127254	10:53	0.98	42.3	—
R-45 S1	2/7/2017	CAMO-17-129411	12:18	1.01	43.4	—
R-45 S2	8/19/2009	CAMO-09-10255	12:47	1.65	9.01	5.97
R-45 S2	11/16/2009	CAMO-10-4771	12:45	1.58	9.94	7.47
R-45 S2	1/27/2010	CAMO-10-9735	12:30	1.49	8.65	8.20
R-45 S2	11/19/2010	CAMO-11-1281	11:10	1.35	10.8	9.45
R-45 S2	11/6/2012	CAMO-13-24367	11:07	1.28	12.5	14.0
R-45 S2	11/6/2013	CAMO-14-45769	11:48	1.18	13.2	13.7
R-45 S2	1/14/2014	CAMO-14-49680	10:47	1.05	—	13.9
R-45 S2	5/7/2014	CAMO-14-75518	11:18	1.24	15.7	—
R-45 S2	8/27/2014	CAMO-14-84013	13:02	1.27	—	—
R-45 S2	11/5/2014	CAMO-15-90236	13:35	1.27	16.6	—
R-45 S2	2/19/2015	CAMO-15-92504	11:38	1.27	17.2	—
R-45 S2	5/4/2015	CAMO-15-95808	14:05	1.29	16.2	—
R-45 S2	8/5/2015	CAMO-15-102611	13:13	1.13	18.4	—
R-45 S2	11/11/2015	CAMO-16-106129	14:02	1.24	18.1	—
R-45 S2	2/10/2016	CAMO-16-110045	13:55	1.17	18.3	—
R-45 S2	5/10/2016	CAMO-16-115283	14:02	1.23	17.3	—
R-45 S2	7/28/2016	CAMO-16-124299	13:08	1.09	20.1	—
R-45 S2	11/17/2016	CAMO-17-127255	12:57	1.25	20.0	—
R-45 S2	2/7/2017	CAMO-17-129412	14:19	1.2	19.0	—
R-50 S1	5/27/2010	CAMO-10-17421	11:03	1.09	55.0461	57.0
R-50 S1	11/16/2010	CAMO-11-1313	15:54	1.24	67.0	66.2
R-50 S1	11/9/2012	CAMO-13-24368	12:17	1.04	96.3	100
R-50 S1	11/12/2013	CAMO-14-45770	16:02	0.97	83.9	69.2
R-50 S1	1/15/2014	CAMO-14-49681	14:35	0.98	112.0	98.6
R-50 S1	5/20/2014	CAMO-14-75519	12:05	0.98	126.0	—
R-50 S1	7/22/2014	CAMO-14-84014	11:03	1.03	106.0	—
R-50 S1	11/14/2014	CAMO-15-90237	11:23	0.99	84.6	—
R-50 S1	2/23/2015	CAMO-15-92505	11:30	0.98	117.0	—

Table 3.0-1 (continued)

Location ID	Date Sampled	Field Sample ID	Time	$\delta^{53}\text{Cr}$ (‰)	Cr ($\mu\text{g/L}$)	Cr(VI) ($\mu\text{g/L}$)
R-50 S1	5/8/2015	CAMO-15-95810	11:45	1.07	114.0	—
R-50 S1	8/5/2015	CAMO-15-102612	15:04	0.9	103.0	—
R-50 S1	11/9/2015	CAMO-16-106131	12:39	1.03	95.7	—
R-50 S1	2/16/2016	CAMO-16-110046	14:13	1.01	139.0	—
R-50 S1	5/12/2016	CAMO-16-115285	12:02	0.97	146.0	—
R-50 S1	7/27/2016	CAMO-16-124300	11:49	0.86	107.0	—
R-50 S1	11/18/2016	CAMO-17-127257	12:16	0.93	117.0	—
R-50 S1	2/21/2017	CAMO-17-129413	12:20	0.85	133.0	—
R-50 S2	5/27/2010	CAMO-10-18980	16:38	1.88	6.0953	4.40
R-50 S2	11/16/2010	CAMO-11-1315	14:00	1.01	7.01	4.21
R-50 S2	11/9/2012	CAMO-13-24369	16:04	1.12	4.25	4.10
R-50 S2	11/12/2013	CAMO-14-45771	14:18	1.13	3.56	—
R-50 S2	1/15/2014	CAMO-14-49682	12:54	1.07	3.34	3.40
R-50 S2	5/19/2014	CAMO-14-75520	13:25	1.03	4.56	—
R-50 S2	7/24/2014	CAMO-14-84015	13:18	1.06	6.39	—
R-50 S2	11/13/2014	CAMO-15-90238	14:43	1.21	3.77	—
R-50 S2	2/23/2015	CAMO-15-92506	15:45	1.2	4.0	—
R-50 S2	5/11/2015	CAMO-15-95811	14:25	1.15	3.87	—
R-50 S2	8/5/2015	CAMO-15-102613	13:07	0.9	3.73	—
R-50 S2	11/9/2015	CAMO-16-106132	16:32	1.1	3.68	—
R-50 S2	2/9/2016	CAMO-16-110047	12:53	1.11	3.95	—
R-50 S2	5/3/2016	CAMO-16-115286	14:47	1.06	5.29	—
R-50 S2	8/8/2016	CAMO-16-124301	13:14	1.05	3.94	—
R-50 S2	11/18/2016	CAMO-17-127258	15:05	0.92	4.35	—
R-62	6/6/2012	CAMO-12-14078	12:31	1.05	135.0	—
R-62	11/8/2012	CAMO-13-24370	10:58	1.01	128.0	—
R-62	11/12/2013	CAMO-14-45774	13:15	0.95	148.0	136
R-62	6/26/2014	CAMO-14-83984	09:27	0.95	240.0	—
R-62	11/17/2014	CAMO-15-90240	14:41	1.02	104.0	—
R-62	5/12/2015	CAMO-15-95814	15:12	1.02	134.0	—
R-62	11/19/2015	CAMO-16-106135	11:15	1.01	161.0	—
R-62	5/9/2016	CAMO-16-115289	14:43	0.9	187.0	—
R-62	11/16/2016	CAMO-17-127260	12:46	0.9	200.0	—
R-67	12/3/2015	CASA-16-106065	12:13	2.01	7.11	—
R-67	2/3/2016	CASA-16-110069	14:52	2.75	6.12	—
R-67	5/10/2016	CAMO-16-115290	11:30	2.21	4.68	—
R-67	11/16/2016	CASA-17-127296	09:38	1.84	7.88	—
R-67	2/16/2017	CASA-17-129341	11:39	1.84	8.51	—
SCI-1	8/22/2007	UF070800SCI101	09:50	0.44	22.1	—

Table 3.0-1 (continued)

Location ID	Date Sampled	Field Sample ID	Time	$\delta^{53}\text{Cr}$ (‰)	Cr ($\mu\text{g/L}$)	Cr(VI) ($\mu\text{g/L}$)
SCI-1	11/16/2007	CASA-08-7412	16:20	0.35	16.5	—
SCI-1	2/22/2008	CASA-08-10569	11:45	0.51	17.1	16.0
SCI-1	5/21/2008	CASA-08-16502	10:54	0.234	15.2	13.6
SCI-1	8/19/2008	CASA-08-14367	12:36	0.37	15.0	14.6
SCI-1	11/13/2008	CASA-09-872	13:35	0.32	11.7	14.2
SCI-1	5/6/2009	CASA-09-8267	10:44	0.43	12.6	13.0
SCI-1	11/19/2013	CASA-14-45718	12:33	0.28	8.68	—
SCI-1	11/12/2014	CASA-15-90263	12:35	0.22	10.2	—
SCI-1	2/12/2016	CASA-16-110070	12:00	-0.34	—	—
SCI-1	5/13/2016	CASA-16-115494	12:03	-0.07	11.9	—
SCI-1	8/2/2016	CASA-16-124351	9:38	-0.04	—	—
SCI-1	11/15/2016	CASA-17-127307	10:35	0.12	9.16	—
SCI-2	10/21/2008	CASA-09-502	13:31	1.17	563	660
SCI-2	11/18/2008	CASA-09-960	12:20	1.22	489.0	665
SCI-2	2/13/2009	CASA-09-2991	14:40	1.22	593.0	633
SCI-2	5/6/2009	CASA-09-8315	14:20	1.06	658.0	622
SCI-2	8/4/2009	CASA-09-10368	11:15	1.1	510.0	511
SCI-2	11/17/2009	CASA-10-3894	09:55	1.1	637.0	596
SCI-2	2/8/2010	CASA-10-12690	11:53	1.15	553	560
SCI-2	11/16/2010	CASA-11-1362	11:15	1.07	512.0	559
SCI-2	11/12/2014	CASA-15-90264	10:39	1.15	416.0	—
SCI-2	11/13/2015	CASA-16-106261	10:59	1.17	418.0	—
SCI-2	2/11/2016	CASA-16-110071	10:43	1.11	355.0	—
SCI-2	5/18/2016	CASA-16-115495	10:32	1.11	371.0	—
SCI-2	8/2/2016	CASA-16-124352	11:18	1.12	385.0	—
SCI-2	11/18/2016	CASA-17-127308	11:50	1.12	354.0	—
SIMR-2	10/23/2015	CASA-16-106066	10:18	1.08	5.01	—
SIMR-2	11/24/2015	CASA-16-106262	15:41	1.1	5.29	—
SIMR-2	2/18/2016	CAMO-16-110050	11:14	1.05	6.75	—
SIMR-2	5/17/2016	CAMO-16-115291	14:47	1.02	5.44	—
SIMR-2	11/21/2016	CAMO-17-127261	10:47	0.97	4.89	—

* — = not available.

Table 3.0-2
Summary of CrPZ Well Data

Location ID	Date Sampled	Field Sample ID	Time Sampled	$\delta^{53}\text{Cr}$ (‰)	Cr ($\mu\text{g/L}$)
CRPZ-1	7/20/2015	CrCH1-15-102153	14:12	0.78	430.75
CRPZ-1	7/20/2015	CrCH1-15-102154	16:40	0.87	406.22
CRPZ-1	2/8/2016	CrCH1-16-110478	17:00	0.99	431.21
CRPZ-1	1/23/2017	CrCH1-17-129732	17:00	0.9	349.5
CRPZ-1	1/24/2017	CrCH1-17-129980	14:00	0.83	355.37
CRPZ-1	1/25/2017	CrCH1-17-129735	13:20	0.86	346.66
CRPZ-1	1/26/2017	CrCH1-17-129981	13:55	0.88	349.87
CRPZ-1	1/27/2017	CrCH1-17-129984	12:00	0.8	343.52
CRPZ-2 S1	7/9/2015	CrCH2-15-102161	12:13	1.0	83.89
CRPZ-2 S1	3/28/2016	CrCH2-16-110502	14:36	1.09	75.05
CRPZ-2 S1	3/29/2016	CrCH2-16-110504	13:40	0.99	102.44
CRPZ-2 S1	3/30/2016	CrCH2-16-110505	13:05	0.97	105.42
CRPZ-2 S1	3/31/2016	CrCH2-16-110506	13:55	0.96	124.57
CRPZ-2 S1	4/1/2016	CrCH2-16-110507	13:10	0.95	128.73
CrPZ-2 S1	07/11/2016	CrCH2-16-123324	10:30	2.84	10.928
CrPZ-2 S1	7/20/2016	CrCH2-16-123328	10:05	1.8	13.015
CrPZ-2 S1	8/5/2016	CrCH2-16-123335	10:10	1.34	24.162
CrPZ-2 S1	8/22/2016	CrCH2-16-123342	10:25	1.25	33.79
CrPZ-2 S1	9/7/2016	CrCH2-16-123510	9:45	1.69	58.205
CrPZ-2 S1	9/23/2016	CrCH2-16-123557	9:55	1.31	44.619
CrPZ-2 S1	9/30/2016	CrCH2-16-123560	10:10	0.99	53.846
CrPZ-2 S1	10/14/2016	CrCH2-16-123566	10:25	1.04	55.121
CrPZ-2 S1	10/28/2016	CrCH2-16-123532	10:45	1.05	62.643
CrPZ-2 S1	11/9/2016	CrCH2-16-123577	10:55	1.31	72.361
CrPZ-2 S1	11/10/2016	CrCH2-16-123578	12:30	1.25	58.415
CrPZ-2 S1	11/23/2016	CrCH2-16-123582	10:40	1.28	59.969
CrPZ-2 S1	12/7/2016	CrCH2-17-128862	12:05	1.14	63.234
CrPZ-2 S1	12/21/2016	CrCH2-17-128856	15:00	1.35	59.278
CrPZ-2 S1	1/9/2017	CrCH2-17-128857	11:35	1.19	44.616
CrPZ-2 S1	1/13/2017	CrCH2-17-128859	10:30	1.18	70.572
CrPZ-2 S1	2/8/2017	CrCH2-17-128860	15:00	1.2	73.366
CrPZ-2 S1	2/15/2017	CrCH2-17-129559	13:40	1.17	57.747
CrPZ-2 S1	2/27/2017	CrCH2-17-129562	11:10	1.25	62.556
CRPZ-2 S2	7/14/2015	CrCH2-15-102164	17:32	1.31	35.01
CRPZ-2 S2	7/14/2015	CrCH2-15-102165	16:03	1.33	29.78
CRPZ-2 S2	2/22/2016	CrCH2-16-110496	16:15	1.27	46.9

Table 3.0-2 (continued)

Location ID	Date Sampled	Field Sample ID	Time Sampled	$\delta^{53}\text{Cr}$ (‰)	Cr ($\mu\text{g/L}$)
CRPZ-2 S2	2/24/2016	CrCH2-16-110497	13:33	1.21	40.04
CRPZ-2 S2	2/25/2016	CrCH2-16-110498	13:30	1.28	36.07
CRPZ-2 S2	2/26/2016	CrCH2-16-110499	13:50	1.26	34.47
CRPZ-3	7/13/2015	CrCH3-15-102170	13:15	1.09	324.63
CRPZ-3	7/13/2015	CrCH3-15-102171	15:50	1.07	322.65
CRPZ-3	7/13/2015	CrCH3-15-102172	18:20	1.1	338.88
CRPZ-3	4/4/2016	CrCH3-16-110514	11:53	1.21	336.66
CRPZ-3	4/4/2016	CrCH3-16-110515	13:37	1.22	333.61
CRPZ-3	4/5/2016	CrCH3-16-110516	13:30	1.17	322.4
CRPZ-3	4/6/2016	CrCH3-16-110517	13:45	1.18	351.62
CRPZ-4	7/8/2015	CrCH4-15-102176	14:28	2.12	5.7
CRPZ-4	7/8/2015	CrCH4-15-102177	16:56	1.41	5.8
CRPZ-4	7/8/2015	CrCH4-15-102178	19:22	1.33	5.69
CRPZ-4	3/7/2016	CrCH4-16-110526	13:23	1.51	14.88
CRPZ-4	3/8/2016	CrCH4-16-110528	13:35	1.04	14.0
CRPZ-4	3/9/2016	CrCH4-16-110529	13:48	1.15	13.37
CRPZ-4	3/10/2016	CrCH4-16-110530	13:50	1.0	12.98
CRPZ-4	3/11/2016	CrCH4-16-110531	13:15	0.98	11.58
CRPZ-5	7/15/2015	CrCH5-15-102182	12:43	1.17	81.31
CRPZ-5	7/15/2015	CrCH5-15-102183	15:10	1.2	89.25
CRPZ-5	7/15/2015	CrCH5-15-102184	17:40	1.1	89.26
CRPZ-5	4/13/2016	CrCH5-16-110538	13:38	0.97	258.24
CRPZ-5	4/14/2016	CrCH5-16-110541	13:50	1.08	253.23
CRPZ-5	4/15/2016	CrCH5-16-110542	13:15	1.06	252.9

Table 3.0-3
Summary of Data from CrEX-1, CrEX-3, CrIN Wells and Regional Aquifer Pump Tests

Location ID	Date Sampled	Field Sample ID	Time Sampled	$\delta^{53}\text{Cr}$ (‰)	Cr ($\mu\text{g/L}$)	Cr(VI) ($\mu\text{g/L}$)
CrEX-1	10/27/2014	Cr-Ex-15-90406	09:40	1.11	139.99	—*
CrEX-1	11/3/2014	Cr-Ex-15-90404	15:16	1.1	169.62	—
CrEX-1	11/12/2014	Cr-Ex-15-90410	10:22	1.17	179.28	—
CrEX-1	11/17/2014	Cr-Ex-15-90414	10:07	1.13	171.11	—
CrEX-1	11/24/2014	Cr-Ex-15-90408	15:25	1.12	167.71	—
CrEX-1	12/1/2014	Cr-Ex-15-90951	15:16	1.21	166.26	—
CrEX-1	12/8/2014	Cr-Ex-15-90953	10:58	0.98	168.22	—
CrEX-1	12/16/2014	Cr-Ex-15-91487	15:08	1.07	154.4	—
CrEX-1	12/22/2014	Cr-Ex-15-91488	10:00	1.06	161.92	—
CrEX-1	1/14/2015	VS-CrEx1-V2-92563	13:52	1.05	137.68	—
CrEX-3	09/15/2016	CrEX3-16-123292	10:30	1.03	156.41	—
CrEX-3	10/14/2016	CrEX3-17-126943	10:20	1.33	175.97	—
CrEX-3	11/07/2016	CrEX3-17-127067	10:15	0.89	180.34	—
CrIN-1	7/20/2016	CrIN1-16-124242	09:02	1.09	82.5	—
CrIN-3	9/9/2016	CrIN3-16-125988	15:00	3.03	43.6	—
CrIN-4	6/22/2016	CrIN4-16-123244	15:00	1.58	97.8	—
CrIN-5	8/4/2016	CrIN5-16-124705	16:00	3.51	54.3	—
R-28	8/28/2013	Cr28-13-41262	14:00	1.02	341.18	361
R-28	8/30/2013	Cr28-13-41265	10:32	1.37	315.12	340
R-28	9/9/2013	Cr28-13-41339	10:28	1.04	347.79	317
R-28	9/17/2013	Cr28-13-41483	13:33	1.04	321.18	302
R-28	9/18/2013	Cr28-13-41486	11:30	1.02	320.17	308
R-28	9/26/2013	Cr28-13-41341	12:15	1.03	299.85	302
R-28	9/30/2013	Cr28-13-41343	10:14	1.09	293.56	297
R-28	10/3/2013	Cr28-13-42048	13:17	1.04	297.85	298.4
R-28	10/11/2013	Cr28-13-42279	10:54	1.0	281.19	292
R-28	10/17/2013	Cr28-13-42401	11:35	1.06	300.13	278
R-28	10/24/2013	Cr28-13-42554	10:03	0.98	291.97	286
R-28	10/31/2013	Cr28-13-45580	13:05	1.03	273.61	282
R-28	11/7/2013	Cr28-13-45911	8:47	1.04	252.9	269.8
R-28	11/14/2013	Cr28-13-45910	12:36	1.06	287.58	280.3
R-28	11/21/2013	Cr28-13-49238	11:55	1.05	288.71	273
R-28	11/27/2013	Cr28-14-49449	11:12	1.25	274.54	251
R-28	12/4/2013	Cr28-14-49440	12:00	1.02	264.8	268
R-28	12/11/2013	Cr28-14-49442	11:30	1.2	294.33	274
R-28	12/18/2013	Cr28-14-49623	11:15	1.02	303.91	295

Table 3.0-3 (continued)

Location ID	Date Sampled	Field Sample ID	Time Sampled	$\delta^{53}\text{Cr}$ (‰)	Cr ($\mu\text{g/L}$)	Cr(VI) ($\mu\text{g/L}$)
R-28	1/10/2014	Cr28-14-49622	9:49	1.06	329.01	312
R-28	1/22/2014	Cr28-14-49448	9:47	1.02	334.24	318
R-28	2/3/2014	Cr28-14-49620	09:43	0.99	325.98	323
R-28	2/18/2014	Cr28-14-49618	9:23	0.96	305.45	435
R-28	3/3/2014	Cr28-14-55776	10:37	0.96	317.43	323
R-28	9/19/2016	TRR-28-16-123651	8:45	1.11	365.77	—
R-28	10/10/2016	TRR-28-16-123657	16:45	1.07	44.741	—
R-28	10/20/2016	TRR-28-16-123667	10:05	1.23	88.223	—
R-28	10/30/2016	TRR-28-16-123677	14:34	1.26	107.52	—
R-28	11/10/2016	TRR-28-16-123688	10:20	1.23	311.68	—
R-28	11/21/2016	TRR-28-17-127645	11:00	1.13	372.94	—
R-28	11/30/2016	TRR-28-17-127650	11:20	1.03	459.39	—
R-28	12/9/2016	TRR-28-17-127668	11:35	0.97	522.86	—
R-28	12/20/2016	TRR-28-17-129043	12:00	1.19	503.94	—
R-42	11/14/2008	GW42-09-1014	10:00	2.67	—	—
R-42	11/15/2008	GW42-09-1016	07:50	2.12	—	—
R-42	6/19/2013	Cr-R42-13-36681	08:45	0.9	898.55	973
R-42	6/26/2013	Cr-R42-13-36690	09:00	0.89	846.58	931
R-42	6/28/2013	Cr-R42-13-36686	09:08	0.88	860.26	921
R-42	7/3/2013	Cr-R42-13-36692	10:12	0.9	825.44	899
R-42	7/11/2013	Cr-R42-13-36697	11:55	0.9	851.0	903
R-42	7/17/2013	Cr-R42-13-37846	09:00	0.97	880.08	778
R-42	7/25/2013	Cr-R42-13-38999	8:55	0.94	656.92	779
R-42	8/1/2013	Cr-R42-13-39306	9:10	0.95	780.33	768
R-42	8/4/2013	Cr-R42-13-39376	7:40	0.95	777.42	773
R-42	8/14/2013	Cr-R42-13-40499	8:57	0.99	700.07	730
R-42	8/23/2013	Cr-R42-13-41095	11:51	0.92	743.5	733
R-42	8/24/2013	Cr-R42-13-41094	07:28	0.98	798.69	756
R-42	8/27/2013	Cr-R42-13-41097	10:36	0.95	733.31	607
R-42	8/29/2013	Cr-R42-13-41082	13:50	0.97	672.1	703
R-42	9/1/2013	Cr-R42-13-41086	8:04	0.91	662.61	717
R-42	9/3/2013	Cr-R42-13-41081	11:10	1.01	747.51	739
R-42	9/5/2013	Cr-R42-13-41347	09:34	0.91	772.66	744
R-42	9/10/2013	Cr-R42-13-41465	09:20	0.95	764.93	747
R-42	9/18/2013	Cr-R42-13-41471	10:45	0.98	782.91	772
R-42	9/27/2013	Cr-R42-13-42023	10:10	0.95	816.53	786
R-42	10/3/2013	Cr-R42-13-41458	10:35	0.94	814.71	792
R-42	10/10/2013	Cr-R42-13-42021	11:35	0.94	787.13	789
R-42	10/18/2013	Cr-R42-13-42270	10:25	0.96	802.64	801

Table 3.0-3 (continued)

Location ID	Date Sampled	Field Sample ID	Time Sampled	$\delta^{53}\text{Cr}$ (‰)	Cr ($\mu\text{g/L}$)	Cr(VI) ($\mu\text{g/L}$)
R-42	10/25/2013	Cr-R42-13-42269	10:55	0.95	755.64	811
R-42	10/31/2013	Cr-R42-13-42272	10:15	1.02	891.06	782
R-42	11/7/2013	Cr-R42-13-42271	11:15	0.97	769.61	826
R-42	11/21/2013	Cr-R42-13-49435	13:20	0.95	832.93	823
R-42	12/5/2013	Cr-R42-13-41456	11:16	0.91	895.53	808
R-42	9/7/2016	TRR-42-16-123756	9:50	0.97	244.86	—
R-42	9/14/2016	TRR-42-16-123759	10:10	0.9	336.4	—
R-42	9/26/2016	TRR-42-16-123764	11:20	0.88	485.99	—
R-42	10/7/2016	TRR-42-16-123769	10:10	0.79	623.29	—
R-42	10/21/2016	TRR-42-17-126870	11:05	0.86	671.55	—
R-42	11/7/2016	TRR-42-17-126877	10:35	0.95	654.01	—
R-42	11/23/2016	TRR-42-17-126884	10:30	0.89	694.63	—
R-43	7/21/2014	CrR431-14-85021	10:13	0.92	84.04	—
R-43	8/4/2014	CrR431-14-85146	16:32	0.98	152.66	—
R-43	8/18/2014	CrR431-14-85950	10:39	0.96	126.07	—
R-43	8/25/2014	CrR431-14-86650	13:55	0.91	150.79	—
R-43	9/2/2014	CrR431-14-86649	10:22	1.09	134.4	—
R-43	9/4/2014	CrR431-14-87015	08:41	1.03	110.07	—
R-43	9/10/2014	CrR431-14-87016	09:58	1.07	100.46	—
R-43	9/17/2014	CrR431-14-87017	09:07	0.97	87.59	—
R-62	5/13/2014	Cr-R62-14-77918	10:35	1.25	—	—
R-62	5/27/2014	Cr-R62-14-79815	10:52	1.02	261	—
R-62	6/4/2014	Cr-R62-14-79998	14:26	1.0	243.15	—
R-62	6/11/2014	Cr-R62-14-81250	14:44	0.97	232.83	—
R-62	6/30/2014	Cr-R62-14-84203	15:00	0.91	202.82	—
R-62	7/7/2014	Cr-R62-14-84204	15:10	0.95	214.13	—
R-62	7/14/2014	Cr-R62-14-84664	12:02	1.0	213.16	—
R-62	7/23/2014	Cr-R62-14-84665	10:42	0.96	240.54	—
R-62	7/30/2014	Cr-R62-14-84666	10:12	0.96	243.55	—
SCI-2	10/25/2013	CrSCI2-14-45464	10:15	1.16	383.2	384
SCI-2	10/30/2013	CrSCI2-14-45469	11:15	1.19	341.97	409
SCI-2	11/4/2013	CrSCI2-14-45647	10:00	1.07	341.1	410
SCI-2	11/6/2013	CrSCI2-14-45641	08:25	1.09	444.42	402
SCI-2	11/13/2013	CrSCI2-14-45932	11:10	1.08	433.77	405
SCI-2	11/20/2013	CrSCI2-14-45930	10:30	1.07	395.79	405
SCI-2	11/21/2013	CrSCI2-14-49223	12:30	1.12	414.43	396
SCI-2	11/27/2013	CrSCI2-14-49484	9:55	1.09	406.68	393
SCI-2	12/4/2013	CrSCI2-14-49491	10:30	1.09	369.46	387
SCI-2	12/11/2013	CrSCI2-14-49494	10:30	1.06	404.18	375

Table 3.0-3 (continued)

Location ID	Date Sampled	Field Sample ID	Time Sampled	$\delta^{53}\text{Cr}$ (‰)	Cr ($\mu\text{g/L}$)	Cr(VI) ($\mu\text{g/L}$)
SCI-2	12/18/2013	CrSCI2-14-49639	10:15	1.12	413.91	387
SCI-2	1/7/2014	CrSCI2-14-49642	11:00	1.09	419.0	390
SCI-2	1/13/2014	CrSCI2-14-49638	11:00	1.04	413.58	387
SCI-2	9/24/2014	CrSCI2-14-87535	09:42	1.2	371.74	—
SCI-2	10/15/2014	CrSCI2-14-87536	14:03	1.24	401.99	—
SCI-2	11/7/2014	CrSCI2-14-87537	14:00	1.34	458.94	—

* — = not available.

**Table 4.0-1
Summary of Experimental Data**

Water Source	Reducing Agent	Time (min)	Date Sampled	Sample ID	$\delta^{53}\text{Cr}$	Cr ($\mu\text{g/L}$)	Cr(VI) $\mu\text{g/L}$
R-42	ZVI	0	7/1/2015	R42Z10-15-101886	0.96	—*	940
R-42	ZVI	5	7/1/2015	R42Z11-15-101887	1.18	—	774
R-42	ZVI	15	7/1/2015	R42Z12-15-101888	1.91	—	462
R-42	ZVI	30	7/1/2015	R42Z13-15-101889	1.96	—	454
R-42	ZVI	0	7/1/2015	R42Z20-15-101891	0.94	—	900
R-42	ZVI	5	7/1/2015	R42Z21-15-101892	1.52	—	635
R-42	ZVI	15	7/1/2015	R42Z22-15-101894	3.17	—	250
R-42	ZVI	30	7/1/2015	R42Z23-15-101893	5.32	—	90
R-42	Microbial	—	4/3/2014	Hak-Bio-14-86855	0.98	818.6	—
R-42	Microbial	—	4/9/2014	Hak-Bio-14-86856	1.33	723.5	—
R-42	Microbial	—	4/3/2014	Hak-Bio-14-86855	0.98	818.6	—
R-42	Microbial	—	4/9/2014	Hak-Bio-14-86856	1.33	723.5	—
R-42	Microbial	—	4/11/2014	Hak-Bio-14-86857	1.42	696.6	—
R-42	Microbial	—	4/17/2014	Hak-Bio-14-86858	1.65	660.9	—
R-42	Microbial	—	4/23/2014	Hak-Bio-14-86859	1.91	610.1	—
R-42	Microbial	—	5/1/2014	Hak-Bio-14-86860	2.11	582.2	—
R-42	Microbial	—	5/7/2014	Hak-Bio-14-86861	2.44	521.7	—
R-42	Microbial	—	5/12/2014	Hak-Bio-14-86862	2.61	499.1	—
R-42	Microbial	—	5/15/2014	Hak-Bio-14-86863	2.66	470.6	—
R-42	Microbial	—	5/21/2014	Hak-Bio-14-86864	3.1	412.6	—
R-42	Microbial	—	5/29/2014	Hak-Bio-14-86865	3.6	393.9	—
R-42	Microbial	—	6/5/2014	Hak-Bio-14-86866	4.25	361.1	—
R-42	Microbial	—	6/11/2014	Hak-Bio-14-86867	4.6	306.7	—
R-42	Microbial	—	6/20/2014	Hak-Bio-14-86868	5.43	215.3	—
R-42	Microbial	—	6/24/2014	Hak-Bio-14-86869	5.91	192.0	—
R-42	Microbial	—	7/1/2014	Hak-Bio-14-86870	6.65	158.0	—
R-42	Microbial	—	7/21/2014	Hak-Bio-14-86872	10.23	62.0	—

* — = not available.

LA-UR-18-21450
March 2018
EP2018-0029

Stratigraphic and Sedimentological Studies and their Hydrogeological Features in the Chromium Investigation Area, Los Alamos National Laboratory

Attachment 3



Prepared by the Associate Directorate for Environmental Management

Los Alamos National Laboratory, operated by Los Alamos National Security, LLC, for the U.S. Department of Energy (DOE) under Contract No. DE-AC52-06NA253 and under DOE Office of Environmental Management Contract No. DE-EM0003528, has prepared this document pursuant to the Compliance Order on Consent, signed June 24, 2016. The Compliance Order on Consent contains requirements for the investigation and cleanup, including corrective action, of contamination at Los Alamos National Laboratory. The U.S. government has rights to use, reproduce, and distribute this document. The public may copy and use this document without charge, provided that this notice and any statement of authorship are reproduced on all copies.

CONTENTS

1.0	INTRODUCTION	1
2.0	NEW GEOLOGIC SURFACES IN THE VADOSE ZONE FOR THE SITE GEOLOGIC MODEL	2
2.1	Introduction	2
2.2	Methods	2
2.3	Results	2
2.3.1	Middle and Upper Otowi Stratal Contacts	3
2.3.2	Tholeiite/Alkali Basalt Stratal Contact	4
2.3.3	Lower Puye Formation Stratal Contact	5
2.4	Discussion of Hydrologic Role of Geologic Units in the Vadose Zone	6
2.5	Alignment of Pliocene Volcanic Centers along a Potential Structural Lineament	9
2.6	Summary and Conclusions	12
3.0	LITHOLOGIC CHARACTERIZATION, PARTICLE-SIZE ANALYSIS, HYDRAULIC CONDUCTIVITY ESTIMATES OF SONIC CORES, AND REVISED STRATIGRAPHY	13
3.1	Introduction	13
3.2	Methods	14
3.2.1	Analytical Methods	14
3.3	Results	15
3.3.1	Chromium Core Hole 1 (CrCH-1)	16
3.3.2	Chromium Core Hole 2 (CrCH-2)	17
3.3.3	Chromium Core Hole 3 (CrCH-3)	18
3.3.4	Chromium Core Hole 4 (CrCH-4)	20
3.3.5	Chromium Core Hole 5 (CrCH-5)	21
3.4	Discussion	21
3.4.1	Revised Stratigraphy for Rocks of the Upper Regional Aquifer	22
3.4.2	Distribution of Rock Units Relative to the Regional Water Table	23
3.4.3	Summary of Particle-Size and Lithologic Characteristics of Rocks of the Upper Regional Aquifer	23
3.4.4	Hydrological Implications of Lithologic and Particle-Size Data	25
3.4.5	Provenance and Sedimentology of Miocene and Pliocene Rocks	26
3.5	Summary and Conclusions	27
4.0	REFERENCES AND MAP DATA SOURCES	28
4.1	References	28
4.2	Map Data Source	31

Figures

Figure 1.0-1	Map showing the approximate extent of the hexavalent chromium plume as defined by the 50- μ g/L New Mexico groundwater standard	33
Figure 2.2-1	Examples of elevation-corrected cross-sections used to correlate gamma logs between wells in the Chromium Investigation Area	34
Figure 2.3-1	Chemical classification diagram showing alkali-silica compositions of subsurface lavas beneath the eastern Pajarito Plateau	35
Figure 2.3-2	Borehole gamma and trace element (zirconium, strontium, and barium) plots for the Cerros del Rio basalt in wells MCOBT-4.4 and MCOBT-8.5	36

Figure 2.3-3	Borehole spectral gamma activity for uranium and thorium in the Puye Formation for well R-11	37
Figure 2.4-1	Diagram showing typical internal features in a basalt lava flow (after Reidel et al. 2013).	38
Figure 2.5-1	Vent locations for dacite (blue star), alkali basalt (yellow stars), and tholeiite (green stars) lavas of the Cerros del Rio volcanic field in the eastern Pajarito Plateau. Numbered locations are referred to in the text	39
Figure 2.5-2	Structure contour map for top of dacite lavas near the east end of MDA G in Pajarito Canyon.....	40
Figure 3.2-1	Stratigraphic columns showing geologic contacts and water levels (blue lines) for core holes in Mortandad Canyon	41
Figure 3.3-1	CrCH-1 grain-size variations for beds making up strata in the upper part of the regional aquifer. The CrPZ-1 (completed in the CrCH-1 borehole) and R-28 well screens are shown for reference	42
Figure 3.3-2	CrCH-1 lithologic column showing rock types for individual beds making up strata in the upper part of the regional aquifer.....	43
Figure 3.3-3	Plane-light photomicrograph of Rendija Canyon Rhyodacite in thin section showing the typical phenocryst assemblage (Q= quartz, PL= plagioclase, BT=biotite, CPX=clinopyroxene; not shown are phenocrysts of hornblende, sanidine, and anorthoclase)	44
Figure 3.3-4	CrCH-2 grain-size variations for beds making up strata in the upper part of the regional aquifer	45
Figure 3.3-5	CrCH-2 lithologic column showing rock types for individual beds making up strata in the upper part of the regional aquifer.....	46
Figure 3.3-6	Comparison of the CrCH-2 lithologic column and estimated hydraulic conductivity to the mean grain size (shown as \emptyset arithmetic mean) and sorting characteristics (shown as standard deviation of \emptyset using the method of moments)	47
Figure 3.3-7	Comparison of pumice compositions in CrCH-2 with Bearhead Rhyolite pumices that make up the Miocene pumiceous unit beneath the Pajarito Plateau.....	48
Figure 3.3-8	XRF data comparing dacite clast compositions in the Puye pumiceous subunit of CrCH-2 with dacitic source rocks that contributed detritus to the Puye Formation	49
Figure 3.3-9	CrCH-3 grain-size variations for beds making up strata in the upper part of the regional aquifer	50
Figure 3.3-10	CrCH-3 lithologic column showing rock types for individual beds making up strata in the upper part of the regional aquifer.....	51
Figure 3.3-11	CrCH-4 grain-size variations for beds making up strata in the upper part of the regional aquifer	52
Figure 3.3-12	CrCH-4 lithologic column showing rock types for individual beds making up strata in the upper part of the regional aquifer.....	53
Figure 3.3-13	CrCH-5 grain-size variations for beds making up strata in the upper part of the regional aquifer	54
Figure 3.3-14	CrCH-5 lithologic column showing rock types for individual beds making up strata in the upper part of the regional aquifer.....	55
Figure 3.4-1	Isopach map showing thickness of the Puye pumiceous subunit [Tpf(p)] in the vicinity of the chromium plume (purple) in Mortandad Canyon	56

Figure 3.4-2	Geologic cross-sections for the upper part of the regional aquifer along the axis of the chromium contaminant plume in Mortandad Canyon	57
Figure 3.4-3	Histograms for grain size and estimated hydraulic conductivity of Pliocene and Miocene rocks in the upper regional aquifer beneath Mortandad Canyon	58
Figure 3.4-4	Histograms for bedding thickness of Pliocene and Miocene rocks in the upper regional aquifer beneath Mortandad Canyon	59
Figure 3.4-5	Folk (1980) clastic rock classification applied to the Pliocene and Miocene rocks at the top of the regional aquifer beneath Mortandad Canyon based on particle-size data for cores collected from CrCH-1, CrCH-2, CrCH-3, CrCH-4, and CrCH-5	60
Figure 3.4-6	Histograms showing selected mineralogy for the F4, F5, and F6 particle-size fractions of Pliocene and Miocene rocks in the upper regional aquifer beneath Mortandad Canyon.....	61
Figure 3.4-7	Schematic cross-sections portraying the aquifer hydraulic structure based on particle-size data and estimates of hydraulic conductivity for CrCH-1, CrCH-2, CrCH-3, CrCH-4, and CrCH-5.....	63
Figure 3.4-8	Early Pliocene (~5 Ma) paleo-geographic map for the western Española basin showing the eruption of the Rendija Canyon Rhyodacite from a volcanic center west of the Pajarito fault zone (PFZ) and contemporaneous deposition of the lower Puye Formation in the western Española basin.....	64
Figure 3.4-9	Middle Pliocene (~3 Ma) paleo-geographic map for the western Española basin showing the eruption of numerous overlapping volcanic centers west of the PFZ and contemporaneous deposition of the upper Puye Formation in the western Española basin.....	65

Tables

Table 3.2-1	Sieve Mesh Sizes, Particle-Size Distributions, and Grain-Size Classification for Analysis of Strata from CrCH-1 through CrCH-5	67
Table 3.3-1	Revised Geologic Contacts for Pliocene and Miocene Sedimentary Rocks of the Regional Aquifer in the Chromium Investigation Area	67

Appendixes

Appendix A	Elevations of Stratal Contacts for the Middle Otowi Member, Top of Cerros del Rio Alkali Basalt, and Middle Puye Formation Based on Borehole Gamma Logs
Appendix B	Structural Contour Maps for Geologic Contacts in the Chromium Investigation Area
Appendix C	Lithologic Descriptions for Core Holes CrCH-1, CrCH-2, CrCH-3, CrCH-4, and CrCH-5
Appendix D	Particle-Size Data and Kozney-Carman Estimates of Hydraulic Conductivity for Core Holes CrCH-1, CrCH-2, CrCH-3, CrCH-4, and CrCH-5
Appendix E	XRF and XRD Analyses of Particle-Size Fractions F4, F5, and F6 for Core Holes CrCH-1, CrCH-2, and CrCH-3

1.0 INTRODUCTION

This report summarizes the lithological characteristics and stratigraphic framework of rock units in the Chromium (Cr) Investigation area. New lithostratigraphic surfaces supplement those in the current site geologic model and provide important information about the site's hydrogeological conditions and potential groundwater pathways in the vadose zone and upper regional aquifer. Section 2 contains information on new geologic surface investigations in the vadose zone for the geologic model. Section 3 contains new stratigraphic and sedimentological data for rocks making up the regional aquifer. A map of the Chromium Investigation Area, which includes many of the wells, boreholes, and core holes discussed in this report, is provided in Figure 1.0-1.

Investigations related to chromium contamination are summarized in a number of reports, including the "Interim Measures Investigation Report for Chromium Contamination in Groundwater" (LANL 2006), "Investigation Report for Sandia Canyon" (LANL 2009c) and the "Phase II Investigation Report for Sandia Canyon" (LANL 2012). These investigations have identified the probable chromium source as cooling tower effluent released near the head of Sandia Canyon between 1956 and 1972. Chromium was transported down the canyon in surface-water flow. Infiltration of surface and alluvial water in the Sandia Canyon resulted in percolation of water through the vadose zone, including in perched intermediate groundwater. Sandia Canyon infiltration is the probable source of chromium contamination in the regional aquifer in the vicinity of Mortandad Canyon.

Section 2 reports the results of borehole geophysical logs to identify the orientation of internal bedding features within three stratigraphic units that make up a significant portion of the vadose zone. New geologic contacts based on the geophysical logs provide information about (1) bedding orientations of ash-flow tuffs in the Otowi Member of the Bandelier Tuff, (2) a regional-scale stratigraphic break between alkali basalts and tholeiites in the Cerros del Rio basalts, and (3) a laterally persistent depositional unit within the lower Puye Formation. Structure contour maps for the three new geologic contacts are presented along with those in the current site geologic model to assess the potential role of bedding to influence groundwater pathways through the vadose zone. Based on their dips, it appears that the Puye Formation and underlying Miocene pumiceous deposits are tilted to the south and southeast by post-depositional faulting.

Section 3 characterizes the lithology of Pliocene and Miocene sedimentary rocks that represent the primary chromium contaminant flow paths in the upper regional aquifer and assesses how the hydrogeological properties of these deposits may affect contaminant migration and the selection of remediation alternatives. The units studied include (1) the lower part of Puye Formation, (2) the Puye pumiceous subunit that is newly recognized in this study, and (3) pumiceous sands that are informally called the Miocene pumiceous unit. Particle-size analysis was conducted on samples collected from five sonic core holes drilled along the axis of the chromium plume in Mortandad Canyon (Figure 1.0-1) to discriminate between transmissive and/or impermeable beds based on the distribution of size fractions and sorting. A small subset of core samples was also analyzed using x-ray fluorescence (XRF) and quantitative x-ray diffraction (QXRD) to determine the bulk chemical and mineralogical compositions of fine to medium sand, very fine to fine sand, and silt size fractions, respectively.

A mixture of English and metric units is used in this report. English units are used for drill and core hole depths and elevations to conform with labelling of core and cuttings and conventions used during geophysical logging. English units are commonly used in well completion reports referenced by this document. Metric units are used for data that were the result of sample analyses and other non-drilling data.

2.0 NEW GEOLOGIC SURFACES IN THE VADOSE ZONE FOR THE SITE GEOLOGIC MODEL

2.1 Introduction

This section presents the results from borehole geophysical logs to identify the orientation of internal bedding features within three stratigraphic units that make up a significant portion of the vadose zone. New geologic contacts based on the geophysical logs provide information about (1) bedding orientations of ash-flow tuffs in the Otowi Member of the Bandelier Tuff, (2) a regional-scale stratigraphic break between alkali basalts and tholeiites in the Cerros del Rio basalts, and (3) a laterally persistent depositional unit within the lower Puye Formation. Structure contour maps for the three new geologic contacts are presented with those in the current site geologic model to assess the potential role of bedding to influence groundwater pathways through the vadose zone. This work supplements the site geologic model by identifying additional geologic contacts internal to the major rock units that have the potential to influence vadose zone groundwater pathways and flow directions.

Section 2.2 of this report describes the methods used to identify and map the new geologic contacts. Section 2.3 summarizes the results of the study and discusses the geologic significance of the new geologic surfaces. Section 2.4 discusses the hydrogeological significance of the surfaces in the context of the entire stratigraphic sequence and the role of bedding to influence groundwater pathways through the vadose zone.

2.2 Methods

Borehole geophysical logs were used to identify (1) bedding orientations in the Otowi Member of the Bandelier Tuff, (2) a regional-scale stratigraphic break between alkali basalts and tholeiites in the Cerros del Rio basalts, and (3) a laterally persistent depositional unit within the middle Puye Formation. Natural gamma logs collected by Los Alamos National Laboratory (the Laboratory) and JetWest, Inc., and spectral gamma logs collected by Schlumberger, Inc., were used to identify compositional breaks at stratal boundaries based on changes of gross gamma activity and uranium, thorium, and potassium concentrations as a function of depth. Where available, other geophysical logs (e.g., porosity and elemental capture spectroscopy [ECS] logs) provided supplemental information to identify bedding features that could be correlated between wells. Stratal contacts for the three units were correlated as a series of cross-sections that show gamma activity as a function of depth logs in closely spaced wells. Examples of the correlations are shown in Figure 2.2-1. Correlation of the gamma logs was aided by the relatively dense spacing of wells in the Chromium Investigation Area. Structure contour maps were prepared for each of the three new geologic surfaces by hand contouring the elevations of the identified stratal contacts.

The gamma inflections used to identify stratal contacts are generally abrupt and the selection of the inflection point is generally reproducible to within 5 ft. In some wells, the combination of poor quality logs and/or unfavorable borehole conditions (e.g., signal attenuation by drill casing) resulted in inflections that span a 15-ft interval. Stratal contacts were placed at the base of gamma inflections to provide a consistent methodology for inflection point selection and to minimize potential errors associated with the broader inflection zones.

2.3 Results

The results of this work are discussed below and in the appendixes. Appendix A lists the elevations of the stratal contacts identified in this report. Appendix B presents Figures B-1 through B-10, which show the structure contour maps for the major geologic surfaces in the Chromium Investigation Area based on the current sitewide geologic model (designated WC15c) that was revised in 2015. Appendix B also includes,

in stratigraphic sequence, new structure contour maps for geologic surfaces identified in this study for the middle Otowi Member (Figure B-3), the top of tholeiite and alkali basalt series (Figures B-6 and B-7), and the middle Puye Formation (Figure B-9). These structure contour maps form the basis of the hydrogeological discussion of potential stratigraphic and structural controls on vadose zone pathways in Section 2.4.

2.3.1 Middle and Upper Otowi Stratal Contacts

Natural and spectral gamma activity for the rhyolitic tuffs of the Otowi Member vary as a function of stratigraphic position, generally becoming more radiogenic towards the bottom of the unit (Figure 2.2-1). The progressive trends towards more radiogenic tuffs with depth in the Otowi Member include abrupt shifts to higher gamma activity downhole at several depths in chromium-area wells. Similar depth-related shifts in gamma activity are documented for the Otowi Member in the “Compendium of Technical Reports Related to the Deep Groundwater Investigation for the RDX Project at Los Alamos National Laboratory,” Attachment 2, “Geology of Technical Area 16 and Vicinity, Los Alamos National Laboratory” (LANL 2018). Significant gamma breaks occur (1) at the contact between the Guaje Pumice Bed and Puye Formation or Cerros del Rio basalt, (2) at the contact between the Otowi Member and Guaje Pumice Bed, and (3) in the middle of Otowi Member ash-flow tuffs (Figure 2.2-1). The geologic contacts for (1) and (2) above are captured in the current sitewide geologic model (WC15c), and structure contours for their contacts are presented in Appendix B. The new internal geologic contact for bedding within the Otowi Member is presented below.

The prominent gamma break in the middle of Otowi Member is easily recognized in borehole logs for all wells in the area, and it is reliably correlated between wells. The abrupt change in gamma activity represents a change in the composition of tuffs across the stratal contact. Spectral gamma logs indicate tuffs below the stratal contact contain higher concentrations of uranium and thorium than the tuffs above; potassium concentrations are largely unchanged across the contact. The abrupt gamma shift is interpreted as a depositional boundary representing a brief hiatus in the Otowi eruption, after which a new batch of magma with a slightly less evolved composition was deposited. At Technical Area 16 (TA-16), formation microimager (FMI) logs showed that gamma shifts in the Otowi Member occur at depositional breaks between flow and/or fall units (LANL 2018). Sequences of tuff flow units with similar gamma activity (i.e., tuffs bound by gamma breaks) probably represent phases of the Otowi eruption during which compositionally similar magmas were erupted. Individual flow units were probably deposited in rapid succession over a gently sloping aggrading surface and are likely to have similar bedding orientations.

The structure contour map for the middle Otowi stratal contact is shown in Figure B-3. The middle Otowi stratal contact is a uniform surface that dips approximately 0.92° toward the east-southeast. In contrast, the underlying Guaje Pumice Bed generally dips about 1.15° southward beneath the main chromium infiltration area beneath Sandia and Mortandad Canyons (Figure B-4). The difference in dip azimuths between these units reflects changes in styles of eruptive activity when the Guaje and Otowi tuffs were deposited.

The Guaje Pumice Bed is a plinian fall deposit that blanketed a south-draining paleo valley developed atop a surface underlain by the Puye Formation and Cerros del Rio basalts (Broxton and Reneau 1996). The west flank of the paleo valley included the eastern Jemez Mountain highlands and east-sloping alluvial fans of the western Española basin. The eastern flank consisted of west-facing slopes on Cerros del Rio volcanic highlands that formed on the floor of the Española basin near what today is the east side of the Pajarito Plateau. The paleo-valley surface is preserved beneath the Guaje Pumice Bed that was deposited from an eruption cloud blown eastwards by prevailing winds before deposition. The structure contour map for the base of the Guaje Pumice Bed is a record of that paleo topography (Figure B-4).

The ash-flow tuffs that overlie the Guaje Pumice Bed were erupted during the climactic phase of the Otowi eruption. During catastrophic explosive eruptions of rhyolitic magma, large volumes of pyroclastic material were entrained in rapidly expanding gases and carried into towering eruption columns. Episodic gravitational collapse within the eruption columns resulted in the generation of numerous pyroclastic flows that raced down the east flank of the Sierra de los Valles. These pyroclastic flows were deposited in rapid succession on the western slopes of the Española basin, building up a thick ash-flow tuff sheet. The accumulating pyroclastic flows filled the south-draining paleo valley and eventually overtopped the Cerros del Rio highland to the east. Consequently, Otowi deposits are thick over the paleo drainage and thin over the basaltic highlands. The east-southeast dip of the middle Otowi stratal contact (Figure B-3) represents a brief hiatus in the climactic eruption that separates deposition of tuffs with slightly different compositions; these compositional differences are captured in the natural and spectral gamma logs.

2.3.2 Tholeiite/Alkali Basalt Stratal Contact

Laboratory reports have long documented the widespread occurrence of tholeiite basalt overlying alkali basalt in the Cerros del Rio volcanic field beneath the eastern Pajarito Plateau (e.g., Broxton et al. 1998; LANL 2009c, Appendix N) (e.g. Tholeiites and alkali basalts are distinct chemical subgroups of basalts whose petrogenesis reflect different mantle source regions (Figure 2.3-1). The tholeiites and alkali basalts can be traced continuously 4.8 km from Los Alamos Canyon on the north to Pajarito Canyon on the south and 5 km from well R-1 on the west to well R-9 on the east. More evolved lava types such as trachyandesites, trachytes, and dacites also occur in the volcanic sequence (Figure 2.3-1), but their distribution is restricted to areas east and south of the Chromium Investigation Area (e.g., TA-54), where they always underlie the tholeiites and alkali basalts. Chemical analyses are commonly employed to differentiate between tholeiites and alkali basalts, and extensive XRF data have been collected for samples of basalt from wells in the area (Figures 2.3-1 and 2.3-2). Chemical differences between tholeiites and alkali basalts are also manifested in borehole gamma logs (Figure 2.3-2). Based on spectral gamma logs, tholeiites are depleted in potassium and thorium, and to a lesser extent uranium, relative to alkali basalts, resulting in lower overall gamma activity. Consequently, the borehole gamma logs can be used to correlate the tholeiite/alkali basalt contact between wells, especially when used in conjunction with supporting chemical data (Figure 2.3-2). Structure contour maps for the basalts are shown in Figures B-5, B-6, and B-7.

The tholeiite/alkali basalt contact is interpreted as a paleo surface that represents a major change in magma compositions and vent locations. Although the tholeiite/alkali basalt contact is a depositional surface, the surface probably separates a mosaic of flow units both above and below the contact. Individual lava flows probably do not form sheet-like deposits over the entire tholeiite/alkali basalt subcrop area. Instead, the tholeiite/alkali basalts appear to represent central vent eruptions, and the distributions of individual flows were controlled by an evolving landscape with considerable topographic relief. Therefore, tholeiites overlying the contact with alkali basalt at one location are not likely to be the same as flows elsewhere. Despite these uncertainties, the tholeiite/alkali basalt contact provides useful information about the internal structure of the Cerros del Rio volcanic field, revealing a buried paleo-topographic surface of regional extent and the locations of potential volcanic vents.

A structure contour map for the tholeiite/alkali basalt contact represents the top of the alkali basalt (Figure B-7). Alkali basalts form a broad shield-like volcanic edifice that rises to a summit near wells R-13 and SIMR-2. The shield-like structure is interpreted as a constructional volcanic feature whose summit is the primary vent area for the alkali basalts. The shape of the structure contours indicates the southern half of the alkali/basalt volcanic edifice was little modified by erosion before burial by the subsequent tholeiites. In contrast, the northern part of the volcanic edifice appears to be partly eroded, with drainages developed near wells MCI-10, R-28, and R-35a/b, respectively (Figure B-7). The small circular highland

north of well CrPZ-4 may represent a satellite volcanic vent, but it is more likely an erosional remnant of the main edifice isolated by erosion.

An updated structure contour map for the all Cerro del Rio basalts (Tb4) is shown in Figure B-5. However, Figure B-5 is a composite surface because it includes a second, small-volume tholeiite/alkali basalt succession that overlies the main tholeiite sequence near Mortandad Canyon. This upper tholeiite/alkali basalt succession is described below. Also, the main tholeiite sequence thins and is locally absent where it laps up onto the summit of the older alkali basalt volcano near wells R-13, R-44, and SIMR-2.

The main tholeiite sequence forms a broad shield-like volcanic edifice that rises to a summit near well R-41 near the east side of TA-54 (Figure B-6). The shield-like structure is interpreted as a constructional volcanic feature whose summit is the primary vent area for the tholeiite basalts. Based on this interpretation, it is inferred that tholeiites in the Chromium Investigation Area flowed down the north flank of the tholeiite volcano. The shape of the structure contours indicates the volcanic summit is separated from another tholeiite vent (informally called Reneau volcano in Figure B-6), located south of Pajarito Canyon, by a broad topographic saddle where the flanks of the two volcanos overlap. Small circular highlands on the west and north flanks of the main tholeiite structure, near wells R-53 and LAO-4.5 respectively, may represent small satellite volcanic vents, but this interpretation is uncertain.

The northern flank of the main tholeiite edifice appears to be modified by erosion that resulted in west- and east-draining paleo valleys. Headwaters of east-draining paleo valleys occur near wells LAOI-7 and PM-1 (Figure B-6). The west-draining paleo valley is a narrow, linear drainage that apparently controlled the distribution of a small-volume upper tholeiite/alkali basalt succession that overlies the main tholeiite sequence near Mortandad Canyon.

The upper tholeiite/alkali basalt succession is manifested in borehole gamma logs and XRF data for wells that include MCOBT-4.4, MCOBT-8.5, R-13, R-28, and R-42 (Figures 2.2-1 and 2.3-2). Cross-sections show that the upper tholeiite/alkali basalt succession is much thinner and more limited in distribution than the underlying main tholeiite/alkali basalt sequence (Figure 2.2-1). A structure contour map for the top of the tholeiite in the upper sequence is shown in the inset map of Figure B-6. The upper tholeiite/alkali basalts represent relatively small-scale eruptions and their distribution suggests they flowed westward down a narrow paleo valley eroded into the top of the underlying main tholeiite sequence. The circular highland of basalt near well R-45 is probably a cinder cone that was the source for the upper tholeiites (Figures B-5 and B-6). Well R-45 encountered 68 ft of basaltic cinders at the top of the upper tholeiite, supporting the interpretation of a volcanic vent near this location (Figure 2.2-1).

2.3.3 Lower Puye Formation Stratal Contact

The Puye Formation is an alluvial fan deposit made up of clast- to matrix-supported dacitic gravels and lithic sandstones. The coarsest parts of the deposits contain subangular to subrounded boulders and cobbles of lava and tuff in a poorly sorted matrix of ash, silts, and sands. Thin ash and pumice deposits of dacitic to rhyolitic composition are interbedded with the gravels and sands. The Puye Formation is 200 to 300 ft thick. More detailed descriptions of the lower Puye Formation are presented in section 3.3 of this report. A structure contour map for the top of the Puye Formation is shown in Figure B-8.

In this investigation, review of the borehole gamma logs revealed the presence of a widespread gamma anomaly in the middle of the Puye Formation that is interpreted as a single depositional unit that can be correlated between wells throughout the Chromium Investigation Area. Normally, correlation of individual beds is difficult because strata are commonly discontinuous due to the dynamical depositional and erosional processes that take place in alluvial fans. The anomaly occupies a similar stratigraphic position in adjacent wells and forms a prominent gamma low with sharp, well-defined boundaries (Figures 2.2-1 and 2.3-3). Elevations at the base of the gamma low were identified (Appendix A-3) and hand contoured

to create a structure contour map for the base of the gamma anomaly (Figure B-9). The structure contour map for the low-gamma deposit indicates strata in the middle of the Puye Formation dip approximately 2.4° towards the south and southeast (Figure B-9).

Gamma activities in the Puye Formation, including for the gamma anomaly, reflect chemical variations (specifically uranium, thorium, and potassium) in fanglomerate sediments (Figure 2.3-3). These chemical variations respond to (1) primary chemical variations in the lava clasts that make up the deposits and (2) secondary chemical variations associated with clay alteration and cements. Secondary minerals and cements are sparse to absent in the Puye Formation, so the gamma activity is dominated by primary chemical variations in the lava clasts that make up the deposit. The Puye Formation was deposited as broad, coalescing alluvial fans shed eastward from the Jemez volcanic field into the western Española basin. The source areas for these alluvial-fan deposits were large, overlapping volcanic dome complexes of the Tschicoma Formation that formed the eastern part of the Jemez Mountains. Broadly speaking, the Tschicoma dome complexes can be subdivided into the 5 million year (Ma) Rhyodacite of Rendija Canyon and approximately 3 Ma Dacites of Cerro Grande, Pajarito Mountain, and Caballo Mountain. Section 3.4.5 contains a more detailed discussion of these volcanic centers as sources of detritus for the Puye Formation. The Rhyodacite of Rendija Canyon is a relatively evolved low-silica rhyolite that erupted from a large volcanic complex located near the headwaters of Rendija and Quemazon Canyons. From approximately 5 Ma to 3 Ma, the Rhyodacite of Rendija Canyon was the primary source for much of the fanglomerate in the lower Puye Formation. New volcanic complexes centered near Cerro Grande, Pajarito Mountain, and Caballo Mountain began to erupt approximately 3 million years ago and soon provided significant detritus to the Puye alluvial fans. These younger volcanic units are dacites, and their major and trace element chemistry is less evolved than the Rhyodacite of Rendija Canyon. Uranium and thorium concentrations in the dacites are less than half the concentrations in the Rhyodacite of Rendija Canyon (see Table 2 in Broxton et al. 2007). Potassium concentrations are 25% lower in the dacites.

The chemical differences between low-silica rhyolite and dacite source lavas are reflected in the gamma logs for the Puye Formation. Gamma activity is generally highest in the lower Puye Formation where the fanglomerates are dominated by Rhyodacite of Rendija Canyon detritus (Figure 2.3-3). Gamma activity in the upper Puye Formation is highly variable, reflecting the combined input of both low-silica rhyolite and dacite sources. The low-gamma anomaly is interpreted as dacite-rich sedimentary deposit that is intercalated between deposits dominated by Rhyodacite of Rendija Canyon detritus. The deposits represented by the low-gamma anomaly mark the beginning of significant dacite contributions to the Puye Formation alluvial fans.

The south and southeast internal dip for the Puye Formation is similar to the dip azimuths for the top (Figure B-8) and base of the unit (Figure B-10). Based on their depositional setting and source regions, initial dips for the Puye were probably generally eastward, reflecting deposition on east-sloping alluvial fans in the western Española basin. Dips are approximately 1.95° for the top of the Puye Formation and 3° for the base of the unit, suggesting deposition and tectonism were contemporaneous. The present-day dips indicate that these rocks are tilted southward by post-depositional tectonism.

2.4 Discussion of Hydrologic Role of Geologic Units in the Vadose Zone

Appendix B contains structure contour maps for the major geologic units in the current sitewide geologic model (WC15c), including the new geologic contacts described in section 2.3 above. The following discussion describes how bedding orientations may influence groundwater pathways through the vadose zone. Bedding orientations for geologic units are discussed in descending stratigraphic order.

At unsaturated conditions, movement of moisture in the vadose zone is probably dominated by vertical, gravity-driven flow through porous rocks. Fractures and joints may also play a role in moisture movement through the Cerros del Rio basalt. In porous flow, moisture is likely to be diverted laterally at capillarity barriers associated with bedding contacts. Similarly, confining beds for perched groundwater systems are generally thought to be stratigraphically controlled. Direction of groundwater flow is controlled by the dip of bedding planes at the contacts and within the major stratigraphic units. Groundwater data for monitoring wells in the Chromium Investigation Area indicate that recharge originating as chromium-contaminated surface water in Sandia Canyon has translated generally southward through the vadose zone before entering the regional aquifer near Mortandad Canyon. Bedding orientations within major geologic units of the vadose zone are consistent with the interpretation that southeast translation of chromium-contaminated recharge is the result of lateral diversion associated with dipping geologic contacts.

Thin deposits of Tshirege unit Qbt 1g and Cerro Toledo Formation directly underlie saturated alluvial deposits in the portion of Sandia Canyon that is believed to represent the main infiltration zone for chromium-contaminated surface water. Structure contour maps for these two units suggest canyon-floor infiltration initially encounters tuffs and sediments that were deposited in east-draining paleo valleys whose axes are located beneath the ridge separating Sandia and Mortandad Canyons (Figures B-1 and B-2). Beneath Sandia Canyon, basal contacts for Qbt 1g and the Cerro Toledo Formation dip towards the south and southeast. However, these contacts probably represent the eroded north flanks of the paleo valleys and the valley-filling deposits themselves likely dip towards the east. The Qbt 1g and Cerro Toledo deposits are thin and consequently probably play a minor role in the lateral diversion of percolating moisture. The thickness of Qbt 1g beneath the main infiltration zone is 0–37 ft and the thickness of the Cerro Toledo Formation is 0–38 ft. Both units pinch out eastward as Sandia Canyon becomes incised into the underlying Otowi Member.

The Otowi Member is the thickest and most important geologic unit immediately below the main infiltration zone for chromium contamination. It is 117 to 260 ft thick beneath Sandia Canyon, thinning eastward against the buried Cerros del Rio highland described in section 3.1. Based on gamma data for the middle Otowi stratal contact, bedding in the central portion of the Otowi Member dips uniformly towards the southeast (Figure B-3). For modeling purposes, the Otowi Member is often treated as a single, homogenous hydrogeological unit with isotropic properties. However, stacking of individual flow units results in widespread stratification within the Otowi Member, with the potential to affect hydrologic properties such as vertical anisotropy and preferred groundwater pathways. Grain-size and textural variations between flow units can result in abrupt changes of hydrologic properties at bed contacts. Modeling results for Paintbrush nonwelded tuffs at Yucca Mountain, Nevada, a unit that includes stacked tuffs like the Otowi Member, demonstrate that significant lateral flow can develop in the presence of layered rock that exhibits contrasting fracture matrix hydraulic properties, low percolation flux, and sloping layer interfaces (Wu et al. 2002). Fractures and faults provide downward pathways for laterally diverted percolation fluxes. Bedding orientations for flow units in the Otowi Member suggest that moisture percolating through the Otowi Member will likely be diverted towards the southeast.

The Guaje Pumice Bed is a stratified, porous fall deposit of gravel-sized vitric pumice, quartz and sanidine phenocrysts, and subordinate volcanic lithics. Borehole data indicate the thickness of this unit ranges between 15 ft and 20 ft. As described in section 3.1, the Guaje Pumice Bed mantles the paleo topography that existed before eruption of the Otowi Member. Near the main infiltration zone in Sandia Canyon, the Guaje Pumice Bed dips 1.15° south to southwest (Figure B-4). The Guaje Pumice Bed is potentially important as a groundwater pathway because higher water content and zones of perched saturation occur within this unit at other areas of the Laboratory beneath wet canyons (e.g., Los Alamos Canyon). Although no perched saturation has been identified in the Guaje Pumice Bed beneath Sandia and Mortandad Canyons, high water contents and well-stratified beds within these deposits may divert unsaturated flow to the south and southwest. Silt-rich deposits have been identified at

the top of the underlying Puye Formation over much of the Chromium Investigation Area, and they may contribute to the lateral diversion of moisture.

The Cerros del Rio basalt is a significant hydrogeological unit because it hosts chromium-contaminated perched zones of saturation, and it is a major component of groundwater pathways through the vadose zone. Flow paths through these basalts are highly uncertain because of the complex internal stratigraphy and structure of these rocks. Although geologic uncertainties may prevent identification of exact groundwater pathways, the following discussion provides an assessment of lithologic and structural features that likely control moisture movement through the basalt flow units. This is followed by a brief description of perched groundwater occurrences associated with the Cerros del Rio basalt.

The Cerros del Rio basalt is made up of a thick stack of lava flows separated by interflow breccias. Individual lava flows typically show stratified physical properties that include a brecciated flow top, a dense interior, and a brecciated flow bottom. Figure 2.4-1 is a generalized depiction of the internal zones that make up a single flow unit. However, each flow is unique and there are many variations in the proportions, characteristics, and occurrences of these internal zones. Under saturated conditions (e.g., perched water), groundwater flow through basalts occurs as porous flow in interflow breccias and as fracture flow in the lava flow interior.

Flow breccias represent the upper and lower surfaces of the lava flow that chill rapidly during emplacement and tend to be thin compared with the overall thickness of the flow. These chilled surfaces are commonly disrupted by auto-brecciation as the liquid core of the lava continues to flow. Flow breccias consist of angular, scoriaceous to vesicular fragments of basaltic rubble that form abrupt contacts with massive, vesicular basalt that makes up the flow interior. Flow-top breccias commonly merge with flow-bottom breccias of the overlying flow, forming a highly porous interflow zone that is often laterally extensive. In addition to highly porous breccias, interflow zones may include cinder beds and sedimentary deposits locally. At saturated conditions, porous flow is expected to dominate groundwater flow in interflow zones.

Flow interiors make up the bulk of the flow unit and are made up of massive basalt with variable amounts and sizes of vesicles. The rock matrix of these basalts is dense and generally impermeable to porous flow. At saturated conditions, groundwater flow occurs in the numerous cooling joints that form a dense network of interconnected fractures. Saturated hydraulic conductivity is determined by aperture dimensions, joint density, interconnectivity, and the presence of joint-filling minerals. Cooling joints commonly form in two styles: columnar and entablature. Columnar jointing commonly occurs at the base of the flow interior and consists of mostly vertical polygonal columns. Columnar jointing may also form at the top of some flows. Entablature jointing occurs in the middle and upper part of the flow interior. It is commonly a more complex pattern of joints that consists of numerous, irregular to randomly oriented, small columns (Figure 2.4-1). The cross-cutting and intersecting nature of entablature joints makes them more likely than columnar joints to form well-connected networks of joints that provide high-fracture permeability under saturated conditions. Clay-filled joints are expected to have very low saturated permeability. Locally, tectonic fractures such as faults, shear zones, and tectonic joint sets may be superimposed on the network of cooling joints. These commonly occur in sets of parallel to subparallel, closely spaced fractures that are recognizable in outcrop but are difficult to identify in subsurface borehole data.

Perched groundwater occurs atop a confining bed of the Cerros del Rio basalt at well SCI-1 in Sandia Canyon. The perched saturation is 25 ft and occurs in Puye Formation sands and gravels that lie above an eroded surface of massive tholeiite of the main tholeiite sequence. The top of the Cerros del Rio basalt dips generally westward in this area, but well SCI-1 is located on the north flank of a paleo drainage incised into the basalt, and the erosional surface dips to the southwest (Figure B-5). Perched water at wells MCOI-4 and MCOBT-4.4 in Mortandad Canyon occurs at the top of basalt within the same paleo drainage, suggesting this contact has favorable characteristics for perching groundwater over a wide area.

Perched groundwater also occurs within fractured lavas and interflow breccias in the lower part of the Cerros del Rio basalt at well SCI-2. The perched groundwater occurs within the alkali basalt sequence, and saturation is approximately 45 ft thick. The nature of the perching horizon is poorly understood but may be a massive lava that contains clay-filled fractures near its top (LANL 2009b). The basalts hosting the perched groundwater were deposited over a south to southeast dipping surface that developed on top of the Puye Formation (Figure B-8). Consequently, groundwater flow directions at well SCI-2 may follow the dip of the contact between the Cerros del Rio basalt and the Puye Formation. Lack of perched water in the alkali basalt at wells R-28 and R-42 in Mortandad Canyon suggests that the perched groundwater drains from the basalts and infiltrates the underlying Puye Formation in the area between wells SCI-2 and R-28/R-42.

Based on the discussion in section 3.3, bedding in the middle and lower Puye Formation dips to the south and southeast (e.g., Figures B-9 and B-10). Gravity-driven unsaturated moisture flow through the vadose-zone portion of the Puye Formation will likely include some lateral diversion along bedding planes in these well-stratified sedimentary deposits. Perched saturation appears to be a relatively unimportant component of transport in the middle and lower Puye Formation. A 4-ft zone of perched groundwater was encountered near the top of the lower Puye Formation during the drilling of well R-42 (LANL 2009).

2.5 Alignment of Pliocene Volcanic Centers along a Potential Structural Lineament

As described in section 2.4, rocks of the Cerros del Rio volcanic field make up a significant portion of the stratigraphic sequence in the Chromium Investigation Area, where they play important roles as aquifers for chromium-contaminated perched groundwater and serve as groundwater pathways for local recharge to the regional aquifer. Cerros del Rio volcanic rocks occur entirely in the vadose zone in the vicinity of Mortandad Canyon, and they are generally thought of as playing no hydrologic role in the regional aquifer. In contrast, these volcanic rocks become much thicker southward and make up the upper part of the regional aquifer in the vicinity of Pajarito Canyon near Material Disposal Area (MDA) G. In addition to the volcanic sequence, volcanic vents and their subsurface feeders such as dikes and dike swarms may affect the hydraulic properties of the regional aquifer. The following discussion describes the volcanic vents that were sources of the Cerros del Rio volcanic rocks beneath the eastern Pajarito Plateau and how these vents appear to define a volcanic lineament that may represent a previously unrecognized fault or fracture system. The volcanic lineament and associated feeder dikes near vents may have hydrologic implications for the regional aquifer east of the chromium plume area.

Numerous vents have been mapped for the Cerros del Rio volcanic field in the Caja del Rio east of the Rio Grande and in White Rock Canyon, where they occur as constructional features such as low-relief shield volcanos, cinder cones, and maars (Griggs and Hem 1964; Smith et al. 1970; Kelley 1978; Thompson et al. 2006; Sawyer et al. 2007). Before this investigation, locations of volcanic vents beneath the Pajarito Plateau were poorly known because critical relations are covered by thick deposits of Bandelier Tuff (Dransfield and Gardner 1985; Broxton and Reneau 1996). Over the past two decades, knowledge about Cerros del Rio volcanic rocks beneath the plateau has greatly expanded because of new data provided by wells installed as part of environmental investigations at the Laboratory. Cutting and cores from these wells provide an extensive suite of samples for lithologic, stratigraphic, geochronological, and geochemical studies. Section 2.3.2 of this report describes how tholeiite and alkali basalts of the Cerros del Rio volcanic series were correlated between wells and boreholes using a combination of wireline gamma logs and XRF analyses for major and trace elements in cores and cuttings samples. A major result of that investigation was the generation of structure contour maps that showed the locations of constructional volcanic highlands interpreted as vent areas for many of the basalts. The volcanic vents are discussed below from oldest to youngest.

The most complete subsurface sequence of volcanic rocks occurs in Pajarito Canyon near the east end of MDA G where lava flows 750 to 1000 ft thick range in composition from basalt to dacite, with the more silicic rock types (dacites) occurring at the base of the volcanic pile (oldest units) and less evolved flows (tholeiites and alkali basalts) at the top (youngest units). A series of intermediate composition volcanic rocks (basaltic trachyandesites and trachyandesites) occurs in the stratigraphic interval between the dacites and the basalts. Well data on the spatial distribution of the intermediate-composition volcanic rocks are insufficient to identify their source vents, and they are not discussed further. At the northern end of the volcanic field, in the vicinity of Mortandad Canyon, the subsurface volcanic sequence is made up only of tholeiites and alkali basalts and is 200 to 440 ft thick.

Dacite lavas at the east end of TA-54 form a small dome and flow complex that is well defined by closely spaced wells, including R-22, R-23/23i, R-39, R-41, R-49, and R-57 (#1 in Figure 2.5-1). Detailed descriptions of the chemistry and petrography of this dacite are given in Samuels et al. (2007). A structure contour map for the top of the dacite is shown in Figure 2.5-2. The dome is nearly circular in plan view and about 3800 ft in diameter. The summit of the dome is about 500 ft above its base. A sample of dacite collected from well R-22 yielded an $^{40}\text{Ar}/^{39}\text{Ar}$ age of 2.42 ± 0.12 Ma (Broxton et al. 2007). Dacite flows of similar age occur at other locations beneath the Pajarito Plateau (Samuels et al. 2007) and at Tetilla Peak and Montoso Arroyo in the Caja del Rio (Sawyer et al. 2007). These dacite lavas are similar in composition to Tschicoma lavas exposed in the Jemez Mountain volcanic field (JMVF), but they are slightly younger and lack the coarse-grained, abundant phenocrysts that characterize the Tschicoma Formation. The dacite lavas of the Pajarito Plateau closely overlap the age and distribution of the tholeiitic and alkali lavas of the Pajarito Plateau as well as the Cerros del Rio volcanic field (CdRVF), but their compositions are more evolved than the basalts that make up most of the volcanic field (WoldeGabriel et al. 1996; Thompson et al. 2006). Thus, dacites of the Pajarito Plateau differ in significant ways from dominant rock types found in both the JMVF and CdRVF and they probably reflect a transitional style of magmatism that developed in the region between these adjacent, concurrently active volcanic fields (Samuels et al. 2007).

Alkali basalts form a broad shield volcano that rises to a summit near wells R-13 and SIMR-2 (see discussion in Section 2.3.2 and #2 in Figure 2.5-1). Figure B-7 shows the structure contour map for the upper surface of the alkali basalts and the location of the inferred summit vent. The vent area appears to be located near the northern end of the volcano, and lavas are distributed asymmetrically to the south, possibly reflecting eruption onto a south-dipping regional slope of Puye deposits (Figure B-8). Near the summit vent, the alkali basalts are 310 ft thick at well SIMR-2 and 427 ft thick at well R-13, with the thicker deposits coinciding with a south-southwest-draining pre-volcanic paleo valley that is defined by structure contours at the base of the unit (Figure B-8). A satellite cinder cone is inferred to occur near well R-34, about 3000 ft southeast of the main vent (#3 in Figure 2.5-1), where >300 ft of oxidized alkali basalt scoria occurs at the top of the alkali basalt. The cinder cone's size and shape are uncertain because of limited well coverage, but the thick near-vent cinder deposits place its location near well R-34. A sample of alkali basalt collected from well R-9 yielded an $^{40}\text{Ar}/^{39}\text{Ar}$ age of 2.45 ± 0.10 Ma (Broxton et al. 2001).

Tholeiitic lavas overlie alkali basalts over much of the eastern Pajarito Plateau (see discussion in Section 2.3.2). The source of these tholeiites appears to be three volcanic vents identified as constructional volcanic highlands by structure contours (Figure B-6) and by the presence of thick near-vent deposits. The structure contour maps are based on subsurface data from wells and from extensive outcrops of basalt on the eastern side of the Pajarito Plateau.

The two largest tholeiite volcanos form broad shield-like volcanic edifices that rise to summits located in lower Cañada del Buey north of well R-41 (#4 in Figure 2.5-1) and Reneau volcano in lower Pajarito Canyon (#5 in Figure 2.5-1). The tholeiite volcano near well R-41 appears to be the source of the main tholeiite sequence discussed in Section 2.3.2 and it largely covers the earlier alkali basalt volcano

(#2 in Figure 2.5-1) except for the summit vent area. Near-vent facies are prominent in the tholeiitic volcanic sequence near the R-41 vent and Reneau volcano. Oxidized scoria deposits are 30 to 140 ft thick in wells R-22, R-39, and R-41, and phreatomagmatic deposits are 60 to 215 ft thick at wells R-49 and D-15. Reneau volcano is located about 6000 ft southeast of the R-41 vent. Reneau volcano is largely covered by Bandelier Tuff, but its scoria-rich summit is exposed on the mesa south of Pajarito Canyon near well R-23. A broad topographic saddle separates the Reneau volcano and the R-41 vent, where the flanks of the two volcanos overlap. A sample of tholeiite basalt collected from well R-22 yielded an $^{40}\text{Ar}/^{39}\text{Ar}$ age of 2.50 ± 0.33 Ma (G. WoldeGabriel, unpublished data).

The third tholeiite volcanic vent is a small cinder cone located near well R-45 in Mortandad Canyon (#6 in Figure 2.5-1). The cinder cone is a small circular feature about 2000 ft in diameter that rises about 70 ft above the surrounding basaltic terrain (Figure B-5 and map inset for Figure B-6). This vent appears to be the source of a small-volume upper tholeiite/alkali basalt sequence that overlies the main tholeiite sequence in the vicinity of Mortandad Canyon (see discussion in Section 2.3.2). Well R-45 penetrated 68 ft of oxidized tholeiite scoria at the top of the volcanic sequence, supporting the interpretation of a volcanic vent at this location. Puye Formation deposits overlie Cerros del Rio basalt in other nearby wells, but they are absent above the cinder cone, indicating it was a positive topographic feature during late Puye Formation deposition.

The dacite, alkali basalt, and tholeiite vents described above are aligned along a narrow north-northwest-trending volcanic lineament (Figure 2.5-1), suggesting that vent locations are controlled by a common tectonic structure. Age dates for subsurface dacite, alkali basalt, and tholeiite lavas overlap within analytical error, indicating the volcanos erupted over a short period of time. These eruptions are also temporally correlative to alkali and tholeiitic basalts and evolved lava flows exposed on both sides of White Rock Canyon of the Rio Grande (WoldeGabriel et al. 1996). The alignment of vents suggests that a previously unrecognized fault or fracture system or lineament provided a favorable pathway for magma bodies to rise from their source regions to the surface. Vent alignment along faults is fairly common, and orientation of the alignment is typically a function of the orientation of the tectonic stress field during magma emplacement and the presence of pre-existing crustal structures (e.g., Thompson et al. 2006; Le Corvec et al. 2013; Valentine and Connor 2015). Volcanic vent alignments are usually associated with tensional structures that are perpendicular to the local least principal horizontal stress. Tension results in fault dilation and provides a low-energy path for magmas to rise to the surface.

The hydrologic effect of the north-northwest-trending volcanic lineament on regional groundwater flow east of the chromium plume area is not well understood, but examples of faults acting as hydrologic barriers are common for basin deposits of the Rio Grande Rift (Koning et al. 2007; Caine and Minor 2009; Grauch et al. 2009). Juxtaposed lithologic units of different hydraulic conductivities can reduce hydraulic conductivity across the faults. Additionally, gouge- and clay-filled faults and fractures can act as barriers that change the direction and quantity of groundwater flow in an aquifer and can compartmentalize aquifers. Similarly, dike swarms are common near volcanic vents and they are likely to occupy tectonic structures reflecting the least principal horizontal stress (Valentine and Connor 2015). Dikes are made up of relatively impermeable rocks and can also act as hydraulic barriers where they intrude loosely consolidated sands and gravels that make up the regional aquifer.

The degree to which the north-northwest-trending volcanic features exert an influence on groundwater flow is unclear. In places where faults form a distinct hydrologic boundary, for example the Joyita-Hubbell Faults of the Middle Rio Grande Basin (McAda and Barroll 2002), the water table gradient is steeper downslope of the fault barrier. On the Pajarito Plateau, the mapped features of the volcanic lineament do not closely align with a sharp increase in hydraulic gradient east of the chromium plume, but they are in close proximity (Figure 2.5-1). This may indicate that other related buried tectonic features such as faults or fractures east of the volcanic lineament play a greater role in the hydraulic properties of the regional aquifer.

2.6 Summary and Conclusions

At unsaturated conditions, movement of moisture in the vadose zone is probably dominated by vertical, gravity-driven flow through porous rocks. Moisture is diverted laterally at capillarity barriers associated with bedding contacts. Similarly, confining beds for perched groundwater systems are generally thought to be stratigraphically controlled. The direction of groundwater flow is controlled by the dip of bedding within the major stratigraphic units. Chromium-contaminated surface water infiltrated in Sandia Canyon has translated generally southward through the vadose zone before entering the regional aquifer near Mortandad Canyon. Bedding orientations of the major geologic units are consistent with the interpretation that chromium-contaminated infiltration percolating through the vadose zone is translated to the southeast, south, and southwest as the result of lateral diversion along dipping geologic beds.

A prominent gamma break in the middle of the Otowi Member represents a change in the composition of tuffs across a stratal contact. The abrupt gamma shift is interpreted as a depositional boundary representing a brief hiatus in the Otowi eruption, after which new magma with a slightly less evolved composition was deposited. The structure contour map for the middle Otowi Member indicates that moisture percolation through the tuffs is likely to be diverted along bedding that dips 0.92° toward the southeast.

Tholeiitic lavas overlie alkali basalts over much of the eastern Pajarito Plateau. The tholeiite/alkali basalt contact provides information about the internal structure of the Cerros del Rio basalts, revealing a buried paleo-topographic surface of regional extent that may influence moisture pathways through the middle vadose zone. The structure contour map for tholeiite/alkali basalt contact shows the alkali basalts form a broad, shield-like volcanic edifice that rises to a summit near wells R-13 and SIMR-2. The shield-like structure is interpreted as a constructional volcanic feature whose summit is likely the primary vent area for the alkali basalts. Tholeiites overlying the alkali basalt form a broad shield-like structure that rises to a summit near well R-41 near the east side of TA-54. The shield-like structure is interpreted as a constructional volcanic feature whose summit is likely the primary vent area for the tholeiitic basalts. A narrow, west-draining paleo valley incised into the top of the main tholeiite sequence apparently controlled the distribution of a thin sequence of tholeiite/alkali basalt flows whose distribution is limited to the Mortandad Canyon area. The probable vent for the upper tholeiites is a small cinder cone near well R-45.

A widespread marker bed characterized by low gamma activity was identified within the Puye Formation. The mapped base of the gamma anomaly is interpreted as a stratal contact and indicates that internal bedding in the Puye Formation dips approximately 2.4° towards the south and southeast. Gamma activity is generally greater in the lower Puye Formation, which is dominated by detritus derived from radiogenic low-silica rhyolites of the Rhyodacite of Rendija Canyon. Gamma activity in the upper Puye Formation is highly variable, reflecting the combined input of both Rhyodacite of Rendija Canyon and other, less radiogenic dacite sources. The low-gamma anomaly is interpreted as a dacite-rich sedimentary deposit that is intercalated between deposits dominated by Rhyodacite of Rendija Canyon detritus. The deposits represented by the low-gamma anomaly mark the beginning of significant dacite contributions to the Puye alluvial fans. Present-day dips for the Puye Formation and underlying Miocene pumiceous deposits suggest these rocks are tilted by faulting. Unsaturated moisture flow through the Puye Formation will likely to be diverted to the south and southeast along bedding planes.

Vents that were sources of the Cerros del Rio volcanic rocks beneath the eastern Pajarito Plateau appear to define a north-northwest-trending volcanic lineament east of the chromium plume area. The lineament may represent a previously unrecognized fault or fracture system. The hydrologic effect of the lineament on regional groundwater flow is not well understood, but examples of faults acting as hydrologic barriers are common for basin deposits of the Rio Grande Rift. The volcanic lineament does not closely align with

a sharp increase in hydraulic gradient east of the chromium plume, but it may be related to other buried faults or fractures that play a greater role in the hydraulic properties of the regional aquifer.

New data and interpretations presented in this section augment the sitewide geologic model that is currently used to assess hydrogeological site conditions. The new data provide information about internal bedding features for the three main rock units that make up the vadose zone in the Chromium Investigation Area. These bedding features have the potential to influence groundwater pathways and flow directions. These data are relevant for assessment of groundwater remediation strategies by providing information about groundwater pathways in the site conceptual model and further constraining numerical models examining contaminant transport through the vadose zone.

3.0 LITHOLOGIC CHARACTERIZATION, PARTICLE-SIZE ANALYSIS, HYDRAULIC CONDUCTIVITY ESTIMATES OF SONIC CORES, AND REVISED STRATIGRAPHY

3.1 Introduction

This section presents results of particle-size analysis and chemical and mineralogical data for samples collected from sonic cores obtained from core holes CrCH-1, CrCH-2, CrCH-3, CrCH-4, and CrCH-5 drilled in the Chromium Investigation Area in Mortandad Canyon (Figure 1.0-1). The objective of this study is to (1) characterize the lithology of Pliocene and Miocene sedimentary rocks that represent the primary chromium contaminant flow paths in the upper regional aquifer, (2) define the stratigraphic section, and (3) assess how the hydrogeological properties of these deposits may affect contaminant migration and the selection of remediation alternatives. The cores were collected and processed in accordance with the project objectives highlighted in the “Interim Measures Work Plan for the Evaluation of Chromium Mass Removal” (LANL 2013), which was designed to explore remedial options for chromium contamination in groundwater beneath Mortandad Canyon (LANL 2014). The work plan included collection of cuttings and sonic cores for detailed subsurface geological characterization within the chromium plume (LANL 2013). The core holes are distributed along the axis of the chromium plume beneath Mortandad Canyon (Figure 1.0-1) to delineate rock types along potential groundwater flow paths and to provide a framework for understanding stratification of chromium concentrations in groundwater within the upper part of the regional aquifer. Some core samples were also tested to evaluate natural reduction and/or adsorption capacities for chromium; the results of these laboratory studies are presented in Attachment 6 of this compendium, “Characterization of Natural Attenuation.” Drilling methods and cuttings/core collection procedures used for this investigation are summarized in “Completion Report for Chromium Project Coreholes 1 through 5” (LANL 2015).

The focus of this study is the geologic units that make up the upper regional aquifer in the vicinity of the chromium contaminant plume. These units include (1) the lower part of Pliocene Puye Formation, (2) newly recognized pumice-rich gravels and sands at the base of the Puye Formation called the Puye pumiceous subunit, and (3) pumiceous sands that are informally called the Miocene pumiceous unit. Detailed lithologic characterization and particle-size analysis were performed on selected sonic cores from just above the water table to depths up to 60 ft into the aquifer. Cores representing the individual beds identified by lithologic characterization were sampled and analyzed to determine the particle-size distribution and to discriminate between transmissive and/or impermeable beds. A subset of core samples was also analyzed using XRF and QXRD to characterize the chemistry and mineralogy of the particle-size fractions.

This report also revises geologic contacts in the five core holes based on drill cuttings and/or sonic core for the Puye Formation, Puye pumiceous subunit, Miocene pumiceous unit, and Miocene riverine deposits. In addition, cuttings for eleven other drill holes in the Chromium Investigation Area were examined to assess the stratigraphic contact, distribution, and thickness of the Puye pumiceous subunit

that was newly recognized in this study. Together, these studies help to refine the stratigraphic sequence in the Chromium Investigation Area and support a broader understanding of the sedimentological, volcanic, and tectonic history of the area.

3.2 Methods

During the air rotary drilling of core holes CrCH-1 through CrCH-5, bulk cuttings were collected at 10-ft intervals from the surface to the base of the Cerros del Rio volcanic sequence, and continuous sonic cores were collected in 3- to 5-ft core runs from the top of the lower Puye Formation to the target depth within the Pliocene and Miocene sediments in the upper part of the regional aquifer (LANL 2015). Bulk cuttings from the upper part of the core holes were collected in plastic sample bags. Cores were collected in Lexan tubes or in tubular plastic sleeves depending on the degree of consolidation of the sediments. Samples for initial characterization of cores were collected from both ends and sometimes from the middle of the Lexan tubes or plastic sleeves. These initial samples were used to identify the general lithologic characteristics of the cores and establish stratigraphic contacts, which are presented in the completion report for the core holes (LANL 2015), and to provide samples, including magnetic separations samples, for evaluating natural reduction and/or adsorption capacities for chromium. Results of these initial studies are reported in Attachment 6 of this compendium. This investigation provides a more systematic and detailed sampling of cores to characterize the lithology, contacts, particle-size distributions, chemistry, and mineralogy of geologic units making up the upper regional aquifer and lower vadose zone.

3.2.1 Analytical Methods

During the drilling, cuttings, and cores were regularly delivered to the analytical laboratory and samples were selected, washed, dried, and examined visually and using a binocular microscope. The lithology types and stratigraphic contacts for all selected samples were documented and a stratigraphic section was prepared for each core hole. A subset of the cuttings and cores was selected and processed for chemical and mineralogical analyses. The preliminary lithologic descriptions and the stratigraphic sequences for the core holes were included in the completion report for the core holes (LANL 2015). Some of the geologic contacts reported in the completion report are superseded by new information developed for this investigation (Figure 3.2-1).

3.2.1.1 Lithologic Description and Particle-Size Characterization

Samples selected for detailed lithologic and particle-size characterization were collected from cores representing strata from just above the water table to depths up to 60 ft into the top of the regional aquifer (Appendixes C and D). The number of samples selected from each core was variable and was dictated by the depth of the well, the position of the static water level, and the stratigraphic units intersected (Figure 3.2-1). For example, fewer samples were selected from CrCH-1 compared with other cores because it did not penetrate the base of the Puye Formation.

Cores in Lexan sleeves and plastic sleeves were opened and photographed. Discrete beds within the 3-ft- to 5-ft-long cores were identified, measured for thickness, and carefully described based on color, grain size, clast compositions, clast morphology, sorting, consolidation, and stratification features. Lithologic characteristics were identified using a hand lens and binocular microscope. Each distinct bed was considered a single sample and bagged separately, completely consuming the core. Sample volumes varied according to the thickness of individual beds. Samples were labeled and placed in pans for drying and then sieved. Because of the large volume of the individual samples, subsamples weighing 1.8 to 2.3 kg were selected from each of the samples for particle-size analysis. The subsamples were dry and wet sieved into six particle-size fractions (Table 3.2-1).

Nearly 400 samples were processed for particle-size analysis using the sieve intervals listed in Table 3.2-1. Disaggregated dry samples were transferred to the sieves and mounted on an automatic shaker for 15 min. After sieving, each of the samples was washed and rinsed using PM-4 well water, starting with the coarser fraction (≥ 8 mm) to remove the finer particles attached to the larger rock fragments. The PM-4 water is potable and representative of the regional aquifer and is free of chromium contamination. The remaining fractions were washed with the same solution and rinsed with clean water. At the end of the washing, the solution was combined in a beaker and placed on a counter top for 24-h gravity settling. The residue from the overnight settling represents Fraction 6 (≤ 0.063 mm), and the supernatant, which was transferred to bottles, was left to settle by gravity until the solution became clear. Once the supernatant was clear, it was decanted and the residue, which represents Fraction 7, was transferred to a pan for drying. All particle-size fractions were saved in plastic bags for archiving.

Nearly 70 samples of 3 size fractions (F4—fine to medium sand, F5—very fine to fine sand, and F6—silt) were selected from CrCH-1, CrCH-2, and CrCH-3 for chemical and mineralogical analyses using XRF and x-ray diffraction (XRD) methods, respectively (Appendix E). Though the majority of the sieved samples are dominated by sandy fractions, samples with different particle sizes were selected to evaluate the degree of compositional and mineralogical variations within the sand, silt, and clay fractions. The objective was to identify samples with potential attenuation capacity of chromium.

3.2.1.2 X-ray Fluorescence Spectroscopy

Aliquots of different size fractions from the same sample were pulverized for chemical analysis using the XRF method. Samples were first crushed and homogenized in 5–10-g portions in a tungsten-carbide ball mill. Sample splits were heated at 110°C for 4 h and equilibrated at ambient laboratory conditions for 12 h. To prepare fusion disks, 1.25-g sample splits were mixed with 8.75 g of lithium metaborate-tetraborate flux and heated in a muffle furnace for 30 min at 1015°C. Additional 1-g splits were heated at 1000°C for 60 min, then weighed to determine the loss on ignition (LOI). The total volatile contents (i.e., H₂O, CO₂, F, Cl, S, etc.) in the samples in weight percentage (wt%) were calculated with the LOI method and used in the data reduction program. Elemental concentrations were calculated by comparing x-ray intensities for the samples with those for 17 standards of known composition using “consensus values.” Intensities were reduced using the de Jongh model empirical method to calculate theoretical matrix correction coefficients. Results are presented in Appendix E, Tables E-1, E-3, and E-5.

3.2.1.3 Quantitative X-ray Diffraction

Aliquots of the powdered samples from the chemical analysis were also used for full-pattern QXRD analysis. Specimens were prepared by mixing 1.3 g of bulk powder of each sample with 0.325 g corundum as an internal standard. The mixture was ground and homogenized using acetone in a Brinkmann Grinder (Chipera and Bish 2002). Samples were mounted on glass slides and scanned for 8 or 12 h at a 2 theta range of 2 to 70 deg. X-ray patterns of pure standards and calculated patterns were used to determine the mineralogical compositions of the size fractions. The results are presented in Appendix E, Tables E-2, E-4, and E-6.

3.3 Results

The lithology and particle-size distributions are summarized by core hole in sections 3.3.1 to 3.3.5. Brief descriptions of chemical and mineral data for three particle fractions in selected samples from CrCH-1, CrCH-2, and CrCH-3 are included in sections 3.3.1 to 3.3.3. Appendix C provides detailed lithologic descriptions of the intervals sampled for particle-size characterization in the five core holes. Appendix D presents tables of particle-size data derived from the sieve analysis of core samples. Appendix D includes estimates of the hydraulic conductivity of core samples that were calculated from the particle-size data

using the Kozney-Carman method (Chapuis and Aubertin 2003; Odong 2007; Zhang 2009). Appendix E presents tables and figures for XRF chemical data and XRD mineralogical data of selected samples from CrCH-1, CrCH-2, and CrCH-3.

The stratigraphy and geologic contacts in this report are generally the same as those presented in the completion report for the core holes (LANL 2015). However, as described above, the stratigraphic sequence is revised in this report to include a new subunit designated as the Puye pumiceous subunit [Tpf(p)] after detailed lithologic descriptions of cores showed that rocks formerly assigned to the upper part of the Miocene pumiceous unit instead represent a distinct stratigraphic interval at the base of the Puye Formation. Figure 3.2-1 summarizes the revised stratigraphic columns for the five core holes. Table 3.3-1 presents revised stratigraphic contacts for Miocene and Pliocene rocks of the regional aquifer in the Chromium Investigation Area (Figure 1.0-1).

3.3.1 Chromium Core Hole 1 (CrCH-1)

The CrCH-1 core hole is located on a mesa top on the south side of Mortandad Canyon (Figure 1.0-1). CrCH-1 cores were selected for characterization from the depth interval of 1111.5 to 1136.5 ft. All samples were collected from the Puye Formation because deeper units were not penetrated by the core hole. The static water level was intersected at a depth of 1113 ft. Detailed lithologic descriptions for CrCH-1 cores are presented in Appendix C, section C-1.0. Particle-size data and estimates of Kozney-Carman hydraulic conductivity for CrCH-1 are presented in Appendix D, Table D-1. Information about the particle-size distributions and rock types encountered in CrCH-1 are summarized in Figures 3.3-1 and 3.3-2, respectively.

For detailed lithologic descriptions and particle-size analysis, the 13 strata representing the Puye Formation were obtained from a 25-ft thick section made up of massive, poorly sorted, poorly consolidated, and matrix-supported gravels that contain abundant dacite granules and pebbles embedded in a tuffaceous sandy matrix (Appendix C, section C-1.0, Figure 3.3-2). The gravel and sand in these strata include abundant clasts of Rendija Canyon Rhyodacite, a major component of the dacitic detritus that makes up the Puye Formation. Rendija Canyon Rhyodacite clasts were readily identified by hand lens and microscope using their unique petrographic features, including phenocrysts of quartz + plagioclase + sanidine + anorthoclase + biotite ± clinopyroxene ± hornblende and the presence of common to abundant felty microlites of orthopyroxene in the lava groundmass (Figure 3.3-3). Individual strata identified within the selected cores vary in thickness from about 0.3 ft to 3 ft and represent variable amounts of gravel (26–75%), sand (26–75%), silt (2–29%), and trace amounts of clay (<1.0%) (Figure 3.3-1). Based on the particle-size data, strata making up the Puye Formation are classified as muddy sandy gravel and gravelly muddy sand according to the grain-size classification of Folk (1980) (Figure 3.3-2). Zones of high estimated hydraulic conductivity are associated with sandy gravels with low silt contents (Figures 3.3-1 and 3.3-2).

XRF and XRD analyses were performed on the fine to medium sand (F4), very fine to fine sand (F5), and silt (F6) size fractions for three samples representing the upper, middle, and lower strata of the core interval straddling the water table in CrCH-1 (Appendix E, Figure E-1 and Tables E-1 and E-2). Results from XRF analysis on the three size fractions show the Puye Formation is mostly characterized by silica contents typical of dacitic compositions (Appendix E, Table E-1 and Figure E-1). However, the silt fraction (F6) from the uppermost sample collected above the static water level has a high silica content that is rhyolitic in composition (Appendix E, Figure E-1). Moreover, the silt fractions (F6) from the three samples are characterized by elevated LOI and low SiO₂, Fe₂O₃, and chromium. The mineralogical compositions of the three samples are generally similar, having higher contents of plagioclase, alkali feldspar, quartz, clays, opal CT, cristobalite, and other minor minerals such as clinoptilolite, hematite, and hornblende (Appendix E, Table E-2). However, differences are noted among the size fractions for each sample. For

example, the silty fraction from each of the three samples generally contains lower felsic mineral contents such as plagioclase, quartz, potassium feldspar, or cristobalite and higher secondary mineral fractions such as mica/illite, smectite, clinoptilolite, and opal-CT. The sample at 1128.7–1129.2 ft depth was selected for mineralogical analysis based on the expectation it might be enriched in secondary minerals because of its high silt content (24 wt%). However, XRD data for the sample show low mica/illite contents and no smectite or clinoptilolite compared with the other two samples with relatively low silt contents (Appendix E, Table E-2). The amorphous material (glass) in the CrCH-1 samples is significantly lower (1.8–15.7 wt%) compared with the felsic mineral contents (49–73 wt%). Most of the glass occurs within the fine to very fine sand, whereas the silt fraction contains the least amount (Appendix E, Table E-2).

3.3.2 Chromium Core Hole 2 (CrCH-2)

CrCH-2 was drilled on the canyon floor within the center of the plume northeast of CrCH-1 (Figure 1.0-1). CrCH-2 samples selected for particle-size analysis were collected from the depth interval of 908 to 987 ft. The static water level was intersected at a depth of 903.3 ft within the lowermost part of the Puye Formation. Detailed lithologic descriptions for CrCH-2 cores are presented in Appendix C, section C-2.0. Particle-size data and estimates of Kozney-Carman hydraulic conductivity for CrCH-2 are presented in Appendix D, Table D-2. Information about the particle-size distributions and rock types encountered in CrCH-2 are summarized in Figures 3.3-4 and 3.3-5, respectively. A total of 109 distinct strata were differentiated in the 79-ft core interval selected for particle-size analysis from the Puye Formation, Puye pumiceous subunit, and the Miocene pumiceous unit in CrCH-2 (Figure 3.3-5).

Twenty distinct strata, ranging in thickness from 0.1 ft to 1.6 ft, were identified within a 17-ft section in the lower part of the Puye Formation (Appendix C, section C-2.0, Figure 3.3-5). Puye Formation strata are generally massive, poorly consolidated, and matrix-supported gravels and sands that contain abundant dacite fragments embedded in a tuffaceous matrix (Appendix C, section C-2.0). Rendija Canyon clasts are common in the gravel and sand fractions. Strata are generally light to dark brown with variable shades of gray, red, yellow, and orange. Rocks of the Puye Formation are classified as muddy sandy gravels and subordinate gravelly muddy sand following the particle-size classification of Folk (1980) (Figure 3.3-5). Most strata making up the Puye Formation are very poorly sorted based on the standard deviation of Phi using the method of moments described by Folk (1980) (Figure 3.3-6). Estimates of hydraulic conductivity are greatest in subordinate beds of silt-poor sandy gravels that are narrowly confined to the middle part of the sampled interval.

Nineteen strata were identified within a 14.6-ft section of the Puye pumiceous subunit in CrCH-2 (Appendix C, section C-2.0, Figure 3.3-5). Strata of the Puye pumiceous subunit are generally massive and poorly consolidated sands and matrix-supported gravels that contain variable amounts of rounded white pumice mixed with dacitic lava fragments and embedded in a tuffaceous silty sand matrix. Beds range in color from whitish to dark gray, to reddish orange, to light orangish brown. A key feature of the Puye pumiceous subunit is that it is a hybrid unit that includes characteristics found in underlying and overlying units. For example, approximately 43% of the stratal thickness of the interval is made up of pumice-rich beds that contain rhyolitic lithologies and rock components that are indistinguishable from the underlying Miocene pumiceous unit. XRF data show that pumices from the Puye pumiceous subunit have the same compositions as pumices in the Miocene pumiceous unit (Figure 3.3-7). These pumice-rich strata are intercalated with mixed pumice-lithic beds or lithic-rich beds that include dacite gravels and sands typically found in the overlying Puye Formation.

XRF data show that dacite clasts from the Puye pumiceous subunit have the same compositions as the Rendija Canyon Rhyodacite that is found in the Puye Formation (Figure 3.3-8). As shown in Figures 3.3-4 and 3.3-5, most of the strata in this unit contain significant amounts of silt (13–20 wt%) except for some of the strata from the middle part of the section that are low in silt content (0–13 wt%). The low-silt strata are

dominated by a mixture of gravel (10–64 wt%) and sand (30–76 wt%) and exhibit the highest estimated hydraulic conductivity (Figure 3.3-4, Appendix D, Table D-2).

About 70 strata were identified within a 47-ft section in the upper part of the Miocene pumiceous unit selected for detailed lithologic characterization (Appendix C, section C-2.0, Figure 3.3-5). The Miocene pumiceous unit is dominated by sand with subordinate silt and gravel (Figure 3.3-4). With few exceptions, these pumice-rich sedimentary strata are mostly massive, poorly consolidated, and matrix supported. Subordinate components of the pumiceous sand and gravels include rhyolite lava, obsidian, and felsic crystals. The strata are mostly classified as poorly sorted gravelly muddy sand following Folk (1980) classification (Figures 3.3-5 and 3.3-6). The sediments exhibit a range of colors, including light to dark gray-brown, light orangish to reddish brown, and medium brownish gray (Appendix D, Table D-2). Despite having abundant fine to coarse sand fractions, strata with higher gravel and lower silt contents were noted throughout the section, representing zones of high estimated hydraulic conductivity (Figures 3.3-4 and 3.3-5). A primary ash fall deposit occurs at a depth of 977 to 977.1 ft, whereas a pumice fall deposit occurs at a depth of 985 to 986.6 ft. As discussed in section 4, the primary fall deposits are important for establishing the age of the Miocene pumiceous unit.

XRF and XRD analyses were performed on three size fractions (F4, F5, and F6) for 11 samples representing the Puye Formation, Puye pumiceous subunit, and the Miocene pumiceous unit (Appendix E, Figure E-2 and Tables E-3 and E-4). Concentrations of SiO₂, Fe₂O₃, and chromium, as well as LOI, were plotted against depth to assess the compositional variations within each of the major stratigraphic units (Appendix E, Figure E-2). Generally, the chemical analyses of the Puye Formation and Puye pumiceous subunit reflect their derivation from dacitic source rocks. Compared with the rhyolitic Miocene pumiceous unit, these units are characterized by lower SiO₂ and LOI and higher Fe₂O₃ and chromium, except for one of the samples from the basal part of the Puye pumiceous subunit that contains abundant rhyolite pumice. One sample from the middle part of the Puye pumiceous subunit contains notably high Fe₂O₃ and chromium values.

Mineralogical differences are noted between the different units of CrCH-2 and within the sand and silt size fractions of the individual samples. All samples contain amorphous materials, representing volcanic glass, but contents in the single sample from the Puye Formation (11–23 wt%) are much lower than the Miocene pumiceous unit (45–85 wt%) (Appendix E, Table E-4). The Puye Formation sample contains more plagioclase than quartz and K-feldspar, consistent with its dacitic composition. Three samples from the Puye pumiceous subunit also show variable mineralogical compositions. Two of the upper samples have mineral assemblages that are similar to the Puye Formation, whereas the lower sample contains lower amounts of plagioclase, K-feldspar, and quartz but high amounts of glass because of the abundant pumice. The Miocene pumiceous unit is dominated by volcanic glass and significant amounts of felsic minerals like quartz, plagioclase, and K-feldspar. Secondary minerals like smectite and clinoptilolite are also more abundant in the silt fractions of the Miocene pumiceous unit. In all units, the amounts of glass, plagioclase, K-feldspar, quartz, and cristobalite decrease with size fraction from coarse sand to silt, whereas mica/illite, clinoptilolite and opal-CT are enriched in the silt fraction.

3.3.3 Chromium Core Hole 3 (CrCH-3)

The CrCH-3 well was drilled on the canyon floor within the center of the chromium plume and is located upstream from CrCH-2 and directly north of CrCH-1 (Figure 1.0-1). CrCH-3 samples selected for particle-size analysis were collected from 876 to 991 ft. The static water level was intersected at a depth of 929 ft within the upper part of the Miocene pumiceous unit. Detailed lithologic descriptions for CrCH-3 cores are presented in Appendix C, section C-3.0. Particle-size data and estimates of Kozney-Carman hydraulic conductivity for CrCH-3 are presented in Appendix D, Table D-3. Information about the particle-size distributions and rock types encountered in CrCH-1 are summarized in Figures 3.3-9 and 3.3-10,

respectively. A total of 145 distinct strata were differentiated in the 115-ft of core selected from the Puye Formation, Puye pumiceous subunit, and the Miocene pumiceous unit. Strata range in thickness from 0.1 ft to 4 ft. Lithological descriptions were also made for Miocene riverine deposits from 1019 to 1023 ft (Appendix C, section C-3.0), but these samples were not processed for particle-size analysis.

The 37 strata from the Puye Formation were obtained from a 27.7-ft section made up of massive, poorly consolidated, and matrix-supported gravels and sands that contain abundant dacite fragments embedded in a tuffaceous matrix (Appendix C, section C-3.0). Rendija Canyon clasts are common in the gravel and sand fractions. These strata contain variable amounts of silt (6–52 wt%), sand (24–64 wt%), and gravel (9–60 wt%) (Appendix C, section C-3.0, Figure 3.3-9) and exhibit a range of colors dominated by light to medium brown, light to dark gray, and pinkish gray to reddish brown. The sand content within the Puye Formation is fairly uniform with depth, and the silt content is higher in the upper and lower parts of the sequence (Figure 3.3-9). Gravel contents vary randomly (Figure 3.3-9). Zones with abundant gravel contents are characterized by higher estimated hydraulic conductivity (Figures 3.3-9 and 3.3-10).

The 16 strata from the Puye pumiceous subunit were obtained from a 13-ft section made up of massive, unconsolidated sands and gravels that contain variable amounts of dacite and pumice fragments in a tuffaceous matrix. Pumice-rich beds with few dacite lithic components make up approximately 35% of the stratal thickness of the Puye pumiceous subunit; the remainder of the subunit is made up of mixed pumice-lithic beds or lithic-rich beds. The rhyolitic clasts that make up the pumice-rich strata, including subordinate rhyolite lava and obsidian, are the same as those found in the underlying Miocene pumiceous unit. The dacite lithic components of the mixed pumice-lithic beds and lithic-rich beds are the same as the gravels and sands that make up the overlying Puye Formation, including common Rendija Canyon Rhyodacite clasts. Thin silt-poor sand and gravel beds in the upper part of the pumiceous Puye Formation have high estimated hydraulic conductivities (Figures 3.3-9 and 3.3-10).

The 92 strata from the Miocene pumiceous unit were collected from a 74-ft section containing massive, variably consolidated, poorly sorted, fine to coarse-grained pumiceous sand (Appendixes C, section C-3.0, and D, Table D-3; Figure 3.3-10). In addition to pumice, these strata contain subordinate amounts of rhyolite lava, obsidian, and felsic crystals. Primary pumice fall deposits occur at depths of 965.3 to 966.5 ft and 982.3 to 982.6 ft. Results from the particle-size analysis indicate the strata contain abundant sand (41–82 wt%) and variable amounts of silt (8–48 wt%) and gravel (1–38 wt%) (Figure 3.3-9). Strata with elevated coarse sand and gravel contents yielded the highest estimates of hydraulic conductivity (Figures 3.3-9 and 3.3-10).

XRF and XRD analyses were performed on three size fractions (F4, F5, and F6) for 10 samples, representing the Puye Formation, Puye pumiceous subunit, and Miocene pumiceous unit (Appendix E, Figure E-3 and Tables E-5 and E-6). Concentrations of SiO₂, Fe₂O₃, and chromium, as well as LOI, were plotted against depth to assess the compositional variations within each of the major stratigraphic units (Appendix E, Figure E-3). Generally, the chemistry of the Puye Formation reflects its derivation from dacitic source rocks. This is reflected in lower SiO₂ and LOI and higher Fe₂O₃ and chromium compared with the rhyolitic Miocene pumiceous unit. The three samples selected from the Puye pumiceous subunit contained abundant rhyolite pumice, and their compositions overlap those in the Miocene pumiceous unit. In all units, Fe₂O₃ and chromium concentrations are greatest in the silt (F6) fraction, except for one sample from the base of the Miocene pumiceous unit. The high LOI values in the Puye pumiceous subunit and Miocene pumiceous unit reflect the high abundance of hydrated volcanic glass in these rocks; low LOI is associated with the Puye Formation, which has lower amounts of volcanic glass.

Mineralogical differences are noted between the different units of CrCH-3 and within the sand and silt size fractions of the individual samples (Appendix E, Table E-6). The Puye Formation contains less glass (11–21 wt%) than underlying stratigraphic units (50–75 wt%). Consequently, contents of other mineral components, such as plagioclase, K-feldspar, and quartz; cristobalite and mica/illite (biotite); and

secondary minerals like smectite and clinoptilolite, are significantly greater in the Puye Formation. Plagioclase, K-feldspar, and cristobalite tend to be more highly concentrated in the fine to medium sand fraction (F4) and secondary minerals such as smectite tend to be concentrated in the very fine to fine sand (F5) and silt (F6) fractions.

Three samples from the Puye pumiceous subunit have mineralogical characteristics that are generally similar to the Miocene pumiceous unit, reflecting the pumice-rich nature of the samples selected for analysis. Both the Puye pumiceous subunit and the Miocene pumiceous unit contain abundant volcanic glass and opal-CT; secondary minerals are sparse. In the Miocene pumiceous unit, the fine to medium sand (F4) generally contains more glass than the very fine to fine sand (F5) and silt (F6) fractions. Smectite is concentrated in the silt fraction (F6).

3.3.4 Chromium Core Hole 4 (CrCH-4)

CrCH-4 is located on the canyon floor west and upstream of the CrCH-3 core hole (Figure 1.0-1). CrCH-4 cores selected for particle-size analysis were collected from 876 to 991 ft. The static water level was intersected at 947 ft within Puye pumiceous subunit. Detailed lithologic descriptions for CrCH-4 cores are presented in Appendix C, section C-4.0. Particle-size data and estimates of Kozney-Carman hydraulic conductivity for CrCH-4 are presented in Appendix D, Table D-4. Information about the particle-size distributions and rock types encountered in CrCH-4 are summarized in Figures 3.3-11 and 3.3-12, respectively. A total of 26 distinct strata were differentiated in the 23-ft section selected for particle-size analysis from the Puye Formation, Puye pumiceous subunit, and the Miocene pumiceous unit in CrCH-4.

The nine strata from the Puye Formation were obtained from an 8.5-ft section that consists of massive, poorly sorted, poorly to moderately consolidated, and matrix-supported gravels that contain abundant dacite fragments embedded in a tuffaceous sandy matrix (Appendix C, section C-4.0). Rendija Canyon clasts are common in the gravel and sand fractions. The Puye gravels contain abundant dacite granules and pebbles (up to 4 in. in diameter) (15–51 wt%) embedded in a tuffaceous sandy (34–48 wt%) and silty (7–45 wt%) matrix of rock fragments and minerals (Figures 3.3-11 and 3.3-12). In general, the estimated hydraulic conductivity is greatest in sandy gravels that have a low-silt content (Appendix D, Table D-4, Figures 3.3-11 and 3.3-12). The strata are 0.2- to 2-ft thick and range in color from light orangish brown to various shades of gray. Some strata show localized bedded and finely laminated structures. Scattered carbonaceous fragments identified as charcoal were noted in one of the beds.

The 10 strata from the Puye pumiceous subunit were obtained from a 10.6-ft section of massive, moderately consolidated sands and subordinate gravels that contain variable mixtures of pumice and dacite fragments (Appendix C, section C-4.0, Figure 3.3-12). These strata contain variable amounts of sand (55–84 wt%), gravel (10–30 wt%), and silt (8–33 wt%) (Appendix C, section C-4.0, Figure 3.3-11). Highly pumiceous sands with minor or no dacite lithic components make up approximately 55% of the stratal thickness of the Puye pumiceous subunit; the remainder of the subunit is made up of mixed pumice-lithic beds or lithic-rich beds. The rhyolitic clasts that make up the pumice-rich strata, including subordinate rhyolite lava and obsidian, are the same as those found in the underlying Miocene pumiceous unit. The dacite lithic components of the mixed pumice-lithic beds and lithic-rich beds are the same as the gravels and sands that make up the overlying Puye Formation, including common Rendija Canyon Rhyolite clasts. Strata range in thickness from 0.25 to 1.9 ft. Results from particle-size analysis indicate that the sand-dominated units are associated with the highest estimated hydraulic conductivity values.

Seven samples from a 3.9-ft section were collected in the uppermost part of the Miocene pumiceous unit. These rhyolitic strata consist of light to medium gray, massive, poorly consolidated, medium- to coarse-grain, pumiceous sands (Appendix C, section C-4.0, Figure 3.3-12). The sand fraction (57–74 wt%)

dominates these strata, followed by silt (12–34 wt%) and gravel (8–18 wt%) (Figure 3.3-11). The gravel fraction is made up of pebbles of pumice, rhyolite lava, and obsidian fragments up to 0.5 in. in size. A pumice fall deposit occurs at 953.4 to 954.25 ft. The uppermost strata in the unit have the lowest silt content and the highest estimated hydraulic conductivity (Figure 3.3-11), but the thickness is only 0.3 ft.

3.3.5 Chromium Core Hole 5 (CrCH-5)

CrCH-5 is located on the canyon floor close to the western edge of the Chromium Investigation Area upstream and southwest of the CrCH-4 well (Figure 1.0-1). CrCH-5 samples selected for particle-size analysis were collected from 960 to 1016 ft. The static water level was intersected at 965 ft in the Puye Formation. Detailed lithologic descriptions for CrCH-5 cores are presented in Appendix C, section C-5.0. Particle-size data and estimates of Kozney-Carman hydraulic conductivity for CrCH-4 are presented in Appendix D, Table D-5. Information about the particle-size distributions and rock types encountered in CrCH-5 are summarized in Figures 3.3-13 and 3.3-14, respectively. A total of 53 distinct strata were differentiated in the 56-ft section selected for particle-size analysis from the Puye Formation and Puye pumiceous subunit. Individual beds in the characterized interval were 0.2 to 2.6 ft thick.

The 15 strata from the Puye Formation were obtained from a 17.5-ft section of massive, very poorly sorted, poorly consolidated, and matrix-supported gravels that contain abundant dacite granules and pebbles embedded in a tuffaceous sandy matrix (Appendix C, section C-5.0, Figure 3.3-14). Lithic sands are a subordinate component of the characterized section. These strata contain variable amounts of gravel (18–60 wt%), sand (32–51 wt%), and silt (7–31 wt%) (Appendix C, section C-5.0, Figure 3.3-13). Rendija Canyon clasts are common in the gravel and sand fractions. The color of strata included light grayish to dark brown, light reddish to orangish brown, and light olive. In general, silt contents decrease with depth and the amount of gravel significantly increases. Two zones of high estimated hydraulic conductivity are associated with low-silt and high-gravel strata in the Puye Formation (Figures 3.3-13 and 3.3-14).

The 38 strata from the Puye pumiceous subunit were obtained from a 38.5-ft section, which consists of massive, poorly to moderately consolidated sands and subordinate gravels that contain varying mixtures of pumice and dacite fragments (Appendix C, section C-5.0, Figure 3.3-14). These strata represent variable amounts of sand (20–78 wt%), gravel (4–73 wt%), and silt (5–26 wt%) fractions (Appendix C, section C-5.0, Figure 3.3-13). Highly pumiceous sands made up mostly of pumice fragments and felsic crystals compose about half of the stratal thickness of the Puye pumiceous subunit; the remainder of the subunit is made up of mixed pumice-lithic beds or lithic-rich beds. Sands dominate the upper and lower parts of the characterized interval, and gravels are abundant in the middle (Figure 3.3-14). Within the gravel-rich interval, there is a 3-ft zone that contains abundant gravel (71–73 wt%) and significantly reduced amounts of sand (20–22 wt%) and silt (5–10 wt%); this zone is characterized by high estimated hydraulic conductivity. Strata colors are variable and include white to whitish gray, light to medium gray, light to dark brown, and light to medium reddish brown sediments (Appendix C, section C-5.0). A sandy gravel bed that contains subangular to subrounded clasts of Rendija Canyon Rhyodacite up to 1 in. in diameter occurs at the base of the section.

3.4 Discussion

Detailed lithologic characterizations of sonic cores from CrCH-1 through CrCH-5 coupled with data from particle-size analyses of the same lithologic units have resulted in the refinement of the stratigraphic sequence of the sedimentary units within the lowermost vadose zone and the upper part of the regional aquifer in the Chromium Investigation Area. The lithologic data and particle-size distributions show that aquifer rock units are characterized by localized, highly transmissive hydrogeological pathways that consist of abundant gravel and sandy fractions with low contents of silt. Strata of enhanced hydraulic

conductivity make up a relatively small portion of the aquifer and are intercalated with thicker sections of rocks that are generally less transmissive.

The following sections discuss revisions to the stratigraphy, distribution of rock units relative to the water table, particle-size and lithologic characteristics of rocks in the upper regional aquifer, hydrological implications of the particle-size and lithologic data, and provenance and sedimentology of the Miocene and Pliocene deposits.

3.4.1 Revised Stratigraphy for Rocks of the Upper Regional Aquifer

Figure 3.2-1 is a revised stratigraphic column for the five core holes examined in this investigation and supersedes the geologic contacts in the core hole completion report (LANL 2015). In earlier Laboratory well completion reports including for the chromium core holes, the contact between the Puye Formation and the Miocene pumiceous unit was placed at the abrupt change downhole from dacitic lithic gravels to highly pumiceous sand and gravel. In these previous investigations, the stratigraphic assignments were based on drill cuttings collected at 5-ft intervals. Based on thicknesses of strata determined in this investigation, it is now recognized that drill cuttings collected at 5-ft intervals represent homogenized samples of multiple strata, obscuring some of the details of the stratigraphic sequence.

Collection of continuous core across the Puye Formation and Miocene pumiceous unit provided an unprecedented opportunity to characterize the Pliocene and Miocene rocks that make up the upper regional aquifer. A major finding of this investigation is that some rocks previously assigned to the upper part of the Miocene pumiceous unit form a distinct depositional sequence at the base of the Puye Formation. This sequence, herein called the Puye pumiceous subunit, has lithological, mineralogical, and chemical characteristics transitional between the Puye Formation and the Miocene pumiceous unit. The Puye pumiceous subunit contains pumice-rich beds, including rhyolitic lithologies and rock components that are indistinguishable from the underlying Miocene pumiceous unit. These pumice-rich strata are intercalated with mixed pumice-lithic beds or lithic-rich beds that include dacite gravels and sands that are typically found in the overlying Puye Formation. Dacitic detritus in the Puye pumiceous subunit includes clasts of Rendija Canyon Rhyodacite, a major component of the Puye Formation that is readily identified by its petrographic characteristics (see section 3.3.2). The Rendija Canyon Rhyodacite was erupted approximately 5 million years ago (WoldeGabriel et al. 2007; Broxton et al. 2007), and its presence indicates the Puye pumiceous subunit is Pliocene in age. The hybrid nature of the Puye pumiceous subunit suggests it represents an early stage of Puye deposition when upslope areas contributing to alluvial fans included areas underlain by both the Miocene pumiceous unit and the Rendija Canyon Rhyodacite. The provenance of the Puye pumiceous subunit is discussed further in section 3.4.5. The contact between the Puye formation and Puye pumiceous subunit is defined as the first appearance of highly pumiceous sand and gravel in the core.

The contact between the Puye pumiceous subunit and the Miocene pumiceous unit is defined as the last occurrence of Rendija Canyon Rhyodacite clasts in the core. The Miocene pumiceous unit is a fluvial deposit made up of reworked pumices and ash derived from the Bearhead Rhyolite. The Bearhead Rhyolite was primarily erupted during an episode of rhyolitic volcanism between 6.5 and 7.1 million years ago (McIntosh and Quade 1995; Justet and Spell 2001) Because of their reworked nature, fluvial deposits containing Bearhead Rhyolite pumices could be either Miocene or Pliocene in age. The identification of primary ash- and pumice-fall deposits in the CrCH-2 (section 3.3.2), CrCH-3 (section 3.3.3), and CrCH-4 (section 3.3.4) deposits was important for establishing the Miocene age of these deposits.

The Puye pumiceous subunit appears to be a widespread unit that is present over most of the Chromium Investigation Area. To extend the results from the core studies, cuttings from 11 other wells in the Chromium Investigation Area were reexamined to assess the distribution and thickness of the newly

recognized Puye pumiceous subunit (Table 3.3-1). Chip trays of washed cuttings (core in the case of SCI-2) were examined using a binocular microscope to identify the downhole transitions from dacitic lithic gravels (Puye Formation) to highly pumiceous sand and gravels that contain a significant Rendija Canyon component (Puye pumiceous subunit) and highly pumiceous sand and gravels that have a negligible Rendija Canyon component (Miocene pumiceous unit). As noted above, well cuttings are imperfect samples because they represent homogenized samples of multiple strata, and many details of the stratigraphic sequence are obscured. Drilling methods also affected the reliability of well cuttings. For example, well cuttings collected from open boreholes advanced without the use of drill casing are susceptible to contamination by sloughing of overlying poorly consolidated units. Use of drill casing to advance the borehole minimizes sloughing of unstable borehole walls, but minor contamination of cuttings by overlying units is possible in cases where the casing underreamer cuts a borehole larger than the diameter of the drill casing. Well CrEX-2 was optimized to minimize the annulus between the underreamed borehole and drill casing, but the other wells were overreamed to facilitate the advancement of drill casing. Finally, the air-water circulation of well cuttings from depths of up 1000 ft may result in incomplete evacuation of earlier drilled cuttings, resulting in minor contamination. With these limitations in mind, the contacts for the Puye Formation, Puye pumiceous subunit, and Miocene pumice unit were identified in the 11 boreholes (Table 3.3-1). Where possible, geophysical logs were used as supporting data to evaluate the selected contacts. In a few boreholes, the contact between the Miocene pumiceous unit and Miocene riverine deposits was also documented.

The Puye pumiceous subunit appears to be present in all wells except R-43/SCI-2 and R-62. An isopach map showing the thickness of the Puye pumiceous subunit was prepared from the data presented in Table 3.3-1 (Figure 3.4-1). The Puye pumiceous subunit appears to thicken southward across the Chromium Investigation Area, averaging 10–40 ft thick along the axis of Mortandad Canyon and reaching a maximum thickness >95 ft thick near well CrEX-2. The thickness of the unit south of CrEX-2 has not been examined.

3.4.2 Distribution of Rock Units Relative to the Regional Water Table

Chromium contamination is confined to the upper 50 ft of the regional aquifer throughout the plume area beneath Mortandad Canyon. Based on new stratigraphic data presented in this report, two geologic cross-sections were prepared for the upper part of the regional aquifer along the axis of the chromium contaminant plume in Mortandad Canyon (Figure 3.4-2). These cross-sections roughly parallel the easterly and southeasterly flow directions in the regional aquifer. The combination of south- to southeast-dipping rock units and a nearly flat water table results in the water table crossing into stratigraphically higher units to the east and south. In the northern cross-section, the water table is mostly within the Miocene pumiceous unit between R-42 and CrCH-4, but it occurs in progressively younger Puye Formation strata eastward from R-28 to R-45. In the southern cross-section, the water table is entirely in Pliocene rocks and crosses progressively younger strata to the southeast. These cross-sections show that plume migration is largely blind to aquifer stratigraphy, moving laterally from Miocene rocks in upgradient areas of the chromium plume to Pliocene rocks in the downgradient areas. Nonetheless, local stratigraphic effects are important for groundwater flow at the scale of individual well screens and affect approaches to characterization and remediation of the contaminant plume (see section 3.4.4).

3.4.3 Summary of Particle-Size and Lithologic Characteristics of Rocks of the Upper Regional Aquifer

Particle-size distribution data highlight the broad lithological differences between the stratigraphic units making up the regional aquifer (Figure 3.4-3). The Puye Formation contains much more gravel (mean 39.5 wt%) than the Puye pumiceous subunit (mean 22.4 wt%) and Miocene pumiceous unit (mean 14.1 wt%). The Puye pumiceous subunit and Miocene pumiceous unit contain more sand (mean 62.1 wt%

and 66.1 wt%, respectively) than the Puye Formation (41.1 wt%). On average, the Puye Formation and Miocene pumiceous unit contain ~28% more silt (mean 19.3 wt% and 19.8 wt%, respectively) than the Puye pumiceous subunit (mean 15.5 wt%). Mean Kozeny-Carmen estimates of hydraulic conductivity are strongly skewed by relatively few high conductivity measurements, and median values better represent the population distributions for the three rock units. Estimated hydraulic conductivity in the Puye pumiceous subunit (median 0.97 ft/d) is greater than in the Puye Formation and Miocene pumiceous unit (both with a median 0.55 ft/d).

CrCH-2 particle-size data were used to calculate the mean grain size (as $\bar{\phi}$ arithmetic mean) and to evaluate sorting (as standard deviation of $\bar{\phi}$ using the method of moments) for each of the strata in the Puye Formation, Puye pumiceous subunit, and Miocene pumiceous unit. The particle-size data were converted to $\bar{\phi}$ units and the arithmetic mean and standard deviation of $\bar{\phi}$ were calculated following the methodology of Folk (1980) (Figure 3.3-6). The mean grain sizes for individual CrCH-2 strata reflect the population statistics described above; the mean grain size of the Puye Formation is mostly coarse and very coarse sand, the Miocene pumiceous unit is mostly fine to medium sand, and the Puye pumiceous unit overlaps the two other units. The Puye Formation strata are very poorly sorted, the Miocene pumiceous unit is mostly poorly sorted, and the Puye pumiceous unit contains subequal amounts of poorly sorted and very poorly sorted strata.

The average thickness of strata making up the Puye Formation, Puye pumiceous subunit, and Miocene pumiceous unit tends to decrease downsection (Figure 3.4-4). Puye Formation strata are generally thicker (mean 0.97 ft) than strata of the Puye pumiceous subunit (mean 0.88 ft) and Miocene pumiceous unit (mean 0.74 ft). The tendency towards thicker strata in the Puye Formation and thinner strata in the Miocene pumiceous unit is consistent with observations from borehole video and FMI logs.

The particle-size distribution data were used to classify the rock types making up aquifer units using the nomenclature of Folk (1980) (Figure 3.4-5). The Puye Formation is made up primarily of muddy sandy gravel and subordinate beds of gravelly muddy sand. The Miocene pumiceous unit is classified as gravelly muddy sands with subordinate muddy sand and muddy sandy gravel. Strata in the Puye pumiceous subunit overlap the principal rock types found in the Puye Formation and Miocene pumiceous unit (mostly muddy sandy gravel and gravelly muddy sand), reflecting the hybrid lithologies making up this unit.

The mineralogy of rocks in the regional aquifer varies by stratigraphic unit and particle size. Figure 3.4-6 summarizes selected mineralogical data for size fractions F4 (fine to medium sand), F5 (very fine to fine sand), and F6 (silt) that may affect rock-water interactions relevant to ongoing studies of chromium attenuation by aquifer media. The Puye Formation is made up of lithic gravel and sand, and its mineralogy is dominated by quartzo-feldspathic minerals. The abundance of quartzo-feldspathic minerals tends to decrease in the finer size fractions, whereas abundances of smectite-clinoptilolite and iron-bearing minerals become progressively enriched as the particle size decreases (Figure 3.4-6). Volcanic glass is commonly present in the tuffaceous matrix of the Puye Formation samples, but it is less significant when compared with the pumiceous Puye sediments and the Miocene pumiceous deposits. The Miocene pumiceous unit is primarily made up of pumiceous sand and gravel, and its mineralogy is dominated by volcanic glass and subordinate quartzo-feldspathic minerals. The abundance of glass and quartzo-feldspathic minerals is somewhat less in the F5 and F6 size fractions and, like in the Puye Formation, abundances of smectite-clinoptilolite and iron-bearing minerals are progressively enriched in the finer-grained size fractions (Figure 3.4-6). The mineralogy of the Puye pumiceous subunit overlaps the mineralogy of the Puye Formation and Miocene pumiceous unit, reflecting the hybrid characteristics of this unit. Though not shown in Figure 3.4-6, illite, mica, and opal-CT are typically enriched in the silt fraction for all units (Appendix E, Tables E-2, E-4, and E-6).

3.4.4 Hydrological Implications of Lithologic and Particle-Size Data

Particle-size distributions for continuous core samples collected in CrCH-1, CrCH-2, CrCH-3, CrCH-4, and CrCH-5 provide a unique opportunity to characterize the hydraulic structure of the regional aquifer. Grain size is one factor that influences hydraulic conductivity. The packing of particles in coarse-grain sediments, including gravels and coarse sands, results in large, well-connected intergranular pores that allow for the easy transmission of water. Fine-grain deposits, such as fine sands and silts, have smaller pores that transmit water less readily. The Kozeny-Carman equation is a useful way to estimate hydraulic conductivity using grain-size distribution of sands (Chapuis and Aubertin 2003; Odong 2007; Zhang et al. 2009). The grain size at the 90th percentile of the particle-size distribution, or the grain size at the smallest 10% of the sample, is used to calculate the hydraulic conductivity using the Kozeny-Carman equation.

$$K_m = \left(\frac{\rho g}{\mu}\right) \left[\frac{d_m^2 \phi_m^3}{180(1-\phi)^2}\right] \quad \text{Equation 1}$$

where K_m = saturated hydraulic conductivity of a mixture

d_m = representative particle diameter of the mixture

ρ = fluid density

g = gravitational acceleration

μ = dynamic viscosity

ϕ = porosity of the medium (0.3)

Unit summaries for estimates of hydraulic conductivity are presented in Figure 3.4-3. Mean hydraulic conductivities are strongly skewed by relatively few high conductivity values; therefore, median values are used to represent the population distributions for the three rock units. Estimated hydraulic conductivity in the Puye pumiceous subunit (median 0.97 ft/d) is greater than in the Puye Formation and Miocene pumiceous unit (both with a median 0.55 ft/d). The higher hydraulic conductivity associated with the Puye pumiceous subunit reflects its generally lower silt content relative to the Puye Formation and Miocene pumiceous unit. These unit summaries suggest that, at large scales, the Puye pumiceous subunit is generally more transmissive than the Puye Formation and Miocene pumiceous unit.

Closer inspection of the hydraulic conductivity data shows that individual strata in each of the three main stratigraphic units may play outsized roles in transmission of groundwater in the regional aquifer, and data for individual strata are probably more important than unit statistics for understanding preferential groundwater pathways. The highest hydraulic conductivities occur in 0.2–4-ft-thick strata that are intercalated in relatively thick sequences of rock that are significantly less transmissive (Figures 3.3-2, 3.3-5, 3.3-10, and 3.3-12). Though all aquifer materials are transmissive to some degree, groundwater flow may be concentrated in relatively few (10–20%) high-conductivity strata. The interpretation that groundwater flow may be concentrated in relatively few transmissive strata in a given well has important implications for understanding chromium migration in groundwater and efforts to characterize and remediate the aquifer. A few transmissive strata may dominate the quantity and chemistry of groundwater pumped from characterization and remediation wells. Transmissive strata may contain groundwater that is younger than adjacent less-transmissive strata, and chromium concentrations may differ as well. Rebound of chromium concentrations to former levels following well pumping events is possible, due to chromium exchange between strata with contrasting hydraulic properties. The hydraulic structure of the aquifer intersected by the well screen affects the efficacy of remediation efforts that include pump-and-treat methods and introduction of amendments for in situ treatment and the design and interpretation of characterization activities such as aquifer tests and tracer studies.

Figure 3.4-7 depicts the hydraulic structure of the regional aquifer based on Kozeny-Carman conductivity estimates for the five core holes. The figure is useful for conceptualizing the number, thickness, and vertical distribution of potential preferential pathways. However, key questions remain about the lateral persistence and interconnections between high-conductivity strata that are difficult to answer because of the distance between the core holes and the lack of unique stratigraphic markers for individual strata. Because of differences in the number of transmissive strata found in stratigraphic units among the core holes, some of the strata are probably laterally discontinuous because of facies changes consistent with the nature of many alluvial fan deposits. Although laterally discontinuous, individual transmissive strata are in contact with adjacent depositional beds (above, below, and to the side), some of which are also transmissive. Thus, groundwater likely moves through interconnected transmissive strata that together form networks of preferential pathways that are largely blind to stratal dips and stratigraphic boundaries. As a result, groundwater pathways in the Chromium Investigation Area are dominated by lateral flow that is controlled by low-gradient hydraulic gradients dipping to the east and southeast. The restriction of chromium contamination to the upper 50 ft of the regional aquifer reflects the dominance of lateral flow and limited vertical mixing in the upper part of the regional aquifer.

3.4.5 Provenance and Sedimentology of Miocene and Pliocene Rocks

The Chromium Investigation Area is in the western Española basin of the Rio Grande rift, about 8 km east of the Pajarito fault system that defines the rift margin. The rift shoulder, which includes the eastern part of the Jemez Mountains volcanic field, consists of Miocene mafic to silicic volcanic centers and flows and Pliocene dacitic volcanic sources and flows that form the Sierra de los Valles mountains between the Valles caldera and Pajarito Plateau (Figures 3.4-8 and 3.4-9). The highlands formed by these Miocene and Pliocene volcanic rocks define the footwall of the Pajarito fault system and were the principal sources of sediments shed onto the adjacent rift floor now occupied by the Pajarito Plateau.

The oldest sediments belong to the Miocene riverine deposits of the Chamita Formation (Tcar). These fluvial deposits (13.5–8.5 Ma) of sandy to gravelly channel-fill sediments and intercalated floodplain deposits were derived from the San Luis Basin of southern Colorado, the Taos Range, and the Abiquiu Embayment (Koning et al. 2007). These riverine deposits underlie much of the Pajarito Plateau and were encountered in core hole CrCH-3 and wells R-13, R-15, R-33, R-42, R-43, R-44, R-45, and R-62 in the Chromium Investigation Area. The riverine deposits of the Chamita Formation are overlain by the Miocene pumiceous unit.

The Miocene pumiceous unit is characterized by well-bedded horizons of light-colored, reworked, pumiceous sands and gravels and subordinate primary ash- and pumice-fall deposits. These deposits are largely made up of reworked pumice associated with the Bearhead Rhyolite. The Bearhead Rhyolite erupted during the late Miocene (7.1–6.5 Ma) from volcanic centers in the southern Jemez Mountains (Smith and Lynch 2007); Bearhead Rhyolite is also exposed in north wall of the Valles caldera (Goff et al. 2011). Bearhead pumice falls probably blanketed large areas of the Jemez volcanic highlands. The pumice and ash making up these fall deposits were quickly eroded from the highlands and transported by streams to the western Española basin, where they were deposited as reworked fluvial deposits of the Miocene pumiceous unit. The intercalation of primary Bearhead ash- and pumice-falls in these deposits establishes the Miocene age for this unit.

The Puye pumiceous subunit marks renewed deposition of alluvial fan complexes in the western Española basin during the early Pliocene, following a late Miocene hiatus. The Puye pumiceous subunit is made up of sediments shed from the eastern Jemez volcanic highlands and includes pumiceous detritus reworked from the Miocene pumiceous unit and lithic detritus shed from the newly forming Rendija Canyon Rhyodacite volcanic center. Figure 3.4-8 is schematic paleo-geographic map for the early Pliocene (~5.0 Ma) that shows the distribution of Miocene and Pliocene volcanic rocks along western rift margin that contributed to the early Puye alluvial fans. The Puye pumiceous subunit was

probably deposited during the earliest stages of the Puye fan development at a time when the developing Rendija Canyon Rhyodacite volcanic center was relatively small, and rocks exposed on the footwall of the Pajarito fault system included the Miocene pumiceous unit. Over time the Rendija Canyon Rhyodacite developed into a large structurally high volcanic edifice that became the dominant sediment source for the Puye Formation. By the middle Pliocene (~3 Ma), numerous other dacitic volcanic centers developed on the footwall of the Pajarito fault system, and these new highlands also became major contributors of sediment to the Puye alluvial fan complex (Figure 3.4-9).

Particle-size data collected in this investigation suggest strata making up the Miocene and Pliocene alluvial fan sediments in the Chromium Investigation Area were deposited by moderate- to high-energy streams as indicated by the sand-dominated Miocene pumiceous unit and gravel-dominated Puye Formation. The poor sorting of these rocks also suggests deposition by moderate- to high-energy streams with relatively steep gradients. Stream gradients probably responded to episodic tectonic and volcanic activity along the active western rift margin of the Rio Grande rift.

Except for apparent particle-size differences and color variations, the Puye Formation and Miocene pumiceous unit have similar sedimentological features. They are thin (0.2–2 ft), massive, poorly sorted, unconsolidated, and clast and/or matrix supported except for a few bedded and reverse-graded deposits (Appendix C, Figure 3.4.3-2). These sedimentary features are the results of several factors that are closely related to tectonic, volcanic, and geomorphic processes that occurred along the active western rift margin and adjacent rift floor of the Española Basin. Specifically, the proximity of the provenance area and the depositional environment, which is reflected in short distance alluvial transport and sedimentation, led to the deposition of thin, immature sediment layers (i.e., poorly sorted). Continuous uplift of the rift margin and subsidence in the adjacent rift floor, steep gradients of fault scarps, and the formation of volcanic centers contributed to the complex sedimentological features such as bedding, sorting, grain size, and degree of consolidation noted in the cores and particle-size distributions.

3.5 Summary and Conclusions

Detailed lithologic descriptions coupled with particle-size analyses of sonic cores from CrCH-1 through CrCH-5 provide subsurface geological and hydrogeological information that is relevant to understanding groundwater flow in the regional aquifer and remediation of the chromium plume. The major results of the laboratory-based characterizations of sonic cores are highlighted below.

1. The detailed lithological descriptions of cores from the upper regional aquifer identified a new lithostratigraphic unit called the Puye pumiceous subunit. Unlike the overlying Puye Formation and the underlying Miocene pumiceous unit, which are dominated by dacite lava fragments and pumiceous sand, respectively, the Puye pumiceous subunit represents hybrid strata of dacite-rich and pumice-rich beds. All strata are sedimentary in origin except for a couple of primary pumice fallout and ash deposits within the Miocene pumiceous unit in CrCH-2, CrCH-3, and CrCH-5.
2. Particle-size analyses of sonic cores reveals that hydraulic conductivities for a relatively small number of thin (0.2- to 4-ft-thick) strata in the Puye Formation, the Puye pumiceous subunit, and the Miocene pumiceous unit are significantly greater than those found in thick sequences of overlying and underlying strata. These thin transmissive beds may play outsized roles in transmission of groundwater in the regional aquifer and may control the quantity and chemistry of groundwater pumped from characterization and remediation wells. The distribution of these beds could affect the efficacy of remediation efforts that include pump-and-treat methods and introduction of amendments for in situ treatment. The presence of thin transmissive beds may affect design and interpretation of characterization activities such as aquifer tests and tracer studies.

3. Regional groundwater likely moves through interconnected transmissive strata that together form networks of preferential pathways that are largely blind to stratal dips and stratigraphic boundaries. As a result, regional groundwater pathways are dominated by lateral flow that is controlled by the low-gradient water table that dips to the east and southeast. The restriction of chromium contamination to the upper 50 ft of the regional aquifer reflects the dominance of lateral flow and limited vertical mixing in the upper part of the regional aquifer.
4. The alluvial fan deposits beneath Mortandad Canyon were eroded from volcanic highlands that make up the eastern Jemez Mountains. The detailed lithologic descriptions coupled with chemical and mineralogical data were used to identify the volcanic vents that were the principal sources of these sediments. The temporal and spatial distribution of these vents affected the compositions and lithologic characteristics of sediments making up the regional aquifer.
5. The alluvial fan deposits making up stratigraphic units within the upper regional aquifer consist of beds (0.2–4 ft) of silty to gravelly coarse sandy strata that are mostly poorly sorted, massive, unconsolidated, and matrix to clast supported. Grain sizes generally decrease with depth through the stratigraphic sequence, and the chemistry and mineralogy of these rocks reflect a change in the provenance of the deposits, with dacite sediment dominant the upper part of the sequence and rhyolite sediments dominant in the lower part. Sedimentological features such as changes in clast compositions, bed thicknesses, grain-size variations, lack of sorting, and massive bedding are attributed to the proximity of these deposits to their source areas, the moderate to steep topographic gradient between the sediment source area and the adjacent depositional environment, the episodic uplift and subsidence along the tectonically active western rift margin of the Española basin, and deposition that overlapped with active volcanism in the source areas.

4.0 REFERENCES AND MAP DATA SOURCES

4.1 References

The following reference list includes documents cited in this report.

- Broxton, D., R. Gilkeson, P. Longmire, J. Marin, R. Warren, D. Vaniman, A. Crowder, B. Newman, B. Lowry, D. Rogers, W. Stone, S. McLin, G. WoldeGabriel, D. Daymon, and D. Wycoff. "Characterization Well R-9 Completion Report," Los Alamos National Laboratory report LA-13742-MS, Los Alamos, New Mexico (2001).
- Broxton, D., G. WoldeGabriel, L. Peters, J. Budahn, and G. Luedemann. "Pliocene Volcanic Rocks of the Tschicoma Formation, East-Central Jemez Volcanic Field: Chemistry, Petrography, and Age Constraints," *New Mexico Geological Society Guidebook: 58th Field Conference, Geology of the Jemez Mountains Region II*, pp. 284–295 (2007).
- Broxton, D.E., and S.L. Reneau. "Buried Early Pleistocene Landscapes Beneath the Pajarito Plateau, Northern New Mexico," *New Mexico Geological Society Guidebook: 47th Field Conference, Jemez Mountains Region, New Mexico*, pp. 325–334 (1996).
- Caine, J.S., and Minor, S.A.. "Structural and geochemical characteristics of faulted sediments and inferences on the role of water in deformation, Rio Grande rift, New Mexico," *Geological Society of America Bulletin*, Vol. 121, nos. 9–10, pp. 1325–1340, DOI: 10.1130/B26164.1 (2009).

- Chapuis, R.P., and M. Aubertin. "On the use of the Kozeny-Carman equation to predict the hydraulic conductivity of soils," *Canadian Geotechnical Journal*, 40(3), pp. 616–628, 10.1139/t03-013 (2003).
- Chipera, S.J., and D. Bish. "FULLPAT: A full-pattern quantitative analysis program for X-ray powder diffraction using measured and calculated patterns," *Journal of Applied Crystallography*, Vol. 35, pp. 744–749 (2002).
- Dransfield, B.J., and J.N. Gardner. "Subsurface Geology of the Pajarito Plateau, Española Basin, New Mexico," Los Alamos National Laboratory report LA-10455-MS, Los Alamos, New Mexico (1985).
- Folk, R.L.. "Petrology of Sedimentary Rocks," Hemphill Publishing Company, p. 190, Austin, Texas (1980).
- Goff, F., J.N. Gardner, S.L. Reneau, S.A. Kelley, K.A. Kempter, J.R. Lawrence. "Geologic map of the Valles caldera, Jemez Mountains, New Mexico," New Mexico Bureau of Geology and Mineral Resources, Geologic Map 79, 1:50,000 scale, color, w/30 p. booklet (2011).
- Grauch, V.J.S., J.D. Phillips, D.J. Koning, P.S. Johnson, and V. Bankey. "Geophysical Interpretations of the Southern Española Basin, New Mexico, That Contribute to Understanding Its Hydrogeologic Framework," U.S. Geological Survey Professional Paper 1761, p. 87 (2009).
- Griggs, R.L., and J.D. Hem. "Geology and Ground-Water Resources of the Los Alamos Area, New Mexico," U.S. Geological Survey Water Supply Paper 1753, Washington, D.C. (1964).
- Justet, L., and T.L. Spell. "Effusive Eruptions from a Large Silicic Magma Chamber: The Bearhead Rhyolite, Jemez Volcanic Field, NM," *Journal of Volcanology and Geothermal Research*, Vol. 107, pp. 241–264 (2001).
- Kelley, V.C.. "Geology of Española Basin, New Mexico," Map 48, ISSN: 0545-2899, New Mexico Bureau of Mines and Mineral Resources, Socorro, New Mexico (1978).
- Koning, D.J., D. Broxton, D., Sawyer, D. Vaniman, and J. Shomaker, D.L.. "Surface and Subsurface Stratigraphy of the Santa Fe Group Near White Rock and the Buckman Areas of the Espanola Basin, North-Central New Mexico," New Mexico Geological Society Guidebook: 58th Field Conference, Geology of the Jemez Mountains Region II, pp. 209-224 (2007).
- Koning, D.J., S. Aby, and S. Finch. "Where is the water? – a preliminary assessment of hydrogeologic characteristics of lithostratigraphic units near Española, north-central New Mexico", New Mexico Geological Society Guidebook, 58th Field Conference, Geology of the Jemez Mountains Region II, 2007, p. 475–484 (2007b).
- LANL (Los Alamos National Laboratory). "Interim Measures Investigation Report for Chromium Contamination in Groundwater," Los Alamos National Laboratory document LA-UR-06-8372, Los Alamos, New Mexico (2006).
- LANL (Los Alamos National Laboratory). "Completion Report for Regional Aquifer Well R-42," Los Alamos National Laboratory document LA-UR-09-0217, Los Alamos, New Mexico (2009a).

- LANL (Los Alamos National Laboratory). "Completion Report for Wells R-43 and SCI-2," Los Alamos National Laboratory document LA-UR-09-1337, Los Alamos, New Mexico (2009b).
- LANL (Los Alamos National Laboratory). "Investigation Report for Sandia Canyon," Los Alamos National Laboratory document LA-UR-09-6450, Los Alamos, New Mexico (2009c).
- LANL (Los Alamos National Laboratory). "Phase II Investigation Report for Sandia Canyon," Los Alamos National Laboratory document LA-UR-12-24593, Los Alamos, New Mexico (2012).
- LANL (Los Alamos National Laboratory). "Interim Measures Work Plan for the Evaluation of Chromium Mass Removal," Los Alamos National Laboratory document LA-UR-13-22534, Los Alamos, New Mexico (2013).
- LANL (Los Alamos National Laboratory). "Drilling Work Plan for Chromium Project Coreholes," Los Alamos National Laboratory document LA-UR-14-24829, Los Alamos, New Mexico (2014).
- LANL (Los Alamos National Laboratory). "Completion Report for Chromium Project Coreholes 1 through 5," Los Alamos National Laboratory document LA-UR-15-23197, Los Alamos, New Mexico (2015).
- LANL (Los Alamos National Laboratory). "Compendium of Technical Reports Related to the Deep Groundwater Investigation of RDX-Contaminated Groundwater at Los Alamos National Laboratory," Attachment 2, "Geology of Technical Area 16 and Vicinity, Los Alamos National Laboratory," Los Alamos National Laboratory document LA-UR-15-23126, Los Alamos, New Mexico (2018).
- Le Bas, M. J., R.W. Le Maitre, A. Streckeisen, and B. Zanettin. "A chemical classification of volcanic rocks based on the total alkali-silica diagram," *Journal of Petrology*, Vol. 27, pp. 745–750 (1986).
- Le Corvec, R.P., K.B. Spörli, J. Rowland, and J. Lindsay. "Spatial distribution and alignments of volcanic centers: Clues to the formation of monogenetic volcanic fields," *Earth Science Reviews*, Vol. 124, pp. 96–114 (2013).
- McAda, D.P., and P. Barroll. "Simulation of Ground-Water Flow in the Middle Rio Grande Basin Between Cochiti and San Acacia, New Mexico," U.S. Geological Survey Water-Resources Investigations Report 2002-4200, p.81 (2002).
- McIntosh, W.C. and J. Quade. "⁴⁰Ar/³⁹Ar geochronology of tephra layers in the Santa Fe Group, Espanola Basin, New Mexico," New Mexico Geological Society Guidebook: 46th Field Conference, Guidebook, pp. 279–287 (1995).
- Odong, Justine. "Evaluation of empirical formulae for determination of hydraulic conductivity based on grain-size analysis," *Journal of American Science*, Vol. 3.3, pp. 54–60 (2007).
- Reidel, S.P., V.E. Camp, T.L. Tolan, and B.S. Martin. "The Columbia River flood basalt province: Stratigraphy, areal extent, volume, and physical volcanology, in the Columbia River Flood Basalt Province," Geological Society of America Special Paper 497, pp. 1–43 (2013).

- Samuels, K.E., D.E. Broxton, D.T. Vaniman, G. WoldeGabriel, J.A. Wolff, D.D. Hickmott, E.C. Kluk, and M.M. Fittipaldo. "Distribution of Dacite Lavas beneath the Pajarito Plateau, Jemez Mountains, New Mexico," *New Mexico Geological Society Guidebook: 58th Field Conference, Geology of the Jemez Mountains Region II*, pp. 296–308 (2007).
- Sawyer, D.A., S.A. Minor, R.A. Thompson, R.R. Shroba, G.A. Smith, D.P. Dethier, V.J.S. Grauch, and T.R. Brandt. "Geologic Map of the Cochiti Pueblo Area, New Mexico," *U.S. Geological Survey Professional Paper 1720, Plate 2*, Reston, Virginia (2007).
- Smith, R.L., R.A. Bailey, and C.S. Ross. "Geologic Map of the Jemez Mountains, New Mexico," *U.S. Geological Survey Miscellaneous Investigations Series, Map I-571*, Washington, D.C. (1970).
- Smith, G.A. and S.D. Lynch. "Interplay of Miocene Rift Tectonics and Rhyolitic magmatism in the Southern Jemez Mountains, New Mexico," *New Mexico Geological Society Guidebook: 58th Field Conference, Geology of the Jemez Mountains Region II*, pp. 262–267 (2007).
- Thompson, R.A., D.A. Sawyer, M.R. Hudson, V.G.S. Grauch, and W.C. McIntosh. "Cenozoic volcanism of the La Bajada constriction area, New Mexico," *U.S. Geological Survey Professional Paper 1720*, pp. 43–60 (2006).
- Valentine G.A., and C.B. Connor, 2015. "Basaltic volcanic fields," *The Encyclopedia of Volcanoes*, 2nd Edition, pp. 423–439, doi: 10.1016/B978-0-12-385938-9.00023-7 (2015).
- WoldeGabriel, G., A.W. Laughlin, D.P. Dethier, and M. Heizler. "Temporal and Geochemical Trends of Lavas in White Rock Canyon and the Pajarito Plateau, Jemez Volcanic Field, New Mexico, USA," *Los Alamos National Laboratory document LA-UR-96-583*, Los Alamos, New Mexico (1996).
- WoldeGabriel, G., A.P. Naranjo, M.M. Fittipaldo. "Distribution, Geochemistry, and Correlation of Pliocene Tephra in the Pajarito Plateau," *New Mexico Geological Society Guidebook: 58th Field Conference, Geology of the Jemez Mountains Region II*, pp. 275–283 (2007).
- Wu, Y.-S., W. Zhang, L. Pan, J. Hinds, and G.S. Bodvarsson. "Modeling Capillary Barriers in Unsaturated Fractured Rock," *Water Resources Research*, Vol. 38, No. 11, pp. 1255–1259 (2002).
- Zhang, Z.F., A.L. Ward, and J.M. Keller. "U.S. Department of Energy, Pacific Northwest National Laboratory. Determining the Porosity and Saturated Hydraulic Conductivity of Binary Mixtures," *PNNL Publication 18801* (2009).

4.2 Map Data Source

Hillshade; Los Alamos National Laboratory, ER-ES, As published;
\\slip\gis\Data\HYP\LiDAR\2014\Bare_Earth\BareEarth_DEM_Mosaic.gdb; 2014.

Point features; As published; EIM data pull; 2017.

Chromium plume > 50 ppb; Los Alamos National Laboratory, ER-ES, As published;
\\slip\gis\GIS\Projects\13-Projects\13-0065\shp\chromium_plume_2.shp; 2018.

Structures; Los Alamos National Laboratory, KSL Site Support Services, Planning, Locating and Mapping Section; 06 January 2004; as published 29 November 2010.

Drainage channel; Los Alamos National Laboratory, ER-ES, As published, GIS projects folder; \\slip\gis\GIS\Projects\15-Projects\15-0080\project_data.gdb\correct_drainage; 2017.

Technical Area Boundaries; Los Alamos National Laboratory, Site Planning & Project Initiation Group, Infrastructure Planning Office; September 2007; as published 13 August 2010.

Unpaved roads; Los Alamos National Laboratory, ER-ES, As published, GIS projects folder; \\slip\gis\GIS\Projects\14-Projects\14-0062\project_data.gdb\digitized_site_features\digitized_roads; 2017.

U.S. Census populated places; Los Alamos National Laboratory, ER-ES, As published, GIS projects folder; \\slip\gis\GIS\Data\ESRI\census\places.sdc\places; 2018

Rivers; Los Alamos National Laboratory, ER-ES, As published, GIS projects folder; \\slip\gis\GIS\Data\ESRI\hydro\rivers.sdc\rivers; 2018.

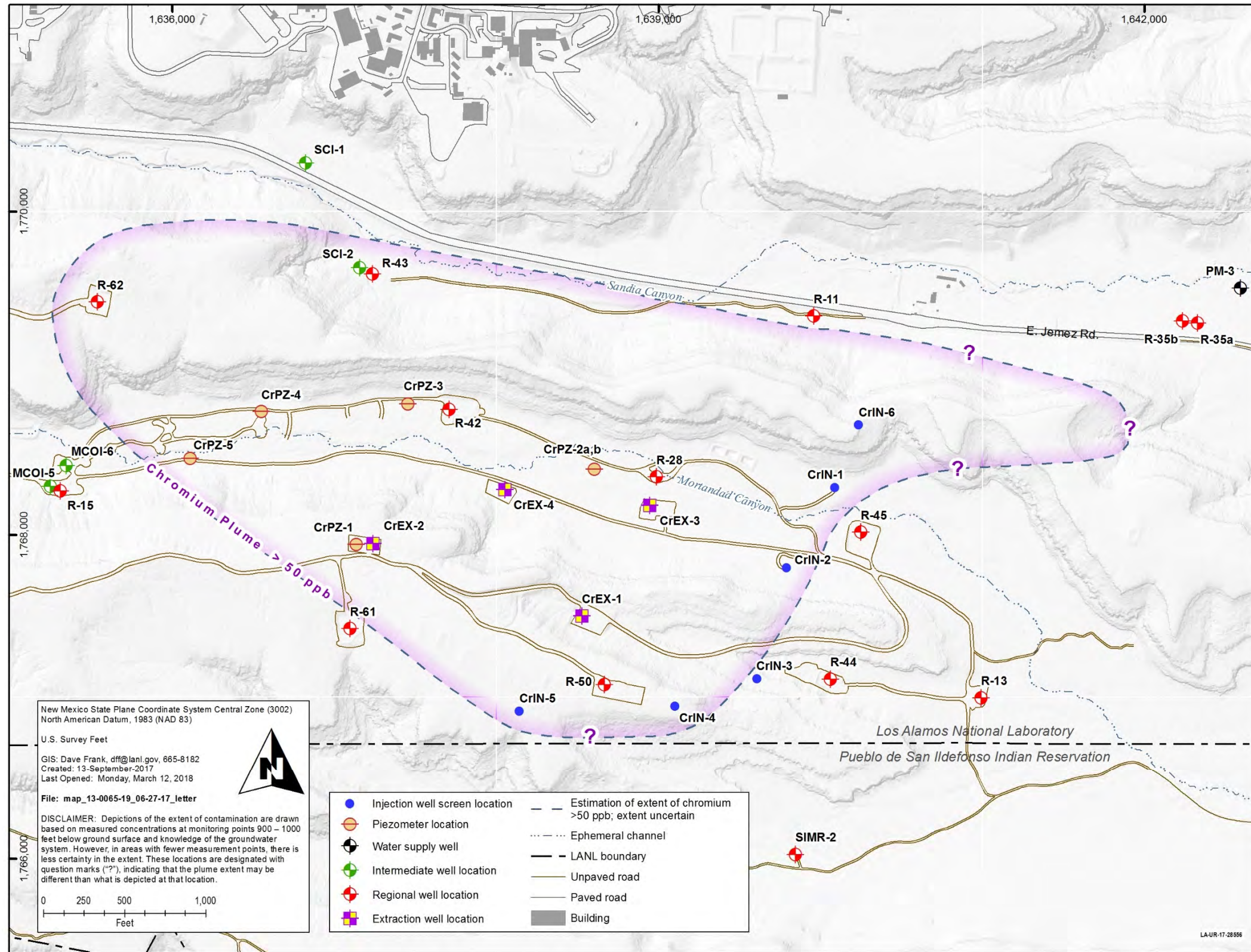


Figure 1.0-1 Map showing the approximate extent of the hexavalent chromium plume as defined by the 50-µg/L New Mexico groundwater standard. Locations of monitoring wells, piezometers, extraction wells and injection wells are also shown.

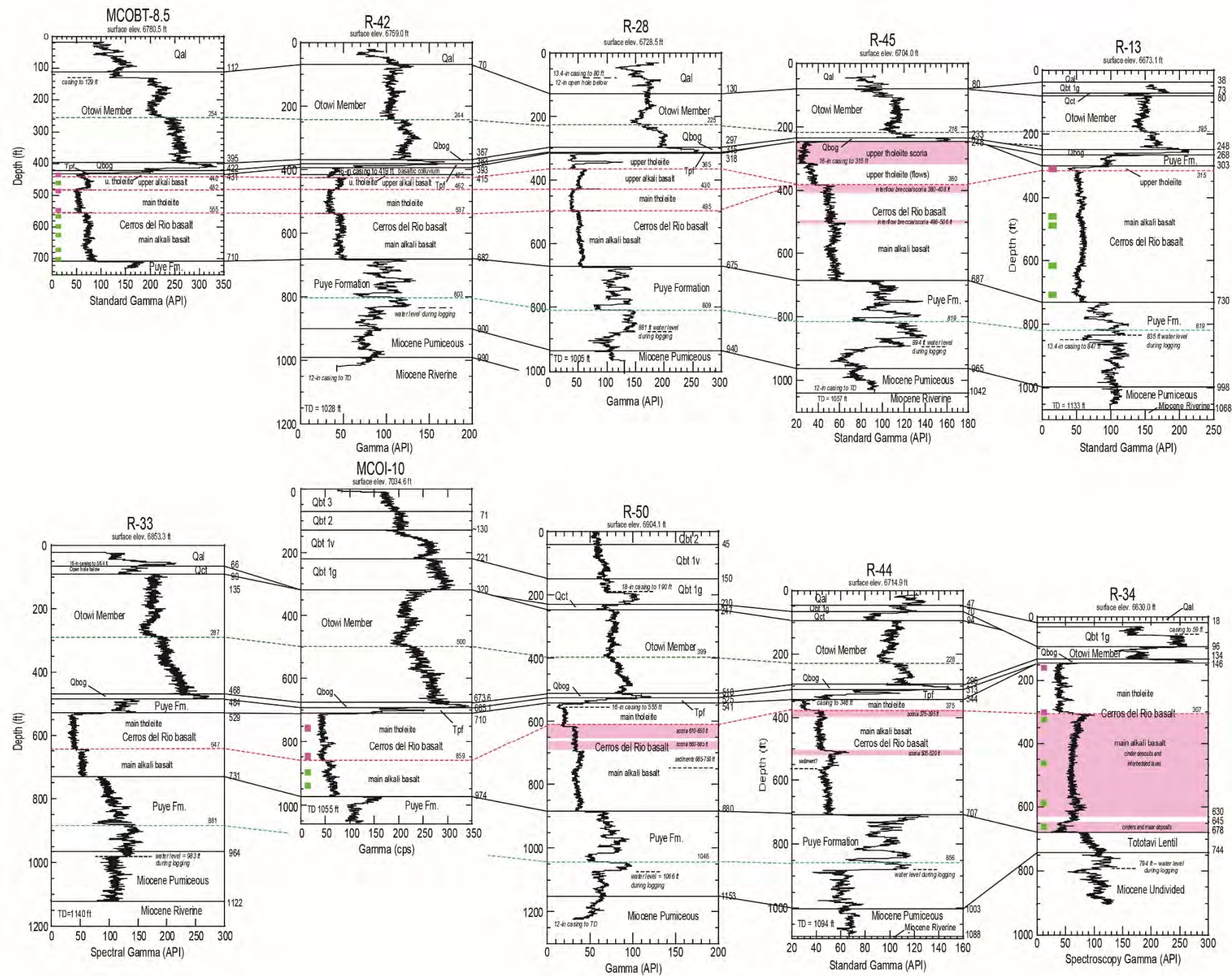


Figure 2.2-1 Examples of elevation-corrected cross-sections used to correlate gamma logs between wells in the Chromium Investigation Area. Three new geologic contacts were correlated between wells based on the gamma logs: (1) internal bedding in the Otowi Member (dashed green line), (2) stratigraphic breaks between tholeiites and alkali basalt (dashed red lines), and (3) a low-gamma deposit in the Puye Formation (dashed blue line). Gamma and spectral gamma logs with API (American Petroleum Institute) units were collected by Schlumberger, Inc., and gamma logs with counts per second (cps) units were collected by the Laboratory. Colored boxes indicate confirmation of tholeiites (red) and alkali basalt (green) by XRF analyses of cuttings.

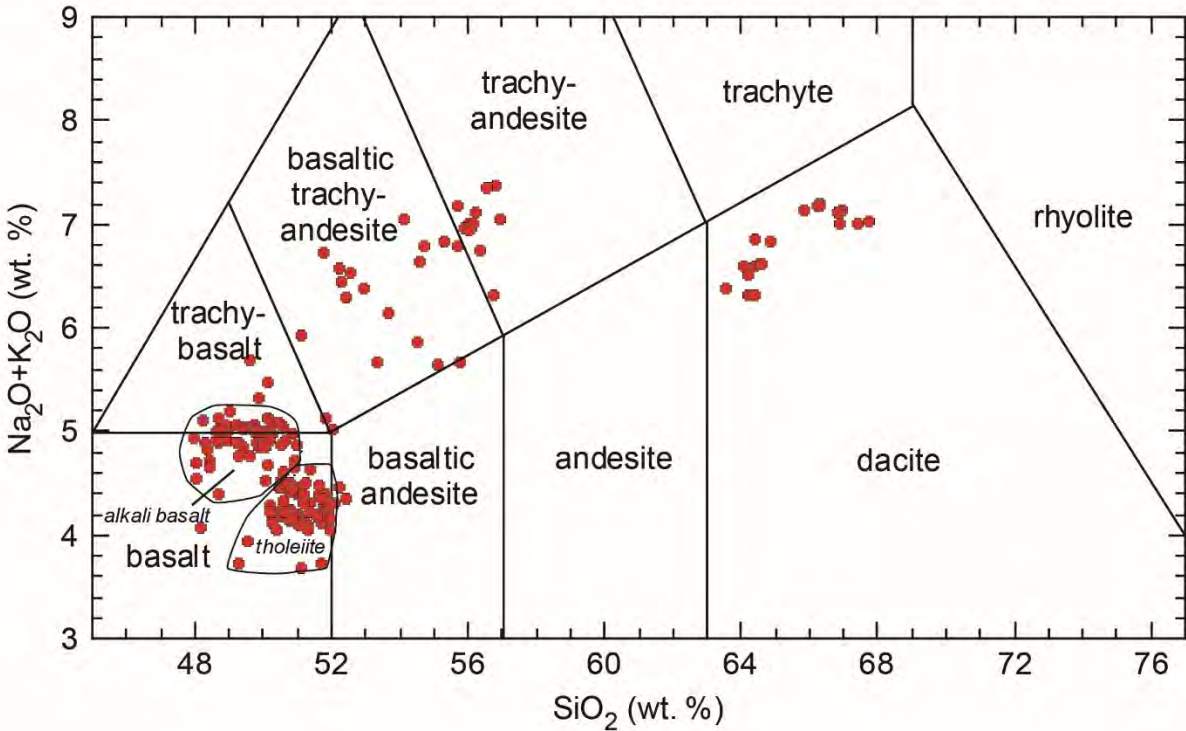


Figure 2.3-1 Chemical classification diagram showing alkali-silica compositions of subsurface lavas beneath the eastern Pajarito Plateau. Tholeiites and alkali basalt subgroups are shown superimposed on the basalt-trachybasalt fields. Basaltic trachyandesite, trachyandesite, and some of the dacites underlie tholeiites and alkali basalts at TA-54. Other dacites occur beneath the western Pajarito Plateau where basalt is mostly absent. Diagram modified from Le Bas et al. (1986). Major element concentrations by XRF data (WoldeGabriel and Broxton, unpublished data).

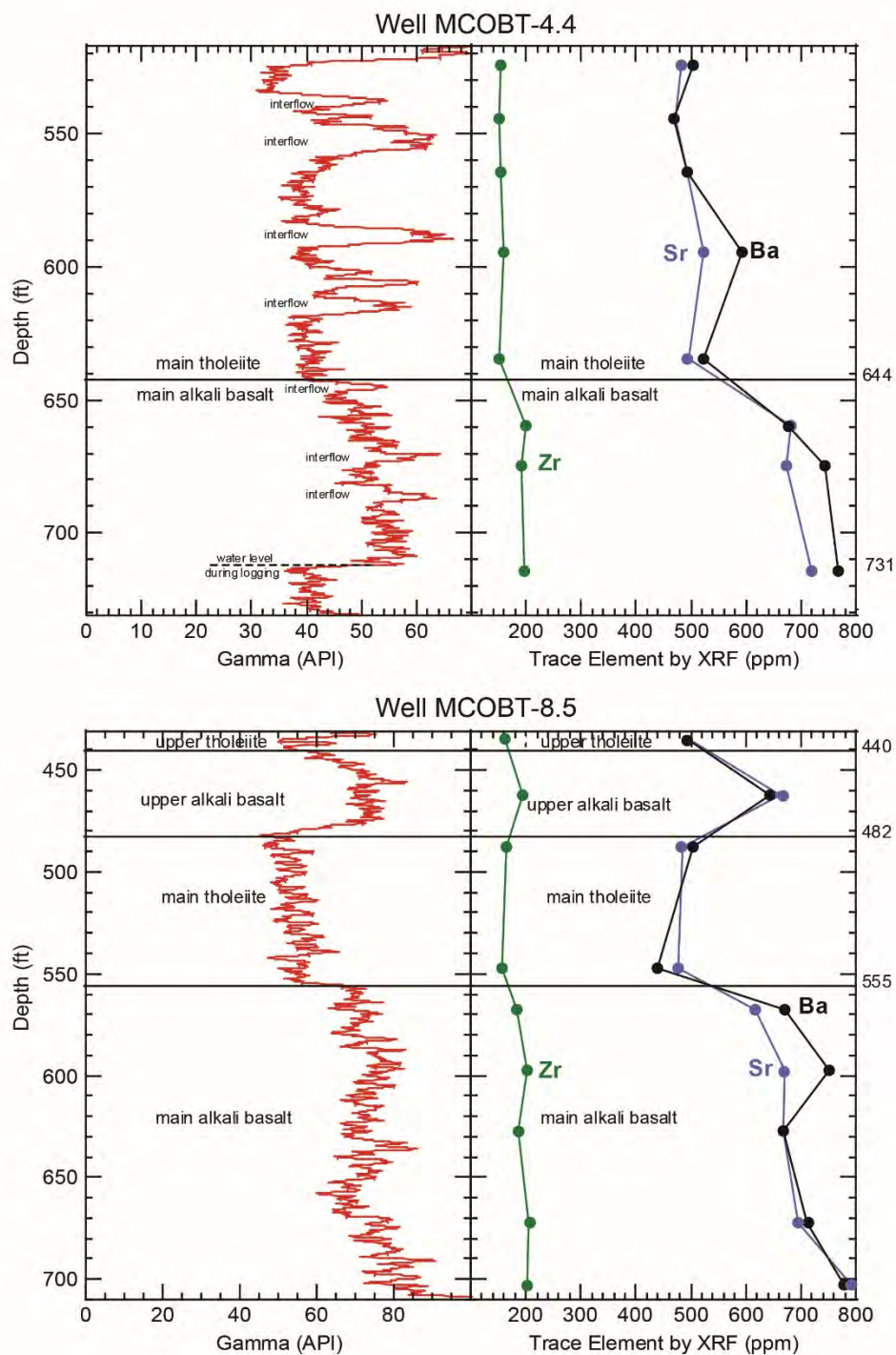


Figure 2.3-2 Borehole gamma and trace element (zirconium, strontium, and barium) plots for the Cerros del Rio basalt in wells MCOBT-4.4 and MCOBT-8.5. Differentiation of tholeiites and alkali basalts based on gamma activity is supported by XRF chemical data collected for cuttings samples (WoldeGabriel and Broxton, unpublished data).

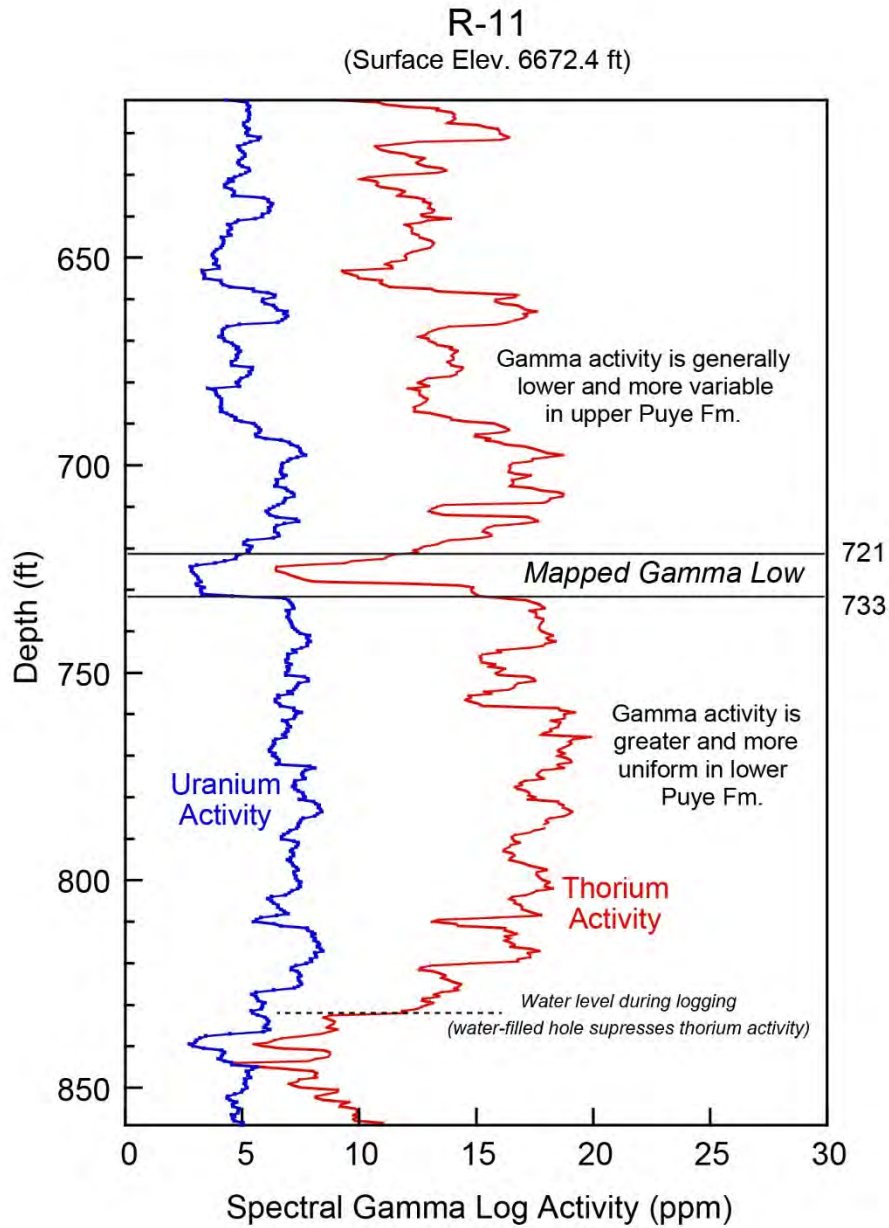


Figure 2.3-3 Borehole spectral gamma activity for uranium and thorium in the Puye Formation for well R-11. Log data collected by Schlumberger, Inc. in an open borehole.

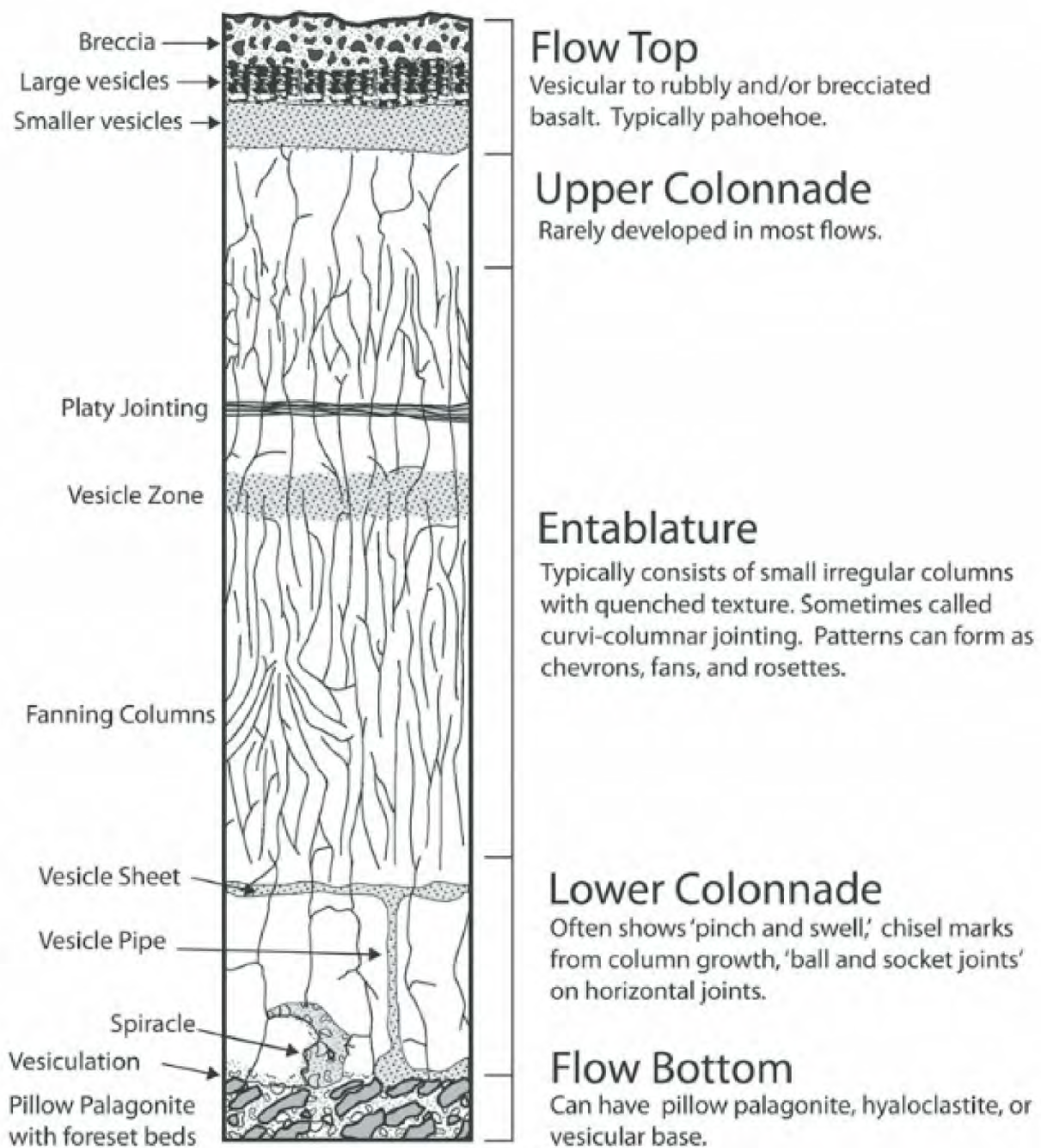


Figure 2.4-1 Diagram showing typical internal features in a basalt lava flow (after Reidel et al. 2013). The figure is idealized and not all features are present for every flow.

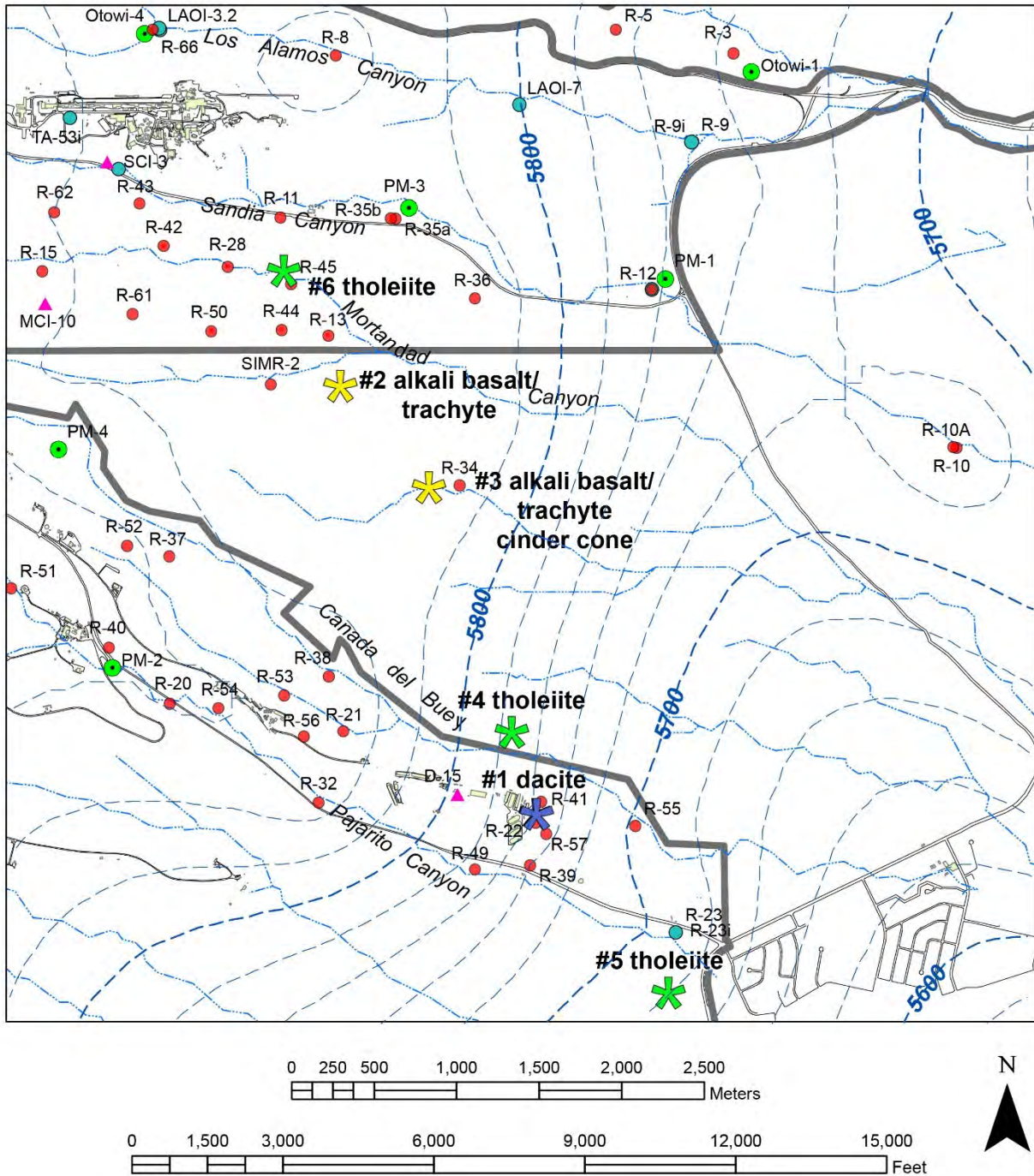


Figure 2.5-1 Vent locations for dacite (blue star), alkali basalt (yellow stars), and tholeiite (green stars) lavas of the Cerros del Rio volcanic field in the eastern Pajarito Plateau. Numbered locations are referred to in the text. The alignment of the vents suggests these magmas were erupted along a common tectonic structure. Water table map (elevation in ft) for the regional aquifer shown as blue dashed lines. Wells include regional monitoring wells (red circles), perched-zone wells (aqua circles), boreholes (pink triangles), and municipal supply wells (green circles).

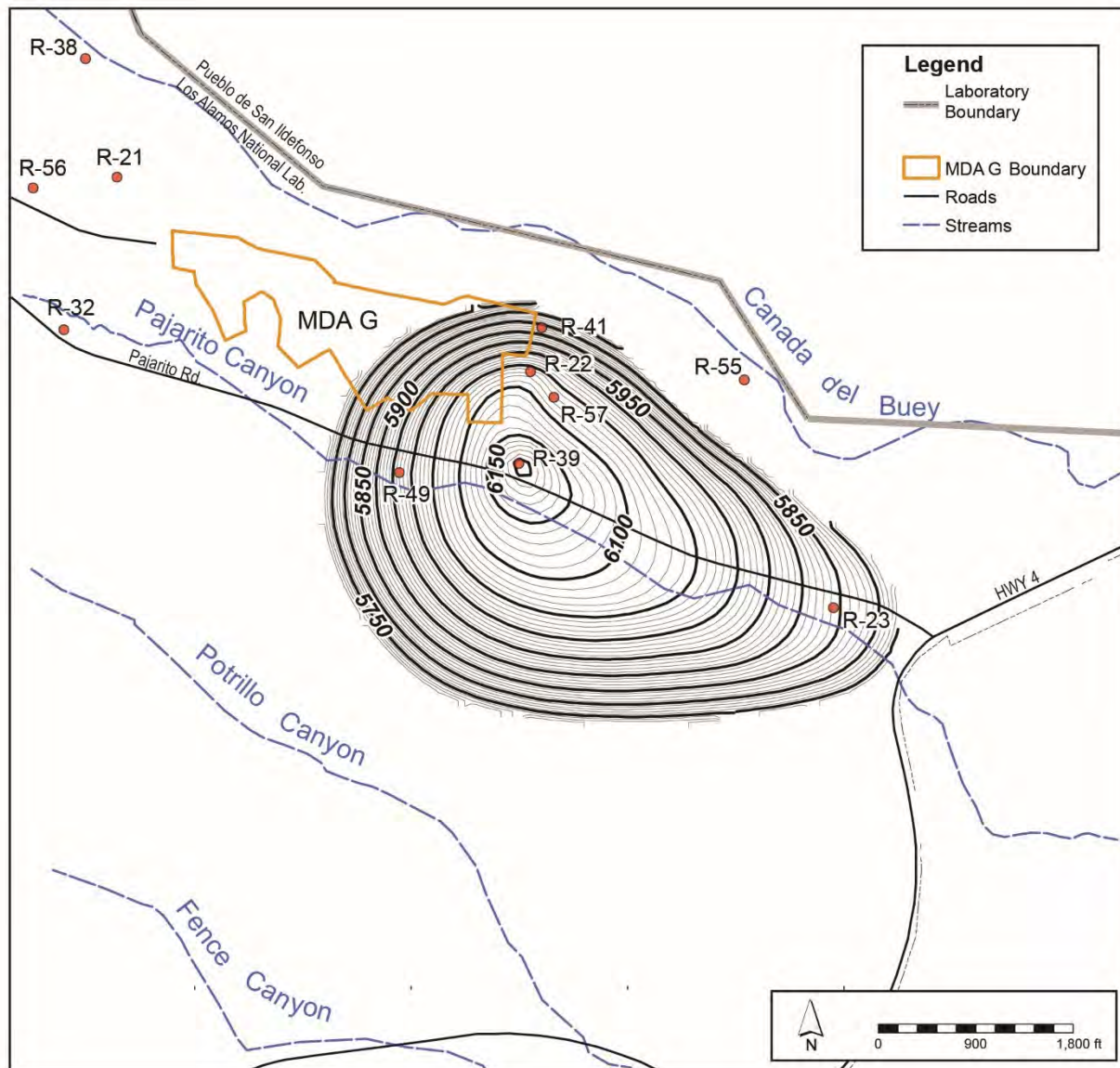


Figure 2.5-2 Structure contour map for top of dacite lavas near the east end of MDA G in Pajarito Canyon. Map taken from the WC15c sitewide geologic model.

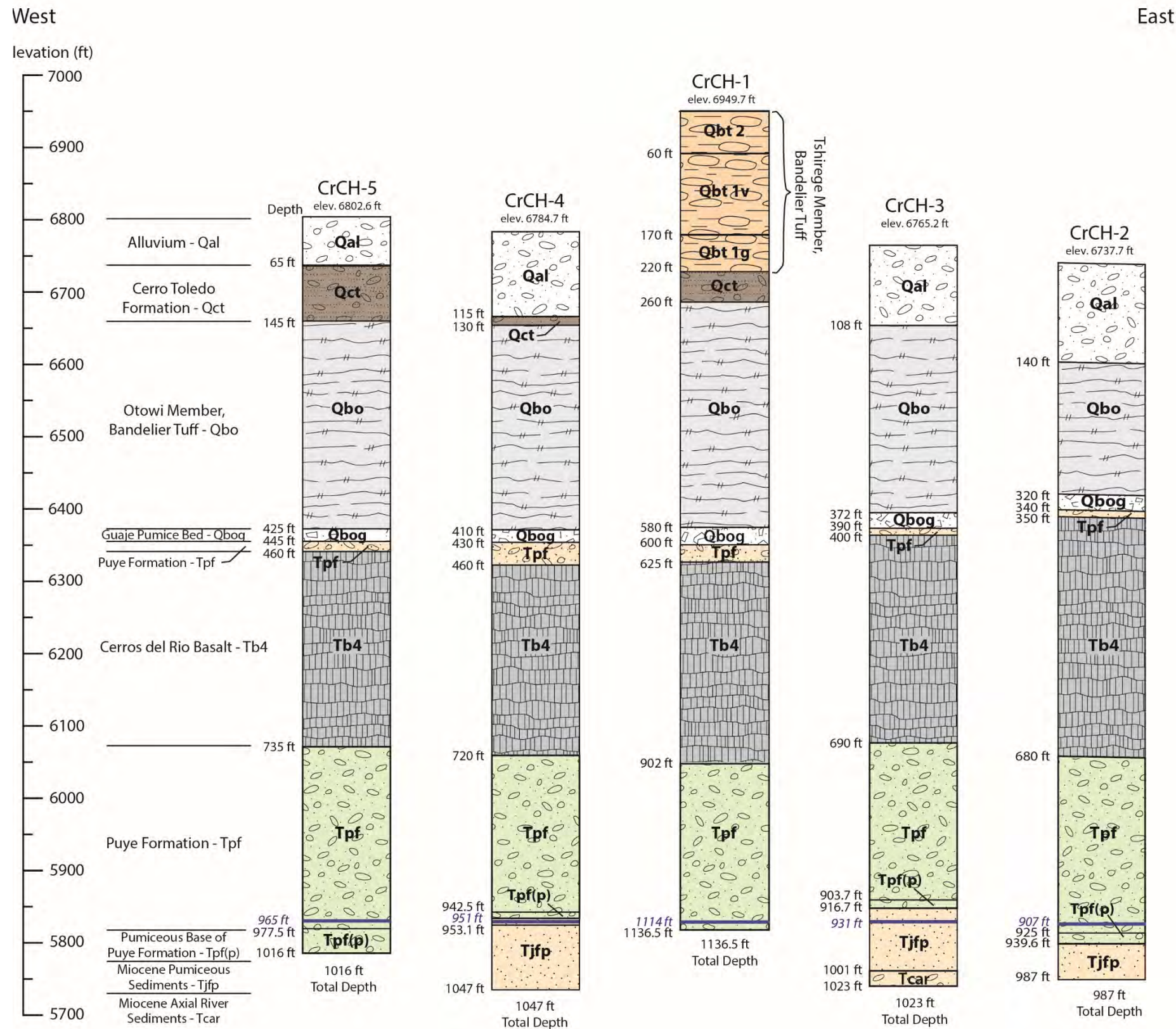


Figure 3.2-1 Stratigraphic columns showing geologic contacts and water levels (blue lines) for core holes in Mortandad Canyon

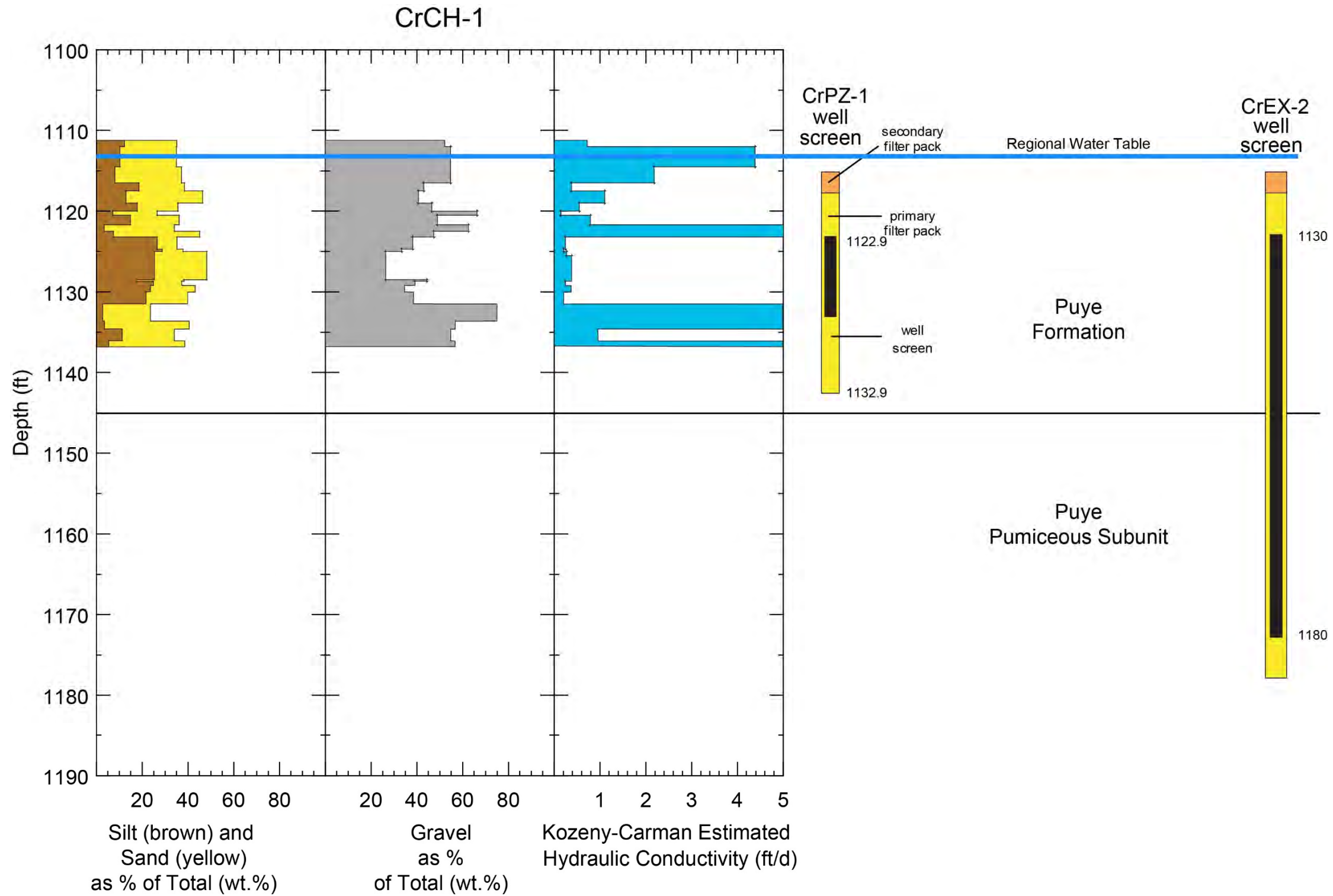


Figure 3.3-1 CrCH-1 grain-size variations for beds making up strata in the upper part of the regional aquifer. The CrPZ-1 (completed in the CrCH-1 borehole) and R-28 well screens are shown for reference. The contact between the Puye Formation and the Puye pumiceous subunit is based on well CrEX-2, which is located on the same drill pad. CrEX-2 did not fully penetrate the Puye pumiceous unit at a total depth of 1240 ft.

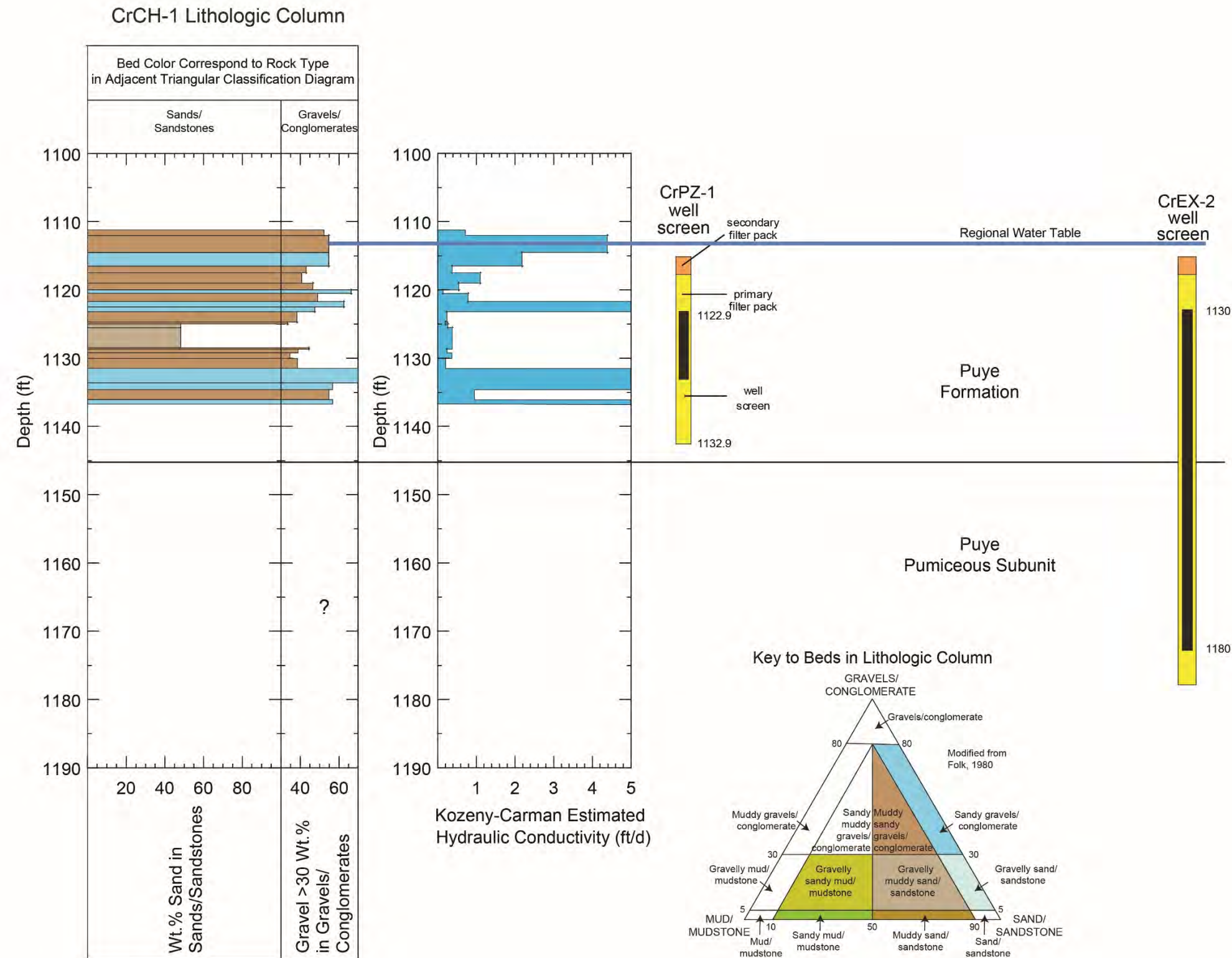


Figure 3.3-2 CrCH-1 lithologic column showing rock types for individual beds making up strata in the upper part of the regional aquifer. The CrPZ-1 (completed in the CrCH-1 borehole) and R-28 well screens are shown for reference. The contact between the Puye Formation and the Puye pumiceous subunit is based on well CrEX-2, which is located on the same drill pad. CrEX-2 did not fully penetrate the Puye pumiceous subunit at a total depth of 1240 ft.

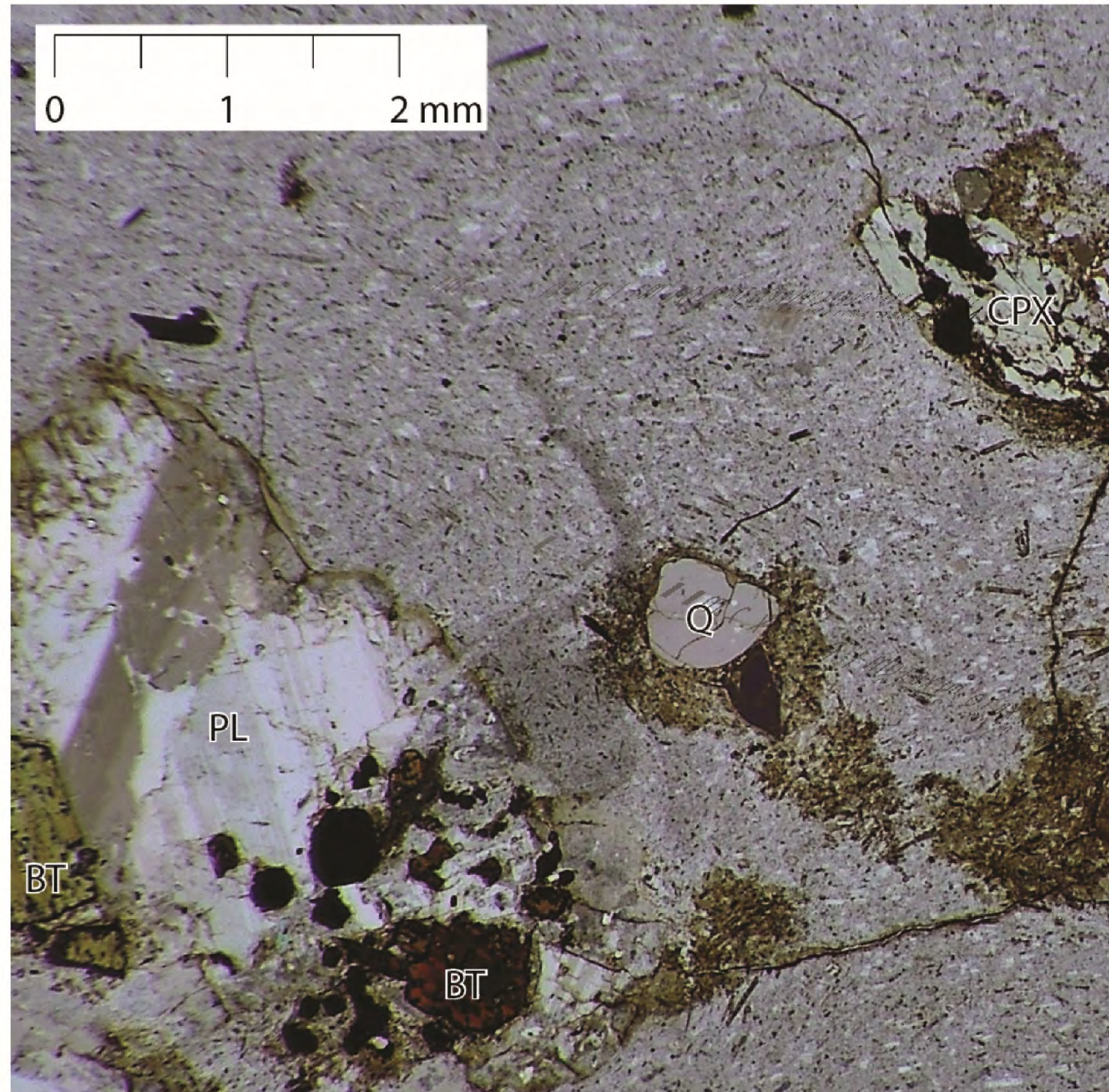


Figure 3.3-3 Plane-light photomicrograph of Rendija Canyon Rhyodacite in thin section showing the typical phenocryst assemblage (Q= quartz, PL= plagioclase, BT=biotite, CPX=clinopyroxene; not shown are phenocrysts of hornblende, sanidine, and anorthoclase). The rod-shaped microlites distributed throughout the groundmass are magnesium-rich orthopyroxene, which are commonly oxidized to a bronze-red color. Orthopyroxene microlites in the groundmass are unique to the Rendija Canyon Rhyodacite and are readily identifiable with a hand lens or binocular microscope.

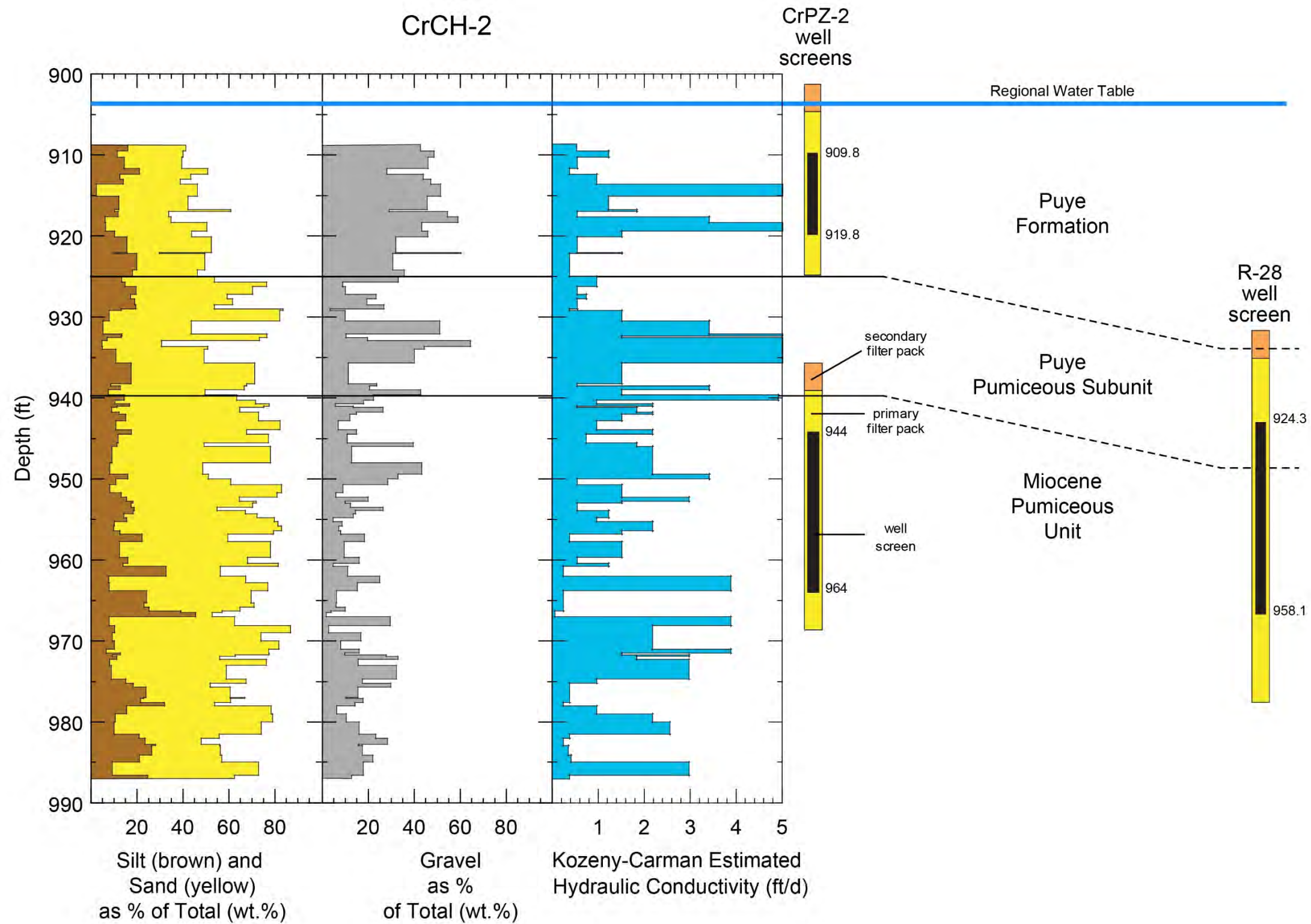


Figure 3.3-4 CrCH-2 grain-size variations for beds making up strata in the upper part of the regional aquifer. CrPZ-2 (completed in the CrCH-2 borehole) and R-28 well screens are shown for reference.

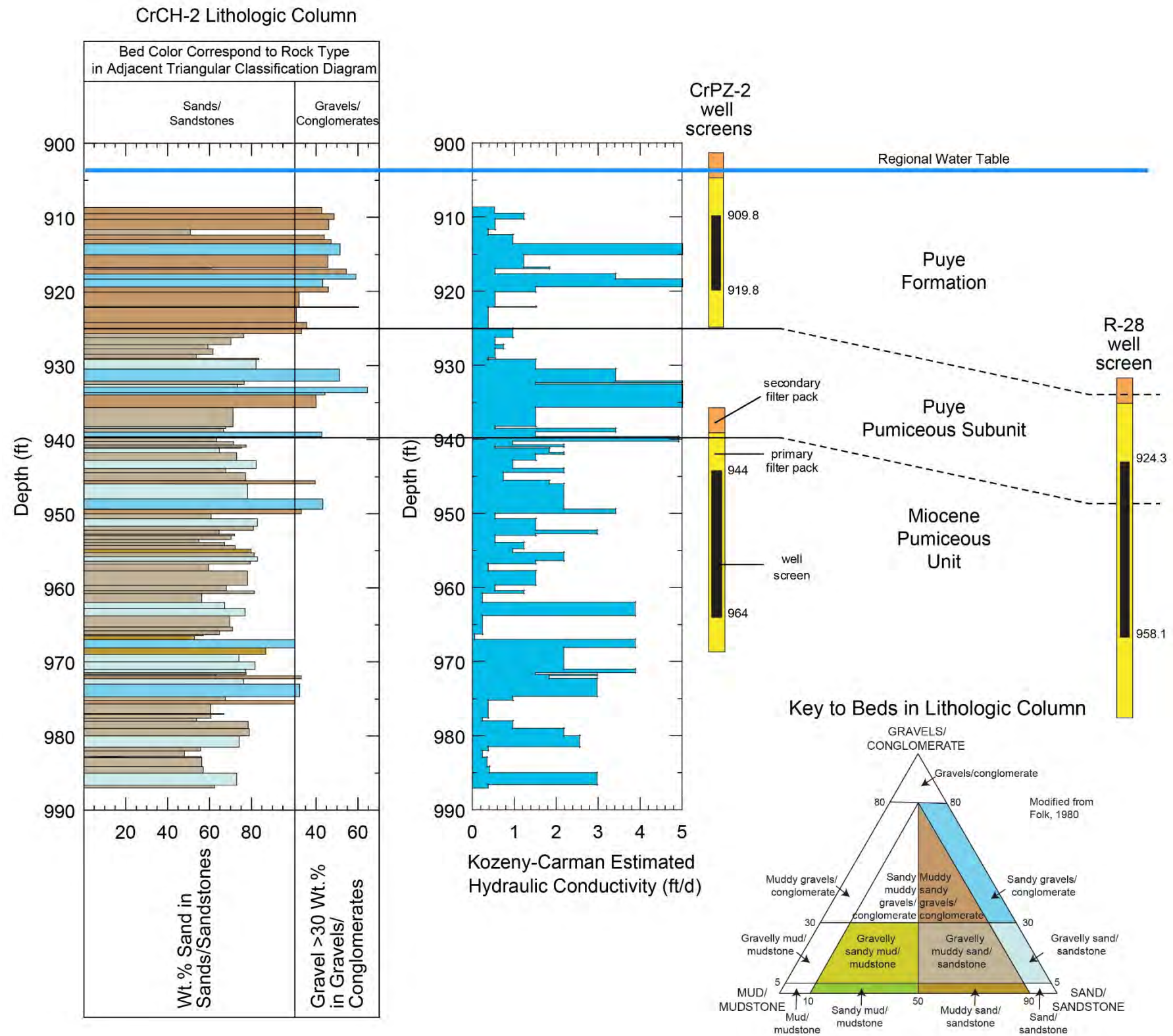


Figure 3.3-5 CrCH-2 lithologic column showing rock types for individual beds making up strata in the upper part of the regional aquifer. CrPZ-2 (completed in the CrCH-2 borehole) and R-28 well screens are shown for reference.

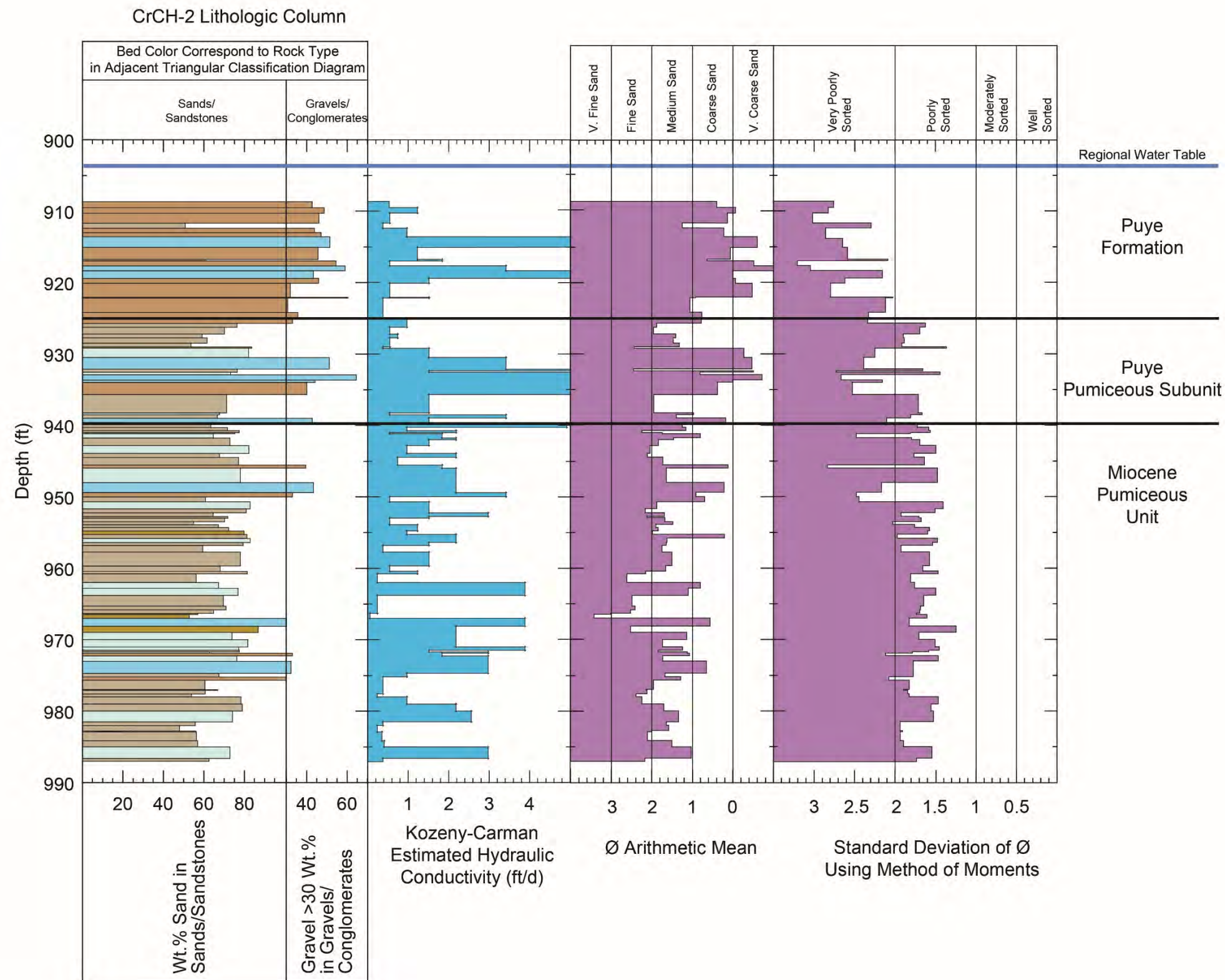


Figure 3.3-6 Comparison of the CrCH-2 lithologic column and estimated hydraulic conductivity to the mean grain size (shown as Ø arithmetic mean) and sorting characteristics (shown as standard deviation of Ø using the method of moments). The Ø arithmetic mean and standard deviation of Ø were calculated from the CrCH-2 sieve data following the methodology of Folk (1980).

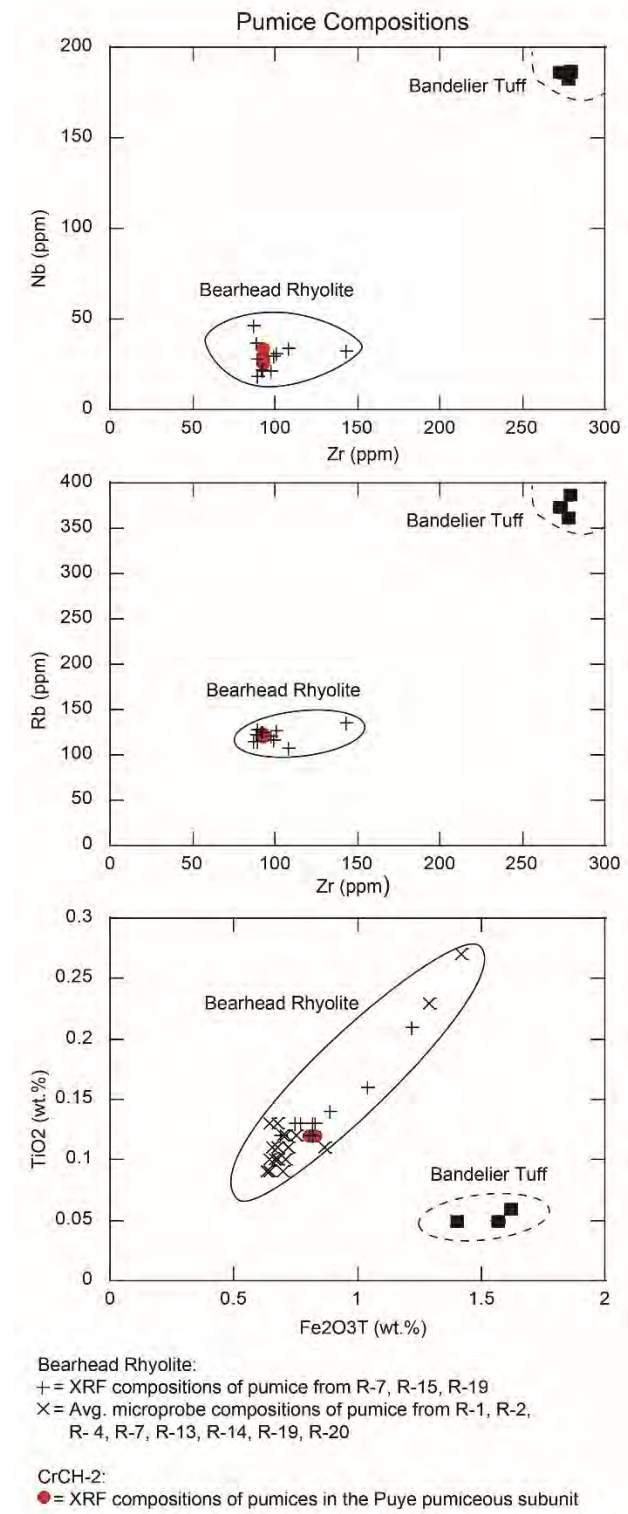


Figure 3.3-7 Comparison of pumice compositions in CrCH-2 with Bearhead Rhyolite pumices that make up the Miocene pumiceous unit beneath the Pajarito Plateau. The CrCH-2 XRF data represent pumices collected from three depth intervals in the Puye pumiceous subunit. Bandelier Tuff compositions shown for reference.

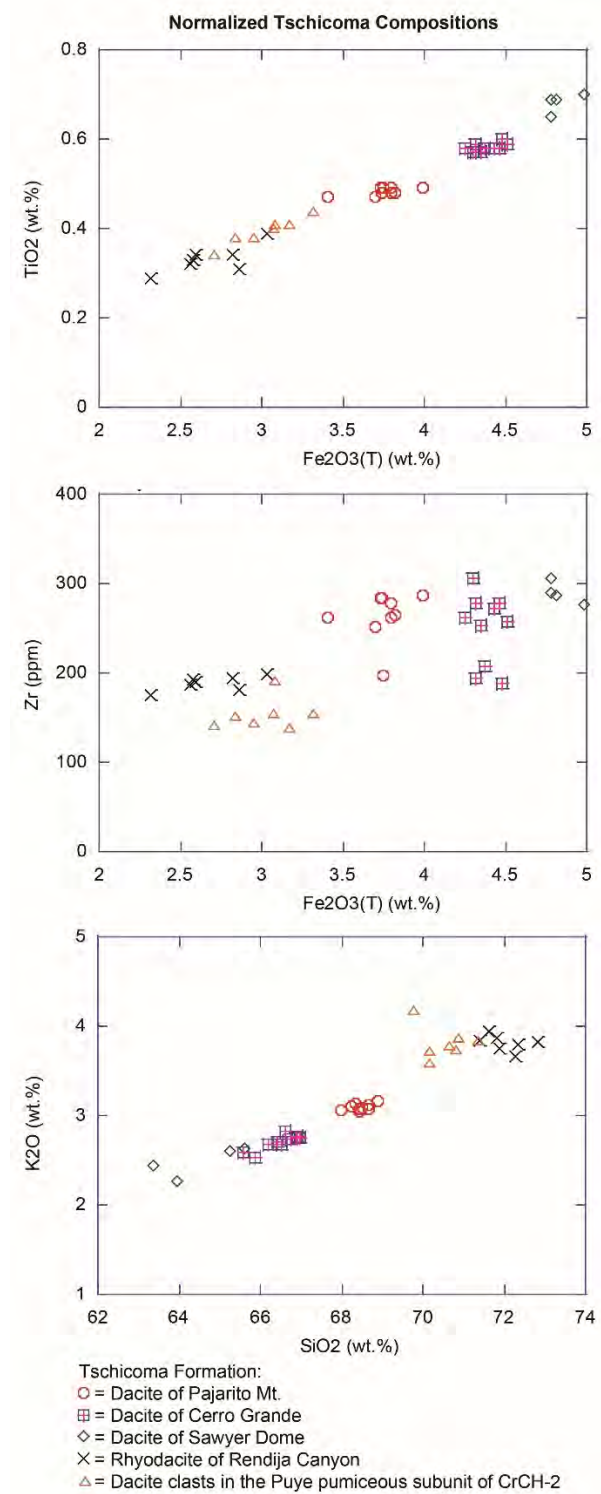
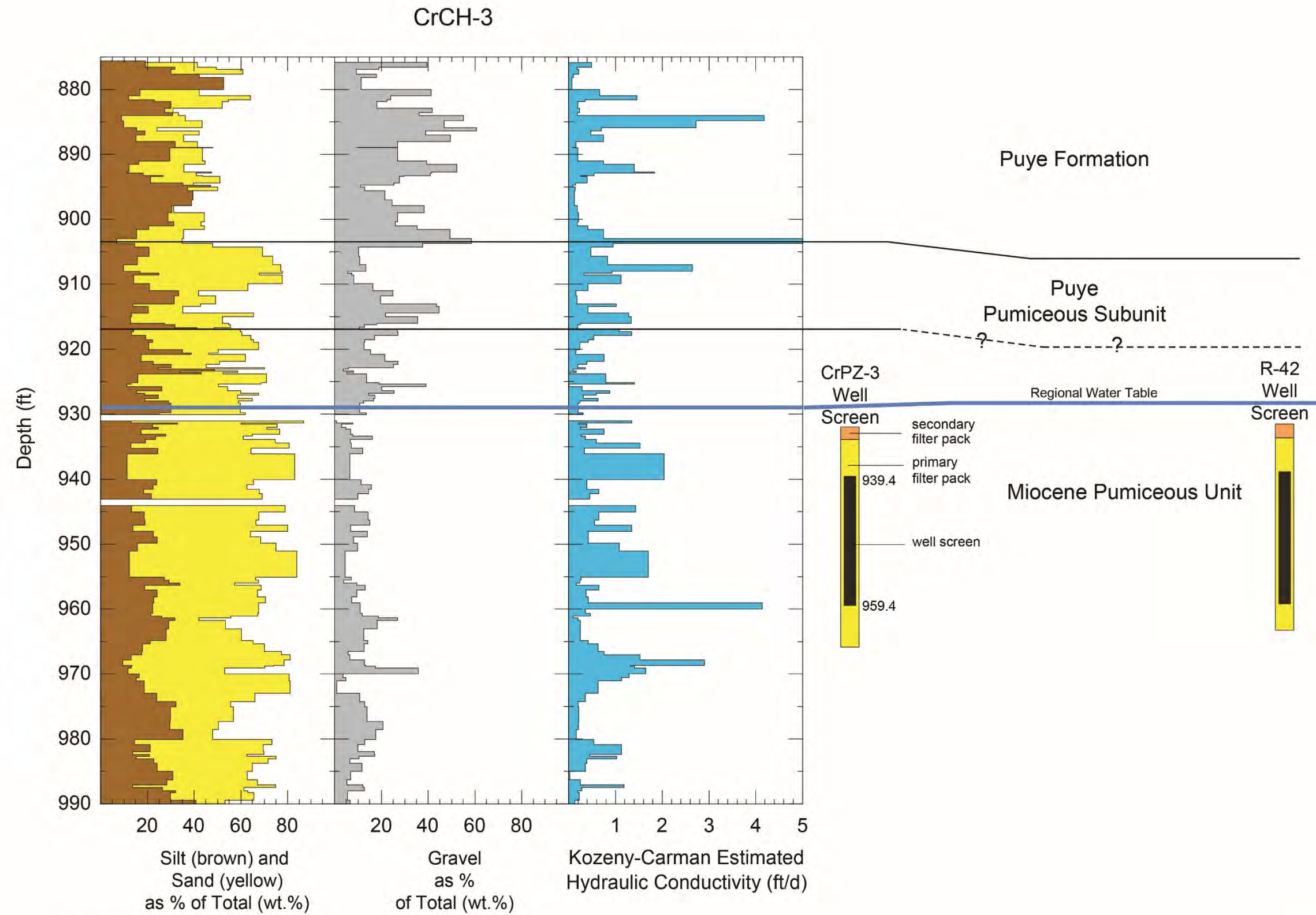


Figure 3.3-8 XRF data comparing dacite clast compositions in the Puye pumiceous subunit of CrCH-2 with dacitic source rocks that contributed detritus to the Puye Formation. The CrCH-2 dacite clasts are similar in chemistry to those found in the Rendija Canyon Rhyodacite, a major component of the gravels making up the lower part of the Puye Formation.



Note: Gaps indicate no core collected

Figure 3.3-9 CrCH-3 grain-size variations for beds making up strata in the upper part of the regional aquifer. CrPZ-3 (completed in the CrCH-3 borehole) and R-42 well screens are shown for reference.

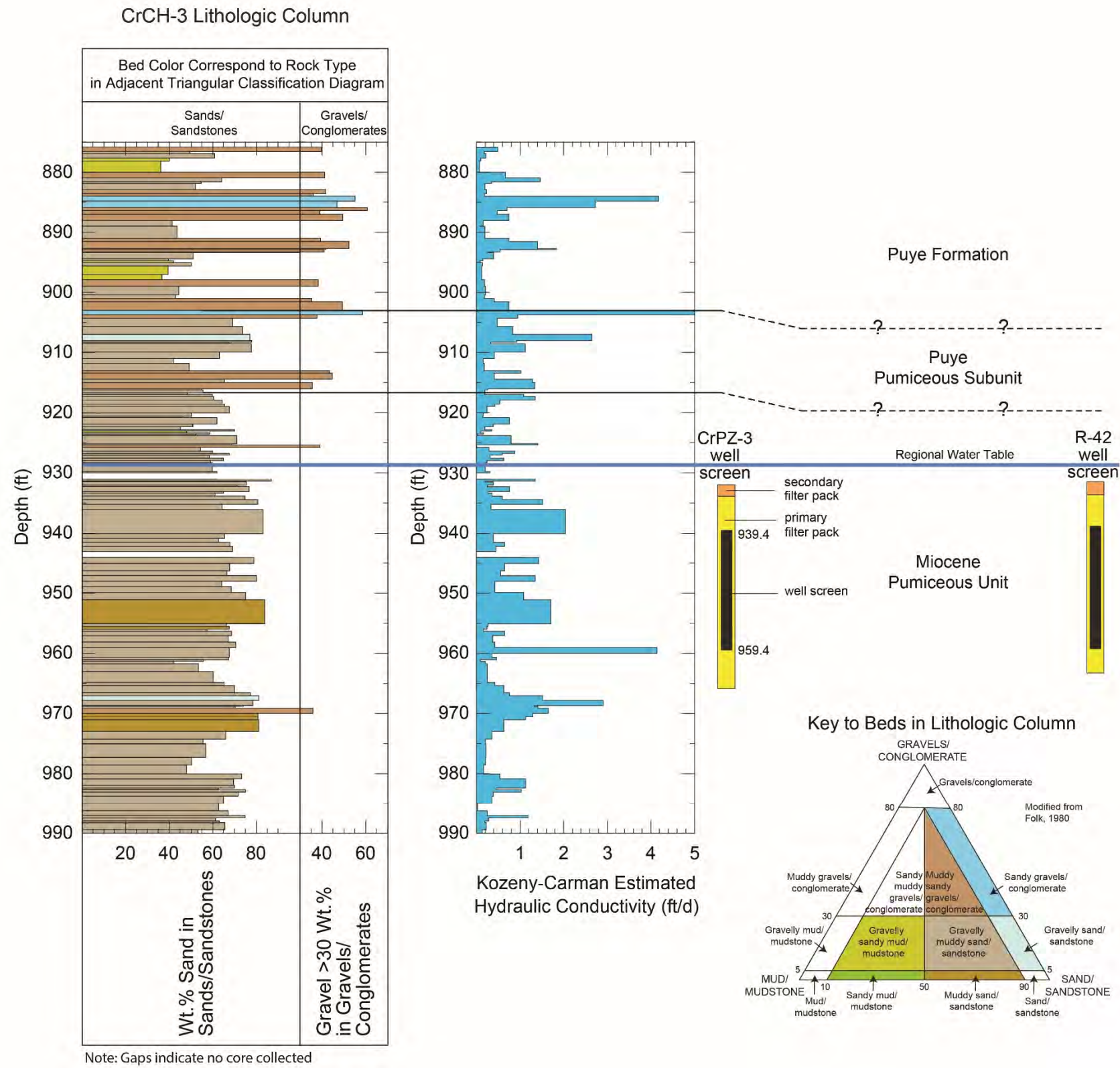


Figure 3.3-10 CrCH-3 lithologic column showing rock types for individual beds making up strata in the upper part of the regional aquifer. CrPZ-3 (completed in the CrCH-3 borehole) and R-42 well screens are shown for reference.

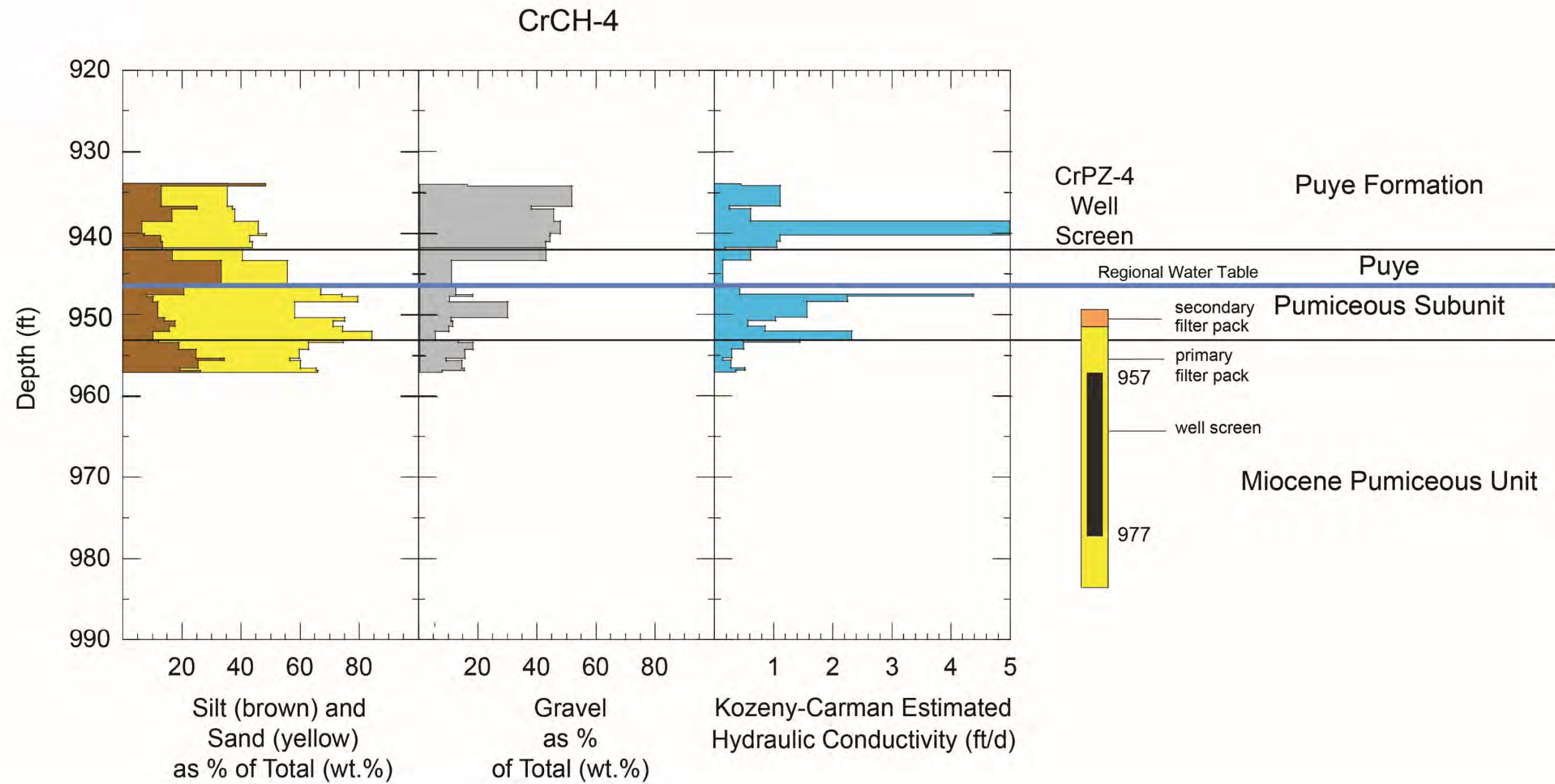


Figure 3.3-11 CrCH-4 grain-size variations for beds making up strata in the upper part of the regional aquifer. CrPZ-4 well screen, which was completed in the CrCH-4 bore hole, is shown for reference.

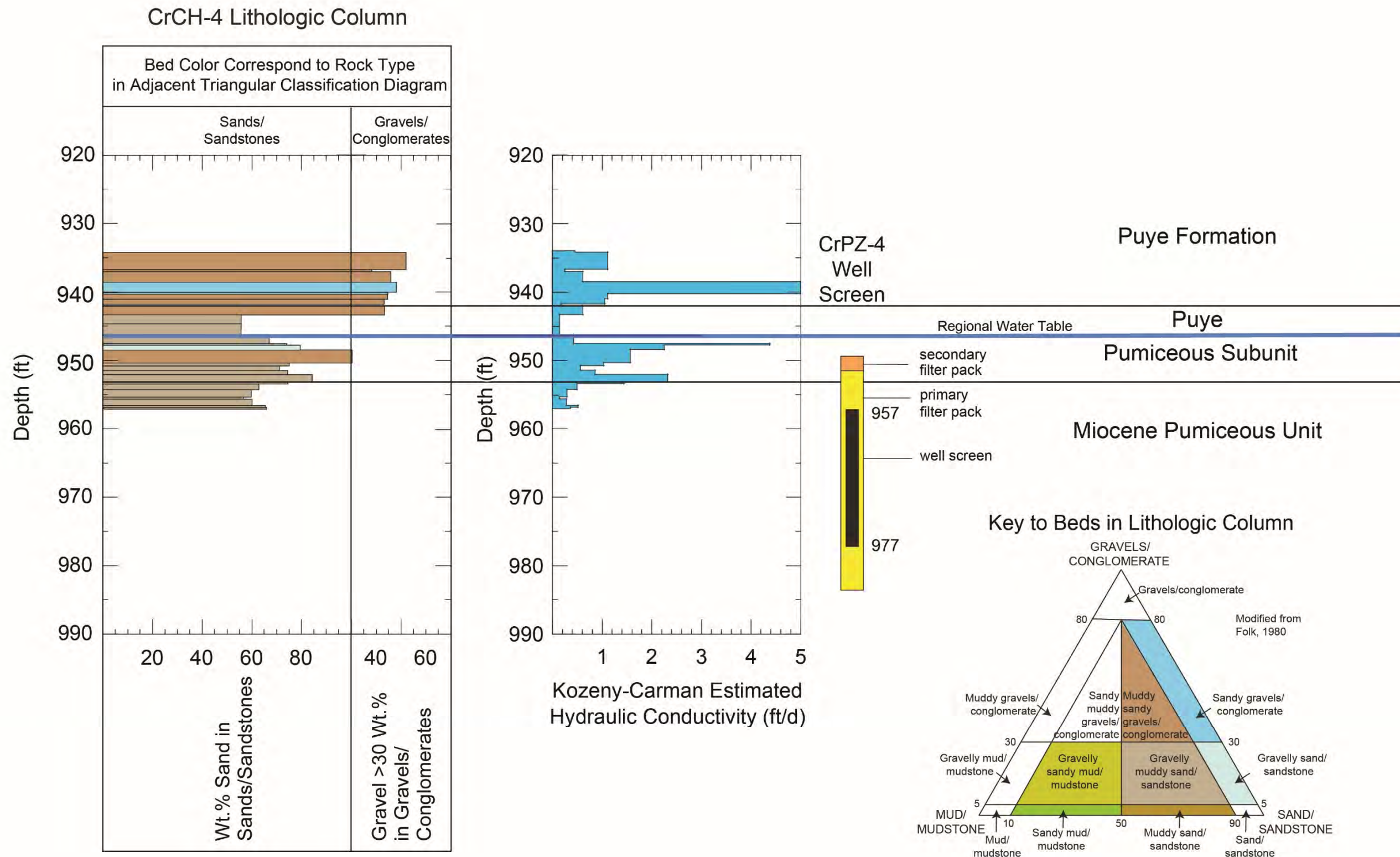


Figure 3.3-12 CrCH-4 lithologic column showing rock types for individual beds making up strata in the upper part of the regional aquifer. CrPZ-4 well screen, which was completed in the CrCH-4 bore hole, is shown for reference.

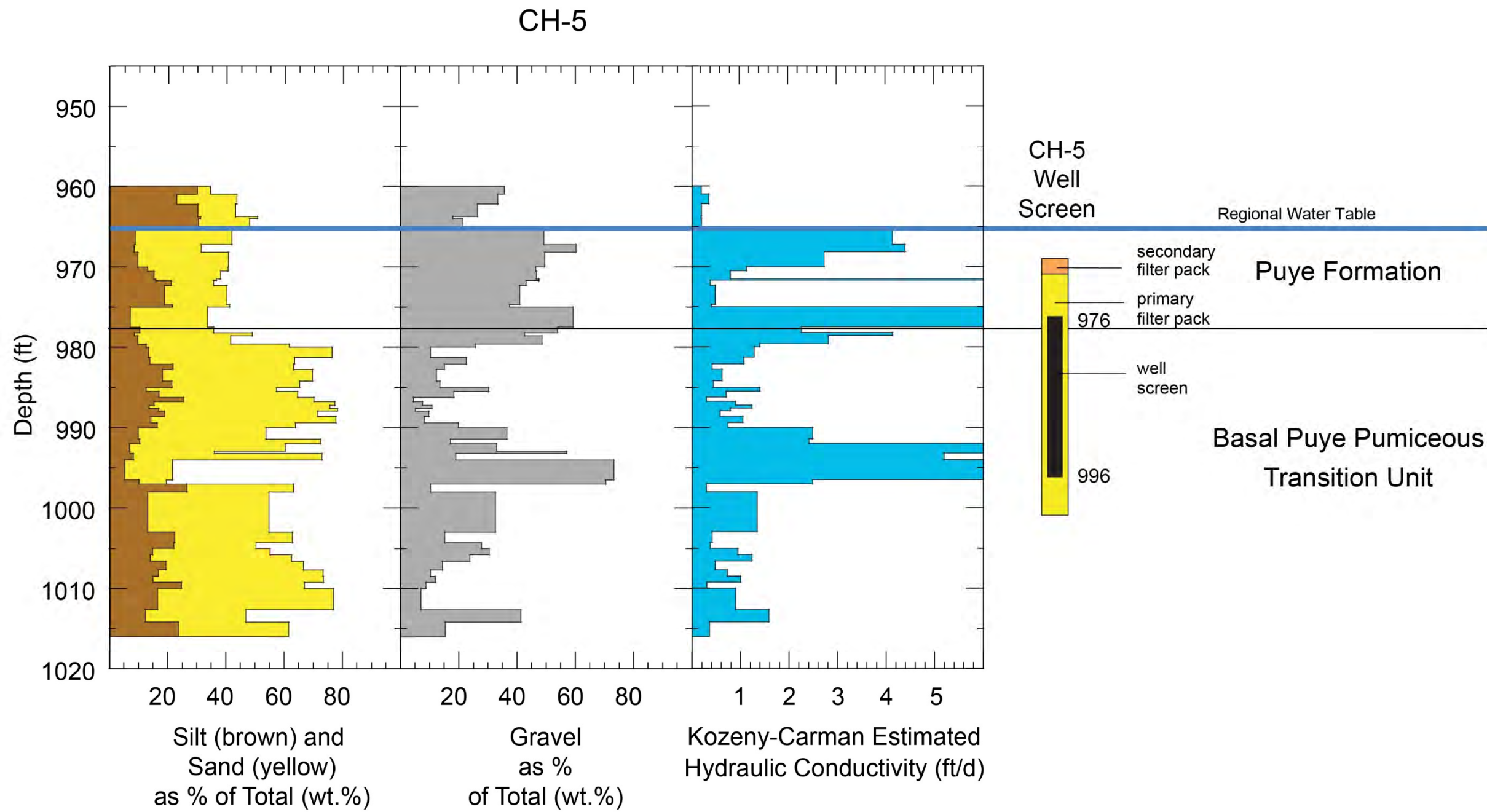


Figure 3.3-13 CrCH-5 grain-size variations for beds making up strata in the upper part of the regional aquifer. CrPZ-5 well screen, which was completed in the CrCH-5 bore hole, is shown for reference.

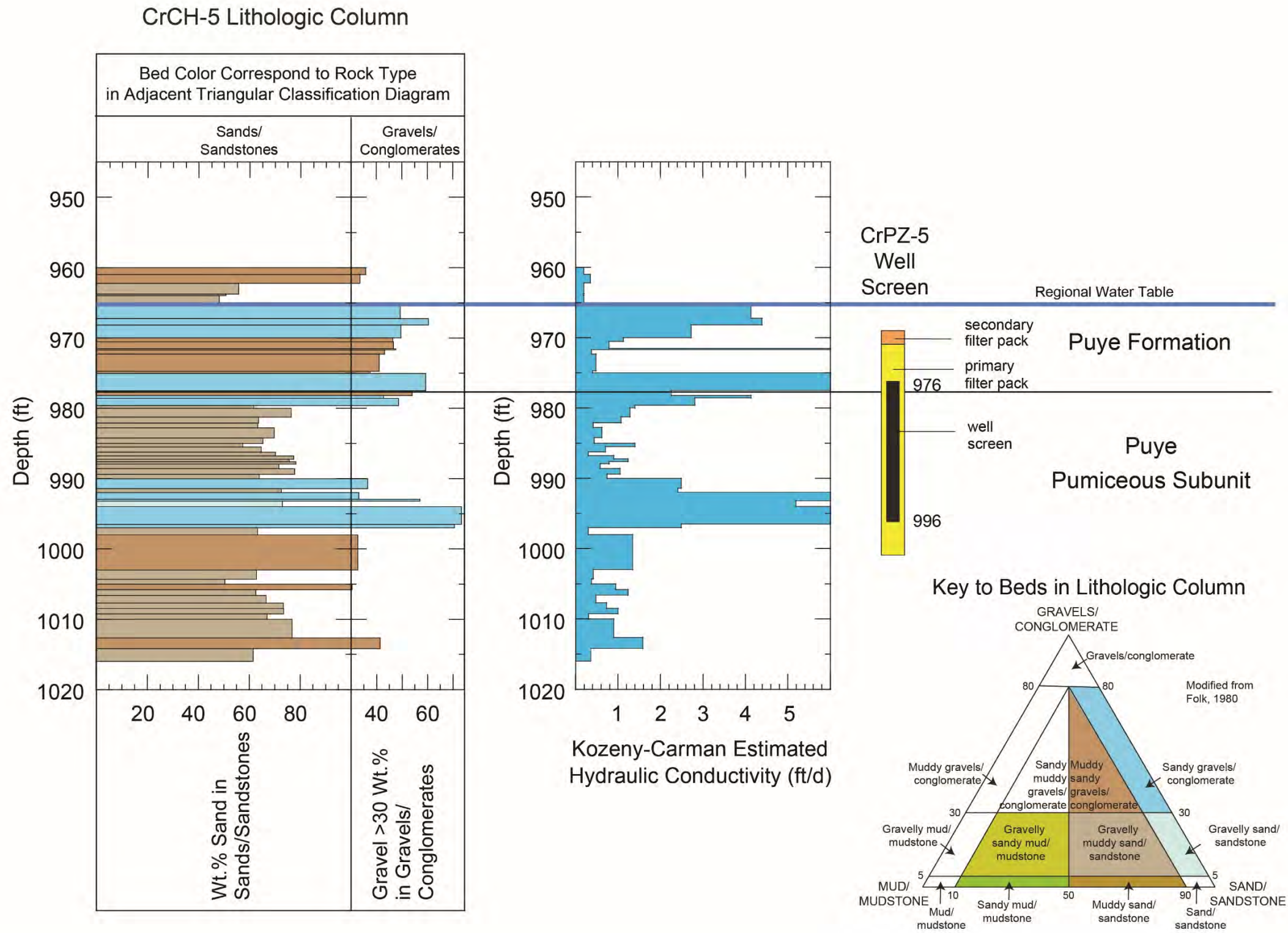


Figure 3.3-14 CrCH-5 lithologic column showing rock types for individual beds making up strata in the upper part of the regional aquifer. CrPZ-5 well screen, which was completed in the CrCH-5 bore hole, is shown for reference.

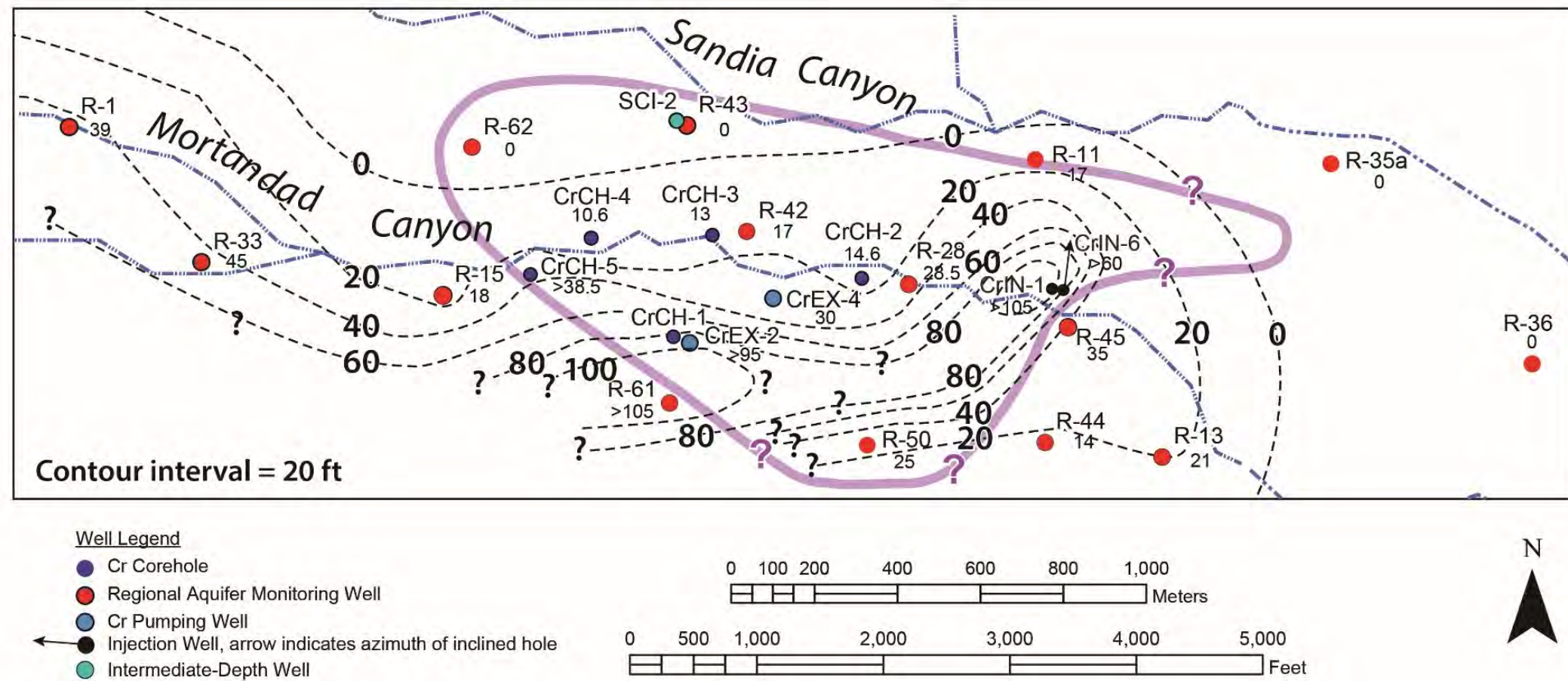


Figure 3.4-1 Isopach map showing thickness of the Puye pumiceous subunit [Tpf(p)] in the vicinity of the chromium plume (purple) in Mortandad Canyon. Only wells where the thickness of Tpf(p) was determined are shown.

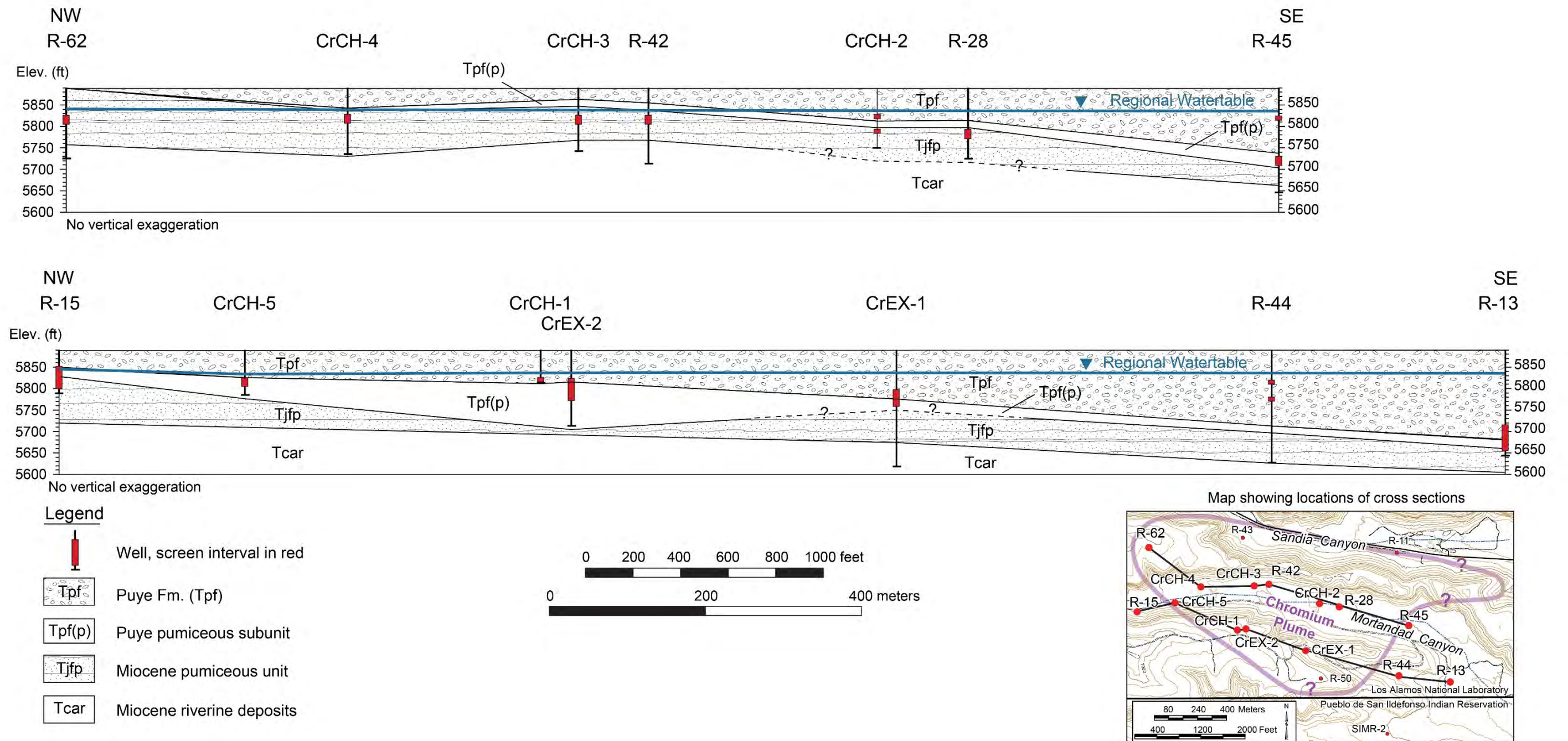


Figure 3.4-2 Geologic cross-sections for the upper part of the regional aquifer along the axis of the chromium contaminant plume in Mortandad Canyon

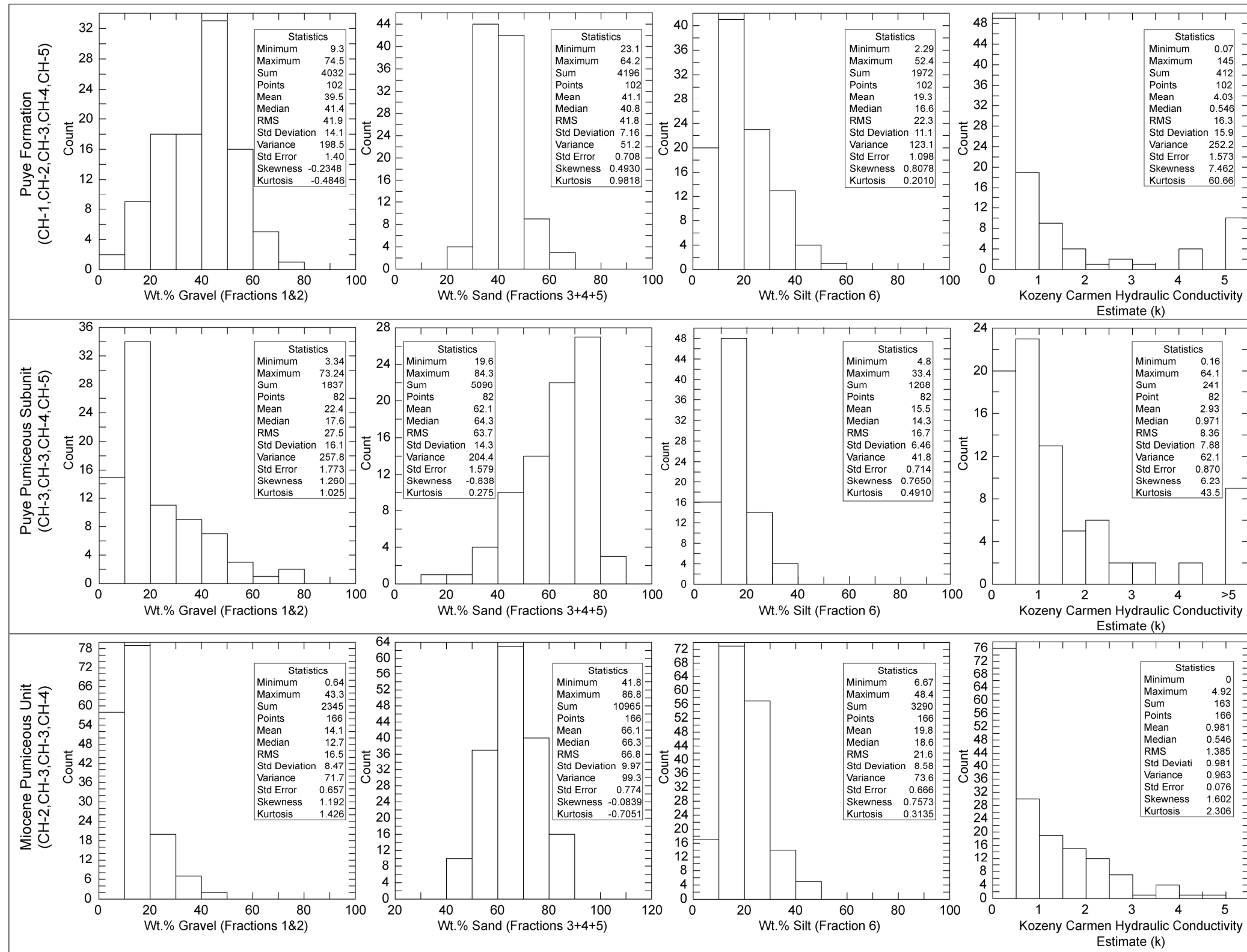


Figure 3.4-3 Histograms for grain size and estimated hydraulic conductivity of Pliocene and Miocene rocks in the upper regional aquifer beneath Mortandad Canyon

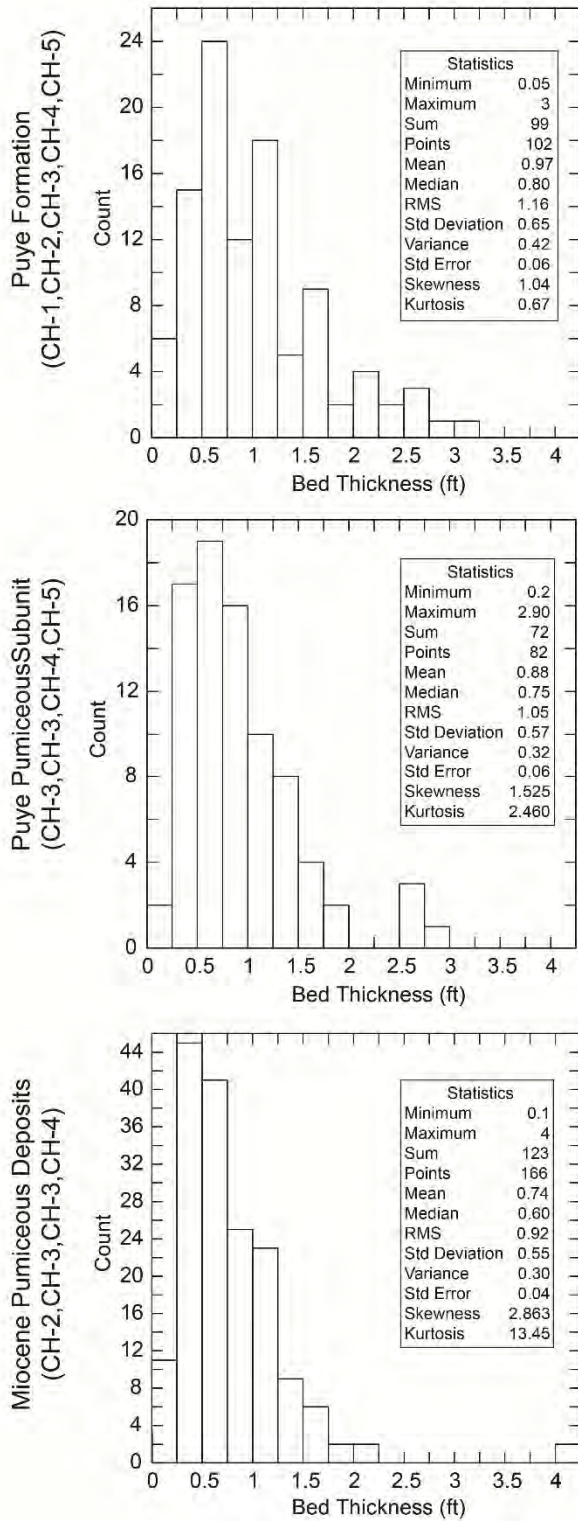


Figure 3.4-4 Histograms for bedding thickness of Pliocene and Miocene rocks in the upper regional aquifer beneath Mortandad Canyon

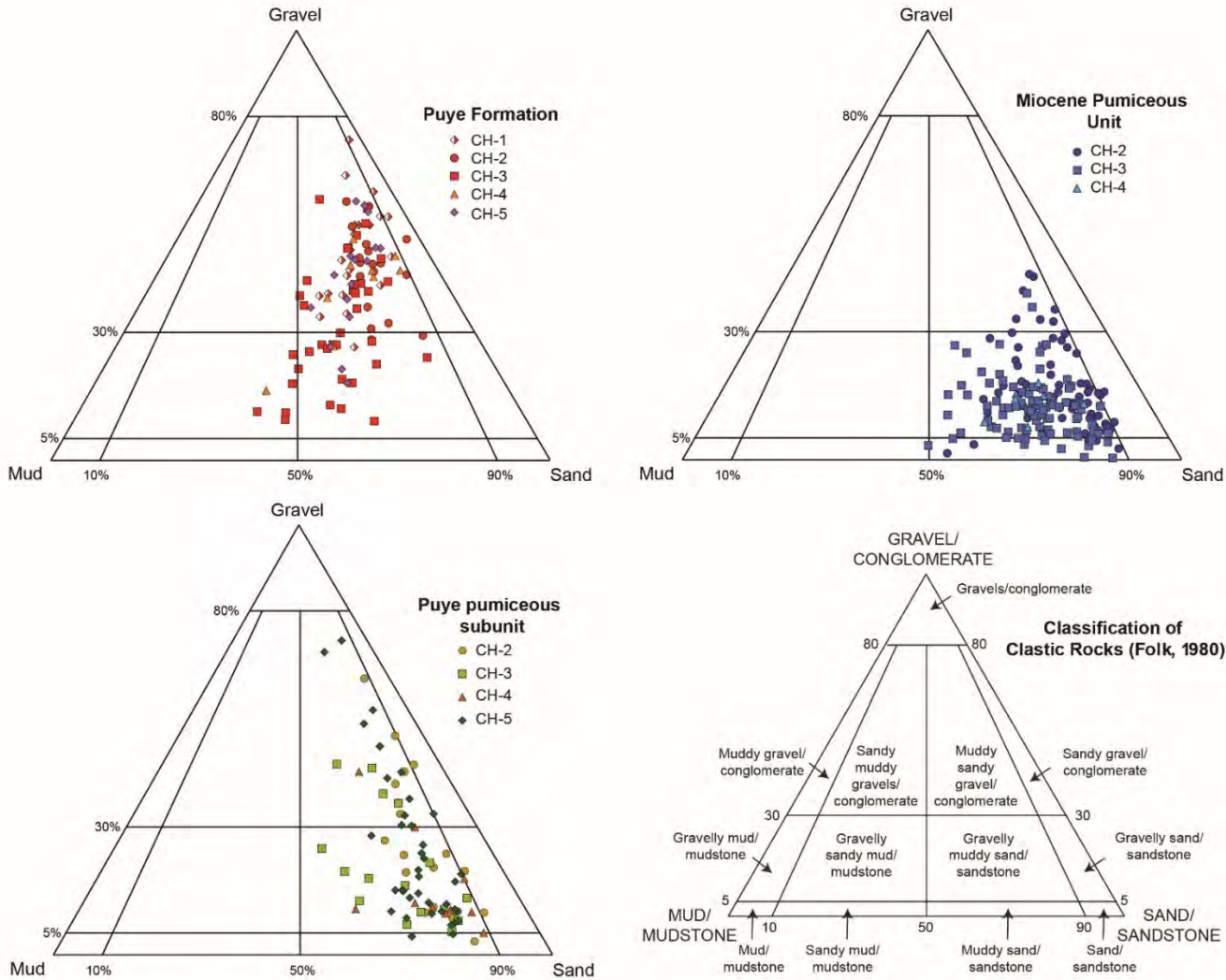


Figure 3.4-5 Folk (1980) clastic rock classification applied to the Pliocene and Miocene rocks at the top of the regional aquifer beneath Mortandad Canyon based on particle-size data for cores collected from CrCH-1, CrCH-2, CrCH-3, CrCH-4, and CrCH-5

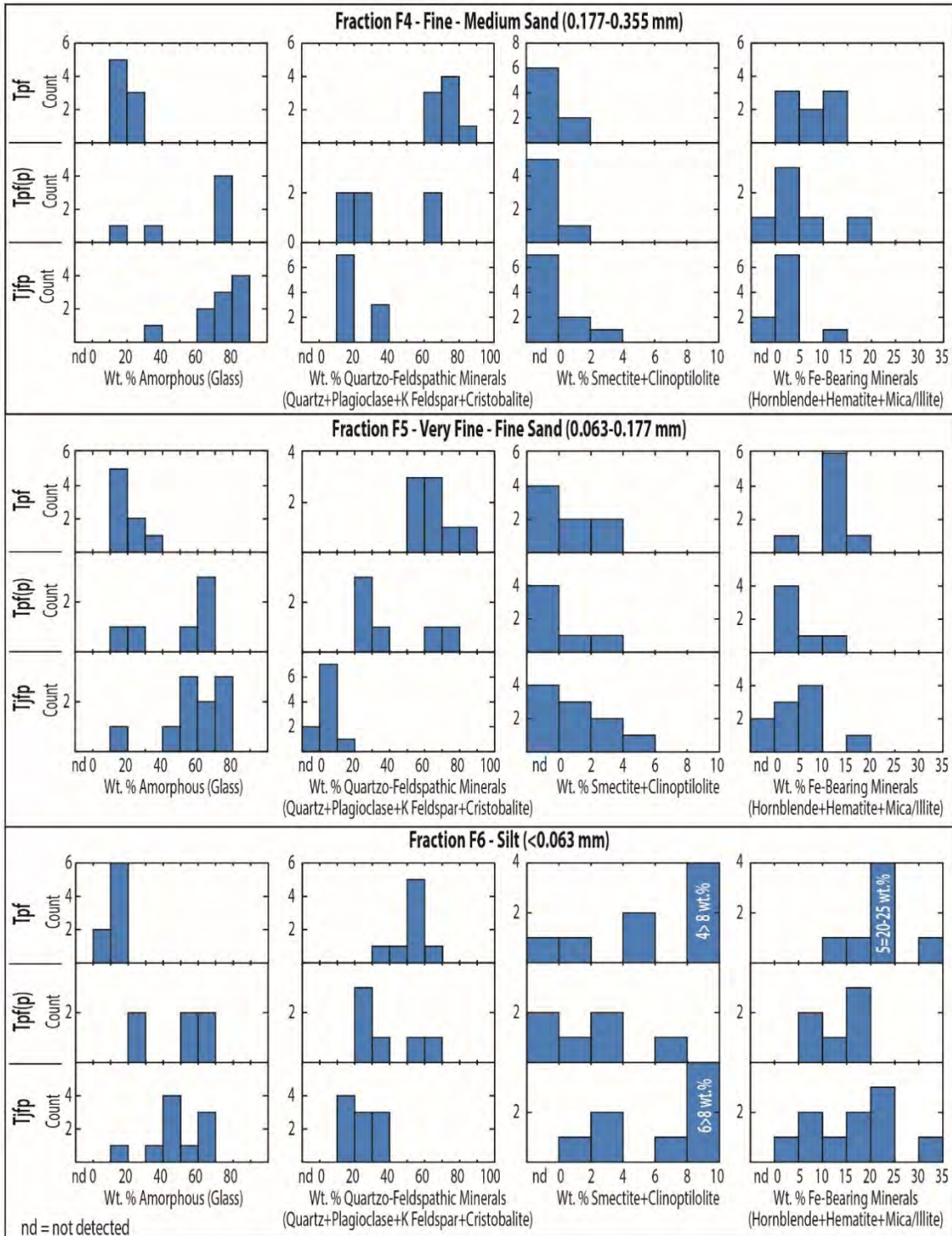


Figure 3.4-6 Histograms showing selected mineralogy for the F4, F5, and F6 particle-size fractions of Pliocene and Miocene rocks in the upper regional aquifer beneath Mortandad Canyon. Rock units include the Puye Formation (Tpf), Puye pumiceous subunit [Tpf(p)], and Miocene pumiceous unit (Tjfp). nd indicates Not detected by XRD

.

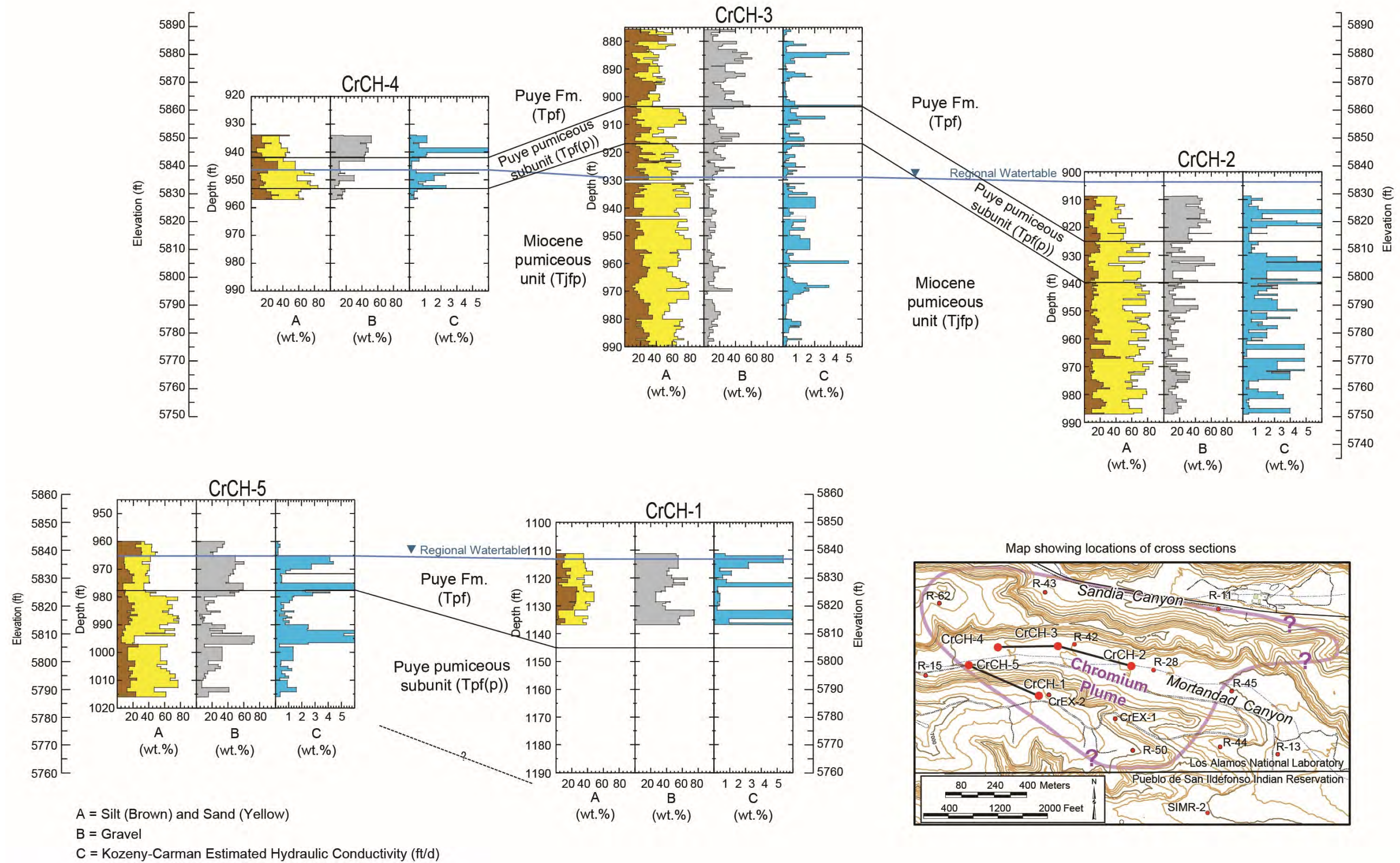


Figure 3.4-7 Schematic cross-sections portraying the aquifer hydraulic structure based on particle-size data and estimates of hydraulic conductivity for CrCH-1, CrCH-2, CrCH-3, CrCH-4, and CrCH-5

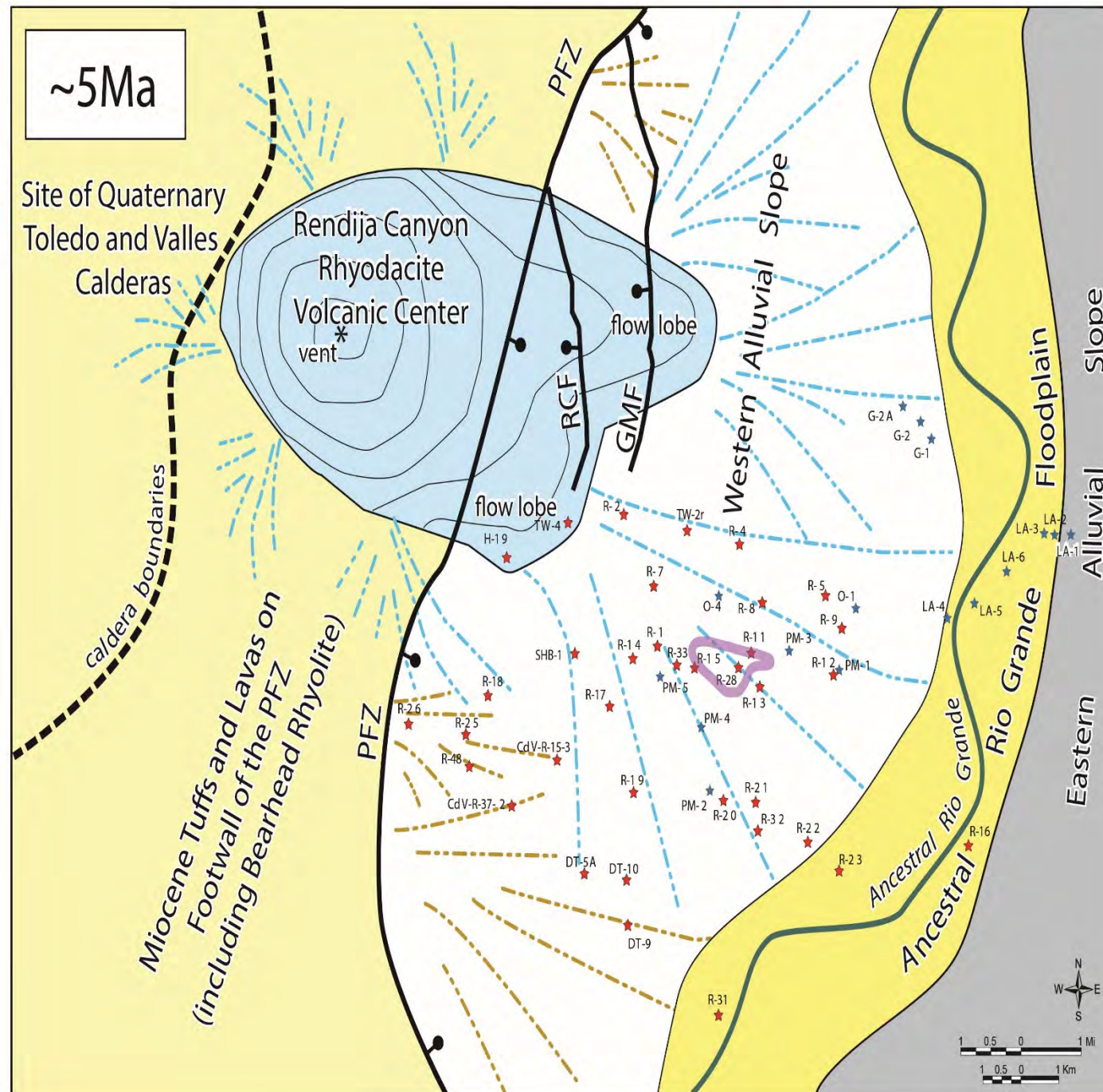


Figure 3.4-8 Early Pliocene (~5 Ma) paleo-geographic map for the western Española basin showing the eruption of the Rendija Canyon Rhyodacite from a volcanic center west of the Pajarito fault zone (PFZ) and contemporaneous deposition of the lower Puye Formation in the western Española basin. Volcanism coincides with tectonism along the PFZ, and the high terrane of the volcanic center is a major source of detritus in alluvial fans that accumulate in the subsiding basin (dashed blue lines). Alluvial fans (brown dashed lines) are also shed from areas of the uplifted footwall block that are underlain by a low- to moderate-relief terrane of Miocene tuffs and lavas that included the Paliza Canyon Formation and Bearhead Rhyolite. Initially, Puye deposits of Tpf(p) in the Chromium Investigation Area (near well R-28) are largely derived from erosion of Miocene Bearhead pumiceous sediments (Tjfp) exposed on the footwall and western alluvial slope but include detritus shed from the early Rendija Canyon volcanic center. As the volcanic center grows, the Rendija Canyon quickly becomes the dominant source of detritus in the Puye Formation. Lobes of lava flow into the western basin. The early Pliocene alluvial fans terminate at the ancestral Rio Grande, which is located 5 to 8 km west of the modern Rio Grande. The location of the Quaternary Toledo and Valles Calderas and selected municipal supply wells (blue stars) and monitoring and test wells (red stars) are shown for spatial reference. RCF = Rendija Canyon fault and GMF = Guaje Mountain fault. Chromium plume >50 ppb shown in purple.

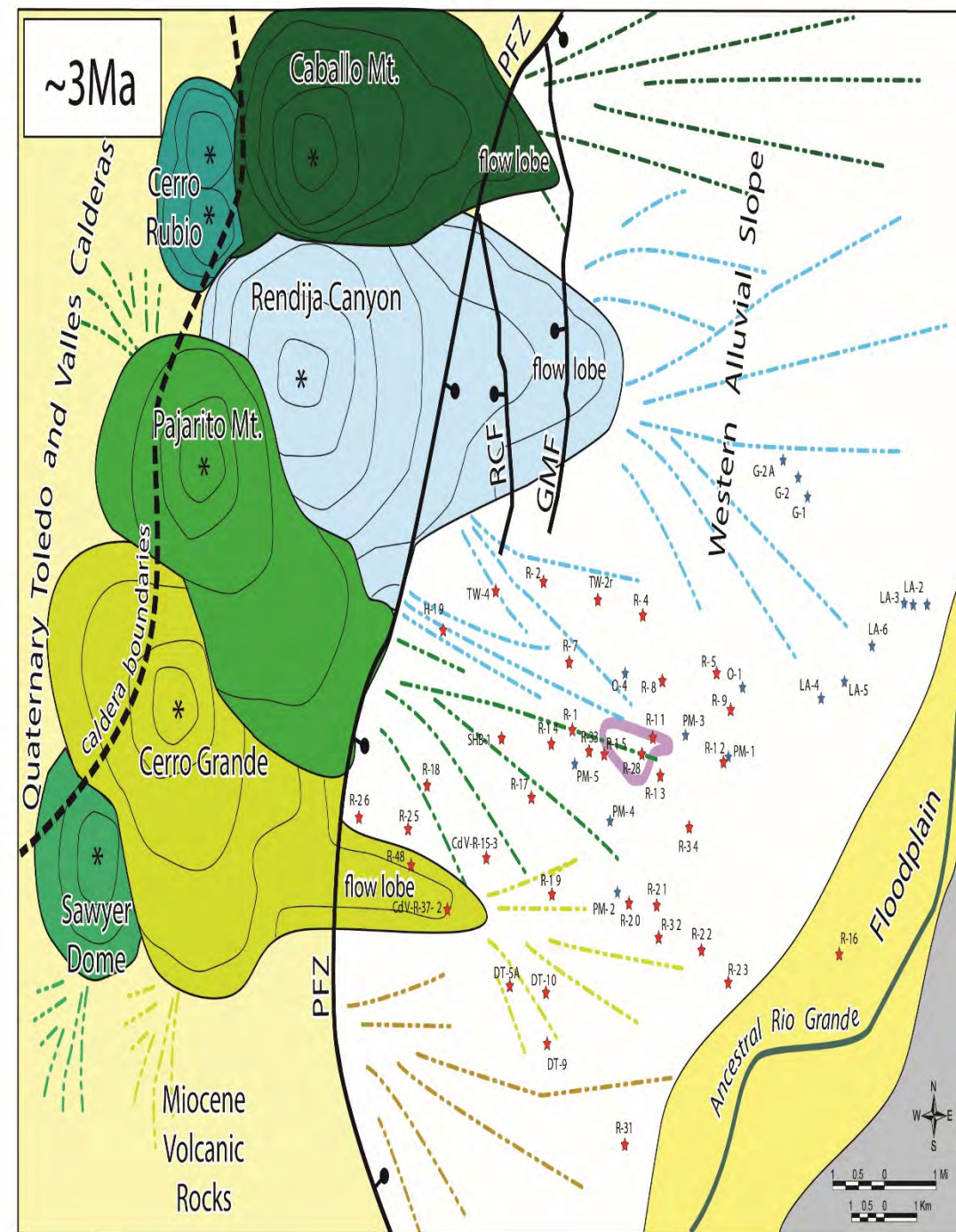


Figure 3.4-9 Middle Pliocene (~3 Ma) paleo-geographic map for the western Española basin showing the eruption of numerous overlapping volcanic centers west of the PFZ and contemporaneous deposition of the upper Puye Formation in the western Española basin. The high terrane formed by the volcanic centers makes up the present-day Sierra de los Valles and is a major source of detritus in coalescing alluvial fans that accumulate in the western Española basin (dashed lines colored by source). Lobes of lava flow into the western basin; the Cerro Grande lobe and part of the Rendija Canyon lobe (near H-19) were subsequently buried by younger Puye deposits. Prograding middle Pliocene alluvial fans push the ancestral Rio Grande eastward to a position similar to the modern Rio Grande. The location of the Quaternary Toledo and Valles Calderas and selected municipal supply wells (blue stars) and monitoring and test wells (red stars) are shown for spatial reference. RCF = Rendija Canyon fault and GMF = Guaje Mountain fault. Chromium plume >50 ppb shown in purple.

Table 3.2-1
Sieve Mesh Sizes, Particle-Size Distributions,
and Grain-Size Classification for Analysis of Strata from CrCH-1 through CrCH-5

U.S. Standard Sieve Mesh #	Fraction	Particle Size (mm)	Phi Size	Grain-Size Classification
5/16 in.	1	≥8	≤-3	Pebbles and cobbles
12-5/16 in.	2	1.7-8	-0.8- -3	Very coarse sand to pebbles
45-12	3	0.355-1.7	1.5- -0.8	Medium to very coarse sand
80-45	4	0.177-0.355	2.5-1.5	Fine to medium sand
230-80	5	0.063-0.177	4-2.5	Very fine to fine sand
≤230	6	≤0.063	≥4	Silt plus clay
>24 h gravity settling	7	≤2 μm	≥9	Clay

Table 3.3-1
Revised Geologic Contacts for Pliocene and Miocene Sedimentary
Rocks of the Regional Aquifer in the Chromium Investigation Area

Well	Tpf/Tpf(p) Contact – Depth in ft (Elev. in ft)	Tpf(p)/Tjfp Depth in ft (Elev. in ft)	Tjfp/Tcar Contact – Depth in ft (Elev. in ft)	Tpf(p) Thickness (ft)	Tjfp Thickness (ft)	Drilling Method	Borehole Geophysics	Comments
CrCH-1 (core)	~1145 (~5797.7)	n/a	n/a	n/a	n/a	Cored	Gamma log only; not deep enough for identifying contacts	Geologic contacts are poorly constrained because coring terminated in Tpf at a depth of 1136.5 ft, before penetrating units Tpf(p) and Tjfp. All of the cores collected above 1136.5 ft depth are characterized by lithic-rich dacitic gravels and sands containing sparse to absent pumice. Additional constraints on contacts was afforded by material embedded in the bottom of a core string that dropped several hundred feet while being tripped out of the completed borehole. The material retrieved from the bottom of the core string consisted of highly pumiceous sand and gravel that is presumably Tpf(p). The Tpf/Tpf(p) contact is placed at ~1145 ft, the same depth the contact was encountered at CrEX-2 on the same drill pad.
CrCH-2 (core)	925 (5812.7)	939.6 (5798.1)	>987 (<5750.7)	14.6	>47.4	Cored	Gamma log only; not deep enough for identifying contacts	Typical Tpf, above a depth of 925 ft, is represented by lithic-rich dacitic gravels and sands containing sparse to absent pumice. In Tpf(p), from 925-939.6 ft depth, pumice abundances notably increase in an interval characterized by mixed lithic-pumiceous deposits that include common Rendija lava clasts. In Tjfp, below 939.6 ft depth, the cuttings are highly pumiceous and Rendija lava clasts are absent. The borehole TD is 987 ft depth.
CrCH-3 (core)	903.7 (5861.5)	916.7 (5848.5)	1001 (5764.2)	13	84.3	Cored	Gamma log only; not useful for identifying contacts	Typical Tpf, above a depth of 903.7 ft, is represented by lithic-rich dacitic gravels and sands containing sparse to absent pumice. In Tpf(p), from 903.73-916.7 ft depth, pumice abundances notably increase in an interval characterized by mixed lithic-pumiceous deposits that include common Rendija lava clasts. In Tjfp, below 916.7 ft depth, the cuttings are highly pumiceous and Rendija lava clasts are absent. Core from 991-1019 ft depth was not examined; core from 1019-1023 ft (TD) depth is made up of Tcar riverine gravels and sands.
CrCH-4 (core)	942.5 (5842.2)	953.1 (5831.6)	>1047 (<5737.7)	10.6	>98.6	Cored	Gamma log only; log run in completed well and not useful for identifying contacts	Typical Tpf, above a depth of 943.3 ft, is represented by lithic-rich dacitic gravels and sands containing sparse to absent pumice. In Tpf(p), from 943.3-948.4 ft depth, pumice abundances notably increase in an interval characterized by mixed lithic-pumiceous deposits that include common Rendija lava clasts. In Tjfp, below 953.1 ft depth, the cuttings are highly pumiceous and Rendija lava clasts are absent. Core from 957-1047 ft (TD) depth was not examined.

Table 3.3-1 (continued)

Well	Tpf/Tpf(p) Contact – Depth in ft (Elev. in ft)	Tpf(p)/Tjfp Depth in ft (Elev. in ft)	Tjfp/Tcar Contact – Depth in ft (Elev. in ft)	Tpf(p) Thickness (ft)	Tjfp Thickness (ft)	Drilling Method	Borehole Geophysics	Comments
CrCH-5 (core)	977.5 (5825.1)	>1016 (<5786.6)	n/a	>38.5	n/a	Cored	Gamma log only; not useful for identifying contacts	Typical Tpf, above a depth of 977.5 ft, is represented by lithic-rich dacitic gravels and sands containing sparse to absent pumice. In Tpf(p), from 977.5-1016 ft (TD) depth, pumice abundances notably increase in an interval characterized by mixed lithic-pumiceous deposits that include common Rendija lava clasts. The borehole was not deep enough to penetrate the base of Tpf(p).
CrEX-2	1145 (5807)	>1240 (<5712)	n/a	>95	n/a	11-in drill casing advanced to TD	JetWest gamma and neutron logs; not useful for identifying contacts	Typical Tpf, above a depth of 1145 ft, is represented by lithic-rich dacitic gravels and sands containing sparse to absent pumice. In Tpf(p), from 1145-1230 ft depth, pumice abundances notably increase in an interval characterized by highly-pumiceous deposits that include common to abundant Rendija lava clasts at depths of 1145-1155 ft and 1205-1240 ft. The borehole was not deep enough to penetrate the base of Tpf(p).
CrEX-4 (washed cuttings)	925 (5828)	955 (5798)	1015 (5738)	30	>60	14-in drill casing advanced to TD	JetWest gamma and neutron logs; not useful for identifying contacts	Typical Tpf, above a depth of 925 ft, is represented by lithic-rich dacitic gravels and sands containing sparse to absent pumice. In Tpf(p), from 925-955 ft depth, pumice abundances notably increase in an interval characterized by highly-pumiceous deposits that include common to abundant Rendija lava clasts. Upper and lower Tpf(p) contacts are placed in middle of 10-ft cuttings intervals where the transition takes place. In Tjfp, from 955-1015 ft depth, the cuttings contain abundant Bearhead pumice, rhyolite lava, and perlite sand and gravel. Rendija lava clasts are sparse throughout the interval and may represent incomplete evacuation of drill cuttings from overlying Tpf. The transition between Tjfp and Tcar occurs in the 1010- to 1020-ft cuttings interval and the contact is placed at 1015 ft.
CrIN-1 (washed cuttings)	955 (5753)	>1060 (<5648)	n/a	>105	n/a	14-in drill casing advanced to TD	JetWest gamma and neutron logs; not useful for identifying contacts	Typical Tpf, above a depth of 955 ft, is represented by lithic-rich dacitic gravels and sands containing sparse to absent pumice. In Tpf(p), the upper contact is placed at 955 ft depth, in the middle of the 950- to 960-ft cuttings interval where Bearhead pumices become abundant. Tpf(p) is characterized by mixed lithic-pumiceous cuttings that include common to abundant Rendija lava clasts.
CrIN-6 (washed cuttings)	933.5 (5774.5)	>994.2 (<5714)	n/a	>60.7	n/a	14-in drill casing advanced to TD	JetWest gamma and neutron logs; not useful for identifying contacts	Borehole drilled inclined 25° from vertical; depths of contacts corrected to show true depth below the drill pad. Typical Tpf, above a depth of 933.5 ft, is represented by lithic-rich dacitic gravels and sands containing sparse to absent pumice. In Tpf(p), Bearhead pumices become abundant and lithologies include mixed lithic-pumiceous cuttings that include common Rendija lava clasts.
R-1 (sieved cuttings in chip trays)	985 (5900)	1024 (5861)	>1165 (<5720)	39	>141	Drilled as an uncased open drill hole.	Full suite of Schlumberger open-hole logs.	Typical Tpf, above a depth of 985 ft, is represented by lithic-rich dacitic gravels and sands containing sparse to absent pumice. The Tpf/Tpf(p) contact is above the water level and was not imaged by the FMI log. However, there is an increase in porosity below 985 ft. In Tpf(p), from 985-1024 ft depth, pumice abundance notably increases in an interval characterized by mixed lithic-pumiceous deposits that include abundant Rendija lava clasts. The FMI log shows a sharp transition at 1024 ft depth from thick sands and gravelly sands above to thinner sands beds below. Also, porosity and conductivity increase below this contact. In Tjfp, from 1024-1165 ft depth, the cuttings are highly pumiceous, although Rendija lava clasts are relatively common throughout the interval (to the TD of 1165 ft depth). The occurrence of Rendija lava clasts in Tjfp is assumed to be the result of sloughing and incomplete evacuation of Tpf cuttings in an uncased open borehole.
R-11 (washed cuttings)	866 (5806)	883 (5789)	>926.5 (<5745.5)	17	>43.5	Drilled as an uncased open drill hole.	Full suite of Schlumberger open-hole logs.	Typical Tpf, above a depth of 866 ft, is represented by lithic-rich dacitic gravels and sands containing sparse to absent pumice. The Tpf/Tpf(p) contact is imaged by the FMI log and is marked by a transition from thick cobble and gravel beds in Tpf to thinner sandy and gravelly beds in Tpf(p). Porosity is greater and density is less in Tpf(p) relative to Tpf. Tpf(p) cuttings are characterized by mixed lithic-pumiceous deposits that include abundant Rendija lava clasts and subordinate Bearhead pumice. In Tjfp, from 883-926.5 ft depth, the cuttings contain abundant Bearhead pumice, rhyolite lava, and perlite sand and gravel. Rendija lava clasts are sparse in Tjfp and are assumed to be the result of sloughing and incomplete evacuation of Tpf cuttings in an uncased open borehole. Relative to Tpf(p), Tjfp is characterized by 1) an increase in porosity, 2) a slight decrease in ECS silica and an increase in ECS iron, and 3) decreases in spectral gamma potassium and uranium.
R-13 (sieved cuttings in chip trays)	991 (5682.1)	1012 (5661.1)	1068 (5605.1)	21	56	12-in drill casing advanced to 1089 ft; open-hole drilling from 1089 to 1133 ft. After reaching TD, the 12-in casing was removed so open hole	Full suite of Schlumberger open-hole logs.	The cuttings data indicate geologic contacts that are 6-7 ft deeper than those indicated by the geophysical logs. We consider the depth control provided by the Schlumberger wireline logs to be more reliable than the depth control for cuttings. Consequently, we used the geophysical logs to define the Tpf/Tpf(p) and Tpf(p)/Tjfp contacts. Typical Tpf, above a depth of 998 ft, is represented by cuttings of lithic-rich dacitic gravels and sands containing sparse to absent pumice. The Tpf/Tpf(p) contact appears to be at a depth of 991 ft based on the FMI log that shows a dramatic change downhole from thick boulder and cobble beds to thinner sandy beds. The bedding transition at 991 ft depth is accompanied downhole by: 1) an increase in spectral-gamma potassium and thorium, 2) a decrease in bulk density, 3) an increase in neutron porosity, and 4) an increase in ECS silica and decrease in ECS iron. In Tpf(p), from 998-1018 ft depth, cuttings alternate between highly pumiceous deposits with common Rendija lavas and pumice-poor gravelly zones with abundant Rendija clasts. The FMI log suggests the Tpf(p)/Tjfp contact is at a depth of at 1012 ft depth where there is a sharp transition downhole from thick sands and

Table 3.3-1 (continued)

Well	Tpf/Tpf(p) Contact – Depth in ft (Elev. in ft)	Tpf(p)/Tjfp Depth in ft (Elev. in ft)	Tjfp/Tcar Contact – Depth in ft (Elev. in ft)	Tpf(p) Thickness (ft)	Tjfp Thickness (ft)	Drilling Method	Borehole Geophysics	Comments
						geophysical logs could be collected below 847 ft.		gravelly sands to thinner sands beds. Also, density decreases and porosity and conductivity increase below 1012 ft depth. In Tjfp, from 1012 to 1068 ft depth, the cuttings are highly pumiceous and Rendija lava clasts are rare to absent. We assume the rare Rendija clasts in this interval are contaminants left over from incomplete evacuation of Tpf cuttings as the borehole advanced. The contact between Tjfp and Tcar riverine deposits is sharp at 1068 ft in cuttings.
R-15 (washed cuttings)	973 (5847)	991 (5829)	1100 (5720)	18	109	12-in drill casing advanced to TD	Gamma log only; not useful for identifying contacts	Typical Tpf, above a depth of 973 ft, is represented by lithic-rich dacitic gravels and sands containing sparse to absent pumice. In Tpf(p), from 973-991 ft depth, pumice abundances notably increase in an interval mixed lithic-pumiceous deposits that include common Rendija lava clasts. In Tjfp, from 991-1100 ft depth, pumice abundances notably increase (generally >50% of the cuttings) in an interval that contains rare to absent Rendija lava clasts. We assume the rare Rendija clasts in this interval are contaminants left over from incomplete evacuation of Tpf cuttings as the borehole advanced.
R-28 (sieved cuttings in chip trays)	939 (5789.5)	967.5 (5761)	>1005 (<5723.5)	28.5	>37.5	Drilled as an uncased open drill hole.	Full suite of Schlumberger open-hole logs.	Typical Tpf represented by lithic-rich dacitic gravels and sands in cuttings containing sparse to absent pumice above a depth of 940 ft. The base of Tpf is placed at 939 ft where the FMI log shows a sharp transition downhole from thick boulder and cobble beds to thinner sandy beds. The contact at 939 ft depth coincides with (downhole): 1) an increase in spectral-gamma potassium and thorium, 2) a decrease in bulk density, 3) an increase in neutron porosity, and 4) an increase in ECS silica and a decrease in ECS iron. Tpf(p) is represented cuttings in the 940-970 ft depth interval which are characterized by deposits rich in Rendija lava clasts and subordinate (5-30%) white pumices. The Tpf(p)/Tjfp contact is placed at 967.6 ft depth where the FMI log shows a transition to thick-bedded sands above to thinner beds of sand below; this bedding change is accompanied downhole by 1) a slight decrease in neutron porosity and 2) a slight decrease in ECS silica and an increase in ECS iron. In Tjfp, from 967.5-1005 ft (TD) depth, there is a sharp increase in pumice abundance (50% or greater), although Rendija lavas are also fairly common. The occurrence of Rendija lava clasts in Tjfp is assumed to be the result of sloughing and incomplete evacuation of Tpf cuttings in an uncased open borehole.
R-33 (sieved cuttings in chip trays)	965 (5888.3)	1010 (5843.3)	1122 (5731.3)	45	112	Drilled as an uncased open drill hole.	Full suite of Schlumberger open-hole logs.	Typical Tpf, above a depth of 970 ft, is represented by cuttings of lithic-rich dacitic gravels and sands containing sparse to absent pumice. The Tpf/Tpf(p) contact appears to be at a depth of 965 ft based on downhole changes in the geophysical logs, including: 1) an increase in spectral-gamma potassium and thorium, 2) a decrease in bulk density, 3) an increase in neutron porosity, and 4) an increase ECS silica and a decrease in ECS iron. Tpf(p) is tentatively identified in the 965-1010 ft depth interval where pumice abundances notably increase in deposits characterized by mixed lithic-pumiceous deposits that include abundant Rendija lava clasts. Note that cuttings returns were of poor quality through much of this interval, especially from 985-1005 ft depth, which had no cuttings returns. Tpf(p), In Tjfp, from 1010-1120 ft depth, cuttings are highly pumiceous (>50%), but 1-5% Rendija lava clasts are present throughout the interval. The occurrence of Rendija lava clasts in Tjfp is assumed to be the result of sloughing and incomplete evacuation of Tpf cuttings in an uncased open borehole. Borehole geophysical logs show a uniform increase in electrical conductivity below 1015 ft, possibly reflecting more abundant silt and very fine sand in Tjfp. Tcar riverine gravels and sands first appear in 1120-1125 ft cuttings interval.
R-35a	Base of Tpf at 882 (5741.1)	Tpf(p) absent	900 (5723.1)	0	12	10-in drill casing advanced to TD	Limited suite of Schlumberger cased-hole logs.	Typical Tpf, above a depth of 882 ft, is represented by cuttings of lithic-rich dacitic gravels and sands containing sparse to absent pumice. Tpf(p) appears to be absent and the Tpf is underlain by Tjfp that is made up of highly pumiceous Bearhead sands and gravels. Rendija lava clasts in Tjfp are rare to absent. The contact between Tjfp and Tcar, at a depth of 900 ft, is marked by the abrupt appearance of riverine deposits of well-rounded gravels made up of intermediate and felsic lavas and 5-10% quartzite and lithic-crystal sands containing minor microcline. The Tjfp/Tcar contact coincides with an abrupt decrease in gamma activity downhole. Tcar riverine deposits occur between depths of 900 and 935 ft. Below 935 ft, Tcar is primarily made up of subangular to subrounded dacitic gravels and sands containing variable amounts of silt and pumice. These Tcar dacitic gravels probably represent Miocene basin-fill derived from the Jemez Mountain volcanic field. Miocene basalt Tb2 was encountered 1136- to 1144-ft depth.
R-36	Base of Tpf at 800 (5791.4)	Tpf(p) absent	Tjfp absent	0	0	10-in drill casing advanced to TD	Gamma log only; run inside drill casing at TD of 865 ft	Tpf is made up of a typical assemblage of lithic-rich dacitic gravels and sands 545- to 575-ft and 705-ft to 800-ft depth intervals. Tpf deposits in the 575- to 705-ft depth interval is a thick sequence of riverine deposits that include variable amounts of Rendija Rhyodacite clasts. The contact between Tpf and Tcar, at a depth of 800 ft, is marked by the abrupt appearance of riverine deposits of well-rounded gravels made up of intermediate and felsic lavas and 5-10% quartzite and lithic-crystal sands containing minor microcline. The Tpf/Tcar contact coincides with an abrupt decrease in gamma activity downhole.
R-42 (sieved cuttings in chip trays)	903 (5856)	920 (5839)	990 (5769)	17	70	12-in drill casing advanced to TD	Limited suite of Schlumberger cased-hole logs.	Typical Tpf, above a depth of 905 ft, is represented by lithic-rich dacitic gravels and sands containing sparse to absent pumice. The Tpf contact is placed at 903 ft where a sharp downhole decrease in bulk density occurs in borehole geophysical logs. In Tpf(p), from 903-920 ft depth, pumice abundances notably increase in an interval characterized by mixed lithic-pumiceous cuttings that include common Rendija lava clasts. In Tjfp, from 920-990 ft depth, the cuttings are highly

Table 3.3-1 (continued)

Well	Tpf/Tpf(p) Contact – Depth in ft (Elev. in ft)	Tpf(p)/Tjfp Depth in ft (Elev. in ft)	Tjfp/Tcar Contact – Depth in ft (Elev. in ft)	Tpf(p) Thickness (ft)	Tjfp Thickness (ft)	Drilling Method	Borehole Geophysics	Comments
								pumiceous and Rendija lava clasts are rare to absent. The upper contact for Tcar riverine deposits is placed at 990 ft, which marks the first appearance of well-rounded intermediate lava and sparse quartzite.
R-43 (sieved cuttings in chip trays)	Base of Tpf at 835 (5897.7)	Tpf(p) absent	905 (5827.7)	0	70	12-in drill casing advanced to TD	Gamma log only; it does not extend to the depths of the geologic contacts of interest.	Typical Tpf, above a depth of 835 ft, is represented by lithic-rich dacitic gravels and sands containing sparse to absent pumice. Mixed lithic-pumiceous deposits of Tpf(p) appear to be absent at well R-43. The Tpf/Tjfp contact is placed at 835 ft where pumice concentrations suddenly increase (>50%) and persist to 905 ft; Rendija lava clasts are rare to absent throughout this interval. We assume the rare Rendija lava clasts below 835 ft are contaminants left over from incomplete evacuation of drill cuttings from overlying Tpf. Tcar riverine gravels and sands first appear in 905-910 ft cuttings interval.
R-44 (sieved cuttings in chip trays)	1003 (5711.9)	1017 (5697.9)	1088 (5626.9)	14	71	12-in drill casing advanced to TD	Limited suite of Schlumberger cased-hole logs.	Typical Tpf, above 1000 ft depth, is represented by lithic-rich dacitic gravels and sands containing sparse to absent pumice. The contact is placed at 1003 ft in the the 1000-1005 ft cuttings interval, which is marked by a downhole increase in spectral-gamma potassium and a decrease in spectral gamma thorium and bulk density. In Tpf(p), from 1003-1017 ft depth, pumice abundances notably increase in cuttings characterized by mixed lithic-pumiceous clasts that include common Rendija lava. In Tjfp, from 1017-1088 ft depth, the cuttings are highly pumiceous and Rendija lava clasts are rare to absent; The contact at 1017 ft is marked by a downhole increase in spectral-gamma activity (primarily as increases in potassium and thorium) and by increases in ECS silica and bulk density. We assume the rare Rendija lava clasts in Tjfp are contaminants left over from incomplete evacuation of drill cuttings from overlying Tpf. Tcar riverine gravels and sands first appear at a depth of 1088 ft.
R-45 (sieved cuttings in chip trays)	965 (5739)	1000 (5704)	1042 (5662)	35	42	12-in drill casing advanced to TD	Limited suite of Schlumberger cased-hole logs.	Typical Tpf, above a depth of 965 ft, is represented by lithic-rich dacitic gravels and sands containing sparse to absent pumice. In Tpf(p), from 965-1000 ft depth, pumice abundance notably increases in an interval characterized by mixed lithic-pumiceous deposits that include common Rendija lava clasts. In Tjfp, from 1000-1042 ft depth, the cuttings are highly pumiceous and Rendija lava clasts are rare to absent. The contact at 1000 ft is marked by downhole increases in ECS silica and spectral-gamma activity (primarily as an increase in potassium), and by a downhole decrease in ECS Fe. We assume the rare Rendija lava clasts in Tjfp are contaminants left over from incomplete evacuation of drill cuttings from overlying Tpf. Tcar riverine gravels and sands first appear at a depth of 1042 ft.
R-50	1155 (5749.1)	1180 (5724.1)	>1225 (<5679.1)	25	>45	12-in drill casing advanced to TD	Limited suite of Schlumberger cased-hole logs.	Typical Tpf, above a depth of 1155 ft, is represented by lithic-rich dacitic gravels and sands containing sparse to absent pumice. In Tpf(p), from 1155-1180 ft depth, pumice abundance notably increases in an interval characterized by mixed lithic-pumiceous deposits that include common Rendija lava clasts. In Tjfp, below 1180 ft depth, the cuttings are highly pumiceous and Rendija lava clasts are rare to absent. We assume the rare Rendija lava clasts in Tjfp are contaminants left over from incomplete evacuation of drill cuttings from overlying Tpf.
R-61	1160 (5780)	>1265 (<5675)	n/a	>105	n/a	12-in drill casing advanced to TD	Gamma log only; not useful for identifying contacts	Typical Tpf, above a depth of 1160 ft, is represented by lithic-rich dacitic gravels and sands containing sparse to absent pumice. In Tpf(p), below 1160 ft depth, deposits are generally highly pumiceous but include intervals of mixed pumiceous-lithic sands and gravels that include variable amounts of Rendija lava clasts ranging from sparse to common. Rendija clasts are especially common below 1235 ft depth.
R-62 (sieved cuttings in chip trays)	Base of Tpf at 1095 (5889.9)	Tpf(p) absent	1228 (5756.9)	0	133	12-in drill casing advanced to TD	Gamma log only; not useful for identifying contacts	Typical Tpf, above a depth of 1095 ft, is represented by lithic-rich dacitic gravels and sands containing sparse to absent pumice. Tpf(p), in the 1095-1100 ft depth interval, is characterized by mixed lithic-pumiceous cuttings that include common Rendija lava clasts. In Tjfp, below 1100 ft depth, the cuttings are highly pumiceous and Rendija lava clasts are rare to absent. We assume the rare Rendija lava clasts in Tjfp are contaminants left over from incomplete evacuation of drill cuttings from overlying Tpf. Tcar riverine gravels and sands first appear in 1225-1230 ft cuttings interval and the contact is placed at 1228 ft depth.
SCI-2 (core)	>827 (<5905.7)	<856.5 (>5876.2)	n/a	n/a	n/a	Cored	Gamma log only; not useful for identifying contacts	Core is missing between depths of 827 and 856.5 ft. Rendija lava clasts are absent in core between depths of 856.5 and 889.7 ft. Cuttings from nearby well R-43 provide more complete documentation of critical contacts at this location. Though samples were limited, SCI-2 core is consistent with the contacts based on R-43 well cuttings.

Appendix A

*Elevations of Stratal Contacts for the Middle Otowi Member,
Top of Cerros del Rio Alkali Basalt, and Middle Puye
Formation Based on Borehole Gamma Logs*

Appendix A presents tables listing the elevations of stratal contacts for the middle Otowi Member, top of Cerros del Rio alkali basalt, and middle Puye Formation. The data presented are based on borehole gamma logs.

Table A-1
Depths and Elevations of Gamma Break for
Middle Otowi Member of the Bandelier Tuff

Well	Surface Elev. (ft)	Depth (ft)	Elev. (ft)	Comment
CrEX-1	6829	325	6504	
CrEX-2	6950	436	6514	
CrEX-3	6736	235	6501	
CrCH-2	6738	235	6503	
CrCH-3	6765	247	6518	
CrCH-4	6785	260	6525	
CrCH-5	6803	274	6529	
CrIN-1	6708	210	6498	
CrIN-2	6731	240	6491	
CrIN-3	6728	243	6489	Inclined borehole, depth is inclined depth.
CrIN-4	6896	406	6500	Inclined borehole, depth is inclined depth.
CrIN-5	6904	447	6503	Inclined borehole, depth is inclined depth.
CrIN-6	6708	238	6492	Inclined borehole, depth is inclined depth.
MCI-1	7106	400	6706	
MCI-10	7035	500	6535	
MCOBT-4.4	6836	275	6561	
MCOBT-8.5	6781	254	6527	
R-1	6885	294	6591	
R-11	6672	175	6497	
R-13	6673	195	6478	
R-14	7062	412	6650	
R-15	6820	280	6540	
R-17	6922	356	6566	
R-28	6729	225	6504	
R-33	6853	287	6566	
R-42	6759	244	6515	
R-43	6733	210	6523	
R-44	6715	228	6487	
R-45	6704	216	6488	
R-50	6904	399	6505	
R-61	6940	429	6511	
R-62	6985	433	6552	

Table A-1 (continued)

Well	Surface Elev. (ft)	Depth (ft)	Elev. (ft)	Comment
R-67	7123	431	6692	
SCC-2	6724	195	6529	
SCC-3	6713	189	6524	
SCC-4	6709	183	6526	
SCC-5	6684	176	6508	
SCC-6	6619	152	6467	
SCI-1/SCC-1	6738	196	6542	
SCI-3	6747	196	6551	
SIMR-2	6702	213	6489	
TA-53i	6987	424	6563	

**Table A-2
Depths and Elevations of Gamma Break for
Top of the Main Alkali Basalt Sequence**

Well	Surface Elev. (ft)	Depth (ft)	Elev. (ft)	Comment
54-24399	6793	557	6236	
CrEX-1	6829	582	6247	
CrEX-2	6950	654	6296	
CrEX-3	6736	503	6233	
CrCH-1	6950	652	6298	
CrCH-2	6738	494	6232	
CrCH-3	6765	530	6235	
CrCH-4	6785	504	6281	
CrCH-5	6803	572	6231	
CrIN-1	6708	388	6320	
CrIN-2	6731	415	6316	
CrIN-3	6728	404	6334	Inclined borehole, depth is inclined depth.
CrIN-4	6896	585	6324	Inclined borehole, depth is inclined depth.
CrIN-5	6904	694	6278	Inclined borehole, depth is inclined depth.
CrIN-6	6708	418	6329	Inclined borehole, depth is inclined depth.
LAOI-7	6458	150	6308	
MCI-10	7035	859	6176	XRF* data available
MCOBT-4.4	6836	644	6192	XRF data available
MCOBT-8.5	6781	555	6226	XRF data available
Otowi-1	6400	147	6253	XRF data available
R-1	6885	679	6206	

Table A-2 (continued)

Well	Surface Elev. (ft)	Depth (ft)	Elev. (ft)	Comment
R-10	6362	204	6158	
R-11	6672	368	6304	
R-12	6500	280	6220	XRF data available
R-13	6673	315	6358	XRF data available
R-15	6820	645	6175	XRF data available
R-20	6694	439	6255	XRF data available
R-21	6656	406	6250	XRF data available
R-22	6651	451	6200	XRF data available
R-28	6729	495	6234	
R-32	6638	456	6182	XRF data available
R-33	6853	647	6206	
R-34	6630	305	6325	XRF data available
R-35a	6623	333	6290	
R-36	6591	305	6286	
R-37	6871	567	6304	XRF data available
R-38	6669	354	6315	
R-40	6719	497	6222	XRF data available
R-41	6661	476	6185	XRF data available
R-42	6759	537	6222	
R-43	6733	483	6250	
R-44	6715	375	6340	
R-45	6704	380	6324	
R-50	6904	610	6294	
R-51	6762	567	6195	
R-53	6690	430	6260	
R-54	6680	438	6242	
R-55	6534	373	6161	
R-56	6781	544	6237	
R-57	6648	406	6242	
R-61	6940	670	6270	
R-62	6985	738	6247	
R-9	6383	180	6203	XRF data available
SCI-3	6747	530	6217	
SIMR-2	6702	340	6362	

* XRF = X-ray fluorescence.

Table A-3
Depths and Elevations of Gamma Break
at Base of Gamma Low in the Puye Formation

Well	Surface Elev. (ft)	Depth (ft)	Elev. (ft)	Comment
CrEX-1	6829	937	5892	
CrEX-2	6950	1035	5915	
CrEX-3	6736	825	5911	
CrCH-1	6950	1042	5908	
CrCH-2	6738	816	5922	
CrCH-3	6765	806	5959	
CrCH-4	6785	836	5949	Uncertain contact
CrIN-1	6708	801	6907	
CrIN-2	6731	842	5889	
CrIN-3	6728	897	5857	Inclined borehole, depth is inclined depth.
CrIN-4	6896	1056	5860	Inclined borehole, depth is inclined depth.
CrIN-5	6904	1158	5850	Inclined borehole, depth is inclined depth.
CrIN-6	6708	880	5910	Inclined borehole, depth is inclined depth.
R-1	6885	876	6009	
R-11	6672	733	5939	
R-13	6673	819	5854	
R-15	6820	870	5950	
R-28	6729	809	5920	
R-33	6853	881	5972	
R-35a	6623	720	5903	
R-42	6759	803	5956	
R-43	6733	731	6002	
R-44	6715	856	5859	Uncertain contact
R-45	6704	819	5885	
R-50	6904	1046	5858	
R-62	6985	992	5993	
R-6	6996	796	6200	
R-61	6940	1070	5870	
R-66	6627	490	6137	Provides constraints north of study area.
R-67	7123	1087	6036	Provides constraints north of study area.
R-8	6545	450	6095	Provides constraints north of study area.

Appendix B

*Structural Contour Maps for Geologic Contacts
in the Chromium Investigation Area*

Appendix B presents structural contour maps based on borehole gamma logs and showing stratal contacts for the middle Otowi Member, top of Cerros del Rio alkali basalt, and middle Puye Formation.

B-3

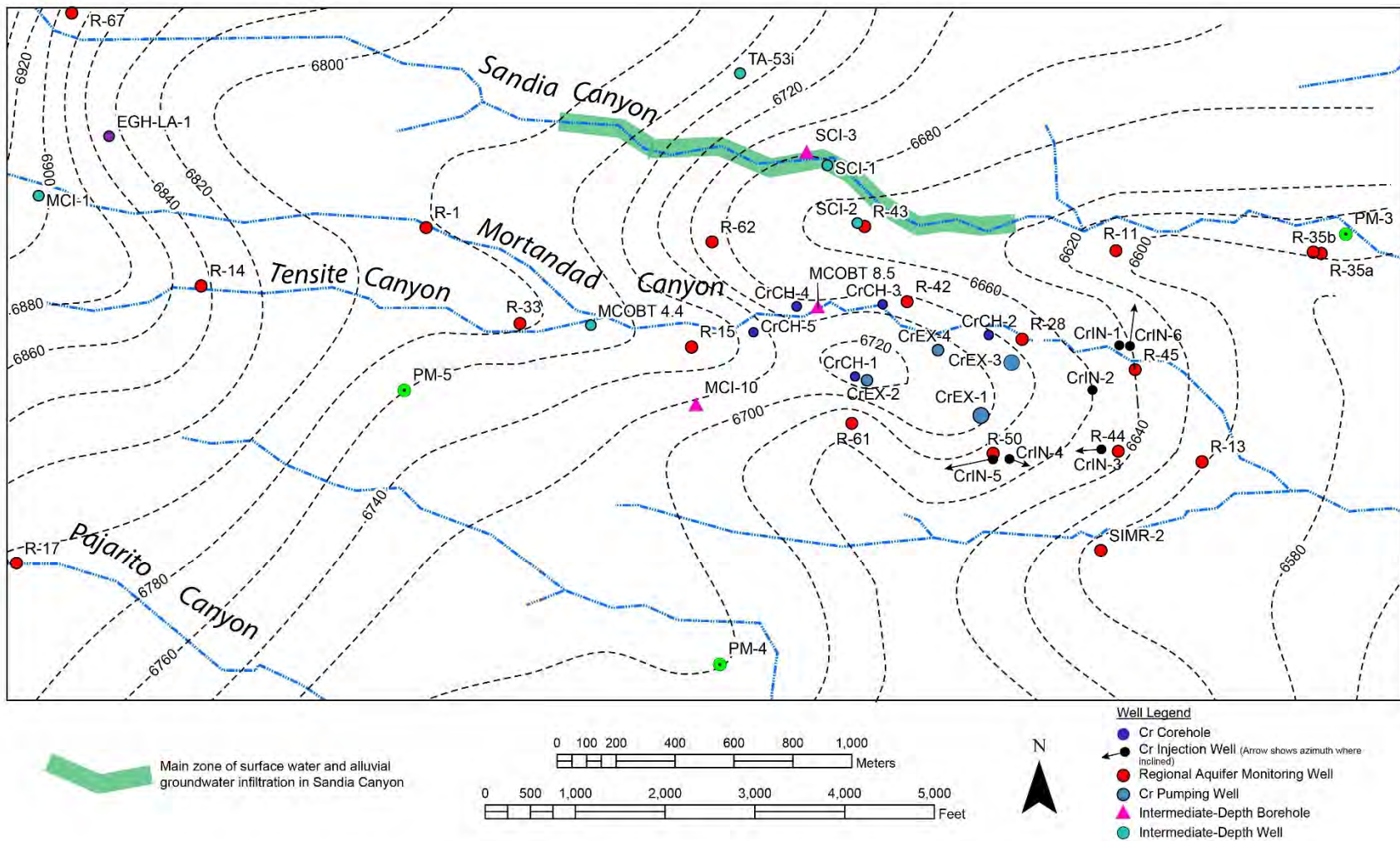


Figure B-1 Structure contour map for base of Tshirege Member subunit Qbt 1g. Contours based on the sitewide geologic model. Wells installed after 2015 shown for reference.

B-5

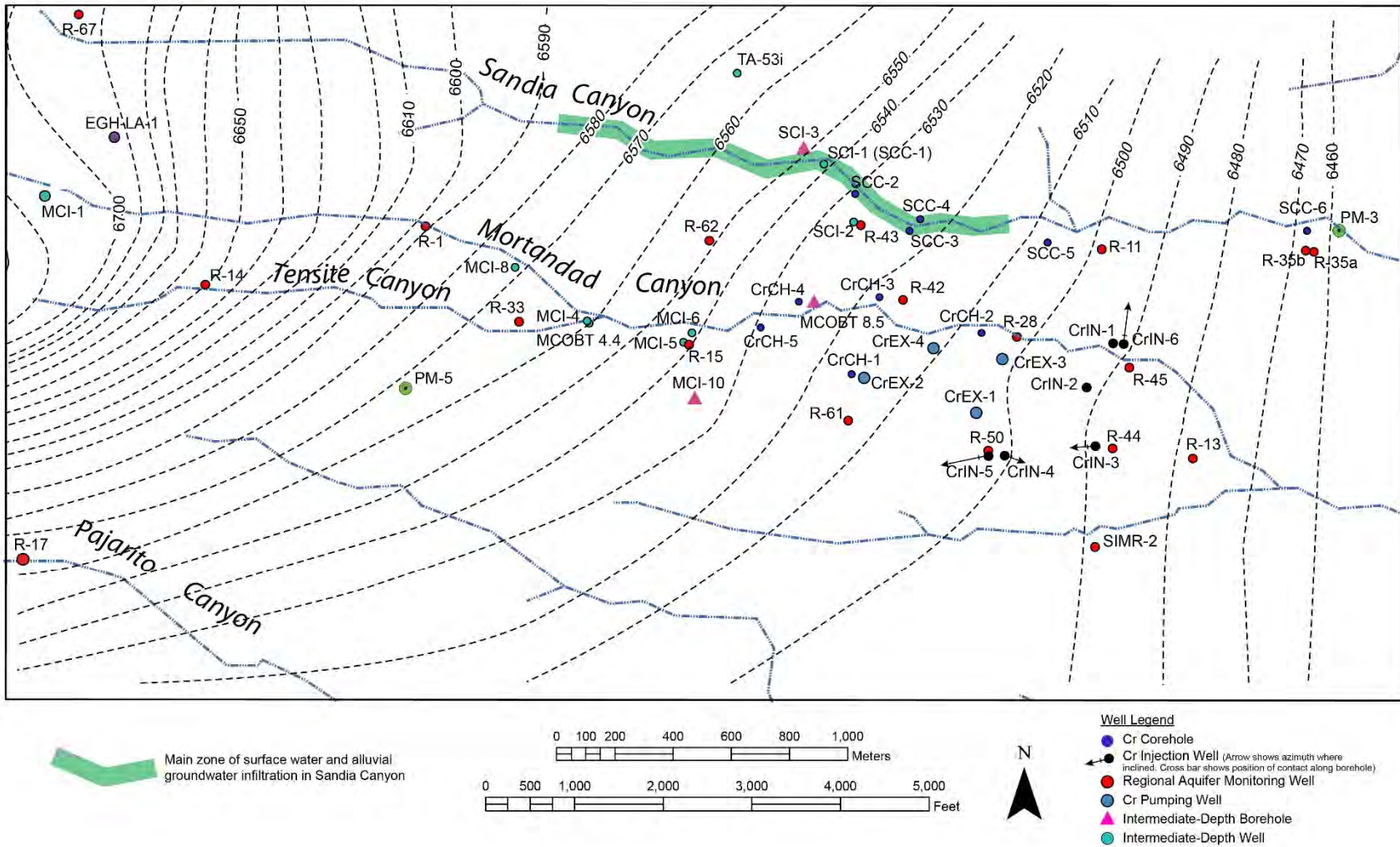


Figure B-3 Structure contour map for stratal contact in middle of Otowi Member identified using borehole gamma logs

B-7

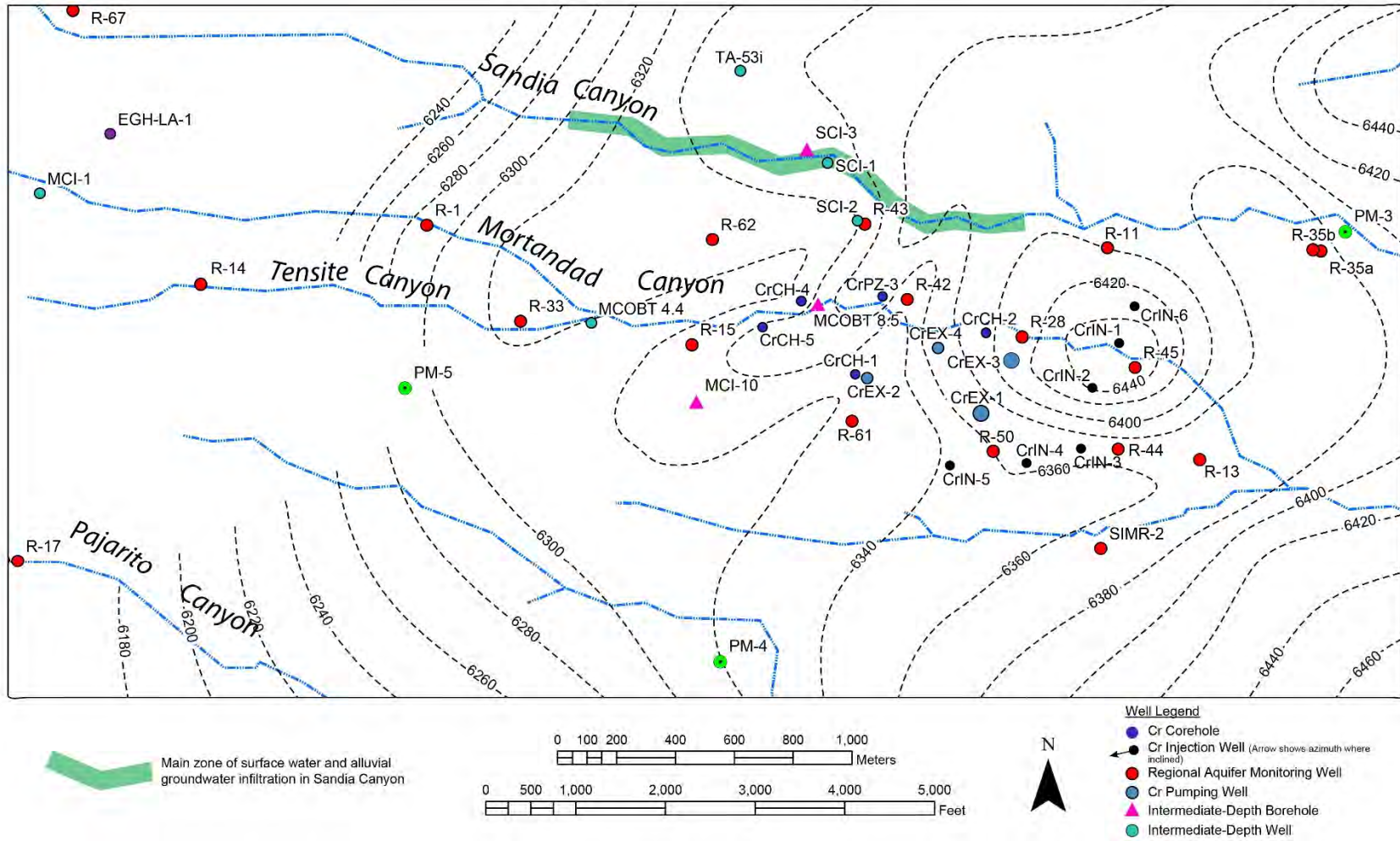


Figure B-5 Structure contour map for Cerros del Rio basalt (Tb4 undivided). Shows eroded top of all Tb4 basalt types (tholeiites and alkali basalts) regardless of source areas. Contours based on the sitewide geologic model. Wells installed after 2015 shown for reference.

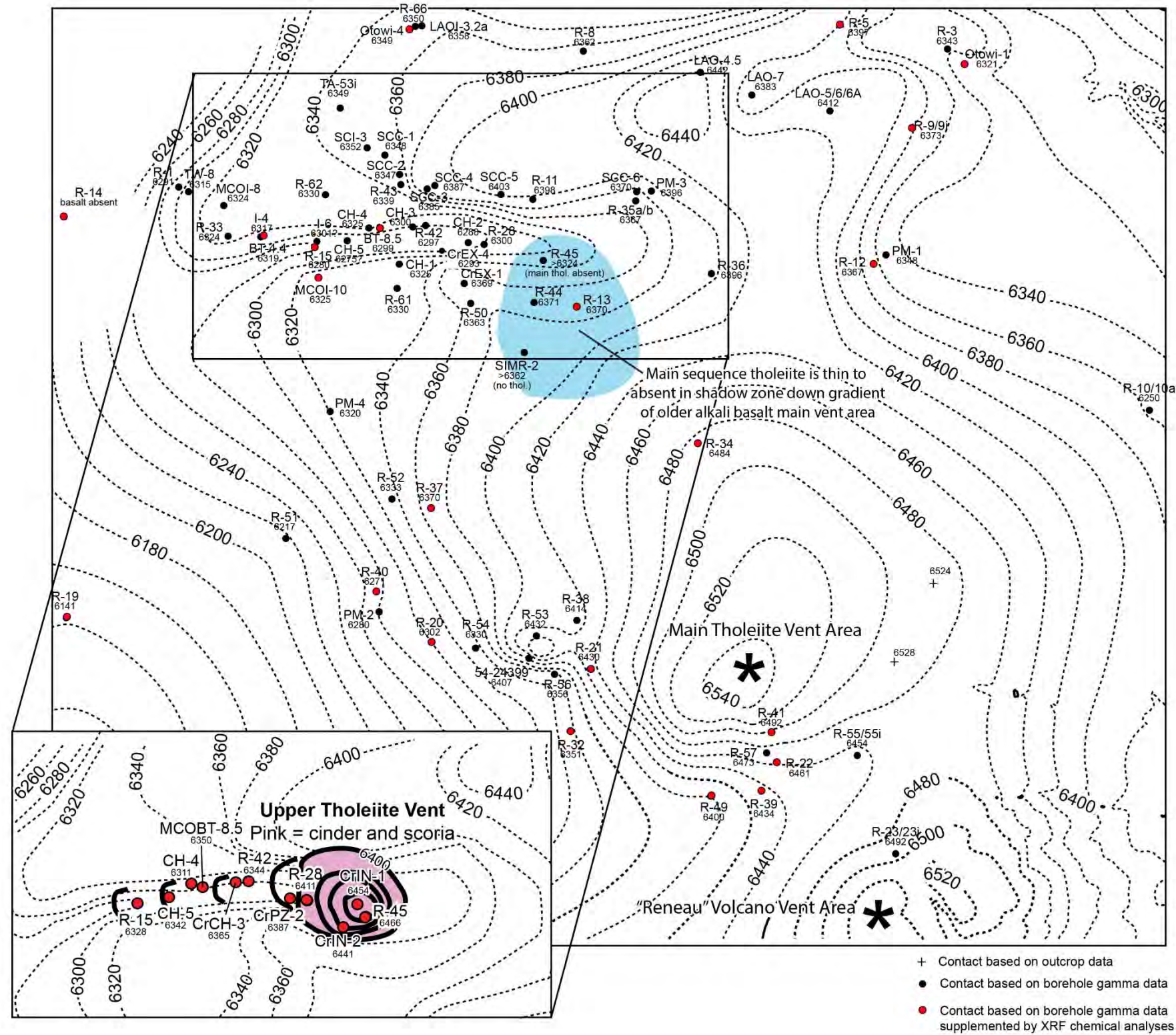


Figure B-6 Structure contour map for top of tholeiites of the main tholeiites/alkali basalt sequence of the Cerros del Rio basalt. The inset map shows the top of the tholeiites in upper tholeiites/alkali basalt sequence (thick black contours) superimposed on the top of the main tholeiite structure contours (dashed lines). The upper tholeiite/alkali basalt flows are present only in wells shown in inset.

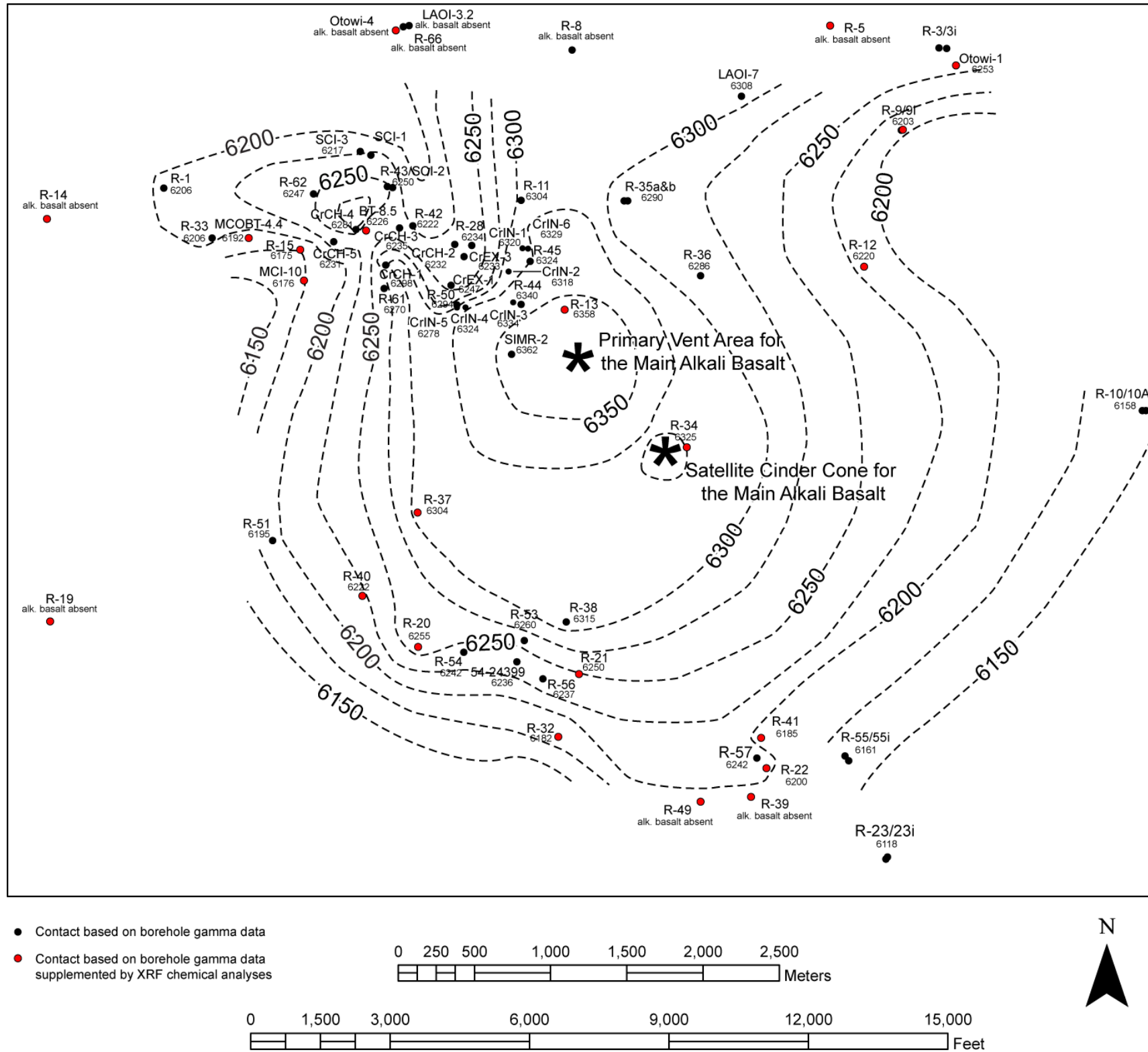


Figure B-7 Structure contour map for top of alkali basalt of the main tholeiite/alkali basalt sequence of the Cerros del Rio basalt

B-11

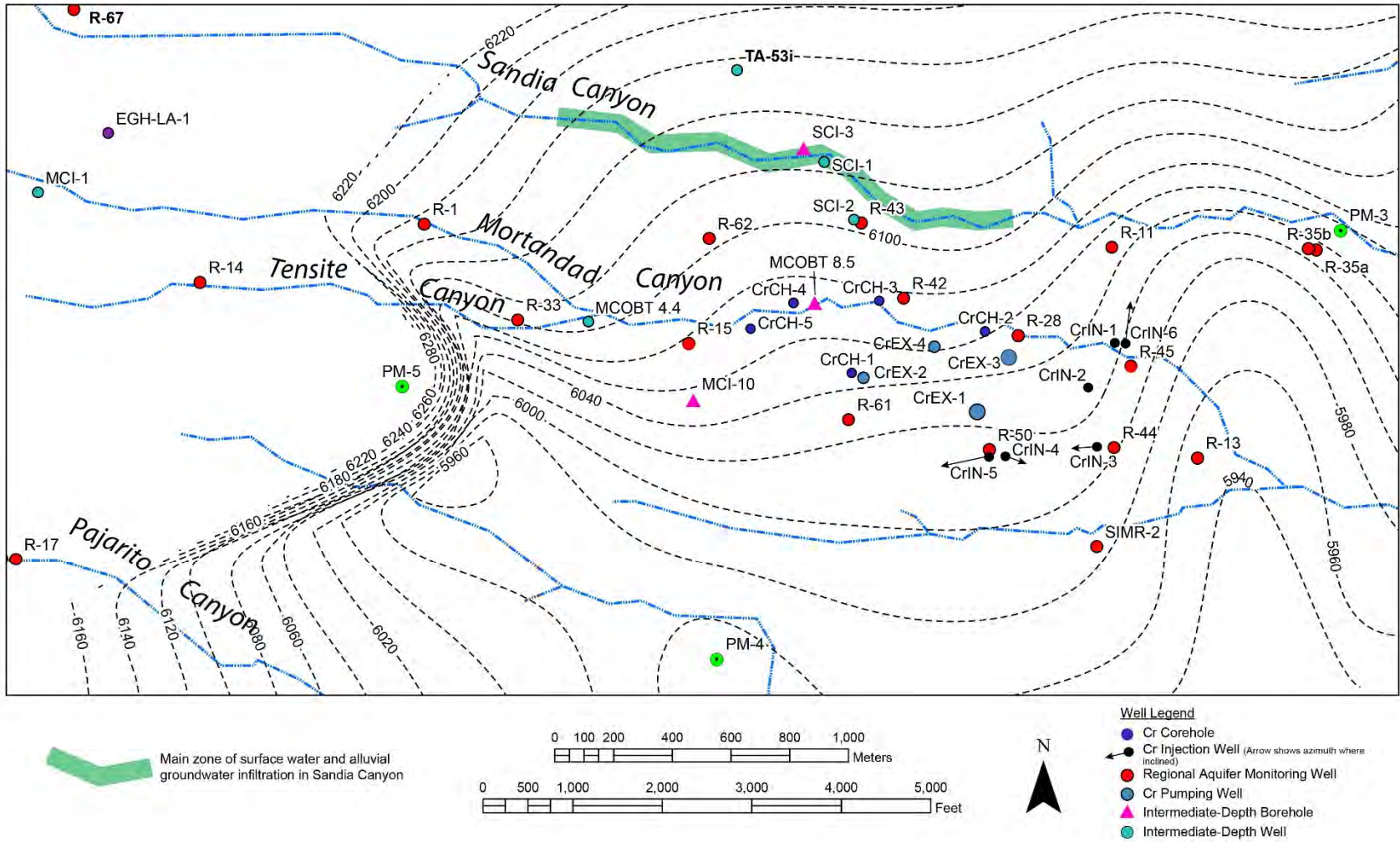


Figure B-8 Structure contour map for base of Cerros del Rio basalt. Contours based on the sitewide geologic model. Wells installed after 2015 shown for reference.

B-12

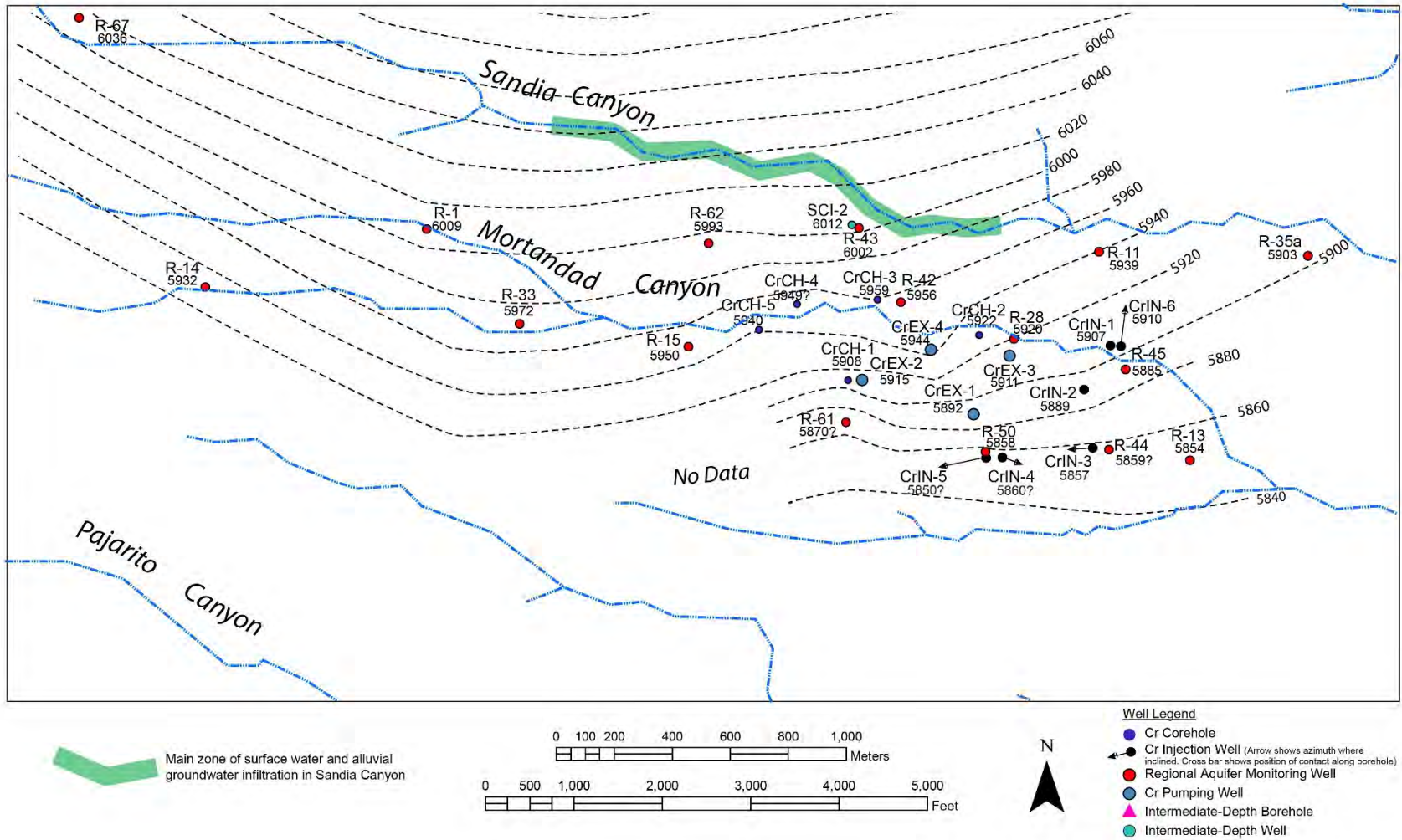


Figure B-9 Structure contour map for stratal contact in middle of Puye Formation identified using borehole gamma logs

B-13

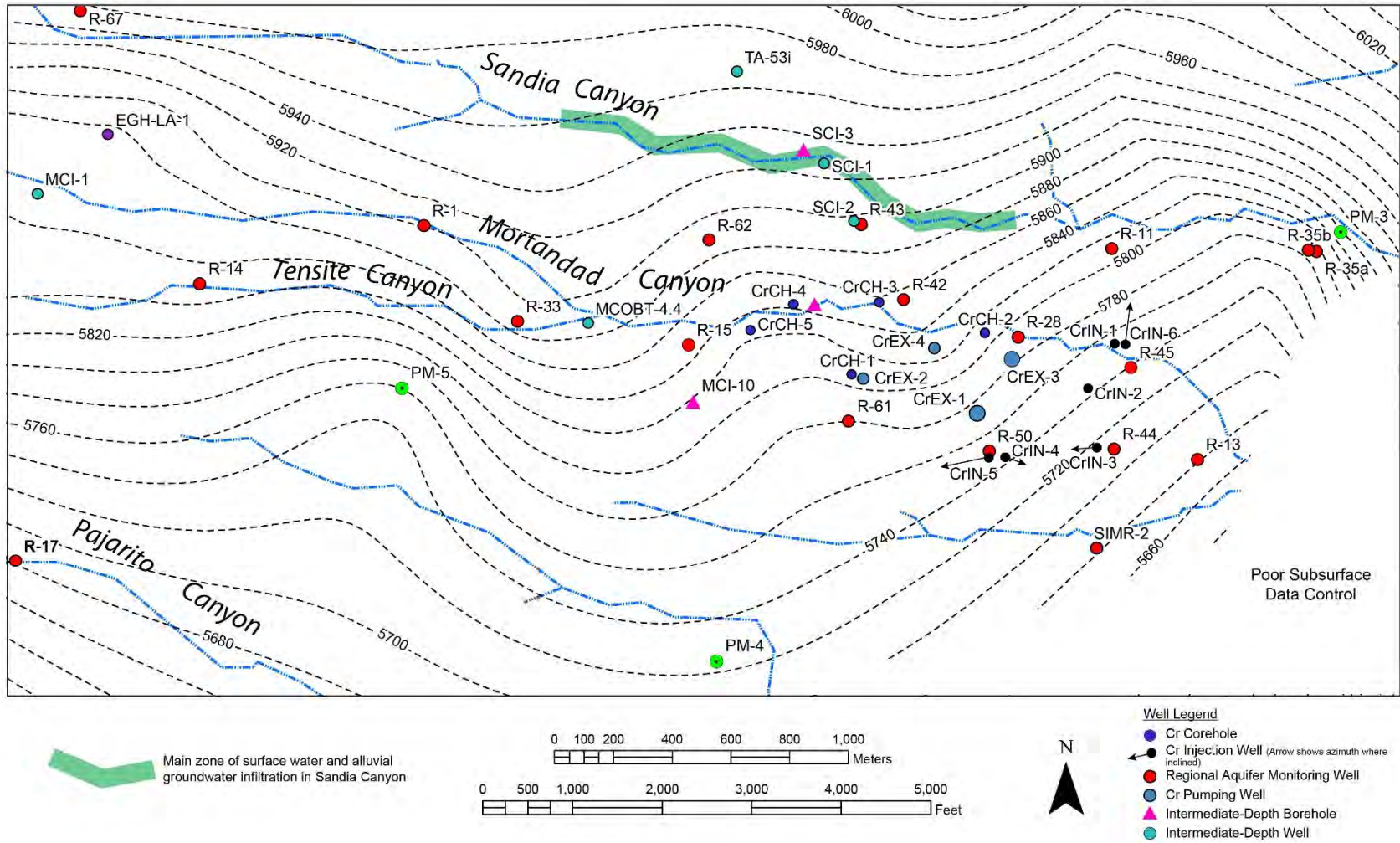


Figure B-10 Structure contour map for base of Puye Formation. Contours based on the sitewide geologic model. Wells installed after 2015 shown for reference.

Appendix C

*Lithologic Descriptions for Core Holes CrCH-1,
CrCH-2, CrCH-3, CrCH-4, and CrCH-5*

C-1.0 CORE HOLE CrCH-1 LITHOLOGIC DESCRIPTIONS

Note: All footages are measured from the bottom of core tubes. The colors in the descriptions reflect damp to wet cores except for run 60, in which the core hole had been previously opened and was slightly damp to dry.

Core Hole CrCH-1, Run 52 Drilled Interval 1111.5–1114.5 ft Drilled 3 ft and Recovered 5 ft

Core Hole CrCH-1 above 1111.5 ft (Slough?)

Possible slough. Light brown, poorly consolidated, silty lithic-crystal sand and gravel.

Core Hole CrCH-1 1111.5–1112 ft (Tpf)

Clean brown, medium- to coarse-grain, poorly consolidated, lithic-crystal sand and gravel containing dark gray dacite granules. The hydraulic conductivity estimated by the Kozeny-Carman method is 0.744 ft/d.

Core Hole CrCH-1 1112–1114.5 ft (Tpf)

Medium brown sandy gravel with abundant matrix- and clast-supported pebbles of dark gray dacite up to 0.75 in. The matrix is a medium-grain, lithic-crystal sand with a minor silt component. The uppermost 0.2 ft of this unit is stained by slight oxidation. This interval is uniform in appearance and contains no obvious bedding breaks. The hydraulic conductivity estimated by the Kozeny-Carman method is 4.385 ft/d.

Core Hole CrCH-1, Run 53 Drilled Interval 1114.5–1117.5 ft Drilled 3 ft and Recovered 3 ft

Core Hole CrCH-1 1114.5–1116.5 ft (Tpf)

Orange-brown sandy gravel with both clast-supported and matrix-supported dark gray dacite gravel up to 1.5-in. The matrix is a medium-to coarse-grain, lithic-crystal sand with a minor silt component. The interval contains no obvious bedding breaks. The hydraulic conductivity estimated by the Kozeny-Carman method is 2.185 ft/d.

Core Hole CrCH-1 1116.5–1117.5 ft (Tpf)

Oxidized orange-tan, gravel-rich, fine- to medium-grain lithic-crystal sand with abundant matrix-supported, dark gray dacite granules and gravel (up to 1 in). Interval contains a significant amount of fine sand and silt. The hydraulic conductivity estimated by the Kozeny-Carman method is 0.379 ft/d.

Core Hole CrCH-1, Run 54 Drilled Interval 1117.5–1120 ft Drilled 30 in. and Recovered 30 in. (Lexan)

Core Hole CrCH-1 1117.5–1119 ft (Tpf)

Brown sandy gravel with subangular to subrounded, granules and pebbles of dark gray dacite up to 1 in. supported in a medium-grain lithic sand matrix. No pumice observed. The bed is massive, moderately consolidated, and poorly sorted. The hydraulic conductivity estimated by the Kozeny-Carman method is 1.096 ft/d.

Core Hole CrCH-1 1119–1120 ft (Tpf)

Brown sandy gravel with subangular to subrounded granules and pebbles of dark gray dacite up to 1 in. supported in a fine- to medium-grain lithic sand matrix. No pumice observed. Upper 2 in. of bed is oxidized to orange-brown. The bed is massive, moderately to strongly consolidated, and poorly sorted. The hydraulic conductivity estimated by the Kozeny-Carman method is 0.546 ft/d.

Core Hole CrCH-1, Run 55

Drilled Interval 1120–1122.5 ft

Drilled 30 in. and Recovered 40 in. (Lexan; extra footage at top of core run discarded for final report)

Core Hole CrCH-1 1120–1120.5 ft (Tpf)

Brown, gravelly, medium- to coarse-grain sand with abundant subangular and subrounded granules and pebbles of dark gray dacite up to 1 in. No pumice observed. The bed is massive, strongly consolidated, and poorly sorted. Bed appears to be partly disrupted, possibly by drilling. The core has a 1-in. rim of silty fine sand that appears to have been mobilized from the underlying bed. The hydraulic conductivity estimated by the Kozeny-Carman method is 0.146 ft/d.

Core Hole CrCH-1 1120.5–1121.7 ft (Tpf)

Light reddish brown, gravelly, coarse-grain sand with abundant, matrix-supported, subangular and subrounded granules and pebbles of dark gray dacite. No pumice observed. The bed is massive, strongly consolidated, and poorly sorted. The hydraulic conductivity estimated by the Kozeny-Carman method is 0.787 ft/d.

Core Hole CrCH-1 1121.7–1122.5 ft (Tpf)

Brown coarse-grain sand with common to abundant, matrix-supported, subangular and subrounded granules and pebbles of dark gray dacite up to 1 in. The bed is normally graded with gravels concentrated in the lower half. The upper contact is sharp but not planar. No pumice observed. The bed is massive, moderately to strongly consolidated, and poorly sorted. The hydraulic conductivity estimated by the Kozeny-Carman method is 39.467 ft/d.

Core Hole CrCH-1, Run 56

Drilled Interval 1122.5–1125.5 ft

Drilled 36 in. and Recovered 46 in.; did not sample 12 in. of highly disrupted core at top of run (Lexan)

Core Hole CrCH-1 1122.5–1123.2 ft (Tpf)

Brown, gravelly, coarse-grain sand with abundant subrounded granules and pebbles of dark gray dacite up to 1 in. The bed is massive, moderately consolidated, and poorly sorted. The hydraulic conductivity estimated by the Kozeny-Carman method is 5.478 ft/d.

Core Hole CrCH-1 1123.2–1124.7 ft (Tpf)

Light reddish-brown, gravelly, coarse-grain, lithic sand with subangular to subrounded clasts of dark gray dacite. The sandy matrix is reversely graded, and is fine- to medium grain at the base and coarse grain in the upper part. The bed is massive, moderately consolidated, and poorly sorted. The hydraulic conductivity estimated by the Kozeny-Carman method is 0.243 ft/d.

Core Hole CrCH-1 1124.7–11225 ft (Tpf)

Medium brown gravel with clast-supported, subangular to subrounded pebbles of dark gray dacite up to 1.5 in. The matrix is sparse and is fine- to medium-grain sand. The bed is massive, poorly consolidated, and poorly sorted. The hydraulic conductivity estimated by the Kozeny-Carman method is 0.208 ft/d.

Core Hole CrCH-1 1125–1125.5 ft (Tpf)

Reddish brown medium- to coarse-grain sand with sparse, subangular to subrounded granules and small pebbles of dark gray dacite. The bed is massive, moderately consolidated, and poorly sorted. The hydraulic conductivity estimated by the Kozeny-Carman method is 0.208 ft/d.

Core Hole CrCH-1, Run 57

Drilled Interval 1125.5-1128.5 ft

Drilled 3 ft and Recovered 5 ft

Core Hole CrCH-1 above 1125.5 ft (Slough?)

Possible slough. Uniform brown medium- to coarse-grain, poorly consolidated, lithic-crystal sand and gravel containing small pebbles of dark gray dacite.

Core Hole CrCH-1 1125.5–1128.5 ft (Tpf)

Orange-brown sandy gravel with abundant matrix-supported pebbles of dark gray subrounded dacite. The matrix is a coarse-grain, lithic-crystal sand with a substantial silt component. The matrix of the 1127.9–1128.5 ft interval contains a slightly greater silt component. This interval is slightly stained by oxidation and contains no obvious bedding breaks. The hydraulic conductivity estimated by the Kozeny-Carman method is 0.379 ft/d.

Core Hole CrCH-1, Run 58

Drilled Interval 1128.5–1131.5 ft

Drilled 3 ft and Recovered 5 ft

Core Hole CrCH-1 above 1128.5 ft (Slough?)

Possible slough. Brown, gravel-rich, medium- to coarse-grain, poorly consolidated, lithic-crystal sand containing abundant matrix-supported pebbles of dark gray dacite up to 1 in. Slight orangish brown oxidation in lowermost 0.25 ft of the interval.

Core Hole CrCH-1 1127.9–1128.5 ft (Tpf)

Light brown, gravel-rich silt and fine- to coarse-grain sand with abundant matrix-supported pebbles of dark gray dacite up to 1 in. The matrix appears to be dominated by silt-sized material and may contain some clay. The hydraulic conductivity estimated by the Kozeny-Carman method is 0.379 ft/d.

Core Hole CrCH-1 1128.7–1129.2 ft (Tpf)

Brown sandy gravel with abundant matrix-supported pebbles of dark gray dacite up to 1.5 in. The matrix is light brown, poorly sorted, coarse-grain sand to silt. The hydraulic conductivity estimated by the Kozeny-Carman method is 0.243 ft/d.

Core Hole CrCH-1 1129.2–1130 ft (Tpf)

Yellow-brown, gravel-rich silt and fine- to coarse-grain sand with granules of dark gray dacite. The matrix appears to contain substantial tuffaceous material (ash and pumice fragments). The hydraulic conductivity estimated by the Kozeny-Carman method is 0.379 ft/d.

Core Hole CrCH-1 1130–1131.5 ft (Tpf)

Brown gravel-rich silt and fine- to coarse-grain lithic-crystal sand containing ~10% of dark gray dacite. The interval contains irregular, patchy zones with yellow-brown discoloration. The hydraulic conductivity estimated by the Kozeny-Carman method is 0.243 ft/d.

Core Hole CrCH-1, Run 59
Drilled Interval 1132.5–1134.5 ft
Drilled 12 in. and Recovered 12 in. (Lexan)

Core Hole CrCH-1 1132.5–1133.5 ft (Tpf)

Light brown, gravelly, coarse-grain sand with abundant, subrounded granules and pebbles of dark gray dacite up to 1.25 in. The bed is massive, moderately consolidated, and poorly sorted. The hydraulic conductivity estimated by the Kozeny-Carman method is 145.00 ft/d.

Core Hole CrCH-1 1133.5–1134.5 ft (Tpf)

Light orangish brown, coarse-grain sand with common, subrounded granules and pebbles of dark gray dacite. The bed is gravelly at the base and becomes finer upwards. The bed is massive, moderately consolidated, and poorly sorted. The matrix may be somewhat tuffaceous, but no pumice was observed. The hydraulic conductivity estimated by the Kozeny-Carman method is 58.328 ft/d.

Core Hole CrCH-1, Run 60
Drilled Interval 1134.5–1136.5 ft
Drilled 2 ft and Recovered 5 ft

Core Hole CrCH-1 above 1134.5 ft (Slough?)

Possible slough. Light-brown sandy gravel like the 1134.5–1136 ft interval below. This sample is segregated from the 1134.5–1136 ft interval because driller's notes indicate the core run represents only 2 ft of penetration. The upper 0.3 ft of this interval is an orangish tan, fine- to coarse-grain tuffaceous sand.

Core Hole CrCH-1 1134.5–1136 ft (Tpf)

Light-brown sandy gravel with abundant matrix-supported pebbles (up to 1 to 2 in.) of dark gray subrounded dacite. The matrix is a coarse-grain, lithic-crystal sand that contains abundant ash and small pumice fragments. The hydraulic conductivity estimated by the Kozeny-Carman method is 0.971 ft/d.

Core Hole CrCH-1 1136–1136.5 ft (Tpf)

Slightly oxidized light brown, gravelly, medium-grain sand with matrix-supported granules of dark gray dacite. The matrix is a coarse-grain, lithic-crystal sand that contains some ash and small pumice fragments. The hydraulic conductivity estimated by the Kozeny-Carman method is 13.656 ft/d.

The Tpf/Tpf(p) contact is deeper than the total depth (TD) of 1136.5 ft.

C-2.0 CORE HOLE CrCH-2 LITHOLOGIC DESCRIPTIONS

Note: All footages are measured from the bottom of core tubes. The colors in the descriptions reflect damp to wet cores except where noted.

Core Hole CrCH-2, Run 55

Drilled Interval 908–915 ft

Drilled 7 ft and Recovered 7 ft (Core saved in two plastic sleeves)

Note: There is overlap in the footages listed on the core bags for core run 55 (908–915 ft; in two bags) and core run 56 (913–917 ft). The log books in the sample prep lab were corrected to indicate that core run 55 should be listed as 908–913 ft. Because we did not describe these cores in sequence, the overlap in depths of the core runs was not known, and the 7 ft of recovered core for run 55 was measured from the base of the unit and labelled as usual—thus overlapping core run 56. The samples for runs 55 and 56 have unique sample numbers and are easily distinguished. However, the core depths for run 55 will need to be rectified at some point to restrict samples to the 908–913 ft depth interval. (Rectification 091216 by DB: the sample core hole, CrCH-2 913.83–915 ft, is treated as possible slough; the core hole interval CrCH-2 912.38–913.83 ft can overlap the top of the underlying run 56.)

Core Hole CrCH-2 908–909.5 ft (Tpf)

Gray-brown gravel-rich sand with subrounded dark gray dacite granules and pebbles up to 2 in. supported by a matrix of silt-rich fine- to coarse-grain lithic sand. The interval is graded, with the gravel clasts becoming less abundant upwards. This interval is poorly sorted and poorly consolidated. The hydraulic conductivity estimated by the Kozeny-Carman method is 0.546 ft/d.

Core Hole CrCH-2 909.5–910.29 ft (Tpf)

Gray-brown sandy gravel supported by a matrix of coarse-grain lithic sand. Gravel clasts are dark gray dacite granules and pebbles up to 1.25 in. This interval is poorly sorted and poorly consolidated. The hydraulic conductivity estimated by the Kozeny-Carman method is 1.229 ft/d.

Core Hole CrCH-2 910.29–911.67 ft (Tpf)

Brown, gravel-rich and silt-rich, fine- to coarse-grain sand. Matrix-supported gravel clasts are subrounded, dark gray granules and pebbles of dacite up to 2 in. The interval is graded, with the gravel clasts becoming smaller and less abundant upwards. The upper half of the interval is oxidized to a reddish brown color. This interval is poorly sorted and poorly consolidated. The hydraulic conductivity estimated by the Kozeny-Carman method is 0.546 ft/d.

Core Hole CrCH-2 911.67–912.38 ft (Tpf)

Brown, gravel-rich and silt-rich, fine- to coarse-grain lithic-crystal sand with matrix-supported granules of white pumice (common) and dark lava (sparse). The sandy matrix also contains common small, white pumice. Interval is moderately poorly consolidated. The hydraulic conductivity estimated by the Kozeny-Carman method is 0.379 ft/d.

Core Hole CrCH-2 912.38–913.83 ft (Tpf)

Orange-brown gravel-rich and silty sand. This interval is like the underlying unit, but the matrix is more fine grained. Matrix-supported, rounded, dark gray dacite granules and pebbles up to 3 in. make up 20–30% of the unit. The matrix is predominately silt-rich fine- to coarse-grain sand. This interval is poorly sorted and poorly consolidated. The hydraulic conductivity estimated by the Kozeny-Carman method is 0.971 ft/d.

Core Hole CrCH-2 913.83–915 ft (Tpf)

Possible slough. Brown, gravel-rich, lithic-crystal sand. Matrix-supported, rounded, dark gray dacite granules and pebbles up to 1.5 in. make up 40–50% of the unit. The matrix is predominately silty fine- to coarse-grain sand. This interval is poorly sorted and poorly consolidated. The middle of the unit contains the most abundant and largest gravel clasts. The contact with the overlying unit is sharp. The hydraulic conductivity estimated by the Kozeny-Carman method is 0.546 ft/d.

Core Hole CrCH-2, Run 56
Drilled Interval 913–917 ft
Drilled 4 ft and Recovered 5 ft

Core Hole CrCH-2 <913 ft; 12 in. of excess core

Possible slough. Same description as interval below; appears to be continuous with no obvious break. Dark orangish brown sandy gravel with subangular to subrounded dark gray dacite granules and pebbles up to 1-in. supported by a matrix of silt to coarse-grain tuffaceous sand. This interval is poorly sorted and moderately well consolidated. The hydraulic conductivity estimated by the Kozeny-Carman method is 0.546 ft/d.

Core Hole CrCH-2 913–913.6 ft (Tpf)

Dark orangish brown sandy gravel with subangular to subrounded dark gray dacite granules and pebbles up to 1 in. supported by a matrix of silty coarse-grain tuffaceous sand. This interval is poorly sorted and moderately well consolidated. The hydraulic conductivity estimated by the Kozeny-Carman method is 0.971 ft/d.

Core Hole CrCH-2 913.6–915.1 ft (Tpf)

Medium orangish brown sandy gravel with subangular to subrounded dark gray dacite granules and pebbles up to 2 in. supported by a matrix of coarse-grain tuffaceous sand. This interval is moderately well sorted and moderately well consolidated. Like the overlying unit, but has a somewhat lighter color and contains less fines. The hydraulic conductivity estimated by the Kozeny-Carman method is 10.257 ft/d.

Core Hole CrCH-2 915.1–915.75 ft (Tpf)

Medium brown, gravel-rich, crystal-lithic-tuffaceous coarse-grain sand with abundant subangular to subrounded dark gray dacite granules and pebbles up to 0.75 in. Gravel clasts are supported by a silty sandy matrix. This interval is massive, well sorted, and moderately well consolidated. The hydraulic conductivity estimated by the Kozeny-Carman method is 1.229 ft/d.

Core Hole CrCH-2 915.75–916.75 ft (Tpf)

Sample removed by previous sampling.

Core Hole CrCH-2 916.75–917 ft (Tpf)

Light brown-gray, gravel-rich, coarse-grain crystal-lithic sand. Sand contains granules of subrounded dark gray dacite up to 0.5 in. This interval is massive, well sorted, and moderately well consolidated. The hydraulic conductivity estimated by the Kozeny-Carman method is 1.836 ft/d.

Core Hole CrCH-2, Run 57

Drilled Interval 917–921 ft

Drilled 4 ft and Recovered 4 ft

Core Hole CrCH-2 917–917.66 ft (Tpf)

Reddish brown gravel supported by a matrix of silty fine- to coarse-grain sand. Gravel clasts are dark gray dacite granules and pebbles up to 1.5 in. Pumice is absent. This interval is poorly sorted and poorly consolidated. The hydraulic conductivity estimated by the Kozeny-Carman method is 0.546 ft/d.

Core Hole CrCH-2 917.66–918.32 ft (Tpf)

Brown gravel supported by a matrix of coarse-grain sand. Gravel clasts are subrounded, dark gray granules and pebbles of dacite up to 2 in. This interval is well sorted and poorly consolidated. The hydraulic conductivity estimated by the Kozeny-Carman method is 3.414 ft/d.

Core Hole CrCH-2 918.32–919.4 ft (Tpf)

Brown, gravel-rich, coarse-grain lithic-crystal sand with matrix-supported granules and pebbles of dark lava clasts up to 1 in. The sandy matrix also contains abundant small, white pumice. Interval is well sorted and poorly consolidated. The hydraulic conductivity estimated by the Kozeny-Carman method is 8.740 ft/d.

Core Hole CrCH-2 919.4–920.1 ft (Tpf)

Reddish brown gravel supported by a matrix of silty coarse-grain sand. Abundant granules and pebbles are dark gray dacite up to 1.5 in. Sparse white pumice is present in the sandy matrix. This interval is well sorted and poorly consolidated. The hydraulic conductivity estimated by the Kozeny-Carman method is 1.517 ft/d.

Core Hole CrCH-2 920.1–921 ft (Tpf)

Medium brown, gravel-rich, coarse-grain lithic-crystal sand. Matrix-supported gravel clasts are dark gray dacite granules and pebbles up to 1 in. White pumice is common in the sandy matrix. This interval is poorly sorted and poorly consolidated.

Core Hole CrCH-2, Run 58

Drilled Interval 921–925 ft

Drilled 4 ft and Recovered 4.66 ft

Core Hole CrCH-2 <921 ft; 8 in. of excess core (Tpf)

Possible slough. Brown, gravel-rich, tuffaceous-lithic-crystal sand with abundant angular to subrounded dark gray dacite granules and pebbles up to 2 in. Gravel clasts are supported by a matrix of silt to coarse-grain tuffaceous sand. The matrix contains abundant volcanic ash but only sparse pumice fragments. This interval is massive, poorly sorted, well consolidated, and gravels become coarser upwards. The hydraulic conductivity estimated by the Kozeny-Carman method is 0.971 ft/d.

Core Hole CrCH-2 921–922.08 ft (Tpf)

Brown, gravel-rich, tuffaceous-lithic-crystal sand with ~50% subangular to rounded dark gray dacite granules and pebbles up to 0.5 in. Gravel clasts are supported by a matrix of silt to coarse-grain tuffaceous sand. The matrix contains abundant volcanic ash but only sparse pumice fragments. The unit has a slight yellowish coloration and appears to become slightly finer upwards. This interval is massive, poorly sorted, and well consolidated; it is likely a debris flow deposit. There are scattered patches of iron staining up to 1 in. from the core rim. These may be oxidized iron fillings or could be natural. The hydraulic conductivity estimated by the Kozeny-Carman method is 0.546 ft/d.

Core Hole CrCH-2 922.08–922.17 ft (Tpf)

Brown sandy gravel with subangular to subrounded dark gray dacite granules and pebbles supported in a coarse-grain tuffaceous-lithic-crystal sand. This unit is a thin bed with sharp contacts with overlying and underlying thick massive beds. The matrix appears to contain fewer fines than adjacent units and is notably less-well consolidated. The hydraulic conductivity estimated by the Kozeny-Carman method is 1.517 ft/d.

Core Hole CrCH-2 922.17–924.2 ft (Tpf)

Yellowish brown, gravel-rich, tuffaceous-lithic-crystal sand with ~40% angular to subrounded dark gray dacite granules and pebbles up to 1.5 in. Gravel clasts are supported by a matrix of silt to coarse-grain tuffaceous sand. The matrix contains abundant volcanic ash but only sparse pumice fragments. The unit is like the overlying unit, but it has the yellow staining throughout and the matrix appears to be slightly more coarse grain. Base of unit is marked by a 2-in. dark gray dacite pebble. This interval is massive, poorly sorted, and well consolidated; it is likely a debris flow deposit. There are scattered patches of iron staining scattered throughout the core, including the interior. The hydraulic conductivity estimated by the Kozeny-Carman method is 0.379 ft/d.

Core Hole CrCH-2 924.2–925 ft (Tpf)

Brown, gravel-rich, tuffaceous-lithic-crystal sand with ~35% angular to subrounded dark gray dacite granules and pebbles up to 1.5 in. Gravel clasts are supported by a matrix of silt to coarse-grain sand. The matrix contains abundant volcanic ash but only sparse pumice fragments. The upper part of the unit has a slight yellowish coloration. This interval is poorly sorted and moderately well consolidated; it is likely a debris flow deposit. The hydraulic conductivity estimated by the Kozeny-Carman method is 0.379 ft/d.

Tpf/Tpf(p) Contact–925 ft

Core Hole CrCH-2, Run 59
Drilled Interval 925-929 ft
Drilled 4 ft and Recovered 4 ft

Core Hole CrCH-2 925–925.7 ft [Tpf(p)]

Orangish brown, gravel- and silt-rich, fine- to coarse-grain tuffaceous sand with ~45% matrix-supported dark gray dacite pebbles up to 0.5 in. Matrix contains abundant tan ash and sparse small pumice fragments. Interval is poorly sorted and moderately well consolidated. The hydraulic conductivity estimated by the Kozeny-Carman method is 0.971 ft/d.

Core Hole CrCH-2 925.7–926.25 ft [Tpf(p)]

Orangish brown, coarse-grain tuffaceous sand that grades down into pumiceous gravelly sand. Gravel clasts are rounded pumice; no lava clasts. Interval is poorly sorted and moderately well consolidated. The hydraulic conductivity estimated by the Kozeny-Carman method is 0.971 ft/d.

Core Hole CrCH-2 926.25–927.2 ft [Tpf(p)]

Orangish gray-brown, silty, fine- to coarse-grain tuffaceous sand that grades down into pumiceous gravelly sand. Matrix-supported gravel clasts are rounded vitric pumice up to 0.5 in. Unit is like the overlying interval in its overall characteristics. One 2-in. rounded dark gray lava clast marks the base of the interval. Interval is poorly sorted and moderately well consolidated. The hydraulic conductivity estimated by the Kozeny-Carman method is 0.546 ft/d.

Core Hole CrCH-2 927.2–927.75 ft [Tpf(p)]

Reddish orange-brown, silty, fine- to coarse-grain tuffaceous sand that grades down into pumiceous gravelly coarse-grain sand. The upper sand contains sparse dark gray dacite up to 1 in. The lower gravelly sand contains abundant matrix-supported granules and pebbles of rounded vitric pumice up to 0.5 in. The base of the interval is a clast-supported gravel made up of pumice and sparse dark gray dacite. The unit is like two overlying intervals in its overall characteristics. The base of the interval is a clast-supported gravel made up of pumice and sparse dark gray dacite. The hydraulic conductivity estimated by the Kozeny-Carman method is 0.744 ft/d.

Core Hole CrCH-2 927.75–928.5 ft [Tpf(p)]

Grayish orange-brown, gravelly and silty, fine- to coarse-grain tuffaceous sand that grades down into pumiceous gravelly coarse-grain sand. Abundant granules and pebbles of pumice are vitric and subrounded. Interval contains lava clasts up to 0.5 in. throughout. Dark gray dacite is more abundant in the sandy matrix and gravel clasts than in the overlying units. The unit is slightly graded but not as much as the overlying units. Interval is poorly sorted and poorly consolidated. The core is wet and somewhat muddy. The hydraulic conductivity estimated by the Kozeny-Carman method is 0.546 ft/d.

Core Hole CrCH-2 928.5–929 ft [Tpf(p)]

Brownish white clast-supported pumice gravel. The unit is almost entirely granules and pebbles of vitric, subangular to subrounded pumice that become finer towards the base. The unit is very poorly consolidated. The hydraulic conductivity estimated by the Kozeny-Carman method is 0.379 ft/d.

Core Hole CrCH-2, Run 60
Drilled Interval 929–934 ft
Drilled 5 ft and Recovered 5.5 ft

Note: The extra 0.5 ft of recovery appears to be stretching and separations of soft core within core plastic sleeve; will adjust the footages to indicate a 5-ft core run. Also, sides of core deformed plastically and are pulled up along outside margins where core extruded into plastic sleeve. Footages are measured from center of core run, and care was taken not to mix stratigraphic units in the sampling.

Core Hole CrCH-2 929–929.2 ft [Tpf(p)]

Brown fine- to medium-grain crystal sand. Dominated by felsic crystals but contains sparse dark lava grains and sparse white pumice. Interval is uniform and well sorted. The hydraulic conductivity estimated by the Kozeny-Carman method is 1.517 ft/d.

Core Hole CrCH-2 929.2–930.1 ft [Tpf(p)]

Brown fine- to coarse-grain crystal-lithic sand and gravel. Dominated by felsic crystals but contains minor dark lava grains and sparse white, rounded pumice. Interval is uniform, well sorted, partially consolidated, and contains no bedding features. The hydraulic conductivity estimated by the Kozeny-Carman method is 3.414 ft/d.

Core Hole CrCH-2 930.5–932.1 ft [Tpf(p)]

Dark gray-brown gravel and coarse-grain lithic sand. The interval lacks pumice and is poorly consolidated. A basal clast-supported, subrounded gravel of medium- to dark gray lava granules and pebbles (up to 1 in.) grades upward into a well-sorted coarse-grain lithic sand with numerous matrix-supported pebbles up to 0.5 in. A 1-in. gravel caps the upper coarse sand. Numerous rust spots on outside of core suggests drilling-induced oxidized iron filings are present. The hydraulic conductivity estimated by the Kozeny-Carman method is 24.278 ft/d.

Core Hole CrCH-2 932.1–932.35 ft [Tpf(p)]

Light gray-tan fine- to medium-grain tuffaceous sand. Very clean and very well sorted. No lava lithics are present. The hydraulic conductivity estimated by the Kozeny-Carman method is 1.517 ft/d.

Core Hole CrCH-2 932.35–932.56 ft [Tpf(p)]

Dark gray-brown gravel and coarse-grain lithic sand. Interval is normally graded. A basal clast-supported gravel of dark gray-brown lava granules and pebbles grades upward into a coarse-grain lithic sand. Sparse white pumice is scattered throughout the interval. The hydraulic conductivity estimated by the Kozeny-Carman method is 6.069 ft/d.

Core Hole CrCH-2 932.56–932.9 ft [Tpf(p)]

Light brown, gravelly, medium- to coarse-grain tuffaceous sand of mostly white vitric pumice. Interval is normally graded, being coarse-grain at the base and becoming finer upwards. Larger pumice clasts at base are matrix-supported and up to 0.5 in. Also contains subordinate amounts of dark gray lava grains that are much less abundant than the pumice. Interval is well sorted and slightly consolidated. The hydraulic conductivity estimated by the Kozeny-Carman method is 6.069 ft/d.

Core Hole CrCH-2 932.9–933.66 ft [Tpf(p)]

Medium gray-brown, coarse-grain, lithic-tuffaceous pebble gravel of mostly dark gray to brown, subrounded lava clasts. Also contains subordinate amounts of white vitric pumice up to 0.5 in. The coarse sandy matrix is free of silt and fine sand. The hydraulic conductivity estimated by the Kozeny-Carman method is 19.015 ft/d.

Core Hole CrCH-2 933.66–934 ft [Tpf(p)]

White clast-supported pumice gravel with well-sorted vitric pumice lapilli up to 0.5 in. Red-brown lava clasts up to 0.25 in. are sparsely distributed throughout the interval. The matrix is free of silt and fine sand. The hydraulic conductivity estimated by the Kozeny-Carman method is 6.692 ft/d.

Core Hole CrCH-2, Run 61
Drilled Interval 934–939 ft
Drilled 5 ft and Recovered 4 ft 9 in.

Core Hole CrCH-2 934–935.7 ft [Tpf(p)] (Missing 0.3 ft of core run assigned to this interval)

Gray brown, gravelly, coarse- to very coarse-grain lithic-tuffaceous sand with abundant matrix-supported subangular to subrounded pebbles of dark gray lava up to 1 in. Sand is dominantly dark gray lava, subordinate pumice, minor ash-rich fine-grain sand and silt. This interval is poorly sorted and poorly consolidated. The hydraulic conductivity estimated by the Kozeny-Carman method is 1.517 ft/d.

Core Hole CrCH-2 935.7–938.25 ft [Tpf(p)]

Light orange-brown, silt-rich, fine- to coarse-grain tuffaceous sand with sparse matrix-supported granules and pebbles of white rounded pumice up to 0.5 in. This interval is massive, poorly sorted, and poorly consolidated. Top and bottom contacts with adjacent units are sharp. The interval appears to contain zones where coarse lithic sand and gravel like those found in the overlying unit are juxtaposed to the dominant fine- to medium-grain tuffaceous sand. These features are interpreted to be lithic sand and gravels that were mobilized into near-vertical open fractures from the overlying unit. The hydraulic conductivity estimated by the Kozeny-Carman method is 0.546 ft/d.

Core Hole CrCH-2 938.25–938.5 ft [Tpf(p)]

Dark gray, gravelly, coarse-grain lithic-tuffaceous sand with matrix-supported granules and pebbles of pumice up to 1 in. The sandy matrix is dominated by dark lava grains, but it also contains small, white, rounded pumice as a subordinate component. Interval is moderately well sorted and poorly consolidated. The hydraulic conductivity estimated by the Kozeny-Carman method is 3.414 ft/d.

Core Hole CrCH-2 938.5–939 ft [Tpf(p)]

Light orange-brown, gravelly, fine- to coarse-grain tuffaceous sand with abundant matrix-supported rounded pebbles of white pumice (dominant) and dark gray lava (subordinate) up to 0.5 in. Sand is dominantly pumice and ash with minor dark gray lava. This interval is poorly sorted. The hydraulic conductivity estimated by the Kozeny-Carman method is 1.517 ft/d.

Core Hole CrCH-2, Run 62
Drilled Interval 939–942 ft
Drilled 3 ft and Recovered 3 ft

Core Hole CrCH-2 939–939.6 ft [Tpf(p)]

Dark gray very coarse lithic sand to lithic fine gravel. The lithic sand/fine gravel is dominantly sand and abundant granules of dark gray lava up to 0.25 in. White pumice granules are sparse. This interval is moderately well sorted and poorly consolidated. The unit is severely mixed with the lithic sand/fine gravel occupying the outer parts of the core and a lithic-pumiceous sand mixture that was apparently mobilized and intruded the center part of the core from the underlying unit; we assume this is a drilling artifact. Sampling was confined to the lithic sand/fine gravel. This is the deepest occurrence of gravels that include the Rendija Canyon Rhyodacite, an indicator of the Puye Formation. The hydraulic conductivity estimated by the Kozeny-Carman method is 4.916 ft/d.

Tpf(p)/Tjfp Contact–939.6 ft

Core Hole CrCH-2 939.6–940.3 ft (Tjfp)

Light brown-gray, gravelly, coarse-grain tuffaceous sand with abundant matrix-supported, rounded pebbles of white pumice. The sandy matrix is dominantly white vitric pumice fragments with sparse, small, dark gray lava grains. The unit coarsens upwards with white pumice clasts up to 0.5 in. becoming more abundant in the upper part. The interval is moderately well sorted in the lower 2/3 of the unit that is dominated by coarse sand, and it is less well sorted in the pebbly upper part where the matrix is made up of fine- to coarse-grain sand. The hydraulic conductivity estimated by the Kozeny-Carman method is 0.971 ft/d.

Core Hole CrCH-2 940.3–940.7 ft (Tjfp)

White clast-supported pumice sand and gravel with granules of white vitric pumice lapilli up to 0.25 in. Small, dark gray lava clasts are sparsely distributed throughout the interval but slightly concentrated towards the base of the unit. The unit is poorly consolidated, well sorted, and highly porous. The hydraulic conductivity estimated by the Kozeny-Carman method is 2.185 ft/d.

Core Hole CrCH-2 940.7–941 ft (Tjfp)

Light brown-gray, fine- to coarse-grain pumiceous sand. The sand contains sparse dark gray lava grains and may include a silt component. The unit is poorly sorted and moderately consolidated. The hydraulic conductivity estimated by the Kozeny-Carman method is 0.546 ft/d.

Core Hole CrCH-2 941–941.7 ft (Tjfp)

Gray-brown, fine- to very-coarse-grain, lithic-tuffaceous sand with sparse granules and pebbles of dark gray lava up to 0.5 in. The sand is dominantly rounded dark gray lava and sparse white pumice. The unit is poorly sorted and moderately consolidated. The hydraulic conductivity estimated by the Kozeny-Carman method is 1.836 ft/d.

Core Hole CrCH-2 941.17–941.75 ft (Tjfp)

Brown clast-supported pumice gravel at the base of the unit, grading upwards to a tuffaceous, coarse-grain sand at the top of the unit. The lower gravel contains pebbles of dense pumice up to 2 in. The unit is poorly sorted and moderately consolidated. The hydraulic conductivity estimated by the Kozeny-Carman method is 2.185 ft/d.

Core Hole CrCH-2 941.75–942 ft (Tjfp)

Light brownish gray, gravelly, medium- to coarse-grain tuffaceous-lithic sand with subrounded to rounded granules of dark gray lava and pumice up to 0.25 in. The unit is massive, moderately well sorted, and moderately consolidated. The hydraulic conductivity estimated by the Kozeny-Carman method is 1.517 ft/d.

Core Hole CrCH-2, Run 63

Drilled Interval 942–946 ft

Drilled 4 ft and Recovered 4 ft

Core Hole CrCH-2 942–942.8 ft (Tjfp)

Orange brown, silty, fine- to coarse-grain tuffaceous sand with sparse, matrix-supported pebbles of white vitric pumice and dark gray lavas up to 0.75 in. The sandy matrix is made up of subrounded to rounded vitric pumice fragments, subordinate felsic crystals, and sparse, dark, lava grains. The interval is graded with the sand matrix somewhat more coarse grain at the base of the unit than in the upper part. A single, anomalous 3-in. rounded cobble of white, dense, pumice with abundant small biotite phenocrysts occurs

at the top of the interval. The interval is poorly sorted and poorly consolidated. The hydraulic conductivity estimated by the Kozeny-Carman method is 0.971 ft/d.

Core Hole CrCH-2 942.8–943.9 ft (Tjfp)

Gray-brown, fine- to coarse-grain tuffaceous sand. A few rounded, matrix-supported granules of white vitric pumice and dark gray lavas are present near the base of the interval. The interval is well sorted and poorly consolidated. The hydraulic conductivity estimated by the Kozeny-Carman method is 2.185 ft/d.

Core Hole CrCH-2 943.9–944.47 ft (Tjfp)

Light brown, gravelly, fine-grain tuffaceous sand with abundant matrix-supported granules and pebbles of white vitric pumice (up to 0.5 in.) and dark gray lava (up to 1 in.). The interval is massive, poorly sorted, and poorly consolidated. The hydraulic conductivity estimated by the Kozeny-Carman method is 0.744 ft/d.

Core Hole CrCH-2 944.47–945.55 ft (Tjfp)

Light brown, coarse-grain tuffaceous sand. The interval has sparse granules and pebbles. The interval is graded with the sand matrix in the lower half somewhat coarser than the upper half. The interval is massive, fairly well sorted, and poorly consolidated. The hydraulic conductivity estimated by the Kozeny-Carman method is 1.836 ft/d.

Core Hole CrCH-2 945.55–946 ft (Tjfp)

Medium to dark gray, gravel-rich, silt-rich, fine- to coarse-grain tuffaceous sand. The poorly sorted matrix is made up of pumice fragments, ash, subordinate felsic crystals, and sparse dark lava grains. The interval contains matrix-supported granules and pebbles of sparse white pumice and common, dark gray lava (up to 2.25 in.). A single, anomalous 2.5-in. rounded cobble of white, dense, pumice occurs at the top of the interval. The interval is densely compacted and well consolidated. The hydraulic conductivity estimated by the Kozeny-Carman method is 0.971 ft/d.

Core Hole CrCH-2, Run 64

Drilled Interval 946–950 ft

Drilled 4 ft and Recovered 4 ft 10 in.

Core Hole CrCH-2 <946 ft; 10 in. of excess core (Tpf)

Possible slough. Light brown, gravelly, fine- to coarse-grain tuffaceous sand with subrounded dark gray lava and white pumice granules and pebbles up to 2 in. supported by a matrix of fine- to coarse-grain lithic sand. There is more of a coarse-sand component in the matrix, which is dominated by fine to medium sand as in the underlying unit, except for the coarse-sand component. This interval is poorly sorted and lacks bedding. The hydraulic conductivity estimated by the Kozeny-Carman method is 2.185 ft/d.

Core Hole CrCH-2 946–948 ft (Tpf)

Light brown, fine- to coarse-grain tuffaceous sand. Granules of sparse, subrounded dark gray lava and white pumice granules and pebbles are supported by the poorly sorted sandy matrix. This interval is massive and lacks bedding. The hydraulic conductivity estimated by the Kozeny-Carman method is 2.185 ft/d.

Core Hole CrCH-2 948–949.4 ft (Tpf)

Gray-brown to medium brown, gravel-rich, coarse-grain lithic sand with matrix-supported granules and pebbles of dark lava up to 0.5 in. The sandy matrix is dominated by dark lava grains, but it also contains small, white pumice as a subordinate component. Interval is well sorted and poorly consolidated. This interval is notable for the large amount of oxidized iron fillings scattered throughout, including in the interior of the core. The hydraulic conductivity estimated by the Kozeny-Carman method is 3.414 ft/d.

Core Hole CrCH-2 949.4–949.6 ft (Tpf)

Reddish brown matrix-supported gravel with a silt-rich fine- to coarse-grain sandy matrix. Gravel clasts are granules and pebbles of rounded white pumice (common) and dark lava (less common). The interval is poorly sorted. The hydraulic conductivity estimated by the Kozeny-Carman method is 3.414 ft/d.

Core Hole CrCH-2 949.6–950 ft (Tpf)

Light to medium brown, gravel-rich, coarse-grain tuffaceous sand with matrix-supported granules of white pumice and dark gray lava. There are two cobble-sized (3 in.) dense pumice granule in the interval. The interval is well sorted and poorly consolidated. The hydraulic conductivity estimated by the Kozeny-Carman method is 1.517 ft/d.

**Core Hole CrCH-2, Run 65
Drilled Interval 950–953 ft
Drilled 3 ft and Recovered 3 ft 6 in.**

Core Hole CrCH-2 <950 ft; 6 in. of excess core (Tpf)

Possible slough. Medium brown, gravel-rich, coarse-grain tuffaceous sand with abundant rounded white pumice in the sandy matrix. Sparse granules and pebbles of pumice and dark lava (up to 0.25 in.) are supported by the sandy matrix. The interval is well sorted. The contact with the underlying unit is sharp. The hydraulic conductivity estimated by the Kozeny-Carman method is 0.546 ft/d.

Core Hole CrCH-2 950–950.7 ft (Tpf)

Gray-brown, gravel-rich, silty, fine- to medium-grain tuffaceous sand with abundant matrix-supported, rounded to subrounded, dark gray lava granules, pebbles, and cobbles up to 3 in. The sandy matrix is dominated by rounded pumice fragments. This interval is massive, unconsolidated, and poorly sorted. The hydraulic conductivity estimated by the Kozeny-Carman method is 1.517 ft/d.

Core Hole CrCH-2 950.7–951.7 ft (Tpf)

Medium brown, fine- to medium-grain tuffaceous sand with very sparse matrix-supported granules and pebbles of pumice up to 0.5 in. Sand is graded from coarser at the base, to finer in the middle, and coarser at the top of the unit. This interval is well sorted and moderately consolidated. The hydraulic conductivity estimated by the Kozeny-Carman method is 2.974 ft/d.

Core Hole CrCH-2 951.7–952.25 ft (Tpf)

Gray-brown, silty, fine- to medium-grain lithic-tuffaceous sand with sparse matrix-supported granules and pebbles of pumice up to 0.5 in. Dark gray lava grains are more abundant than pumice in the sandy matrix. Sand is slightly graded, being somewhat coarser at the base and finer in the upper part of the unit. This interval is well sorted. The hydraulic conductivity estimated by the Kozeny-Carman method is 1.517 ft/d.

Core Hole CrCH-2 952.25–952.75 ft (Tpf)

Light orangish brown, gravelly and silty, fine-grain tuffaceous sand with matrix-supported rounded granules and pebbles of pumice up to 0.5 in. Dark gray lava clasts are relatively rare. This interval is poorly sorted and moderately well consolidated. The hydraulic conductivity estimated by the Kozeny-Carman method is 0.971 ft/d.

Core Hole CrCH-2 952.75–953 ft (Tpf)

Light brown, silt-rich, fine- to medium-grain tuffaceous-lithic sand with sparse matrix-supported granules of pumice. Abundant dark gray lava grains in the sandy matrix are more fine grain than the sandy rounded pumice component. This interval is massive, poorly sorted, and moderately well consolidated. Contact with overlying unit is sharp. The hydraulic conductivity estimated by the Kozeny-Carman method is 0.546 ft/d.

Core Hole CrCH-2, Run 66
Drilled Interval 953–957 ft
Drilled 4 ft and Recovered 5 ft

Core Hole CrCH-2 < 953 ft; 12 in. of excess core

Possible slough. Mixed interval of light brownish gray, gravelly and silty, coarse-grain lithic-tuffaceous sand. A 1-in.-thick purplish gray, medium-grain sand in middle of unit appears to be mobilized to the edge of the core where it forms a thin layer on the core rim. The upper part of the interval is a uniform coarse-grain lithic-tuffaceous sand with abundant granules of dark gray lava up to 0.25 in. The upper sand is well sorted and moderately consolidated. The hydraulic conductivity estimated by the Kozeny-Carman method is 0.546 ft/d.

Core Hole CrCH-2 953–953.5 ft (Tjfp)

Mixed interval of core with an upward-tapering conical zone of poorly sorted, light gray-brown, coarse-grain tuffaceous sand that is surrounded by purplish brown clay and gray medium-grain sand in a zone up to 0.5 in. thick. Sampling is confined to the interior tuffaceous sand, which is the lithology that is representative of this depth interval. The interior sand contains silt-rich, fine- to coarse-grain, dark gray lava clasts up to 0.5 in. The interior sand is coarse grain, poorly sorted and moderately well consolidated. The hydraulic conductivity estimated by the Kozeny-Carman method is 0.546 ft/d.

Core Hole CrCH-2 953.5–953.9 ft (Tjfp)

Light gray-brown, gravel-rich and silty, fine- to coarse-grain pumiceous sand with granules and pebbles of rounded, dense pumice. The sand is poorly sorted and moderately well consolidated. The top of the unit is a mixed interval with an upward-tapering conical zone of the pumiceous sand surrounded by material that appears to be derived from the overlying unit (not sampled). The hydraulic conductivity estimated by the Kozeny-Carman method is 0.546 ft/d.

Core Hole CrCH-2 953.9–954.3 ft (Tjfp)

Gray-brown, silt-rich, fine- to coarse-grain tuffaceous-lithic sand with sparse granules of pumice. The sand is poorly sorted and moderately well consolidated. The top of the unit is a mixed interval with an upward-tapering conical zone of the tuffaceous-lithic sand surrounded by material that appears to be derived from the overlying unit (not sampled). The hydraulic conductivity estimated by the Kozeny-Carman method is 1.229 ft/d.

Core Hole CrCH-2 954.3–954.8 ft (Tjfp)

Gray-brown, silty, fine- to coarse-grain tuffaceous sand with up to 30% white pumice clasts and sparse, rounded dark gray lava clasts. The sand is massive, poorly sorted, and moderately well consolidated. The hydraulic conductivity estimated by the Kozeny-Carman method is 1.229 ft/d.

Core Hole CrCH-2 954.8–955.25 ft (Tjfp)

Gray-brown, medium- to coarse-grain lithic-tuffaceous sand with sparse, subangular pumice granules up to 0.25 in. The unit is slightly graded, fining upwards. The sand is well sorted and moderately well consolidated. The hydraulic conductivity estimated by the Kozeny-Carman method is 0.971 ft/d.

Core Hole CrCH-2 955.25–955.8 ft (Tjfp)

Light brown, gravel-rich, fine- to coarse-grain pumiceous sand with abundant granules and pebbles of pumice and dark gray lava up to 0.5 in. The sand is well sorted and well consolidated. An unusual 0.25- to 0.5-in.-thick zone of dark brown clay occurs along the rim of the core; we assume this is a drilling artifact and did not sample it. The hydraulic conductivity estimated by the Kozeny-Carman method is 2.185 ft/d.

Core Hole CrCH-2 955.8–956.4 ft (Tjfp)

Medium brown, coarse-grain pumiceous-lithic sand with sparse granules of white pumice. The unit is slightly graded, fining upwards. The sand contains subequal pumice and lava and is well sorted and well consolidated. The upper part of the unit shows faint bedding. The hydraulic conductivity estimated by the Kozeny-Carman method is 2.185 ft/d.

Core Hole CrCH-2 956.4–957 ft (Tjfp)

Medium gray, coarse-grain lithic-tuffaceous sand with subrounded to rounded granules of white pumice and dark gray lava lithics. Lava is more abundant than pumice in the sand matrix. The unit is massive, well sorted, and moderately well consolidated. The hydraulic conductivity estimated by the Kozeny-Carman method is 1.517 ft/d.

Core Hole CrCH-2, Run 67

Drilled Interval 957–962 ft

Drilled 5 ft and Recovered 5 ft

Core Hole CrCH-2 956.8–957.7 ft (Tjfp)

Light orange-brown, gravelly and pumice-rich, silty, fine- to coarse-grain tuffaceous sand that contains abundant dark-lava grains as part of the sandy matrix. Granules and pebbles of lava are sparse and matrix-supported. Outer margins of the core up to 1 in. thick display an unusual concentration of gray silt and fine sand that is probably an artifact of the sonic drilling. The interval is poorly sorted. The hydraulic conductivity estimated by the Kozeny-Carman method is 0.379 ft/d.

Core Hole CrCH-2 957.7–959.7 ft (Tjfp)

Light orange-brown, coarse-grain tuffaceous sand that contains abundant dark-lava grains as part of the sandy matrix. Although the interval is generally uniform in character, there is a bed of coarse-grain, gravelly sand from 958.5 to 958.75 ft that contains abundant white pumice. Interval is well sorted. The hydraulic conductivity estimated by the Kozeny-Carman method is 1.517 ft/d.

Core Hole CrCH-2 959.7–960.4 ft (Tjfp)

Light orange-brown, coarse-grain tuffaceous sand containing abundant small, white vitric pumice granules. Interval is poorly sorted. Outer margins of the core display an unusual concentration of silt and fine sand that is probably an artifact of the sonic drilling. The hydraulic conductivity estimated by the Kozeny-Carman method is 0.546 ft/d.

Core Hole CrCH-2 960.4–960.8 ft (Tjfp)

Light orange-brown, silty, fine- to medium-grain tuffaceous sand. Pumice clasts are very small. The interval is uniform in character and contains no obvious bedding. Interval is well sorted. The hydraulic conductivity estimated by the Kozeny-Carman method is 1.229 ft/d.

Core Hole CrCH-2 960.8–962 ft (Tjfp)

Tan to light brown silt and fine-grain tuffaceous sand containing 10-15% matrix-supported, white vitric pumice up to 1 in. Interval is well sorted. The base of the interval, from 961.7 to 962 ft, is relatively pumice rich. The interval 960.8 to 961.2 ft also contains abundant pebbles of pumice granules, some of which are surrounded by slight oxidation. The hydraulic conductivity estimated by the Kozeny-Carman method is 0.243 ft/d.

Core Hole CrCH-2, Run 68
Drilled Interval 962–967 ft
Drilled 5 ft and Recovered 5 ft

Core Hole CrCH-2 962–962.8 ft (Tjfp)

Light gray-brown, gravel-rich, coarse-grain tuffaceous sand with abundant matrix-supported granules and pebbles of pumice and gray lavas. Interval is well sorted and poorly consolidated. The hydraulic conductivity estimated by the Kozeny-Carman method is 3.884 ft/d.

Core Hole CrCH-2 962.8–963.8 ft (Tjfp)

Light orange-brown, coarse-grain tuffaceous sand with sparse granules of white vitric pumice and gray lavas. Interval is well sorted and poorly consolidated. The hydraulic conductivity estimated by the Kozeny-Carman method is 3.884 ft/d.

Core Hole CrCH-2 963.8–965.3 ft (Tjfp)

Orangish gray-brown, silt-rich, fine- to coarse-grain tuffaceous sand with matrix-supported granules and pebbles of white vitric pumice and gray lavas up to 2 in. The top of the interval from 963.8 to 964 ft is a slightly more oxidized, clast-free, light-brown, fine- to medium-grain tuffaceous sand. The footage from 964 to 964.25 ft is a pumice-rich gravel bed. Interval is poorly sorted. The hydraulic conductivity estimated by the Kozeny-Carman method is 0.243 ft/d.

Core Hole CrCH-2 965.3–965.8 ft (Tjfp)

Light to medium brown, fine- to coarse-grain tuffaceous sand with granules of white vitric pumice and gray lava. A possible small fault juxtaposes orangish tan silt with small pumice and lava clasts against the medium- to coarse-grain sand along a high-angle plane cutting the core. The possible fault zone is about 0.5- to 0.75-in. wide and the fine silts show a closely spaced foliation parallel to the fault. There is no cementation associated with the possible fault. Interval is poorly sorted. The hydraulic conductivity estimated by the Kozeny-Carman method is 0.243 ft/d.

Core Hole CrCH-2 965.8–966.3 ft (Tjfp)

Light orangish brown, fine-grain sand and silt with matrix-supported clasts of white vitric pumice and gray lavas up to 0.5 in. Closely spaced high-angle fractures cut the core in this interval. The fracture zone is 0.25 in. wide and contains an unidentified dark material that seems to coat sand grains. Interval is fairly well sorted. The hydraulic conductivity estimated by the Kozeny-Carman method is 0.243 ft/d.

Core Hole CrCH-2 966.3–966.5 ft (Tjfp)

Light grayish brown silt and fine-grain sand that is sorted and compacted. The interval appears to contain bedding 0.15 to 0.25 ft thick. The hydraulic conductivity estimated by the Kozeny-Carman method is 0.061 ft/d.

Core Hole CrCH-2 966.5–967 ft (Tjfp)

Light brown silt and fine-grain sand that appears to be laminated and compacted. There are patchy zones containing white pumice clasts. The hydraulic conductivity estimated by the Kozeny-Carman method is 0.061 ft/d.

Core Hole CrCH-2, Run 69

Drilled Interval 967–970 ft

Drilled 3 ft and Recovered 3 ft

Core Hole CrCH-2 967–968.1 ft (Tjfp)

Gray-brown, very coarse–grain tuffaceous-lithic sand to fine gravel. Contains subequal subangular to subrounded sand and granules of white pumice and dark gray lavas. Interval is slightly graded, fining upwards. The interval is well sorted and unconsolidated. This unit is similar to the 969 to 970 ft interval. The hydraulic conductivity estimated by the Kozeny-Carman method is 3.884 ft/d.

Core Hole CrCH-2 968.1–969 ft (Tjfp)

Brown, fine- to medium-grain tuffaceous sand with a minor component of dark gray lava sand. Interval is gravel free, well sorted, and slightly consolidated. The hydraulic conductivity estimated by the Kozeny-Carman method is 2.185 ft/d.

Core Hole CrCH-2 969–970 ft (Tjfp)

Gray-brown, very coarse–grain tuffaceous-lithic sand to fine gravel. Contains subequal rounded sand and granules of white pumice and dark gray lavas. Interval is slightly graded, fining upwards. The interval is gravel free, well sorted, and unconsolidated. The hydraulic conductivity estimated by the Kozeny-Carman method is 2.185 ft/d.

Core Hole CrCH-2, Run 70

Drilled Interval 970–973 ft

Drilled 3 ft and Recovered 3.4 ft

Core Hole CrCH-2 <970 ft; 5 in. of excess core

Possible slough. Gray-brown mixed interval of adjacent zones of vertically segregated medium-grain sand next to lithic gravel (up to 0.25 in) with sparse pumice. Interval is capped by massive medium- to coarse-grain sand. The sample is possible slough. The hydraulic conductivity estimated by the Kozeny-Carman method is 3.414 ft/d.

Core Hole CrCH-2 970–971 ft (Tjfp)

Gray-brown, fine- to coarse-grain tuffaceous-lithic sand. Contains subequal tuffaceous material and dark gray lava. Interval is slightly graded, fining upwards. The interval is fairly well sorted and poorly consolidated. The hydraulic conductivity estimated by the Kozeny-Carman method is 2.185 ft/d.

Core Hole CrCH-2 971–971.5 ft (Tjfp)

Brown, very coarse grain tuffaceous-lithic sand to fine gravel (mostly <0.25 in.). Contains subequal rounded pumice and dark gray lavas. The matrix contains little silt. Interval is well sorted and poorly consolidated. The hydraulic conductivity estimated by the Kozeny-Carman method is 3.884 ft/d.

Core Hole CrCH-2 971.5–971.7 ft (Tjfp)

Dark gray-brown, silty, fine- to medium-grain tuffaceous-lithic sand with sparse granules of rounded dark gray lava and white pumice. Possible grading with slight coarsening of matrix upwards. Interval is fairly well sorted and poorly consolidated. The hydraulic conductivity estimated by the Kozeny-Carman method is 1.517 ft/d.

Core Hole CrCH-2 971.7–971.9 ft (Tjfp)

Light brown, gravel-rich, fine- to coarse-grain tuffaceous-lithic sand with common matrix-supported granules and pebbles of rounded white pumice. Dark lava clasts are sparse. The matrix may contain some silt and fine sand. Interval is poorly sorted and poorly consolidated. The hydraulic conductivity estimated by the Kozeny-Carman method is 2.974 ft/d.

Core Hole CrCH-2 971.9–972.25 ft (Tjfp)

Light brown tuffaceous fine gravel with a coarse-grain sand matrix. The gravel is both matrix- and clast-supported. The gravel is made up of larger rounded dark gray lava up to 0.75 in. and smaller white pumice up to 0.5 in. Interval is poorly sorted. The hydraulic conductivity estimated by the Kozeny-Carman method is 1.836 ft/d.

Core Hole CrCH-2 972.25–973 ft (Tjfp)

Light to medium brown, gravelly, fine- to medium-grain tuffaceous sand with common matrix-supported granules and pebbles of rounded dark gray lava and white pumice (up to 0.25 in.). The unit contains slightly more pumice in the upper part. The lowermost 2 in. of the unit is somewhat whiter and finer grain than the sands above. The unit is fairly well sorted and moderately consolidated. The hydraulic conductivity estimated by the Kozeny-Carman method is 2.974 ft/d.

Core Hole CrCH-2, Run 71

Drilled Interval 973–978 ft

Drilled 5 ft and Recovered 5 ft

Note: This core run showed considerable mixing of zones along the margins of the core. A rind of silt and fine sand surrounding the upper core interior appears to have been mobilized from the lower. Also, contacts in the lower intervals show upward drag along their outer margins. The mixing probably took place when soft plastic core was extruded into the plastic sleeve from the core barrel. Sampling was restricted to undisturbed areas in the center of the core that preserved the stratigraphic succession, and possible mobilized zones, such as the upper rind on the outer part of the core, were excluded.

Core Hole CrCH-2 973–974.7 ft (Tjfp)

Dark gray-brown, very coarse grain tuffaceous-lithic sand to fine gravel. Contains subequal rounded sand and granules of white pumice and dark gray lavas. Contains sparse lava pebbles. Sand grains are rounded to subrounded. Interval is well sorted. Some medium sand in the matrix, but little or no silt and fine sand. The hydraulic conductivity estimated by the Kozeny-Carman method is 2.974 ft/d.

Core Hole CrCH-2 974.7–975.25 ft (Tjfp)

Brown gravelly and silty fine- to coarse-grain tuffaceous sand with common rounded pumice granules. Interval has poor sorting and is poorly to moderately consolidated. The hydraulic conductivity estimated by the Kozeny-Carman method is 0.971 ft/d.

Core Hole CrCH-2 975.25–975.7 ft (Tjfp)

Gray-brown lithic gravel. Gravel is made up of matrix-supported rounded to subrounded granules and pebbles of dark gray lava clasts. The matrix is silt and fine- to coarse-grain tuffaceous-lithic sand matrix. Pumice is very sparse in the gravel. Interval is poorly sorted and poorly consolidated. The hydraulic conductivity estimated by the Kozeny-Carman method is 0.379 ft/d.

Core Hole CrCH-2 975.7–977 ft (Tjfp)

Reddish brown gravelly silt and fine- to coarse-grain tuffaceous sand with rounded pumice up to 0.25 in. The interval is slightly graded, fining upwards, and becomes somewhat darker in color in the upper part. The matrix contains considerable silt and sorting is poor. The unit is moderately consolidated. The hydraulic conductivity estimated by the Kozeny-Carman method is 0.379 ft/d.

Core Hole CrCH-2 977–977.1 ft (Tjfp)

Light gray to tan-white, fine-grain, vitric ash bed (possible ash fall) with sparse subrounded pumice up to 0.25 in. The bed is slightly graded (fining upwards) and moderately well consolidated. The hydraulic conductivity estimated by the Kozeny-Carman method is 0.379 ft/d.

Core Hole CrCH-2 977.1–977.6 ft (Tjfp)

Light brown, gravelly, fine-grain tuffaceous sand and silt with common granules and pebbles of pumice up to 0.25 in. The interval is graded, fining upwards. The interval is poorly sorted and moderately consolidated. The hydraulic conductivity estimated by the Kozeny-Carman method is 0.379 ft/d.

Core Hole CrCH-2 977.6–978 ft (Tjfp)

Reddish brown silt and fine- to medium-grain tuffaceous sand with granules of pumice and rare dark lava clasts up to 0.5 in. The unit is poorly sorted and moderately consolidated. The hydraulic conductivity estimated by the Kozeny-Carman method is 0.243 ft/d.

Core Hole CrCH-2, Run 72
Drilled Interval 978–982 ft
Drilled 4 ft and Recovered 4 ft

Core Hole CrCH-2 978–979 ft (Tjfp)

Brown, silty, fine- to coarse-grain tuffaceous sand with some matrix-supported granules of white pumice. Interval is poorly sorted and moderately consolidated. Interval contains dark gray patches of medium- to coarse-grain crystal-rich sand that may be fracture fill or a segregation induced by drilling. The hydraulic conductivity estimated by the Kozeny-Carman method is 0.971 ft/d.

Core Hole CrCH-2 979–980 ft (Tjfp)

Brown, medium- to coarse-grain tuffaceous sand with matrix-supported clasts of white, rounded pumice up to 0.5 in. and subordinate gray lava granules. Interval is poorly sorted and moderately consolidated. Interval contains dark gray patches of fine- to medium-grain crystal-rich sand that may be fracture fill or a segregation induced by drilling. The hydraulic conductivity estimated by the Kozeny-Carman method is 2.185 ft/d.

Core Hole CrCH-2 980–981.5 ft (Tjfp)

Gray-brown, gravelly, coarse-grain lithic-tuffaceous sand. The matrix is dominated by dark gray lava, and white pumice is subordinate. The matrix contains relatively few fines. Unit grades upwards to a medium-grain sand. Interval is fairly well sorted and poorly consolidated. The hydraulic conductivity estimated by the Kozeny-Carman method is 2.564 ft/d.

Core Hole CrCH-2 981.5–982 ft (Tjfp)

Reddish brown, gravel-rich and silty, fine- to coarse-grain, tuffaceous sand with abundant matrix-supported granules and pebbles of subrounded white pumice (up to 0.75 in.) and sparse dark gray lava. Interval is massive, poorly sorted, and moderately consolidated. The hydraulic conductivity estimated by the Kozeny-Carman method is 0.379 ft/d.

Core Hole CrCH-2, Run 73
Drilled Interval 982–987 ft
Drilled 5 ft and Recovered 5 ft

Core Hole CrCH-2 982–982.75 ft (Tjfp)

Light brown, gravel-rich silt and fine-grain tuffaceous sand with rounded matrix-supported granules of white pumice and subordinate dark gray lavas. Interval is poorly sorted and moderately consolidated. The hydraulic conductivity estimated by the Kozeny-Carman method is 0.243 ft/d.

Core Hole CrCH-2 982.75–982.9 ft (Tjfp)

Light brownish gray, gravelly and silt-rich, coarse-grain tuffaceous sand with abundant matrix-supported granules of white pumice and subordinate dark gray lavas. Interval is poorly sorted and moderately consolidated. The hydraulic conductivity estimated by the Kozeny-Carman method is 0.243 ft/d.

Core Hole CrCH-2 982.9–984.16 ft (Tjfp)

Brown, gravelly silt and fine-grain tuffaceous sand with matrix-supported granules of white pumice in the lower part. Cracks or fractures in the interval are filled with coarse- to very coarse-grain pumice and dark lava grains. The hydraulic conductivity estimated by the Kozeny-Carman method is 0.350 ft/d.

Core Hole CrCH-2 984.16–985 ft (Tjfp)

Light to medium brown, gravel- and silt-rich, coarse-grain tuffaceous sand with abundant matrix-supported granules and pebbles of white pumice and subordinate dark gray lavas. The unit is graded and becomes more fine grain upwards. Pebbles are mostly <0.25 in., but one is 0.5 in. Interval is poorly sorted and moderately consolidated. The hydraulic conductivity estimated by the Kozeny-Carman method is 0.410 ft/d.

Core Hole CrCH-2 985–986.6 ft (Tjfp)

Brownish white pumice fall with sparse grains of dark gray lavas. Angular to subrounded pumice clasts are white vitric, and up to 0.25 in. Interval is well sorted and lacks fine ash in the matrix. The unit is poorly consolidated. Note: the lower 1 ft of interval was removed by previous sampling. A split of the earlier sampled material contained abundant ash, leading to the belief that the lower part of interval was fine grain. The hydraulic conductivity estimated by the Kozeny-Carman method is 2.974 ft/d.

Core Hole CrCH-2 986.6–987 ft (Tjfp)

Reddish brown, gravelly silt and fine- to coarse-grain tuffaceous sand with matrix-supported silt-coated granules of white pumice. The unit is slightly graded and becomes more fine grain upwards. Interval is poorly sorted and moderately consolidated. The hydraulic conductivity estimated by the Kozeny-Carman method is 0.379 ft/d.

C-3.0 CORE HOLE CrCH-3 LITHOLOGIC DESCRIPTIONS

Note: All footages are measured from the bottom of core tubes. The colors in the descriptions reflect damp to wet cores except where noted.

Core Hole CrCH-3 Run 54 (Lexan)

Drilled Interval 876–880 ft

Drilled 48 in. and Recovered 58 in. (extra footage at top of core run discarded for final report)

Core Hole CrCH-3 876–876.6 ft (Tpf)

Light brown, silty and sandy gravel with common matrix-supported granules and pebbles of dark lava up to 0.5 in. Sparse granules of white pumice are present. The sandy matrix is fine to coarse grain. The bed has crude reverse grading with larger clasts concentrated in the middle and top. The bed is massive, well consolidated, and poorly sorted. The hydraulic conductivity estimated by the Kozeny-Carman method is 0.493 ft/d.

Core Hole CrCH-3 876–876.64 ft (Tpf)

Very thin bed of brown, very fine- to fine-grain sand with very sparse granules of dark lava. The bed is massive, well consolidated, and well sorted. Transmissivity is poor. No sieve data was collected for this thin interval.

Core Hole CrCH-3 876.64–876.96 ft (Tpf)

Light brown, fine- to medium-grain sand with ~15% matrix-supported granules and pebbles of white pumice up to 0.25 in. Sparse granules of dark lava are present. The bed contains faint horizontal bedding. The bed is well consolidated and moderately sorted. The hydraulic conductivity estimated by the Kozeny-Carman method is 0.175 ft/d.

Core Hole CrCH-3 876.96–877 ft (Tpf)

Very thin bed of dark brown, fine-grain sand. The bed is massive, well consolidated, and well sorted. Transmissivity is poor. Like all beds in this core run, the unit is densely compacted; this may be an artifact of coring. No sieve data was collected for this thin interval.

Core Hole CrCH-3 877–877.66 ft (Tpf)

Light brown, fine- to coarse-grain silty sand with common matrix-supported granules of dark gray lava. Sparse granules of white pumice are present; these are slightly more concentrated near the bottom of the bed. The bed is massive, well consolidated, and poorly to moderately sorted. The hydraulic conductivity estimated by the Kozeny-Carman method is 0.219 ft/d.

Core Hole CrCH-3 877.66–877.75 ft (Tpf)

Medium to dark brown, fine-grain sand with very sparse granules of dark lava. The bed is massive, well consolidated, and well sorted. Transmissivity is poor. No sieve data was collected for this thin interval.

Core Hole CrCH-3 877.75–878.2 ft (Tpf)

Light brown silt and fine-grain sand with common matrix-supported granules and pebbles of white pumice and dark lava up to 0.25 in. The dark lava clasts tend to be granules (i.e., smaller). The bed is massive, well consolidated, and poorly sorted. The hydraulic conductivity estimated by the Kozeny-Carman method is 0.103 ft/d.

Core Hole CrCH-3 878.2–880 ft (Tpf)

Light to medium brown, gravelly, silt and fine-grain sand with ~10% matrix-supported granules and pebbles of dark lava up to 0.5 in. There are no pumice clasts. The bed is normally graded, fining upwards. The lower part of the bed contains faint stratification and the upper part is massive. The bed is well consolidated and poorly sorted. The hydraulic conductivity estimated by the Kozeny-Carman method is 0.073 ft/d.

Core Hole CrCH-3 Run 55

Drilled Interval 880–884 ft

Drilled 48 in. and Recovered 60 in. (extra footage at top of core run discarded for final report)

Core Hole CrCH-3 880–881 ft (Tpf)

Light brownish gray gravel with a matrix of coarse-grain sand supporting subangular to subrounded granules and pebbles of dacite up to 2 in. Includes sparse rounded pumice up to 0.25 in. Interval is reverse graded with sands yielding to clast-supported gravels upwards in the section. Small rust spots in center of core may be oxidized iron fillings. The bed is well consolidated and poorly sorted. The hydraulic conductivity estimated by the Kozeny-Carman method is 0.661 ft/d.

Core Hole CrCH-3 881–881.6 ft (Tpf)

Light grayish brown, gravelly, coarse-grain sand with subangular to subrounded granules and rare pebbles of dacite up to 1 in. Includes sparse sand-size pumice. The bed is massive, poorly consolidated, and poorly to moderately sorted. The hydraulic conductivity estimated by the Kozeny-Carman method is 1.457 ft/d.

Core Hole CrCH-3 881.6–881.9 ft (Tpf)

Medium gray, gravelly and silty, medium- to coarse-grain sand with subrounded granules of dacite. Interval appears to be crudely bedded. Clasts from underlying bed are partly intermixed in basal 2 in. of this bed. The bed is moderately consolidated and moderately well sorted. The hydraulic conductivity estimated by the Kozeny-Carman method is 0.350 ft/d.

Core Hole CrCH-3 881.9–882.9 ft (Tpf)

Reddish brown, silty, coarse-grain sand with thin, slightly deformed, medium-brown interbedded fine- to medium-grain sand. The coarse-grain sand contains subangular to subrounded granules and pebbles of dacite and sparse granules of white pumice. Some dacite clasts are coarsely vesicular and may represent scoria. The bed is moderately well consolidated and poorly sorted. The hydraulic conductivity estimated by the Kozeny-Carman method is 0.197 ft/d.

Core Hole CrCH-3 882.9–883.6 ft (Tpf)

Light purplish gray gravel with a matrix of silt and fine- to medium-grain sand supporting up to 40% angular to subangular granules and pebbles of dacite up to 1.5 in. Some dacite clasts are coarsely vesicular and may represent scoria. The bed is massive, moderately consolidated, and poorly sorted. The hydraulic conductivity estimated by the Kozeny-Carman method is 0.231 ft/d.

Core Hole CrCH-3 883.6–884 ft (Tpf)

Grayish brown gravel with a matrix of silt and fine- to coarse-grain sand with upward common matrix-supported, angular to subangular granules and pebbles of dacite up to 0.5 in. Interval contains minor pumice granules. The base of the interval is poorly consolidated and contains higher concentrations of matrix-supported pebbles than above. The middle of the interval is somewhat bedded. The upper portion of the interval is sandy and moderately consolidated. Sorting is poor throughout the interval. Transmissivity is good in the lower gravel-rich bed and poor in the upper sandy part. Note: the lower 3.5 in. of the Lexan tube was empty. The hydraulic conductivity estimated by the Kozeny-Carman method is 0.186 ft/d.

Core Hole CrCH-3 Run 56 (bag; core is dried out)

Drilled Interval 884–888 ft

Drilled 48 in. and Recovered 48 in.

Core Hole CrCH-3 884–884.8 ft (Tpf)

Grayish light-brown sandy gravel with pebbles of subangular to subrounded dacite up to 2 in. Clasts are supported in a matrix of fine- to coarse-grain lithic-crystal sand. The bed is massive, unconsolidated, and poorly sorted. The hydraulic conductivity estimated by the Kozeny-Carman method is 4.181 ft/d.

Core Hole CrCH-3 884.8–885.9 ft (Tpf)

Grayish light-brown gravel with a matrix of fine- to coarse-grain lithic-crystal sand supporting ~30% granules and pebbles of subangular to subrounded dacite up to 1 in. The bed is massive, poorly consolidated, and poorly sorted. The hydraulic conductivity estimated by the Kozeny-Carman method is 2.725 ft/d.

Core Hole CrCH-3 885.9–886.4 ft (Tpf)

Light pinkish gray gravel with a matrix of silt and fine- to coarse-grain sand that supports granules and pebbles of dacite up to 2 in. The sandy matrix appears to be dominated by ash with minor amounts of lithics and crystals. The interval is unusually well consolidated, but it is not cemented by calcite (does not effervesce in HCl). The bed is massive and moderately sorted. The hydraulic conductivity estimated by the Kozeny-Carman method is 0.702 ft/d.

Core Hole CrCH-3 886.4–887 ft (Tpf)

Orangish gray gravel with a matrix of silt and fine- to coarse-grain sand that supports subangular to subrounded granules and pebbles of dacite up to 1.5 in. The bed is massive, unconsolidated, and poorly sorted. The hydraulic conductivity estimated by the Kozeny-Carman method is 0.476 ft/d.

Core Hole CrCH-3 887–888 ft (Tpf)

Light brown sandy gravel made up of 30–40% subangular to subrounded granules and pebbles of dacite. Clasts are supported in a matrix of silty fine- to coarse-grain tuffaceous sand. The bed is massive, generally unconsolidated, and poorly sorted. Small areas of the bed show greater consolidation. The hydraulic conductivity estimated by the Kozeny-Carman method is 0.744 ft/d.

Core Hole CrCH-3 Run 57

Drilled Interval 888–891 ft

Drilled 36 in. and Recovered 60 in. (extra footage at top of core run discarded for final report)

Core Hole CrCH-3 888–888.95 ft (Tpf)

Light brownish gray, gravelly, silt and fine- to coarse-grain sand with 10–15% matrix-supported, subangular to subrounded granules and pebbles of brown and gray dacite up to 0.5 in. The interval contains fewer larger pebbles than the overlying bed. No pumice clasts occur in this interval. The bed is massive, moderately consolidated, and poorly sorted. The hydraulic conductivity estimated by the Kozeny-Carman method is 0.155 ft/d.

Core Hole CrCH-3 888.95–889 ft (Tpf)

Medium brownish gray silt and fine-grain sand. This thin interval contains few granule-sized clasts and forms a partly disrupted thin interbed between two thicker gravelly sands. The bed is massive, moderately consolidated, and moderately well sorted. The hydraulic conductivity estimated by the Kozeny-Carman method is 0.087 ft/d.

Core Hole CrCH-3 889–891 ft (Tpf)

Bedded sequence dominated by light brownish gray, gravelly, silt and fine- to coarse-grain sand with abundant matrix-supported, subangular to subrounded granules and pebbles of dacite up to 0.5 in. These dominant beds are massive, strongly consolidated, and poorly sorted. Up to seven thin beds of medium brown-gray silty fine sand are interbedded within the primary fine- to coarse-grain, tuffaceous sand; these

thin interbeds are similar to the overlying 888.95–889 ft bed. The hydraulic conductivity estimated by the Kozeny-Carman method is 0.197 ft/d.

Core Hole CrCH-3 Run 58

Drilled Interval 891–895 ft

Drilled 48 in. and Recovered 60 in. (extra footage at top of core run discarded for final report)

Core Hole CrCH-3 891–891.5 ft (Tpf)

Reddish brown gravel with a matrix of silt and fine- to coarse-grain lithic sand that supports subangular granules and pebbles of dark dacite up to 2 in. (but generally <0.5 in.). The interval is notably oxidized. The bed is massive, moderately well consolidated, and poorly sorted. The hydraulic conductivity estimated by the Kozeny-Carman method is 0.744 ft/d.

Core Hole CrCH-3 891.5–892.7 ft (Tpf)

Grayish brown gravel with a matrix of silt and fine- to coarse-grain lithic sand that supports subrounded granules and pebbles of dark dacite up to 1.5 in. Pumice is sparsely distributed throughout the sand fraction. The bed is massive, moderately well consolidated, and poorly sorted. The hydraulic conductivity estimated by the Kozeny-Carman method is 1.398 ft/d.

Core Hole CrCH-3 892.7–892.9 ft (Tpf)

Grayish brown gravel with a matrix of fine- to coarse-grain lithic sand that supports subrounded granules and pebbles of dark dacite up to 0.5 in. Pumice is moderately abundant throughout the sand matrix. The bed is faintly bedded, poorly consolidated, and poorly sorted. The hydraulic conductivity estimated by the Kozeny-Carman method is 1.836 ft/d.

Core Hole CrCH-3 892.9–893.3 ft (Tpf)

Light brown gravel with a matrix of silty fine- to coarse-grain lithic sand that supports subangular to subrounded granules and pebbles of dark dacite up to 0.5 in. The bed is massive, moderately well consolidated, and poorly sorted. The hydraulic conductivity estimated by the Kozeny-Carman method is 0.546 ft/d.

Core Hole CrCH-3 893.3–893.4 ft (Tpf)

Grayish brown, gravelly, silt and fine- to coarse-grain sand with pumice and lava granules. Contains some coarse-grain dacite sand. The lower part of the interval is bedded and the upper part is massive. The bed is moderately well consolidated and fairly well sorted. The hydraulic conductivity estimated by the Kozeny-Carman method is 0.255 ft/d.

Core Hole CrCH-3 893.4–894.4 ft (Tpf)

Light brown, gravelly, silt and fine- to coarse-grain tuffaceous sand with abundant, matrix-supported granules and pebbles of dark dacite and white pumice up to 0.25 in. The interval is bedded at the top and bottom and massive in the middle. The bed is massive, moderately well consolidated, and poorly sorted. The hydraulic conductivity estimated by the Kozeny-Carman method is 0.395 ft/d.

Core Hole CrCH-3 894.4–894.75 ft (Tpf)

Gray-brown silt and fine- to coarse-grain sand with abundant, matrix-supported granules and pebbles of dark dacite up to 0.25 in. and sparse granules of white pumice. The bed is moderately well consolidated and poorly sorted. The hydraulic conductivity estimated by the Kozeny-Carman method is 0.146 ft/d.

Core Hole CrCH-3 894.75–895 ft (Tpf)

Medium gray silt and fine- to coarse-grain sand with sparse, matrix-supported granules and pebbles of dark dacite up to 0.5 in. The bed is massive, moderately well consolidated, and poorly sorted. The hydraulic conductivity estimated by the Kozeny-Carman method is 0.087 ft/d.

Core Hole CrCH-3 Run 59

Drilled Interval 895–899 ft

Drilled 48 in. and Recovered 60 in. (extra footage at top of core run discarded for final report)

Core Hole CrCH-3 895–895.3 ft (Tpf)

Light to medium brown silt and coarse-grain pumiceous sand with sparse, matrix-supported granules and pebbles of dark dacite up to 0.5 in. Pumice is abundant throughout the coarse sand fraction. The interval contains common clay-lined pores that may represent soil development. The bed is massive, moderately well consolidated, and poorly to moderately sorted. The hydraulic conductivity estimated by the Kozeny-Carman method is 0.146 ft/d.

Core Hole CrCH-3 895.3–896 ft (Tpf)

Reddish brown silt and fine- to coarse-grain sand with sparse, matrix-supported, subrounded granules and pebbles of dark dacite up to 2 in. Granules of pumice are sparsely distributed in the upper part of the bed. The bed is massive, moderately well consolidated, and poorly to moderately sorted. The hydraulic conductivity estimated by the Kozeny-Carman method is 0.137 ft/d.

Core Hole CrCH-3 896–897.4 ft (Tpf)

Reddish brown, gravelly, silt and fine- to coarse-grain sand with 5–10% matrix-supported granules and pebbles of dark dacite up to 1 in. No pumice observed in this bed. The bed is massive, moderately well consolidated, and poorly to moderately sorted. The hydraulic conductivity estimated by the Kozeny-Carman method is 0.119 ft/d.

Core Hole CrCH-3 897.4–898.2 ft (Tpf)

Reddish brown silt and medium- to coarse-grain sand with abundant, subangular to subrounded granules and pebbles of dark dacite up to 0.25 in. The lower 0.5 ft of the bed is characterized by fine-scale, interbedded layers of purplish gray, well-sorted, fine-grain sand that are <0.25 in. thick. Most of the bed is massive, moderately well consolidated, and poorly sorted. The hydraulic conductivity estimated by the Kozeny-Carman method is 0.119 ft/d.

Core Hole CrCH-3 898.2–899 ft (Tpf)

Light brown gravel with a matrix of silt and fine- to coarse-grain sand that supports granules and pebbles up to 2 in. The bed is massive, poorly to moderately well consolidated, and poorly sorted. The hydraulic conductivity estimated by the Kozeny-Carman method is 0.186 ft/d.

Core Hole CrCH-3 Run 60

Drilled Interval 899–903 ft

Drilled 48 in. and Recovered 36 in. (plastic sleeve with possible settling; distributed the missing 12 in.; core is dry)

Core Hole CrCH-3 899–900.4 ft (Tpf)

Medium orangish brown, gravelly, silt and fine- to coarse-grain sand with ~15% matrix-supported, subangular granules and pebbles of dark gray dacite up to 1.5 in. The bed is massive, unconsolidated, and poorly sorted. The hydraulic conductivity estimated by the Kozeny-Carman method is 0.208 ft/d.

Core Hole CrCH-3 900.4–901 ft (Tpf)

Light grayish brown, gravelly, silt and fine- to coarse-grain sand with ~15% matrix-supported, subangular granules and pebbles of dark gray dacite up to 1 in. Also contains sparse pumice granules. The bed is massive, moderately well consolidated, and poorly sorted. The hydraulic conductivity estimated by the Kozeny-Carman method is 0.186 ft/d.

Core Hole CrCH-3 901–901.6 ft (Tpf)

Gray–pinkish brown, coarse-grain, gravelly and silty, fine- to coarse-grain sand with sparse subangular to subrounded granules and pebbles of dark gray dacite up to 1 in. Bed also contains sparse white, rounded pumice. The bed is massive, moderately well consolidated, and poorly sorted. The hydraulic conductivity estimated by the Kozeny-Carman method is 0.410 ft/d.

Core Hole CrCH-3 901.6–903 ft (Tpf)

Light brownish gray gravel with a matrix of coarse-grain sand with abundant matrix-supported, subangular to subrounded granules and pebbles of dark gray dacite up to 1 in. Bed also contains sparse white, rounded pumice. The bed is massive, poorly to moderately well consolidated, and poorly sorted. The hydraulic conductivity estimated by the Kozeny-Carman method is 0.744 ft/d.

Core Hole CrCH-3 Run 61

Drilled Interval 903–907 ft

Drilled 48 in. and Recovered 60 in. (extra footage at top of core run discarded for final report)

Core Hole CrCH-3 903–903.7 ft (Tpf)

Light reddish brown gravel with a matrix of coarse-grain sand supporting subangular to subrounded granules and pebbles of dark dacite up to 1.5 in. Gravel clasts are entirely Rendija Canyon Rhyodacite. The coarse sand matrix is oxidized. The bed shows slight normal grading. The lower 2 to 3 in. of the bed contains sparse white pumice that was probably eroded from the underlying bed. The bed is massive, moderately consolidated, and poorly sorted. The hydraulic conductivity estimated by the Kozeny-Carman method is 14.582 ft/d.

Tpf/Tpf(p) Contact–903.7 ft

Core Hole CrCH-3 903.7–904.3 ft [Tpf(p)]

Light orangish brown, gravelly, coarse-grain pumiceous sand with sparse, matrix-supported granules and rare pebbles up to 0.5 in. The sandy matrix is dominated by tuffaceous sand but includes 5–10% dark lava, including rhyolite, perlite, and dacite. The interval appears to have faint bedding and is oxidized. The bed is moderately well consolidated and poorly to moderately sorted. The hydraulic conductivity

estimated by the Kozeny-Carman method is 0.947 ft/d. Beginning of pumice-rich deposits that make up the base of the Puye Formation.

Core Hole CrCH-3 904.3–905.7 ft [Tpf(p)]

Light orangish brown, silty, fine- to coarse-grain pumiceous sand with sparse, matrix-supported granules of pumice. An isolated 1.5-in. pumice clast occurs in the middle of the bed. The granules include sparse black obsidian. The bed is massive, moderately well consolidated, and moderately sorted. The hydraulic conductivity estimated by the Kozeny-Carman method is 0.476 ft/d.

Core Hole CrCH-3 905.7–907 ft [Tpf(p)]

Light grayish brown, fine- to coarse-grain pumiceous sand with sparse matrix-supported granules of pumice and obsidian. The sandy matrix is dominated by tuffaceous sand (pumice and shards), but it contains ~10% dark lava, including rhyolite, perlite, and dacite. The bed is massive, well consolidated, and moderately sorted. The hydraulic conductivity estimated by the Kozeny-Carman method is 0.831 ft/d.

Core Hole CrCH-3 Run 62

Drilled Interval 907–911 ft

Drilled 48 in. and Recovered 60 in. (extra footage at top of core run discarded for final report)

Core Hole CrCH-3 907–908 ft [Tpf(p)]

Medium brown, medium- to coarse-grain mixed lithic and pumiceous sand with granules of white pumice and dark gray and reddish brown lava (perlite, rhyolite, and dacite). Lava granules are more abundant than in the overlying bed. Rare pebbles are up to 0.25 in. The interval is faintly bedded. The bed is poorly consolidated and poorly to moderately sorted. The hydraulic conductivity estimated by the Kozeny-Carman method is 2.644 ft/d.

Core Hole CrCH-3 908–908.3 ft [Tpf(p)]

Light grayish brown, fine- to medium-grain pumiceous sand with rare granules of white pumice and dark gray lava near the bottom of the bed. The interval is faintly bedded. The uniform fine sand is moderately well consolidated and moderately sorted. The hydraulic conductivity estimated by the Kozeny-Carman method is 0.923 ft/d.

Core Hole CrCH-3 908.3–908.6 ft [Tpf(p)]

Medium brown, silt and fine- to coarse-grain pumiceous sand with sparse granules of white pumice and dark gray lava near base. The interval is faintly bedded. The bed is moderately well consolidated and poorly to moderately sorted. The hydraulic conductivity estimated by the Kozeny-Carman method is 0.321 ft/d.

Core Hole CrCH-3 908.6–909.9 ft [Tpf(p)]

Light brown, coarse-grain tuffaceous sand with sparse granules of scoria, dark gray lava, and white pumice, a few up to 0.5 in. The lower half of the interval contains thin interbeds of medium-gray silt to fine-grain sand up to 0.3 mm thick. Overall, there is general fining upwards of the interval. The bed is moderately well consolidated and poorly to moderately sorted. The hydraulic conductivity estimated by the Kozeny-Carman method is 1.122 ft/d.

Core Hole CrCH-3 909.9–911 ft [Tpf(p)]

Bedded sequence dominated by brownish white, coarse-grain, mixed pumiceous and lithic sand with seven thin (0.2–0.8 mm) medium-gray, moderately well-sorted silt or fine-grained sand. The pumiceous sand contains granules and pebbles of pumice and dark gray lava (rhyolite and dacite) up to 0.5 in. The pumiceous sand fines upwards and the upper 4 in. is oxidized to an orangish brown color (possible soil development). A single lava clast is 1.5 in., but lava clasts are generally smaller than pumice clasts. The pumiceous sand is massive, moderately well consolidated, and poorly sorted. Transmissivity is good in the pumiceous sand and poor in the silt or fine-grain sand. The hydraulic conductivity estimated by the Kozeny-Carman method is 0.231 ft/d.

Core Hole CrCH-3 Run 63

Drilled Interval 911–913 ft

Drilled 24 in. and Recovered 60 in. (extra footage at top of core run discarded for final report)

Core Hole CrCH-3 911–911.8 ft [Tpf(p)]

Bedded interval of light brown, gravelly and silty, coarse-grain lithic sand with abundant subangular to subrounded granules and pebbles of Rendija Canyon Rhyodacite up to 1.5 in. The interval contains up to six thin beds of medium gray, well-sorted silt or fine-grain sand. The dominant coarse-grain sand is massive, well consolidated, and poorly sorted. The hydraulic conductivity estimated by the Kozeny-Carman method is 0.155 ft/d.

Core Hole CrCH-3 911.8–913 ft [Tpf(p)] (Interval dried out)

Light yellowish brown, gravelly and silty, coarse-grain lithic sand with common subangular to subrounded granules and pebbles of Rendija Canyon Rhyodacite up to 0.25 in. The core is dense and strongly consolidated and has a bleached appearance that may be the result of heating near the bottom of the core barrel; the bottom of the Lexan tube is melted and deformed. The bed is massive and poorly to moderately sorted. The hydraulic conductivity estimated by the Kozeny-Carman method is 0.175 ft/d.

Core Hole CrCH-3 Run 64

Drilled Interval 913–916 ft

Drilled 36 in. and Recovered 36 in. (Lexan)

Core Hole CrCH-3 913–913.4 ft [Tpf(p)]

Light brownish gray gravel with a matrix of coarse-grain, mixed lithic and pumiceous sand that supports pebbles and cobbles of subrounded, dark gray dacite up to 3 in. and subordinate pebbles of white pumice up to 0.5 in. The dacite clasts are monolithologic and contain abundant hornblende and biotite phenocrysts; these may be from Cerro Rubio or Sawyer Dome. No Rendija Canyon Rhyodacite clasts found. The bed is massive, poorly to moderately well consolidated, and poorly sorted. The hydraulic conductivity estimated by the Kozeny-Carman method is 1.020 ft/d.

Core Hole CrCH-3 913.4–914.4 ft [Tpf(p)]

Light grayish brown cobble bed with a silty fine- to coarse-grain, mixed lithic and pumiceous sandy matrix. Clasts are matrix-supported, subangular to subrounded, dark gray dacite up to 3.5 in.; similar to the hornblende-biotite dacite described in the overlying bed. A few Rendija Canyon Rhyodacite clasts found in washed gravel. Gravel clasts include subordinate white pumice. The bed is massive, poorly to moderately well consolidated, and poorly sorted. The hydraulic conductivity estimated by the Kozeny-Carman method is 0.410 ft/d.

Core Hole CrCH-3 914.4–915 ft [Tpf(p)]

Light brown, coarse-grain, mixed lithic and pumiceous sand with 5–10% granules of white pumice up to 0.25 in. The bed is massive, poorly consolidated, and poorly sorted. The hydraulic conductivity estimated by the Kozeny-Carman method is 1.284 ft/d.

Core Hole CrCH-3 915–916 ft [Tpf(p)]

Light brown, pebbly, coarse-grain, mixed lithic and pumiceous sand with ~10% matrix-supported, rounded granules and pebbles of dark gray lava up to 1.5 in. A few Rendija Canyon Rhyodacite clasts found in washed gravel. Also contains abundant granules of white pumice. The bed is massive, unconsolidated, and poorly sorted. The hydraulic conductivity estimated by the Kozeny-Carman method is 1.341 ft/d.

Core Hole CrCH-3 Run 65
Drilled Interval 916–920 ft
Drilled 48 in. and Recovered 48 in. (Lexan)

Core Hole CrCH-3 916–916.25 ft [Tpf(p)]

Yellowish brown silt and fine- to coarse-grain mixed lithic and pumiceous sand with common matrix-supported, subrounded granules of dark gray lava up to 0.25 in. Also contains very sparse granules of white pumice. The bed is massive, well consolidated, and poorly sorted. The matrix contains numerous isolated clay-lined pores that may be indicative of soil development. The hydraulic conductivity estimated by the Kozeny-Carman method is 0.255 ft/d. Contact with underlying bed is irregular, possibly as a drilling artifact.

Core Hole CrCH-3 916.25–916.7 ft [Tpf(p)]

Light pinkish gray silt and fine- to coarse-grain mixed lithic and pumiceous sand with abundant matrix-supported granules of white pumice up to 0.25 in. and sparse granules of dark gray lava. A few Rendija Canyon Rhyodacite clasts found in washed granules; this is the deepest occurrence of these types of clasts. The bed is massive, moderately well consolidated, and poorly sorted. The hydraulic conductivity estimated by the Kozeny-Carman method is 0.197 ft/d. Contact with overlying and underlying beds is disrupted, possibly because of drilling.

Tpf(p)/Tjfp Contact–916.7 ft

Core Hole CrCH-3 916.7–916.9 ft (Tjfp)

Yellowish brown silt and fine-grain sand with sparse subrounded granules of dark gray lava up to 0.25 in. The interval may have faint bedding. The bed is generally massive, well consolidated, and fairly well sorted. The matrix contains numerous isolated clay-lined pores that may be indicative of soil development. The hydraulic conductivity estimated by the Kozeny-Carman method is 0.119 ft/d. Similar in thickness and color to the 916- to 916.25-ft interval, but fine grained.

Core Hole CrCH-3 916.9–917.25 ft (Tjfp)

Pink–reddish gray, coarse-grain sand with matrix-supported granules and pebbles of white pumice and dark gray lava up to 1 in. The bed shows slight upward fining of clast sizes. The bed is massive, poorly consolidated, and poorly sorted. The hydraulic conductivity estimated by the Kozeny-Carman method is 1.071 ft/d. The lower contact of the bed is sharp whereas the upper contact is irregular and disrupted.

Core Hole CrCH-3 917.25–917.8 ft (Tjfp)

Light reddish brown, coarse-grain pumiceous sand with matrix-supported granules and pebbles of white pumice (mostly granules but some pebbles up to 0.5 in.). Dark lava sand and granules are rare. The bed is massive, moderately well consolidated, and poorly sorted. The hydraulic conductivity estimated by the Kozeny-Carman method is 1.341 ft/d. The upper contact of the bed is sharp, but the lower contact is transitional to the underlying pumiceous deposit.

Core Hole CrCH-3 917.8–918.5 ft (Tjfp)

White to very light tan, medium- to very coarse-grain pumiceous sand and granular gravel. Dominated by white rounded pumice in all grain sizes. Sparse dark lava occurs in the sandy matrix. The bed is irregularly infiltrated by tan fine sand from the overlying bed. The bed is massive, moderately-well consolidated, and poorly sorted. The hydraulic conductivity estimated by the Kozeny-Carman method is 0.528 ft/d.

Core Hole CrCH-3 918.5–918.9 ft (Tjfp)

Tan–grayish brown, silty, fine- to coarse-grain pumiceous sand with common granules and sparse pebbles of white pumice up to 0.25 in. The bed is massive, moderately to well consolidated, and poorly sorted. The hydraulic conductivity estimated by the Kozeny-Carman method is 0.410 ft/d. The interval may be faintly bedded.

Core Hole CrCH-3 918.9–920 ft (Tjfp)

Reddish brown, silty, fine- to coarse-grain tuffaceous sand with sparse granules and very sparse pebbles of white pumice up to 0.5 in. The bed is normally graded with gravels concentrated near the base of the unit. The bed is poorly to moderately well consolidated and poorly sorted. The hydraulic conductivity estimated by the Kozeny-Carman method is 0.231 ft/d.

Core Hole CrCH-3 Run 66

Drilled Interval 920–923 ft

Drilled 36 in. and Recovered 38 in., extra 2 in. distributed (Lexan)

Core Hole CrCH-3 920–920.5 ft (Tjfp)

Light yellowish brown silt and fine- to coarse-grain tuffaceous sand with sparse granules and pebbles of dark gray and red-brown lava up to 0.25 in. A single dense glassy 1.5-in. pumice clast in the lower more gravelly part of the bed. The bed becomes finer grain upwards. The bed is well consolidated and moderately well sorted. The matrix contains numerous isolated clay-lined pores that may be indicative of soil development. The hydraulic conductivity estimated by the Kozeny-Carman method is 0.146 ft/d. There may be a certain amount of drilling-induced mixing with light grayish brown coarse-grain sand.

Core Hole CrCH-3 920.5–920.75 ft (Tjfp)

Light yellowish brown silt and fine- to medium-grain tuffaceous sand with sparse granules and pebbles of dark gray lava up to 0.25 in. The bed is massive, well consolidated, and moderately well sorted. The matrix contains numerous isolated clay-lined pores that may be indicative of soil development. The hydraulic conductivity estimated by the Kozeny-Carman method is 0.137 ft/d. The bed exhibits drilling-induced deformation.

Core Hole CrCH-3 920.75–921.8 ft (Tjfp)

Light pinkish brown, silty, coarse-grain sand with common, matrix-supported granules and pebbles of rhyolite, dark gray lava, and subordinate white pumice. Larger gravel clasts occur near the base of the bed with a single 2-in. dense glassy pumice clast at the basal contact. The bed becomes finer grain upwards. The bed is moderately well consolidated and poorly sorted. The hydraulic conductivity estimated by the Kozeny-Carman method is 0.744 ft/d. No Rendija Canyon Rhyodacite clasts observed in washed gravels.

Core Hole CrCH-3 921.8–922.25 ft (Tjfp)

Light pinkish brown, silty, fine- to coarse-grain sand with common, matrix-supported granules and pebbles of dark gray lava and white pumice up to 1 in. Also contains sparse but conspicuous black obsidian granules and small pebbles. The bed is moderately well consolidated and poorly sorted. The hydraulic conductivity estimated by the Kozeny-Carman method is 0.380 ft/d. The interval contains two thin interbeds of dark olive-gray silt or fine sand up to 3 mm thick.

Core Hole CrCH-3 922.25–922.75 ft (Tjfp)

Bedded sequence of eight laminated medium-brown fine-grain sands 2–5 mm thick that are distributed in the main lithology of grayish brown silt and fine- to coarse-grain tuffaceous sand with abundant, matrix-supported granules and pebbles of dark gray lava and white pumice up to 0.5 in. Lava clasts include banded rhyolite. The bed is moderately well consolidated and poorly sorted. The hydraulic conductivity estimated by the Kozeny-Carman method is 0.186 ft/d.

Core Hole CrCH-3 922.75–923 ft (Tjfp)

Light reddish brown, silty, fine- to coarse-grain tuffaceous sand with common, matrix-supported granules of lava and sparse pebbles of dense pumice. The bed is reversely graded, becoming more gravelly upwards. The bed is poorly consolidated and poorly sorted. The hydraulic conductivity estimated by the Kozeny-Carman method is 0.350 ft/d.

Core Hole CrCH-3 Run 67

Drilled Interval 923–927 ft

Drilled 48 in. and Recovered 58 in. (Lexan; extra footage at top of core run discarded for final report)

Core Hole CrCH-3 923–923.25 ft (Tjfp)

Yellowish olive-brown silt and fine-grain sand (lacks larger clasts). The bed is massive, very well consolidated, and fairly well sorted. The hydraulic conductivity estimated by the Kozeny-Carman method is 0.087 ft/d. The matrix contains sparse isolated clay-lined pores that may be indicative of soil development.

Core Hole CrCH-3 923.25–923.5 ft (Tjfp)

Pinkish gray silt and fine- to coarse-grain tuffaceous sand with sparse rounded granules and small pebbles of subequal pumice and dark lava up to 0.25 in. The bed is massive, well consolidated, and fairly well sorted. The hydraulic conductivity estimated by the Kozeny-Carman method is 0.155 ft/d. The basal contact shows some mixing with the underlying unit. The matrix contains isolated clay-lined pores that may be indicative of soil development.

Core Hole CrCH-3 923.5–923.75 ft (Tpf)

Yellowish brown, silty, fine- to medium-grain sand with sparse granules of dark lava. The bed is massive, very well consolidated, and fairly well sorted. The hydraulic conductivity estimated by the Kozeny-Carman method is 0.0.013 ft/d. The basal contact undulates and may be deformed by drilling.

Core Hole CrCH-3 923.75–925.1 ft (Tjfp)

Pinkish gray, coarse-grain tuffaceous sand with abundant granules of rounded white pumice and sparse rounded pebbles of dark lava up to 0.5 in. The center of the bed contains two thin interbeds of dark olive-brown fine-grain sand. Overall, the main sequence fines upward. The bed is poorly consolidated and poorly sorted. The hydraulic conductivity estimated by the Kozeny-Carman method is 0.787 ft/d.

Core Hole CrCH-3 925.1–925.3 ft (Tjfp)

Reddish, coarse-grain tuffaceous sand with abundant granules of rounded white pumice and sparse granules and pebbles of rounded dark lava up to 0.5 in. The bed is massive, moderately well consolidated, and poorly sorted. The hydraulic conductivity estimated by the Kozeny-Carman method is 1.398 ft/d.

Core Hole CrCH-3 925.3–925.7 ft (Tjfp)

Light grayish brown, coarse-grain tuffaceous sand with abundant matrix-supported granules of rounded white pumice and common granules and pebbles of rounded dark lava up to 0.5 in. The bed is massive, poorly consolidated, and poorly sorted. The hydraulic conductivity estimated by the Kozeny-Carman method is 1.903 ft/d.

Core Hole CrCH-3 925.7–926.3 ft (Tjfp)

Bedded sequence of light grayish brown silt and fine- to coarse-grain tuffaceous sand with abundant matrix-supported granules of rounded white pumice and obsidian and sparse pebbles of dark lava up to 1 in. The interval contains nine thin interbeds of well-sorted dark olive-gray silt up to 0.5 cm. The main sequence bed is moderately well consolidated and poorly sorted. The hydraulic conductivity estimated by the Kozeny-Carman method is 0.281 ft/d.

Core Hole CrCH-3 926.3–926.7 ft (Tjfp)

Light brownish gray, coarse-grain tuffaceous sand with abundant matrix-supported rounded granules and pebbles of white pumice and dark lava up to 0.5 in. The bed is massive, poorly to moderately well consolidated, and poorly sorted. The bed is reversely graded, with gravels concentrated in the upper part. The hydraulic conductivity estimated by the Kozeny-Carman method is 0.876 ft/d.

Core Hole CrCH-3 926.7–927 ft (Tjfp)

Light reddish brown, silty, coarse-grain tuffaceous sand with abundant granules of white pumice and sparse granules of dark lava up to 0.25 in. The bed is massive, poorly consolidated, and poorly sorted. The hydraulic conductivity estimated by the Kozeny-Carman method is 0.583 ft/d.

Core Hole CrCH-3 Run 68
Drilled Interval 927–930 ft
Drilled 36 in. and Recovered 36 in. (Lexan)

Core Hole CrCH-3 927–927.5 ft (Tjfp)

Grayish brown, silty, coarse-grain tuffaceous sand with granules and pebbles of white pumice and subordinate dark gray lava up to 0.5 in. The bed is reversely graded, becoming more gravelly upwards. The bed is moderately well consolidated and poorly sorted. The hydraulic conductivity estimated by the Kozeny-Carman method is 0.307 ft/d.

Core Hole CrCH-3 927.5–927.9 ft (Tjfp)

Light pinkish brown, fine- to coarse-grain tuffaceous sand with granules and pebbles of white pumice and subordinate dark gray lava up to 0.5 in. The bed is normally graded, becoming more or less gravelly upwards. The bed is moderately well consolidated and poorly sorted. The hydraulic conductivity estimated by the Kozeny-Carman method is 0.621 ft/d.

Core Hole CrCH-3 927.9–928.25 ft (Tjfp)

Medium brown silt and fine- to coarse-grain tuffaceous sand. Gravel is absent. The bed is massive, well consolidated, and moderately well sorted. The matrix in the lower half of the bed contains numerous isolated clay-lined pores that may be indicative of soil development. The hydraulic conductivity estimated by the Kozeny-Carman method is 0.231 ft/d.

Core Hole CrCH-3 928.25–929.7 ft (Tjfp)

Light-brown silt and fine- to coarse-grain tuffaceous sand. Gravel is absent to sparse. The lower part of the bed is a dark lithic sand with sparse white pumice granules and gravel up to 0.5 in. The bed is normally graded, becoming finer upwards, including enclaves of silty fine-grain sand. The bed is well consolidated and moderately well sorted. The bed contains numerous isolated clay-lined pores that may be indicative of soil development. The hydraulic conductivity estimated by the Kozeny-Carman method is 0.197 ft/d.

Core Hole CrCH-3 929.7–930 ft (Tjfp)

Light reddish brown, silty, fine- to coarse-grain tuffaceous sand with common, matrix-supported granules and pebbles of white pumice and dark gray lava up to 0.5 in. The bed is massive, moderately well consolidated, and poorly sorted. The bed contains numerous isolated clay-lined pores that may be indicative of soil development; some are elongated along the contact. The hydraulic conductivity estimated by the Kozeny-Carman method is 0.307 ft/d.

Core Hole CrCH-3 Run 71 (bag)
Drilled Interval 931–933 ft
Drilled 24 in. and Recovered 27 in.; extra 3 in. of core exactly like and added to 931–931.3-ft interval

Core Hole CrCH-3 931–931.3 ft (Tjfp)

Gray silt and medium- to coarse-grain tuffaceous sand. The sand is uniform with no granules or pebbles. The bed is massive, poorly consolidated, and well sorted. The hydraulic conductivity estimated by the Kozeny-Carman method is 1.341 ft/d.

Core Hole CrCH-3 931.3–931.5 ft (Tjfp)

Light orangish brown silt and fine-grain tuffaceous sand with sparse granules of white pumice. The bed is massive, moderately consolidated, and well sorted. The hydraulic conductivity estimated by the Kozeny-Carman method is 0.197 ft/d. The bed is partly disrupted by intrusion of material from the overlying bed.

Core Hole CrCH-3 931.5–932 ft (Tjfp)

Gray, silty, fine- to coarse-grain tuffaceous sand. The sand is uniform with no granules or pebbles. The bed is poorly consolidated and well sorted. The hydraulic conductivity estimated by the Kozeny-Carman method is 0.397 ft/d. The bed is generally massive but contains a <1-in.-thick, orangish brown, silty bed in the 931.67–931.75-ft interval that is disrupted and could not be discretely sampled.

Core Hole CrCH-3 932–932.25 ft (Tjfp)

Medium reddish brown, silty, fine- to coarse-grain sand with sparse granules and small pebbles of white pumice up to 0.5 in. The sand is uniform with no granules or pebbles. The bed is massive, well consolidated, and poorly sorted. The hydraulic conductivity estimated by the Kozeny-Carman method is 0.243 ft/d. The top of the bed is disrupted by intrusion from gray sand from the overlying bed (not sampled).

Core Hole CrCH-3 932.25–933 ft (Tjfp)

Reddish brown, fine- to coarse-grain tuffaceous sand with sparse granules and pebbles of white pumice and dark gray lava. The bed is massive, poorly consolidated, and moderately well sorted. The hydraulic conductivity estimated by the Kozeny-Carman method is 0.744 ft/d.

Core Hole CrCH-3 Run 72 (bag)

Drilled Interval 933–936 ft

Drilled 36 in. and Recovered 30 in.; assume uniform compaction; add 1 in. for every 6 in. drilled

Core Hole CrCH-3 933–933.3 ft (Tjfp)

Light brown silt and fine- to medium-grain tuffaceous sand containing sparse granules and small pebbles of white, vitric pumice and dark gray lava. The bed is massive, moderately consolidated, and moderately well sorted. The hydraulic conductivity estimated by the Kozeny-Carman method is 0.255 ft/d.

Core Hole CrCH-3 933.3–933.8 ft (Tjfp)

Light brown, silty, fine- to coarse-grain tuffaceous sand containing abundant matrix-supported granules and pebbles of rounded, white, vitric pumice. The bed is massive, poorly consolidated, and poorly sorted. The hydraulic conductivity estimated by the Kozeny-Carman method is 0.350 ft/d.

Core Hole CrCH-3 933.8–934.4 ft (Tjfp)

Light to medium brown, silty, fine- to coarse-grain tuffaceous sand. The bed is massive, poorly consolidated, and well sorted. The hydraulic conductivity estimated by the Kozeny-Carman method is 0.583 ft/d.

Core Hole CrCH-3 934.4–935.2 ft (Tjfp)

Light brownish gray, medium- to coarse-grain tuffaceous sand. The bed is massive, poorly consolidated, and well sorted. The hydraulic conductivity estimated by the Kozeny-Carman method is 1.517 ft/d.

Core Hole CrCH-3 935.2–936 ft (Tjfp)

Light to medium brown, silty, coarse-grain tuffaceous sand with sparse white pumice granules. The bed is massive, poorly consolidated, and well sorted. The hydraulic conductivity estimated by the Kozeny-Carman method is 0.321 ft/d.

Core Hole CrCH-3 Run 73 (bag)

Drilled Interval 936–940 ft

Drilled 48 in. and Recovered 48 in.

Note: Unusual core run makeup of a sandy sequence that could be considered one bed. The core was re-bagged into 1-ft increments by previous samplers with the 937–938-ft interval removed for testing. There is little to no mineralogical, grain size, and color difference among the 1-ft bags. Based on the similarity of the sieve data for each 1-ft bag, the entire interval is treated as a single thick bed. For the entire core run, there is a slight fining upwards.

Core Hole CrCH-3 938–939 ft (Tjfp)

Light to medium brownish gray, medium-grain, tuffaceous sand. The sandy matrix contains a mixture of broken pumice, perlite, felsic crystal, and lava grains. The bed slightly coarser and lacks the granules found above in the 936–937-ft interval. The bed is massive, unconsolidated, and moderately well sorted. The 937–938-ft interval was removed by earlier workers for sequential leaching. The hydraulic conductivity estimated by the Kozeny-Carman method is 2.042 ft/d.

Core Hole CrCH-3 Run 74

Drilled Interval 940–943 ft

Drilled 36 in. and Recovered 32 in. (plastic sleeve with possible settling; distributed the missing 4 in.)

Core Hole CrCH-3 940–940.8 ft (Tjfp)

Medium brown, silty, fine-grain tuffaceous sand with abundant, matrix-supported, rounded granules of pumice (and sparse pebble-size pumice). The bed is massive, moderately consolidated, and poorly to moderately sorted. The hydraulic conductivity estimated by the Kozeny-Carman method is 0.379 ft/d.

Core Hole CrCH-3 940.8–941.5 ft (Tjfp)

Light gray, silty, fine- to coarse-grain pumiceous sand with abundant, matrix-supported, rounded granules of pumice and sparse dark lava granules. The bed is massive, poorly to moderately consolidated, and poorly to moderately sorted. The hydraulic conductivity estimated by the Kozeny-Carman method is 0.378 ft/d. Contacts with overlying and underlying beds partly disrupted by drilling, and mixing of zones occurs (avoided in sampling).

Core Hole CrCH-3 941.5–942.2 ft (Tjfp)

Brown, fine- to coarse-grain tuffaceous sand with sparse rounded granules of pumice and sparse pebbles of dark lavas. The bed is massive, moderately consolidated, and poorly to moderately sorted. The hydraulic conductivity estimated by the Kozeny-Carman method is 0.641 ft/d. Contacts with overlying and underlying beds partly disrupted by drilling, and mixing of zones occurs (avoided in sampling).

Core Hole CrCH-3 942.2–943 ft (Tjfp)

Grayish brown, silty, fine- to coarse-grain tuffaceous sand with sparse rounded granules of pumice and sparse pebbles of dark lavas up to 0.5 in. The bed is massive, moderately consolidated, and poorly to moderately sorted. The hydraulic conductivity estimated by the Kozeny-Carman method is 0.442 ft/d. May have very faint bedding.

Core Hole CrCH-3 Run 75
Drilled Interval 944–947 ft
Drilled 36 in. and Recovered 36 in.

Note: There were two Lexan core tubes labeled Run 75, 944–947 ft. Based on the continuity of core colors and lithologies to overlying and underlying core runs, this core run was elected as representative and all data was discarded for the other core tube.

Core Hole CrCH-3 944–945 ft (Tjfp)

Grayish brown, fine- to coarse-grain tuffaceous sand with subrounded pebbles of dark lava up to 0.5 in. and abundant rounded white pumice granules. The bed is massive, moderately consolidated, and poorly to moderately sorted. The hydraulic conductivity estimated by the Kozeny-Carman method is 1.428 ft/d. The outer margin of core is gray in color and may reflect segregation or migration of fines to the core margins because of drilling.

Core Hole CrCH-3 945– 946.2 ft (Tjfp)

Grayish brown, fine- to coarse-grain tuffaceous sand with common granules of rounded, white pumice and less common pebbles of dark lava up to 0.5 in. The bed is massive, moderately consolidated, and poorly to moderately sorted. The hydraulic conductivity estimated by the Kozeny-Carman method is 0.641 ft/d. The outer margin of core is gray in color and may reflect segregation or migration of fines to the core margins because of drilling.

Core Hole CrCH-3 946.2–947 ft (Tjfp)

Light brownish gray, medium- to coarse-grain tuffaceous sand with common granules of rounded, white pumice and rare granules of dark lava up to 0.5 in. The bed is moderately consolidated and poorly to moderately sorted. The hydraulic conductivity estimated by the Kozeny-Carman method is 0.543 ft/d. The bed is mixed with irregular pods of reddish brown silty clay that may reflect drilling-induced segregation of fines.

Core Hole CrCH-3 Run 76 (bag)
Drilled Interval 947–951 ft
Drilled 48 in. and Recovered 42 in.; assume uniform compaction, depths corrected uniformly

Core Hole CrCH-3 947–948 ft (Tjfp)

Light brown, fine- to coarse-grain tuffaceous sand. Small white pumice throughout the sand fraction. The bed is massive, moderately consolidated, and well sorted. The hydraulic conductivity estimated by the Kozeny-Carman method is 1.341 ft/d.

Core Hole CrCH-3 948–948.8 ft (Tjfp)

Light brown, silty, fine- to medium-grain tuffaceous sand containing ~10% matrix-supported granules and pebbles of white, vitric pumice up to 0.5 in. Sparse dark gray lava is a component of the sand fraction. The bed is massive, moderately consolidated, and poorly sorted. The hydraulic conductivity estimated by the Kozeny-Carman method is 0.410 ft/d.

Core Hole CrCH-3 948.8–949.8 ft (Tjfp)

Light grayish brown, silty, fine-grain tuffaceous sand with abundant matrix-supported granules and small pebbles of rounded, white pumice up to 0.25 in. Matrix is dominated by fine sand. The bed is massive, moderately consolidated, and poorly sorted. The hydraulic conductivity estimated by the Kozeny-Carman method is 0.410 ft/d.

Core Hole CrCH-3 949.8–951 ft (Tjfp)

Light brown, fine- to coarse-grain tuffaceous sand with matrix-supported granules of white pumice and very sparse dark gray lava. Fewer pumice granules than the overlying bed. The bed is massive, moderately consolidated, and well sorted. The hydraulic conductivity estimated by the Kozeny-Carman method is 1.071 ft/d. One 0.75-in. oxidized iron filling found in sample.

Core Hole CrCH-3 Run 77

Drilled Interval 951–955 ft

Drilled 48 in. and Recovered 36 in.; 12 in. of core previously removed for geochemical analyses (Lexan)

Core Hole CrCH-3 951–955 ft (Tjfp)

The entire core run is lithologically similar and is treated as a single depositional unit. Light grayish brown, fine- to coarse-grain tuffaceous sand with subangular to subrounded granules of gray rhyolite lava and white pumice. Rare lava pebbles are up to 0.5 in. The bed is massive, poorly to moderately consolidated, and poorly sorted. The hydraulic conductivity estimated by the Kozeny-Carman method is 1.700 ft/d. The bed contains sparse isolated clay-lined pores that may be indicative of soil development.

Core Hole CrCH-3 Run 78

Drilled Interval 955–959 ft

Drilled 48 in. and Recovered 53 in. (Lexan; extra footage at top of core run discarded for final report)

Core Hole CrCH-3 955–955.5 ft (Tjfp)

Medium gray silt and fine- to coarse-grain tuffaceous sand with sparse granules of white pumice. The matrix is dominated by pumice, ash, felsic crystals, and subordinate dark gray lava. The bed is massive, well consolidated, and moderately sorted. The hydraulic conductivity estimated by the Kozeny-Carman method is 0.255 ft/d.

Core Hole CrCH-3 955.5–955.9 ft (Tjfp)

Light gray silt and fine- to medium-grain tuffaceous sand with thin white ashy laminae that are deformed by drilling(?) The bed becomes more fine grain upwards. The bed is well consolidated and moderately sorted. The hydraulic conductivity estimated by the Kozeny-Carman method is 0.231 ft/d. This bed marks the base of a very light colored stratigraphic sequence that overlies in sharp contact a dark reddish brown sequence.

Core Hole CrCH-3 955.9–956.3 ft (Tjfp)

Reddish brown silt and fine- to medium-grain tuffaceous sand with no larger clasts. A single 0.25-in. clast of dense pumice occurs at the base of the bed. The bed is massive, moderately well consolidated and moderately sorted. The bed becomes more fine grain upwards. The hydraulic conductivity estimated by the Kozeny-Carman method is 0.155 ft/d. The bed appears to be internally deformed, possibly because of drilling.

Core Hole CrCH-3 956.3–957 ft (Tjfp)

Light reddish brown, fine- to medium-grain tuffaceous sand with common, matrix-supported granules and small pebbles of dense pumice. The sandy matrix contains stretched and deformed white pumice. The bed is massive, well consolidated, and poorly sorted. The hydraulic conductivity estimated by the Kozeny-Carman method is 0.641 ft/d. The bed appears to be internally deformed, possibly because of drilling.

Core Hole CrCH-3 957–958.1 ft (Tjfp)

Light brown, silty, fine- to medium-grain tuffaceous sand with sparse, rounded, white pumice up to 1 in. The bed is massive, well consolidated, and poorly sorted. The hydraulic conductivity estimated by the Kozeny-Carman method is 0.364 ft/d.

Core Hole CrCH-3 958.1–959 ft (Tjfp)

Grayish brown, silty, fine- to coarse-grain tuffaceous sand with sparse dense pumice clasts. The sand fraction contains abundant pumice. The bed is massive, moderately well consolidated, and poorly sorted. The hydraulic conductivity estimated by the Kozeny-Carman method is 0.410 ft/d. The bed appears to be slightly deformed, possibly because of drilling.

Core Hole CrCH-3 Run 79

Drilled Interval 959–963 ft

Drilled 48 in. and Recovered 43 in. (plastic sleeve with possible settling; distributed the missing 5 in.)

Core Hole CrCH-3 959–959.9 ft (Tjfp)

Grayish brown, silty, fine- to medium-grain tuffaceous sand with sparse rounded granules of pumice and subordinate granules of dark lava. The bed is massive, moderately consolidated, and moderately sorted. The hydraulic conductivity estimated by the Kozeny-Carman method is 4.131 ft/d.

Core Hole CrCH-3 959.9–960.6 ft (Tjfp)

Light brownish gray, silty, fine- to medium-grain tuffaceous sand with sparse rounded granules of pumice and subordinate granules of dark lava. The bed is massive, poorly consolidated, and poorly sorted. The hydraulic conductivity estimated by the Kozeny-Carman method is 0.350 ft/d.

Core Hole CrCH-3 960.6–961 ft (Tjfp)

Light brown, silty, fine- to medium-grain tuffaceous sand with sparse rounded granules of pumice. The bed is massive, poorly consolidated, and moderately sorted. The hydraulic conductivity estimated by the Kozeny-Carman method is 0.459 ft/d. Some mixing with underlying bed because of drilling.

Core Hole CrCH-3 961–961.3 ft (Tjfp)

Reddish brown silt with sparse rounded granules of pumice. The bed is massive, moderately well consolidated, and well sorted. The hydraulic conductivity estimated by the Kozeny-Carman method is 0.087 ft/d.

Core Hole CrCH-3 961.3–961.7 ft (Tjfp)

Brownish gray silt and fine- to coarse-grain tuffaceous sand with abundant matrix-supported, rounded granules and pebbles of pumice up to 1 in. The bed is massive, poorly consolidated, and poorly sorted. The hydraulic conductivity estimated by the Kozeny-Carman method is 0.197 ft/d.

Core Hole CrCH-3 961.7–963 ft (Tjfp)

Brown, gravelly, silt and fine-grain tuffaceous sand with abundant matrix-supported, rounded granules and rare pebbles of pumice up to 1.5 in. The bed is massive, moderately well consolidated, and poorly sorted. The hydraulic conductivity estimated by the Kozeny-Carman method is 0.243 ft/d.

Core Hole CrCH-3 Run 80
Drilled Interval 963–967 ft
Drilled 48 in. and Recovered 48 in. (Lexan)

Core Hole CrCH-3 963–964.75 ft (Tjfp)

Light brown silt and fine- to medium-grain tuffaceous sand with sparse granules and pebbles of pumice and rare dark lava up to 1 in. The bed is massive, moderately well consolidated, and moderately sorted. The hydraulic conductivity estimated by the Kozeny-Carman method is 0.243 ft/d. The bed contains numerous isolated clay-lined pores that may be indicative of soil development.

Core Hole CrCH-3 964.75–965.3 ft (Tjfp)

Grayish brown, silty, medium- to coarse-grain pumiceous sand with sparse granules and pebbles of pumice and dark lava up to 0.25 in. The sand fraction contains abundant pumice. The bed is massive, well consolidated, and moderately well sorted. The hydraulic conductivity estimated by the Kozeny-Carman method is 0.410 ft/d. The upper contact of the bed is deformed, possibly because of drilling.

Core Hole CrCH-3 965.3–966.5 ft (Tjfp)

White pumice fall deposit. Coarse- to very coarse-grain subangular sand and granular pumice are matrix supported. The bed also contains sparse dark lava in the sand fraction in the lower part of the unit. The base of the unit contains dark laminae of brown, stained material that is deformed into an upward-pointing cone. The bed is massive, moderately well consolidated, and moderately well sorted. The hydraulic conductivity estimated by the Kozeny-Carman method is 0.621 ft/d.

Core Hole CrCH-3 966.5–967 ft (Tjfp)

Light brown, silty, fine- to coarse-grain tuffaceous sand with sparse granules of white pumice. The bed is massive, poorly consolidated, and poorly sorted. The hydraulic conductivity estimated by the Kozeny-Carman method is 0.743 ft/d.

Core Hole CrCH-3 Run 81 (bag)

Drilled Interval 967–971 ft

Drilled 48 in. and Recovered 45 in.; assume uniform compaction, depths corrected uniformly

Core Hole CrCH-3 967–967.75 ft (Tjfp)

Grayish brown, fine- to coarse-grain tuffaceous sand with ~5% matrix-supported granules and small pebbles of white pumice and lesser dark gray lava. The bed is massive, unconsolidated, and moderately well sorted. The hydraulic conductivity estimated by the Kozeny-Carman method is 1.517 ft/d.

Core Hole CrCH-3 967.75–968.6 ft (Tjfp)

Grayish brown, coarse-grain tuffaceous sand with matrix-supported granules and pebbles of dark gray lava and white pumice up to 0.5 in. The bed is massive, poorly consolidated, and poorly sorted. The hydraulic conductivity estimated by the Kozeny-Carman method is 2.890 ft/d.

Core Hole CrCH-3 968.6–968.75 ft (Tjfp)

Light brown, fine- to coarse-grain tuffaceous sand with sparse granules of white pumice and dark gray lava. The bed is massive, unconsolidated, and moderately well sorted. The hydraulic conductivity estimated by the Kozeny-Carman method is 1.312 ft/d.

Core Hole CrCH-3 968.75–969 ft (Tjfp)

Light brown, fine- to coarse-grain tuffaceous sand with matrix-supported granules of dark gray lava and lesser white pumice. Dark gray lava is more abundant than pumice in the sand fraction. The bed is massive, unconsolidated, and moderately well sorted. The hydraulic conductivity estimated by the Kozeny-Carman method is 1.398 ft/d.

Core Hole CrCH-3 969–969.9 ft (Tjfp)

Light brown, coarse- to very-coarse-grain, gravelly sand with abundant matrix-supported granules and pebbles of dark gray lava and white pumice up to 0.5 in. Dark gray lava is much more abundant than pumice in the sand fraction. The bed is massive, unconsolidated, and poorly sorted. The hydraulic conductivity estimated by the Kozeny-Carman method is 1.641 ft/d.

Core Hole CrCH-3 969.9–970.5 ft (Tjfp)

Light brown, fine-grain tuffaceous sand. The bed lacks granules and is massive, moderately consolidated, and well sorted. The hydraulic conductivity estimated by the Kozeny-Carman method is 1.284 ft/d.

Core Hole CrCH-3 970.5–971 ft (Tjfp)

Light brown, fine- to coarse-grain tuffaceous sand that is fining upwards. The bed is massive, unconsolidated, and moderately well sorted. The hydraulic conductivity estimated by the Kozeny-Carman method is 1.122 ft/d.

Core Hole CrCH-3 Run 82
Drilled Interval 971–975 ft
Drilled 48 in. and Recovered 48 in.

Note: Sample included a Lexan tube and 1-ft plastic sleeve marked as bottom of run. The plastic sleeve contents matched the bottom of the Lexan tube that was partly empty.

Core Hole CrCH-3 971–972.9 ft (Tjfp)

Medium gray, silty, fine- to coarse-grain crystal and tuffaceous sand with no larger clasts. Lower part of interval appears to be faintly bedded and more consolidated than upper part. The base of the bed is deformed with an upper-pointing cone of material derived from the underlying bed; this is probably a drilling artifact. Most of the bed is massive, poorly to moderately well consolidated, and moderately sorted. The hydraulic conductivity estimated by the Kozeny-Carman method is 0.622 ft/d.

Core Hole CrCH-3 972.9–974.2 ft (Tjfp)

Reddish brown, silty, fine- to coarse-grain tuffaceous sand with abundant, matrix-supported granules of pumice and subordinate dark lava. Maximum clast size is 0.25 in. Bed is oxidized and may be altered by possible soil development. Dark lava clasts are more common in the lower part of the bed and are up to 0.5 in. The bed is massive, moderately well consolidated, and poorly sorted. The hydraulic conductivity estimated by the Kozeny-Carman method is 0.350 ft/d.

Core Hole CrCH-3 974.2–975 ft (Tjfp)

Light brownish gray, gravelly, silt and fine-grain tuffaceous sand with abundant, matrix-supported, rounded granules and pebbles of pumice up to 0.5 in. The bed is massive, moderately well consolidated, and poorly sorted. The hydraulic conductivity estimated by the Kozeny-Carman method is 0.197 ft/d.

Core Hole CrCH-3 Run 83 (bag)
Drilled Interval 976.5–980 ft
Drilled 42 in. and Recovered 36 in.; assume uniform compaction, depths corrected uniformly

Core Hole CrCH-3 976.5–977.25 ft (Tjfp)

Light brown silt and fine- to coarse-grain tuffaceous sand containing ~10% matrix-supported granules and pebbles of rounded, white, vitric pumice up to 0.25 in. Trace dark gray lava is a component of the sand fraction. The bed is massive, moderately consolidated, and moderately well sorted. The hydraulic conductivity estimated by the Kozeny-Carman method is 0.208 ft/d.

Core Hole CrCH-3 977.25–978.5 ft (Tjfp)

Light brown to white, gravelly, silt and fine- to coarse-grain sand with matrix-supported granules and sparse pebbles of subangular, white, vitric pumice up to 1 in. Matrix appears to contain abundant silt and clay(?). Trace dark gray lava is a component of the sand fraction. The bed is massive, well consolidated, and poorly sorted. The hydraulic conductivity estimated by the Kozeny-Carman method is 0.205 ft/d.

Core Hole CrCH-3 978.5–980 ft (Tjfp)

Light grayish brown silt and fine-grain tuffaceous sand containing abundant matrix-supported granules and rare small pebbles of white, vitric pumice up to 0.25 in. The bed is characterized by small, unconnected cavities throughout that may represent bioturbation(?). Thin, subhorizontal veinlets filled with white secondary minerals occur in the bed; the secondary minerals are soft and do not react with HCl. The bed is massive, moderately well consolidated, and poorly sorted. The hydraulic conductivity estimated by the Kozeny-Carman method is 0.155 ft/d.

Core Hole CrCH-3 Run 84
Drilled Interval 980–983 ft
Drilled 36 in. and Recovered 36 in. (plastic sleeve)

Core Hole CrCH-3 980–980.8 ft (Tjfp)

Grayish brown, fine- to coarse-grain tuffaceous sand with common, matrix-supported, subrounded to rounded granules and rare pebbles of pumice up to 0.5 in. The bed appears to fine upwards. The bed is massive, moderately well consolidated, and poorly sorted. The hydraulic conductivity estimated by the Kozeny-Carman method is 0.528 ft/d. The core has a rind of coarse sandy material that may be due to mobilization of sand during drilling.

Core Hole CrCH-3 980.8–981.9 ft (Tjfp)

Grayish brown silt and very fine-grain tuffaceous sand (no larger clasts). The bed is massive, moderately well consolidated, and well sorted. The hydraulic conductivity estimated by the Kozeny-Carman method is 1.122 ft/d. The core has a rind of very coarse sandy material that may be due to mobilization of sand during drilling. There appears to be some intrusion of the underlying unit into this bed.

Core Hole CrCH-3 981.9–982.3 ft (Tjfp)

Brownish gray, medium- to coarse-grain tuffaceous sand with common, matrix-supported, rounded granules and pebbles of pumice and dark lava up to 0.75 in. The bed is massive, poorly consolidated, and poorly sorted. The hydraulic conductivity estimated by the Kozeny-Carman method is 1.122 ft/d. The core contains a few rust spots from oxidation of iron fillings.

Core Hole CrCH-3 982.3–982.6 ft (Tjfp)

White, very coarse-grain tuffaceous sand or fine gravel made up of clast-supported, subangular to angular granules of pumice up to 0.25 in. The bed is faintly bedded, poorly consolidated, and poorly sorted. Transmissivity is good. The core has a rind of coarse sandy material that may be due to mobilization of sand during drilling. Contacts with overlying and underlying beds partly disrupted by drilling, and mixing of zones occurs (avoided in sampling). The bed may be a primary fall deposit. The hydraulic conductivity estimated by the Kozeny-Carman method is 0.442 ft/d.

Core Hole CrCH-3 982.6–983 ft (Tjfp)

Light brownish gray, fine- to coarse-grain tuffaceous sand with abundant, matrix-supported, rounded granules of pumice up to 0.25 in. Also contains subordinate granules of dark lava. The bed is massive, moderately well consolidated, and poorly sorted. The hydraulic conductivity estimated by the Kozeny-Carman method is 1.020 ft/d.

Core Hole CrCH-3 Run 85

Drilled Interval 983–987 ft

Drilled 48 in. and Recovered 60 in. (The extra 12 in. of core was evenly distributed throughout the core run.)

Core Hole CrCH-3 983–983.7 ft (Tjfp)

Medium gray, silty, medium- to coarse-grain tuffaceous sand with sparse, subrounded granules of pumice up to 0.25 in. The sandy matrix contains subordinate dark lava. The bed is massive, moderately well consolidated, and poorly sorted. The hydraulic conductivity estimated by the Kozeny-Carman method is 0.379 ft/d.

Core Hole CrCH-3 983.7–984.9 ft (Tjfp)

Gray, silty, medium- to coarse-grain tuffaceous sand with common, matrix-supported granules of pumice and dark lava. Basal part of bed is deformed with an upper-pointing cone of material derived from the underlying bed; this is probably a drilling artifact. The bed is massive, moderately well consolidated, and poorly sorted. The hydraulic conductivity estimated by the Kozeny-Carman method is 0.350 ft/d.

Core Hole CrCH-3 984.9–986.2 ft (Tjfp)

Reddish brown silt and fine-grain tuffaceous sand with sparse granules of dark gray lava up to 0.25 in. Pumice granules are rare. Bed is oxidized and may be altered by possible soil development. The bed is massive, moderately well consolidated, and moderately sorted. The hydraulic conductivity estimated by the Kozeny-Carman method is 0.018 ft/d. Top of bed is irregular and partly intrudes the overlying bed.

Core Hole CrCH-3 986.2–987 ft (Tjfp)

Gray–reddish brown silt and fine- to medium-grain tuffaceous sand with common, matrix-supported granules of pumice and dark lava at the base, which then disappear upwards. Bed is oxidized and may be altered by possible soil development. The bed is massive, moderately well consolidated, and moderately to well sorted (except for base). The hydraulic conductivity estimated by the Kozeny-Carman method is 0.243 ft/d.

Core Hole CrCH-3 Run 86 (bag)

Drilled Interval 987–991 ft

Drilled 48 in. and Recovered 48 in.

Core Hole CrCH-3 987–987.4 ft (Tjfp)

Light brownish gray, medium- to very coarse-grain tuffaceous sand containing minor granules of white, vitric pumice and sparse, dark gray lava. The bed is massive, unconsolidated, and fairly well sorted. Finer sand is concentrated along the margins of the core, possibly representing exfiltration to the edges during drilling. There also appears to be some fingering of this bed into the top of the underlying bed; this may be due to soft sediment mobilization during drilling. The hydraulic conductivity estimated by the Kozeny-Carman method is 1.175 ft/d.

Core Hole CrCH-3 987.4–987.9 ft (Tjfp)

Light gray, silty, fine- to medium-grain pumiceous sand. The sandy matrix is dominated by white, vitric pumice that may be slightly altered. The bed is highly disrupted (by drilling?). The bed is generally massive, unconsolidated, and fairly well sorted. The hydraulic conductivity estimated by the Kozeny-

Carman method is 0.268 ft/d. The bed appears to be disrupted by intrusion by the overlying bed; the intruded material was avoided during sampling.

Core Hole CrCH-3 987.9–988.2 ft (Tjfp)

Possible soil. Reddish brown silt and fine-grain sand with some possible clay. Contains sparse granules and rare small pebbles of dark gray lava up to 0.25 in. The bed is massive, well consolidated, and well sorted. The hydraulic conductivity estimated by the Kozeny-Carman method is 0.186 ft/d.

Core Hole CrCH-3 988.2–989.4 ft (Tjfp)

Possible soil. Brownish red silt and fine- to medium-grain sand with some possible clay. Contains sparse granules of white pumice, which are concentrated in the upper part of the bed (reverse grading). Lower part of bed contains some stratification, and the upper part is more massive. Very sparse dark gray lava is a component of the sand fraction. The bed is moderately well consolidated and well sorted. The hydraulic conductivity estimated by the Kozeny-Carman method is 0.219 ft/d. Finer sand is concentrated along the margins of the core, possibly representing exfiltration to the edges during drilling; this was avoided during sampling.

Core Hole CrCH-3 989.4–991 ft (Tjfp)

Possible soil. Reddish brown silt and fine-grain sand with ~20% granules of matrix-supported dark gray lava up to 0.2 in. and sparse white pumice. Bed is normally graded, with fewer granules upwards. The bed is well consolidated and poorly sorted. The hydraulic conductivity estimated by the Kozeny-Carman method is 0.119 ft/d. Finer sand is concentrated along the margins of the core, possibly representing exfiltration to the edges during drilling; this was avoided during sampling. Small pockets at the top of the unit contain concentrations of coarse pumiceous sand and lava; these may be burrows.

Core Hole CrCH-3 Run 95 (bag)

Drilled Interval 1019–1023 ft

Drilled 48 in. and Recovered 48 in.

Note: Although sampled, these cores were not processed for particle-size fractions.

Core Hole CrCH-3 1019–1019.8 ft (Tcar–riverine)

Medium brown, gravelly, coarse-grain lithic-crystal sand with ~5–10% matrix-supported pebbles and cobbles of well-rounded, dark gray and brown intermediate-composition lava up to 3 in. The sandy matrix contains crystals and well-rounded dark lava and clear to milky quartzite. The bed is massive, unconsolidated, and poorly sorted. Transmissivity is moderate to good.

Core Hole CrCH-3 1019.8–1020.7 ft (Tcar–riverine)

Medium grayish brown, gravelly, coarse-grain lithic-crystal sand with ~5–10% matrix-supported pebbles and cobbles of rounded, dark gray intermediate-composition lava and minor quartzite up to 4 in. This bed is slightly lighter in color than the overlying bed. The bed is massive, unconsolidated, and poorly sorted. Transmissivity is good.

Core Hole CrCH-3 1020.7–1021.5 ft (Tcar–riverine)

Yellowish medium-brown, medium-grain, magnetite-rich lithic-crystal sand with sparse matrix-supported pebbles of rounded, dark gray intermediate-composition lava and minor quartzite. The magnetite is highly concentrated in thin–very thin horizontal stringers. The interval is bedded, unconsolidated, and well sorted. Transmissivity is good.

Core Hole CrCH-3 1021.5–1022.1 ft (Tcar–riverine)

Medium brown, gravelly, coarse-grain lithic-crystal sand with ~10% matrix-supported pebbles of rounded, dark gray intermediate-composition lava and minor quartzite up to 1.5 in. The bed is massive.

Core Hole CrCH-3 1022.1–1023 ft (Tcar–riverine)

Brownish gray, gravelly, coarse-grain lithic-crystal sand with ~10-20% matrix-supported pebbles of rounded, dark gray intermediate-composition lava and quartzite up to 3 in. Orange, well-cleaved microcline is present as sparse crystals up to 0.75 in. The bed is massive, poorly consolidated, and poorly sorted. Transmissivity is moderate to good. The largest quartzite cobble (3 in.) is sharply angular and is probably a remnant of a larger clast broken during coring.

C-4.0 CORE HOLE CrCH-4 LITHOLOGIC DESCRIPTIONS

Note: All footages are measured from the bottom of core tubes. Colors reflect damp to wet cores except where noted.

Core Hole CrCH-4, Run 48 (Lexan)

Drilled Interval 934–938.5 ft

Drilled 54 in. and Recovered 54 in.

Core Hole CrCH-4 934–934.2 ft (Tpf)

Lower part of bed is dark brown and upper part is dark brownish gray. Faintly laminated fine- to medium-grain sand with no larger clasts. The upper part of the bed is massive. The bed contains a number of small pieces of carbonaceous material identified under the microscope as charcoal. Overall, the bed is well consolidated and fairly well sorted. The hydraulic conductivity estimated by the Kozeny-Carman method is 0.476 ft/d.

Core Hole CrCH-4 934.2–936.7 ft (Tpf)

Light orangish brown sandy gravel with matrix-supported, subrounded and subangular granules and pebbles of grayish brown dacite up to 4 in. The matrix is medium- to coarse-grain lithic-crystal sand. Fine reworked pumice is concentrated in a 1-in. zone near the top of the bed. Overall the bed is normally graded, becoming somewhat finer upwards. The bed is well consolidated and poorly sorted. The hydraulic conductivity estimated by the Kozeny-Carman method is 1.122 ft/d.

Core Hole CrCH-4 936.7–937 ft (Tpf)

Light brown silty sand with common matrix-supported, subrounded and subangular granules and pebbles of grayish brown dacite up to 0.5 in. The bed is massive, well consolidated, and poorly sorted. The hydraulic conductivity estimated by the Kozeny-Carman method is 0.268 ft/d.

Core Hole CrCH-4 937–938.5 ft (Tpf)

Light orangish brown, gravelly, medium- to coarse-grain sand with abundant matrix-supported, subrounded and subangular granules and pebbles of grayish brown dacite up to 0.75 in. Gravel is concentrated in the lower part of the bed and the bed fines upwards. The bed is massive, well consolidated, and poorly sorted. The lower part is somewhat less consolidated. The hydraulic conductivity estimated by the Kozeny-Carman method is 0.622 ft/d.

Core Hole CrCH-4, Run 49 (Lexan)

Drilled Interval 938–942 ft

Drilled 48 in. and Recovered 60 in. (extra footage distributed into 48-in. interval)

Note: There is a 0.5-ft overlap in the recorded drill intervals for Runs 48 and 49.

Core Hole CrCH-4 938–940 ft (Tpf)

Light orangish brown sandy gravel with matrix-supported, subangular to subrounded granules and pebbles of dacite up to 2.5 in. White pumice granules are very sparse. The matrix is fine- to coarse-grain sand and may be tuffaceous. The bed is massive, well consolidated, and poorly sorted. The hydraulic conductivity estimated by the Kozeny-Carman method is 7.682 ft/d.

Core Hole CrCH-4 940–940.25 ft (Tpf)

Light orangish brown, gravelly, coarse-grain sand with numerous pumice in the sand fraction. The gravel fraction consists of subangular to subrounded granules of dacite. The bed is massive, poorly consolidated, and poorly to moderately sorted. The hydraulic conductivity estimated by the Kozeny-Carman method is 9.484 ft/d.

Core Hole CrCH-4 940.25–941 ft (Tpf)

Light orangish brown, gravelly, fine- to medium-grain sand with common matrix-supported, subrounded to subangular granules and pebbles of dacite up to 1 in. The bed is massive, well consolidated, and poorly sorted. The hydraulic conductivity estimated by the Kozeny-Carman method is 1.122 ft/d.

Core Hole CrCH-4 941–941.75 ft (Tpf)

Light brown, fine- to coarse-grain sand with abundant granules of dacite. The bed is massive, moderately well consolidated and poorly sorted. A 0.25-in. layer of gray-brown silt or fine-grain sand occurs near the base of the bed. The hydraulic conductivity estimated by the Kozeny-Carman method is 1.071 ft/d.

Core Hole CrCH-4 941.75–942 ft (Tpf)

Bedded medium gray silt with individual layers up to 0.5 in. thick. There is also a 0.5-in. layer of medium- to coarse-grain pumiceous sand. Overall the interval is moderately consolidated and well sorted. The hydraulic conductivity estimated by the Kozeny-Carman method is 0.197 ft/d.

Tpf/Tpf(p) Contact–942.5 ft

Core Hole CrCH-4, Run 50 (Sausage)

Drilled Interval 942.5–947.5 ft

Drilled 60 in. and Recovered 55 in. (settled in plastic sleeve)

Note: there is no 942–942.5 interval in either Runs 49 or 50 (interval not sampled).

Core Hole CrCH-4 942.5–943.3 ft [Tpf(p)]

Light orangish brown, silty, gravelly, sand with abundant matrix-supported, subrounded pebbles of dacite up to 1.5 in. Clasts are supported in a matrix of tuffaceous sand. The bed is massive, poorly consolidated, and poorly sorted. The hydraulic conductivity estimated by the Kozeny-Carman method is 0.622 ft/d.

Core Hole CrCH-4 943.3–946.2 ft [Tpf(p)]

Medium brown, massive fine- to medium-grain sand with common granules and small pebbles of white pumice and dark gray lava. A single flow-banded 3-in. obsidian clast occurs at the top of the bed. The tuffaceous nature of the bed is striking compared with all overlying core intervals. Rendija Canyon granules are confirmed by microscope. Overall, the bed is moderately consolidated and fairly well sorted. A 0.5-in.-thick gravel with subrounded lava occurs in the middle of the bed. The hydraulic conductivity estimated by the Kozeny-Carman method is 0.155 ft/d.

Core Hole CrCH-4 946.2–947.5 ft [Tpf(p)]

Medium gray, medium- to coarse-grain pumiceous sand. No larger clasts are present. The sandy matrix is dominated by broken pumice with very minor amounts of lithics and crystals. The bed is massive, poorly consolidated, and moderately well sorted. The hydraulic conductivity estimated by the Kozeny-Carman method is 0.442 ft/d.

Core Hole CrCH-4, Run 51 (Lexan)

Drilled Interval 947.5–952 ft

Drilled 4.5 ft and Recovered 5 ft (extra footage at top of core run discarded as slough)

Core Hole CrCH-4 947.5–947.75 ft [Tpf(p)]

Light brownish gray, medium- to coarse-grain pumiceous sand with sparse granules and small pebbles of dark lava up to 0.25 in. The sandy matrix is dominated by pumice and felsic crystals. The bed is massive, poorly to moderately well consolidated, and moderately well sorted. The hydraulic conductivity estimated by the Kozeny-Carman method is 4.385 ft/d.

Core Hole CrCH-4 947.75–948.4 ft [Tpf(p)]

Medium brownish gray, fine- to coarse-grain pumiceous sand with common subrounded granules and pebbles of pumice and dark lava up to 1 in. The sandy matrix is dominated by pumice and felsic crystals. The bed is massive, moderately well consolidated, and poorly to moderately sorted. Contains sparse Rendija Canyon lava clasts. The hydraulic conductivity estimated by the Kozeny-Carman method is 2.258 ft/d.

Core Hole CrCH-4 948.4–950.3 ft [Tpf(p)]

Medium brownish gray pumiceous gravel with abundant rounded granules and pebbles of porphyritic glassy rhyolite up to 2 in. The matrix is dominated by coarse-grain sand of pumice and felsic crystals. The bed is massive, moderately well consolidated, and poorly sorted. The hydraulic conductivity estimated by the Kozeny-Carman method is 1.579 ft/d.

Core Hole CrCH-4 950.3–950.75 ft [Tpf(p)]

Medium brownish gray, medium-grain pumiceous sand with sparse subrounded granules and small pebbles of dark lava up to 0.25 in. The sandy matrix is dominated by pumice and felsic crystals. The bed is massive, moderately well consolidated, and poorly to moderately sorted. The hydraulic conductivity estimated by the Kozeny-Carman method is 1.045 ft/d.

Core Hole CrCH-4 950.75– 951.4 ft [Tpf(p)]

Mottled white to light gray sequence of pumiceous sands and gravels. The two sequences have coarse-grain pumiceous sand with a minor lava component in the lower parts and grade upwards into gravels that contain granules and small pebbles of pumice up to 0.25 in. (reverse grading). The bed is moderately well consolidated and poorly sorted. The hydraulic conductivity estimated by the Kozeny-Carman method is 0.583 ft/d.

Core Hole CrCH-4 951.4–952 ft [Tpf(p)]

Brown, gravelly, pumiceous sand with matrix-supported, subrounded granules and pebbles of pumice up to 1 in. The bed is stratified with gravelly zones at the top and bottom and a sandy zone in the middle. The bed is moderately well consolidated and poorly sorted. The hydraulic conductivity estimated by the Kozeny-Carman method is 0.876 ft/d.

**Core Hole CrCH-4, Run 52 (Lexan)
Drilled Interval 952–957 ft
Drilled 60 in. and Recovered 60 in.**

Core Hole CrCH-4 952–953.1 ft [Tpf(p)]

Medium gray, coarse-grain pumiceous sand with sparse granules of pumice. Pumice is abundant throughout the coarse sand fraction, and dark lava is a minor component. The bed is massive, poorly to moderately well consolidated, and poorly to moderately sorted. The hydraulic conductivity estimated by the Kozeny-Carman method is 2.333 ft/d.

Tpf(p)/Tjfp Contact–953.1 ft

Core Hole CrCH-4 953.1–953.4 ft (Tjfp)

Light gray, medium- to coarse-grain pumiceous sand with minor matrix-supported granules and pebbles of white pumice and sparse reddish-brown lava up to 0.5 in. The sandy matrix is dominated by pumice and felsic crystals; dark lava grains are a subordinate component of the sand. The bed appears to be slightly reversely graded. The bed is poorly sorted. The hydraulic conductivity estimated by the Kozeny-Carman method is 1.457 ft/d.

Core Hole CrCH-4 953.4–954.25 ft (Tjfp)

White pumice bed. Fine gravel of white, angular to subangular pumice that is mostly <0.25 in. The bed is massive, moderately well consolidated, and moderately well sorted. The bed is a possible fall deposit. The hydraulic conductivity estimated by the Kozeny-Carman method is 0.510 ft/d.

Core Hole CrCH-4 954.25–955.3 ft (Tjfp)

Reddish brown, fine- to coarse-grain tuffaceous sand with sparse granules and pebbles of dark gray lava up to 0.5 in. The matrix is dominated by tuffaceous material with subordinate dark lava grains. The base of the bed contains sparse granules of pumice and obsidian. The bed is reversely graded, moderately well consolidated, and poorly sorted. The hydraulic conductivity estimated by the Kozeny-Carman method is 0.307 ft/d.

Core Hole CrCH-4 955.3–955.6 ft (Tjfp)

Reddish brown, gravelly and silty fine-grain sand with common matrix-supported angular granules and pebbles of lava up to 1 in. The matrix is notably fine grain. The bed is massive, moderately well consolidated, and poorly sorted. The hydraulic conductivity estimated by the Kozeny-Carman method is 0.155 ft/d.

Core Hole CrCH-4 955.6–956.5 ft (Tjfp)

Medium grayish brown, medium- to coarse-grain pumiceous sand. Generally, fines upwards (normal grading). Base of bed includes a fine gravel of pumice and dark gray lava up to 0.5 in. The bed is massive and moderately well sorted except for the gravelly base. The hydraulic conductivity estimated by the Kozeny-Carman method is 0.294 ft/d.

Core Hole CrCH-4 956.5–956.8 ft (Tjfp)

Medium grayish brown, fine- to coarse-grain tuffaceous sand with sparse granules and pebbles of pumice and dark gray lava up to 0.5 in. The bed is massive, poorly consolidated, and poorly sorted. The bed is partly disrupted, possibly because of drilling. The hydraulic conductivity estimated by the Kozeny-Carman method is 0.528 ft/d.

Core Hole CrCH-4 956.8–957 ft (Tjfp)

Reddish brown, fine- to medium-grain tuffaceous sand. The sand is massive and uniform except for very sparse granules of pumice. The bed is poorly consolidated and moderately well sorted. The bed is partly disrupted, possibly because of drilling. The hydraulic conductivity estimated by the Kozeny-Carman method is 0.379 ft/d.

C-5.0 CORE HOLE CrCH-5 LITHOLOGIC DESCRIPTIONS

Note: All footages are measured from the bottom of core tubes. Colors reflect damp to wet cores except where noted.

Core Hole CrCH-5, Run 45 (Sausage)

Drilled Interval 960–965 ft

Drilled 60 in. and Recovered 60 in.

Core Hole CrCH-5 960–961 ft (Tpf)

Grayish brown, gravelly, fine- to coarse-grain lithic sand with abundant matrix-supported, subrounded granules and pebbles of dark gray dacite up to 1.5 in. The bed is massive, poorly consolidated, and poorly sorted. The hydraulic conductivity estimated by the Kozeny-Carman method is 0.197 ft/d.

Core Hole CrCH-5 961–962.2 ft (Tpf)

Light orangish brown, gravelly, fine-grain sand with abundant matrix-supported, subrounded granules and pebbles of dark gray dacite up to 1.5 in. Clasts are less common, and the matrix is finer than the overlying bed. The bed is massive, moderately well consolidated, and poorly sorted. The bed is likely a debris flow deposit. The hydraulic conductivity estimated by the Kozeny-Carman method is 0.350 ft/d.

Core Hole CrCH-5 962.2–963.75 ft (Tpf)

Light reddish brown, silty, fine-grain tuffaceous sand with sparse subrounded granules and pebbles of dark gray dacite up to 1 in. Sparse pumice occurs in the sandy matrix. The bed is massive, moderately well consolidated, and poorly sorted. The hydraulic conductivity estimated by the Kozeny-Carman method is 0.197 ft/d.

Core Hole CrCH-5 963.75–964 ft (Tpf)

Light olive-gray, medium- to coarse-grain tuffaceous sand with granules of pumice. Bed is very uniform and may be a Tschicoma fall deposit. Mafic crystals (some quite small and needle-like) are abundant in the sandy fraction and in the pumice. The bed is massive, poorly consolidated, and fairly well sorted. The hydraulic conductivity estimated by the Kozeny-Carman method is 0.186 ft/d.

Core Hole CrCH-5 964–965 ft (Tpf)

Brownish gray, medium- to coarse-grain sand. The sand is a mixture of lava lithics and tuffaceous material. The bed becomes gravelly towards the base. The bed is massive, poorly consolidated, and poorly sorted. The hydraulic conductivity estimated by the Kozeny-Carman method is 0.197 ft/d.

Core Hole CrCH-5, Run 46 (Sausage)

Drilled Interval 965–970 ft

Drilled 60 in. and Recovered 60 in.

Core Hole CrCH-5 965–967.25 ft (Tpf)

Brown, gravelly, medium- to coarse-grain lithic sand with abundant matrix-supported, subangular to subrounded granules and pebbles of dark gray dacite up to 0.5 in. The bed is reversely graded with oxidized coarse-grain sand in the lower third and gravelly sand in the upper two-thirds. Pumice is rare to absent. The bed is poorly consolidated and poorly sorted. Overall, the bed is fines poor. The hydraulic conductivity estimated by the Kozeny-Carman method is 4.131 ft/d.

Core Hole CrCH-5 967.25–968.2 ft (Tpf)

Light reddish brown, gravelly, fine- to coarse-grain lithic sand with matrix-supported, subrounded granules and pebbles of dark gray dacite up to 0.5 in. and sparse granules of pumice up to 0.25 in. The bed is massive, poorly consolidated, and poorly sorted. The hydraulic conductivity estimated by the Kozeny-Carman method is 4.385 ft/d.

Core Hole CrCH-5 968.2–970 ft (Tpf)

Reddish brown, coarse-grain lithic sand with sparse subangular to subrounded granules and pebbles of dark gray dacite up to 0.5 in. The sand tends to be oxidized and contains thin, intercalated, gravelly sands that are less oxidized. Pumice is sparse throughout the bed. The bed is poorly consolidated and poorly sorted. The hydraulic conductivity estimated by the Kozeny-Carman method is 4.385 ft/d. The bed marks the position of the regional water table.

Core Hole CrCH-5, Run 47 (Sausage)

Drilled Interval 970–975 ft

Drilled 60 in. and Recovered 60 in.

Core Hole CrCH-5 970–970.5 ft (Tpf)

Dark brown, coarse-grain lithic sand with abundant matrix-supported, subrounded granules and pebbles of dark gray dacite up to 0.5 in. The bed is massive, poorly consolidated, and poorly sorted. The hydraulic conductivity estimated by the Kozeny-Carman method is 1.122 ft/d.

Core Hole CrCH-5 970.5–971.5 ft (Tpf)

Reddish brown, medium- to coarse-grain sand with abundant matrix-supported, subrounded granules and pebbles of dark gray dacite up to 1 in. The bed is massive, poorly consolidated, and poorly sorted. The hydraulic conductivity estimated by the Kozeny-Carman method is 0.787 ft/d.

Core Hole CrCH-5 971.5–971.75 ft (Tpf)

Dark gray, silty, fine- to coarse-grain sand with common matrix-supported, subrounded granules of dark gray dacite. The bed is massive, poorly consolidated, and poorly sorted. The hydraulic conductivity estimated by the Kozeny-Carman method is 9.484 ft/d.

Core Hole CrCH-5 971.75–972.3 ft (Tpf)

Reddish brown sandy gravel with abundant matrix-supported, subrounded granules and pebbles of dark gray dacite up to 1.5 in. and sparse granules of pumice. The bed is massive, poorly consolidated, and poorly sorted. The hydraulic conductivity estimated by the Kozeny-Carman method is 0.379 ft/d.

Core Hole CrCH-5 972.3–974.7 ft (Tpf)

Reddish brown to gray sandy gravel with abundant matrix-supported, subrounded to subangular granules and pebbles of dark gray dacite up to 2 in. The matrix is a coarse-grain lithic sand. An orange 0.5-in-thick pumiceous sand occurs near the top of the bed; otherwise the bed is pumice poor. Overall, the bed is massive, poorly consolidated, and poorly sorted. The hydraulic conductivity estimated by the Kozeny-Carman method is 0.476 ft/d.

Core Hole CrCH-5 974.7–975 ft (Tpf)

Reddish brown, coarse-grain tuffaceous sand with abundant matrix-supported, subrounded to subangular granules of dark gray dacite up to 0.25 in. The bed is massive, moderately well consolidated, and poorly sorted. The hydraulic conductivity estimated by the Kozeny-Carman method is 0.395 ft/d.

Core Hole CrCH-5, Run 48 (Sausage)

Drilled Interval 975–980 ft

Drilled 60 in. and Recovered 56 in. (distributed the missing 4 in.)

Core Hole CrCH-5 975–977.5 ft (Tpf)

Grayish brown sandy gravel with subrounded to subangular granules and pebbles of dark lava up to 1 in. The matrix is made up of medium- to coarse-grain sand. Pumice is absent. The bed is massive, poorly consolidated, and poorly sorted. The hydraulic conductivity estimated by the Kozeny-Carman method is 9.484 ft/d.

Tpf/Tpf(p) Contact–977.5 ft

Core Hole CrCH-5 977.5–978.2 ft [Tpf(p)]

Light reddish brown, fine- to coarse-grain sand with matrix-supported granules of dark lava and subordinate white pumice. The matrix is made up of medium- to coarse-grain sand. The bed is massive, moderately well consolidated, and poorly sorted. The hydraulic conductivity estimated by the Kozeny-Carman method is 2.258 ft/d.

Core Hole CrCH-5 978.2–978.6 ft [Tpf(p)]

Light brown, coarse-grain pumiceous sand with abundant matrix-supported granules of pumice and subordinate dark lava up to 0.25 in. The bed is massive, moderately well consolidated, and poorly sorted. The hydraulic conductivity estimated by the Kozeny-Carman method is 4.131 ft/d.

Core Hole CrCH-5 978.6–979.6 ft [Tpf(p)]

Light brownish gray. Gravelly, coarse-grain sand with abundant matrix-supported, subrounded to subangular pebbles of dark lava up to 1 in. and subordinate white pumice up to 0.25 in. The bed is massive, moderately well consolidated, and poorly sorted. The hydraulic conductivity estimated by the Kozeny-Carman method is 2.807 ft/d.

Core Hole CrCH-5 979.6–980 ft [Tpf(p)]

Grayish brown, coarse-grain pumiceous sand with granules of white pumice up to 0.25 in. The bed is massive, moderately well consolidated, and poorly sorted. A small area of oxidation occurs in the center of the core. The hydraulic conductivity estimated by the Kozeny-Carman method is 1.398 ft/d.

Core Hole CrCH-5, Run 49 (Sausage)

Drilled Interval 980–985 ft

Drilled 60 in. and Recovered 56 in. (distributed the missing 4 in.)

Core Hole CrCH-5 980–981.25 ft [Tpf(p)]

Light brown, medium- to coarse-grain sand with sparse granules and pebbles of pumice and dark lava. The sandy matrix is a mixture of lava grains, crystals, and white pumice. The bed is massive, poorly consolidated, and poorly to moderately sorted. The hydraulic conductivity estimated by the Kozeny-Carman method is 1.284 ft/d.

Core Hole CrCH-5 981.25–982.1 ft [Tpf(p)]

White to tan, gravelly, coarse-grain pumiceous sand with matrix-supported subrounded granules and pebbles of pumice up to 1 in. The bed is massive except for a 0.25-in.-thick bedded sand at the base of the interval. The bed is poorly consolidated, and poorly sorted. The hydraulic conductivity estimated by the Kozeny-Carman method is 1.071 ft/d.

Core Hole CrCH-5 982.1–982.75 ft [Tpf(p)]

Reddish brown, fine-grain tuffaceous sand with sparse granules of pumice in the upper part of the bed and a 2-in.-thick gravel at the top of the bed. The bed is moderately well consolidated and moderately sorted. The hydraulic conductivity estimated by the Kozeny-Carman method is 0.410 ft/d.

Core Hole CrCH-5 982.75–984.25 ft [Tpf(p)]

Reddish brown, fine- to coarse-grain tuffaceous sand with sparse granules of pumice and rare dark lava. The bed oxidized throughout, and oxidation is more intense in the upper part. The bed is massive, moderately well consolidated, and poorly sorted. The hydraulic conductivity estimated by the Kozeny-Carman method is 0.622 ft/d.

Core Hole CrCH-5 984.25–985 ft [Tpf(p)]

Light brownish tan, coarse-grain pumiceous sand with no larger clasts. The sandy matrix is dominated by subrounded pumice and rare lava grains. The bed is massive, poorly consolidated, and poorly to moderately sorted. The hydraulic conductivity estimated by the Kozeny-Carman method is 0.442 ft/d.

Core Hole CrCH-5, Run 50 (Sausage)

Drilled Interval 985–990 ft

Drilled 60 in. and Recovered 60 in.

Core Hole CrCH-5 985–985.5 ft [Tpf(p)]

Medium brown, tuffaceous, coarse-grain sand with sparse granules and pebbles of pumice and dark lava. The bed appears to be disrupted by the drilling process. The bed is massive, poorly consolidated, and poorly to moderately sorted. The hydraulic conductivity estimated by the Kozeny-Carman method is 1.398 ft/d.

Core Hole CrCH-5 985.5–986.25 ft [Tpf(p)]

Light brown, pumiceous, coarse-grain sand with abundant rounded granules of pumice and sparse granules of dark lava. The sandy matrix is dominated by pumice. The bed is massive, poorly consolidated, and poorly sorted. The hydraulic conductivity estimated by the Kozeny-Carman method is 0.702 ft/d.

Core Hole CrCH-5 986.25–986.75 ft [Tpf(p)]

Light brown, fine- to medium-grain tuffaceous sand with sparse granules of pumice. There are no apparent lava clasts. The bed is massive, moderately well consolidated, and poorly sorted. The hydraulic conductivity estimated by the Kozeny-Carman method is 0.294 ft/d.

Core Hole CrCH-5 986.75–987.2 ft [Tpf(p)]

Light grayish brown, medium- to coarse-grain tuffaceous sand with abundant granules of dark lava up to 0.25 in. Pumice is sparse and mostly in the sand fraction. The bed is massive, poorly consolidated, and poorly sorted. The hydraulic conductivity estimated by the Kozeny-Carman method is 0.900 ft/d.

Core Hole CrCH-5 987.2–987.6 ft [Tpf(p)]

Grayish brown, coarse-grain pumiceous sand with abundant granules of pumice and dark lava up to 0.25 in. Pumice is sparse and mostly in the sand fraction. The bed is massive, poorly consolidated, and poorly sorted. The hydraulic conductivity estimated by the Kozeny-Carman method is 1.229 ft/d.

Core Hole CrCH-5 987.6–987.9 ft [Tpf(p)]

Light brownish gray, medium- to coarse-grain lithic-tuffaceous sand. Contains no larger clasts. The sandy matrix is a mixture of lava grains and subordinate tuffaceous material. The bed is massive, poorly consolidated, and poorly sorted. The hydraulic conductivity estimated by the Kozeny-Carman method is 0.787 ft/d.

Core Hole CrCH-5 987.9–988.6 ft [Tpf(p)]

Brownish gray, coarse-grain pumiceous sand with abundant granules of rounded pumice and sparse granules of dark lava up to 0.25 in. The sandy matrix is a mixture of lava grains and subordinate tuffaceous material. The bed is massive, poorly consolidated, and poorly sorted. The hydraulic conductivity estimated by the Kozeny-Carman method is 0.583 ft/d.

Core Hole CrCH-5 988.6–989.4 ft [Tpf(p)]

Bedded white and light brown, medium-grain pumiceous sand with no larger clasts. The bed consists of alternating white and light brown massive layers that are 0.5 in. thick. The bed is poorly consolidated and moderately well sorted. The hydraulic conductivity estimated by the Kozeny-Carman method is 1.045 ft/d.

Core Hole CrCH-5 989.4–990 ft [Tpf(p)]

Whitish gray, coarse-grain pumiceous sand with abundant granules of rounded pumice up to 0.25 in. Lava clasts are absent. Fines are rare in the sandy matrix. The bed is massive, poorly consolidated, and poorly sorted. The hydraulic conductivity estimated by the Kozeny-Carman method is 0.744 ft/d.

Core Hole CrCH-5, Run 51 (Sausage)

Drilled Interval 990–994 ft

Drilled 48 in. and Recovered 48 in.

Core Hole CrCH-5 990–991.4 ft [Tpf(p)]

Brown, gravelly, tuffaceous, fine-grain sand with matrix-supported granules and pebbles of dark lava up to 0.5 in. Pumice is abundant throughout the sand fraction. The bed is massive, poorly consolidated, and poorly sorted. The hydraulic conductivity estimated by the Kozeny-Carman method is 2.486 ft/d.

Core Hole CrCH-5 991.4–992 ft [Tpf(p)]

Brown, coarse-grain tuffaceous sand with sparse granules and pebbles of dark lava up to 0.5 in. The sandy matrix contains abundant tuffaceous materials. The bed is massive, poorly consolidated, and poorly sorted. The hydraulic conductivity estimated by the Kozeny-Carman method is 2.409 ft/d.

Core Hole CrCH-5 992–992.9 ft [Tpf(p)]

Brown, gravelly, coarse-grain sand with abundant matrix-supported granules and pebbles of dark lava up to 1 in. Pumice is sparse and present only in the sand fraction. The bed is massive, poorly consolidated, and poorly sorted. The hydraulic conductivity estimated by the Kozeny-Carman method is 9.867 ft/d.

Core Hole CrCH-5 992.9–993.2 ft [Tpf(p)]

Brown, gravelly, medium-grain sand with abundant matrix-supported subangular to subrounded granules and pebbles of dark lava up to 2 in. Granules of pumice are also abundant. The bed is massive, poorly consolidated, and poorly sorted. The hydraulic conductivity estimated by the Kozeny-Carman method is 16.524 ft/d.

Core Hole CrCH-5 993.2–994 ft [Tpf(p)]

Brown, coarse-grain lithic-crystal sand with sparse granules and pebbles of dark lava up to 0.5 in. Pumice is sparse in the sand fraction. The bed is massive, moderately well consolidated, and poorly to moderately sorted. The hydraulic conductivity estimated by the Kozeny-Carman method is 5.193 ft/d.

Core Hole CrCH-5, Run 52 (Sausage)

Drilled Interval 994–998 ft

Drilled 4 ft and Recovered 4 ft

Core Hole CrCH-5 994–996.5 ft [Tpf(p)]

Dark brownish gray sandy gravel with subrounded clasts of Rendija Canyon lava. The lower and upper part of the bed is a gravel and the central part a gravelly sand. The sand fraction is a coarse lithic sand with sparse white pumice present near the base of the bed. The bed is massive, poorly consolidated, and poorly sorted. The hydraulic conductivity estimated by the Kozeny-Carman method is 64.109 ft/d.

Core Hole CrCH-5 996.5–997 ft [Tpf(p)]

Light to medium gray pumice and lithic gravel with a silty matrix. The gravel is dominated by subrounded pebbles of dark lava up to 1 in. Pumice granules up to 0.25 in. are also abundant (notably more abundant than the overlying bed). Silty material may have migrated into the gravel from the underlying bed. The bed is massive, poorly consolidated, and poorly sorted. The core is notably wet. The hydraulic conductivity estimated by the Kozeny-Carman method is 2.486 ft/d.

Core Hole CrCH-5 997–998 ft [Tpf(p)]

Reddish brown, tuffaceous silt and fine-grain sand. The bed is massive, moderately well consolidated, and well sorted. The fine sand abundance increases upwards. The hydraulic conductivity estimated by the Kozeny-Carman method is 0.294 ft/d.

Core Hole CrCH-5, Run 53 (Sausage)

Drilled Interval 942.5–947.5 ft

Drilled 48 in. and Recovered 43 in. (settled in plastic sleeve)

Note: the interval 998–1002 was apparently not sampled.

Core Hole CrCH-5 1002–1003 ft [Tpf(p)]

Brown, gravelly, coarse-grain tuffaceous sand with abundant angular to subrounded granules and small pebbles of dark gray lava up to 1 in. and granular subrounded pumice up to 0.25 in. The bed is massive, poorly consolidated, and poorly sorted. The hydraulic conductivity estimated by the Kozeny-Carman method is 1.341 ft/d.

Core Hole CrCH-5 1003–1004.3 ft [Tpf(p)]

Light reddish brown, medium- to coarse-grain pumiceous sand with common subrounded granules of pumice and sparse dark gray lava. The bed is massive, poorly to moderately consolidated, and poorly sorted. The hydraulic conductivity estimated by the Kozeny-Carman method is 0.410 ft/d.

Core Hole CrCH-5 1004.3–1005 ft [Tpf(p)]

White, coarse-grain pumiceous sand with abundant granular subrounded pumice up to 0.25 in. The sandy matrix is dominated by broken pumice with very minor amounts of lithics and crystals. The bed is massive, poorly consolidated, and poorly sorted. The hydraulic conductivity estimated by the Kozeny-Carman method is 0.379 ft/d.

Core Hole CrCH-5, Run 54 (Sausage)

Drilled Interval 1005–1010 ft

Drilled 60 in. and Recovered 54 in. (missing footage distributed through core interval)

Core Hole CrCH-5 1005–1005.8 ft ([Tpf(p)]

White pumiceous sand with abundant granules of matrix-supported, rounded to subrounded granules of pumice up to 0.25 in. The matrix is fine- to coarse-grain pumiceous sand with sparse dark lava grains. The bed is massive, unconsolidated, and poorly sorted. The hydraulic conductivity estimated by the Kozeny-Carman method is 0.947 ft/d.

Core Hole CrCH-5 1005.8–1006.6 ft [Tpf(p)]

Medium reddish brown, pumiceous sand with subrounded granules of pumice up to 0.25 in. The bed is massive, moderately well consolidated, and poorly sorted. The hydraulic conductivity estimated by the Kozeny-Carman method is 1.229 ft/d.

Core Hole CrCH-5 1006.6–1007.7 ft [Tpf(p)]

White pumiceous sand with common rounded granules of pumice up to 0.25 in. The matrix is coarse-grain pumiceous sand. The bed is massive, poorly consolidated, and poorly sorted. The hydraulic conductivity estimated by the Kozeny-Carman method is 0.476 ft/d.

Core Hole CrCH-5 1007.7–1008.5 ft [Tpf(p)]

Reddish brown, fine- to coarse-grain pumiceous sand with sparse granules of pumice. The bed is massive, poorly to moderately well consolidated, and poorly to moderately sorted. The hydraulic conductivity estimated by the Kozeny-Carman method is 0.722 ft/d.

Core Hole CrCH-5 1008.5–1009.25 ft [Tpf(p)]

Gray–reddish brown, fine- to medium-grain sand with sparse granules of dark lava up to 0.25 in. Pumice is rare. The bed is massive, moderately well consolidated, and poorly sorted. The hydraulic conductivity estimated by the Kozeny-Carman method is 0.996 ft/d.

Core Hole CrCH-5 1009.25–1010 ft [Tpf(p)]

Reddish brown, fine- to medium-grain tuffaceous sand with sparse granules of pumice and dark lava. The bed is massive, poorly to moderately well consolidated, and poorly sorted. The hydraulic conductivity estimated by the Kozeny-Carman method is 0.307 ft/d.

Core Hole CrCH-5, Run 55 (Sausage)

Drilled Interval 1010–1016 ft

Drilled 72 in. and Recovered 56 in. (probably because of settling in plastic sleeve; distributed contacts to make 72 in.)

Core Hole CrCH-5 1010–1012.6 ft [Tpf(p)]

Light brown (dry color), gravelly and silty coarse-grain tuffaceous sand with granules and small pebbles of pumice and dark lava up to 0.25 in. The bed is massive, moderately well consolidated, and poorly sorted. The lower part of the bed is disrupted and intruded by the underlying bed. The hydraulic conductivity estimated by the Kozeny-Carman method is 0.900 ft/d.

Core Hole CrCH-5 1012.6–1014.2 ft [Tpf(p)]

Light brownish gray, sandy gravel with abundant matrix-supported, subrounded and subangular granules and pebbles of Rendija Canyon lava up to 1 in. Pumice granules are sparse. The matrix is fine- to coarse-grain tuffaceous sand. Overall the bed is reversely graded, becoming coarser upwards. The bed is poorly consolidated and poorly sorted. The top and bottom of the bed are disrupted and intruded by adjacent beds. Scattered rust spots could be oxidized iron fillings. The hydraulic conductivity estimated by the Kozeny-Carman method is 1.579 ft/d.

Core Hole CrCH-5 1014.2–1016 ft [Tpf(p)]

Light reddish brown, fine- to medium-sand with common matrix-supported, rounded granules and small pebbles of pumice up to 0.25 in.; also contains sparse Rendija Canyon lava granules. The bed is massive, moderately well consolidated, and poorly to moderately sorted. The bed represents a dramatic color change from the overlying beds. The hydraulic conductivity estimated by the Kozeny-Carman method is 0.364 ft/d.

The Tpf(p)/Tjfp contact is deeper than the TD of 1016 ft.

Appendix D

Particle-Size Data and Kozney-Carman Estimates of Hydraulic Conductivity for Core Holes CrCH-1, CrCH-2, CrCH-3, CrCH-4, and CrCH-5

Appendix D presents particle-size data and Kozney-Carman estimates of hydraulic conductivity for core holes CrCH-1, CrCH-2, CrCH-3, CrCH-4, and CrCH-5.

Table D-1
Particle-Size Data and Hydraulic Conductivity for CrCH-1

Core Hole CrCH-1—Puye Formation															
Drilled Interval (ft)	Sieve-Size Classifications				Pebbles and Cobbles in Size (>8 mm)	Very Coarse Sand to Pebbles (1.7 mm–8 mm)	Medium to Very Coarse Sand (0.355 mm–1.7 mm)	Fine to Medium Sand (0.177 mm– 0.355 mm)	Very Fine to Fine Sand (0.177 mm– 0.063 mm)	Silt (<0.063 mm)	24 Hour Gravity Settled	Total (%)	All Gravel	Fine to Very Coarse Sand	Hydraulic Conductivity Estimate (k) (ft/d)
	Upper Depth (ft)	Midpoint (ft)	Bottom Depth (ft)	Bed thickness (ft)	Fraction 1 (weight %)	Fraction 2 (wt%)	Fraction 3 (wt%)	Fraction 4 wt %)	Fraction 5 (wt%)	Fraction 6 (wt%)	Fraction 7 (wt%)		Fraction 1 + Fraction 2	Fraction 3 + Fraction 4 + Fraction 5	
CrCH-1 1111.5–1112	1111.5	1111.75	1112	0.5	18.26	34.26	22.20	6.60	6.22	12.18	0.28	100	52.52	35.02	0.744
CrCH-1 1112–1114.5	1112	1113.25	1114.5	2.5	26.37	28.20	20.03	7.94	6.85	10.30	0.31	100	54.57	34.81	4.385
CrCH-1 1114.5–1116.5	1114.5	1115.5	1116.5	2	21.55	33.11	21.24	9.50	6.36	8.10	0.13	100	54.66	37.11	2.185
CrCH-1 1116.5–1117.5	1116.5	1117	1117.5	1	16.72	25.65	18.47	6.56	12.88	18.29	1.42	100	42.37	37.91	0.379
CrCH-1 1117.5–1119	1117.5	1119	1118.25	0.75	11.31	29.35	29.89	8.01	8.39	12.91	0.14	100	40.66	46.29	1.096
CrCH-1 1119–1120	1119	1120	1119.5	0.5	20.53	25.86	18.65	6.91	9.87	17.76	0.41	100	46.39	35.44	0.546
CrCH-1 1120–1120.5	1120	1120.5	1120.25	0.25	19.01	47.22	18.88	4.07	3.57	7.14	0.11	100	66.24	26.52	0.146
CrCH-1 1120.5–1121.7	1120.5	1121.7	1121.1	0.6	9.34	39.50	22.85	6.26	6.94	14.84	0.28	100	48.84	36.04	0.787
CrCH-1 1121.7–1122.5	1121.7	1122.5	1122.1	0.4	18.13	44.34	24.18	6.59	3.29	3.46	0.01	100	62.47	34.06	39.467
CrCH-1 1122.5–1123.2	1122.5	1123.2	1122.85	0.35	11.46	35.94	29.86	7.35	7.86	7.45	0.08	100	47.40	45.07	5.478
CrCH-1 1123.2–1124.7	1123.2	1124.7	1123.95	0.75	8.26	29.65	18.12	7.22	9.59	26.26	0.89	100	37.91	34.93	0.243
CrCH-1 1124.7–1125	1124.7	1125	1124.85	0.15	15.68	16.16	18.44	8.39	9.22	27.41	4.69	100	31.85	36.05	0.208
CrCH-1 1125–1125.5	1125	1125.5	1125.25	0.25	7.24	19.00	21.09	11.07	15.80	25.24	0.57	100	26.24	47.95	0.268
CrCH-1 1125.5–1128.5	1125.5	1127	1128.5	3	12.89	26.07	21.02	8.54	11.79	19.70	-	100	38.96	41.34	0.379
CrCH-1 1127.9–1128.7	1127.9	1128.3	1128.7	0.8	18.03	25.91	23.97	8.71	5.27	17.23	0.87	100	43.94	37.95	0.379
CrCH-1 1128.7–1129.2	1128.7	1128.95	1129.2	0.5	14.37	24.20	19.87	8.68	7.95	24.25	0.68	100	38.57	36.50	0.243
CrCH-1 1128.7 ft + 18 in. to top—slough	1128.7	1128.7	1128.7	0	9.43	31.10	35.73	9.38	6.71	7.53	0.12	100	40.53	51.82	4.916
CrCH-1 1129.2–1130	1129.2	1129.6	1130	0.8	5.70	28.26	23.98	9.09	9.49	22.93	0.56	100	33.96	42.55	0.379
CrCH-1 1130–1131.5	1130	1130.75	1131.5	1.5	9.27	28.93	23.96	7.05	8.49	21.50	0.81	100	38.20	39.50	0.243
CrCH-1 1132.5–1133.5	1132.5	1133.5	1133	0.5	18.61	55.84	18.61	3.28	1.20	2.38	0.06	100	74.46	23.10	145.000
CrCH-1 1133.5–1134.5	1133.5	1134.5	1134	0.5	8.28	48.36	32.02	4.79	3.12	3.38	0.05	100	56.64	39.93	58.328
CrCH-1 1134.5–18"	1134.5	1134.5	1134.5	0	11.60	27.90	29.02	10.00	8.62	12.72	0.14	100	39.50	47.64	0.971
CrCH-1 1134.5–1136	1134.5	1135.25	1136	1.5	17.25	37.49	23.53	5.78	4.75	11.18	0.02	100	54.74	34.06	0.971
CrCH-1 1136–1136.5	1136	1136.25	1136.5	0.5	17.15	39.60	27.20	6.66	4.38	4.97	0.04	100	56.74	38.25	13.656

Table D-2
Particle-Size Data and Hydraulic Conductivity for CrCH-2

Core Hole CrCH-2—Puye Formation															
Drilled Interval (ft)	Sieve-Size Classifications				Pebbles and Cobbles in Size (>8 mm)	Very Coarse Sand to Pebbles (1.7 mm–8 mm)	Medium to Very Coarse Sand (0.355 mm–1.7 mm)	Fine to Medium Sand (0.177 mm–0.355 mm)	Very Fine to Fine Sand (0.177 mm–0.063 mm)	Silt (<0.063 mm)	24 Hour Gravity Settled	Total (%)	All Gravel	Fine to Very Coarse Sand	Hydraulic Conductivity Estimate (k) (ft/d)
	Upper Depth (ft)	Midpoint (ft)	Bottom Depth (ft)	Bed thickness (ft)											
CrCH-2 908–909.5	908	908.75	909.5	1.5	13.55	29.23	22.05	7.89	11.17	15.93	0.18	100.00	42.78	41.11	0.546
CrCH-2 909.5–910.29	909.5	909.895	910.29	0.79	16.31	31.56	22.19	6.93	10.16	11.18	1.69	100.00	47.87	39.27	1.229
CrCH-2 910.29–911.67	910.29	910.98	911.67	1.38	20.12	24.95	17.91	7.40	13.46	14.12	2.04	100.00	45.07	38.77	0.546
CrCH-2 911.67–912.38	911.67	912.025	912.38	0.71	5.32	22.09	25.90	8.98	14.74	20.55	2.42	100.00	27.41	49.63	0.379
CrCH-2 912.38–913.83	912.38	913.105	913.83	1.45	16.78	25.57	20.26	7.09	14.54	12.20	3.57	100.00	42.35	41.88	0.971
CrCH-2 913.83–915	913.83	914.415	915	1.17	19.36	30.84	24.03	7.36	7.24	10.94	0.23	100.00	50.20	38.63	0.546
CrCH-2 12 in. of core above 913 ft	913	913	913	0	12.92	32.48	21.00	7.86	9.99	15.36	0.40	100.00	45.40	38.84	0.546
CrCH-2 913–913.6	913	913.3	913.6	0.6	12.04	34.79	24.89	6.02	7.75	13.92	0.60	100.00	46.82	38.66	0.971
CrCH-2 913.6–915.1	913.6	914.35	915.1	1.5	19.52	31.56	27.43	9.28	9.22	2.28	0.71	100.00	51.08	45.94	10.257
CrCH-2 915.1–915.75	915.1	915.925	916.75	1.65	10.92	34.54	28.28	7.29	6.50	11.97	0.49	100.00	45.46	42.07	1.229
CrCH-2 916.75–917	916.75	916.875	917	0.25	5.90	23.12	38.18	12.94	9.54	10.22	0.09	100.00	29.01	60.67	1.836
CrCH-2 917–917.66	917	917.33	917.66	0.66	30.04	24.28	17.38	7.82	8.58	11.78	0.11	100.00	54.33	33.78	0.546
CrCH-2 917.66–918.32	917.66	917.99	918.32	0.66	30.25	27.04	20.14	7.10	6.52	5.93	3.02	100.00	57.29	33.76	3.414
CrCH-2 918.32–919.4	918.32	918.86	919.4	1.08	5.35	37.51	34.84	8.92	6.22	6.35	0.81	100.00	42.86	49.99	8.740
CrCH-2 Above 921 ft—possible slough	921	921	921	0	11.50	35.27	25.96	7.11	7.81	11.86	0.49	100.00	46.77	40.88	0.971
CrCH-2 922.08–921	921	921.54	922.08	1.08	11.39	48.70	20.86	4.77	4.04	10.02	0.23	100.00	60.09	29.66	0.546
CrCH-2 922.08–922.17	922.08	922.125	922.17	0.09	2.51	29.28	27.60	15.35	9.09	15.57	0.59	100.00	31.79	52.05	1.517
CrCH-2 922.17–924.2	922.17	923.185	924.2	2.03	2.53	27.85	30.16	8.03	10.75	19.61	1.06	100.00	30.39	48.94	0.379
CrCH-2 924.2–925	924.2	924.6	925	0.8	5.18	30.06	28.85	6.99	9.87	17.85	1.21	100.00	35.24	45.71	0.379
Core Hole CrCH-2—Pumiceous Puye Subunit															
CrCH-2 925–925.7	925	925.35	925.7	0.7	7.84	24.98	25.49	13.51	14.44	13.26	0.48	100.00	32.82	53.44	0.971
CrCH-2 925.7–926.25	925.7	925.975	926.25	0.55	0.61	8.16	32.19	22.72	20.85	14.76	0.72	100.00	8.76	75.76	0.971
CrCH-2 926.25–927.2	926.25	926.725	927.2	0.95	0.17	9.78	32.88	17.42	19.64	19.60	0.51	100.00	9.95	69.95	0.546
CrCH-2 927.2–927.75	927.2	927.475	927.75	0.55	1.77	21.65	27.73	13.55	17.87	17.32	0.10	100.00	23.42	59.16	0.744
CrCH-2 927.75–928.5	927.75	928.125	928.5	0.75	0.75	18.65	40.56	0.59	20.45	18.90	0.10	100.00	19.40	61.60	0.546
CrCH-2 928.5–929	928.5	928.75	929	0.5	0.72	25.92	29.16	8.96	15.36	19.45	0.44	100.00	26.64	53.48	0.379
CrCH-2 929–929.2	929	929.1	929.2	0.2	0.05	3.28	18.64	28.65	36.16	13.12	0.10	100.00	3.33	83.44	1.517
CrCH-2 929.2–930.1	929.2	929.85	930.5	1.3	0.00	9.98	37.81	24.16	20.02	7.94	0.09	100.00	9.98	81.99	3.414
CrCH-2 930.5–932.1	930.5	931.3	932.1	1.6	8.92	42.18	36.24	4.42	2.97	5.25	0.02	100.00	51.10	43.63	24.278

Table D-2 (continued)

Core Hole CrCH-2—Puye Formation															
Drilled Interval (ft)	Sieve-Size Classifications				Pebbles and Cobbles in Size (>8 mm)	Very Coarse Sand to Pebbles (1.7 mm–8 mm)	Medium to Very Coarse Sand (0.355 mm–1.7 mm)	Fine to Medium Sand (0.177 mm–0.355 mm)	Very Fine to Fine Sand (0.177 mm–0.063 mm)	Silt (<0.063 mm)	24 Hour Gravity Settled	Total (%)	All Gravel	Fine to Very Coarse Sand	Hydraulic Conductivity Estimate (k) (ft/d)
	Upper Depth (ft)	Midpoint (ft)	Bottom Depth (ft)	Bed thickness (ft)											
Core Hole CrCH-2—Pumiceous Puye Subunit															
CrCH-2 932.1–932.35	932.1	932.225	932.35	0.25	2.77	7.53	9.83	14.69	52.09	13.10	-	100.00	10.30	76.60	1.517
CrCH-2 932.35–932.56	932.35	932.455	932.56	0.21	16.89	37.83	22.97	9.50	7.50	5.29	0.01	100.00	54.73	39.97	6.069
CrCH-2 932.56–932.9	932.56	932.73	932.9	0.34	0.00	19.69	50.52	15.06	7.71	6.99	0.03	100.00	19.69	73.29	6.069
CrCH-2 932.9–933.66	932.9	933.28	933.66	0.76	7.46	56.97	22.23	4.05	4.46	4.81	0.02	100.00	64.43	30.74	19.015
CrCH-2 933.66–934	933.66	933.83	934	0.34	5.29	39.08	31.92	9.22	9.58	4.88	0.02	100.00	44.37	50.72	6.692
CrCH-2 934–935.7	934	934.85	935.7	1.7	11.35	28.46	23.89	11.20	13.95	10.76	0.39	100.00	39.81	49.04	1.517
CrCH-2 935.7–938.25	935.7	936.975	938.25	2.55	1.22	10.02	26.20	22.33	22.12	17.32	0.79	100.00	11.24	70.65	0.546
CrCH-2 938.25–938.5	938.25	938.375	938.5	0.25	1.05	22.57	37.49	15.35	14.56	8.62	0.37	100.00	23.62	67.40	3.414
CrCH-2 938.5–939	938.5	938.75	939	0.5	2.19	18.30	27.92	18.30	20.25	12.75	0.28	100.00	20.49	66.48	1.517
CrCH-2 939–939.6	939	939.3	939.6	0.6	3.33	39.42	32.53	8.46	8.68	7.57	0.02	100.00	42.76	49.66	4.916
Core Hole CrCH-2—Miocene Pumiceous Unit															
CrCH-2 939.6–940.3	939.6	939.95	940.3	0.7	0.43	21.85	33.80	15.56	13.85	14.35	0.15	100.00	22.27	63.22	0.971
CrCH-2 940.3–940.7	940.3	940.5	940.7	0.4	0.15	17.75	43.59	13.98	13.91	10.44	0.18	100.00	17.90	71.48	2.185
CrCH-2 940.7–941	940.7	940.85	941	0.3	0.07	5.70	28.55	18.41	30.37	16.76	0.14	100.00	5.77	77.33	0.546
CrCH-2 941–941.17	941	941.085	941.17	0.17	3.00	10.43	26.61	18.32	30.16	11.26	0.21	100.00	13.43	75.10	1.836
CrCH-2 941.17–941.75	941.17	941.46	941.75	0.58	13.39	12.92	27.50	17.84	19.29	8.94	0.12	100.00	26.31	64.64	2.185
CrCH-2 941.75–942	941.75	941.875	942	0.25	2.52	12.24	34.91	19.85	17.86	12.28	0.36	100.00	14.75	72.61	1.517
CrCH-2 942–942.8	942	942.4	942.8	0.8	1.25	10.75	28.87	20.63	23.33	15.11	0.06	100.00	12.00	72.83	0.971
CrCH-2 942.8–943.9	942.8	943.35	943.9	1.1	0.59	6.29	26.98	23.20	32.06	10.86	0.03	100.00	6.88	82.23	2.185
CrCH-2 943.9–944.47	943.9	944.185	944.47	0.57	2.14	12.62	16.90	15.48	35.19	17.51	0.16	100.00	14.75	67.57	0.744
CrCH-2 944.47–945.55	944.47	945.01	945.55	1.08	1.30	9.50	31.95	22.66	22.35	11.88	0.34	100.00	10.81	76.97	1.836
CrCH-2 945.55–946	945.55	945.775	946	0.45	20.47	18.79	26.03	13.30	9.64	11.23	0.55	100.00	39.26	48.96	0.971
CrCH-2 <946 ft 10 in.—excess core	946	946	946	0	0.46	14.73	32.49	19.36	23.09	9.80	0.06	100.00	15.20	74.94	2.185
CrCH-2 946–948	946	947	948	2	0.00	12.66	33.39	16.93	27.66	9.14	0.22	100.00	12.66	77.98	2.185
CrCH-2 948–949.4	948	948.7	949.4	1.4	4.06	39.21	28.71	9.76	10.07	8.14	0.05	100.00	43.27	48.54	3.414
CrCH-2 949.4–949.6	949.4	949.7	950	0.6	9.35	23.51	22.42	11.25	17.27	15.96	0.24	100.00	32.85	50.95	3.414
CrCH-2 949.6–950	949.6	949.8	950	0.4	16.74	18.38	32.92	12.77	12.09	7.05	0.05	100.00	35.12	57.78	1.517
CrCH-2 <950 ft 6 in.—excess core	950	949.8	949.6	-0.4	3.60	24.23	31.29	14.26	13.99	12.58	0.05	100.00	27.84	59.54	0.546
CrCH-2 950–950.7	950	950.35	950.7	0.7	12.20	16.11	29.35	18.11	12.99	10.71	0.53	100.00	28.31	60.45	1.517
CrCH-2 950.7–951.7	950.7	951.2	951.7	1	0.24	8.71	28.53	23.12	31.12	8.18	0.10	100.00	8.95	82.77	2.974

Table D-2 (continued)

Core Hole CrCH-2—Puye Formation															
Drilled Interval (ft)	Sieve-Size Classifications				Pebbles and Cobbles in Size (>8 mm)	Very Coarse Sand to Pebbles (1.7 mm–8 mm)	Medium to Very Coarse Sand (0.355 mm– 1.7 mm)	Fine to Medium Sand (0.177 mm– 0.355 mm)	Very Fine to Fine Sand (0.177 mm– 0.063 mm)	Silt (<0.063 mm)	24 Hour Gravity Settled	Total (%)	All Gravel	Fine to Very Coarse Sand	Hydraulic Conductivity Estimate (k) (ft/d)
	Upper Depth (ft)	Midpoint (ft)	Bottom Depth (ft)	Bed thickness (ft)	Fraction 1 (wt%)	Fraction 2 (wt%)	Fraction 3 (wt%)	Fraction 4 (wt%)	Fraction 5 (wt%)	Fraction 6 (wt%)	Fraction 7 (wt%)		Fraction 1 + Fraction 2	Fraction 3 + Fraction 4 + Fraction 5	
CrCH-2 951.7–952.25	951.7	951.975	952.25	0.55	0.25	5.64	27.28	21.30	32.18	13.19	0.16	100.00	5.89	80.76	1.517
CrCH-2 952.25–952.75	952.25	952.5	952.75	0.5	3.19	16.67	21.35	14.25	28.73	15.48	0.32	100.00	19.86	64.34	0.971
CrCH-2 952.75–953	952.75	952.875	953	0.25	1.23	8.62	24.30	20.48	26.92	18.22	0.23	100.00	9.84	71.70	0.546
CrCH-2 >953 ft 12 in.—excess slough	953	953	953	0	6.01	14.75	32.56	20.77	9.67	15.50	0.74	100.00	20.76	63.00	0.546
CrCH-2 953–953.5	953	953.25	953.5	0.5	0.27	11.99	35.83	21.24	13.12	17.47	0.09	100.00	12.26	70.19	0.546
CrCH-2 953.5–953.9	953.5	953.7	953.9	0.4	3.06	23.24	19.51	14.25	20.95	18.85	0.14	100.00	26.30	54.71	0.546
CrCH-2 953.9–954.3	953.9	954.1	954.3	0.4	1.29	13.17	24.49	19.87	22.76	18.37	0.05	100.00	14.46	67.12	1.229
CrCH-2 954.3–954.8	954.3	954.55	954.8	0.5	0.36	13.02	26.22	20.74	25.04	14.23	0.40	100.00	13.38	72.00	1.229
CrCH-2 954.8–955.25	954.8	955.025	955.25	0.45	0.18	4.45	36.47	23.80	19.45	15.51	0.15	100.00	4.63	79.72	0.971
CrCH-2 955.25–955.8	955.25	955.525	955.8	0.55	0.00	8.58	25.83	28.61	26.82	10.15	0.01	100.00	8.58	81.26	2.185
CrCH-2 955.8–956.4	955.8	956.1	956.4	0.6	0.17	7.00	41.12	23.64	18.04	9.89	0.13	100.00	7.18	82.80	2.185
CrCH-2 956.4–957	956.4	956.6	956.8	0.4	0.00	7.92	42.04	21.27	16.05	12.64	0.07	100.00	7.92	79.36	1.517
CrCH-2 956.8–957.7	956.8	957.25	957.7	0.9	1.81	16.58	27.10	14.16	18.16	22.15	0.05	100.00	18.38	59.42	0.379
CrCH-2 957.7–959.7	957.7	958.7	959.7	2	0.25	9.15	45.40	18.25	13.72	12.27	0.97	100.00	9.39	77.37	1.517
CrCH-2 959.7–960.4	959.7	960.05	960.4	0.7	0.32	15.59	29.83	19.77	18.39	15.96	0.15	100.00	15.90	67.98	0.546
CrCH-2 960.4–960.8	960.4	960.6	960.8	0.4	0.11	4.55	26.30	30.01	24.92	13.86	0.26	100.00	4.65	81.23	1.229
CrCH-2 960.8–962	960.8	961.4	962	1.2	1.09	9.71	15.69	14.83	24.07	31.74	2.86	100.00	10.81	54.59	0.243
CrCH-2 962.0–962.8	962	962.4	962.8	0.8	2.56	22.37	39.41	15.96	11.82	7.78	0.10	100.00	24.92	67.20	3.884
CrCH-2 962.8–963.8	962.8	963.3	963.8	1	0.17	14.95	49.56	12.25	14.77	7.87	0.44	100.00	15.11	76.58	3.884
CrCH-2 963.8–965.3	963.8	964.55	965.3	1.5	0.34	5.78	21.82	21.65	26.08	24.15	0.20	100.00	6.12	69.54	0.243
CrCH-2 965.3–965.8	965.3	965.55	965.8	0.5	0.54	5.38	23.95	21.88	24.97	23.03	0.25	100.00	5.92	70.80	0.243
CrCH-2 965.8–966.3	965.8	966.05	966.3	0.5	0.94	8.90	16.91	14.95	32.59	25.05	0.67	100.00	9.84	64.44	0.243
CrCH-2 966.3–966.5	966.3	966.4	966.5	0.2	0.00	3.73	20.93	12.56	23.31	38.91	0.55	100.00	3.73	56.81	0.061
CrCH-2 966.5–967	966.5	966.75	967	0.5	0.00	1.64	13.37	10.95	26.27	43.65	4.12	100.00	1.64	50.59	0.061
CrCH-2 967–968.1	967	967.55	968.1	1.1	2.61	26.90	41.57	11.80	9.18	7.91	0.04	100.00	29.51	62.54	3.884
CrCH-2 968.1–969	968.1	968.55	969	0.9	0.00	2.81	15.51	27.14	44.15	10.34	0.05	100.00	2.81	86.80	2.185
CrCH-2 969–970	969	969.5	970	1	2.25	14.49	42.38	17.12	14.37	9.23	0.16	100.00	16.74	73.87	2.185
CrCH-2 5 in. above 970 ft	970	970	970	0	2.17	17.13	35.04	17.16	20.86	7.49	0.14	100.00	19.31	73.06	3.414
CrCH-2 970–971	970	970.5	971	1	0.45	7.56	35.69	23.54	22.50	10.18	0.07	100.00	8.02	81.73	2.185
CrCH-2 971–971.5	971	971.25	971.5	0.5	0.39	15.59	38.77	20.08	18.46	6.67	0.04	100.00	15.99	77.31	3.884
CrCH-2 971.5–971.7	971.5	971.6	971.7	0.2	0.70	9.08	31.22	21.09	25.08	12.68	0.13	100.00	9.78	77.40	1.517
CrCH-2 971.7–971.9	971.7	971.8	971.9	0.2	2.03	25.86	22.14	18.73	21.89	9.30	0.06	100.00	27.90	62.75	2.974

Table D-2 (continued)

Core Hole CrCH-2—Puye Formation															
Drilled Interval (ft)	Sieve-Size Classifications				Pebbles and Cobbles in Size (>8 mm)	Very Coarse Sand to Pebbles (1.7 mm–8 mm)	Medium to Very Coarse Sand (0.355 mm–1.7 mm)	Fine to Medium Sand (0.177 mm–0.355 mm)	Very Fine to Fine Sand (0.177 mm–0.063 mm)	Silt (<0.063 mm)	24 Hour Gravity Settled	Total (%)	All Gravel	Fine to Very Coarse Sand	Hydraulic Conductivity Estimate (k) (ft/d)
	Upper Depth (ft)	Midpoint (ft)	Bottom Depth (ft)	Bed thickness (ft)	Fraction 1 (wt%)	Fraction 2 (wt%)	Fraction 3 (wt%)	Fraction 4 (wt%)	Fraction 5 (wt%)	Fraction 6 (wt%)	Fraction 7 (wt%)		Fraction 1 + Fraction 2	Fraction 3 + Fraction 4 + Fraction 5	
CrCH-2 971.9–972.25	971.9	972.075	972.25	0.35	4.77	28.00	18.02	10.55	27.38	11.16	0.11	100.00	32.78	55.95	1.836
CrCH-2 972.25–973	972.25	972.625	973	0.75	0.97	14.67	19.18	26.24	30.79	8.07	0.09	100.00	15.64	76.20	2.974
CrCH-2 973–974.7	973	973.85	974.7	1.7	0.78	31.36	34.59	13.41	10.60	8.78	0.48	100.00	32.14	58.60	2.974
CrCH-2 974.7–975.25	974.7	974.95	975.2	0.5	1.84	15.61	24.91	19.08	23.14	14.99	0.43	100.00	17.45	67.13	0.971
CrCH-2 975.25–975.7	975.2	975.45	975.7	0.5	3.09	26.42	20.22	13.04	18.16	18.28	0.80	100.00	29.51	51.42	0.379
CrCH-2 975.7–977	975.7	976.35	977	1.3	0.85	14.18	24.73	16.61	17.34	23.19	3.09	100.00	15.03	58.68	0.379
CrCH-2 977–977.1	977	977.05	977.1	0.1	2.19	8.02	24.66	21.14	20.96	22.82	0.21	100.00	10.21	66.76	0.379
CrCH-2 977.1–977.6	977.1	977.35	977.6	0.5	2.28	15.32	14.29	14.17	31.80	21.46	0.67	100.00	17.60	60.27	0.379
CrCH-2 977.6–978	977.6	977.8	978	0.4	0.63	13.31	19.62	11.05	21.98	31.22	2.19	100.00	13.94	52.65	0.243
CrCH-2 978–979	978	978.5	979	1	0.11	6.17	21.87	27.69	28.58	15.43	0.16	100.00	6.27	78.14	0.971
CrCH-2 979–980	979	979.5	980	1	0.77	9.66	32.76	23.00	23.02	10.59	0.20	100.00	10.44	78.77	2.185
CrCH-2 980–981.5	980	980.75	981.5	1.5	0.18	15.72	37.56	19.71	16.61	10.00	0.21	100.00	15.90	73.89	2.564
CrCH-2 981.5–982	981.5	981.75	982	0.5	1.88	21.29	21.68	12.39	21.49	20.81	0.46	100.00	23.17	55.56	0.379
CrCH-2 982–982.75	982	982.375	982.75	0.75	0.76	27.26	19.11	8.81	19.50	23.27	1.29	100.00	28.02	47.41	0.243
CrCH-2 982.75–982.9	982.75	982.825	982.9	0.15	0.70	15.01	28.37	11.39	16.05	27.99	0.48	100.00	15.72	55.81	0.243
CrCH-2 982.9–984.16	982.9	983.53	984.16	1.26	1.96	15.29	20.06	10.27	25.37	26.10	0.95	100.00	17.25	55.69	0.350
CrCH-2 984.16–985	984.16	984.58	985	0.84	0.82	21.23	31.85	9.96	15.01	21.06	0.07	100.00	22.04	56.82	0.410
CrCH-2 985–986.6	985	985.8	986.6	1.6	0.12	17.67	48.12	13.08	11.51	9.32	0.18	100.00	17.79	72.71	2.974
CrCH-2 986.6–987	986.6	986.8	987	0.4	0.37	12.15	23.01	17.72	20.94	24.41	1.40	100.00	12.52	61.67	0.379

Table D-3
Particle-Size Data and Hydraulic Conductivity for CrCH-3

Core Hole CrCH-3—Puye Formation															
Drilled Interval (ft)	Sieve-Size Classifications				Pebbles and Cobbles in Size (>8 mm)	Very Coarse Sand to Pebbles (1.7 mm–8 mm)	Medium to Very Coarse Sand (0.355 mm–1.7 mm)	Fine to Medium Sand (0.177 mm–0.355 mm)	Very Fine to Fine Sand (0.177 mm–0.063 mm)	Silt (<0.063 mm)	24 Hour Gravity Settled	Total (%)	All Gravel	Fine to Very Coarse Sand	Hydraulic Conductivity Estimate (k) (ft/d)
	Upper Depth (ft)	Midpoint (ft)	Bottom Depth (ft)	Bed thickness (ft)											
CrCH-3 <876 0 ft 4 in.—excess core, possible slough	908	908.75	909.5	1.5	13.55	29.23	22.05	7.89	11.17	15.93	0.18	100.00	42.78	41.11	0.546
CrCH-3 <876 4 ft 10 in.—excess core, possible slough	909.5	909.895	910.29	0.79	16.31	31.56	22.19	6.93	10.16	11.18	1.69	100.00	47.87	39.27	1.229
CrCH-3 876–876.6	910.29	910.98	911.67	1.38	20.12	24.95	17.91	7.40	13.46	14.12	2.04	100.00	45.07	38.77	0.546
CrCH-3 876.64–876.96	911.67	912.025	912.38	0.71	5.32	22.09	25.90	8.98	14.74	20.55	2.42	100.00	27.41	49.63	0.379
CrCH-3 877–877.66	912.38	913.105	913.83	1.45	16.78	25.57	20.26	7.09	14.54	12.20	3.57	100.00	42.35	41.88	0.971
CrCH-3 877.75–878.2	913.83	914.415	915	1.17	19.36	30.84	24.03	7.36	7.24	10.94	0.23	100.00	50.20	38.63	0.546
CrCH-3 878.2–880	913	913	913	0	12.92	32.48	21.00	7.86	9.99	15.36	0.40	100.00	45.40	38.84	0.546
CrCH-3 879–879.3	913	913.3	913.6	0.6	12.04	34.79	24.89	6.02	7.75	13.92	0.60	100.00	46.82	38.66	0.971
CrCH-3 879.3–879.7	913.6	914.35	915.1	1.5	19.52	31.56	27.43	9.28	9.22	2.28	0.71	100.00	51.08	45.94	10.257
CrCH-3 879.7–880.3	915.1	915.925	916.75	1.65	10.92	34.54	28.28	7.29	6.50	11.97	0.49	100.00	45.46	42.07	1.229
CrCH-3 880.3–881	916.75	916.875	917	0.25	5.90	23.12	38.18	12.94	9.54	10.22	0.09	100.00	29.01	60.67	1.836
CrCH-3 881–881.6	917	917.33	917.66	0.66	30.04	24.28	17.38	7.82	8.58	11.78	0.11	100.00	54.33	33.78	0.546
CrCH-3 881.6–881.9	917.66	917.99	918.32	0.66	30.25	27.04	20.14	7.10	6.52	5.93	3.02	100.00	57.29	33.76	3.414
CrCH-3 881.9–882.9	918.32	918.86	919.4	1.08	5.35	37.51	34.84	8.92	6.22	6.35	0.81	100.00	42.86	49.99	8.740
CrCH-3 882.9–883.6	919.4	919.75	920.1	0.7	13.15	32.60	29.38	7.57	6.73	10.26	0.32	100.00	45.74	43.68	1.517
CrCH-3 883.6–884	921	921	921	0	11.50	35.27	25.96	7.11	7.81	11.86	0.49	100.00	46.77	40.88	0.971
CrCH-3 884–884.8	884	884.8	884.4	0.4	21.38	33.62	22.57	7.97	5.63	8.67	0.16	100.00	55.00	36.17	4.181
CrCH-3 884.8–885.9	884.8	885.9	885.35	0.55	11.55	35.26	28.66	8.38	6.25	9.70	0.20	100.00	46.81	43.29	2.725
CrCH-3 885.9–886.4	885.9	886.4	886.15	0.25	39.40	20.99	15.12	4.27	4.55	15.20	0.47	100.00	60.38	23.94	0.702
CrCH-3 886–887.4	886	887.4	886.7	0.7	20.19	33.41	21.28	6.25	6.59	11.80	0.47	100.00	53.60	34.13	1.428
CrCH-3 886.4–887	886.4	887	886.7	0.3	16.58	21.87	20.29	10.38	11.16	18.72	1.01	100.00	38.45	41.83	0.476
CrCH-3 887–888	887	888	887.5	0.5	20.16	28.94	21.05	7.61	6.64	14.90	0.70	100.00	49.09	35.30	0.744
CrCH-3 887.4–887.8	887.4	887.8	887.6	0.2	31.85	18.79	17.36	8.27	8.69	14.61	0.42	100.00	50.65	34.32	0.831
CrCH-3 887.8–888.95	887.8	888.95	888.375	0.575	7.49	19.04	20.11	7.50	13.29	31.26	1.31	100.00	26.53	40.90	0.155
CrCH-3 888.95–889	888.95	889	888.975	0.025	0.00	9.31	18.60	10.27	13.02	46.84	1.96	100.00	9.31	41.89	0.087
CrCH-3 889–891	889	891	890	1	5.97	20.61	22.78	8.48	11.70	28.97	1.50	100.00	26.58	42.95	0.197
CrCH-3 890–890.2	890	890.2	890.1	0.1	16.13	20.31	19.70	5.05	14.41	24.39	-	100.00	36.44	39.17	0.307
CrCH-3 890.2–91	890.2	891	890.6	0.4	13.87	20.75	23.94	8.39	14.23	17.61	1.20	100.00	34.62	46.57	0.583

Table D-3 (continued)

Core Hole CrCH-3—Puye Formation															
Drilled Interval (ft)	Sieve-Size Classifications				Pebbles and Cobbles in Size (>8 mm)	Very Coarse Sand to Pebbles (1.7 mm–8 mm)	Medium to Very Coarse Sand (0.355 mm– 1.7 mm)	Fine to Medium Sand (0.177 mm– 0.355 mm)	Very Fine to Fine Sand (0.177 mm– 0.063 mm)	Silt (<0.063 mm)	24 Hour Gravity Settled	Total (%)	All Gravel	Fine to Very Coarse Sand	Hydraulic Conductivity Estimate (k) (ft/d)
	Upper Depth (ft)	Midpoint (ft)	Bottom Depth (ft)	Bed thickness (ft)	Fraction 1 (wt%)	Fraction 2 (wt%)	Fraction 3 (wt%)	Fraction 4 (wt%)	Fraction 5 (wt%)	Fraction 6 (wt%)	Fraction 7 (wt%)		Fraction 1 + Fraction 2	Fraction 3 + Fraction 4 + Fraction 5	
CrCH-3 <876 0 ft 4 in.— excess core, possible slough	908	908.75	909.5	1.5	13.55	29.23	22.05	7.89	11.17	15.93	0.18	100.00	42.78	41.11	0.546
CrCH-3 <876 4 ft 10 in.— excess core, possible slough	909.5	909.895	910.29	0.79	16.31	31.56	22.19	6.93	10.16	11.18	1.69	100.00	47.87	39.27	1.229
CrCH-3 876–876.6	910.29	910.98	911.67	1.38	20.12	24.95	17.91	7.40	13.46	14.12	2.04	100.00	45.07	38.77	0.546
CrCH-3 876.64–876.96	911.67	912.025	912.38	0.71	5.32	22.09	25.90	8.98	14.74	20.55	2.42	100.00	27.41	49.63	0.379
CrCH-3 877–877.66	912.38	913.105	913.83	1.45	16.78	25.57	20.26	7.09	14.54	12.20	3.57	100.00	42.35	41.88	0.971
CrCH-3 877.75–878.2	913.83	914.415	915	1.17	19.36	30.84	24.03	7.36	7.24	10.94	0.23	100.00	50.20	38.63	0.546
CrCH-3 878.2–880	913	913	913	0	12.92	32.48	21.00	7.86	9.99	15.36	0.40	100.00	45.40	38.84	0.546
CrCH-3 879–879.3	913	913.3	913.6	0.6	12.04	34.79	24.89	6.02	7.75	13.92	0.60	100.00	46.82	38.66	0.971
CrCH-3 879.3–879.7	913.6	914.35	915.1	1.5	19.52	31.56	27.43	9.28	9.22	2.28	0.71	100.00	51.08	45.94	10.257
CrCH-3 879.7–880.3	915.1	915.925	916.75	1.65	10.92	34.54	28.28	7.29	6.50	11.97	0.49	100.00	45.46	42.07	1.229
CrCH-3 880.3–881	916.75	916.875	917	0.25	5.90	23.12	38.18	12.94	9.54	10.22	0.09	100.00	29.01	60.67	1.836
CrCH-3 891–891.5	891	891.5	891.25	0.25	18.65	20.53	24.58	6.16	13.73	16.03	0.34	100.00	39.17	44.46	0.744
CrCH-3 891.5–892.7	891.5	892.7	892.1	0.6	31.72	20.52	22.04	6.78	6.79	11.93	0.20	100.00	52.24	35.62	1.398
CrCH-3 892.7–892.9	892.7	892.9	892.8	0.1	17.07	24.40	30.38	7.68	9.27	11.02	0.17	100.00	41.47	47.33	1.836
CrCH-3 892.9–893.3	892.9	893.3	893.1	0.2	22.95	17.71	21.75	7.85	11.02	17.93	0.80	100.00	40.66	40.62	0.546
CrCH-3 893.3–893.4	893.3	893.4	893.35	0.05	11.68	17.75	21.19	10.10	12.12	26.35	0.80	100.00	29.43	43.41	0.255
CrCH-3 893.4–894.4	893.4	894.4	893.9	0.5	8.18	19.45	29.72	7.41	13.73	21.12	0.39	100.00	27.63	50.86	0.395
CrCH-3 894.4–894.75	894.4	894.75	894.575	0.175	10.27	14.77	21.43	6.69	11.03	34.57	1.25	100.00	25.04	39.14	0.146
CrCH-3 894.75–895	894.75	895	894.875	0.125	2.75	8.22	19.78	9.78	12.02	46.33	1.12	100.00	10.97	41.57	0.087
CrCH-3 894.5–894.9	894.5	894.9	894.7	0.2	1.34	10.49	26.59	6.62	18.32	34.46	2.18	100.00	11.83	51.53	0.146
CrCH-3 894.9–895.6	894.9	895.6	895.25	0.35	3.25	9.55	20.88	6.80	22.09	36.78	0.65	100.00	12.79	49.78	0.137
CrCH-3 895.6–897	895.6	897	896.3	0.7	4.72	16.59	15.90	6.15	17.31	39.03	0.31	100.00	21.31	39.36	0.119
CrCH-3 897–897.9	897	897.9	897.45	0.45	6.05	16.84	14.15	5.99	13.97	35.91	7.09	100.00	22.89	34.10	0.119
CrCH-3 897.9–899	897.9	899	898.45	0.55	16.19	20.23	13.95	5.89	9.82	28.89	5.04	100.00	36.42	29.66	0.186
CrCH-3 899–900.4	899	900.4	899.7	0.7	9.76	16.83	22.33	8.20	13.31	28.38	1.20	100.00	26.59	43.84	0.208
CrCH-3 900.4–901	900.4	901	900.7	0.3	7.81	17.64	21.98	7.07	12.92	30.30	2.29	100.00	25.45	41.97	0.186
CrCH-3 901–901.6	901	901.6	901.3	0.3	8.40	26.68	25.00	8.78	10.21	20.18	0.75	100.00	35.07	44.00	0.410
CrCH-3 901.6–903	901.6	903	902.3	0.7	20.09	28.81	21.72	7.45	5.94	15.20	0.79	100.00	48.90	35.11	0.744
CrCH-3 902–902.5	902	902.5	902.25	0.25	16.65	36.15	21.66	5.76	6.02	13.34	0.42	100.00	52.80	33.43	1.071

Table D-3 (continued)

Core Hole CrCH-3—Puye Formation															
Drilled Interval (ft)	Sieve-Size Classifications				Pebbles and Cobbles in Size (>8 mm)	Very Coarse Sand to Pebbles (1.7 mm–8 mm)	Medium to Very Coarse Sand (0.355 mm–1.7 mm)	Fine to Medium Sand (0.177 mm–0.355 mm)	Very Fine to Fine Sand (0.177 mm–0.063 mm)	Silt (<0.063 mm)	24 Hour Gravity Settled	Total (%)	All Gravel	Fine to Very Coarse Sand	Hydraulic Conductivity Estimate (k) (ft/d)
	Upper Depth (ft)	Midpoint (ft)	Bottom Depth (ft)	Bed thickness (ft)											
Core Hole CrCH-3—Pumiceous Puye Subunit															
CrCH-3 902.5–903.7	902.5	903.7	903.1	0.6	16.92	41.61	25.76	4.95	4.01	6.64	0.12	100.00	58.53	34.71	14.582
CrCH-3 903.7–904.3	903.7	904.3	904	0.3	7.66	29.79	25.25	9.81	12.53	14.32	0.64	100.00	37.45	47.59	0.947
CrCH-3 904.3–905.7	904.3	905.7	905	0.7	0.27	9.63	24.61	19.92	22.89	19.99	2.71	100.00	9.89	67.42	0.476
CrCH-3 905.7–907	905.7	907	906.35	0.65	0.56	10.15	33.74	22.33	17.07	15.41	0.74	100.00	10.71	73.14	0.831
CrCH-3 906–907.1	906	907.1	906.55	0.55	0.97	14.36	44.20	20.19	12.24	7.81	0.23	100.00	15.33	76.62	4.181
CrCH-3 907.1–908	907.1	908	907.55	0.45	1.03	12.36	44.37	20.55	11.66	9.55	0.47	100.00	13.39	76.58	2.644
CrCH-3 908–908.3	908	908.3	908.15	0.15	0.57	4.97	17.95	27.77	31.88	16.54	0.32	100.00	5.54	77.60	0.923
CrCH-3 908–908.9	908	908.9	908.45	0.45	8.58	43.87	23.56	6.21	6.33	11.05	0.39	100.00	52.45	36.11	1.705
CrCH-3 908.3–908.6	908.3	908.6	908.45	0.15	0.69	6.58	29.93	17.26	20.34	24.65	0.54	100.00	7.27	67.54	0.321
CrCH-3 908.6–909.9	908.6	909.9	909.25	0.65	0.14	8.03	37.59	21.43	18.26	13.95	0.61	100.00	8.17	77.28	1.122
CrCH-3 908.9–909.3	908.9	909.3	909.1	0.2	7.79	29.88	24.69	7.93	9.67	19.60	0.44	100.00	37.66	42.30	0.442
CrCH-3 909.9–911	909.9	911	910.45	0.55	3.77	12.47	28.82	17.23	16.72	20.61	0.39	100.00	16.23	62.77	0.410
CrCH-3 909.3–911.1	909.3	911	910.15	0.85	5.87	21.41	21.97	10.39	13.14	25.69	1.54	100.00	27.27	45.50	0.268
CrCH-3 911.1–911.8	911.1	911.8	911.45	0.35	4.90	19.59	20.26	10.26	10.65	32.58	1.75	100.00	24.49	41.18	0.155
CrCH-3 911.8–913	911.8	913	912.4	0.6	3.60	15.47	22.03	13.15	12.84	30.46	2.46	100.00	19.07	48.02	0.175
CrCH-3 913–913.4	913	913.4	913.2	0.2	23.16	20.25	20.06	11.58	10.98	13.70	0.27	100.00	43.41	42.61	1.020
CrCH-3 913.4–914.4	913.4	914.4	913.9	0.5	27.99	16.45	15.38	8.57	11.06	20.17	0.37	100.00	44.44	35.01	0.410
CrCH-3 914.4–915	914.4	915	914.7	0.3	5.18	16.38	30.57	17.57	16.79	12.94	0.57	100.00	21.56	64.93	1.284
CrCH-3 915–916	915	916	915.5	0.5	13.09	22.21	25.38	14.57	11.98	12.46	0.32	100.00	35.30	51.92	1.341
CrCH-3 916–916.25	916	916.25	916.125	0.125	1.88	15.80	23.94	13.39	16.40	26.62	1.98	100.00	17.68	53.73	0.255
CrCH-3 916.25–916.7	916.25	916.7	916.475	0.225	0.64	12.03	19.77	14.32	20.91	31.32	1.02	100.00	12.67	54.99	0.197
Core Hole CrCH-3—Miocene Pumiceous Unit															
CrCH-3 916.7–916.9	916.7	916.9	916.8	0.1	1.16	9.22	16.80	12.41	18.15	40.02	2.24	100.00	10.38	47.36	0.119
CrCH-3 916.9–917.25	916.9	917.25	917.075	0.175	5.20	21.42	30.00	14.89	14.53	13.84	0.12	100.00	26.61	59.43	1.071
CrCH-3 917.25–917.8	917.25	917.8	917.525	0.275	0.58	26.34	31.59	12.16	16.27	12.83	0.24	100.00	26.92	60.01	1.341
CrCH-3 917.8–918.5	917.8	918.5	918.15	0.35	0.28	16.67	34.34	13.22	16.41	18.91	0.18	100.00	16.94	63.97	0.528
CrCH-3 918.5–918.9	918.5	918.9	918.7	0.2	0.82	11.85	23.25	15.44	26.03	21.80	0.80	100.00	12.68	64.72	0.410
CrCH-3 918.9–920	918.9	920	919.45	0.55	0.53	11.77	21.65	18.08	27.26	20.11	0.60	100.00	12.30	66.99	0.231
CrCH-3 920–920.5	920	920.5	920.25	0.25	2.83	12.06	16.36	15.85	16.69	33.86	2.34	100.00	14.90	48.90	0.146
CrCH-3 920.5–920.75	920.5	920.75	920.625	0.125	2.24	12.67	12.26	12.88	19.90	37.61	2.43	100.00	14.92	45.04	0.137
CrCH-3 920.75–921.8	920.75	921.8	921.275	0.525	2.97	18.21	30.22	16.34	14.80	16.90	0.55	100.00	21.18	61.36	0.744
CrCH-3 921.8–922.25	921.8	922.25	922.025	0.225	7.32	19.56	20.29	14.09	16.13	22.08	0.52	100.00	26.89	50.52	0.380

Table D-3 (continued)

Core Hole CrCH-3—Puye Formation															
Drilled Interval (ft)	Sieve-Size Classifications				Pebbles and Cobbles in Size (>8 mm)	Very Coarse Sand to Pebbles (1.7 mm–8 mm)	Medium to Very Coarse Sand (0.355 mm– 1.7 mm)	Fine to Medium Sand (0.177 mm– 0.355 mm)	Very Fine to Fine Sand (0.177 mm– 0.063 mm)	Silt (<0.063 mm)	24 Hour Gravity Settled	Total (%)	All Gravel	Fine to Very Coarse Sand	Hydraulic Conductivity Estimate (k) (ft/d)
	Upper Depth (ft)	Midpoint (ft)	Bottom Depth (ft)	Bed thickness (ft)	Fraction 1 (wt%)	Fraction 2 (wt%)	Fraction 3 (wt%)	Fraction 4 (wt%)	Fraction 5 (wt%)	Fraction 6 (wt%)	Fraction 7 (wt%)		Fraction 1 + Fraction 2	Fraction 3 + Fraction 4 + Fraction 5	
CrCH-3 922.2–922.75	922.2	922.75	922.475	0.275	0.79	8.11	17.48	17.17	17.01	39.43	-	100.00	8.90	51.66	0.410
CrCH-3 922.25–922.75	922.25	922.75	922.5	0.25	2.62	21.31	13.22	14.74	15.12	28.64	4.35	100.00	23.93	43.08	0.186
CrCH-3 22.75–923	922.75	923	922.875	0.125	0.76	4.98	25.52	17.83	26.04	24.17	0.70	100.00	5.74	69.39	0.350
CrCH-3 922.75–923.1	922.75	923.1	922.925	0.175	0.00	4.56	20.41	21.73	19.39	31.76	2.15	100.00	4.56	61.53	0.175
CrCH-3 923.1–923.25	923.1	923.25	923.175	0.075	0.00	3.46	13.92	12.43	20.60	47.32	2.26	100.00	3.46	46.95	0.087
CrCH-3 923.25–923.5	923.25	923.5	923.375	0.125	0.00	7.86	21.13	15.49	21.42	33.33	0.77	100.00	7.86	58.04	0.155
CrCH-3 923.5–923.75	923.5	923.75	923.625	0.125	0.30	4.60	17.02	15.27	18.12	41.28	3.41	100.00	4.91	50.40	0.013
CrCH-3 923.75–925.1	923.75	925.1	924.425	0.675	0.57	12.90	34.63	19.73	16.25	15.59	0.34	100.00	13.47	70.61	0.787
CrCH-3 925.1–925.3	925.1	925.3	925.2	0.1	2.08	16.74	32.43	19.39	16.50	12.65	0.21	100.00	18.82	68.32	1.398
CrCH-3 925.3–925.7	925.3	925.7	925.5	0.2	14.44	24.35	24.44	13.89	11.87	10.87	0.14	100.00	38.79	50.20	1.903
CrCH-3 925.7–926.3	925.7	926.3	926	0.3	2.25	17.65	21.84	15.90	15.95	25.58	0.83	100.00	19.91	53.69	0.281
CrCH-3 926.3–926.7	926.3	926.7	926.5	0.2	3.00	22.19	29.52	14.59	15.49	15.02	0.19	100.00	25.19	59.61	0.876
CrCH-3 926.7–927	926.7	927	926.85	0.15	0.70	13.50	30.59	16.43	20.28	18.42	0.09	100.00	14.20	67.30	0.583
CrCH-3 927–927.5	927	927.5	927.25	0.25	6.70	10.39	25.05	16.61	16.38	24.28	0.59	100.00	17.09	58.05	0.307
CrCH-3 927.5–927.9	927.5	927.9	927.7	0.2	1.58	14.89	21.97	19.55	22.94	18.63	0.45	100.00	16.47	64.45	0.621
CrCH-3 927.9–928.25	927.9	928.25	928.075	0.175	0.50	11.75	23.24	13.47	22.06	28.83	0.15	100.00	12.25	58.77	0.231
CrCH-3 928.25–929.7	928.25	929.7	928.975	0.725	0.78	9.79	24.43	15.86	18.94	29.58	0.62	100.00	10.56	59.24	0.197
CrCH-3 929.7–930	929.7	930	929.85	0.15	0.46	12.91	22.94	16.22	22.38	24.63	0.46	100.00	13.37	61.54	0.307
CrCH-3 931–931.3	931	931.3	931.15	0.15	0.00	0.63	45.09	25.57	15.40	12.57	0.73	100.00	0.63	86.07	1.341
CrCH-3 931.3–931.5	931.3	931.5	931.4	0.1	0.95	6.60	16.18	17.05	26.40	32.43	0.41	100.00	7.54	59.62	0.197
CrCH-3 931.5–932	931.5	932	931.75	0.25	0.39	2.35	27.57	24.30	22.82	21.78	0.80	100.00	2.74	74.68	0.379
CrCH-3 932–932.25	932	932.25	932.125	0.125	0.44	4.18	25.53	21.88	22.72	24.08	1.17	100.00	4.63	70.13	0.243
CrCH-3 932.25–933	932.25	933	932.625	0.375	0.19	6.48	28.71	25.32	22.21	16.89	0.20	100.00	6.67	76.24	0.744
CrCH-3 933–933.3	933	933.3	933.15	0.15	1.17	6.40	19.67	17.82	26.90	27.37	0.66	100.00	7.58	64.39	0.255
CrCH-3 933.3–933.8	933.3	933.8	933.55	0.25	0.68	15.09	19.19	20.57	20.47	22.94	1.06	100.00	15.77	60.23	0.350
CrCH-3 933.8–934.4	933.8	934.4	934.1	0.3	0.27	6.24	27.69	23.73	22.86	18.82	0.39	100.00	6.51	74.29	0.583
CrCH-3 934.4–935.2	934.4	935.2	934.8	0.4	1.66	5.23	33.47	24.27	22.52	12.60	0.25	100.00	6.89	80.26	1.517
CrCH-3 935.2–936	935.2	936	935.6	0.4	2.35	9.35	28.26	17.91	17.48	23.90	0.74	100.00	11.70	63.66	0.321
CrCH-3 936–937	936	937	936.5	0.5	0.58	5.66	33.43	28.65	19.95	11.48	0.26	100.00	6.24	82.03	1.836
CrCH-3 938–939	938	939	938.5	0.5	0.00	6.30	41.94	26.43	14.51	10.70	0.11	100.00	6.30	82.88	2.042
CrCH-3 939–940	939	940	939.5	0.5	0.30	8.23	45.97	23.15	13.38	8.81	0.16	100.00	8.53	82.49	3.234
CrCH-3 940–940.8	940	940.8	940.4	0.4	0.78	10.34	18.70	14.21	31.80	23.37	0.80	100.00	11.12	64.71	0.379
CrCH-3 940.8–941.5	940.8	941.5	941.15	0.35	0.87	14.65	28.21	16.88	17.15	22.01	0.22	100.00	15.52	62.25	0.379

Table D-3 (continued)

Core Hole CrCH-3—Puye Formation															
Drilled Interval (ft)	Sieve-Size Classifications				Pebbles and Cobbles in Size (>8 mm)	Very Coarse Sand to Pebbles (1.7 mm–8 mm)	Medium to Very Coarse Sand (0.355 mm– 1.7 mm)	Fine to Medium Sand (0.177 mm– 0.355 mm)	Very Fine to Fine Sand (0.177 mm– 0.063 mm)	Silt (<0.063 mm)	24 Hour Gravity Settled	Total (%)	All Gravel	Fine to Very Coarse Sand	Hydraulic Conductivity Estimate (k) (ft/d)
	Upper Depth (ft)	Midpoint (ft)	Bottom Depth (ft)	Bed thickness (ft)	Fraction 1 (wt%)	Fraction 2 (wt%)	Fraction 3 (wt%)	Fraction 4 (wt%)	Fraction 5 (wt%)	Fraction 6 (wt%)	Fraction 7 (wt%)		Fraction 1 + Fraction 2	Fraction 3 + Fraction 4 + Fraction 5	
CrCH-3 941.5–942.2	941.5	942.2	941.85	0.35	0.69	13.60	24.51	19.02	24.08	17.98	0.13	100.00	14.29	67.60	0.641
CrCH-3 942.2–943	942.2	943	942.6	0.4	0.36	9.32	22.00	23.30	23.11	21.17	0.75	100.00	9.68	68.41	0.442
CrCH-3 944–945*	944	945*	944	0	0.44	7.86	27.58	28.26	22.49	12.88	0.50	100.00	8.29	78.33	1.428
CrCH-3 945–946.2*	945	946.2*	945	0	0.82	13.25	25.29	17.11	24.86	18.30	0.37	100.00	14.07	67.26	0.641
CrCH-3 946.2–947*	946.2	947*	946.2	0	0.22	14.67	34.99	15.89	15.07	18.50	0.65	100.00	14.90	65.95	0.543
CrCH-3 944–944.8	944	944.8	944.4	0.4	0.00	17.43	35.29	12.80	13.85	20.37	0.26	100.00	17.43	61.94	0.175
CrCH-3 944.8–945.3	944.8	945.3	945.05	0.25	0.00	12.44	24.94	12.54	23.66	24.62	1.80	100.00	12.44	61.14	0.321
CrCH-3 945.3–945.9	945.3	945.9	945.6	0.3	0.45	18.57	23.53	12.69	24.24	20.02	0.51	100.00	19.02	60.46	0.510
CrCH-3 945.9–946.3	945.9	946.3	946.1	0.2	0.54	27.42	24.90	12.49	17.01	17.51	0.13	100.00	27.96	54.40	0.641
CrCH-3 946.3–947	946.3	947	946.65	0.35	0.00	12.35	18.82	13.49	24.50	29.03	1.81	100.00	12.35	56.81	0.208
CrCH-3 947–948	947	948	947.5	0.5	0.26	6.34	26.43	27.50	25.42	13.43	0.62	100.00	6.61	79.35	1.341

Table D-4
Particle-Size Data and Hydraulic Conductivity for CrCH-4

Core Hole CrCH-4—Puye Formation															
Drilled Interval (ft)	Sieve-Size Classifications				Pebbles and Cobbles in Size (>8 mm)	Very Coarse Sand to Pebbles (1.7 mm–8 mm)	Medium to Very Coarse Sand (0.355 mm–1.7 mm)	Fine to Medium Sand (0.177 mm–0.355 mm)	Very Fine to Fine Sand (0.177 mm–0.063 mm)	Silt (<0.063 mm)	24 Hour Gravity Settled	Total (%)	All Gravel	Fine to Very Coarse Sand	Hydraulic Conductivity Estimate (k) (ft/d)
	Upper Depth (ft)	Midpoint (ft)	Bottom Depth (ft)	Bed thickness (ft)											
CrCH-4 934–934.2	934	934.1	934.2	0.2	4.71	11.10	16.37	8.37	9.84	46.91	2.69	100.00	15.82	34.58	0.476
CrCH-4 934.2–936.7	934.2	935.45	936.7	2.5	13.13	38.10	20.30	7.26	7.81	12.97	0.44	100.00	51.22	35.38	1.122
CrCH-4 936.7–937	936.7	936.85	937	0.3	10.20	27.22	19.71	7.67	9.37	24.88	0.95	100.00	37.42	36.74	0.268
CrCH-4 937–938.5	937	937.75	938.5	1.5	14.29	30.93	22.94	7.78	7.06	16.51	0.49	100.00	45.22	37.78	0.622
CrCH-4 938–940	938	939	940	2	36.59	10.93	28.54	9.96	7.42	6.52	0.03	100.00	47.52	45.93	7.682
CrCH-4 940–940.25	940	940.125	940.25	0.25	12.38	31.73	34.65	8.20	5.67	7.25	0.13	100.00	44.10	48.52	9.484
CrCH-4 940.25–941	940.25	940.625	941	0.75	16.57	27.42	24.44	9.65	8.75	12.94	0.22	100.00	43.99	42.85	1.122
CrCH-4 941–941.75	941	941.375	941.75	0.75	8.32	34.23	27.24	8.27	8.31	13.32	0.31	100.00	42.55	43.82	1.071
CrCH-4 941.75–942	941.75	941.875	942	0.25	3.57	22.62	25.17	12.58	5.83	29.20	1.03	100.00	26.19	43.58	0.197
CrCH-4 942.5–943.3	942.5	942.9	943.3	0.8	10.96	31.33	24.74	6.44	8.97	16.59	0.97	100.00	42.29	40.15	0.622
Core Hole CrCH-4—Pumiceous Puye subunit															
CrCH-4 943.3–946.2	943.3	944.75	946.2	2.9	1.24	9.52	20.19	14.18	20.91	33.06	0.90	100.00	10.76	55.28	0.155
CrCH-4 946.2–947.5	946.2	946.85	947.5	1.3	0.00	12.19	31.17	19.03	16.48	20.56	0.57	100.00	12.19	66.68	0.442
CrCH-4 947.5–947.75	947.5	947.625	947.75	0.25	0.00	17.89	45.71	18.58	9.83	7.94	0.05	100.00	17.89	74.12	4.385
CrCH-4 947.75–948.4	947.75	948.075	948.4	0.65	1.54	8.57	41.71	22.23	15.37	10.31	0.28	100.00	10.11	79.30	2.258
CrCH-4 948.4–950.3	948.4	949.35	950.3	1.9	7.69	22.12	27.55	17.78	12.90	11.91	0.05	100.00	29.81	58.24	1.579
CrCH-4 950.3–950.75	950.3	950.525	950.75	0.45	0.72	9.92	34.78	22.93	17.09	14.23	0.33	100.00	10.64	74.80	1.045
CrCH-4 950.75–951.4	950.75	951.075	951.4	0.65	0.17	11.02	40.83	17.34	12.88	17.68	0.10	100.00	11.18	71.04	0.583
CrCH-4 951.4–952	951.4	951.7	952	0.6	0.77	9.05	29.75	21.42	23.28	15.69	0.04	100.00	9.83	74.45	0.876
CrCH-4 952–953.1	952	952.55	953.1	1.1	0.20	5.13	42.76	26.47	15.09	10.32	0.03	100.00	5.33	84.32	2.333
Core Hole CrCH-4—Miocene Pumiceous Unit															
CrCH-4 953.1–953.4	953.1	953.25	953.4	0.3	0.78	12.43	43.62	18.59	12.30	12.19	0.08	100.00	13.21	74.52	1.457
CrCH-4 953.4–954.25	953.4	953.825	954.25	0.85	0.80	17.26	31.52	15.90	15.55	18.94	0.03	100.00	18.06	62.97	0.510
CrCH-4 954.25–955.3	954.25	954.775	955.3	1.05	1.14	14.19	25.58	17.35	16.49	24.61	0.64	100.00	15.33	59.42	0.307
CrCH-4 955.3–955.6	955.3	955.45	955.6	0.3	0.36	8.54	22.68	14.34	19.20	34.12	0.78	100.00	8.90	56.21	0.155
CrCH-4 955.6–956.5	955.6	956.05	956.5	0.9	0.19	14.07	26.40	13.93	19.51	25.30	0.59	100.00	14.26	59.85	0.294
CrCH-4 956.5–956.8	956.5	956.65	956.8	0.3	0.61	14.43	27.00	16.67	21.39	19.19	0.71	100.00	15.04	65.07	0.528
CrCH-4 956.8–957	956.8	956.9	957	0.2	0.31	7.43	29.10	2.26	34.38	26.15	0.37	100.00	7.73	65.75	0.379

Table D-5
Particle-Size Data and Hydraulic Conductivity for CrCH-5

Core Hole CrCH-5—Puye Formation															
Drilled Interval (ft)	Sieve-Size Classifications				Pebbles and Cobbles in Size (>8 mm)	Very Coarse Sand to Pebbles (1.7 mm–8 mm)	Medium to Very Coarse Sand (0.355 mm–1.7 mm)	Fine to Medium Sand (0.177 mm–0.355 mm)	Very Fine to Fine Sand (0.177 mm–0.063 mm)	Silt (<0.063 mm)	24 Hour Gravity Settled	Total (%)	All Gravel	Fine to Very Coarse Sand	Hydraulic Conductivity Estimate (k) (ft/d)
	Upper Depth (ft)	Midpoint (ft)	Bottom Depth (ft)	Bed thickness (ft)											
CrCH-5 960–961	960	960.5	961	1	11.40	23.90	18.30	6.52	9.79	29.37	0.73	100.00	35.30	34.61	0.197
CrCH-5 961–962.2	961	961.6	962.2	1.2	15.30	17.77	15.51	8.85	19.00	22.60	0.96	100.00	33.07	43.36	0.35
CrCH-5 962.2–963.75	962.2	962.975	963.75	1.55	10.51	15.75	14.37	7.73	21.03	30.01	0.59	100.00	26.26	43.13	0.197
CrCH-5 963.75–964	963.75	963.875	964	0.25	1.49	16.46	23.04	11.05	16.77	30.99	0.20	100.00	17.94	50.87	0.186
CrCH-5 964–965	964	964.5	965	1	2.89	18.18	23.56	9.76	14.54	30.18	0.89	100.00	21.07	47.86	0.197
CrCH-5 965–967.25	965	966.125	967.25	2.25	10.63	38.68	28.42	7.76	5.86	8.62	0.02	100.00	49.31	42.05	4.131
CrCH-5 967.25–968.2	967.25	967.725	968.2	0.95	15.04	45.20	19.38	5.95	6.27	8.11	0.06	100.00	60.23	31.60	4.385
CrCH-5 968.2–970	968.2	969.1	970	1.8	12.67	36.79	27.34	7.62	6.00	9.55	0.04	100.00	49.46	40.96	2.725
CrCH-5 970–970.5	970	970.25	970.5	0.5	4.43	41.81	26.18	7.23	7.21	12.83	0.31	100.00	46.23	40.63	1.122
CrCH-5 970.5–971.5	970.5	971	971.5	1	11.53	34.98	24.66	6.91	6.48	15.11	0.33	100.00	46.51	38.05	0.787
CrCH-5 971.5–971.7	971.5	971.6	971.7	0.2	16.56	30.55	22.66	6.44	7.44	15.51	0.83	100.00	47.11	36.54	9.484
CrCH-5 971.75–972.3	971.75	972.025	972.3	0.55	16.28	26.74	19.36	7.33	9.02	20.93	0.34	100.00	43.02	35.71	0.379
CrCH-5 972.3–974.7	972.3	973.5	974.7	2.4	11.22	29.59	21.62	8.77	9.81	18.62	0.37	100.00	40.81	40.20	0.476
CrCH-5 974.7–975	974.7	974.85	975	0.3	10.37	26.87	21.93	8.37	10.71	21.17	0.58	100.00	37.24	41.01	0.395
CrCH-5 975–977.5	975	976.25	977.5	2.5	15.15	44.09	22.79	5.94	5.05	6.87	0.11	100.00	59.24	33.78	9.484
Core Hole CrCH-5—Pumiceous Puye subunit															
CrCH-5 977.5–978.2	977.5	977.85	978.2	0.7	12.15	41.66	23.64	6.08	6.11	10.14	0.22	100.00	53.81	35.83	2.258
CrCH-5 978.2–978.6	978.2	978.4	978.6	0.4	9.66	32.97	31.97	9.24	7.87	8.29	0.00	100.00	42.63	49.08	4.131
CrCH-5 978.6–979.6	978.6	979.1	979.6	1	15.20	33.40	22.01	10.23	9.49	9.54	0.13	100.00	48.60	41.72	2.807
CrCH-5 979.6–980	979.6	979.8	980	0.4	8.25	17.45	30.71	17.49	13.61	12.32	0.17	100.00	25.70	61.81	1.398
CrCH-5 980–981.25	980	980.625	981.25	1.25	0.04	10.28	35.37	23.63	17.42	13.14	0.10	100.00	10.33	76.43	1.284
CrCH-5 981.25–982.1	981.25	981.675	982.1	0.85	1.97	20.66	34.34	16.78	12.53	13.66	0.06	100.00	22.63	63.66	1.071
CrCH-5 982.1–982.75	982.1	982.425	982.75	0.65	1.32	13.56	26.80	16.06	19.65	21.36	1.25	100.00	14.88	62.51	0.41
CrCH-5 982.75–984.25	982.75	983.5	984.25	1.5	0.47	11.78	28.92	20.16	20.06	17.74	0.88	100.00	12.25	69.13	0.622
CrCH-5 984.25–985	984.25	984.625	985	0.75	1.20	12.27	24.77	17.53	22.91	21.08	0.25	100.00	13.46	65.21	0.442

Table D-5 (continued)

Core Hole CrCH-5—Puye Formation															
Drilled Interval (ft)	Sieve-Size Classifications				Pebbles and Cobbles in Size (>8 mm)	Very Coarse Sand to Pebbles (1.7 mm–8 mm)	Medium to Very Coarse Sand (0.355 mm– 1.7 mm)	Fine to Medium Sand (0.177 mm– 0.355 mm)	Very Fine to Fine Sand (0.177 mm– 0.063 mm)	Silt (<0.063 mm)	24 Hour Gravity Settled	Total (%)	All Gravel	Fine to Very Coarse Sand	Hydraulic Conductivity Estimate (k) (ft/d)
	Upper Depth (ft)	Midpoint (ft)	Bottom Depth (ft)	Bed thickness (ft)	Fraction 1 (wt%)	Fraction 2 (wt%)	Fraction 3 (wt%)	Fraction 4 (wt%)	Fraction 5 (wt%)	Fraction 6 (wt%)	Fraction 7 (wt%)		Fraction 1 + Fraction 2	Fraction 3 + Fraction 4 + Fraction 5	
CrCH-5 985–985.5	985	985.25	985.5	0.5	0.81	29.37	30.28	13.96	13.07	12.34	0.17	100.00	30.18	57.31	1.398
CrCH-5 985.5–986.25	985.5	985.875	986.25	0.75	0.53	17.86	28.95	18.41	17.31	16.83	0.11	100.00	18.39	64.67	0.702
CrCH-5 986.25–986.75	986.25	986.5	986.75	0.5	0.13	4.30	21.96	26.51	21.35	25.06	0.69	100.00	4.43	69.83	0.294
CrCH-5 986.75–987.2	986.75	986.975	987.2	0.45	0.26	7.23	31.76	28.06	17.32	15.04	0.32	100.00	7.49	77.14	0.9
CrCH-5 987.2–987.6	987.2	987.4	987.6	0.4	0.32	10.45	35.73	21.36	18.45	13.36	0.34	100.00	10.77	75.53	1.229
CrCH-5 987.6–987.9	987.6	987.75	987.9	0.3	0.00	5.04	26.71	29.72	21.72	16.63	0.18	100.00	5.04	78.16	0.787
CrCH-5 987.9–988.6	987.9	988.25	988.6	0.7	0.17	9.59	25.81	23.70	22.06	18.53	0.14	100.00	9.76	71.57	0.583
CrCH-5 988.6–989.4	988.6	989	989.4	0.8	0.29	7.83	37.29	26.00	14.49	14.02	0.08	100.00	8.12	77.78	1.045
CrCH-5 989.4–990	989.4	989.7	990	0.6	0.67	19.26	30.31	18.80	14.66	16.13	0.17	100.00	19.92	63.78	0.744
CrCH-5 990–991.4	990	990.7	991.4	1.4	12.22	24.21	15.10	16.03	22.69	9.72	0.04	100.00	36.43	53.81	2.486
CrCH-5 991.4–992	991.4	991.7	992	0.6	3.95	13.24	31.16	27.87	13.60	10.11	0.08	100.00	17.19	72.63	2.409
CrCH-5 992–992.9	992	992.45	992.9	0.9	14.79	18.16	44.01	10.50	5.90	6.62	0.02	100.00	32.95	60.41	9.867
CrCH-5 992.9–993.2	992.9	993.05	993.2	0.3	34.50	22.57	27.16	5.36	3.58	6.77	0.05	100.00	57.08	36.11	16.524
CrCH-5 993.2–994	993.2	993.6	994	0.8	0.30	18.68	58.69	8.27	5.94	8.01	0.11	100.00	18.98	72.90	5.193
CrCH-5 994–996.5	994	995.25	996.5	2.5	13.26	59.97	16.35	2.13	3.26	5.01	0.01	100.00	73.23	21.75	64.109
CrCH-5 996.5–997	996.5	996.75	997	0.5	28.69	41.80	9.31	4.49	5.79	9.83	0.09	100.00	70.49	19.59	2.486
CrCH-5 997–998	997	997.5	998	1	0.28	9.89	16.88	19.73	25.82	26.12	1.29	100.00	10.17	62.42	0.294
CrCH-5 1002–1003	1002	1002.5	1003	1	3.05	29.53	30.18	12.81	11.78	12.59	0.06	100.00	32.58	54.76	1.341
CrCH-5 1003–1004.3	1003	1003.65	1004.3	1.3	0.38	14.76	25.23	14.91	22.45	21.70	0.57	100.00	15.14	62.59	0.410
CrCH-5 1004.3–1005	1004.3	1004.65	1005	0.7	0.81	27.04	28.85	8.93	12.49	21.62	0.25	100.00	27.85	50.28	0.379
CrCH-5 1005–1005.8	1005	1005.4	1005.8	0.8	1.02	29.36	30.97	12.06	12.22	14.34	0.03	100.00	30.38	55.25	0.947
CrCH-5 1005.8–1006.6	1005.8	1006.2	1006.6	0.8	0.48	23.19	32.45	10.70	18.95	13.46	0.76	100.00	23.67	62.11	1.229
CrCH-5 1006.6–1007.7	1006.6	1007.15	1007.7	1.1	0.18	14.30	42.79	12.33	11.29	18.81	0.30	100.00	14.47	66.41	0.476
CrCH-5 1007.6–1008.5	1007.6	1008.05	1008.5	0.9	0.11	10.16	39.41	19.22	14.38	16.21	0.51	100.00	10.27	73.02	0.722
CrCH-5 1008.5–1009.25	1008.5	1008.88	1009.25	0.75	0.33	11.64	38.87	18.25	16.17	14.41	0.33	100.00	11.97	73.29	0.996
CrCH-5 1009.25–1010	1009.25	1009.63	1010	0.75	0.60	8.01	28.66	22.06	15.27	23.76	1.64	100.00	8.61	65.98	0.307
CrCH-5 1010–1012.6	1010	1011.3	1012.6	2.6	0.79	6.29	26.18	23.31	27.21	15.92	0.29	100.00	7.08	76.70	0.900
CrCH-5 1012.5–1014.2	1012.5	1013.35	1014.2	1.7	8.23	33.00	21.03	13.22	12.69	11.76	0.07	100.00	41.23	46.94	1.579
CrCH-5 1014.2–1016	1014.2	1015.1	1016	1.8	2.40	12.76	21.20	18.27	21.69	23.01	0.67	100.00	15.16	61.16	0.364

Appendix E

*XRF and XRD Analyses of Particle-Size Fractions F4, F5,
and F6 for Core Holes CrCH-1, CrCH-2, and CrCH-3*

Appendix E presents x-ray fluorescence (XRF) and x-ray diffraction (XRD) analyses of particle-size fractions F4, F5, and F6 for core holes CrCH-1, CrCH-2, and CrCH-3.

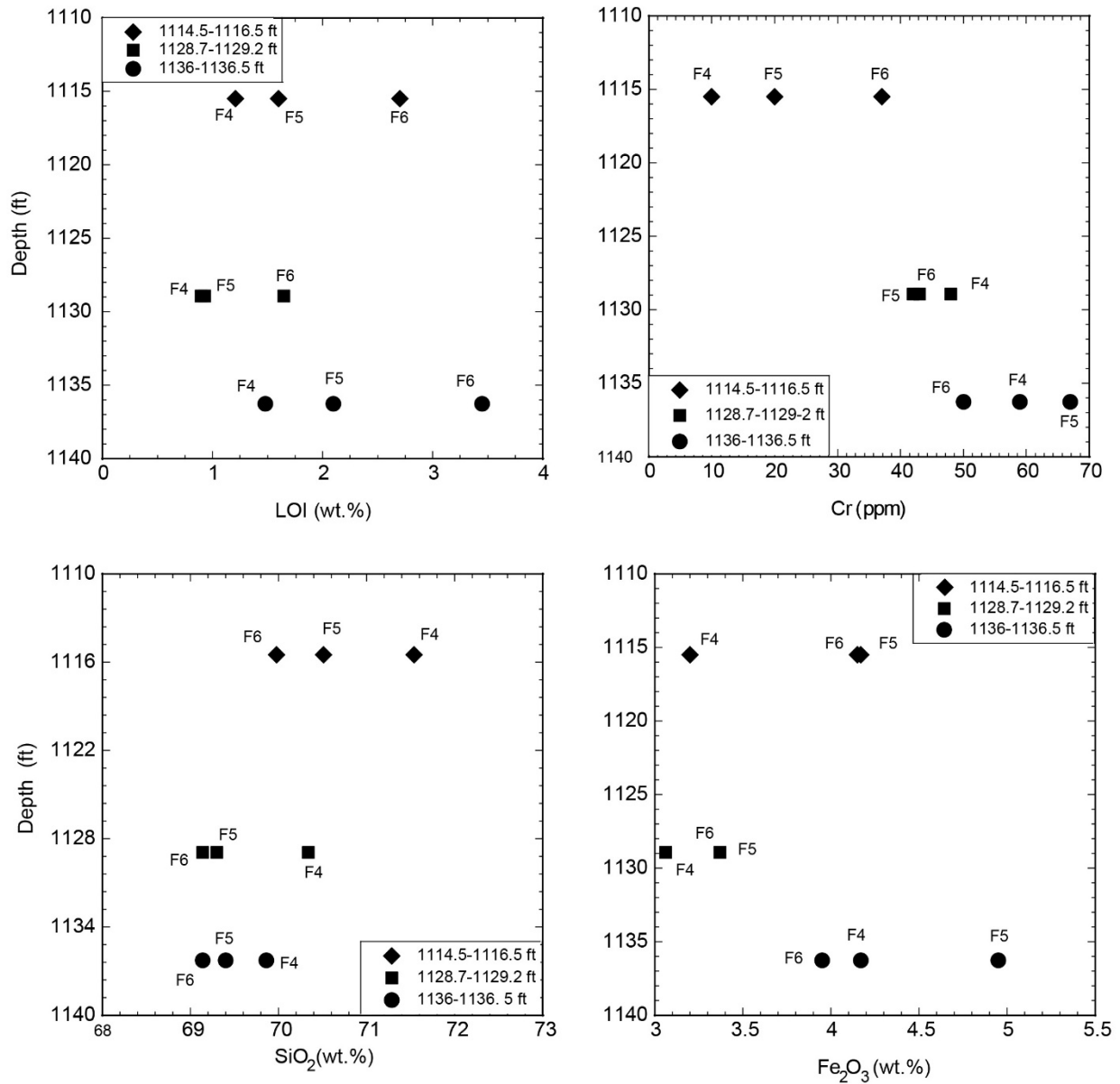


Figure E-1 Plots of major oxides versus depth of fine- to medium sand (F4), very fine to fine sand (F5), and silt (F6) fractions of core hole CrCH-1 core samples from the Puye Formation (Tpf)

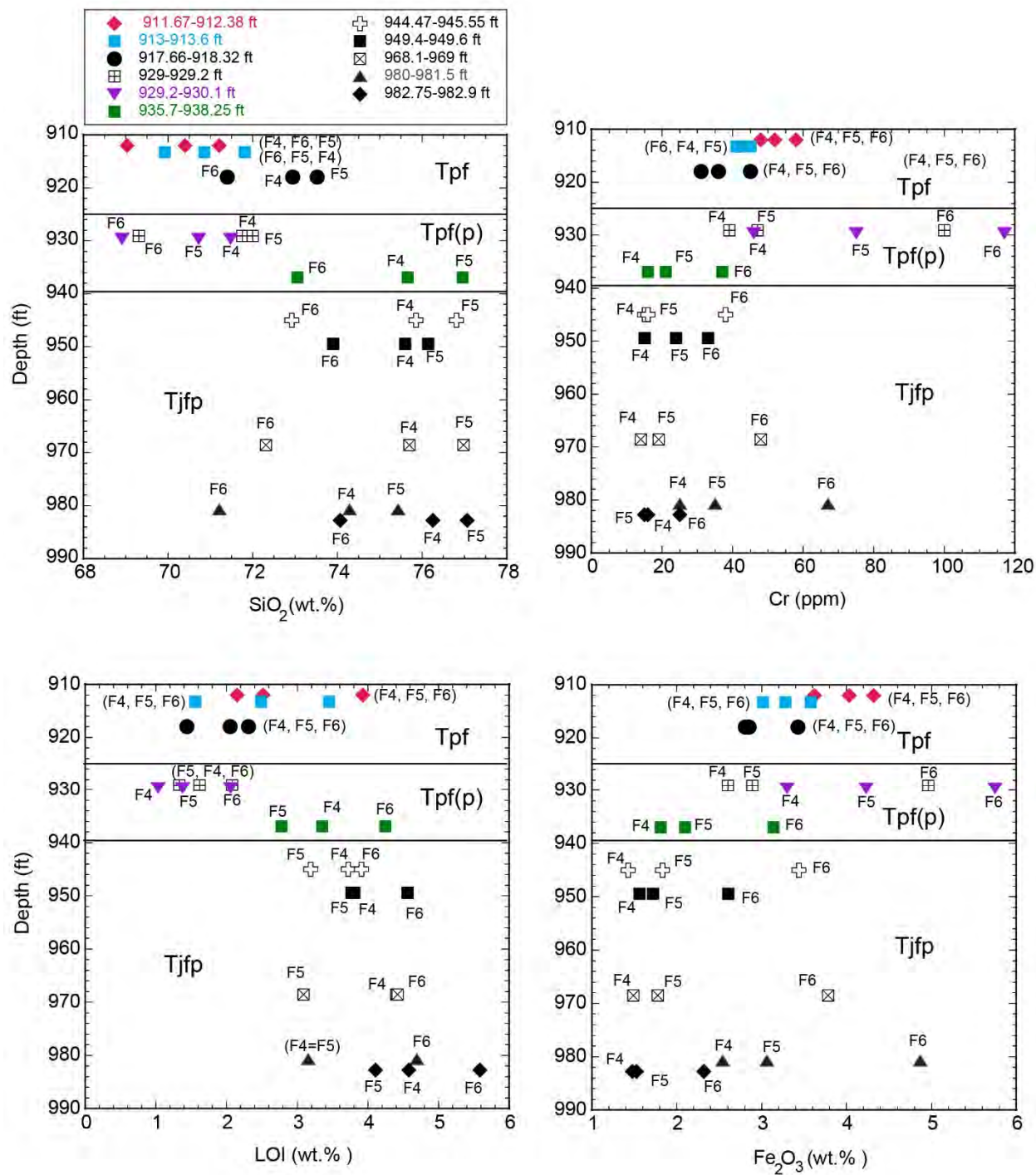


Figure E-2 Plots of major oxides versus depth of fine- to medium sand (F4), very fine to fine sand (F5), and silt (F6) fractions of core hole CrCH-2 core samples from the Puye Formation (Tpf), Puye pumiceous subunit [Tpf(p)], and Miocene pumiceous unit (Tjfp)

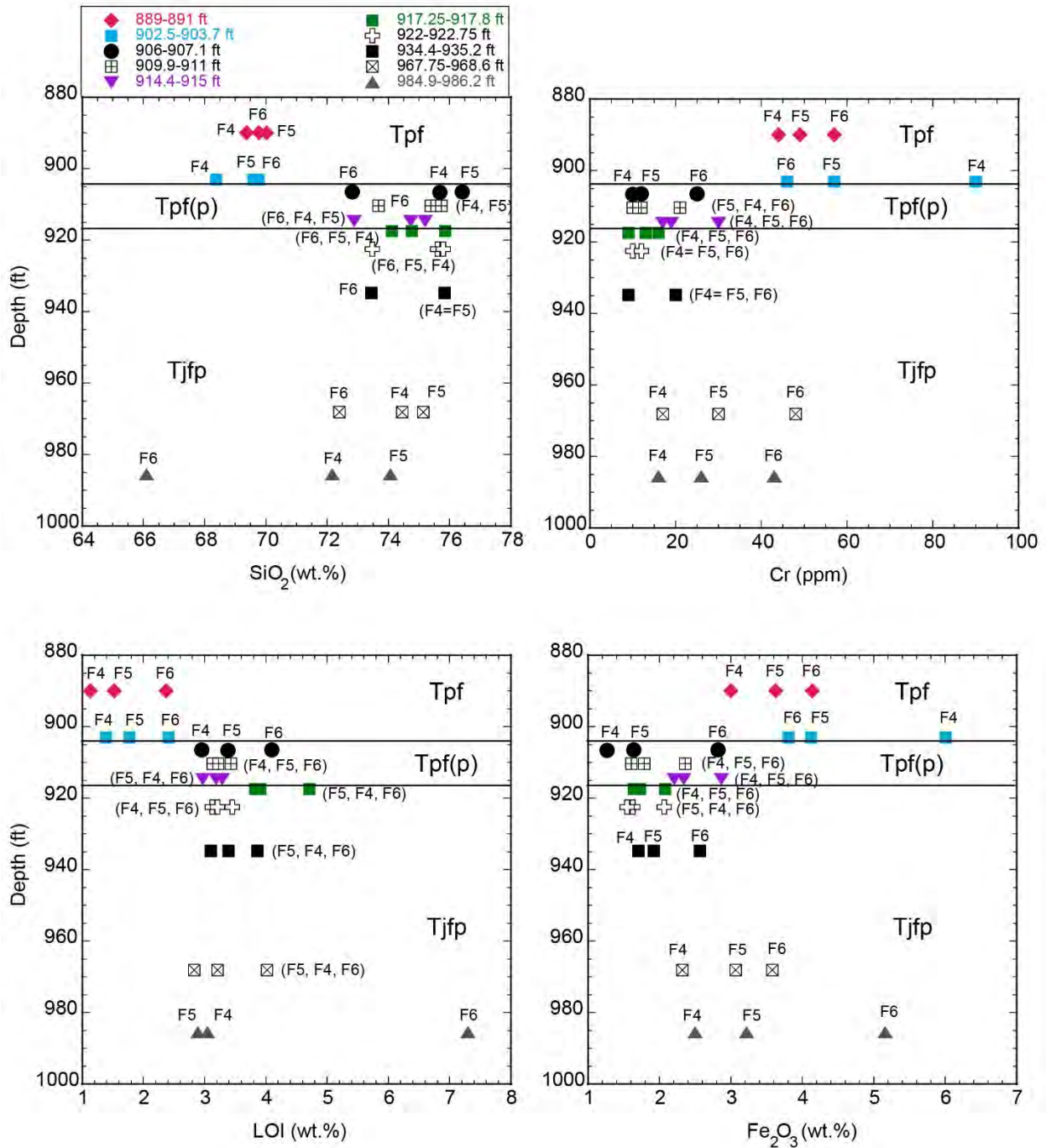


Figure E-3 Plots of major oxides versus depth of fine- to medium sand (F4), very fine to fine sand (F5), and silt (F6) fractions of core hole CrCH-3 core samples from the Puye Formation (Tpf), Puye pumiceous subunit [Tpf(p)], and Miocene pumiceous unit (Tjfp)

Table E-1
Major and Trace Element Compositions of F4, F5, and F6
Sand and Silt Fractions of Core Hole CrCH-1 Core Samples from the Puye Formation

Element/ Compound	Sample ID								
	CrCH1 1114.5- 1116.5 F4 ^a	CrCH1 1114.5- 1116.5 F5 ^b	CrCH1 1114.5- 1116.5 F6 ^c	CrCH1 1128.7- 1129.2 F4	CrCH1 1128.7- 1129.2 F5	CrCH1 1128.7- 1129.2 F6	CrCH1 1136- 1136.5 F4	CrCH1 1136- 1136.5 F5	CrCH1 1136- 1136.5 F6
	Stratigraphic Unit								
	Tpfd	Tpf	Tpf	Tpf	Tpf	Tpf	Tpf	Tpf	Tpf
SiO ₂	70.56	69.24	67.96	69.59	68.53	67.88	68.26	67.56	67.32
TiO ₂	0.37	0.49	0.56	0.37	0.45	0.45	0.43	0.57	0.53
Al ₂ O ₃	14.03	13.93	13.97	14.64	15.03	15.04	14.61	13.90	14.09
Fe ₂ O ₃	3.15	4.08	4.05	3.02	3.34	3.30	4.10	4.83	3.81
MgO	1.22	1.43	1.95	1.36	1.59	1.64	1.40	1.75	2.04
MnO	0.047	0.054	0.065	0.051	0.060	0.059	0.058	0.069	0.068
CaO	2.63	2.73	2.45	2.83	2.82	2.80	3.07	3.03	2.74
Na ₂ O	3.55	3.31	2.80	3.68	3.54	3.50	3.52	3.08	2.50
K ₂ O	3.00	2.88	3.14	3.31	3.42	3.39	2.81	2.78	2.94
P ₂ O ₅	0.074	0.084	0.176	0.082	0.111	0.113	0.108	0.149	0.331
Total	98.632	98.207	97.116	98.937	98.892	98.176	98.357	97.715	96.364
LOI ^e	1.21	1.60	2.70	0.90	0.93	1.65	1.48	2.10	3.45
V ₂ O ₅	0.0082	0.0120	0.0102	0.0075	0.0080	0.0082	0.0121	0.0150	0.0104
V	46	67	57	42	45	46	68	84	58
Cr ₂ O ₃	0.0061	0.0086	0.0098	0.0070	0.0061	0.0063	0.0086	0.0098	0.0073
Cr	42	59	67	48	42	43	59	67	50
NiO	0.0037	0.0041	0.0047	0.0048	0.0050	0.0048	0.0045	0.0052	0.0041
Ni	29	32	37	38	39	38	35	41	32
CuO	0.0013	0.0025	0.0046	0.0014	0.0051	0.0053	0.0018	0.0029	0.0183
Cu	10	20	37	11	41	42	14	23	146
ZnO	0.0046	0.0174	0.0065	0.0044	0.0059	0.0059	0.0055	0.0074	0.0098
Zn	37	139	52	35	47	47	44	59	78
Rb ₂ O	0.0074	0.0074	0.0101	0.0089	0.0096	0.0097	0.0071	0.0078	0.0102
Rb	68	68	92	81	88	89	65	71	93
SrO	0.0434	0.0445	0.0380	0.0454	0.0448	0.0442	0.0501	0.0487	0.0396
Sr	367	376	321	384	379	374	424	412	335
Y ₂ O ₃	0.0017	0.0023	0.0029	0.0018	0.0022	0.0020	0.0015	0.0023	0.0032
Y	13	18	23	14	17	16	12	18	25

Table E-1 (continued)

Element/ Compound	Sample ID								
	CrCH1 1114.5- 1116.5 F4 ^a	CrCH1 1114.5- 1116.5 F5 ^b	CrCH1 1114.5- 1116.5 F6 ^c	CrCH1 1128.7- 1129.2 F4	CrCH1 1128.7- 1129.2 F5	CrCH1 1128.7- 1129.2 F6	CrCH1 1136- 1136.5 F4	CrCH1 1136- 1136.5 F5	CrCH1 1136- 1136.5 F6
	Stratigraphic Unit								
	Tpf ^d	Tpf	Tpf	Tpf	Tpf	Tpf	Tpf	Tpf	Tpf
ZrO ₂	0.0181	0.0450	0.0434	0.0188	0.0223	0.0216	0.0209	0.0424	0.0353
Zr	134	333	321	139	165	160	155	314	261
Nb ₂ O ₅	0.0046	0.0051	0.0063	0.0057	0.0066	0.0069	0.0043	0.0051	0.0063
Nb	16	18	22	20	23	24	15	18	22
BaO	0.0894	0.0857	0.0899	0.0897	0.0977	0.0942	0.0821	0.0818	0.0830
Ba	801	768	805	803	875	844	735	733	743
PbO	0.0011	0.0012	0.0016	0.0011	0.0011	0.0014	0.0005	0.0013	0.0026
Pb	10	11	15	10	10	13	5	12	24
Total	100.03	100.04	100.04	100.03	100.04	100.04	100.04	100.04	100.04

Note: Concentrations are in weight percent for major elements and parts per million (ppm) for trace elements.

^a F4 = Fine- to medium sand.

^b F5 = Very fine- to fine sand.

^c F6 = Silt.

^d Tpf = Puye Formation.

^e LOI = Loss on ignition.

Table E-2
Quantitative Mineralogical Compositions of F4, F5, and F6 Sand and
Silt Fractions of Core Hole CrCH-1 Core Samples from the Bottom of the Puye Formation

Sample ID	Stratigraphic Unit	Hornblende	Smectite	Mica/Illite	Clinoptilolite	Hematite	Opal-C/CT	Cristobalite	Quartz	K-Feldspar	Plagioclase	Amorphous	Total
CrCH-1 1114.5-1116.5F4 ^a	Tpf ^b	0.2	— ^c	11.0	—	0.6	2.0	7.0	15.5	12.1	39.2	12.5	100.1
CrCH-1 1114.5-1116.5F5 ^d	Tpf	0.4	—	11.1	—	0.6	0.8	4.4	15.3	9.3	44.8	13.4	100.1
CrCH-1 1114.5-1116.5F6 ^e	Tpf	0.6	7.8	20.5	1.1	0.9	9.2	4.9	9.7	10.3	33.2	1.8	100.0
CrCH-1 1128.7-1129.2F4	Tpf	—	—	1.6	—	0.4	—	11.7	9.4	16.0	46.8	13.9	99.8
CrCH-1 1128.7-1129.2F5	Tpf	0.2	—	3.7	—	0.5	—	8.0	8.7	13.7	50.3	15.0	100.1
CrCH-1 1128.7-1129.2F6	Tpf	—	—	12.4	—	0.6	4.5	9.1	5.7	18.0	33.9	15.7	99.9
CrCH-1 1136-1136.5F4	Tpf	0.2	—	8.5	—	0.8	0.7	5.5	13.5	10.3	47.7	12.0	99.3
CrCH-1 1136-1136.5F5	Tpf	0.4	—	14.5	—	0.4	4.8	2.9	11.9	9.4	41.0	14.7	100.0
CrCH-1 1136-1136.5F6	Tpf	0.5	8.9	23.8	1.9	0.5	4.0	4.7	9.8	8.0	30.7	7.1	99.9

Note: Mineral abundances are in weight percent (wt%).

^a F4 = Fine- to medium sand.

^b Tpf = Puye Formation.

^c — = Not detected.

^d F5 = Very fine- to fine sand.

^e F6 = Silt.

Table E-3
Major and Trace Element Compositions of F4, F5, and F6 Sand and Silt Fractions
of Core Hole CrCH-2 Core Samples from the Puye Formation, Puye Pumiceous Subunit, and Miocene Pumiceous Unit

Element/Compound	Sample ID									
	CrCH2 911.67- 912.38 F4 ^a	CrCH2 911.67- 912.38 F5 ^b	CrCH2 911.67- 912.38 F6 ^c	CrCH2 913-913.6 F4	CrCH2 913-913.6 F5	CrCH2 913-913.6 F6	CrCH2 917.66- 918.32 F4	CrCH2 917.66- 918.32 F5	CrCH2 917.66- 918.32 F6	CrCH2 929-929.2 F4
	Stratigraphic Unit									
	Tpf ^d	Tpf	Tpf	Tpf	Tpf	Tpf	Tpf	Tpf	Tpf	Tpf(p) ^e
SiO ₂	67.43	69.29	67.50	70.57	68.98	67.40	71.78	71.90	69.63	70.47
TiO ₂	0.42	0.52	0.63	0.35	0.41	0.44	0.34	0.41	0.50	0.30
Al ₂ O ₃	14.94	13.22	13.58	13.89	14.12	14.43	13.36	12.78	13.21	14.21
Fe ₂ O ₃	3.54	3.92	4.14	2.97	3.20	3.45	2.77	2.78	3.35	2.55
MgO	1.60	1.77	1.91	1.29	1.70	1.95	1.05	1.27	1.88	1.08
MnO	0.06	0.07	0.07	0.05	0.06	0.07	0.05	0.05	0.06	0.05
CaO	3.30	2.86	2.59	2.39	2.42	2.33	2.17	2.19	2.53	2.18
Na ₂ O	3.50	2.70	2.25	3.46	3.17	2.84	3.37	2.98	2.76	3.55
K ₂ O	2.79	2.82	2.99	3.22	3.20	3.33	3.41	3.28	3.28	3.77
P ₂ O ₅	0.11	0.13	0.24	0.08	0.11	0.16	0.11	0.15	0.33	0.08
Total	97.68	97.30	95.88	98.28	97.35	96.39	98.41	97.79	97.52	98.23
LOI ^f	2.15	2.52	3.93	1.56	2.49	3.45	1.44	2.05	2.31	1.62
V ₂ O ₅	0.01	0.01	0.01	0.01	0.01	0.01	0.01	0.01	0.01	0.01
V	55.00	65.00	64.00	40.00	44.00	42.00	38.00	37.00	47.00	30.00
Cr ₂ O ₃	0.01	0.01	0.01	0.01	0.01	0.01	0.00	0.01	0.01	0.01
Cr	48.00	52.00	58.00	42.00	45.00	41.00	31.00	36.00	45.00	39.00
NiO	0.00	0.00	0.00	0.00	0.00	0.01	0.00	0.00	0.00	0.00

Table E-3 (continued)

Element/Compound	Sample ID									
	CrCH2 911.67- 912.38 F4 ^a	CrCH2 911.67- 912.38 F5 ^b	CrCH2 911.67- 912.38 F6 ^c	CrCH2 913-913.6 F4	CrCH2 913-913.6 F5	CrCH2 913-913.6 F6	CrCH2 917.66- 918.32 F4	CrCH2 917.66- 918.32 F5	CrCH2 917.66- 918.32 F6	CrCH2 929-929.2 F4
	Stratigraphic Unit									
	Tpf ^d	Tpf	Tpf	Tpf	Tpf	Tpf	Tpf	Tpf	Tpf	Tpf(p) ^e
Ni	34.00	34.00	30.00	29.00	36.00	40.00	26.00	25.00	32.00	28.00
CuO	0.00	0.00	0.01	0.00	0.00	0.00	0.00	0.00	0.01	0.00
Cu	16.00	13.00	40.00	14.00	22.00	24.00	13.00	17.00	41.00	16.00
ZnO	0.01	0.01	0.01	0.01	0.01	0.01	0.00	0.01	0.01	0.00
Zn	50.00	52.00	61.00	112.00	46.00	56.00	39.00	43.00	53.00	38.00
Rb ₂ O	0.01	0.01	0.01	0.01	0.01	0.01	0.01	0.01	0.01	0.01
Rb	67.00	75.00	94.00	78.00	85.00	98.00	81.00	86.00	96.00	92.00
SrO	0.06	0.05	0.04	0.04	0.03	0.03	0.03	0.03	0.03	0.04
Sr	483.00	403.00	330.00	305.00	294.00	275.00	288.00	286.00	285.00	305.00
Y ₂ O ₃	0.00	0.00	0.00	0.00	0.00	0.00	0.00	0.00	0.00	0.00
Y	14.00	19.00	26.00	13.00	18.00	20.00	15.00	18.00	27.00	17.00
ZrO ₂	0.02	0.04	0.05	0.02	0.03	0.02	0.02	0.03	0.04	0.02
Zr	169.00	267.00	339.00	131.00	213.00	163.00	155.00	256.00	297.00	112.00
Nb ₂ O ₅	0.01	0.00	0.01	0.01	0.01	0.01	0.01	0.01	0.01	0.01
Nb	18.00	17.00	22.00	22.00	21.00	24.00	23.00	22.00	26.00	23.00
BaO	0.09	0.09	0.09	0.09	0.08	0.09	0.09	0.09	0.09	0.09
Ba	763.00	765.00	815.00	809.00	753.00	794.00	816.00	773.00	790.00	826.00
PbO	0.00	0.00	0.00	0.00	0.00	0.00	0.00	0.00	0.00	0.00
Pb	7.00	12.00	14.00	11.00	8.00	16.00	11.00	9.00	11.00	11.00
Total	100.04	100.04	100.04	100.03	100.03	100.03	100.03	100.03	100.04	100.03

Table E-3 (continued)

Element/Compound	Sample ID									
	CrCH2 929-929.2 F5	CrCH2 929-929.2 F6	CrCH2 929.2-930.1 F4	CrCH2 929.2-930.1 F5	CrCH2 929.2-930.1 F6	CrCH2 935.7-938.25 F4	CrCH2 935.7-938.25 F5	CrCH2 935.7-938.25 F6	CrCH2 944.47- 945.55 F4	CrCH2 944.47- 945.55 F5
	Stratigraphic Unit									
	Tpf(p)	Tpf(p)	Tpf(p)	Tpf(p)	Tpf(p)	Tpf(p)	Tpf(p)	Tpf(p)	Tjfp ^a	Tjfp
SiO ₂	70.93	67.73	70.63	69.62	67.35	73.02	74.71	69.84	72.95	74.25
TiO ₂	0.36	0.59	0.35	0.50	0.64	0.27	0.35	0.46	0.20	0.30
Al ₂ O ₃	13.75	13.48	13.94	13.38	13.30	12.33	11.45	12.93	12.44	11.79
Fe ₂ O ₃	2.85	4.84	3.26	4.17	5.62	1.75	2.04	3.00	1.38	1.77
MgO	1.37	2.04	1.09	1.58	1.92	0.65	0.74	1.38	0.45	0.63
MnO	0.06	0.09	0.06	0.07	0.09	0.07	0.06	0.08	0.07	0.06
CaO	2.57	2.58	2.48	2.65	2.47	1.12	1.31	1.46	0.87	1.17
Na ₂ O	3.33	2.90	3.59	3.26	2.83	2.74	2.39	2.10	3.11	2.59
K ₂ O	3.22	3.32	3.33	3.11	3.38	4.52	3.98	4.23	4.66	4.07
P ₂ O ₅	0.09	0.15	0.08	0.10	0.15	0.05	0.06	0.11	0.03	0.05
Total	98.51	97.73	98.81	98.44	97.73	96.51	97.08	95.59	96.16	96.68
LOI	1.33	2.08	1.03	1.38	2.06	3.36	2.78	4.25	3.72	3.19
V ₂ O ₅	0.01	0.01	0.01	0.01	0.01	0.00	0.01	0.01	0.00	0.00
V	37.00	59.00	39.00	56.00	68.00	24.00	35.00	51.00	17.00	26.00
Cr ₂ O ₃	0.01	0.01	0.01	0.01	0.02	0.00	0.00	0.01	0.00	0.00
Cr	47.00	100.00	46.00	75.00	117.00	16.00	21.00	37.00	15.00	16.00
NiO	0.00	0.01	0.00	0.00	0.01	0.00	0.00	0.00	0.00	0.00
Ni	30.00	48.00	29.00	36.00	47.00	11.00	13.00	15.00	10.00	9.00
CuO	0.00	0.00	0.00	0.00	0.01	0.00	0.00	0.00	0.00	0.00
Cu	16.00	32.00	12.00	17.00	42.00	11.00	10.00	39.00	4.00	8.00
ZnO	0.00	0.01	0.01	0.01	0.01	0.00	0.00	0.01	0.00	0.00

Table E-3 (continued)

Element/Compound	Sample ID									
	CrCH2 929-929.2 F5	CrCH2 929-929.2 F6	CrCH2 929.2-930.1 F4	CrCH2 929.2-930.1 F5	CrCH2 929.2-930.1 F6	CrCH2 935.7-938.25 F4	CrCH2 935.7-938.25 F5	CrCH2 935.7-938.25 F6	CrCH2 944.47- 945.55 F4	CrCH2 944.47- 945.55 F5
	Stratigraphic Unit									
	Tpf(p)	Tpf(p)	Tpf(p)	Tpf(p)	Tpf(p)	Tpf(p)	Tpf(p)	Tpf(p)	Tjfp ^a	Tjfp
Zn	39.00	69.00	43.00	48.00	72.00	35.00	32.00	56.00	32.00	32.00
Rb ₂ O	0.01	0.01	0.01	0.01	0.01	0.01	0.01	0.01	0.01	0.01
Rb	78.00	87.00	77.00	75.00	88.00	103.00	94.00	112.00	102.00	95.00
SrO	0.04	0.04	0.04	0.04	0.04	0.02	0.02	0.02	0.01	0.02
Sr	358.00	313.00	343.00	354.00	301.00	135.00	184.00	165.00	100.00	170.00
Y ₂ O ₃	0.00	0.00	0.00	0.00	0.00	0.00	0.00	0.00	0.00	0.00
Y	14.00	25.00	14.00	20.00	29.00	24.00	22.00	29.00	22.00	20.00
ZrO ₂	0.02	0.05	0.02	0.04	0.07	0.02	0.03	0.04	0.01	0.02
Zr	171.00	365.00	141.00	319.00	510.00	145.00	210.00	324.00	110.00	174.00
Nb ₂ O ₅	0.01	0.01	0.01	0.01	0.01	0.01	0.01	0.01	0.01	0.01
Nb	20.00	25.00	22.00	23.00	27.00	24.00	22.00	24.00	26.00	20.00
BaO	0.09	0.09	0.09	0.09	0.08	0.08	0.08	0.08	0.09	0.09
Ba	799.00	781.00	842.00	765.00	746.00	759.00	744.00	750.00	769.00	771.00
PbO	0.00	0.00	0.00	0.00	0.00	0.00	0.00	0.00	0.00	0.00
Pb	14.00	13.00	11.00	10.00	19.00	13.00	12.00	14.00	11.00	6.00
Total	100.04	100.05	100.03	100.04	100.05	100.03	100.03	100.04	100.03	100.03

Table E-3 (continued)

Element/Compound	Sample ID									
	CrCH2 944.47- 945.55 F6	CrCH2 949.4-949.6 F4	CrCH2 949.4-949.6 F5	CrCH2 949.4-949.6 F6	CrCH2- 968.1-969 F4	CrCH2 968.1-969 F5	CrCH2 968.1-969 F6	CrCH2 980-981.5 F4	CrCH2 980-981.5 F5	CrCH2 980-981.5 F6
	Stratigraphic Unit									
	Tjfp	Tjfp	Tjfp	Tjfp	Tjfp	Tjfp	Tjfp	Tjfp	Tjfp	Tjfp
SiO ₂	69.93	72.62	73.17	70.42	72.28	74.50	68.98	71.83	72.93	67.74
TiO ₂	0.59	0.20	0.25	0.39	0.21	0.29	0.63	0.30	0.43	0.49
Al ₂ O ₃	12.87	12.53	12.15	12.88	12.53	11.71	12.85	12.57	11.52	12.95
Fe ₂ O ₃	3.30	1.50	1.65	2.49	1.42	1.73	3.61	2.46	2.96	4.64
MgO	1.28	0.51	0.57	0.97	0.51	0.70	1.38	0.70	0.79	1.39
MnO	0.08	0.07	0.07	0.07	0.07	0.05	0.08	0.08	0.08	0.10
CaO	1.74	0.90	1.00	1.39	0.89	1.41	1.90	1.26	1.39	1.53
Na ₂ O	2.26	3.06	2.70	2.34	2.80	2.57	2.21	3.16	2.64	2.15
K ₂ O	3.74	4.66	4.51	4.29	4.73	3.78	3.65	4.28	3.90	4.05
P ₂ O ₅	0.12	0.03	0.03	0.06	0.04	0.05	0.12	0.05	0.05	0.10
Total	95.91	96.06	96.10	95.29	95.49	96.77	95.40	96.69	96.69	95.13
LOI	3.91	3.81	3.77	4.56	4.40	3.09	4.42	3.16	3.16	4.70
V ₂ O ₅	0.01	0.00	0.00	0.01	0.00	0.00	0.01	0.00	0.01	0.01
V	60.00	19.00	20.00	37.00	17.00	25.00	63.00	28.00	41.00	52.00
Cr ₂ O ₃	0.01	0.00	0.00	0.00	0.00	0.00	0.01	0.00	0.01	0.01
Cr	38.00	15.00	24.00	33.00	14.00	19.00	48.00	25.00	35.00	67.00
NiO	0.00	0.00	0.00	0.00	0.00	0.00	0.00	0.00	0.00	0.00
Ni	17.00	10.00	11.00	14.00	8.00	11.00	17.00	13.00	16.00	20.00
CuO	0.00	0.00	0.00	0.00	0.00	0.00	0.01	0.00	0.00	0.01
Cu	28.00	7.00	10.00	32.00	6.00	12.00	64.00	5.00	8.00	67.00
ZnO	0.01	0.01	0.00	0.01	0.00	0.00	0.01	0.01	0.01	0.01

Table E-3 (continued)

Element/Compound	Sample ID									
	CrCH2 944.47- 945.55 F6	CrCH2 949.4-949.6 F4	CrCH2 949.4-949.6 F5	CrCH2 949.4-949.6 F6	CrCH2- 968.1-969 F4	CrCH2 968.1-969 F5	CrCH2 968.1-969 F6	CrCH2 980-981.5 F4	CrCH2 980-981.5 F5	CrCH2 980-981.5 F6
	Stratigraphic Unit									
	Tjfp	Tjfp	Tjfp	Tjfp	Tjfp	Tjfp	Tjfp	Tjfp	Tjfp	Tjfp
Zn	53.00	49.00	36.00	49.00	32.00	33.00	57.00	40.00	41.00	65.00
Rb ₂ O	0.01	0.01	0.01	0.01	0.01	0.01	0.01	0.01	0.01	0.01
Rb	105.00	102.00	102.00	109.00	105.00	87.00	98.00	89.00	86.00	107.00
SrO	0.03	0.01	0.02	0.02	0.01	0.03	0.03	0.02	0.02	0.02
Sr	230.00	100.00	129.00	182.00	98.00	218.00	233.00	156.00	187.00	171.00
Y ₂ O ₃	0.00	0.00	0.00	0.00	0.00	0.00	0.00	0.00	0.00	0.00
Y	30.00	22.00	21.00	23.00	22.00	19.00	29.00	20.00	20.00	28.00
ZrO ₂	0.05	0.01	0.02	0.03	0.02	0.02	0.06	0.02	0.03	0.05
Zr	399.00	101.00	141.00	200.00	113.00	148.00	421.00	120.00	232.00	381.00
Nb ₂ O ₅	0.01	0.01	0.01	0.01	0.01	0.00	0.01	0.01	0.01	0.01
Nb	23.00	25.00	23.00	23.00	25.00	16.00	24.00	25.00	22.00	25.00
BaO	0.09	0.09	0.09	0.09	0.07	0.09	0.08	0.10	0.09	0.08
Ba	833.00	805.00	773.00	825.00	641.00	787.00	752.00	931.00	835.00	754.00
PbO	0.00	0.00	0.00	0.00	0.00	0.00	0.00	0.00	0.00	0.00
Pb	11.00	13.00	6.00	10.00	12.00	14.00	9.00	11.00	7.00	12.00
Total	100.04	100.03	100.03	100.03	100.02	100.03	100.05	100.03	100.03	100.04

Table E-3 (continued)

Element/Compound	Sample ID		
	CrCH2 982.75-982.9 F4	CrCH2 982.75-982.9 F5	CrCH2 982.75-982.9 F6
	Stratigraphic Unit		
	Tjfp	Tjfp	Tjfp
SiO ₂	72.65	73.79	69.82
TiO ₂	0.19	0.22	0.31
Al ₂ O ₃	12.30	11.80	13.01
Fe ₂ O ₃	1.41	1.47	2.19
MgO	0.46	0.56	1.15
MnO	0.07	0.07	0.07
CaO	0.71	0.94	1.18
Na ₂ O	2.65	2.42	2.05
K ₂ O	4.81	4.45	4.42
P ₂ O ₅	0.03	0.04	0.07
Total	95.28	95.75	94.27
LOI	4.58	4.11	5.59
V ₂ O ₅	0.00	0.00	0.01
V	16.00	19.00	33.00
Cr ₂ O ₃	0.00	0.00	0.00
Cr	16.00	15.00	25.00
NiO	0.00	0.00	0.00
Ni	9.00	9.00	14.00
CuO	0.00	0.00	0.01
Cu	6.00	16.00	68.00
ZnO	0.00	0.01	0.01

Table E-3 (continued)

Element/Compound	Sample ID		
	CrCH2 982.75-982.9 F4	CrCH2 982.75-982.9 F5	CrCH2 982.75-982.9 F6
	Stratigraphic Unit		
	Tjfp	Tjfp	Tjfp
Zn	32.00	45.00	55.00
Rb ₂ O	0.01	0.01	0.01
Rb	103.00	100.00	115.00
SrO	0.01	0.01	0.02
Sr	78.00	126.00	127.00
Y ₂ O ₃	0.00	0.00	0.00
Y	22.00	19.00	26.00
ZrO ₂	0.01	0.02	0.02
Zr	99.00	117.00	183.00
Nb ₂ O ₅	0.01	0.01	0.01
Nb	27.00	21.00	23.00
BaO	0.11	0.10	0.08
Ba	944.00	880.00	746.00
PbO	0.00	0.00	0.00
Pb	8.00	19.00	16.00
Total	100.03	100.03	100.03

Note: Concentrations are in weight percent for major elements and parts per million (ppm) for trace elements.

^a F4 = Fine- to medium sand.

^b F5 = Very fine- to fine sand.

^c F6 = Silt.

^d Tpf = Puye Formation.

^e Tpf(p) = Puye pumiceous subunit.

^f LOI = Loss on ignition.

^g Tjfp = Miocene pumiceous unit.

Table E-4
Quantitative Mineralogical Compositions of F4, F5, and F6 Sand and Silt Fractions
of Core Hole CrCH-2 Core Samples from the Puye Formation, Puye Pumiceous Subunit, and Miocene Pumiceous Unit

Sample ID	Stratigraphic Unit	Hornblende	Smectite	Mica/Illite	Clinoptilolite	Hematite	Opal-C/CT	Cristobalite	Quartz	K-Feldspar	Plagioclase	Amorphous	Total
CrCH-2 911.67-912.38F4 ^a	Tpf ^b	1.2	— ^c	10.0	0.1	0.3	2.7	3.8	10.4	7.9	38.1	25.5	100.0
CrCH-2 911.67-912.38F5 ^d	Tpf	1.4	1.9	12.1	0.4	0.2	2.5	2.6	18.1	6.5	28.8	25.5	100.0
CrCH-2 911.67-912.38F6 ^e	Tpf	1.5	12.1	22.6	1.9	0.4	0.9	2.4	12.3	4.9	21.1	19.8	99.9
CrCH-2 913-913.6F4	Tpf	—	—	9.0	—	0.7	5.1	7.5	9.7	15.2	37.1	13.9	98.2
CrCH-2 913-913.6F5	Tpf	0.2	3.5	13.6	—	0.6	5.2	5.9	10.5	9.8	34.9	15.9	100.1
CrCH-2 913-9913.6F6	Tpf	—	8.6	23.7	0.8	0.7	4.4	7.7	4.8	10.7	28.4	10.2	100.0
CrCH-2 917.66-9918.32F4	Tpf	—	—	1.5	—	0.3	—	5.8	13.3	11.6	44.7	22.8	100.0
CrCH-2 917.66-9918.32F5	Tpf	—	—	12.0	—	0.5	4.8	4.0	16.3	8.7	30.1	23.2	99.6
CrCH-2 917.66-9918.32F6	Tpf	0.4	—	31.8	1.9	0.4	14.6	2.3	7.7	7.9	21.6	11.5	100.1
CrCH-2 929-9929.2F4	Tpf(p) ^f	—	—	5.0	—	0.4	3.6	7.7	9.1	12.5	31.5	30.3	100.1
CH-2 929-9929.2F5	Tpf(p)	0.5	—	2.6	—	0.6	—	4.3	12.4	10.6	49.3	19.5	99.8
CrCH-2 929-9929.2F6	Tpf(p)	0.8	2.4	15.1	—	0.5	4.8	5.1	10.7	10.1	28.4	22.0	99.9
CrCH-2 929.2-9930.1F4	Tpf(p)	0.3	—	14.6	—	0.5	3.2	6.7	8.8	9.9	41.2	15.4	100.4
CrCH-2 929.2-9930.1F5	Tpf(p)	0.2	—	9.3	—	0.6	2.7	4.8	11.7	9.5	38.9	21.3	99.0
CrCH-2 929.2-9930.1F6	Tpf(p)	0.5	—	11.4	—	1.0	—	5.1	6.4	10.7	40.3	24.4	99.8
CrCH-2 935.7-9938.25F4	Tpf(p)	—	0.9	4.9	—	—	—	—	8.1	2.5	11.7	71.5	99.6
CrCH-2 935.7-9938.25F5	Tpf(p)	—	3.2	9.8	—	—	—	—	21.0	4.5	11.1	50.3	99.9
CrCH-2 935.7-9938.25F6	Tpf(p)	—	7.7	16.0	—	0.2	—	—	8.4	2.6	12.4	52.4	99.7
CrCH-2 944.47-9944.55F4	Tjfp ^g	—	—	—	—	—	—	—	4.1	2.9	8.5	84.5	100.0
CrCH-2 944.47-9944.55F5	Tjfp	—	1.0	3.8	—	—	—	—	21.1	3.7	14.8	57.2	101.6
CrCH-2 944.47-944.55F6	Tjfp	0.2	10.6	16.0	1.7	0.4	—	—	16.0	3.5	13.9	37.9	100.2
CrCH-2 949.4-949.6F4	Tjfp	—	—	—	—	0.2	—	—	3.2	2.7	10.8	84.8	101.7

Table E-4 (continued)

Sample ID	Stratigraphic Unit	Hornblende	Smectite	Mica/Illite	Clinoptilolite	Hematite	Opal-C/CT	Cristobalite	Quartz	K-Feldspar	Plagioclase	Amorphous	Total
CrCH-2 949.4-949.6F5	Tjfp	—	—	—	—	—	—	—	10.5	3.3	9.4	76.7	99.9
CrCH-2 949.4-949.6F6	Tjfp	—	7.8	11.2	1.0	0.2	—	—	10.9	4.0	15.7	51.7	102.6
CrCH-2 968.1-969F4	Tjfp	—	—	—	—	—	—	—	3.4	2.7	7.7	86.1	99.9
CrCH-2 968.1-969F5	Tjfp	0.3	2.5	4.9	—	—	—	—	22.3	4.0	20.3	45.9	100.2
CrCH-2 968.1-969F6	Tjfp	0.6	11.4	14.4	0.3	0.2	—	—	10.3	2.1	17.6	43.1	100.0
CrCH-2 980-981.5F4	Tjfp	—	—	1.1	—	—	—	—	6.7	5.4	18.4	68.1	99.7
CrCH-2 980-981.5F5	Tjfp	—	—	5.7	—	0.2	—	—	19.1	4.0	16.6	54.0	99.6
CrCH-2 980-981.5F6	Tjfp	0.5	12.3	19.2	—	0.3	—	—	8.2	2.3	12.8	44.3	99.9
CrCH-2 982.75-982.9F4	Tjfp	—	1.7	4.7	—	—	—	—	5.3	3.9	8.9	75.4	99.9
CrCH-2 982.75-982.9F5	Tjfp	—	2.5	5.8	—	—	—	—	14.5	4.0	10.7	62.3	99.8
CrCH-2 982.75-982.9F6	Tjfp	—	15.4	21.1	1.5	—	—	—	5.9	1.8	7.1	47.0	99.8

Note: Mineral abundances are in weight percent (wt%).

^a F4 = Fine- to medium sand.

^b Tpf = Puye Formation.

^c — = Not detected.

^d F5 = Very fine- to fine sand.

^e F6 = Silt.

^f Tpf(p) = Puye pumiceous subunit.

^g Tjfp = Miocene pumiceous unit.

Table E-5

**Major and Trace Element Compositions of F4, F5, and F6 Sand and Silt Fractions
of Core Hole CrCH-3 Core Samples from the Puye Formation, Puye Pumiceous Subunit, and Miocene Pumiceous Unit**

Element/Compound	Sample ID									
	CrCH3 889-891 F4 ^a	CrCH3 889-891 F5 ^b	CrCH3 889-891 F6 ^c	CrCH3 902.5- 903.7 F4	CrCH3 902.5- 903.7 F5	CrCH3 902.5- 903.7 F6	CrCH3 906-907.1 F4	CrCH3 906-907.1 F5	CrCH3 906-907.1 F6	CrCH3 909.9-911 F4
	Stratigraphic Unit									
	Tpf ^d	Tpf	Tpf	Tpf	Tpf	Tpf	Tpf(p) ^e	Tpf(p)	Tpf(p)	Tpf(p)
SiO ₂	68.46	68.83	67.98	67.31	68.22	67.95	73.05	74.07	69.72	72.87
TiO ₂	0.34	0.45	0.61	0.57	0.51	0.50	0.17	0.25	0.43	0.21
Al ₂ O ₃	15.44	14.29	13.92	13.78	14.40	14.64	12.67	12.01	13.25	12.54
Fe ₂ O ₃	2.96	3.57	4.03	5.92	4.04	3.71	1.22	1.59	2.70	1.56
MgO	1.25	1.54	1.85	1.70	1.63	1.75	0.40	0.52	1.12	0.46
MnO	0.051	0.061	0.074	0.080	0.069	0.078	0.065	0.065	0.075	0.070
CaO	3.35	3.24	3.02	2.88	3.01	2.75	0.89	1.06	1.61	0.97
Na ₂ O	3.84	3.30	2.77	3.25	3.15	2.81	3.29	2.89	2.49	3.34
K ₂ O	2.92	2.92	2.98	2.84	2.92	3.08	4.72	4.42	4.24	4.60
P ₂ O ₅	0.091	0.106	0.188	0.092	0.102	0.148	0.033	0.045	0.115	0.036
Total	98.70	98.30	97.43	98.43	98.05	97.42	96.50	96.92	95.74	96.66
LOI ^f	1.13	1.52	2.37	1.39	1.77	2.41	3.38	2.95	4.10	3.22
V ₂ O ₅	0.0077	0.0100	0.0114	0.0171	0.0116	0.0093	0.0025	0.0043	0.0075	0.0032
V	43	56	64	96	65	52	14	24	42	18
Cr ₂ O ₃	0.0064	0.0072	0.0083	0.0132	0.0083	0.0067	0.0015	0.0018	0.0037	0.0018
Cr	44	49	57	90	57	46	10	12	25	12
NiO	0.0038	0.0041	0.0045	0.0066	0.0048	0.0048	0.0009	0.0014	0.0019	0.0010

Table E-5 (continued)

Element/Compound	Sample ID									
	CrCH3 889-891 F4 ^a	CrCH3 889-891 F5 ^b	CrCH3 889-891 F6 ^c	CrCH3 902.5- 903.7 F4	CrCH3 902.5- 903.7 F5	CrCH3 902.5- 903.7 F6	CrCH3 906-907.1 F4	CrCH3 906-907.1 F5	CrCH3 906-907.1 F6	CrCH3 909.9-911 F4
	Stratigraphic Unit									
	Tpf ^d	Tpf	Tpf	Tpf	Tpf	Tpf	Tpf(p) ^e	Tpf(p)	Tpf(p)	Tpf(p)
Ni	30	32	35	52	38	38	7	11	15	8
CuO	0.0011	0.0016	0.0036	0.0019	0.0016	0.0061	0.0005	0.0004	0.0041	0.0005
Cu	9	13	29	15	13	49	4	3	33	4
ZnO	0.0043	0.0056	0.0074	0.0085	0.0068	0.0076	0.0038	0.0043	0.0065	0.0044
Zn	34	45	59	68	54	61	30	34	52	35
Rb ₂ O	0.0073	0.0077	0.0093	0.0081	0.0091	0.0103	0.0115	0.0108	0.0120	0.0112
Rb	67	70	85	74	83	94	105	99	110	102
SrO	0.0617	0.0572	0.0491	0.0439	0.0473	0.0419	0.0117	0.0163	0.0220	0.0129
Sr	522	484	415	371	400	354	99	138	186	109
Y ₂ O ₃	0.0013	0.0019	0.0029	0.0020	0.0020	0.0024	0.0028	0.0027	0.0036	0.0027
Y	10	15	23	16	16	19	22	21	28	21
ZrO ₂	0.0176	0.0332	0.0444	0.0307	0.0349	0.0265	0.0139	0.0189	0.0354	0.0143
Zr	130	246	329	227	258	196	103	140	262	106
Nb ₂ O ₅	0.0049	0.0057	0.0057	0.0060	0.0060	0.0072	0.0077	0.0066	0.0069	0.0074
Nb	17	20	20	21	21	25	27	23	24	26
BaO	0.0853	0.0884	0.0945	0.0803	0.0830	0.0883	0.0831	0.0817	0.0864	0.0836
Ba	764	792	846	719	743	791	744	732	774	749
PbO	0.0010	0.0011	0.0015	0.0016	0.0016	0.0022	0.0011	0.0015	0.0017	0.0015
Pb	9	10	14	15	15	20	10	14	16	14
Total	100.03	100.04	100.05	100.04	100.04	100.04	100.02	100.02	100.03	100.02

Table E-5 (continued)

Element/Compound	Sample ID									
	CrCH3 909.9-911 F5	CrCH3 909.9-911 F6	CrCH3 914.4-915 F4	CrCH3 914.4-915 F5	CrCH3 914.4-915 F6	CrCH3 917.25- 917.8 F4	CrCH3 917.25- 917.8 F5	CrCH3 917.25- 917.8 F6	CrCH3 922.25- 922.75 F4	CrCH3 922.25- 922.75 F5
	Stratigraphic Unit									
	Tpf(p)	Tpf(p)	Tpf(p)	Tpf(p)	Tpf(p)	Tjfp ^a	Tjfp	Tjfp	Tjfp	Tjfp
SiO ₂	73.27	71.04	72.25	72.86	70.37	72.78	71.81	70.54	73.15	73.28
TiO ₂	0.26	0.36	0.29	0.36	0.46	0.24	0.27	0.30	0.22	0.24
Al ₂ O ₃	12.21	12.99	12.47	12.12	13.08	12.27	13.52	12.99	12.45	12.39
Fe ₂ O ₃	1.73	2.28	2.14	2.27	2.77	1.57	1.66	1.98	1.57	1.50
MgO	0.48	0.79	0.54	0.65	0.99	0.53	0.67	0.99	0.44	0.41
MnO	0.070	0.073	0.078	0.075	0.074	0.068	0.064	0.072	0.069	0.069
CaO	1.02	1.41	1.06	1.17	1.70	0.93	1.07	1.27	0.95	0.93
Na ₂ O	3.10	2.90	3.32	2.99	2.83	2.86	2.50	2.30	3.32	3.18
K ₂ O	4.57	4.50	4.51	4.34	4.17	4.67	4.42	4.62	4.54	4.65
P ₂ O ₅	0.038	0.081	0.038	0.045	0.092	0.051	0.060	0.116	0.033	0.029
Total	96.75	96.42	96.68	96.89	96.53	95.96	96.06	95.16	96.75	96.67
LOI	3.13	3.43	3.19	2.97	3.29	3.91	3.82	4.71	3.12	3.21
V ₂ O ₅	0.0043	0.0068	0.0046	0.0055	0.0082	0.0036	0.0046	0.0050	0.0036	0.0029
V	24	38	26	31	46	20	26	28	20	16
Cr ₂ O ₃	0.0015	0.0031	0.0025	0.0028	0.0044	0.0013	0.0019	0.0023	0.0015	0.0015
Cr	10	21	17	19	30	9	13	16	10	10
NiO	0.0014	0.0018	0.0019	0.0015	0.0019	0.0010	0.0010	0.0014	0.0011	0.0011
Ni	11	14	15	12	15	8	8	11	9	9
CuO	0.0008	0.0029	0.0008	0.0014	0.0033	0.0006	0.0015	0.0063	0.0009	0.0006
Cu	6	23	6	11	26	5	12	50	7	5

Table E-5 (continued)

Element/Compound	Sample ID									
	CrCH3 909.9-911 F5	CrCH3 909.9-911 F6	CrCH3 914.4-915 F4	CrCH3 914.4-915 F5	CrCH3 914.4-915 F6	CrCH3 917.25- 917.8 F4	CrCH3 917.25- 917.8 F5	CrCH3 917.25- 917.8 F6	CrCH3 922.25- 922.75 F4	CrCH3 922.25- 922.75 F5
	Stratigraphic Unit									
	Tpf(p)	Tpf(p)	Tpf(p)	Tpf(p)	Tpf(p)	Tjfp ^a	Tjfp	Tjfp	Tjfp	Tjfp
ZnO	0.0046	0.0056	0.0058	0.0051	0.0064	0.0045	0.0049	0.0066	0.0043	0.0044
Zn	37	45	46	41	51	36	39	53	34	35
Rb ₂ O	0.0110	0.0114	0.0108	0.0106	0.0107	0.0116	0.0114	0.0137	0.0110	0.0108
Rb	101	104	99	97	98	106	104	125	101	99
SrO	0.0143	0.0207	0.0149	0.0177	0.0268	0.0123	0.0155	0.0148	0.0131	0.0130
Sr	121	175	126	150	227	104	131	125	111	110
Y ₂ O ₃	0.0030	0.0033	0.0030	0.0029	0.0037	0.0027	0.0029	0.0034	0.0029	0.0028
Y	24	26	24	23	29	21	23	27	23	22
ZrO ₂	0.0200	0.0324	0.0170	0.0267	0.0498	0.0151	0.0211	0.0234	0.0154	0.0182
Zr	148	240	126	198	369	112	156	173	114	135
Nb ₂ O ₅	0.0077	0.0072	0.0074	0.0074	0.0066	0.0072	0.0069	0.0077	0.0083	0.0074
Nb	27	25	26	26	23	25	24	27	29	26
BaO	0.0804	0.0883	0.0886	0.0843	0.0932	0.0908	0.0794	0.0737	0.0888	0.0836
Ba	720	791	794	755	835	813	711	660	795	749
PbO	0.0018	0.0016	0.0017	0.0013	0.0020	0.0018	0.0015	0.0016	0.0014	0.0013
Pb	17	15	16	12	19	17	14	15	13	12
Total	100.03	100.03	100.03	100.03	100.04	100.02	100.03	100.03	100.03	100.03

Table E-5 (continued)

Element/Compound	Sample ID									
	CrCH3 922.25- 922.75 F6	CrCH3 934.4- 935.2 F4	CrCH3 934.4- 935.2 F5	CrCH3 934.4- 935.2 F6	CrCH3 967.75- 968.6 F4	CrCH3 967.75- 968.6 F5	CrCH3 967.75- 968.6 F6	CrCH3 984.9- 986.2 F4	CrCH3 984.9- 986.2 F5	CrCH3 984.9- 986.2 F6
	Stratigraphic Unit									
	Tjfp	Tjfp	Tjfp	Tjfp	Tjfp	Tjfp	Tjfp	Tjfp	Tjfp	Tjfp
SiO ₂	70.84	73.18	73.39	70.49	71.95	72.89	69.36	69.84	71.81	61.19
TiO ₂	0.30	0.23	0.29	0.39	0.31	0.48	0.53	0.34	0.46	0.61
Al ₂ O ₃	13.40	12.30	12.15	13.04	12.55	11.67	13.00	14.02	12.50	15.79
Fe ₂ O ₃	2.00	1.65	1.86	2.47	2.24	2.97	3.43	2.42	3.12	4.78
MgO	0.89	0.36	0.50	0.95	0.70	0.89	1.21	1.18	1.48	3.31
MnO	0.071	0.076	0.071	0.077	0.078	0.078	0.082	0.070	0.070	0.079
CaO	1.45	0.85	1.06	1.43	1.26	1.49	1.57	2.19	1.93	2.11
Na ₂ O	3.00	3.14	2.91	2.59	3.15	2.60	2.32	3.04	2.22	1.09
K ₂ O	4.41	4.69	4.50	4.46	4.35	3.88	4.19	3.58	3.25	3.27
P ₂ O ₅	0.066	0.034	0.048	0.102	0.050	0.064	0.104	0.105	0.119	0.335
Total	96.41	96.50	96.78	96.00	96.64	97.01	95.79	96.78	96.95	92.56
LOI	3.45	3.39	3.10	3.86	3.21	2.83	4.02	3.05	2.89	7.30
V ₂ O ₅	0.0052	0.0030	0.0043	0.0068	0.0048	0.0082	0.0096	0.0066	0.0093	0.0134
V	29	17	24	38	27	46	54	37	52	75
Cr ₂ O ₃	0.0018	0.0013	0.0013	0.0029	0.0025	0.0044	0.0070	0.0023	0.0038	0.0063
Cr	12	9	9	20	17	30	48	16	26	43
NiO	0.0015	0.0010	0.0013	0.0019	0.0017	0.0020	0.0022	0.0020	0.0024	0.0036
Ni	12	8	10	15	13	16	17	16	19	28
CuO	0.0016	0.0008	0.0010	0.0044	0.0006	0.0016	0.0068	0.0014	0.0019	0.0051
Cu	13	6	8	35	5	13	54	11	15	41
ZnO	0.0045	0.0046	0.0049	0.0065	0.0056	0.0064	0.0091	0.0048	0.0059	0.0111
Zn	36	37	39	52	45	51	73	38	47	89

Table E-5 (continued)

Element/Compound	Sample ID									
	CrCH3 922.25- 922.75 F6	CrCH3 934.4- 935.2 F4	CrCH3 934.4- 935.2 F5	CrCH3 934.4- 935.2 F6	CrCH3 967.75- 968.6 F4	CrCH3 967.75- 968.6 F5	CrCH3 967.75- 968.6 F6	CrCH3 984.9- 986.2 F4	CrCH3 984.9- 986.2 F5	CrCH3 984.9- 986.2 F6
	Stratigraphic Unit									
	Tjfp	Tjfp	Tjfp	Tjfp	Tjfp	Tjfp	Tjfp	Tjfp	Tjfp	Tjfp
Rb ₂ O	0.0110	0.0112	0.0112	0.0124	0.0102	0.0097	0.0118	0.0091	0.0102	0.0152
Rb	101	102	102	113	93	89	108	83	93	139
SrO	0.0216	0.0112	0.0156	0.0197	0.0193	0.0241	0.0218	0.0421	0.0343	0.0215
Sr	183	95	132	167	163	204	184	356	290	182
Y ₂ O ₃	0.0030	0.0029	0.0028	0.0038	0.0027	0.0029	0.0042	0.0025	0.0028	0.0047
Y	24	23	22	30	21	23	33	20	22	37
ZrO ₂	0.0190	0.0146	0.0219	0.0353	0.0180	0.0432	0.0639	0.0177	0.0324	0.0249
Zr	141	108	162	261	133	320	473	131	240	184
Nb ₂ O ₅	0.0080	0.0077	0.0077	0.0080	0.0069	0.0060	0.0074	0.0057	0.0054	0.0074
Nb	28	27	27	28	24	21	26	20	19	26
BaO	0.0942	0.0707	0.0749	0.0759	0.1075	0.0926	0.0895	0.1041	0.0890	0.0707
Ba	844	633	671	680	963	829	802	932	797	633
PbO	0.0011	0.0009	0.0017	0.0015	0.0012	0.0013	0.0019	0.0019	0.0009	0.0024
Pb	10	8	16	14	11	12	18	18	8	22
Total	100.03	100.02	100.03	100.03	100.03	100.04	100.05	100.03	100.04	100.05

Note: Concentrations are in weight percent for major elements and parts per million (ppm) for trace elements.

^a F4 = Fine- to medium sand.

^b F5 = Very fine- to fine sand.

^c F6 = Silt.

^d Tpf = Puye Formation.

^e Tpf(p) = Puye pumiceous subunit.

^f LOI = Loss on ignition.

^g Tjfp = Miocene pumiceous unit.

Table E-6
Quantitative Mineralogical Compositions of F4, F5, and F6 Sand and
Silt Fractions of Core Samples from the Puye Formation, Puye Pumiceous Subunit, and Miocene Pumiceous Unit

Sample ID	Stratigraphic Unit	Hornblende	Smectite	Mica/Illite	Clinoptilolite	Hematite	Opal-C/CT	Cristobalite	Quartz	K-Feldspar	Plagioclase	Amorphous	Total
CrCH-3 889-891F4 ^a	Tp ^b	0.7	— ^c	3.3	—	0.2	—	4.7	7.8	10.1	51.6	21.5	99.9
CrCH-3 889-891F5 ^d	Tpf	0.3	0.2	9.6	—	0.2	0.7	3.1	11.0	6.7	36.6	31.9	100.3
CrCH-3 889-891F6 ^e	Tpf	2.0	4.1	21.6	1.1	0.3	6.2	2.8	12.5	6.0	31.6	11.8	100.0
CrCH-3 902.5-903.7F4	Tpf	0.1	1.5	13.4	0.4	0.8	4.4	6.6	8.7	14.5	36.0	13.7	100.1
CrCH-3 902.5-903.7F5	Tpf	0.2	0.1	10.6	0.1	0.5	4.7	4.5	8.2	10.7	44.6	15.3	99.5
CrCH-3 902.5-903.7F6	Tfp(p) ^f	0.2	4.3	17.5	0.6	0.7	12.2	5.5	5.5	11.1	31.5	11.0	100.1
CrCH-3 906-907.1F4	Tfp(p)	0.1	—	3.1	—	—	8.1	0.4	1.4	2.1	11.5	75.9	102.7
CrCH-3 906-907.1F5	Tfp(p)	0.1	—	2.0	—	—	5.9	0.1	9.2	3.5	9.8	69.3	99.9
CrCH-3 906-907.1F6	Tfp(p)	0.2	3.8	14.2	—	0.6	3.1	0.9	7.1	3.8	15.2	51.0	99.9
CrCH-3 909.9-911F4	Tfp(p)	—	—	—	—	—	5.6	1.3	4.0	2.9	9.2	76.7	99.7
CrCH-3 909.9-911F5	Tfp(p)	—	0.3	4.6	—	—	7.6	0.5	6.0	1.9	12.8	68.6	102.0
CrCH-3 909.9-911F6	Tfp(p)	—	0.6	5.5	—	0.3	7.0	0.9	5.3	3.5	12.8	64.0	99.9
CrCH-3 914.4-915F4	Tfp(p)	—	—	0.9	—	0.2	0.9	2.2	1.0	4.0	14.6	76.0	99.8
CrCH-3 914.4-915F5	Tfp(p)	0.1	—	2.2	—	0.2	4.8	1.1	8.8	3.6	11.5	67.8	100.1
CrCH-3 914.4-915F6	Tfp(p)	0.2	—	5.2	—	0.3	2.1	1.3	7.9	3.7	18.7	60.6	100.0
CrCH-3 917.25-917.8F4	Tjfp ^g	—	0.5	3.8	—	—	5.4	0.1	4.3	3.0	7.3	75.6	100.0
CrCH-3 917.25-917.8F5	Tjfp	—	0.3	3.6	—	0.2	—	0.9	5.6	4.2	12.7	72.5	100.0
CrCH-3 917.25-917.8F6	Tjfp	—	2.5	5.5	—	—	4.6	—	9.6	4.0	9.7	63.9	99.8
CrCH-3 922.25-922.75F4	Tjfp	—	—	—	—	0.2	7.3	1.6	1.9	3.9	10.3	74.6	99.8
CrCH-3 922.25-922.75F5	Tjfp	—	—	—	—	—	4.4	1.2	3.8	2.8	10.3	77.4	99.9
CrCH-3 922.25-922.75F6	Tjfp	—	1.4	—	—	0.6	2.7	2.1	3.4	6.9	17.1	65.9	100.1

Table E-6 (continued)

Sample ID	Stratigraphic Unit	Hornblende	Smectite	Mica/Illite	Clinoptilolite	Hematite	Opal-C/CT	Cristobalite	Quartz	K-Feldspar	Plagioclase	Amorphous	Total
CrCH-3 934.4-935.2F4	Tjfp	0.2	—	—	—	—	6.7	1.1	2.4	2.8	8.0	80.4	101.7
CrCH-3 934.4-935.2F5	Tjfp	0.2	—	3.0	—	—	5.6	0.6	9.6	4.2	11.6	65.1	99.9
CrCH-3 934.4-935.2F6	Tjfp	—	4.0	8.0	—	0.2	5.9	0.1	6.1	2.8	10.7	62.1	99.9
CrCH-3 967.75-968.6F4	Tjfp	—	—	—	—	0.2	3.0	1.1	5.8	6.2	19.2	61.8	97.2
CrCH-3 967.75-968.6F5	Tjfp	—	1.3	5.1	—	0.2	4.4	0.2	14.5	5.4	17.7	51.3	100.1
CrCH-3 967.75-968.6F6	Tjfp	—	6.8	20.1	1.0	0.4	6.7	0.1	6.8	1.8	10.3	45.7	99.7
CrCH-3 984.9-986.2F4	Tjfp	0.7	3.1	13.6	—	0.2	4.1	1.3	11.8	4.0	21.9	39.2	99.9
CrCH-3 984.9-986.2F5	Tjfp	0.4	4.9	17.7	0.5	0.3	1.6	0.4	21.0	4.8	31.5	17.1	100.2
CrCH-3 984.9-986.2F6	Tjfp	—	23.8	40.7	—	0.4	4.1	0.2	5.0	1.2	7.0	17.3	99.7

Note: Mineral abundances are in weight percent (wt%).

^a F4 = Fine- to medium sand.

^b Tpf = Puye Formation.

^c — = Not detected.

^d F5 = Very fine- to fine sand.

^e F6 = Silt.

^f Tpf(p) = Puye pumiceous subunit.

^g Tjfp = Miocene pumiceous unit.

LA-UR-18-21450
March 2018
EP2018-0030

Analysis of Groundwater Geochemical Fingerprints for Identification of Source Areas in the Chromium Project Area

Attachment 4



Prepared by the Associate Directorate for Environmental Management

Los Alamos National Laboratory, operated by Los Alamos National Security, LLC, for the U.S. Department of Energy (DOE) under Contract No. DE-AC52-06NA253 and under DOE Office of Environmental Management Contract No. DE-EM0003528, has prepared this document pursuant to the Compliance Order on Consent, signed June 24, 2016. The Compliance Order on Consent contains requirements for the investigation and cleanup, including corrective action, of contamination at Los Alamos National Laboratory. The U.S. government has rights to use, reproduce, and distribute this document. The public may copy and use this document without charge, provided that this notice and any statement of authorship are reproduced on all copies.

CONTENTS

1.0	INTRODUCTION	1
2.0	METHODS	1
2.1	Fingerprint Constituents	1
2.2	Data Sources	1
2.3	Data Normalization	1
2.4	Context for Data Interpretation	3
3.0	RESULTS AND DISCUSSION	3
4.0	CONCLUSIONS	5
5.0	REFERENCES	6
5.1	References	6
5.2	Map Data Sources	6

Figures

Figure 2.3-1	Isotopic ranges for different nitrate sources (after Davis et al., 2015)	7
Figure 2.4-1	Different types of releases from canyons (LA–Los Alamos [includes DP Canyon], S–Sandia, M–Mortandad) and their hypothetical fingerprint plots	9
Figure 3.0-1	Contaminant domains as identified from fingerprint diagrams	10
Figure 3.0-2	Cr/SO ₄ ratios for regional aquifer wells	11

Tables

Table 2.3-1	UTL and MDL Values Used to Normalize Contaminant Concentrations	13
Table 2.3-2	Range of Data for Each Isotopic Signature in the Intermediate and Regional Aquifer and the Background Range Used to Normalize the Data to a Common Scale	13
Table 2.3-3	Scheme Showing How Nitrate and Sulfate Isotopic Signatures Were Scaled	14

Plate

Plate 1	Contaminant fingerprint diagrams for wells located in and around the chromium plume	
---------	---	--

1.0 INTRODUCTION

Anthropogenic contaminant concentrations and isotopic signatures from regional aquifer wells associated with the chromium plume were used to create visual “fingerprint” patterns of contamination. Fingerprint patterns were compared in order to assign regional aquifer wells to a contaminant domain. By comparison to fingerprint patterns of intermediate aquifer wells, and accounting for spatial and temporal variation in contaminant release and knowledge of aquifer hydrology, contaminant domains were associated with different contaminant sources. Chromium/sulfate (Cr/SO_4) ratios were also examined in this context.

2.0 METHODS

2.1 Fingerprint Constituents

Six chemical constituents (chlorate, sulfamethoxazole, chromium, 1,4-dioxane, perchlorate and tritium) were chosen to discriminate between different locations and times of release. Perchlorate, tritium and 1,4-dioxane are excellent tracers of releases associated with plutonium processing, which occurred in Effluent/Mortandad Canyon and Los Alamos/DP Canyon. Chromium is associated with cooling tower discharges into Sandia Canyon. Chlorate is often associated with modern sewage treatment processes (though it can also occur with perchlorate). The antibiotic sulfamethoxazole is also associated with the release of sewage and is therefore related to releases in Sandia Canyon. In addition, five isotopic signatures (^{36}Cl , ^{129}I , ^{18}O of nitrate, ^{15}N of nitrate, ^{34}S of sulfate) were examined. The New Mexico Environment Department Oversight Bureau (NMED-OB) has done extensive analyses of ^{36}Cl and ^{129}I , which are typically related to plutonium processing. NMED-OB has also looked at sulfate isotope signals because their isotopic signatures can help to distinguish specific contaminant sources.

2.2 Data Sources

The data used in this analysis cover the period January 2010 through September 2017. Filtered samples are necessary to provide accurate dissolved concentrations or isotope values for some species. Data from those filtered groundwater sample analysis were used as appropriate. Time series were plotted for each constituent to see if outliers were present. Any points that were clearly outside the range and trend of the vast majority of the data were removed. For CrPZ-2 S1 and CrPZ-2 S2, only data after August 2016 were used. All nitrate concentration data were reported as nitrate as nitrogen.

2.3 Data Normalization

Concentration data were normalized using the aquifer appropriate background upper tolerance limit (UTL) or the weighted average method detection limit (MDL) for that analyte. For constituents that have a natural background concentration, UTLs were used, while MDLs were used for constituents that were solely anthropogenic. The UTLs and MDLs used for the normalization are present in Table 2.3-1. All values below the UTL and MDL were set to 1. All data are plotted in box and whisker diagrams with the latest data plotted as a solid black diamond symbol and non-detects plotted at 1 with a white fill; visually obvious temporal trends were represented with arrows. Perched-intermediate groundwater and regional aquifer data were treated separately, as they have different background chemistry and contaminant concentration ranges.

Isotopic data are presented in similar fashion but were normalized and scaled relative to background ranges as determined from wells with background chemistry in consultation with NMED staff. This process was most straightforward for ^{36}Cl and ^{129}I where it was necessary only to distinguish between background and contamination. For these isotopes, the minimum and maximum values of each isotope were determined separately for the perched-intermediate and regional aquifers (see Table 2.3-2). If the values were within the background range, a value of 0 was assigned. If values were greater than the background range, the difference between the measured value and applicable background value were scaled from 0 to 3, with the maximum value for that isotope in a given aquifer corresponding to 3.

For $\delta^{15}\text{N}$ and $\delta^{18}\text{O}$ of nitrate, isotopic ranges for three potential contaminant sources were determined from known modern sources (e.g., sewage treatment plants, commercial nitric acid) and from the literature. The three contaminant sources considered are modern sewage, old sewage, and nitric acid. Regional aquifer background isotopic signatures were also considered (Davis et al. 2015). The terms “old” and “modern” are relative. No specific timeframe should be inferred. Modern refers to source signatures that can be measured today from active processes, whereas old refers to signatures inferred based on knowledge of historic processes.

Modern LANL sewage and nitric acid have unique isotopic signatures whereas ‘old sewage’ and background nitrate fields strongly overlap (Figure 2.3-1).

In Figure 2.3-1, the least processed sewage values (from the literature) have $\delta^{15}\text{N}$ values of approximately 0–7‰, strongly overlapping with the background nitrate isotope field. Well R-10a, though not specifically included in this study, provides further insight into the potential isotopic signature of old sewage. This well has nitrate concentrations slightly above the background UTL but a nitrate isotope signature that falls within the background range. Simple isotopic mass balance mixing calculations suggest that the nitrate source at this well must also have an isotopic signature similar to background. It is clear from the isotopic signature that anthropogenic nitrate in this well is not derived from nitric acid. The most likely source, particularly in light of literature values for less treated sewage, is older sewage that had not undergone modern treatment processes.

The old sewage/background isotopic data overlap was resolved using the nitrate concentration along with the isotope signature for each sample. If nitrate concentrations were higher than the background UTL and $\delta^{15}\text{N}$ was between 0 and 7‰, the sample was considered to have an old sewage signal; the difference between the measured value and applicable threshold value (7‰) was scaled from 0 to –1, with the minimum value for $\delta^{15}\text{N}$ within this grouping corresponding to –1. Data that fell within this isotopic range, but with concentrations less than the background UTL, were assigned a value of 0, representing background. $\delta^{15}\text{N}$ data greater than 7‰ were considered a modern sewage signal and adjusted to a scale from 0 to 3 in a manner analogous to ^{36}Cl and ^{129}I . No data existed that had both $\delta^{15}\text{N}$ greater than 7‰ and $\delta^{18}\text{O}$ greater than 12‰ (see next paragraph). Few nitric acid signatures were found in the data set. Those few samples dominated by nitric acid (based primarily on ^{18}O of nitrate; both “normal” and anomalously low $\delta^{15}\text{N}$ nitric acid) were arbitrarily assigned a value of 0 and are noted accordingly. This is shown in Table 2.3-3.

For $\delta^{18}\text{O}$ of nitrate, the following rules were used. If $\delta^{18}\text{O}$ of nitrate is greater than 12‰, the values were considered a nitric acid signal and adjusted to a scale from 0 to 3 in a manner analogous to ^{36}Cl and ^{129}I . Samples with isotopically distinct nitric acid (negative $\delta^{15}\text{N}$) were assigned a value of 3. Any values less than 12‰ but with positive ^{15}N were considered sewage, with no discrimination between old and modern and were scaled from 0 to –1 with the minimum isotopic value corresponding to –1 (Table 2.3-3).

Source-term measurements of $\delta^{34}\text{S}$ and $\delta^{18}\text{O}$ of sulfate from modern sewage, cooling-tower effluent, sulfuric acid, and background sulfate fail to completely bound sulfate isotopic signatures in regional and perched-intermediate aquifer wells within the chromium plume (based on NMED-OB data). This is particularly true for $\delta^{18}\text{O}$ of sulfate. However, modern sewage and sulfuric acid sources (including cooling tower discharge) seem to have $\delta^{34}\text{S}$ values less than 6‰. Background sulfate has $\delta^{34}\text{S}$ greater than 6‰ within the local regional aquifer. However, several wells with sulfate concentrations above the background UTL have similar $\delta^{34}\text{S}$ to background. Using similar arguments to those used to define the nitrate isotopic signature of old sewage, it is inferred that old sewage has $\delta^{34}\text{S}$ greater than 6‰. However, there is lower confidence in this assumption relative to the inferred nitrate isotope signature of old sewage. Well R-36, however, provides an interesting case study. The $\delta^{34}\text{S}$ of this well falls within the background range, but sulfate concentrations are above the background UTL. An isotopic mass balance approach suggests the $\delta^{34}\text{S}$ of the contaminant source must also be in the background range, greater than 6‰. Since the signal looks nothing like that of modern sewage, sulfuric acid, or cooling-tower discharge, it is inferred by a process of elimination that this signal is likely related to old sewage.

As such, the information derived from $\delta^{34}\text{S}$ isotopes is given less weight in the interpretation than other isotopic signatures. All isotope samples that had a sulfate concentration below the UTL were considered background and assigned a value of 0. The rest of the data, with sulfate concentrations above UTL, were separated into different source terms. Values with SO_4 above the background UTL and $\delta^{34}\text{S}$ above 6‰ were considered to be from an undefined source but potentially indicative of an old sewage signal and were adjusted to a scale from 0 to 3. Data with sulfate concentrations above the UTL and less than 6‰ were considered a modern sewage or sulfuric acid/cooling tower signal and adjusted to a scale from 0 to -1 (Table 2.3-3).

2.4 Context for Data Interpretation

To aid the reader in interpreting fingerprint diagrams, examples of potential source-term fingerprints are provided in Figure 2.4-1.

3.0 RESULTS AND DISCUSSION

Fingerprint data are shown in Plate 1. Visual pattern matching is necessarily somewhat subjective and no two well fingerprints will be exactly alike. The fingerprints are grouped into five categories or contaminant domains using best judgement, and taking into account known hydrologic constraints. These domains are shown in Figure 3.0-1. Domains are shown for upper screen of wells only.

The domains, along with source-term assignments, are described below. The discussion is focused on groupings of wells with similar signatures rather than on each individual well. Anomalous or confusing signatures are discussed in more detail.

Background (R-13 and SIMR-2)

These wells, located outside of the estimated chromium plume perimeter, have background or non-detect contaminant concentrations and background isotopic signatures.

Lower Sandia Canyon, Los Alamos Canyon, +/- Mortandad Canyon Source (R-42, R-28, R-50 S1, CRPZ-1, CRPZ-2 S1; CRPZ-3, CRPZ-5, CREX-1, CREX-3)

These wells encompass the centroid of the chromium plume. They form a very distinct fingerprint that looks like a sine wave for major contaminants and a prominent W for isotopes (Plate 1). For the most part, these wells have elevated concentrations of each of the key contaminants, though chromium, sulfamethoxazole, and tritium tend to have the strongest signals. Contaminant signatures towards the edge of the chromium plume centroid can be somewhat depressed (e.g., R-50 S1). The most prominent isotope signals are a clear modern sewage signal and elevated ^{129}I . Note that the deep screen at CrPZ-2 appears to belong to the Older Releases domain described below.

This combination of contaminant signatures, along with a position relative to perched-intermediate and regional aquifer flow paths, suggests a Sandia Canyon (chromium, chlorate, modern sewage, sulfamethoxazole) and Los Alamos/DP Canyon contaminant source (chlorate, tritium, perchlorate, and possibly 1,4-dioxane), possibly with additional plutonium processing–related contributions from Mortandad Canyon. These wells are believed to be affected by alluvial water infiltration occurring in lower reaches of Sandia Canyon (LANL 2012).

Los Alamos Canyon perched-intermediate well fingerprint patterns are elevated in tritium and perchlorate, and, interestingly, in chlorate (Plate 1). We speculate that this chlorate might be a breakdown or equilibration product of perchlorate. Chlorate is substantially elevated in Sandia Canyon perched-intermediate wells, probably due to chlorate from modern sewage treatment processes (LANL 2012, Plate 1). Chromium, sulfamethoxazole, and modern sewage components also appear in these wells. North-to-south hydrologic gradients within the perched-intermediate groundwater occurrences along with a combination of plutonium processing–related contaminants and contaminants derived from cooling-tower discharges and sewage releases from Sandia Canyon demonstrate mixing of sources within the perched-intermediate groundwater occurrences beneath Sandia Canyon. The ^{129}I in Sandia Canyon perched-intermediate wells is likely associated with Los Alamos/DP Canyon sources, though may have been flushed out of the perched-intermediate groundwater more proximal to sources.

Upper Sandia Canyon + Los Alamos Canyon Source (R-62, R-43 S1, R11)

Well R-62 has a similar fingerprint pattern to that of the Lower Sandia Canyon, Los Alamos Canyon, +/- Mortandad Canyon domain, but much less of a Los Alamos Canyon plutonium-processing signature (lower 1,4-dioxane, perchlorate, and tritium) (Plate 1). The tritium present in this well may not represent anthropogenic tritium, but rather atmospheric tritium inputs from historical precipitation transported along relatively fast hydrologic pathways to the regional aquifer. The presence of ^{129}I suggests that there must be some Los Alamos/DP Canyon source, though this may be minor. Given the location of this well, the contamination is believed to be related to infiltration further up Sandia Canyon than the location of infiltration affecting chromium plume centroid wells.

Based on hydrologic considerations and fingerprint patterns, well R-43 S1 is thought to be a more dilute member of the same domain as R-62, with additional plutonium processing-related inputs from Los Alamos/DP Canyon based on isotope signatures (Plate 1). Well R-11 is believed to have an even more dilute signal than these other two wells.

Mortandad Canyon Source (R-15, CRPZ-4, and R-50S1)

Wells R-15 and CRPZ-4 are characterized in particular by elevated perchlorate, tritium and ^{36}Cl (Plate 1). Their nitrate and sulfate isotope signatures are consistent with an old sewage source. This old sewage could be derived from Mortandad Canyon and may include a component signature from Tensite Canyon. The upper screen at R-50 has an isotopic fingerprint pattern that appears to be intermediate between the

plume centroid and the Mortandad source, suggesting mixed domains at this location. Piezometer CRPZ-4 looks like an “island” in Figure 3.0-1, suggesting a nearby drip point with Mortandad-derived contaminants dominating at this location. The fingerprints for these regional aquifer wells share some similarities (elevated perchlorate, tritium, and ^{36}Cl) with nearby perched-intermediate wells MCOI-5 and MCOI-6 (Plate 1). There is likely a significant hydrologic connection between these wells and wells in the regional aquifer that are dominated by the Mortandad domain. The fingerprints of the perched-intermediate wells likely reflect recent mixing with Sandia contaminant sources (LANL 2012), the signals of which may not have manifested in the regional aquifer. One interesting facet of these wells is that they are the only wells to show a clear nitric acid signature in the nitrate isotope data.

Older Releases (R-43 S2, R-35a, R-35b, CRPZ-2 S2, R-45 S1 and S2, R-44 S1, R-36)

This contaminant domain includes wells near the downgradient periphery of the chromium plume. They tend to have more muted signals of chromium, plutonium processing–related constituents, and old sewage. While clearly showing older inputs from a temporal sense, the physical sources for these wells are likely to be the same as for the Lower Sandia, Los Alamos Canyon, +/- Mortandad Canyon Source domain.

Among these wells, R-36 is particularly interesting. Note the very strong old sewage signature suggested by $\delta^{34}\text{S}$ and the somewhat higher perchlorate and tritium values compared with other wells in this grouping. These results could be suggestive of a stronger component of contamination sourced from Los Alamos/DP Canyons and possibly even from Pueblo Canyon (reflecting old sewage inputs and earliest plutonium processing at the lab that released into Acid/Pueblo Canyons).

Chromium/sulfate ratios tend to support the domains identified above (Figure 3.0-2). Since sulfate is likely to be conservative in the oxidizing regional aquifer, changes in Cr/SO_4 ratios are likely to reflect either reduction of hexavalent chromium $\text{Cr}(\text{VI})$ to trivalent chromium $\text{Cr}(\text{III})$ or temporal or spatial variation in the source-term ratios of these contaminants in various forms of contaminant discharge. Given the relative paucity of evidence for $\text{Cr}(\text{VI})$ reduction in the regional aquifer, the latter is the more likely explanation. (See the following attachments of this compendium: Attachment 1, “Results and Implications of Field Tracer Testing and Long-Term Pump Tests within the Chromium Plume at Los Alamos National Laboratory from 2013 to 2017,” and Attachment 6, “Characterization of Natural Attenuation.”)

Background wells have the lowest Cr/SO_4 , as do wells R-14 and CrPZ-4 in the Mortandad domain. All of the wells in the Older Releases domain have low to intermediate Cr/SO_4 , while wells in the plume centroid have the highest Cr/SO_4 . Wells R-62 and R-43 S1 also have higher ratios. Well R-11 does not fit this pattern, with low Cr/SO_4 ; contaminant signatures in this well may be a precursor to those seen at R-43 S1 and R-62. The chromium injection wells (CrIN 1–6) had insufficient data to formulate fingerprint diagrams. Their Cr/SO_4 ratios, however, were used in identifying domains shown in Figure 3.0-1.

4.0 CONCLUSIONS

Fingerprint diagrams of regional aquifer wells clearly define contaminant source domains that can be related to contaminant releases that manifest within the chromium plume and along flow paths monitored in perched-intermediate wells associated with the chromium plume. This visual approach is a good complement to more quantitative strategies designed to identify contaminant sources, flow pathways, and mixing zones (See Attachment 5 of this compendium, “Evaluation of Potential Source Areas for the Chromium Plume Using Machine Learning Data Analysis of Geochemical Data.”)

5.0 REFERENCES AND MAP DATA SOURCES

5.1 References

The following reference list includes documents cited in this report.

Davis, P., J. Syme, J.M. Heikoop, J. Fessenden-Rahn, G. Perkins, B. Newman, A. Chrystal, and S. Hagerty. "Quantifying Uncertainty in Stable Isotope Mixing Models," *Journal of Geophysical Research – Biogeosciences*, Vol. 120, pp. 903–923, doi:10.1002/2014JG002839 (2015).

LANL (Los Alamos National Laboratory). "Groundwater Background Investigation Report, Revision 4," Los Alamos National Laboratory document LA-UR-10-4827, Los Alamos, New Mexico (2010).

LANL (Los Alamos National Laboratory). "Phase II Investigation Report for Sandia Canyon," Los Alamos National Laboratory document LA-UR-12-24593, Los Alamos, New Mexico (2012).

LANL (Los Alamos National Laboratory). "Groundwater Background Investigation Report, Revision 5," Los Alamos National Laboratory document LA-UR-16-27907, Los Alamos, New Mexico (2016).

5.2 Map Data Sources

Hillshade; Los Alamos National Laboratory, ER-ES, As published; \\slip\gis\Data\HYP\LiDAR\2014\Bare_Earth\BareEarth_DEM_Mosaic.gdb; 2014.

Point features; As published; EIM data pull; 2017.

Structures; Los Alamos National Laboratory, KSL Site Support Services, Planning, Locating and Mapping Section; 06 January 2004; as published 29 November 2010.

Technical Area Boundaries; Los Alamos National Laboratory, Site Planning & Project Initiation Group, Infrastructure Planning Office; September 2007; as published 13 August 2010.

Average Cr/SO4; Los Alamos National Laboratory, ER-ES, As published; \\slip\gis\GIS\Projects\17-Projects\17-0073\project_data.gdb\point\ratios_CRSO4_bubbles; 2018.

Regional groundwater contour May 2017, 4-ft interval; Los Alamos National Laboratory, ER-ES, As published; \\slip\gis\GIS\Projects\16-Projects\16-0027\project_data.gdb\line\contour_wl2017may_2ft; 2017.

Paved Road Arcs; Los Alamos National Laboratory, FWO Site Support Services, Planning, Locating and Mapping Section; 06 January 2004; as published 29 November 2010.

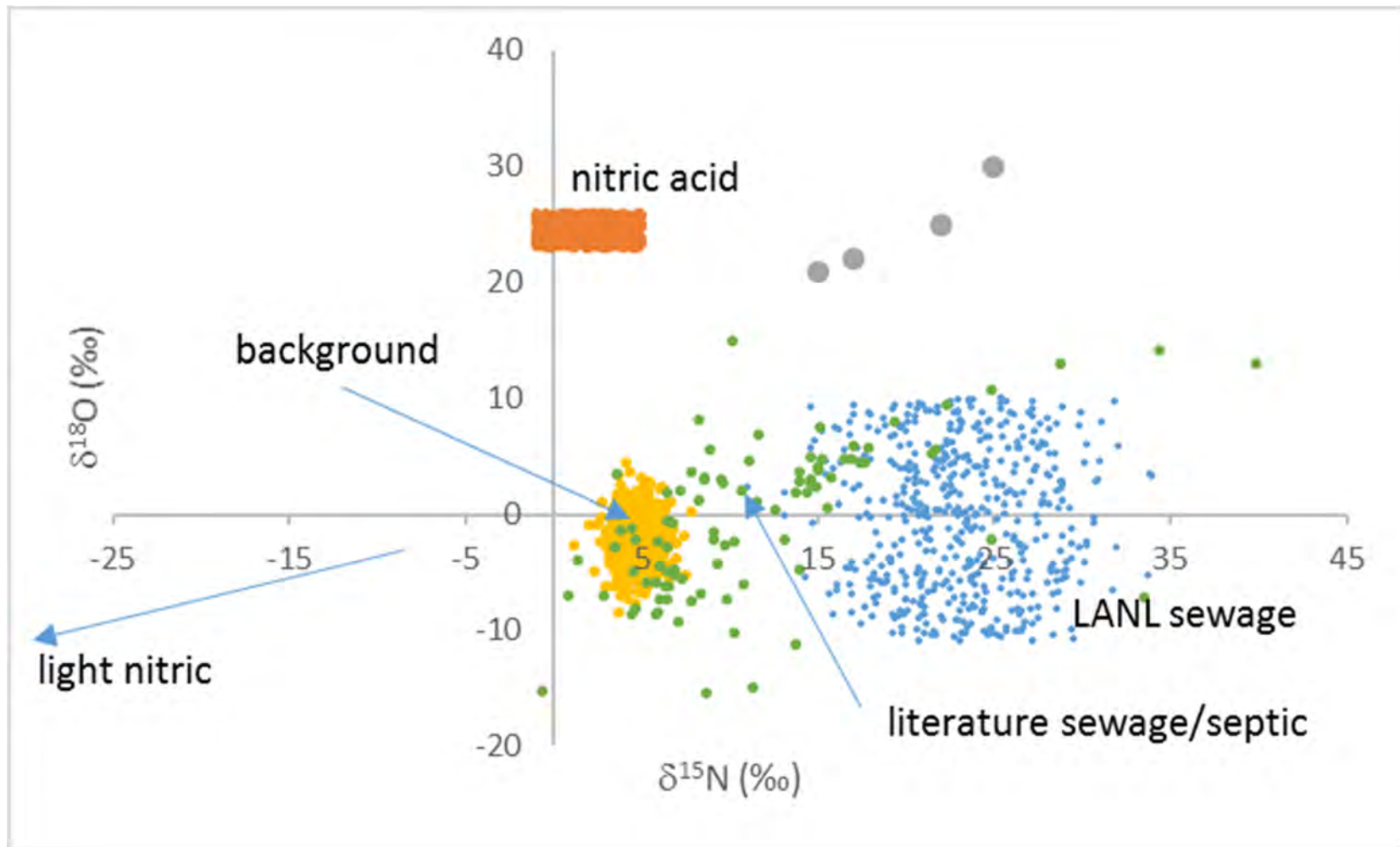


Figure 2.3-1 Isotopic ranges for different nitrate sources (after Davis et al., 2015). Regional aquifer nitrate is shown in yellow. Modern sewage (as determined from local sewage discharges) is shown in blue. Literature values for sewage, which includes nitrate associated with minimal sewage treatment (e.g., septic systems and manure), are shown in green. Nitric acid is shown in orange. Note that in the case of background, nitric acid, and LANL sewage, each point is not a discrete measurement, but rather the result of Monte Carlo sampling of a probability distribution function (see Davis et al., 2015). The arrow labeled “light nitric” refers to a nitric acid discharge that was anomalously enriched in ^{14}N .

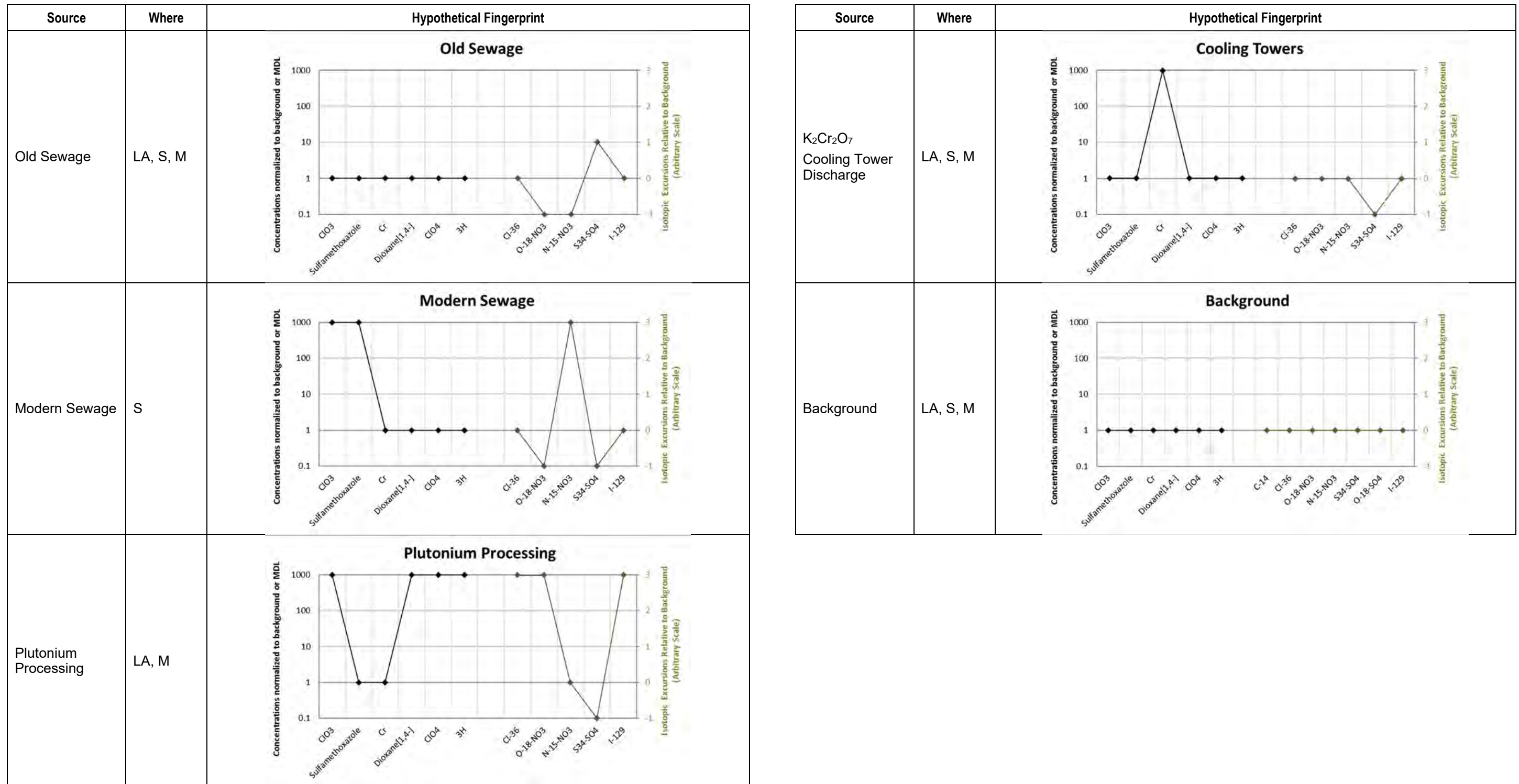


Figure 2.4-1 Different types of releases from canyons (LA–Los Alamos [includes DP Canyon], S–Sandia, M–Mortandad) and their hypothetical fingerprint plots

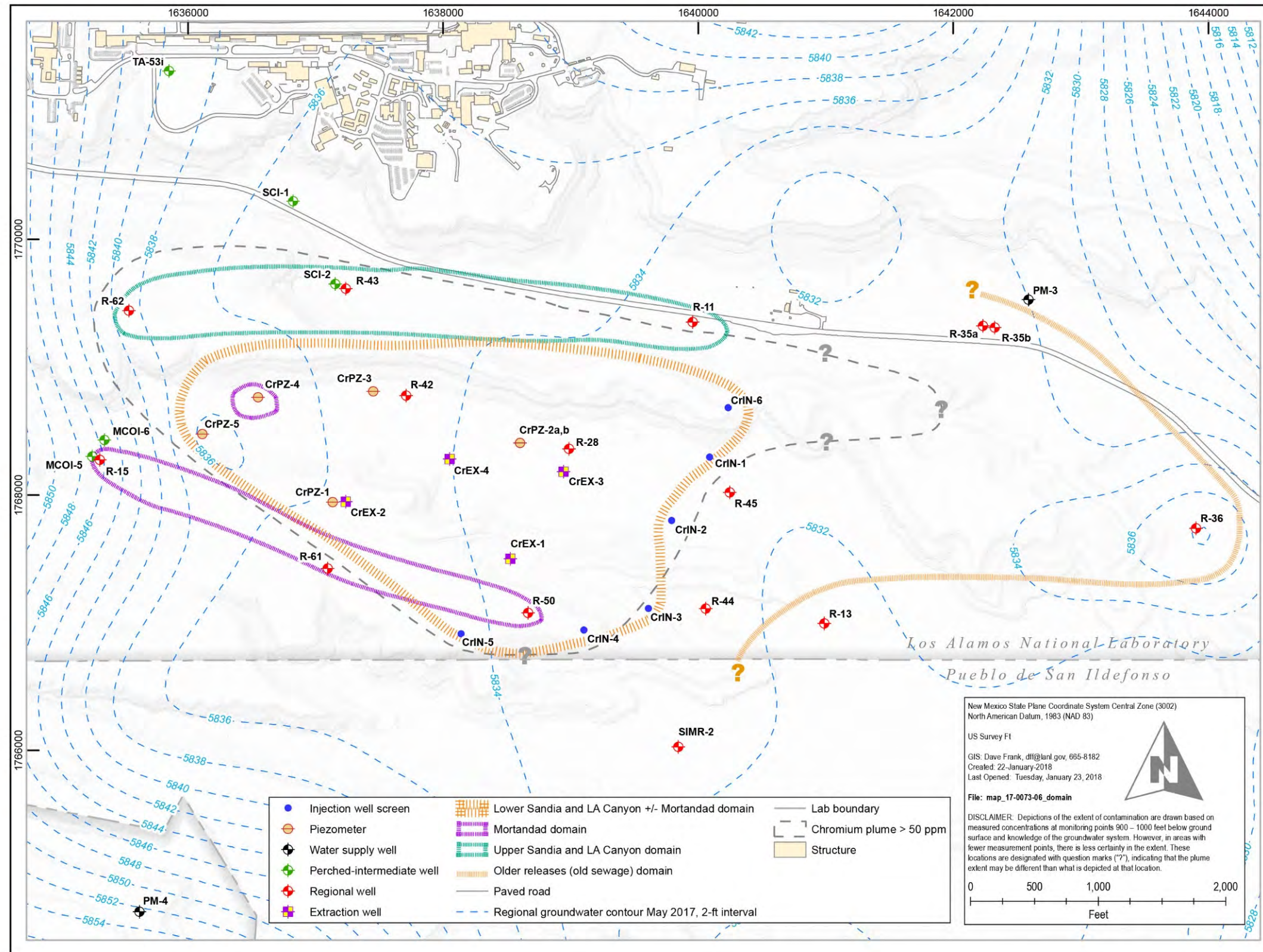


Figure 3.0-1 Contaminant domains as identified from fingerprint diagrams

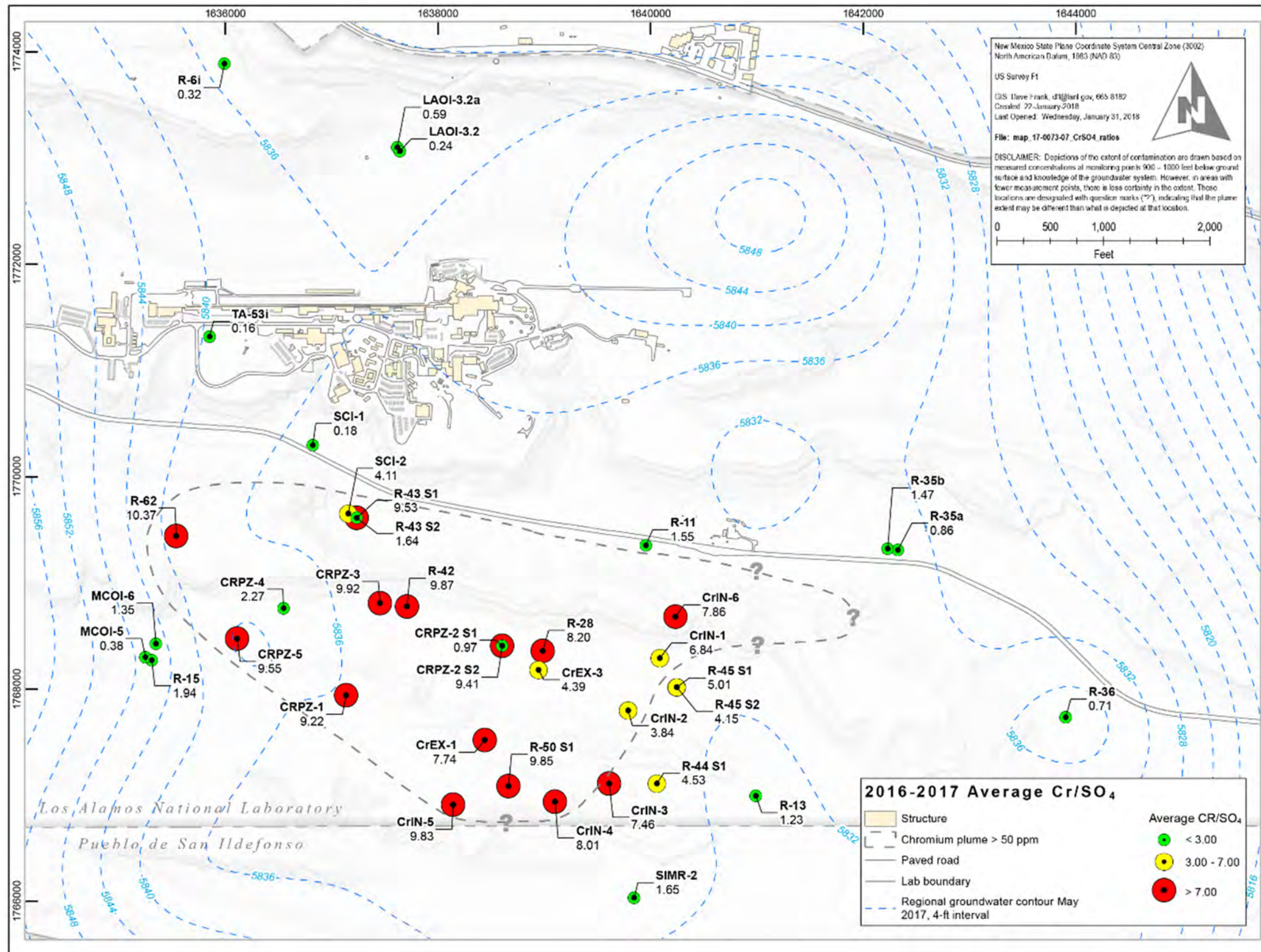


Figure 3.0-2 Cr/SO₄ ratios for regional aquifer wells

Table 2.3-1
UTL and MDL Values Used to Normalize Contaminant Concentrations

Constituent	Aquifer	UTL/MDL	Unit	Source
Chlorate	Perched-Intermediate	0.0015	mg/L	Weighted Average Intermediate MDL ^a
	Regional	0.0014	mg/L	Average Regional MDL ^a
Perchlorate	Perched-Intermediate	0.2700	µg/L	GBIR ^b , Revision 5 pg. 51 (LANL 2016)
	Regional	0.4140	µg/L	GBIR, Revision 5 pg. 52
Chromium	Perched-Intermediate	4.74	µg/L	GBIR, Revision 4 pg. 71(LANL 2010)
	Regional	7.48	µg/L	GBIR, Revision 5 pg. 52
Dioxane[1,4-]	Perched-Intermediate	2.40	µg/L	Weighted Average Intermediate MDL*
	Regional	0.1544	µg/L	Weighted Average Regional MDL*
Nitrate-Nitrite as Nitrogen	Perched-Intermediate	0.459	mg/L	GBIR, Revision 5 pg. 51
	Regional	0.769	mg/L	GBIR, Revision 5 pg. 52
Sulfate	Perched-Intermediate	7.1	mg/L	GBIR, Revision 5 pg. 51
	Regional	4.59	mg/L	GBIR, Revision 5 pg. 52
Sulfamethoxazole	Perched-Intermediate	0.7295	ng/L	Weighted Average Intermediate MDL*
	Regional	0.7342	ng/L	Average Regional MDL*
Tritium	Perched-Intermediate	36.08	pCi/L	GBIR, Revision 4 pg. 73
	Regional	6.26	pCi/L	GBIR, Revision 4 pg. 81

^a Weighted average of all the report MDLs for that aquifer and particular species.

^b GBIR = Groundwater Background Information Report.

Table 2.3-2
Range of Data for Each Isotopic Signature
in the Intermediate and Regional Aquifer and the
Background Range Used to Normalize the Data to a Common Scale

Isotopic Signature	Unit	Aquifer	Data Range Min	Data Range Max	Background Range
δ ³⁶ Cl	Ratio	Intermediate	37.39	12,900	<961
		Regional	147	3680	
δ ¹²⁹ I	Ratio	Intermediate	185.87	17,367	<1E-13
		Regional	22.8	11,688	
δ ¹⁴ C	‰	Intermediate	1.2425	7.1584	<1.1
		Regional	0.3875	0.8713	
δ ¹⁵ N-NO ₃	‰	Intermediate	-22.57	28.16	<7
		Regional	2.46	17.252	
δ ¹⁸ O-NO ₃	‰	Intermediate	-3.37	16.249	<12
		Regional	-6.35	3.4	
δ ³⁴ S-SO ₄	‰	Intermediate	2.7	6	>6
		Regional	2.6	8	

Table 2.3-3
Scheme Showing How Nitrate and Sulfate Isotopic Signatures Were Scaled

 $\delta^{34}\text{S-SO}_4$

Scaled Value	Source	$\delta^{34}\text{S-SO}_4$	SO_4
0 to 3	Old sewage	>6	>UTL
0	Background	-	<UTL
-1 to 0	Modern Sewage or Sulfuric Acid	<6	>UTL

 $\delta^{15}\text{N-NO}_3$

Scaled Value	Source	$\delta^{15}\text{N-NO}_3$	$\delta^{18}\text{O-NO}_3$	NO_3
0 to 3	Modern sewage	>7	-	-
0	Background	0-7	-	<UTL
0	MCOI-5 Nitric Acid	-	>12	-
0	MCOI-6 Nitric Acid	<0	-	-
-1 to 0	Old sewage	0-7	<12	>UTL

 $\delta^{18}\text{O-NO}_3$

Scaled Value	Source	$\delta^{15}\text{N-NO}_3$	$\delta^{18}\text{O-NO}_3$	NO_3
3	MCOI-6 Nitric Acid	<0	-	-
0 to 3	Nitric Acid	>0	>12	-
0	Background	-	-	<UTL
-1 to 0	Sewage (old and modern)	>0	<12	>UTL

LA-UR-18-21450
March 2018
EP2018-0031

Evaluation of Potential Source Areas for the Chromium Plume Using Machine Learning Data Analyses of Geochemical Data

Attachment 5

Prepared by the Associate Directorate for Environmental Management

Los Alamos National Laboratory, operated by Los Alamos National Security, LLC, for the U.S. Department of Energy (DOE) under Contract No. DE-AC52-06NA253 and under DOE Office of Environmental Management Contract No. DE-EM0003528, has prepared this document pursuant to the Compliance Order on Consent, signed June 24, 2016. The Compliance Order on Consent contains requirements for the investigation and cleanup, including corrective action, of contamination at Los Alamos National Laboratory. The U.S. government has rights to use, reproduce, and distribute this document. The public may copy and use this document without charge, provided that this notice and any statement of authorship are reproduced on all copies.

CONTENTS

1.0 OBJECTIVE 1

2.0 METHODOLOGY 1

3.0 RESULTS AND DISCUSSION 2

 3.1 Sources..... 3

 3.2 Key Observations 4

4.0 SUMMARY 6

5.0 REFERENCES 6

Figures

Figure 3.0-1 Observed versus estimated geochemical concentrations at all the site monitoring wells over time 7

Figure 3.2-1 Transient mixing ratios of the seven groundwater types (sources) identified to be present at the site-monitoring wells. 17

Figure 3.2-2 Spatial maps of transient mixing ratios of the seven groundwater types (sources) identified to be present at the site monitoring wells 27

Tables

Table 3.0-1 Transient Geochemical Concentrations Applied in the NTFk Analysis 39

Table 3.0-2 Geochemical Concentrations Associated with the Seven Groundwater Types (Sources) Identified to be Mixed with Background Regional Groundwater at the Site Monitoring Wells..... 45

1.0 OBJECTIVE

The objective of this analysis was to use a novel approach for evaluation of geochemical variability within the chromium plume area for the purpose of identifying spatially or temporally unique source areas (groundwater types) within the overall chromium plume footprint. Different originating sources of contamination and/or groundwater geochemical signatures that have been modified through water-rock interaction can mix in the vadose zone or within the regional aquifer. The method described in this report attempts to deconvolve data from individual wells to identify original contaminant release sources and potential breakthrough locations in the regional aquifer. Identification of source areas may provide insight into plume dynamics and plume evolution, and support optimization of remediation strategies.

2.0 METHODOLOGY

This evaluation uses an approach in which “unsupervised” machine learning (ML) methods are employed for objective and robust analysis of monitoring data from the chromium plume for the purpose of identifying potential sources that help explain potential unique or mixed geochemical domains within the plume. The approach applied here uses a novel unsupervised ML method for a model referred to as blind source separation (BSS), specifically designed for interpretation of geochemical data (Vesselinov et al. 2017). BSS analyses provide a useful additional approach and line of evidence for interpretation of the site geochemical data to supplement existing statistical and modeling techniques. The ML BSS techniques robustly and objectively identify the groundwater types represented by groundwater data. Statistical methods frequently require assumptions about the statistical properties of the analyzed data (e.g. normal distribution); however, ML BSS techniques do not make assumptions about the statistical properties of the processed data (Alexandrov and Vesselinov 2014).

The monitoring of contaminant plume migration typically relies on monitoring well data that informs spatiotemporal geochemical characteristics of the contaminated groundwater flowing through the aquifer. These records are then used to infer flow and transport properties of the aquifer and contaminant source characteristics (location, loading transients, etc.) that are essential for reliable assessment of the contamination hazards and risks.

Identifying the aquifer and contaminant source properties is difficult when geochemical data represent a single source, and this identification is even more difficult when there are multiple sources. The geochemistry of the chromium plume represents multiple mixed sources for which the specific mixing ratios are typically unknown. To provide more detailed information on sources and mixing ratios, a new ML methodology and computational framework called rNMF (Robust Nonnegative Matrix Factorization) was developed for inverse analysis and source identification based on nonnegative matrix factorization (NMF) techniques. The rNMF framework is based on work for model-free inverse analysis of water-level (pressure) data (Alexandrov and Vesselinov 2014) and includes the three different BSS algorithms described below: (1) NMFk, (2) ShiftNMFk, and (3) GreenNMFk.

1. NMFk (Nonnegative Matrix Factorization + k-means clustering analysis) is developed to decouple the mixed observational data from wells and to find the number of contaminant sources that may be present in well data, based only on the robustness of the reconstructed solutions, and without any additional information about the contaminant sources, aquifer properties, or the physical/biogeochemical processes of contaminant transport in the aquifer.

2. ShiftNMFk takes into account transients in the observations and the velocity of contaminant migration (in this case, representative of advective transport; e.g., shifts in the peak breakthrough arrivals), which results in delays (time shifts) in the recorded signals; the unknown time shift is identified only based on the transient observations. ShiftNMFk identifies (a) the number of contaminant sources, (b) the source locations (i.e., breakthrough locations into the regional aquifer), (c) the signal delays, and (d) velocity of signal propagation (advective transport velocity).
3. GreenNMFk, like ShiftNMFk, performs NMF decomposition of the observed transient contaminant signals (e.g., changes in the contaminant breakthrough shapes), but accounts for the physics of the contaminant transport process (using “Green functions” of advection-diffusion equation Alexandrov and Vesselinov 2014). GreenNMFk identifies (a) the number of contaminant sources; (b) the source locations (i.e., breakthrough locations into the regional aquifer), (c) the transients in the source releases, (d) advective transport velocity, and (e) transport dispersivities (assuming a Fickian dispersion model).

The work related to the development of the rNMF theory, methods, and computational frameworks resulted in a U.S. Patent Application, filed by Los Alamos National Laboratory, titled: “*Source Identification by Nonnegative Matrix Factorization Combined with Semi-Supervised Clustering*,” Inventors: B.S. Alexandrov, V.V. Vesselinov et al., LANS Ref. No: S-133, 364, KS Ref. No. 8472-97415-01 U.S. Provisional App. No. 62/381, 486. The patent application was submitted in August 2017.

Initial matrix factorization results were recently published for the chromium site (Vesselinov et al., 2017 602858). However, in addition to the matrix techniques in the matrix ML methods discussed above, a novel unsupervised ML based on Nonnegative Tensor Factorization (NTF) has been developed, called NTFk, which allows analysis of multi-dimensional data (NMF applicability is limited to two-dimensional datasets). NTFk can be applied to perform analyses of the spatial and temporal behavior of the observed geochemical data. The analyses discussed below are performed using the NTFk method, which allows for accounting of transients of source mixing.

3.0 RESULTS AND DISCUSSION

The ML NTFk analysis presented here are based on data from the following wells and well screens: R-67, R-14 S1, R-1, R-15, R-62, R-43 S1, R-43 S2, R-42, R-28, R-50 S1, R-11, R-45 S1, R-45 S2, R-44 S1, SIMR-2, R-13, R-35a, R-35b, and R-36 (see Figure 1.0-1 in the main text of this compendium).

The data include representative recent measurement for eight different geochemical species: chromium (Cr), chloride (Cl⁻), perchlorate (ClO₄), tritium (³H), nitrate (NO₃), calcium (Ca), magnesium (Mg), and sulfate (SO₄).

This dataset was analyzed to define the potential groundwater sources (groundwater types) that are represented as geochemical mixtures in the monitoring well data over time. The NTFk analysis accounts for the mixing of different groundwater types, where some of the types might be associated with background groundwater types and others might be caused by contamination sources.

The geochemical data applied in the NTFk are presented in Table 3.0-1; here the data is multi-dimensional (tensorial) because it has both spatial (well locations) and temporal (sampling events) dependencies. The data in Table 3.0-1 represents annual averages for each year between 2005 and 2016. There are 12 geochemical time snapshots in total.

Based on the data in Table 3.0-1, the NTFk analysis automatically identified seven sources (groundwater types) based on the methodology similar to the one outlined in Vesselinov et al. (2017). The number of sources is identified by the NTFk algorithm by evaluation of the quality and robustness of the obtained solutions. The solution quality is based on a comparison between the data and ML reproduction of the data (as presented in Figure 3.0-1, discussed below). The solution robustness is based on clustering, as discussed in Vesselinov et al. (2017).

The concentrations of each of the eight different geochemical species prior to mixing with regional aquifer water for the seven sources (groundwater types) are presented in Table 3.0-2. These are the concentrations of the estimated groundwater types that are mixed to reproduce the observed groundwater at the wells. As discussed below, there are two background groundwater types that represent changes in the background groundwater types, potentially because of geochemical processes. These processes might be caused by heterogeneity in the aquifer materials and/or mixing of groundwater types with contrasting geochemical properties. The dominant geochemical species associated with each of the seven sources are shown in bold in Table 3.0-2.

Figure 3.0-1 shows the observed versus estimated geochemical concentrations (from Table 3.0-1) at monitoring wells over time. The estimated concentrations are based on NTFk ML analysis with seven distinct groundwater types. The NTFk does a good job of accurately reproducing the geochemical transients observed at the monitoring wells.

Analyzing the data presented in Table 3.0-2, it is apparent that all the identified sources (groundwater types) have distinct geochemistry. Sources 1, 2, 4, 5 and 6 are clearly associated with contaminant sources because of the presence of constituent concentrations above background. Sources 3 and 7 represent the non-contaminated groundwater signature in the plume area (“background”). The variations in the mixing of these two background groundwater types represent variability in the background compositions, potentially as a result of some mixing with contaminated groundwater sources. The temporal dynamics of sources 7 and 3 may represent geochemical reactions occurring in the aquifer because of mixture of groundwater with different geochemistry or heterogeneity in the aquifer materials causing changes in the groundwater geochemistry.

3.1 Sources

Source 1 has values elevated for Cr, Cl⁻, NO₃, Ca, Mg, and SO₄. This is the main source of chromium that constitutes the majority of the plume footprint. The source is a combination of historical blowdown from the power plant located at the head of Sandia Canyon and treated sewage effluent from NPDES Outfall 01A-001 (LANL 2009). The estimated chromium concentration of about 3000 ppb is close to the source concentrations estimated using other data-analysis and modeling techniques (see Attachment 9 of this compendium “Groundwater Modeling Status Report”).

Source 2 has elevated ClO₄, which is a known contaminant in effluent from the Radioactive Liquid Wastewater Treatment Facility (RLWTF) in Mortandad Canyon (LANL 2009).

Source 4 has elevated NO₃, and this is also potentially a Los Alamos, Sandia or Mortandad Canyon contamination source, the difference being whether the nitrate is related to a sewage source originating from sanitary wastewater released into Sandia Canyon or a nitric acid source originating from historical releases from the RLWTF in Mortandad Canyon (LANL 2009). If the nitrate is a Sandia Canyon source, the lack of chromium suggests infiltration of young surface water that post-dates cessation of chromium releases.

Source 5 has elevated tritium. Also elevated are Cr, Cl⁻, Ca, Mg, and SO₄. This is potentially a mixed source where contaminants originating along Los Alamos, Sandia and Mortandad Canyons are mixing in perched groundwater before their arrival at the regional aquifer. The tritium may be originating from either historical releases from the RLWTF in Mortandad Canyon, or from sources in DP Canyon (SWMU 21-011[k]) or Los Alamos Canyon (Omega West Reactor) (LANL 2009).

Source 6 has elevated Cl⁻, Ca, Mg, and SO₄ and Cr. This might be groundwater originating from the same source as earlier chromium-contaminated water, but it has very low or nondetectable concentrations of ³H because the source of these constituents post-dated cessation of chromium releases in 1972. Therefore, this source might reflect more recent infiltration through the vadose zone. This source might be associated with recent Sandia Canyon effluent-dominated infiltration that post-dates chromium releases. The infiltration pathways of Sources 6 and 1 might be similar.

3.2 Key Observations

The evolution of how the seven groundwater types are represented and mixed at each monitoring well is presented in Figure 3.2-1. Note that the mixing ratios for each period of record for each well add to 1.

Summaries of the transient mixing ratios for each well are presented below. The well order approximately follows the direction of the groundwater flow from west to east.

Limited data are available for R-67. R-67 is dominated by background sources 3 and 7, but their contribution might be decreasing. The contribution of Source 4 might be increasing.

R-14 is dominated by background sources 3 and 7. There are no significant mixing transients at this well.

R-1 is dominated by background sources 3 and 7. There are no significant mixing transients at this well.

R-15 is predominantly influenced by source 2 (ClO₄), which appears to show an increasing contribution over time.

R-62 is dominated by background sources 3 and 7. At this well, the impact of source 7 is decreasing, but the impact of sources 1, 2, 4 and 5 is increasing over time.

R-43 S1 is dominated by source 4, although the contribution seems to be diminishing over time. The contribution of source 1 appears to be sharply increasing with time.

R-43 S2 is observing increasing contribution of source 4 and 6 over time. In comparison to R-43 S1, this might be caused by slow vertical groundwater flow and transport from the shallow portions of the aquifer into deeper portions. There is anomalous behavior in 2010.

R-42 observes all seven groundwater types. The mixing ratios for background source 7 are decreasing over time, and the mixing ratios for source 6 are increasing over time. The mixing ratios may suggest a peak mixing ratio for sources 1 and 5 in 2013.

Similar to R-42, R-28 also observes all seven groundwater types. Also similar to R-42, the mixing ratios for background source 7 are slightly decreasing over time, and the mixing ratio for source 6 is slightly increasing over time. Source 4 seems to be decreasing over time. There is anomalous behavior in 2014, which might represent the effects of field testing.

R-50 is dominated by background sources 3 and 7; however, their contributions are changing over time. There is a small increase of source 1 in this well, which represents the increase of chromium concentrations.

R-11 mixing ratios show increasing contributions of sources 4 and 6 over time. Source 2 might be increasing as well. Background sources 3 and 7 show significant decreases, and sources 1 and 5 might be decreasing slightly with time.

R-45 S1 is predominantly impacted by sources 3, 4, and 7. The proportions of sources 1, 2, 4 and 5 are increasing over time, and background sources 3 and 7 are decreasing.

In contrast, R-45 S2 is dominated by background sources 3 and 7. The contribution of source 4 is decreasing over time. However, sources 1, 2 and 5 are slightly increasing over time. The difference in the behavior of source 4 in R-45 S1 (increasing) and R-45 S2 (decreasing) is interesting, and potentially suggests complex groundwater flow/transport conditions and/or differences in the geochemical processes associated with different hydrostratigraphic units.

R-44 S1 is dominated by sources 3, 4, and 7. The contribution of sources 1 and 2 is slightly increasing over time.

R-13 is dominated by background sources 3 and 7; there is a slight increase over time of source 4. Also, there is a slight decrease over time in the contribution of Source 7.

R-35a is dominated by background sources 3 and 7; however, sources 2 and 6 are potentially present at this well in low proportions.

R-35b is dominated by sources 3 and 7; however, sources 2, 4 and 6 are potentially present at this well. There are no important mixing transients at this well.

R-36 appears to show all groundwater types except source 1. This is surprising, considering the well location and the mixing ratios observed at nearby wells. The signature (fingerprint) of the mixing ratios of the groundwater types at this well is unique and sharply different from what is observed at all the other monitoring wells in this assessment. R-36 shows background concentrations of chromium, but low concentrations of other constituents, including nitrate and tritium. Data from R-36 may represent an area of infiltration from an entirely different source than that examined for other wells in this evaluation.

Limited data are available for SIMR-2. SIMR-2 is dominated by background sources 3 and 7. There seems to be no important mixing transients at this well, which is expected considering the well location. It is important to note that SIMR-2 is affected by low proportions of sources 2, 4, and 6. Because of the short period of record for the well, it is difficult to make important conclusions about mixing transients.

The mixing information presented in Figure 3.2-1 is also shown as spatial maps in Figure 3.2-2. The maps depict the transient mixing ratios of the seven groundwater types (sources) identified as present at the site monitoring wells. The maps show the mixing ratio of each source (groundwater type). The mixing ratios are estimated at the wells and interpolated in space between the wells using Kriging interpolation technique. The maps represent 12 temporal snapshots of mixing different sources (groundwater types) from 2005 to 2016 based on the averaged geochemical data (Table 3.0-1).

Here, we perform analysis of the series of maps in Figure 3.2-2.

Sources 1, 5 and 6 are centered in the area of R-28 and R-42. The changes in the shape of the estimated spatial extent of these sources (groundwater types) are predominantly driven by the addition of new monitoring wells over the years (see Table 3.0-1). Nevertheless, the spatial extent of these sources appears to be well constrained. The major difference between sources 1, 5 and 6 is that source 5 is not dominant in R-62 and R-43; however, sources 1 and 6 are present at R-62 and R-43.

Source 2 is centered in the area of R-15. The spatial extent of source 2 appears to be well constrained.

Source 4 is centered in the area of R-43 and R-11; it has been also observed in R-62 and R-15. However, its impact seems to be diminishing at the R-62/R-15 area and increasing at R-11 in recent years. The transients in the mixing ratios between 2008 and 2013 (snapshots for source 4 in Figure 3.2-2) may suggest impacts of lateral plume migration or shifts in the infiltration pathways.

Sources 7 and 3 represent the background groundwater types. Source 3 represents the temporal and spatial dynamics of the Cl, Ca, and Mg geochemical species related to background groundwater. Diminished background mixing ratios are shown in the area of the chromium plume (area of the wells detecting sources 1, 5 and 6). The temporal dynamics of the lowered mixing ratios in the area of chromium plume represents shifts in the mixing of contaminated and background groundwater.

4.0 SUMMARY

The methodology used in the “unsupervised” ML BSS analysis can be coupled with other methods and lines of evidence to discern plume variability and evolution. The results to date should be considered a work in progress and a potentially valuable tool to guide remediation strategies.

5.0 REFERENCES

The following reference list includes documents cited in this report.

Alexandrov, B.S., and V. Vesselinov. “Blind Source Separation for Groundwater Pressure Analysis Based on Nonnegative Matrix Factorization,” *Water Resources Research*, Vol. 50, pp. 7332–7347 (2014).

LANL (Los Alamos National Laboratory). “Investigation Report for Sandia Canyon,” Los Alamos National Laboratory document LA-UR-09-6450, Los Alamos, New Mexico (2009).

Vesselinov, V.V., B.S. Alexandrov, and D. O'Malley. “Contaminant Source Identification Using Semi-Supervised Machine Learning,” *Journal of Contaminant Hydrology*, pp. 1–9. (2017).

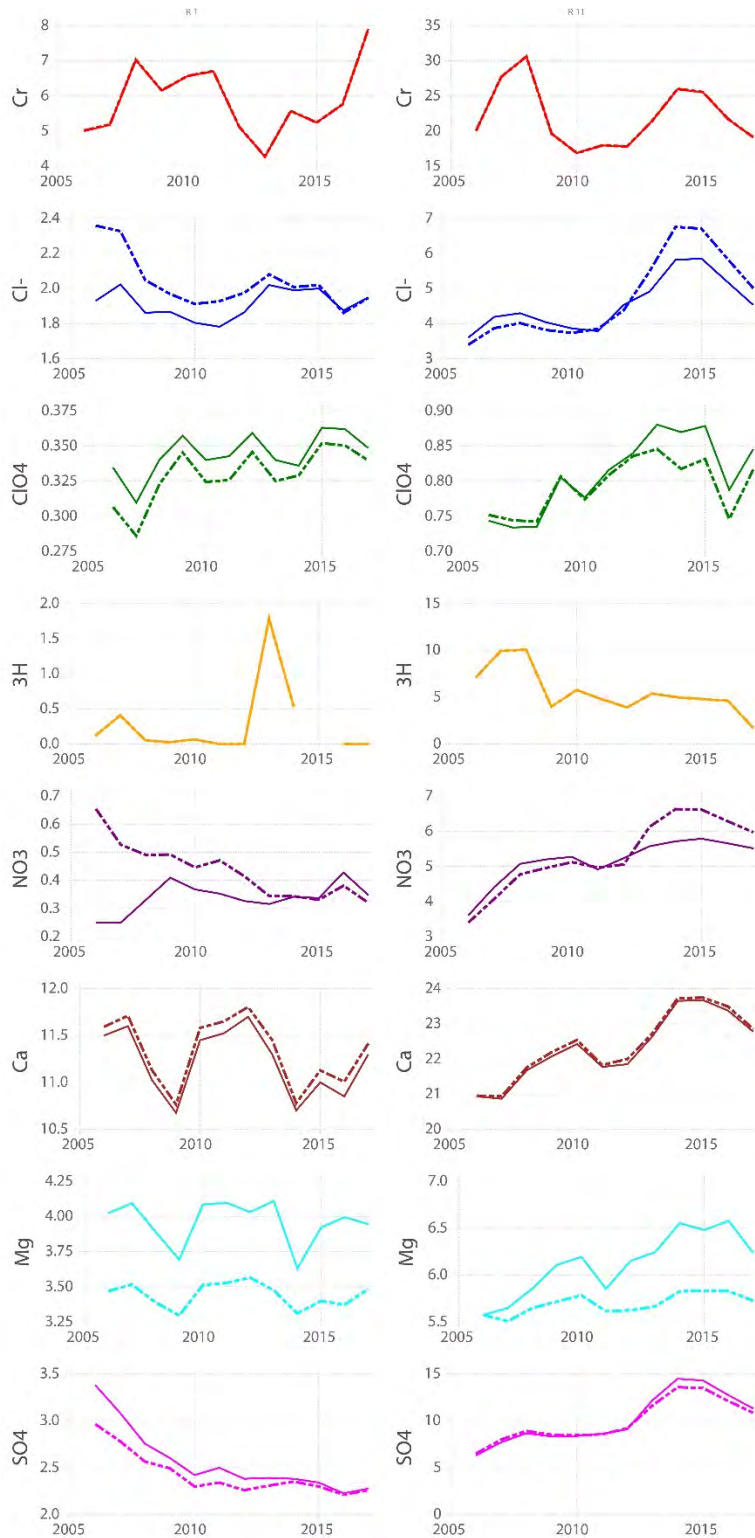


Figure 3.0-1 Observed versus estimated geochemical concentrations at all the site monitoring wells over time. Observed data are presented in Table 3.0-1. The estimated concentrations are based on NTFk ML analysis with seven distinct groundwater types (Table 3.0-2).



Figure 3.0-1 (continued) Observed versus estimated geochemical concentrations at all the site monitoring wells over time. Observed data are presented in Table 3.0-1. The estimated concentrations are based on NTFk ML analysis with seven distinct groundwater types (Table 3.0-2).

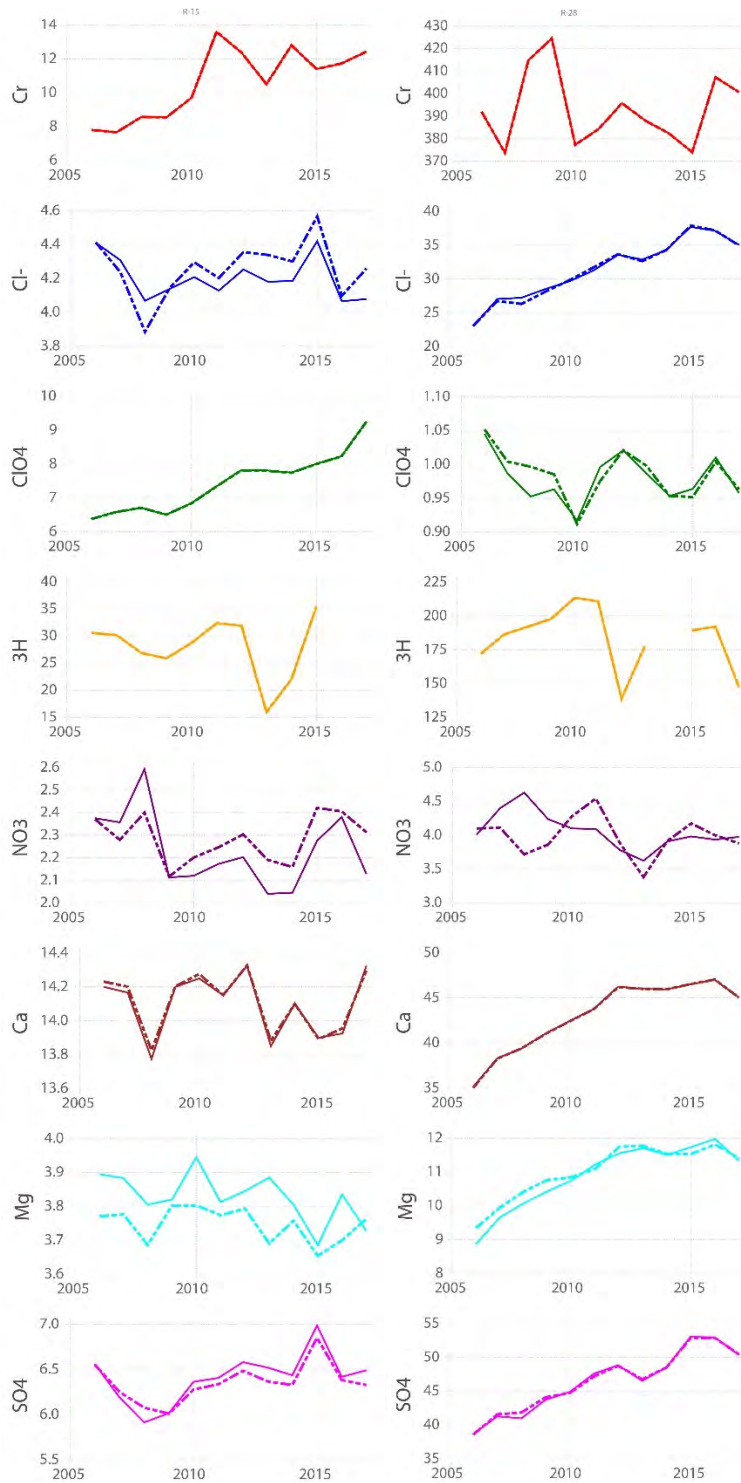


Figure 3.0-1 (continued) Observed versus estimated geochemical concentrations at all the site monitoring wells over time. Observed data are presented in Table 3.0-1. The estimated concentrations are based on NTFk ML analysis with seven distinct groundwater types (Table 3.0-2).

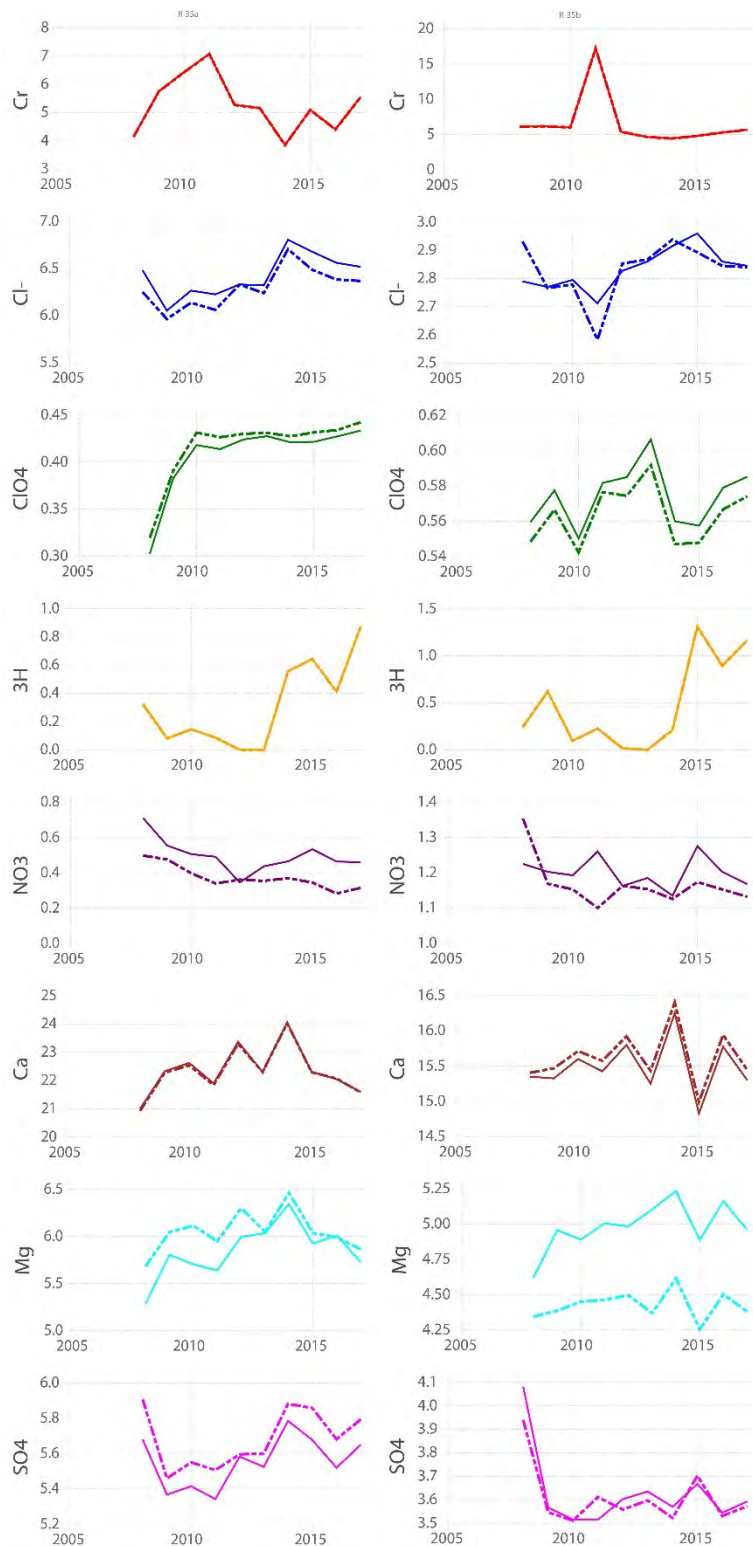


Figure 3.0-1 (continued) Observed versus estimated geochemical concentrations at all the site monitoring wells over time. Observed data are presented in Table 3.0-1. The estimated concentrations are based on NTFk ML analysis with seven distinct groundwater types (Table 3.0-2).

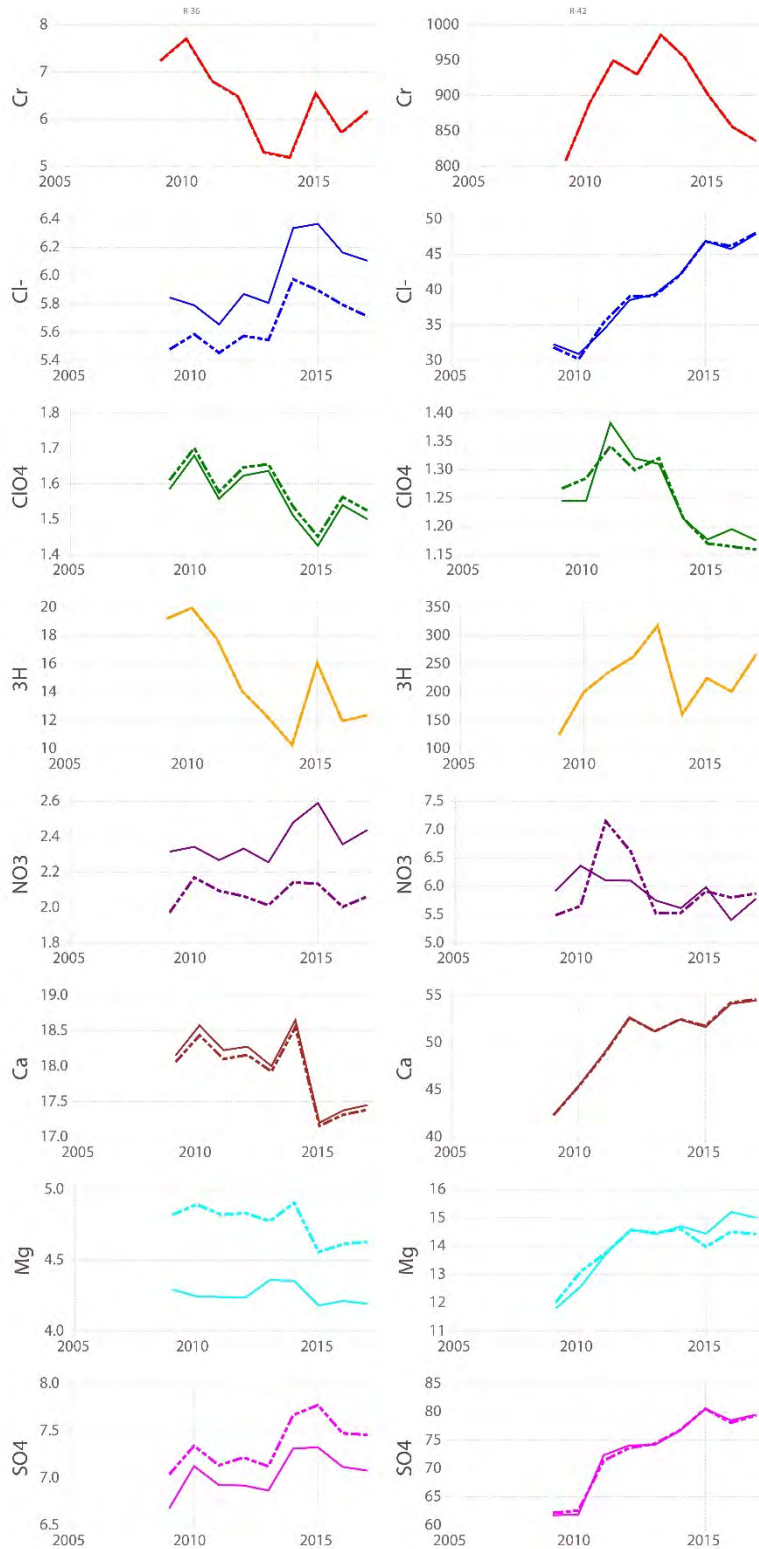


Figure 3.0-1 (continued) Observed versus estimated geochemical concentrations at all the site monitoring wells over time. Observed data are presented in Table 3.0-1. The estimated concentrations are based on NTFk ML analysis with seven distinct groundwater types (Table 3.0-2).

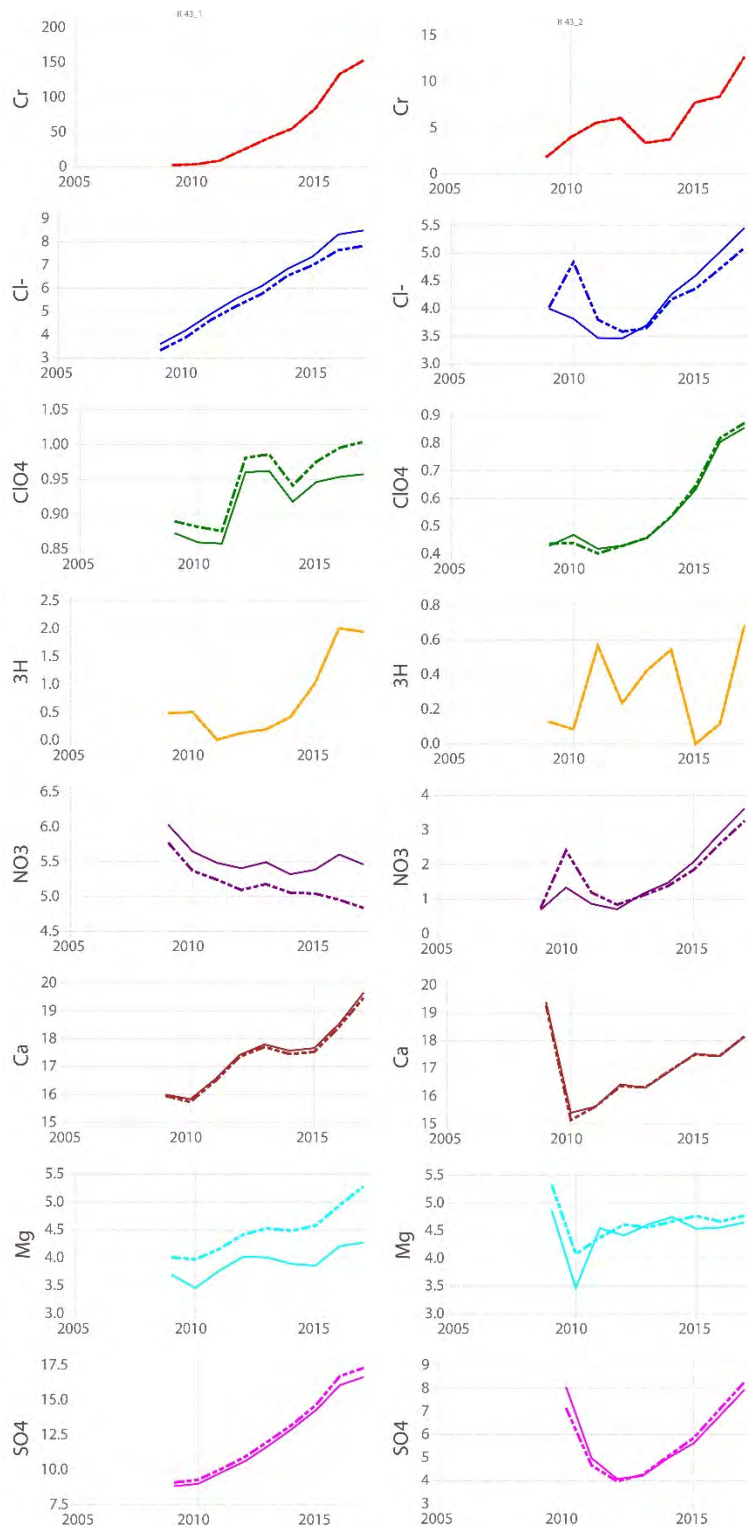


Figure 3.0-1 (continued) Observed versus estimated geochemical concentrations at all the site monitoring wells over time. Observed data are presented in Table 3.0-1. The estimated concentrations are based on NTFk ML analysis with seven distinct groundwater types (Table 3.0-2).

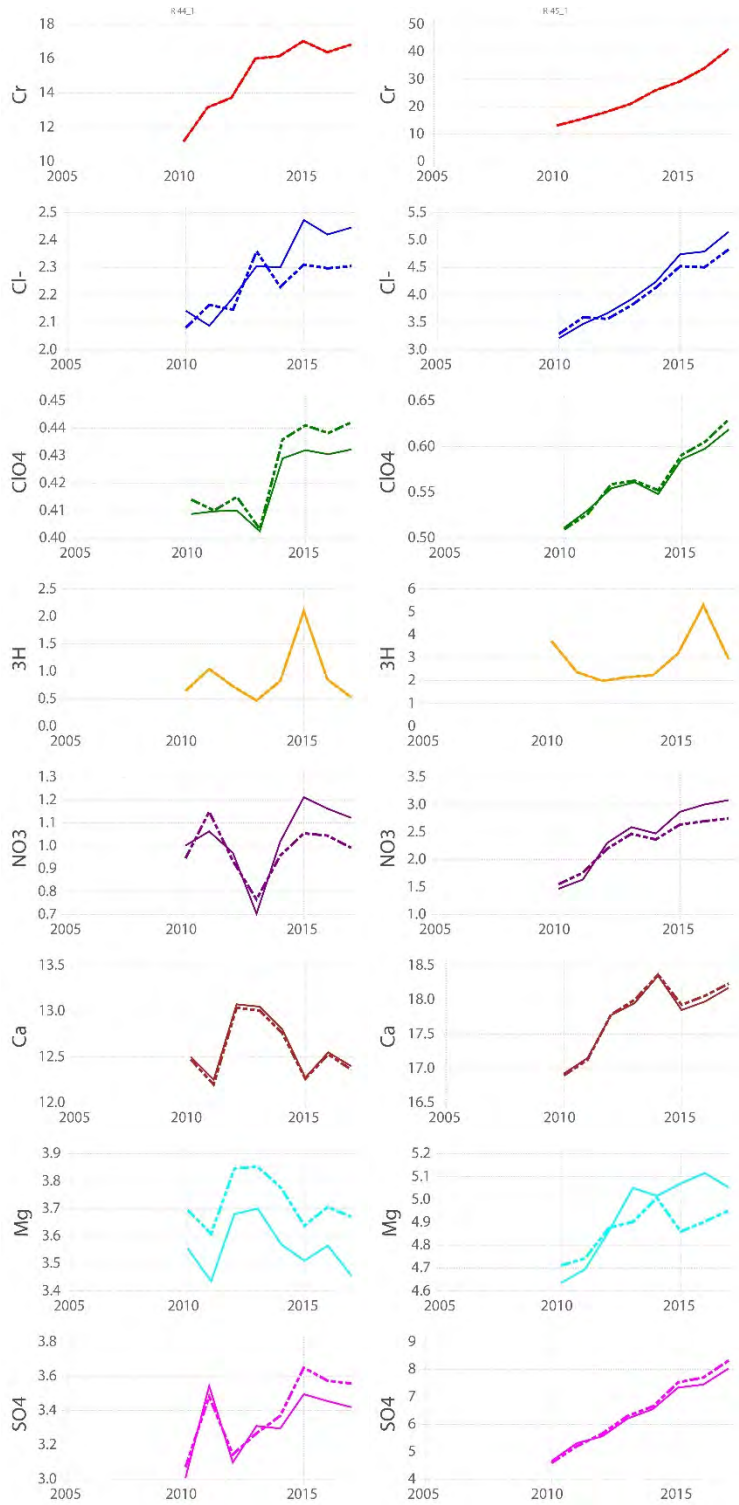


Figure 3.0-1 (continued) Observed versus estimated geochemical concentrations at all the site monitoring wells over time. Observed data are presented in Table 3.0-1. The estimated concentrations are based on NTFk ML analysis with seven distinct groundwater types (Table 3.0-2).

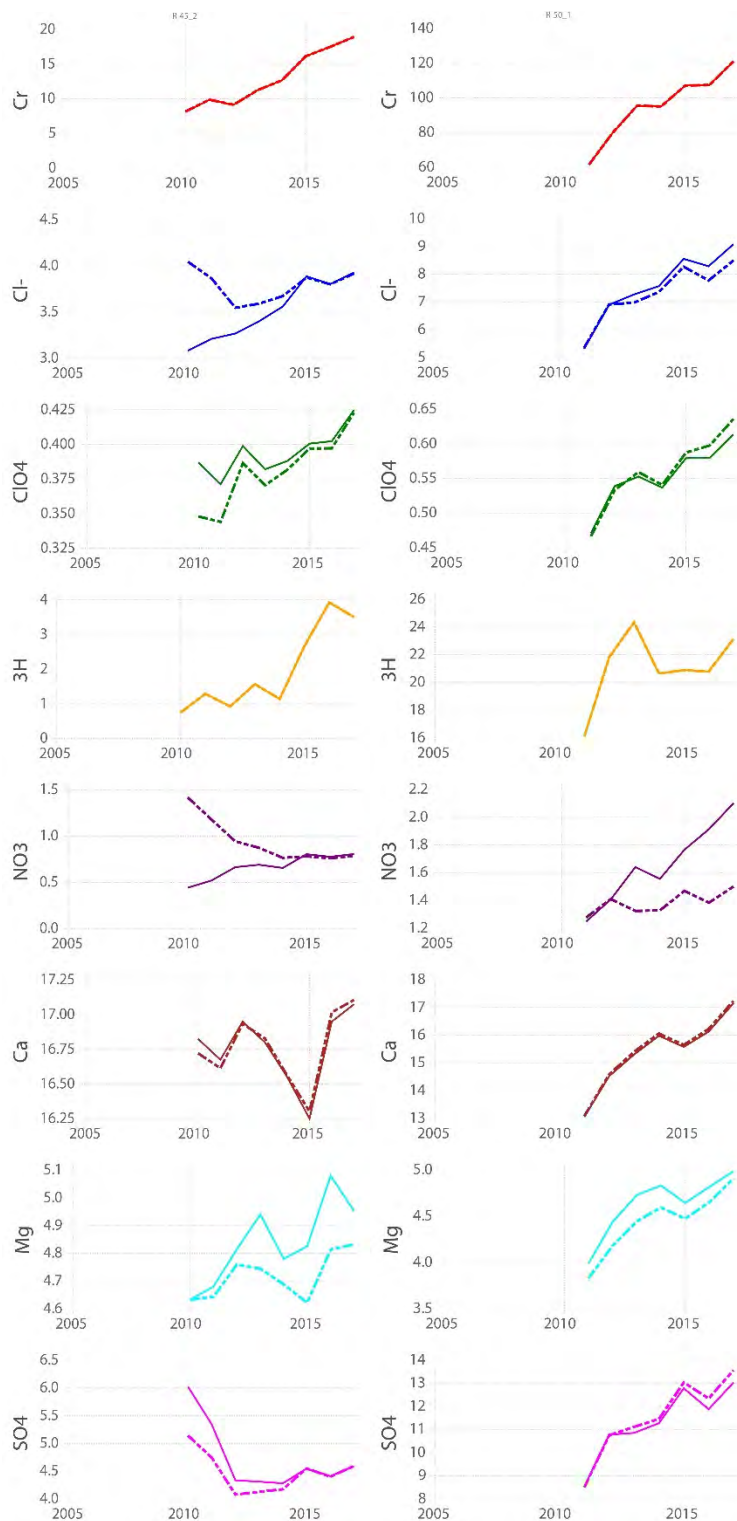


Figure 3.0-1 (continued) Observed versus estimated geochemical concentrations at all the site monitoring wells over time. Observed data are presented in Table 3.0-1. The estimated concentrations are based on NTFk ML analysis with seven distinct groundwater types (Table 3.0-2).

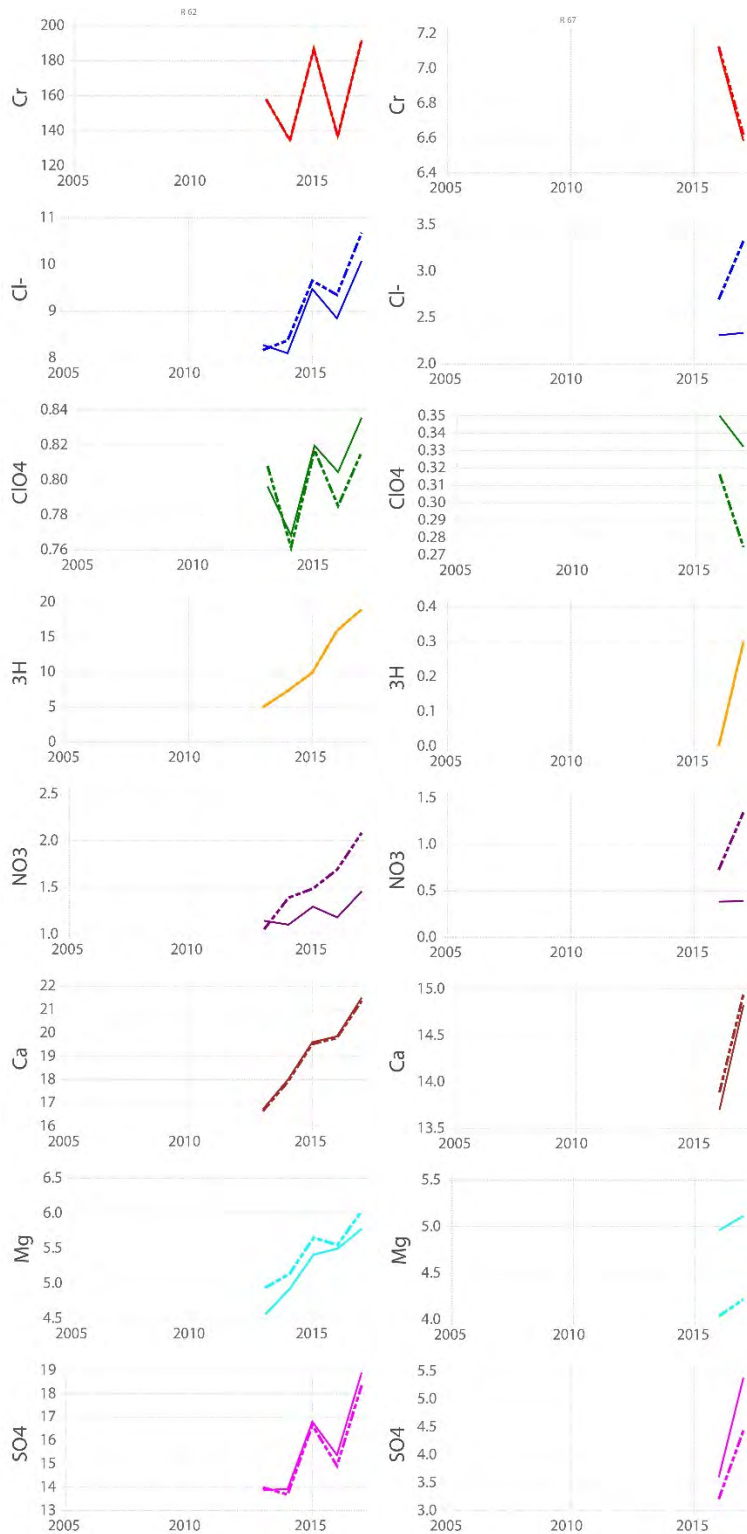


Figure 3.0-1 (continued) Observed versus estimated geochemical concentrations at all the site monitoring wells over time. Observed data are presented in Table 3.0-1. The estimated concentrations are based on NTFk ML analysis with seven distinct groundwater types (Table 3.0-2).

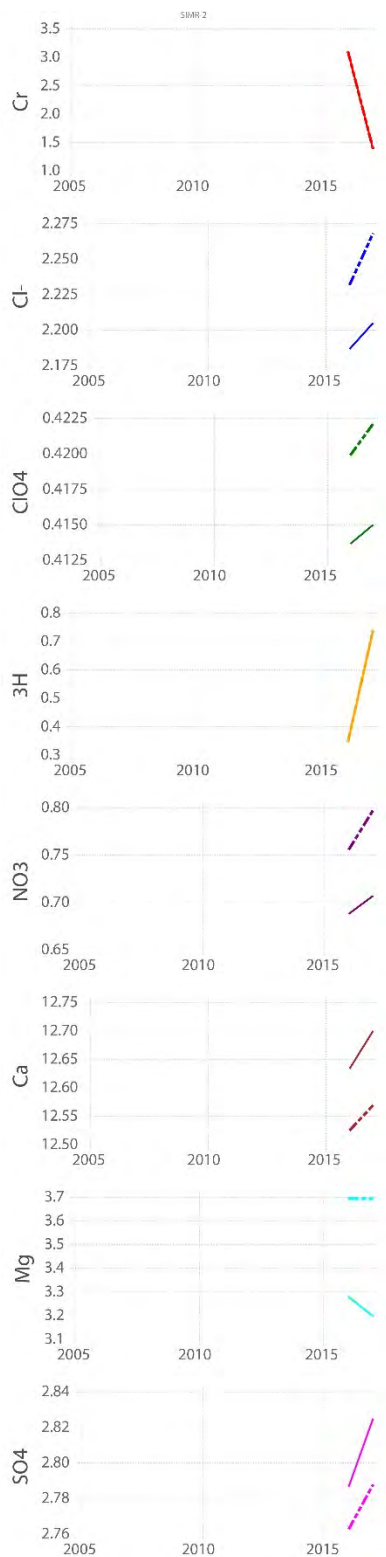


Figure 3.0-1 (continued) Observed versus estimated geochemical concentrations at all the site monitoring wells over time. Observed data are presented in Table 3.0-1. The estimated concentrations are based on NTFk ML analysis with seven distinct groundwater types (Table 3.0-2).

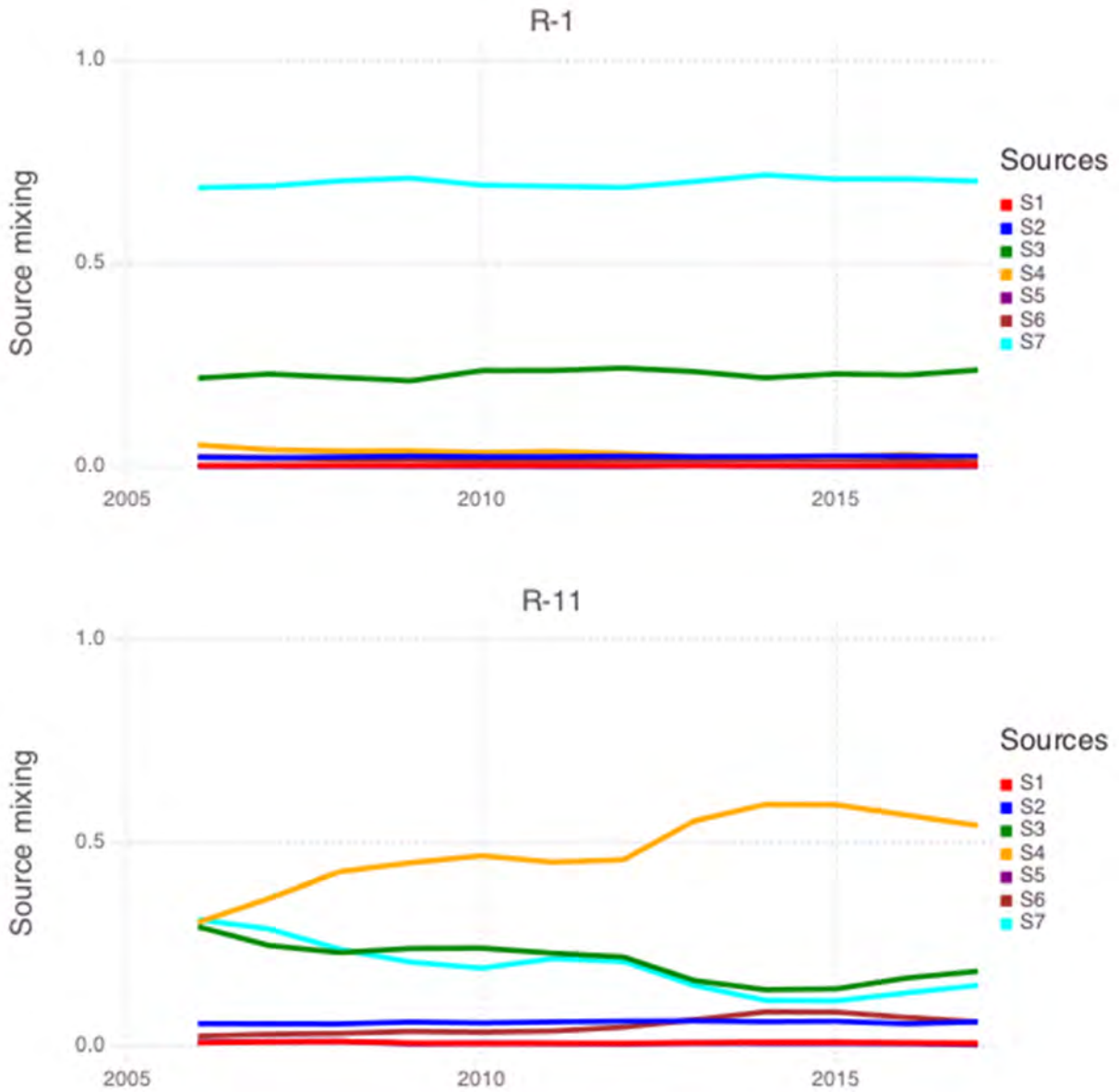


Figure 3.2-1 Transient mixing ratios of the seven groundwater types (sources) identified to be present at the site-monitoring wells. The mixing ratios add up to 1 for each time frame.

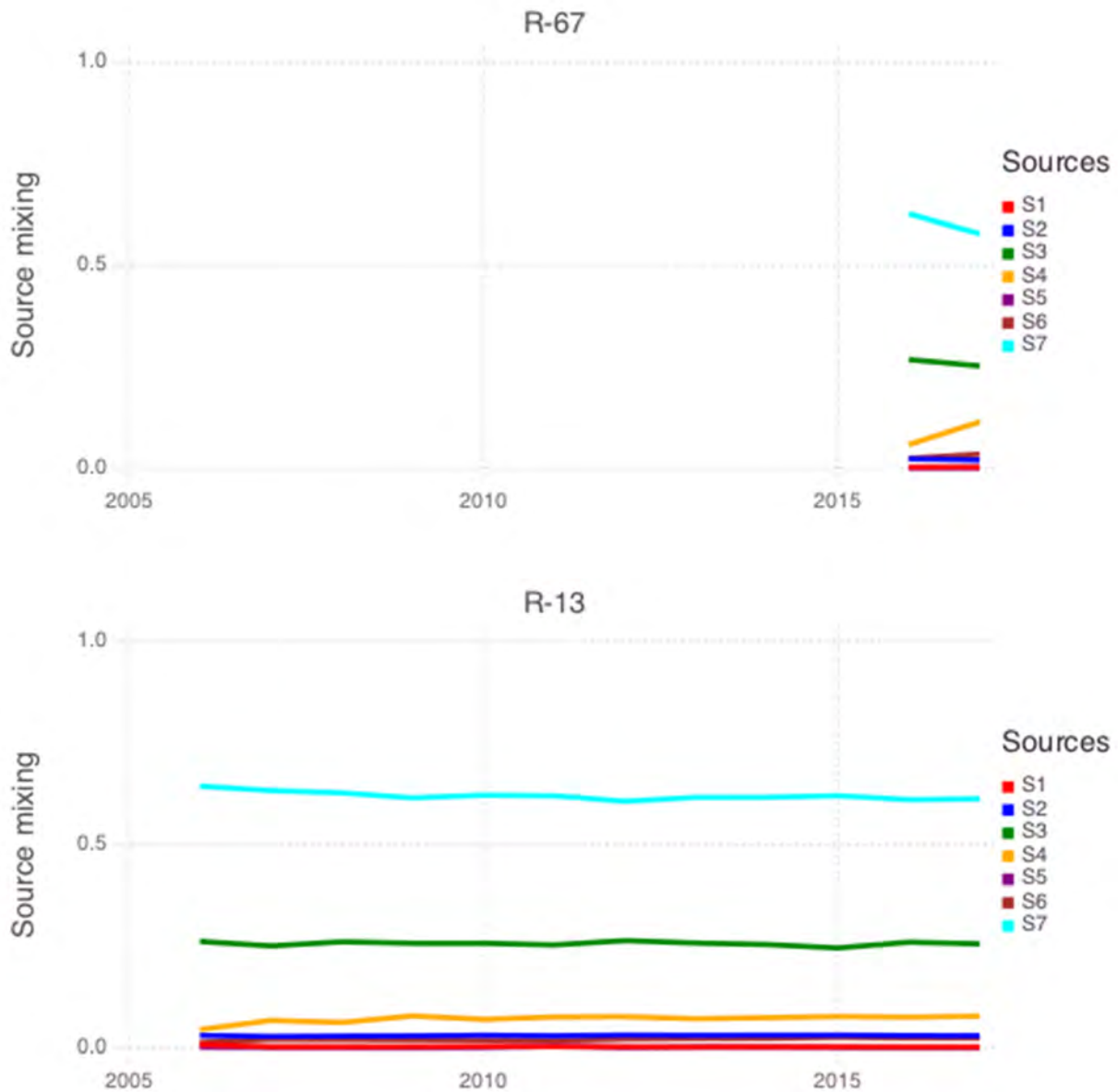


Figure 3.2-1 (continued) Transient mixing ratios of the seven groundwater types (sources) identified to be present at the site-monitoring wells. The mixing ratios add up to 1 for each time frame.

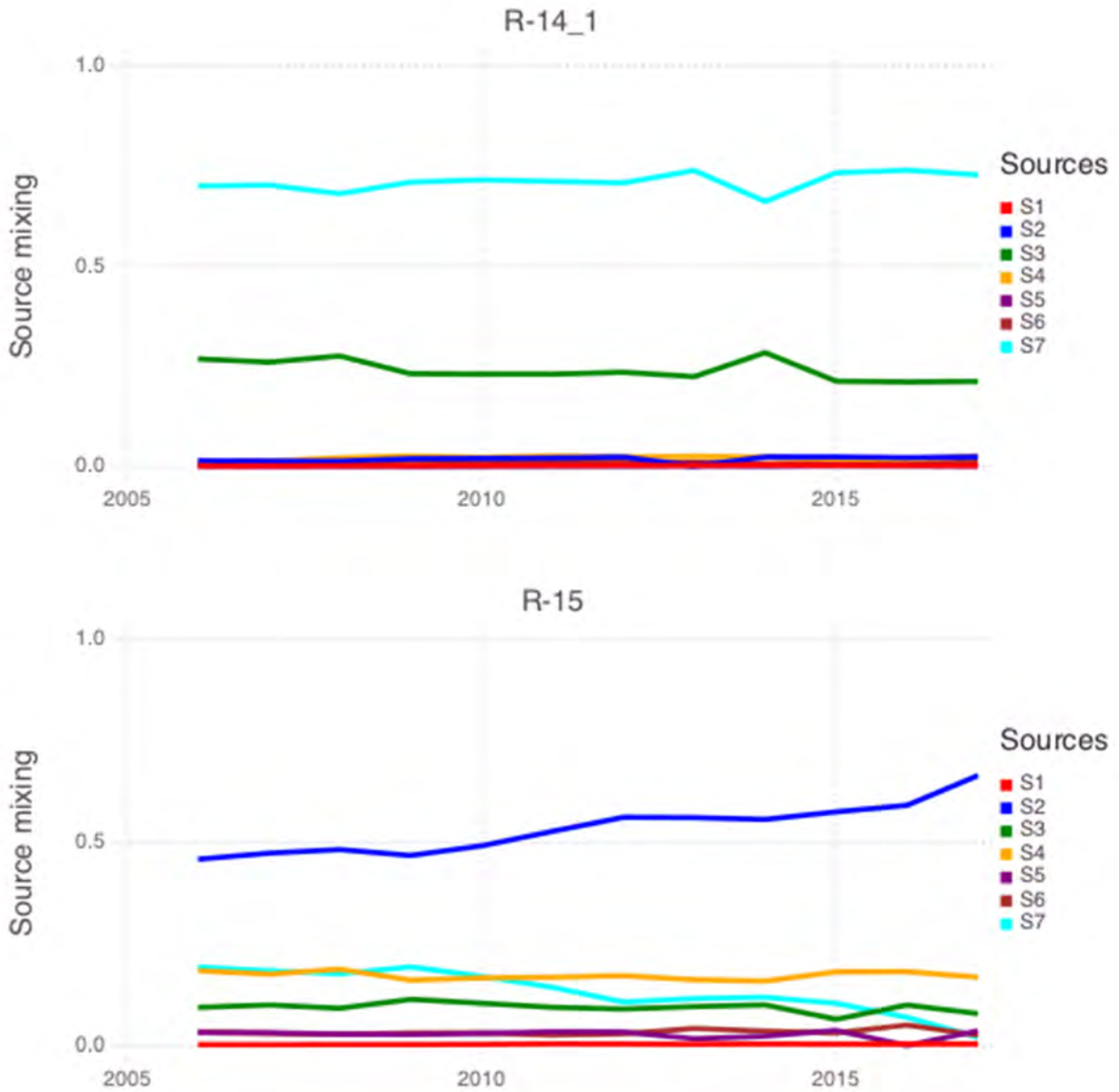


Figure 3.2-1 (continued) Transient mixing ratios of the seven groundwater types (sources) identified to be present at the site-monitoring wells. The mixing ratios add up to 1 for each time frame.

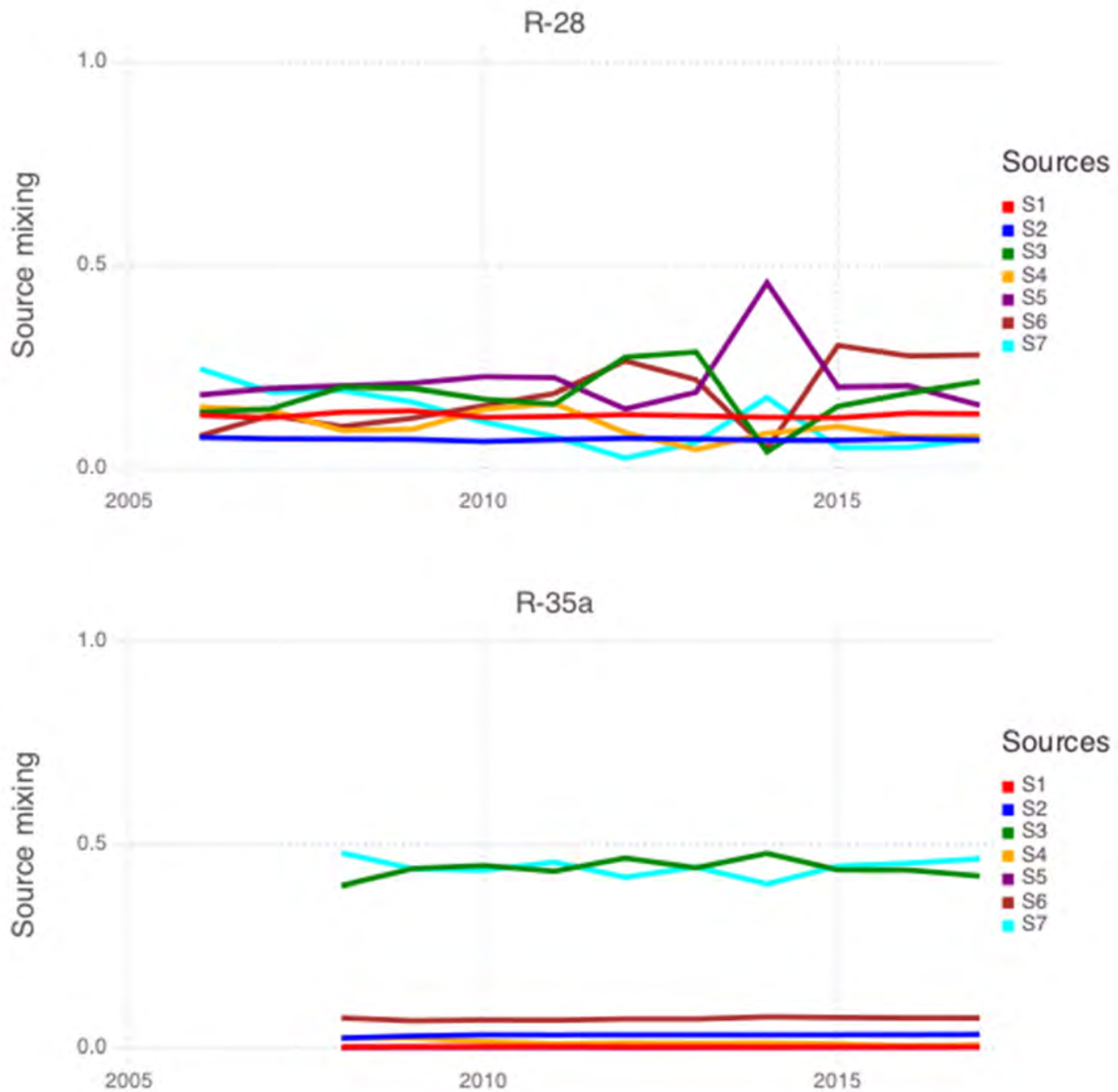


Figure 3.2-1 (continued) Transient mixing ratios of the seven groundwater types (sources) identified to be present at the site-monitoring wells. The mixing ratios add up to 1 for each time frame.

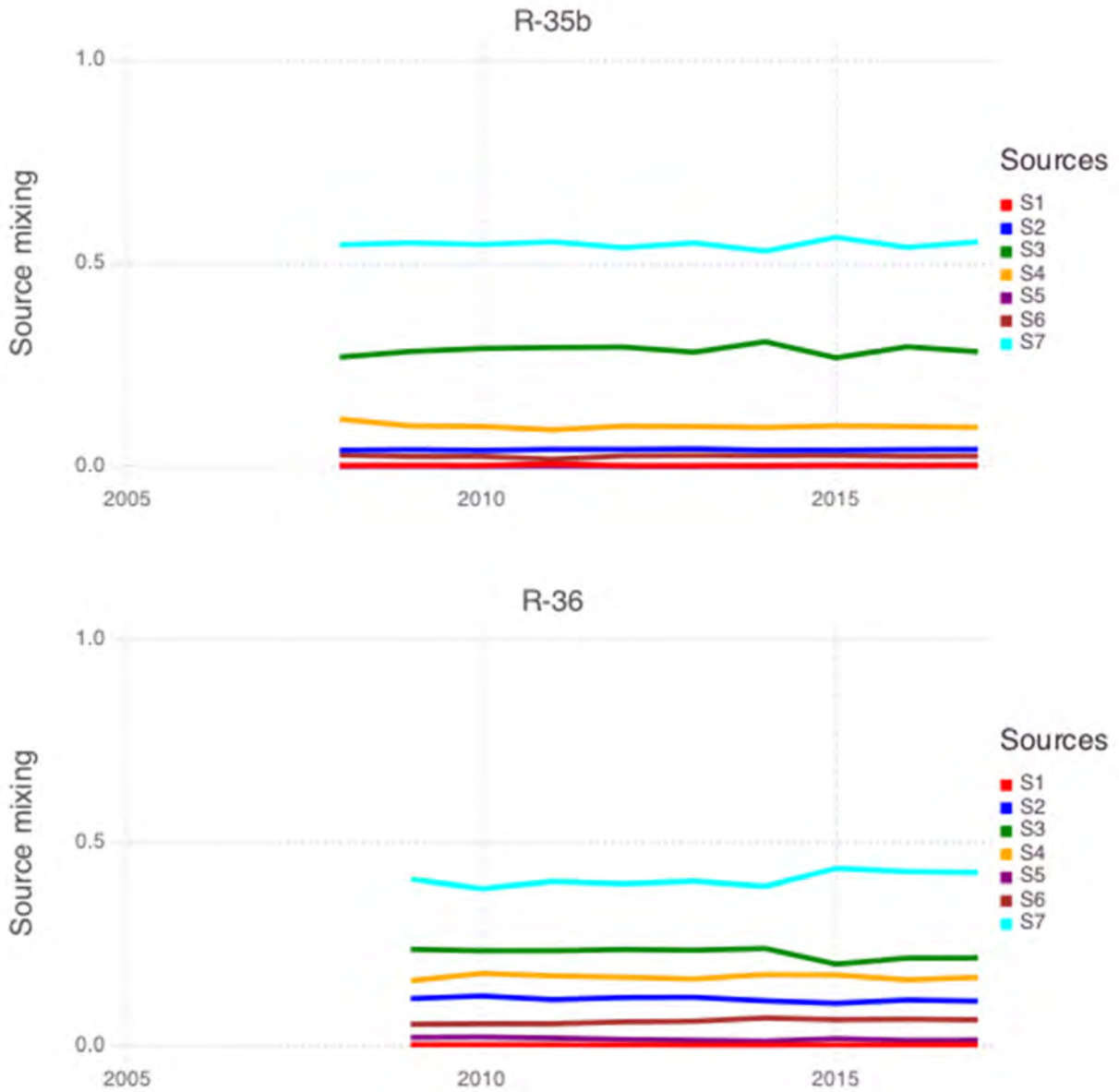


Figure 3.2-1 (continued) Transient mixing ratios of the seven groundwater types (sources) identified to be present at the site-monitoring wells. The mixing ratios add up to 1 for each time frame.

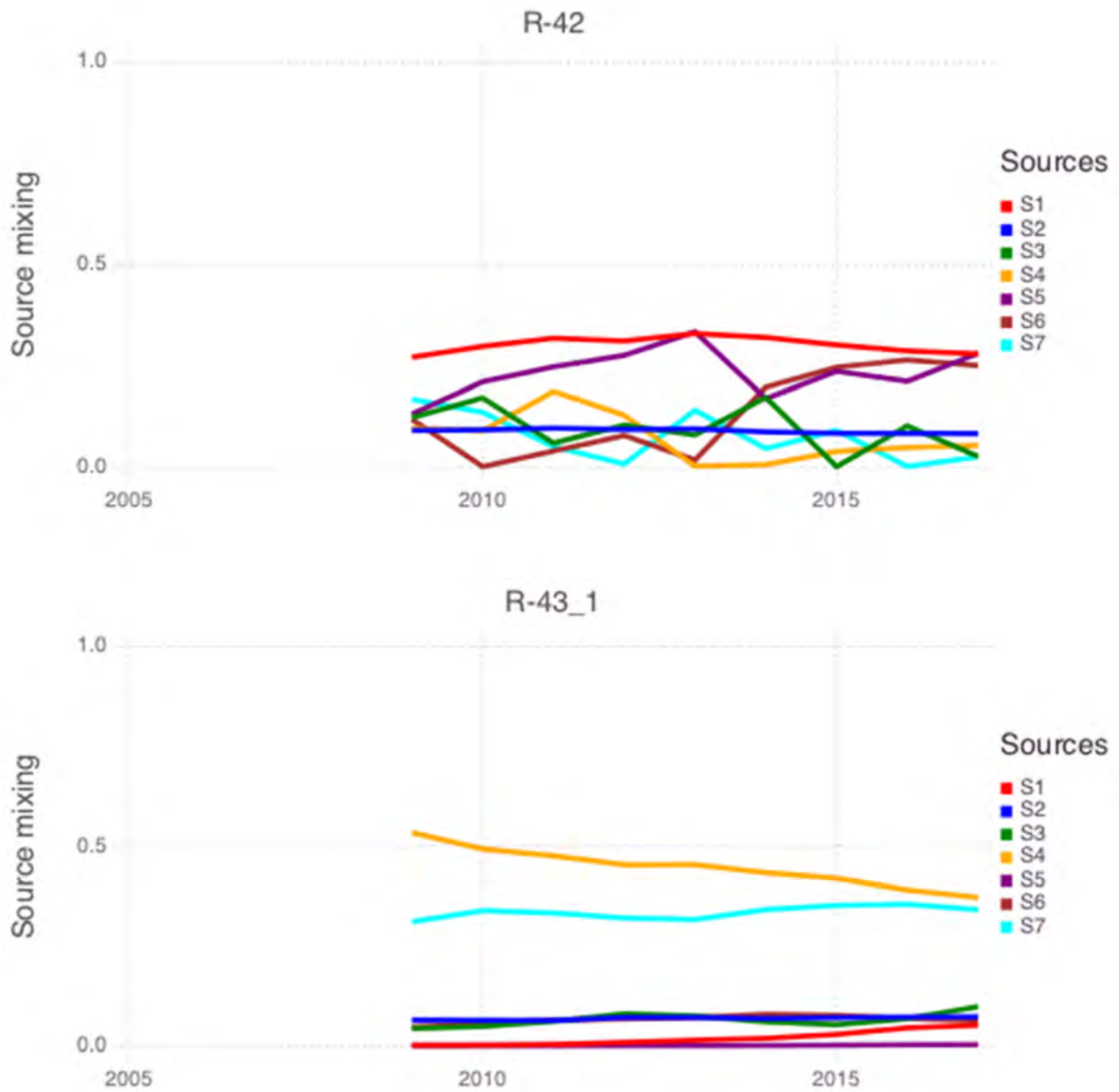


Figure 3.2-1 (continued) Transient mixing ratios of the seven groundwater types (sources) identified to be present at the site-monitoring wells. The mixing ratios add up to 1 for each time frame.

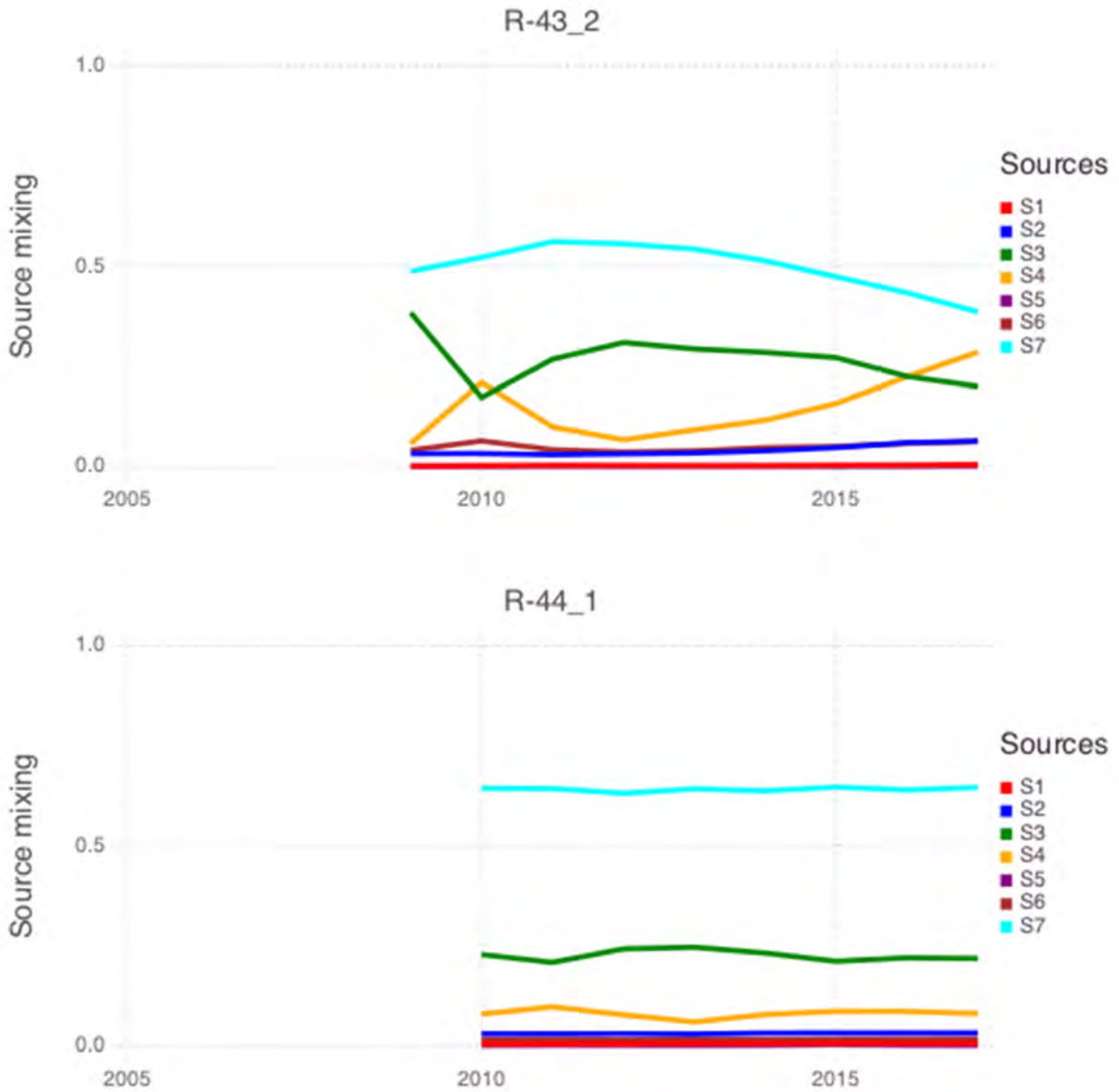


Figure 3.2-1 (continued) Transient mixing ratios of the seven groundwater types (sources) identified to be present at the site-monitoring wells. The mixing ratios add up to 1 for each time frame.

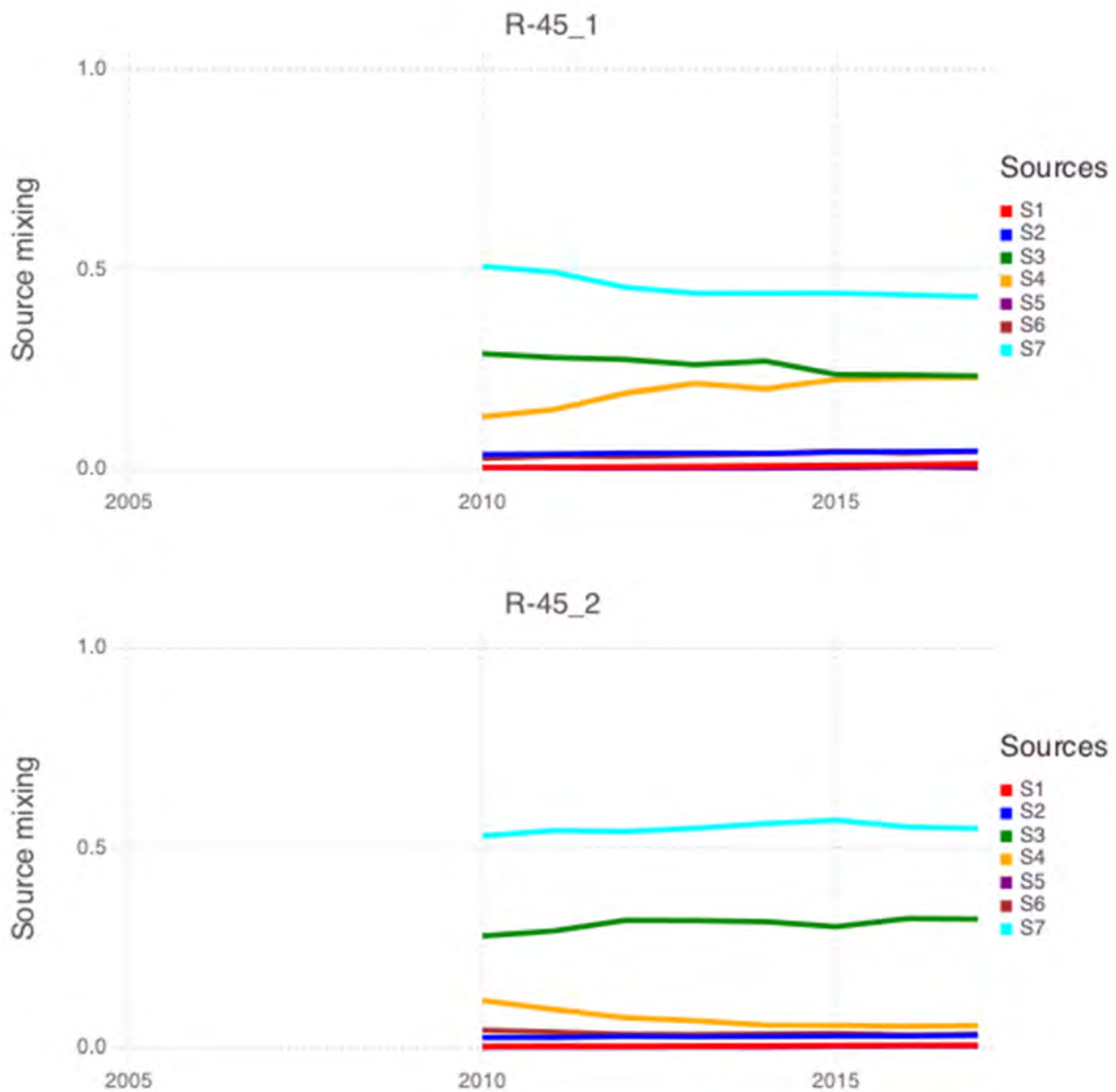


Figure 3.2-1 (continued) Transient mixing ratios of the seven groundwater types (sources) identified to be present at the site-monitoring wells. The mixing ratios add up to 1 for each time frame.

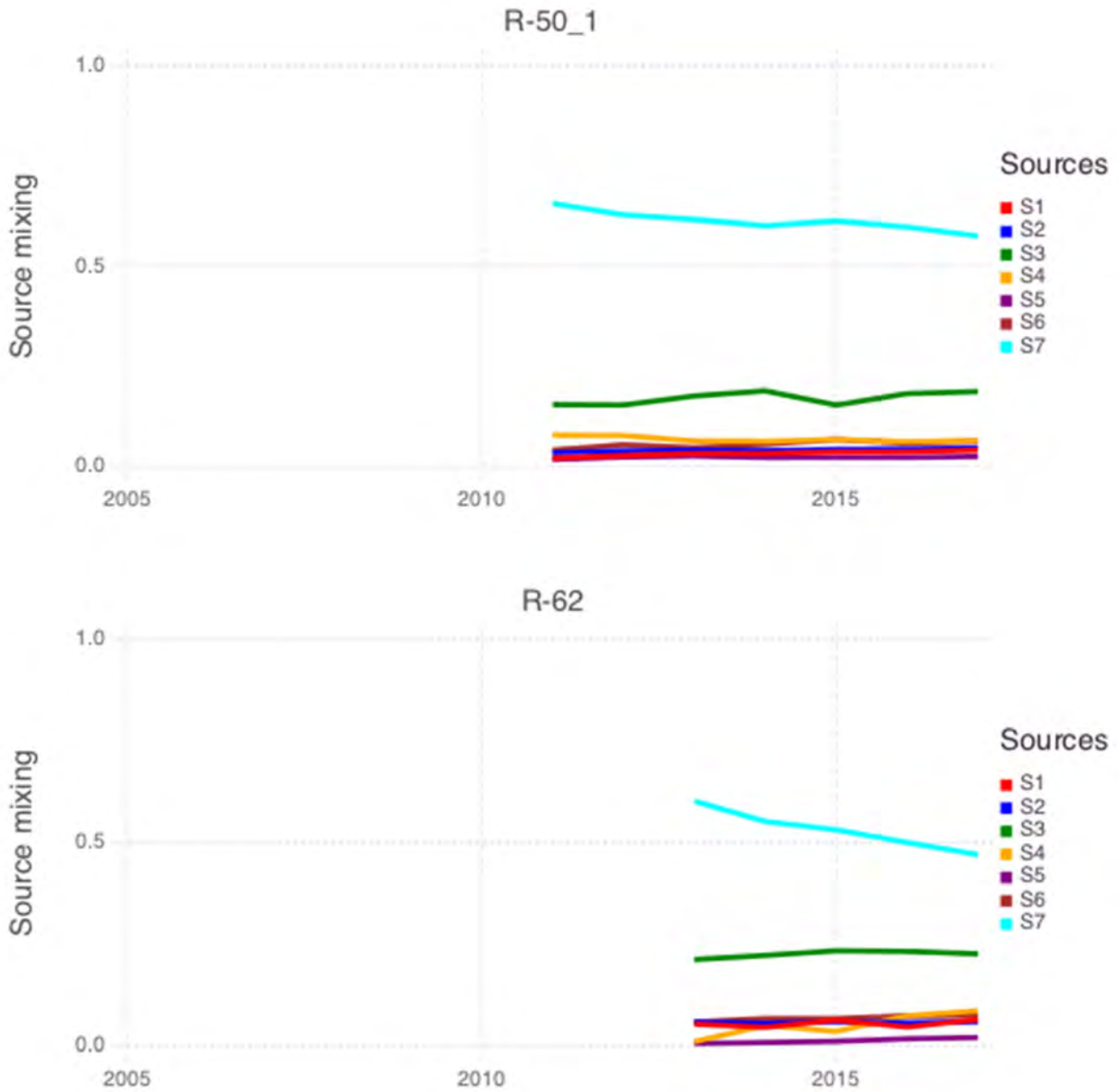


Figure 3.2-1 (continued) Transient mixing ratios of the seven groundwater types (sources) identified to be present at the site-monitoring wells. The mixing ratios add up to 1 for each time frame.

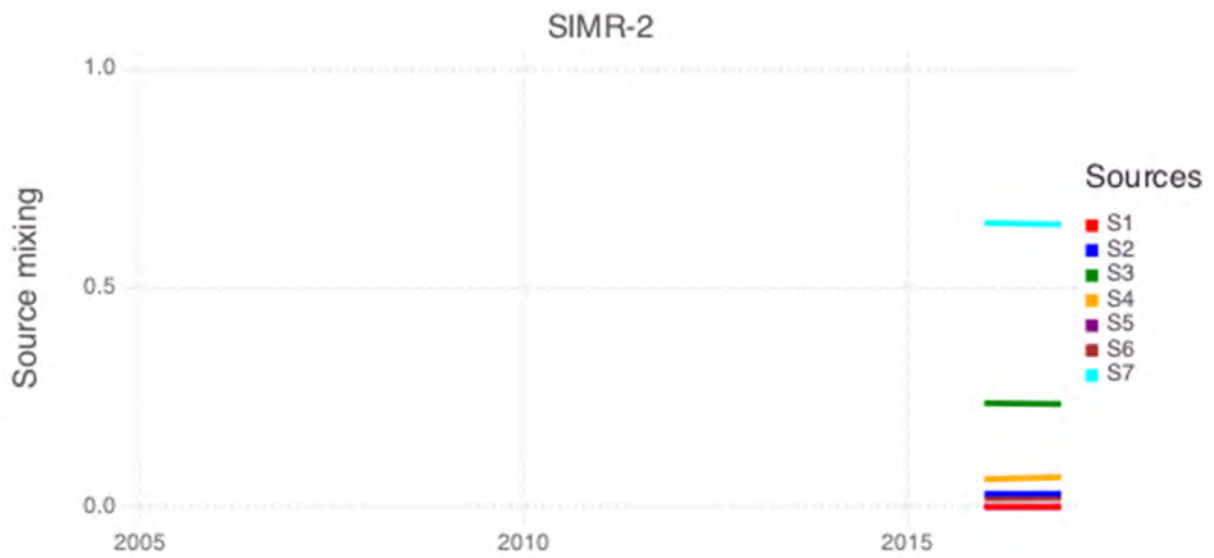


Figure 3.2-1 (continued) Transient mixing ratios of the seven groundwater types (sources) identified to be present at the site-monitoring wells. The mixing ratios add up to 1 for each time frame.

January 2005 – December 2005

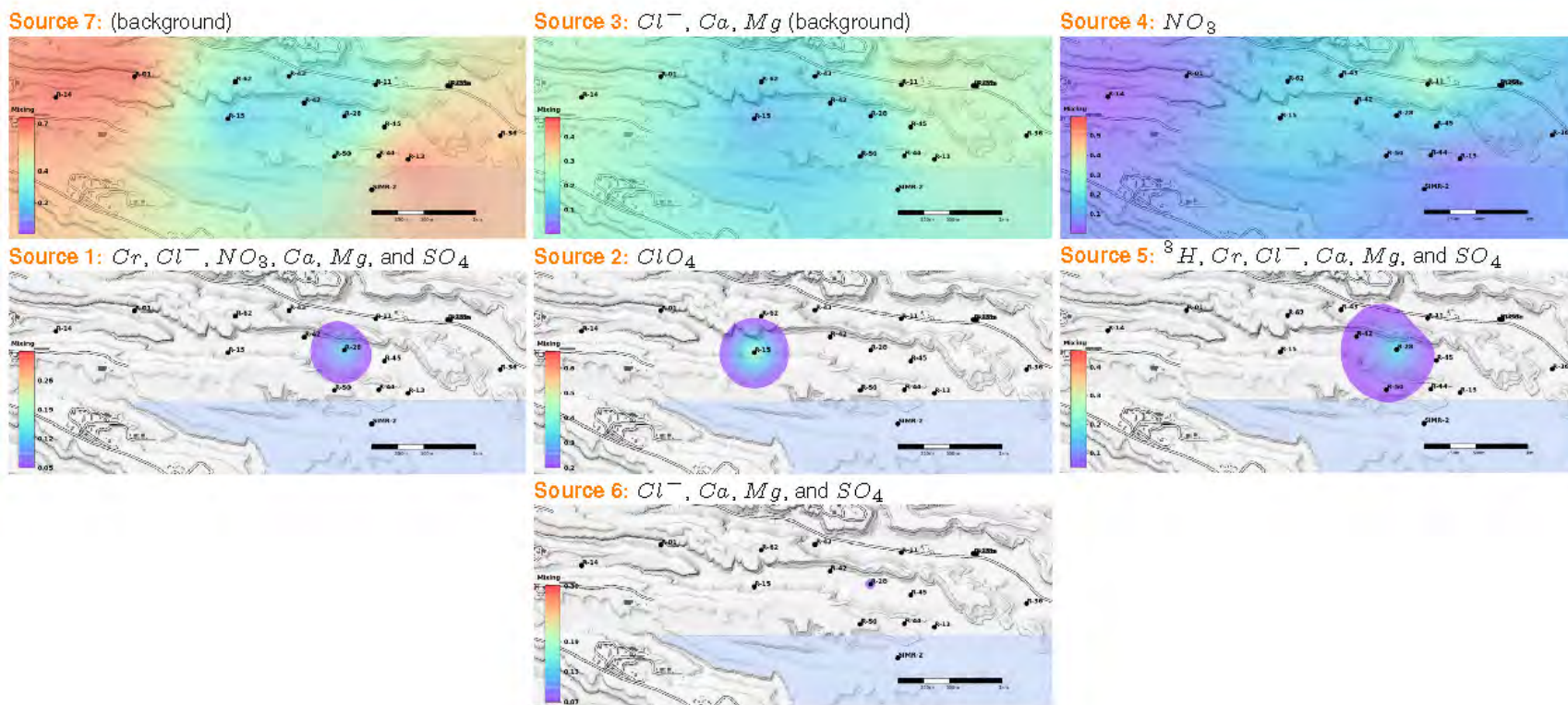
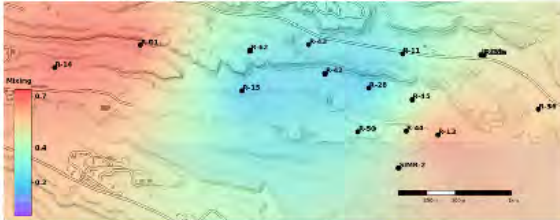


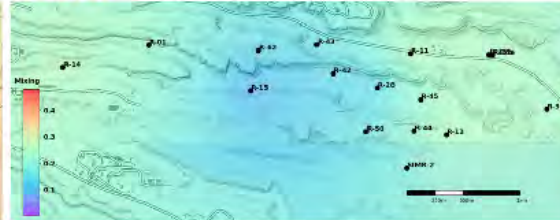
Figure 3.2-2 Spatial maps of transient mixing ratios of the seven groundwater types (sources) identified to be present at the site monitoring wells. The maps show the mixing ratio of each source (groundwater type). The mixing ratios are estimated at the wells and interpolated in space between the wells using an interpolation technique. The maps represent 12 temporal snapshots from 2005 to 2016.

January 2006 – December 2006

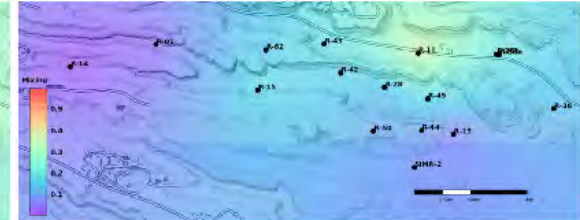
Source 7: (background)



Source 3: Cl^- , Ca , Mg (background)



Source 4: NO_3



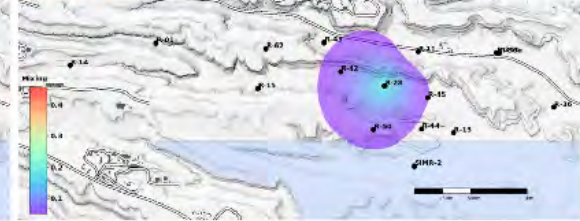
Source 1: Cr , Cl^- , NO_3 , Ca , Mg , and SO_4



Source 2: ClO_4



Source 5: 8H , Cr , Cl^- , Ca , Mg , and SO_4



Source 6: Cl^- , Ca , Mg , and SO_4

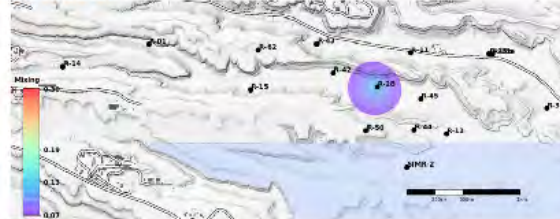
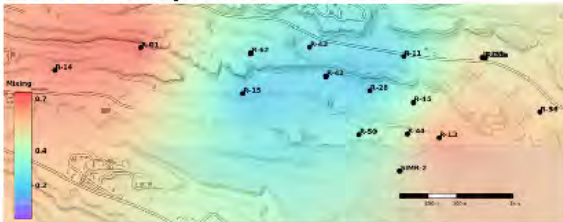


Figure 3.2-2 (continued)

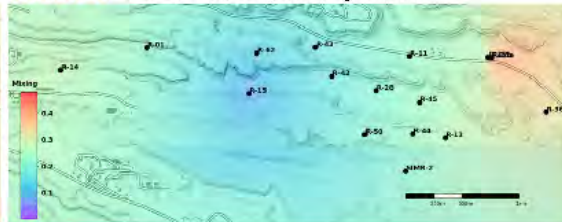
Spatial maps of transient mixing ratios of the seven groundwater types (sources) identified to be present at the site monitoring wells. The maps show the mixing ratio of each source (groundwater type). The mixing ratios are estimated at the wells and interpolated in space between the wells using an interpolation technique. The maps represent 12 temporal snapshots from 2005 to 2016.

January 2007 – December 2007

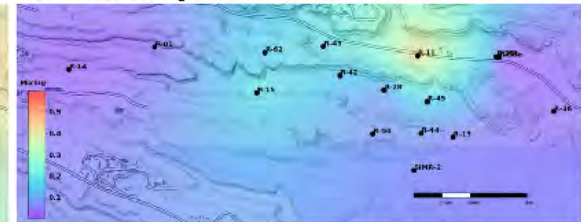
Source 7: (background)



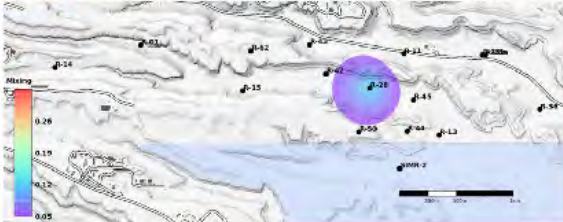
Source 3: Cl^- , Ca , Mg (background)



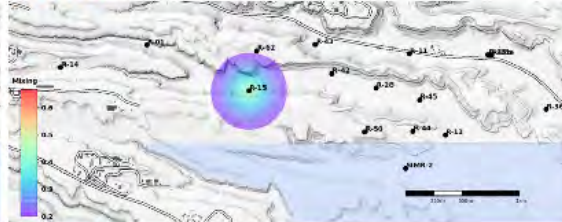
Source 4: NO_3



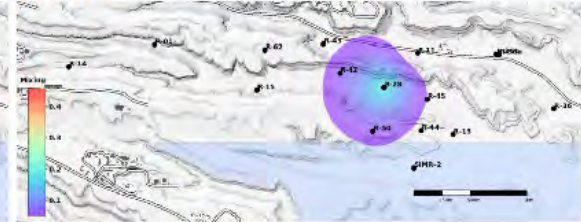
Source 1: Cr , Cl^- , NO_3 , Ca , Mg , and SO_4



Source 2: ClO_4



Source 5: 8H , Cr , Cl^- , Ca , Mg , and SO_4



Source 6: Cl^- , Ca , Mg , and SO_4

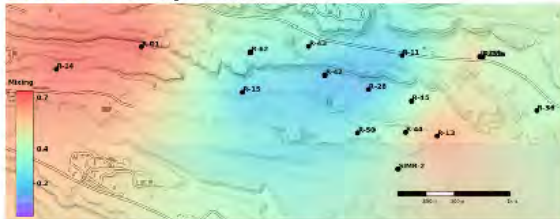


Figure 3.2-2 (continued)

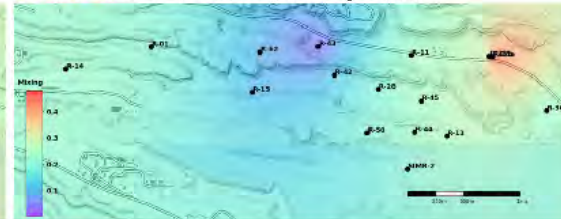
Spatial maps of transient mixing ratios of the seven groundwater types (sources) identified to be present at the site monitoring wells. The maps show the mixing ratio of each source (groundwater type). The mixing ratios are estimated at the wells and interpolated in space between the wells using an interpolation technique. The maps represent 12 temporal snapshots from 2005 to 2016.

January 2008 – December 2008

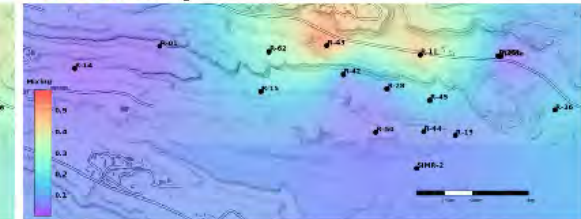
Source 7: (background)



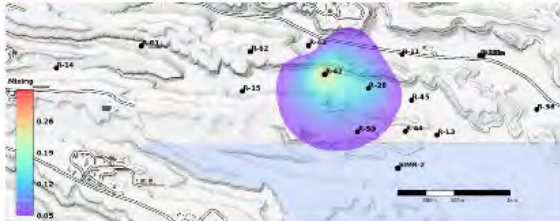
Source 3: Cl^- , Ca , Mg (background)



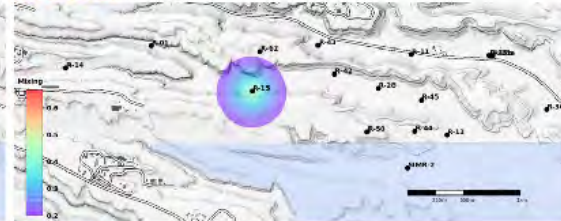
Source 4: NO_3



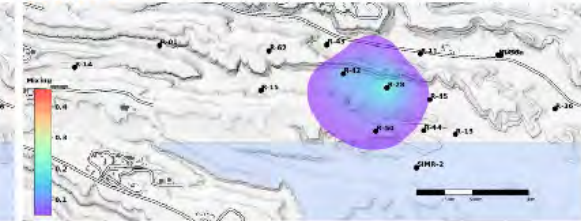
Source 1: Cr , Cl^- , NO_3 , Ca , Mg , and SO_4



Source 2: ClO_4



Source 5: 8H , Cr , Cl^- , Ca , Mg , and SO_4



Source 6: Cl^- , Ca , Mg , and SO_4

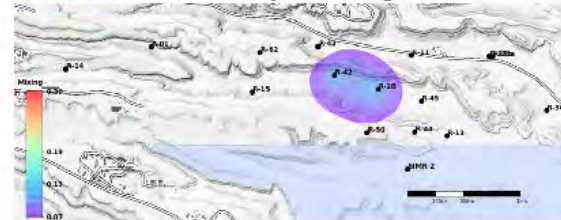
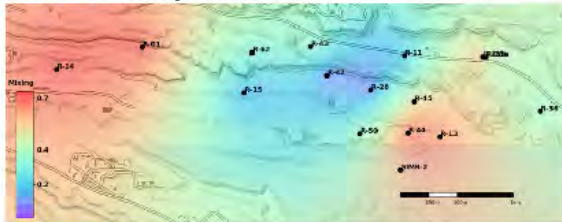


Figure 3.2-2 (continued)

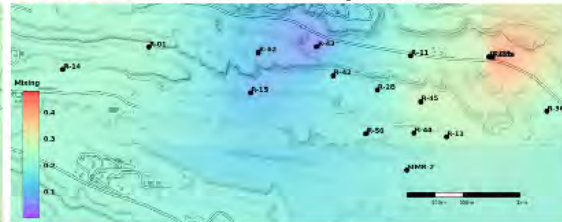
Spatial maps of transient mixing ratios of the seven groundwater types (sources) identified to be present at the site monitoring wells. The maps show the mixing ratio of each source (groundwater type). The mixing ratios are estimated at the wells and interpolated in space between the wells using an interpolation technique. The maps represent 12 temporal snapshots from 2005 to 2016.

January 2009 – December 2009

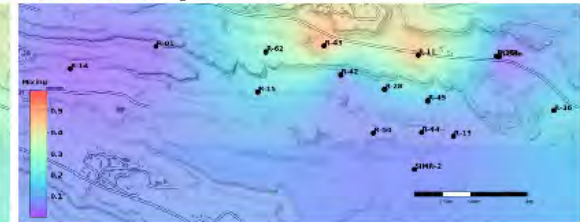
Source 7: (background)



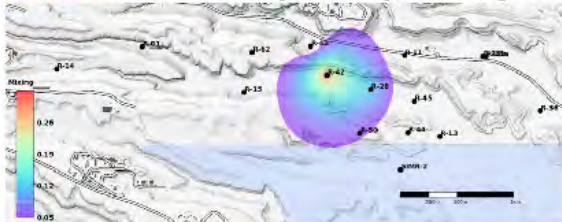
Source 3: Cl^- , Ca , Mg (background)



Source 4: NO_3



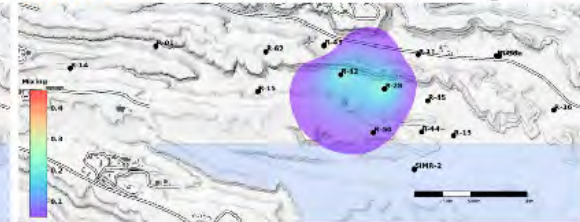
Source 1: Cr , Cl^- , NO_3 , Ca , Mg , and SO_4



Source 2: ClO_4



Source 5: 8H , Cr , Cl^- , Ca , Mg , and SO_4



Source 6: Cl^- , Ca , Mg , and SO_4



Figure 3.2-2 (continued)

Spatial maps of transient mixing ratios of the seven groundwater types (sources) identified to be present at the site monitoring wells. The maps show the mixing ratio of each source (groundwater type). The mixing ratios are estimated at the wells and interpolated in space between the wells using an interpolation technique. The maps represent 12 temporal snapshots from 2005 to 2016.

January 2010 – December 2010

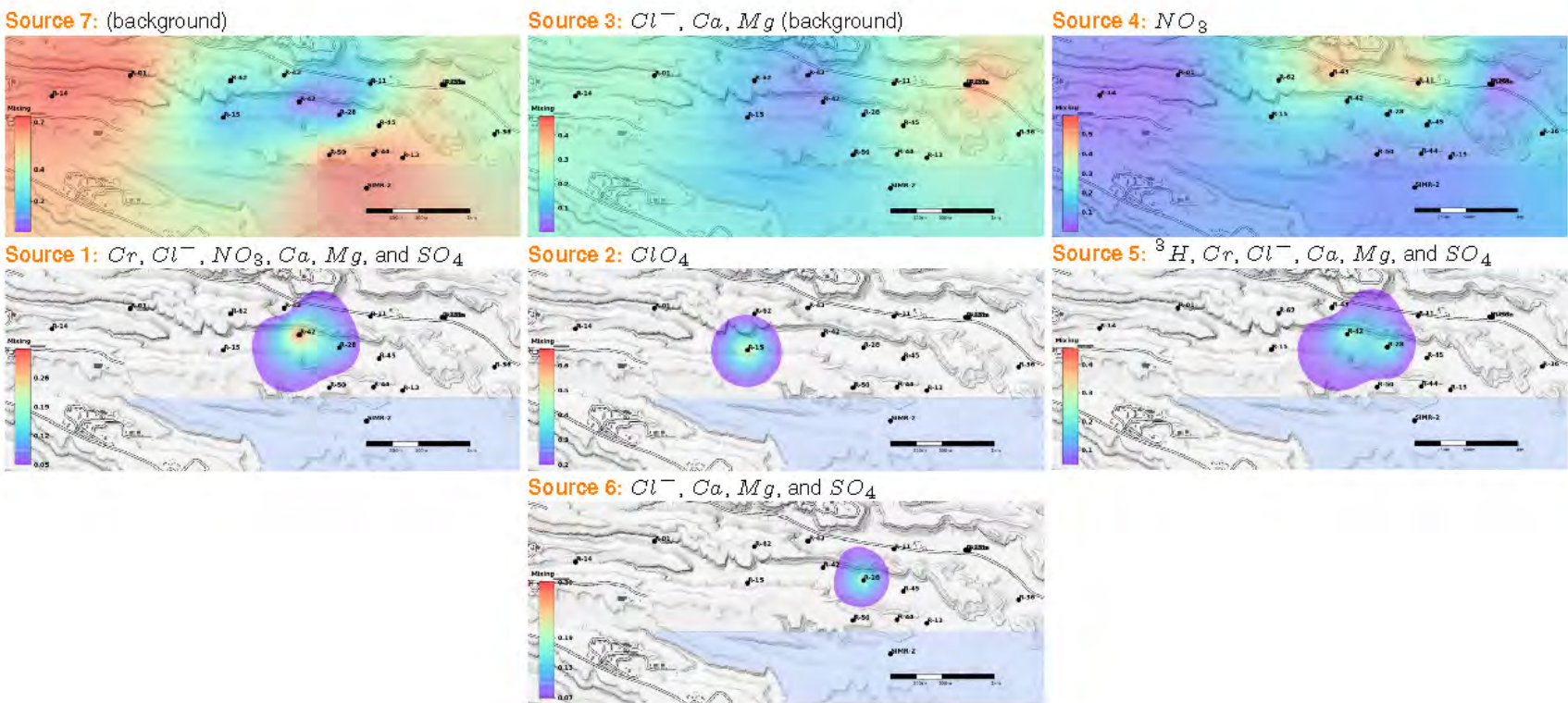
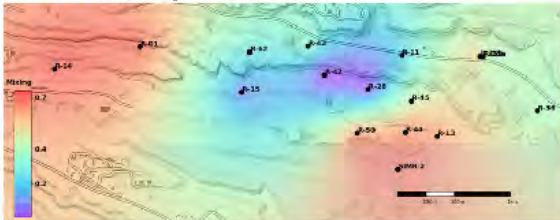


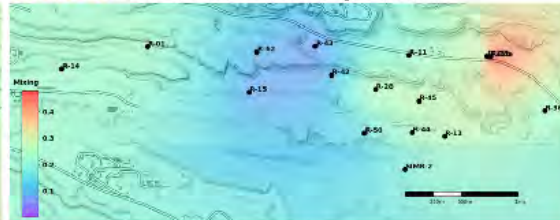
Figure 3.2-2 (continued) Spatial maps of transient mixing ratios of the seven groundwater types (sources) identified to be present at the site monitoring wells. The maps show the mixing ratio of each source (groundwater type). The mixing ratios are estimated at the wells and interpolated in space between the wells using an interpolation technique. The maps represent 12 temporal snapshots from 2005 to 2016.

January 2011 – December 2011

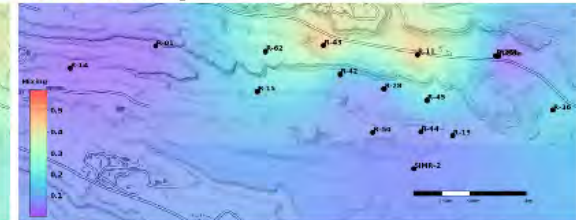
Source 7: (background)



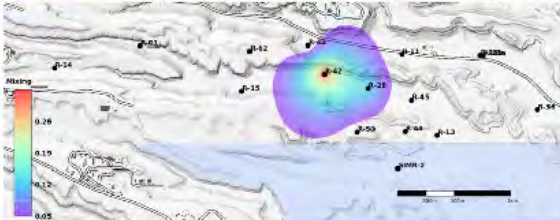
Source 3: Cl^- , Ca , Mg (background)



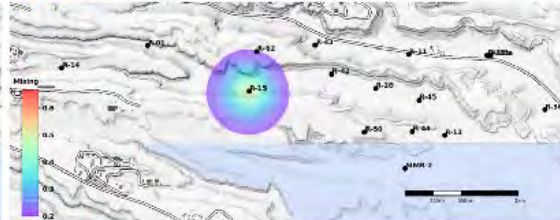
Source 4: NO_3



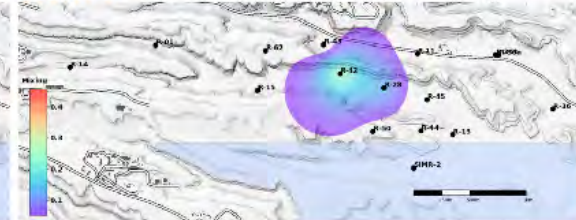
Source 1: Cr , Cl^- , NO_3 , Ca , Mg , and SO_4



Source 2: ClO_4



Source 5: 8H , Cr , Cl^- , Ca , Mg , and SO_4



Source 6: Cl^- , Ca , Mg , and SO_4

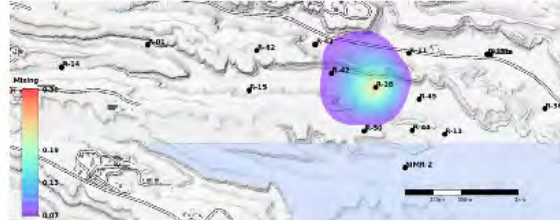
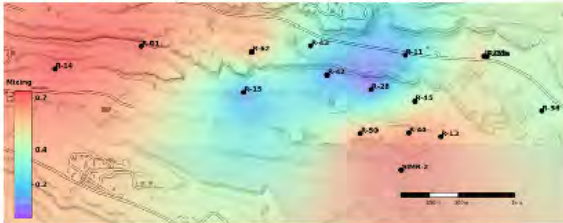


Figure 3.2-2 (continued)

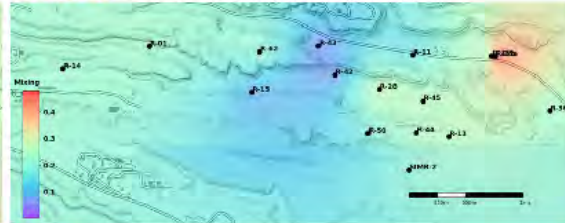
Spatial maps of transient mixing ratios of the seven groundwater types (sources) identified to be present at the site monitoring wells. The maps show the mixing ratio of each source (groundwater type). The mixing ratios are estimated at the wells and interpolated in space between the wells using an interpolation technique. The maps represent 12 temporal snapshots from 2005 to 2016.

January 2012 – December 2012

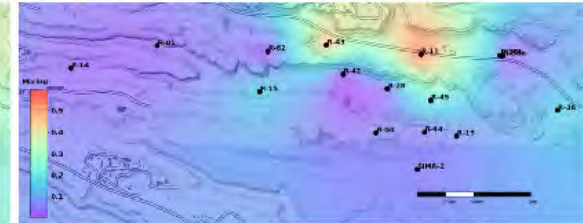
Source 7: (background)



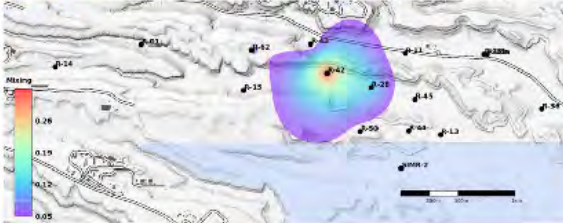
Source 3: Cl^- , Ca , Mg (background)



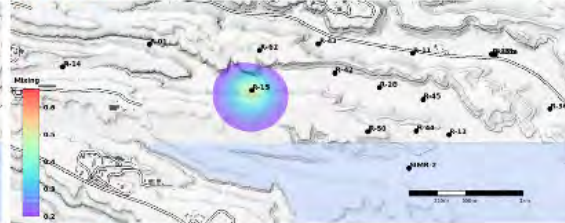
Source 4: NO_3



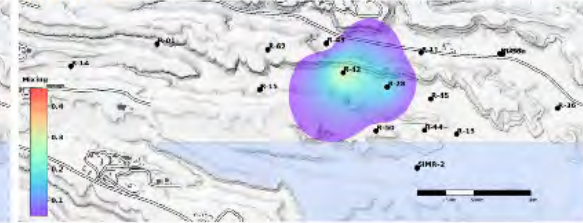
Source 1: Cr , Cl^- , NO_3 , Ca , Mg , and SO_4



Source 2: ClO_4



Source 5: 3H , Cr , Cl^- , Ca , Mg , and SO_4



Source 6: Cl^- , Ca , Mg , and SO_4

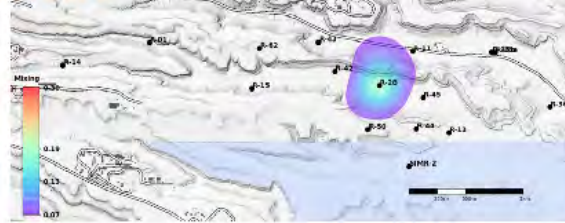
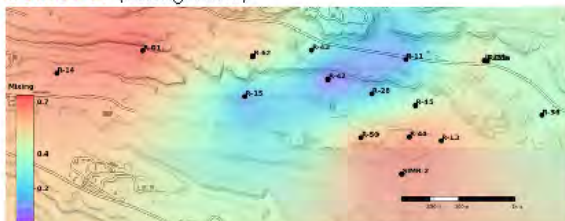


Figure 3.2-2 (continued)

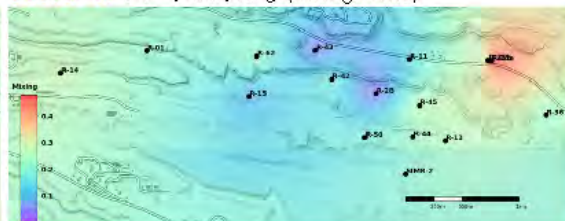
Spatial maps of transient mixing ratios of the seven groundwater types (sources) identified to be present at the site monitoring wells. The maps show the mixing ratio of each source (groundwater type). The mixing ratios are estimated at the wells and interpolated in space between the wells using an interpolation technique. The maps represent 12 temporal snapshots from 2005 to 2016.

January 2013 – December 2013

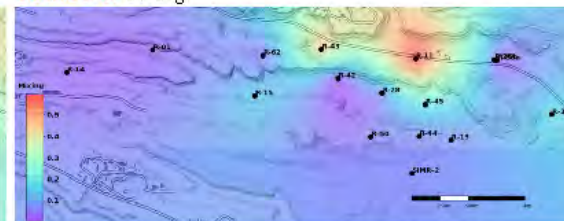
Source 7: (background)



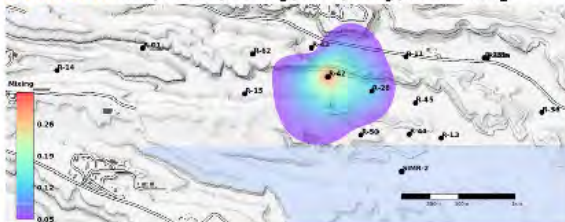
Source 3: Cl^- , Ca , Mg (background)



Source 4: NO_3



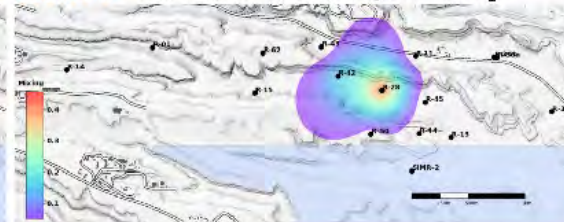
Source 1: Cr , Cl^- , NO_3 , Ca , Mg , and SO_4



Source 2: ClO_4



Source 5: 8H , Cr , Cl^- , Ca , Mg , and SO_4



Source 6: Cl^- , Ca , Mg , and SO_4

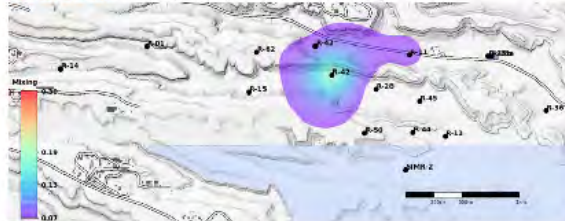
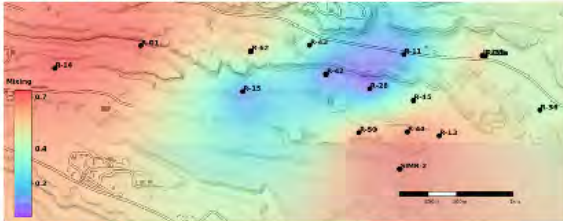


Figure 3.2-2 (continued)

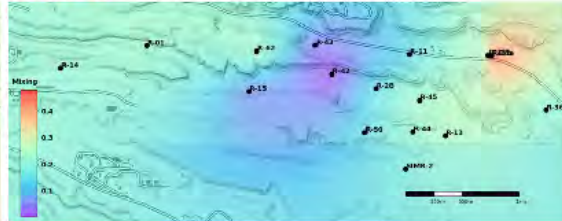
Spatial maps of transient mixing ratios of the seven groundwater types (sources) identified to be present at the site monitoring wells. The maps show the mixing ratio of each source (groundwater type). The mixing ratios are estimated at the wells and interpolated in space between the wells using an interpolation technique. The maps represent 12 temporal snapshots from 2005 to 2016.

January 2014 – December 2014

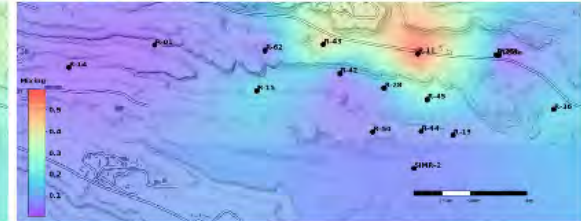
Source 7: (background)



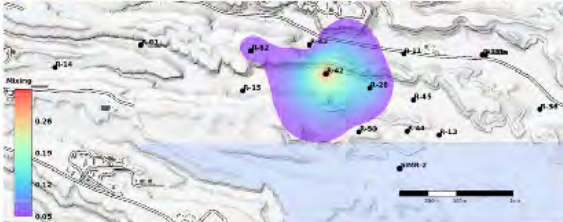
Source 3: Cl^- , Ca , Mg (background)



Source 4: NO_3



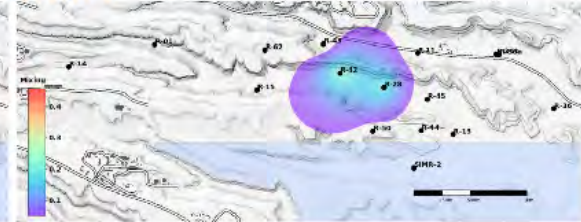
Source 1: Cr , Cl^- , NO_3 , Ca , Mg , and SO_4



Source 2: ClO_4



Source 5: 8H , Cr , Cl^- , Ca , Mg , and SO_4



Source 6: Cl^- , Ca , Mg , and SO_4

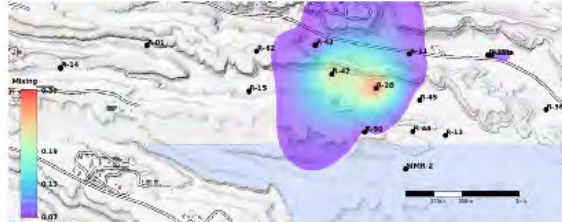
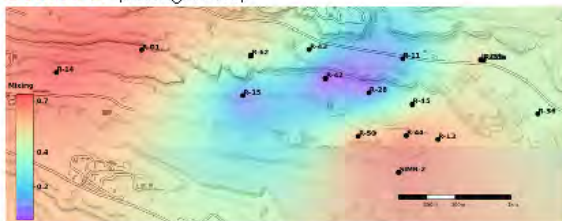


Figure 3.2-2 (continued)

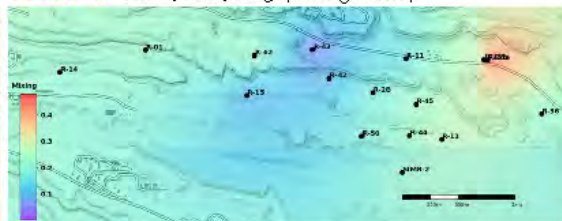
Spatial maps of transient mixing ratios of the seven groundwater types (sources) identified to be present at the site monitoring wells. The maps show the mixing ratio of each source (groundwater type). The mixing ratios are estimated at the wells and interpolated in space between the wells using an interpolation technique. The maps represent 12 temporal snapshots from 2005 to 2016.

January 2015 – December 2015

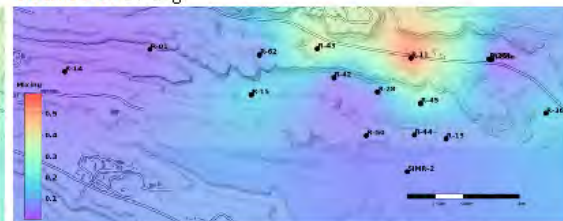
Source 7: (background)



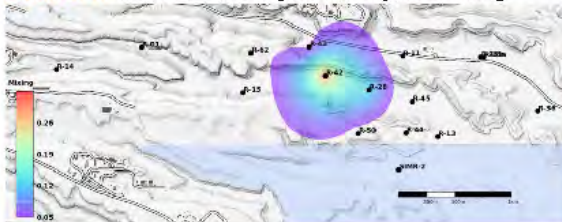
Source 3: Cl^- , Ca , Mg (background)



Source 4: NO_3



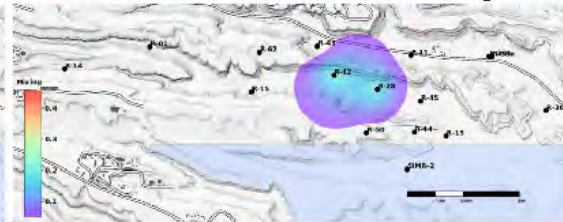
Source 1: Cr , Cl^- , NO_3 , Ca , Mg , and SO_4



Source 2: ClO_4



Source 5: 8H , Cr , Cl^- , Ca , Mg , and SO_4



Source 6: Cl^- , Ca , Mg , and SO_4

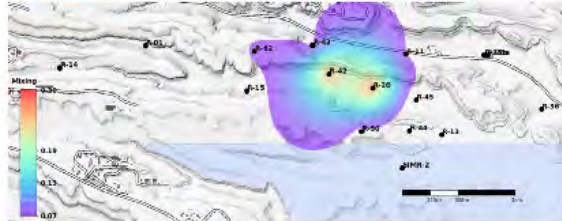
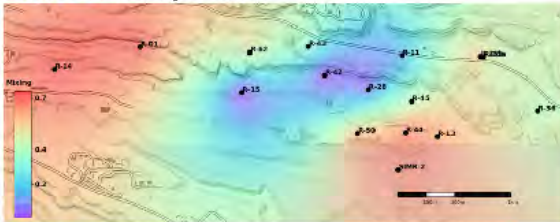


Figure 3.2-2 (continued)

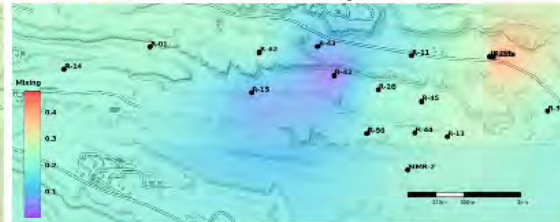
Spatial maps of transient mixing ratios of the seven groundwater types (sources) identified to be present at the site monitoring wells. The maps show the mixing ratio of each source (groundwater type). The mixing ratios are estimated at the wells and interpolated in space between the wells using an interpolation technique. The maps represent 12 temporal snapshots from 2005 to 2016.

January 2016 – December 2016

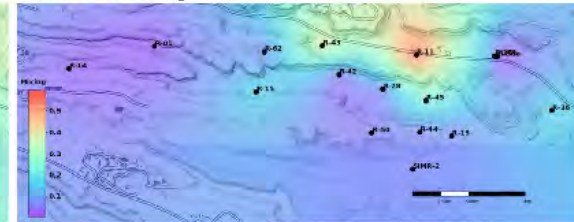
Source 7: (background)



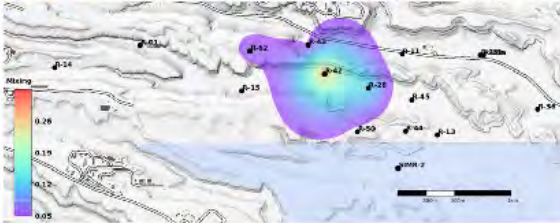
Source 3: Cl^- , Ca , Mg (background)



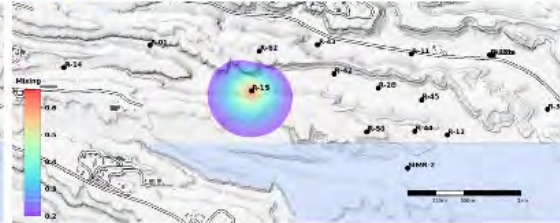
Source 4: NO_3



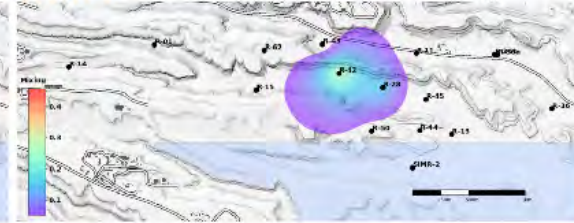
Source 1: Cr , Cl^- , NO_3 , Ca , Mg , and SO_4



Source 2: ClO_4



Source 5: 8H , Cr , Cl^- , Ca , Mg , and SO_4



Source 6: Cl^- , Ca , Mg , and SO_4

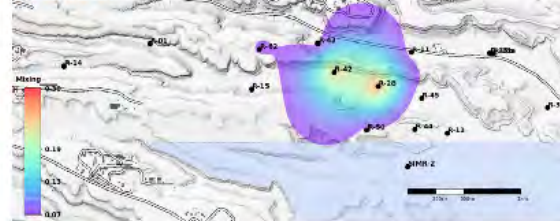


Figure 3.2-2 (continued)

Spatial maps of transient mixing ratios of the seven groundwater types (sources) identified to be present at the site monitoring wells. The maps show the mixing ratio of each source (groundwater type). The mixing ratios are estimated at the wells and interpolated in space between the wells using an interpolation technique. The maps represent 12 temporal snapshots from 2005 to 2016.

Table 3.0-1
Transient Geochemical Concentrations Applied in the NTFk Analysis

2005 Species								
Wells	Cr (µg/L)	Cl-(mg/L)	ClO4 (µg/L)	3H (pCi/L)	NO3 (mg/L)	Ca (mg/L)	Mg (mg/L)	SO4 (mg/L)
R-67	—*	—	—	—	—	—	—	—
R-14 S1	1.6	1.5	0.2	0.7	0.1	12.0	3.5	1.4
R-1	5.0	1.9	0.3	0.1	0.2	11.5	4.0	3.4
R-15	7.8	4.4	6.4	30.6	2.4	14.2	3.9	6.6
R-62	—	—	—	—	—	—	—	—
R-43 S1	—	—	—	—	—	—	—	—
R-43 S2	—	—	—	—	—	—	—	—
R-42	—	—	—	—	—	—	—	—
R-28	392.0	23.0	1.0	171.8	4.0	35.1	8.9	38.6
R-50 S1	—	—	—	—	—	—	—	—
R-11	20.0	3.6	0.7	7.1	3.6	20.9	5.6	6.3
R-45 S1	—	—	—	—	—	—	—	—
R-45 S2	—	—	—	—	—	—	—	—
R-44 S1	—	—	—	—	—	—	—	—
SIMR-2	—	—	—	—	—	—	—	—
R-13	—	2.2	0.4	0.4	0.6	—	—	3.1
R-35a	—	—	—	—	—	—	—	—
R-35b	—	—	—	—	—	—	—	—
R-36	—	—	—	—	—	—	—	—
2006 Species								
Wells	Cr (µg/L)	Cl-(mg/L)	ClO4 (µg/L)	3H (pCi/L)	NO3 (mg/L)	Ca (mg/L)	Mg (mg/L)	SO4 (mg/L)
R-67	—	—	—	—	—	—	—	—
R-14 S1	2.4	1.7	0.2	0.0	0.1	11.9	3.5	1.8
R-1	5.2	2.0	0.3	0.4	0.2	11.6	4.1	3.1
R-15	7.7	4.3	6.6	30.2	2.4	14.2	3.9	6.2
R-62	—	—	—	—	—	—	—	—
R-43 S1	—	—	—	—	—	—	—	—
R-43 S2	—	—	—	—	—	—	—	—
R-42	—	—	—	—	—	—	—	—
R-28	373.8	27.0	1.0	186.3	4.4	38.3	9.7	41.3
R-50 S1	—	—	—	—	—	—	—	—
R-11	27.7	4.2	0.7	9.9	4.4	20.9	5.6	7.7
R-45 S1	—	—	—	—	—	—	—	—
R-45 S2	—	—	—	—	—	—	—	—
R-44 S1	—	—	—	—	—	—	—	—
SIMR-2	—	—	—	—	—	—	—	—
R-13	4.5	2.2	0.4	0.1	0.7	13.3	3.3	3.0
R-35a	—	—	—	—	—	—	—	—
R-35b	—	—	—	—	—	—	—	—
R-36	—	—	—	—	—	—	—	—

Table 3.0-1 (continued)

2007 Species								
Wells	Cr (µg/L)	Cl-(mg/L)	ClO4 (µg/L)	3H (pCi/L)	NO3 (mg/L)	Ca (mg/L)	Mg (mg/L)	SO4 (mg/L)
R-67								
R-14 S1	3.8	1.6	0.2	0.2	0.1	12.7	3.6	1.8
R-1	7.0	1.9	0.3	0.1	0.3	11.0	3.9	2.8
R-15	8.6	4.1	6.7	26.8	2.6	13.8	3.8	5.9
R-62	–	–	–	–	–	–	–	–
R-43 S1	–	–	–	–	–	–	–	–
R-43 S2	–	–	–	–	–	–	–	–
R-42	–	–	–	–	–	–	–	–
R-28	414.8	27.2	1.0	191.9	4.6	39.4	10.1	41.0
R-50 S1	–	–	–	–	–	–	–	–
R-11	30.6	4.3	0.7	10.1	5.1	21.7	5.9	8.7
R-45 S1	–	–	–	–	–	–	–	–
R-45 S2	–	–	–	–	–	–	–	–
R-44 S1	–	–	–	–	–	–	–	–
SIMR-2	–	–	–	–	–	–	–	–
R-13	5.2	2.2	0.4	0.0	0.6	13.6	3.4	2.9
R-35a	4.2	6.5	0.3	0.3	0.7	21.0	5.3	5.7
R-35b	6.1	2.8	0.6	0.2	1.2	15.4	4.6	4.1
R-36	–	–	–	–	–	–	–	–
2008 Species								
Wells	Cr (µg/L)	Cl-(mg/L)	ClO4 (µg/L)	3H (pCi/L)	NO3 (mg/L)	Ca (mg/L)	Mg (mg/L)	SO4 (mg/L)
R-67	–	–	–	–	–	–	–	–
R-14 S1	3.3	1.7	0.3	0.0	0.2	11.2	3.4	2.2
R-1	6.2	1.9	0.4	0.0	0.4	10.7	3.7	2.6
R-15	8.6	4.1	6.5	25.9	2.1	14.2	3.8	6.0
R-62	–	–	–	–	–	–	–	–
R-43 S1	3.0	3.6	0.9	0.5	6.0	16.0	3.7	8.8
R-43 S2	1.8	4.0	0.4	0.1	0.7	19.4	4.9	
R-42	808.0	32.3	1.2	125.1	5.9	42.3	11.8	61.8
R-28	424.5	28.5	1.0	197.8	4.2	41.1	10.4	43.7
R-50 S1	–	–	–	–	–	–	–	–
R-11	19.6	4.0	0.8	4.0	5.2	22.1	6.1	8.3
R-45 S1	–	–	–	–	–	–	–	–
R-45 S2	–	–	–	–	–	–	–	–
R-44 S1	–	–	–	–	–	–	–	–
SIMR-2	–	–	–	–	–	–	–	–
R-13	5.3	2.2	0.4	0.0	0.8	13.8	3.4	3.0
R-35a	5.8	6.1	0.4	0.1	0.6	22.3	5.8	5.4
R-35b	6.2	2.8	0.6	0.6	1.2	15.3	5.0	3.6
R-36	7.3	5.8	1.6	19.2	2.3	18.2	4.3	6.7

Table 3.0-1 (continued)

2009 Species								
Wells	Cr (µg/L)	Cl-(mg/L)	ClO4 (µg/L)	3H (pCi/L)	NO3 (mg/L)	Ca (mg/L)	Mg (mg/L)	SO4 (mg/L)
R-67	–	–	–	–	–	–	–	–
R-14 S1	4.8	1.7	0.3	0.0	0.3	11.0	3.3	2.0
R-1	6.6	1.8	0.3	0.1	0.4	11.5	4.1	2.4
R-15	9.7	4.2	6.8	28.7	2.1	14.3	3.9	6.4
R-62	–	–	–	–	–	–	–	–
R-43 S1	3.6	4.2	0.9	0.5	5.6	15.8	3.5	9.0
R-43 S2	4.0	3.8	0.5	0.1	1.3	15.4	3.5	8.1
R-42	889.0	30.9	1.2	200.0	6.4	45.4	12.6	61.9
R-28	377.3	29.7	0.9	213.3	4.1	42.5	10.7	44.9
R-50 S1	–	–	–	–	–	–	–	–
R-11	16.9	3.9	0.8	5.8	5.3	22.4	6.2	8.4
R-45 S1	13.2	3.2	0.5	3.7	1.5	16.9	4.6	4.7
R-45 S2	8.1	3.1	0.4	0.7	0.4	16.8	4.6	6.0
R-44 S1	11.2	2.1	0.4	0.6	1.0	12.5	3.6	3.0
SIMR-2	–	–	–	–	–	–	–	–
R-13	7.9	2.2	0.4	0.0	0.7	13.6	3.5	3.0
R-35a	6.4	6.3	0.4	0.1	0.5	22.6	5.7	5.4
R-35b	6.0	2.8	0.6	0.1	1.2	15.6	4.9	3.5
R-36	7.7	5.8	1.7	19.9	2.3	18.6	4.2	7.1
2010 Species								
Wells	Cr (µg/L)	Cl-(mg/L)	ClO4 (µg/L)	3H (pCi/L)	NO3 (mg/L)	Ca (mg/L)	Mg (mg/L)	SO4 (mg/L)
R-67	–	–	–	–	–	–	–	–
R-14 S1	5.6	1.6	0.3	0.4	0.3	11.0	3.5	2.0
R-1	6.7	1.8	0.3	0.0	0.4	11.5	4.1	2.5
R-15	13.6	4.1	7.3	32.3	2.2	14.2	3.8	6.4
R-62	–	–	–	–	–	–	–	–
R-43 S1	9.3	4.9	0.9	0.0	5.5	16.6	3.8	9.8
R-43 S2	5.5	3.5	0.4	0.6	0.9	15.6	4.5	5.0
R-42	949.8	34.4	1.4	235.0	6.1	48.9	13.7	72.4
R-28	384.3	31.3	1.0	210.8	4.1	43.8	11.2	47.6
R-50 S1	61.4	5.3	0.5	16.1	1.2	13.1	4.0	8.5
R-11	18.0	3.8	0.8	4.8	4.9	21.8	5.9	8.6
R-45 S1	15.5	3.5	0.5	2.4	1.6	17.2	4.7	5.3
R-45 S2	9.9	3.2	0.4	1.3	0.5	16.7	4.7	5.3
R-44 S1	13.2	2.1	0.4	1.0	1.1	12.3	3.4	3.5
SIMR-2	–	–	–	–	–	–	–	–
R-13	6.4	2.2	0.4	2.9	0.8	13.7	3.4	3.1
R-35a	7.1	6.2	0.4	0.1	0.5	21.9	5.6	5.3
R-35b	17.2	2.7	0.6	0.2	1.3	15.4	5.0	3.5
R-36	6.8	5.7	1.6	17.7	2.3	18.2	4.2	6.9

Table 3.0-1 (continued)

2011 Species								
Wells	Cr (µg/L)	Cl-(mg/L)	ClO4 (µg/L)	3H (pCi/L)	NO3 (mg/L)	Ca (mg/L)	Mg (mg/L)	SO4 (mg/L)
R-67	–	–	–	–	–	–	–	–
R-14 S1	6.4	1.7	0.3	0.4	0.3	11.1	3.4	1.9
R-1	5.1	1.9	0.4	0.0	0.3	11.7	4.0	2.4
R-15	12.4	4.3	7.8	31.9	2.2	14.3	3.8	6.6
R-62	–	–	–	–	–	–	–	–
R-43 S1	25.0	5.6	1.0	0.1	5.4	17.4	4.0	10.6
R-43 S2	6.1	3.5	0.4	0.2	0.7	16.4	4.4	4.1
R-42	930.0	38.5	1.3	261.8	6.1	52.7	14.6	74.1
R-28	395.8	33.6	1.0	138.8	3.8	46.3	11.6	48.8
R-50 S1	80.1	6.9	0.5	21.8	1.4	14.5	4.4	10.8
R-11	17.8	4.5	0.8	3.9	5.2	21.9	6.2	9.1
R-45 S1	18.1	3.7	0.6	2.0	2.3	17.8	4.9	5.6
R-45 S2	9.1	3.3	0.4	0.9	0.7	17.0	4.8	4.3
R-44 S1	13.7	2.2	0.4	0.7	1.0	13.1	3.7	3.1
SIMR-2	–	–	–	–	–	–	–	–
R-13	4.3	2.3	0.4	0.0	0.8	14.1	3.5	3.1
R-35a	5.3	6.3	0.4	0.0	0.3	23.4	6.0	5.6
R-35b	5.4	2.8	0.6	0.0	1.2	15.8	5.0	3.6
R-36	6.5	5.9	1.6	14.1	2.3	18.3	4.2	6.9
2012 Species								
Wells	Cr (µg/L)	Cl-(mg/L)	ClO4 (µg/L)	3H (pCi/L)	NO3 (mg/L)	Ca (mg/L)	Mg (mg/L)	SO4 (mg/L)
R-67	–	–	–	–	–	–	–	–
R-14 S1	5.7	1.6		0.8	0.3	10.6	3.5	2.0
R-1	4.3	2.0	0.3	1.8	0.3	11.3	4.1	2.4
R-15	10.5	4.2	7.8	15.9	2.0	13.9	3.9	6.5
R-62	158.0	8.3	0.8	5.0	1.1	16.7	4.6	13.9
R-43 S1	40.9	6.1	1.0	0.2	5.5	17.8	4.0	11.8
R-43 S2	3.4	3.7	0.5	0.4	1.2	16.3	4.6	4.2
R-42	985.8	39.4	1.3	317.0	5.7	51.2	14.4	74.2
R-28	388.0	32.9	1.0	178.0	3.6	46.0	11.7	46.5
R-50 S1	95.5	7.3	0.6	24.3	1.6	15.3	4.7	10.9
R-11	21.5	4.9	0.9	5.4	5.6	22.7	6.2	12.2
R-45 S1	21.0	3.9	0.6	2.1	2.6	18.0	5.1	6.2
R-45 S2	11.2	3.4	0.4	1.6	0.7	16.8	4.9	4.3
R-44 S1	16.0	2.3	0.4	0.5	0.7	13.1	3.7	3.3
SIMR-2	–	–	–	–	–	–	–	–
R-13	4.2	2.4	0.4	1.0	0.7	13.9	3.5	3.2
R-35a	5.2	6.3	0.4	0.0	0.4	22.3	6.0	5.5
R-35b	4.7	2.9	0.6	0.0	1.2	15.3	5.1	3.6
R-36	5.3	5.8	1.6	12.3	2.3	18.0	4.4	6.9

Table 3.0-1 (continued)

2013 Species								
Wells	Cr (µg/L)	Cl-(mg/L)	ClO4 (µg/L)	3H (pCi/L)	NO3 (mg/L)	Ca (mg/L)	Mg (mg/L)	SO4 (mg/L)
R-67	–	–	–	–	–	–	–	–
R-14 S1		1.7	0.3	0.0	0.3			1.8
R-1	5.6	2.0	0.3	0.5	0.3	10.7	3.6	2.4
R-15	12.8	4.2	7.7	22.1	2.0	14.1	3.8	6.4
R-62	134.5	8.1	0.8	7.3	1.1	18.0	4.9	13.9
R-43 S1	54.8	6.8	0.9	0.4	5.3	17.6	3.9	13.0
R-43 S2	3.8	4.3	0.5	0.5	1.5	16.9	4.7	5.0
R-42	954.0	42.2	1.2	161.0	5.6	52.4	14.7	76.7
R-28	382.4	34.3	1.0		3.9	46.0	11.5	48.5
R-50 S1	95.1	7.6	0.5	20.6	1.6	16.0	4.8	11.3
R-11	26.0	5.8	0.9	5.0	5.7	23.7	6.6	14.5
R-45 S1	25.9	4.2	0.5	2.2	2.5	18.4	5.0	6.6
R-45 S2	12.7	3.6	0.4	1.1	0.7	16.6	4.8	4.3
R-44 S1	16.2	2.3	0.4	0.8	1.0	12.8	3.6	3.3
SIMR-2	–	–	–	–	–	–	–	–
R-13	4.9	2.4	0.4	0.8	0.7	13.8	3.4	3.2
R-35a	3.9	6.8	0.4	0.6	0.5	24.1	6.3	5.8
R-35b	4.4	2.9	0.6	0.2	1.1	16.3	5.2	3.6
R-36	5.2	6.3	1.5	10.3	2.5	18.7	4.4	7.3
2014 Species								
Wells	Cr (µg/L)	Cl-(mg/L)	ClO4 (µg/L)	3H (pCi/L)	NO3 (mg/L)	Ca (mg/L)	Mg (mg/L)	SO4 (mg/L)
R-67	–	–	–	–	–	–	–	–
R-14 S1	5.7	1.8	0.3	1.5	0.3	10.2	3.3	1.9
R-1	5.2	2.0	0.4		0.3	11.0	3.9	2.3
R-15	11.4	4.4	8.0	35.5	2.3	13.9	3.7	7.0
R-62	186.7	9.5	0.8	9.9	1.3	19.6	5.4	16.8
R-43 S1	84.2	7.4	0.9	1.0	5.4	17.7	3.9	14.3
R-43 S2	7.7	4.6	0.6	0.0	2.1	17.5	4.5	5.6
R-42	900.3	46.9	1.2	224.5	6.0	51.6	14.4	80.5
R-28	374.0	37.7	1.0	189.3	4.0	46.5	11.7	53.0
R-50 S1	107.2	8.6	0.6	20.9	1.8	15.6	4.6	12.8
R-11	25.5	5.9	0.9	4.8	5.8	23.7	6.5	14.3
R-45 S1	29.1	4.7	0.6	3.2	2.9	17.9	5.1	7.3
R-45 S2	16.2	3.9	0.4	2.7	0.8	16.3	4.8	4.5
R-44 S1	17.0	2.5	0.4	2.1	1.2	12.3	3.5	3.5
SIMR-2	–	–	–	–	–	–	–	–
R-13	4.4	2.5	0.4	0.3	0.8	13.6	3.3	3.4
R-35a	5.1	6.7	0.4	0.6	0.5	22.3	5.9	5.7
R-35b	4.8	3.0	0.6	1.3	1.3	14.8	4.9	3.7
R-36	6.6	6.4	1.4	16.1	2.6	17.2	4.2	7.3

Table 3.0-1 (continued)

2015 Species								
Wells	Cr (µg/L)	Cl-(mg/L)	ClO4 (µg/L)	3H (pCi/L)	NO3 (mg/L)	Ca (mg/L)	Mg (mg/L)	SO4 (mg/L)
R-67	7.1	2.3	0.4	0.0	0.4	13.7	5.0	3.6
R-14 S1	5.6	1.7	0.3	1.3	0.4	10.0	3.3	1.8
R-1	5.8	1.9	0.4	0.0	0.4	10.9	4.0	2.2
R-15	11.7	4.1	8.2		2.4	13.9	3.8	6.4
R-62	136.8	8.8	0.8	15.9	1.2	19.9	5.5	15.4
R-43 S1	133.3	8.3	1.0	2.0	5.6	18.5	4.2	16.1
R-43 S2	8.4	5.0	0.8	0.1	2.9	17.5	4.6	6.8
R-42	856.0	45.8	1.2	201.0	5.4	54.1	15.2	78.5
R-28	407.3	37.1	1.0	192.0	3.9	47.0	12.0	53.0
R-50 S1	107.4	8.3	0.6	20.8	1.9	16.1	4.8	11.9
R-11	21.7	5.2	0.8	4.6	5.7	23.4	6.6	12.8
R-45 S1	34.0	4.8	0.6	5.3	3.0	18.0	5.1	7.4
R-45 S2	17.5	3.8	0.4	3.9	0.8	17.0	5.1	4.4
R-44 S1	16.4	2.4	0.4	0.9	1.2	12.6	3.6	3.5
SIMR-2	3.1	2.2	0.4	0.3	0.7	12.6	3.3	2.8
R-13	3.8	2.4	0.4	0.0	0.8	14.0	3.6	3.2
R-35a	4.4	6.6	0.4	0.4	0.5	22.1	6.0	5.5
R-35b	5.3	2.9	0.6	0.9	1.2	15.8	5.2	3.5
R-36	5.7	6.2	1.5	12.0	2.4	17.4	4.2	7.1
2016 Species								
Wells	Cr (µg/L)	Cl-(mg/L)	ClO4 (µg/L)	3H (pCi/L)	NO3 (mg/L)	Ca (mg/L)	Mg (mg/L)	SO4 (mg/L)
R-67	6.6	2.3	0.3	0.3	0.4	14.8	5.1	5.4
R-14 S1	6.0	1.6	0.3	0.4	0.5	10.2	3.3	1.8
R-1	7.9	2.0	0.3	0.0	0.3	11.3	3.9	2.3
R-15	12.4	4.1	9.3	34.6	2.1	14.3	3.7	6.5
R-62	191.8	10.1	0.8	18.9	1.5	21.5	5.8	18.9
R-43 S1	153.0	8.5	1.0	1.9	5.5	19.7	4.3	16.7
R-43 S2	12.7	5.5	0.9	0.7	3.6	18.2	4.7	7.9
R-42	836.0	47.9	1.2	266.5	5.8	54.5	15.0	79.5
R-28	400.7	35.1	1.0	147.6	4.0	45.0	11.3	50.3
R-50 S1	121.0	9.1	0.6	23.1	2.1	17.2	5.0	13.0
R-11	19.1	4.5	0.8	1.7	5.5	22.8	6.2	11.3
R-45 S1	41.0	5.2	0.6	2.9	3.1	18.2	5.1	8.0
R-45 S2	18.9	3.9	0.4	3.5	0.8	17.1	5.0	4.6
R-44 S1	16.8	2.4	0.4	0.5	1.1	12.4	3.5	3.4
SIMR-2	1.4	2.2	0.4	0.7	0.7	12.7	3.2	2.8
R-13	4.1	2.4	0.4	0.0	0.7	13.9	3.4	3.3
R-35a	5.6	6.5	0.4	0.9	0.5	21.6	5.7	5.7
R-35b	5.7	2.8	0.6	1.2	1.2	15.3	5.0	3.6
R-36	6.2	6.1	1.5	12.4	2.4	17.5	4.2	7.1

Note: Average concentrations for each year between 2005 and 2016 are computed; there are 12 time snapshots in total.

*- = No data available.

**Table 3.0-2
Geochemical Concentrations Associated with the
Seven Groundwater Types (Sources) Identified to be Mixed
with Background Regional Groundwater at the Site Monitoring Wells**

Sources	Species							
	Cr (µg/L)	Cl- (mg/L)	ClO4 (µg/L)	3H (pCi/L)	NO3 (mg/L)	Ca (mg/L)	Mg (mg/L)	SO4 (mg/L)
S1	2970.22	63.06	0.00	0.00	13.94	73.37	24.74	171.02
S2	0.79	0.35	13.87	0.00	0.49	5.27	1.71	0.61
S3	0.24	3.62	0.00	0.00	0.01	40.77	10.90	0.06
S4	0.48	0.14	0.00	0.00	10.49	21.09	5.00	10.18
S5	20.53	50.57	0.00	949.53	2.39	66.54	14.89	49.63
S6	1.46	64.24	0.00	0.00	2.81	50.92	10.43	68.08
S7	0.10	0.03	0.00	0.00	0.01	0.43	0.78	0.88

Note: Dominant geochemical species associated with each source are in bold.

LA-UR-18-21450
March 2018
EP2018-0032

Characterization of Natural Attenuation

Attachment 6



Prepared by the Associate Directorate for Environmental Management

Los Alamos National Laboratory, operated by Los Alamos National Security, LLC, for the U.S. Department of Energy (DOE) under Contract No. DE-AC52-06NA253 and under DOE Office of Environmental Management Contract No. DE-EM0003528, has prepared this document pursuant to the Compliance Order on Consent, signed June 24, 2016. The Compliance Order on Consent contains requirements for the investigation and cleanup, including corrective action, of contamination at Los Alamos National Laboratory. The U.S. government has rights to use, reproduce, and distribute this document. The public may copy and use this document without charge, provided that this notice and any statement of authorship are reproduced on all copies.

CONTENTS

1.0	INTRODUCTION	1
2.0	EXPERIMENTS TO EVALUATE DIRECT UPTAKE OF CR(VI) ON AQUIFER SEDIMENTS	1
2.1	Introduction	1
2.2	Chronology of Cr(VI) Uptake Experiments	2
2.3	Highlights of Cr(VI) Uptake Experiment Results	5
2.4	Conclusions from Cr(VI) Uptake Experiments	9
3.0	SEQUENTIAL LEACHING EXPERIMENTS TO LEACH ANTHROPOGENIC CHROMIUM FROM AQUIFER SEDIMENTS.....	10
3.1	Introduction	10
3.2	Biotite and Bentonite Acid Leaching Experiments.....	11
3.2.1	Materials	11
3.2.2	Evaluation of Leaching Effectiveness	11
3.2.3	Evaluation of Method Detection Limit with Biotite and Bentonite.....	12
3.3	Sequential Leaching of Aquifer Sediment Samples	13
3.3.1	Samples.....	13
3.3.2	Four Sets of Sequential Acid Leaching Experiments.....	13
3.3.3	Sequential Acid Leaching Results.....	13
3.4	Conclusions from Sequential Leaching Experiments	15
4.0	SUMMARY OF SYNCHROTRON EXPERIMENTS TO EVALUATE CR(VI) REDUCTION TO CR(III) ON OUTCROP MATERIALS OR SONIC CORE HOLE SEDIMENTS.....	15
5.0	REFERENCES.....	17

Figures

Figure 2.3-1	Normalized ^3HHO and Cr(VI) concentrations (concentrations divided by injection concentration, C/Co) and flow rate (mL/h) as a function of volume eluted in four column experiments in which R-42 water spiked with ^3HHO was injected for approximately 2 pore volumes followed by unspiked R-42 water.....	19
Figure 2.3-2	Results of batch uptake experiments conducted on zero-valent iron filings at various solution-to-solid mass ratios (see legend)	20
Figure 2.3-3	Results of batch uptake experiments conducted on different fractions separated from bulk sonic core from CrCH-4, 967 ft below land surface (BLS)	20
Figure 2.3-4	Cr(VI) uptake on drillers' bentonite used in sonic core hole completions as a function of starting concentration of Cr(VI) at a pH of ~ 8.5	21
Figure 2.3-5	Cr(VI) batch uptake on R-42 sediments used in the R-42 column experiment shown in Figure 2.3-1	21
Figure 2.3-6	pH dependence of Cr(VI) uptake on sediments from CrCH-5, 998–1005 ft BLS.	22
Figure 2.3-7	Cr(VI) uptake onto material from CrCH-5, 998–1005 ft BLS, which did not settle by gravity after 120 h, and subsequent desorption of Cr(VI) after exposure to Los Alamos tap water	22
Figure 2.3-8	Hydraulic conductivity (as deduced from particle-size distribution data using the Kozeny-Carman equation) vs depth for lithologically distinct intervals in CrCH-1 and CrCH-2.....	23

Figure 2.3-9	Cr(VI) batch uptake after 504 h of sediment contact with R-42 water vs hydraulic conductivity (as deduced from particle-size distribution data using the Kozeny-Carman equation) for the red data points of Figure 2.3-8	23
Figure 3.1-1	Workflow of sequential alkaline leaching procedure.....	24
Figure 3.1-2	Workflow of sequential acid leaching procedure.	25
Figure 3.2-1	Cumulative chromium leached from biotite exposed to Cr(VI) solutions as a function of leaching step in three experiments with duplicate samples in each experiment (solid lines).	26
Figure 3.2-2	Cumulative chromium leached from bentonite exposed to Cr(VI) solutions as a function of leaching step in two experiments with duplicate samples in each experiment (solid lines)	26
Figure 3.2-3	Cumulative log Cr vs log Fe of leachates from uncontaminated aquifer samples (black), unexposed biotite (green), and unexposed bentonite (red).....	27
Figure 3.2-4	Cumulative log Cr vs log Fe of leachates from Cr(VI)-exposed and unexposed biotite samples.....	28
Figure 3.2-5	Cumulative log Cr vs log Fe of leachates from Cr(VI)-exposed and unexposed bentonite samples.....	28
Figure 3.2-6	Cumulative Cr/Fe ratios of 0.1 M HNO ₃ leachates from Cr(VI)-exposed biotite samples minus Cr/Fe ratio of leachates from unexposed biotite samples vs Cr(VI) uptake on exposed samples	29
Figure 3.2-7	Cumulative Cr/Fe ratios of 0.1 M HNO ₃ leachates from Cr(VI)-exposed bentonite samples minus Cr/Fe ratio of leachates from unexposed bentonite samples vs Cr(VI) uptake on exposed samples	29
Figure 3.3-1	Cumulative log Cr vs log Fe of leachates from both contaminated and uncontaminated samples in first set of leaching experiments after 0.1 M HNO ₃ leaching steps (blue) and 2 M HNO ₃ leaching steps (red).	30
Figure 3.3-2	Cumulative log Cr vs log Fe of leachates from samples in first set of leaching experiments after 2 M HNO ₃ leaching steps.....	30
Figure 3.3-3	Cumulative log Cr vs log Fe of leachates from samples in first set of leaching experiments after 0.1 M HNO ₃ leaching steps.....	31
Figure 3.3-4	Cumulative log Cr vs log Fe of leachates from samples in second set of leaching experiments (0.1 M HNO ₃ leaching)	31
Figure 3.3-5	Cumulative log Cr vs log Fe of leachates from samples in third set of leaching experiments (0.1 M HNO ₃ leaching), color coded by degree of magnetism of samples ..	32
Figure 3.3-6	Cumulative log Cr vs log Fe of leachates from samples in third set of leaching experiments (0.1 M HNO ₃ leaching), color coded by contaminated or uncontaminated ..	32
Figure 3.3-7	Cumulative log Cr vs log Fe of leachates from samples in fourth set of leaching experiments (0.1 M HNO ₃ leaching), color coded by degree of magnetism of samples (see legend)	33
Figure 3.3-8	Cumulative log Cr vs log Fe of leachates from all final 0.1 M HNO ₃ leaches, color coded by contaminated (red) vs uncontaminated (black).....	34
Figure 4.0-1	XANES spectra of Cr(III)/Cr(VI) standards	34
Figure 4.0-2	XANES spectra of chromite-a, chromite-b, uvarovite, Sandia Canyon wetland sample with chromium concentration of 17 µg/g, and Cr(VI)-spiked biotite with chromium concentration of 18 µg/g	35

Figure 4.0-3 XANES spectra of Sandia wetland sample and various outcrop (Puye formation) samples after exposure to Cr(VI) solutions..... 35

Figure 4.0-4 Micro-XRF maps of “Ren-2 < 2um sample” before (top left) and after (top right) exposure to 5 ppm Cr(VI) solution, and the corresponding XANES spectra of numbered “hot spots” present in the mapped samples (bottom, directly below corresponding map). 36

Figure 4.0-5 Time sequence of XANES spectra of a suspension of 0.25–0.7-µm fines in a solution that was initially 20 mg/L Cr(VI) 37

Tables

Table 2.3-1 Particle-Size Fractions Separated from Sonic Core Samples for Last Set of Cr(VI) Uptake Experiments..... 39

Table 3.2-1 Chemical Composition of Bentonite and Biotite from XRF Expressed as Oxides in Weight%..... 39

Table 3.2-2 Results of Trace Elements in the Bentonite and Biotite In ppm (mg/kg) as Determined by XRF 39

Table 3.3-1 Field Samples Used In Sequential Acid Leaching Tests 40

Table 3.3-2 Differences in Sample Preparation and Leaching Steps in the Four Sets of Sequential Leaching Experiments 41

1.0 INTRODUCTION

Between 2013 and 2016, several laboratory experiments were conducted to evaluate the potential for regional aquifer sediments to reduce hexavalent chromium [Cr(VI)] to trivalent chromium [Cr(III)], thus providing natural attenuation of Cr(VI) in the regional aquifer. These experiments included the following:

- Cr(VI) “uptake” experiments, in which an aquifer sediment sample was placed in contact with a solution containing a known amount of Cr(VI), either in a batch experiment or a column experiment, and the amount of Cr(VI) removed from solution was measured
- Sequential leaching experiments, in which aquifer sediment samples were leached with successively more aggressive solutions to remove anthropogenic Cr associated with the sediments
- X-ray synchrotron experiments to confirm that Cr(VI) reduction to Cr(III) can potentially occur on aquifer sediments

The methods, results, and implications of each of these types of experiments are presented in the three main sections that compose the remainder of this report. Section 2 covers the Cr(VI) uptake experiments, section 3 covers the sequential leaching experiments, and section 4 summarizes the x-ray synchrotron experiments.

2.0 EXPERIMENTS TO EVALUATE DIRECT UPTAKE OF CR(VI) ON AQUIFER SEDIMENTS

2.1 Introduction

Between 2013 and 2016, several laboratory experiments were conducted to evaluate the potential for regional aquifer sediments to directly uptake Cr(VI). Most of these were batch experiments in which a sediment sample was placed in contact with a solution containing a known amount of Cr(VI), typically water from regional aquifer monitoring well R-42, which has the highest Cr(VI) concentrations of any location in the plume, ranging from 800 to 1000 µg/L Cr(VI). The batch experiments are very straightforward; they involve measuring Cr(VI) concentrations in the water both before and after contact with the sediment to determine the amount of Cr(VI) that became associated with the sediment during the contact period. Typically, a set of “control” experiments with no sediment in the batch reactors is run in parallel with reactors that contain sediments, and any decrease in Cr(VI) in the sediment-containing reactors relative to the controls can be taken as an indication of Cr(VI) uptake on the sediments. This method allows any Cr(VI) association with the reactor walls to be identified and accounted for. In cases where Cr(IV) uptake on the sediments was indicated, desorption experiments were sometimes conducted to determine if the Cr(VI) association with the sediments was reversible. These experiments were conducted by decanting off as much of the chromium-bearing water from the reactors as possible and replacing it with water containing no Cr(VI), and then measuring how much Cr(VI) was in the water after a certain contact period. Desorption was indicated by an excess of Cr(VI) in the aqueous phase after accounting for the Cr(VI) that remained in the residual aqueous phase after the decanting step.

The remainder of this section first provides a brief narrative of the chronology and evolution of methodology in the Cr(VI) uptake experiments. This narrative is provided because many potential pitfalls were encountered in measuring Cr(VI) uptake, and some of these pitfalls are suspected to have led to a significant overestimation of Cr(VI) uptake on both vadose zone and regional aquifer sediments that were documented in a 2009 project report (LANL 2009, Appendix I). Although it is not conventional to report problems that led to erroneous results, the intent here is to avoid a repetition of such problems in any future uptake experiments and also to provide justification for discounting many results that might

otherwise be interpreted optimistically (i.e., suggesting more natural attenuation of Cr(VI) than actually exists). After the chronology, most of the remainder of this section is dedicated to reporting the highlights of the uptake experiments. Finally, this section concludes with a summary of what the results collectively mean for natural attenuation of Cr(VI) in the regional aquifer.

2.2 Chronology of Cr(VI) Uptake Experiments

Many different batch uptake experiments were conducted over a 3+ y period, and this subsection provides a brief summary of the evolution of the variations in the approaches taken as observations were made with each successive iteration. Note that previous batch experiments (LANL 2009, Appendix I) were conducted to measure Cr(VI) uptake on aquifer sediments, and these had indicated a substantial amount of uptake on many different sediment samples, including samples from both above and below the water table. Even column experiments on some of these samples had indicated significant Cr(VI) uptake in some cases. However, the batch experiments were run at very large solution-to-solid mass ratios (35 mL of water to every gram of sediment), where any small decrease in the concentration of Cr(VI) would translate to a relatively large amount of inferred uptake on the sediments. It was suspected that the Cr(VI) uptake on the sediments was being overestimated in these experiments, especially given that geochemical trends in monitoring wells at the periphery of the chromium plume indicated that Cr(VI) concentrations were increasing essentially in tandem with concentrations of nonreactive anions (e.g., SO_4^- and Cl^-) that were known to be associated with surface sources (see Appendix B of Attachment 1 of this compendium, "Results and Implications of Field Tracer Testing and Long-Term Pump Tests within the Chromium Plume at Los Alamos National Laboratory from 2013 to 2017"). Most of the batch and column test data from this earlier work indicated that Cr(VI) should have never been observed in the monitoring wells if it were attenuated to the extent suggested in the lab experiments. Crushing of the sediment samples was found to enhance Cr(VI) uptake in these experiments. Also, metallic iron contamination was found in some, but not all, of the samples, and it was shown to increase Cr(VI) uptake when it was present. However, even uncrushed samples believed to be free of metallic iron exhibited Cr(VI) uptake, suggesting that Cr(VI) should be delayed by a factor of at least 10 relative to nonreactive anions in monitoring wells, which was inconsistent with field observations that indicated almost identical transport of Cr(VI) and the anions.

For the reasons discussed above, the decision was made to conduct additional batch and column uptake experiments to better quantify the interactions of Cr(VI) with aquifer sediments. To avoid potential biases introduced by iron contamination and crushing of grains (i.e., exposing of fresh surfaces not present in the aquifer), an initial round of experiments was conducted using outcrop materials. These materials were taken from a Puye Formation exposure in Rendija canyon, well to the north of the Cr(VI) plume area, and they were collected with no possibility of iron contamination and without crushing of the sediments. The experiments were conducted using R-42 water at a solution to sediment ratio of 5 mL to every gram of sediment, and they were conducted over a pH range from 5.8 to 8.8. When these experiments showed no appreciable uptake of Cr(VI) on any of the sediments at any of the pH values, an additional set of batch experiments was conducted in a similar manner on magnetically separated heavy mineral grains from selected outcrop materials. Experiments were also conducted on a very fine clay-sized fraction (estimated to be less than 2 μm in diameter) that was separated by gravity settling from one of the samples. Additionally, biotite and muscovite samples from commercially available mineral stocks were used in some of the batch reactors to serve as samples that were expected to exhibit Cr(VI) uptake. The biotite samples indeed took up a considerable amount of Cr(VI), and it was found that this Cr(VI) did not subsequently desorb, leading to the conclusion that the biotite served as a good proxy for a mineral that was capable of reducing Cr(VI) to Cr(III). The other batch reactors showed significant Cr(VI) uptake only on the <2- μm fraction of the outcrop material separated by gravity settling, and the Cr(VI) uptake could not be subsequently desorbed from this sample. A portion of this sample was later analyzed by x-ray

absorption near-edge spectroscopy (XANES) at the Stanford Synchrotron Research Laboratory (SSRL), and evidence for Cr(VI) reduction to Cr(III) was found (by comparing samples that had been exposed and not exposed to a Cr(VI) solution—see section 4 of this report). Batch experiments were also conducted using fines collected from below the water table in R-42 during drilling (fines that washed out of the cuttings returned to the surface during drilling, with the rationale that these should not contain iron), and these materials showed no evidence of any Cr(VI) uptake.

In parallel with the batch experiments, four column experiments were conducted in which R-42 water was injected along with a conservative tracer (^3HHO). Two of the columns were packed with material from wells drilled into the chromium plume (one was disaggregated Miocene pumiceous core taken from above the water table in SCI-2, and the other was the same R-42 cuttings material that was used in the batch experiments described at the end of the last paragraph). The other two columns were packed with outcrop material taken from Rendija Canyon and White Rock Canyon, respectively, with the former being representative of material from the Puye Formation and the latter considered representative of Miocene pumiceous material. There was no apparent retardation of Cr(VI) in any of the four columns.

In late 2014, five core holes were drilled into the regional aquifer in the Cr(VI) plume area using a sonic-advance coring method. It was thought that the core material from these holes would be ideal for use in batch uptake experiments because the sonic method typically has high core recoveries without significant loss of any particular size fraction, and it should not create fresh surfaces in the core or introduce as much artificial iron as a conventional rotary coring method might. Also, the sonic core material was arguably more representative of the regional aquifer sediments than any of the outcrop materials, which had not been exposed to groundwater, or than the R-42 fines materials that had washed out of cuttings. Initial batch experiments with sonic core from the first core hole indicated small amounts of Cr(VI) uptake, but it soon became apparent that the sonic method was introducing metallic iron fragments into the core that were having a large influence on Cr(VI) uptake. One of the first indications of this problem was the much lower than expected Cr(VI) concentrations that were being measured in pore waters extracted from the cores. This prompted close examinations of the core, and indeed iron fragments were identified in many core intervals.

Several batch experiments were then conducted in which iron was either left in the sonic core or carefully removed, and in one case an experiment was conducted using just the iron fragments as the “sediment.” These experiments collectively indicated that

1. iron fragments were not easy to remove from the core samples, and removing them typically entailed also removing some magnetic minerals that might contribute some Cr(VI) uptake and
2. when iron was painstakingly removed from core samples by hand under a microscope, Cr(VI) uptake was essentially negligible, even after crushing the sediments and with very small solution-to-solid mass ratios (as low as 10 mL of water to 8 g of sediments).

An experiment with iron fragments taken from the sonic core indicated that the fragments were capable of uptake that corresponded to Cr(VI) partition coefficients exceeding 10,000 mL/g in a matter of hours, which essentially meant that any tiny amount of undetected metallic iron in a sediment sample would render an uptake measurement erroneous.

These results were taken to be a strong potential indication of why the batch experiments conducted before 2010 may have shown such large amounts of Cr(VI) uptake; i.e., it is possible that very small amounts of metallic iron may have been present in the samples that went undetected but nevertheless may have exerted a significant influence on the results. The results also made it very clear that using sonic core materials without some careful pretreatment to screen for and remove iron fragments was certain to result in overestimation of Cr(VI) uptake on the sediments, and hence an overestimation of natural attenuation provided by the sediments.

A separate set of experiments indicated that the Wyoming bentonite that the drilling contractor used in the completions of the piezometers that were installed in the sonic core holes after coring was quite efficient at taking up Cr(VI) from solution, provided the solution pH was less than about 9.5. These experiments were conducted because it was suspected that the Cr(VI) concentrations in samples taken from the piezometers might be biased low because of the presence of the bentonite. Additional batch uptake experiments were conducted with the bentonite and also with biotite samples from a commercially available mineral stock to serve as controls in sequential leaching experiments that were done to determine if there was anthropogenic chromium associated with aquifer sediments taken from parts of the chromium plume that were known to be contaminated. The “sediments” from these uptake experiments were used to determine how efficient the sequential leaching steps were at removing anthropogenic chromium and also which leaching steps resulted in the greatest removal of anthropogenic chromium. These experiments are discussed in section 3 of this report. The relevance of these experiments to the current section is that they demonstrated that the batch uptake method worked well to measure definitive chromium uptake on nonaquifer materials that were not contaminated with iron fragments. They also served to demonstrate that some uptake occurred in cases where there was apparently some nonmetallic reduced iron present, as reduced iron was believed to be present in both the bentonite and biotite samples.

Given the collective experience described above, the decision was made to conduct additional experiments in the following ways to try to remove artifacts associated with iron fragments and to better quantify Cr(VI) uptake on aquifer sediments:

- Experiments were conducted using material from near the bottom of sonic core hole 5 (CrCH-5) that was treated with a magnet to remove magnetic material. These experiments were conducted with 40 mL of R-42 water in contact with 2 g of sediment, with the primary intent being to see if there was a dependence of Cr(VI) uptake on pH. pH values were varied from about 4 to 9.
- Experiments with very small solution-to-solid mass ratios (typically on the order of 1 mL of solution to 4 g of solids), which were much closer to the ratios expected in the aquifer, were conducted in centrifuge tubes containing filter inserts. Essentially, what amounted to wet sediment was loaded onto the filters in the tubes, and each time a sample was collected, the tube was spun to force some of the solution through the filter for analysis. The unanalyzed solution was then returned to the sediment and the process was repeated to collect more samples. Control experiments were conducted to ensure that no Cr(VI) was lost to the filters or the centrifuge tubes. These experiments were conducted using both the R-42 fine sediments that had previously exhibited no Cr(VI) uptake (at 5 mL of solution to 1 g of sediment) and also using sonic core material from several different intervals that represented different lithologies in the chromium plume. All of the sonic core materials were sieved to a very fine size fraction (<63 μm) after removing magnetic materials with a strong magnet.
- Experiments were conducted on fractions of the same sonic core materials that were selected for the above experiments, except the materials used in these experiments were separated by gravity settling for different amounts of time (most of them after first removing magnetic material with magnets and sieving). The gravity settling was intended to be an independent method of removing residual iron fragments, with the idea being that the iron fragments should settle rapidly, and the material remaining suspended should be free of iron. These experiments also served as a check on whether the Cr(VI) uptake on the very fine gravity-separated sediments of the outcrop material (discussed above) was reproducible in the aquifer sediments. It was suspected that Cr(VI) uptake might occur primarily on such very fine sediments.

Selected results from the experiments described above are presented in the remainder of this section, with emphasis on the most recent sets of experiments because they are believed to be the most representative for Cr(VI) uptake in the regional aquifer. However, as will be shown, even these experiments have some anomalous results that suggest the possibility of iron fragment contamination, which may underscore the difficulty of removing iron fragments from sediment samples.

2.3 Highlights of Cr(VI) Uptake Experiment Results

Figure 2.3-1 shows the results of the four column experiments that were conducted before drilling the sonic core holes. These experiments were designed with groundwater residence times of approximately 2 d, and with linear flow velocities that were intended to be similar to flow velocities in the contaminated aquifer (~15 cm/d; which is a velocity that is still considered reasonable for much of the plume area). The water used in all experiments was taken from R-42, with a Cr(VI) concentration of about 900 µg/L. Figure 2.3-1 shows that the Cr(VI) transported essentially identically to ³H₂O in three of the columns, and the Cr(VI) breakthrough in the other column actually preceded that of the ³H₂O, which can be explained only by some sort of anion exclusion process that kept Cr(VI) from diffusing into pores in the rock grains. The concentrations of Cr(VI) decreased in some, but not all, of the columns after the flow rate was decreased significantly. This initially suggested a rate-limited adsorption or reduction process, but the dependence of the Cr(VI) concentrations on flow rate did not follow expectations for a first-order rate process because a single rate constant was not capable of matching the Cr(VI) concentrations observed at both the high- and low flow rates. A definitive explanation for this behavior was not pursued, but it was speculated that different amounts of microbial activity capable of reducing Cr(VI) may have occurred over time in the different columns, which were not sterilized in any way and were not injected with sterile/filtered water. The conclusion was that the column experiments provided no clear-cut evidence of any natural attenuation of Cr(VI) in the regional aquifer, but the results did suggest that biostimulation might be a viable remediation strategy.

Figure 2.3-2 shows the results of some batch experiments in which zero-valent iron was used as the solid phase in contact with R-42 water. These experiments were conducted after it became apparent that iron fragments from the sonic coring bit were present in at least some of the sonic core material and that Cr(VI) concentrations in pore water spun out of the core seemed to be lower than expected [relative to other constituents that are generally correlated with Cr(VI) within the plume area]. It is apparent from Figure 2.3-2 that zero-valent iron very rapidly reduces Cr(VI) to Cr(III). Reduction was ultimately confirmed by chromium isotope ratio measurements conducted on samples taken from such experiments (see Attachment 2 of this compendium, "Isotopic Signatures of Hexavalent Chromium in the Regional Aquifer: Evaluation of Natural Attenuation"). After these experiments were conducted, it was obvious that any sonic core material used in uptake experiments would have to be carefully processed to remove iron fragments. A subsequent experiment using a core interval from CrCH-3 that was particularly high in iron fragments revealed that simply hand-picking out iron fragments was not sufficient for removing all artifacts caused by iron because the material with and without iron fragments both showed significant amounts of Cr(VI) uptake, and the difference between them was not significant.

Figure 2.3-3 shows the results of an uptake experiment conducted on core material from CrCH-4 that was very painstakingly separated into different fractions, including three tiny pieces of metallic iron found in the core. The other fractions included a >1.41-mm (14 mesh sieve) magnetic fraction, a <1.41-mm magnetic fraction, a "heavy, nonmagnetic mineral" fraction, and an ultrafine fraction that looked like a very fine white powder. Of all the uptake experiments conducted, this experiment represents one of the most thorough separations of sonic core into different fractions that avoided or included iron fragments. Figure 2.3-3 shows that with the exception of the smaller magnetic particles, which demonstrated a small amount of apparent uptake, none of the fractions except the iron fragments showed appreciable uptake of

Cr(VI). The uptake on the iron fragments was all the more remarkable considering the extreme solution-to-solid mass ratio for this fraction. The Cr(VI) uptake on the iron fragments after 145 h was calculated to be a staggering 960 μg Cr(VI) per g of iron. Some of the larger magnetic and heavy material grains were then re-exposed to R-42 water after crushing them to generate fresh surfaces, and there was still no appreciable uptake observed on the crushed grains. Note that CrCH-4 was ultimately found to be essentially free of Cr(VI) contamination, so it could not be argued that the natural material had been pre-exposed to Cr(VI) contamination that may have exhausted its ability to further reduce Cr(VI).

Figure 2.3-4 shows the results of uptake experiments on some of the bentonite that was used by the drillers when completing the sonic core holes as 2-in. piezometers. Some of these experiments were used to provide starting material for sequential leaching experiments in which the bentonite was used as an example of a material that was known to have anthropogenic Cr(VI) associated with it. The experiment with different starting concentrations of Cr(VI) was conducted to determine if there was a maximum Cr(VI) uptake per unit mass of bentonite at a given pH (it appears to be about 12 μg per g of bentonite at pH \sim 8.5). However, it is also apparent that the uptake of Cr(VI) on bentonite is strongly pH dependent (with very little uptake at a pH greater than about 9.5). These results show that the bentonite used in piezometer completions could potentially artificially depress observed Cr(VI) concentrations, although how much depression and for how long will depend on both groundwater pH and on how much bentonite was dispersed into the screened interval during the completion of the piezometer.

Figure 2.3-5 shows the results of an experiment conducted using the R-42 cuttings material that was used in one of the four columns of Figure 2.3-1. The Cr(VI) concentrations in the column experiment decreased by 10–15% after the flow rate through the column was slowed down, and this material had exhibited no evidence of iron contamination in any previous experiments. Furthermore, this was the only one of the column materials that actually came from the Cr(VI)-contaminated regional aquifer, so it was a good candidate for measuring small amounts of attenuation, such as those suggested by the column results at the lower flow rate. This batch uptake experiment differed from previous uptake experiments in that it had a very small solution-to-solid mass ratio that was much closer to being representative of the aquifer itself than any previous batch experiment (starting at 16 g of sediment per 4 g of R-42 water, which translates to a porosity of about 40%). The experiments were conducted in centrifuge tubes equipped with filters, with what amounted to sediments wetted with R-42 water being loaded onto the filters. The centrifuge tubes were spun each time to extract enough water through the filters to do a Cr(VI) measurement by ultraviolet-visible (UV-Vis) spectroscopy, and then any unused water spun through the filter was returned to the wet sediment. Because of the small solution-to-solid mass ratio, these experiments were very sensitive to any small amount of Cr(VI) uptake on the sediments, and Figure 2.3-5 shows that there was indeed a small amount of uptake, amounting to about 0.04 to 0.05 μg Cr(VI) per g of sediment. If this amount of uptake had been observed in the column experiment, the Cr(VI) should have been delayed in breakthrough relative to the ^3HHO by about 10 mL (out of about a 100-mL pore volume in the column, so about a 10% delay in Cr(VI) breakthrough). This was clearly not observed in the column experiment, and the subsequent decrease in Cr(VI) concentrations after the flow rate was decreased amounted to an apparent uptake of about 0.35 μg Cr(VI) per g of sediment in the column, which is 7–9 times greater than what was observed in the batch experiment. This result lends support to the speculation that some microbial activity may have been stimulated in the column, causing some reduction/uptake of Cr(VI).

Figure 2.3-6 shows the results of experiments conducted on material taken from near the bottom of CrCH-5 to investigate the pH dependence of Cr(VI) uptake. The sediments in these experiments were not treated carefully to remove iron contamination, and the Cr(VI) uptake on the sediments at aquifer pHs proved to be nearly 2 orders of magnitude higher than in the experiments of Figure 2.3-5. While this was taken as an indication that the sediments were probably tainted with some iron, the results of the experiments are shown here to illustrate the sort of pH dependence of uptake that might be expected for

natural sediments, and it also illustrates that even with iron likely present, uptake is relatively low at aquifer pHs, which are near 8. Note that while not as extreme as the pH dependence observed for bentonite, and also not extending to pHs that are as high as for bentonite, the pH dependence of the Cr(VI) uptake on CrCH-5 sediments is at least qualitatively consistent with the pH dependence of bentonite (i.e., greater uptake at lower pH).

Figure 2.3-7 shows the results of experiments conducted on “ultrafine” material that was obtained from the same CrCH-5 sediments as in Figure 2.3-6. The ultrafine material was obtained by gravity settling, and it consisted of material that did not settle after 120 h of being suspended in deionized water. Other fractions of this material were collected after 1, 5, and 60 min of settling, and also after 48 h of settling. The hope was that iron fragments would settle rapidly, and at some point the unsettled material would be free of iron contamination. The experiments were conducted at a much smaller solution-to-solid mass ratio than the experiments of Figure 2.3-6 (less than 1:1 vs about 20:1 for Figure 2.3-6), thus making them much more sensitive to small amounts of uptake. Somewhat surprisingly, all the unsettled mass fractions exhibited no apparent uptake of Cr(VI) except for the finest size fraction that did settle in 120 h (i.e., the ultrafine fraction). This result suggests that the iron apparently was removed with larger particles that settled in the first minute of the settling process, which seems rather astonishing. The Cr(VI) uptake on this material amounted to about 0.3 μg Cr(VI) per g of sediment, but considering that this material was less than 1% of the overall mass of the starting material, this result implies that the starting material would have had an uptake of less than 0.003 μg Cr(VI) per g of sediment, or over an order of magnitude lower than what was observed for uptake on the R-42 cuttings (Figure 2.3-5).

Desorption experiments were also conducted on this material using Los Alamos tap water as the desorbing solution, and as Figure 2.3-7 shows, initial desorption appeared to be almost complete, but a large fraction of the desorbed Cr(VI) became reassociated with the sediments after several hundred hours passed. The rapid desorption is attributed to oxidants present in tap water from the use of the mixed oxidant (MIOX) process by Los Alamos County to introduce sodium hypochlorite (bleach) and other oxidants into tap water to control microbial contamination. These oxidants are suspected to have caused reoxidation and liberation of reduced chromium on the sediments, but over time as the oxidants were consumed (their lifetime is relatively short), some of the liberated Cr(VI) was re-reduced to Cr(III) and became reassociated with the sediments. This was the only batch experiment conducted at circum-neutral pH that ever exhibited any appreciable desorption (reoxidation) of chromium from a sediment onto which Cr(VI) had been uptaken, and it was also the only batch experiment ever conducted with tap water. Because the analysis method for chromium was UV-Vis spectroscopy, which detects only Cr(VI), not Cr(III), the liberated chromium must have been Cr(VI). These results are shown here to illustrate that a strong oxidant is apparently capable of reoxidizing Cr(III) that has been uptaken on sediments, but in this case the oxidant was apparently not abundant enough to exhaust the reduction capacity of the sediments, so some of the Cr(VI) became reassociated with the sediments. An important implication of these results, which were rather unexpected, is that certain oxidants (such as sodium hypochlorite) might be very efficient at reoxidizing and desorbing anthropogenic Cr(III) that has been uptaken onto sediments. The use of such oxidants in sequential leaching experiments was never pursued because this discovery was made after all the sequential leaching experiments were completed.

A final set of Cr(VI) uptake experiments was conducted using sediments from several different sonic core hole intervals taken from below the water table in the chromium plume that were selected for their variability in lithology, and also for their variability in apparent hydraulic conductivity. Each core interval was sieved into six size fractions (Table 2.3-1), and the smallest fraction (<0.063 mm) was further separated by gravity settling in deionized water into material that did and did not settle in 24 h. The hydraulic conductivity of the core intervals was not measured directly but rather was estimated by using the particle-size distribution data in the Kozeny-Carman equation (Chapuis and Aubertin 2003;

Odong 2007; Zhang et al. 2009). Based on what had been learned in previous experiments (described above), the <0.063-mm material that did and did not settle in 24 h was the only material used in the uptake experiments (larger materials appeared to contribute negligibly to uptake in previous experiments). The <0.063-mm material was preprocessed by running a strong neodymium magnet over it to remove magnetic material before settling. This was intended to remove any iron fragment artifacts, but it also removed some magnetic minerals from the sediments. Uptake experiments were also repeated on the R-42 sediments that were used to generate the data of Figure 2.3-5 (as well as a portion of this material with magnetic minerals removed). Experiments were also repeated on the CrCH-5 material that was used to generate the data of Figures 2.3-6 and 2.3-7 (processed the same way as the other sonic core hole sediments described above, using the material from the <0.063-mm size fraction that did and did not settle after 24 h).

Figure 2.3-8 shows, on a plot of deduced hydraulic conductivity vs depth, the intervals that were selected for uptake experiments (all from CrCH-1 and CrCH-2) among all the sonic core intervals that were separated into different particle-size fractions and for which hydraulic conductivity was estimated (hydraulic conductivity was not estimated for the CrCH-5 sample). It is apparent that the materials used for uptake testing have representation from different stratigraphic units and over a range of hydraulic conductivities. Note that the stratification of the aquifer into thin layers of different hydraulic conductivities is apparent in Figure 2.3-8. Figure 2.3-9 shows the apparent uptake of Cr(VI) on the different materials that settled within 24 h after 504 h of contact with R-42 water vs the hydraulic conductivity deduced from the Kozeny-Carman equation. These uptakes are corrected for the mass fraction of bulk sediments that was associated with the material that settled in 24 h (i.e., the uptake on the material tested was multiplied by this mass fraction, with the assumption that there would have been no uptake on the remaining materials). It is apparent that there is not a strong correlation between Cr(VI) uptake and hydraulic conductivity. It is also apparent that the average mass-corrected Cr(VI) uptake on the sonic core hole sediments is in relatively good agreement with the uptake observed on the R-42 sediments in the experiments of Figure 2.3-5, which were 0.04–0.05 μg Cr(VI) per g of sediment. However, in the repeat experiments on these same sediments, virtually no measurable Cr(VI) uptake was observed on either the bulk material or the material with magnetic minerals removed. In the case of the CrCH-5 material, the uptake on the <0.063-mm size fraction that settled in 24 h (~ 0.04 $\mu\text{g/g}$) was comparable with the uptake on the other sonic core hole sediments, and it was about 2 orders of magnitude lower than in the earlier experiments on this bulk material. This result clearly points to the likely presence of iron fragments in the earlier experiments.

In the experiments on the sonic core material that did not settle in 24 h, the mass-corrected Cr(VI) uptake values were never larger than 0.0046 $\mu\text{g/g}$, and many of the intervals had no measurable uptake. The CrCH-5 sediment that did not settle exhibited a mass-corrected uptake of 0.001 $\mu\text{g/g}$, which compares reasonably well with the 0.003 $\mu\text{g/g}$ observed in the experiments on material from this same interval that did not settle after 120 h (Figure 2.3-7). Interestingly, the mass fraction of the material that did not settle after 24 h (0.36 wt%) was smaller than the mass fraction that did not settle after 120 h in the earlier experiments (0.84 wt%), and the material that did not settle in 24 h in the earlier experiments showed no measurable Cr(VI) uptake in those experiments. Inconsistencies such as this probably reflect minor variations in experimental technique by different individuals.

Note that the Cr(VI) analytical method used in all the uptake experiments was UV-Vis spectroscopy (specifically, UV absorbance). This method measures only Cr(VI) and does not measure any Cr(III) in solution, although this was not considered problematic because any Cr(III) formed in any of the experiments should have rapidly adsorbed to the sediments or precipitated from solution. The UV-Vis method is subject to some uncertainties, and it is normally not considered to be the best method for quantitative chromium concentration measurements, but it was used for the uptake experiments because

it provided rapid turnaround times. UV absorbance measurements can be affected by differences in the preparation of reagents used in making measurements, errors in mixing/diluting water samples with reagent solutions, fingerprints or dust/dirt on measurement vials, using different measurement vials for different measurements, orienting the same measurement vials in different directions in the light chamber, and variability in turbidity of solutions. The latter source of error was particularly a concern in the experiments with the very fine particle fractions that did not rapidly settle by gravity. All of these potential sources of error were minimized to the extent possible, but they still contributed to uncertainty and error in the measurements because uptake was often deduced from relatively small differences in UV absorbance. In general, errors were minimized by using small solution-to-solid mass ratios because this tends to increase differences in Cr(VI) concentrations before and after uptake.

2.4 Conclusions from Cr(VI) Uptake Experiments

Collectively, the Cr(VI) uptake experiments suggest that there is very little uptake of Cr(VI) on regional aquifer sediments. Early experiments, including those conducted before 2010 (LANL 2009, Appendix I), had indicated that considerable Cr(VI) uptake might be occurring on some aquifer sediments, but in light of the experiments reported here, it seems very likely that any previously reported large uptakes were caused by iron contamination in the sediment/core samples. Such iron contamination had not been previously evaluated carefully, and experiments with zero-valent iron and iron fragments separated from sonic core samples clearly showed that even very small amounts of iron contamination could have a large effect on uptake measurements.

Although Cr(VI) uptake appears to be very minimal on aquifer sediment samples that are not contaminated with iron fragments, it cannot be said to be zero. Synchrotron experiments and uptake experiments using extremely fine material that was separated by gravity settling (and thus less likely to be contaminated by iron) have indicated that a small amount of Cr(VI) uptake can occur on some aquifer materials. The uptake experiments collectively suggest an upper-bound uptake on the order of 0.05 μg Cr(VI) per g of sediment. To put this value in perspective, if this much anthropogenic chromium were associated with sediments within the plume, and the average aqueous Cr(VI) concentration in the plume were 300 $\mu\text{g}/\text{L}$ (and the average porosity in the plume was 0.25), then the ratio of anthropogenic chromium on sediments to chromium in solution would be $\sim 1.33:1$. Effectively, this means that Cr(VI) arrivals at various observation points within the plume should be delayed relative to a nonreactive species by a factor of 2.33. This delay would be predicted to be a factor of 1.4 if average Cr(VI) concentrations in the plume were 1000 $\mu\text{g}/\text{L}$, and a factor of 5 if average concentrations were 100 $\mu\text{g}/\text{L}$. Given that concentrations at the plume periphery are less than 100 $\mu\text{g}/\text{L}$, one might expect Cr(VI) to be significantly delayed in its arrival relative to nonreactive species in monitoring wells at the plume periphery. However, delays in Cr(VI) arrivals relative to nonreactive species like Cl^- and SO_4^{2-} are not observed at all in plume periphery wells (Appendix B of Attachment 1 of this compendium). These species also have anthropogenic origins and should have entered the regional aquifer at times similar to Cr(VI). Thus, the field data show no indications that Cr(VI) uptake in the aquifer is anything close to the upper bound value of 0.05 $\mu\text{g}/\text{g}$ from the laboratory uptake experiments. Given the extreme sensitivity of the laboratory uptake measurements to iron contamination, and the fact that iron contamination was ubiquitous throughout the sonic core sediment samples and was difficult to remove, one cannot rule out the possibility that the higher laboratory uptake measurements reflect iron contamination. Indeed, this would be the only way to reconcile the highest lab uptake measurements with the field observations.

It is important to note that the experiments producing the highest Cr(VI) uptake values were conducted with sediments that settled by gravity relatively rapidly (or were not separated at all by gravity). These sediments are considered more likely to contain iron contamination than sediments that did not settle rapidly. The highest mass-weighted uptake values on material that did not settle within 24 h was about

0.004 to 0.005 $\mu\text{g Cr(VI)}$ per g of sediment, or about an order of magnitude lower than the upper bound for the materials that settled rapidly. These values are more compatible with the field observations, although they would still predict a delay in Cr(VI) arrival times relative to nonreactive species of about a factor of 1.4 at an average Cr(VI) concentration of 100 $\mu\text{g/L}$.

3.0 SEQUENTIAL LEACHING EXPERIMENTS TO LEACH ANTHROPOGENIC CHROMIUM FROM AQUIFER SEDIMENTS

3.1 Introduction

As a complement to the Cr(VI) uptake experiments described in the previous section, several attempts were made to determine if there was any anthropogenic Cr(VI) associated with aquifer sediments by conducting sequential leaching experiments on the sediments. In principle, an alkaline leach should remove any Cr(VI) that is adsorbed to the sediments by anion exchange, and acid leaching should remove Cr(III) that has been reduced on sediment surfaces. Successively more aggressive acid leaches can help determine how strongly associated Cr(III) is with the sediments, although stronger acid leaches will also tend to remove considerable Cr(III) that is part of the native minerals in the sediments and not anthropogenically deposited. Acid leaches should also remove most, if not all, the Cr(VI) that is present on surfaces. Samples from contaminated portions of the aquifer must always be compared with similar samples from uncontaminated portions to determine if the chromium leached from a contaminated sample represents an excess relative to the chromium leached from uncontaminated samples. It is also helpful to test the methods by conducting control experiments on samples with known amounts of chromium purposely deposited onto them. Commercially available biotite and bentonite (the latter used by the drilling contractor when completing the sonic core holes as piezometers) were used for this purpose because Cr(VI) uptake was significant on both materials.

Alkaline leaching experiments, which were conducted on biotite, bentonite, and numerous aquifer sediments by employing three successive leaches using a solution of 0.05 M NaHCO_3 + 0.05 M Na_2CO_3 with pH ~ 10 (Figure 3.1-1) at first indicated that as much as 0.1–0.4 $\mu\text{g Cr(VI)}$ per g of sediment was being desorbed from contaminated sediments. However, the field-scale alkaline leaching experiment conducted in well R-42 (discussed in Attachment 1 of this compendium) did not show any evidence of Cr(VI) desorption, and it should have resulted in highly elevated concentrations of Cr(VI) if even the smallest amounts of Cr(VI) that appeared to be desorbed in the laboratory experiments were desorbed in the field because this well has the highest aqueous Cr(VI) concentrations of any in the chromium plume. This result was taken to be an indication that the laboratory alkaline leaching experiments may have simply washed some Cr(VI) off of the sediments that deposited on the surfaces as the sediments dried out before testing. Also, only a small percentage of the Cr(VI) that was uptaken onto biotite and bentonite samples was leached by alkaline leaching, and much of this came in the first leaching step, which indicated that it was likely aqueous carryover from the uptake experiments that were conducted to load the Cr(VI) onto the sediments. Because the alkaline leaching results were considered inconclusive, these leaching experiments were conducted only for the first two of four rounds of sequential leach testing on aquifer sediments, and they are not discussed further in this section. Additional alkaline leach testing was not pursued partly in recognition that even if there is a small amount of Cr(VI) anion exchange occurring on aquifer sediments, this type of adsorption should be fully reversible, and thus it will not provide as effective of a natural attenuation remedy as the reduction of Cr(VI) to Cr(III).

The workflow for the sequential acid leaching procedure is shown in Figure 3.1-2. In addition to removing anthropogenic Cr(III) present from the sediments, the acid leaches should have also been effective at liberating Cr(VI) that was associated with the sediments. The 2 M HNO_3 leach was used only in the early leaching experiments because it became evident that it was removing such a large amount of naturally

occurring chromium from the sediments that any anthropogenic chromium would be almost impossible to detect given the variability in naturally occurring chromium leached from one sediment to the next. Section 3.2 presents the results of acid leaching experiments that were conducted on biotite and bentonite samples [both with and without Cr(VI) deposited onto them] to test the acid leaching method and also to determine a practical detection limit of the method for each material. Section 3.3 presents the results of the four separate sets of acid leaching experiments performed on aquifer sediments. The progression of the four sets of experiments reflects a learning progression as the experiments were conducted and they also reflect what was learned in the biotite and bentonite leaching experiments, which were conducted after the first set of aquifer sediment experiments.

3.2 Biotite and Bentonite Acid Leaching Experiments

3.2.1 Materials

Commercially available biotite (Wards Scientific) and bentonite (used by the drilling contractor when completing the sonic core holes as piezometers) were used as test samples to evaluate the acid leaching methods. An additional interest with the bentonite experiments was to evaluate the potential for artificial suppression of Cr(VI) concentrations in water samples collected from the sonically drilled piezometers caused by the bentonite being used in their completions. Quantitative x-ray fluorescence (XRF) data for the biotite and bentonite are provided in Tables 3.2-1 (major elements) and 3.2-2 (trace elements), respectively.

3.2.2 Evaluation of Leaching Effectiveness

Several experiments were conducted in which biotite and/or bentonite were exposed to Cr(VI) solutions, and the amount of Cr(VI) that became associated with these materials was measured in the same manner as in uptake experiments (see section 2). Given that Cr(VI) uptake was substantial on both materials, it is likely that the Fe₂O₃ reported in Table 3.2-1 for each material was at least partially in the form of reduced iron (Fe²⁺), which is capable of reducing Cr(VI) to Cr(III). Once the Cr(VI) uptake on the samples was measured, the biotite and/or bentonite was removed from the Cr(VI) solution, washed, and then subjected to the sequential acid leaching procedure. Nonexposed samples of the biotite and bentonite were also subjected to the leaching procedure along with the exposed samples. Figure 3.2-1 shows the results of sequential acid leaching on biotite, and Figure 3.2-2 shows the results for bentonite.

In Figure 3.2-1 it is apparent that more Cr(VI) was actually leached from the biotite by the 0.1 M HNO₃ (4th, 5th, and 6th steps) than was taken up on the biotite in the uptake experiments. This result is difficult to explain, although it is possible that more Cr(VI) was uptaken on the biotite between the time the aqueous sample was taken for the uptake measurement and the time that the biotite was actually removed from the Cr(VI) solution. Regardless of this discrepancy, it is apparent that the 0.1 M HNO₃ leach was quite effective at removing the uptaken chromium, and not much natural chromium was leached from the unexposed biotite until the 2 M HNO₃ was employed (7th, 8th, and 9th steps). In contrast, the leaching of Cr(VI) taken up on the bentonite was incomplete, and only a small fraction of the Cr(VI) was leached until the 2 M HNO₃ was employed. The bentonite also contained very little natural chromium leached.

These results indicated that the 0.1 M HNO₃ should be sufficient to remove anthropogenic chromium from aquifer sediments that behave like biotite, and the 2 M HNO₃ steps may actually be somewhat detrimental for such sediments because they contribute mostly natural chromium, which will tend to dilute the anthropogenic chromium signal. However, if aquifer materials behave more like bentonite, leaching with 2 M HNO₃ will be required to remove most of the anthropogenic chromium. After conducting one set of experiments on aquifer sediments using all nine acid leaching steps, it became apparent that the amount of chromium leached from the sediments by the 2 M HNO₃ greatly exceeded any reasonable amount of

anthropogenic chromium that might have become associated with the sediments. Even sediments that came from uncontaminated areas of the regional aquifer yielded large amounts of chromium in the 2 M HNO₃ leaches. Amounts of chromium leached from both contaminated and uncontaminated sediments by the 2 M HNO₃ ranged from 1 to 10 µg of chromium per g of sediment, which is about 2 orders of magnitude larger than the Cr(VI) uptake observed in any of the uptake experiments discussed in section 2 (an upper bound of 0.05 µg/g). It also became apparent in the first set of sediment leaching experiments that the amounts of chromium and iron leached from the sediments were highly correlated, which is not surprising given that the two elements are often found together in minerals. Figure 3.2-3 is a log-log crossplot of chromium vs iron leached from uncontaminated sediments in the first set of leaching experiments, along with the chromium vs iron data for the unexposed biotite and bentonite in the experiments that produced the data of Figures 3.2-1 and 3.2-2. It is apparent that the chromium and iron are highly correlated for all materials, although the uncontaminated sediments (which include different size fractions and both magnetic and nonmagnetic fractions) have greater Cr/Fe ratios than either the biotite or the bentonite. Figure 3.2-4 is a log-log cross-plot of Fe vs Cr leached for both exposed and unexposed biotite, and Figure 3.2-5 is an analogous plot for exposed and unexposed bentonite. Figure 3.2-4 shows that the 0.1 M HNO₃ leaches provide better log separation of the Cr/Fe ratios leached from the exposed vs unexposed biotite than the 2 M HNO₃ leaches. Also, Figure 3.2-5 shows that the 0.1 M HNO₃ leaches provide similar log separation between the Cr/Fe ratios leached from the exposed vs unexposed bentonite as with the exposed vs unexposed biotite in Figure 3.2-4, despite the fact that the majority of the chromium was leached from the bentonite by the 2 M HNO₃. Furthermore, the log separation between the Cr/Fe ratios for the exposed vs unexposed bentonite did not improve for the 2 M HNO₃ leaches relative to the 0.1 M HNO₃ leaches.

Given all the above observations, and recognizing the difficulty associated with measuring small amounts of anthropogenic chromium when leaching ever larger amounts of chromium, it was decided that the 2 M HNO₃ leaching steps would not be employed after the first set of sediment leaching experiments. The 0.1 M HNO₃ leaches were deemed sufficient, and in fact optimal, for detecting small amounts of anthropogenic chromium even if they did not remove all of the available anthropogenic chromium from a given sample. Also, because there is greater variability in absolute iron and chromium amounts leached from aquifer sediments than there is in the Cr/Fe ratios leached from the sediments, it was decided that examining differences in leached Cr/Fe ratios between contaminated and uncontaminated sediments was a better way to detect anthropogenic chromium than simply examining the differences in chromium leached from the sediments.

3.2.3 Evaluation of Method Detection Limit with Biotite and Bentonite

An additional set of sequential acid leaching experiments with biotite and bentonite was conducted to estimate the effective detection limit of the method with 0.01 M and 0.1 M HNO₃ leaches. In these experiments, biotite and bentonite samples were exposed to solutions with different Cr(VI) concentrations [including no Cr(VI)] so that different amounts of chromium would be taken up on them. Then all the samples were subjected to the sequential acid leaching procedure. Figure 3.2-6 is a plot of the excess Cr/Fe ratio leached from Cr(VI)-exposed biotite samples vs the amount of Cr(VI) uptaken on the samples, and Figure 3.2-7 is an analogous plot for bentonite. The “excess Cr/Fe ratio” is the Cr/Fe ratio leached from a sample exposed to Cr(VI) minus the Cr/Fe ratio from a sample not exposed to Cr(VI). In each case, the ratios are calculated from the cumulative amounts of chromium and iron leached from all six steps of the sequential leaching procedure. Each of the data points in Figures 3.2-6 and 3.2-7 represents the average of two duplicate measurements of a Cr(VI)-exposed sample minus the average of two duplicate measurements of a sample not exposed to Cr(VI). Two sets of experiments were conducted for the biotite, so two data sets are shown in Figure 3.2-6. The x-intercepts of the linear regression lines shown in Figures 3.2-6 and 3.2-7 correspond to the Cr(VI) uptakes for which the Cr/Fe ratio of the

leachates from Cr(VI)-exposed sediments cannot be distinguished from the Cr/Fe ratio of leachates from unexposed sediments. These intercepts are taken to be the effective detection limits of the sequential leaching procedure for measuring Cr(VI) uptake on the biotite or bentonite, and they are relatively large compared with the amounts of Cr(VI) that became associated with aquifer sediments in the Cr(VI) uptake experiments discussed in the previous section (an upper bound of about 0.05 $\mu\text{g/g}$). Given that the bentonite and biotite are relatively homogeneous materials that should have much less variability in background levels of chromium, iron, and Cr/Fe ratios than what was leached from aquifer sediments taken from different parts of the aquifer, it was recognized that detecting anthropogenic chromium in sequential leaching experiments would be a challenge. Nevertheless, four separate sets of aquifer sediment leaching experiments were conducted, including the first set mentioned above, to look for evidence of anthropogenic chromium on sediments from contaminated portions of the aquifer. These experiments are discussed in the next section.

3.3 Sequential Leaching of Aquifer Sediment Samples

3.3.1 Samples

Table 3.3-1 lists all the aquifer sediment samples that were used in sequential acid leaching experiments. The samples are divided into four categories distinguished by sample type and purpose. The last column of Table 3.3-1 lists the experiment set number in which the samples were used (see section 3.3.2).

3.3.2 Four Sets of Sequential Acid Leaching Experiments

Four separate sets of sequential leaching experiments were conducted, with the primary differences between the sets being the different methods of sample preparation (although the last two sets had the same sample preparation method and differed only in that the final set used samples only from uncontaminated horizons in sonic core holes). Leaching with 2 M HNO_3 was employed only in the first set of experiments, with the remaining sets involving only three 0.01 M HNO_3 leaches followed by three 0.1 M HNO_3 leaches (Figure 3.1-2). Table 3.3-2 summarizes the differences in the four sets of tests. The solution (leachate)-to-solid mass ratio in most tests was 10:1 (20-mL to 2-g solids in each leaching step), although when only small amounts of sediment material were available for a particular size/magnetic fraction, the ratio was sometimes increased. Also, when material was plentiful, a smaller ratio was sometimes used. The leaching results did not seem to show much dependence on the solution-to-solid mass ratio, so this variable is not discussed further.

3.3.3 Sequential Acid Leaching Results

The results from the sequential acid leaching experiments are presented here as a series of crossplots of log Cr leached vs log Fe leached, similar to Figures 3.2-3 through 3.2-5. Figure 3.3-1 shows the cumulative amounts of chromium and iron leached through the 0.1 M HNO_3 steps and through the 2 M HNO_3 steps from the first set of experiments, irrespective of which type of sample was leached. It is apparent that the 2 M HNO_3 steps effectively serve to extend the trend(s) observed in the 0.1 M HNO_3 steps. Differences between contaminated and uncontaminated samples for these two different acid leaching strengths are shown in Figures 3.3-2 (2 M HNO_3) and 3.3-3 (0.1 M HNO_3). The contaminated samples, shown as red symbols in both figures, appear to have somewhat greater Cr/Fe ratios than the uncontaminated samples, suggesting that some anthropogenic chromium may have been leached. However, in Figure 3.3-3, the vertical separation between the dashed lines corresponds to the effective detection limit for chromium of the 0.1 M HNO_3 leaching steps for biotite (taken to be 1 μg chromium/g sediment), and it is apparent that differences between the contaminated and uncontaminated samples generally fall within this detection limit range. Given the scatter in the data, and the inevitable differences

in chromium and iron contents of sediments taken from different portions of the aquifer, it would be difficult to claim with certainty that any anthropogenic chromium was leached.

Figure 3.3-4 summarizes the results from the second set of experiments, which involved samples that were all potentially in contact with Cr(VI) in either the unsaturated zone or saturated zone. All of the samples were either from the Puye Formation or from the Cerros del Rio basalt. It is apparent that the sonic core hole samples from the regional aquifer had larger Cr/Fe ratios in leachates than any of the unsaturated zone samples, and the basalt samples had much smaller Cr/Fe ratios than any of the Puye samples. This data set is considered inconclusive because all of the samples were potentially in contact with Cr(VI) contamination.

Figure 3.3-5 shows the results from the third set of experiments, with three different colored symbols used for the three different types of magnetic separation of the samples, irrespective of where the samples came from. It is clear that the more magnetic samples have greater amounts of both iron and chromium leached from them. Figure 3.3-6 shows the same data as Figure 3.3-5 but color-coded according to whether the sample came from a contaminated portion of the aquifer or not. One of the contaminated samples was actually “contaminated” in the laboratory in a Cr(VI) uptake experiment; this sample (from CrCH-5, 1001 ft) came from an uncontaminated horizon, and it was used in an uptake experiment without removing iron filings contamination that might be present (and iron filings were later confirmed). Thus, it was considered to provide good representation of a sample with anthropogenic Cr(VI) uptake that most likely occurred on iron contamination. The exact amount of Cr(VI) associated with the sample was not known because the sample was used in a qualitative experiment in which the sediments were just being conditioned with contaminated water in preparation for a biostimulation experiment (it was not a formal uptake experiment). In Figure 3.3-6 it is apparent that it is difficult to see any conclusive difference between the contaminated and uncontaminated samples.

Figure 3.3-7 shows the results of the final set of experiments, with three different colored symbols for the three different types of magnetic separation of the samples. In this set of experiments, all the samples were taken from horizons within sonic core holes that were believed to be free of Cr(VI) contamination, and the primary purpose of the experiments was to increase the baseline of data for uncontaminated horizons.

Figure 3.3-8 shows the results of all four sets of experiments plotted together, with red symbols used for contaminated samples and black symbols used for uncontaminated samples (and blue x's for the basalt samples). The vertical difference between dashed lines corresponds to the effective detection limit for Cr(VI) uptake on biotite; these lines are not extended beyond a leached chromium value of 10 $\mu\text{g/g}$ because the lines converge to where their difference (1 $\mu\text{g/g}$) cannot be distinguished on a log-log plot. It is apparent from Figure 3.3-8 that the red contaminated data points seem to fall slightly to the upper left of the black uncontaminated data points, suggesting a small amount of chromium uptake may have occurred on the contaminated sediments. However, other than the contaminated data points at the extreme upper right of the plot (which are all samples that likely contained iron filings contamination), all of the contaminated data points have nearby uncontaminated data points that fall within the vertical separation of the dashed lines that correspond to the effective detection limit for uptake on biotite.

Figure 3.3-8 also shows a pair of lines that correspond to the range of Cr/Fe ratios measured in strong acid leaches (2 M HNO_3 only) of iron filings taken directly from a sonic coring bit, and also iron filings removed from a contaminated section of sonic core itself. These lines indicate that any iron contamination could impart a false chromium signal on the sediments regardless of whether or not the filings came in contact with any Cr(VI) contamination.

No attempt is made here to present any comparisons of contaminated vs uncontaminated sediments from specific lithologies. Such comparisons suggest that there may be a slightly greater amount of anthropogenic chromium associated with Miocene pumiceous sediments than Puye or Puye pumiceous subunit sediments, although the suggestion of anthropogenic chromium on either type of sediment is rather unconvincing given the effective detection limit of chromium associated with biotite and also the overall scatter in the data.

3.4 Conclusions from Sequential Leaching Experiments

The results from the sequential acid leaching experiments are generally consistent with the uptake experiments discussed in the previous section in that they suggest little or no uptake of anthropogenic chromium on regional aquifer sediments taken from the chromium plume area. By simple examination of Figure 3.3-8, one might conclude an uptake of as much as 0.2 to 1 $\mu\text{g Cr(VI)}$ per g of sediment in the plume area, which is somewhat greater than the upper bound of 0.05 $\mu\text{g Cr(VI)/g}$ reported for the uptake experiments. This estimate is not corrected for the mass fraction of sediments that were actually leached (as the uptake experiment estimates were), but the tendency for slightly higher Cr/Fe ratios in contaminated samples appears to persist for all mass fractions in Figure 3.3-8. However, it must be acknowledged that the sequential leaching method is less precise than the uptake experiments because it relies on comparing results from contaminated and uncontaminated sediments, whereas the uptake experiments involve a direct measurement of Cr(VI) uptake on any given sample. Also, the sequential leach testing of biotite and bentonite exposed to Cr(VI) indicated a method detection limit for anthropogenic Cr(VI) of no better than about 1 $\mu\text{g Cr(VI)/g}$ (and closer to 5 $\mu\text{g Cr(VI)/g}$ for bentonite). It must also be acknowledged that the sequential leaching method is subject to the same biases caused by the presence of anthropogenic iron contamination as the uptake experiments. The Cr(VI) uptake experiments showed that anthropogenic iron can result in orders of magnitude more Cr(VI) uptake than appears to occur on natural sediments, and such uptake will be reflected in sequential leaching experiments if iron contamination is present.

4.0 SUMMARY OF SYNCHROTRON EXPERIMENTS TO EVALUATE CR(VI) REDUCTION TO CR(III) ON OUTCROP MATERIALS OR SONIC CORE HOLE SEDIMENTS

Two sets of experiments were conducted at x-ray synchrotron facilities that qualitatively verified the ability of at least a small subset of aquifer materials to reduce Cr(VI) to Cr(III). The experiments were conducted at SSRL at Stanford, CA, and at the Advanced Photon Source (APS) at Argonne National Laboratory, IL. Synchrotron-based XANES is a powerful method for distinguishing Cr(VI) and Cr(III), because of the prominent pre-edge peak at 5995 eV for Cr(VI) in a tetrahedral coordination and the higher energy of the main edge for Cr(VI) relative to Cr(III) (in an octahedral coordination) (Peterson et al. 1997). XANES spectra of a series of standards containing varying amounts of Cr(VI) relative to Cr(III) are shown in Figure 4.0-1. In addition, micro XRF can map elemental distributions of chromium and other metal elements, especially iron, in minerals, revealing their spatial correlations.

In the first set of synchrotron experiments, both Cr(VI)-exposed and unexposed samples of the <2 μm size fraction of the Puye outcrop sample from Rendija Canyon that had exhibited considerable Cr(VI) uptake in batch experiments (mentioned in the second paragraph of section 2.2) were taken to SSRL, where XANES and micro-x-ray mapping were conducted on both samples. Additionally, XANES spectra were obtained for other Cr(VI)-exposed outcrop samples that did not exhibit any Cr(VI) uptake in batch experiments. The XANES spectra of the outcrop samples were compared with the XANES spectra of three mineral "standards" known to contain only Cr(III), and also two samples that were known to have reduced Cr(VI) from solution to Cr(III). One of the latter two samples was a biotite sample taken from a

batch Cr(VI) uptake experiment, and the other sample was a sediment taken from the Sandia wetland source area of the chromium plume that was known to have an anthropogenic Cr(III) content of about 17 ppm.

The XANES spectra of the three Cr(III) “standards,” the biotite, and the wetland sample are shown in Figure 4.0-2. The spectra of the biotite and wetland samples clearly lack the Cr(VI) pre-edge peak, and they were taken to be representative of samples that reduced Cr(VI) from solution to Cr(III). The Cr(III) standards are shown to illustrate that their XANES spectra differ from the samples exposed to Cr(VI) solutions, despite the fact that none of the samples appears to contain any Cr(VI).

Figure 4.0-3 shows the XANES spectra of the wetland sample along with the spectra for three of the outcrop samples. The “Ren-2 <2 μm+Cr” sample is the only outcrop sample that took Cr(VI) out of solution, and it is apparent that its spectra is quite similar to the wetland sample (and the biotite sample of Fig. 4.0-2). The other two outcrop samples, which did not take any Cr(VI) out of solution, have spectra that are similar to the Cr(III) standards of Figure 4.0-2. Thus, the spectrum of the “Ren-2 <2 μm+Cr” sample suggests that the Cr(VI) that was uptaken onto this sample was reduced to Cr(III) in a manner similar to the Cr(VI) that was uptaken onto the wetland sample and the biotite.

Figure 4.0-4 shows the results of micro-XRF mapping (top) and spot-XANES (bottom) of both unexposed (left) and Cr(VI)-exposed (right) fractions of the <2 μm Puye outcrop sample. The samples were fixed on a microscope slide with double-backed tape for the measurements. The micro-XRF maps show that both maps have chromium “hot spots”, which tended to be highly correlated with iron “hot spots” (not shown). However, some of the chromium hot spots in the Cr(VI)-exposed sample have XANES spectra that are similar to the Cr(VI)-exposed samples of Figure 4.0-3, whereas all the hot spots in the unexposed sample have XANES signatures that are consistent with no Cr(VI) uptake. While these data are clearly qualitative, they suggest that the Cr(VI) that was uptaken onto the outcrop sample was reduced to Cr(III). Also, unlike Figure 4.0-3, Figure 4.0-4 shows a direct comparison of the same sample that was both exposed and not exposed to Cr(VI).

The second set of synchrotron experiments was conducted at APS, and it involved the use of a “clay-size” fraction of material isolated by gravity settling from a sonic core hole sample collected from CrCH-1 at a depth of 1121 ft (just below the water table). The sample was estimated (based on Stokes settling calculations) to have a size range of 0.25–0.7 μm, and it composed about 0.9 wt% of the sonic core sample. This fine material was dispersed in a 20-mg/L Cr(VI) solution at APS, and XANES spectra were collected as a function of time. Some of the spectra are shown in Figure 4.0-5, and it is apparent that the Cr(VI) pre-edge peak diminished over time, which suggests that the Cr(VI) in solution was gradually reduced on the fine suspended particles. These data indicate that very fine material from regional aquifer sediments appear to be capable of reducing Cr(VI) to Cr(III). Quantitative estimates of Cr(VI) uptake values in these experiments were not possible because the solid-to-solution mass ratio was not controlled. While uptake was obviously significant, it must be kept in mind that any uptake estimate would have to be multiplied by 0.009 (the mass fraction of the fine material in the sample) to be converted to a bulk sediment basis.

5.0 REFERENCES

The following reference list includes documents cited in this report.

- Chapuis, R.P., and M. Aubertin. "On the Use of the Kozeny-Carman Equation to Predict the Hydraulic Conductivity of Soils," *Canadian Geotechnical Journal*, Vol. 40, No. 3, pp. 616–628, 10.1139/t03-013 (2003).
- LANL (Los Alamos National Laboratory). "Investigation Report for Sandia Canyon," Los Alamos National Laboratory document LA-UR-09-6450, Los Alamos, New Mexico (2009).
- Odong, J. "Evaluation of Empirical Formulae for Determination of Hydraulic Conductivity Based on Grain-size Analysis," *Journal of American Science* Vol. 3, No. 3, pp. 54–60 (2007).
- Peterson M., G.E. Brown Jr., G.A. Parks, and C.L. Stein. "Differential Redox and Sorption of Cr(III/VI) on Natural Silicate and Oxide Minerals: EXAFS and XANES Results," *Geochimica et Cosmochimica Acta*, Vol. 61, No. 16, pp. 3399–3412 (1997).
- Zhang, Z.F., A.L. Ward, and J.M. Keller. "Determining the Porosity and Saturated Hydraulic Conductivity of Binary Mixtures," Pacific Northwest National Laboratory publication 18801, Retrieved from http://www.pnl.gov/main/publications/external/technical_reports/PNNL-18801.pdf (2009).

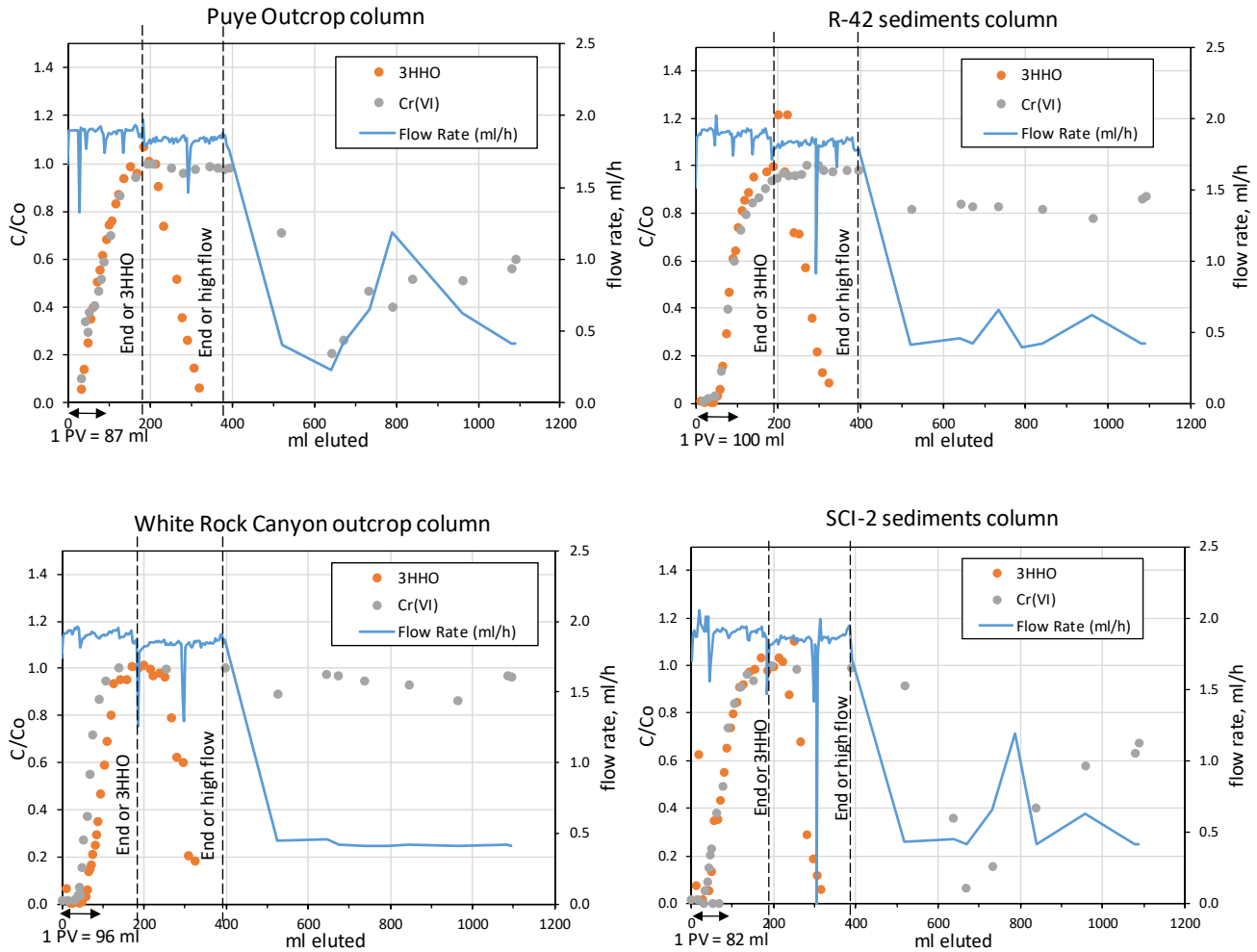


Figure 2.3-1 Normalized ^3HHO and Cr(VI) concentrations (concentrations divided by injection concentration, C/C_0) and flow rate (mL/h) as a function of volume eluted in four column experiments in which R-42 water spiked with ^3HHO was injected for approximately 2 pore volumes followed by unspiked R-42 water. Columns in left-hand plots were packed with outcrop material, and columns in right-hand plots were packed with core or cuttings samples from R-42 and SCI-2. 1 PV = 1 column pore volume.

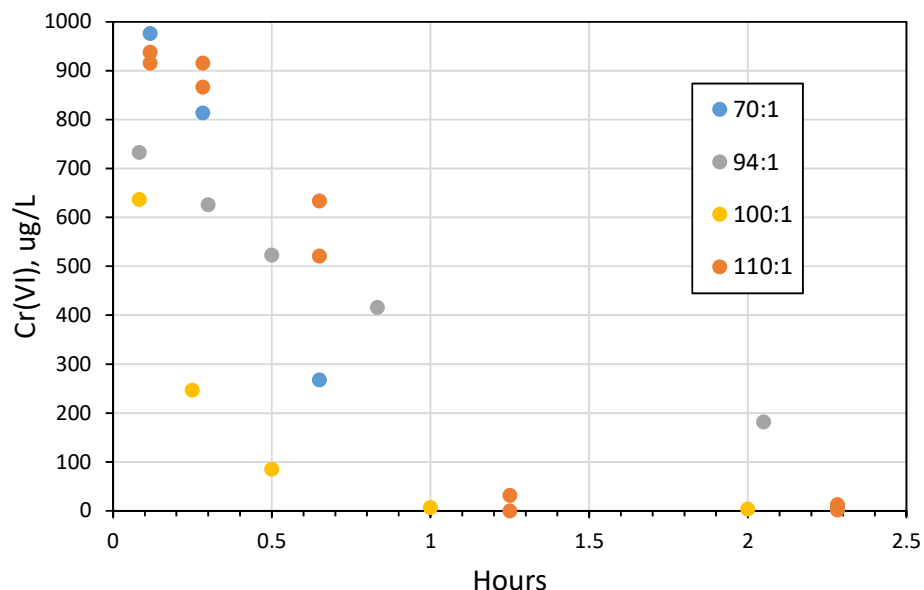


Figure 2.3-2 Results of batch uptake experiments conducted on zero-valent iron filings at various solution-to-solid mass ratios (see legend). All experiments were conducted using R-42 water with a starting concentration of 900–1000 $\mu\text{g/L}$ Cr(VI), and the y-axis is the concentration of Cr(VI) remaining in solution. Chromium uptakes ranged from 50 to 100 $\mu\text{g Cr/g}$, but they did not represent the full capacity of the zero-valent iron for Cr(VI).

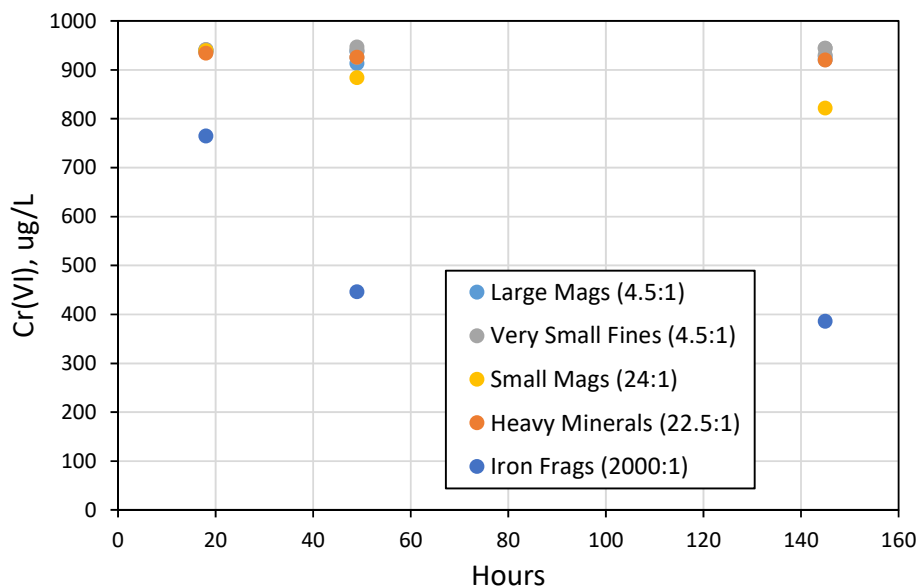


Figure 2.3-3 Results of batch uptake experiments conducted on different fractions separated from bulk sonic core from CrCH-4, 967 ft below land surface (BLS). All experiments were conducted using R-42 water with a starting concentration of $\sim 950 \mu\text{g/L}$ Cr(VI), and the y-axis is the concentration of Cr(VI) remaining in solution. The iron fragments were separated from the core material. Numbers in parentheses in the legend are the solution-to-solid mass ratio for each fraction.

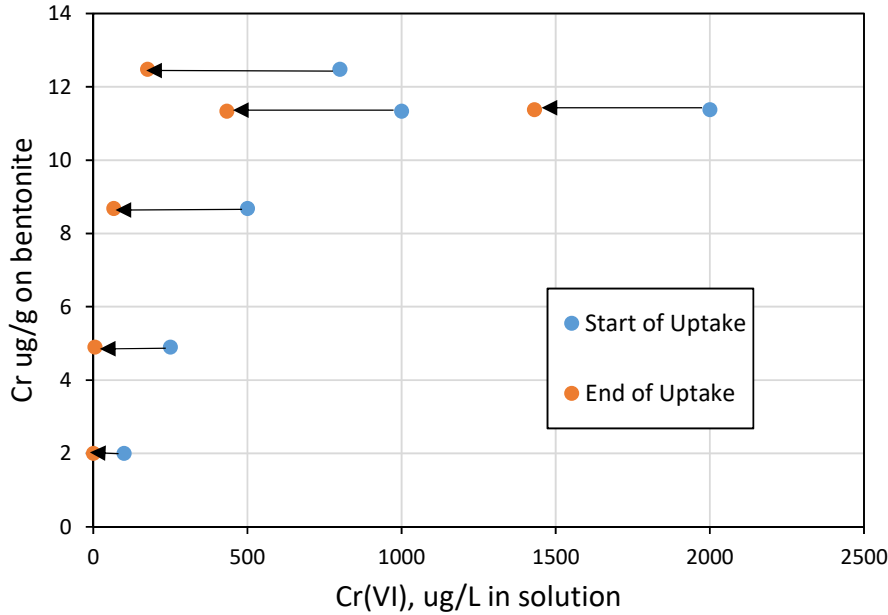


Figure 2.3-4 Cr(VI) uptake on drillers’ bentonite used in sonic core hole completions as a function of starting concentration of Cr(VI) at a pH of ~8.5. Arrows graphically illustrate Cr(VI) uptake on bentonite (difference between starting and ending concentrations in solution). Cr(VI) uptake peaked at about 12 μg/g of bentonite once the starting Cr(VI) concentration exceeded 500 μg/L in solution. Experiments were conducted at a solution-to-solid mass ratio of 20:1. Note that Cr(VI) uptake on bentonite was greater at lower pH and less at higher pH.

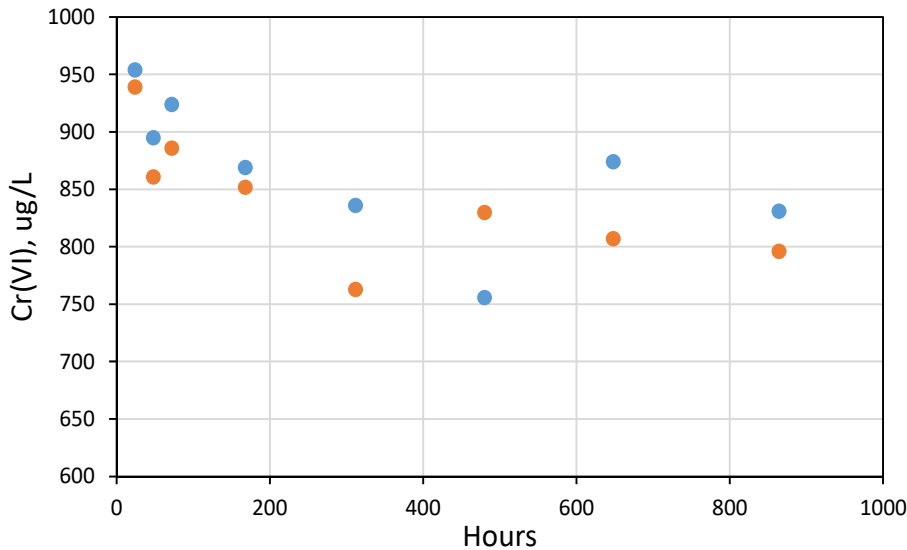


Figure 2.3-5 Cr(VI) batch uptake on R-42 sediments used in the R-42 column experiment shown in Figure 2.3-1. The two symbols are duplicate experiments. All experiments were conducted using R-42 water with a starting concentration of ~1000 μg/L Cr(VI), and the y-axis is the concentration of Cr(VI) remaining in solution. The initial solution-to-solid mass ratio was 1:4, and the final ratio was about 1:7. Cr(VI) uptake on the sediments at the end of the experiment was 0.04 to 0.05 μg Cr(VI) per g of sediment.

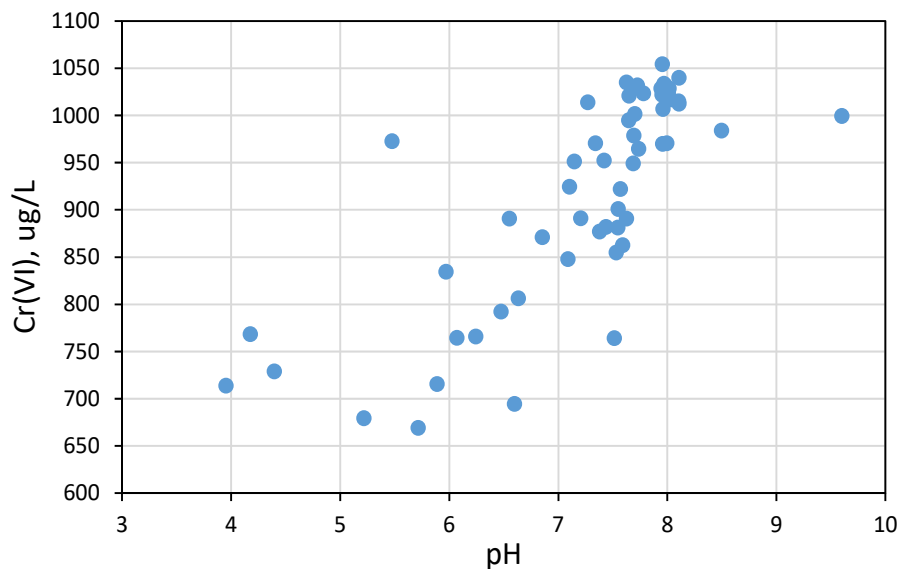


Figure 2.3-6 pH dependence of Cr(VI) uptake on sediments from CrCH-5, 998–1005 ft BLS. Experiments were conducted at a solution-to-solid mass ratio of 20:1 and starting Cr(VI) concentrations from 1036 to 1050 $\mu\text{g/L}$, and the y-axis is the concentration of Cr(VI) remaining in solution. These sediments were later discovered to contain iron contamination, so uptake far exceeded that observed in any iron-free experiments, but the pH dependence of uptake was considered to be qualitatively representative of uptake on aquifer sediments.

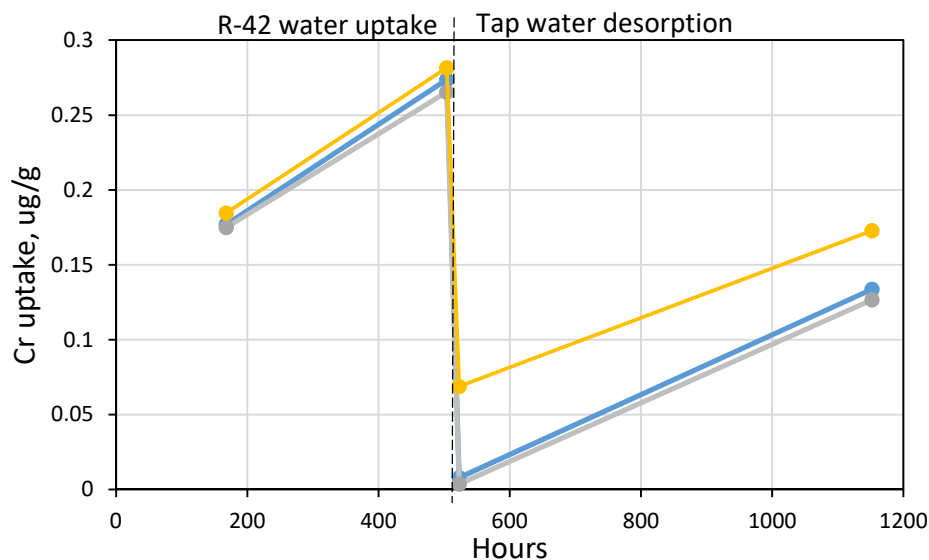


Figure 2.3-7 Cr(VI) uptake onto material from CrCH-5, 998–1005 ft BLS, which did not settle by gravity after 120 h, and subsequent desorption of Cr(VI) after exposure to Los Alamos tap water. Solution-to-solid mass ratios ranged from about 0.7:1 to 1.4:1.

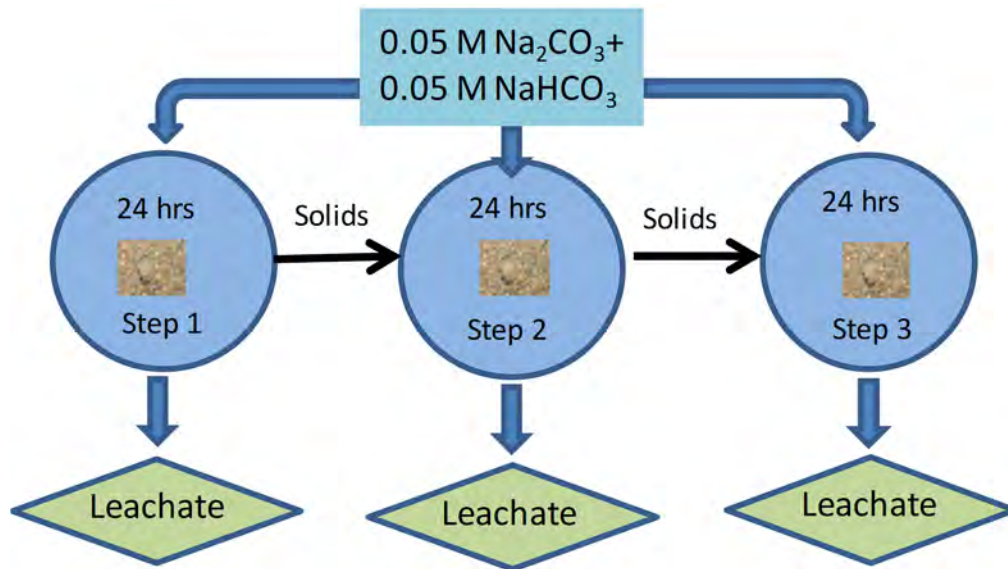


Figure 3.1-1 Workflow of sequential alkaline leaching procedure. Leachate to solid mass ratio was 10:1 in most tests.

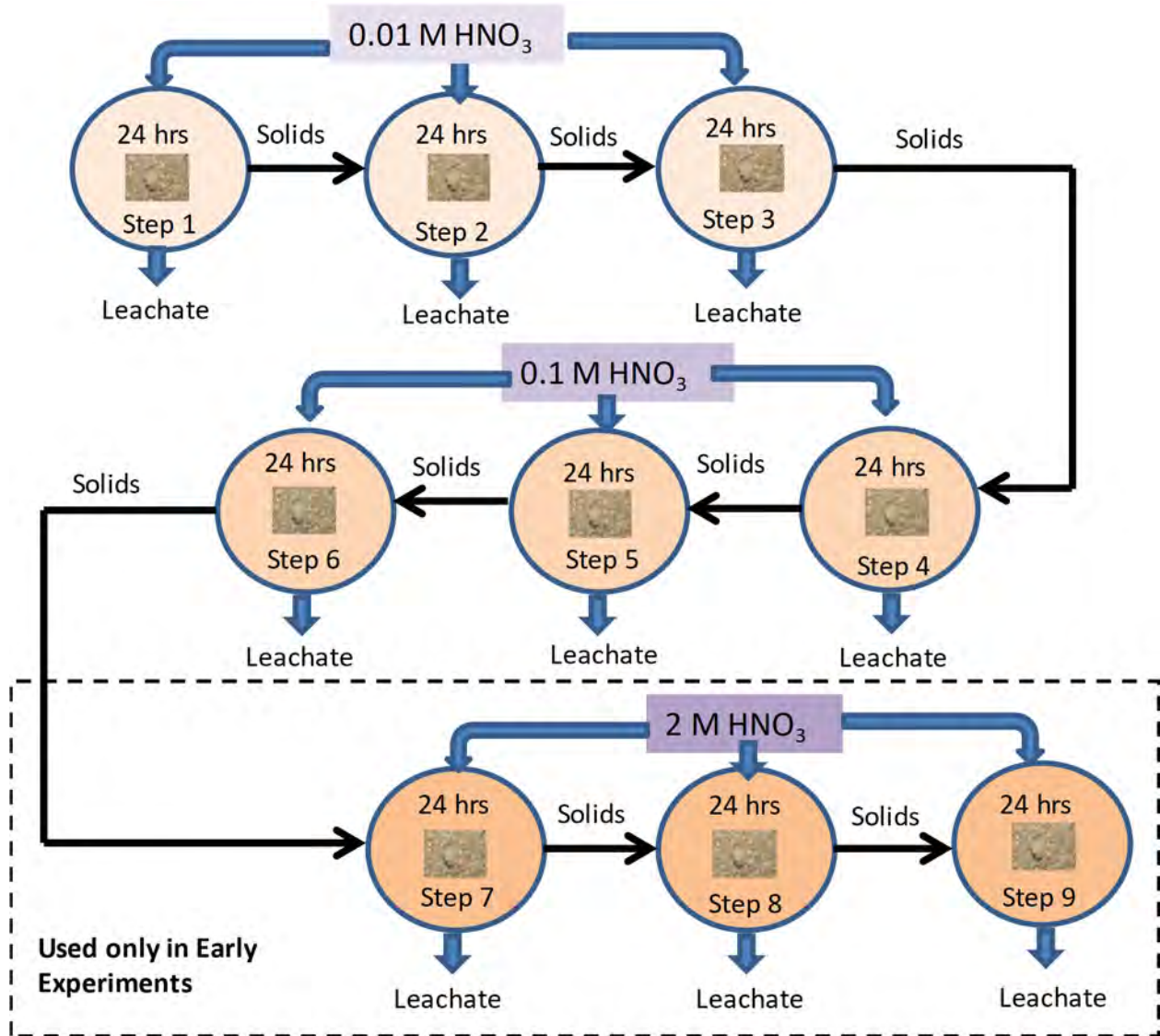


Figure 3.1-2 Workflow of sequential acid leaching procedure. Leachate to solid mass ratio was 10:1 in most tests. Note that the 2 M HNO₃ steps were used only in early experiments.

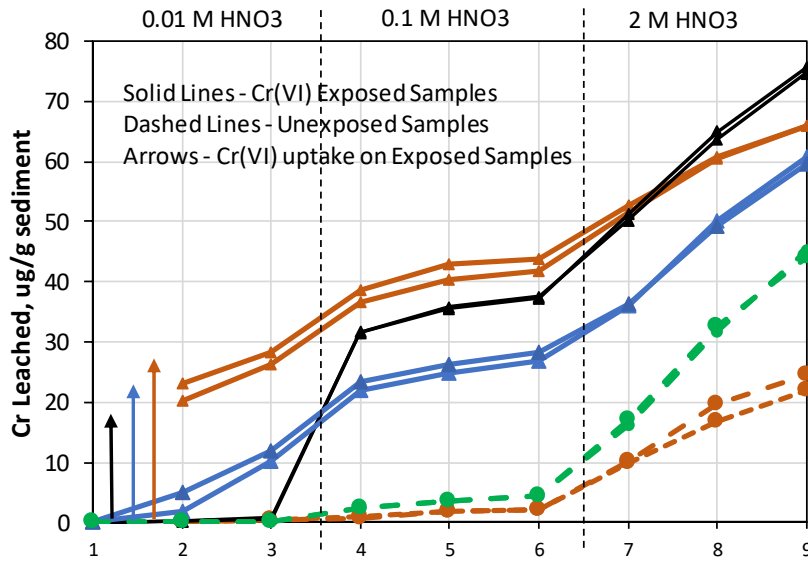


Figure 3.2-1 Cumulative chromium leached from biotite exposed to Cr(VI) solutions as a function of leaching step in three experiments with duplicate samples in each experiment (solid lines). Green dashed lines correspond to unexposed samples leached at same time as black and blue solid lines, and brown dashed lines correspond to unexposed samples leached at same time as brown solid lines. The arrows indicate the Cr(VI) uptake measured on the corresponding solid-line samples before leaching. Only two 0.01 M HNO₃ steps were used for the samples associated with the brown lines.

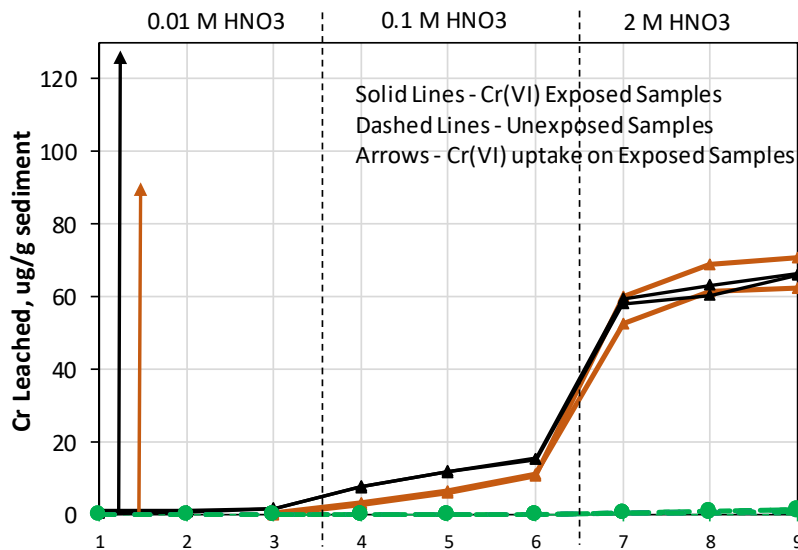


Figure 3.2-2 Cumulative chromium leached from bentonite exposed to Cr(VI) solutions as a function of leaching step in two experiments with duplicate samples in each experiment (solid lines). Green dashed lines correspond to unexposed samples. The arrows indicate the Cr(VI) uptake measured on the corresponding solid-line samples before leaching.

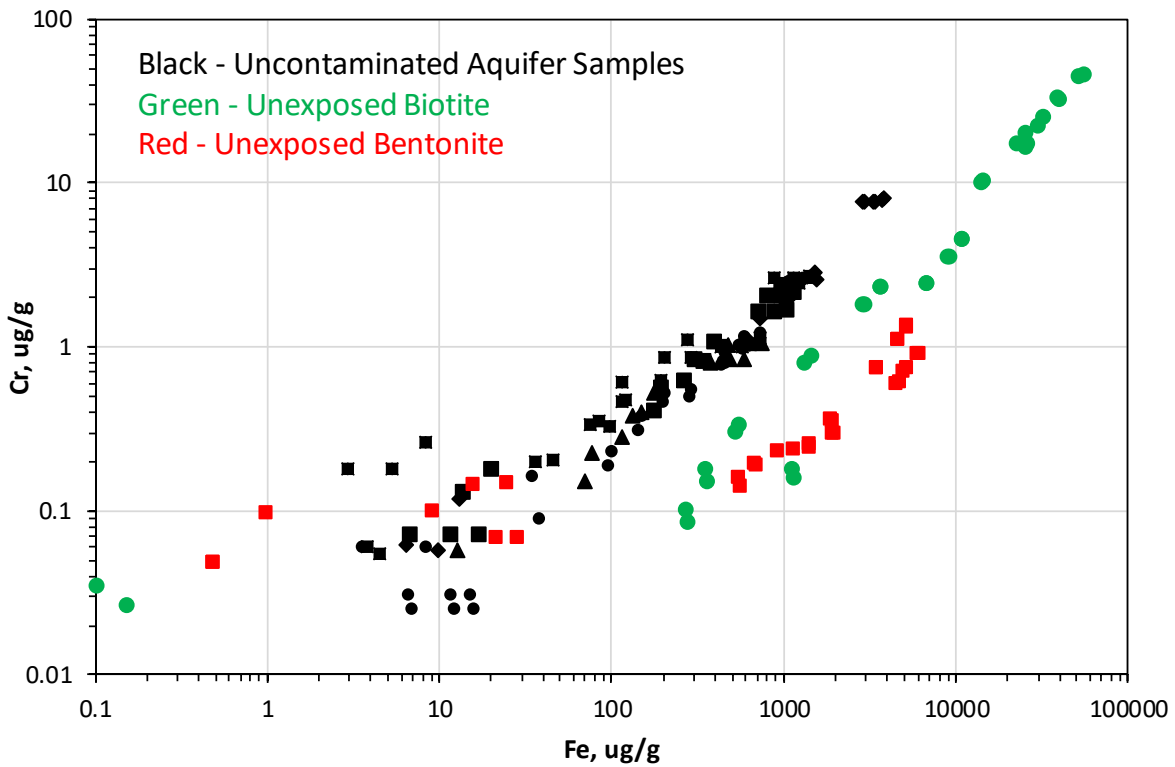


Figure 3.2-3 Cumulative log Cr vs log Fe of leachates from uncontaminated aquifer samples (black), unexposed biotite (green), and unexposed bentonite (red). Data for all nine steps of sequential acid leaching (0.01 M, 0.1 M, and 2 M HNO_3) are shown (cumulative amounts after each step). Aquifer samples have higher Cr/Fe ratios than either biotite or bentonite.

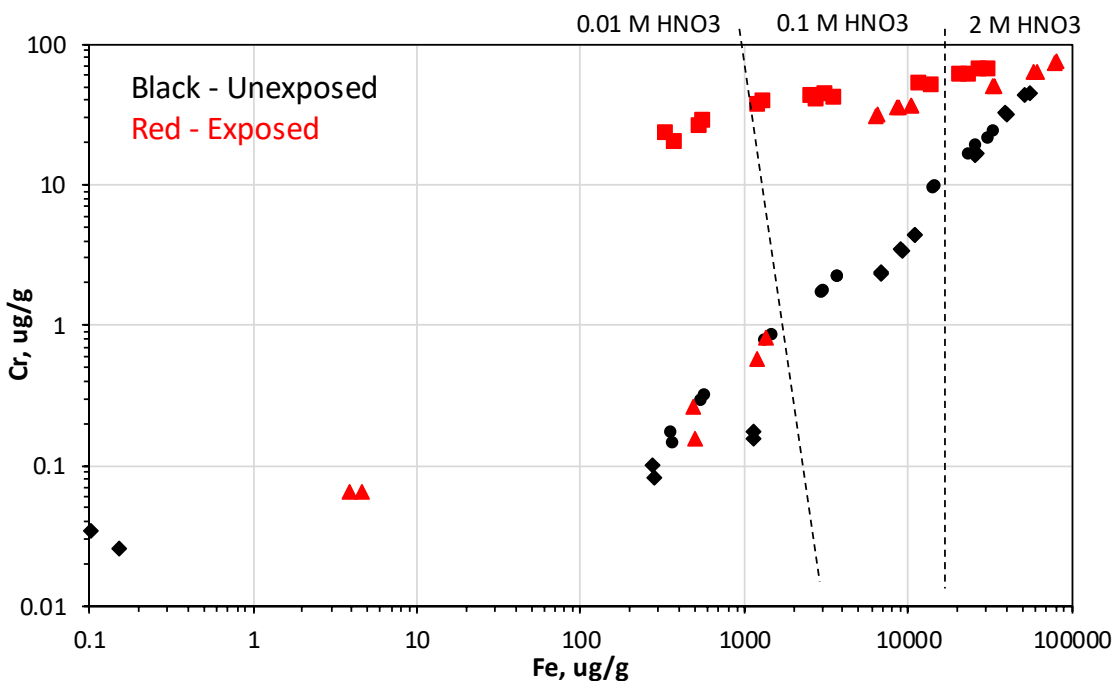


Figure 3.2-4 Cumulative log Cr vs log Fe of leachates from Cr(VI)-exposed and unexposed biotite samples. Leachates are from experiments of Figure 3.2-1.

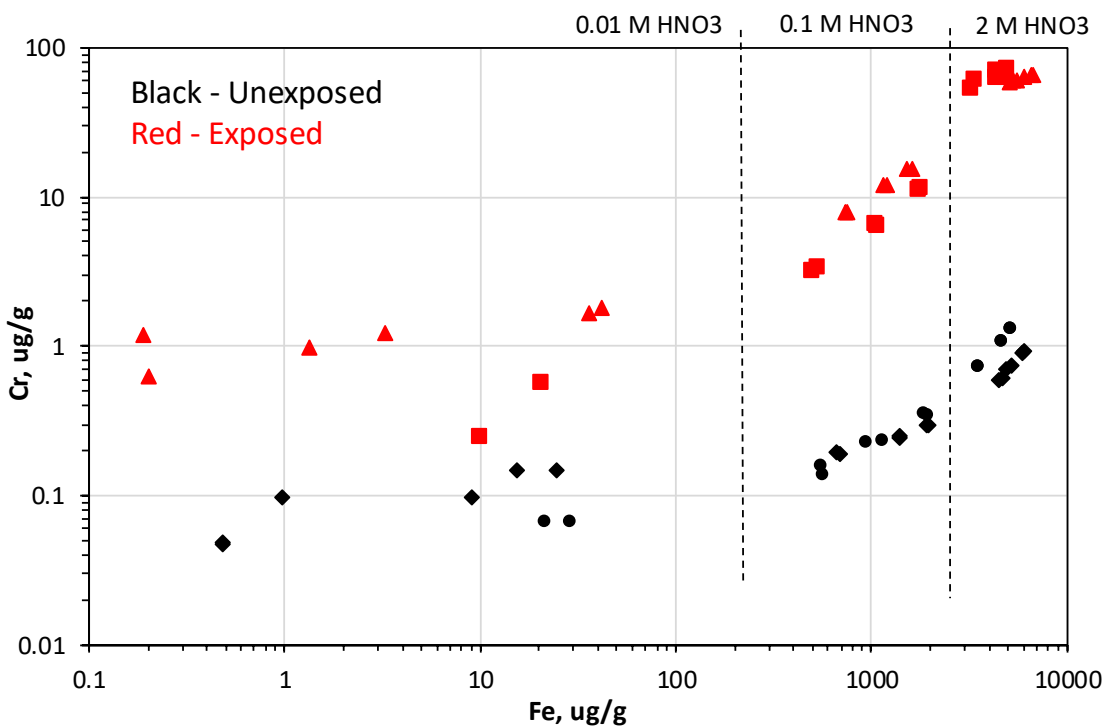


Figure 3.2-5 Cumulative log Cr vs log Fe of leachates from Cr(VI)-exposed and unexposed bentonite samples. Leachates are from experiments of Figure 3.2-2.

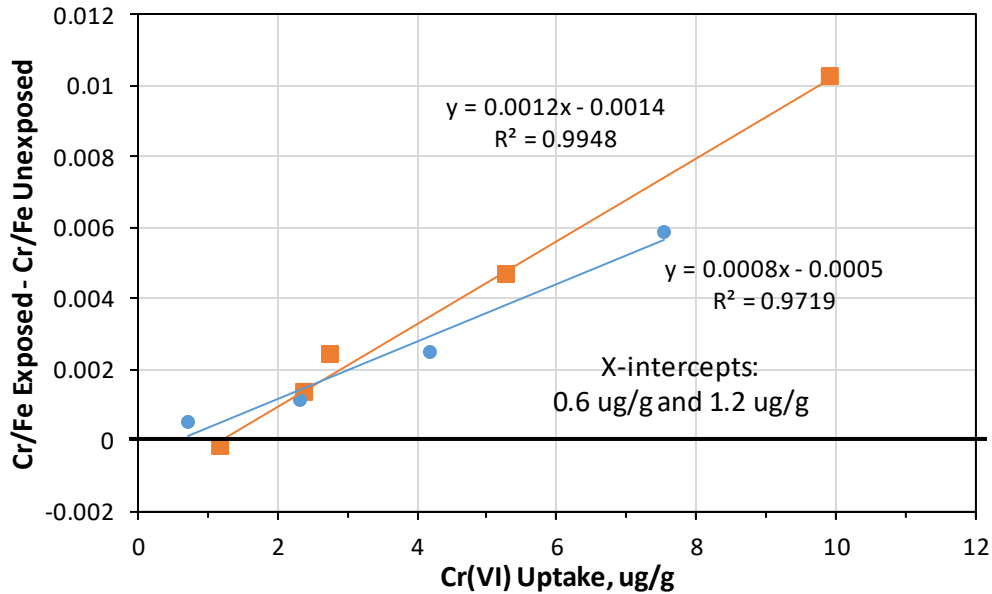


Figure 3.2-6 Cumulative Cr/Fe ratios of 0.1 M HNO₃ leachates from Cr(VI)-exposed biotite samples minus Cr/Fe ratio of leachates from unexposed biotite samples vs Cr(VI) uptake on exposed samples. Each data point is the average of two duplicate measurements. X-intercepts of linear regression lines are estimates of method detection limit for Cr(VI) uptake on biotite.

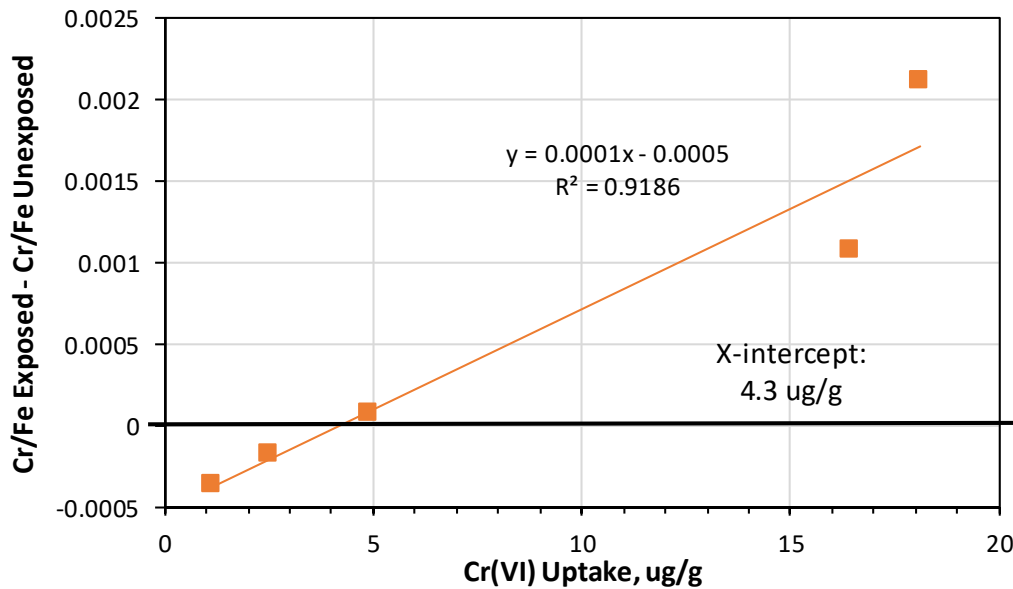


Figure 3.2-7 Cumulative Cr/Fe ratios of 0.1 M HNO₃ leachates from Cr(VI)-exposed bentonite samples minus Cr/Fe ratio of leachates from unexposed bentonite samples vs Cr(VI) uptake on exposed samples. Each data point is the average of two duplicate measurements. X-intercept of linear regression line is estimate of method detection limit for Cr(VI) uptake on bentonite.

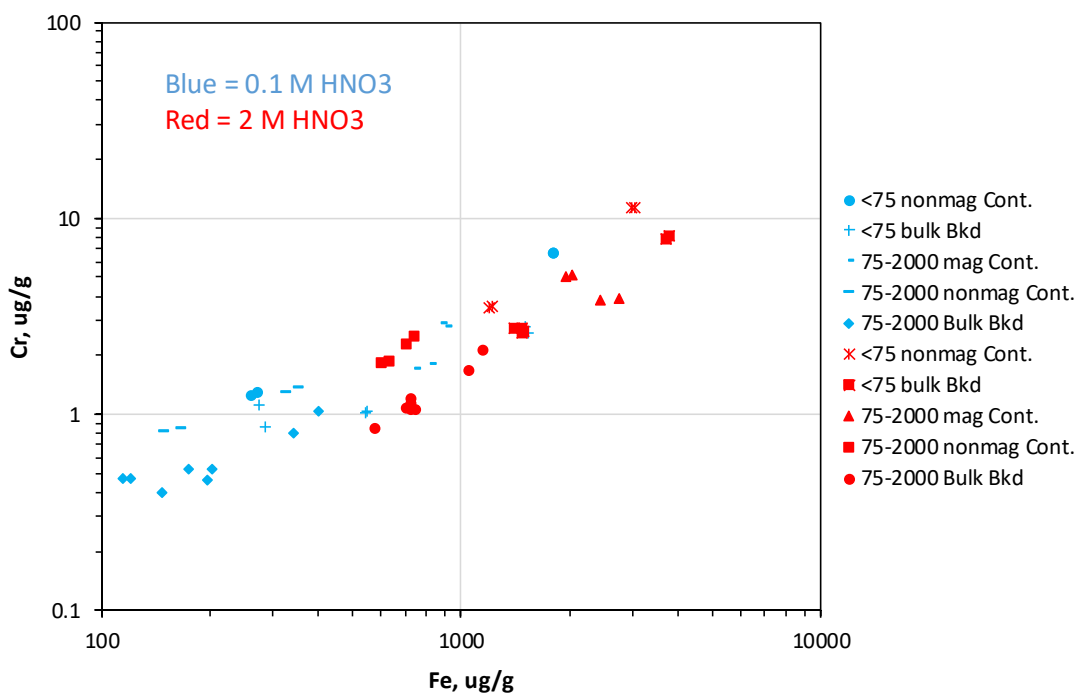


Figure 3.3-1 Cumulative log Cr vs log Fe of leachates from both contaminated and uncontaminated samples in first set of leaching experiments after 0.1 M HNO₃ leaching steps (blue) and 2 M HNO₃ leaching steps (red).

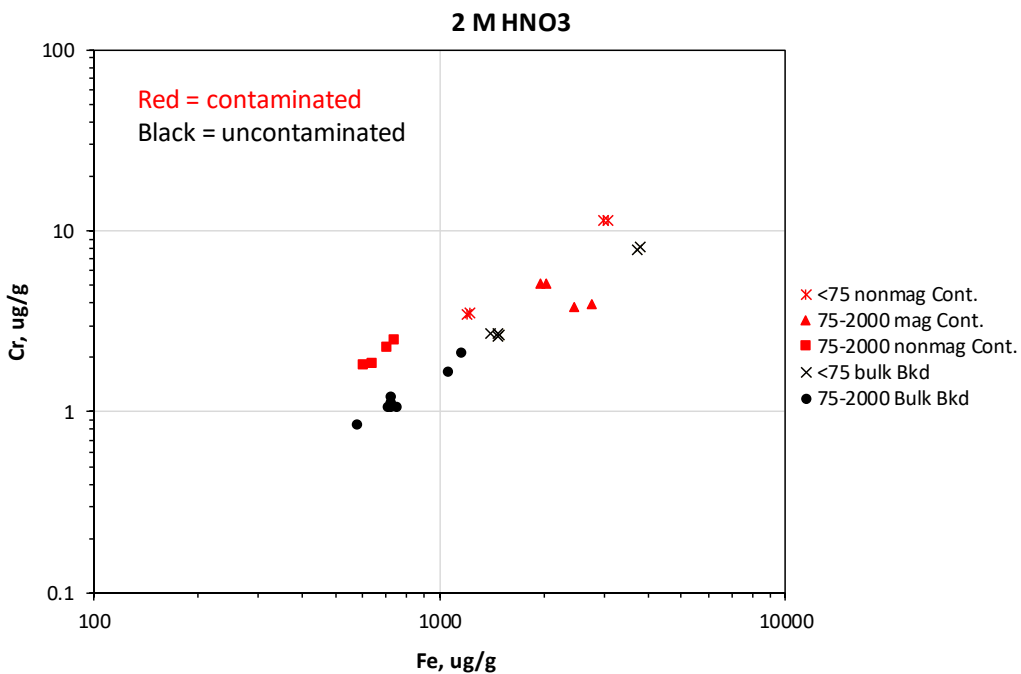


Figure 3.3-2 Cumulative log Cr vs log Fe of leachates from samples in first set of leaching experiments after 2 M HNO₃ leaching steps

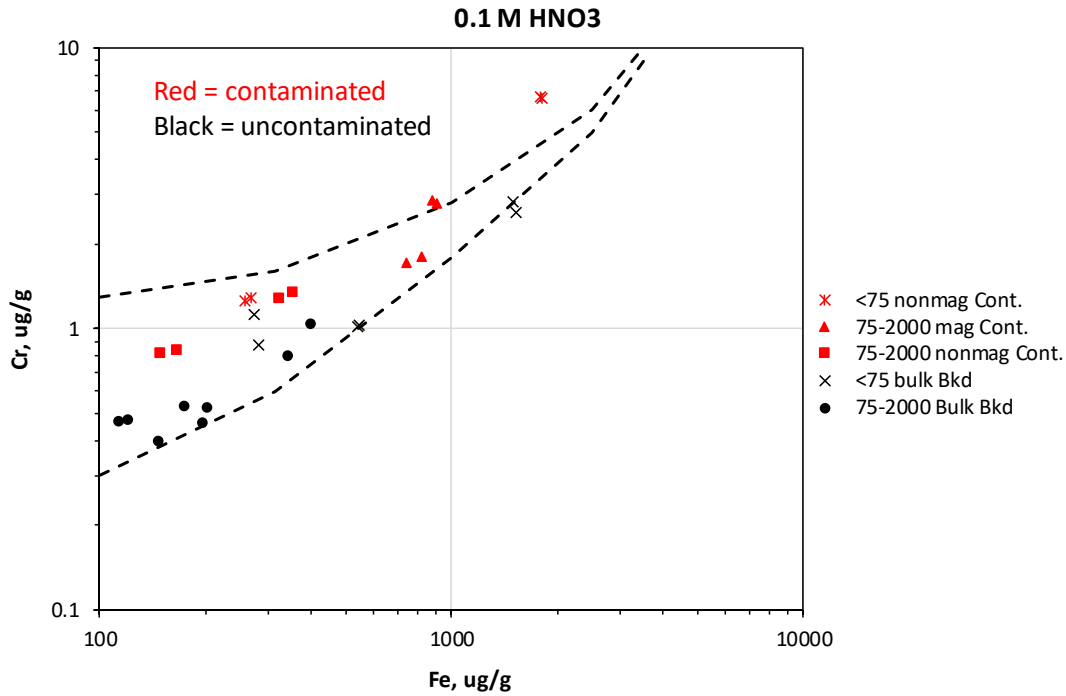


Figure 3.3-3 Cumulative log Cr vs log Fe of leachates from samples in first set of leaching experiments after 0.1 M HNO₃ leaching steps. Vertical difference between dashed lines corresponds to 1 μg Cr(VI)/g, which is approximately the method detection limit for biotite.

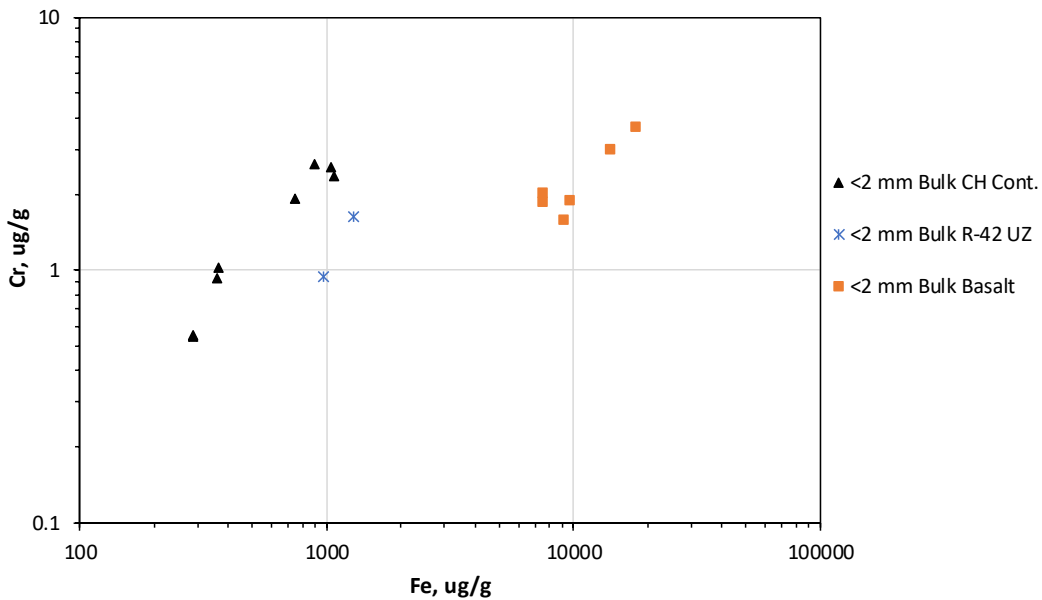


Figure 3.3-4 Cumulative log Cr vs log Fe of leachates from samples in second set of leaching experiments (0.1 M HNO₃ leaching). All samples were considered potentially contaminated.

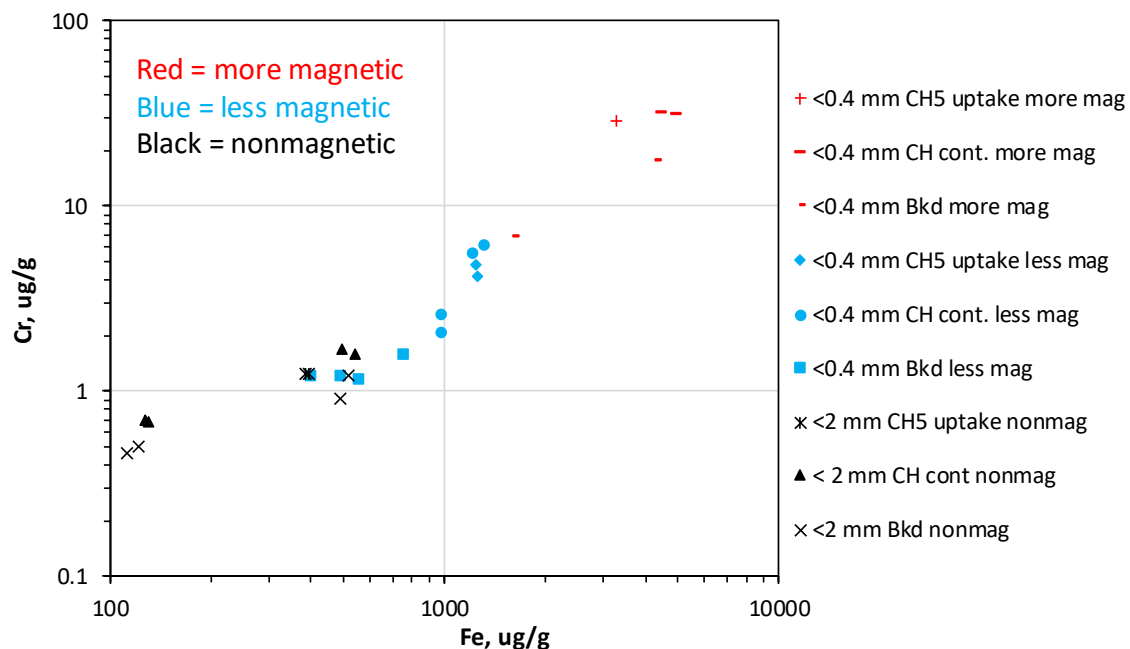


Figure 3.3-5 Cumulative log Cr vs log Fe of leachates from samples in third set of leaching experiments (0.1 M HNO₃ leaching), color coded by degree of magnetism of samples

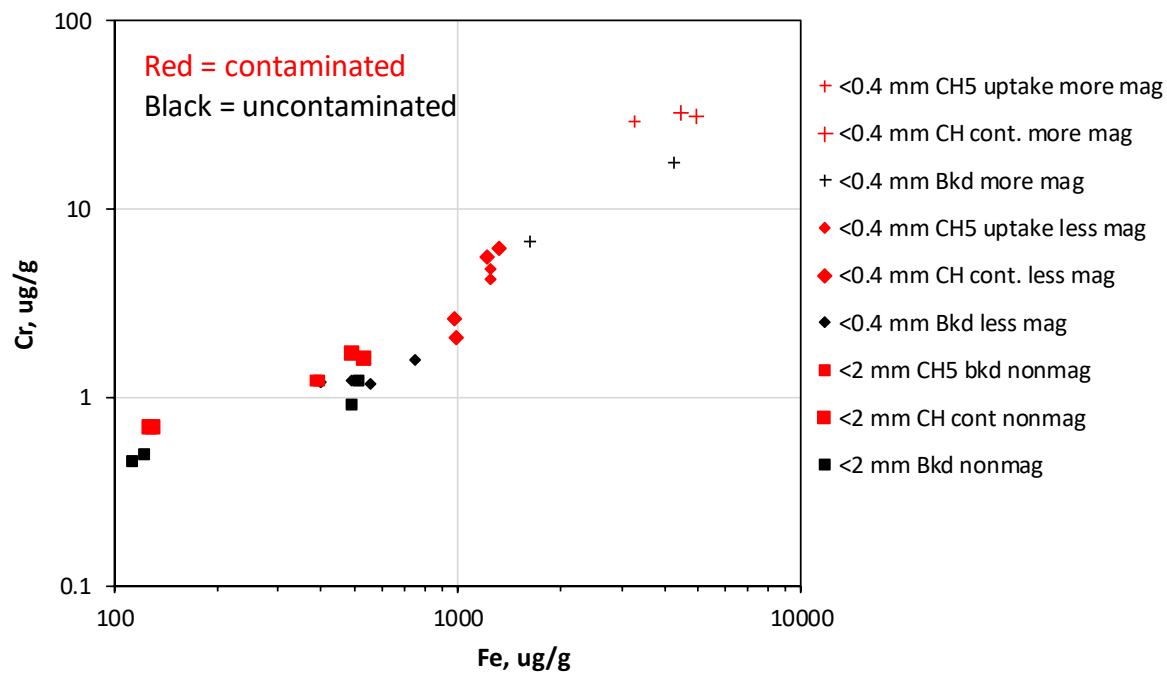


Figure 3.3-6 Cumulative log Cr vs log Fe of leachates from samples in third set of leaching experiments (0.1 M HNO₃ leaching), color coded by contaminated or uncontaminated

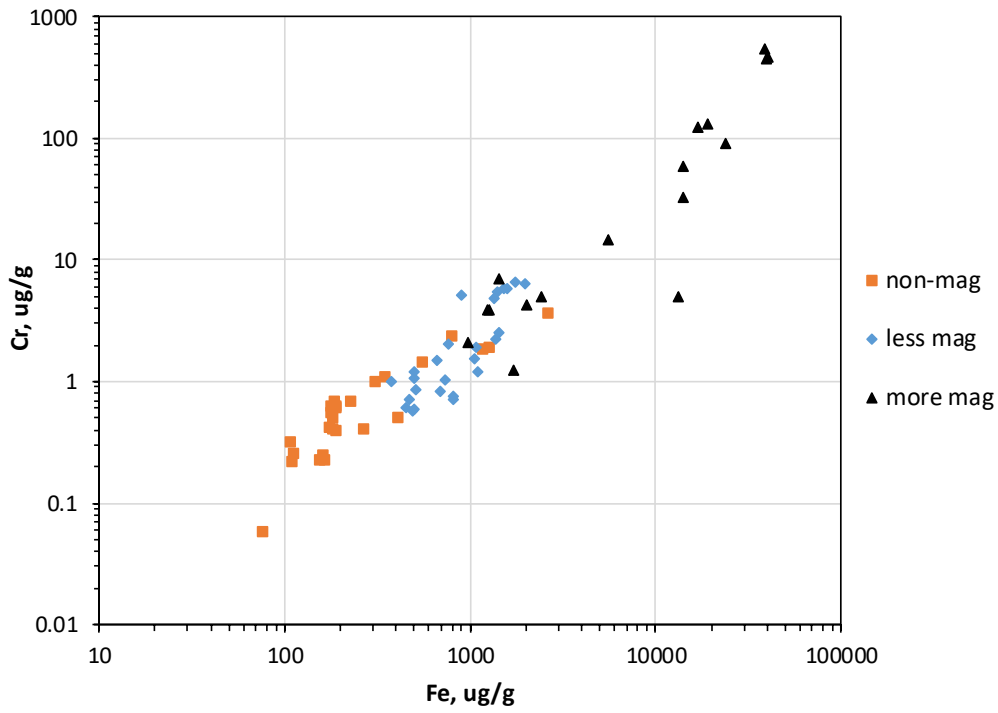


Figure 3.3-7 Cumulative log Cr vs log Fe of leachates from samples in fourth set of leaching experiments (0.1 M HNO_3 leaching), color coded by degree of magnetism of samples (see legend). All samples were believed to be uncontaminated.

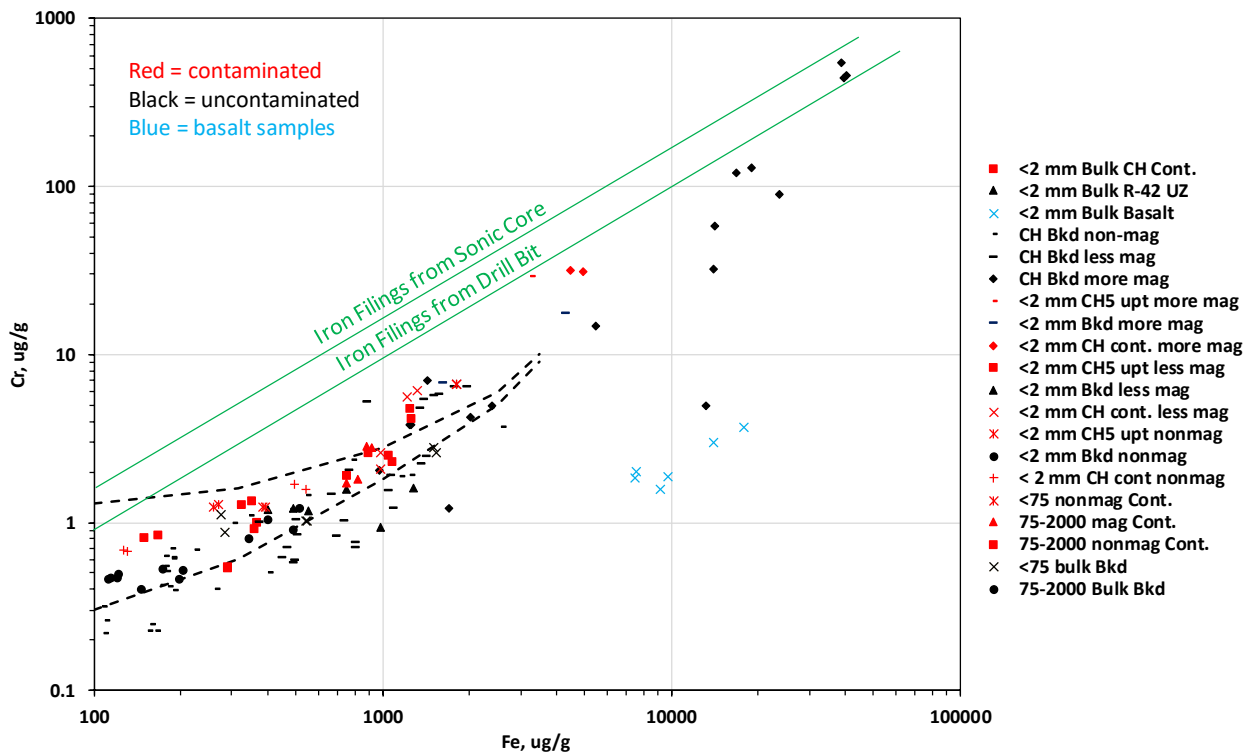


Figure 3.3-8 Cumulative log Cr vs log Fe of leachates from all final 0.1 M HNO₃ leaches, color coded by contaminated (red) vs uncontaminated (black). Basalt samples (potentially contaminated) are shown in blue. Vertical difference between dashed lines corresponds to 1 µg Cr(VI)/g, which is approximately the method detection limit for biotite. Green lines represent Cr/Fe ratios in one 2 M HNO₃ leach of iron filings removed from sonic core and of filings shaved off a sonic drill bit, respectively.

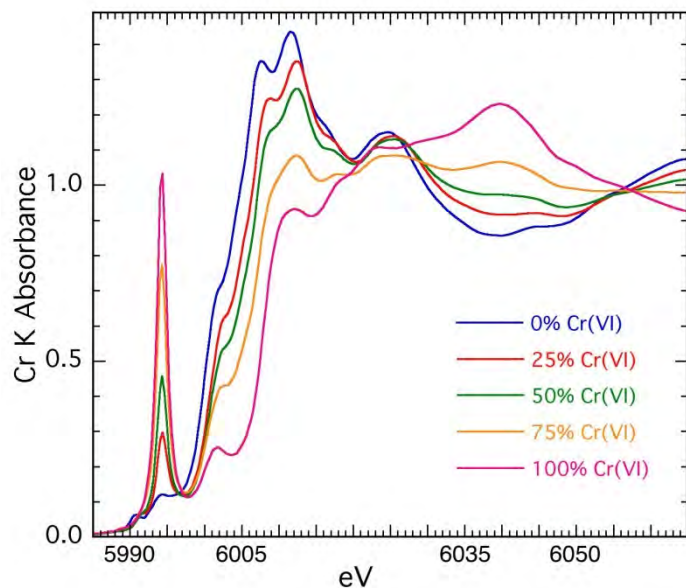


Figure 4.0-1 XANES spectra of Cr(III)/Cr(VI) standards

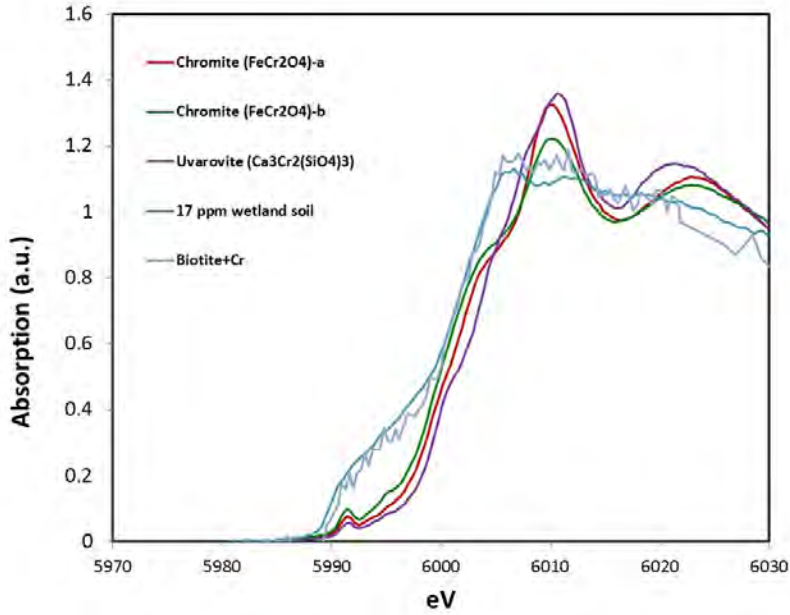


Figure 4.0-2 XANES spectra of chromite-a, chromite-b, uvarovite, Sandia Canyon wetland sample with chromium concentration of 17 $\mu\text{g/g}$, and Cr(VI)-spiked biotite with chromium concentration of 18 $\mu\text{g/g}$

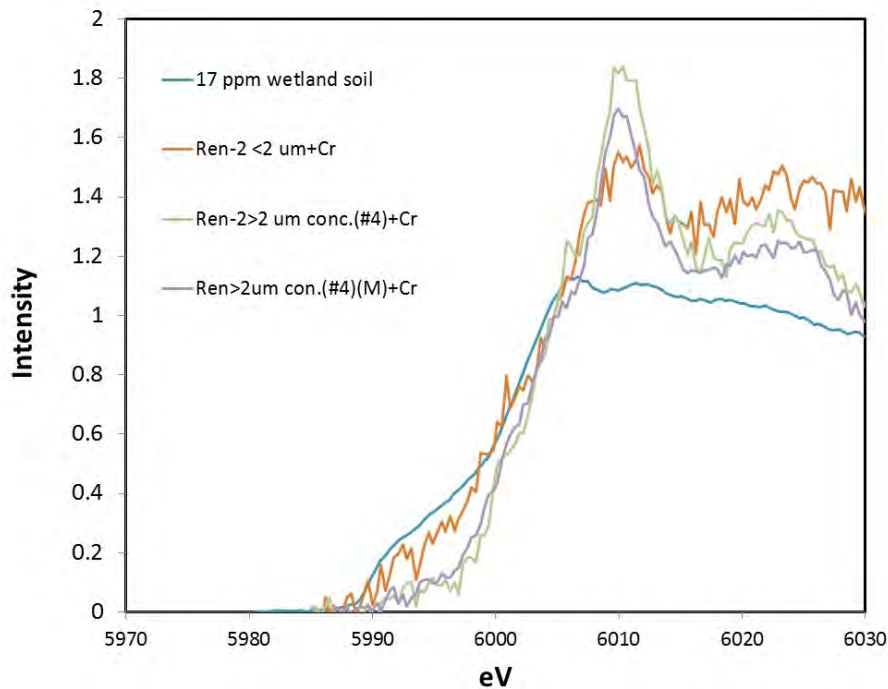


Figure 4.0-3 XANES spectra of Sandia wetland sample and various outcrop (Puye formation) samples after exposure to Cr(VI) solutions

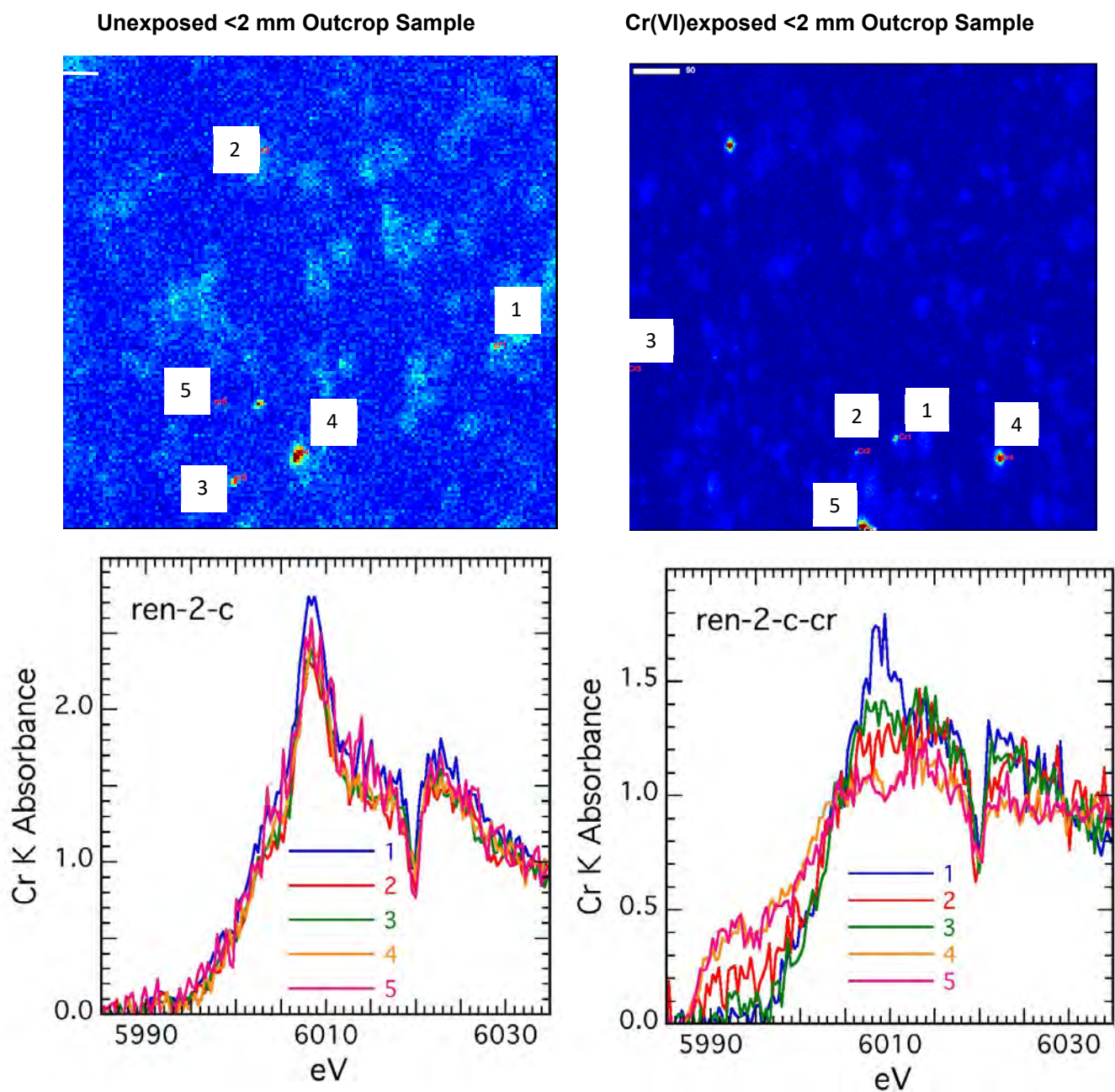


Figure 4.0-4 Micro-XRF maps of “Ren-2 < 2um sample” before (top left) and after (top right) exposure to 5 ppm Cr(VI) solution, and the corresponding XANES spectra of numbered “hot spots” present in the mapped samples (bottom, directly below corresponding map).

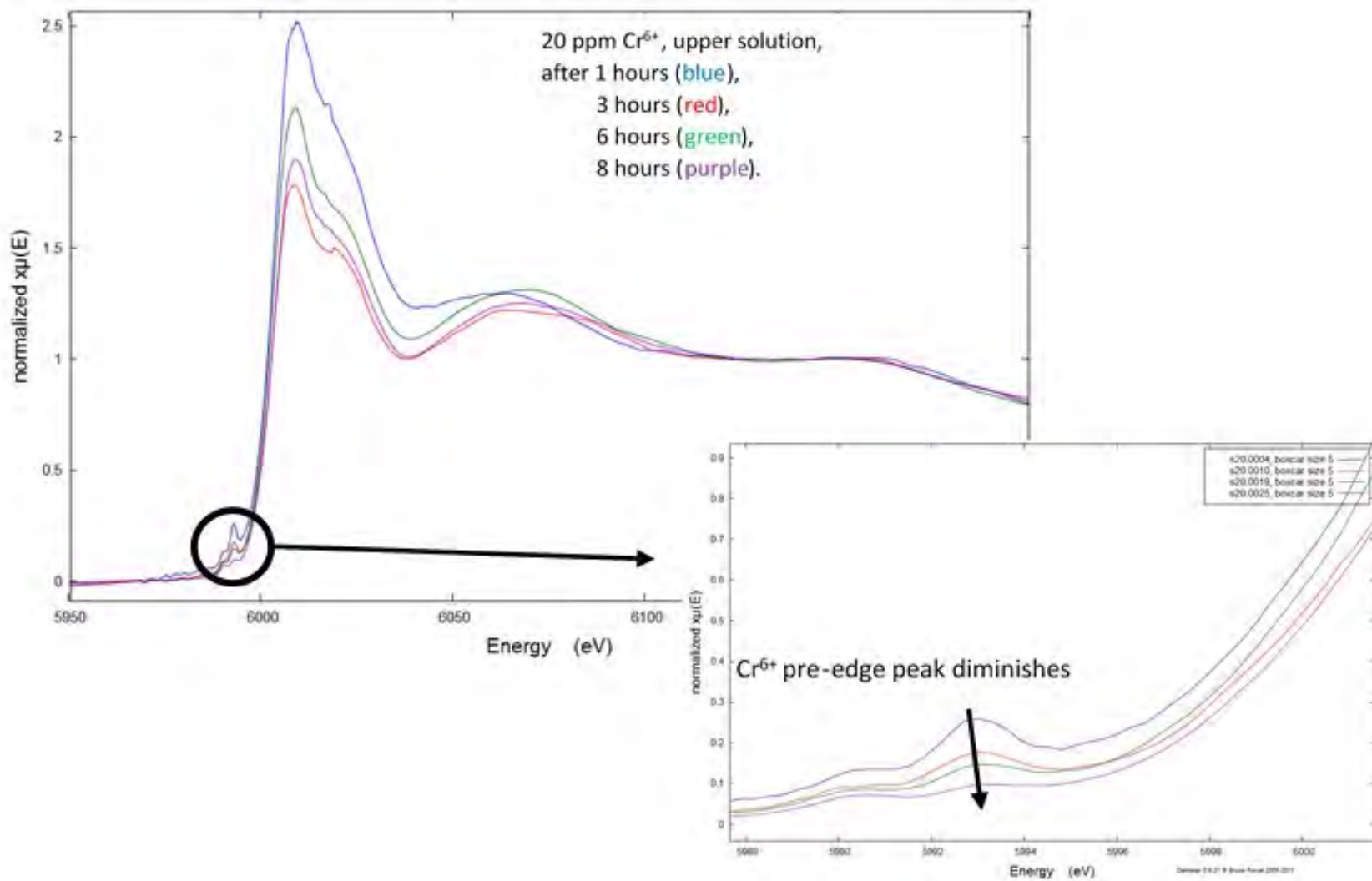


Figure 4.0-5 Time sequence of XANES spectra of a suspension of 0.25–0.7- μm fines in a solution that was initially 20 mg/L Cr(VI). The fines were isolated by gravity setting from a sonic core hole sample taken from core hole CrCH-1, and they represented 0.9 wt% of the sediment sample.

**Table 2.3-1
Particle-Size Fractions Separated from
Sonic Core Samples for Last Set of Cr(VI) Uptake Experiments**

Fraction	Particle Size
1	> 8 mm
2	1.4 mm–8 mm
3	0.355 mm–1.4 mm
4	0.177 mm–0.355 mm
5	0.063 mm–0.177 mm
6	< 0.063 mm + material that settled after 24 h
7	Material that did not settle after 24 h

Note: Only fractions 6 and 7 were used in uptake experiments, but the mass distribution for all seven fractions was used for hydraulic conductivity estimates using the Kozeny-Carman equation.

**Table 3.2-1
Chemical Composition of Bentonite and Biotite from XRF Expressed as Oxides in Weight%**

	Na ₂ O	MgO	Al ₂ O ₃	SiO ₂	P ₂ O ₅	K ₂ O	CaO	TiO ₂	MnO	Fe ₂ O ₃	LOI ^c	Total
Ben ^a	2.79	1.63	16.92	66.79	0.077	0.9	1.03	0.18	0.032	3.59	5.92	99.85
Bio ^b	0.48	15.29	11.06	41.95	0.014	9.69	0.16	2.26	0.576	17.41	0.79	99.68

^a Ben = Bentonite.

^b Bio = Biotite.

^c LOI = Loss on ignition, which is caused by water and/or organic compounds in the sample.

**Table 3.2-2
Results of Trace Elements in the Bentonite
and Biotite In ppm (mg/kg) as Determined by XRF**

	V	Cr	Ni	Cu	Zn	Rb	Sr	Y	Zr	Nb	Ba	Pb
Ben ^a	16	0	0	0	79	32	277	31	145	37	876	12
Bio ^b	109	25	0	0	1212	729	18	14	42	132	896	38

Note: The amount of chromium in the bentonite is below the method detection limits, in contrast to the significant abundance of chromium in biotite.

^a Ben = Bentonite.

^b Bio = Biotite.

**Table 3.3-1
Field Samples Used In Sequential Acid Leaching Tests**

Sample Type and Purpose	Bore Hole	Depth (BLS), ft	Lithological Unit	Set Number
Vadose-zone sediments from conventional core within chromium plume footprint that could potentially contain Cr(VI) contamination	R-42	500	Basalt, Tb4	2
	R-42	530	Basalt, Tb4	2
	R-43	620	Basalt, Tb4	2
	R-43	695	Puye Formation, Tpf	2
Regional aquifer sediments from conventional core taken from outside of chromium plume that represent lithologies identified within the chromium plume	R-60	1350–1355	Puye Formation	1, 3
	R-60	1380–1385	Puye Formation	1, 3
	R-64	1290–1295	Miocene pumiceous	1, 3
	R-64	1345–1350	Miocene pumiceous	1, 3
Regional aquifer sediments from sonic core holes taken from horizons believed to contain Cr(VI) contamination	CrCH-2	887	Puye Formation, Tpf	2
	CrCH-2	900	Puye Formation, Tpf	2
	CrCH-5	955	Puye Formation, Tpf	2
	CrCH-5	960	Puye Formation, Tpf	2
	CrCH-5	980	Puye Formation, Tpf	1, 3
	CrCH-3	937	Miocene pumiceous	1, 3
Regional aquifer sediments from sonic core holes taken from horizons believed to be free of Cr(VI) contamination (used as background samples)	CrCH-2	929	Puye Formation, Tpf	4
	CrCH-2	934	Puye Formation, Tpf	4
	CrCH-5	998	Puye Formation, Tpf	4
	CrCH-5	1002	Puye Formation, Tpf	3, 4
	CrCH-5	1010	Puye Formation, Tpf	4
	CrCH-5	1011	Puye Formation, Tpf	4
	CrCH-2	981	Miocene pumiceous	4
	CrCH-4	977	Miocene pumiceous	4
	CrCH-4	987	Miocene pumiceous	4
	CrCH-4	1042	Miocene pumiceous	4
	CrCH-5	1016	Miocene pumiceous	4
	CrCH-6	1253	Miocene pumiceous	4
	CrCH-6	1257	Miocene pumiceous	4

Note: Terminology taken from Attachment 3 of this compendium, "Stratigraphic and Sedimentological Studies and their Hydrogeological Features in the Chromium Investigation Area, Los Alamos National Laboratory": Tb4 = Cerros del Rio Basalts, Tpf = Puye Formation, Tpf(p) = Puye pumiceous subunit, and Tjfp = Miocene pumiceous unit.

Table 3.3-2
Differences in Sample Preparation and
Leaching Steps in the Four Sets of Sequential Leaching Experiments

Experiment Set	Sample Preparations				HNO ₃ Leaches (3 each)
Set 1 (contaminated)	75–2000 μm, nonmagnetic ^a	75–2000 μm, magnetic ^a	<75 μm, nonmagnetic ^a	<75 μm, magnetic ^a	0.01, 0.1, 2 M
Set 1 (background)	75–2000 μm, no magnetic separations		<75 μm, no magnetic separations		0.01, 0.1, 2 M
Set 2	All samples <2000 μm (no magnetic separation)				0.01, 0.1 M
Set 3 (all samples)	<2000 μm, nonmagnetic ^a	<355 μm, less magnetic ^b	<355 μm, more magnetic ^b		0.01, 0.1 M
Set 4 (all samples)	<2000 μm, nonmagnetic ^a	<355 μm, less magnetic ^b	<355 μm, more magnetic ^b		0.01, 0.1 M

^a Separated using a neodymium hand magnet.

^b Magnetic materials <2000-μm were isolated with a neodymium hand magnet, then they were sieved to <355 μm, and then a Frantz was employed with different magnetic field strengths to obtain “less” and “more” magnetic fractions. The “less” magnetic fraction was assumed to be free of iron contamination, and the “more” magnetic fraction was thought to likely contain iron contamination.

LA-UR-18-21450
March 2018
EP2018-0033

Bioremediation Bench-Scale Studies

Attachment 7

Prepared by the Associate Directorate for Environmental Management

Los Alamos National Laboratory, operated by Los Alamos National Security, LLC, for the U.S. Department of Energy (DOE) under Contract No. DE-AC52-06NA253 and under DOE Office of Environmental Management Contract No. DE-EM0003528, has prepared this document pursuant to the Compliance Order on Consent, signed June 24, 2016. The Compliance Order on Consent contains requirements for the investigation and cleanup, including corrective action, of contamination at Los Alamos National Laboratory. The U.S. government has rights to use, reproduce, and distribute this document. The public may copy and use this document without charge, provided that this notice and any statement of authorship are reproduced on all copies.

CONTENTS

1.0	OBJECTIVE	1
2.0	MATERIALS AND METHODS.....	1
2.1	Groundwater and Sediment Sampling.....	1
2.2	Characterization of Microbial Diversity	2
2.3	Bacterial Growth and Cr(VI) Reduction Kinetics	2
2.4	Column Biostimulation and Chromium Reduction	3
2.5	Analytical Procedures.....	4
2.5.1	Analysis of Ferrous Iron	4
2.5.2	Scanning Electron Microscopy Characterization	5
3.0	RESULTS.....	5
3.1	Batch Studies.....	5
3.1.1	Microbial Community Analysis	5
3.1.2	Microbial Growth Stimulated by Acetate and Molasses.....	5
3.1.3	Reduction of Nitrate, Sulfate, Chromate, and Iron in Liquid Cultures Biostimulated with Molasses and Acetate.....	6
3.1.4	Microbial Community Analysis of Reactors Biostimulated with Acetate	7
3.2	Column Studies	7
3.2.1	Chromium Reduction in Packed Columns	7
3.2.2	Natural Attenuation of Cr(VI) by Sediments from the Chromium Plume Area	8
3.2.3	Attenuation of Cr(VI) by Sediments Biostimulated with Acetate and Molasses.....	8
3.2.4	Microbial Diversity in the Column Sediments.....	9
3.2.5	SEM Characterization of Bioreduction Products.....	10
4.0	DISCUSSION	10
5.0	CONCLUSION	15
6.0	REFERENCES AND MAP DATA SOURCES	15
6.1	References	15
6.2	Map Data Sources.....	18

Figures

Figure 2.1-1	Map showing the footprint of the chromium plume in the regional aquifer beneath Los Alamos National Laboratory.....	19
Figure 3.1-1	Graphic representation of the microbial diversity at the phylum or groundwater collected from sampling well R-42	21
Figure 3.1-2	Microbial growth in R-42 water stimulated by either 1.4 g/L sodium acetate or 1.8 g/L molasses	22
Figure 3.1-3	Microbial growth in reactors biostimulated with molasses and incubated anaerobically. Initial conditions are: Water used from R-42 with 888 µg/L Cr(VI). Initial pH = 8.8 and final pH = 4.85.....	23
Figure 3.1-4	Microbial growth in saturated sediments samples from CH-3 amended with various acetate concentrations and incubated statically in the dark under anaerobic conditions	24

Figure 3.1-5	Microbial growth in saturated sediments samples from CH-3 amended with various molasses concentrations and incubated statically in the dark under anaerobic conditions	24
Figure 3.1-6	Nitrate reduction in R-42 water amended with 0.82 g/L acetate and incubated anaerobically in the presence and absence of sediments	25
Figure 3.1-7	Sulfate reduction in R-42 water amended with 0.82 g/L acetate and incubated anaerobically in the presence and absence of sediments	26
Figure 3.1-8	Chromate reduction in liquid cultures amended with 0.82 g/L acetate and incubated anaerobically in the presence and absence of sediments	27
Figure 3.1-9	Concentration of ferrous iron in the different reactors stimulated with acetate	28
Figure 3.1-10	Acetate consumption in liquid cultures amended with 0.82 g/L acetate and incubated anaerobically in the presence and absence of sediments	29
Figure 3.1-11	Bioreduction of chromate in reactors amended with molasses in the absence and presence sediments	30
Figure 3.1-12	Chromate reduction by molasses under sterile conditions	31
Figure 3.1-13	Changes in pH during the microcosm experiment biostimulated with molasses	32
Figure 3.1-14	Graphic representation of (A) microbial diversity and (B) a comparison of the microbial diversity at the phylum level between the microbial diversity in the groundwater (CBN.20), in the water of strictly anaerobic reactors stimulated with acetate (CBN.1), in the micro-oxic biostimulated reactors stimulated with acetate (CBN.7), in the column outlets stimulated with acetate (ASH49), and in the column inlets stimulated with acetate (ASH50)	33
Figure 3.2-1	Breakthrough curves showing the transport of chromate along with the tritium conservative tracer for columns filled with sediments from the chromium plumes area. (a) column filled with sediments from outcrop sediments (Ren 121213-03), (b) column filled with sediments from outcrop sediments (R-42 Fines depth 930-935), (c) column filled with sediments from outcrop sediments (WC-006 3-27-14), (d) column filled with sediments from Puye sediments in SCI-2	35
Figure 3.2-2	Chromium attenuation in column 3 biostimulated by the injection of 2.4 pore volumes of a solution containing 0.82 g/L (10 mM) ae	37
Figure 3.2-3	Chromium attenuation in column 1 biostimulated by the injection of 4.8 pore volumes of a solution containing 0.82 g/L (10 mM) acetate followed by 15.4 pore volumes of a solution containing 0.08 g/L (0.1mM) ace	37
Figure 3.2-4	Chromium breakthrough in column 2 biostimulated by the injection of 2.3 pore volumes of a solution containing 3.4 g/L molasses	38
Figure 3.2-5	Chromium breakthrough in column 2 biostimulated by the injection of 4.8 pore volumes of a solution containing 3.4 g/L (10 mM) molasses followed by 12.6 pore volumes of a solution containing 0.34 g/L molasses	38
Figure 3.2-6	Flow rate for column 4 biostimulated with an injection of R-42 water amended with molasses	39
Figure 3.2-7	Flow rate for column 2 biostimulated with two successive injection of R-42 water amended with molasses	39
Figure 3.2-8	Graphic representation of microbial diversity at the phylum level in the column biostimulated with acetate	40

Figure 3.2-9 Graphic representation of microbial diversity at the phylum level in the column biostimulated with molasses 41

Figure 3.2-10 SEM images of microorganisms and biofilm coatings on sediment grains and EDS spectra 42

Figure 4.0-1 Observed rate of Cr(VI) reduction by cell suspensions of microbes grown anaerobically by biostimulation of R-42 water with acetate..... 43

Figure 4.0-2 Breakthrough of Cr(VI), acetate, and iodine tracer from a column in response to two successive injections of an acetate pulse 43

Figure 4.0-3 Breakthrough curves showing pH, molasses, and tritium transport through column 2 during the injection of molasses for 3.2 pore volumes..... 44

Tables

Table 2.4-1 Parameters of the Column Used in the Natural Attenuation and Biostimulation Studies . 45

Table 4.0-1 Diversity Indices of Column Samples 45

1.0 OBJECTIVE

The objective of the studies detailed in this report is to characterize the bacterial community in the regional aquifer at LANL, examine if microbial activity is affecting chromium speciation under current conditions, and evaluate the potential use of in situ biostimulation to reduce chromium mobility in regional aquifer and the effect of biostimulation on groundwater quality. This report presents a detailed examination of the microbial community structure in the regional aquifer within the chromium plume, and how the community structure changes in closed reactors and columns packed with material representative of the regional aquifer following biostimulation with sodium acetate and molasses. It also provided the basis for development of a field pilot-scale amendments test using molasses for in situ remediation of chromium.

Before this study was undertaken, very little was known on the potential contribution of microbes to chromium attenuation at the regional aquifer at the Los Alamos National Laboratory (LANL or the Laboratory) site. However, reduction of Cr(VI) to trivalent chromium [Cr(III)] through bacterial activity has been extensively examined both in the laboratory and the field through pilot studies at other sites (Brodie et al. 2011; Han et al. 2010; Katsaveli et al. 2012; Stewart et al. 2007; Xiao et al. 2014). Many individual bacteria and bacterial consortia have been reported to reduce Cr(VI) aerobically (Ozturka et al. 2012; Bopp and Ehrlich 1988; McLean et al. 2000), anaerobically (Priester et al. 2006; Guha et al. 2001; Cheung and Gu 2003), or both. Aerobic chromate reduction is pronounced in microbial species that tolerate high concentrations of chromate. Many *Pseudomonas* and *Bacillus* species have been shown to reduce Cr(VI) to Cr(III) under aerobic conditions (Han et al. 2010; Xiao et al. 2014; Bopp and Ehrlich 1988). The exact mechanism of reduction is not well understood, but is often attributed to reaction of Cr(VI) with bacterial exudates such as extracellular DNA, secreted exopolymers, and other bacterial metabolites (Ozturka et al. 2012; Priester et al. 2006). Reduction of Cr(VI) through anaerobic respiration is very common, especially in environments harboring a significant population of denitrifying bacteria. Bacteria such as *Shewanella alga* and *Aeromonas dechromatica* have been shown to reduce Cr(VI) anaerobically (Guha et al. 2001; Cheung et al. 2006). Sulfate-reducing bacteria such as *Desulfovibrio desulfuricans* and *D. vulgaris* have also been reported to reduce Cr(VI) (Guha et al. 2001; Fude et al. 1994; Tebo and Obraztsova 1998; Cheung and Gu 2003). Studies of anaerobic Cr(VI) reduction seem to indicate that chromium is processed by microorganisms as a co-metabolite used along with other electron acceptors available to support bacterial respiration. Some reports also indicate that it can be used by microorganisms to support microbial growth (Tebo and Obraztsova 1998; Cheung and Gu 2003). It is evident from the literature that bacteria capable of reducing chromium are abundant, and natural attenuation of Cr(VI) through microbial activity is likely under both aerobic and anaerobic conditions.

2.0 MATERIALS AND METHODS

2.1 Groundwater and Sediment Sampling

Groundwater used in the batch and column experiments was obtained from the regional aquifer at monitoring location R-42, located at the center of the chromium plume area (Figure 2.1-1). The well was purged with at least three casing volumes before the samples were taken. The water samples were stored in the dark at 4°C in plastic carboys until used. Chemical analysis of the R-42 water showed that it was relatively oxidizing and was characterized by the presence of dissolved oxygen (DO) at concentrations which ranged from 5.9 to 6.9 mg/L, pH of 7.49 ± 0.1 , and oxidation reduction potential (ORP) from 77 to 200 mV. Concentrations of dissolved iron and manganese were $<50 \mu\text{g/L}$ and $6 \mu\text{g/L}$, respectively, indicating that very little reduction is occurring naturally in the aquifer. The concentration of dissolved chromium ranged between 840 and 940 $\mu\text{g/L}$, and was present as hexavalent chromium [Cr(VI)]. The water also contained relatively stable concentrations of sulfate and nitrate measured

consistently between 80 to 100 mg/L and 30 to 50 mg/L, respectively. The concentration of total organic carbon ranged from 0.4 to 1.7 mg/L. The sediment samples used in the microcosm experiments were sampled from the Puye Formation using a core sample obtained from sonic drilling from the center of the chromium plume. Sonic drilling does not generally introduce any drilling fluids or water and is believed to preserve the original composition of the microbial population and geochemical parameters of the aquifer. The core samples were stored at 4°C for the initial 24 hours and then subsamples of about 100 g were packed in 50 mL centrifuge tubes and stored at -20°C. Sediments collected from two outcrop samples of the Puye Formation were also used in this study. The outcrop samples were sterilized before they were used in any experiments. The sediment samples from the Puye Formation were dominated by plagioclase and K-feldspars with a total feldspars content ranging from 29 to 54.1 wt%. Smectitic material constituted on average less than 5 wt% and amorphous content ranged from 9 to 44 wt%. Altogether, these major groups of minerals amounted to 70% to 90% of the sample. The chemical composition of the amorphous materials was dominated by silicon oxides and aluminum oxides with traces of iron oxides, magnesium oxides and calcium oxides (Woldegabriel et al. 2007).

2.2 Characterization of Microbial Diversity

DNA was extracted from microbes from unfiltered groundwater obtained from sampling well R-42, groundwater sampled from biostimulated reactors, and sediments obtained from biostimulated columns. The water samples were filtered through a vacuum-filtration system equipped with polycarbonate filters having 47 mm diameter and 0.2 µm pore size (Thermo Scientific) to separate the microbes from the water. The material retained on the filter was mobilized and placed in 2.0 mL conical centrifuge tubes and subjected to a DNA-extraction procedure. Total DNA was extracted from each filter membrane following the method of The UltraClean Microbial DNA Isolation kit (MO BIO). DNA extraction from the column sediments was performed similarly by using 0.4 g of the sediments directly. The purified DNA was eluted in 25 µl of clean deionized (DI) water and stored at -20°C until it was subjected to polymerase chain reaction (PCR) analysis. DNA extracts were used to amplify 16S rRNA genes using bacterial 16S rRNA specific primers (515F-806R [GTGCCAGCMGCCGCGGTAA and GGACTACHVGGGTWTCTAAT, respectively]). Amplicons were purified using a solid-phase reversible immobilization (SPRI) bead clean-up step, quantitated by picogreen assay, normalized, pooled, and then sequenced on an Illumina Solexa instrument. The sequencing run resulted in >1 million reads per sample with an average read length of 295 bp. The samples were filtered to retain those sequences longer than 250 bp with an average quality score of greater than or equal to 30. Sequence data were processed by using the QIIME software package v1.6.0 (Caporaso et al. 2012). Operational taxonomic units (OTUs) were clustered at the 97% similarity level. OTUs were assigned to 16S rRNA gene database (<http://greengenes.secondgenome.com/>) to generate taxa summary bar plots. Alpha diversity analysis was performed using QIIME script (alpha_rarefaction.py). Principle Component Coordinated Analysis (PCoA) was implemented using QIIME based on the Jaccard distance. The National Center for Biotechnology Information (NCBI) Blast was used to assign representative sequences to genus or species levels.

2.3 Bacterial Growth and Cr(VI) Reduction Kinetics

Two independent microcosm experiments were set up to examine Cr(VI) reduction under stimulated and non-stimulated conditions. The first microcosm experiment was set up using sediment samples obtained by sonic drilling from well CrCH-3 (Figure 2.1-1) and water from sampling well R-42. The second microcosm experiment was performed in slurry reactors using sediments from the outcrop samples and groundwater from R-42. The microcosm experiments were designed to test microbial growth and chromate reduction under various geochemical conditions of electron acceptors availability (i.e., oxygen, nitrate, sulfate, chromate, and iron), the availability of carbon substrates (i.e., acetate and molasses), and the level of saturation of the sediments (i.e., no sediment, slurry, and saturated sediments).

The first microcosm experiment was setup in 100 mm by 15 cm sterile polystyrene Petri dishes filled with 20 g of sediments from CrCH-3. The sediments were amended with 8.0 mL of groundwater from R-42 and an aliquot of either molasses or sodium acetate as a carbon source. The final concentrations of acetate in the sediments were 0, 1.6, 8.2 and 16 g/L and the concentrations of molasses were 0, 3.6, 18, or 36 g/L. The Petri dishes were incubated statically in a glove bag filled with argon and covered with a black tarp to reduce light exposure during the incubation. At fixed time intervals individual Petri dishes were removed from the glove bag and processed to quantify microbial growth, and molasses and acetate concentrations. Microbial growth was quantified by direct cell counts performed on sediments that were separated by suspending 1.0 g of sediments in 10 mL of water. After vortexing, the suspensions were centrifuged at 2000 rotations per minute (RPM) to separate the sediment particles from the supernatant. Cell counts in the supernatant were determined by direct cell counts and converted to cell counts per gram of sediments. The pore water was removed by centrifugation of the sediment placed in two part centrifuge tubes with built in filters. All geochemical parameters of the water including the concentrations of molasses and acetate were measured in the pore water.

The second microcosm experiment was performed in sealed 150 mL serum vials equipped by thick rubber stoppers and tested both molasses and acetate amendments. The individual reactors received 100 mL of R-42 water and an aliquot of either sodium acetate or molasses. The concentration of acetate was fixed at 0.82 g/L, and for molasses the concentration was fixed at 1.8 g/L. For each carbon source a total of seven triplicate reactors were prepared with different initial geochemical conditions. Three sets of triplicates contained 1.0 g of sterile sediments from outcrop sample, Rend-121213, and the other three sets did not contain sediment. Sterile controls were prepared with and without sediments. All reactors were purged initially with argon for 15 min to create anaerobic conditions. Sampling was performed once a week by removing 3.0 mL of solution via syringes equipped with needles. The samples were filtered through a 0.22 μm polycarbonate syringe filter before analysis. Bacterial growth was monitored by reading the OD₆₀₀ of the supernatant extracted from the vials. The OD readings were converted to cell numbers using a correlation established by direct cell counts of one of the cultures from the same batch. A separate calibration curve was created for each carbon substrate.

2.4 Column Biostimulation and Chromium Reduction

The reduction of Cr(VI), as well as nitrate, sulfate and iron(III), by treated local sediments was tested in a set of column experiments. Four glass columns, 30 cm long with a diameter of 2.6 cm, were used for the column biostimulation experiments. The columns were thoroughly washed and rinsed with DI water prior to packing. Packing materials for the two columns were sediment samples sieved to yield particles ranging in size between 2.0 and 75.0 μm . The first column was packed with sediment from the Rendija Canyon outcrop sample, Ren 121213-03, and the second column with <2mm Puye sediment from SCI-2. The third column was packed with sediments from the Water Canyon outcrop sample (WC-006 3-27-14), and the fourth column was packed with <2mm Puye sediments from SCI-2 (Table 2.4-1). The columns were weighed before and after packing with dry, sieved sediment samples to determine the exact mass of the sediment in each column. The packed columns were autoclaved for 30 min at 120°C to sterilize the sediments. The columns were saturated by first evacuating them under vacuum, then filling them with R-42 water treated with an ion exchange resin to remove Cr(VI). The two columns were covered with aluminum foil during the entire run and were aligned vertically with flow from bottom to top. Syringe pumps (KD Scientific) were used to maintain a controlled flow rate with minimal pulsing. A flow rate of 2.0 mL/h, which corresponds to a linear velocity of 20-30 cm/day (110 m/year), was set as the target velocity for both columns. Each column was connected to two syringe pumps mounted in parallel and a fraction collector which collected the eluted fractions in 10 mL plastic test tubes. Individual fractions were collected every 3 hours and analyzed for Cr(VI) and other parameters. The pore volume of the different columns varied between 82 and 100 mL and the porosity was calculated to be 68%. The water was spiked with an aliquot

of tritiated water (^3HHO) used as a conservative solute tracer in the experiment. The columns were tested for their capacity to attenuate chromium either by reduction or sorption by the injection of a pulse of R-42 water amended with ^3HHO used as a tracer. The water used in this experiment was collected from R-42 just prior to the experiment and contained a bacteria native contaminated area.

Following the initial studies of Cr(IV) natural attenuation, the first and second columns were stimulated by injecting short pulses of acetate solutions, which lasted 2.39 and 4.89 pore volumes respectively, introduced at the inlet of the column. The acetate was mixed with R-42 water at the column inlet to achieve an acetate concentration of 0.82 g/L. The third and fourth columns were stimulated by injecting short pulses of molasses solutions, which lasted 4.68 and 2.31 pore volumes respectively, introduced at the inlet of the column. The molasses was mixed with R-42 water at the column inlet to achieve a concentration of 1.8 g/L. The flow rate for all injections was set to 0.4 mL/h. At the completion of the biostimulation injections, the flow rate was increased to 2.0 mL/h and the injection water was changed to R-42 water without any amendments additions. The effluents were monitored for over 50 pore volumes for columns one and three and to over 100 pore volumes for columns two and four. The effluents from the columns were monitored until chromium concentration breakthrough approached the initial concentration in the influent water. The already stimulated columns were treated with several sequential pulse injections of sodium acetate and molasses to probe their response to repeated injections of biostimulants.

2.5 Analytical Procedures

Cr(IV) concentration was analyzed spectrophotometrically using a modified procedure of the U.S. Environmental Protection Agency (EPA) method 7196A. Briefly, a solution of 5 diphenylcarbazide was prepared by dissolving 0.02g in 100 mL DI water acidified with 5.0 mL of 1.0 M HCl. Equal volumes on this solution and water samples containing dissolved Cr(VI) were then mixed. The solutions were left to equilibrate for 10 min before reading the absorbance at 542 nm which is correlated to the concentration of Cr(VI) using a calibration curve produced using known Cr(VI) standards. The method is very sensitive and has a detection limit of a few parts per billion. Acetate was analyzed using a Dionex Summit HPLC system using procedures available in the literature (Duke et al. 2007; Bowman and Gibbens 1992). The flow rate used was 0.5 mL/min and the mobile phase was composed of 60% KH_2PO_4 at 30 mM (pH=2.57) and 40% methanol. The column used was C18 Acclaim 120 (Thermo Scientific). Absorbance detection wavelength was 222 nm. Acetate standards were analyzed by ion chromatography (IC) following EPA method 300 on a Dionex DX-600 system. Molasses concentration was quantified indirectly by measuring the total organic carbon (TOC) content of the water. A calibration curve was established which correlated the concentration of molasses in solution to TOC readings.

2.5.1 Analysis of Ferrous Iron

Water samples were analyzed for ferrous iron content by a modification of procedures described in the literature for ferrous iron analysis in the presence of ferric iron. The water samples were diluted to 100 mL using 0.02 M sulfuric acid to bring the concentration of leached ferrous iron to tens of $\mu\text{g/L}$ levels. The samples were analyzed for Fe(II) by the bathophenanthroline method. A 0.1 mL aliquot of the solution was mixed with 0.9 mL of a 0.1 M solution of a 2-(N-morpholino)ethanesulfonic acid (MES) buffer and a 1.0 mL of a solution containing 0.01% 1,10-Phenanthroline (Ricca Chemical Company). The solutions turn orange immediately in the presence of Fe(II) which forms a strong complex with 1,10-Phenanthroline. The pH of the solutions analyzed was between 2.5 and 4. The solutions were analyzed by UV-visible spectroscopy at 554 nm. All solutions were analyzed 10 to 15 min after mixing to insure complete ferrous iron complexation by 10-Phenanthroline. The concentration of Fe(II) was determined by comparing the readings of the unknown solution to a calibration curve established using known Fe(II) standards treated under the exact same conditions.

2.5.2 Scanning Electron Microscopy Characterization

Samples were prepared for scanning electron microscopy (SEM) analysis by affixing sediment grains and cell suspension residues to aluminum stubs with carbon tape. The samples were carbon or gold-coated before analysis. The analyses were performed with an FEITM Inspect F scanning electron microscope SEM. Imaging with the SEM was performed using a 5.0 to 15.0 kV accelerating voltage and a spot size of 1.5 to 3.0. Energy dispersive x-ray spectroscopy (EDX) performed at 20 kV and a 3.0 spot for size was used for elemental analyses of selected sediment grains. The samples were analyzed before and after biostimulation to identify the area of chromium deposition and to seek any evidence of ion and chromium correlations.

3.0 RESULTS

3.1 Batch Studies

3.1.1 Microbial Community Analysis

Microbial community analysis of groundwater sampled from monitoring well R-42 had fairly consistent cell counts. On average cell counts varied from 5×10^4 to 5×10^5 cells/mL which is consistent with cell counts for deep groundwater aquifers (Hazen et al. 1991). Gene sequence analysis was used to study the microbial community in freshly collected groundwater from monitoring well R-42 as well as in the acetate and molasses biostimulated columns. The groundwater samples from R-42 were dominated by Proteobacteria, which represented 58.2 % of the overall bacterial population [α -Proteobacteria (25.5%), β -Proteobacteria (12.7%), γ -Proteobacteria (13.7%), δ -Proteobacteria (6.2%)]. Other phyla in significant abundance (>1%) included Firmicutes, Acidobacteria, Actinobacteria, Bacteroidetes, Chloroflexi, NC10, Fibrobacteres, Nitrospirae, Planctomyces, Verrucomicrobia. In the Proteobacteria, Caulobacteraceae (9.7%), Comamonadaceae (7.9%) and Legionellaceae (9.7%) were among the dominant families (Figure 3.1-1). Members of the Caulobacteraceae possess the capability to reduce Fe(III) in an environment in which nutrients are limited, and have been shown to exhibit resistance to heavy metals (Li et al. 2013). The Comamonadaceae phylotypes are associated with denitrification, e.g., in wastewater (Khan et al. 2002). Legionellaceae occur in diverse environments and include some well-studied human pathogens (Li et al. 2013). Strains in these families are commonly found in groundwater ecosystems (Flynn et al. 2013). One of the OTUs shared 99–100% identity with a number of *Polaromonas* spp., and the second was closely related (99% similarity) to multiple *Acidovorax* spp. Members of the *Polaromonas* genus are found in a variety of pristine oligotrophic environments, are known for their ability to degrade complex hydrocarbon pollutants, and can be enriched under nitrate reducing conditions (Yagi et al. 2009; Yelton et al. 2013). *Acidovorax* spp. sharing 99–100% similarity to sequences found in R-42 water have been identified in Cr(VI)- and Cr(III)-contaminated industrial wastewaters (Katsaveli et al. 2012) and Cr(VI)-contaminated groundwater from the U.S. Department of Energy's Hanford Site in Washington state (Brodie et al. 2011). Overall, the microbial population in R-42 has the density and the metabolic ability to reduce nitrate and therefore should also be able to reduce chromium as a co-metabolite. However, both nitrate and Cr(VI) are very stable in R-42 water. This is probably because of the low availability of carbon substrates that can serve as electron donors.

3.1.2 Microbial Growth Stimulated by Acetate and Molasses

Two independent studies were performed to characterize microbial growth in R-42 water and saturated sediments. The first experiment was performed in liquid cultures with and without addition of sediments in sealed serum vials under strict anaerobic conditions and examined the ability of acetate and molasses to stimulate the growth of the microbial population present in R-42 water. The data in Figure 3.1-2 show the

rate of microbial growth as function of time for reactors stimulated by the addition of acetate and molasses. The data show more vigorous growth in the reactors amended with 1.8 g/L molasses relative to the reactors amended with 1.4 g/L acetate. There was no visible growth in the control reactors without a carbon source amendment. Full growth was achieved in less than 10 days after which no visible increase in cell numbers was observed. A slight decrease in cell numbers was noticed at longer incubation times (data not shown). The growth rate was significantly dependent on the concentration of the amendments at lower concentrations. Higher concentrations of molasses enhanced the rate of microbial growth, however, limited enhancement of microbial growth was observed for molasses concentrations exceeding 1.8 g/L (Figure 3.1-3).

The second microcosm experiment examined microbial growth in saturated sediments from CrCH-3 amended with acetate or molasses and incubated in the dark statically under anaerobic conditions. The data in Figures 3.1-4a and 3.1-5b show the rate of microbial growth as a function of time for three different concentrations of molasses and acetate. The data show that full growth is reached very quickly for both amendments. The concentration of the amendment used does not have a marked influence on the rate of cell growth. All reactors seem to converge to the same cell density independent of the initial concentration of the carbon source. However, the sediments amended with molasses grow to higher cell numbers relative to the sediments amended with acetate. This is consistent with the liquid cultures presented in Figure 3.1-2, which also show that at equivalent concentrations molasses stimulate microbial growth to higher cell numbers than acetate.

3.1.3 Reduction of Nitrate, Sulfate, Chromate, and Iron in Liquid Cultures Biostimulated with Molasses and Acetate

3.1.3.1 Biostimulation Using Acetate as a Carbon Source

The data in Figures 3.1-6-9 show the rate of nitrate, sulfate, chromate, and iron reduction in liquid cultures biostimulated with acetate. Nitrate was rapidly consumed in all reactors that received acetate while it remained fairly constant in all control reactors without acetate and the sterile reactors (Figure 3.1-6). The sampling frequency was insufficient to capture the rapid decay of nitrate which was complete within the first week of incubation. The presence of sediment did not influence the rate of nitrate reduction. The concentration of sulfate remained constant in all reactors, including the controls, suggesting that sulfate reduction was not significant (Figure 3.1-7). The reduction of Cr(VI) was relatively slow and depended on the presence of sediments. Chromium reduction did not proceed to any significant degree in the first month of incubation and was faster in reactors with sediments (Figure 3.1-8). No reduction was observed in the heat-killed controls and in the controls without acetate. The presence of sediments only affected reactors with active microorganisms, which indicates that chromate sorption/transformation by sediments is negligible in the absence of bacterial activity. The pH of all reactors varied between 7.45 and 8.23 but did not change dramatically or affect the rate of chromate reduction (Figure 3.1-9). The level of ferrous iron concentration remained below detection in all reactors (data not shown). Acetate concentrations decreased slightly in the first week of incubation in the active reactors but remained stable afterward (Figure 3.1-10). The concentration of acetate remained stable in the sterile controls.

3.1.3.2 Biostimulation Using Molasses as a Carbon Source

Chromate concentration was measured in the liquid cultures biostimulated with molasses and incubated anaerobically. The data in Figure 3.1-11 show that Cr(VI) was not measurable in any of the reactors including the sterile controls. However, Cr(VI) remained stable and did not change significantly in any of the controls that did not receive molasses. The presence of sediments did not affect Cr(VI) concentrations even after more than two months of incubation. This indicates that Cr(VI) is likely reduced chemically by

association with molasses. To validate this observation, a set of control experiments was performed by incubating sterile filtered molasses with chromate. The data in Figure 3.1-12 show the profile of Cr(VI) concentration over time at different molasses concentrations. At longer incubation times of more than 50 days, the concentrations of Cr(VI) were near the detection limit (data not shown). The rate of chromate reduction is significantly enhanced at higher molasses concentrations. Under the conditions of our microcosm experiment of 1.8 g/L molasses, complete reduction was observed within 24 hours. Ferrous iron was detected in samples with active microbes after the first week of incubation. The pH of the media dropped very rapidly after the reactors were sealed and stabilized between 4.5 and 5.2 (Figure 3.1-13). Sterile control reactors decreased slightly but stabilized to approximately pH 6.5. The sediments did not affect the pH.

3.1.4 Microbial Community Analysis of Reactors Biostimulated with Acetate

Changes in microbial community composition of groundwater was investigated for the reactors biostimulated with acetate only since the benchtop experiments with molasses revealed that chromate was mainly reduced abiotically by reaction of chromate with molasses. Gene sequence analysis was used to study the microbial community in acetate-biostimulated reactors sealed under strict anaerobic conditions. Biostimulation of groundwater in sealed reactors lessened bacterial diversity and resulted in different community compositions in the anaerobic reactors (Figure 3.1-14). Proteobacteria constitute 96.3% of the overall population in the biostimulated reactors. The level of Firmicutes also was stimulated by acetate. Three phyla including Nitrospirae (5.9%), NC10 (5.2%) and Fibrobacteres (2.0%) present in the R-42 groundwater were no longer detectable after acetate amendment. Moreover, members of the Chloroflexi, constituting 1.6% of the bacteria present in R-42 water reduced to 0.3% in the sample biostimulated with acetate. These data suggest that acetate has a positive effect on the selection of Proteobacteria and Firmicutes, but suppressed Nitrospirae, NC10, Chloroflexi and Fibrobacteres. In general, acetate did not cause biostimulation of the most abundant genera. In contrast, growth of the genera *Oleomonas*, *Pseudomonas*, *Xanthobacter*, *Azospira*, present in low numbers in R-42 groundwater, was commonly stimulated by acetate. A drastic increase in growth was observed for *Pseudomonas* representing over half of the total population in the reactors biostimulated with acetate anaerobically. A drastic increase in growth was observed for *Dechloromonas* (37.2%) and *Novosphingobium* (19.4%) under strict anaerobic condition. *Dechloromonas* and *Pseudomonas* are known for their versatile metabolic abilities. Both can utilize acetate as a carbon source.

Many *Pseudomonas* species such as *P. putida*, *P. aeruginosa*, *P. fluorescens* are known to reduce chromium (Wolterink et al. 2005; Heylen et al. 2006). Sequences of the most abundant *Pseudomonas* are closely related to *P. fluorescens* (98% sequence identify). Model experiments have revealed that nitrate reduction is tightly linked to chromate reduction (Vainshtein et al. 2003). Sequences of *Dechloromonas* are related to a nitrate reducer *Dechloromonas hortensis* (96% sequence identify) (Wolterink et al. 2005). While the bacterial phenotypes cannot be determined based on 16S rRNA gene comparisons, the utilization of acetate and reduction of chromium strongly suggest that the observed *Pseudomonas* and *Dechloromonas* OTUs are involved in chromium reduction.

3.2 Column Studies

3.2.1 Chromium Reduction in Packed Columns

Column experiments were performed to (1) evaluate the response of microorganisms from R-42 to biostimulation under continuous flow conditions and high sediment to water ratio; (2) evaluate the long-term geochemical changes in water chemistry; (3) determine chromium reduction kinetics and rebound times, and (4) evaluate the potential mobilization of adverse effects of other constituents such as arsenic.

Four identical columns were filled with different sediments and were run by injecting R-42 groundwater containing 942 µg/L Cr(VI) under slightly different biostimulation conditions. The first two columns were biostimulated by the injection of acetate and the third and fourth columns were biostimulated by the addition of molasses. All columns were initially tested to evaluate the natural capacity of the sediments to attenuate Cr(VI) followed by a biostimulation period induced by the addition of carbon substrate amendment to the R-42 water injected through the column.

3.2.2 Natural Attenuation of Cr(VI) by Sediments from the Chromium Plume Area

The four columns packed with sediments representative of regional aquifer sediments were tested for their ability to attenuate chromate through sorption/reduction in the absence of any microbial activity. All columns were packed with dry sediments and sterilized by autoclaving to limit the activity of bacteria associated with sediments. The sterile columns were saturated with sterile filtered R-42 which was treated by ion exchange resin to remove Cr(VI). The columns were run at a constant flow by the injection of R-42 water amended with a spike of tritiated water used as a conservative tracer. The data in Figure 3.2-1a–d show the concentration breakthrough curves of chromate along with the conservative tracer for the different columns. The data show that there is very little to no natural attenuation of chromium before biostimulation for all columns. The profiles of Cr(VI) concentration breakthrough matched the concentration breakthrough of the tritium tracer. Chromate transport through the column sediments in column 2 (R-42 fines) is slightly retarded relative to tritium, and in column 3 (filled with sediments from Water Canyon [WC-006 3-27-14]) chromate exited the column slightly faster than the conservative tracer, signifying that there might be some anion exclusion process that slightly enhanced chromate transport. There was no measurable differences in the transport of tritium and chromate observed in columns 1 and 4, which were filled with Puye sediments from Rendija Canyon [(Ren 121213-03) and SCI-2, respectively].

3.2.3 Attenuation of Cr(VI) by Sediments Biostimulated with Acetate and Molasses

Following the natural attenuation studies which demonstrated that the sediments used in all four columns had no measurable attenuation capacity, the columns were biostimulated by the injection of R-42 water along with a pulse of either sodium acetate or molasses. Note that though the columns were sterilized before the start of the experiments, on average 4 pore volumes of R-42 water was injected through each column during the natural attenuation studies. The injection of R-42 water, containing on average 1×10^5 bacteria/mL, inoculated the column sediment with microbes present in R-42 water. Biostimulation was initiated for each column by the injection of either acetate or molasses. The first column was filled with sterile sediments from Ancho Canyon, and was biostimulated by the injection of R-42 water amended with sodium acetate at a concentration of 0.82 g/L (10 mM) for 3.9 pore volumes, followed by 15 pore volumes of a solution containing 0.08 g/L acetate and 50 pore volumes of R-42 water without any amendments (Figure 3.2-2). The third column was filled with sterile sediments from Rendija Canyon, and was biostimulated by continuous injection of 2.4 pore volumes of R-42 water amended with 0.82 g/L (10 mM) acetate, followed by an additional 5 pore volumes pure R-42 water without any amendments (Figure 3.2-3). The second column filled with sterile sediments from R-42 fines was biostimulated by the injection of 4.68 pore volumes R-42 water amended with molasses at a concentration of 3.4 g/L followed by 12.6 pore volumes of a solution containing 0.34 g/L of molasses and 50 pore volumes of R-42 water without any amendments (Figure 3.2-4). The fourth column filled with sterile Puye sediments from SCI-2 was biostimulated by continuous injection of 2.31 pore volumes R-42 water amended with molasses at a concentration of 3.4 g/L and monitored for Cr(VI) attenuation for an additional 20 pore volumes without any additional molasses (Figure 3.2-5). The water residence time was approximately 47 hours for all columns. During the entire run the column effluents were collected using fraction collectors and were

monitored for pH, acetate concentration, molasses, Cr(VI), and nitrate. The flow rate fluctuated slightly but was mostly maintained at approximately 1.89 mL/hour (Figures 3.2-6 and 3.2-7).

The data in Figures 3.2-4 and 3.2-5 show the profile of chromium concentration breakthrough for the columns biostimulated with molasses. The data show that the column biostimulated with a single short pulse of molasses completely removed Cr(VI) from the influent water for approximately 16 pore volumes. Chromium concentration in the effluents fluctuated but trended up continually. The concentration of Cr(VI) never reached the concentration of influent water (860 µg/L) signifying continued Cr(VI) attenuation. The data from the column biostimulated for a longer period of time at a lower concentration of molasses showed no breakthrough of chromium at any point during the experiment.

The data show that the attenuation capacity of the sediments is dependent on the biostimulation duration. Longer attenuation capacities are achieved with longer biostimulation periods. Relatively lower concentrations of biostimulant applied for longer periods of time created larger attenuation capacities relative to high concentrations of biostimulant applied for short periods of time. The data from the column breakthrough curve show that the concentration of Cr(VI) in the effluents fluctuated significantly over time and was very sensitive to the flow rate. A reduction in the flow rate resulted in immediate reduction of chromium concentrations in the column effluents.

3.2.4 Microbial Diversity in the Column Sediments

The diversity of the microbial community in the acetate-stimulated column was also reduced compared to R-42 water (Figure 3.2-8). The microbial community in acetate-stimulated column sediments was primarily comprised of *Proteobacteria*. Interestingly, members of *Verrucomicrobia* were specifically enriched in the column. The combined taxa (*Proteobacteria* + *Verrucomicrobia*) comprised 86% in both the influent (bottom) and effluent (top) ends of the acetate column. Three OTUs from the *Comamonadaceae* family, exhibiting 99–100% similarity to various *Pelomonas*, *Acidovorax*, and *Curvibacter* spp., comprised 51% (influent end) and 62% (effluent end) of the β -*Proteobacteria* sequence types. Each of these genera possesses the ability to reduce nitrate.

Members of the α -*Proteobacteria* comprised a greater fraction of the total bacterial community in the column (approximately 19% in both ends of column). Two of the most abundant OTUs of the α -*Proteobacteria* in the column were classified as *Caulobacteraceae* sequences that exhibited 100% identity with typed *Caulobacter* (40% of the α -*proteobacteria* sequences) and *Brevundimonas* (17% of the α -*proteobacteria* sequences) species. Members of these two genera are often found in nutrient-limited environments where their propensity to form stalk cells for attachment and swarmer cells for mobility increases population fitness. A number of *Brevundimonas* species are capable of denitrification. A third abundant α -*proteobacteria* OTU found in the column (17% of the α -*proteobacteria* sequences) was 100% similar to sequences from two *Afipia* species (*Afipia birgiae* and *Afipia massiliensis*) isolated from a hospital water supply (La Scola et al. 2000). Of note, the genome of *Afipia birgiae* was sequenced and genes involved in chromium resistance were found. Additionally, four sequences found in a trivalent chromium precipitation tank share 100% similarity with this OTU (Flynn et al. 2013). A member of this genus was isolated also from a nitrate- and uranium-contaminated aquifer at Oak Ridge Reservation, TN and was shown to reduce nitrate to nitrogen gas during growth (Wolterink et al. 2005).

A single OTU belonging to the γ -*Proteobacteria* was detected in the column, comprising 4.0% and 9.1% of the total bacterial community found in the influent and effluent ends, respectively. This phylotype shares 99% similarity to several *Pseudoxanthomonas* species, including several linked to Cr(VI) reduction in the presence of acetate or methanol (Tekerekopoulou et al. 2010; Sahinkaya et al. 2013).

A single *Verrucomicrobia* sequence-type was present in all samples, comprising 7% and 19% of the total bacterial sequences found in the influent and effluent ends of the acetate column respectively. This OTU was classified as a member of the *Opitutaceae* family, but only shared 93% similarity to its closest, cultured neighbor, a strain of *Opitutus terrae*. *Verrucomicrobia* are commonly found in aquifers and sediments, but the biogeochemical traits of *Opitutus terrae* or related microorganisms that allow them to thrive in these environments are unclear. One OTU classified in the *Sporolactobacillaceae* family was also found in the effluent end of the acetate column, comprising 5.4% of all bacterial sequences in that sample. This OTU was classified in the *Sporolactobacillaceae* family of the *Firmicutes*.

In the molasses column, there was a greater divergence in the composition of the dominant taxa between the influent and effluent ends of the column (Figure 3.2-10). The influent end of the molasses column was primarily comprised of β -proteobacteria (65%) and *Verrucomicrobia* (28%), whereas the dominant members in the effluent end of the column were almost equally split amongst the β -proteobacteria (30%) and *Verrucomicrobia* (27%) and Bacteroidetes (28%). It is not surprising that the bacterial community was more heterogeneous in the molasses column since this energetic substrate supported greater bacterial growth and biomass in the influent end of the column than did acetate, which in turn would have resulted in a greater redox gradient through the length of the molasses column.

3.2.5 SEM Characterization of Bioreduction Products

Scanning electron microscopy investigations were performed on the initial sediments, the biostimulated sediments collected from the biostimulated column, and on residues from the biostimulated reactors containing no sediments, to examine the association of chromium with the biomass and the minerals in the sediments. Figure 3.2-10 shows a composite picture of SEM images of the microbial cells obtained from a biostimulated reactors incubated in the absence of sediments. The images show massive chromium precipitation on the surface of the cells and biofilm (a). Nanospheres ranging in size between 10 to 50 nm are observed on the microbial cells (b). Energy dispersive spectroscopy (EDS) analysis of the nanospheres confirms the presence of chromium, but it is not clear if other elements are also present (c). It is worth noting the absence of iron in the composition of the precipitated chromium. In contrast, SEM obtain for sediment grains collected from the biostimulated column show biofilm coatings on the surface of the grains (e,f) and a strong correlation of iron and chromium, which were found to be collated in all samples analyzed. In the presence of sediment, no observations were made of any well-defined features with increased chromium. Grains which did not contain any iron did not show any chromium. This suggests that in the presence of sediment, chromium tends to accumulate on the surface of iron minerals. This suggests that Cr(VI) is either reduced indirectly by reaction with Fe(II) accumulated on the minerals to form a Fe(III)-Cr(III) mineral phase or that Cr(VI) is reduced directly by microbes but preferentially precipitates on the surface of iron phases to form a mixed Fe(III)-Cr(III) mineral phase. Examinations by the extended x-ray absorption fine structure (EXAFS) method (results not presented) does suggest that Cr(III) precipitated in the presence of sediments forms a mixed Fe(III)-Cr(III) mineral phase.

4.0 DISCUSSION

Cell density in groundwater from well R-42 ranged from 5×10^4 to 2×10^6 bacteria/mL, decreasing with the amount of water pumped before sampling. It could indicate that the cell counts are strongly influenced by the microenvironment within the sampling interval. Groundwater from R-42 had 750 to 900 CFU/mL. Biostimulation with acetate and molasses in sealed reactors and saturated sediments promoted rapid microbial growth and slightly higher cell densities. However, molasses was more effective at stimulating microbial growth. For most of the experiments presented in this report, the concentrations of acetate used (0.8 g/L) were lower than the concentrations of molasses used (3.4 g/L), making direct comparison of growth stimulation difficult. However, the biostimulation of the saturated sediments used concentrations of

acetate up to 16 g/L and did not record a significant enhancement in microbial density relative to lower acetate concentrations (Figure 3.1-4). This was also true for molasses for which higher molasses concentrations did not necessarily induce higher biomass generation. In general, it was determined that molasses biostimulated microbes to higher cell densities compared to acetate for equivalent concentrations. However, higher molasses and acetate concentrations accelerated microbial growth relative to lower concentrations (Figure 3.1-4 and Figure 3.1-5). The average cell densities established after the initial exponential growth in sediments stimulated under anoxic conditions with acetate were $7.5 \times 10^8 \pm 6 \times 10^8$ cells/g and for molasses the cell numbers were about an order of magnitude higher averaging $5.0 \times 10^9 \pm 3 \times 10^9$ bacteria/g. The cell numbers in the liquid cultures were also lower in acetate biostimulated reactors relative to molasses (Figure 3.1-4 and Figure 3.1-4). Growth in the biostimulated columns varied between the bottom (influent) and top of the column (outlet). At the bottom of the column, microbial density in the sediments biostimulated with acetate was 2.0×10^7 cells/g and at the top of the column was 4.4×10^6 cells/g. Cell numbers in the columns biostimulated with molasses were about an order of magnitude higher compared to acetate. Overall the data reflects the ability of both acetate and molasses to biostimulate the microorganisms present in R-42 groundwater under anaerobic conditions. However, molasses seems to stimulate the growth of higher cell densities relative to acetate. The cell density is an important parameter that is hard to determine accurately, especially in the presence of sediments. The cell numbers reported here are intended to provide a qualitative parameter for modeling efforts that may be implemented for consideration of remedial alternatives for the chromium plume.

Overall, the results of microbial diversity studies using groundwater from R-42, and the microcosm experiments, indicate that bacteria capable of denitrification are abundant in the source groundwater and that these microorganisms dominated the R-42 microcosm experiments. β -proteobacteria, in particular *Acidovorax* spp., have been found to dominate under denitrifying conditions during periods of Cr(VI) reduction in soils and sediments from different sources (McLean et al. 2000). Additionally, several of the genera detected in the R-42 microcosm experiments (i.e. *Acidovorax*, *Dechloromonas*, *Sediminibacterium*) were previously observed in columns/microcosms containing Hanford Site groundwater and sediments when lactate and polylactate compounds were tested as electron donors to support Cr(VI) reduction under denitrifying conditions (Xiao et al. 2014). These results combined with the water chemistry analysis indicate that, with acetate as the electron donor, Cr(VI) reduction was supported under denitrifying conditions in the R-42 microcosm experiment.

Microbial diversity examination in the column stimulated with acetate also shows a reduction in the microbial diversity relative to R-42 water, and a marked difference in the microbial diversity between the inlet and outlet of the column (Figure 3.2-8, Table 4.0-1). However, the biostimulation with acetate specifically enriched microbial genera that possess the ability to reduce nitrate. *Acidovorax* spp., sharing 99–100% similarity to sequences found in the acetate microcosm, have been identified in Cr(VI)- and Cr(III)-contaminated industrial wastewaters (Katsaveli et al. 2012) and Cr(VI)-contaminated groundwater from the Hanford Site (Brodie et al. 2011). The two other predominant β -Proteobacteria OTUs found in the acetate-stimulated columns (31% and 34% of the β -Proteobacteria sequence types in the influent and effluent ends of the column, respectively) were from the *Rhodocyclaceae* family and shared 100% identity to sequences from various *Azoarcus* and *Azospira* spp. Members of these two genera are well-known denitrifiers. Select members (including several that share 100% identity to the OTUs found here) couple iron-oxidation with nitrate reduction to support growth (Tekerekopoulou et al. 2010). The β -Proteobacteria comprised a greater fraction of the community in sediment obtained from the influent (51.5%) than from the effluent end of the columns (37.3%). Based on the phylogenetic identity of these strains, it can be posited that a handful of β -proteobacteria genera (e.g. *Acidovorax*, *Pelomonas*, *Azospira*, *Azoarcus*, *Curvibacter* and unclassified β -proteobacteria) stimulated in the column were adept at utilizing nitrate as a terminal electron acceptor under the experimental conditions. Different subsets of these organisms thrived with acetate serving as the electron donor. It is possible that high levels of denitrification,

particularly at the influent end of the columns resulted in a nitrate gradient that decreased from the bottom (influent) to the top (effluent) of the columns.

The composition of the β -proteobacteria differed substantially between the molasses- and acetate-fed columns at the OTU level. The dominant β -proteobacteria OTU in the molasses column could not be classified with confidence at the family level and exhibited just 96% similarity to its nearest neighbor sequence as determined by Basic Local Alignment Search Tool (BLAST) analysis. This OTU comprised 84% and 38% β -proteobacteria sequence types in the molasses column at the influent and effluent ends, respectively. This equates to 54% and 11% of the total bacterial sequences found in the two ends of the column. Apparently, this novel phylotype is extremely competitive when fed molasses under the experimental conditions. This phylotype is not specifically adapted to polysaccharide utilization, however, as it comprised 8.3% and 0.1% of the β -proteobacteria OTUs identified in the influent and effluent ends of the acetate column, respectively. Because it is not closely related to characterized isolates or environmental clones linked to biogeochemical processes, its physiological traits cannot be speculated.

In both the acetate- and molasses-fed columns, the β -proteobacteria comprised a greater fraction of the community in sediment obtained from the influent (52% to 65%) versus the effluent end of the columns (30% to 37%). Based on the phylogenetic identity of these strains it can be posited that a handful of β -proteobacteria genera (e.g. *Acidovorax*, *Pelomonas*, *Azospira*, *Azoarcus*, *Curvibacter* and unclassified β -proteobacteria) were adept at utilizing nitrate as a terminal electron acceptor under the experimental conditions and that different subsets of these organisms thrived with either molasses or acetate serving as the electron donor. It is possible that high levels of denitrification, particularly at the influent end of the columns, resulted in a nitrate gradient that decreased from the bottom (influent) to top (effluent) of the columns.

One of the striking differences between the acetate- and molasses-fed columns was the abundance of *Bacteroidetes* in the effluent end of the latter. *Bacteroidetes* phylotypes comprised 2.5% to 2.8% of the total bacterial sequences in the acetate column and 1.1% of the total in the influent end of the molasses column; however, they contributed 27.9% of the total in the effluent end of the molasses column. The most abundant of these OTUs (13.3% of the total sequences in the effluent end of the molasses column) was in the *Sphingobacteriaceae* family and 99% similar to several *Pedobacter* species. Members of this genus inhabit a variety of habitats, but of particular interest are a major component of the microbial community in the subsurface at the Hanford Site. Genome analysis of four *Pedobacter* isolates from the Hanford Site revealed a chemoheterotrophic metabolism, under aerobic and microaerophilic conditions, with the genes encoding a number of extracellular carbohydrate-active enzymes for growth on complex polysaccharides and transporters for more labile sugars. Thus, it is possible that these microorganisms derived energy directly from molasses, but the physio-chemical conditions in the effluent end of the column provided a superior environment for growth than those in the influent end of the column (this OTU comprised just 0.5% of the total sequences in the influent end). Alternatively, since molasses supported such robust growth, it is also possible that *Pedobacter* spp. in the effluent end of the column is involved in the degradation or digestion of dead cells and extracellular substances produced and transported from the influent end. The second most abundant *Bacteroidetes* OTU in the molasses column was found exclusively in the effluent end, where it comprised 9.7% of the total sequences, and belonged to the *Chitinophagaceae* (but could not be classified at the genus level). Similar sequences comprised a significant proportion of the bacterial community in an aerobic/anoxic deammonification bioreactor, where it was suggested that *Chitinophagaceae* were acting as predators or saprotrophs of other microorganisms in the system. Finally, *Bdellovibrionaceae* sequences (δ -proteobacteria) most closely related to various predatory *Bdellovibrio* spp. (96% similarity) comprised 1.6% of the sequences in the effluent end of the molasses column, but less than 0.05% in each of the other column samples. Overall, these observations could indicate that a substantial proportion of the *Bacteroidetes* species found in the effluent end of the molasses column could be involved in dead-cell recycling.

A third *Bacteroidetes* OTU common in the effluent end of the molasses column (2.7% of the total sequences) was also classified in the *Chitinophagaceae* family and was 100% similar to the 16S rRNA gene from *Sediminibacterium salmoneum*. *Sediminibacterium* spp. are capable of coupling Fe(II)-oxidation to nitrate reduction and have been found in various chromium-contaminated waters. This OTU was also present in the acetate column where it comprised 0.7% to 1.1% of the bacterial community.

Of particular note, *Nitrospira* sequences (*Nitrospirae* phylum) were detected in the effluent end of the molasses column, where they comprised 1.4% of the total. These results indicate that in the influent end of the molasses column, denitrification is either incomplete or nitrate reduction occurs at such a high rate that nitrite accumulates at concentrations that support growth of the nitrite-oxidizing *Nitrospira* spp. *Nitrospira* sequences were not found in the acetate column and comprised just 0.01% of the total in the influent end of the molasses column.

The acetate microcosm studies show that nitrate was rapidly consumed in all reactors that received acetate while it remained fairly constant in all control reactors without acetate, and that sulfate remained stable under all conditions. The concentrations of ferrous iron remained below detection in all reactors, indicating that either iron reduction did not occur or that ferrous iron precipitated as ferrous iron hydroxides. However, acidifying the sediments did not lead to the release of any ferrous iron, which is interpreted as an indication that iron reduction did not occur. The reduction of Cr(VI) did not proceed to any significant degree until all nitrate was reduced. The rate of chromate reduction varied significantly between reactors, as indicated by the large error bars in the Cr(VI) concentration (Figure 3.1-8). This variability was mainly driven by the cell numbers. The reactors with higher cell numbers reduced chromate more rapidly than reactors with lower cell numbers. This interpretation was checked by performing an independent experiment in which Cr(VI) reduction was examined in cell suspensions under non-growth conditions under strict anaerobic conditions as a function of microbial cell density. The data in Figure 4.0-1 show that the rate of chromate reduction increases exponentially as the density of the microbial cell increases. In these experiments, acetate was provided as the sole electron acceptor and no competing electron acceptors (i.e., nitrate, iron, and sulfate) were present. The data from the acetate microcosm experiment show that acetate can effectively stimulate the microbes present in R-42 water to drive chromate reduction. Nitrate is shown to strongly inhibit chromate reduction. However, nitrate is consumed very rapidly and does not seem to limit chromate reduction. On the contrary, our microbial diversity analysis has shown enrichment of denitrifying bacteria, which seem to also reduce chromate under anoxic conditions. The presence of nitrate might be beneficial by helping to rapidly shape the microbiome to effectively reduce nitrate and create conditions favorable to chromate reduction. Tests of how the microbiome would change if no nitrate were present were not conducted because most of the groundwater in the contamination area contains appreciable amounts of nitrate.

Biostimulation of the column sediments using acetate was very effective at creating conditions favorable for chromate reduction. The data in Figure 3.2-2 show the breakthrough of chromate from the column biostimulated with acetate for a short period of time. The sediments developed a short chromate attenuation capacity. The concentration Cr(VI) in the effluents exceeded 50 ppb after the injection of only 1.7 pore volumes of R-42 water containing 860 µg/L Cr(VI). The concentration of Cr(VI) in the effluent water fluctuated considerably and decreased significantly each time the flow rate was decreased, but never reached the influent concentration at any time during the experiment. The ratio between the period of complete Cr(VI) removal (meaning less than 50 ppb) and the duration of biostimulation (acetate injection) was 0.7, indicating very little reducing capacity was built in the column, and its rapid depletion in the absence of acetate. The results from column 2, biostimulated for a longer period of time, show that chromium was also depleted from the column effluents as soon as acetate was added to the influent water (Figure 3.2-3). Chromium concentrations in the effluent water exceeded 50 ppb after the injection of 29 pore volumes following the end of acetate addition. The ratio between the period of complete Cr(VI) removal and the duration of biostimulation period was 1.4. The data from the acetate column experiments

show that acetate was very effective at creating conditions favorable for chromate reduction. Furthermore, the microbial diversity data show that acetate favorably created strong denitrification conditions, especially at the inlet of the column, and therefore shape the microbiome to favorably reduce chromate. However, acetate is not accumulated in the columns and the capacity of the sediments to reduce Cr(VI) is rapidly diminished in the absence of acetate. Addition of acetate to the already stimulated column results in an immediate and complete removal of chromium from the column effluents. The data in Figure 4.0-2 show the breakthrough curve of Cr(VI), acetate, and iodine used as a conservative tracer in column 2, following additions of two short pulses of acetate. The data is consistent with the data presented in the initial biostimulation runs and shows that the ratio between the period of complete removal of chromium to less than 50 µg/L and the period of active addition of the acetate amendment is about 0.7. The data show that acetate was not retained in the column and that only 14% of acetate was effectively used or accumulated in the column. The moles equivalent consumed/accumulated was 0.26 mmol and resulted in the removal of 0.01 mmol of Cr(VI). It is worth noting that the average residence time of about 47 hours was sufficient to completely reduce chromium and nitrate, whereas in the batch experiments incubation time of 60 to 100 days were needed to completely remove chromium from solution. This suggests that the reduction mechanism in the column experiments could be entirely different from that observed in the sealed reactors. Indirect reduction of Cr(VI) by reduced sediments is likely, but given the very strong dependence of Cr(VI) reduction on the presence of acetate, it is more likely that Cr(VI) is directly reduced by microbes. The very high solid (including biomass) to liquid ratio in the column does create conditions that seem favorable to Cr(VI) reduction. It is also likely that sediments are playing a role in catalyzing Cr(VI) reduction by facilitating surface precipitation of Cr(III).

Chromate reduction in the microcosm reactors biostimulated with molasses shows that chromate is reduced chemically by reaction with molasses. This is in agreement with other reports from the literature which have also shown that chromate is rapidly reduced by sugars and sugar metabolites. Vinasse, a product of alcohol production from sugar beet molasses was shown to reduction of Cr(VI) in acidic solution and ambient temperature within hours (Altundogan et al. 2004). Sugarcane molasses has also been shown to reduce Cr(VI) to Cr(III) abiotically at pH values that range from 2.0 to 6.1 (Zi-Fang et al. 2015). In these microcosm experiments, chromate was reduced within a few hours before any microbial growth is recorded and is clearly attributed to abiotic processes. The pH dropped significantly in all active reactors with live cells and varied between 4.5 and 5.5. The low pH resulted in the mobilization of ferrous iron, which was produced in all reactors with active cells and molasses. The concentration of arsenic remained below detection limit and was consistent with the low abundance of arsenic in the aquifer sediments used in our experiments.

The breakthrough curves showing the transport of Cr(VI) through sediments biostimulated with molasses are consistent with the data from the microcosm experiments and show complete removal of Cr(VI) from the effluents immediately after molasses was introduced in the column. It is likely that Cr(VI) was reduced chemically rather than through the activity of metal-reducing bacteria. The breakthrough curves show an elevated baseline when molasses is present. This is an artifact from increased baseline because of the presence of molasses. However, there is no Cr(VI) in any of the samples analyzed in any of the effluents samples collected while molasses was being injected into the column. The pH drop correlated perfectly with the injection of molasses. The data in Figure 4.0-4 show the profile of molasses concentration in the column effluents and the pH of the effluents. The data also show that the pH returned to neutral when all the molasses exited the column. This transient low pH is very important because it can drive the dissolution of stainless steel associated with well components. The concentration of Cr(VI) in the effluent water was below the detection limit of our method. The column stimulated with 2.3 pore volumes of molasses (column 4) completely removed chromium from solution ([Cr(VI) <50ppb]) for 13 pore volumes. The ratio between the pore volumes of biostimulation and complete Cr(VI) is for approximately 5.7. This ratio was not determined for the columns biostimulated for a longer period of time because Cr(VI) was not

detected in the effluents after more than 100 pore volumes of R-42 water injection. The results from the columns biostimulated with molasses clearly show that molasses was very effective at creating long-lasting conditions favorable to Cr(VI) attenuation. However, for both columns, transient low pH conditions were created and could negatively impact the water chemistry of the water. Analysis of the effluent samples from our columns did not show elevated concentration of undesirable metals. Effectively the concentration of arsenic was below 7 ppb in all samples measured.

5.0 CONCLUSION

In this study we examined the microbial diversity of groundwater within the chromium-contaminated portion of the regional aquifer and how it evolved after biostimulation. The study found that the bacterial community in groundwater is dominated by proteobacteria, which represented 58.2% of the overall bacterial population: α -proteobacteria (25.5%), β -proteobacteria (12.7%), γ -proteobacteria (13.7%), and δ -proteobacteria (6.2%).

Laboratory studies of biostimulation showed increased cell numbers but reduction in microbial diversity. The microbial community in the sediments stimulated with acetate was primarily comprised of β -proteobacteria, α -proteobacteria, γ -proteobacteria and Verrucomicrobia. In general, this study revealed that both molasses and acetate can be used as carbon substrates to stimulate microbes capable of reducing Cr(VI). However, molasses induced the buildup of higher biomass and provided a longer reduction capacity than acetate. Molasses transformation to organic acids created low pH condition of between 4.5 and 5. The study highlights the importance of the initial geochemical conditions in shaping the microbiome. It also makes the case for establishment of reducing conditions favorable to Cr(VI) reduction, but shows how difficult it is to maintain an effective and lasting reducing environment capable of supporting long-term Cr(VI) reduction. These data were used to design a field pilot-study, which is described in the Pilot-Scale Amendments Testing Work Plan for Chromium in Groundwater beneath Mortandad Canyon (LANL 2017).

6.0 REFERENCES AND MAP DATA SOURCES

6.1 References

The following reference list includes documents cited in this report.

- Altundogan H.S., A. Ozer, and F. Tümen. "A Study on the Reduction of Hexavalent Chromium in Aqueous Solutions by Vinasse," *Environmental Technology* Vol. 25, No. 11, pp. 1257–1263 (2004).
- Bopp L.H., and H.L. Ehrlich. "Chromate Resistance and Reduction in *Pseudomonas Fluorescens* Strain LB300," *Archive of Microbiology*, Vol. 150, No. 5, pp. 426–431 (1988).
- Brodie E.L., D.C. Joyner, B. Faybishenko, M.E. Conrad, C. Rios-Velazquez, J. Malave, R. Martinez, B. Mork, A. Willett, S. Koenigsberg, D.J. Herman, M.K. Firestone, and T.C. Hazen. "Microbial Community Response to Addition of Polylactate Compounds to Stimulate Hexavalent Chromium Reduction in Groundwater," *Chemosphere*, Vol. 85, pp. 660–665 (2011).
- Bowman R.S., and J.F. Gibbens. "Difluorobenzoates as Nonreactive Tracers in Soil and Groundwater," *Ground Water*, Vol. 30, No. 1, pp. 8–14 (1992).

- Caporaso J.G., C.L. Lauber, W.A. Walters, D. Berg-Lyons, J. Huntley, N. Fierer, S.M. Owens, J. Betley, L. Fraser, M. Bauer, N. Gormley, J.A. Gilbert, G. Smith, and R. Knight. "Ultra-high-throughput Microbial Community Analysis on the Illumina Hiseq and Miseq Platforms," *The ISME Journal*, Vol. 6, No. 8, pp. 1621–1624 (2012).
- Cheung K.H., and J.D. Gu. "Reduction of Chromate (CrO₄(2-)) by an Enrichment Consortium and an Isolate of Marine Sulphate-reducing Bacteria," *Chemosphere*, Vol. 52, pp.1523–1529 (2003).
- Cheung K.H., H.Y. Lai, and J.D. Gu. "Associated Hexavalent Chromium Reductase of *Bacillus Megaterium* TKW3 with Induced Expression," *Journal of Microbiology and Biotechnology*, Vol. 16, pp. 855–862 (2006).
- Duke C.L., R.C. Roback, P.W. Reimus, R.S. Bowman, T.L. McLing, K.E. Bake, and L.C. Hull. "Elucidation of Flow and Transport Processes in a Variably Saturated System of Interlayered Sediment and Fractured Rock Using Tracer Tests," *Vadose Zone Journal*, Vol. 6, No. 4, pp. 855–867 (2007).
- Flynn T.M., R.A. Sanford, H. Ryu, C.M. Bethke, A.D. Levine, N.J. Ashbolt, and J.W. Santo Domingo. "Functional Microbial Diversity Explains Groundwater Chemistry in a Pristine Aquifer," *BMC Microbiology*, Vol. 13, No. 146 (2013).
- Fude L., B. Harris, M.M. Urrutia, and T.J. Beveridge. "Reduction of Cr(VI) by a Consortium of Sulfate-reducing Bacteria (SRB III)," *Applied and Environmental Microbiology*, Vol. 60:1525–1531 (1994).
- Guha H., K. Jayachandran, and F. Maurrassec. "Kinetics of Chromium (VI) Reduction by a Type Strain *Shewanella* Alga under Different Growth Conditions," *Environmental Pollution*, Vol. 115, pp. 209–218 (2001).
- Han R., J.T. Geller, L. Yang, E.L. Brodie, R. Chakraborty, J.T. Larsen, and H.R. Beller. "Physiological and Transcriptional Studies of Cr (VI) Reduction under Aerobic and Denitrifying Conditions by an Aquifer-derived *Pseudomonad*," *Environmental Science & Technology*, Vol 44, pp. 7491–7497 (2010).
- Hazen C.T., L. Jimenez, G. Lopez de Victoria, and C.B. Fliermans. "Comparison of Bacteria from Deep Subsurface Sediment and Adjacent Groundwater," *Microbial Ecology* Vol. 22, pp. 293–304 (1991).
- Heylen K., B. Vanparys, L. Wittebolle, W. Verstraete, N. Boon, and P. De Vos. "Cultivation of Denitrifying Bacteria: Optimization of Isolation Conditions and Diversity Study," *Applied and Environmental Microbiology* Vol. 72, pp. 2637–2643 (2006).
- Katsaveli K., D. Vayenas, G. Tsiamis, and K. Bourtzis. "Bacterial Diversity in Cr(VI) and Cr(III)-contaminated Industrial Wastewaters," *Extremophiles*, Vol. 16, pp. 285–296 (2012).
- Khan S.T., Y. Horiba, M. Yamamoto, and A. Hiraishi. "Members of the Family Comamonadaceae as Primary Poly(3-hydroxybutyrate-co-3-hydroxyvalerate)-degrading Denitrifiers in Activated Sludge as Revealed by a Polyphasic Approach," *Applied and Environmental Microbiology*, Vol. 68, pp. 3206–3214 (2002).
- La Scola B., R.J. Birtles, M.N. Mallet, and D. Raoult. *Massilia* gen. nov. in "Validation of Publication of New Names and New Combinations Previously Effectively Published Outside the IJSEM," List no. 73. *International Journal of Systematic and Evolutionary Microbiology*, Vol. 50, pp. 423–424 (2000).

- LANL (Los Alamos National Laboratory). "Pilot-Scale Amendments Testing Work Plan for Chromium in Groundwater beneath Mortandad Canyon," Los Alamos National Laboratory document LA-UR-17-25406, Los Alamos, New Mexico (2017).
- Li J.W., X.T. Peng, H.Y. Zhou, J.T. Li, and Z.L. Sun. "Molecular Evidence for Microorganisms Participating in Fe, Mn, and S Biogeochemical Cycling in Two Low-temperature Hydrothermal Fields at the Southwest Indian Ridge," *Journal of Geophysical Research*, Vol. 118, pp. 665–679 (2013).
- McLean J.S., T.J. Beveridge, and D. Phipps. "Isolation and Characterization of a Chromium-reducing Bacterium from a Chromated Copper Arsenate-contaminated Site," *Environmental Microbiology*, Vol. 2, pp. 611–619 (2000).
- Ozturka S., K. Tayfun, A. Belma, and T. Sema. "Removal and Reduction of Chromium by *Pseudomonas* spp. and their Correlation to Rhamnolipid Production," *Journal of Hazardous Materials*, Vols. 231–232, pp. 64–69 (2012).
- Priester J.H., S.G. Olson, S.M. Webb, M.P. Neu, L.E. Hersman, and P.A. Holden. "Enhanced Exopolymer Production and Chromium Stabilization in *Pseudomonas putida* Unsaturated Biofilms," *Applied and Environmental Microbiology*, Vol. 72, No. 3, pp. 1988–1996 (2006).
- Sahinkaya E., A. Kilic, B. Calimlioglu, and Y. Toker. "Simultaneous Bioreduction of Nitrate and Chromate using Sulfur-based Mixotrophic Denitrification Process," *Journal of Hazardous Materials*, Vol. 262, pp. 234–239 (2013).
- Stewart D.I., I.T. Burke, and R.J.G. Mortimer. "Stimulation of Microbial Mediated Chromate Reduction in Alkaline Soil-Water Systems," *Geomicrobiology Journal*, Vol. 24, pp. 655–669 (2007).
- Tebo B.M., and A.Y. Obraztsova. "Sulfate-reducing Bacterium Grows with Cr(VI), U(VI), Mn(IV), and Fe(III) as Electron Acceptors," *FEMS Microbiology Letters*, Vol. 162, pp. 193–198 (1998).
- Tekerlekopoulou A.G., G. Tsiamis, E. Dermou, S. Siozios, K. Bourtzis, and D.V. Vayenas. "The Effect of Carbon Source on Microbial Community Structure and Cr(VI) Reduction Rate," *Biotechnology and Bioengineering* Vol. 107, pp. 478–487 (2010).
- Vainshtein M., P. Kuschik, J. Mattusch, A. Vatsourina, and A. Wiessner. "Model Experiments on the Microbial Removal of Chromium from Contaminated Groundwater," *Water Research*, Vol. 37, pp. 1401–1405 (2003).
- Woldegabriel, G., A.P. Naranjo, and M.M. Fittipaldo. "Distribution, Geochemistry, and Correlations Pliocene Tephra in the Pajarito Plateau," *New Mexico Geological Society Guidebook, 58th Field Conference*, pp. 275–283 (2007).
- Wolterink A., S. Kim, M. Muusse, I.S. Kim, P.J.M. Roholl, C.G. Van Ginkel, A.J.M. Stams, and S.W.M. Kengen. "Dechloromonas Hortensis sp. nov. and Strain ASK-1, Two Novel (Per)chlorate-Reducing Bacteria, and Taxonomic Description of Strain GR-1," *International Journal of Systematic and Evolutionary Microbiology*, Vol. 55, pp. 2063–2068 (2005).
- Xiao W., X. Yang, Z. He, and T. Li. "Chromium-resistant Bacteria Promote the Reduction of Hexavalent Chromium in Soils," *Journal of Environmental Quality*, Vol. 43, pp. 507–516 (2014).

Yagi J.M., D. Sims, T. Brettin, D. Bruce, and E.L. Madsen. "The Genome of Polaromonas Naphthalenivorans Strain CJ2, Isolated from Coal Tar-contaminated Sediment, Reveals Physiological and Metabolic Versatility and Evolution through Extensive Horizontal Gene Transfer," *Environmental Microbiology*, Vol. 11, pp. 2253–2270 (2009).

Yelton A.P., K.H. Williams, J. Fournelle, K.C. Wrighton, K.M. Handley, and J.F. Banfield. "Vanadate and Acetate Biostimulation of Contaminated Sediments Decreases Diversity, Selects for Specific Taxa, and Decreases Aqueous V5+ Concentration," *Environmental Science & Technology* Vol. 47, pp. 6500–6509 (2013).

Chen, Z.F., Y.S. Zhao, J.W. Zhang, and J. Bai. "Mechanism and Kinetics of Hexavalent Chromium Chemical Reduction with Sugarcane Molasses," *Water, Air, & Soil Pollution*, Vol. 226, No. 363 (2015).

6.2 Map Data Sources

Hillshade; Los Alamos National Laboratory, ER-ES, As published;
\\slip\gis\Data\HYP\LiDAR\2014\Bare_Earth\BareEarth_DEM_Mosaic.gdb; 2014.

Point features; As published; EIM data pull; 2017.

Chromium plume > 50 ppb; Los Alamos National Laboratory, ER-ES, As published;
\\slip\gis\GIS\Projects\13-Projects\13-0065\shp\chromium_plume_2.shp; 2018.

Structures; Los Alamos National Laboratory, KSL Site Support Services, Planning, Locating and Mapping Section; 06 January 2004; as published 29 November 2010.

Drainage channel; Los Alamos National Laboratory, ER-ES, As published, GIS projects folder;
\\slip\gis\GIS\Projects\15-Projects\15-0080\project_data.gdb\correct_drainage; 2017.

Technical Area Boundaries; Los Alamos National Laboratory, Site Planning & Project Initiation Group, Infrastructure Planning Office; September 2007; as published 13 August 2010.

Unpaved roads; Los Alamos National Laboratory, ER-ES, As published, GIS projects folder;
\\slip\gis\GIS\Projects\14-Projects\14-0062\project_data.gdb\digitized_site_features\digitized_roads; 2017.

U.S. Census populated places; Los Alamos National Laboratory, ER-ES, As published, GIS projects folder; \\slip\gis\GIS\Data\ESRI\census\places.sdc\places; 2018.

Rivers; Los Alamos National Laboratory, ER-ES, As published, GIS projects folder;
\\slip\gis\GIS\Data\ESRI\hydro\rivers.sdc\rivers; 2018.

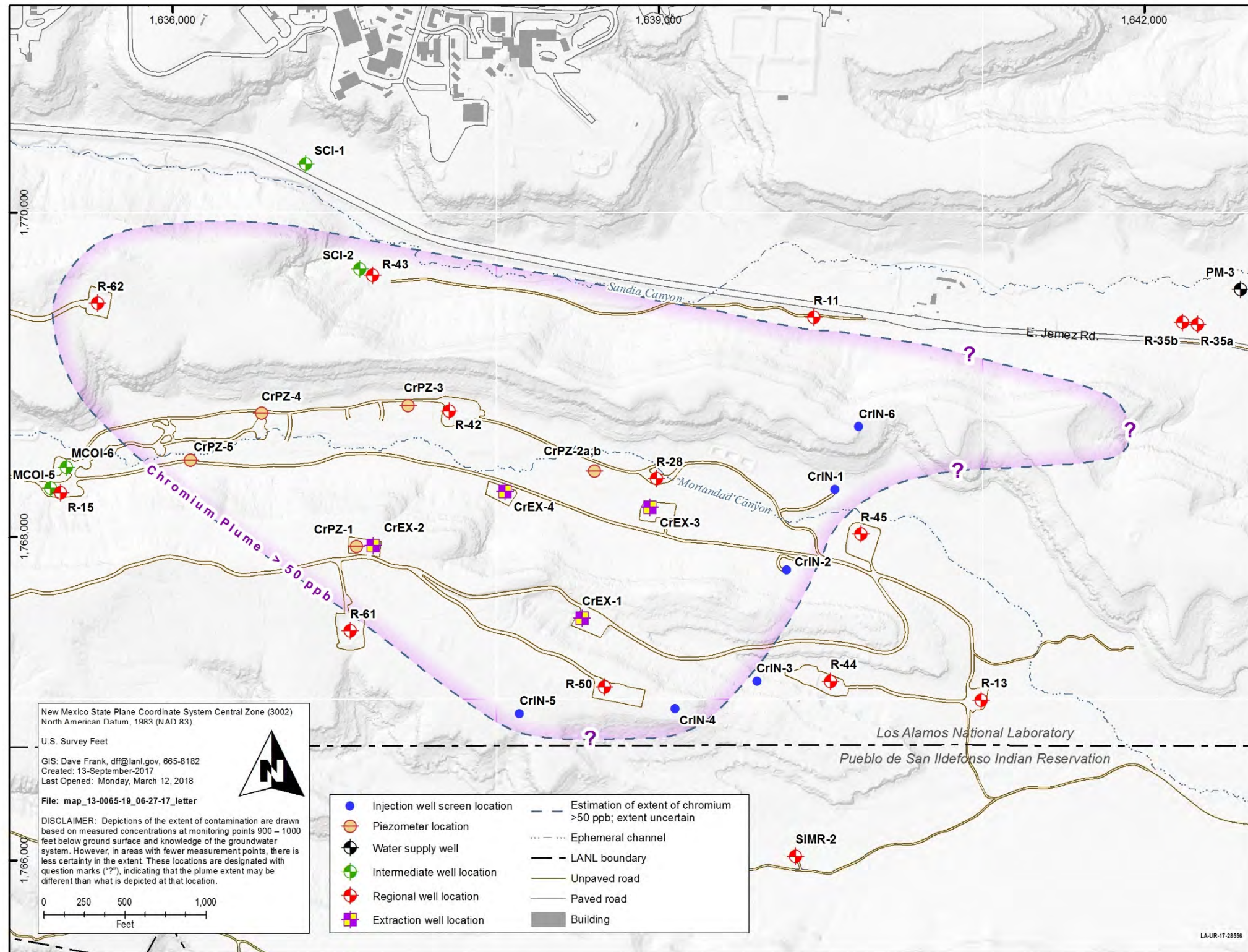


Figure 2.1-1 Map showing the footprint of the chromium plume in the regional aquifer beneath Los Alamos National Laboratory. Groundwater monitoring wells interrogating the regional aquifer (red), the deep intermediate aquifer (green), nearby water-supply wells (blue/black), and groundwater contours are shown.

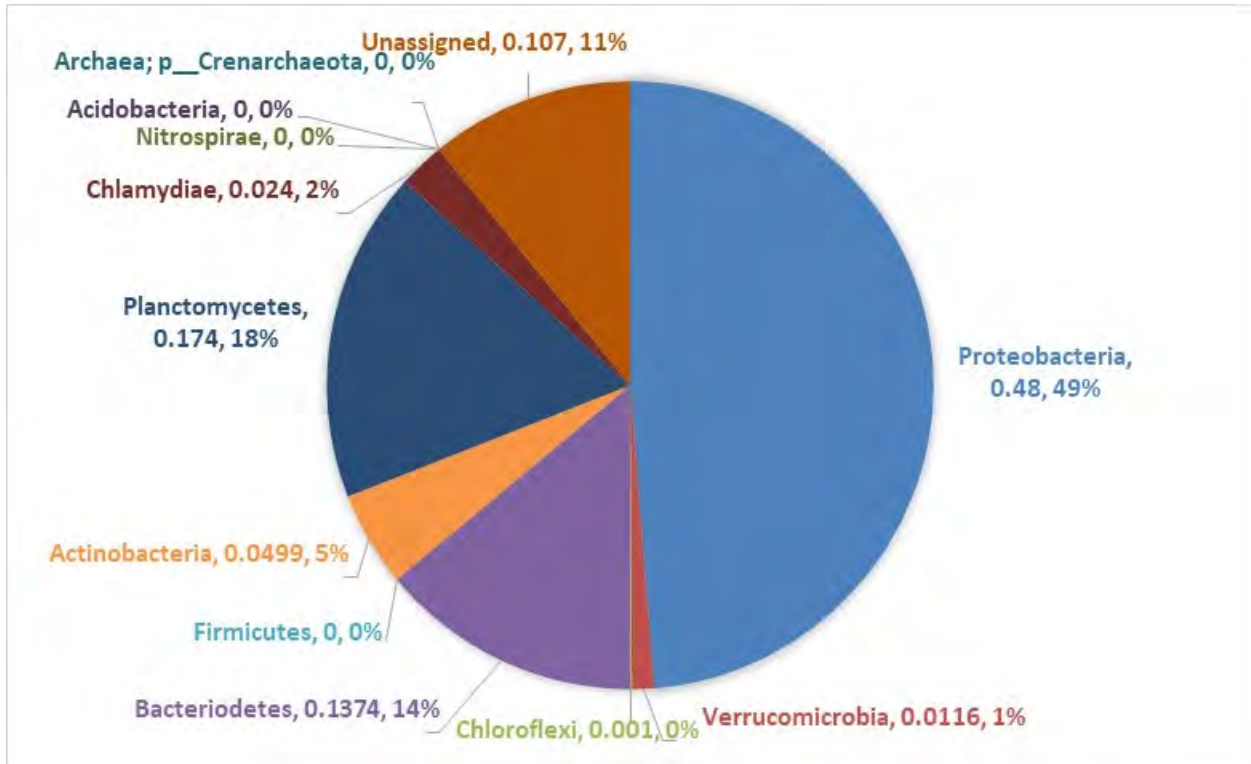


Figure 3.1-1 Graphic representation of the microbial diversity at the phylum or groundwater collected from sampling well R-42

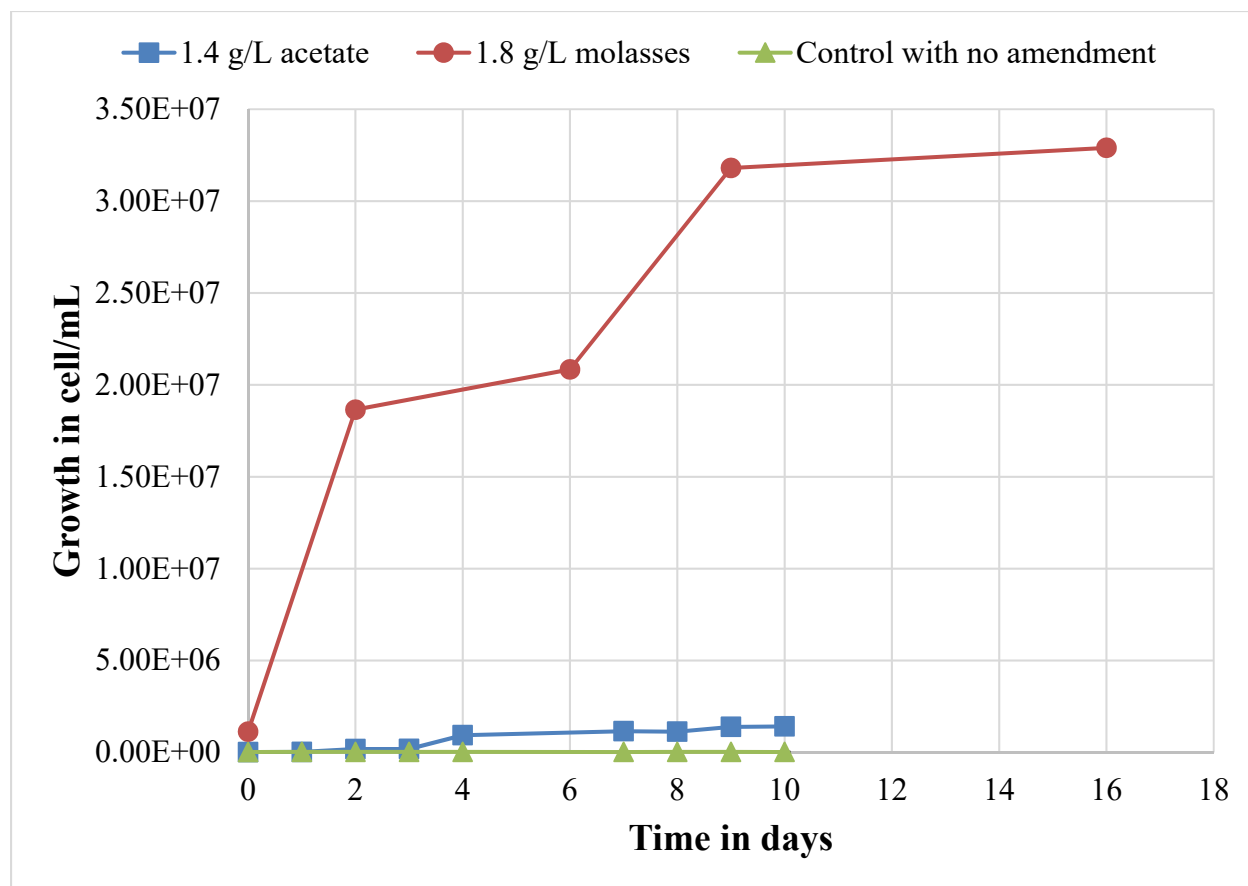


Figure 3.1-2 Microbial growth in R-42 water stimulated by either 1.4 g/L sodium acetate or 1.8 g/L molasses. Cell numbers were determined by reading the optical density at 600 nm which were converted to cell numbers using calibration curves establishes specifically for each carbon source. The water parameters of the R-42 water are as described in the materials section.

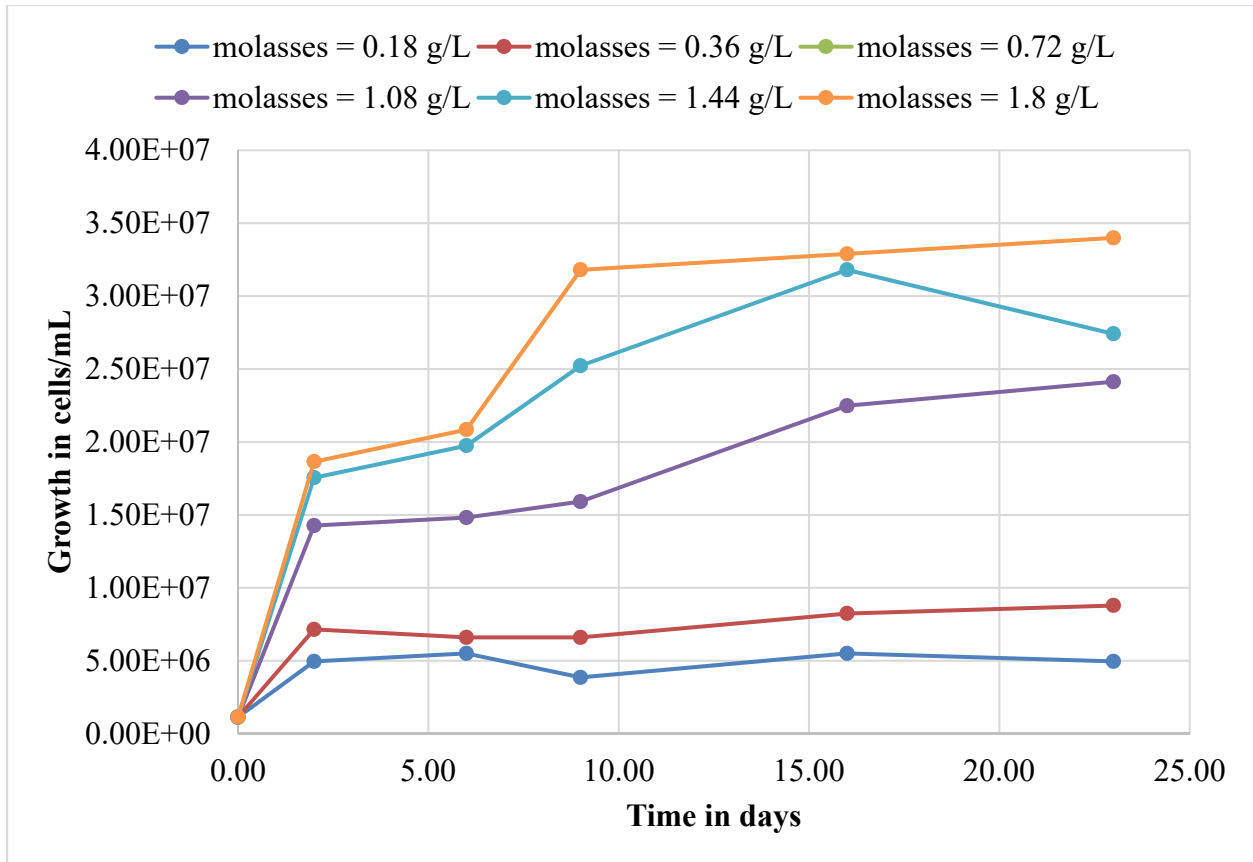


Figure 3.1-3 Microbial growth in reactors biostimulated with molasses and incubated anaerobically. Initial conditions are: Water used from R-42 with 888 $\mu\text{g/L}$ Cr(VI). Initial pH = 8.8 and final pH = 4.85.

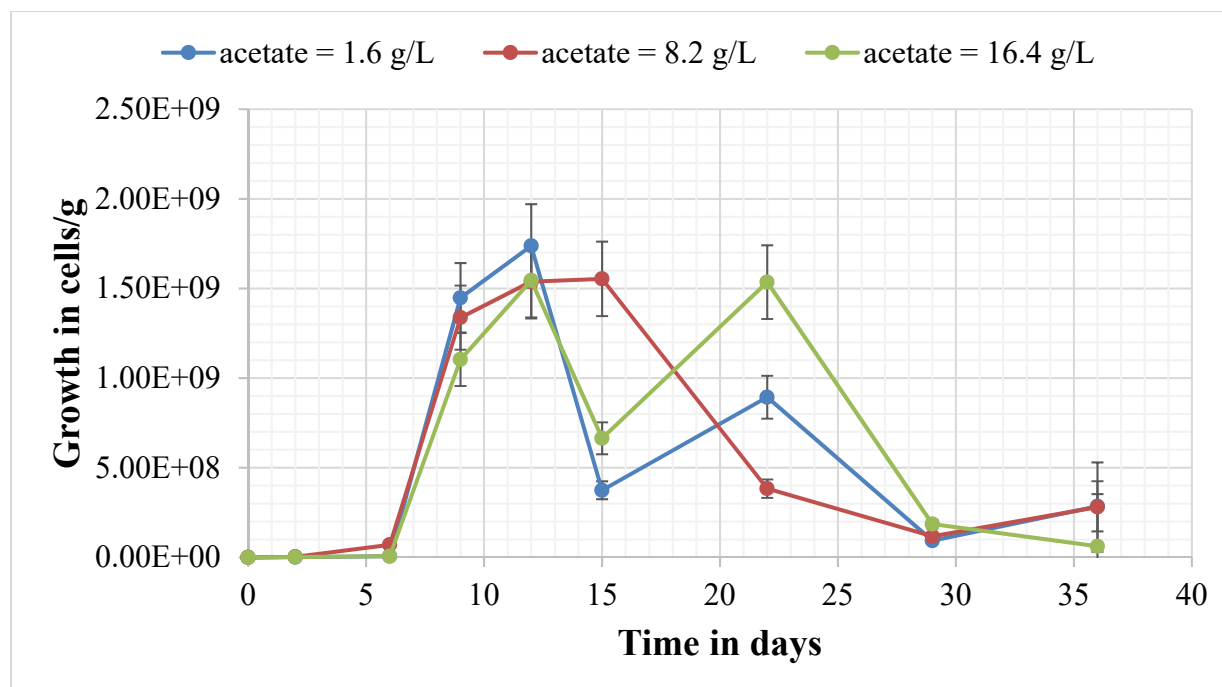


Figure 3.1-4 Microbial growth in saturated sediments samples from CH-3 amended with various acetate concentrations and incubated statically in the dark under anaerobic conditions

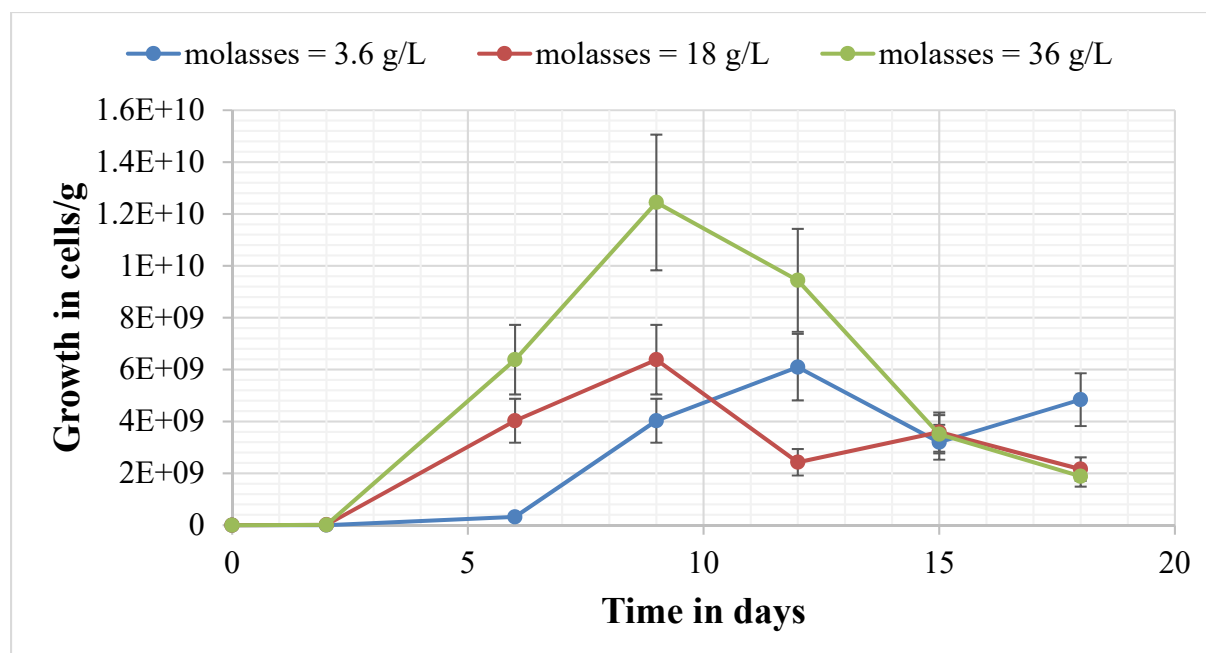


Figure 3.1-5 Microbial growth in saturated sediments samples from CH-3 amended with various molasses concentrations and incubated statically in the dark under anaerobic conditions

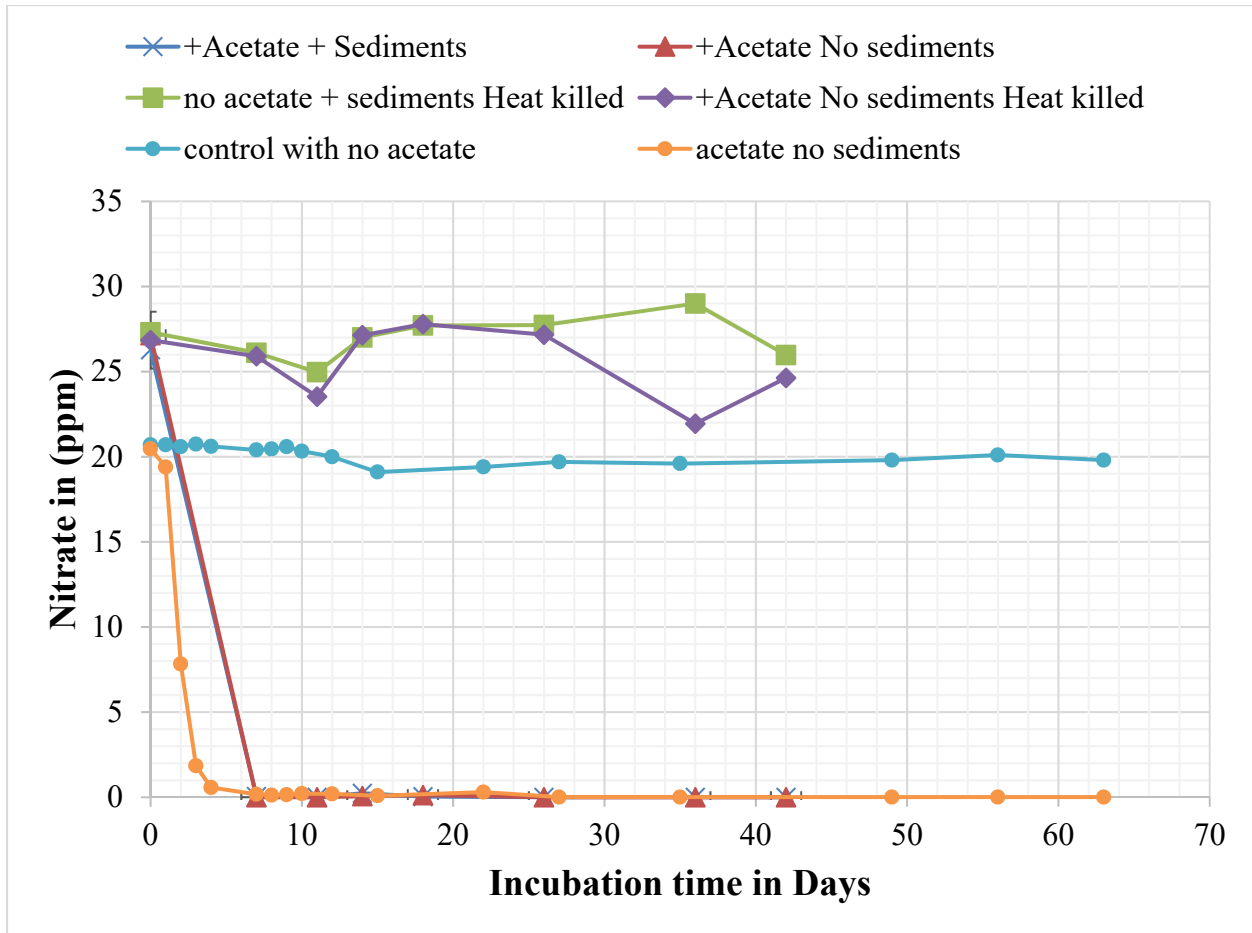


Figure 3.1-6 Nitrate reduction in R-42 water amended with 0.82 g/L acetate and incubated anaerobically in the presence and absence of sediments. Reactors received 100 mL of R-42 water and 1.0 g of sediments. R-42 water chemistry is presented in the materials and methods section.

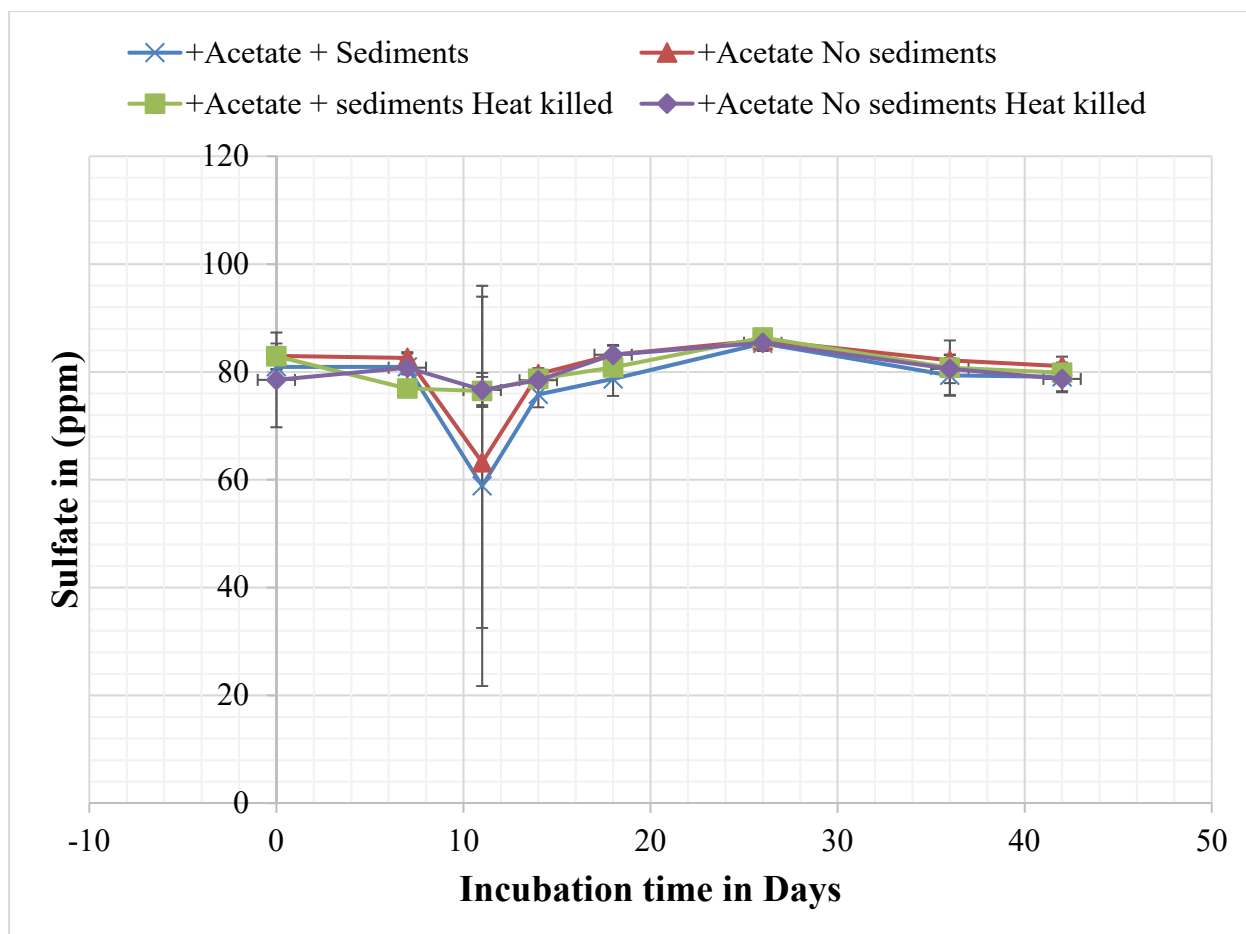


Figure 3.1-7 Sulfate reduction in R-42 water amended with 0.82 g/L acetate and incubated anaerobically in the presence and absence of sediments. Reactors received 100 mL of R-42 water and 1.0 g of sediments. R-42 water chemistry is presented in the materials and methods section.

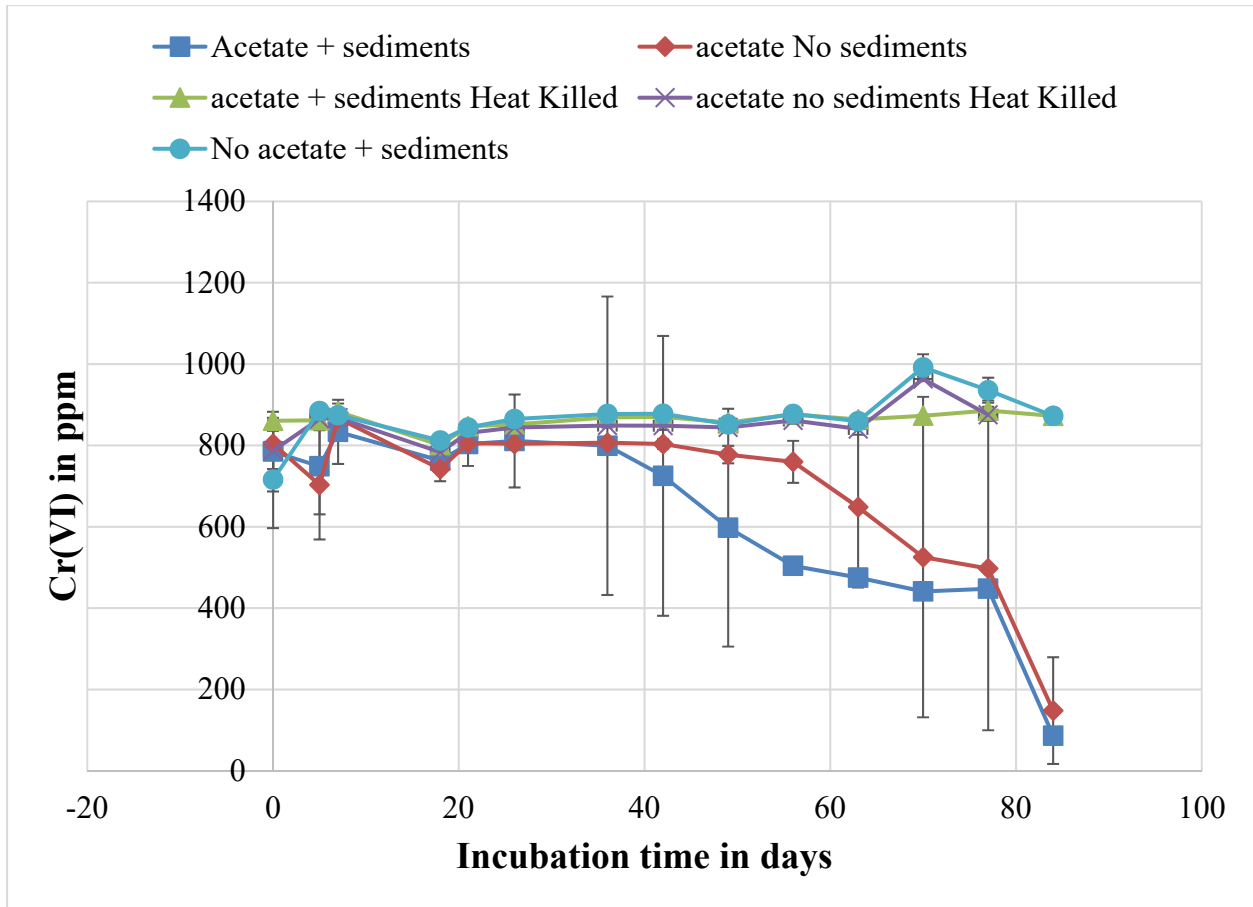


Figure 3.1-8 Chromate reduction in liquid cultures amended with 0.82 g/L acetate and incubated anaerobically in the presence and absence of sediments. Reactors received 100 mL of R-42 water and 1.0 g of sediments. Heat killed control reactors were autoclaved to sterilize the reactors.

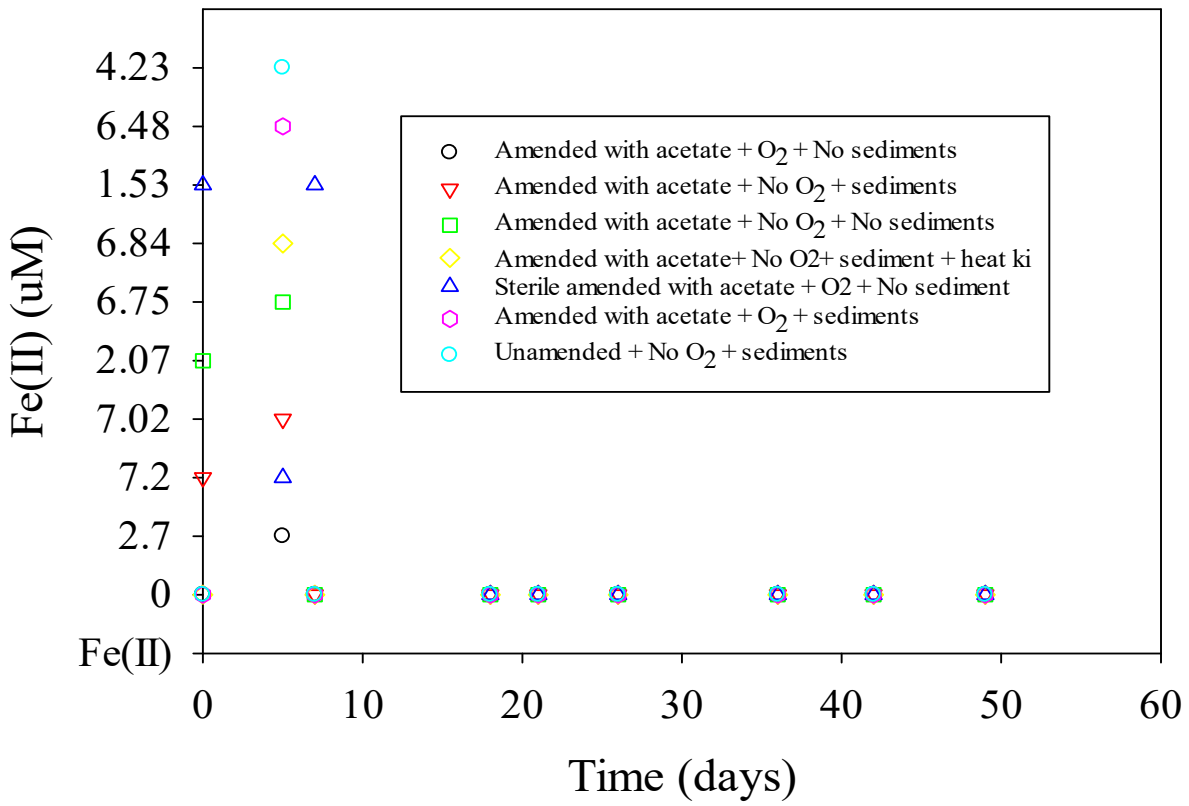


Figure 3.1-9 Concentration of ferrous iron in the different reactors stimulated with acetate

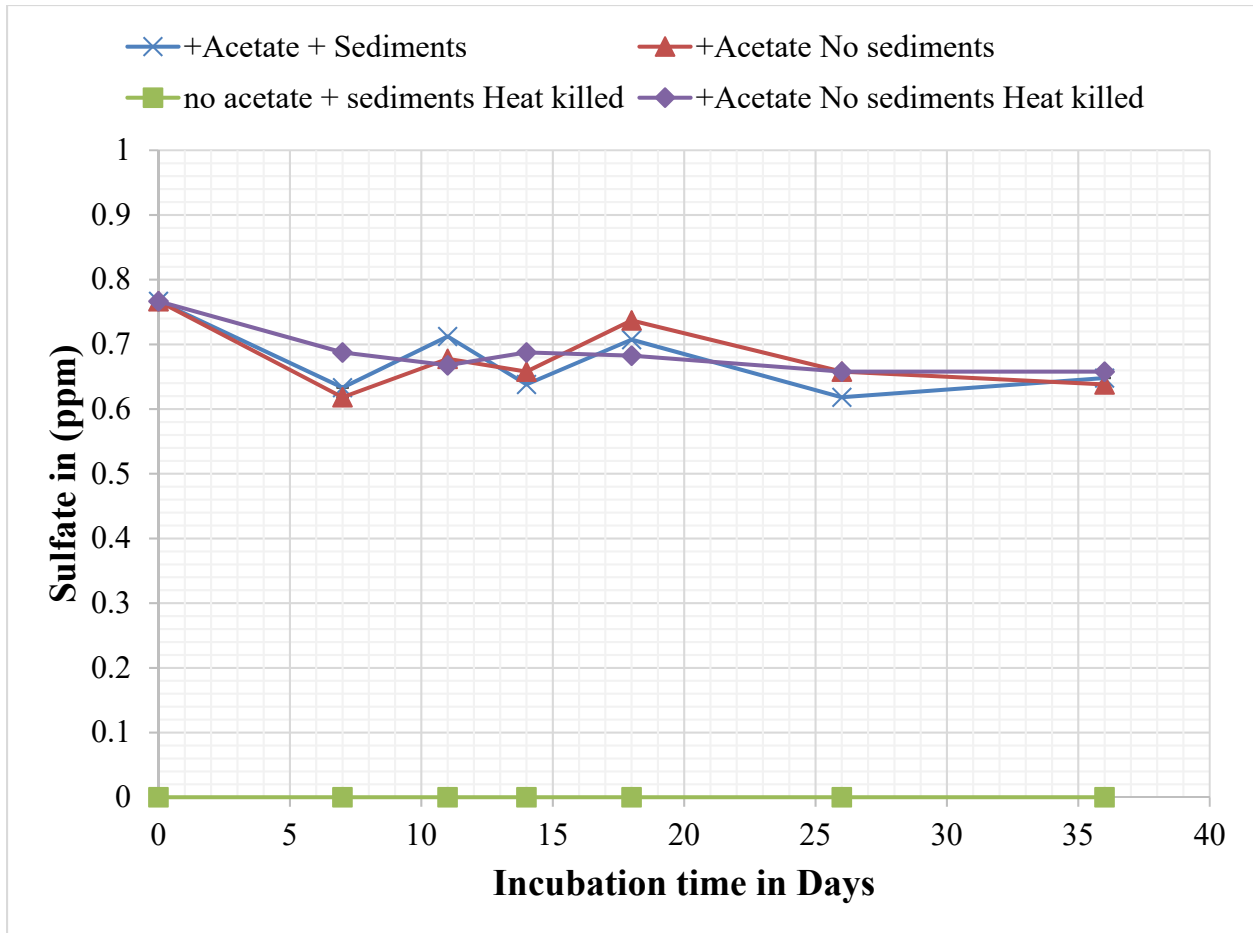


Figure 3.1-10 Acetate consumption in liquid cultures amended with 0.82 g/L acetate and incubated anaerobically in the presence and absence of sediments. Reactors received 100 mL of R-42 water and 1.0 g of sediments. Heat killed control reactors were autoclaved to sterilize the reactors.

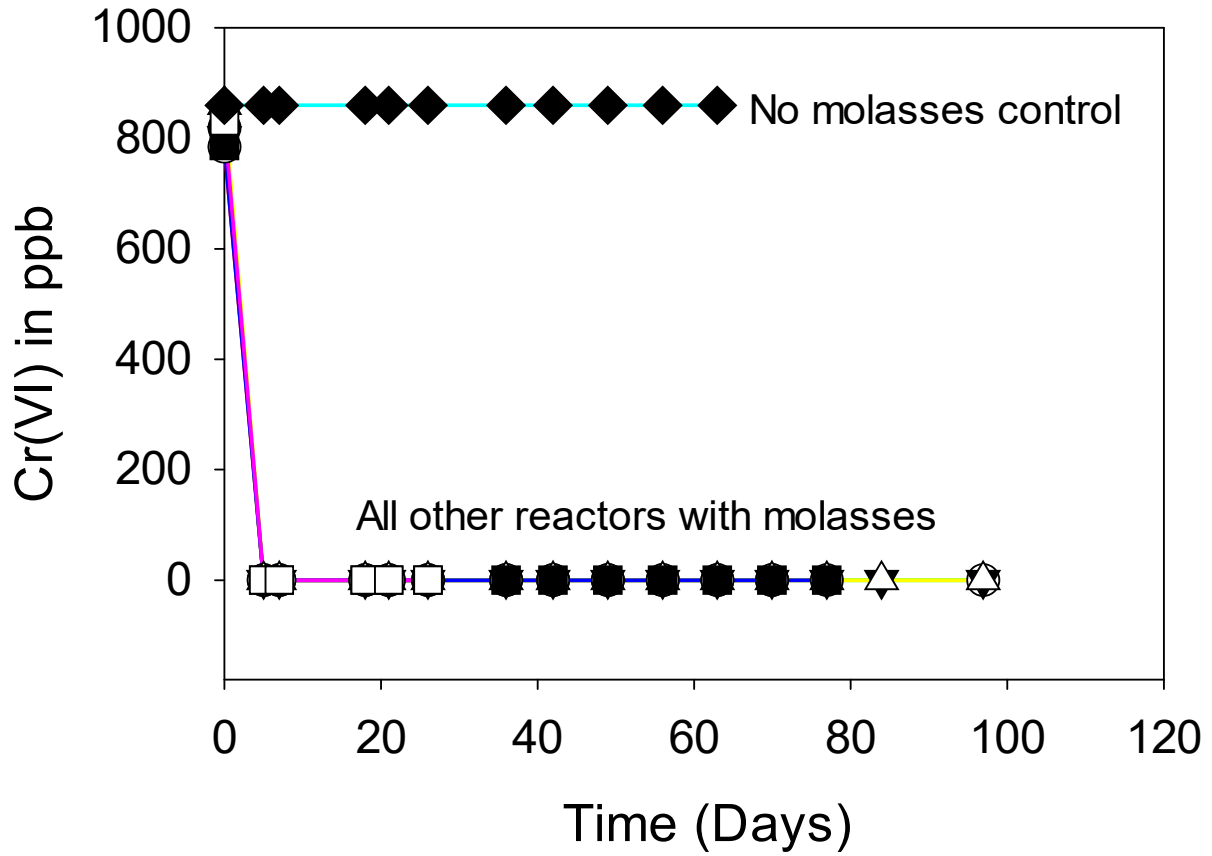


Figure 3.1-11 Bioreduction of chromate in reactors amended with molasses in the absence and presence sediments. A control with degassed R-42 water was setup as a control without addition of molasses.

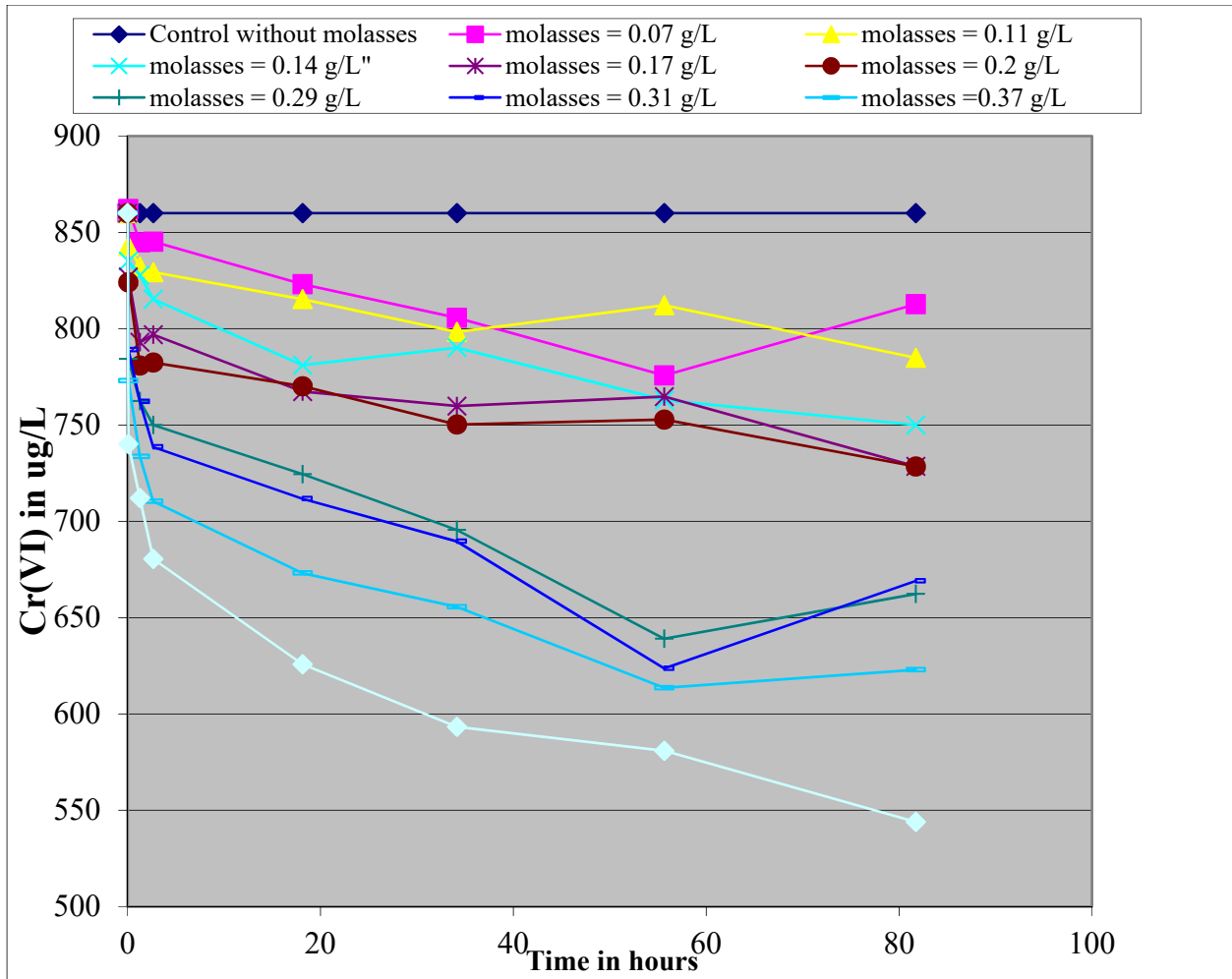


Figure 3.1-12 Chromate reduction by molasses under sterile conditions. Molasses was sterile filtered using 0.2 μm syringe filters. The pH of the groundwater was pH = 8.8 and did not change.



Figure 3.1-13 Changes in pH during the microcosm experiment biostimulated with molasses. The molasses concentration was fixed in all reactors to 1.8 g/L.

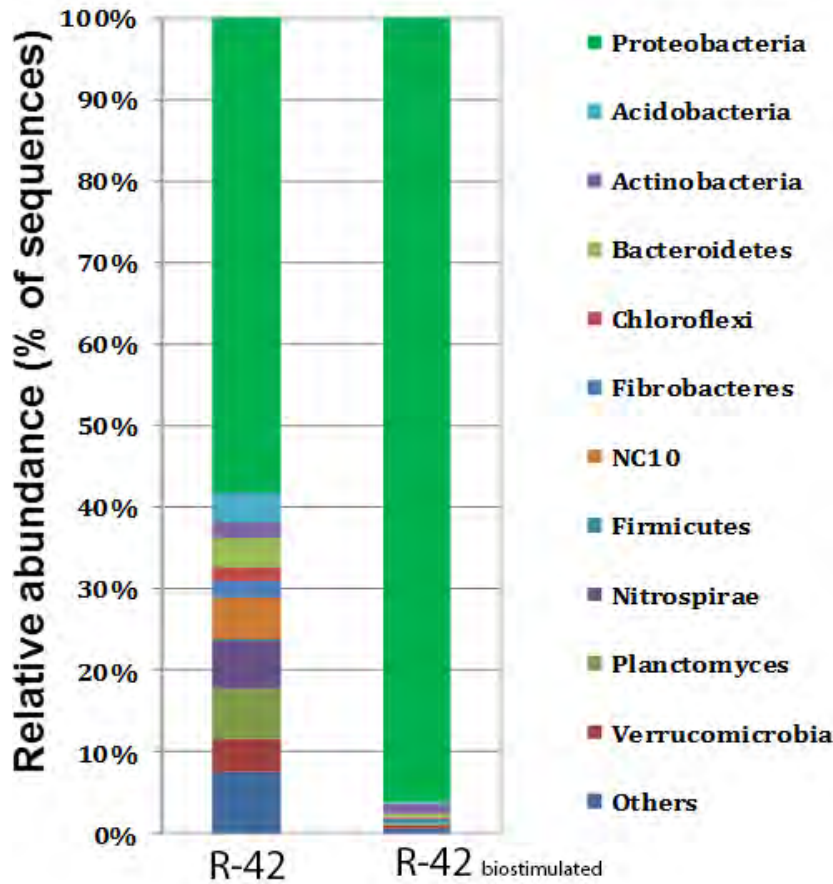


Figure 3.1-14 Graphic representation of (A) microbial diversity and (B) a comparison of the microbial diversity at the phylum level between the microbial diversity in the groundwater (CBN.20), in the water of strictly anaerobic reactors stimulated with acetate (CBN.1), in the micro-oxic biostimulated reactors stimulated with acetate (CBN.7), in the column outlets stimulated with acetate (ASH49), and in the column inlets stimulated with acetate (ASH50).

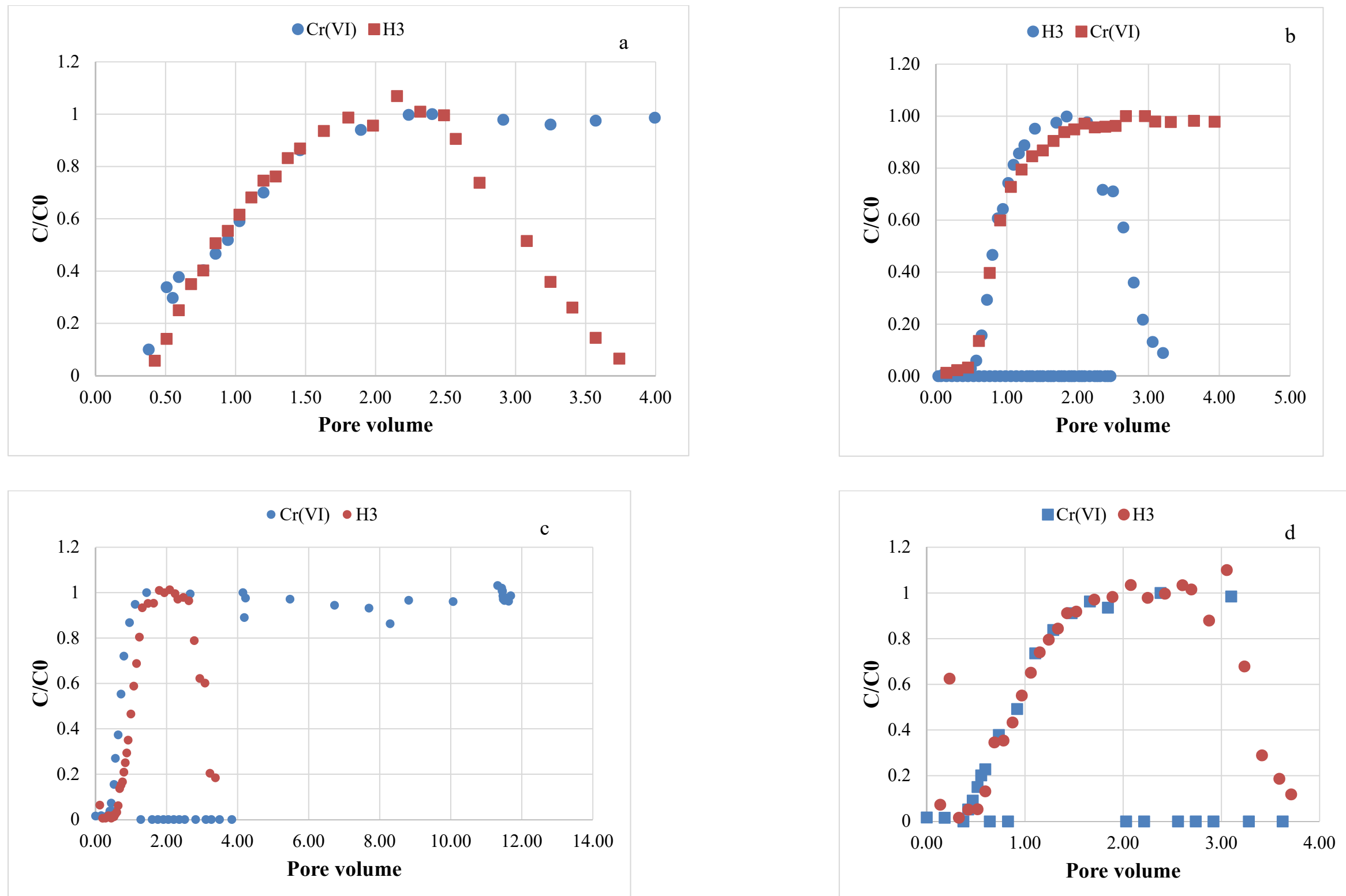


Figure 3.2-1 Breakthrough curves showing the transport of chromate along with the tritium conservative tracer for columns filled with sediments from the chromium plumes area. (a) column filled with sediments from outcrop sediments (Ren 121213-03), (b) column filled with sediments from outcrop sediments (R-42 Fines depth 930-935), (c) column filled with sediments from outcrop sediments (WC-006 3-27-14), (d) column filled with sediments from Puye sediments in SCI-2. All columns were run under saturated conditions at a flow rate of 2.0 mL/h.

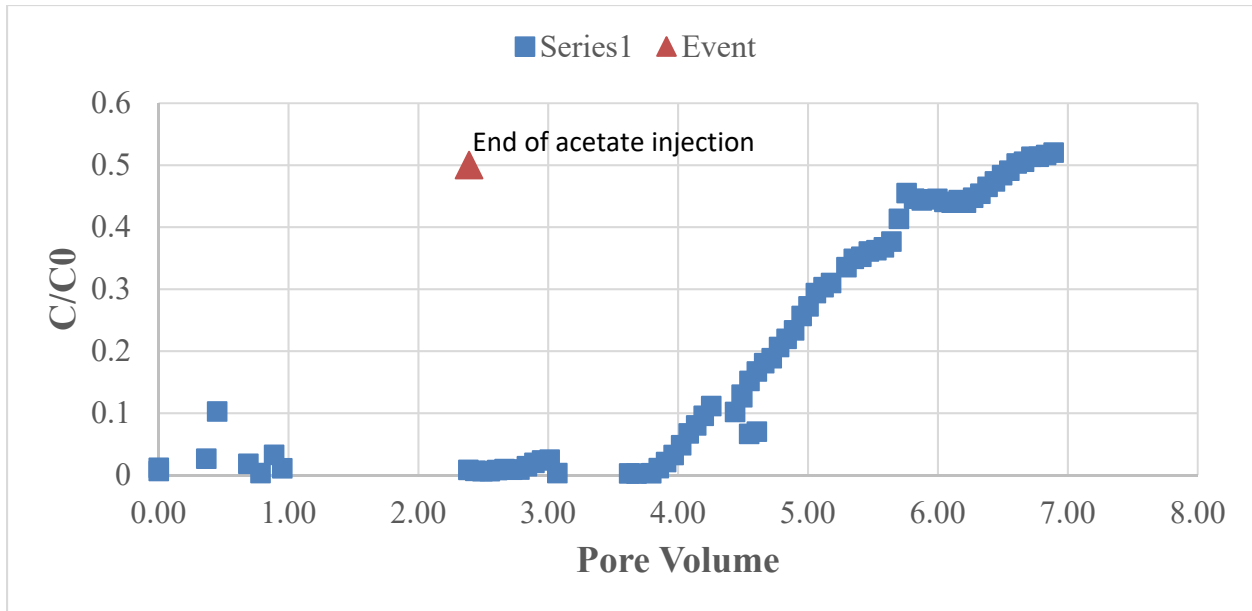


Figure 3.2-2 Chromium attenuation in column 3 biostimulated by the injection of 2.4 pore volumes of a solution containing 0.82 g/L (10 mM) ace

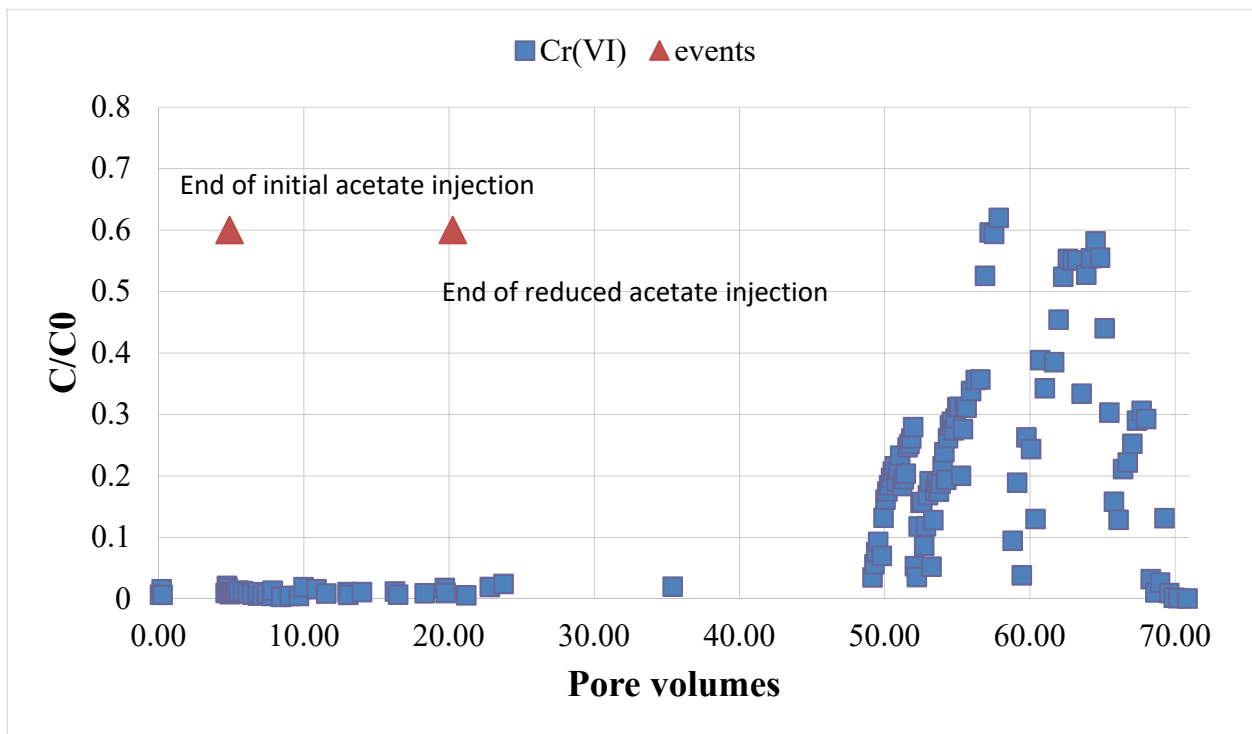


Figure 3.2-3 Chromium attenuation in column 1 biostimulated by the injection of 4.8 pore volumes of a solution containing 0.82 g/L (10 mM) acetate followed by 15.4 pore volumes of a solution containing 0.08 g/L (0.1mM) ace

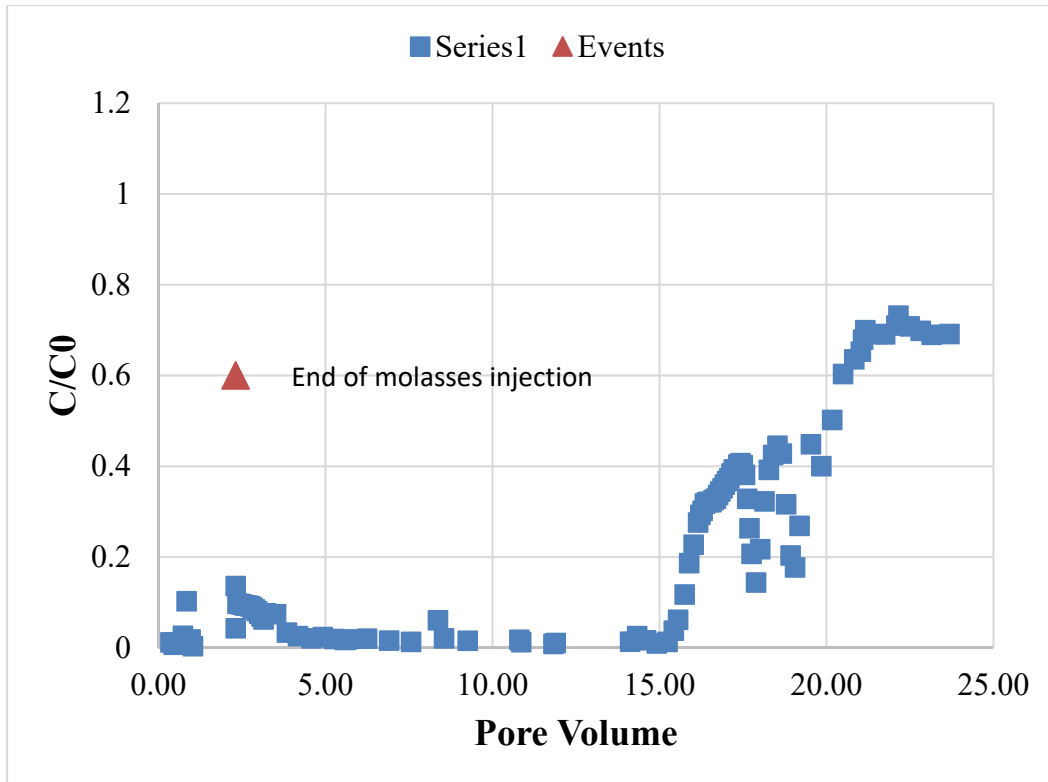


Figure 3.2-4 Chromium breakthrough in column 2 biostimulated by the injection of 2.3 pore volumes of a solution containing 3.4 g/L molasses

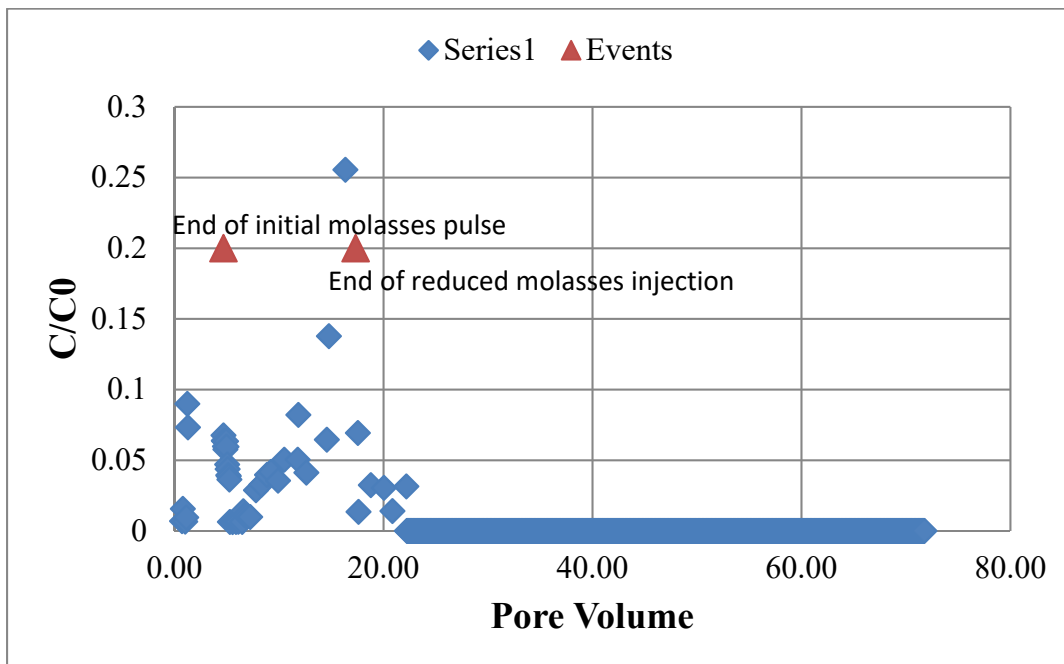


Figure 3.2-5 Chromium breakthrough in column 2 biostimulated by the injection of 4.8 pore volumes of a solution containing 3.4 g/L (10 mM) molasses followed by 12.6 pore volumes of a solution containing 0.34 g/L molasses

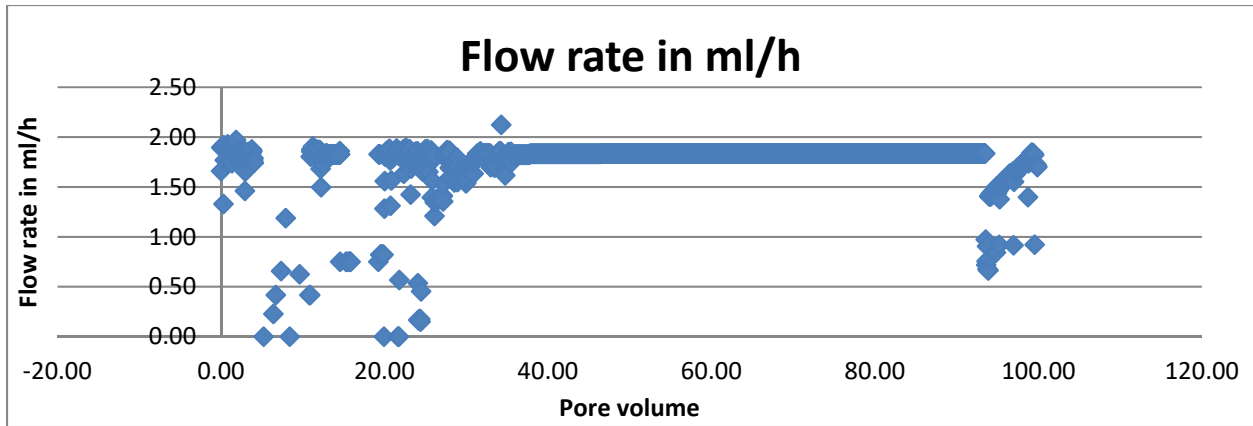


Figure 3.2-6 Flow rate for column 4 biostimulated with an injection of R-42 water amended with molasses

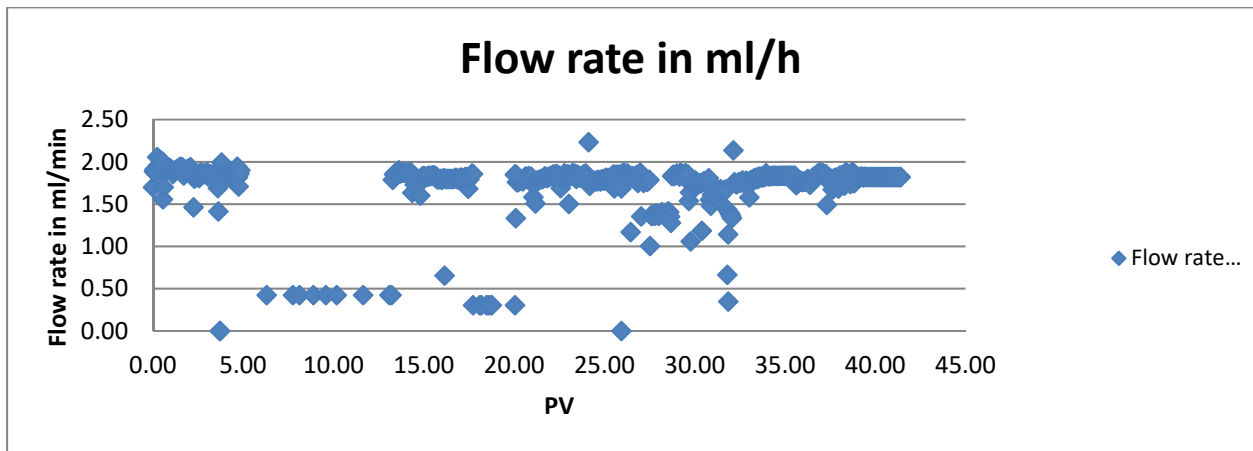


Figure 3.2-7 Flow rate for column 2 biostimulated with two successive injection of R-42 water amended with molasses

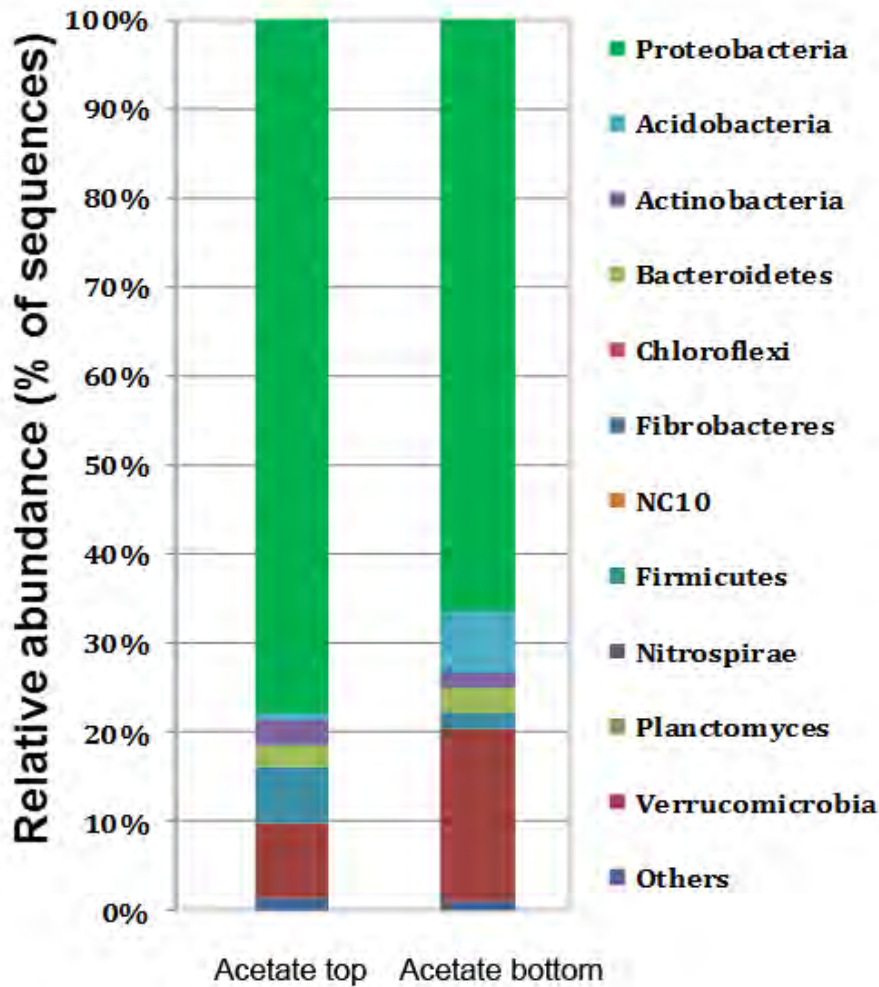


Figure 3.2-8 Graphic representation of microbial diversity at the phylum level in the column biostimulated with acetate. The data show a representation of the microbial diversity in sediments collected at the inlet (bottom) and outlet (top) of the column.

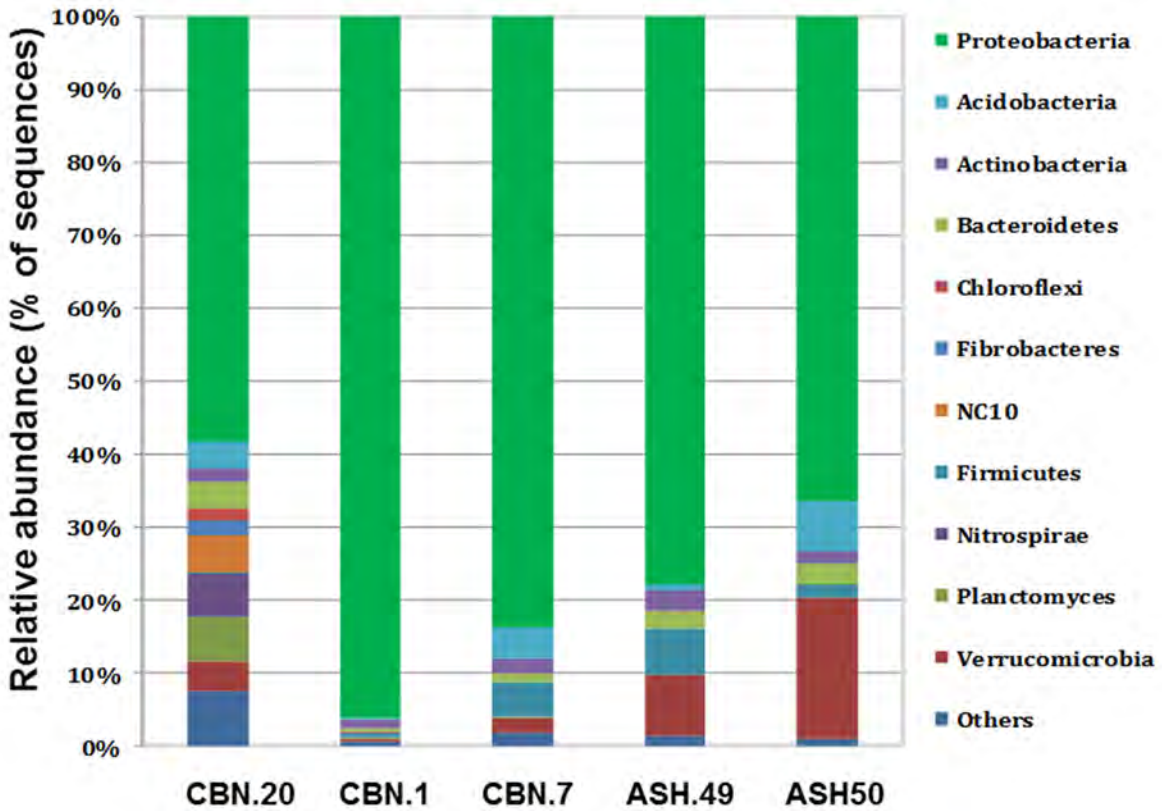


Figure 3.2-9 Graphic representation of microbial diversity at the phylum level in the column biostimulated with molasses. The data show a representation of the microbial diversity in sediments collected at the inlet (bottom) and outlet (top) of the column.

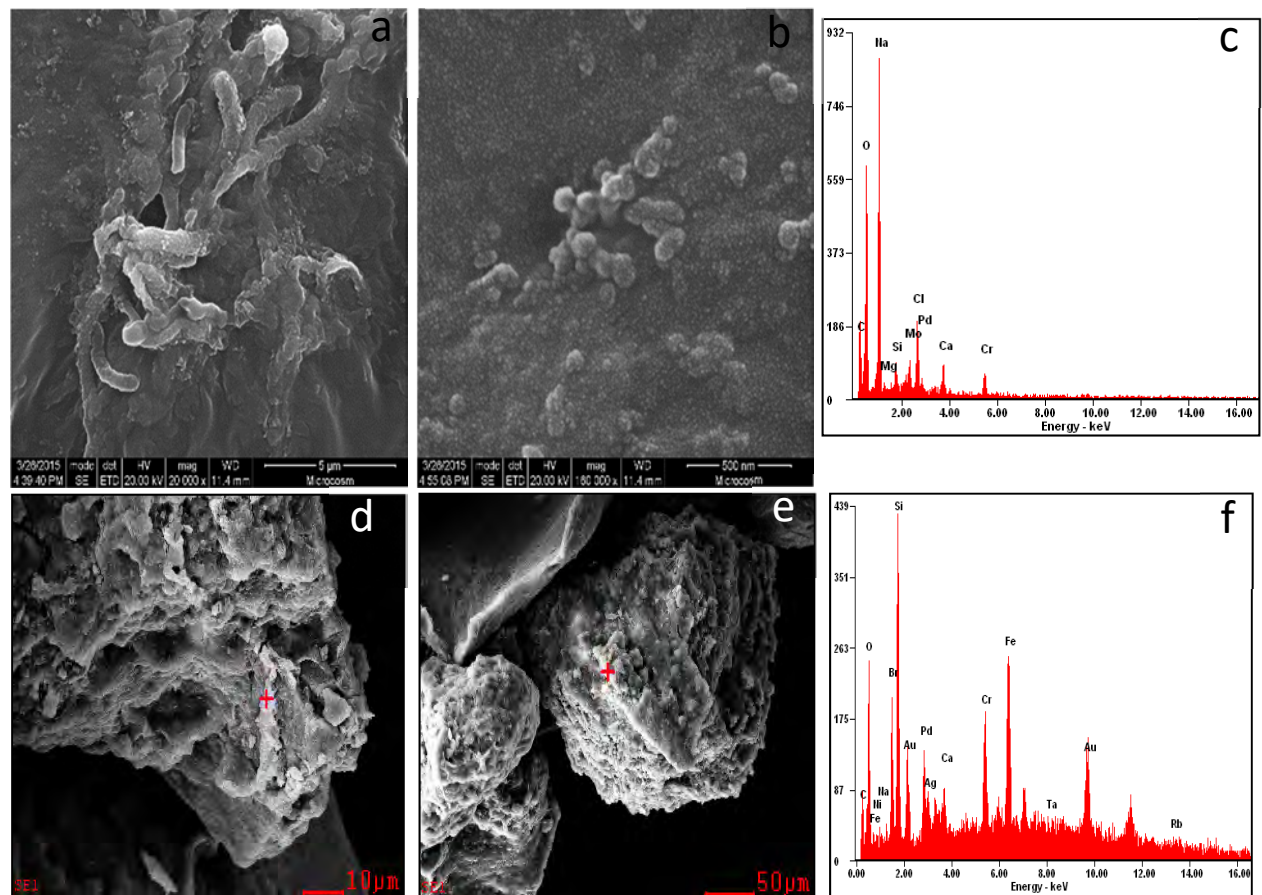


Figure 3.2-10 SEM images of microorganisms and biofilm coatings on sediment grains and EDS spectra. (a) Microbial cells coated with massive Cr(III) precipitates; (b) spherical aggregates of biogenic Cr(III) precipitates; (c) EDS spectrum of the surface of biofilm containing chromium precipitates; (d, e) sediment grains with biofilm coatings; (f) EDS spectrum from the surface of sediment grains coated with biofilm.

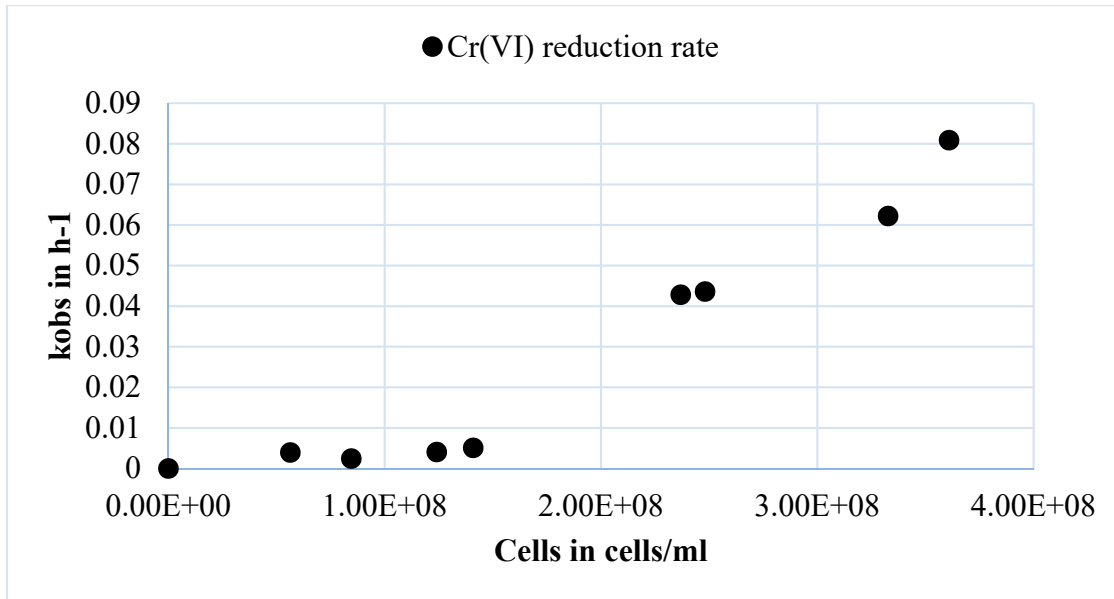


Figure 4.0-1 Observed rate of Cr(VI) reduction by cell suspensions of microbes grown anaerobically by biostimulation of R-42 water with acetate. The observed rates were determined by fitting the Cr(VI) concentration decay by a mono exponential equation. Cell numbers were determined by direct cell counts.

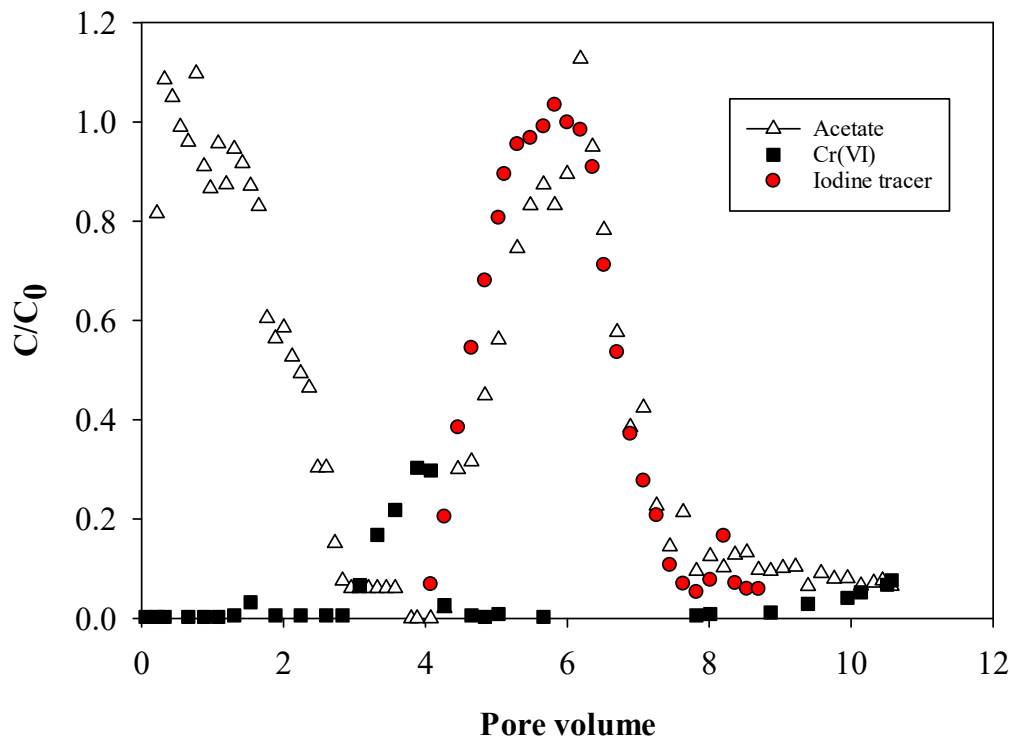


Figure 4.0-2 Breakthrough of Cr(VI), acetate, and iodine tracer from a column in response to two successive injections of an acetate pulse

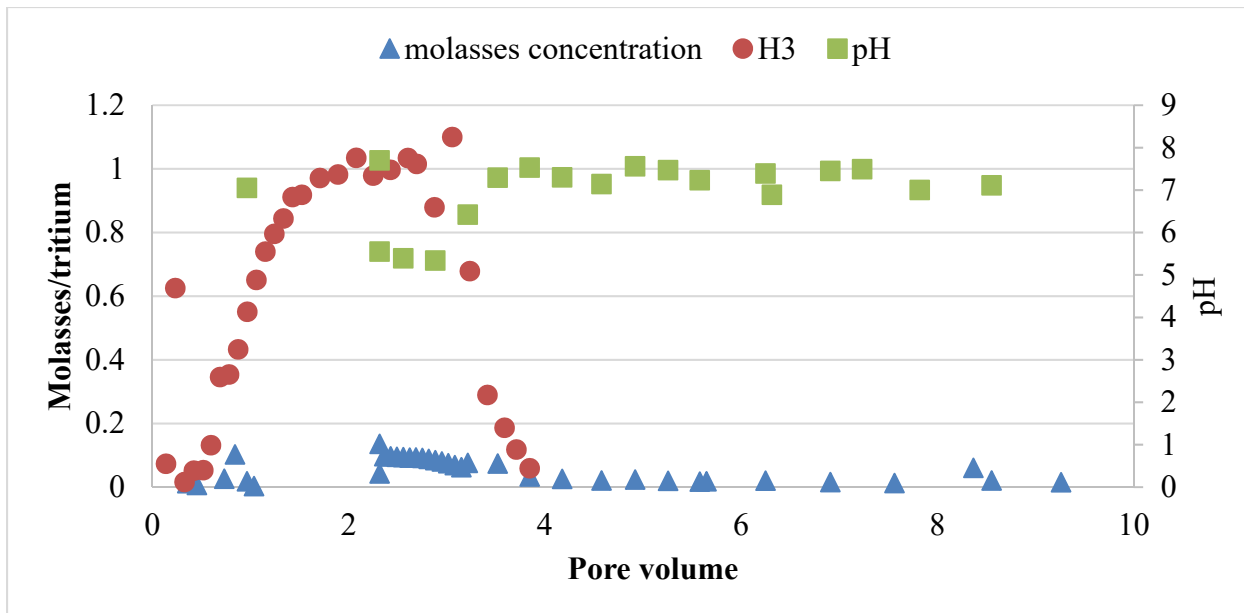


Figure 4.0-3 Breakthrough curves showing pH, molasses, and tritium transport through column 2 during the injection of molasses for 3.2 pore volumes

Table 2.4-1
Parameters of the Column Used in the Natural Attenuation and Biostimulation Studies

Column Parameters	Column 1	Column 2	Column 3	Column 4
Sediments used	Ren 121213-03	R-42 Fines 930-935	WC-006 3-27-14 <2mm	SCI-2 <2mm
Pore volume	86.85	100.01	95.81	82.39
Biostimulant	Acetate	Molasses	Acetate	Molasses
Flow rate	1.8 ml/h	1.8 ml/h	2.0 ml/h	2.0 ml/h

Table 4.0-1
Diversity Indices of Column Samples

Sample	Number of Sequences	Richness ^a	Chao 1*	Phylogenetic Diversity*
Acetate influent (column bottom)	30,766	205	294	18.2
Acetate effluent (column top)	28,706	183	245	16.3
Molasses influent (column bottom)	16,967	161 (169)	204	14.6
Molasses effluent (column top)	35,151	254	341	20.1

* Analysis performed after sequence number was normalized to n=14,370

LA-UR-18-21450
March 2018
EP2018-0034

Chemical Remediation Bench-Scale Studies

Attachment 8

Prepared by the Associate Directorate for Environmental Management

Los Alamos National Laboratory, operated by Los Alamos National Security, LLC, for the U.S. Department of Energy (DOE) under Contract No. DE-AC52-06NA253 and under DOE Office of Environmental Management Contract No. DE-EM0003528, has prepared this document pursuant to the Compliance Order on Consent, signed June 24, 2016. The Compliance Order on Consent contains requirements for the investigation and cleanup, including corrective action, of contamination at Los Alamos National Laboratory. The U.S. government has rights to use, reproduce, and distribute this document. The public may copy and use this document without charge, provided that this notice and any statement of authorship are reproduced on all copies.

CONTENTS

1.0	INTRODUCTION	1
2.0	CONCEPTUAL MODEL	1
3.0	METHODS AND MATERIALS	2
3.1	Blank Batch Experiments	2
3.2	Comparison of Buffer Solutions.....	3
3.3	Batch Experiments with Sediments.....	3
3.4	Column Experiments	4
3.5	Analytical Techniques.....	4
3.5.1	UV-Vis analysis: $S_2O_4^{2-}$, SO_3^{2-}	5
3.5.2	Iodometric Titration.....	5
3.5.3	Ion Chromatography (SO_4^{2-}) and ICP-MS	5
4.0	RESULTS AND DISCUSSION	6
4.1	Blank Experiments.....	6
4.1.1	Dithionite and Degradation Products through Time	6
4.1.2	Proposed Reaction of Dithionite Degradation and Kinetic Rate Law.....	7
4.1.3	Buffer Solution Selection.....	9
4.2	Sediment Characterization	9
4.3	Batch and Column Experiments with Sediment	10
4.3.1	Batch Experiments—Dithionite Degradation and Chromium Uptake	10
4.3.2	Column Experiments	11
5.0	CONCLUSIONS	14
6.0	REFERENCES	15

Figures

Figure 4.1-1	Dithionite decomposition through time in HCO_3^- -buffered (A), $EDTA/OH^-$ -buffered (B), and unbuffered (C) solutions.....	17
Figure 4.1-2	Concentrations of SO_3^{2-} (A, B), H_2S (C, D), and SO_4^{2-} (E, F) through time in HCO_3^- -buffered (A, C, E) and $EDTA/OH^-$ -buffered (B, D, F) solutions	18
Figure 4.1-3	pH through time in HCO_3^- -buffered (A), $EDTA/OH^-$ -buffered (B), and unbuffered (C) solutions	19
Figure 4.1-4	Percent recovery of S relative to the starting amount in HCO_3^- -buffered (A) and $EDTA/OH^-$ -buffered (B) solutions	19
Figure 4.1-5	Simulation of experiments conducted in the HCO_3^- -buffered solution. Panel (A) shows the dithionite concentration, and Panel (B) shows pH.....	20
Figure 4.1-6	Simulation of experiments conducted in the $EDTA/OH^-$ -buffered solution. Panel (A) shows the dithionite concentration, and Panel (B) shows pH.....	20
Figure 4.1-7	Decomposition of $S_2O_4^{2-}$ in various buffer solutions left open to the atmosphere and accompanying pH measurements	21
Figure 4.1-8	Anaerobic decomposition of dithionite in background solutions of HCO_3^- , SO_3^{2-} , and $HCO_3^- + SO_3^{2-}$	22

Figure 4.3-1	Dithionite decomposition in batch experiments with four different sediments (identified by depth [ft] from CrCH-2) with 10 mL of solution for every 5 g sediment.....	22
Figure 4.3-2	Iron generation in batch experiments with four different sediments (identified by depth [ft] from CrCH-2) with 10 mL of solution for every 5 g sediment.....	23
Figure 4.3-3	Release of Cr (A) and As (B) from batch sediments.....	24
Figure 4.3-4	pH of column eluent	25
Figure 4.3-5	Breakthrough curves of cations and anions in the Miocene pumiceous column experiment and corresponding predictions of the 1-D transport model.....	26
Figure 4.3-6	Post-experiment Fe and Cr profiles in Miocene pumiceous column and prediction of penetration distance by dithionite (dummy surface species, arbitrary units).....	27
Figure 4.3-7	Cr(VI) breakthroughs in the two dithionite column experiments.	27

Tables

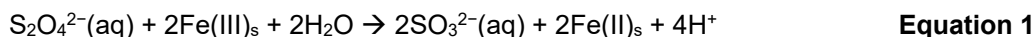
Table 3.3-1	Size Fraction Abundance as Percent of Whole Rock and Estimates of Hydraulic Conductivity for CrCH-2 Sediment Samples.....	29
Table 4.1-1	Secondary Species with Corresponding Mass Action Laws and Equilibrium Constants (K) Used in the Numerical Model.....	29
Table 4.1-2	Additional Calibrated Parameters Used in the Numerical Model.....	29
Table 4.2-1	XRF Data for Bulk Sediment Samples from CH-2 Used In Batch Experiments (A) and Sediments from CH-2 and CH-3 Used in Column Experiments (B)	30
Table 4.2-2	XRD Data for Sediment Samples Used in the Column Experiments	31
Table 4.2-3	BET Surface-Area Measurements for Sediments Used in Batch and Column Experiments	31
Table 4.3-1	Chromium Concentrations in Solutions after Injection of 1% Chromium Solution to Dithionite-Treated Sediments	31

1.0 INTRODUCTION

This report presents the results of studies conducted to evaluate potential chemical amendments that may be used for remediation of chromium contamination in the groundwater beneath Mortandad Canyon, within the boundary of Los Alamos National Laboratory. Chemical amendments are considered a potentially favorable approach for remediation because of the abundance of naturally occurring iron in the aquifer at Los Alamos. Ferrous iron is generally considered an effective reductant of aqueous hexavalent chromium [Cr(VI)] because it is naturally abundant, and the products of the redox reaction, ferric oxide [Fe(III)] and trivalent chromium [Cr(III)], coprecipitate (Amonette et al. 1994). This study provided data that supported an ongoing field pilot-scale study to evaluate the efficacy of a chemical amendment for in situ treatment of chromium.

2.0 CONCEPTUAL MODEL

In oxidized aquifers, Fe(III) (hydr)oxides are the predominant iron species in the sediments. Therefore, treatment of Cr(VI) from reduction by ferrous oxide [Fe(II)] requires the creation of an in situ redox environment which first reduces Fe(III) associated with aquifer sediments to Fe(II). Amendment deployments at other sites have successfully employed sodium dithionite ($\text{Na}_2\text{S}_2\text{O}_4^{2-}$), which is a strong reductant (Amonette et al. 1994). Sodium dithionite treatments have successfully treated plumes of Cr(VI) by reducing structural Fe(III) to Fe(II), which then serves as an electron donor to Cr(VI) (Amonette et al. 1994). Sodium dithionite reacts with the solid-phase Fe(III) in sediments according to



in which SO_3^{2-} represents reduced S species (e.g., H_2S , SO_3^{2-} , $\text{S}_4\text{O}_6^{2-}$) (Amonette et al. 1994). The reduced sulfur species should eventually oxidize to sulfate in an oxic groundwater system, and thus the risk of introducing harmful reaction products (e.g., H_2S) to the aquifer is minimal.

Unfortunately, the data currently available in the literature on the degradation rate of dithionite and its decomposition products are inconsistent. One of the factors influencing determined decomposition rates of dithionite and, thus partially explaining scattering of the data, is the pH at which experiments were performed. Dithionite decomposition is slower in anaerobic, alkaline solutions and reportedly follows pseudo-first-order decay (Amonette et al. 2004). However, even in an alkaline solution, the data on dithionite decomposition is inconsistent. One explanation for such discrepancies is the extent of containment of the experimental solutions. If the suggestion of the formation of H_2S as the decomposition product of dithionite is correct (Wayman and Lem 1970), poor containment of the system should inevitably lead to losses of this component from the solution and acceleration of the decomposition of dithionite. These losses can potentially occur as degassing of the solution due to formation of H_2S gas (even in inert gas-filled compartments, such as gloveboxes), or if solutions are not protected from the atmosphere, due to oxidation of H_2S by atmospheric oxygen. Note that the majority of experimental studies prevented oxygen intrusion but did not take any special precaution to address the outgassing of H_2S , and therefore the studies may have underestimated the dithionite degradation rate. Moreover, the vast majority of the studies available in the literature on the decomposition of dithionite have been performed for durations not exceeding 2 wk, primarily due to quick decomposition of dithionite. However, if this quick decomposition is caused by the effects discussed above (e.g., poor containment of the solutions), these data can be misleading for modeling anaerobic aquifers in which confined conditions with respect to gas exchange often exist and in which the residence time of dithionite can potentially be significantly longer.

The groundwater in the regional aquifer is oxic (6–8 ppm dissolved O₂), and as such, dissolved chromium has remained in the soluble Cr(VI) form. Furthermore, another study included in this compendium indicated that the sediments have little capacity to naturally attenuate the chromium (Attachment 6, “Characterization of Natural Attenuation”). As a result, sodium dithionite is being considered as a potential remedial alternative because it is a strong reducing agent that could provide in situ treatment of the chromium plume. This study also sought to answer whether the reaction would liberate any undesirable byproducts (e.g., arsenic, manganese).

3.0 METHODS AND MATERIALS

The initial experiments investigated the stability of dithionite in thoroughly contained systems without the presence of sediment to determine whether proper containment of the systems decreased the degradation rate of dithionite, and if so, would expand the dithionite lifetime up to months. Batch experiments in blank solutions were also conducted to determine the most appropriate buffer for the field injections. These experiments were necessary to simulate the behavior of dithionite during a field injection, which is best represented by a closed system, to estimate whether dithionite would degrade before spreading into the aquifer.

Upon completion of the blank experiments, batch and column experiments were performed with dithionite in the presence of sediments to determine the reduction capacity of aquifer sediments after treatment with S₂O₄²⁻. Batch experiments involved injecting dithionite into anoxic vials containing sediment to simulate a closed system such as a confined aquifer, followed by addition of Cr(VI). Additionally, two sediment columns were constructed and injected with S₂O₄²⁻, after which the contaminated groundwater was injected until the reduction capacity of the sediments was exhausted.

A semi-empirical model of dithionite consumption and Fe(II) production was then developed from the laboratory batch experiments. The mathematical expressions for dithionite consumption and iron production were then incorporated into a one-dimensional (1-D) finite-difference model that accounts for cation exchange (Williams et al. 2013) to make forward predictions of observations in the dithionite column transport experiments, as well as observations to date in the field dithionite experiment at regional aquifer monitoring well R-42. The model is presented in section 4.0 along with the experimental data.

3.1 Blank Batch Experiments

Experiments involved determination of the concentrations of dithionite and its decomposition products in solutions contained in sealed 10-mL glass ampules. Considering that the typical pH observed in the solutions of treated aquifers ranges from 7 to 10, experiments were performed in three types of solutions: (1) 0.1 M sodium bicarbonate (Certified ACS [American Chemical Society], Fisher scientific; pH = 7.8–8.3), hereafter referred to as the HCO₃⁻ buffered solutions, (2) 1 wt% ethylenediaminetetraacetic acid (EDTA), disodium salt dehydrate, 0.6 wt% potassium carbonate, 0.5 wt% potassium hydroxide, and 0.4 wt% potassium borate (pH = 9.8–10; Fisher Scientific pH 10 buffer solution), hereafter referred to as the EDTA/OH⁻ buffered solutions, and (3) in pH-unbuffered deionized water. Dithionite solutions were prepared by dissolving Na₂S₂O₄ (Laboratory Grade, Fisher Scientific) in the above solutions. Experiments were performed with solutions having three initial concentrations of dithionite, 0.1 M, 0.05 M, and 0.025 M, which were chosen to encompass the range of concentrations used in previous field injections (Istok et al. 1999). Before the addition of dithionite salt, all solutions were degassed under vacuum and thereafter intensively purged with argon gas to remove any traces of oxygen. Solutions were transferred via syringe into argon-purged glass ampules. The ampules were immediately flame-sealed to prevent oxygen intrusion into the solutions and potential losses of H₂S out of them. A cloudy appearance was observed in the unbuffered 0.05 M and 0.025 M solutions, which disappeared in less than 1 d. All glass ampules used in

the study were filled the same day (total of 108 ampules) and left undisturbed until sampled. Sampling of the solutions was performed after 1, 3, 7, 10, 14, 29, 45, 55, 66, 78, 86, and 105 d from the beginning of the experiment. Each sampling involved opening of 9 ampules (0.1 M, 0.05 M, and 0.025 M each in HCO_3^- buffered solutions, EDTA/OH^- buffered solutions, and unbuffered solutions) and determination of S species and pH. Sampling was performed immediately after opening the ampule, and analyses for all analytes were conducted as quickly as possible.

3.2 Comparison of Buffer Solutions

Dithionite decomposes rapidly in unbuffered aqueous solution, and previous studies employ carbonate and/or hydroxide buffers to increase the pH to 10–11 and stabilize dithionite (Amonette et al. 1994). However, in aquifers that are nearly saturated with respect to calcite, which is the case here, increasing the pH can lead to calcite precipitation and subsequent clogging of pore spaces within the aquifer. Therefore, a buffer that will increase the stability of dithionite in solution without raising the pH or alkalinity is required in such aquifers. Two experiments were conducted to test the efficacy of hypothesized products of dithionite decomposition as appropriate buffers.

A series of dithionite solutions containing different combinations of Na_2SO_3 and Na_2S buffers was mixed in 500-mL polyethylene bottles. Each combination (no buffer, NaSO_3 , $\text{Na}_2\text{SO}_3 + \text{Na}_2\text{S}$, Na_2S , and $\text{Na}_2\text{SO}_3 + \text{Ar}$) was made at concentrations of 0.05 M, 0.1 M, and 0.3 M dithionite. The variation in Na_2SO_3 concentrations was identical to that of the dithionite, whereas the concentration of Na_2S in all experiments was 0.001 M. Dithionite concentrations were measured by ultraviolet-visible (UV-Vis) spectrometry as outlined in section 3.5.1 at 0, 1.5, 2.5, and 5.5 h. The pH of each solution was also measured at each sampling interval.

Another set of experiments was conducted in glass vials with rubber stoppers to compare the efficacy of SO_3^{2-} and HCO_3^- buffers without the influence of oxygen. In this set, 0.05 M solutions of dithionite were made in argon-purged solutions of (1) 0.1 M HCO_3^- with and without 0.1 M SO_3^{2-} and (2) only 0.1 M SO_3^{2-} . Samples were taken via syringe for UV-Vis and pH analysis over a total time period of 600 h.

3.3 Batch Experiments with Sediments

Four sediments collected as cores from varying depths beneath the water table of core hole 2 (CrCH-2) in Mortandad Canyon were selected for the batch experiments. The sediments were sieved and the size fractions with grain sizes <0.355 mm (medium sand and finer) were used for the experiments (Table 3.3-1). The magnetic fraction of the samples was removed by a neodymium magnet to ensure the exclusion of any iron filings added to the sediment during drilling. From each sediment sample, 5-g portions were placed into 20-mL glass ampules. Next, 10-mL of sodium dithionite solutions of varying concentrations (0.025 M, 0.05 M, or 0.1 M) were prepared by adding sodium dithionite salt (Laboratory Grade, Fisher Scientific) to a 0.1 M sodium bicarbonate (Certified ACS, Fisher scientific; pH = 7.8–8.3) solution in a polyethylene bottle. Before addition of the dithionite salt, the HCO_3^- solution was degassed under vacuum and purged with argon gas to remove oxygen. The solutions were subsequently transferred to syringes for injection into the ampules. The glass ampules were immediately flame-sealed to prevent dithionite reaction with oxygen. All ampules (108 total) were filled the same day and remained undisturbed until analysis. The ampules were then opened for analysis 1, 2, 3, 7, 11, 16, 24, 43, and 140 d after sealing.

3.4 Column Experiments

Approximately 230 g of sediment from each of two core holes in Mortandad Canyon was selected for the column experiments. CrCH-2 sediments from depths between 917.66 and 918.32 ft represent the dacitic Puye Formation and sediments from core hole 3 (CrCH-3) between 934.4 and 935.2 ft represent the rhyolitic Miocene pumiceous unit. Only sediments that were sieved to grain sizes less than 0.355 mm were used in the columns, although the very finest material that did not settle after 24 h of gravity settling in water was also excluded from the columns to avoid plugging of the columns by fines. The magnetic fraction of the samples was removed by a neodymium magnet to ensure the exclusion of any iron filings added to the sediment during drilling. The mineralogy and elemental composition of the sediments for both the batch and column experiments were determined by x-ray diffraction (XRD) and x-ray fluorescence (XRF).

The sediments were tightly packed into Kontes Chromaflex glass columns (2.5 x 30 cm) with plastic luer lock fittings. Air space at the column outlet was packed with steel wool, which also acts to filter sediment from escaping the column. Polyetheretherketone (PEEK) tubing was used at both the inlet and outlet of the columns. The inlet tubing was attached to 140 cm³ Monoject syringes controlled by KD Scientific syringe pumps. The flow rate was set to 1.2 mL/h, and samples were collected every 3 h using a Teledyne ISCO FOXY Jr. fraction collector. The columns were flushed with deaerated R-42 water for ~ 2 pore volumes (1 pore volume = 60 mL) before addition of dithionite solution.

The columns were then injected with a solution of sodium dithionite to reduce the structural Fe(III) in the sediment. The injection solution was made with Na₂S₂O₄ salt (Fisher Scientific) to a concentration of 0.05 M in deionized water that had been degassed with argon for ~ 1 h. Before the deionized water was degassed, lithium bromide salt was added to a concentration of 400 ppm and thoroughly mixed with the deionized water on a shaker table. In conjunction with the addition to Na₂S₂O₄ salt, Na₂SO₃ salt was added as a buffer to a concentration of 0.05 M.

A total of ~ 110 mL of dithionite solution was injected through the columns over 4 d (~2 pore volumes). Subsequently, non-deaerated R-42 water was injected in the columns until breakthrough of chromium was detected. After ~23 pore volumes, the flow rate was increased to 2.4 mL/h for ~3 pore volumes of R-42 injection water. The flow rate was then decreased to 0.6 mL/h for ~1 pore volume, followed by an increase to 4.8 mL/h for ~4 pore volumes. Flow was then restored to 1.2 mL/h for the remainder of the experiment. Flow-rate changes were employed to test the kinetics of Cr(VI) and NO₃⁻ reduction in the columns after observations that Cr(VI) was strongly immobilized in the column, whereas NO₃⁻ eluted without reduction. The experiment was complete when Cr(VI) breakthrough was detected.

After completion of the column experiments, the sediment was frozen and cut into 1-cm sections. The sediment was leached with 2 M HNO₃ for 1 d and then centrifuged and the supernatant filtered (0.45 μm) for analysis by inductively coupled plasma–mass spectrometry (ICP-MS) and inductively coupled plasma–optical emission spectroscopy (ICP-OES).

3.5 Analytical Techniques

For each sampling event involving dithionite, solutions were analyzed for concentrations of dithionite, sulfide, sulfite, thiosulfate, and sulfate. Additionally, pH was determined and, to control the mass balance of sulfur, total concentration of sulfur species able to interact with iodine (dithionite, sulfide, sulfite, thiosulfate, and polythionates, except S₂O₆²⁻).

3.5.1 UV-Vis analysis: $\text{S}_2\text{O}_4^{2-}$, SO_3^{2-}

When a vial was broken for sampling, an aliquot was immediately taken for UV-Vis analysis (dithionite, sulfite, and thiosulfate) on a Shimadzu UV-2600 spectrophotometer. UV-Vis spectra of experimental solutions were recorded in a flow-through cuvette under strictly oxygen-free conditions for the wavelengths ranging from 190 to 400 nm with an increment of 1 nm. A glass vial, containing 50 mL distilled water and 1 mL of 0.1 M HCO_3^- , which was continuously purged with argon, was connected with Tygon tubing to the cuvette. Continuous circulation of the solution between the vial and the cuvette was forced by peristaltic pump.

Dithionite concentrations were measured at a wavelength of 350 nm (Amonette et al. 2004). Sulfite was determined at a wavelength of 200 nm. Although the $\text{S}_2\text{O}_3^{2-}$ and SO_3^{2-} UV-Vis spectra overlap, both deconvolution of the UV-Vis spectra and titration with formaldehyde described below indicated negligible thiosulfate formation. Owing to the near-immediate partial degradation of dithionite, calibrating the UV-Vis spectral signal of dithionite-bearing solutions is essential, yet nontrivial. Known amounts of dithionite salt were added to glass vials pre-purged with argon gas and sealed with rubber stoppers. The buffer solutions were then added by syringe through the rubber stoppers. Upon complete dissolution of the salt, an aliquot was extracted by syringe and UV-Vis spectra were recorded. Another aliquot was taken for iodometric titration to determine dissolved sulfur species as described below. The latter indicated that ~50% of the dithionite underwent immediate decomposition.

3.5.2 Iodometric Titration

Another aliquot of sample was taken for iodometric titration, which determines total reduced sulfur species (Danehy and Zubritsky 1974; Szekeres 1974). This technique was used to determine a mass balance as it measures the concentration of all sulfur species except oxidized sulfur (i.e., SO_4^{2-}), elemental sulfur, and $\text{S}_2\text{O}_6^{2-}$. In some selected samples, $\text{S}_2\text{O}_3^{2-}$ was also determined through iodometric titration with formaldehyde (Danehy and Zubritsky, 1974; Szekeres, 1974), but these analyses determined that thiosulfate formation was negligible.

The concentrations of dissolved sulfide sulfur (H_2S , HS^-) in the solutions were determined by precipitation with cadmium acetate and iodometric back titration. The technique involves precipitation of sulfide sulfur in the form of insoluble cadmium sulfide (by adding an aliquot of cadmium acetate), separation of the precipitate from the solution by centrifuging or filtration, and the aforementioned iodometric back titration of the solid precipitate in an aliquot having an excess of hydrogen chloride and iodine by sodium thiosulfate (Szekeres 1974).

3.5.3 Ion Chromatography (SO_4^{2-}) and ICP-MS

Oxidized sulfur (i.e., SO_4^{2-} analysis) was determined on a Dionex ICS-2100 Ion Chromatography System. The aliquots that were not analyzed immediately after sampling, were immediately frozen to stop decomposition of dithionite and preclude continuous accumulation of decomposition products. Concentrations of the main metal suite in post-experimental solutions were determined using the ICP-MS and ICP-OES techniques.

Any sulfur in excess of the independently determined $\text{S}_2\text{O}_4^{2-}$, SO_3^{2-} , HS^- , SO_4^{2-} and $\text{S}_2\text{O}_3^{2-}$ can be attributed to zero valent sulfur, some of the polythionate species, and/or elemental sulfur involved in polysulfane chains.

4.0 RESULTS AND DISCUSSION

4.1 Blank Experiments

4.1.1 Dithionite and Degradation Products through Time

Concentrations of dithionite, its hydrolysis products, and pH of the solutions determined during the experiments are reported in Figures 4.1-1 through 4.1-3. Figure 4.1-1 shows the decomposition of dithionite through time. The first measurement was taken 1 d after solutions were prepared. At this stage, determined concentrations of dithionite represented only a fraction of dithionite initially placed in the solution. This fraction systematically decreases with decreasing pH. For example, for HCO_3^- -buffered solutions (pH = 7.5 to 7.1), recovery of dithionite after 1 d was 26 to 30% of the initial concentrations (Fig. 4.1-1a). Conversely, in the EDTA/OH^- buffered solutions having pH = 9.1–9.7, this value ranged from 68 to 78% (Fig. 4.1-1b). It is likely that during the first days after solution preparation dithionite undergoes complex re-equilibration with its hydrolysis products: the first three samples taken demonstrated a relative increase of dithionite concentrations with respect to concentrations determined during day 1. For example, after 2 d, the concentrations of dithionite in the HCO_3^- -buffered solutions increased from 26–30% of the initial concentrations to 33–42%, and in the EDTA/OH^- -buffered solutions, some solutions demonstrated nearly 92% of initial concentrations of dithionite. Subsequent samples, however, showed prolonged decrease in concentrations. The unbuffered solutions experienced rapid loss of dithionite. Although the 0.1 M solution persisted for 2–3 weeks, the 0.05 M and 0.025 M solutions had no measureable dithionite after the first day (Fig. 4.1-1c). Because of the rapid loss of dithionite in the unbuffered solutions, it would be impractical to consider an unbuffered dithionite deployment, so the remainder of this paper focuses on the behavior of dithionite in the buffered solutions. For the solutions buffered in HCO_3^- , dithionite disappeared after 29 d in the 0.1 M solution, whereas the disappearance was 55 and 78 d in the 0.05 M and 0.025 M solutions, respectively (Figure 4.1-1a). Similarly, the solutions buffered with EDTA/OH^- experienced more rapid loss for the 0.1 M solution than for the 0.05 and 0.025 M solutions. However, dithionite persisted much longer in all of the EDTA/OH^- -buffered solutions compared with the HCO_3^- -buffered solutions, lasting until 105 d in the 0.1 M solution, and remaining present until the end of the experiment (105 d; Figure 4.1-1b) in the 0.05 and 0.025 M solutions.

The hydrolysis products determined in the experiments demonstrate distinctively different behavior. Sulfite (SO_3^{2-}) and sulfide (HS^-) are found in nearly equimolar concentrations in effectively all sampled solutions (Figure 4.1-2, a–d). Both of these species do not show a definitive variation with time. The large temporal variability of the concentrations of SO_3^{2-} may be due, in part, to experimental errors. In order to prevent saturating the UV-Vis detector, a very small amount of sample (0.05 mL) was diluted substantially (1210 times). The accuracy of the syringe is 0.01 mL, and thus the error with the SO_3^{2-} measurements may be as high as 20%. However, it is apparent that in all samples, the SO_3^{2-} concentrations experience an initial increase similar to that of $\text{S}_2\text{O}_4^{2-}$. Sulfite in the HCO_3^- -buffered samples then appears to plateau before dropping off at around 50–60 d (Figure 4.1-2a). Sulfite in the EDTA/OH^- buffered samples, however, decreases at around 30 d but then increases by the end of the experiment (Figure 4.1-2b). Sulfite accounts for between 2 and 12% of the total sulfur in EDTA/OH^- -buffered solutions and between 3 and 20% in HCO_3^- -buffered solutions.

In HCO_3^- buffered solutions, the concentration of SO_4^{2-} decreases with time (Figure 4.1-2e). In the first two samples, SO_4^{2-} accounts for about 33% of total sulfur, but by the completion of the experiment accounts for between 5 and 20%. A similar pattern is seen with the 0.1-M sample in EDTA/OH^- -buffered solution, in which the percentage of SO_4^{2-} accounting for total sulfur drops from 33% to 5%. However, the 0.05 and 0.025 M solutions have relatively steady SO_4^{2-} concentrations through time (Figure 4.1-2f).

In all samples, the pH decreases through time, and the decrease is more pronounced with increasing concentrations for the HCO_3^- -buffered and EDTA/OH^- solutions, whereas the pH of the 0.1 M unbuffered solution is higher than either the 0.05 M or 0.025 M unbuffered solutions (Figure 4.1-3, a–c). More specifically, in the HCO_3^- -buffered solutions, the pH drops from 7.5 to 7.3 in the 0.025 M solution, from 7.3 to 7.0 in the 0.05 M solution, and from 7.0 to 6.8 in the 0.1 M solution (Figure 4.1-3a). Similarly, in the EDTA/OH^- -buffered solution, the pH drops from 9.7 to 9.6 in the 0.025 M solution, from 9.5 to 9.2 in the 0.05 M solution, and from 9.1 to 7.9 in the 0.1 M solution (Figure 4.1-3b).

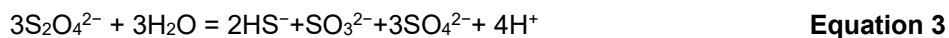
4.1.2 Proposed Reaction of Dithionite Degradation and Kinetic Rate Law

Faster degradation of dithionite at lower pH is consistent with previous studies (Amonette et al. 2004). However, accounting for all previously reported major degradation products (i.e., SO_3^{2-} , $\text{S}_2\text{O}_3^{2-}$) in these experiments demonstrates that a substantial proportion of sulfur cannot be accounted for in near neutral solutions (pH = 7.5 to 7.1). The sum of the sulfur species determined in these experiments was only 68 to 78% of the initial total sulfur concentrations on the first day of the experiments and demonstrated continuous decrease with time (Figure 4.1-4a). At alkaline conditions (pH = 9.0–9.7), measured sulfur species accounted for almost 100% of initial total sulfur concentrations during the first 30 d of the experiment (Figure 4.1-4b). The species that account for missing sulfur are not detectable by the present methods, and therefore can be represented by either zero valent sulfur, some of the polythionate species, and/or elemental sulfur involved in polysulfane chains. The initial unbuffered solutions became milky white, suggesting the formation of colloidal sulfur at low pH.

In addition to elemental sulfur, which appeared to be important only at very low pH (unbuffered solutions), dithionite decomposition may produce polythionates. The decomposition of polythionates produces sulfate, elemental sulfur, and hydrogen ions and is thus consistent with the analytically measured products (Meyer and Ospina 1982). These observations lead to the hypothesis that formation of polythionate $\text{S}_4\text{O}_6^{2-}$ has occurred in these solutions, and that the hydrolysis reaction of dithionite can be expressed as follows:



This reaction progresses to a lesser extent as pH increases, consistent with polythionates having greater stability at low pH and undergoing decomposition at higher pH (Meyer and Ospina, 1982). The reaction depicted in Equation 2 therefore is a proxy for the more rapid process of dithionite degradation observed at near-neutral pH. The stoichiometry of the reaction depicted in Equation 2 accounts for the initial production of protons and polythionates (i.e., unaccounted-for sulfur species) observed in HCO_3^- -buffered experiments at each dithionite concentration. Because the various polythionates and elemental sulfur could not be directly measured, it is possible that the $\text{S}_4\text{O}_6^{2-}$ term represents the summation of other unaccounted-for sulfur species. Nevertheless, at higher pH values and on longer time scales, this term becomes less important and the reaction is better represented as



This reaction is used in the following kinetic discussion as it describes the long-term degradation of dithionite.

A numerical model was formulated to quantify the kinetics of dithionite degradation in the HCO_3^- - and $\text{EDTA}/\text{NaOH}^-$ -buffered experiments. The unbuffered experiments were not modeled because degradation was so rapid that it was considered impractical to consider using dithionite without buffering. No attempt was made to model the very rapid initial degradation of dithionite; rather the first-measured dithionite concentrations and pHs effectively served as initial conditions in the model. To allow for quantitative

comparison of the HCO_3^- - and EDTA/NaOH^- -buffered experiments, a kinetic model was developed based upon the experimentally deduced stoichiometry (Equation 3) for both sets of experiments. The kinetic rate expression assumed first-order dependence on dithionite concentration and a fractional-order dependence on proton activity:

$$\frac{dC_i}{dt} = S_i k \{H^+\}^\alpha \{S_2O_4^{2-}\}, \quad \text{Equation 4}$$

where C_i and S_i are the concentration at each time step and stoichiometry of the i^{th} chemical component in Equation 3, t is time (s), k is the kinetic rate constant, α is a fractional exponent, and $\{S_2O_4^{2-}\}$ and $\{H^+\}$ are the respective dithionite and proton activities at each time step. The inclusion of a fractional-order dependence on proton activity reflects an autocatalytic process in which there is no additional generation or consumption of protons beyond that described in Equation 3. The model also includes Na^+ , along with HCO_3^- as a representative buffer. It was assumed that $\text{S}_2\text{O}_4^{2-}$, H_2O , SO_3^{2-} , HS^- , SO_4^{2-} , H^+ , Na^+ , and HCO_3^- could be modeled as total components in order to include equilibrium reactions with secondary species dictated by the laws of mass action. This approach allows for a more accurate calculation of proton activity. The model includes the secondary species and corresponding mass action laws shown in Table 4.1-1, which are taken from the EQ3/6 database (Wolery 1992). Activity coefficients were calculated in each time step using the Debye-Hückel equation.

Equation 3 was coupled to Equation 4 in PFLOTRAN (Lichtner et al. 2017a, b) using its “reaction-sandbox” interface (Hammond 2015). To fit the experimental data, model calibration was required. The primary parameters were k and α . An additional adjustable parameter needed to match the observed pH trends was the effective buffering capacity of the solutions, which was incorporated into the model as an equivalent concentration of bicarbonate ($[\text{HCO}_3^-]_{\text{eff}}$) for each set of experiments. Calibration was achieved using the open-source code MADS (Vesselinov and Harp 2012). The model parameters were calibrated using inverse analysis (using Levenberg-Marquardt optimization) to reproduce the experimental observations as defined in the MADS problem setup. Experimental measurements of $[\text{S}_2\text{O}_4^{2-}]$ and pH were used as calibration targets.

Equation 5 shows the parameterized kinetic rate law:

$$\frac{dC_i}{dt} = S_i 10^{-4.81} \{H^+\}^{0.24} \{S_2O_4^{2-}\}, \quad \text{Equation 5}$$

where $\frac{dC_i}{dt}$ has units of $\text{mol l}^{-1} \text{s}^{-1}$. Results of model calibration are shown in Figures 4.1-5 and 4.1-6, and additional calibrated model parameters for the two sets of experiments are shown in Table 4.1-2. In general, the kinetic rate model with equilibrium speciation was capable of fitting the $[\text{S}_2\text{O}_4^{2-}]$ and pH data for both the HCO_3^- -buffered and EDTA/OH^- -buffered experiments. The parameter $[\text{HCO}_3^-]_{\text{eff}}$ for the HCO_3^- buffered solutions (0.329 M) was found to be higher than the 0.1-M HCO_3^- used, which is most likely due to equilibrium reactions of sulfur species (e.g., $\text{H}_2\text{S}_4\text{O}_6(\text{aq})$, HS_4O_6^-) not considered in the model. The high calibrated value of $[\text{HCO}_3^-]_{\text{eff}}$ for the EDTA/OH^- -buffered experiments (0.570 M) was likely due to the complex buffers used in stock buffer solution.

Equation 5 was used to estimate half-lives of each experiment by treating $10^{-4.81} \{H^+\}_i^{0.24}$ as a pseudo-first-order rate constant, where $\{H^+\}_i$ is the initial proton activity calculated using the calibrated value of pH_i , and normalizing by the stoichiometric coefficient of $\text{S}_2\text{O}_4^{2-}$ in Equation 3. The estimated half-lives for the HCO_3^- -buffered experiments were 9.06, 10.6, and 12.4 d for the 0.1, 0.05, and 0.025 M dithionite concentrations, respectively, resulting in a mean half-life of 10.7 d. The estimated half-lives for the EDTA/OH^- -buffered experiments were 27.2, 34.2, and 39.5 d for 0.1 M, 0.05 M, and 0.025 M dithionite concentrations respectively, resulting in a mean half-life of 33.6 d. The mean values represent single best estimates that consider all initial starting concentrations for a given pH while also assuming that the half-

life varies with pH but not dithionite concentration (pseudo first-order). The longer half-life reported at the higher pH in the present study relative to the half-lives reported by Amonette et al. (2004) at a similar pH is most likely the result of preventing any gases from either entering or leaving the glass-sealed ampoules in the current study. It is well known that oxygen reacts rapidly with dithionite, and care was taken in both studies to minimize or eliminate oxygen, but the present study also prevented the egress of gases from the reaction vessels. Amonette et al. (2004) does not mention any measures taken to prevent H₂S egress (which can occur through many types of vessel caps or stoppers), and keeping the H₂S in the reaction vessels in the present study is believed to have slowed the degradation of dithionite because it maintained a higher concentration of the degradation product(s) HS⁻/S²⁻ in solution.

Although the rate law (Equation 5) can effectively predict the post-rapid-hydrolysis degradation rate as a function of pH, several lines of evidence suggest that assuming the reaction depicted in Equation 3 accounts for all dithionite degradation and using only the limited assemblage of species and reactions in Table 4.1-1 greatly oversimplifies the system. The fact that the pH trends in the experiments can be matched only if the initial effective pH buffering of the system (the first ~ 3 d) is treated as an adjustable parameter is one such line of evidence. Also, as S₂O₄²⁻ concentrations decrease with time, the concentrations of reaction products SO₄²⁻, SO₃²⁻, and HS⁻ (Equation 3) all either decrease or stay relatively constant instead of increasing as the reaction (Equation 3) would predict. Instead, it is the concentration(s) of the unaccounted-for reduced sulfur species, which are not considered in the model, that consistently increase with time. These observations combined suggest that (1) there are unaccounted-for reaction products that are involved in hydrolysis and acid-base reactions that affect pH in ways not considered by the model, and (2) the sulfur chemistry evolves in a complex manner as a result of interactions between reduced and oxidized sulfur reaction products that are not thermodynamically compatible.

4.1.3 Buffer Solution Selection

The results of the buffer experiments are shown in Figures 4.1-7 and 4.1-8. Figure 4.1-7 illustrates the rapid decomposition of dithionite in the presence of oxygen without a carbonate buffer. The concentration drops more rapidly at higher concentrations, demonstrating the first-order dependence on dithionite concentration of the rate constant (Amonette et al. 1994). The presence of Na₂S adds negligible stability to the dithionite, but all solutions with SO₃²⁻ (SO₃²⁻, SO₃²⁻ + Na₂S, SO₃²⁻ + Ar) are noticeably more stable through time. Not surprisingly, the stability of dithionite corresponds to the ability of the buffer to maintain a neutral pH. In the case with just S₂O₄²⁻ and with S₂O₄²⁻ + Na₂S, the pH drops rapidly below 4, coincident with a drop in the S₂O₄²⁻ concentration. The results of this experiment suggest that SO₃²⁻ is an effective buffer for slowing the decomposition of dithionite and the production of H⁺. The addition of Na₂S or argon to NaSO₃ solutions does not appreciably enhance the buffering capacity of SO₃²⁻.

Figure 4.1-8 demonstrates the relative effectiveness of HCO₃⁻ vs SO₃²⁻, in which it is apparent that there is no discernable difference in the longevity of dithionite between the two buffers. Although the concentration of dithionite is quantifiable to 600 h with the bicarbonate buffer, the concentrations in all solutions past 300 h is negligible. These experiments suggest that sulfite is as effective as bicarbonate in extending the lifetime of dithionite in aqueous solution.

4.2 Sediment Characterization

XRF data for the samples in both the batch and column experiments are shown in Table 4.2-1, XRD data for the column experiments are shown in Table 4.2-2, and Brunauer-Emmett-Teller (BET) surface area measurements are shown in Table 4.2-3. The sediment samples from both CrCH-2 and CrCH-3 contain predominantly aluminosilicate material. Material sampled from CrCH-2 consists largely of plagioclase,

whereas material sampled from CrCH-3 is mostly amorphous material, presumably rhyolite glass. The iron content of the CrCH-3 material is less than 1% (0.90%) and of the CrCH-2 material ranges between 1.20 and 2.36%. The chromium content of the sediments ranges from 7 to 32 ppm, and the highest concentrations in the CrCH-2 material are between 913 and 918 ft below ground surface, which also coincides with the highest iron content. This interval also has the highest surface area (Table 4.2.-3). The surface area of all CrCH-2 samples is greater than that of CrCH-3.

4.3 Batch and Column Experiments with Sediment

4.3.1 Batch Experiments—Dithionite Degradation and Chromium Uptake

The decomposition of dithionite is shown in Figure 4.3-1. The pH remained constant (6.8–7.4) throughout the sampling period, indicating that the HCO_3^- buffering was sufficient. For all three concentrations of dithionite treatments, the dithionite concentration decreased by greater than half after 1 d. In addition to consumption of dithionite by reaction with iron (Equation 1), dithionite decomposes in near-neutral to alkaline solution by hydrolysis (Section 4.1 demonstrated the near-immediate rapid disproportionation of dithionite upon addition to aqueous solution to about half of the initial concentration followed by slower and prolonged decay). A comparison of dithionite decomposition in Figures 4.1-1 and 4.3-1 indicates that the initial concentration of dithionite measured in the presence of the sediments is consistently about 0.01 M less than in absence of sediments. Furthermore, it is apparent in Figure 4.3-2 that there is almost an immediate increase in dissolved iron concentrations of about 1 mM regardless of what the starting concentration of dithionite was. This leads to the conclusion that irrespective of the dithionite starting concentration or type of sediment, there is a very rapid consumption of about 2×10^{-5} mol of dithionite per gram of sediment and a rapid generation of about 2×10^{-6} mol of iron per gram of sediment when excess dithionite comes in contact with aquifer sediments. Also, the subsequent increase in iron concentrations after the very rapid reaction appears to be directly proportional to the amount of remaining dithionite that has degraded beyond the first 0.01 M that is rapidly consumed. Although not shown here, manganese concentrations followed trends very similar to the iron concentrations of Figure 4.3-2 except that they were about an order of magnitude lower than the iron concentrations, resulting in the rapid generation of about 2×10^{-7} mol of manganese per gram of sediment. The black curves in Figure 4.3-1 correspond to the predictions of a first-order rate expression for dithionite decomposition *after* the rapid decomposition for starting concentrations of 0.05 and 0.1 M (a decay curve for a starting dithionite concentration of 0.025 M is not shown because effectively all of the dithionite was consumed by the rapid decomposition). Note that the first-order dithionite decay rate constant used to generate the curves of Figure 4.3-1 is about a factor of 2.7 larger than the pseudo-first-order rate constant given by Equation 5, so dithionite degradation proceeds slightly faster in the presence of sediments than in their absence (after the very rapid degradation). However, the solid-to-solution mass ratio was not varied in the lab experiments to determine if there is a dependence of the decay rate in the presence of sediments on this ratio.

The black curves in Figure 4.3-2 show that the measured iron concentrations are predicted very well if it is assumed that 0.35 mol of iron are generated for every mole of dithionite consumed after the initial rapid decay. However, a final set of samples taken at 150 d (not shown in Figure 4.3-1) was considerably lower in iron concentrations than the last data points shown in Figure 4.3-2, suggesting that the liberated aqueous Fe(II) is eventually resorbed to or precipitated onto the sediment.

Arsenic concentrations in the batch experiments increased to levels above the U.S. Environmental Protection Agency (EPA) drinking water standard (10 ppb; Figure 4.3-3b), but by the conclusion of the experiment, they were mostly below the standard. Chromium concentrations were all well below the 50 ppb New Mexico Environment Department (NMED) standard, except for an unexplained peak around 50 d (Figure 4.3-3a).

Based on the observations discussed above, the following semi-empirical set of equations is adopted to describe the degradation of dithionite and generation of iron in the presence of aquifer sediments at pH ~7:

$$\frac{dC_{S_2O_4}}{dt} = -k_1 \frac{\rho_B}{\phi} \left[1 - \left(\frac{s}{s_{max}} \right)^{10} \right] - k_2 C_{S_2O_4}, \quad \text{Equation 6}$$

$$\frac{ds}{dt} = k_1 \left[1 - \left(\frac{s}{s_{max}} \right)^{10} \right], \quad \text{Equation 7}$$

$$\frac{dC_{Fe(II)}}{dt} = 0.1k_1 \frac{\rho_B}{\phi} \left[1 - \left(\frac{s}{s_{max}} \right)^{10} \right] + 0.35k_2 C_{S_2O_4}, \quad \text{Equation 8}$$

$$\frac{dC_{SO_4}}{dt} = 1.1k_1 \frac{\rho_B}{\phi} \left[1 - \left(\frac{s}{s_{max}} \right)^{10} \right] + 1.35k_2 C_{S_2O_4}, \quad \text{Equation 9}$$

where $k_1 = 0.002$ mol/g-h, $k_2 = 0.003$ h⁻¹, $s_{max} = 2 \times 10^{-5}$ mol/g sediment, ρ_B = bulk density in g/cm³, ϕ = porosity, and s is a dummy surface species concentration that serves to shut off the rapid dithionite consumption reaction after 2×10^{-5} mol of dithionite has been consumed per gram sediment. The first term on the right side of Equation 6 corresponds to the rapid consumption of 2×10^{-5} mol/g sediment of dithionite in the presence of sediments, and the second term corresponds to the slower decay of dithionite that occurs after the rapid consumption. The $\left(\frac{s}{s_{max}} \right)^{10}$ term in Equation 6 serves to keep the rapid dithionite consumption rate high until s is almost equal to s_{max} . The value of 0.002 mol/g-h for k_1 is somewhat arbitrary, but it is large enough to ensure that 2×10^{-5} mol/g of sediment are consumed in a very short time, while it is not so large as to cause instabilities in a numerical model. The value of $k_2 = 0.003$ h⁻¹ is the decay constant used to generate the curves of Figure 4.3-1. The coefficients in Equation 7 ensure that the moles of Fe(II) generated per mole of dithionite consumed match the experimental data (Figure 4.3-1), and the coefficients in Equation 9 serve to maintain charge balance after the loss of dithionite and the generation of Fe(II). Equation 9 is consistent with the experimental data in that a little over 1 mol of sulfate was measured in the batch reactors per mole of dithionite consumed.

In the batch experiments in which the four different sediments shown in Figures 4.3-1 and 4.3-2 were treated with a 1 M dithionite solution and then introduced to a 1% Cr(VI) solution to determine Cr(VI) reduction capacity, the amount of Cr(VI) reduced on the treated sediments ranged from 0.015 to 0.025 mol Cr(VI) per mole of dithionite introduced, which is about 2 to 4 times larger than in the column experiments (Table 4.3-1). However, the Cr(VI) reduction per unit mass of sediments was nearly 2.5 orders of magnitude larger than in the column experiments, and it would have taken anywhere from 30% to 99% of the entire inventory of iron in the sediments to account for the amount of Cr(VI) reduced if Fe(II) were entirely responsible for the reduction. Furthermore, the reduction capacity of the sediments did not appear to correlate at all with their iron content (measured by XRF) or with specific surface area determined by N₂ adsorption. Most of the literature on the remediation of Cr(VI) with dithionite attributes the benefits of dithionite to the Fe(II) that is produced, but these results suggest that Fe(II) accounts for at best only a portion of reductive capacity generated by dithionite. It seems that reductive capacity is much better predicted by the amount of dithionite introduced to a system than any characteristic of the sediments, such as iron content or specific surface area.

4.3.2 Column Experiments

Dithionite concentrations were measured by UV-Vis spectrometry in the injection solution immediately after preparation and again at the end of the injection. Over the 4-d injection, the dithionite concentration of the injection solution decreased from 0.05 M to 0.02 M. Although the syringe was closed off from the atmosphere, the material is not totally impervious to oxygen intrusion. Therefore, loss of dithionite over

the 4-d injection is expected. The reaction depicted in Equation 1 indicates that acidity is generated during the dithionite reduction of Fe(III) and subsequent reduction of Cr(VI). The measured pH of the eluent drops abruptly from a background value of ~9 to 2 during the dithionite injection (Figure 4.3-4).

The bromide conservative tracer indicates the timing of the dithionite injection, which confirms that 110 mL of the solution was injected over 4 d (Figure 4.3-5). Sulfate, an oxidation product of both sulfite and dithionite, eluted coincidentally with bromine (Figure 4.3-5). A total of 0.0165 mol of sulfur in excess of SO_4^{2-} from R-42 was injected from the 0.05 M $\text{S}_2\text{O}_4^{2-}/\text{SO}_3^{2-}$ mix. A total of 0.00665 and 0.00941 mol of SO_4^{2-} in excess of the R-42 concentration was eluted during the injection through the CH-2 (Puye) and CH-3 (Miocene pumiceous) columns, respectively, indicating that only 40% and 57% of the initially reduced sulfur oxidized to SO_4^{2-} . The remaining sulfur may have oxidized to an intermediate sulfur species (e.g., SO_3^{2-}) or precipitated in the sediment. It is not possible to distinguish whether the SO_4^{2-} is a reaction product from hydrolysis of dithionite or from a redox reaction with sedimentary Fe(III). Therefore, it is uncertain how much sedimentary Fe(III) was reduced by the dithionite injection. The nitrate decreases during the time of the injection, suggesting that nitrate in R-42 water is reduced by the dithionite. However, the nitrate returns to background R-42 concentration immediately after the injection, indicating that the treated sediment does not reduce nitrate (Figure 4.3-5). Chloride behaves conservatively throughout the entire experiment, maintaining the background R-42 concentration of ~50 ppm (Figure 4.3-5).

The divalent cations, strontium, calcium, manganese, and magnesium, as well as potassium, show an increase in concentration around 60 mL, coincident with the breakthrough of the injection solution (Figure 4.3-5). These observations suggest that a cation exchange mechanism occurs owing to the lithium and sodium injection. The 110 mL of dithionite solution injected into the column contained the 400-ppm lithium bromide (tracer), and Na^+ from 0.05 M Na_2SO_3 and 0.05 M $\text{Na}_2\text{S}_2\text{O}_4$. The total number of moles of lithium and sodium injected into the column was therefore 0.0005 and 0.022, respectively. After the injection, ~95% of both lithium and sodium are recovered in the eluent, whereas the concentrations of calcium, magnesium, strontium, and potassium in the eluent are below the concentrations of the injection water, suggesting that some amount is then reabsorbed to the sediment.

The column experiments were modeled numerically using Equations 6–9 to simulate 1-D reactive transport in porous media while accounting for cation exchange of up to 9 cations (Williams et al. 2013). This model was used because it was apparent from the column experiments that cation exchange played a significant role in the fate and transport of Fe(II). Figure 4.3-5 shows the breakthrough curves of selected cations and anions in the column experiment with the Miocene pumiceous sediments, and the right-hand plot shows the predicted breakthrough curves from the model. The model used published values of cation exchange selectivity coefficients for all the cations, so the only parameters that were adjusted to match the data were the longitudinal dispersivity in the column (matched using the bromide breakthrough curve) and the cation exchange capacity (CEC) of the sediments (matched using the shapes of the cation breakthrough curves). The breakthrough curves for the column packed with Puye sediments (not shown) looked very similar to those of Figure 4.3-5, and adjustments of less than 10% to the column dispersivity and CEC values relative to the Miocene pumiceous column were sufficient to match the observations. The model parameters have not yet been formally optimized to match the data. Adjustment of the selectivity coefficients for the various cations should provide better matches to the individual cation breakthrough curves, particularly for calcium and magnesium, which appear to be underpredicted during the intermediate portion of the tests. However, these species are of little consequence for the behavior of dithionite and its effect on the reduction capacity of the sediments. It was considered far more important to capture the behavior of Fe(II), which has implications for the subsequent reduction of Cr(VI). The Fe(II) breakthrough curves were quite well predicted by the model, although the model predicts an earlier first arrival of Fe(II) than was observed in both columns. The recovery of Fe(II) from both columns was reasonably well matched.

Figure 4.3-6 shows the profiles of iron and chromium that were leached from the sediments of the Miocene pumiceous column. Of particular interest is the dramatic increase in iron concentrations leached from the sediments that occurs about two-thirds of the distance from the column inlet. These data suggest that aggressive dissolution of iron from the sediments reached only about two-thirds of the way into the columns. Although iron concentrations on the sediments were not formally accounted for in the model, Figure 4.3-6 shows that the modeled surface concentrations of the dummy species that corresponds to the rapid consumption of dithionite appears to reach about the same distance into the column as the depleted iron concentrations. This prediction assumes that about half the dithionite decayed before the dithionite solution ever entered the column, and the difference between the locations of the inflection in iron concentrations and the calculated penetration of the dummy species could easily be explained by a slight inaccuracy in this assumption.

Although only partial sediment leaching data were available for the Puye column at the time of writing this paper, preliminary indications are that the dithionite distance penetrated into this column was similar to that of the Miocene pumiceous column. The chromium profile in Figure 4.3-7 indicates that there is not a strong spatial dependence of where Cr(VI) was reduced and precipitated in the columns. This implies that the reductive capacity imparted to the sediments by the dithionite does not appear to be limited to regions where aggressive iron dissolution occurred and presumably where the dithionite reached. It is possible that the elevated iron concentrations in the final one-third of the column, which were likely deposited by cation exchange, provide as much reduction capacity as the depleted sediments in the first two-thirds of the column, but reduced sulfur species are also suspected to play an important role in Cr(VI) reduction. Note that the chromium recovery from the sediments was within about 20% of what was calculated to be deposited in the column based on the breakthrough curves of the Cr(VI).

Figure 4.3-7 shows the breakthrough curves of Cr(VI) in both columns. The Puye column exhibited about 35% more Cr(VI) reduction capacity than the Miocene pumiceous column. This is considered quite similar for the two sediments, and it does not appear to be strongly correlated to the iron content of the sediments, which was 1.9 wt% for the Puye vs 0.9 wt% for the Miocene pumiceous (determined by XRF). Also, the amount of iron that was leached from the untreated sediments by a 2 M HNO₃ leach was about 2.5 times larger for the Puye sediments than for the Miocene pumiceous sediments (about 0.013 wt% vs 0.005 wt%, corresponding to approximately 0.5% of the total iron in the sediments measured by XRF in both cases). The greater reduction capacity of the Puye sediments may be related to the fact that more Fe(II) appeared to be retained in this column than in the Miocene pumiceous column. The recovery of dissolved iron from the Miocene pumiceous column was nearly twice that from the Puye column (about 15 mg vs about 8 mg, corresponding to about 0.75% of the total iron in the Miocene pumiceous column and about 0.2% of the total iron in the Puye column), which may be a reflection of the mineralogy of the sediments: the Puye sediment consists of largely crystalline minerals, whereas the Miocene sediment consists mostly of glass, which is more susceptible to leaching. The reduction capacities of the sediments in the two columns, expressed as moles of Cr(VI) reduced per mole of dithionite introduced, were 6.3×10^{-3} mol Cr(VI)/mole for the Miocene pumiceous sediments and 8.5×10^{-3} mol Cr(VI)/mole for the Puye sediments. These numbers would approximately double if the dithionite concentration is corrected for the amount of dithionite that was believed to have actually entered the columns after the rapid decomposition. If the entire mass of sediments in each column was considered to be "treated", then the reduction capacity expressed as moles of Cr(VI) per gram of treated sediment would be 1.6×10^{-7} mol Cr(VI)/g for the Miocene pumiceous column and 2.0×10^{-7} mol Cr(VI)/g for the Puye column.

5.0 CONCLUSIONS

Although the chemistry associated with sodium dithionite reactions is complex and many mechanistic details remain poorly understood, sodium dithionite appears to be a viable chemical reductant that should be capable of establishing an in situ permeable reactive barrier in the regional aquifer that can immobilize many pore volumes of Cr(VI)-contaminated groundwater. Batch experiments conducted in flame-sealed glass reactors without sediments present confirmed a complex aqueous dithionite degradation process, with both a rapid initial degradation process that proceeded to a greater extent at lower pH, followed by a much slower degradation process that was also pH dependent. The lifetime of dithionite under anoxic conditions was found to be greater than previously reported, presumably because reaction products such as H₂S gas were more efficiently prevented from escaping than in any previous experiments. This has important implications for field deployments because it suggests that dithionite may be able to travel further away from injection wells in an aquifer before degrading than previously thought. Batch experiments with sediments showed that the presence of sediments causes the rapid reaction of about 2×10^{-5} mol of dithionite per gram of sediment beyond the initial rapid degradation of dithionite in the absence of sediments. During this rapid reaction period, about 2×10^{-6} mol of dissolved Fe²⁺ and 2×10^{-7} mol of dissolved Mn²⁺ per gram of sediment were produced, and these quantities were found to be similar for four different aquifer sediments tested. After the initial rapid reaction, any remaining dithionite was consumed about 2.7 times faster in the presence of sediments than in their absence, and about 0.35 mol of Fe²⁺ and 0.035 mol of Mn²⁺ were produced for every mole of dithionite consumed. Concentrations of arsenic and other metals observed in the experiments generally stayed below EPA maximum concentration levels.

Column experiments showed that the injection of two pore volumes of a 0.05 M sodium dithionite solution buffered with 0.05 M of Na₂SO₃ resulted in a Cr(VI) reduction capacity ranging from about 6×10^{-3} to 9×10^{-3} mol Cr(VI)/mole dithionite introduced. These capacities were measured by injecting non-deaerated R-42 water [Cr(VI) concentrations of about 900 µg/L] through the columns until Cr(VI) broke through in the column effluents. R-42 water nominally has a dissolved oxygen concentration of 6-7 mg/L and a nitrate concentration of 25–30 mg/L. Nitrate was not reduced by the dithionite-treated sediments, but some of the oxygen was probably reduced (dissolved oxygen was not measured in the column effluents because the effluents became oxygenated before measurements could be made). The dithionite-treated sediments effectively prevented Cr(VI) breakthrough for 30 to 50 column pore volumes. Arsenic and other metal concentrations generally remained below their EPA maximum concentration limits except during the dithionite pulse. After chromium breakthrough was complete, the columns were frozen and cut into 1-cm long sections, and each section was acid leached to determine the spatial distribution of chromium, iron and other constituents on the sediments. The results revealed that chromium was rather evenly distributed throughout the columns, but the iron distribution in the sediments in one of the columns suggested that the dithionite had reached only about two-thirds of the way through the column before being consumed. The mass of sediments in the first two-thirds of the column corresponds to the mass that would be predicted to rapidly consume all the injected dithionite if the rapid consumption were the same as in the batch experiments (i.e., 2×10^{-5} mol of dithionite per gram of sediment).

One of the main conclusions from the dithionite laboratory experiments is that, contrary to conventional wisdom, the reduction capacity imparted to sediments does not appear to be derived almost exclusively from the reaction of dithionite with Fe(III) phases to form Fe(II). Rather, there also appears to be a significant, perhaps dominant, contribution from reduced sulfur species that are generated by the decomposition of dithionite. More work is needed to understand and quantify this contribution. The implication is that dithionite treatments may depend much less on sediment characteristics (such as iron content, mineralogy, and specific surface area) than previously thought. A semi-empirical kinetic model was developed that, when coupled with a 1-D mass transfer model that accounts for cation exchange, can predict dithionite consumption and penetration into an aquifer, as well as Fe(II) generation within the aquifer.

6.0 REFERENCES

The following reference list includes documents cited in this report.

- Amonette, J.E., J.E. Szecsody, H.T. Schaef, J.C. Templeton, Y.A. Gorby, and J. S. Fruchter. "Abiotic Reduction of Aquifer Materials by Dithionite: A Promising In-Situ Remediation Technology," in G.W. Gee and N.R. Wing (Eds.), *In-Situ Remediation: Scientific Basis for Current and Future Technologies*, pp. 851–881, Columbus: Battelle (1994).
- Danehy, J.P., and C.W. Zubritsky. "Iodometric Method for the Determination of Dithionite, Bisulfite, and Thiosulfate in the Presence of Each Other and Its Use in Following the decomposition of Aqueous Solutions of Sodium Dithionite," *Analytical Chemistry*, Vol. 46, No. 3, pp. 391–395 (1974).
- Hammond, G.E. "PFLOTRAN: Recent Developments Facilitating Massively-Parallel Reactive Biogeochemical Transport," presented at American Geophysical Union Fall Meeting, 2015, <https://agu.confex.com/agu/fm15/meetingapp.cgi/Paper/61587> (2015).
- Istok, J.D., J.E. Amonette, C.R. Cole, J.S. Fruchter, M.D. Humphrey, J.E. Szecsody, S.S. Teel, V.R. Vermeul, M.D. Williams, and S.B. Yabusaki. "In Situ Redox Manipulation by Dithionite Injection: Intermediate-scale Laboratory Experiments," *Ground Water*, Vol. 37, No. 6, pp. 884–889 (1999).
- Lichtner, P.C., G.E. Hammond, C. Lu, S. Karra, G. Bisht, B. Andre, R.T. Mills, J. Kumar, and J.M. Frederick. *PFLOTRAN User Manual*, <http://www.documentation.pflotran.org> (2017a).
- Lichtner, P.C., G.E. Hammond, C. Lu, S. Karra, G. Bisht, B. Andre, R.T. Mills, J. Kumar, and J.M. Frederick. PFLOTRAN Webpage, <http://www.pflotran.org> (2017b).
- Meyer, B., and M. Ospina. "Raman Spectrometric Study of the Thermal Decomposition of Aqueous Tri- and Tetrathionate," *Phosphorus and Sulfur and the Related Elements*, Vol. 14, No. 1, pp. 23–36 (1982).
- Szekeres, L. "Analytical Chemistry of the Sulfur Acids," *Talanta*, Vol. 21, No. 1, pp. 1–44 (1974).
- Vesselinov, V., and D. Harp. "Model Analysis and Decision Support (MADS) for Complex Physics Models," in XIX International Conference on Water Resources—CMWR (2012).
- Wayman, M., and W.J. Lem. "Decomposition of Aqueous Dithionite. Part II. A Reaction Mechanism for the Decomposition of Aqueous Sodium Dithionite," *Canadian Journal of Chemistry*, Vol. 48, No. 5, pp. 782–787 (1970).
- Williams, M.D., P.W. Reimus, V.R. Vermeul, P.E. Rose, C.A. Dean, T.B. Watson, D.L. Newell, K.B. Leecaster, and E.M. Brauser. "Development of Models to Simulate Tracer Tests for Characterization of Enhanced Geothermal Systems," in Pacific Northwest National Laboratory document PNNL-22486, Ch. 5, Richland, WA (2013).
- Wolery, T.J. *EQ3/6: A Software Package for Geochemical Modeling of Aqueous Systems: Package Overview and Installation Guide*, version 7.0, pp. 1–65, Lawrence Livermore National Laboratory, Livermore, CA (1992).

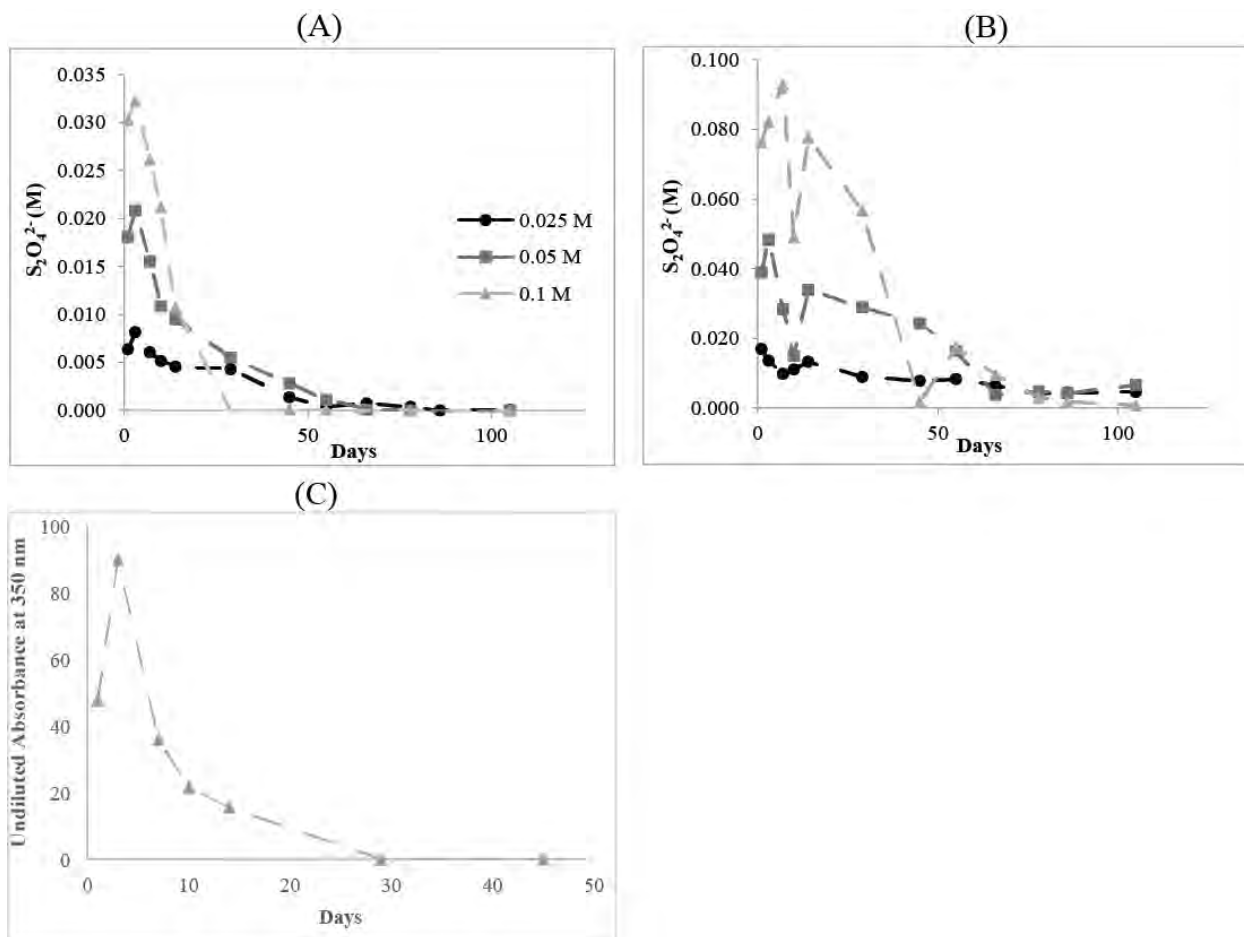


Figure 4.1.1 Dithionite decomposition through time in HCO_3^- -buffered (A), EDTA/ OH^- -buffered (B), and unbuffered (C) solutions.

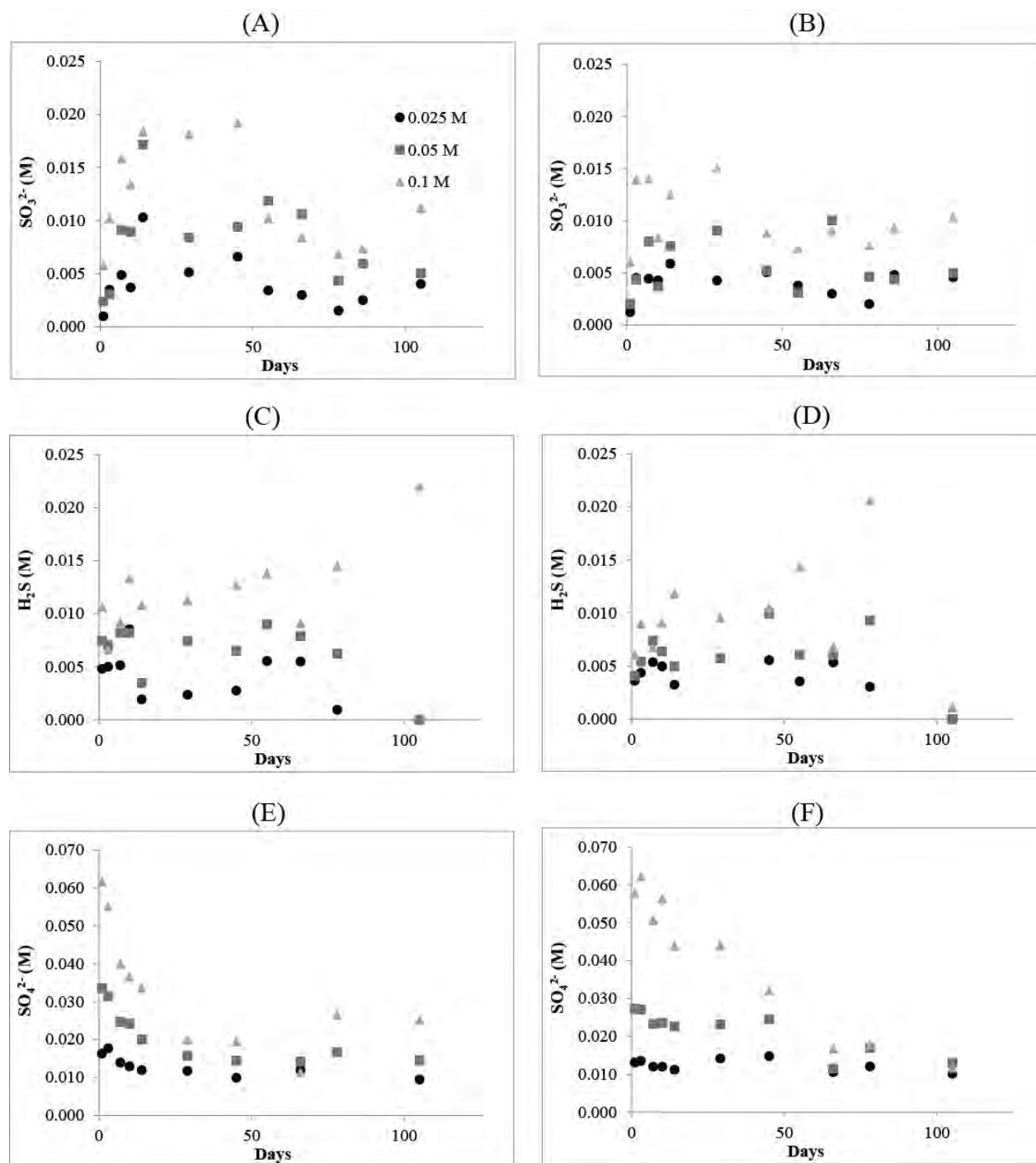


Figure 4.1-2 Concentrations of SO₃²⁻ (A, B), H₂S (C, D), and SO₄²⁻ (E, F) through time in HCO₃⁻-buffered (A, C, E) and EDTA/OH⁻-buffered (B, D, F) solutions

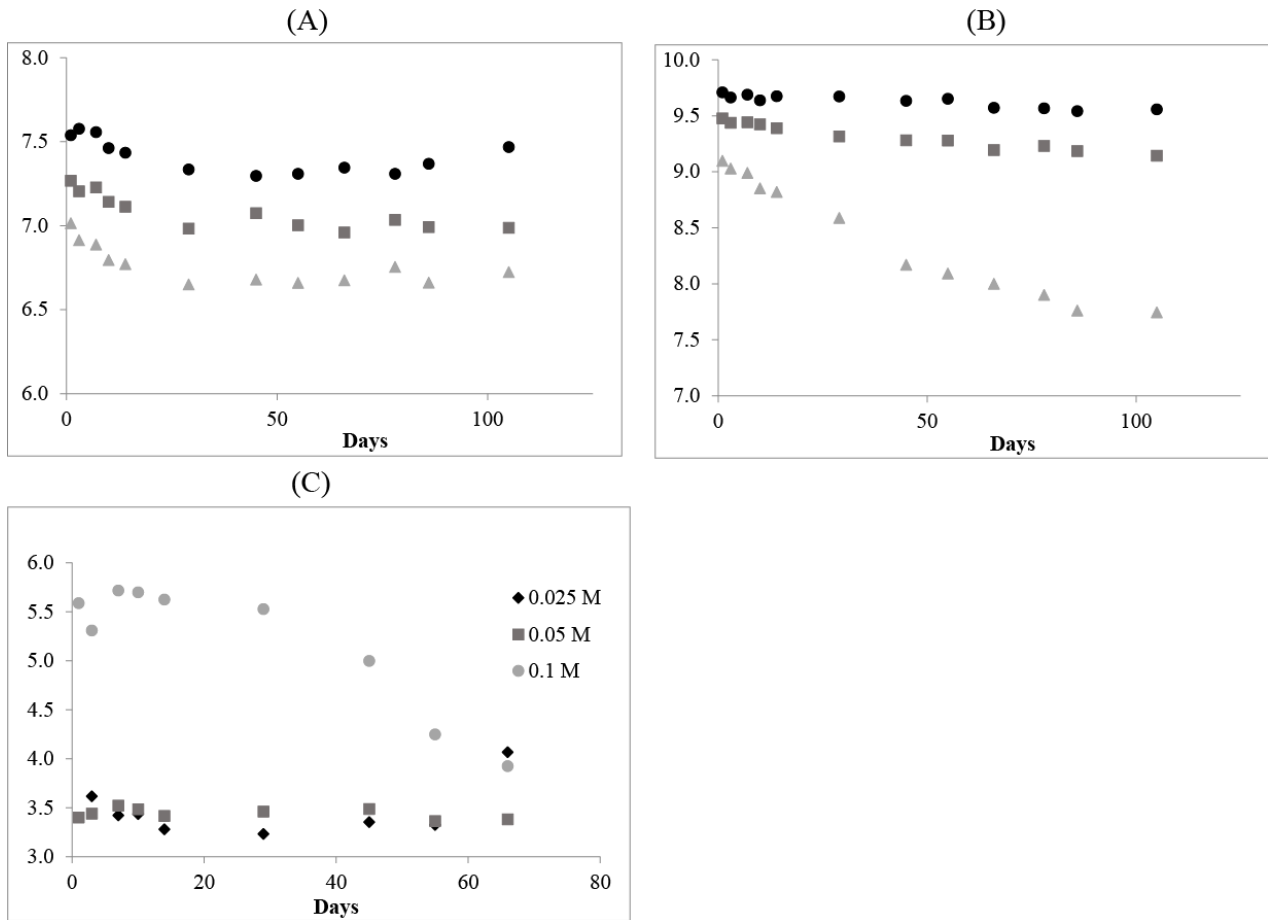


Figure 4.1-3 pH through time in HCO_3^- -buffered (A), EDTA/OH^- -buffered (B), and unbuffered (C) solutions

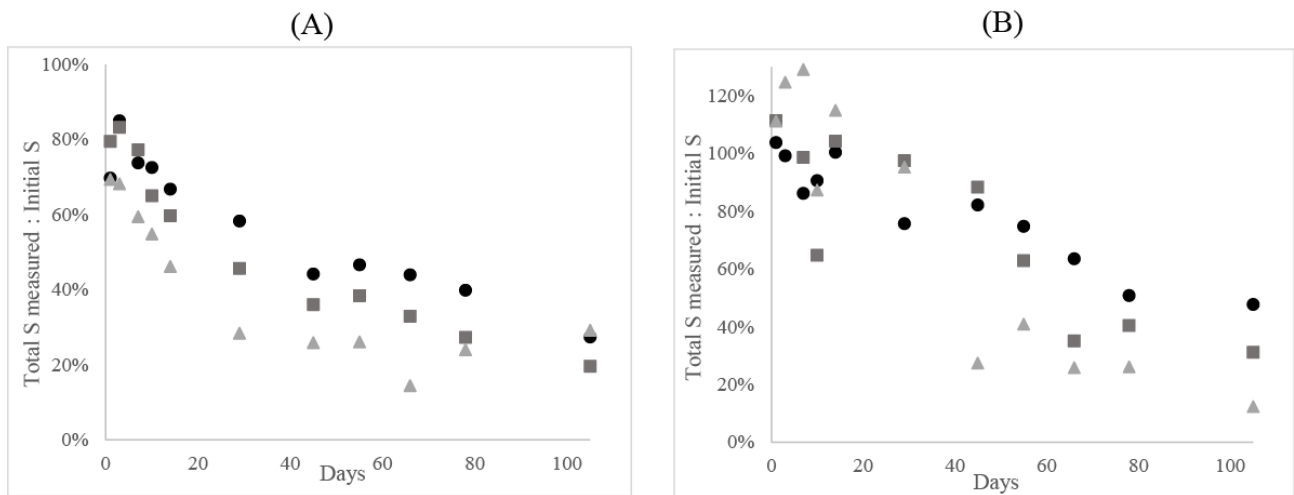


Figure 4.1-4 Percent recovery of S relative to the starting amount in HCO_3^- -buffered (A) and EDTA/OH^- -buffered (B) solutions

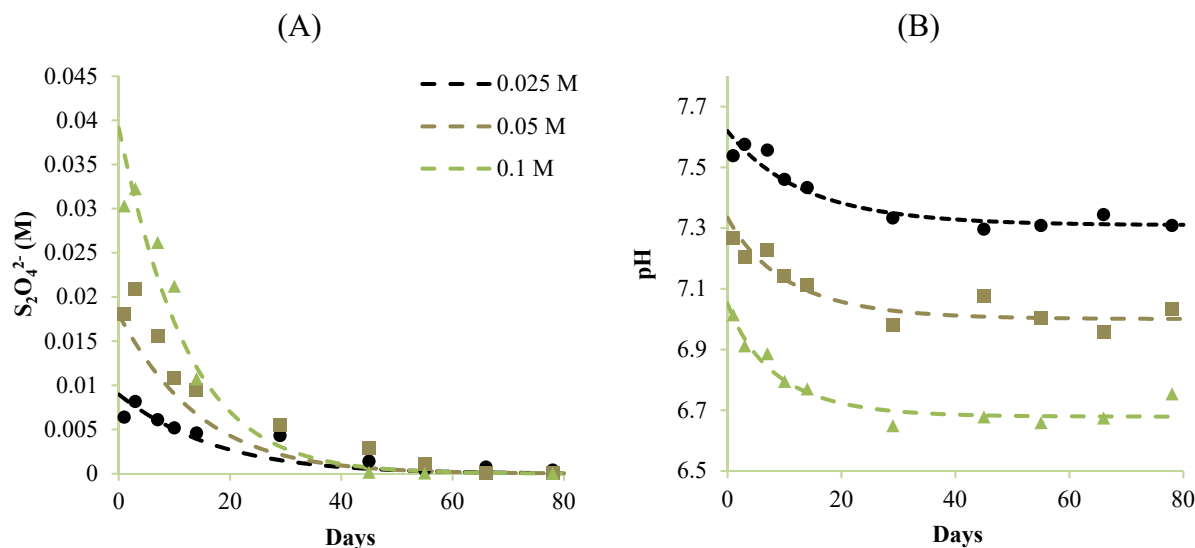


Figure 4.1-5 Simulation of experiments conducted in the HCO_3^- -buffered solution. Panel (A) shows the dithionite concentration, and Panel (B) shows pH. The figure compares calibrated model curves (dashed lines) and experimental data (points) for the different concentrations of dithionite used in these experiments.

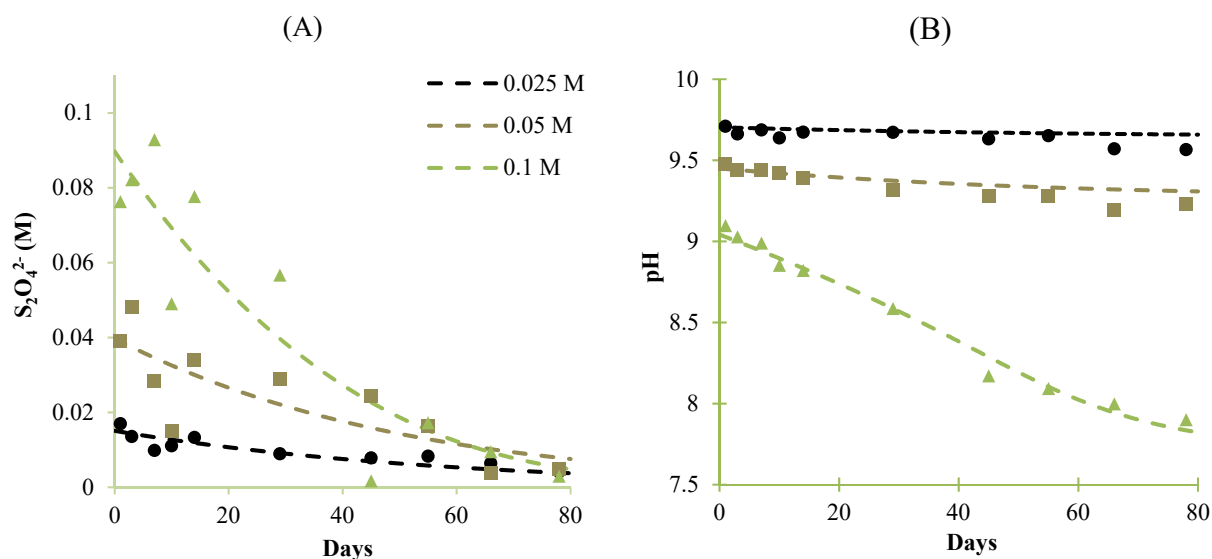


Figure 4.1-6 Simulation of experiments conducted in the $EDTA/OH^-$ -buffered solution. Panel (A) shows the dithionite concentration, and Panel (B) shows pH. The figure compares calibrated model curves (dashed lines) and experimental data (points) for the different concentrations of dithionite used in these experiments.

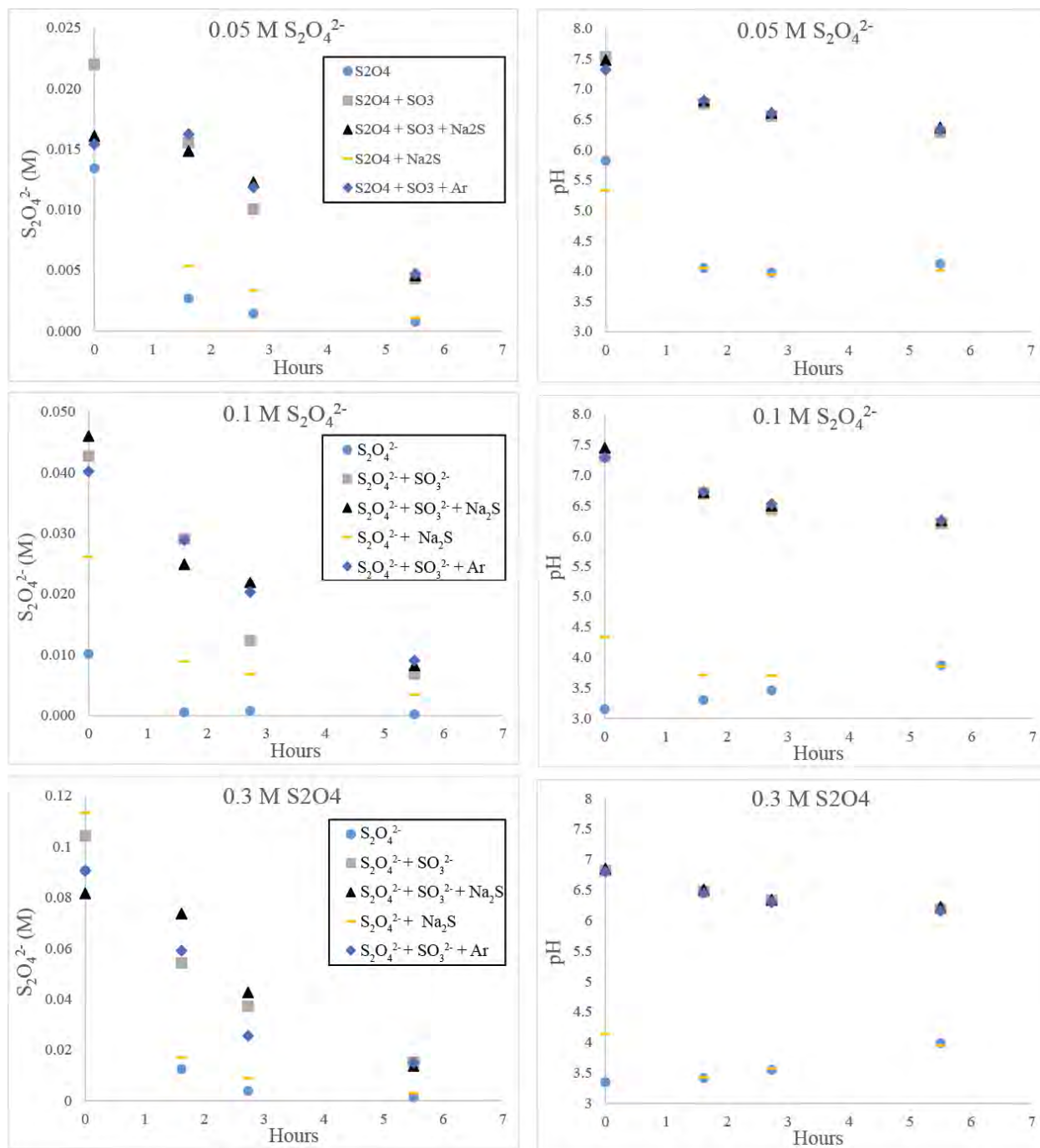


Figure 4.1-7 Decomposition of $S_2O_4^{2-}$ in various buffer solutions left open to the atmosphere and accompanying pH measurements

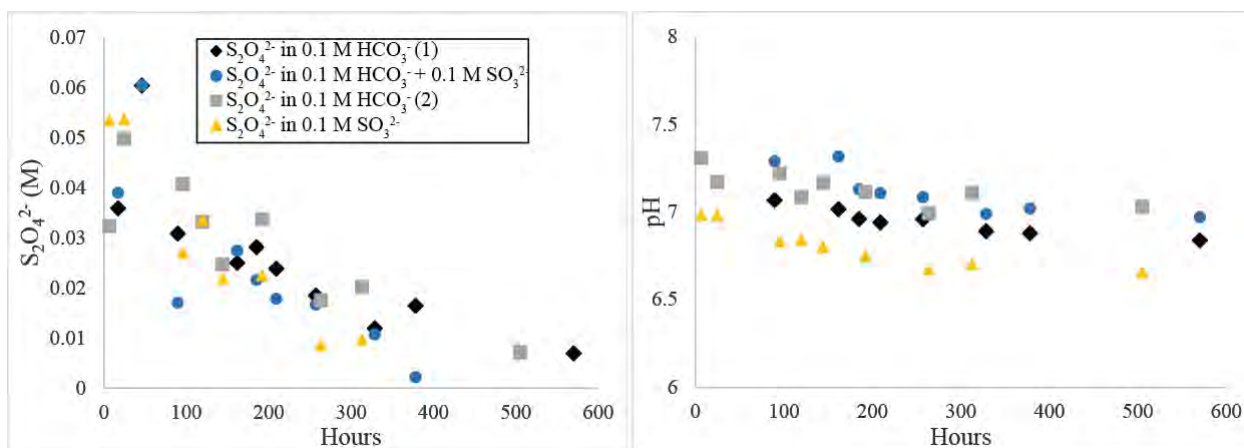


Figure 4.1-8 Anaerobic decomposition of dithionite in background solutions of HCO_3^- , SO_3^{2-} , and $\text{HCO}_3^- + \text{SO}_3^{2-}$

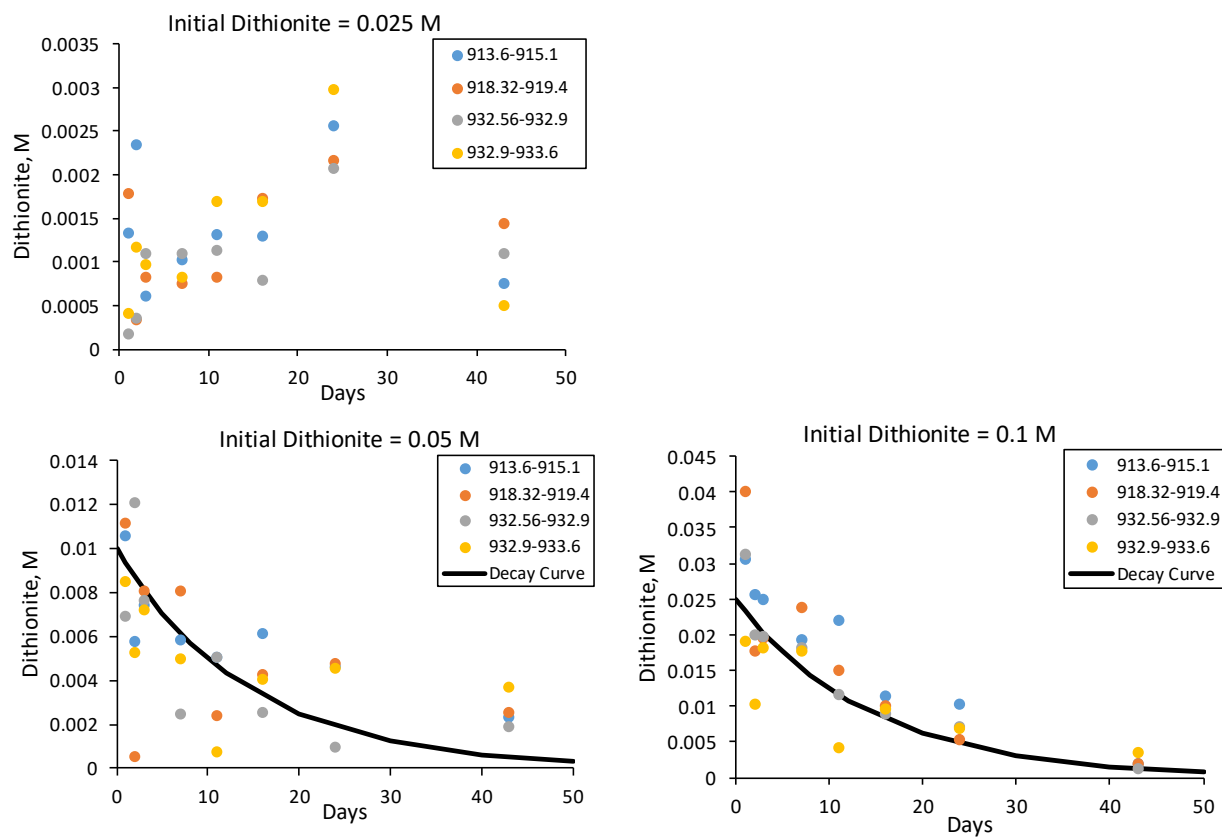


Figure 4.3-1 Dithionite decomposition in batch experiments with four different sediments (identified by depth [ft] from CrCH-2) with 10 mL of solution for every 5 g sediment. Curves were generated using the kinetic model discussed in text.

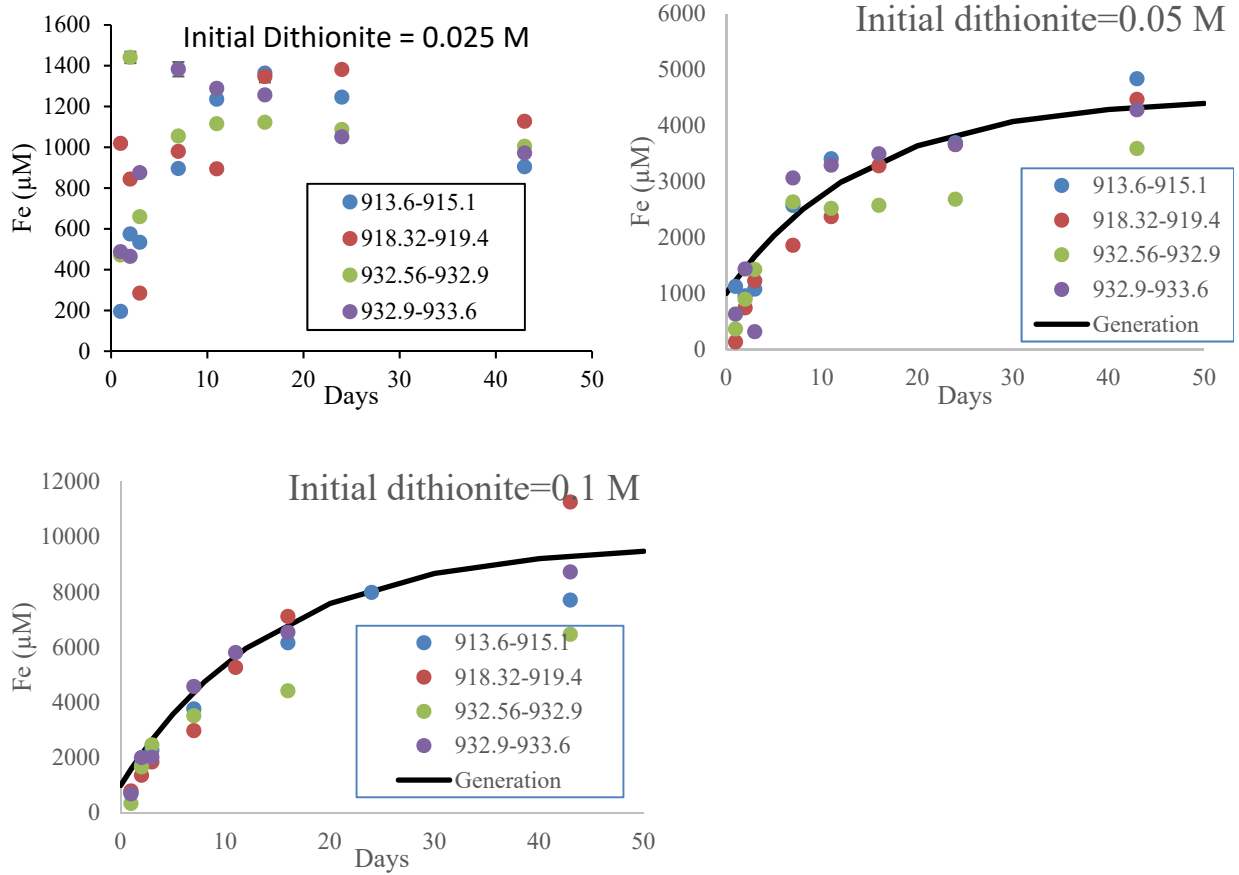
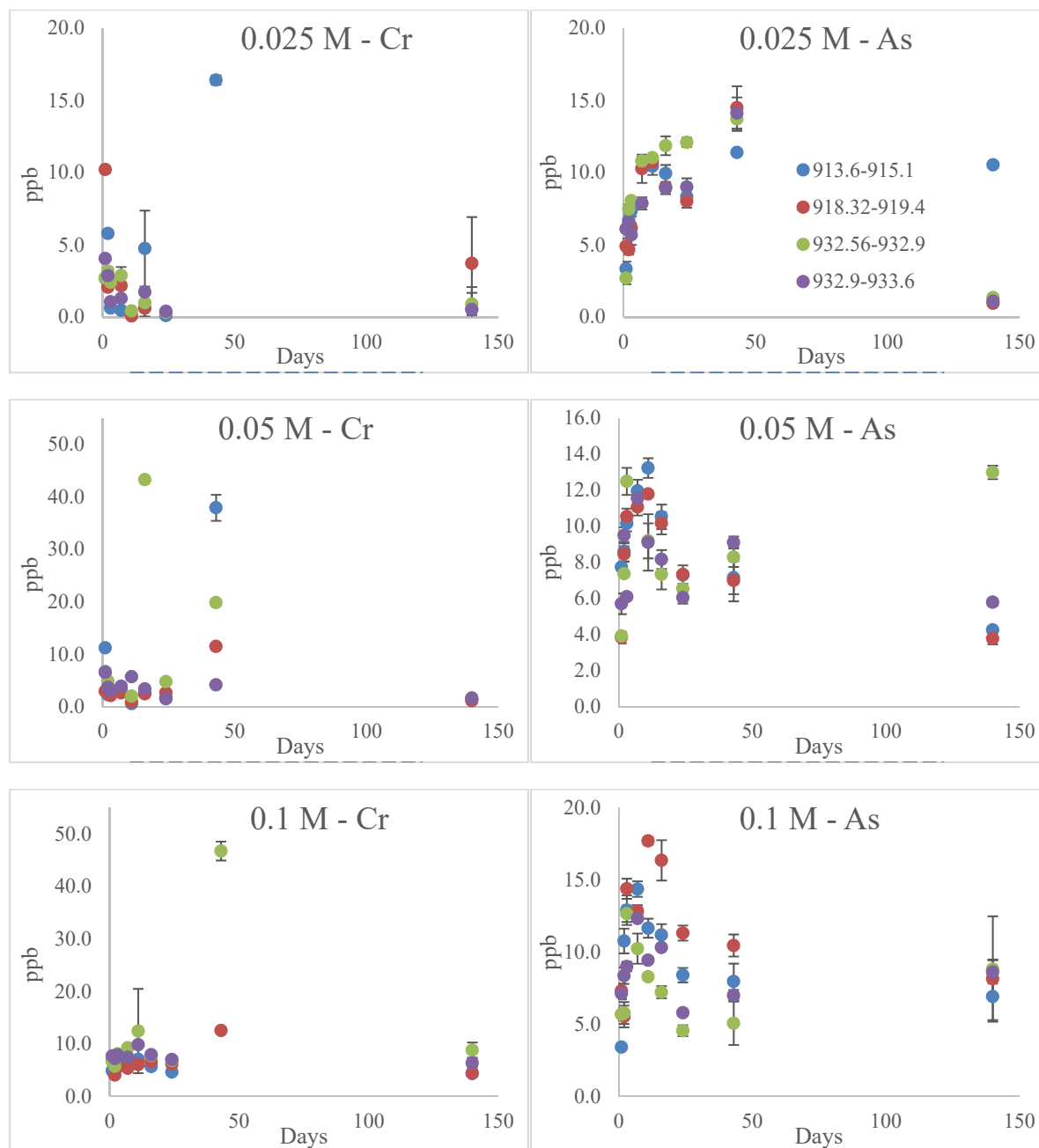


Figure 4.3-2 Iron generation in batch experiments with four different sediments (identified by depth [ft] from CrCH-2) with 10 mL of solution for every 5 g sediment. Curves were generated using the kinetic model discussed in text.



A.

B.

Figure 4.3-3 Release of Cr (A) and As (B) from batch sediments. The molarity indicates the starting concentration of the dithionite solution.

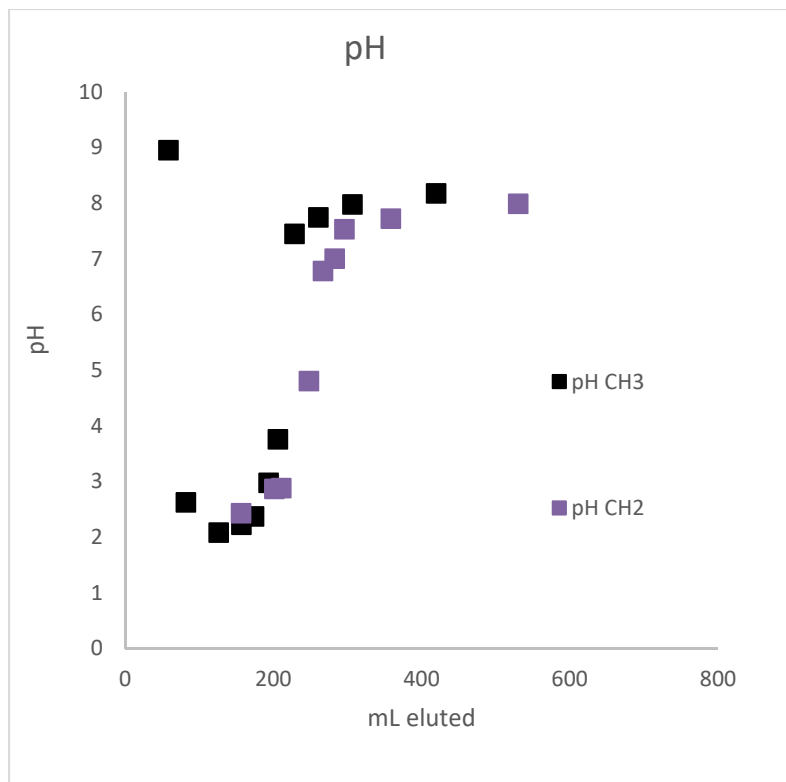


Figure 4.3-4 pH of column eluent

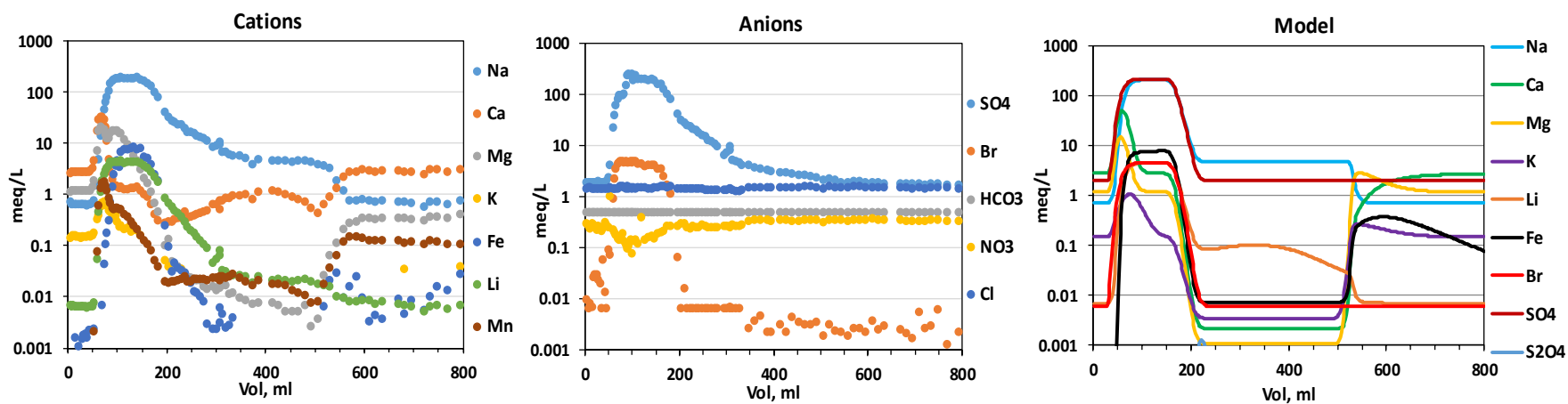


Figure 4.3-5 Breakthrough curves of cations and anions in the Miocene pumiceous column experiment and corresponding predictions of the 1-D transport model

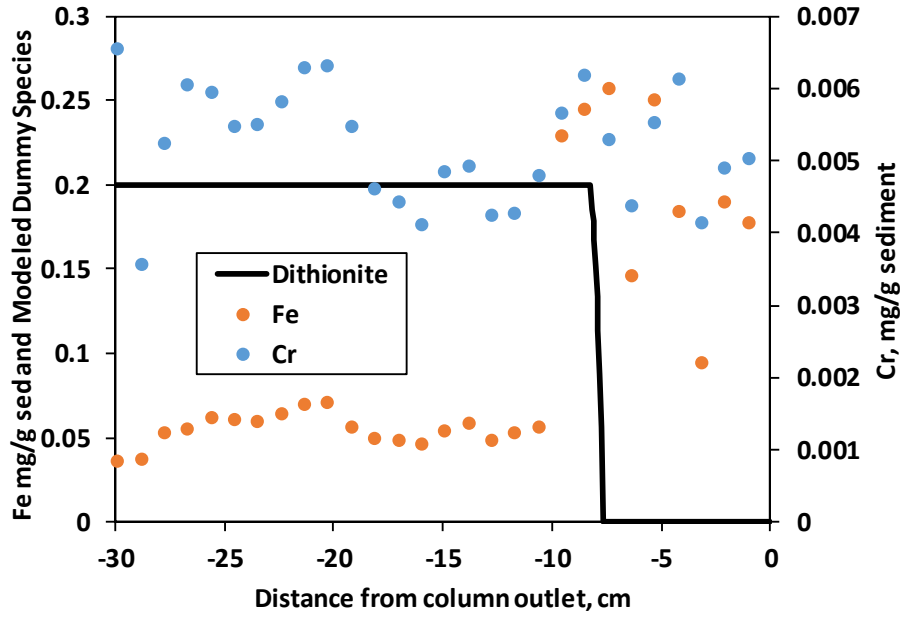


Figure 4.3-6 Post-experiment Fe and Cr profiles in Miocene pumiceous column and prediction of penetration distance by dithionite (dummy surface species, arbitrary units).

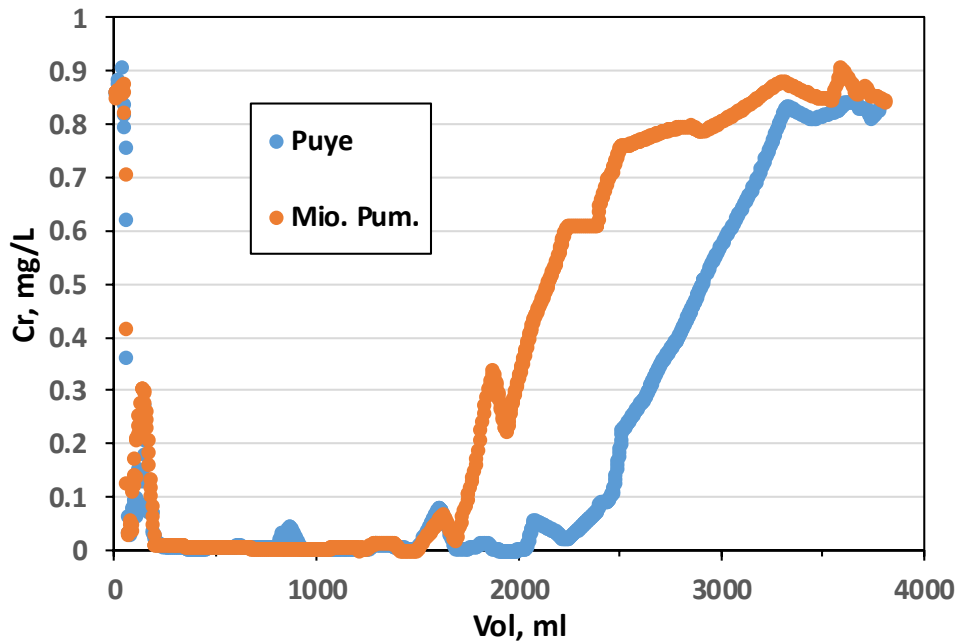


Figure 4.3-7 Cr(VI) breakthroughs in the two dithionite column experiments.

Table 3.3-1
Size Fraction Abundance as Percent of Whole Rock
and Estimates of Hydraulic Conductivity for CrCH-2 Sediment Samples

Sample Depth (ft)	% Fraction 3 (0.355–0.177 mm)	% Fraction 4 (0.177–0.063 mm)	% Fraction 5 (< 0.063 mm)	Kozeny Carmen Estimate of K	Lithologic Unit
913.6–915.1	11.64	11.56	2.85	10.257	Puye Fm. (Tpf)
918.32–919.4	9.51	6.63	6.76	8.74	Puye Fm. (Tpf)
932.9–933.66	4.38	4.82	5.19	19.015	pumiceous Puye [Tpf(p)]
932.56–932.9	15.06	7.71	6.99	6.069	pumiceous Puye [Tpf(p)]

Note: Lithologic units are the same as those described in Attachment 3 of this compendium, "Stratigraphic and Sedimentological Studies and their Hydrogeological Features in the Chromium Investigation Area, Los Alamos National Laboratory."

Table 4.1-1
Secondary Species with Corresponding Mass Action Laws
and Equilibrium Constants (K) Used in the Numerical Model

Secondary Species	Mass Action Law	K
OH ⁻	OH ⁻ + H ⁺ ↔ H ₂ O	10 ^{14.0}
CO ₃ ²⁻	CO ₃ ²⁻ + H ⁺ ↔ HCO ₃ ⁻	10 ^{10.3}
CO ₂ (aq)	CO ₂ (aq) + H ₂ O ↔ H ⁺ + HCO ₃ ⁻	10 ^{-6.34}
HSO ₃ ⁻	HSO ₃ ⁻ ↔ H ⁺ + SO ₃ ²⁻	10 ^{-7.21}
H ₂ SO ₃ (aq)	H ₂ SO ₃ (aq) ↔ 2H ⁺ + SO ₃ ²⁻	10 ^{-9.21}
HSO ₄ ⁻	HSO ₄ ⁻ ↔ H ⁺ + SO ₄ ²⁻	10 ^{-1.98}
H ₂ SO ₄ (aq)	H ₂ SO ₄ (aq) ↔ 2H ⁺ + SO ₄ ²⁻	10 ^{1.02}
NaCO ₃ ⁻	NaCO ₃ ⁻ + H ⁺ ↔ HCO ₃ ⁻ + Na ⁺	10 ^{9.81}
NaHCO ₃ (aq)	NaHCO ₃ (aq) ↔ HCO ₃ ⁻ + Na ⁺	10 ^{-0.154}
NaOH(aq)	NaOH(aq) + H ⁺ ↔ H ₂ O + Na ⁺	10 ^{14.8}
NaSO ₄ ⁻	NaSO ₄ ⁻ ↔ SO ₄ ²⁻ + Na ⁺	10 ^{-0.820}
H ₂ S(aq)	H ₂ S(aq) ↔ H ⁺ + HS ⁻	10 ^{-6.99}

Table 4.1-2
Additional Calibrated Parameters Used in the Numerical Model

Parameter	Unit	pH 8.3	pH 10
pH _i , 0.1 M S ₂ O ₄ ⁻²	n/a*	7.15	9.14
pH _i , 0.05 M S ₂ O ₄ ⁻²	n/a	7.43	9.55
pH _i , 0.025 M S ₂ O ₄ ⁻²	n/a	7.71	9.81
[S ₂ O ₄ ⁻²] _i , 0.1 M S ₂ O ₄ ⁻²	M	0.0391	0.0897
[S ₂ O ₄ ⁻²] _i , 0.05 M S ₂ O ₄ ⁻²	M	0.0180	0.0397
[S ₂ O ₄ ⁻²] _i , 0.025 M S ₂ O ₄ ⁻²	M	0.00897	0.0151
[HCO ₃ ⁻] _{eff}	M	0.329	0.570

* n/a = Not applicable.

Table 4.2-1
XRF Data for Bulk Sediment Samples from CH-2 Used In
Batch Experiments (A) and Sediments from CH-2 and CH-3 Used in Column Experiments (B)

Sample	Na ₂ O%	MgO%	Al ₂ O ₃ %	SiO ₂ %	P ₂ O ₅ %	K ₂ O%	CaO%	TiO ₂ %	MnO%	Fe ₂ O ₃ %	V ppm	Cr ppm
918.32	3.2	0.98	12	75	0.084	3.3	1.9	0.26	0.042	1.9	19	26
913.6	3.4	1.2	13	71	0.093	3.4	2.4	0.32	0.048	2.4	29	32
932.56	2.9	0.41	12	73	0.033	4.9	0.87	0.17	0.057	1.2	12	9.0
932.9	3.0	0.68	12	73	0.058	4.6	1.2	0.25	0.059	1.7	19	17
Sample	Ni ppm	Cu ppm	Zn ppm	Rb ppm	Sr ppm	Y ppm	Zr ppm	Nb ppm	Ba ppm	Pb ppm	LOI*%	
918.32	25	8.0	27	73	260	12	120	18	910	9.0	0.83	
913.6	29	12	30	84	320	13	150	20	800	10	1.0	
932.56	9.0	3.0	31	107	100	22	110	23	820	13	3.4	
932.9	18	8.0	32	102	150	20	130	25	850	11	2.7	

(A)

Sample	Na ₂ O%	MgO%	Al ₂ O ₃ %	SiO ₂ %	P ₂ O ₅ %	K ₂ O%	CaO%	TiO ₂ %	MnO%	Fe ₂ O ₃ %	V ₂ O ₅	V ppm
CH-2 917.66-918.32	3.	0.98	12	74	0.097	3.4	2.0	0.27	0.042	1.9	0.0037	21
CH-3 934.4-935.2	3.3	0.19	12	75	0.021	4.8	0.69	0.13	0.060	0.90	0.0016	9.0
Sample	Cr ppm	Ni ppm	Cu ppm	Zn ppm	Rb ppm	Sr ppm						
CH-2 917.66-918.32	26.0	23	14.	29	82	290						
CH-3 934.4-935.2	7.0	8	5.0	39	110	73						
Sample	Y ppm	Zr ppm	Nb ppm	Ba ppm	Pb ppm	LOI%						
CH-2 917.66-918.32	16	180	20	840	14	1.19						
CH-3 934.4-935.2	23	100	29	620	13	3.3						

(B)

* LOI = Loss on ignition.

Table 4.2-2
XRD Data for Sediment Samples Used in the Column Experiments

Sample	Hornblende	Smectite	Mica/illite	Clinoptilolite	Hematite	Opal-C/CT	Cristobalite	Quartz	K-Feldspar	Plagioclase	Amorphous	Total
CH-3 934.4-935.2 F4	0.2	—	—	—	—	6.7	1.1	2.4	2.8	8.0	80.4	101.7
CH-3 934.4-935.2 F5	0.2	—	3.0	—	—	5.6	0.6	9.6	4.2	11.6	65.1	99.9
CH-3 934.4-935.2 F6	—	4.0	8.0	—	0.2	5.9	0.1	6.1	2.8	10.7	62.1	99.9
CH-2 917.66-918.32 F4	—	—	1.5	—	0.3	—	5.8	13.3	11.6	44.7	22.8	100.0
CH-2 917.66-918.32 F5	—	—	12.0	—	0.5	4.8	4.0	16.3	8.7	30.1	23.2	99.6
CH-2 917.66-918.32 F6	0.4	—	31.8	1.9	0.4	14.6	2.3	7.7	7.9	21.6	11.5	100.1

Notes: F4, F5, and F6 refer to the fraction size of the sediments, with 4 containing fine to medium sand (0.177 mm–0.355 mm), fraction 5 very fine to fine sand (0.063 mm–0.177 mm) and fraction 6 silt (<0.063 mm). Dashes indicate an insignificant contribution to the total mineral assemblage.

Table 4.2-3
BET Surface-Area Measurements for
Sediments Used in Batch and Column Experiments

Sample	Surface Area (m ² /g)
CH-2 913.6-915.1	3.2289
CH-2 917.66-918.3	3.8053
CH-2 918.32-919.4	2.6024
CH-2 932.56-932.8	1.3666
CH-2 932.9-933.6	1.5024
CH-3 934.4-935.2	0.8965

Table 4.3-1
Chromium Concentrations in
Solutions after Injection of 1%
Chromium Solution to Dithionite-Treated Sediments

Sample	Chromium (ppm)	Sediment Uptake (mg Cr/kg sediment)
Blank (no soil)	1223.2	
CH-2 913.6-915.1	536.72	1510.3
CH-2 918.32-919.4	338.22	1947.0
CH-2 932.5-932.9	55.587	2568.8
CH-2 932.9-933.6	399.77	1811.6

LA-UR-18-21450
March 2018
EP2018-0035

Groundwater Modeling Status Report

Attachment 9

Prepared by the Associate Directorate for Environmental Management

Los Alamos National Laboratory, operated by Los Alamos National Security, LLC, for the U.S. Department of Energy (DOE) under Contract No. DE-AC52-06NA253 and under DOE Office of Environmental Management Contract No. DE-EM0003528, has prepared this document pursuant to the Compliance Order on Consent, signed June 24, 2016. The Compliance Order on Consent contains requirements for the investigation and cleanup, including corrective action, of contamination at Los Alamos National Laboratory. The U.S. government has rights to use, reproduce, and distribute this document. The public may copy and use this document without charge, provided that this notice and any statement of authorship are reproduced on all copies.

CONTENTS

1.0	DESCRIPTION OF MODELS	1
1.1	Three-Dimensional Coupled Vadose-Zone/Regional-Aquifer Model	1
1.1.1	Computational Grid	2
1.1.2	Model Setup	2
1.1.3	Calibrated Model Parameters	3
1.2	Regional-Scale Aquifer Model	3
1.3	Biogeochemical Remediation Model	5
1.3.1	Using CHROTRAN to Model Bioamendment Remediation	6
1.3.2	Using CHROTRAN to Model Chemical Remediation	6
2.0	MODEL RESULTS AND UNCERTAINTY ANALYSES	7
2.1	Three-Dimensional Coupled Vadose-Zone/Regional-Aquifer Model	7
2.2	Regional-Scale Aquifer Model	8
2.3	Biochemical Remediation Model	9
2.3.1	Biochemical Remediation with Molasses	9
2.3.2	Geochemical Remediation with Sodium Dithionite	9
2.3.3	Comparison of Molasses and Dithionite Injection in a Hypothetical Scenario	9
2.3.4	Relative Impact of Abiotic Reduction and Bioreduction with Molasses Amendment	10
2.3.5	Simulation of Biofouling	10
2.3.6	Simulation of Geochemical Remediation along a Flow Path	11
2.3.7	Local Sensitivity Analysis	11
2.3.8	Global Sensitivity Analysis	12
3.0	COMPUTATION FRAMEWORK CAPABILITIES (MADS)	13
4.0	REFERENCES	15

Figures

Figure 1.1-1	Lateral model domain (yellow line) of the 3-D vadose-zone/regional-aquifer model of the Laboratory chromium site	19
Figure 1.1-2	Block diagram showing the computational grid of the chromium 3-D vadose-zone / regional-aquifer model	19
Figure 1.1-3	Block diagram showing the computational grid and locations of three hydraulic windows in the perched water zone above the regional aquifer	20
Figure 1.2-1	Block diagram showing the grid used for the regional-scale aquifer model	20
Figure 2.1-1	Block diagram showing the 3-D shape of the simulated perched water zone above the regional aquifer. In the figure, the full saturation is shown in red	21
Figure 2.1-2	Block diagram showing the 3-D structure of the simulated groundwater flow between the perched horizon and the regional aquifer when the flow occurs along three hydraulic windows as depicted in Figure 1.1-3	22
Figure 2.1-3	Maps showing “true” (top) and simulated (bottom) thicknesses of the perched saturated zone.	23
Figure 2.1-4	Simulated vs observed thicknesses of the perched-intermediate saturated zone at 11 calibration target locations.	24

Figure 2.2-1	The model-predicted (black) vs the observed (red) water-level declines (drawdowns) at the site monitoring wells.....	25
Figure 2.2-2	The model-predicted (black line) vs the observed (red dots) chromium concentrations at the site monitoring wells.....	27
Figure 2.2-4	Maps of model-predicted contaminant sources; the number, size, shape, location, start time, and concentrations of the contaminant sources are estimated automatically during the model calibration.....	31
Figure 2.2-5	Maps of model-predicted chromium concentrations in 2017 and 2018.....	32
Figure 2.2-6	Model-predicted pumping effects on the regional-aquifer water table caused by the municipal water-supply wells.	33
Figure 2.2-7	Model-predicted chromium concentrations (solid gray lines) vs observed chromium concentrations (red circles) at various site wells.	36
Figure 2.3-1	Map showing simulation of the injection of a biostimulant (molasses) and a biological inhibitor (ethanol) at R-28.	37
Figure 2.3-2	Map showing simulation of the injection of a strong chemical reducing agent (sodium dithionite) at CrPZ-3.....	38
Figure 2.3-3	CHROTRAN breakthrough concentration curves for Cr(VI) at an observation point located 10 m downstream of the injection well.....	38
Figure 2.3-4	Maps showing predicted Cr(VI) concentrations (ppb) in a heterogeneous, Cr(VI)-contaminated aquifer 470 d after treatment, under four different scenarios.....	39
Figure 2.3-5	Simulation of biomass fouling that could occur during in situ bioremediation.....	40
Figure 2.3-6	Simulation of the release of a sodium dithionite treatment solution along a 1-D flow path.....	41
Figure 2.3-7	Local sensitivity analysis of biochemical treatment model. See Table 2.3-1 for a description of the parameters.	41
Figure 2.3-8	Local sensitivity analysis of geochemical treatment model.....	42
Figure 2.3-9	Global sensitivity analysis (eFAST) of geochemical treatment model.....	42
Figure 3.0-1	An example MCMC analysis of the regional-aquifer model.....	43
Figure 3.0-2	Conceptual map of a representative site that is used to demonstrate the MADS approach to decision analysis.....	44
Figure 3.0-3	Application of BIGDT to optimize use of extraction wells to ensure contaminants in groundwater do not exceed a specified threshold at a compliance boundary.....	45

Tables

Table 2.1-1 Simulated and Observed Perched Water Zone Thickness at 11 Locations 47

Table 2.1-2 Estimated and Calibration-Target Groundwater Fluxes in Three Hydraulic Windows 47

Table 2.1-3 Simulated and Calibration-Target Chromium Travel Time through Vadose Zone 47

Table 2.1-4 Simulated and Observed Chromium Concentration at Well MCOI-5 48

Table 2.1-5 Simulated and Observed Chromium Concentration at Well MCOI-6 48

Table 2.1-6 Name, Meaning, and Estimated Values of Adjustable Parameters Estimated through
Model Calibration 49

Table 2.3-1 Description of Parameters Used for Sensitivity Analysis of Molasses Treatment Model . 50

Table 2.3-2 Description of Parameters Used for Sensitivity Analysis of Dithionite Treatment Model . 50

Appendix

Appendix A CHROTRAN: A Massively Parallel Numerical Simulator for In Situ Biogeochemical
Reduction of Heavy Metals in Heterogeneous Aquifers

1.0 DESCRIPTION OF MODELS

1.1 Three-Dimensional Coupled Vadose-Zone/Regional-Aquifer Model

The coupled vadose-zone/regional-aquifer model is designed to represent the groundwater flow and contaminant transport in the vadose zone and the regional aquifer in the chromium contamination area. Spatially, the model domain includes Mortandad, Sandia, and Los Alamos Canyons. A map of the spatial extent of the model domain is shown in Figure 1.1-1. Vertically, the model extends from ground surface to a distance of about 100 m below the regional-aquifer water table including the entire vadose zone. Figure 1.1-2 shows the entire model with hexahedral grid.

The major goals of these model analyses are the following:

1. Simulate groundwater flow and contaminant transport conditions at the site.
2. Predict the fate of contaminant mass in the vadose zone in the future, including the future impacts on the regional-aquifer concentrations.
3. Represent the system behavior under different future natural and mitigation scenarios.

To achieve these goals, a series of model analyses are being performed, which currently predominantly target Goal 1 above.

Various types of model analyses (model inversions and calibrations, sensitivity analyses, uncertainty analyses, etc.) are carried out using the open-source code MADS (Model Analysis & Decision Support) as described in section 3.0 (Vesselinov and O'Malley 2016), and forward model runs including flow and transport modeling are accomplished using the Finite Element Heat and Mass Transfer Code (FEHM) (Zyvoloski et al. 2015).

Currently, the chromium three-dimensional (3-D) coupled vadose-zone/regional-aquifer model is calibrated to

- reproduce the perching of infiltrated groundwater on the top of the Cerros del Rio (CdR) basalts within the vadose zone along the infiltration pathway. The goal here is that the model be capable of reproducing the occurrences of perched-intermediate saturation beneath Sandia and Mortandad Canyons.
- match the model-predicted saturation thickness with existing observations obtained from the monitoring wells in the perched-intermediate zone beneath Sandia and Mortandad Canyons.
- obtain groundwater and contaminant-mass fluxes through “hydraulic windows” (Figure 1.1-3) through the CdR basalts in the vadose zone, reproducing those estimated by the large-scale regional-aquifer models and informed by the sitewide geologic model presented in Attachment 3 of this compendium, “Stratigraphic and Sedimentological Studies and their Hydrogeological Features in the Chromium Investigation Area, Los Alamos National Laboratory.”
- achieve advective travel times through the vadose zone consistent with existing site data and knowledge. Based on previous model analyses and site data, the advective flow path through the vadose zone along a predominantly vertical flow path is estimated to be on the order of about 5 y; however, 3-D complex flow paths that include vertical flow through the vadose zone and horizontal flow along perching horizons may take longer (Vesselinov et al. 2013).

1.1.1 Computational Grid

This model includes new hydrostratigraphic surface contours and evaluations based on new drill hole data and the most current geologic framework model. For this model domain, the most notable difference from earlier versions is the added detail to the top of the CdR basalt (Tb4). The changes result in recognition of topography on top of the CdR that includes erosional drainage features and better characterization of the relationship between the basalts and the overlying Puye Formation and Otowi Member. Where the top of the basalt now has steeper contours, the higher elevations make for thinner Puye Formation (Tpf3) deposits. The result is that Tpf3 is thin to absent over the higher Tb4 terrain. The Guaje Pumice Bed (Qbog) and overlying Otowi tuffs (Qbof) sit directly on basalt where Tpf3 is missing.

The stacked mesh is made up of selected surfaces, and layers are divided proportionally between layer pairs for the vertical spacing. The layers in this mesh that conform to surfaces are: the land surface; the top of the basalts, Tb4, and dacites, Tvt2; and the water table surface. The bottom is flat at 1675 m elevation, about -100 m from the lowest point of water table elevations. The information is interpolated onto the grid nodes, and the nodes above the ground surface are removed.

The grid nodes are connected into tetrahedral elements based on the Delaunay criteria (George 1997). After constructing and checking the grid, attributes are assigned to grid nodes and model setup files are written for input into FEHM simulations. The numerical grid was developed using the Los Alamos Grid Generation Toolbox (LaGriT) software package (George 1997). LaGriT reports a successful matrix for this mesh with positive Voronoi volumes and zero negative coefficients on the interior of the grid (George 1997).

1.1.2 Model Setup

The model setup files are written for use in simulations using FEHM.

Based on detailed preliminary model analyses that consider computational time, convergence, and accuracy, a conceptual model accounting for water-phase-only flow and transport was adopted based on Richard's Equation. A van Genuchten relative-permeability capillary-pressure model is used, and vadose-zone permeabilities of various geologic units are represented as a function of saturation.

The initial and boundary conditions for the flow simulations in the 3-D coupled vadose-zone/regional-aquifer chromium model are set as follows:

- The perched-intermediate zones are initially assigned to constant hydrostatic pressure head and full saturation.
- The perched-intermediate water-table locations are fixed by assigning constant hydrostatic pressure head and full saturation (equal to 1) to all nodes within the areas of saturation.
- The boundary nodes that are part of the perched-intermediate groundwater zones are assigned to constant hydrostatic pressure head and full saturation.
- Permeability reduction is applied to the bottom of the perched-intermediate zones.
- Based on the information from the large-scale regional-aquifer models, three hydraulic windows are defined in the vadose zone model, allowing downward water flow through these windows from the perched-intermediate groundwater zones within the vadose zone towards the regional aquifer.

The contaminant transport of chromium is solved by the classical advective dispersion equation (ADE) as defined in the "trac" macro of the FEHM. Specifics related to the "trac" macro format and inputs are described in the FEHM manual (Zyvoloski et al. 2015). Groundwater flow and contaminant transport simulations are carried out sequentially, assuming steady-state groundwater flow conditions.

1.1.3 Calibrated Model Parameters

A series of model parameters is estimated automatically through model calibration. The model calibration is performed using a modified version of the Levenberg-Marquardt algorithm as coded in MADS (Vesselinov et al. 2016). There are a total of 23 model parameters to be estimated, including

- uniform anisotropic permeability of nodes within the three hydraulic windows (3),
- uniform anisotropic permeability of nodes above, within, and below the basalt (3),
- porosity of nodes above, within, and below the basalt (3),
- inverse of air entry head in van Genuchten formula for nodes above, within, and below the basalt (3),
- power n in van Genuchten formula for nodes above, within, and below the basalt (3),
- infiltration rates at the ground surface (1),
- canyon infiltration fluxes along Los Alamos, Sandia, and Mortandad Canyons (3),
- water influx from western boundary, which represents the unknown inflow within the regional aquifer outside of the model domain (1),
- chromium concentration at inlet nodes (1),
- time when chromium arrival into the regional aquifer begins (1), and
- time when chromium arrival into the regional aquifer ends (1).

1.1.3.1 Calibration Targets

Four types of measurements are applied as calibration targets in the perched-intermediate groundwater in the process of model inversion, including

1. thickness of perched-intermediate zones at 11 locations. Some of these locations are based on the observations at existing monitoring wells. The rest are defined based on the data analyses performed by Attachment 3 of this compendium, which accounts for the 3-D structure of geology and groundwater flow.
2. fluxes of groundwater arrival at the top of the regional aquifer estimated by the large-scale regional-aquifer model (discussed in section 1.2 of this report).
3. advective travel times through the vadose zone.
4. year-average chromium concentration from 2005 to 2016 for six wells: MCOI-4, MCOI-5, MCOI-6, SCI-1, SCI-2, and TA-53i.

1.2 Regional-Scale Aquifer Model

The Los Alamos National Laboratory (the Laboratory or LANL) site model is designed to represent the groundwater flow and contaminant transport in the regional aquifer at the Laboratory site. The current model is 3-D with a spatial model domain encompassing the entire Pajarito Plateau. The top of the model is defined by the regional-aquifer water table.

The regional-scale aquifer model spans a domain with the Jemez Mountains as the approximate western boundary and the Rio Grande as the eastern boundary. The model grid (see Figure 1.2-1) contains 766,283 nodes and 4,659,062 elements with local refinement in the area of the chromium plume. The local refinement enables the model to include accurate locations for wells within the area of the chromium plume that are used in the model calibration effort. The top of the grid matches the water table. The model represents hydrologic flow and transport using spatially heterogeneous permeability (permeability is also anisotropic) and specific storage. The model includes several areas where there is local groundwater recharge. Some of these groundwater recharge areas are also breakthrough areas (“sources”) of chromium contamination. The model also includes pumping from municipal water-supply wells and from tests performed in the area of the chromium plume.

The computational grid includes nodes that are connected into tetrahedral elements based on the Delaunay criteria (George 1997). After constructing and checking the grid, attributes are assigned to grid nodes and model setup files are written for input into FEHM simulations. LaGriT reports a successful matrix for this mesh, with positive Voronoi volumes and lack of negative coefficients on the interior of the grid; this process guarantees that the FEHM simulations using the created grid will not have numerical errors caused by poor grid quality. .

The model is built through model inversion, which is the process of establishing models that derive from actual field observations. The model properties are estimated by calibration against observed field data. Prior information about the model properties is provided in the form of prior information about plausible parameter ranges. However, these ranges are defined to be wide enough to capture existing uncertainties.

The model accounts for transients in the municipal water-supply pumping occurring on the Pajarito Plateau. The model also simulates the pumping at the chromium site during long-term field tests (e.g., the pumping at R-28, R-42, CrEX-1, and CrEX-3). The drawdown responses at site monitoring wells to the water-supply and site pumping are key pieces of information allowing characterization of aquifer heterogeneity at the chromium site during the model inversion.

The model also simulates the chromium transport using advective-dispersion partial-differential equations. The model estimates the location and shape of the contamination sources as a part of the inverse process. The model also estimates flux of infiltration from the vadose zone and contaminant concentration directly at the entry point into the regional aquifer. The other important information allowing characterization of aquifer heterogeneity at the chromium site is the chromium concentrations observed at the site monitoring wells. The chromium concentrations also provide information about the transport properties of the regional aquifer.

In summary, the model is calibrated to reproduce

- regional-aquifer water levels from existing monitoring points,
- transients in the hydraulic drawdowns in the regional aquifer caused by water-supply pumping and project-related pumping activities, and
- chromium concentration transients observed in regional-aquifer monitoring wells.

In total, there are more than 143,549 calibration targets, which include 196 transient chromium concentration values; 109,108 transient drawdown values caused by the municipal water-supply pumping; and 34,421 transient drawdown values caused by the pumping at the chromium site. Different weights are applied to different calibration targets to reflect the importance and magnitude of the calibration values.

It is important to note that this calibration data set does not include 2016 and 2017 data. A new calibration data set, which includes the 2016 data, has 479,872 entries. Even more will be added in the calibration process when the 2017 data are added in the model calibration process.

The model parameters estimated in the calibration process are

- aquifer permeability (accounting for 3-D anisotropy and heterogeneity) (137 parameters),
- aquifer storativity (accounting for 3-D heterogeneity) (74 parameters),
- aquifer transport properties (advective transport porosity, dispersivities) (4 parameters),
- characteristics of contamination sources (location, size, strength, etc.) (19 parameters), and
- model internal and external boundary conditions (8 parameters).

The contaminant transport of chromium is solved by the classical ADE as defined in the “trac” macro of the FEHM. Specifics related to the “trac” macro format and inputs are described in the FEHM manual (Zyvoloski et al. 2015).

In total, 242 model parameters are calibrated. The model calibration is performed using a modified version of the Levenberg-Marquardt algorithm as coded in MADS (Vesselinov et al. 2016).

Various types of model analyses (model inversions and calibrations, sensitivity analyses, uncertainty analyses, etc.) are carried out using MADS (Vesselinov and O'Malley, 2016), and forward model runs, including flow and transport modeling, are accomplished using FEHM (Zyvoloski et al. 2015).

1.3 Biogeochemical Remediation Model

The primary goal of in situ remediation of chromium-contaminated groundwater is to geochemically reduce hexavalent chromium, [Cr(VI)], to its immobile, benign oxidation state, trivalent chromium [Cr(III)]. A multi-dimensional reactive transport model of relevant biogeochemical processes is valuable for evaluating the deployment of various amendments for in situ remediation in the aquifer. To this end, CHROTRAN (Chromium Transport Bio-Chemical Remediation Code) was developed as a comprehensive modeling tool used to evaluate potential bioremediation strategies for chromium. CHROTRAN provides a framework for modeling biostimulation, biodegradation, chemical degradation, growth inhibition, and biocide effects. There have previously existed no general software tools appropriate for modeling all of these complex, interacting processes. CHROTRAN is optimized for modeling biogeochemical remediation of Cr(VI), but it is of sufficient generality that it may be used for bioremediation of other metals and a wide range of organic contaminants. Appendix A of this attachment includes a detailed description of CHROTRAN capabilities. The following section describes the use of the latest CHROTRAN release (version 1.2) for analysis of potential in situ remediation of chromium. Biochemical remediation of chromium using molasses and geochemical remediation using sodium dithionite are described separately below.

The following is further addressed in Appendix A. The CHROTRAN mathematical model is provided as a convenient, open-source software package based upon the existing code, PFLOTRAN (Lichtner, 2017a 2017b), which has modularity and “reaction sandbox” capability that allows model implementation without changes to its flow and transport code. CHROTRAN can harness the existing capabilities of PFLOTRAN, which allows for simulations of complex models with a large number of computational cells and degrees of freedom. The Fortran source-code files for CHROTRAN, along with input files for the examples, are freely available at <https://github.com/chrotran/release>. Additional information regarding CHROTRAN is available at <http://chrotran.lanl.gov>.

1.3.1 Using CHROTRAN to Model Bioamendment Remediation

In situ biochemical remediation of chromium-contaminated groundwater using molasses as a biostimulant is currently undergoing pilot-scale testing at the Laboratory's chromium site. The injection of molasses can achieve remediation objectives because it can initiate direct reduction by microbes (Wang and Xiao 1995; Okeke 2008; Hansen et al. 2017a) and indirect reduction by substrates such as ferrous iron and sulfide compounds resulting from anaerobic respiration. The biochemical model includes full dynamics for all relevant species that occur both in situ and in the treatment solution. Refer to Appendix A of this attachment and Hansen et al. (2017b) for a full description of the biochemical treatment model. Since CHROTRAN is optimized to model chromium remediation, the full suite of biochemical processes implemented in CHROTRAN is used to model this treatment method. In the exploratory models conducted for bioremediation to date, the following species, whose dynamics are governed by physical and biochemical aquifer processes, were considered:

- **Cr(VI)**, the contaminant to be remediated,
- **Molasses**, a carbon source that serves as the biostimulant and abiotic reductant,
- **Biomass**, a collection of microbial cells and their associated extracellular material,
- **Ethanol**, a conservative amendment that serves as a microbial growth inhibitor, and
- **Biocide**, an amendment that kills excess biomass and is consumed in the process.

The injection of a biostimulant solution into chromium-contaminated groundwater results in the following reactions, which are modeled in CHROTRAN. After a molasses solution is injected into the groundwater, its transport is retarded because of adsorption onto sediments. This is a reversible process and is modeled using a mobile-immobile mass transfer reaction. The direct (abiotic) reduction of Cr(VI) occurs with molasses as the electron donor in an oxidation-reduction reaction. This reaction is known to possess fast kinetics (Chen et al. 2015; Hansen et al. 2017b) and can use molasses in either the mobile or immobile phase. Bioreduction is a far more complex phenomenon that could involve multiple cell-metabolic or extracellular processes. In CHROTRAN, these processes are abstracted into a single reaction that is controlled by the concentration of Cr(VI) and biomass. Biomass concentration is controlled by a multitude of other reactions, which are explicitly modeled and are now summarized. Biomass growth occurs as it consumes molasses. However, the growth rate may be slowed because of cell stress induced by biomass crowding. Similarly, the inclusion of ethanol in the treatment solution inhibits excessive biomass growth. Natural death and decay return biomass to background levels if it is left unstimulated. Finally, biomass death can also be induced through the inclusion of a biocide as an amendment. The inclusion of either a bio-inhibitor or biocide in the treatment solution is beneficial if excessive growth near the injection well poses the risks of preventing the dispersal of molasses or causing clogging (i.e., a decrease in porosity/permeability). The bio-clogging effect is also explicitly modeled; the degree of clogging in a certain region depends upon the local biomass concentration.

1.3.2 Using CHROTRAN to Model Chemical Remediation

In situ geochemical remediation of chromium-contaminated groundwater is also currently undergoing pilot-scale testing at the Laboratory's chromium site. The injection of sodium dithionite, a strong chemical reductant, is capable of reducing iron in sediments from ferric iron [Fe(III)] to ferrous iron [Fe(II)], which can be present on mineral surfaces within the aquifer or occur in the aqueous phase. Surface-bound Fe(II) becomes a long-term, stationary source of reductant capable of geochemically reducing dissolved Cr(VI) to Cr(III). This process is referred to as in situ redox manipulation (ISRM). CHROTRAN is capable of modeling the entire process of ISRM using sodium dithionite. Along with simulation of in situ reduction of Cr(VI), it is also capable of modeling other important processes that may influence remediation, such

as mineral precipitation/dissolution, aqueous speciation, and pH. Because of the oxic nature of the regional groundwater at the site, relevant reactions with dissolved oxygen are also modeled. Refer to Appendix A of this attachment for a full description of the dithionite geochemical remediation model.

The specific geochemical reactions that enable simulation of in situ dithionite treatment using CHROTRAN are summarized here. Dissolved dithionite is known to be unstable and is prone to degradation (i.e., disproportionation), especially in the presence of sediments (Amonette et al. 1994). Thus, a dithionite degradation reaction is included in the model. The kinetics of this reaction is higher at low pH, so the injectant is buffered with bicarbonate, and the associated buffering reactions are also included in the model. Dithionite is also highly reactive with dissolved oxygen, so a bimolecular reaction that consumes both of these species is also included. Injected dithionite that does not degrade or react with oxygen is available to reduce iron associated with aquifer sediments, which results in the formation of an ISRM zone with Fe(II) bound to sediments. Fe(II) can subsequently reduce any dissolved oxygen or Cr(VI) that passes through the ISRM zone. Chromium that is reduced to Cr(III) quickly precipitates as Cr(OH)₃(s), a highly insoluble secondary phase. Finally, the groundwater is assumed to be in equilibrium with calcite. These reactions are primarily assumed to be kinetically limited, with the exception of aqueous pH buffering effects. Kinetic rate laws were formulated after an extensive literature review (see Appendix A of this attachment). Relevant geochemical species include oxidants [dissolved oxygen, Cr(IV) as HCrO₄], the injected reductant and associated degradation products (dithionite, sulfate, sulfite, and thiosulfate), Fe(II) bound to mineral surfaces, pH and pH buffers [H⁺, OH⁻, CO₃⁻², H₂CO₃(aq)], minerals, [Fe(OH)₃(s), Cr(OH)₃(s), CaCO₃(s)], and other relevant dissolved ions (Na⁺, Fe⁺³, Ca⁺², Cr⁺³).

2.0 MODEL RESULTS AND UNCERTAINTY ANALYSES

2.1 Three-Dimensional Coupled Vadose-Zone/Regional-Aquifer Model

Figure 2.1-1 shows the simulated perched-intermediate water zone; Figure 2.1-2 shows the simulated perched-intermediate water zone with three hydraulic windows; and Figure 2.1-3 shows the observed and simulated thicknesses of the perched-intermediate water zone. The model reproduces the thickness of the perched-intermediate zones on top of the CdR basalts, and the predicted saturation thickness matches reasonably well with existing observations from monitoring wells. Here, the applied modeling approach makes a simplifying assumption that the top of the basalt is the perching horizon, even though some of the significant perching takes place near the bottom of the basalt (e.g., SCI-2, MCOI-5, and MCOI-6) as well. Still, the model predicts increased saturation within the basalts as well, because of grid vertical resolution, which ranges between 10 and 20 m in the area of the basalts.

The simulated thickness is quantitatively compared with data at the 11 calibration-target locations, as shown in Table 2.1-1 and Figure 2.1-4. The data applied to calibrate the model and reproduce the thickness of the perched-intermediate zone of saturation is extracted from spatial interpretation of the existing site data. The simulated fluxes in three hydraulic windows and chromium travel time through the vadose zone are calibrated well with observations (Tables 2.1-2 and 2.1-3). The simulated concentrations compare relatively well with observations at wells MCOI-5 and MCOI-6 (Tables 2.1-4 and 2.1-5). Table 2.1-6 lists the 23 adjustable parameters and their estimated values obtained through model inversions.

The site 3-D coupled vadose-zone/regional-aquifer model is currently well calibrated to reproduce the current groundwater flow in the subsurface. The model reproduces the spatial shape of the perched horizons, and the simulated fluxes of groundwater arrival at the top of the regional aquifer are consistent with the regional-aquifer model discussed in section 1.2. It is important to note that the regional aquifer is calibrated using much more data than the model discussed here. The regional aquifer is calibrated against transient water levels and chromium concentrations observed at more than 15 regional monitoring wells and accounts for municipal and field-test pumping conducted at the site.

However, the current model is overpredicting the mobile-phase [Cr(VI)] mass in the vadose zone as estimated from pore water and perched-intermediate zone water-quality data. Additional model analyses are being performed to improve the model calibration to calculate more accurately the estimated Cr(VI) mass in the vadose zone.

2.2 Regional-Scale Aquifer Model

The groundwater flow and contaminant transport in the regional-scale aquifer model are calibrated by exploring (1) aquifer heterogeneity, (2) contaminant source attributes (e.g., location, size, and contaminant concentration at multiple source zones representing dripping of contaminant from the vadose zone into the regional aquifer), and (3) properties of groundwater flow and contaminant transport in the regional aquifer (including aquifer dispersivity). The groundwater flow and contaminant transport in these models are currently calibrated against all the transient data for the hydraulic pressures and chromium contaminant concentration observed in the regional aquifer. The calibration is performed using advanced optimization methods running in parallel and coded in MADS (see section 3 of this report).

Figures 2.2-1 and 2.2-2 illustrate the calibration of the model to the water-level and chromium concentration data from monitoring wells. Figure 2.2-3 presents the model-predicted heterogeneity and anisotropy in the hydraulic conductivity along the top of the regional aquifer. The anisotropy in hydraulic conductivity along the x, y and z axes are shown in Figure 2.2-3a, 2.2-3b, and 2.2-3c, respectively. The model estimates the aquifer heterogeneity and anisotropy based on the calibration data. The hydraulic conductivity is conditioned on the prior information about aquifer heterogeneity based on past pumping tests.

Figure 2.2-4 depicts the model-predicted contaminant sources (breakthrough areas) at the top of the regional aquifer. The number, size, shape, location, start time, and concentrations of the contaminant sources are estimated automatically during the model calibration. No prior knowledge is applied. The model estimates the contaminant source properties based on the provided calibration data. The figure shows the estimated four contaminant sources, the start times (in calendar years), their size, and concentrations (as log transformed values).

Figure 2.2-5 presents two snapshots of the model-predicted chromium concentrations in 2017 and 2018. The concentrations do not depict the mixed concentrations that might be present in a monitoring well, but rather they are the potential concentrations in an extremely thin layer right at the water table and could not be measured in any type of real monitoring well. They should effectively be considered relative concentrations with dispersion from the initial breakthrough locations. The model predictions are based on the best calibrated model and do not depict existing uncertainties.

Figure 2.2-6 shows the model-predicted pumping effects caused by the municipal water-supply wells. The figure shows the model-predicted pumping effects on the regional-aquifer water table caused by the municipal water-supply wells. The changes in the hydraulic heads presented in Figure 2.2-6 are relative to the model-predicted water levels circa May 2011. In the period between May 2011 and December 2014, some of the municipal wells are experiencing only rebounds, because of decreases in the water-supply pumping (e.g., PM-2 and O-4). PM-5 is observing only pressure declines. PM-4 has rebound and decline periods. PM-3 and PM-1 maps are not shown in Figure 2.2-6 because these wells are predicted to produce no drawdown of the regional water table at the chromium site.

Figure 2.2-7 summarizes the model-predicted chromium concentrations vs observed chromium concentrations at various site wells. Note that these predictions are based on a model that did not have CrIN-6 data as a calibration target. The best estimate of the chromium concentration at CrIN-6 in 2017 is about ~250 ppb, which matches well with the actual chromium concentrations observed at CrIN-6.

2.3 Biochemical Remediation Model

The following example studies illustrate the ability of CHROTRAN to simulate biochemical and geochemical remediation of chromium-contaminated groundwater and how it may be used to aid in the design of both pilot-scale field studies and long-term remediation strategies. In these studies, the background and inflow Cr(VI) concentration are assumed to be constant. The inflow Cr(VI) concentration is equal to the background concentration. More specific model terms and constraints based on field observations of ongoing pilot-scale studies can eventually be used to estimate the effects of in situ remediation strategies.

2.3.1 Biochemical Remediation with Molasses

Figure 2.3-1 shows the results of a two-dimensional (2-D) case study that uses CHROTRAN to simulate injection of a molasses treatment solution at the site (in the presented case, injection is performed at R-28). The purpose of this study is to estimate effects (spatial and temporal) of an injection of a biostimulant on Cr(VI) concentrations at a well downstream (e.g., CrIN-1). In the simulation, preferential flow occurs with a mean pore water velocity of 1 m/d (~3.3 ft/d) to the east of the injection location. A 0.01 M molasses treatment solution is injected at R-28 for 20 d at a flow rate of 10 gallons per minute (gpm). The solution also includes ethanol as a biological inhibitor, and the abiotic reduction of Cr(VI) by molasses is modeled. The bioreduction rate is assumed to be fast, so biomass (i.e., bioreduction) plays an important role in Cr(VI) remediation. The figure shows the concentration of Cr(VI) removed [i.e., reduced to Cr(III)] as a result of bioremediation 10 mo after the injection. A large amount of Cr(VI) (3 kg) has been converted to Cr(III) by this time, and relatively fast pore water velocities result in a large zone of influence downstream of the injection well. However, additional injections would be required and Cr(VI) concentrations would have to be measured for a longer period of time before significant declines in Cr(VI) concentrations are observed at CrIN-1.

2.3.2 Geochemical Remediation with Sodium Dithionite

Figure 2.3-2 shows the results of a 2-D case study that uses CHROTRAN to simulate injection of a buffered sodium dithionite treatment solution (in the presented example, injection occurs at the CrPZ-3 location). The purpose of this study is to estimate the effects of an injection of a chemical reductant on Cr(VI) concentrations at a well downstream (e.g., R-42). In the simulation, preferential flow occurs with a mean pore water velocity of 0.1 m/d (~0.33 ft/d) to the east. A 0.01 M dithionite treatment solution is injected for 20 d at a flow rate of 10 gpm. The figure shows the concentration of Cr(VI) removed [reduced to Cr(III)] 11 mo after the injection. Although a large amount of Cr(VI) (0.6 kg) has been removed by this time, relatively slow pore water velocities prevent the migration of the treated groundwater to a substantial distance downstream, resulting in no change in Cr(VI) concentration at R-42 within the modeled duration.

2.3.3 Comparison of Molasses and Dithionite Injection in a Hypothetical Scenario

The CHROTRAN model enables comparisons of various deployment strategies. The results of model runs can be used to inform deployment strategies, spatial density of deployment locations, frequency of required redeployment, and expected longevity of treatments. Figure 2.3-3 shows the results of a 2-D study that compares CHROTRAN biochemical (molasses) and geochemical (dithionite) remediation. A treatment solution is injected for 20 d, and chromium concentrations are monitored at a single observation

point downgradient of the injection well. To evaluate the performance of the different remediation strategies, the concentration of either molasses or dithionite in the treatment solution is varied. Similarities in the initial decrease in Cr(VI) concentrations in all cases is due to dilution [the treatment solution has 0 ppb Cr(VI)]. Despite dilution effects, the figure shows that the Cr(VI) concentration at the observation well decreases for all of the test cases, albeit to varying degrees. Naturally, the remediation schemes with the highest concentration of amendment provide the most effect treatment of Cr(VI). The initial, partial rebound in Cr(VI) that occurs in some of the bioremediation simulations is due to the fact that, in these cases, abiotic reduction of Cr(VI) by molasses alone only provides partial treatment and biomass is not yet well established, causing minimal bioreduction in the period shortly after injection. This study shows the ability of CHROTRAN to model both biochemical and geochemical remediation and its potential value as a decision-support tool to aid in the design of effective in situ remediation strategies for chromium-contaminated groundwater.

2.3.4 Relative Impact of Abiotic Reduction and Bioreduction with Molasses Amendment

Figure 2.3-4 shows the simulated co-injection of molasses (electron donor) and ethanol (nonlethal bio-inhibitor) into a single well drilled in a heterogeneous aquifer. This study explores the competition between direct abiotic reduction of Cr(VI) by molasses and bio-reduction of Cr(VI), which exists since both reduction pathways consume the electron donor, along with the impact of suppressing the biomass growth. Four related simulations are performed on the same 2-D heterogeneous hydraulic conductivity field with the same injection duration; they differ in chemical kinetics, only. Both zero and moderate direct abiotic reduction are considered, as well as injection with and without ethanol. The injection fluid chemistry always has Cr(VI) concentration equal to the initial Cr(VI) concentration, ensuring that no chromium disappearance is due to dilution. The figure shows that little persistent reduction due to biomass alone occurs with the model parameters specified (the bioreduction rate is assumed to be slow), although ethanol co-injection does increase the biomass footprint, which has a noticeable and persistent effect. By contrast, the rapid abiotic reduction of Cr(VI) by molasses has more impact, because molasses has a large reducing capacity and has a retardation factor of around 150 (Shashidhar et al. 2006), allowing for the formation of a persistent permeable reactive zone around the well. Better performance in the presence of ethanol occurs because ethanol co-injection prevents excessive consumption of molasses by the biomass, allowing molasses to reduce Cr(VI) over a larger area.

2.3.5 Simulation of Biofouling

Figure 2.3-5 shows simulated hydraulic conductivity reduction that may occur in the aquifer because of biofouling and the use of biocide associated with introduction of a biostimulant. Initially, an acetate biostimulant is injected into a well within a 2-D, homogeneous permeability domain. The acetate amendment is subsequently replaced with the biocide for the remainder of the simulation. The figure shows a sequence of quiver plots representing the velocity field at nine points in time superimposed on the biomass concentration. During the first 400 d of the simulation, biomass concentration grows in the vicinity of the well, causing a drop in hydraulic conductivity until no influx occurs there. Only ambient flow is apparent, flowing around the impermeable barrier near the well. At this point, the biomass has become useless for bioremediation, as contaminated groundwater no longer travels through it. However, at 400 d, a biocide is introduced into the injection fluid and effectively eliminates biomass in the vicinity of the well. The region containing biocide is relatively sterile and grows outward until the biomass concentration approaches background, and the initial flow regime is recovered at 416 d. This cycle could be performed indefinitely to counteract the negative impact of biofouling and increase remediation performance.

2.3.6 Simulation of Geochemical Remediation along a Flow Path

Figure 2.3-6 shows the simulated release of a sodium dithionite solution along a contaminated, one-dimensional (1-D) flow path. Four different CHROTRAN simulations that varied in the concentration of sodium dithionite in the injectant were conducted. Figure 2.3-6A shows the variation of observed Cr(VI) concentrations through time at an observation well located 10 m downstream of the injection location. The figure shows that remediation performance is heavily dependent upon the dithionite concentration. Figure 2.3-6B shows the spatial distribution of reduced Fe(II) in aquifer sediments at several times after the injection of a high concentration of dithionite solution. The figure shows that a rebound in observed Cr(VI) to background levels occurs as the source of Fe(II) reductant is depleted. In this model, after 1 yr, most of the Fe(II) has been removed from the system (passivated), indicating that a re-injection of amendment would be required.

2.3.7 Local Sensitivity Analysis

Local sensitivity analysis was performed on the chromium remediation model using the open-source code MADS (<http://mads.lanl.gov>), a model analysis and decision support tool written in the high-performance computing language Julia (see section 3 of this report). Sensitivity analyses are important to identify model parameters that are critical for the obtained model predictions. In general there are local and global sensitivity methods. The local sensitivity methods evaluate parameter sensitivity in the vicinity of the optimal parameter data set; typically, this optimal parameter data set is identified through model inversion or based on literature data. The global sensitivity analyses explore the importance of model parameters within predefined parameter ranges. Again, these parameter ranges can be identified through model inversion or based on literature data.

The method uses local gradients of the model output as model parameters that are simultaneously perturbed (Gustafson et al. 1996; Vesselinov 2000; Vesselinova et al. 2016). These gradients are used to calculate a Jacobian (\mathbf{J}) matrix with dimensions that correspond to the number of model parameters and the desired number of model outputs. A covariance matrix is then computed as $[\mathbf{J}^T\mathbf{J}]^{-1}$ and is analyzed using eigenanalysis. The estimated covariance matrix in this case represents the local parameter uncertainty and sensitivity related to the predefined initial guesses for the model parameters. In the more general case, when calibration data are available, the covariance matrix represents the local parameter uncertainty and sensitivity related to the estimated optimal model parameters representing the calibration data. The computed eigenvectors represent the contribution of each model parameter to the model output during perturbation of all parameters, and the dominance of each eigenvector is inversely related to its computed eigenvalue. Eigenvectors are ordered by magnitude of the respective eigenvalues. The more important eigenvectors are to the left. Parameters with large absolute eigenvector components (close to 1 and -1) are more dominant in characterizing the respective eigenvector. This method also quantifies correlation between parameters. Parameters that have an important contribution in the same eigenvector are correlated. Positive correlation occurs if the contributions of these parameters possess the same sign, and negative correlation occurs if the signs are opposite. Local sensitivity analysis was conducted separately for both the biochemical remediation model (molasses amendment) and the geochemical remediation model (dithionite amendment).

Table 2.3-1 describes the model parameters and Figure 2.3-7 shows the results of the biochemical remediation model local sensitivity analysis. Based upon the first two eigenvectors in Figure 2.3-7, the model appears to be most sensitive to perturbation of λ_{B_1} (biomass growth rate constant) and λ_{B_2} (biomass natural decay rate constant). It follows that λ_{B_1} and λ_{B_2} would be the most well-constrained parameters during model calibration. These parameters are important because they control the amount of biomass present in the system; biomass is required for bio-reduction of Cr(VI) to occur. Based upon eigenvectors 3–6 in Figure 2.3-7, moderately sensitive/constrained parameters include Γ_{CD} (abiotic reduction rate

constant), K_D (the molasses Monod constant [Monod 1949]), K_I (bio-inhibitor Monod inhibition constant [Monod 1949]), and λ_C (the chromium bio-reduction rate constant). The model is only moderately sensitive to perturbations of Γ_{CD} because it only controls chromium reduction when molasses is present in the system (i.e., during or immediately after injection). Both K_D and K_I influence the biomass growth rate, but the model appears to be less sensitive to these parameters as opposed to the kinetic rate constants in the biomass rate expressions (i.e., λ_{B_1} and λ_{B_2}). The moderate sensitivity to λ_C indicates that the bio-reduction rate expression is more strongly controlled by biomass concentration. Based upon eigenvectors 7 and 8 in Figure 2.3-7, the least sensitive and most unconstrained parameters are K_B (biomass Monod inhibition constant [Monod 1949]) and K_C (chromium bio-reduction Monod constant [Monod 1949]).

Table 2.3-2 describes the model parameters and Figure 2.3-8 shows the results of the geochemical remediation model local sensitivity analysis. Based upon the first eigenvector in Figure 2.3-8, the model appears to be most sensitive to perturbation of $k_{S_2O_4^{2-}disp}$ (dithionite degradation rate constant) and $k_{\equiv Fe(II)-HCrO_4^-}$ [$\equiv Fe(II)$ reduction of chromium rate constant]. It follows that $k_{S_2O_4^{2-}disp}$ and $k_{\equiv Fe(II)-HCrO_4^-}$ would be the most well-constrained parameters during model calibration. Based upon eigenvectors 2–5 in Figure 2.3-8, moderately sensitive/constrained parameters include $k_{S_2O_4^{2-}O_2(aq)}$ (dithionite reduction of oxygen rate constant), $k_{S_2O_4^{2-}Fe(OH)_3(s)}$ [dithionite reduction of $Fe(III)$ sediments rate constant], $k_{\equiv Fe(II)-O_2(aq)}$ [$\equiv Fe(II)$ reduction of oxygen rate constant], and $wt\%_{Fe(OH)_3(s)}$ [weight percent of total solids that are $Fe(III)$ sediments]. The parameter $k_{S_2O_4^{2-}disp}$ is important because it directly controls the mass of nondegraded dithionite that is available to create the ISRM zone. The parameter $k_{\equiv Fe(II)-HCrO_4^-}$ is important because it controls the rate at which the ISRM zone reduces $Cr(VI)$. Thus, model analysis reveals that the combined influence of $k_{S_2O_4^{2-}disp}$, $k_{\equiv Fe(II)-HCrO_4^-}$, and their associate reactions provides the strongest control on ISRM behavior and, thus, the overall effectiveness of in situ geochemical remediation. The parameters $k_{S_2O_4^{2-}O_2(aq)}$ and $k_{\equiv Fe(II)-O_2(aq)}$ control the kinetics of reactions that involve oxygen. The moderate sensitivity of the model to perturbation of these parameters indicates that the mass of dissolved oxygen is not sufficient to substantially alter ISRM behavior, despite the assumption that the aquifer is saturated with respect to oxygen. The parameters $k_{S_2O_4^{2-}Fe(OH)_3(s)}$ and $wt\%_{Fe(OH)_3(s)}$ control the kinetics of reactions that involve $Fe(III)(s)$. The moderate sensitivity of the model to perturbation of these parameters could indicate that even extremely small amounts of $Fe(III)$ minerals are sufficient to create an ISRM zone and provide a long-term capacity to reduce $Cr(VI)$, which would make ISRM viable over a wider range of site geologies.

2.3.8 Global Sensitivity Analysis

The extended Fourier Amplitude Sensitivity Test (eFAST; Saltelli et al. 1999) was employed for global sensitivity analysis of the geochemical (dithionite) remediation model. This variance-based method allows for efficient analysis of both first-order (i.e., main effect) and higher-order (i.e., total effect) sensitivity indices for each model parameter. The main effect measures the output variance caused when a single model parameter is perturbed and is averaged over variations in the other model parameters (Sobol, 1993). The total effect measures the output variance caused as a single model parameter is perturbed but is also averaged over variations in the remaining model parameters. Results of global sensitivity analysis of the geochemical remediation model using eFAST are shown in Figure 2.3-9. The figure visualizes results by plotting the total and main effect of each parameter over simulated time. Both the total and main effect scale relative sensitivity such that calculated values for each parameter range from 0 to 1. At a given time, the total and main effect values that approach 1 are classified as the most influential parameters. Conversely, the total and main effect values close to 0 indicate less influential parameters. If the shapes of the total and main effect curves are similar, the parameters are more independent. Differences in the shapes of the total and main effect curves could indicate that the analyzed parameters are correlated.

Figure 2.3-9 shows that both the total and main effect reaffirm local sensitivity analysis results. The results demonstrate a strong dependence of the geochemical remediation model on $k_{S_2O_4^{-2}\text{-disp}}$ and $k_{\equiv Fe(II)\text{-HCrO}_4^-}$. This analysis also indicates that the model appears to be less sensitive to $k_{S_2O_4^{-2}\text{-O}_2(aq)}$, $k_{\equiv Fe(II)\text{-O}_2(aq)}$, and $k_{S_2O_4^{-2}\text{-Fe(OH)}_3(s)}$, which is also similar to the local sensitivity analysis. However, the global sensitivity analysis shows that the model is highly sensitive to $wt\%_{Fe(OH)_3(s)}$, unlike the local sensitivity analysis, especially at later times. Comparing the total and main effects reveals the curve shapes for the most influential parameters ($k_{S_2O_4^{-2}\text{-disp}}$, $k_{\equiv Fe(II)\text{-HCrO}_4^-}$, $wt\%_{Fe(OH)_3(s)}$, and $k_{S_2O_4^{-2}\text{-Fe(OH)}_3(s)}$) are similar, indicating that these parameters behave independently. Analysis of the time-dependence of the relative sensitivity of each parameter in Figure 2.3-9 provides additional insight that can be used to aid in experimental design. The most striking result shown in the figure is the significance of multiple parameters at ~15 d. Fifteen days marks the time at which the release of the amendment solution containing dithionite ceases. Global sensitivity analysis reveals that this time period is of critical importance, and possibly the most difficult to interpret, because of the influence of multiple parameters (and thus their associated reactions). In an actual experiment, increasing the sampling interval during this time could provide valuable additional data. These data could then be used to more accurately calibrate the model and interpret experimental results. Towards the end of the simulations, only two parameters ($k_{S_2O_4^{-2}\text{-disp}}$ and $wt\%_{Fe(OH)_3(s)}$) control model behavior. If model calibration is successful using the early-time data from an experiment, it follows that the sampling interval can be decreased at late times. If model calibration using early-time data is questionable, late-time data could then be used to more accurately constrain parameter values for $k_{S_2O_4^{-2}\text{-disp}}$ and $wt\%_{Fe(OH)_3(s)}$. Used in this manner, global sensitivity analysis becomes a valuable decision support tool that can help lead to a better understanding of the remediation of chromium-contaminated groundwater at the Laboratory and improve confidence in predictive capabilities.

3.0 COMPUTATION FRAMEWORK CAPABILITIES (MADS)

MADS is a Laboratory-developed open-source code (<http://mads.lanl.gov>). MADS is designed to perform various types of model analyses including uncertainty quantification, sensitivity analyses, machine learning, model selection, and decision analyses.

The source code is available on github (<https://github.com/madsjulia>). A user manual and references to the publications presenting the theory behind the MADS algorithms are publicly available online at <http://mads.lanl.gov> and <http://madsjulia.github.io/Mads.jl>. MADS is easy to install on any computer (PC/Mac/Linux; laptops/HPC clusters/cloud frameworks). MADS is written in Julia (<http://julia-lang.org>) and can be internally or externally coupled with any existing external model simulator such as FEHM, PFLOTRAN, CHROTRAN, ModFlow, MT3D, etc. MADS is specifically designed for high-performance computing and includes advanced tools for automatic bookkeeping of model results for efficient restarts and reruns; these MADS capabilities are critical for the model analyses performed for the chromium projects because a typical model analyses such as a model calibration requires more than 20 d to be performed in parallel using 1024 processors and frequently requires restarts. The sensitivity, uncertainty, and decision analyses require even more computational time.

Unit-testing and code-coverage analyses are performed periodically to improve code testing, verification, and validation. New unit tests are regularly added and required with addition of new features. New unit tests are also implemented when bugs are found. Unit tests are automatically executed with each change of the code submitted at the MADS website using a cloud service. The unit test results are publicly available at <https://travis-ci.org/madsjulia>. Code coverage analyses are also performed automatically with each change of the code submitted at the MADS website to the master branch using a cloud service. The coverage results are also publicly available at <https://coveralls.io/github/madsjulia>.

All the MADS functions are fully documented at <http://madsjulia.github.io/Mads.jl/Modules/Mads>. The website lists all the MADS modules and functions. All the input and output parameters of all the MADS functions are provided as wells. Examples are also provided.

All the MADS unit tests can be executed through the MADS command `Mads.test()` under Julia. `Mads.test()` executes all the unit tests and performs comparisons against "gold standard" results stored in "gold standard" files.

MADS has been applied to perform analyses related to various types of tasks related to the Chromium project. These include

- Model analysis
 - ❖ Model calibration
 - ❖ Sensitivity analysis
 - ❖ Uncertainty quantification
 - ❖ Model selection and averaging
 - ❖ Model reduction
- Surrogate modeling based on advanced machine-learning methods
- Risk assessment and decision analysis
 - ❖ Monitoring well siting
 - ❖ Siting of injection and extraction wells
 - ❖ Evaluation of contamination risks associated with chromium concentrations in the regional aquifer
 - ❖ Evaluation of intermediate measures and remedial scenarios

MADS contains advanced unique capabilities for quantifying uncertainty and supporting decision-making under uncertainty. Similar capabilities are not available in any of the other tools frequently used for similar analyses such as DAKOTA (<https://dakota.sandia.gov>), PSUADE (<https://computation.llnl.gov/projects/psuade-uncertainty-quantification>), PEST (<http://www.pesthomepage.org>), and UCODE (<http://igwmc.mines.edu/freeware/ucode>).

Figure 3.0-1 shows the uncertain chromium transients predicted from a Markov Chain Monte Carlo (MCMC) analysis of the regional-aquifer model. MADS can leverage these uncertainty quantification capabilities to enable robust decision making. Figure 3.0-1 is an example that is directly relatable to the chromium contamination.

A simple demonstration of uncertainty analysis capabilities of MADS can be also found online at http://madsjulia.github.io/Mads.jl/Examples/bayesian_sampling.

MADS also includes a unique Bayesian Information-Gap Decision Theory (BIGDT) capability that leverages the MCMC framework discussed above. This method is applied to a problem that is representative of the Laboratory's chromium plume. Figure 3.0-2 shows a schematic map of a hypothetical representative site that is used to demonstrate application of BIGDT to a decision scenario. The representative site shares some commonalities with the Laboratory's chromium site including a network of ~30 monitoring wells surrounding the contaminant plume, a compliance boundary where concentrations must be kept below a concentration threshold, supply wells in the vicinity of the contaminant plume, three extraction wells that can be used in various combinations for pump-and-treat

near the boundary, and uncertain model parameters that govern the flow of groundwater and transport of the contaminant. In this problem, three potential remedial options are considered. The first involves using all three extraction wells. The second involves only using the central extraction well. The third involves using the two outer extraction wells but not the central extraction well.

Figure 3.0-3 shows the results of applying BIGDT to this decision scenario. As expected, the first remedial option using all three extraction wells provides the most robustness against uncertainty. Somewhat surprisingly, the second option (use of central extraction well only) provides more robustness against uncertainty than the third option (use of the two outer extraction wells). This result arises from the fact that the central well is the crucial well for successful pump-and-treat here. When only the two outer wells are used, the contaminated groundwater can flow between them, resulting in an exceedance of the concentration threshold across the hypothetical compliance boundary. The following conclusions can be drawn from this analysis:

1. The approach that used only the central extraction well provides almost as much robustness against uncertainty as the approach that uses all the extraction wells, making it a potentially viable option. The decision to use all the extraction wells could be justified if additional robustness is desired and could be seen as a conservative decision.
2. Using the two outer extraction wells without using the central extraction well would not meet remediation goals, and employing this remedy would be a bad decision. It is expected to fail, and provides no robustness against uncertainty. If a two-well remedy is desired, an alternative design should be considered such as employing two closely spaced wells straddling the original central well location.

An additional simple decision analyses demonstration is available online at http://madsjulia.github.io/Mads.jl/Examples/bigdt/source_termination.

More examples of MADS applications can be viewed and downloaded at <http://madsjulia.github.io/Mads.jl/Examples>.

4.0 REFERENCES

The following reference list includes documents cited in this report.

- Amonette, J.E., J.E. Szecsody, H.T. Schaef, Y.A. Gorby, J.S. Fruchter, and J.C. Templeton. "Abiotic Reduction of Aquifer Materials by Dithionite: A Promising In-Situ Remediation Technology," Pacific Northwest Laboratory technical report PNL-SA-24505 (1994).
- Chen, Z.F., Y.S. Zhao, J.W. Zhang, and J. Bai. "Mechanism and Kinetics of Hexavalent Chromium Chemical Reduction with Sugarcane Molasses," *Water, Air, & Soil Pollution*, Vol. 226, pp. 1–9, <https://doi.org/10.1007/s11270-015-2629-6>, (2015).
- George, D. "Unstructured 3D Grid Toolbox for Modeling and Simulation," Los Alamos National Laboratory document LA-UR-97-3052, presented at the 1997 Workshop on Computational Electronics and Nanoelectronics, Urbana, Illinois, October 20–22 (1997).
- Gustafson, P., C Srinivasan, and L. Wasserman. "Local Sensitivity Analysis," *Bayesian Statistics*, Vol. 5, pp. 197–210, (1996).

- Hansen, S.K., H. Boukhalfa, S. Karra, D. Wang, and V.V. Vesselinov. "Chromium (VI) Reduction in Acetate- and Molasses Amended Natural Media: Empirical Model Development," Los Alamos National Laboratory document LA-UR-17-30690, Los Alamos, New Mexico (2017a).
- Hansen, S.K., S. Pandey, S. Karra, and V.V. Vesselinov. "CHROTRAN 1.0: A Mathematical and Computational Model for In Situ Heavy Metal Remediation in Heterogeneous Aquifers," *Geoscientific Model Development*, Vol. 10, pp. 4525-4538 (2017b).
- Lichtner, P.C., G.E. Hammond, C. Lu, S. Karra, G. Bisht, B. Andre, R.T. Mills, J. Kumar, and J.M. Frederick. *PFLOTRAN User Manual*, available at: <http://www.documentation.pflotran.org>, last access: 12 December (2017a).
- Lichtner, P.C., G.E. Hammond, C. Lu, S. Karra, G. Bisht, B. Andre, R.T. Mills, J. Kumar, and J.M. Frederick. PFLOTRAN web page, available at: <http://www.pflotran.org>, last access: 12 December (2017b).
- Monod, J. "The Growth of Bacterial Cultures," *Annual Review of Microbiology*, Vol. 3, pp. 371-394, <https://doi.org/10.1146/annurev.mi.03.100149.002103>, (1949).
- Okeke, B.C. "Bioremoval of Hexavalent Chromium from Water by a Salt Tolerant Bacterium, *Exiguobacterium* sp. GS1," *Journal of Industrial Microbiology & Biotechnology*, Vol. 35, pp. 1571-1579, <https://doi.org/10.1007/s10295-008-0399-5> (2008).
- Saltelli, A., S. Tarantola, and K.P.S Chan. "A Quantitative Model-Independent Method for Global Sensitivity Analysis of Model Output," *Technometrics*, Vol. 41, No. 1, pp. 39-56, (1999).
- Shashidhar, T., P. Ligy, and S.M. Bhallamudi. "Bench-scale Column Experiments to Study the Contaminant of Cr(VI) in Confined Aquifers by Bio-transformation," *Journal of Hazardous Materials*, Vol. 131, Nos. 1-3, pp. 200-209 (2006).
- Sobol, I.M. "Sensitivity Estimates for Nonlinear Mathematical Models," *Mathematical Modelling and Computational Experiments*, Vol. 1, No. 4, pp. 407-414, (1993).
- Vesselinov, V.V. "Numerical Inverse Interpretation of Pneumatic Tests in Unsaturated Fractured Tuffs at the Apache Leap Research Site," PhD dissertation, University of Arizona (2000).
- Vesselinov, V.V., and D. O'Malley. "Model Analysis of Complex Systems Behavior using MADS," presented at AGU 2016 Fall Meeting, San Francisco, CA (2016).
- Vesselinov, V.V., D. Katzman, D. Broxton, K. Birdsell, S. Reneau, D. Vaniman, P. Longmire, J. Fabryka-Martin, J. Heikoop, M. Ding, D. Hickmott, E. Jacobs, T. Goering, D.R. Harp, and P. Mishra. "Data and Model-Driven Decision Support for Environmental Management of a Chromium Plume at Los Alamos National Laboratory (LANL)," Waste Management Symposium 2013, Session 109: ER Challenges: Alternative Approaches for Achieving End State, Phoenix, AZ, February 28, 2013, online peer-reviewed publication at <http://wmsym.org> (2013).
- Vesselinov, V.V., D. O'Malley, Y. Lin, and S. Hansen. "MADS.jl: Model Analyses and Decision Support in Julia" (2016).
- Vesselinova, N., B.S. Alexandrov, and M.E. Wall. "Dynamical Model of Drug Accumulation in Bacteria: Sensitivity Analysis and Experimentally Testable Predictions," *PLoS One*, Vol. 11, No. 11:e0165899 (2016).

Wang, Y.T., and C. Xiao, "Factors Affecting Hexavalent Chromium Reduction in Pure Cultures of Bacteria," *Water Research*, Vol. 29, pp. 2467–2474, [https://doi.org/10.1016/0043-1354\(95\)00093-Z](https://doi.org/10.1016/0043-1354(95)00093-Z), (1995).

Zyvoloski, G.A., B.A. Robinson, Z.V. Dash, S. Kelkar, H.S. Viswanathan, R.J. Pawar, P.H. Stauffer, T.A. Miller, and C. Shaoping, *Software Users Manual (UM) for the FEHM Application Version 3.1–3.X*, p. 329, Los Alamos National Laboratory document LA-UR-12-24493, Los Alamos, New Mexico (2015).

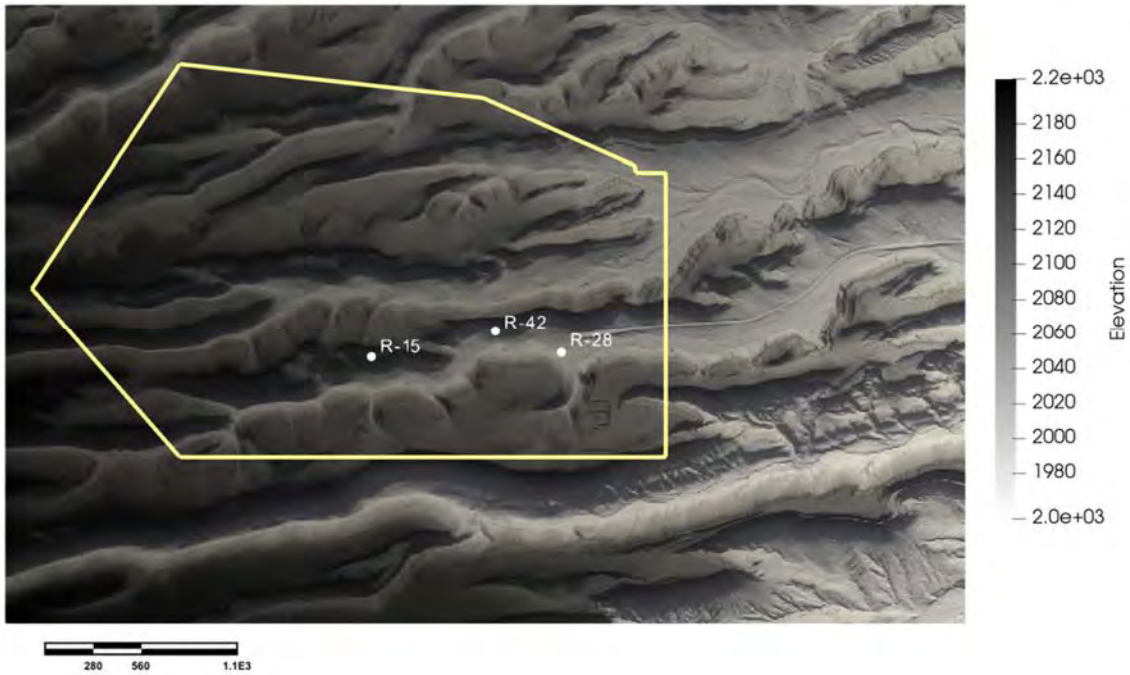


Figure 1.1-1 Lateral model domain (yellow line) of the 3-D vadose-zone/regional-aquifer model of the Laboratory chromium site. The gray-shaded relief presents the ground surface (the units of ground-surface elevations and spatial coordinates are in meters). Some the regional aquifer wells along Mortandad Canyon are also shown in the map.

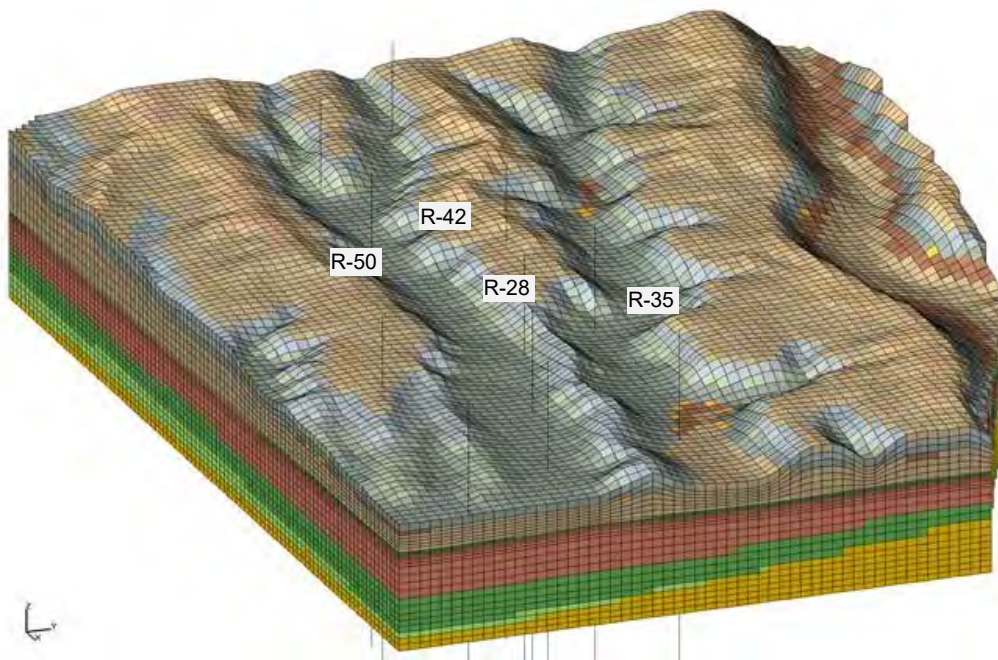


Figure 1.1-2 Block diagram showing the computational grid of the chromium 3-D vadose-zone / regional-aquifer model. View is towards the northwest and the canyons, from left to right, are Mortandad, Sandia, and Los Alamos. Vertical lines show well locations. Y-axis indicates north.

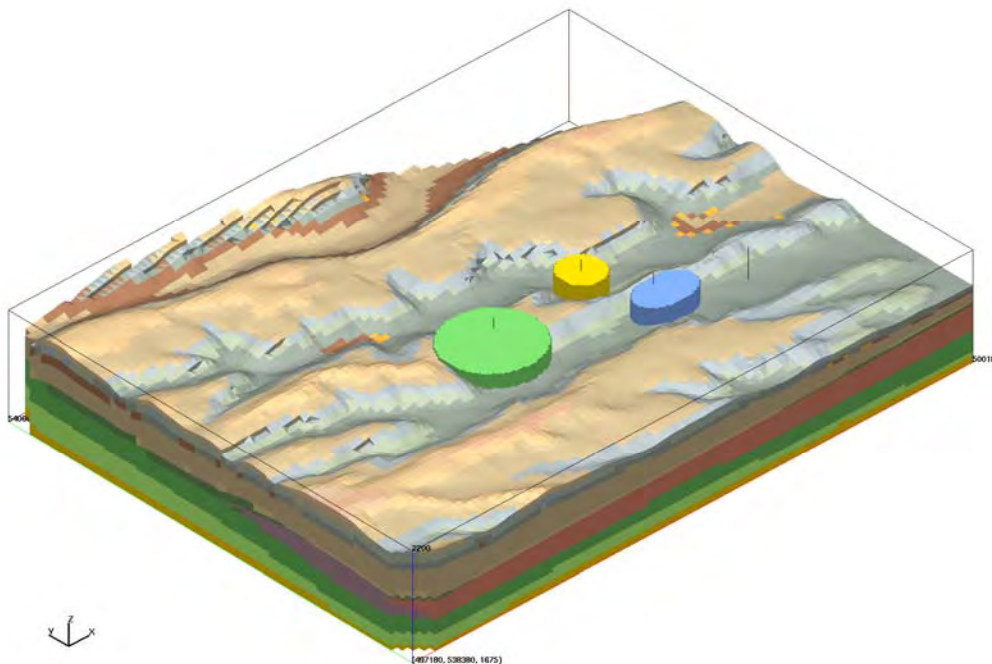


Figure 1.1-3 Block diagram showing the computational grid and locations of three hydraulic windows in the perched water zone above the regional aquifer. Each ellipse is intersected by the reduction zone inside the basalts and near well locations R-42, R-62, and R-43. View is towards the northeast with the y-axis indicating north.

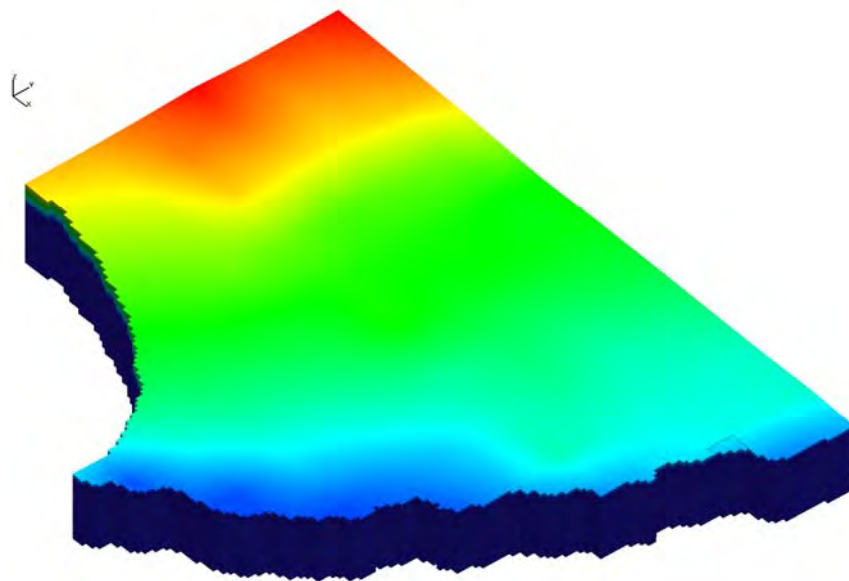


Figure 1.2-1 Block diagram showing the grid used for the regional-scale aquifer model. View is towards the northwest and the y-axis indicates north. The coloring represents the elevation of the regional-aquifer water table in 2012. The red regions to the west are high pressures in the area of mountain-front recharge beneath the Sierra de los Valles. The blue regions to the east represent the impact of discharge near the Rio Grande.

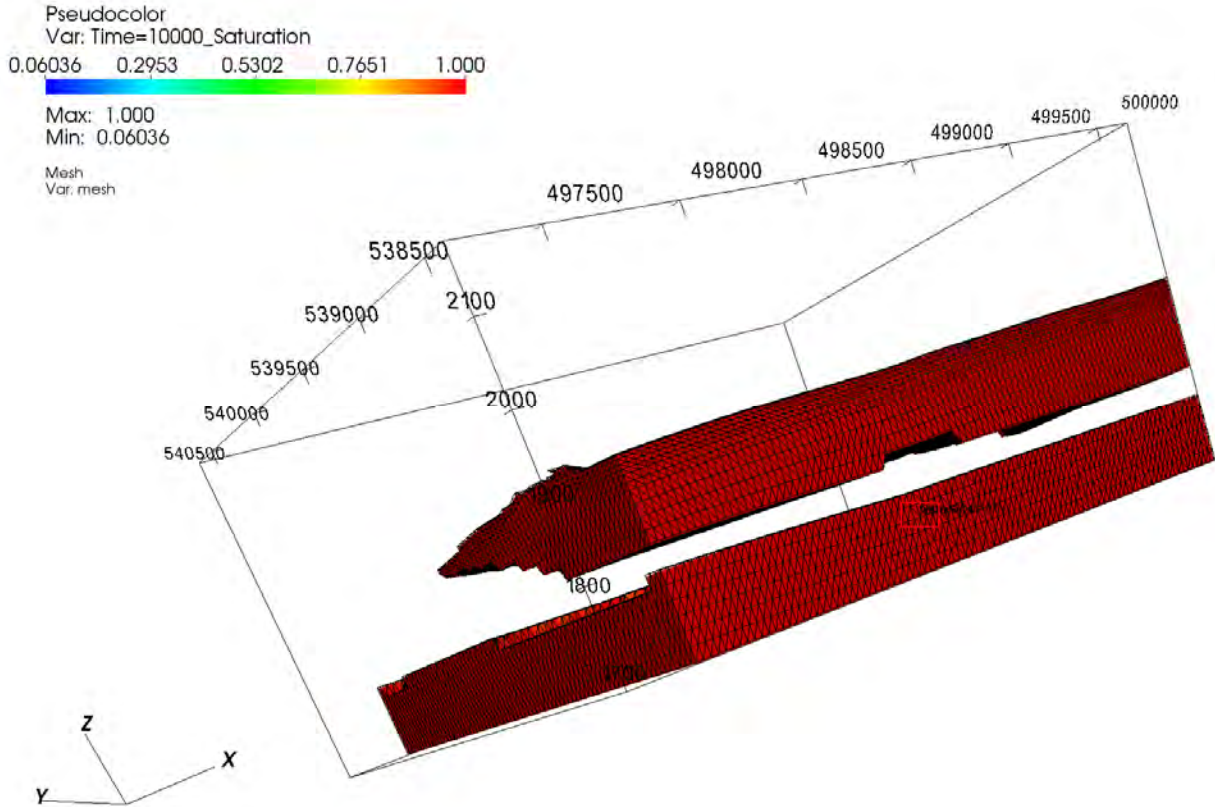


Figure 2.1-1 Block diagram showing the 3-D shape of the simulated perched water zone above the regional aquifer. In the figure, the full saturation is shown in red. To produce the figure, model nodes with saturation less than 0.3 are blanked out to depict the separation between the perched saturated zone (red region on the top) and the regional aquifer (brick-shaped red region on the bottom). The perched saturated zone is clearly separated from the regional aquifer in the 3-D coupled vadose-zone/regional-aquifer model.

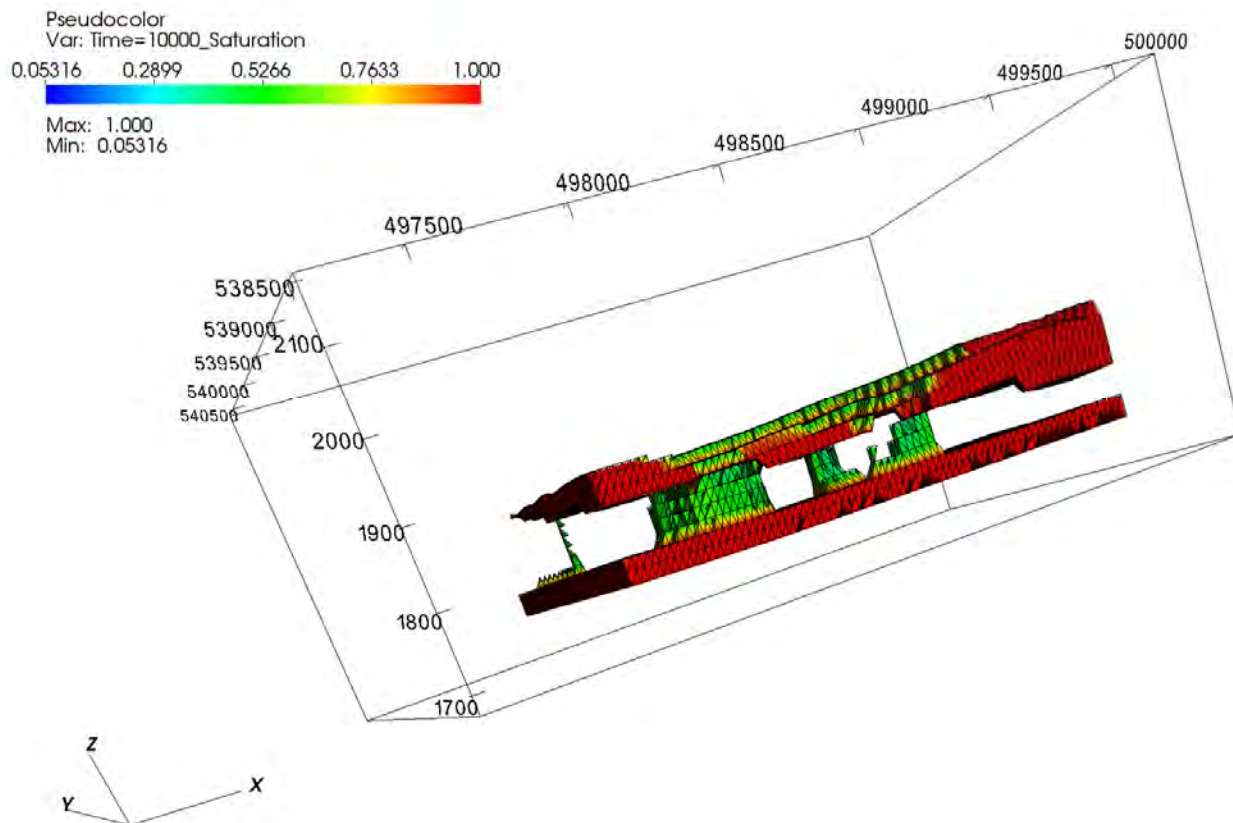


Figure 2.1-2 Block diagram showing the 3-D structure of the simulated groundwater flow between the perched horizon and the regional aquifer when the flow occurs along three hydraulic windows as depicted in Figure 1.1-3. In the figure, the full saturation is shown in red and minimum saturation is shown in blue. To produce the figure, model nodes with saturation less than 0.3 are blanked out to depict the separation between the perched saturated zone (red region on the top) and the regional aquifer (brick-shaped red region on the bottom). The perched saturated zone is clearly separated from the regional aquifer in the 3-D coupled vadose-zone/regional-aquifer model. The partly saturated flow between the perched horizon and the regional aquifer along the three hydraulic windows can be seen in green.

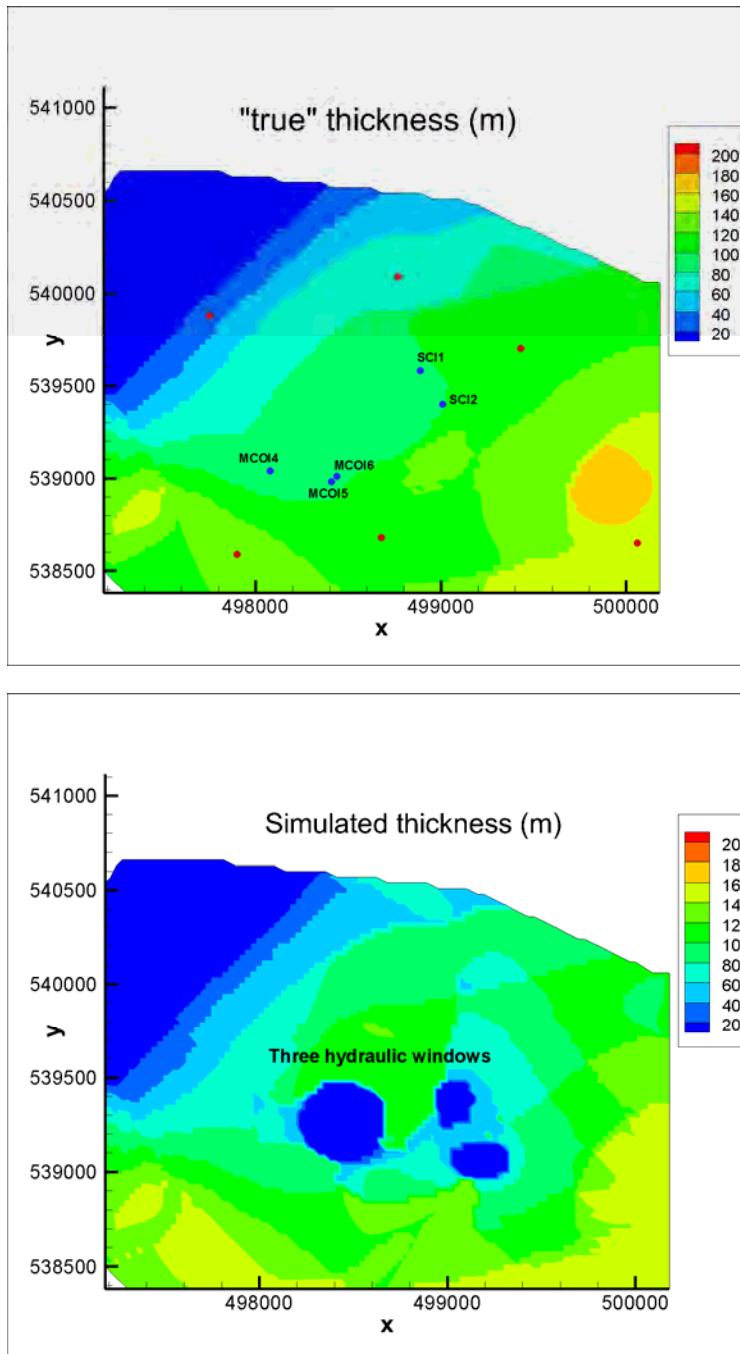


Figure 2.1-3 Maps showing “true” (top) and simulated (bottom) thicknesses of the perched saturated zone. Areas of thinner (blue) and thicker (red) perched zones are in the north-west and south-east quadrants, respectively. The top map shows the locations of the existing wells used in the calibration (blue dots) and locations of additional points (red dots) used to improve the characterization of the saturated thickness. The bottom map also shows the location of the three hydraulic windows applied in the model; the hydraulic windows define the locations of vertical flow from the perched zone towards the regional aquifer.

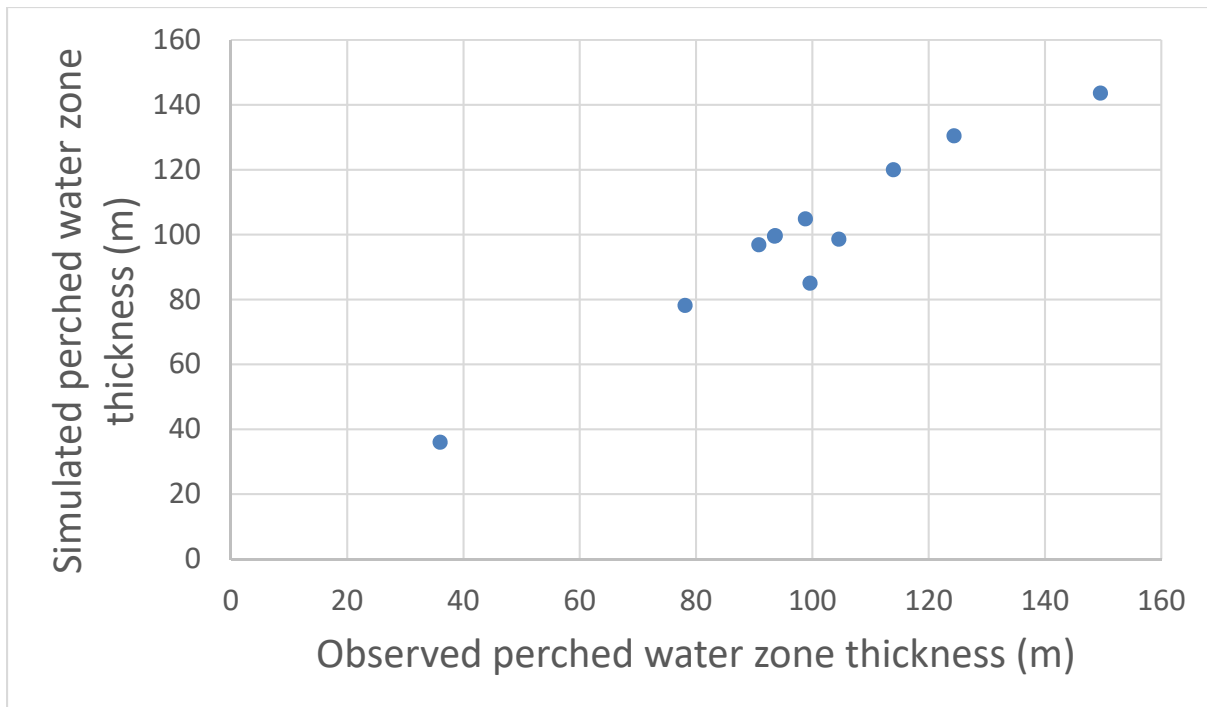


Figure 2.1-4 Simulated vs observed thicknesses of the perched-intermediate saturated zone at 11 calibration target locations. Perfect matches will be along 1:1 line.

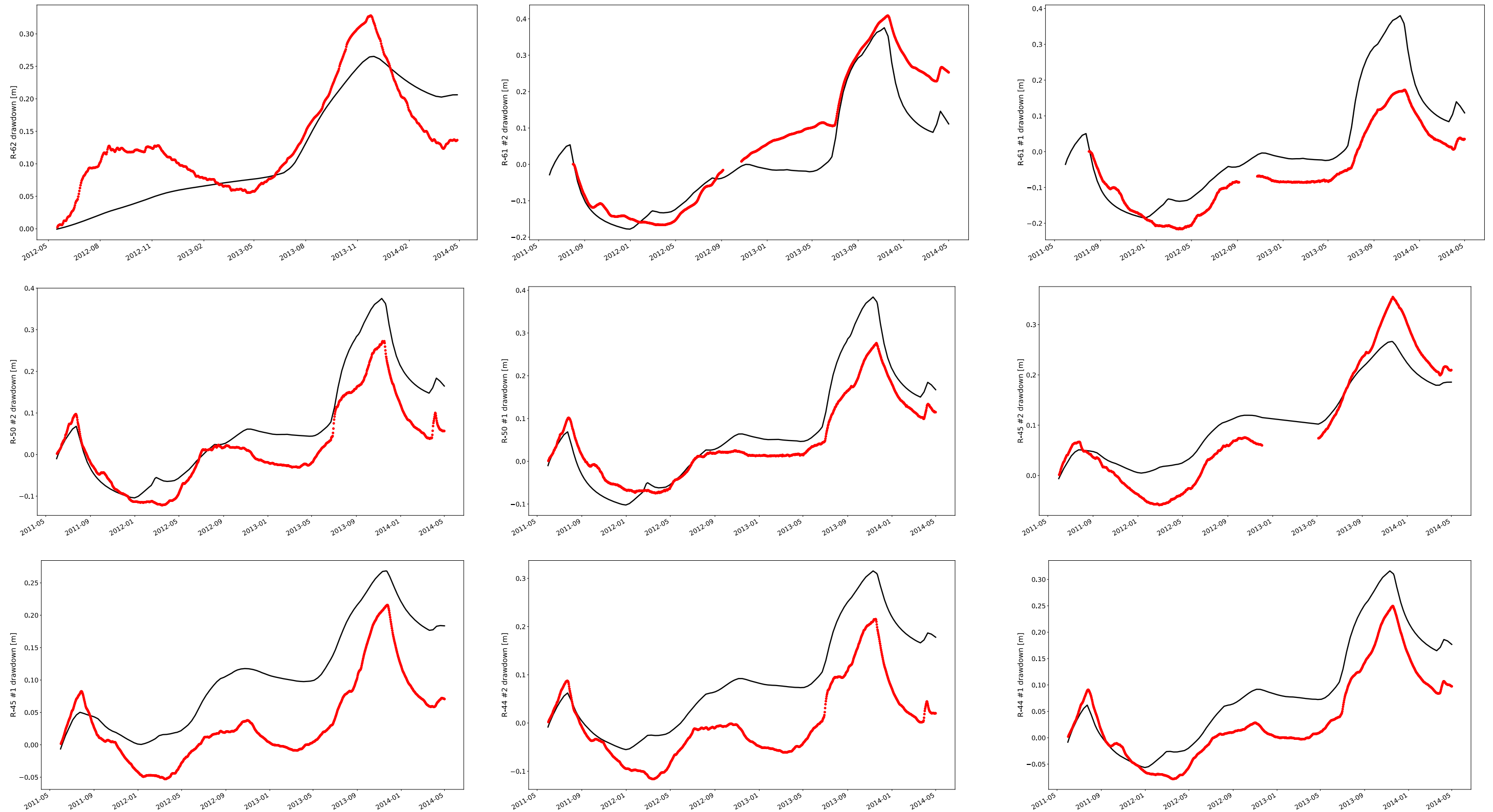


Figure 2.2-1 The model-predicted (black) vs the observed (red) water-level declines (drawdowns) at the site monitoring wells

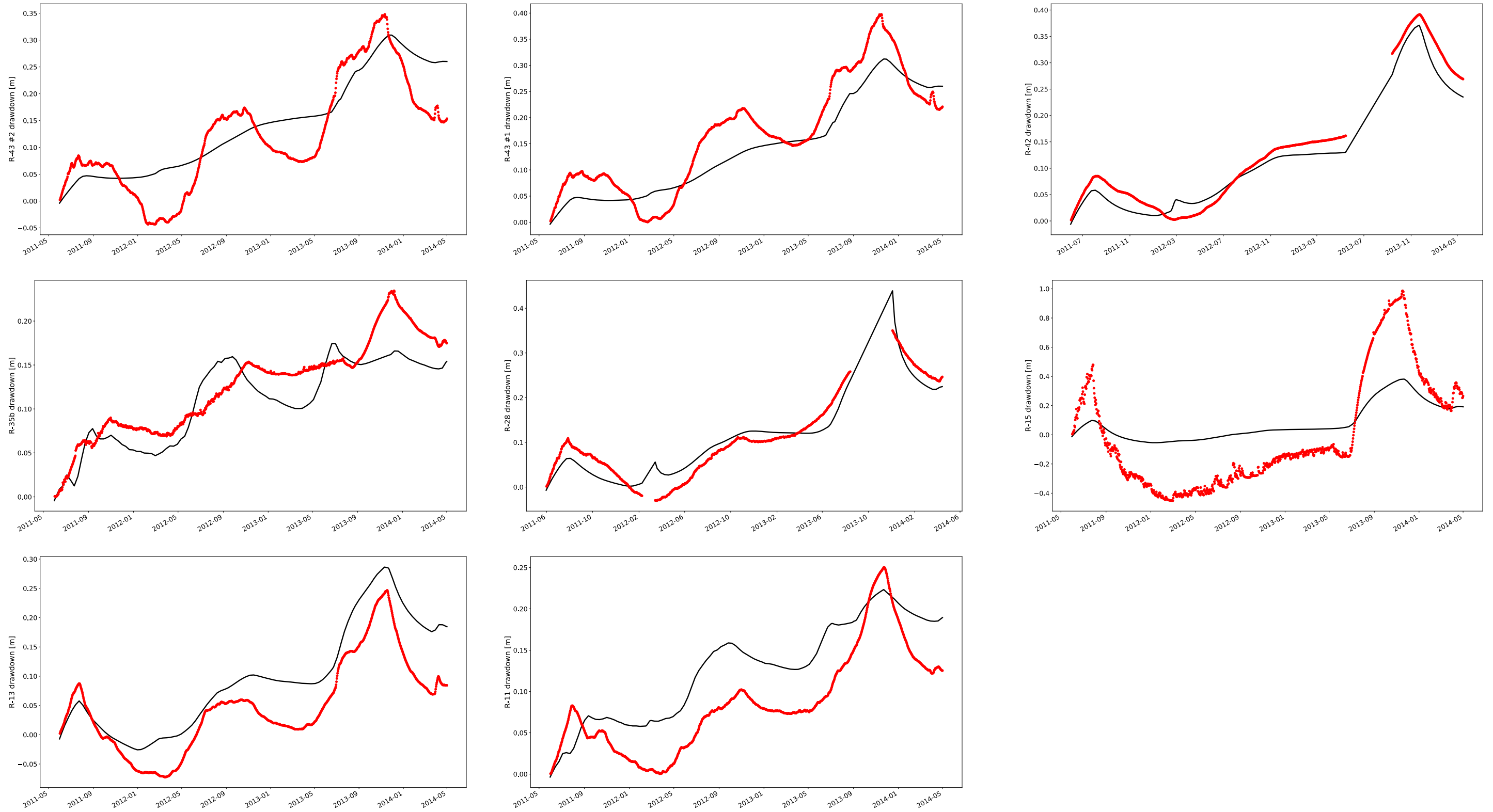


Figure 2.2-1 (continued) The model-predicted (black) vs the observed (red) water-level declines (drawdowns) at the site monitoring wells

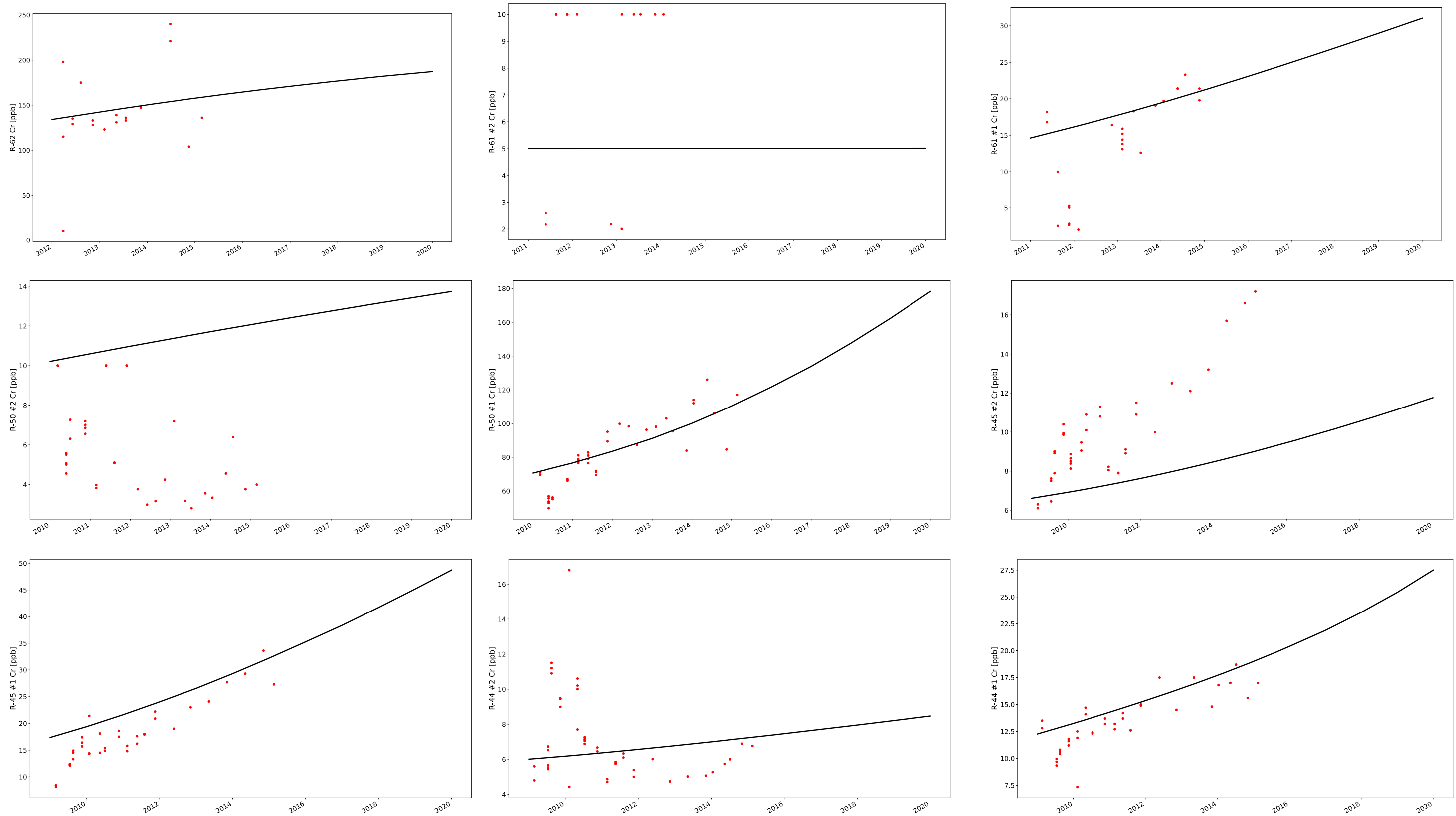


Figure 2.2-2 The model-predicted (black line) vs the observed (red dots) chromium concentrations at the site monitoring wells. The predicted concentrations are based on the best values estimated for the model parameters. These concentrations also represented the “central” tendencies of the multiple realizations presented in Figure 2.2-7 below.

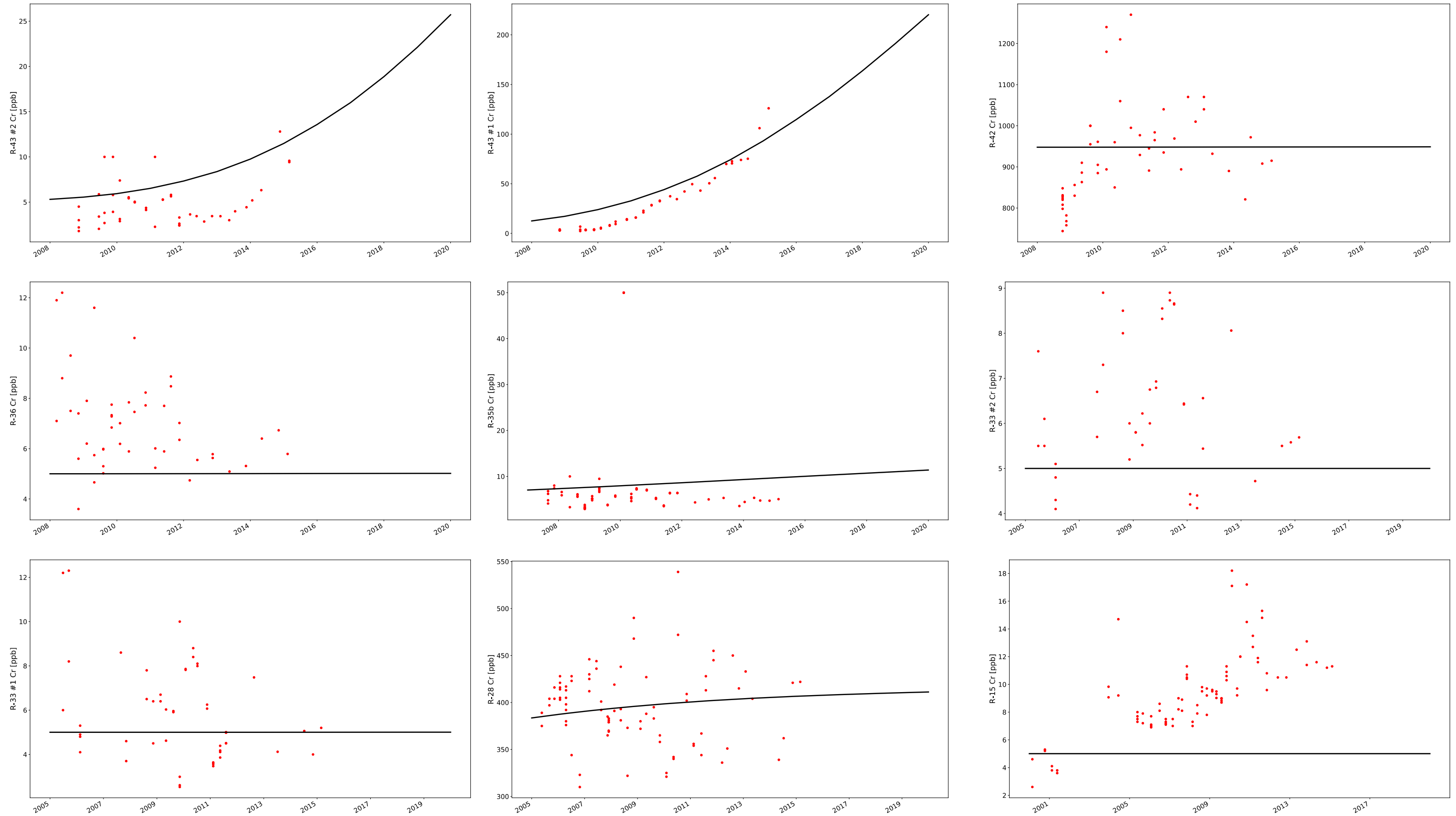


Figure 2.2-2 (continued) The model-predicted (black line) vs the observed (red dots) chromium concentrations at the site monitoring wells. The predicted concentrations are based on the best values estimated for the model parameters. These concentrations also represented the “central” tendencies of the multiple realizations presented in Figure 2.2-7 below.

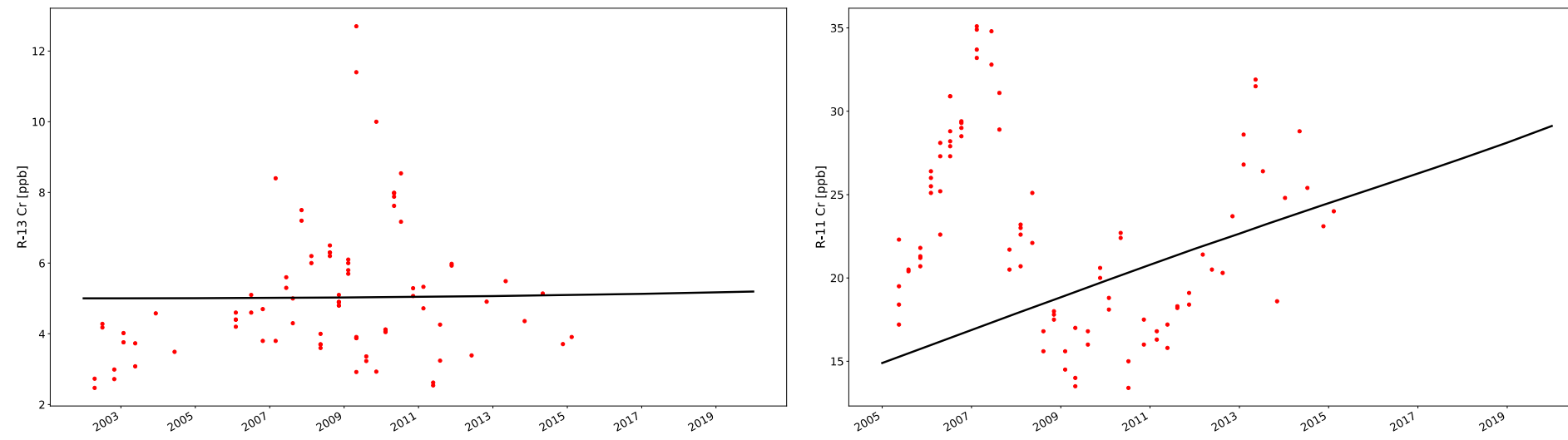
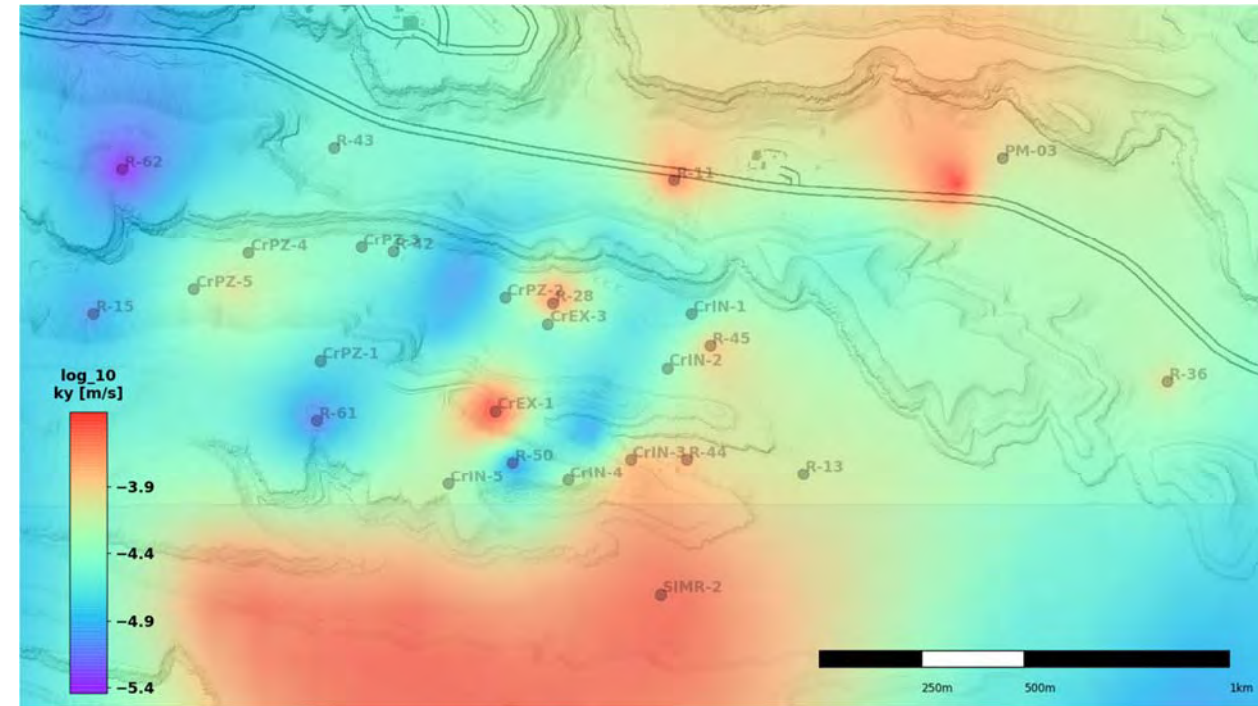
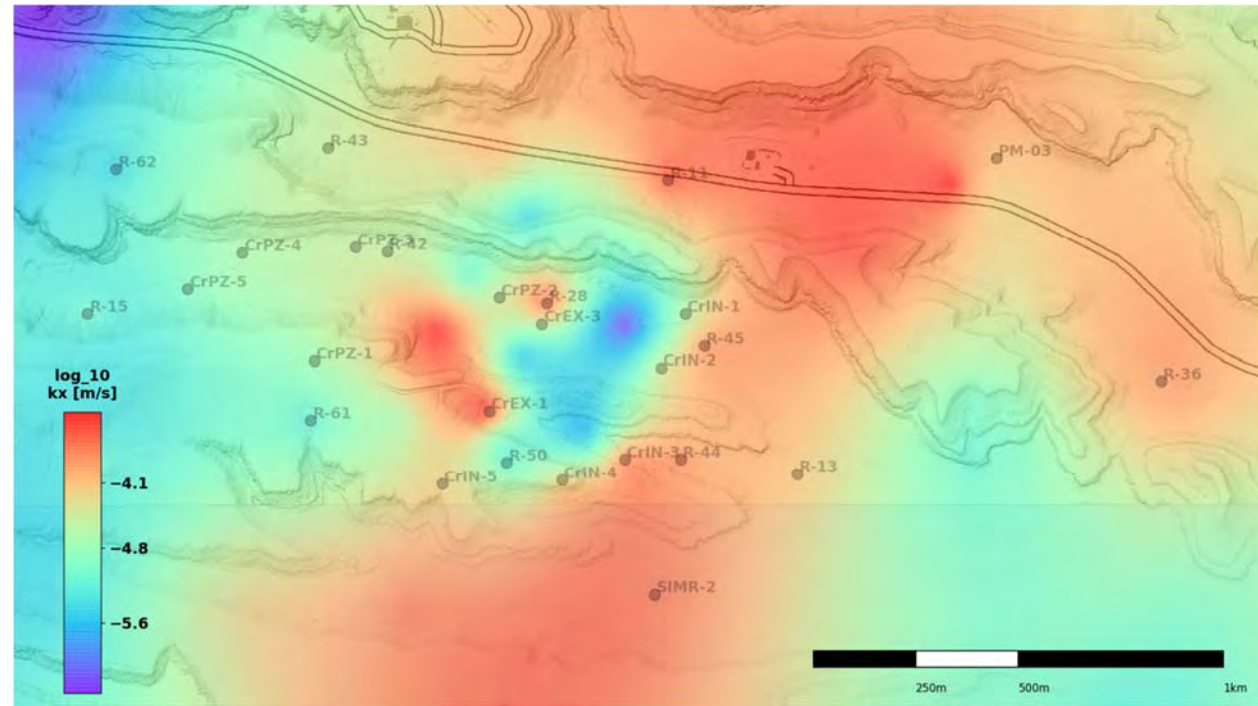
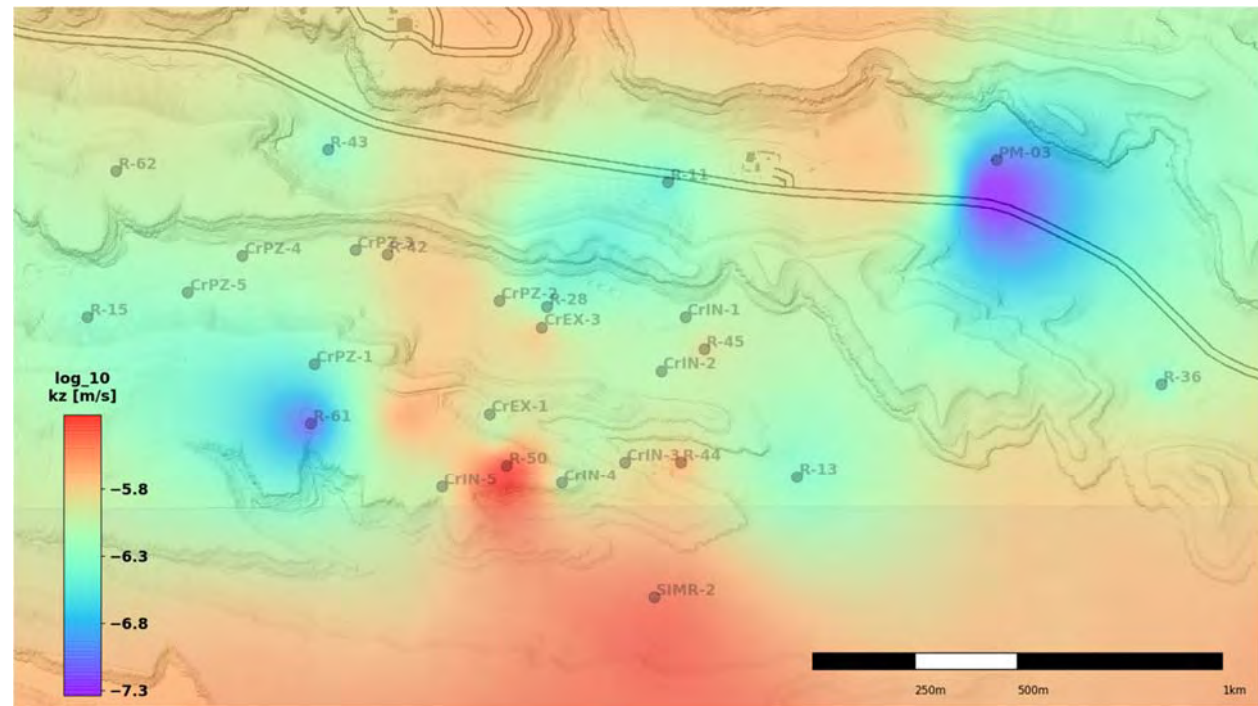


Figure 2.2-2 (continued) The model-predicted (black line) vs the observed (red dots) chromium concentrations at the site monitoring wells. The predicted concentrations are based on the best values estimated for the model parameters. These concentrations also represented the “central” tendencies of the multiple realizations presented in Figure 2.2-7 below.



(a)

(b)



(c)

Figure 2.2-3 Maps of model-predicted heterogeneity and anisotropy in the hydraulic conductivity along the top of the regional aquifer; hydraulic conductivity along x, y, and z axes (north-south, east-west, and vertical axes, respectively) are shown in the a, b, and c graphs above

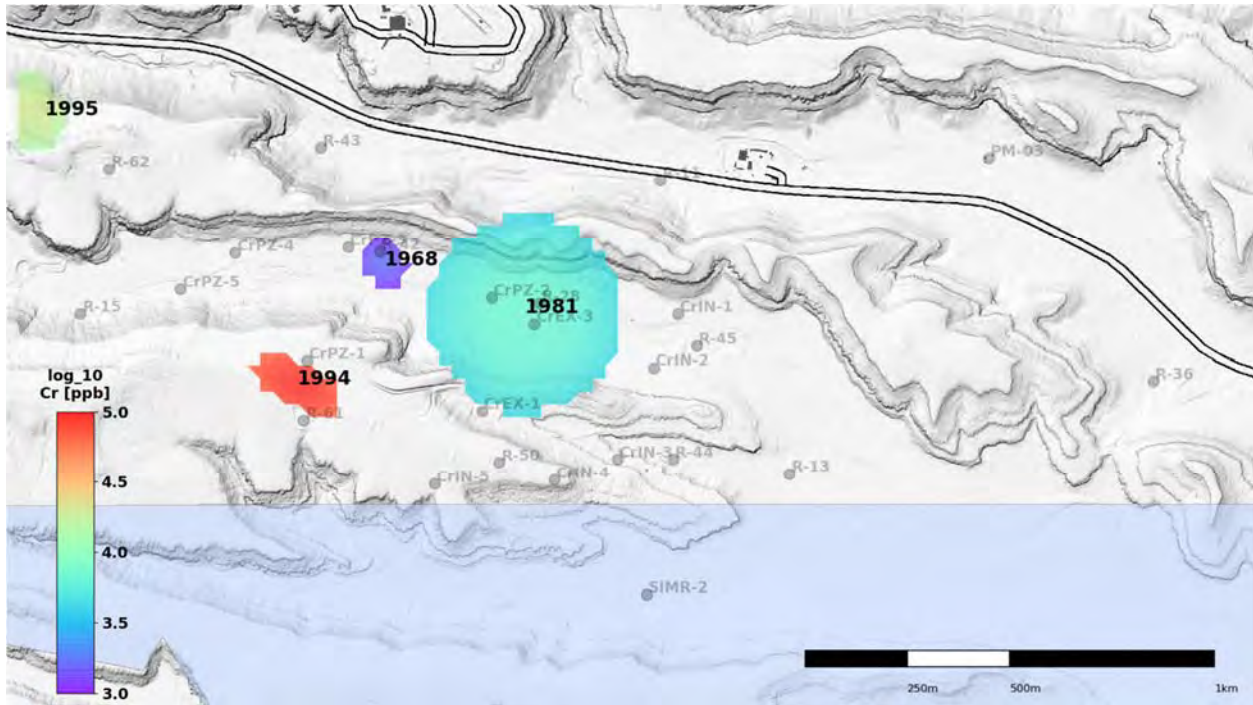
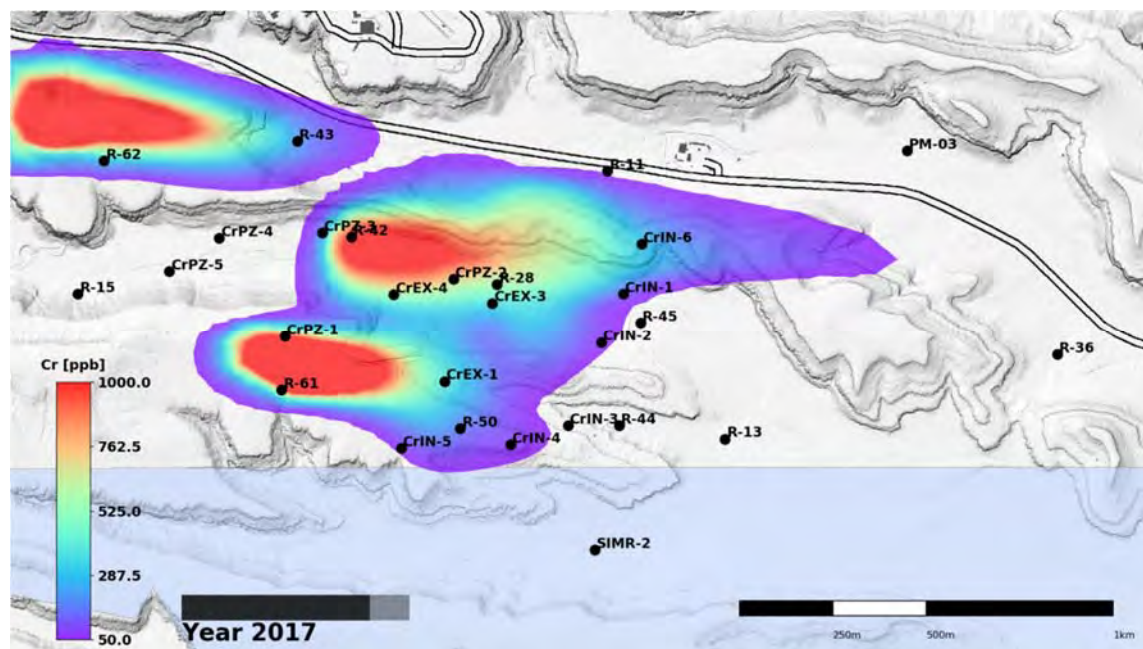
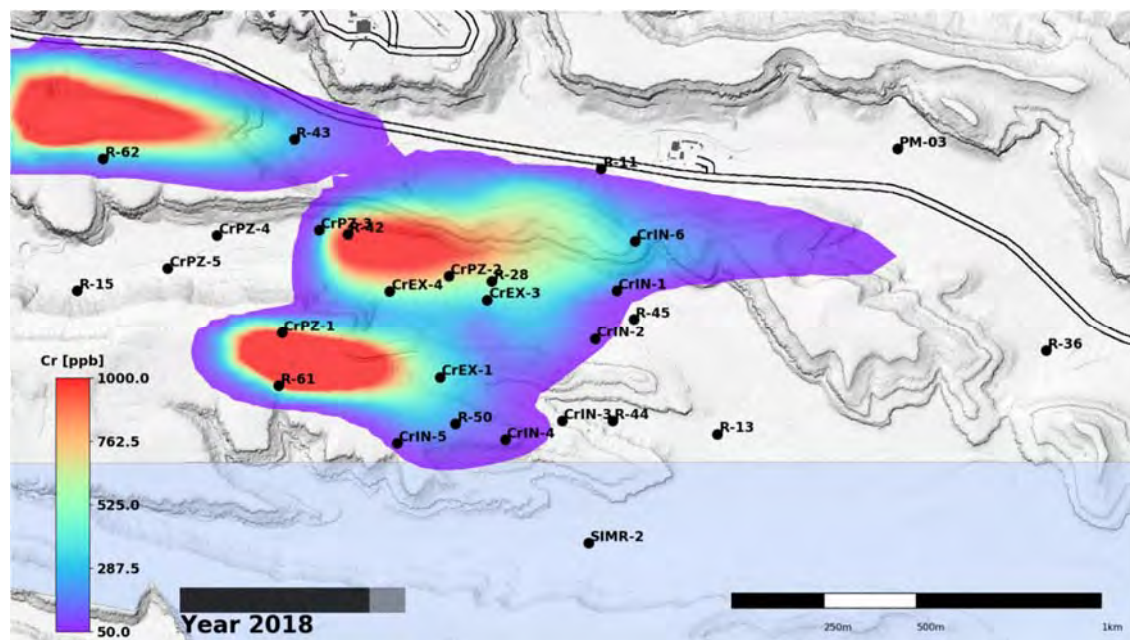


Figure 2.2-4 Maps of model-predicted contaminant sources; the number, size, shape, location, start time, and concentrations of the contaminant sources are estimated automatically during the model calibration. The figure shows the estimated four contaminant sources, the start times (in calendar years), their size, and concentrations (as log transformed values).

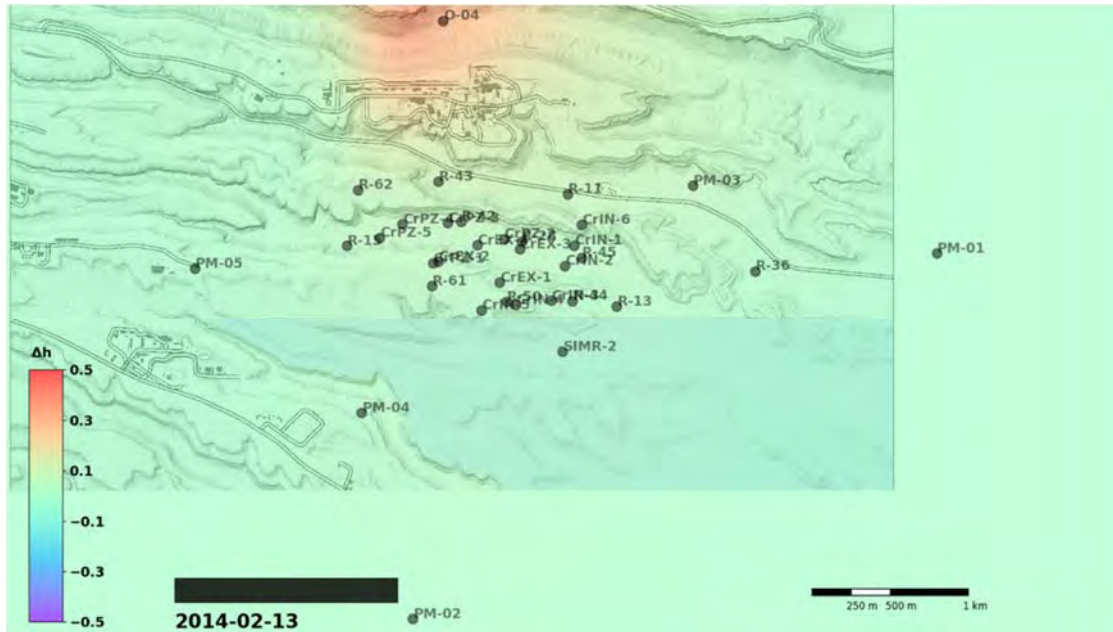


(a)

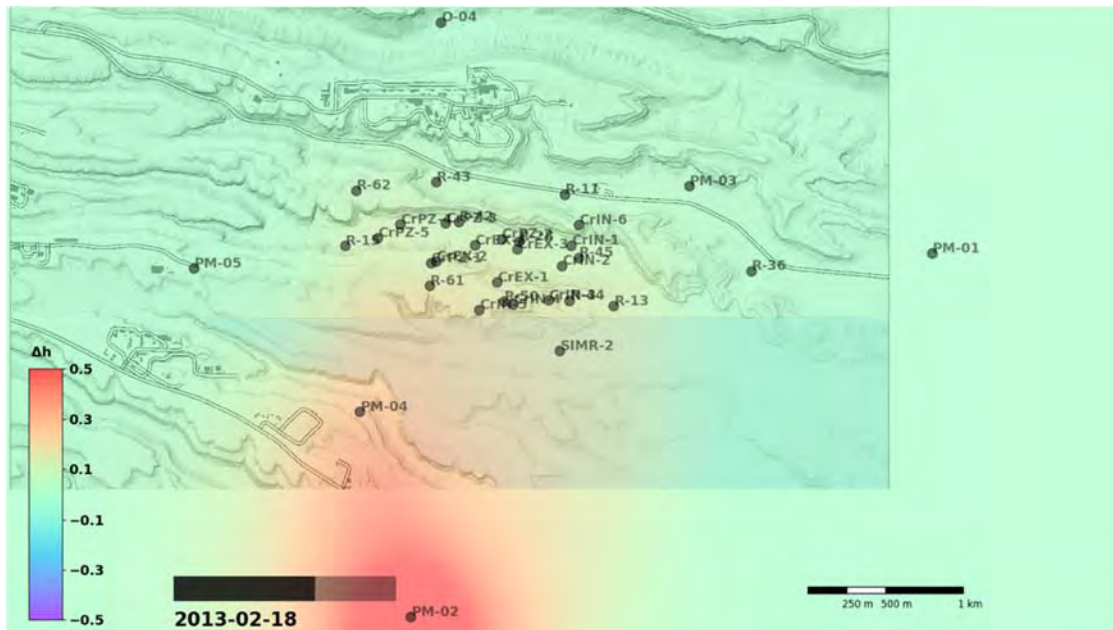


(b)

Figure 2.2-5 Maps of model-predicted chromium concentrations in 2017 and 2018. Concentrations are depicted as the value in a thin layer right at the water table and do not represent concentrations that might be measured in a monitoring well. The concentration gradients can be considered as relative modeled concentrations rather than absolute model predictions for mixed groundwater concentrations at wells.

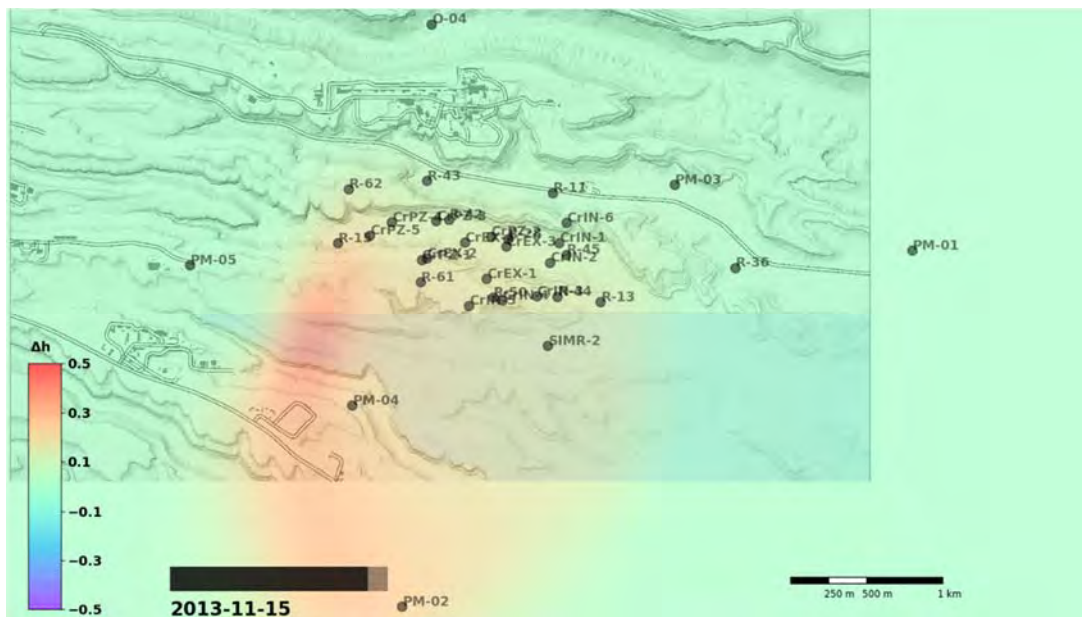


(a) rebound of the hydraulic heads in the vicinity of O-4 in February 2014

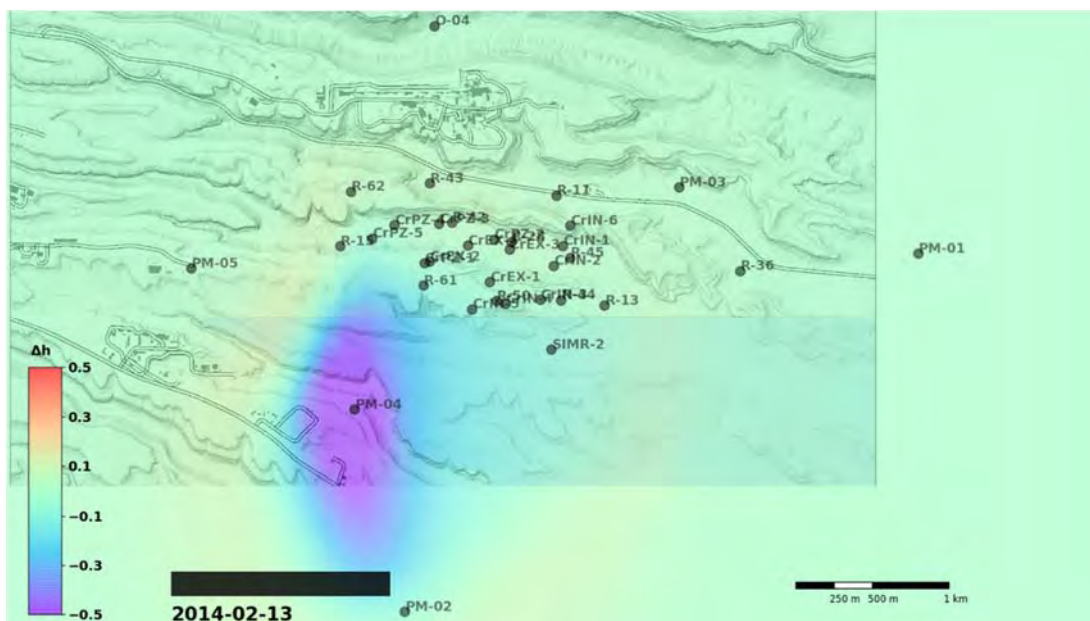


(b) rebound of the hydraulic heads in the vicinity of PM-2 in February 2014

Figure 2.2-6 Model-predicted pumping effects on the regional-aquifer water table caused by the municipal water-supply wells. The changes in the hydraulic heads presented above are relative to the model-predicted water levels circa May 2011. In the period between May 2011 and December 2014, some of the municipal wells are experiencing only rebounds, because of decreases in the water-supply pumping (e.g., PM-2, and O-4). PM-5 is observing only pressure declines. PM-4 has rebound and decline periods. PM-3 and PM-1 maps are not shown because these wells are predicted to produce no drawdown of the regional water table at the chromium site.



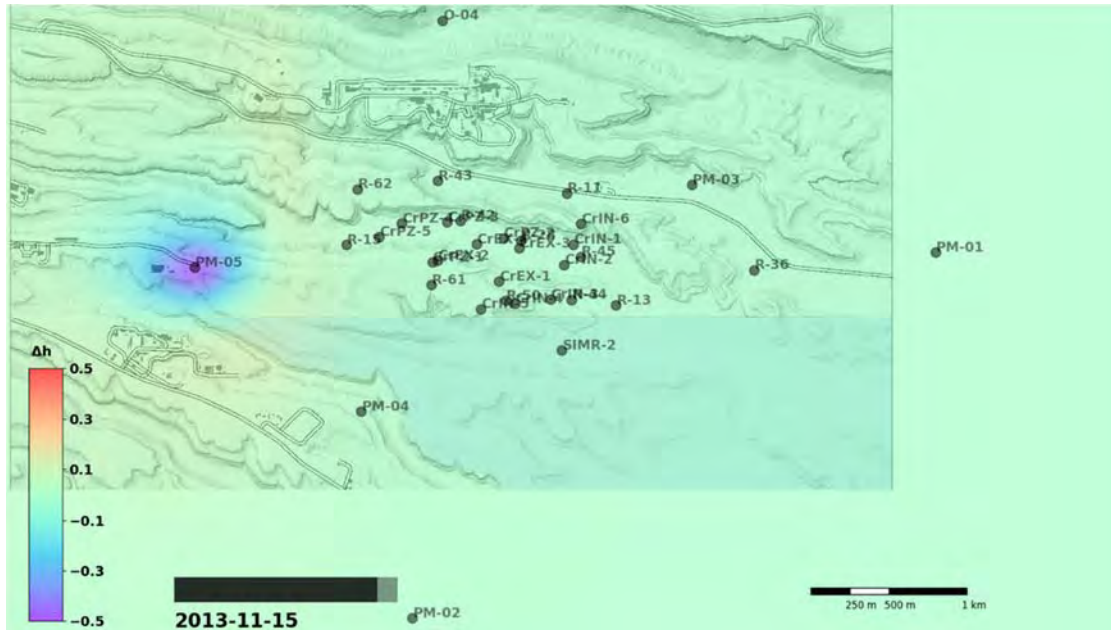
(c) rebound of the hydraulic heads in the vicinity of PM-4 in November 2013



(d) decline of the hydraulic heads in the vicinity of PM-4 in February 2014

Figure 2.2-6 (continued)

Model-predicted pumping effects on the regional-aquifer water table caused by the municipal water-supply wells. The changes in the hydraulic heads presented above are relative to the model-predicted water levels circa May 2011. In the period between May 2011 and December 2014, some of the municipal wells are experiencing only rebounds, because of decreases in the water-supply pumping (e.g., PM-2, and O-4). PM-5 is observing only pressure declines. PM-4 has rebound and decline periods. PM-3 and PM-1 maps are not shown because these wells are predicted to produce no drawdown of the regional water table at the chromium site.



(e) decline of the hydraulic heads in the vicinity of PM-5 in November 2014

Figure 2.2-6 (continued)

Model-predicted pumping effects on the regional-aquifer water table caused by the municipal water-supply wells. The changes in the hydraulic heads presented above are relative to the model-predicted water levels circa May 2011. In the period between May 2011 and December 2014, some of the municipal wells are experiencing only rebounds, because of decreases in the water-supply pumping (e.g., PM-2, and O-4). PM-5 is observing only pressure declines. PM-4 has rebound and decline periods. PM-3 and PM-1 maps are not shown because these wells are predicted to produce no drawdown of the regional water table at the chromium site.

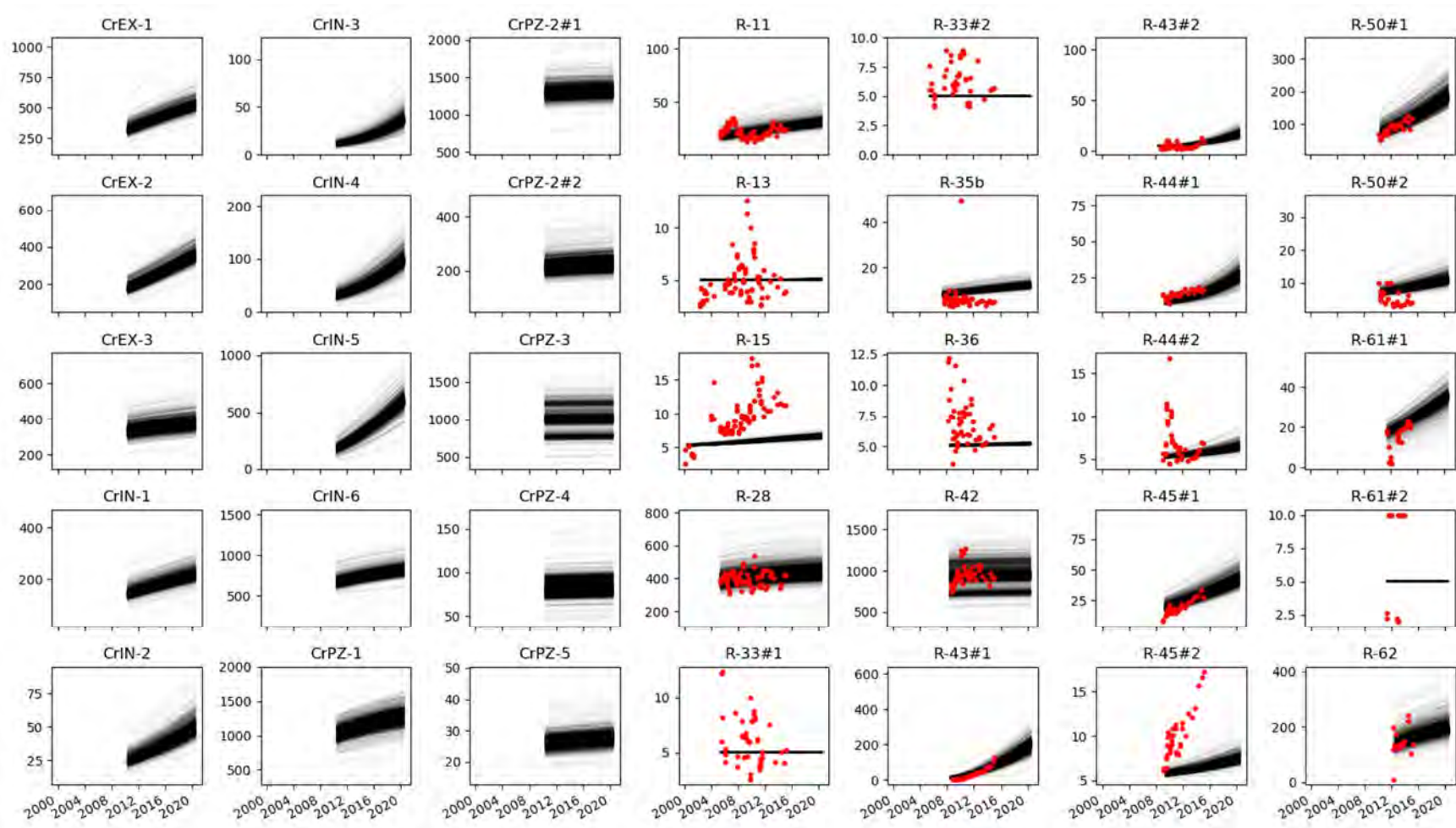


Figure 2.2-7 Model-predicted chromium concentrations (solid gray lines) vs observed chromium concentrations (red circles) at various site wells. The plots in the figure depict the confidence bounds as shown in regions of overlapping solid gray lines. Note that these predictions are based on a model that did not have CrIN-6 data as a calibration target. The best estimate of the chromium concentration at CrIN-6 in 2017 is about ~250 ppb, which matches the actual concentration at CrIN-6 when it was drilled.

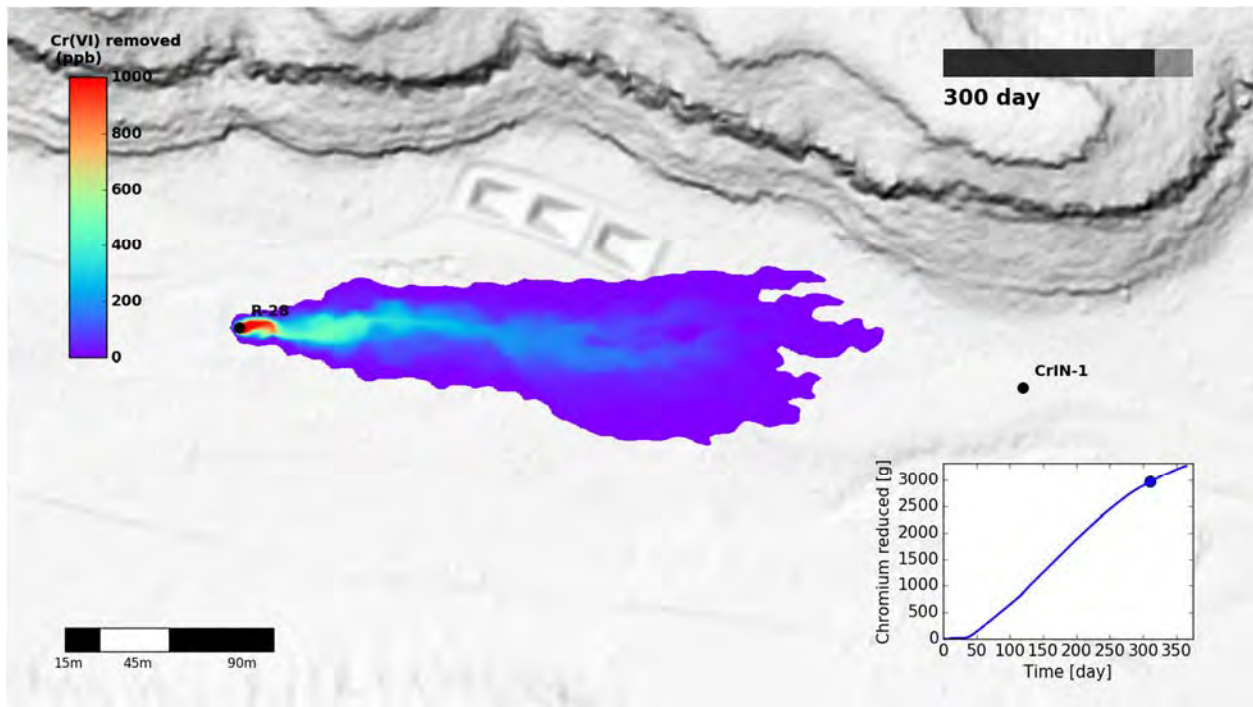


Figure 2.3-1 Map showing simulation of the injection of a biostimulant (molasses) and a biological inhibitor (ethanol) at R-28. The figure shows the concentration of Cr(VI) removed as a result of remediation 10 mo after the injection. A large amount of Cr(VI) has been removed by this time, and relatively fast pore water velocities (1 m/d; ~3.3 ft/d) result in a large zone of influence downgradient of the injection well. However, a significant decrease in Cr(VI) concentrations has not occurred in CrIN-1 after 10 mo.

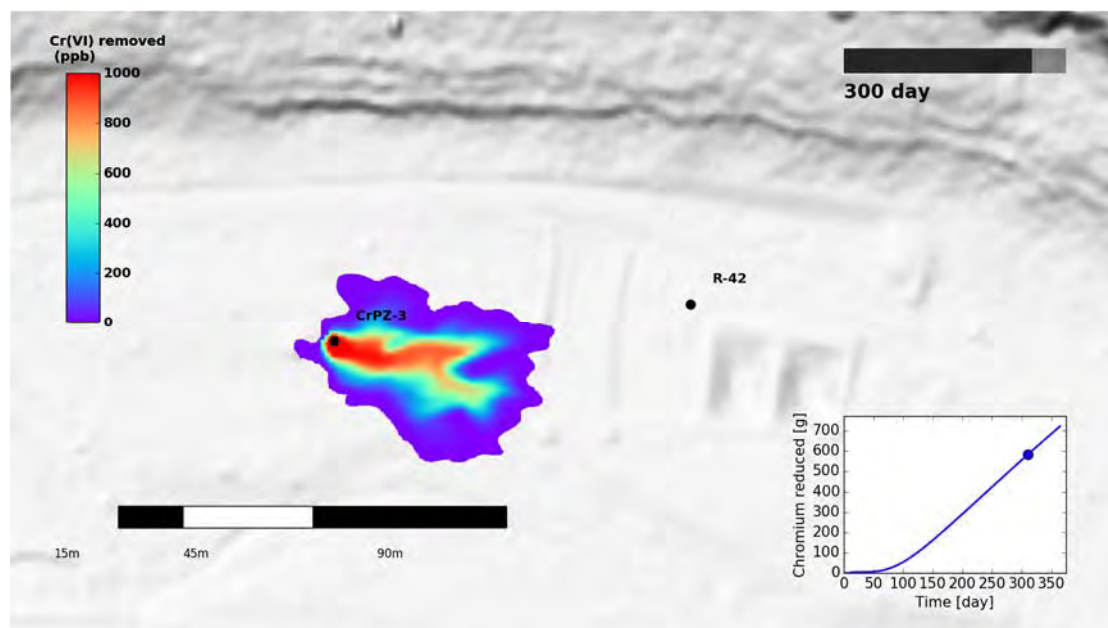


Figure 2.3-2 Map showing simulation of the injection of a strong chemical reducing agent (sodium dithionite) at CrPZ-3. The figure shows the concentration of Cr(VI) removed as a result of remediation 11 mo after the injection. Although a large amount of Cr(VI) has been removed by this time, relatively slow pore water velocities (0.1 m/d; ~0.33 ft/d) prevent the migration of the treated plume to R-42.

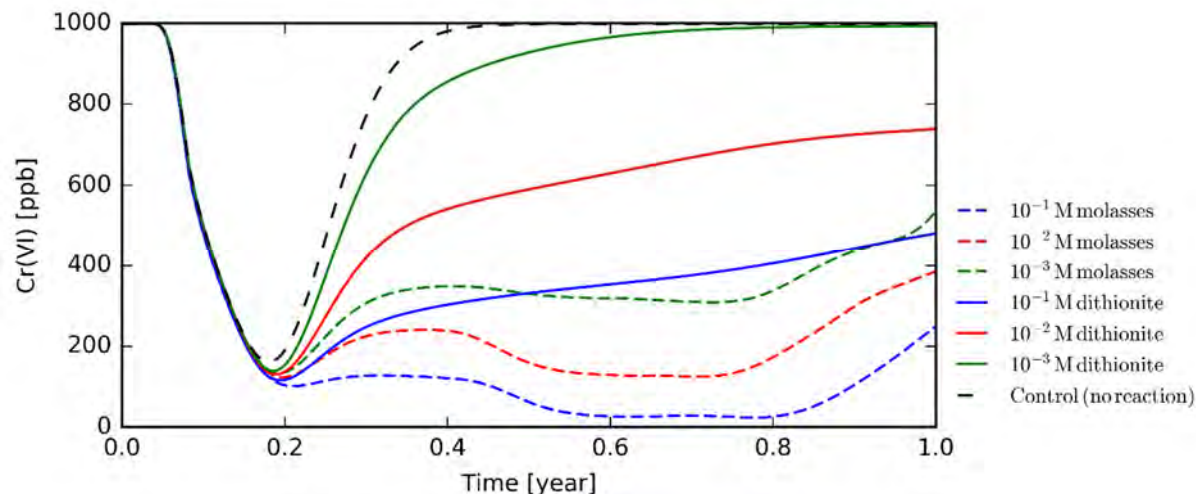


Figure 2.3-3 CHROTRAN breakthrough concentration curves for Cr(VI) at an observation point located 10 m downstream of the injection well. The results are taken from 2-D simulations in a heterogeneous permeability aquifer with mean pore water velocities of ~1 m/d (3.3 ft/d). Colored dashed lines represent CHROTRAN simulations that model the injection of a biostimulant (molasses), the solid lines represent CHROTRAN simulations that model the injection of a chemical reductant (dithionite), and the black dashed line shows dilution effects (no reaction). All simulations result in the decrease of Cr(VI) downstream, but the long-term effectiveness of treatment is heavily dependent upon the mass of amendment being injected.

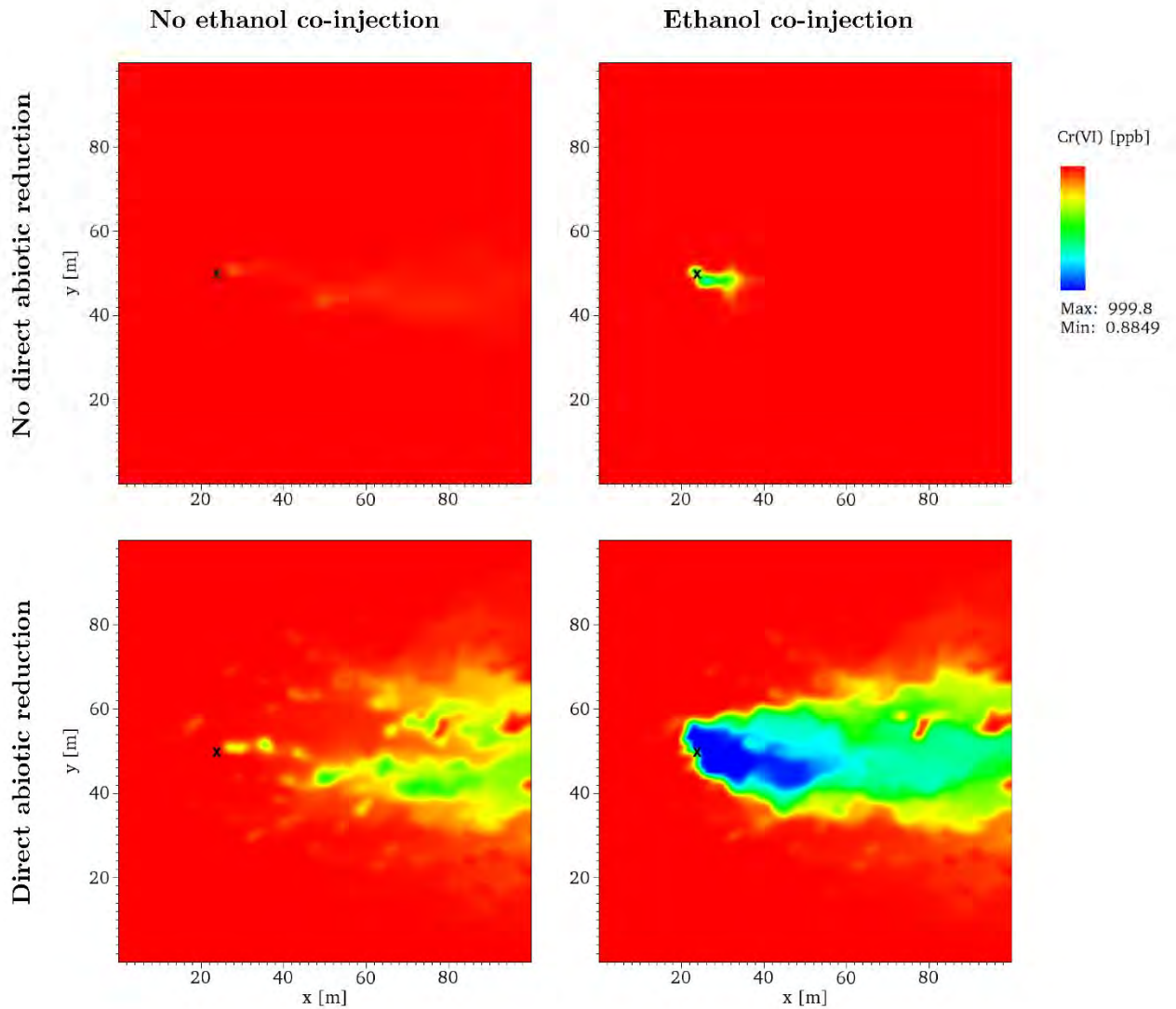


Figure 2.3-4 Maps showing predicted Cr(VI) concentrations (ppb) in a heterogeneous, Cr(VI)-contaminated aquifer 470 d after treatment, under four different scenarios. Scenarios with and without co-injection of ethanol and with and without direct abiotic reduction of Cr(VI) by molasses are shown. The injection well location is denoted by a black cross. The simulation where direct abiotic reduction is modeled and ethanol is co-injected (bottom right) results in the most effective in situ remediation.

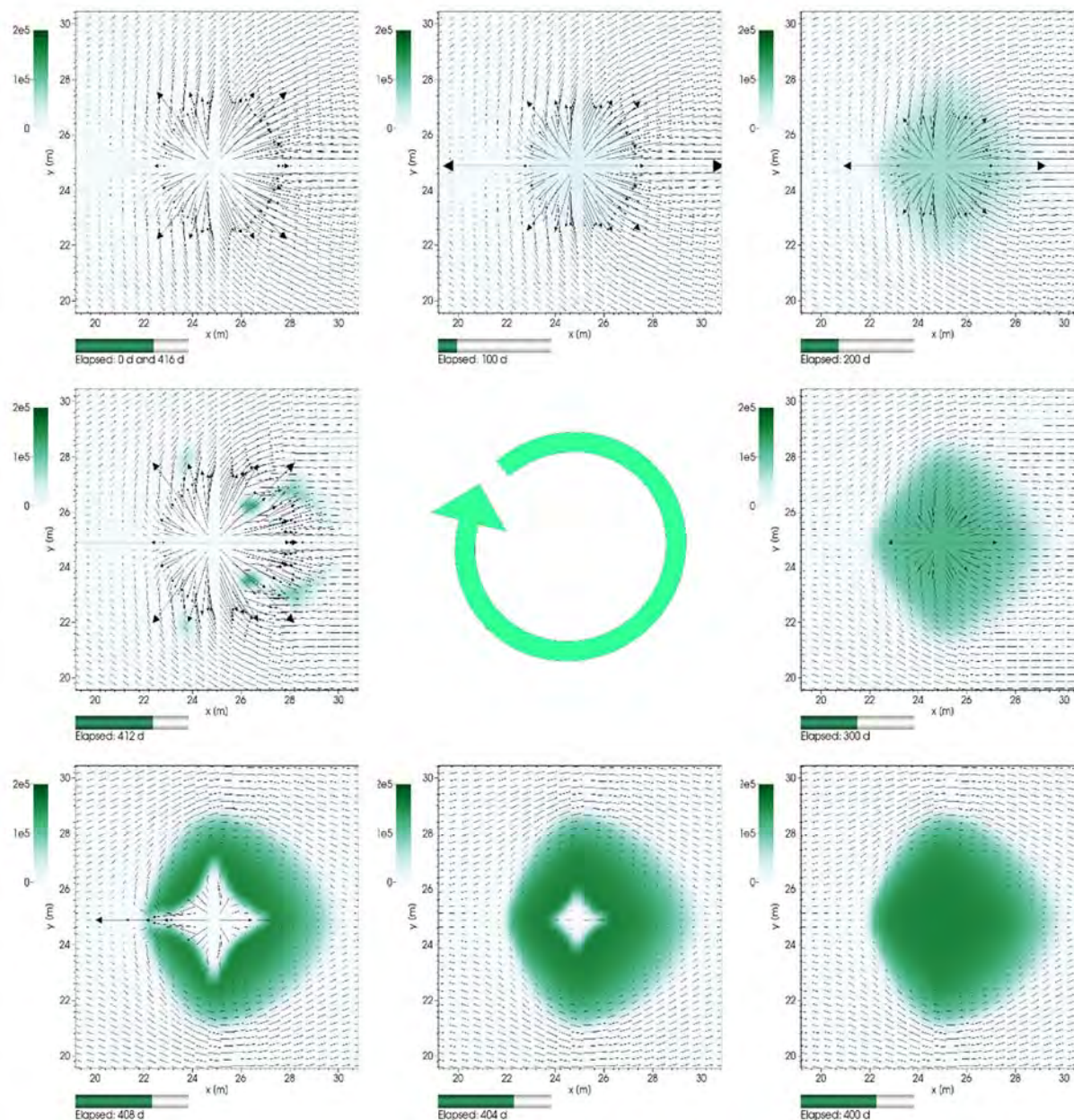


Figure 2.3-5 Simulation of biomass fouling that could occur during in situ bioremediation. The figure shows groundwater velocities overlaid upon biomass concentration. Velocity magnitude is indicated by arrow length and direction by arrow orientation; biomass concentration [g m^{-3}] is indicated by green intensity. The initial condition is shown in the upper-left corner, with time increasing in the clockwise direction. The biostimulant is first injected without a biocide, resulting in the growth of biomass that clogs the system. Groundwater velocities within the area of remediation decrease significantly until flow stops within the remediation area (bottom right). Biocide is then injected into the system, which reduces biomass concentrations and restores groundwater velocities to the initial state at 416 d.

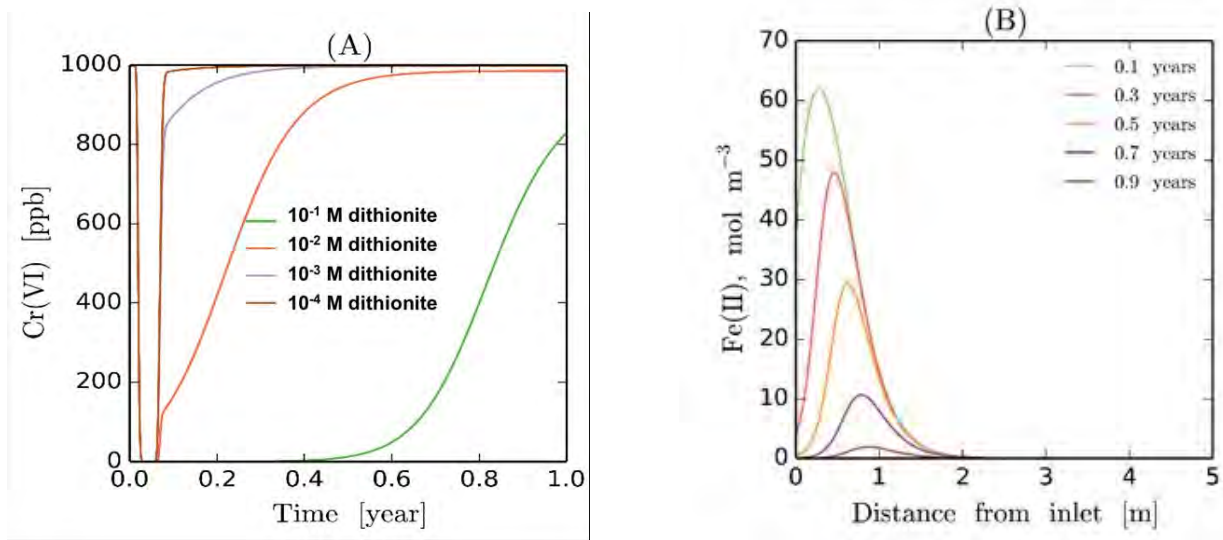


Figure 2.3-6 Simulation of the release of a sodium dithionite treatment solution along a 1-D flow path. Panel (A) shows the time evolution of Cr(VI) concentration at a well located 10 m downstream of the injection location for four different concentrations of dithionite in the injectant. The figure illustrates that a high concentration of dithionite is required to have prolonged decreases in the observed Cr(VI) downstream. When the concentration of dithionite is too low, the concentration of Cr(VI) quickly rebounds in the observation well. Panel (B) shows the spatial distribution of surface-bound Fe(II) at five different times for a 10^{-1} M dithionite injection. Fe(II) remains as a reductant of Cr(VI) long after dithionite is flushed from the system. However, it eventually depletes, resulting in the rebound in the Cr(VI) concentration in the observation well seen in panel (A).

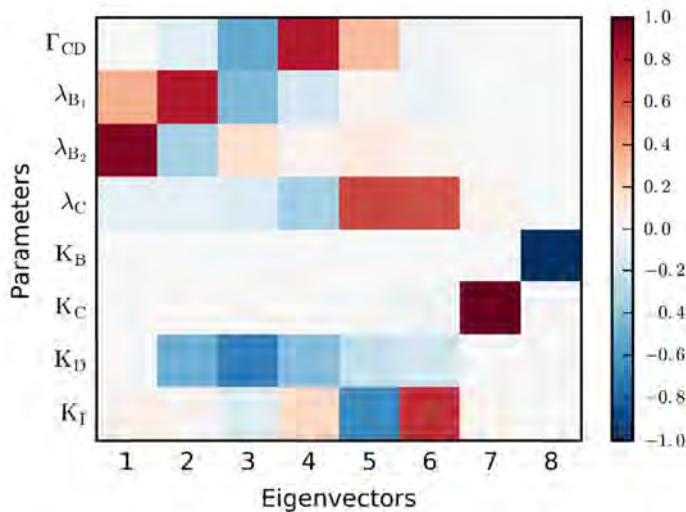


Figure 2.3-7 Local sensitivity analysis of biochemical treatment model. See Table 2.3-1 for a description of the parameters. The figure presents the eigenvectors of the estimated parameter covariance matrix, which defines the parameter uncertainty and sensitivity.

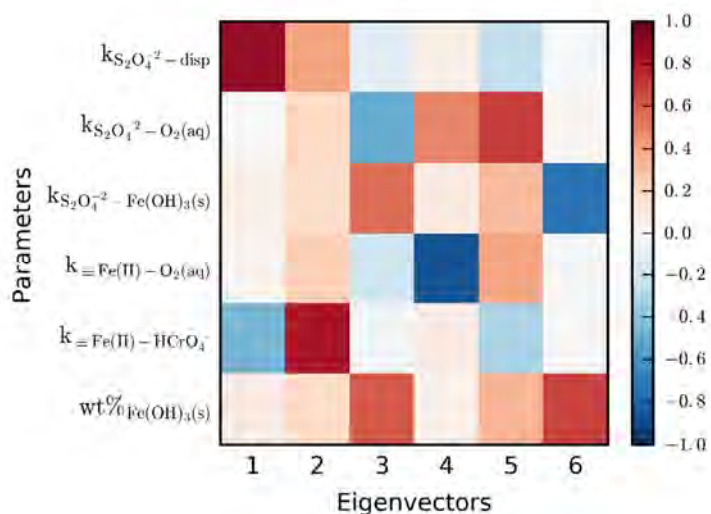


Figure 2.3-8 Local sensitivity analysis of geochemical treatment model. See Table 2.3-2 for a description of the parameters. The figure presents the eigenvectors of the estimated parameter covariance matrix, which defines the parameter uncertainty and sensitivity.

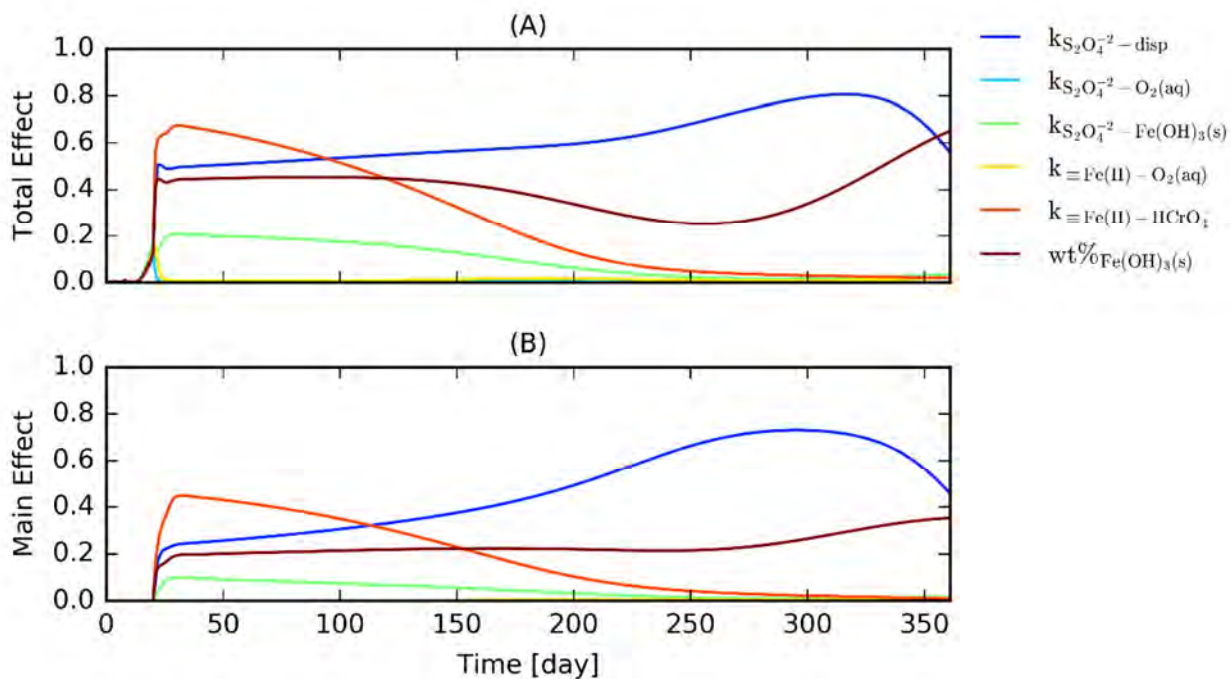


Figure 2.3-9 Global sensitivity analysis (eFAST) of geochemical treatment model. See Table 2.3-2 for a description of the parameters.

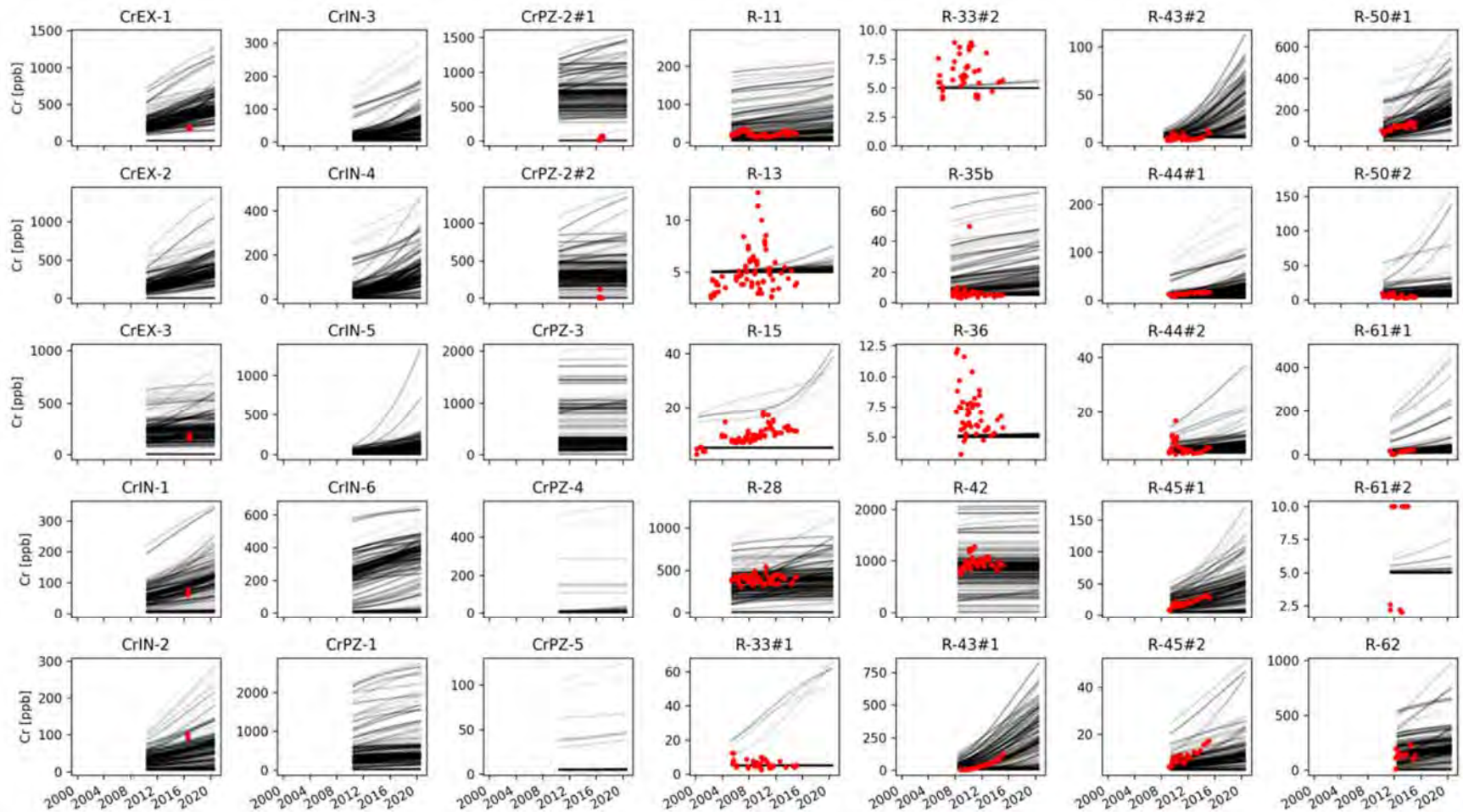


Figure 3.0-1 An example MCMC analysis of the regional-aquifer model. Shown are the sampled model predictions (grey lines) in comparison with the observational data (red dots) for the chromium transients.

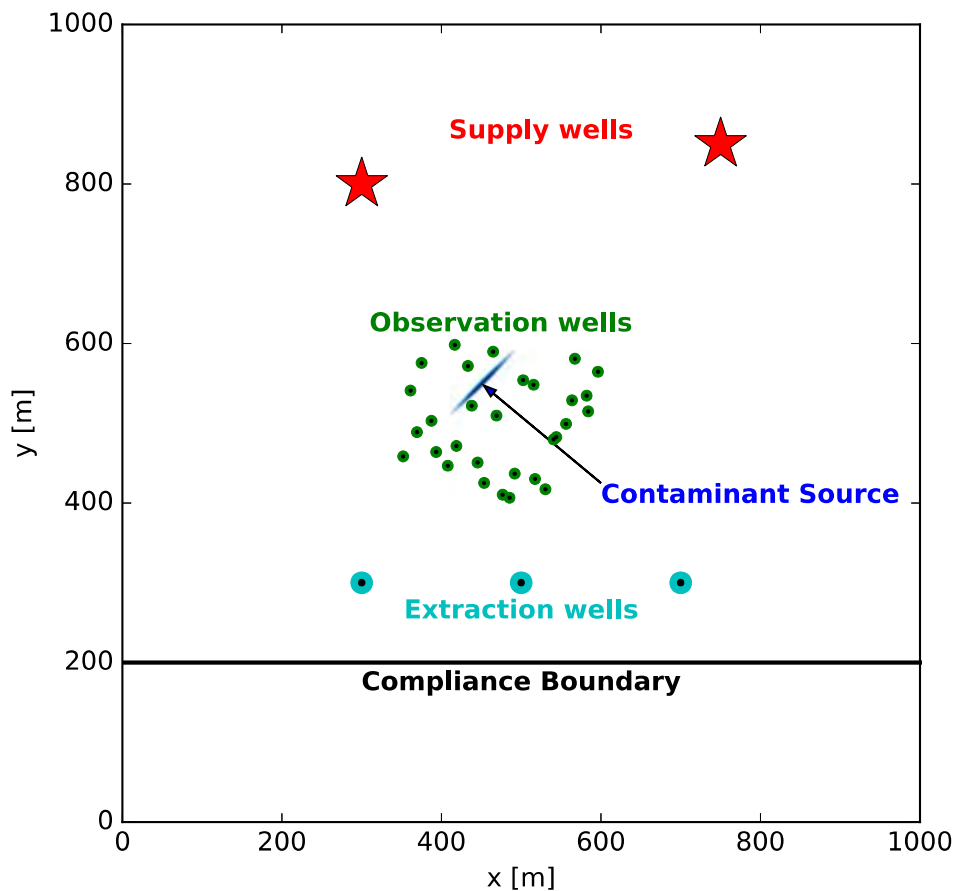


Figure 3.0-2 Conceptual map of a representative site that is used to demonstrate the MADS approach to decision analysis. Groundwater flow direction is southward. The green dots denote the locations of wells that are used for monitoring the plume evolution; the red stars denote the locations of water supply wells; the cyan dots denote the locations of potential extraction wells; and the black line denotes the compliance boundary. Along the compliance boundary and further to the south, concentrations of the contaminant cannot exceed a specified threshold. The blue ellipse denotes the location where the contaminant enters the aquifer from the vadose zone.

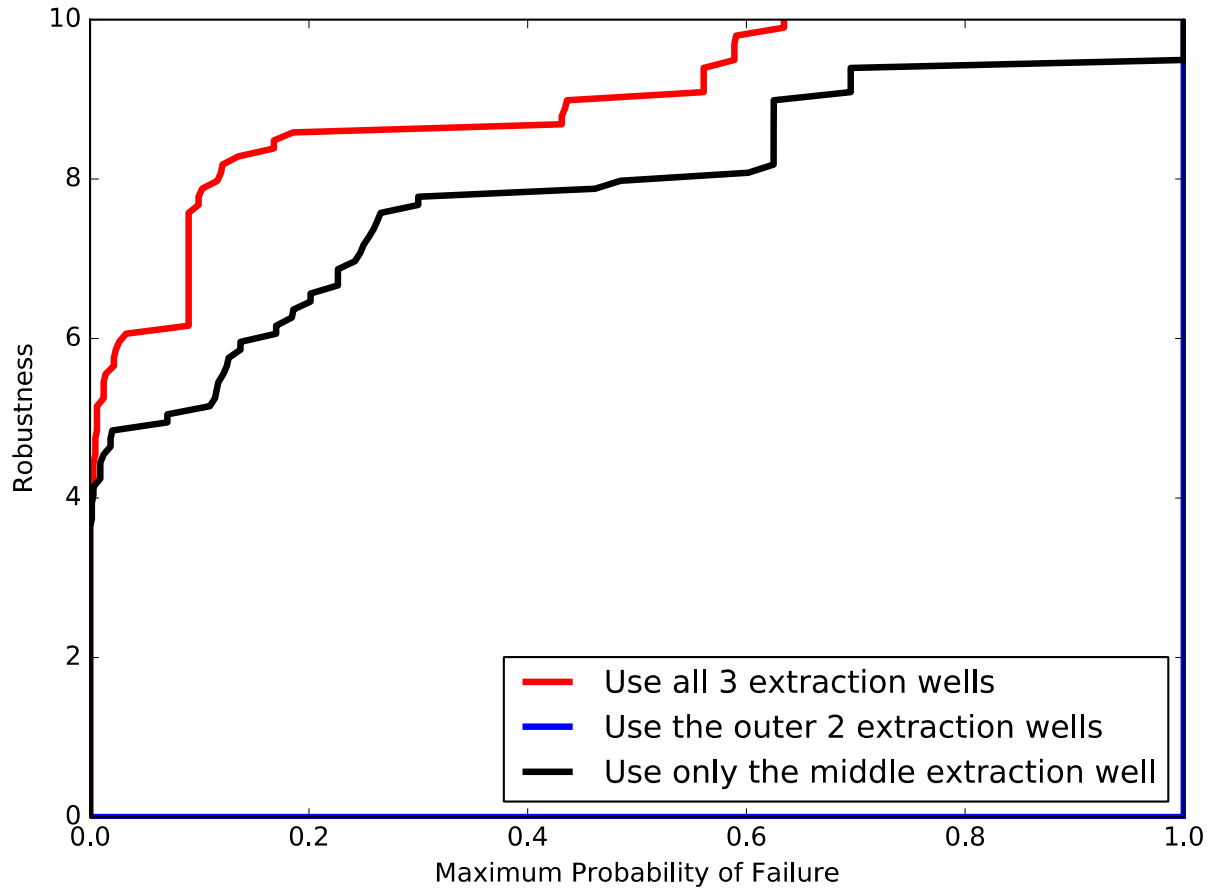


Figure 3.0-3 Application of BIGDT to optimize use of extraction wells to ensure contaminants in groundwater do not exceed a specified threshold at a compliance boundary. For a given probability of failure at the compliance boundary, the robustness against uncertainty is shown for each of the three remedies considered. Note that the use of two extraction wells fails to meet remediation goals, and the plot is at 0 on the y axis until the maximum probability of failure is 1, where robustness increases to >9. The robustness against uncertainty quantifies how wrong the physical and probabilistic models can be while still ensuring that the probability of an undesirable outcome remains below the maximum probability of failure (as plotted along the x axis).

**Table 2.1-1
Simulated and Observed Perched
Water Zone Thickness at 11 Locations**

Location Label	Observed Thickness (M)	Estimated Thickness (M)
T722	124	130
T996	150	145
T1051	115	120
T2052	93	99
T2154	93	99
T2243	91	96
T3486	100	85
T4088	98	104
T4510	104	98
T5060	36	36
T5801	78.1	78.1

Note: the simulated values are estimated through model calibration.

**Table 2.1-2
Estimated and Calibration-Target
Groundwater Fluxes in Three Hydraulic Windows**

Window Label	Calibration-Target Flux in Hydraulic Windows (kg/s)	Estimated Flux in Hydraulic Windows (kg/s)
w1	0.394	0.394
w2	0.0081	0.0086
w3	0.0216	0.0214

Note: The estimated fluxes are obtained through model calibration of the 3-D coupled vadose-zone/regional-aquifer model discussed here. The calibration-target fluxes are obtained through model calibration of the 3-D regional-aquifer model discussed in Section 1.2.

**Table 2.1-3
Simulated and Calibration-Target Chromium Travel Time through Vadose Zone**

	Calibration-Target Chromium Travel Time through Vadose Zone (yr)	Simulated Chromium Travel Time through Vadose Zone (yr)
Travel Time	10	10.2

Note: The simulated travel times are obtained through model calibration of the 3-D coupled vadose-zone/regional-aquifer model discussed here. The calibration-target fluxes are estimated based on past analyses and site data.

Table 2.1-4
Simulated and Observed Chromium Concentration at Well MCOI-5

Year	Observed Chromium Concentration (ppb)	Simulated Chromium Concentration (ppb)
2005	3.30	3.16
2006	2.85	4.06
2007	2.92	5.10
2008	6.09	6.28
2009	6.09	7.57
2010	6.44	8.96
2011	4.48	10.39
2012	4.56	11.84
2013	7.29	13.26
2014	5.95	14.59
2015	5.20	15.80
2016	9.32	16.86

Note: the simulated values are estimated through model calibration.

Table 2.1-5
Simulated and Observed Chromium Concentration at Well MCOI-6

Year	Observed Chromium Concentration (ppb)	Simulated Chromium Concentration (ppb)
2005	54.41	19.29
2006	45.10	24.63
2007	34.19	30.80
2008	38.11	37.73
2009	46.73	45.29
2010	54.74	53.31
2011	57.64	61.58
2012	61.05	69.84
2013	72.55	77.83
2014	72.67	85.29
2015	74.78	91.00
2016	78.64	97.75

Note: the simulated values are estimated through model calibration.

**Table 2.1-6
Name, Meaning, and Estimated Values of
Adjustable Parameters Estimated through Model Calibration**

Parameter Name	Parameter Meaning	Estimated Value
logk1	logarithm of the permeability (m ²) of nodes within the three hydraulic windows	-15.575
logk2		-17.628
logk3		-16.681
logkab	logarithm of the permeability (m ²) of nodes above, within, and below the basalts	-11.385
logkbs		-12.564
logkbl		-12.009
rab	porosity of nodes above, within, and below the basalts	0.207
rbs		0.049
rbl		0.092
rp3ab	inverse of air entry head for nodes above, within, and below the basalts	0.578
rp3bs		2.993
rp3bl		2.994
aab	power n in van Genuchten formula for nodes above, within, and below the basalts	1.791
abs		1.474
abl		1.942
infil	infiltration rates at the ground surface (kg/s)	0.124
mc_flux	Mortandad Canyon infiltration rates (kg/s)	0.062
sc_flux	Sandia Canyon infiltration rates (kg/s)	6.441
lc_flux	Los Alamos Canyon infiltration rates (kg/s)	0.683
west_flux	Water influx from western boundary (kg/s)	71.782
crbc	Injection chromium concentration at inlet nodes (mol/kg)	67.332
crst	Time when chromium injection begins (d)	14525.9
cret	Time when chromium injection ends (d)	18221.3

Table 2.3-1
Description of Parameters Used for
Sensitivity Analysis of Molasses Treatment Model

Symbol	Description
Γ_{CD}	Direct (abiotic) reduction rate constant
λ_{B_1}	Biomass growth rate constant
λ_{B_2}	Biomass natural decay rate constant
λ_C	Chromium bioreduction rate constant
K_B	Biomass Monod inhibition constant* (biomass crowding)
K_C	Chromium bioreduction Monod constant
K_D	Molasses (electron donor) Monod constant
K_I	Ethanol (inhibitor) Monod inhibition constant

* Monod 1949.

Table 2.3-2
Description of Parameters Used for
Sensitivity Analysis of Dithionite Treatment Model

Symbol	Description
$k_{S_2O_4^{2-}-disp}$	Rate constant, dithionite degradation
$k_{S_2O_4^{2-}-O_2(aq)}$	Rate constant, dithionite reduction of oxygen
$k_{S_2O_4^{2-}-Fe(OH)_3(s)}$	Rate constant, dithionite reduction of Fe(III) sediments
$k_{\equiv Fe(II)-O_2(aq)}$	Rate constant, Fe(II) reduction of oxygen
$k_{\equiv Fe(II)-HCrO_4^-}$	Rate constant, Fe(II) reduction of chromium
$wt\%_{Fe(OH)_3(s)}$	Weight percent of total solids, Fe(III) sediments

Appendix A

*CHROTRAN: A Massively Parallel Numerical Simulator
for In Situ Biogeochemical Reduction
of Heavy Metals in Heterogeneous Aquifers*

A-1.0 INTRODUCTION

CHROTRAN (Chromium Transport Bio-Chemical Remediation Code) is a novel biogeochemical simulator capable of modeling the governing processes of in situ remediation of chromium, hexahydro-1,3,5-trinitro-1,3,5-triazine (RDX), and other contaminants in heterogeneous aquifers. CHROTRAN features full coupling between groundwater flow and reactive transport, allowing for three-dimensional simulation of the complex interactions of hydrology and biogeochemistry that occur during contaminant transport and remediation. CHROTRAN is based upon the existing PFLOTRAN code framework (Lichtner et al. 2017a, b), leveraging existing capabilities to model multi-component flow and reactive transport using highly parallelized computational solvers. CHROTRAN provides a framework for modeling biostimulation, biodegradation, abiotic degradation, growth inhibitors, and biocides, which can be used to evaluate remediation of chromium along with a variety of other contaminants. The CHROTRAN framework also considers specific processes related to chromium remediation by sodium dithionite, a strong chemical reductant with unique oxidation-reduction behavior. These key features allow CHROTRAN to simulate sophisticated, multiscale biogeochemical remediation processes and aid in the design of field pilot studies and long-term deployments at the Los Alamos National Laboratory (LANL) contamination sites.

CHROTRAN is open-source software that can be redistributed and/or modified under the terms of the GNU Lesser General Public License as published by the Free Software Foundation. The Fortran source code files for CHROTRAN, along with input files for the examples are freely available at <https://github.com/chrotran/release>. Additional information regarding CHROTRAN is available at <http://chrotran.lanl.gov>. Please refer to Hansen et al. (2017a) for a more detailed description of model development and implementation. CHROTRAN allows for simulations employing complex models with a large number of computational cells and unknown variables. Because of the abstraction of the model and its parametric flexibility, CHROTRAN can also be used to model the in situ remediation of groundwater contaminated with heavy metals besides chromium, along with a wide range of organic contaminants. These include but are not limited to explosives (e.g., RDX), hydrocarbons, chlorinated solvents, pesticides, and volatile organic compounds.

A-2.0 USING CHROTRAN TO MODEL BIOCHEMICAL REMEDIATION

CHROTRAN biochemical remediation simulations account for spatial and temporal transients of (1) the heavy metal to be remediated, (2) introduced amendments (e.g., through well injection), and (3) biomass growth and decay. The introduced amendments can include (1) an electron donor (e.g., molasses), (2) a nontoxic conservative bio-inhibitor (e.g., ethanol), and (3) a biocide (e.g., dithionite). In addition, direct abiotic reduction by donor-metal interaction, as well as donor-driven biomass growth and bioreduction, are explicitly modeled in CHROTRAN. Other critical governing processes, such as donor sorption, bio-fouling and biomass death, are also modeled.

A-2.0-1 Key Features

The following summarizes the key processes involved in CHROTRAN bioremediation simulations.

- **Direct abiotic reaction between introduced electron donor and contaminant:** Experimental results (Chen et al. 2015; Hansen et al. 2017b) have established a rapid direct redox reaction of hexavalent chromium [Cr(VI)] to trivalent chromium [Cr(III)] when molasses is used as an electron donor.

- **Indirect Monod kinetics:** CHROTRAN models Cr(VI) biotic degradation based upon Monod kinetics of microorganism growth (Monod 1949; Wang and Xiao 1995; Okeke 2008; Hansen et al. 2017b).
- **Biofouling/Bioclogging:** CHROTRAN adjusts flow parameters such as porosity and hydraulic conductivity to account for biomass growth. This feature can be used to represent buildup of biological material near the amendment injection wells, which interferes with amendment injection and may rapidly consume electron donors.
- **Biomass crowding:** CHROTRAN accounts for changes in the biomass growth if biomass becomes overly dense. This causes cell stress, which reduces the rate of further growth.
- **Amendment additives:** CHROTRAN simulates the impact of bio-inhibitors and biocides injected to control biomass density near the amendment injection wells. This helps the spread of injected electron donors farther from the well before they are consumed by microorganisms.
- **Multiple donor consumption pathways:** CHROTRAN accounts for different biogeochemical models of electron donor consumption.

A-2.0-2 Relevant Species

CHROTRAN bioremediation simulations model five species whose dynamics are governed by physical and biogeochemical aquifer processes:

- **Aqueous contaminant(s)** to be remediated.
- **Immobile and mobile electron donors**, with mass exchange between the two states.
- **Biomass**, a collection of microbial consortia and their associated extracellular material.
- **Biomass-growth inhibitor**, represented as a conservative species, whose increasing concentration decreases microbial growth.
- **Biocide**, which reacts directly with biomass and is consumed.

These species interact in the following manner:

- **Biomass growth:** the biomass growth reaction irreversibly consumes the donor to produce biomass. The process rate is linearly proportional to the biomass concentration and controlled by the contaminant concentration through Monod kinetics. Two inhibition effects are accounted for: (1) biomass crowding attenuates growth rate as the biomass concentration rises, (2) biomass growth rate is reduced as the concentration of nonlethal inhibitor increases.
- **Bioreduction:** removal of the contaminant by the biomass; the process rate is linearly proportional to the biomass concentration and controlled by the contaminant concentration through Monod kinetics. The contaminant reduction is not directly tied to any particular biological process.
- **Biocide reaction:** an interphase bimolecular reaction between the biocide and the biomass based on a second-order mass action rate law, with the added condition that the biomass concentration cannot fall below a specified minimum.
- **Biomass natural decay:** If left unstimulated (without electron donor), the biomass decays based on a first-order process and returns to its natural background level represented by a specified minimum biomass concentration.
- **Biomass respiration:** consumption of the electron donor by biomass for purposes of life maintenance, unrelated to growth.

- **Abiotic reduction:** an aqueous-phase reaction between the electron donor and the contaminant based on a second-order mass action rate law.
- **Mobile-immobile mass transfer:** a process with first-order kinetics representing sorptive retardation of the electron donor.

A-3.0 USING CHROTRAN TO MODEL SODIUM DITHIONITE TREATMENT (GEOCHEMICAL REMEDIATION)

In situ geochemical remediation of aquifers contaminated with chromium involves the injection of a strong chemical reductant into sediments containing redox-sensitive elements. In the case of iron-bearing sediments, this results in the reduction of ferric iron [Fe(III)] to ferrous iron [Fe(II)], which binds to mineral surfaces and becomes a long-term, stationary source of reductant capable of transforming dissolved Cr(VI) to Cr(III). This process is referred to as in situ redox manipulation (ISRM). In the past, simple numerical models have been used by others (Amonette et al. 1994; Istok et al. 1999; Williams et al. 2000; Chilakapati et al. 2000) to help quantify certain steps of this process. However, a unified predictive model that combines all of the important steps that occur throughout the remediation process has not previously been developed. Such a model is critical to quantitatively evaluate remediation design strategies for field deployment. CHROTRAN is capable of modeling the entire process of ISRM using sodium dithionite from laboratory to field scale. Along with simulation of in situ reduction of Cr(VI), it is also capable of modeling other important processes that may influence remediation, such as mineral precipitation/dissolution, aqueous speciation, and pH.

A-3.0-1 Key Features

The following reactions are included to accurately model in situ remediation of Cr(VI) through the injection of a sodium dithionite amendment. These reactions are assumed to be kinetically limited, and rate laws were formulated after an extensive literature review (Morello et al. 1964; Creutz and Sutin 1974; Eary and Rai 1989; Rubio et al. 1992; Amonette et al. 1994; Buerge and Hug 1997, 1999; Istok et al. 1999; Williams et al. 2000; Chilakapati et al. 2000; Williams and Scherer 2001; Bond and Fendorf 2003).

- **Reduction of Fe(III) sediments by dithionite:** CHROTRAN accounts for Fe(III) and its reduction to Fe(II) by dithionite, which results in the formation of an ISRM zone (Istok et al. 1999; Williams et al. 2000).
- **Reduction of Cr(VI) by reduced iron sediments:** CHROTRAN models the reduction of and subsequent immobilization of Cr(VI) as it passes through the ISRM zone and reacts with Fe(II). This results in decreased Cr(VI) concentrations downstream of the ISRM zone but also decreases the concentration of Fe(II) within the ISRM zone.
- **Loss of dithionite through disproportionation:** Dissolved dithionite is known to be unstable and is prone to degradation through disproportionation reactions, which are accelerated in the presence of sediments (Amonette et al. 1994). This reaction is included in CHROTRAN and decreases the overall availability of dithionite, causing less reduction of Fe(III).
- **Loss of dithionite through reactions with oxygen:** In an aerobic aquifer, dissolved oxygen will also react with dithionite through redox reactions. This will also decrease the amount of injected dithionite available to reduce Fe(III) and is an important limiting factor of ISRM accounted for in CHROTRAN.
- **Oxidation of Fe(II) sediments by oxygen:** Surface-bound Fe(II) is capable of reducing other dissolved oxidants, which reduces the overall capacity of the ISRM zone to reduce Cr(VI). In an aerobic aquifer, dissolved oxygen will most likely be the dominant oxidant. The oxidation of Fe(II) sediments by dissolved oxygen is included in CHROTRAN.

A-3.0-2 Relevant Species

CHROTRAN geochemical remediation simulations model the following species whose dynamics are governed by physical and geochemical aquifer processes:

- **Oxidants:** CHROTRAN accounts for dissolved oxygen, Cr(VI), and Fe(III). Oxygen and Cr(VI) exist in the aqueous phase and Fe(III) is represented in the solid phase as a mineral precipitate.
- **Injected reductant and its reaction products:** The injected reductant is sodium dithionite, which dissociates to sodium and dithionite. The reaction products of the different reactions involving dithionite are sulfate, sulfite, and thiosulfate.
- **Reduced species:** Dithionite reduces Fe(III) precipitates to Fe(II) bound to mineral surfaces. Surface-complexed Fe(II) is subsequently capable of reducing Cr(VI) to Cr(III) in the aqueous phase.
- **pH and pH buffers:** The degradation of dithionite is strongly pH dependent, as the kinetics of the reaction is greatly accelerated at high pH. CHROTRAN simulates pH changes that result from the redox reactions outlined above. In addition, the model accounts for injectant pH buffering (e.g., potassium bicarbonate, calcium carbonate).
- **Other aqueous species:** Equilibrium speciation is also included in CHROTRAN to estimate the concentrations of secondary aqueous species (e.g., OH^- , CO_3^{2-} , $\text{H}_2\text{CO}_3(\text{aq})$, HCrO_4^-). These species influence the ionic strength, charge balance, and pH of the groundwater.
- **Mineral species and their dissolved constituents:** Both Cr(III) and Fe(III) are highly insoluble and readily precipitate in neutral to alkaline pH groundwater. For this reason, mineral precipitation is included in CHROTRAN to account for the fate of Cr(III) as chromium hydroxide and Fe(III) as ferric hydroxide. CHROTRAN considers the potential release of carbonates through the dissolution of minerals such as calcite, which will influence pH.

A-4.0 REFERENCES

The following reference list includes documents cited in this report.

- Amonette, J.E., J.E. Szecsody, H.T. Schaef, Y.A. Gorby, J.S. Fruchter, and J.C. Templeton. "Abiotic Reduction of Aquifer Materials by Dithionite: A Promising In-Situ Remediation Technology," Pacific Northwest Laboratory technical report PNL-SA-24505 (1994).
- Bond, D.L., and S. Fendorf. "Kinetics and Structural Constraints of Chromate Reduction by Green Rusts," *Environmental Science & Technology*, Vol. 37, No. 12, pp. 2750–2757 (2003).
- Buerge, I.J., and S.J. Hug. "Kinetics and pH Dependence of Chromium (VI) Reduction by Iron (II)," *Environmental Science & Technology*, Vol. 31, No. 5, pp. 1426–1432 (1997).
- Buerge, I.J., and S.J. Hug. "Influence of mineral Surfaces on chromium (VI) Reduction by Iron (II)," *Environmental Science & Technology*, Vol. 33, No. 23, pp. 4285–4291 (1999).
- Chen, Z.F., Y.S. Zhao, J.W. Zhang, and J. Bai. "Mechanism and Kinetics of Hexavalent Chromium Chemical Reduction with Sugarcane Molasses," *Water, Air, & Soil Pollution*, Vol. 226, pp. 1–9, <https://doi.org/10.1007/s11270-015-2629-6> (2015).
- Chilakapati, A., M. Williams, S. Yabusaki, C. Cole, and J. Szecsody. "Optimal Design of an In Situ Fe (II) Barrier: Transport Limited Reoxidation," *Environmental Science & Technology*, Vol. 34, No. 24, pp. 5215–5221 (2000).

- Creutz, Carol and Norman Sutin. Kinetics of the reactions of sodium dithionite with dioxygen and hydrogen peroxide. *Inorganic Chemistry*, 13(8):2041–2043, 1974.
- Eary, L.E., and D. Rai. “Kinetics of Chromate Reduction by Ferrous Ions Derived from Hematite and Biotite at 25 Degrees C,” *American Journal of Science*, Vol. 289, No. 2, pp. 180–213 (1989).
- Hansen, S.K., H. Boukhalfa, S. Karra, D. Wang, and V.V. Vesselinov. “Chromium (VI) Reduction in Acetate- and Molasses Amended Natural Media: Empirical Model Development,” Los Alamos National Laboratory document LA-UR-17-30690, Los Alamos, New Mexico (2017a).
- Hansen, S.K., S. Pandey, S. Karra, and V.V. Vesselinov. “CHROTRAN 1.0: A Mathematical and Computational Model for In Situ Heavy Metal Remediation in Heterogeneous Aquifers,” *Geoscientific Model Development*, Vol. 10, pp. 4525–4538 (2017b).
- Istok, J.D., J.E. Amonette, C.R. Cole, J.S. Fruchter, M.D. Humphrey, J.E. Szecsody, S.S. Teel, V.R. Vermeul, M.D. Williams, and S.B. Yabusaki. “In Situ Redox Manipulation by Dithionite Injection: Intermediate-scale Laboratory Experiments,” *Ground Water*, Vol. 37, No. 6, pp. 884–889 (1999).
- Lichtner, P.C., G.E. Hammond, C. Lu, S. Karra, G. Bisht, B. Andre, R.T. Mills, J. Kumar, and J.M. Frederick. *PFLOTRAN User Manual*, available at: <http://www.documentation.pflotran.org>, last access: 12 December (2017a).
- Lichtner, P.C., G.E. Hammond, C. Lu, S. Karra, G. Bisht, B. Andre, R.T. Mills, J. Kumar, and J.M. Frederick. PFLOTRAN web page, available at: <http://www.pflotran.org>, last access: 12 December (2017b).
- Monod, J. “The Growth of Bacterial Cultures,” *Annual Review of Microbiology*, Vol. 3, pp. 371–394, <https://doi.org/10.1146/annurev.mi.03.100149.002103>, (1949).
- Morello, J.A., M.R. Craw, H.P. Constantine, and R.E. Forster. “Rate of Reaction of Dithionite Ion with Oxygen in Aqueous Solution,” *Journal of Applied Physiology*, Vol. 19, No. 3, pp. 522–525, (1964).
- Okeke, B.C. “Bioremoval of Hexavalent Chromium from Water by a Salt Tolerant Bacterium, *Exiguobacterium* sp. GS1,” *Journal of Industrial Microbiology & Biotechnology*, Vol. 35, pp. 1571–1579, <https://doi.org/10.1007/s10295-008-0399-5> (2008).
- Rubio, F.C., M.P. Paez Dueñas, G. Blazquez Garcia, and J.M. Garrido Martin. “Oxygen Absorption in Alkaline Sodium Dithionite Solutions,” *Chemical Engineering Science*, Vol. 47, Nos. 17–18, pp. 4309–4314, (1992).
- Wang, Y.T., and C. Xiao. “Factors Affecting Hexavalent Chromium Reduction in Pure Cultures of Bacteria,” *Water Research*, Vol. 29, pp. 2467–2474, [https://doi.org/10.1016/0043-1354\(95\)00093-Z](https://doi.org/10.1016/0043-1354(95)00093-Z), (1995).
- Williams, M.D., V.R. Vermeul, J.E. Szecsody, and J.S. Fruchter. “100-D area In Situ Redox Treatability Test for Chromate Contaminated Groundwater,” Pacific Northwest National Laboratory technical report PNNL-13349 (2000).
- Williams, A.G.B., and M.M. Scherer. “Kinetics of Cr(VI) Reduction by Carbonate Green Rust,” *Environmental Science & Technology*, Vol. 35, No. 17, pp. 3488–3494 (2001).

Contaminant Fingerprint Diagrams 2010 - September 2017

New Mexico State Plane Coordinate System Central Zone (3002)
 North American Datum, 1983 (NAD 83)
 Feet
 GIS: Dave Frank, atlan@lanl.gov, 605-8182
 Created: 19 September 2017
 Last Opened: Wednesday, January 31, 2018
 File: map_17-0073-02_contaminant_plate
 3
 DISCLAIMER: This map was created for work processes associated with ERES. All other uses for this map should be confirmed with LANL staff.

- D Injection well
- B Piezometer
- A Regional well
- A Perched-intermediate well
- Paved road
- - - Lab boundary
- Structure
- Chromium plume > 50 ppm
- Regional groundwater index contour May 2017, 60-ft interval
- Regional groundwater contour May 2017, 4-ft interval

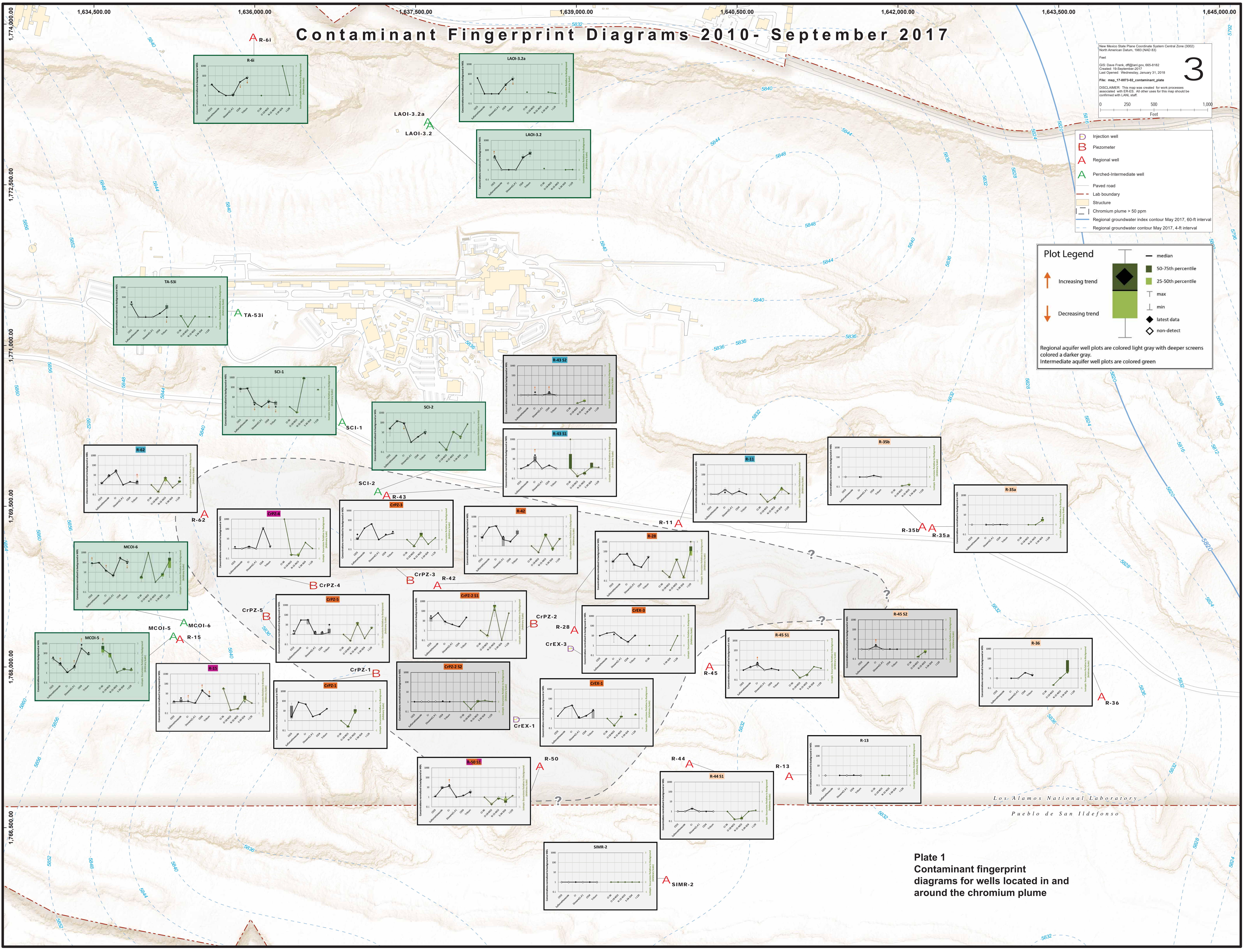
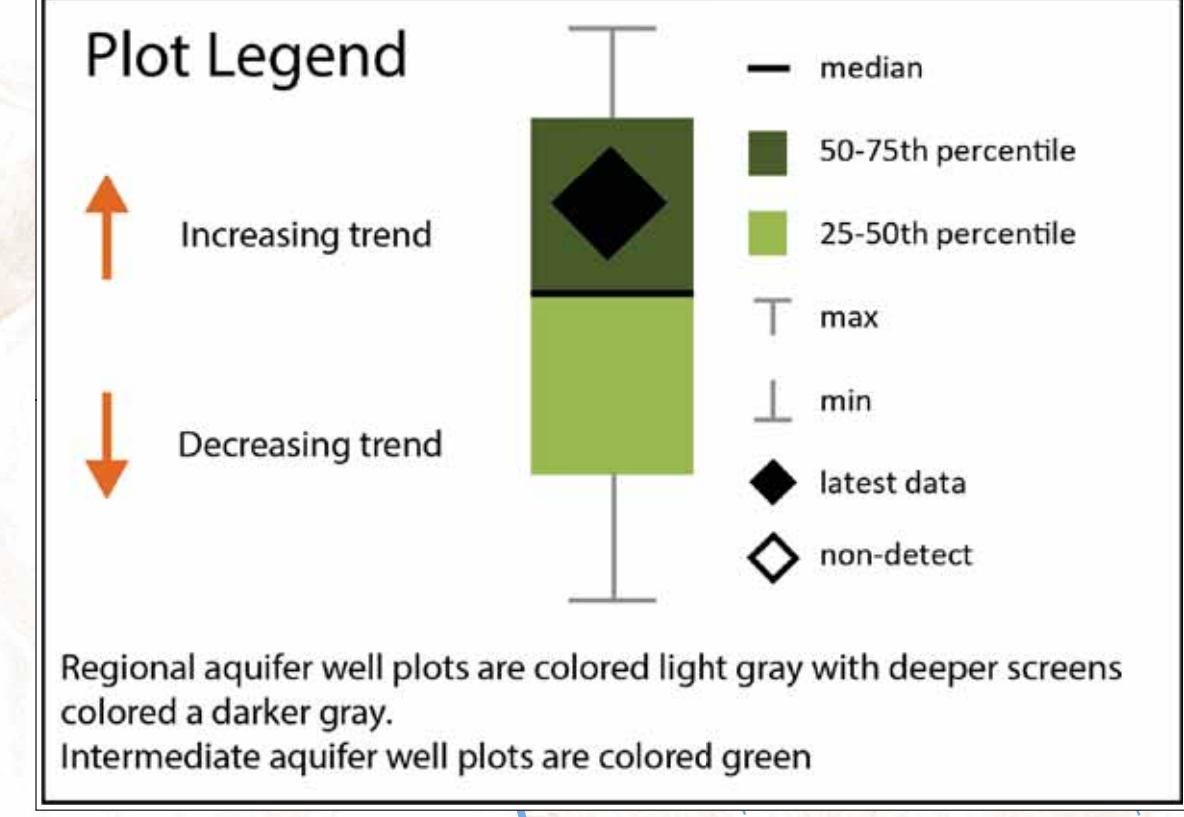


Plate 1
 Contaminant fingerprint diagrams for wells located in and around the chromium plume